Transactions of the ASME®

Technical Editor, LEON M. KEER (1993)

The Technological Institute
Northwestern University
Evanston, IL 60201

APPLIED MECHANICS DIVISION

Chairman, WILLIAM S. SARIC
Secretary, THOMAS A. CRUSE
Associate Technical Editors,
R. ABEYARATNE (1995)
T. R. AKYLAS (1995)
S. A. BERGER (1995)
R. M. BOWEN (1994)
S. K. DATTA (1993)
G. J. DVORAK (1993)
M. E. FOURNEY (1994)
R. L. HUSTON (1994)
D. J. INMAN (1995)
J. T. C. LIU (1993)
X. MARKENSCOFF (1995)
R. M. McMEEKING (1994)
A. K. NOOR (1994)
J. W. RUDNICKI (1995)
W. N. SHARPE, JR. (1994)
C. F. SHIH (1993)
P. D. SPANOS (1995)
F. Y. M. WAN (1995)

BOARD ON COMMUNICATIONS
Chairman and Vice-President
R. E. NICKELL
Members-at-Large
W. BEGELL, T. F. CONRY, T. DEAR,
R. L. KASTOR, J. KITTO, R. MATES,
W. MORGAN, E. M. PATTON,
R. E. REDER, A. VAN DER SLUYS,
F. M. WHITE, B. ZIELS

President, N. H. HURT, JR.
Exec. Dir.
D. L. BELDEN
Treasurer, ROBERT A. BENNETT

PUBLISHING STAFF
Mng. Dir., Publ.,
CHARLES W. BEARDSLEY
Managing Editor,
CORNELIA MONAHAN
Production Editor, JUDY SIERANT
Prod. Asst., MARISOL ANDINO

Transactions of the ASME, Journal of Applied Mechanics (ISSN 0021-8936) is published quarterly (Mar., June, Sept., Dec.) for $160.00 per year by The American Society of Mechanical Engineers, 345 East 47th Street, New York, NY 10017. Second class postage paid at New York, NY and additional mailing offices. POSTMASTER: Send address changes to Transactions of the ASME, Journal of Applied Mechanics, c/o THE AMERICAN SOCIETY OF MECHANICAL ENGINEERS, 22 Law Drive, Box 2300, Fairfield, NJ 07007-2300.

CHANGES OF ADDRESS must be received at Society headquarters seven weeks before they are to be effective. Please send old label and new address.

PRICES: To members, $29.00, annually: to nonmembers, $160.00. Add $20.00 for postage to countries outside the United States and Canada.

STATEMENT from By-Laws. The Society shall not be responsible for statements or opinions advanced in papers or . . . printed in its publications (B7.1, Par. 3).

COPYRIGHT © 1992 by The American Society of Mechanical Engineers. Reprints from this publication may be made on condition that full credit be given the TRANSACTIONS OF THE ASME, JOURNAL OF APPLIED MECHANICS, and the author, and date of publication be stated.

INDEXED by Applied Mechanics Reviews and Engineering Information, Inc. Canadian Goods & Services Tax Registration #126148048.

Journal of Applied Mechanics

Published Quarterly by The American Society of Mechanical Engineers

VOLUME 59 • NUMBER 1 • MARCH 1992

TECHNICAL PAPERS

1 Improved Bounds on the Effective Elastic Moduli of Random Arrays of Cylinders
S. Torquato and F. Lado

7 A Torque-Free Flexible Model Gyro
F. P. J. Rimrott and F. Janabi-Sharifi

16 Stability Properties of a Viscoelastic Column Under a Periodic Force
G. Cederbaum and M. Mond

20 A General Solution for the Pressurized Elastoplastic Tube
David Durban and Michael Kubi

27 Modeling of Creep of Misaligned Short-Fiber Reinforced Ceramic Composites
John R. Pachalis and Tsu-Wei Chou

33 The Optimal Mode of an Approximate Expression of Final Displacement in Dynamic Plastic Response of Structures
Zhu-ping Huang and Li-zhi Sun

39 Three-Dimensional Effective Moduli of Orthotropic and Symmetric Laminates (91-WA/APM-12)
Ajit K. Roy and Stephen W. Tsai

48 Effect of Strain Hardening and Rate Sensitivity on the Dynamic Growth of a Void in a Plastic Material
M. Ortiz and A. Molinari

54 A Complete Acoustic Microscopical Analysis of Multilayered Specimens
T. Kundu

61 Corner Singularities of Three-Dimensional Planar Interface Cracks
F. Ghahremani and C. F. Shih

69 Static Axisymmetric End Problems in Semi-infinite and Finite Solid Cylinders (91-WA/APM-13)
Yoon Young Kim and Charles R. Steele

77 Bonded Bi-material Half-Planes With Semi-elliptical Notch Under Tension Along the Interface
Norio Hasebe, Mikiya Okumura, and Takuji Nakamura

84 Influence of Cracking Direction of Interfacial Fracture in Bicrystals With Symmetric Tilt Boundary
R. Mohan, M. Ortiz, and C. F. Shih

92 On the Contact Zone Model for Interface Cracks
K.-C. Wu

95 Crack-Tip Stress and Deformation Fields in Strain-Softening Nonlinearly Viscoelastic Materials
B. Moran and W. G. Knauss

102 Reflection and Transmission of a Plane Wave by an Array of Cavities in the Interface of Two Solids (91-WA/APM-16)
Yonglin Xu

109 Analysis of the Fully Developed Chute Flow of Granular Materials
Hojin Ahn, Christopher E. Brennen, and Rolf H. Sabersky

120 Boundary Conditions for Rapid Granular Flow: Flat, Frictional Walls
J. T. Jenkins

128 A Viscoelastic Model for the Dynamic Behavior of Saturated Poroelastic Soils
J. P. Bardet

136 Frequency-Dependent Element Mass Matrices
N. J. Fergusson and W. D. Pilkey

140 Inertially Coupled Galloping of Iced Conductors
P. Yu, A. H. Shah, and N. Popplewell

146 On the Behavior of Pretwisted Beams With Irregular Cross-Sections
J. B. Kosmatka

153 Nonlinear Vibrations of Piecewise-Linear Systems by Incremental Harmonic Balance Method
S. L. Lau and W.-S. Zhang

161 Chaotic Dynamics of a Quasi-Periodically Forced Beam
K. Yagasaki

168 The Pseudo-Shakedown of Beams and Plates When Subjected to Repeated Dynamic Loads
Wei Qin Shen and Norman Jones

176 Overdamped and Gyroscopic Vibrating Systems
Lawrence Barkwell and Peter Lancaster

182 A Boundary Element Method Formulation for Design Sensitivities in Steady-State Conduction Convection Problems
Abhijit Chandra and Cho Lik Chan

191 Response of a Liquid Bridge With Rotationally Excited Bottom
Helmut F. Bauer

196 Low-Dimensional Chaos in a Flexible Tube Conveying Fluid (91-WA/APM-17)
M. P. Païdoussis, J. P. Cusumano, and G. S. Copeland

206 Symmetry Reduction of Reynolds Equation and Applications to Film Lubrication
M. L. Abell and W. F. Ames

(Contents continued on Inside Back Cover)

Downloaded 04 May 2010 to 171.66.16.49. Redistribution subject to ASME license or copyright; see http://www.asme.org/terms/Terms_Use.cfm

BRIEF NOTES

Laminated Plates Under Uniformly Distributed and Concentrated Loads
S. Savithri and T. K. Varadan 211

On the Invariance of Flow in a Narrow Channel of Varying Gap
R. Usha 214

Interaction Between an Edge Dislocation and a Lamellar Inhomogeneity With a Slipping Interface
L. Stagni and R. Lizzio 215

Strain-Hardening Creep Relaxation
P. A. Hunneault 217

A Constitutive Model for Bimodular Materials With an Application to Plate Bending
E. Sacco and J. N. Reddy 220

Elastodynamic Behavior of Relatively Thick, Symmetrically Laminated, Anisotropic Circular Shells
Marco Di Sciuva and Erasmo Carrera 222

224 Circumferential Stresses in Curved Beams
Robert D. Cook

225 On General Conditions of Rotordynamic Stability Under Combined Oscillator Axial Forces and Torque
Sunil K. Sinha

228 On the Numerical Evaluation of the Unforced Response of a Duffing Oscillator
G. D. Hahn, J. F. Carney III, and Malcolm H. Ray

230 The Influence of Two-Dimensional End Effects on the Natural Frequencies of Cantilevered Beams Weak in Shear
J. M. Duva and J. G. Simmonds

233 Analysis of a Pendulum on a Rotating Arm
Bertram A. Schmidt and David G. McDowell

234 On Transverse Vibrations of a Rotating Disk of Uniform Strength
Uğur Güven

DISCUSSIONS

236 **Stability of Linear Conservative Gyroscopic Systems, by J. A. Walker—Discussion by B. L. Ly**

237 **Mixing in a Closed Room by the Action of Two Fans, by S. Lichter, A. Dagan, W. B. Underhill, and H. Ayanle—Discussion by F. H. Ling**

238 **Stress Analysis of Multilayered Anisotropic Elastic Media, by B. H. J. Choi and S. Thangjitham—Discussion by Marek-Jerzy Pindera**

239 **The Motion of a Sphere on a Rough Horizontal Plane, by J.-Y. Yang—Discussion by L. Y. Bahar**

240 **The Usefulness of Elementary Theory for the Linear Vibrations of Layered, Orthotropic Elastic Beams and Corrections to Two-Dimensional End Effects, by J. M. Duva and J. G. Simmonds—Discussion by Yi-Yuan Yu**

241 **On Energy Rate Theorems for Linear First-Order Nonholonomic Systems, by John G. Papastavridis—Discussion by T. R. Kane and D. A. Levinson**

242 **Dynamics of Nonholonomic Mechanical Systems Using a Natural Orthogonal Complement, by S. K. Saha and J. Angeles—Discussion by John G. Papastavridis**

BOOK REVIEWS

245 *Dynamic Fracture Mechanics*, by **L. B. Freund** . . . Reviewed by **John W. Hutchinson**

245 *Plasticity Theory*, by **J. Lubliner** . . . Reviewed by **B. Moran**

ANNOUNCEMENTS AND SPECIAL NOTES

32 Symposium on High Performance Computing for Flight Vehicles

94 Books Received by the Office of the Technical Editor List

181 Forum on Industrial and Environmental Applications of Fluid Mechanics—Call for Papers

210 Symposium on Adaptive, Multilevel and Hierarchical Computational Strategies

246 Change of Address Form

247 Worldwide Mechanics Meetings List

250 Second U.S. National Congress on Computational Mechanics

outside back cover Information for Authors

Downloaded 04 May 2010 to 171.66.16.49. Redistribution subject to ASME license or copyright; see http://www.asme.org/terms/Terms_Use.cfm

S. Torquato
Department of Mechanical and Aerospace Engineering and Department of Chemical Engineering,
North Carolina State University,
Raleigh, NC 27695-7910
Mem. ASME

F. Lado
Department of Physics,
North Carolina State University,
Raleigh, NC 27695-8202

Improved Bounds on the Effective Elastic Moduli of Random Arrays of Cylinders

Improved rigorous bounds on the effective elastic moduli of a transversely isotropic fiber-reinforced material composed of aligned, infinitely long, equisized, circular cylinders distributed throughout a matrix are evaluated for cylinder volume fractions up to 70 percent. The bounds are generally shown to provide significant improvement over the Hill-Hashin bounds which incorporate only volume-fraction information. For cases in which the cylinders are stiffer than the matrix, the improved lower bounds provide relatively accurate estimates of the elastic moduli, even when the upper bound diverges from it (i.e., when the cylinders are substantially stiffer than the matrix). This last statement is supported by accurate, recently obtained Monte Carlo computer-simulation data of the true effective axial shear modulus.

1 Introduction

In earlier works (Torquato and Lado, 1988a,b) we computed bounds on the effective axial shear modulus μ_e (or, equivalently, transverse conductivity) and the effective transverse bulk modulus k_e of random arrays of infinitely long, oriented cylindrical fibers in a matrix that improved upon the well-known second-order bounds of Hill (1964) and Hashin (1965, 1970). These third and fourth-order bounds depend upon the key microstructural parameter ζ_2—a multidimensional integral, which was evaluated for the aforementioned model by us in the superposition approximation. Recent computer simulations (described below) indicate that ζ_2 in the superposition approximation is not accurate at high-fiber volume fractions. Moreover, corresponding improved bounds on the effective transverse shear modulus G_e, that depend upon a different microstructural parameter η_2, of random arrays of cylinders have heretofore not been computed.

Rigorous upper and lower bounds on the effective properties of composite materials are useful because: (i) they enable one to test the merits of theories; (ii) as successively more microstructural information is incorporated, the bounds become progressively narrower; (iii) one of the bounds can typically provide a relatively accurate estimate of the property even when the reciprocal bound diverges from it (Torquato, 1985, 1987), a point that has yet to be fully appreciated.

The purpose of this paper is to determine accurate analytical expressions for both ζ_2 and η_2 and thus improved bounds on μ_e, k_e, and G_e for the practically useful model of impenetrable, parallel, infinitely long, equisized, circular cylinders (or circular disks in two dimensions) distributed randomly throughout a matrix. Accurate computer simulations of the true effective axial shear modulus μ_e recently obtained by Kim and Torquato (1990) shall be used to access the accuracy of the improved bounds on μ_e. Note that transversely isotropic, fiber-reinforced materials are characterized by five effective elastic constants but Hill (1964) showed that for such two-component materials it is only necessary to determine three of the constants since the other two can then be easily calculated.

2 Improved Bounds on μ_e, k_e, and G_e

Given only the phase volume fractions, ϕ_1 and ϕ_2, bulk moduli, K_1 and K_2, and shear moduli, G_1 and G_2, of a two-phase transversely isotropic fiber-reinforced material, Hill (1964) and Hashin (1965, 1970) have derived the best possible bounds on μ_e, k_e, and G_e. Silnutzer (1972) derived improved bounds on μ_e and k_e that additionally depend upon two integrals over certain three-point correlation functions. Milton (1982) showed that both integrals can be expressed in terms of a single integral ζ_2 defined as follows:

$$\zeta_2 = \frac{4}{\pi\phi_1\phi_2}\int_0^\infty \frac{dr}{r}\int_0^\infty \frac{ds}{s}\int_0^\pi d\theta\left[S_3(r,s,t) - \frac{S_2(r)S_2(s)}{\phi_2}\right]\cos 2\theta. \tag{1}$$

The quantities $S_2(r)$ and $S_3(r,s,t)$ are, respectively, the probabilities of finding in phase 2 the end points of a line segment of length r and the vertices of a triangle with sides of length r, s and t; θ is the included angle opposite the side of length t. The Silnutzer bounds are referred to as third-order bounds since they are exact up to third order in the difference in the phase properties.

Silnutzer also derived third-order bounds on the effective transverse shear modulus G_e which Milton showed could be expressed in terms of ζ_2 another microstructural parameter η_2 where

Contributed by the Applied Mechanics Division of THE AMERICAN SOCIETY OF MECHANICAL ENGINEERS for publication in the JOURNAL OF APPLIED MECHANICS.

Discussion on this paper should be addressed to the Technical Editor, Prof. Leon M. Keer, The Technological Institute, Northwestern University, Evanston, IL 60208, and will be accepted until two months after final publication of the paper itself in the JOURNAL OF APPLIED MECHANICS. Manuscript received by the ASME Applied Mechanics Division, May 4, 1990; final revision, Mar. 4, 1991.

Copyright © 1992 by ASME
Downloaded 03 May 2010 to 171.66.16.247. Redistribution subject to ASME license or copyright; see http://www.asme.org/terms/Terms_Use.cfm

$$\eta_2 = \frac{16}{\pi\phi_1\phi_2}\int_0^\infty \frac{dr}{r}\int_0^\infty \frac{ds}{s}\int_0^\pi d\theta\left[S_3(r,s,t) - \frac{S_2(r)S_2(s)}{\phi_2}\right]\cos 4\theta. \tag{2}$$

The simplified forms of the Silnutzer third-order bounds (Milton, 1982) for the axial shear modulus, transverse bulk modulus, and transverse shear modulus are, respectively, given by

$$\mu_L^{(3)} \le \mu_e \le \mu_U^{(3)}, \tag{3}$$

where

$$\mu_U^{(3)} = \left[\langle G\rangle - \frac{\phi_1\phi_2(G_2-G_1)^2}{\langle \tilde{G}\rangle + \langle G\rangle_\zeta}\right], \tag{4}$$

$$\mu_L^{(3)} = \left[\langle 1/G\rangle - \frac{\phi_1\phi_2(1/G_2-1/G_1)^2}{\langle 1/\tilde{G}\rangle + \langle 1/G\rangle_\zeta}\right]^{-1}; \tag{5}$$

$$k_L^{(3)} \le k_e \le k_U^{(3)}, \tag{6}$$

where

$$k_U^{(3)} = \left[\langle k\rangle - \frac{\phi_1\phi_2(k_2-k_1)^2}{\langle \tilde{k}\rangle + \langle G\rangle_\zeta}\right], \tag{7}$$

$$k_L^{(3)} = \left[\langle 1/k\rangle - \frac{\phi_1\phi_2(1/k_2-1/k_1)^2}{\langle 1/\tilde{k}\rangle + \langle 1/G\rangle_\zeta}\right]^{-1}; \tag{8}$$

and

$$G_L^{(3)} \le G_e \le G_U^{(3)}, \tag{9}$$

where

$$G_U^{(3)} = \left[\langle G\rangle - \frac{\phi_1\phi_2(G_2-G_1)^2}{\langle \tilde{G}\rangle + \Theta}\right], \tag{10}$$

$$G_L^{(3)} = \left[\langle 1/G\rangle - \frac{\phi_1\phi_2(1/G_2-1/G_1)^2}{\langle 1/\tilde{G}\rangle + \Xi}\right]^{-1}, \tag{11}$$

$$\Theta = [2\langle k\rangle_\zeta\langle G\rangle^2 + \langle k\rangle^2\langle G\rangle_\eta]/\langle k+2G\rangle^2, \tag{12}$$

$$\Xi = 2\langle 1/k\rangle_\zeta + \langle 1/G\rangle_\eta. \tag{13}$$

Here we define $\langle b\rangle = b_1\phi_1 + b_2\phi_2$, $\langle \tilde{b}\rangle = b_1\phi_2 + b_2\phi_1$, $\langle b\rangle_\zeta = b_1\zeta_1 + b_2\zeta_2$, and $\langle b\rangle_\eta = b_1\eta_1 + b_2\eta_2$, where $\zeta_1 = 1-\zeta_2$ and $\eta_1 = 1-\eta_2$. The quantity k_i is the transverse bulk modulus of phase i for transverse compression without axial extension and may be expressed in terms of the isotropic phase moduli as $k_i = K_i + G_i/3$ $(i=1,2)$. Since the microstructural parameters ζ_i and η_i lie in the closed interval [0,1], the above third-order bounds always improve upon the second-order bounds of Hill and Hashin. Note that the problem of determining the effective axial shear modulus μ_e is mathematically equivalent to determining the effective transverse thermal or electrical conductivity (Hashin, 1970).

Fourth-order bounds on the effective transverse conductivity or axial shear modulus μ_e of transversely isotropic fiber-reinforced materials that depend upon the phase properties, ϕ_2, ζ_2, and an integral over the four-point probability function S_4 have been derived by Milton (1981). Employing a phase-interchange theorem, Milton demonstrated that the integral involving S_4 can be expressed in terms of ϕ_2 and ζ_2 only. The fourth-order bounds, for the case $G_2 \ge G_1$, are given by

$$\mu_L^{(4)} \le \mu_e \le \mu_U^{(4)}, \tag{14}$$

where

$$\mu_U^{(4)} = G_2\left[\frac{(G_1+G_2)(G_1+\langle G\rangle) - \phi_2\zeta_1(G_2-G_1)^2}{(G_1+G_2)(G_2+\langle \tilde{G}\rangle) - \phi_2\zeta_1(G_2-G_1)^2}\right] \tag{15}$$

$$\mu_L^{(4)} = G_1\left[\frac{(G_1+G_2)(G_2+\langle G\rangle) - \phi_1\zeta_2(G_2-G_1)^2}{(G_1+G_2)(G_1+\langle \tilde{G}\rangle) - \phi_1\zeta_2(G_2-G_1)^2}\right]. \tag{16}$$

3 Determination of the Parameters ζ_2 and η_2 for Random Arrays of Impenetrable Cylinders

Evaluation of the integrals (1) and (2) requires knowledge of the three-point probability function S_3 for infinitely long, oriented, equisized, impenetrable cylinders (disks in two dimensions). Torquato and Stell (1982) have given an exact infinite series representation of the general n-point function S_n for a two-phase system of arbitrary dimensionality consisting of inclusions (phase 2) distributed throughout a matrix (phase 1). In the special case of a statistically isotropic distribution of identical, impenetrable disks (infinitely long, parallel cylinders) of radius a at an area (volume) fraction ϕ_2, the infinite series for S_n terminates with the nth term (Torquato and Stell, 1985); in the case $n=3$, it is given by

$$S_3(r_{12},r_{13},r_{23}) = S_3^{(1)}(r_{12},r_{13},r_{23}) + S_3^{(2)}(r_{12},r_{13},r_{23}) + S_3^{(3)}(r_{12},r_{13},r_{23}), \tag{17}$$

where

$$S_3^{(1)} = \rho\int m(r_{14})m(r_{24})m(r_{34})d\mathbf{r}_4, \tag{18}$$

$$S_3^{(2)} = \rho^2\int\int m(r_{14})m(r_{24})m(r_{35})g_2(r_{45})d\mathbf{r}_4d\mathbf{r}_5 + \rho^2\int\int m(r_{14})m(r_{25})m(r_{34})g_2(r_{45})d\mathbf{r}_4d\mathbf{r}_5 + \rho^2\int\int m(r_{15})m(r_{24})m(r_{34})g_2(r_{45})d\mathbf{r}_4d\mathbf{r}_5, \tag{19}$$

$$S_3^{(3)} = \rho^3\int\int\int m(r_{14})m(r_{25})m(r_{36})g_3(r_{45},r_{46},r_{56})d\mathbf{r}_4d\mathbf{r}_5d\mathbf{r}_6, \tag{20}$$

with

$$m(r) = \begin{cases} 1, & r<a \\ 0 & r>a. \end{cases} \tag{21}$$

Here, ρ is the number density of disks (cylinders) and therefore the disk area fraction (or cylinder volume fraction) is $\phi_2 = \rho\pi a^2$. Moreover, g_2 is the pair (radial) distribution function and g_3 the triplet distribution function for the particles, while $r_{ij} \equiv |\mathbf{r}_j - \mathbf{r}_i|$. The domain of integration in each of the above integrals in (18)–(20) is the infinite area of the macroscopic sample. Note that S_2 can be obtained from the expression for S_3, Eq. (17), by letting two of the three points coincide.

The combination of (17)–(21) and the key integrals for ζ_2 and η_2 (Eqs. (1) and (2), respectively) shows that one must perform fivefold, sevenfold, and ninefold integrations. For the case of ζ_2, these "cluster" integrals have been greatly simplified by Torquato and Lado (1988a) by expanding angle-dependent terms in the integrands in circular harmonics (i.e., Chebyshev polynomials) and using the orthogonality properties of this basis set. No such simplification of the cluster integrals involved in η_2 has thus far been made. However, before simplifying and evaluating η_2, it is instructive to first describe existing results for ζ_2.

After simplification, Torquato and Lado (1988a) found that for impenetrable disks of unit diameter one has exactly

$$\zeta_2 = \frac{2}{\pi\phi_1}[b_2\phi_2 + b_3\phi_2^2], \tag{22}$$

where

$$b_2 = \frac{\pi}{4}\int_1^\infty dr\,\frac{rg_2(r)}{(r^2-1/4)^2} \tag{23}$$

and

$$b_3 = \sum_{n=2}^\infty \frac{(n-1)}{4^{n-3}}\int_1^\infty \frac{dr}{r^{n-1}}\int_1^r \frac{ds}{s^{n-1}}\int_0^\pi d\theta[g_3(r,s,t) - g_2(r)g_2(s)]T_n(\cos\theta). \tag{24}$$

Downloaded 03 May 2010 to 171.66.16.247. Redistribution subject to ASME license or copyright; see http://www.asme.org/terms/Terms_Use.cfm

In Eq. (24), $T_n(\cos\theta)=\cos(n\theta)$ is the Chehyshev polynomial of the first kind. Note that the original fivefold, sevenfold, and ninefold cluster integrals have been reduced to manageable one and threefold integrals. Observe also that b_2 and b_3 are complicated functions of ϕ_2 as a result of the appearance of the density-dependent quantities g_2 and g_3. Although g_2 is known accurately in the Percus-Yevick approximation (Lado, 1968), g_3 is more problematical and hence Torquato and Lado (1988a) resorted to the commonly used superposition approximation (Hansen and McDonald, 1986)

$$g_3(r_{12},r_{13},r_{23}) \approx g_2(r_{12})g_2(r_{13})g_2(r_{23}) \tag{25}$$

to evaluate the integrals of (24). Recent computer simulation studies (Miller and Torquato, 1990) have shown that use of the superposition approximation gives accurate results provided that ϕ_2 is not large. A striking finding is that the exact expansion of ζ_2 through second order in ϕ_2 yields excellent agreement with the simulation results for a very wide range of volume fractions, i.e., up to the disorder-order phase transition, which for disks occurs at $\phi_2 \approx 0.71$ (Wood, 1968). This indicates that cubic and higher-order terms make negligible contributions to ζ_2 (and to the closely related parameter η_2), even at high densities. For disks this exact expansion

$$\zeta_2 = \frac{\phi_2}{3} - 0.05707\phi_2^2, \tag{26}$$

was also given by Torquato and Lado (1988a), but was not used by them to compute bounds. Therefore, relation (26) is now employed in this study for the range $0 \le \phi_2 \le 0.7$. Note that $\phi_2 = 0.7$ corresponds to approximately 87 percent of the maximum random close-packing volume fraction, $\phi_2^c \simeq 0.81$ (Stillinger, DiMarzio, and Kornegay, 1964).

As already noted, η_2 has yet to be computed for random impenetrable disks. The first step is to simplify the cluster integrals of η_2 which result after substituting (17)–(20) into (2). Following the expansion procedure of Torquato and Lado (1988a), the integral (2) in conjunction with the integrals (18)–(20) can be simplified (after considerable algebra) to yield the exact result that

$$\eta_2 = \frac{8}{\pi\phi_1}[c_2\phi_2 + c_3\phi_2^2], \tag{27}$$

where

$$c_2 = \int_1^\infty dr r g_2(r) W(r), \tag{28}$$

$$W(r) = \frac{\pi}{4(r^2-1/4)^2}\left[1 - \frac{3}{4(r^2-1/4)} - \frac{9}{64(r^2-1/4)^2} + \frac{9}{64(r^2-1/4)^3} + \frac{15}{512(r^2-1/4)^4}\right], \tag{29}$$

$$c_3 = \sum_{n=2}^{\infty} \int_1^\infty dr r \int_1^r ds s \int_0^\pi d\theta [g_3(r,s,t) - g_2(r)g_2(s)]Q_n(r,s,\cos\theta) \tag{30}$$

and

$$Q_n(r,s,\cos\theta) = \frac{1}{4^{n-4}r^{n-2}s^{n-2}}\left\{\frac{(n-1)}{16r^2s^2} + (n-3) \times \left[(n-2) - \frac{n(n-1)}{8r^2}\right]\left[(n-2) - \frac{n(n-1)}{8s^2}\right]\right\} T_n(\cos\theta). \tag{31}$$

By virtue of the appearance of g_2 and g_3, the coefficients c_2 and c_3 of (27) are dependent upon the particle fraction ϕ_2.

We now evaluate the parameter η_2 exactly through second order in ϕ_2. The radial distribution function for impenetrable disks of unit diameter is known exactly through first order in ϕ_2 (Hansen and McDonald, 1986),

$$g_2(r) = H(r-1)[1 + A_2(r)\phi_2], \tag{32}$$

where

$$A_2(r) = \frac{4}{\pi}\left[\pi - 2\sin^{-1}\left(\frac{r}{2}\right) - r\left(1 - \frac{r^2}{4}\right)^{1/2}\right] H(2-r), \tag{33}$$

$$H(x) = \begin{cases} 0, & x<0 \\ 1, & x>0. \end{cases} \tag{34}$$

Substitution of (32) into (28) yields

$$c_2 = \frac{7}{81}\pi + 0.1387\phi_2, \tag{35}$$

which is exact to the order (and number of significant figures) indicated. The coefficient 0.1387 was determined using a one-dimensional trapezoidal rule. The zero-density limit of g_3 is given by the expression

$$g_3(r_{12},r_{13},r_{23}) = H(r_{12}-1)H(r_{13}-1)H(r_{23}-1). \tag{36}$$

Substitution of (36) into (30) and use of the Gaussian-Chebyshev quadrature technique, employed by Torquato and Lado (1988a) to compute ζ_2, gives

$$c_3 = -0.3934, \tag{37}$$

which is exact to zeroth order in ϕ_2 (to the number of significant figures indicated). Finally, combination of (27), (35), and (37) yields, to second order in ϕ_2, that

$$\eta_2 = \frac{56}{81}\phi_2 + 0.0428\phi_2^2. \tag{38}$$

In accordance with the discussion above, we shall employ result (38) in third-order bounds for the effective transverse shear modulus G_e, Eq. (9), for the range $0 \le \phi_2 \le 0.7$. Note that to second order in ϕ_2, $\eta_2 > \zeta_2$ for our model.

In Figs. 1 and 2 we compare our results for the three-point parameters ζ_2 and η_2 for our random model to the few calculations of these quantities for other random microstructures. These include the symmetric-cell material (SCM) with cylindrical cells (Beran and Silnutzer, 1971) for which $\zeta_2 = \eta_2 = \phi_2$ (Milton, 1981) and equisized, fully penetrable cylinders (FPC), i.e., randomly centered cylinders (Torquato and Beasley, 1986a,b; Joslin and Stell, 1986a). Joslin and Stell (1986b) showed that the parameters for the FPC model were insensitive to polydispersivity in size. (Symmetric-cell materials (Miller, 1969) are constructed by partitioning the space into cells of possibly varying shapes and sizes, with cells randomly designated as phase 1 or phase 2 with probabilities ϕ_1 and ϕ_2, respectively.) Note that the linear terms in the respective volume-fractions expansions of the parameters about $\phi_2 = 0$ either exactly or approximately represent ζ_2 and η_2 over the allowable volume fraction range (Torquato and Lado, 1988a). Torquato and Lado (1986) have already given the reasons why the values of ζ_2 and η_2 for distributions of fully penetrable particles always lie above the corresponding results for impenetrable particles, which unlike the former do not form clusters until the maximum allowable random close-packing fraction is reached.

4 Calculation of Improved Bounds on μ_e, k_e, and G_e for Random Arrays of Impenetrable Cylinders

Here we shall utilize the results for the three-point parameters, relations (26) and (38), to compute the improved bounds of Section 2 for equilibrium distributions of infinitely long, oriented, impenetrable cylinders. We will consider cases in which the cylindrical fibers are stiffer than the matrix for the fiber volume range $0 \le \phi_2 \le 0.7$. It is now well known (Torquato, 1985; 1987; 1988a) that in such cases that the lower bounds (rather than the upper bounds) will provide a relatively

Downloaded 03 May 2010 to 171.66.16.247. Redistribution subject to ASME license or copyright; see http://www.asme.org/terms/Terms_Use.cfm

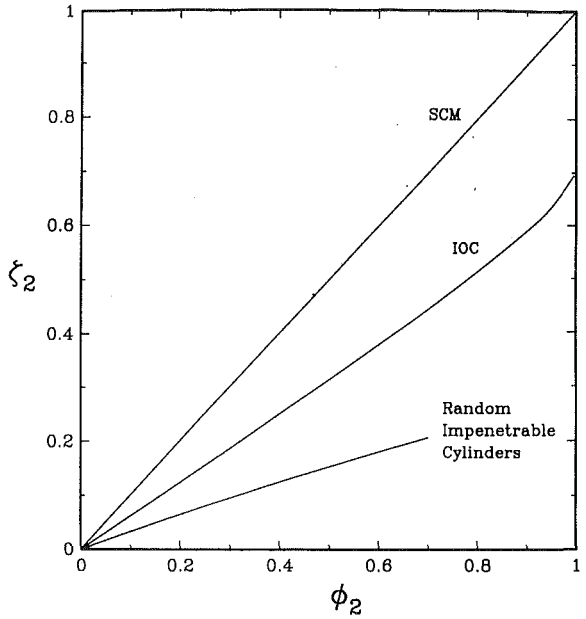

Fig. 1 Three-point parameter ζ_2, defined by Eq. (1), for random arrays of cylinders, including the symmetric-cell material (SCM) with cylindrical cells (Beran and Silnutzer, 1971; Milton, 1982), fully penetrable cylinders (FPC) (Torquato and Beasley, 1986a; Joslin and Stell, 1986a) and the equilibrium distribution of impenetrable cylinders, Eq. (26)

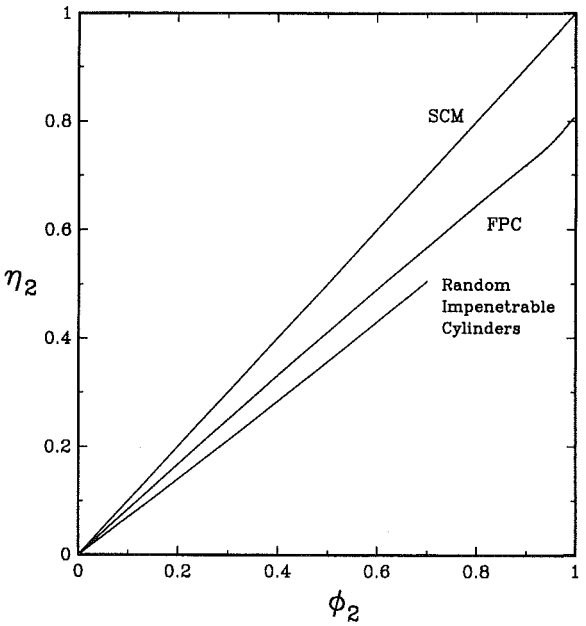

Fig. 2 Three-point parameter η_2, defined by Eq. (2), for random arrays of cylinders, including the symmetric-cell material (SCM) with cylindrical cells (Beran and Silnutzer, 1971; Milton, 1982), fully penetrable cylinders (FPC) (Torquato and Beasley, 1986b; Joslin and Stell, 1986a) and the equilibrium distribution of impenetrable cylinders, Eq. (38)

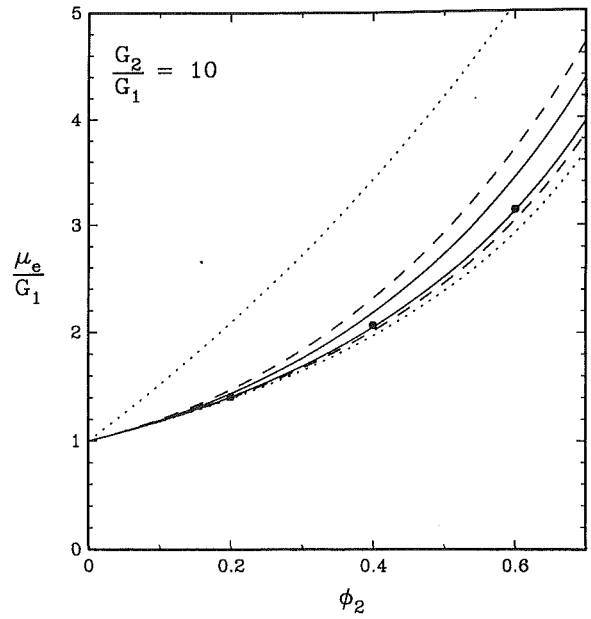

Fig. 3 Bounds on the scaled effective axial shear modulus μ_e/G_1 versus the cylinder volume fraction ϕ_2 at $G_2/G_1 = 10$; ····· second-order bounds (Hashin, 1965; 1970); - - - - third-order bounds (Silnutzer, 1972); and ——— fourth-order bounds (Milton, 1981) for an equilibrium distribution of impenetrable cylinders. The black circles are computer-simulation determinations of the true scaled effective axial shear modulus (Kim and Torquato, 1990).

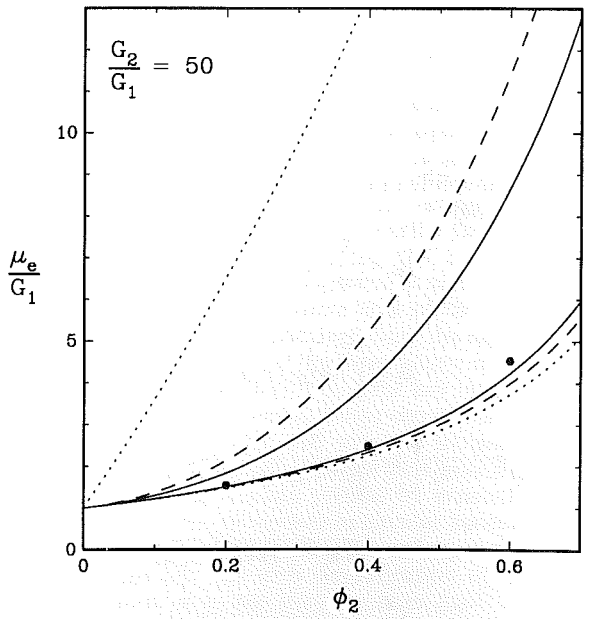

Fig. 4 As in Fig. 3, with $G_2/G_1 = 50$

accurate estimate of the effective parameter (even when the bounds are not tight) since the stiffer phase (fibers) can never form large connected clusters for $0 \le \phi_2 \le 0.7$. Equilibrium distributions of cylinders do not form interparticle contacts until the random close-packing volume fraction $\phi_2^c \simeq 0.81$ is reached (Stillinger, DiMarzio and Kornegay, 1964).

In Fig. 3, we plot third and fourth-order bounds on the scaled effective axial shear modulus μ_e/G_1 (Eqs. (3) and (14)) as a function of the cylinder volume fraction ϕ_2 for a composite with a shear modulus ratio $G_2/G_1 = 10$. Included in this figure is the corresponding second-order bounds derived by Hashin and highly accurate Monte Carlo computer simulation data recently obtained by Kim and Torquato (1990) for the same equilibrium impenetrable-cylinder model for the mathematically equivalent effective transverse conductivity. It is seen that the third-order Silnutzer bounds substantially improve upon the second-order bounds; the fourth-order Milton bounds, in turn, are more restrictive than the third-order bounds and indeed are narrow enough to provide a good estimate of μ_e for a wide range of ϕ_2. As expected, most of the improvement comes in the upper bounds. Note that since the superposition approximation evaluation of ζ_2 (Torquato and Lado, 1988a) overestimates it at high ϕ_2, the effect of using the more accurate relation (26) for ζ_2 is to shift the bounds downward towards the second-order lower bound. Observe also the excellent

Downloaded 03 May 2010 to 171.66.16.247. Redistribution subject to ASME license or copyright; see http://www.asme.org/terms/Terms_Use.cfm

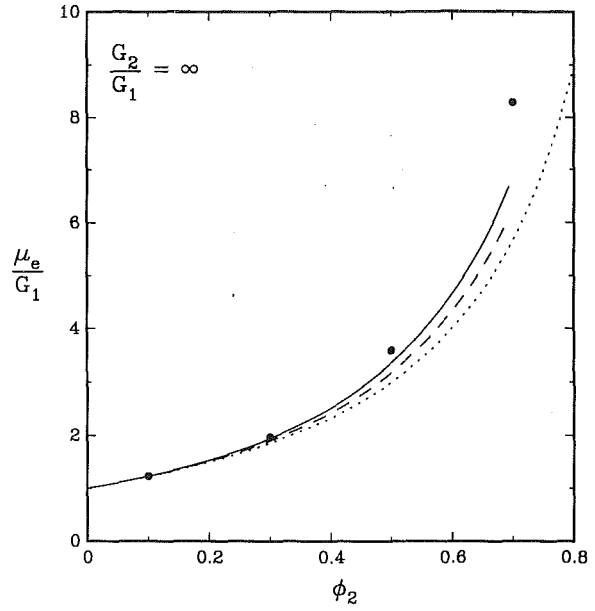

Fig. 5 As in Fig. 3, with $G_2/G_1 = \infty$; upper bounds are not shown since they diverge to infinity in this limit

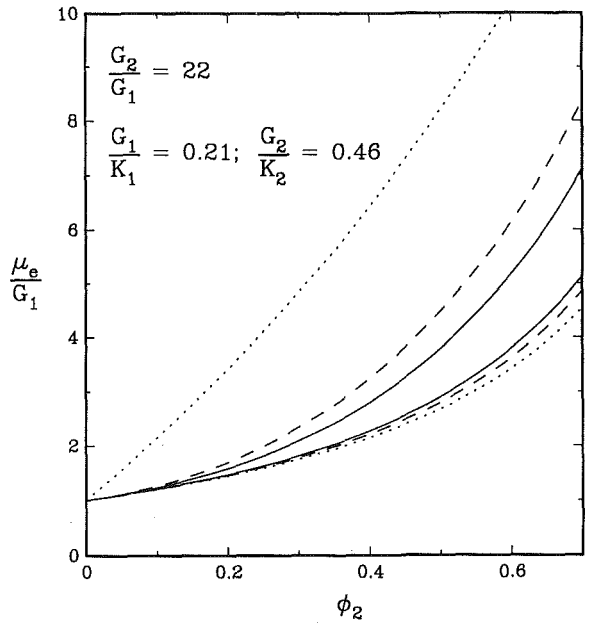

Fig. 6 As in Fig. 3 for a glass-epoxy composite with $G_2/G_1 = 22$, $G_1/K_1 = 0.21$ and $G_2/K_2 = 0.46$. Computer-simulation data are not available in this case.

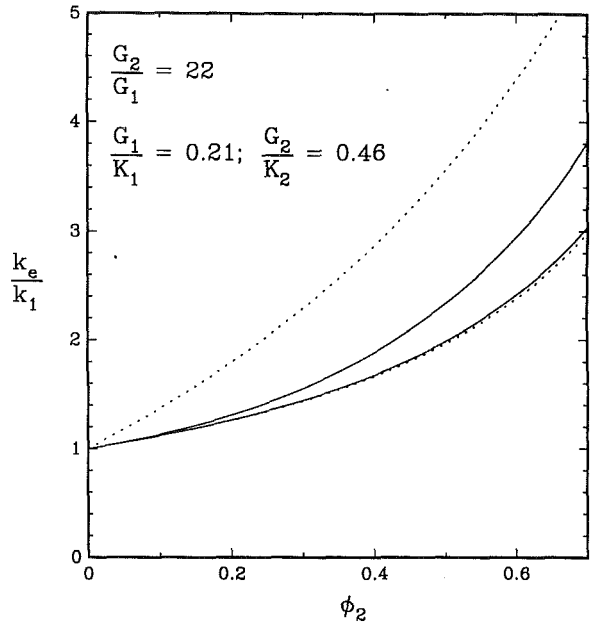

Fig. 7 Bounds on the scaled effective transverse bulk modulus k_e/k_1 versus the cylinder volume fraction ϕ_2 for a glass-epoxy composite for which $G_2/G_1 = 22$, $G_1/K_1 = 0.21$ and $G_2/K_2 = 0.46$; · · · · second-order bounds (Hill, 1964; Hashin, 1965); ——— third-order bounds (Silnutzer, 1972)

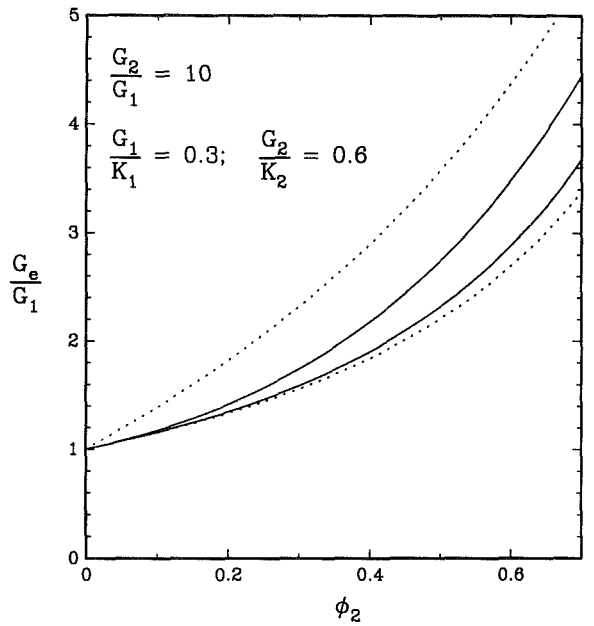

Fig. 8 Bounds on the scaled effective transverse shear modulus G_e/G_1 versus the cylinder volume fraction ϕ_2 for a composite in which $G_2/G_1 = 10$, $G_1/K_1 = 0.3$ and $G_2/K_2 = 0.6$; · · · · second-order bounds (Hill, 1964; Hashin, 1965); ——— third-order bounds (Silnutzer, 1972)

agreement between the computer simulation data and the fourth-order lower bound.

In Fig. 4, we plot the same bounds for the case where the fibers are 50 times more rigid than the matrix ($G_2/G_1 = 50$). Not surprisingly, the bounds widen but, for reasons noted earlier, the fourth-order lower bound still provides an accurate estimate of the effective axial shear modulus for a wide range of cylinder volume fractions.

This latter point is further substantiated by comparing the bounds in the extreme case of super rigid inclusions relative to the matrix ($G_2/G_1 = \infty$) to the computer-simulation data (see Fig. 5). Although all of the upper bounds diverge to infinity here, it is seen that the fourth-order lower bound still provides a good estimate of μ_e for a wide range of ϕ_2.

Figure 6 shows second, third and fourth-order bounds on the scaled effective axial shear modulus μ_e/G_1 for a glass-epoxy composite for which $G_2/G_1 = 22$, $G_1/K_1 = 0.21$ and $G_2/K_2 = 0.46$. Based upon the previous observations, the fourth-order lower bound gives a highly accurate estimate of μ_e for this commonly employed fiber-reinforced material.

Figure 7 depicts the third-order Silnutzer bounds on the scaled effective transverse bulk modulus k_e/k_1 (Eq. (6)) for our model as a function of ϕ_2 for a glass-epoxy composite for which $G_2/G_1 = 22$, $G_1/K_1 = 0.21$, and $G_2/K_2 = 0.46$. Included in the figure are the corresponding second-order bounds (Hill, 1964; Hashin, 1965). The third-order bounds provide significant improvement over the second-order bounds and are tight enough to yield good estimates of k_e for a wide range of cylinder volume fractions.

Downloaded 03 May 2010 to 171.66.16.247. Redistribution subject to ASME license or copyright; see http://www.asme.org/terms/Terms_Use.cfm

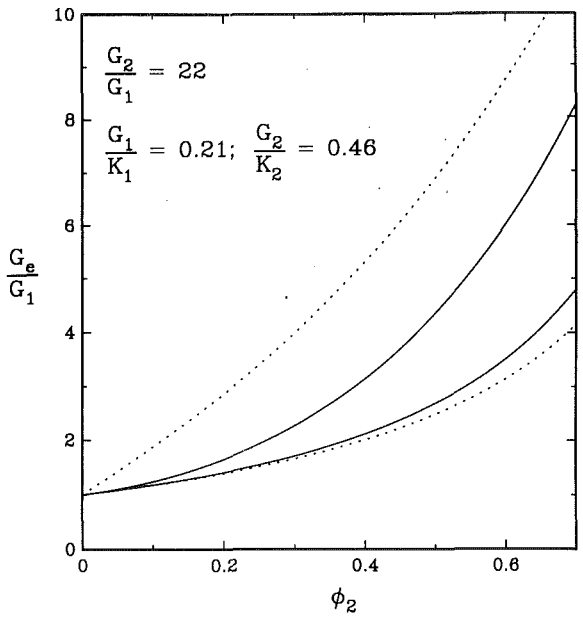

Fig. 9 As in Fig. 8 for a glass-epoxy composite for which $G_2/G_1 = 22$, $G_1/K_1 = 0.21$ and $G_2/K_2 = 0.46$

In Fig. 8, we plot second and third-order bounds on the scaled effective transverse shear modulus G_e/G_1 for our model of a composite with $G_2/G_1 = 10$, $G_1/K_1 = 0.3$ and $G_2/K_2 = 0.6$. Figure 9 shows the same bounds for a glass-epoxy composite with $G_2/G_1 = 22$, $G_1/K_1 = 0.21$ and $G_2/K_2 = 0.46$. Again, the third-order lower bound should yield a good estimate of G_e for a wide range of ϕ_2.

5 Conclusion

Four-point bounds on the effective axial shear modulus and three-point bounds on the effective transverse bulk and shear moduli have been computed for a transversely isotropic, fiber-reinforced material composed of a random array of infinitely long, parallel, impenetrable, circular cylinders for cylinder volume fractions up to 70 percent. This represents the first calculation of such bounds of the transverse bulk and shear moduli for this practically useful model. We exploited a key property of the microstructural parameters ζ_2 and η_2 to accurately compute them for fixed volume fraction ϕ_2, namely, for a large class of random distributions of oriented cylinders (be they overlapping or possessing size distribution), the low-volume fraction expansions of the parameters (which are easily determined) are excellent approximations over a wide range of ϕ_2 (Torquato, 1991). A striking result is that the lower bounds provide remarkably accurate estimates of the elastic moduli, even when the cylinders are much more rigid than the matrix.

Acknowledgments

S. Torquato gratefully acknowledges the support of the Office of Basic Energy Sciences, U.S. Department of Energy, under Grant No. DE-FG05-86ER 13482.

References

Beran, M. J., and Silnutzer, N., 1971, "Effective Electrical, Thermal and Magnetic Properties of Fiber-Reinforced Materials," *Journal of Composite Materials*, Vol. 5, pp. 246–249.

Hansen, J. P., and McDonald, I. R., 1986, *Theory of Simple Liquids*, Academic Press, New York.

Hashin, Z., 1965, "On Elastic Behavior of Fiber Reinforced Materials of Arbitrary Transverse Phase Geometry," *Journal of the Mechanics and Physics of Solids*, Vol. 13, pp. 119–134.

Hashin, Z., 1970, "Theory of Composite Materials," *Mechanics of Composite Materials*, F. W. Wendt, H. Liebowitz, and N. Perrone, eds., Pergamon Press, New York, pp. 201–242.

Hill, R., 1964, "Theory of Mechanical Properties of Fiber-Strengthened Materials—I. Elastic Behavior," *Journal of the Mechanics and Physics of Solids*, Vol. 12, pp. 199–212.

Joslin, C. G., and Stell, G., 1986a, "Bounds on the Properties of Fiber-Reinforced Composites," *Journal of Applied Physics*, Vol. 60, pp. 1607–1610.

Joslin, C. G., and Stell, G., 1986b, "Effective Properties of Fiber-Reinforced Composities: Effects of Polydispersivity in Fiber Diameter," *Journal of Applied Physics*, Vol. 60, pp. 1610–1615.

Kim, I. C., and Torquato, S., 1990, "Determination of the Effective Conductivity of Heterogeneous Media by Brownian Motion Simulation," *Journal of Applied Physics*, Vol. 68, pp. 3892-3903.

Lado, F., 1968, "Equation of State of the Hard-Disk Fluid from Approximate Integral Equations," *Journal of Chemical Physics*, Vol. 49, pp. 3092–3096.

Miller, M. N., 1969, "Bounds for Effective Electrical, Thermal, and Magnetic Properties of Heterogeneous Materials," *Journal of Mathematical Physics*, Vol. 10, pp. 1988–2004.

Miller, C. A., and Torquato, S., 1990, "Effective Conductivity of Hard-Sphere Dispersions," *Journal of Applied Physics*, Vol. 68, pp. 5486–5493.

Milton, G. W., 1981, "Bounds on the Transport and Optical Properties of a Two-Component Composite Material," *Journal of Applied Physics*, Vol. 52, pp. 5294–5304.

Milton, G. W., 1982, "Bounds on the Elastic and Transport Properties of Two-Component Composites," *Journal of the Mechanics and Physics of Solids*, Vol. 30, pp. 177–191.

Silnutzer, N., 1972, "Effective Constants of Statistically Homogeneous Materials," Ph.D. Thesis, University of Pennsylvania, Philadelphia, PA.

Stillinger, F. H., DiMarzio, E. A., and Kornegay, R. L., 1964, "Systematic Approach to Explanation of the Rigid Disk Phase Transition," *Journal of Chemical Physics*, Vol. 40, pp. 1564–1576.

Torquato, S., and Stell, G., 1982, "Microstructure of Two-Phase Random Media. I. The *n*-Point Probability Functions," *Journal of Chemical Physics*, Vol. 77, pp. 2071–2077.

Torquato, S., 1985, "Effective Electrical Conductivity of Two-Phase Disordered Composite Media," *Journal of Applied Physics*, Vol. 58, pp. 3790–3797.

Torquato, S., and Stell, G., 1985, "Microstructure of Two-Phase Random Media. V. The *n*-Point Matrix Probability Functions for Impenetrable Spheres," *Journal of Chemical Physics*, Vol. 82, pp. 980–987.

Torquato, S., and Beasley, J. D., 1986a, "Effective Properties of Fiber-Reinforced Materials: I. Bounds on the Effective Thermal Conductivity of Dispersions of Fully Penetrable Cylinders," *International Journal of Engineering Science*, Vol. 24, pp. 415–433.

Torquato, S., and Beasley, J. D., 1986a, "Effective Properties of Fiber-Reinforced Materials: I. Bounds on the Effective Thermal Conductivity of Dispersions of Fully Penetrable Cylinders," *International Journal of Engineering Science*, Vol. 24, pp. 415–433.

Torquato, S., and Beasley, J. D., 1986b, "Effective Properties of Fiber-Reinforced Materials: II. Bounds on the Effective Elastic Moduli of Dispersions of Fully Penetrable Cylinders," *International Journal of Engineering Science*, Vol. 24, pp. 435–447.

Torquato, S., and Lado, F., 1986, "Effective Properties of Two-Phase Disordered Composite Media: II. Evaluation of Bounds on the Conductivity and Bulk Modulus of Dispersions of Impenetrable Spheres," *Physical Review B*, Vol. 33, pp. 6428–6435.

Torquato, S., 1987, "Thermal Conductivity of Disordered Heterogeneous Media from the Microstructure," *Reviews in Chemical Engineering*, Vol. 4, pp. 151–204.

Torquato, S., and Lado, F., 1988a, "Bounds on the Conductivity of a Random Array of Cylinders," *Proceedings of the Royal Society of London*, Vol. A417, pp. 59–80.

Torquato, S., and Lado, F., 1988b, "Bounds on the Effective Transport and Elastic Properties of a Random Array of Cylindrical Fibers in a Matrix," ASME JOURNAL OF APPLIED MECHANICS, Vol. 55, pp. 347–354.

Torquato, S., 1991, "Random Heterogeneous Media: Microstructure and Improved Bounds on Effective Properties," *Applied Mechanics Reviews*, Vol. 44, pp. 37–76.

Wood, W. W., 1968, "Monte Carlo Calculations for Hard Disks in the Isothermal-Isobaric Ensemble," *Journal of Chemical Physics*, Vol. 48, pp. 415–434.

Downloaded 03 May 2010 to 171.66.16.247. Redistribution subject to ASME license or copyright; see http://www.asme.org/terms/Terms_Use.cfm

A Torque-Free Flexible Model Gyro

F. P. J. Rimrott
Professor,
Fellow ASME.

F. Janabi-Sharifi

Department of Mechanical Engineering,
University of Toronto,
Toronto, Ontario M5S 1A4, Canada

The present investigation is concerned with the behavior of an elastic, oblate, torque-free gyro model. The model has been devised such that it represents accurately arbitrarily large attitudes and arbitrarily large deformations. All simplifying assumptions are incorporated into the model before the theory is applied. The subsequent theoretical development is consequently exact; i.e., the expressions for inertia moments, angular moments, kinetic and elastic energies are all exact. Also, the mass center of the model gyro does not shift within the gyro. Equations remain tractable and the practicing engineer can readily get a feel for the phenomena uncovered. The model is composed of a rigid massless rod connected elastically to a rigid massive disk. At the tip of each rod there is a point mass. The nonlinear equations of quasi-static motion are derived using Euler's law, and a floating coordinate frame. Following the analysis, various numerical examples are investigated and the results are plotted. The total mechanical energy of the system is determined, and the condition for existence of an energy trap state (minimum energy state at an attitude other than zero) is obtained. When trapped, the gyro is in effect rigid, has a stable attitude, and rotates around the principal axis of maximum inertia, which in turn is collinear with the space-fixed angular momentum vector.

1 Introduction

The principal idea underlying the present work is to describe accurately the quasi-static behavior of a specially devised model gyro. The present work parallels that of a number of authors, e.g., Hooker and Margulies (1965) and Scher and Farrenkopf (1974), who have dealt with flexible satellites and flexible gyrostats.

Using the model gyro it can readily be demonstrated that flexible gyros may have energy traps, and that the existence and location of a trap depends on the flexibility of the gyro.

The model gyro is oblate and consists of an axisymmetric massive disk and a flexible axial massless rod with point masses at each tip (Fig. 1). The rod is free to spin with respect to the disk. A physical version might be as shown in Fig. 2. For the model gyro version, every part, excepting disk and tip masses, would have to be massless. The linear spring is axisymmetric and of stiffness k (in Nm/rad), such that it provides a restoring torque of

$$M_s = k\phi \tag{1}$$

where the deformation angle ϕ is the angle between rod and the central axis of the disk and M_s is the moment induced by the spring (Fig. 3).

At each tip of the rod there is a point mass of magnitude m. The total mass of the model gyro is thus $m_D + 2m$. The inertia moments of the model gyro at rest, i.e., when the spring is undeformed ($\phi = 0$ deg) are

$$B_o = A_o = A_D + 2ml^2 \tag{2a}$$

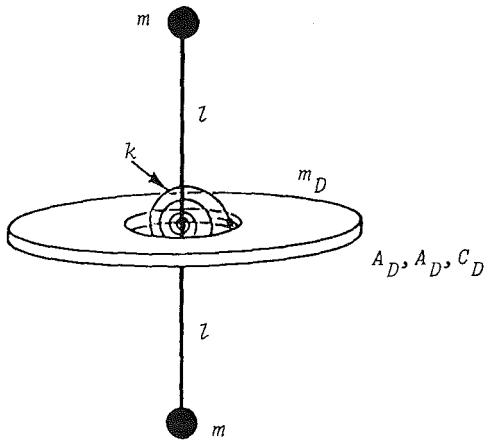

Fig. 1 The model gyro

$$C_o = C_D \tag{2b}$$

where A_D, B_D, and C_D are the principal inertia moments of the disk and $2l$ is the length of the rod. As is seen from Eq. (2), the model gyro is axisymmetric when undeformed, and is oblate if

$$C_o > A_o. \tag{3}$$

2 Gyro Deformation at Different Attitudes

A floating coordinate frame $Cuvz$ is chosen such that its axes are coincident with the disk's principal axes. The $Cuvz$ frame is rotating at an angular velocity Ω (Fig. 3). According to Euler's law,

$$\mathbf{M} = \dot{\mathbf{H}} \tag{4}$$

as a consequence a torque-free ($\mathbf{M} = \mathbf{0}$) gyro, has an angular momentum vector $\mathbf{H}$ of constant magnitude, fixed in space.

Contributed by the Applied Mechanics Division of THE AMERICAN SOCIETY OF MECHANICAL ENGINEERS for publication in the JOURNAL OF APPLIED MECHANICS.

Discussion on this paper should be addressed to the Technical Editor, Prof. Leon M. Keer, The Technological Institute, Northwestern University, Evanston, IL 60208, and will be accepted until two months after final publication of the paper itself in the JOURNAL OF APPLIED MECHANICS. Manuscript received by the ASME Applied Mechanics Division, May 25, 1990; final revision, Nov. 19, 1990.

Copyright © 1992 by ASME
Downloaded 03 May 2010 to 171.66.16.247. Redistribution subject to ASME license or copyright; see http://www.asme.org/terms/Terms_Use.cfm

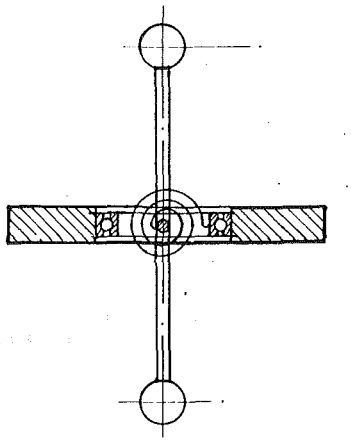

Fig. 2 A physical version of the model gyro

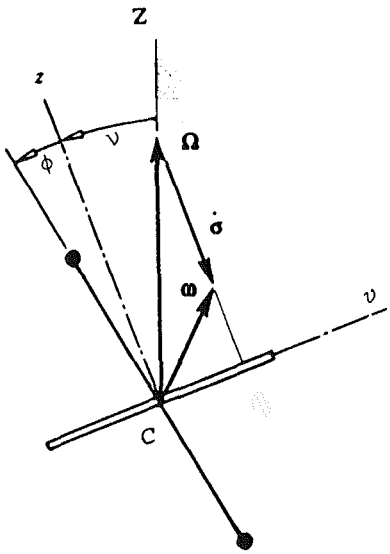

Fig. 3 The model gyro and its angular velocities

Thus, we can set up a space-fixed coordinate frame $CXYZ$ in such a way that the Z-axis is collinear with the $\mathbf{H}$ vector (Fig. 3). The attitude angle ν is measured from the space-fixed Z-axis to the disk's central axis z. Considering that the model gyro consists of two rigid parts: (*i*) *the disk D* and (*ii*) *the dumbbell rod R*, and that under quasi-static conditions the time derivatives of angles ν and ϕ vanish and $\dot{\sigma}=$ constant, the components of the angular momentum of the gyro (Fig. 4) have been shown by Schlegel et al. (1989) to be

$$H_u = 0 \tag{5a}$$

$$H_\nu = A_D\omega_\nu + 2ml^2\Omega\sin(\nu+\phi)\cos\phi \tag{5b}$$

$$H_z = C_D\omega_z + 2ml^2\Omega\sin(\nu+\phi)\sin\phi \tag{5c}$$

where the disk rotates at an angular velocity ω and the rod at an angular velocity Ω, i.e., at the angular velocity of the floating $Cuvz$ coordinate system. The reason for this is that the inertial force field moves at Ω (Rimrott, 1988), and since the dumbbell has no inertia moment about its axis, Ω becomes the angular velocity of the dumbbell rod as well.

The quasi-static conditions, i.e., $\dot{\nu}=\dot{\phi}=0$, apply uniquely when the total mechanical energy is a minimum (or maximum). In all other cases they represent one possible mode of motion out of an infinite number. Since the present paper is concerned with uncovering and describing gyro behavior at minimum mechanical energy, a general expression for the angular momentum involving time derivatives is not needed.

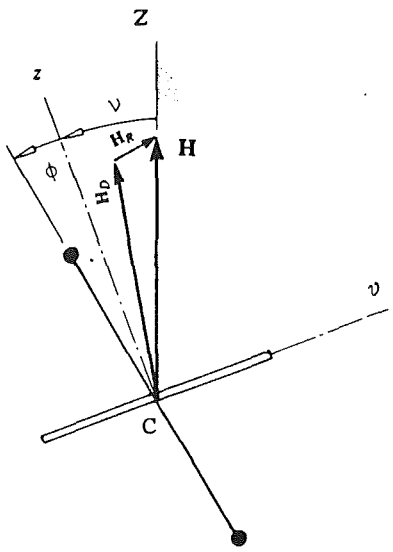

Fig. 4 The angular momentum of the whole system

The ν-components of the angular velocities ω and Ω are related by

$$\omega_\nu = \Omega\sin\nu. \tag{6}$$

Further, the angular momentum component,

$$H_\nu = H\sin\nu. \tag{7}$$

Thus, the ν-component of the angular velocity of the disk, derived from (5*a*), (6), and (7), becomes

$$\omega_\nu = \frac{H\sin\nu}{A_D + 2ml^2\dfrac{\sin(\nu+\phi)\cos\phi}{\sin\nu}}. \tag{8}$$

In a similar manner, the z-component of the angular velocity of the disk can be obtained.

$$\omega_z = \frac{H}{C_D}\left[\cos\nu - \frac{2ml^2\sin(\nu+\phi)\sin\phi}{A_D + 2ml^2\dfrac{\sin(\nu+\phi)\cos\phi}{\sin\nu}}\right] \tag{9}$$

By substituting (8) into (6), one gets, for the magnitude of the rod's angular velocity,

$$\Omega = \frac{H}{A_D + 2ml^2\dfrac{\sin(\nu+\phi)\cos\phi}{\sin\nu}}. \tag{10}$$

The spin rate $\dot{\sigma}$ of the disk is the difference between the disk's and the rod's angular velocity's components in the z-direction, i.e.,

$$\dot{\sigma} = \omega_z - \Omega_z, \tag{11}$$

and by substituting from (9) and (10) into (11), one gets for the spin

$$\dot{\sigma} = \frac{H}{C_D}\left[\cos\nu - \frac{2ml^2\sin(\nu+\phi)\sin\phi + C_D\cos\nu}{A_D + 2ml^2\dfrac{\sin(\nu+\phi)\cos\phi}{\sin\nu}}\right]. \tag{12}$$

The torque, $\mathbf{M}_D$, transmitted from the dumbbell rod to the disk can also be found from Euler's law, with

$$\mathbf{M}_D = \dot{H}_D \tag{13}$$

where $\mathbf{H}_D$ is the angular momentum of the disk, i.e.,

$$\mathbf{H}_D = [\mathbf{e}_u\ \mathbf{e}_\nu\ \mathbf{e}_z]\begin{bmatrix}0\\ A_D\omega_\nu\\ C_D\omega_z\end{bmatrix} \tag{14}$$

Downloaded 03 May 2010 to 171.66.16.247. Redistribution subject to ASME license or copyright; see http://www.asme.org/terms/Terms_Use.cfm

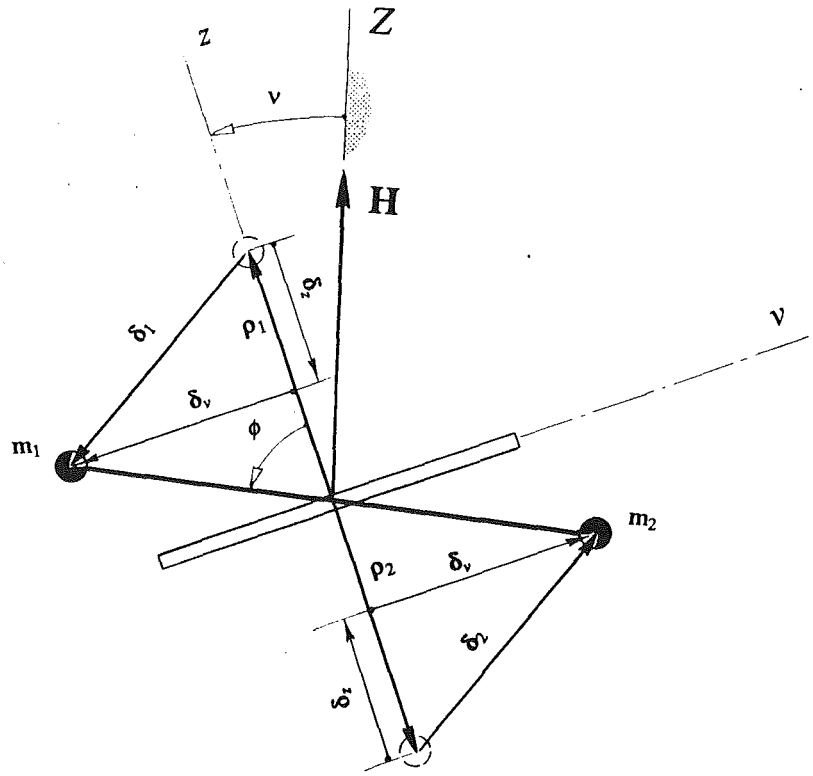

Fig. 5 Position and displacement components

and

$$\dot{\mathbf{H}}_D = \mathring{\mathbf{H}}_D + \Omega \times \mathbf{H}_D. \tag{15}$$

In (15), $\dot{\mathbf{H}}_D$ is the disk's angular momentum rate and $\mathring{\mathbf{H}}_D$ is the relative change rate of the angular momentum of the disk with respect to the *Cuvz* coordinate system. Since $\dot{\omega}_\nu = 0$ and $\dot{\omega}_z = 0$, we can write

$$\mathring{\mathbf{H}}_D = 0. \tag{16}$$

Further,

$$\Omega \times \mathbf{H}_D = \begin{vmatrix} \mathbf{e}_u & \mathbf{e}_\nu & \mathbf{e}_z \\ 0 & \omega_\nu & \Omega_z \\ 0 & A_D\omega_\nu & C_D\omega_z \end{vmatrix}. \tag{17}$$

Thus, the torque transmitted to the disk from the rod is

$$\mathbf{M}_D = [\mathbf{e}_u\ \mathbf{e}_\nu\ \mathbf{e}_z] \begin{bmatrix} 2ml^2\Omega^2 \sin(\nu+\phi)\cos(\nu+\phi) \\ 0 \\ 0 \end{bmatrix}. \tag{18}$$

Since the moment applied by the spring must be equal to the torque transmitted to the disk, one can obtain the deformation angle ϕ, using (1) and (18), as

$$\phi = \frac{\Omega^2}{2\omega_n^2} \sin 2(\nu+\phi) \tag{19}$$

where

$$\omega_n^2 = \frac{k}{2ml^2} \tag{20}$$

is the square of a stiffness parameter, viz. the natural frequency of an oscillating symmetric dumbbell rod with tip masses m and length $2l$ connected elastically at the center to the disk.

Now one can obtain the deformation angle of the rod ϕ at any arbitrary attitude angle ν by using (10) and (19). The result is three curves, as plotted in Fig. 7, for a set of constants given. Figures 8 to 10 show the families of curves obtained for specific cases, with the spring stiffness as parameter.

3 Gyro Energy at Different Attitudes

The total mechanical energy E of a gyro is the sum of its kinetic energy T and its elastic energy V.

$$E = T + V \tag{21}$$

The kinetic energy is the sum of the kinetic energy of the disk and the kinetic energy of the dumbbell rod.

$$T = \frac{1}{2}\left[A_D\omega_\nu^2 + C_D\omega_z^2 + 2ml^2\Omega^2\sin^2(\nu+\phi)\right] \tag{22}$$

The elastic energy is due to the displacement of the spring.

$$V = ml^2\omega_n^2\phi^2 \tag{23}$$

Thus, the total mechanical energy of the system can be written with the help of (22) and (23).

$$E = \frac{1}{2}\left[A_o\omega_\nu^2 + C_o\omega_z^2 + 2ml^2\Omega^2(\sin^2(\nu+\phi) - \sin^2\nu)\right] + ml^2\omega_n^2\phi^2 \tag{24}$$

Using (10), (19), (20), and (24), one can now determine the total mechanical energy of the model gyro at any attitude. This is done for specific cases and plotted in Figs. 13 and 14.

4 Inertia Tensors

The inertia tensor of the model gyro in the floating *Cuvz* coordinate system (Fig. 5) is

$$[I] = \begin{bmatrix} I_{uu} & I_{u\nu} & I_{uz} \\ I_{\nu u} & I_{\nu\nu} & I_{\nu z} \\ I_{zu} & I_{z\nu} & I_{zz} \end{bmatrix} \tag{25}$$

which is composed of inertia moments (I_{uu}, $I_{\nu\nu}$, I_{zz}) and inertia products ($I_{u\nu}$, I_{uz}, $I_{\nu z}$). The inertia moments of the model gyro in the floating coordinate frame used (Fig. 5) are

$$I_{uu} = A_D + 2ml^2 \tag{26a}$$

$$I_{\nu\nu} = A_D + 2ml^2\cos^2\phi \tag{26b}$$

Downloaded 03 May 2010 to 171.66.16.247. Redistribution subject to ASME license or copyright; see http://www.asme.org/terms/Terms_Use.cfm

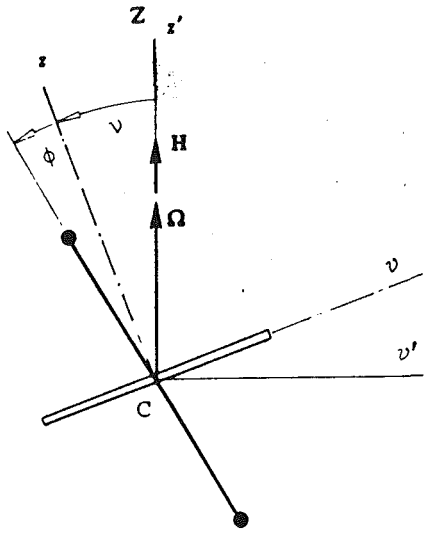

Fig. 6 The $Cu'v'z'$ coordinate system is the principal coordinate system in the trap

$$I_{zz} = C_D + 2ml^2\sin^2\phi. \tag{26c}$$

The inertia products are defined as

$$I_{uv} = -\int_m uv\,dm \tag{27a}$$

$$I_{uz} = -\int_m uz\,dm \tag{27b}$$

$$I_{vz} = -\int_m vz\,dm, \tag{27c}$$

and the position coordinates of an arbitrary mass element dm are

$$u = \rho_u + \delta_u \tag{28a}$$

$$v = \rho_v + \delta_v \tag{28b}$$

$$z = \rho_z + \delta_z \tag{28c}$$

where ρ_u, ρ_v, and ρ_z are the position components of each mass element dm in the *undeformed gyro*. For our case, there are only two point masses m which are displaced. They are located at

$$\rho_u = 0$$

$$\rho_v = 0$$

$$\rho_z = \pm l. \tag{29}$$

The quantities δ_u, δ_v, and δ_z are the displacement components of each mass element dm due to the gyro's deformation (Fig. 5). For our case, the two point masses m have the displacement components

$$\delta_u = 0$$

$$\delta_v = \pm l\sin\phi$$

$$\delta_z = \pm l(1-\cos\phi) \tag{30}$$

where the positive sign is for the lower mass and the negative sign for the upper one. Using (27), (28), (29), and (30), the inertia products can be written as

$$I_{uv} = 0$$

$$I_{uz} = 0$$

$$I_{vz} = 2ml^2\cos\phi\sin\phi. \tag{31}$$

Of special interest also are inertia moments and products expressed by means of another coordinate frame. We consider

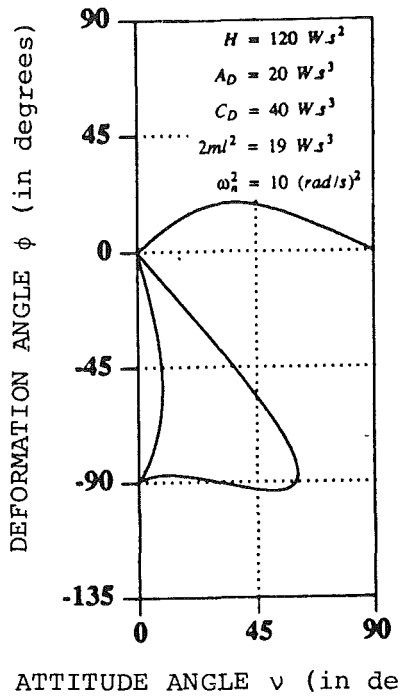

Fig. 7 Deformation angle versus attitude angle according to Eq. (19) for $A_o/C_o = 0.975$ and $\omega_n^2 = 10$ (rad/s)^2

the model gyro (Fig. 6) and choose a $Cu'v'z'$ coordinate frame such that the u'-axis is collinear with the u-axis, and the z'-axis is collinear with the Z-axis (and the **H**-vector), and the v'-axis is chosen such that $Cu'v'z'$ forms a right-handed orthogonal coordinate system. Then

$$I_{u'u'} = A_o \tag{32a}$$

$$I_{v'v'} = \frac{1}{2}[(A_D + C_D) + (A_D - C_D)\cos 2\nu] + 2ml^2\cos^2(\nu+\phi) \tag{32b}$$

$$I_{z'z'} = \frac{1}{2}[(A_D + C_D) - (A_D - C_D)\cos 2\nu] + 2ml^2\sin^2(\nu+\phi) \tag{32c}$$

$$I_{u'v'} = 0 \tag{32d}$$

$$I_{u'z'} = 0 \tag{32e}$$

$$I_{v'z'} = -\frac{C_D - A_D}{2}\sin 2\nu + ml^2\sin 2(\nu+\phi) \tag{32f}$$

where the first term in each of (32b) and (32c) are the inertia moments of the disk, and the second ones are the inertia moments of the rod.

5 Numerical Results

From (10) and (19), one can calculate the deformation angle at any arbitrary attitude angle. Figure 7 shows a typical diagram of deformation angle ϕ of the rod versus the attitude angle ν for given values of H, A_D, C_D, $2ml^2$, and ω_n. A family of these curves can be plotted by changing the stiffness of the spring, i.e., ω_n (Figs. 8, 9, and 10). All diagrams are for oblate ($C_o > A_o$) gyros. Figure 8 is for an almost spherical gyro, i.e., A_o is almost equal to C_o. This type of gyro is more likely to have a trap than the one whose deformation versus attitude characteristics are plotted in Fig. 9, or the almost perfect thin disk, with A_o almost equal to $C_o/2$, whose characteristics are plotted in Fig. 10.

Angular velocity Ω of the rod, angular velocity ω of the disk, and components of gyro angular velocity in the ν and z di-

Downloaded 03 May 2010 to 171.66.16.247. Redistribution subject to ASME license or copyright; see http://www.asme.org/terms/Terms_Use.cfm

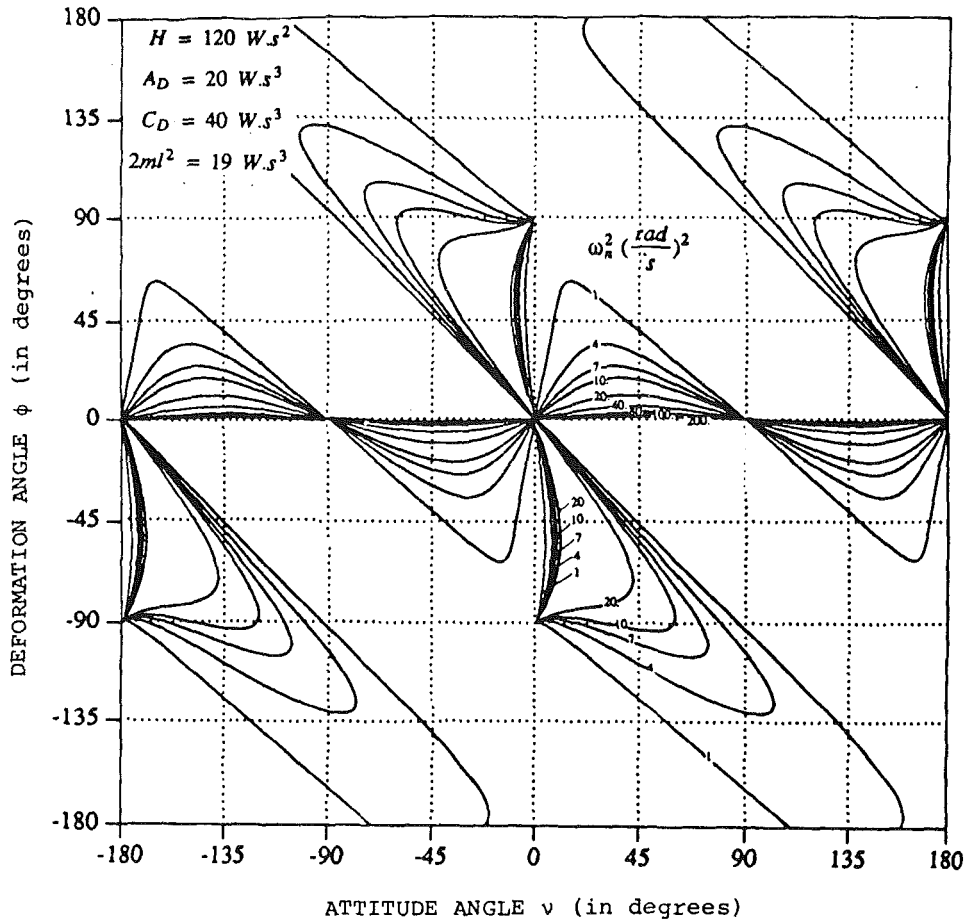

Fig. 8 Deformation angle versus attitude angle according to Eq. (19) for $A_o/C_o = 0.975$

rections can be obtained for any attitude angle (Fig. 11) by using (10), (8), and(9); a solution of (10) and (19) simultaneously gives the deformation angle ϕ, and the magnitude of the disk's angular velocity can be obtained from

$$\omega = \sqrt{\omega_\nu^2 + \omega_z^2}. \tag{33}$$

The spin rate of the disk can be obtained from (12). The result is shown in Fig. 11, which also shows that $\dot{\sigma} = 0$ and $\Omega = \omega$ characterize a trap point. Also using (26) and (31), the values of inertia moments and inertia products at different attitudes and for prescribed parametric values can be obtained (Fig. 12).

In order to ascertain the total mechanical energy of the gyro at different attitude angles, values of A_D, C_D, H, $2ml^2$, and ω_n were entered into (24) for different values of attitude angle with related deformation angles ϕ obtained from (19). The results are shown in Figs. 13 and 14.

6 Energy Trap States

6.1 General Case. Scher and Farrenkopf (1974) studied the energy trap states of dual-spin spacecraft. They showed that flexible spacecraft with internal damping will seek a state at which the whole system rotates with one and the same angular velocity. Also, at that state, there will be no more energy dissipation because the relative spin between the platform and the rotor has vanished. Application of this principle to a single flexible body reveals that the minimum energy state is one of spin about the body's centroidal principal axis of maximum inertia (Pringle, 1966). This result can be extended to the present model gyro if internal damping is included, in which case $\dot{\sigma}$ eventually vanishes since finite energy cannot be dissipated indefinitely. Thus, ultimately the dumbbell stops relative to the disk, and the system, behaving now as a rigid body, has reached a minimum energy state. Since there is no further energy dissipation, that particular state can consequently be represented just as well by an undamped gyro, such as our model.

If we compare Figs. 13 and 14, the concept of a trap state can be better understood. As is seen from Fig. 13, the energy minimum occurs at zero attitude. In Fig. 14, with, e.g., $\omega_n^2 = 10$ $(\text{rad/s})^2$, on the other hand, the energy minimum occurs at $\nu \approx 33.3$ deg (and $\phi \approx 18.9$ deg), i.e., the gyro will be trapped in this state. Also, it is seen that there is no trap after a certain stiffness ($\omega_n^2 = 180$ $(\text{rad/s})^2$ in Fig. 14) is exceeded. The importance of trap points, and their effects in the stability of the flexible gyros and spacecraft are well explained by different authors (e.g., see Scher and Farrenkopf, 1974). The task that remains is to state the condition for an existence of a trap state away from $\nu = 0$ deg for our model.

In a trap state energy minimum angular velocity ($\omega = \Omega$) and angular momentum **H** are collinear, according to the collinearity theorems (Rimrott, 1988). Also, one principal axis of the deformed gyro becomes collinear with the angular momentum **H**, and there is no longer any spin, i.e.,

$$\dot{\sigma} = 0. \tag{34}$$

See also Fig. 11.

Thus, from (12) and (34) one gets

$$\sin 2(\nu_1 + \phi_1) = \frac{C_D - A_D}{2ml^2} \sin 2\nu_1 \tag{35}$$

for a trap state (ν_1, ϕ_1). At this state, the gyro has become kinetically rigid and all parts are moving at one and the same

Downloaded 03 May 2010 to 171.66.16.247. Redistribution subject to ASME license or copyright; see http://www.asme.org/terms/Terms_Use.cfm

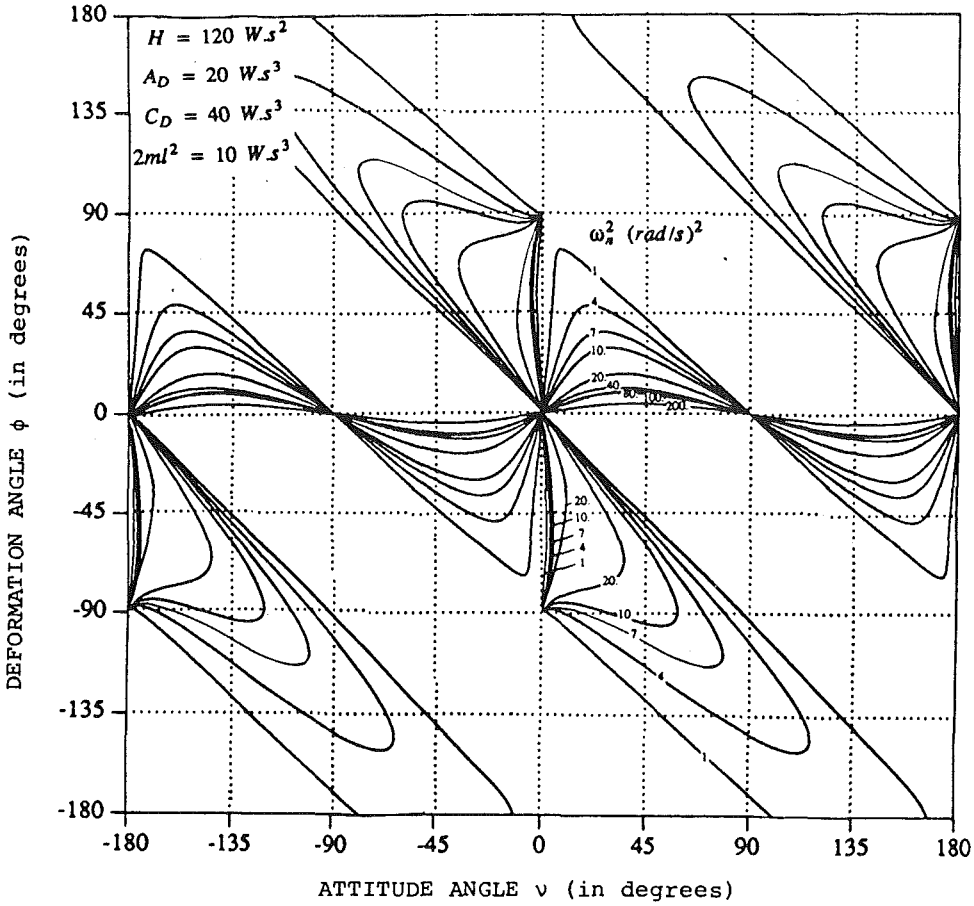

Fig. 9 Deformation angle versus attitude angle according to Eq. (19) for $A_o/C_o = 0.75$

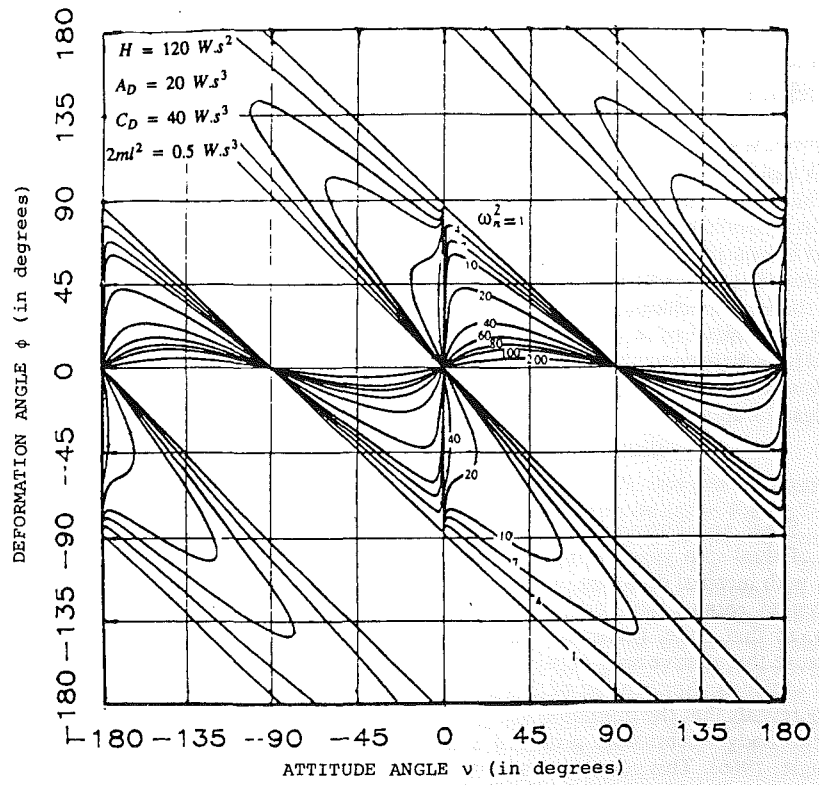

Fig. 10 Deformation angle versus attitude angle according to Eq. (19) for $A_o/C_o = 0.5125$

Downloaded 03 May 2010 to 171.66.16.247. Redistribution subject to ASME license or copyright; see http://www.asme.org/terms/Terms_Use.cfm

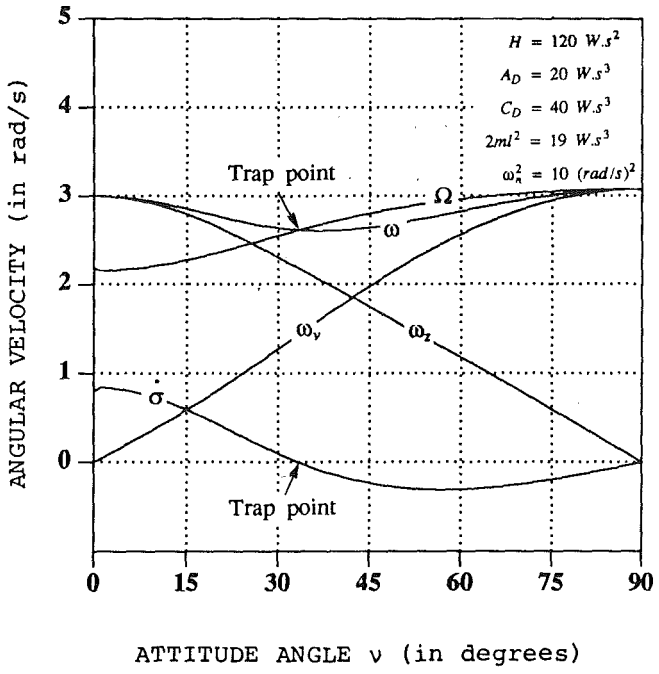

Fig. 11 Angular velocities and spin rate versus attitude angle

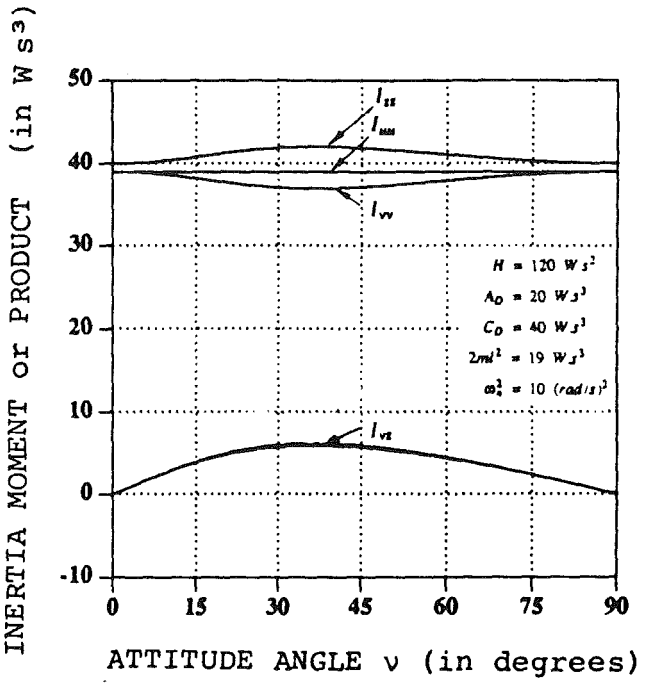

Fig. 12 Inertia moments versus attitude angle

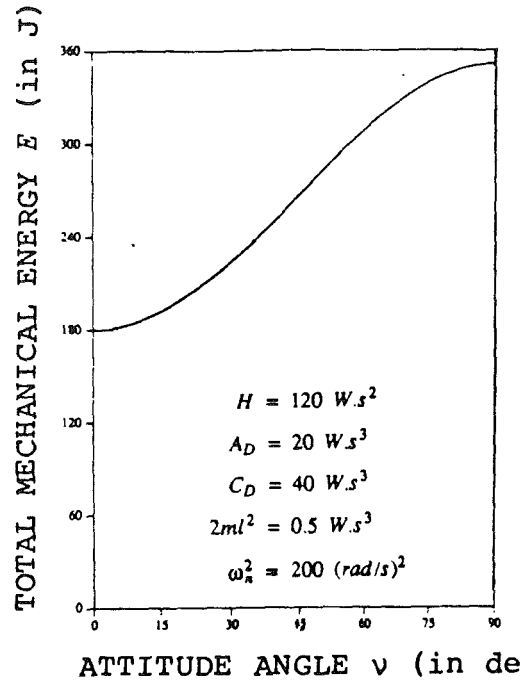

Fig. 13 Total mechanical energy versus attitude angle when there is no trap away from $\nu = 0$ deg

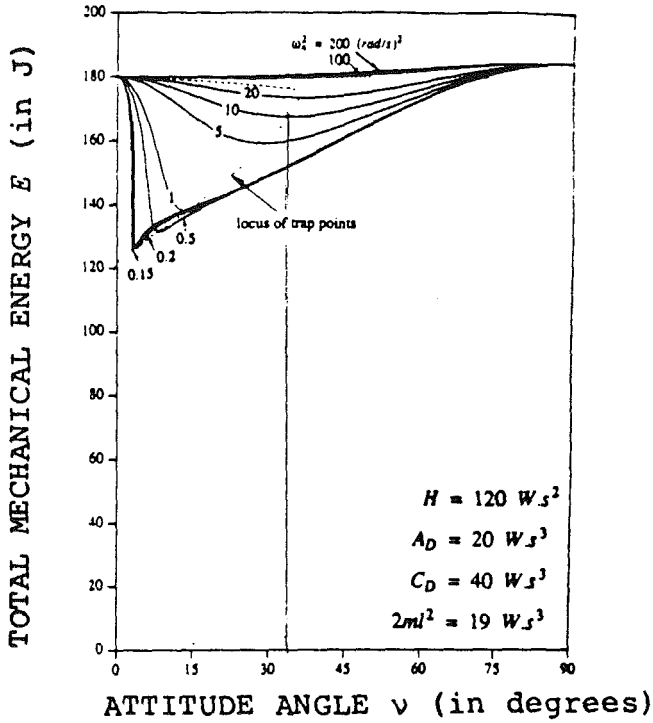

Fig. 14 Total mechanical energy versus attitude angle diagram with trap points away from $\nu = 0$ deg

angular velocity (Fig. 6). For oblate gyros, this typically happens at zero attitude (Fig. 13), but sometimes it happens at attitudes other than zero (Fig. 14).

The minimum energy state occurs at $\nu = \nu_1$, where ω and **H** are also collinear. For this state then, one can see that

$$\omega_{y1} = \omega_1 \sin\nu_1$$

$$\omega_{z1} = \omega_1 \cos\nu_1$$

$$\omega_1 = \Omega_1. \tag{36}$$

By introducing a frequency ratio

$$r_1 = \frac{\omega_1}{\omega_n}, \tag{37}$$

one can write (19) in the form of

$$\phi_1 = \frac{1}{2} r_1^2 \sin 2(\nu_1 + \phi_1). \tag{38}$$

As is to be expected, conditions (35) and (38) can also be obtained by differentiating the *Lagrangian*

$$L = T - V = -ml^2\omega_n^2\phi_2 + \frac{1}{2} A_D\omega_1^2\sin^2\nu + \frac{1}{2} C_D\omega_1^2\cos^2\nu + ml^2\omega_1^2\sin^2(\nu + \phi). \tag{39}$$

Downloaded 03 May 2010 to 171.66.16.247. Redistribution subject to ASME license or copyright; see http://www.asme.org/terms/Terms_Use.cfm

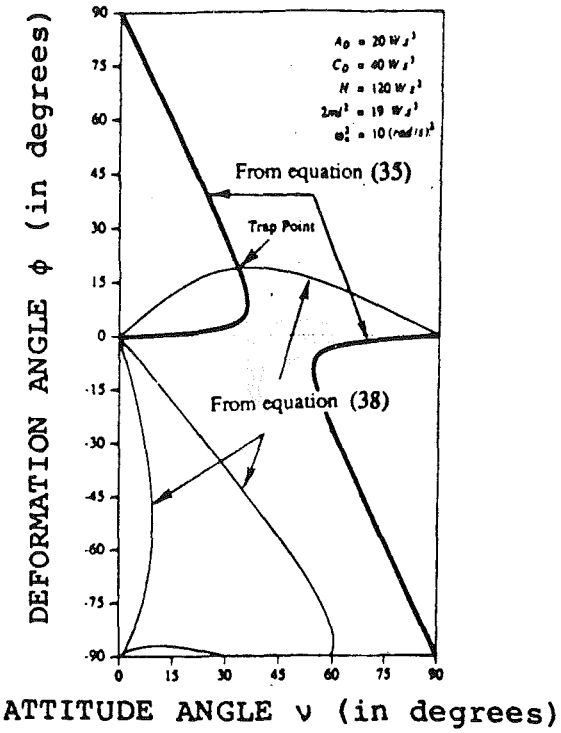

Fig. 15 Detection of a trap point by intersecting curves (35) and (38)

Substitution from (39) into Lagrange's equation for ϕ,

$$\frac{d}{dt}\frac{\partial L}{\partial \dot{\phi}}-\frac{\partial L}{\partial \phi}=0, \tag{40}$$

gives

$$\phi=\frac{1}{2}r_1^2\sin 2(\nu+\phi),$$

which is the same as (38). Also, Lagrange's equation for ν,

$$\frac{d}{dt}\frac{\partial L}{\partial \dot{\nu}}-\frac{\partial L}{\partial \nu}=0, \tag{41}$$

leads to

$$\sin 2(\nu+\phi)=\frac{C_D-A_D}{2ml^2}\sin 2\nu,$$

which is the same as (35).

Equations (35) and (38) are now available to determine the values of the two angles ν_1 and ϕ_1 associated with a trap point. Therefore, a trap point can be found by plotting both equations, i.e., (35) and (38), into a deformation angle versus attitude angle diagram, where the intersection of the two curves will pinpoint the trap (Fig. 15).

To study the inertia moments at trap states, we choose a $Cu'v'z'$ coordinate frame such that the u'-axis coincides with the u-axis, and the z'-axis with the **H**-axis (Fig. 6). Then we can write inertia moments and inertia products as given by Eqs. (32). Figure 16 shows the inertia moments of the gyro with respect to the u', v', z' axes at different attitude angles.

In the trap state the u', v', and z' axes are principal axes, i.e., the inertia products become zero. Therefore,

$$I_{v'z'}=0. \tag{42}$$

Substitution from (32f) gives

$$\sin 2(\nu+\phi)=\frac{C_D-A_D}{2ml^2}\sin 2\nu$$

which is the same condition as (35).

In order to apply Pringle's (1966) rule we differentiate (32b) and (32c) twice with respect to ν, and then substituting from (35) yields

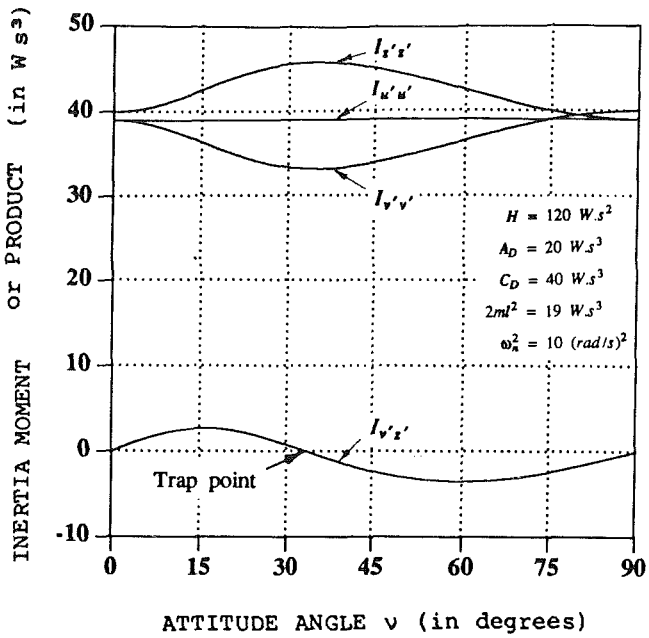

Fig. 16 Inertia moments in $Cu'v'z'$ coordinates for different attitude angles

$$\frac{d^2I_{z'z'}}{d\nu^2}<0$$

$$\frac{d^2I_{v'v'}}{d\nu^2}>0. \tag{43}$$

Therefore, at a trap state, the inertia moment about the z'-axis is maximum and about the v'-axis is a minimum. At a trap state, the now rigidized gyro rotates purely about the principal axis of maximum inertia, and its attitude is stable.

6.2 Condition for Nonexistence of a Trap Point. Curves (35) and (38) are seen (Figs. 15 and 17) to intersect always at $\nu=0$ deg and $\nu=90$ deg. At some other attitude angle $\nu=\nu_1$ an intersection may or may not occur. Considering the steady curvature upward of (35) and the steady curvature downward of (38), an intersection does not occur, and consequently a trap point (other than at $\nu=0$ deg) does not exist, when the slope $\frac{d\phi}{d\nu}$ of (35) is greater than that of (38), both taken at $\nu=\phi=0$ deg (Fig. 17).

From (35) one obtains, for $\nu=\phi=0$ deg,

$$\left(\frac{d\phi}{d\nu}\right)_{35}=\frac{C_D-A_D}{2ml^2}-1 \tag{44}$$

From (38) one obtains, for $\nu=\phi=0$ deg,

$$\left(\frac{d\phi}{d\nu}\right)_{38}=\frac{r_o^2}{1-r_o^2} \tag{45}$$

where at $\nu=0$ deg we have

$$\phi_o=0$$

$$\omega_{v_o}=0$$

$$\omega_{z_o}=\frac{H}{C_D}=\omega_o \tag{46}$$

and a frequency ratio

Downloaded 03 May 2010 to 171.66.16.247. Redistribution subject to ASME license or copyright; see http://www.asme.org/terms/Terms_Use.cfm

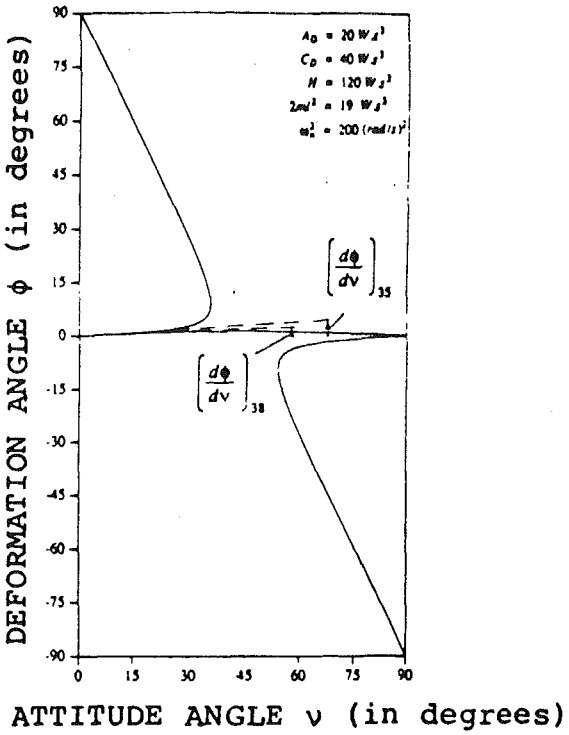

Fig. 17 A trap point does not exist, when the slope of curve (35) is greater than that of (38)

$$r_o = \frac{\omega_o}{\omega_n}. \tag{47}$$

As stated above, no trap point away from $\nu = 0$ deg occurs when

$$\left(\frac{d\phi}{d\nu}\right)_{35} > \left(\frac{d\phi}{d\nu}\right)_{38}, \tag{48}$$

and from a substitution from (44) and (45) into (48) it follows that

$$C_D > A_D + \frac{2ml^2}{1-r_o^2} \tag{49}$$

or

$$C_o > A_o + 2ml^2 \frac{r_o^2}{1-r_o^2} \tag{50}$$

where A_o and C_o are inertia moments of the undeformed gyro. The relation (50) is the same as relation (8.88) in (Rimrott, 1988) for near-rigid gyros. One can determine the shape limit, i.e., C_o limit, of the gyro from relation (50). If the information about the spring stiffness is sought, then inequality (49) can be written as

$$\omega_n > \frac{H}{C_D}\sqrt{\frac{C_D - A_D}{C_D - A_D - 2ml^2}} \tag{51}$$

from which the spring stiffness $k = 2ml^2\omega_n^2$ for no trap can be obtained.

It is interesting to note that for very stiff springs ($r_o \to 0$) inequality (50) requires, for attitude stability at $\nu = 0$ deg, the well-known condition

$$C_o > A_o. \tag{52}$$

For oblate gyros, inequalities (49), (50), and (51) are valid only when r_o is smaller than unity, or more specifically, from inequality (50), when

$$r_o < \sqrt{\frac{C_o - A_o}{C_o - A_o + 2ml^2}}. \tag{53}$$

7 Conclusions

In order to demonstrate that flexible torque-free gyros can be caught in a trap while deformed, the simplest imaginable model gyro was devised. In the first part of the present paper the nonlinear equations of motion were derived for this model gyro, solid is oblate and composed of a rigid massive disk and a rigid massless rod with point masses at the tips, and has disk and rod connected elastically by a linear spring. In the second part the effects of elastic deformation were studied, with particular emphasis on locating traps away from zero attitude and on how these traps can be avoided.

References

Hooker, W. W., and Margulies, G., 1965, "The Dynamical Attitude Equation for an n-body Satellite," *J. Astronautical Sciences*, Vol. 12, pp. 123–128.

Pringle, R., 1966, "On the Stability of a Body with Connected Moving Parts," *AIAA Journal*, Vol. 4, No. 8, pp. 1395–1404.

Rimrott, F. P. F., 1988, *Introductory Attitude Dynamics*, Springer-Verlag, New York, p. 153, 230.

Scher, M. P., and Farrenkopf, R. L., 1974, "Dynamic Trap States of Dual-Spin Spacecraft," *AIAA Journal*, Vol. 12, No. 12, pp. 1721–1725.

Schlegel, V., Guran, A., and Rimrott, F. P. J., "An Elastic Oblate Axisymmetric Reference Gyro for Attitude Studies," *Proceedings, CANCAM'89*, pp. 396–397.

Downloaded 03 May 2010 to 171.66.16.247. Redistribution subject to ASME license or copyright; see http://www.asme.org/terms/Terms_Use.cfm

Stability Properties of a Viscoelastic Column Under a Periodic Force

G. Cederbaum

M. Mond

The Pearlstone Center for Aeronautical Engineering Studies, Department of Mechanical Engineering, Ben-Gurion University of the Negev, Beer-Sheva 84105, Israel

The dynamic stability of a viscoelastic column subjected to a periodic longitudinal load is investigated. The viscoelastic behavior is given in terms of the Boltzmann superposition principle which yields an integro-differential equation of motion. The stability boundaries of this equation are determined analytically by using the multiple-scales method. It is shown that due to the viscoelasticity the stability regions are expanded, relative to the elastic ones, and the time for which a stable system becomes unstable is given. In addition, the stability properties of the viscoelastic column are time dependent and an initially stable system can turn unstable after a finite time, unlike columns that are described by the elastic model.

1 Introduction

The problem of the dynamical stability of elastic structures was investigated by Bolotin (1964), where the behavior is governed by the Mathieu equation and the stability characterizations are given by the Strutt diagram. Extensive bibliography and further results for this problem was given by Evan-Iwanovski in a review paper (1965) and in a monograph (1976).

In the case of a viscoelastic structure the analysis becomes more complicated since the Boltzmann representation of the stress-strain relation, which allows any linear viscoelastic character, leads to an integro-differential equation of motion. To analyze this problem, Matyash (1967) used the averaging method and Stevense (1966) employed the spring-dashpot representation. Szyszkowski and Glockner (1985) and Glockner and Szyszkowski (1987) utilized the Lyapunov concept of stability with the spring-dashpot representation (see also Ziegler, 1968). Lately, the dynamic stability of viscoelastic plates was investigated by Aboudi, Cederbaum, and Elishakoff (1990) by using Lyapunov exponents. This numerical procedure enables to determine whether the structure is stable for a particular set of parameters.

In the present paper we present a solution for the above problem based on the concept of multiple-scales analysis (Bender and Orszag, 1984). It is based on the fact that the relaxation function varies slowly with time and that we are mainly interested in small load amplitudes. The nonharmonic Mathieu equation is derived by using the Bernoulli-Euler hypothesis. The analysis leads to the following analytical results: (i) the time-dependent stability regions are determined, (ii) the time-dependent critical (minimum) value of the load parameter, for which instability occurs, is obtained, and (iii) An expression for the critical time for which the structure, with a given load parameter, will turn unstable. Examples are given for the fully elastic case as well as for the Voigt-Kelvin model for which comparisons of the results can be made with Bolotin's (1964) and for the standard linear solid model.

The above procedure can be easily used to analyse the dynamic stability of viscoelastic plates and shells.

2 Problem Formulation

Consider the problem of the transverse vibrations of a simply-supported column with a uniform cross-section, subjected

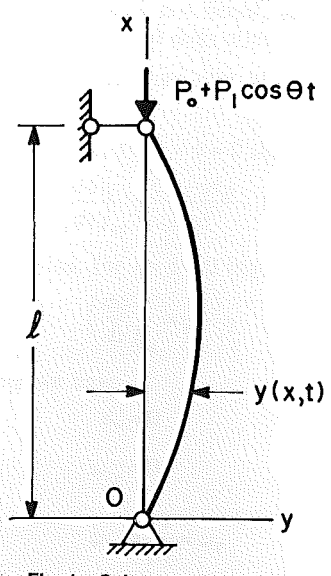

Fig. 1 Column configuration

Contributed by the Applied Mechanics Division of THE AMERICAN SOCIETY OF MECHANICAL ENGINEERS for publication in the JOURNAL OF APPLIED MECHANICS.

Discussion on this paper should be addressed to the Technical Editor, Prof. Leon M. Keer, The Technological Institute, Northwestern University, Evanston, IL 60208, and will be accepted until two months after final publication of the paper itself in the JOURNAL OF APPLIED MECHANICS. Manuscript received by the ASME Applied Mechanics Division, Mar. 12, 1990; final revision, Nov. 29, 1990.

Copyright © 1992 by ASME

Downloaded 03 May 2010 to 171.66.16.247. Redistribution subject to ASME license or copyright; see http://www.asme.org/terms/Terms_Use.cfm

to a periodic longitudinal loading (see Fig. 1). The equation that describes the motion of the column is:

$$\frac{\partial^2 M(x,\,t)}{\partial x^2}+P(t)\,\frac{\partial^2 y(x,\,t)}{\partial x^2}+m\,\frac{\partial^2 y(x,\,t)}{\partial t^2}=0 \qquad (1)$$

where

$$M(x,\,t)=\int_{-h/2}^{h/2} z\sigma(x,\,z,\,t)dz,$$

$\sigma(x,\,z,\,t)$ is the stress component and m is the mass per unit length.

For a viscoelastic material, the stress-strain relation is given by the Boltzmann superposition principle as

$$\sigma(x,\,z,\,t)=E_0\epsilon(x,\,z,\,t)+\int_0^t \dot{E}(t-t')\epsilon(x,\,z,\,t')dt', \qquad (2)$$

where $E(t))$ is the relaxation function while E_0 is its value at $t=0$, i.e, the initial Young modulus of the material.

Assuming small deflections, the strain-displacement relation is given by:

$$\epsilon(x,\,z,\,t)=-z\,\frac{\partial^2 y(x,\,t)}{\partial x^2}. \qquad (3)$$

Using the separation of variables method, the deflection $y(x,\,t)$ can be written in the form:

$$y(x,\,t)=Y(x)f(t), \qquad (4)$$

so that together with Eqs. (2) and (3), the following expression is obtained for the stress couple:

$$M(x,\,t)=I\,\frac{\partial^2 Y(x)}{\partial x^2}\,[E_0 f(t)+\int_0^t \dot{E}(t-t')f(t')dt'], \qquad (5)$$

where I is the second moment of the column cross-section. The equation of motion can now be rewritten in the form:

$$\left[E_0 I\,\frac{d^4 Y(x)}{dx^4}+P(t)\,\frac{d^2 Y(x)}{dx^2}\right]f(t)+mY(x)\,\frac{d^2 f(t)}{dt^2}=$$

$$-E_0 I\,\frac{d^2 Y(x)}{dx^2}\int_0^t \dot{D}(t-t')f(t')dt' \qquad (6)$$

where

$$D(t)=\frac{E(t)}{E_0}.$$

In order to satisfy the boundary conditions of a simply-supported column, the solution is given by the following Fourier sine series:

$$y(x,\,t)=\sum_{k=1}^{\infty} f_k(t)\,\sin\frac{k\pi x}{l}, \qquad (7)$$

where l is the length of the column.

In the following, the main stability region is investigated. To this end only the $k=1$, term in (7) is considered so that $y(x,\,t)$ is in the form given by (4). Let $P_0 = 0$ and

$$\omega^2=\left(\frac{\pi}{l}\right)^4\frac{E_0 I}{m},\ P^*=\left(\frac{\pi}{l}\right)^2 E_0 I,\ \eta=\frac{P_1}{2P^*}, \qquad (8)$$

where P_1 is the loading amplitude. The equation of motion is now in the form:

$$\ddot{f}(t)+\omega^2\,[1-2\eta\cos(\theta t)]f(t)=-\omega^2\int_0^t \dot{D}(t-t')f(t')dt', \qquad (9)$$

where θ is the loading frequency.It is noted that in the pure elastic case, i.e., $\dot{D}=0$, the Mathieu equation is recovered. An extensive investigation of the latter can be found in Mclachlan (1964).

3 Stability Boundaries of the Equation of Motion

In this section the stability properties of the solutions of Eq. (9) are investigated. Since no exact analytical solution is available for Eq. (9), the multiple scale method is employed in order to obtain asymptotic solutions (Bender and Orszag, 1984). The latter method is based on the fact that various physical processes that determine the behavior of the structure take place on distinct time scales. In the system investigated here, three different time scales control its development. The first time scale serves as a reference to the others and hence is considered throughout this work to be of order 1. The second time scale, associated with the loading amplitude is given by $1/\eta$ and is assumed to be much bigger than 1. In order to define the third time scale we assume that $D(t)$ varies slowly with time. This means that the time scale over which D changes is significantly longer than $2\pi/\omega$. The ratio of the former to the latter time scales is denoted by δ which is much smaller than 1. Thus,

$$\dot{D}(t)=\delta\dot{D}(\delta t), \qquad (10)$$

where the dot denotes the derivative with respect to the argument. Szyszkowski and Glockner (1985), assuming that δ is small, expanded the solution for Eq. (9) in power series in δ. Inserting Eq. (10) into Eq. (9) and retaining only terms of lowest order in δ results in the following equation for f:

$$\ddot{f}(t)+\omega^2\,[1-2\eta\cos(\theta t)f(t)=-\delta\omega^2\dot{D}(\delta t)\int_0^t f(t')dt'. \qquad (11)$$

We turn now to finding the boundaries in the $(\omega,\,\theta,\,\eta,\,\delta)$ space which divide the stable from the unstable regions in the limit of small δ and η.

It is noticed that when

$$\omega=\frac{\theta}{2}, \qquad (12)$$

a regular perturbation expansion in δ and η results in solutions that contain terms that are unbounded in time. These terms, known in the literature as secular terms, are unphysical.

In order to eliminate the secular terms, the multiple scales analysis is employed by introducing two new independent variables $\tau=\eta t$ and $\zeta=\delta t$. The latter represents the long time scale introduced to the system by the slow variation of the material moduli while the former long time scale is due to the small loading amplitude. Within the multiscale analysis t, τ, and ζ are considered as three independent variables. As a result, the time derivatives in Eq. (9) are given in terms of the partial derivatives according to

$$\frac{df}{dt}=\frac{\partial f}{\partial t}+\eta\,\frac{\partial f}{\partial \tau}+\delta\,\frac{\partial f}{\partial \zeta}. \qquad (13)$$

In addition, f is expanded in the following form:

$$f(t,\,\tau,\,\zeta)=f_0(t,\,\tau,\,\zeta)+\eta g_1\,(t,\,\tau,\,\zeta)$$
$$+\delta h_1\,(t,\,\tau,\,\zeta)+O(\eta^2,\,\delta^2) \qquad (14)$$

and since the regions of interest are near $\omega=\theta/2$, ω is expanded as

$$\omega^2=\frac{\theta^2}{4}+\eta\omega_1^2+O(\eta^2) \qquad (15)$$

where, to first order in η, ω_1 measures how close half the loading frequency $\theta/2$ is to the natural frequency ω. Expressions (13), (14), and (15) are inserted into Eq. (11) and coefficients of equal powers of δ and η are collected. The lowest order terms yield the following equation for f_0:

$$\frac{\partial^2 f_0}{\partial t^2}+\frac{\theta^2}{4}f_0=0 \qquad (16)$$

and its solution is given by

Downloaded 03 May 2010 to 171.66.16.247. Redistribution subject to ASME license or copyright; see http://www.asme.org/terms/Terms_Use.cfm

$$f_0(t,\tau,\zeta)=A(\tau,\zeta)e^{i\frac{\theta}{2}(t-t_0)}+\text{C.C}, \tag{17}$$

where C.C. stands for complex conjugate.

Terms of first order in δ and η yield the following equations, respectively,

$$\frac{\partial^2 h}{\partial t^2}+\frac{\theta^2}{4}h_1=\left(-i\theta\frac{\partial A}{\partial\zeta}+i\frac{\theta}{2}\dot{D}A\right)e^{i\frac{\theta}{2}(t-t_0)}+\text{NST}+\text{C.C}, \tag{18}$$

$$\frac{\partial^2 g}{\partial t^2}+\frac{\theta^2}{4}g_1=\left(-i\theta\frac{\partial A}{\partial\tau}-\omega_1^2A+\frac{\theta^2}{4}\bar{A}^*\right)e^{i\frac{\theta}{2}(t-t_0)}+\text{NST}+\text{C.C.} \tag{19}$$

The terms on the right-hand side of Eqs. (18) and (19) that multiply exp ($i\theta/2$) are the secular ones since they give rise to unbounded solutions. The rest are nonsecular term (NST). In order to eliminate the secular terms, we require that the coefficients of exp ($i\theta/2$) in each equation vanish. To this end let

$$A(\tau,\zeta)=T(\tau)Z(\zeta); \tag{20}$$

and by inserting expression (20) into Eqs. (18) and (19), one obtains

$$\frac{dZ}{d\zeta}-\frac{1}{2}\dot{D}Z=0 \tag{21}$$

$$\theta\frac{dT}{d\tau}-i\omega_1^2T+i\frac{\theta^2}{4}T^*=0. \tag{22}$$

The solutions of the last two equations are

$$Z(\zeta)=\alpha e^{\frac{1}{2}\int_{t_0}^{\zeta}\dot{D}(\zeta')d\zeta'} \tag{23}$$

and

$$T(\tau)=\beta e^{\frac{1}{\theta}\sqrt{\frac{\theta^4}{16}-\omega_1^4}(\tau-\tau_0)}+\gamma e^{-\frac{1}{\theta}\sqrt{\frac{\theta^4}{16}-\omega_1^4}(\tau-\tau_0)}, \tag{24}$$

respectively, where α, β, and γ are constants.

Due to the slow variation of D, its time derivative is assumed to be constant in the interval $t-t_0$, whose length is of order 1. In this case

$$\dot{D}(\zeta)=\lambda(\zeta_0), \tag{25}$$

where $\zeta_0=\delta t_0$. The dependence on ζ_0 in (25) signifies the fact that the slope of D (ζ) varies from one time interval to the other. Using (25) in (23) and inserting the latter together with Eq. (24) into Eq. (17), the following form for the zeroth-order solution is obtained

$$f_0(t,\tau,\zeta)=A_0e^{\frac{1}{2}\lambda(\zeta_0)(\zeta-\zeta_0)}e^{\pm\frac{1}{\theta}\sqrt{\frac{\theta^4}{16}-\omega_1^4}(\tau-\tau_0)}e^{i\frac{\theta}{2}t-t_0)} \tag{26}$$

where A_0 is a constant, obtained from α, β, and γ. Rewritting τ and ζ in terms of t, we see that instability occurs when

$$\frac{\eta}{\theta}\sqrt{\frac{\theta^2}{16}-\omega_1^4}\geq\frac{1}{2}|\lambda(\zeta_0)|\delta. \tag{27}$$

Hence, with Eq. (15), it can be concluded that for small η and δ the stability boundaries are given by

$$\omega^2=\frac{\theta^2}{4}\left[1\pm\sqrt{\eta^2-\frac{4\lambda^2}{\theta^2}\delta^2}\right]. \tag{28}$$

It is noted that in the pure elastic case, i.e., $\lambda=0$, the classical stability boundaries, as described by the Mathieu equation, are recovered. An example for such a case can be seen in Fig. 3 in the graph denoted by $\zeta_0\to\infty$. As can be seen in the latter, the pure elastic case is unstable for an infinitesimal loading amplitude when $\theta=2\omega$. However, as can be seen from Eq. (28), the stabilizing viscoelastic effects are most pronounced when the loading frequency assumes the value of 2ω.

Form Eq. (27) it s also clear that the critical (minimum) value of the excitation parameter, η_c, for which instability occurs is

$$\eta_c(\zeta_0)=\frac{2|\lambda(\zeta_0)|}{\theta}\delta. \tag{29}$$

Few interesting properties of the system can be inferred from Eq. (28). First we notice that by increasing the viscoelasticity ($\delta\lambda$), the stability region at a given time increases. It can also be seen that for a given ratio ω/θ, the stability region decreases by increasing the loading frequency. Finally, we see that if the loading parameter is less than $\eta_c(0)$, the system is stable. In such a case it is possible to determine the critical time, t_c, for which the system becomes unstable. This critical time is given by the solution of the following implicit equation:

$$\lambda(\delta t_c)=\frac{\eta_c(0)}{2\delta}\theta. \tag{30}$$

To summarize, it is emphasized that, unlike the elastic case, as well as in the elastic case with proportional damping (Bolotin, 1964), the stability properties as derived in this work are time dependent. These include the stability boundaries (Eq. (28)), the critical loading amplitude (Eq. (29)), and the time at which an initially stable system turns unstable (Eq. (30)).

4 Applications

4.1 The Elastic Case. For this case $D(t)=1$ and $\lambda=0$. Hence, the familiar results for the elastic case are recovered, i.e., the stability boundaries and the critical loading parameter are given by:

$$\omega^2=\frac{\theta^2}{4}(1\pm\eta)\text{ and }\eta_c=0, \tag{31}$$

respectively, as in Bolotin (1964).

4.2 The Voigt-Kelvin Model. For this case, Eq. (2) is

$$\sigma(x,z,t)=E_0\epsilon(x,z,t)+E_1\dot{\epsilon}(x,z,t)$$

$$=E_0[\epsilon(x,z,t)+\gamma\dot{\epsilon}(x,z,t);\ \gamma=\frac{E_1}{E_0} \tag{32}$$

so that with Eqs. (3), (4), and (8), Eq. (9) is now in the form

$$\ddot{f}(t)+\omega^2[1-2\eta\cos(\theta t)]f(t)=-\gamma\omega^2\dot{f}(t). \tag{33}$$

By employing the above multiple scale method, it was found that instability occurs when

$$\frac{\eta}{\theta}\sqrt{\frac{\theta^4}{16}-\omega_1^2}\geq\frac{\theta^2}{8}\gamma; \tag{34}$$

and with Eq. (15), the stability boundaries are given by

$$\omega^2=\frac{\theta^2}{4}\left[1\pm\sqrt{\eta^2-\frac{\theta^2}{4}\gamma^2}\right]. \tag{35}$$

For this case, a constant critical load amplitude is given by

$$\eta_c=\frac{\theta}{2}\gamma. \tag{36}$$

Setting $\gamma\omega^2=2\epsilon$ and $\theta=2\omega$, one obtains

$$\eta_c=\frac{2}{\omega}\epsilon, \tag{37}$$

which is the same result derived in Bolotin (1964) for the damped Mathieu equation.

4.3 The Standard Linear Solid Model. The relaxation function in this case is given by:

$$D(t)=a+be^{-\beta\zeta} \tag{38}$$

Downloaded 03 May 2010 to 171.66.16.247. Redistribution subject to ASME license or copyright; see http://www.asme.org/terms/Terms_Use.cfm

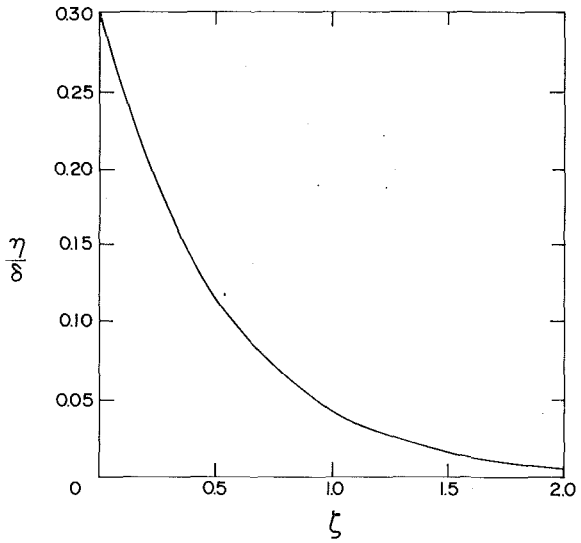

Fig. 2 Variation of η_c/δ versus $\zeta = \delta t$

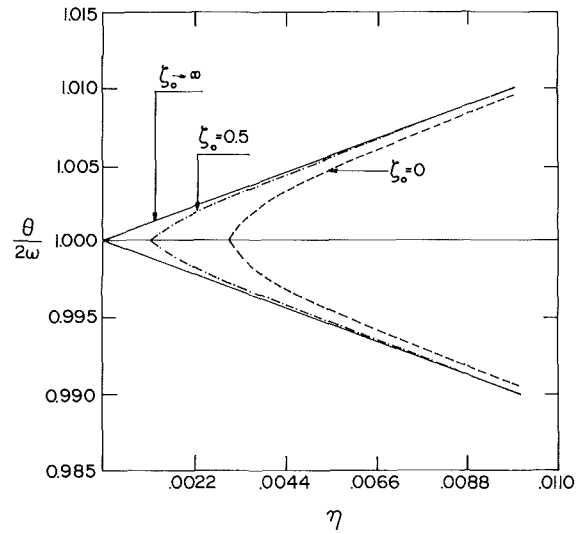

Fig. 3 Stability boundaries for $\zeta_0 = 0$, $\zeta_0 = 50$ and $\zeta_0 \to \infty$

where a, b and β are constants such that $a + b = 1$ (see Eq. (6)). Thus,

$$\dot{D}(\zeta) = -\beta b e^{-\beta\zeta}. \tag{40}$$

As an example, let

$$a = 0.7,\ b = 0.3,\ \beta = 2/\omega,\ \theta = 2\omega \text{ and } \delta = 0.01,$$

for which the following expressions are obtained

$$\eta_c(\zeta_0) = 3 \times 10^{-3} e^{-2\zeta_0},$$

$$\omega^2 = \frac{\theta^2}{4}\left[1 \pm \sqrt{\eta^2 - \eta_c^2(\zeta_0)}\right] \text{ for } \eta \geq \eta_c(0), \tag{41}$$

and

$$t_c = -\frac{1}{\delta\beta} \ln \frac{\eta\theta}{\delta} \frac{1}{2b\beta}. \tag{42}$$

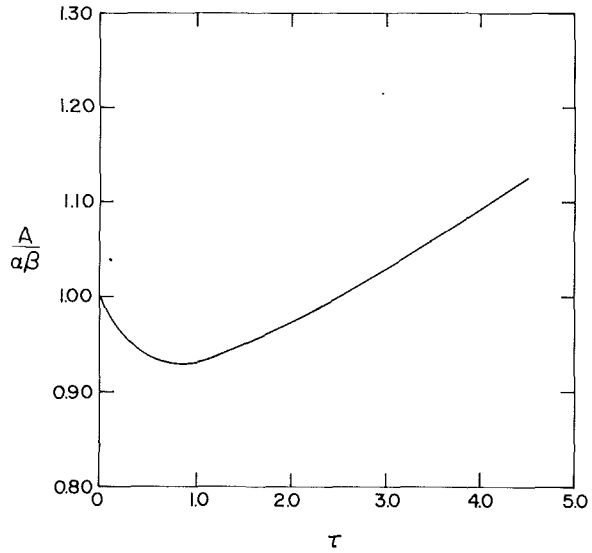

Fig. 4 Variation of the normalized response amplitude versus $\tau = \eta t$ ($\omega_1 = 0.8$)

Figure 2 shows the variations of η_c/δ as a function of $\zeta = \delta t$. The reductin of η_c implies that the instability region is enlarged due to the relaxation phenomenon. In Fig. 3, the instability boundaries at three different times ($\zeta_0 = 0$, $\zeta_0 = 50$, and $\zeta_0 \to \infty$), are plotted. It can be easily seen that the difference between the curves are pronounced for small values of η. This means that as the loading parameter grows, the effect of viscoelasticity becomes less important. Figure 4 shows the variation of the normalized amplitude with τ. As can be seen, the initially stable column turns unstable, and the amplitude of the oscillations grows without bound.

References

Aboudi, J., Cederbaum, G., and Elishakoff, I. 1990, "Stability of Viscoelastic Plates by Lyapunov Exponents," *Journal of Sound and Vibrations*, Vol. 139, No. 3, pp. 459-467.

Bender, C. M., and Orszag, S. A., 1984, *Advanced Mathematical Methods for Scientists and Engineers*, McGraw-Hill International Book Company, Singapore.

Bolotin, V. V., 1964, *The Dynamic Stability of Elastic Systems*, Halden Day, San Francisco.

Evan-Iwanovski, R. M., 1965, "On the Parametric Response of Structures," *Applied Mechanics Reviews V-I*, Vol. 18, pp. 699-702.

Evan-Iwanovski, R. M., 1976, *Resonant Oscillations in Mechanical Systems*, Elsevier, Amsterdam.

Glockner, P. g., and Szyszkowski, W., 1987, "On the Stability of Columns Made of Time Dependent Materials," Chapter 23 Vol. 1 - Structures, in *Encyclopedia of Civil Engineering Practice*, (Vol. 1 - Structures, Chapter 23), Technomic Publishing, pp. 577-626.

Matyash, V. I., 1967, "Dynamic Stability of a Hinged Viscoelastic Bar, *Mechanics of Polymers*, Vol. 2, pp. 293-300.

Mclachlan, N. W., 1964, *Theory and Applications of Mathieu Functions*, Dover Publications, New York.

Stevens, K. K., 1966, "On the Parametric Excitation of a Viscoelastic Column," *AIAA Journal*, Vol. 12, pp. 2111-2116.

Szyszkowski, W., and Glockner, P. G., 1985, "The Stability of Viscoelastic Perfect Columns: A Dynamic Approach," *International Journal of Solid and Structures*, Vol. 6, pp. 545-559.

Ziegler H., 1968, *Principles of Structural Stability* Blaisdell Publication Co.

Downloaded 03 May 2010 to 171.66.16.247. Redistribution subject to ASME license or copyright; see http://www.asme.org/terms/Terms_Use.cfm

A General Solution for the Pressurized Elastoplastic Tube[1]

David Durban

Michael Kubi

Faculty of Aerospace Engineering,
Technion—Israel Institute of Technology,
Haifa 32000, Israel

The problem of a thick-walled cylindrical tube subjected to internal pressure is investigated within the framework of continuum plasticity. Material behavior is modeled by a finite strain elastoplastic flow theory based on the Tresca yield function. The deformation pattern is restricted by the plane-strain condition but arbitrary hardening and elastic compressibility are accounted for. A general solution is given in terms of quadratures. The analysis also includes treatment of a second plastic phase, characterized by corner relations, that may develop at the inner boundary. It is shown that the interface between the two plastic regions moves initially outwards and then, beyond a certain strain level, it moves back inwards. Some useful and simple results are given for thin-walled tubes of hardening materials and for thick-walled elastic/perfectly plastic tubes.

1 Introduction

An exact large strain solution for the pressurized elastoplastic tube is known (Durban, 1979) only under the constraint of elastic incompressibility. That solution, based on the Mises flow rule and on the assumption of plane strain behavior, is valid for any stress-strain hardening characteristic. A more general analysis of this type has been given recently by Durban and Kubi (1990) for plastic-orthotropic solids—including the Tresca Material as a special case—but again with the neglect of elastic compressibility. A numerical finite strain solution for pressurized compressible tubes is described in (Durban, 1988b) within the framework of the J_2 deformation theory.

This paper presents a general solution of the tube problem employing the Tresca yield function and its associated flow rule. The deformation pattern is restricted to plane-strain conditions, but arbitary hardening and elastic compressibility are accounted for.

The small strain version of this analysis for elastic/perfectly plastic solids is originally due to Koiter (1953). His solution was later generalized by Bland (1956) to include strain hardening.

The mathematical model is presented in the next section. We show that the governing field equations can be solved by quadratures with the effective stress as the independent variable. Numerical examples, shown in Section 3, reveal the existence of a bursting pressure where the applied load attains a maximum value. That result is supported by an ad hoc thin wall approximation. Conditions for the onset of a second plastic zone, characterized by corner relations, are determined in detail. It is shown that such a zone cannot appear if the initial radii ratio is smaller than a certain critical value (which depends on material parameters). For thicker tubes, the second zone will start at the inner boundary when the axial and circumferential stress components become equal.

A complete analysis of the corner zone is given in Section 4. Tracing the pressure-expansion behavior of the tube has shown that the interface between the two plastic zones moves initially outward. At a certain load level the location of that interface reaches a maximum and then moves back inwards. Eventually, the interface will hit the inner boundary and the whole tube will again be governed by the single phase solution.

Finally, in Section 5, we consider in detail the case of an elastic/perfectly material. This model can be further analyzed, leading to some useful results. In particular, we derive an expression for the asymptotic pressure sustained by a cylindrical cavity embedded in an infinite medium.

2 The Mathematical Model

A circular cylinder is deforming in an axially symmetric pattern, under plane-strain conditions, due to uniform pressure applied at the inner surface. We wish to determine the strain and stress fields within the cylinder, with particular emphasis on the maximum (bursting) pressure attained along the loading history. The constitutive relations employed here are those of an elastoplastic flow theory based on the Tresca yield function. The only active stress components are, with the usual notation, $(\sigma_r, \sigma_\theta, \sigma_z)$ and we assume that, at least initially, the axial component σ_z takes the intermediate value. Thus,

$$\sigma_r < \sigma_z < \sigma_\theta \tag{1}$$

and the definition of the effective stress follows as

$$\sigma_e = \sigma_\theta - \sigma_r. \tag{2}$$

The plastic strain rates are determined by the normality rule

[1]This work is based on a part of a Thesis by Michael Kubi submitted to the Technion, in partial fulfillment of the requirements for the degree of Master of Science.

Contributed by the Applied Mechanics Division of THE AMERICAN SOCIETY OF MECHANICAL ENGINEERS for publication in the JOURNAL OF APPLIED MECHANICS.

Discussion on this paper should be addressed to the Technical Editor, Prof. Leon M. Keer, The Technological Institute, Northwestern University, Evanston, IL 60208, and will be accepted until two months after final publication of the paper itself in the JOURNAL OF APPLIED MECHANICS. Manuscript received by the ASME Applied Mechanics Division, May 10, 1990; final revision, Nov. 15, 1990.

Copyright © 1992 by ASME
Downloaded 03 May 2010 to 171.66.16.247. Redistribution subject to ASME license or copyright; see http://www.asme.org/terms/Terms_Use.cfm

$$\dot{\epsilon}_r^P = \dot{\Lambda}\frac{\partial \sigma_e}{\partial \sigma_r} = -\dot{\Lambda} \quad \dot{\epsilon}_\theta^P = \dot{\Lambda}\frac{\partial \sigma_e}{\partial \sigma_\theta} = \dot{\Lambda} \quad \dot{\epsilon}_z^P = \dot{\Lambda}\frac{\partial \sigma_e}{\partial \sigma_z} = 0 \tag{3}$$

where Λ is some scalar and the superposed dot stands for differentiation with respect to a timelike parameter. Relations (3) are supplemented by the plastic power equivalence relation

$$\sigma_r \dot{\epsilon}_r^P + \sigma_\theta \dot{\epsilon}_\theta^P + \sigma_z \dot{\epsilon}_z^P = \sigma_e \dot{\epsilon}_P \tag{4}$$

where ϵ_P is the total plastic strain and a known function of the effective stress σ_e. Inserting the strain rates (3) in (4) and using (2), we find that $\dot{\Lambda} = \dot{\epsilon}_P$ and the plastic strain rates become

$$-\dot{\epsilon}_r^P = \dot{\epsilon}_\theta^P = \dot{\epsilon}_P \quad \dot{\epsilon}_z^P = 0. \tag{5}$$

Assuming that the elastic strain rates are given by the standard Hookean relations, we get the elastoplastic constitutive connections

$$\dot{\epsilon}_r = \frac{1}{E}\left[\dot{\sigma}_r - \nu\left(\dot{\sigma}_\theta + \dot{\sigma}_z\right)\right] - \dot{\epsilon}_P \tag{6a}$$

$$\dot{\epsilon}_\theta = \frac{1}{E}\left[\dot{\sigma}_\theta - \nu\left(\dot{\sigma}_z + \dot{\sigma}_r\right)\right] + \dot{\epsilon}_P \tag{6b}$$

$$\dot{\epsilon}_z = \frac{1}{E}\left[\dot{\sigma}_z - \nu\left(\dot{\sigma}_r + \dot{\sigma}_\theta\right)\right] \tag{6c}$$

where (E, ν) are the standard elastic constants. Integrating relations (6) along the loading path results in the deformation-theory type constitutive relations

$$\epsilon_r = \frac{1}{E}\left[\sigma_r - \nu\left(\sigma_\theta + \sigma_z\right)\right] - \epsilon_P \tag{7a}$$

$$\epsilon_\theta = \frac{1}{E}\left[\sigma_\theta - \nu\left(\sigma_z + \sigma_r\right)\right] + \epsilon_P \tag{7b}$$

$$\epsilon_z = \frac{1}{E}\left[\sigma_z - \nu\left(\sigma_r + \sigma_\theta\right)\right]. \tag{7c}$$

However, the plane-strain constant ($\epsilon_z = 0$) implies, via (7c),

$$\sigma_z = \nu(\sigma_r + \sigma_\theta). \tag{8}$$

Substituting (8) back in (7*a-b*) gives the two relations

$$\epsilon_r = \frac{1-\nu^2}{E}\left(\sigma_r - \frac{\nu}{1-\nu}\sigma_\theta\right) - \epsilon_P \tag{9a}$$

$$\epsilon_\theta = \frac{1-\nu^2}{E}\left(\sigma_\theta - \frac{\nu}{1-\nu}\sigma_r\right) + \epsilon_P. \tag{9b}$$

The equilibrium equation can be written in the form

$$\frac{d\sigma_r}{dr} + \frac{1+\dfrac{du}{dr}}{r+u}(\sigma_r - \sigma_\theta) = 0 \tag{10}$$

where r is the material (Lagrangian) radial coordinate and u is the displacement. Recalling the definitions of the logarithmic strain components, namely

$$\epsilon_r = \ln\left(1 + \frac{du}{dr}\right) \quad \epsilon_\theta = \ln\left(1 + \frac{u}{r}\right), \tag{11}$$

we can recast (10), with the aid of (2), into the differential relation

$$d\sigma_r = \sigma_e \exp(\epsilon_r - \epsilon_\theta)\frac{dr}{r}. \tag{12}$$

Eliminating u from (11) gives the plane compatibility equation which can be put as

$$d\epsilon_\theta = \left[\exp\left(\epsilon_r - \epsilon_\theta\right) - 1\right]\frac{dr}{r}. \tag{13}$$

Now, we combine (2) with (9*b*) to obtain

$$\epsilon_\theta = (1-\nu^2)\Sigma + (1-2\nu)(1+\nu)\Sigma_r + \epsilon_P \tag{14}$$

where $\Sigma_r = \sigma_r/E$ and $\Sigma = \sigma_e/E$. Alternatively, we can write (14) in the differential form

$$d\epsilon_\theta = (1-\nu^2+\epsilon_P')d\Sigma + (1-2\nu)(1+\nu)d\Sigma_r \tag{15}$$

where the prime denotes differentiation with respect to Σ. Also, from (9*a*) – (9*b*) and (2) we find that

$$\epsilon_r - \epsilon_\theta = -(1+\nu)\Sigma - 2\epsilon_P. \tag{16}$$

Inserting (16) back in (12)–(13) and replacing $d\epsilon_\theta$ in (13) by (15) we obtain a linear algebraic system for the differentials $d\Sigma_r$, $d\Sigma$, dr/r. This can be conveniently regrouped, with Σ as the independent variable, as

$$d\Sigma_r = -F(\Sigma)d\Sigma \tag{17}$$

$$\frac{dr}{r} = -G(\Sigma)d\Sigma \tag{18}$$

where

$$F(\Sigma) = \frac{(1-\nu^2+\epsilon_P')\Sigma}{\exp[(1+\nu)\Sigma + 2\epsilon_P] + (1-2\nu)(1+\nu)\Sigma - 1} \tag{19}$$

$$G(\Sigma) = \frac{F(\Sigma)}{\Sigma}\exp[(1+\nu)\Sigma + 2\epsilon_P]. \tag{20}$$

Equations (17)–(18) admit the quadrature-type solution

$$P = \int_{\Sigma_b}^{\Sigma_a} F(\Sigma)d\Sigma \tag{21}$$

$$\ln\frac{b}{a} = \int_{\Sigma_b}^{\Sigma_a} G(\Sigma)d\Sigma \tag{22}$$

where P is the internal pressure (nondimensionalized with respect to the elastic modulus E), (a, b) are, respectively, the undeformed inner and outer radii, and (Σ_a, Σ_b) are the values of the nondimensionalized effective stress at $r = (a, b)$, respectively. It is now a matter of ease to solve Eqs. (21)–(22), with specified values of P and b/a, for Σ_a and Σ_b. Note that this solution is valid for any strain-hardening response including elastic/plastic characteristics with a definite yield stress. A simple way of tracing the solution of (21)–(22) is through a semi-inverse method whereby a value of Σ_a is assumed first and the corresponding value of Σ_b is then determined from (22), the associated value of the pressure is obtained from (21), and the scheme is then repeated with a new value of Σ_a.

With the solution of (21)–(22) in hand we get the radial profile of the effective stress, from (18), in the implicit form

$$\ln\frac{r}{a} = \int_{\Sigma}^{\Sigma_a} G(\Sigma)d\Sigma. \tag{23}$$

The corresponding profile of the radial stress follows from (17) as

$$\Sigma_r = -P + \int_{\Sigma}^{\Sigma_a} F(\Sigma)d\Sigma \tag{24}$$

while the circumferential stress component is given, via (2), by

$$\Sigma_\theta = \Sigma_r + \Sigma \tag{25}$$

where $\Sigma_\theta = \sigma_\theta/E$ and Σ_r is expressed by (24). The variation of the radial displacement along the radius is obtained from the second of Eqs. (11) and (14) together with the transformation (23). In particular, the inner surface expansion u_a can be written as

Downloaded 03 May 2010 to 171.66.16.247. Redistribution subject to ASME license or copyright; see http://www.asme.org/terms/Terms_Use.cfm

$$\frac{u_a}{a} = \exp\left[\left(\left(1-\nu^2\right)\Sigma_a - (1-2\nu)(1+\nu)P + \epsilon_{Pa}\right]\right] \tag{26}$$

where ϵ_{Pa} is the value of ϵ_P at $r=a$.

The analysis presented so far is valid only as long as assumption (1) holds. The case where (1) fails will be discussed later.

3 Examples and Further Analysis

Sample curves for the pressure expansion behavior are displayed in Figs. 1(*a*)-(*b*) for three representative metals and two radii ratios. The uniaxial stress-strain curves of these solids are described by the Ramberg-Osgood relation

$$\epsilon = \Sigma + K\Sigma^n \leftrightarrow \epsilon_P = K\Sigma^n \tag{27}$$

where (K, n) are material parameters. The specific values of the material constants used in the computation are

Stainless Steel

$$K = 5.78 \cdot 10^4 \quad n = 3 \quad E = 20.6 \cdot 10^{10}\frac{N}{m^2} \quad \nu = 0.3$$

Aluminum 7075 T6

$$K = 3.94 \cdot 10^{21} \quad n = 10.9 \quad E = 7.24 \cdot 10^{10}\frac{N}{m^2} \quad \nu = 0.32$$

Steel X-200

$$K = 8.85 \cdot 10^{66} \quad n = 34.1 \quad E = 20.8 \cdot 10^{10}\frac{N}{m^2} \quad \nu = 0.27.$$

Failure of assumption (1) has been detected only with the steel X-200 for the thicker tube with $b/a = 8$. At a certain load level σ_z becomes equal to σ_θ on the inner boundary (Fig. 1(*b*)).

The most striking result of Figs. 1(*a*)-1(*b*) is, as expected, the existence of a maximum (bursting) pressure. If that point of instability is attained while assumption (1) is still valid throughout the entire body, then we can use the rate form of (21)-(22) to facilitate a useful relation between Σ_a and Σ_b at the maximum pressure. Thus, from (21)-(22),

$$\dot{P} = F(\Sigma_a)\dot{\Sigma}_a - F(\Sigma_b)\dot{\Sigma}_b \tag{28a}$$

$$0 = G(\Sigma_a)\dot{\Sigma}_a - G(\Sigma_b)\dot{\Sigma}_b \tag{28b}$$

but at bursting $\dot{P}=0$, and relations (28*a*-*b*) may be combined to give, with the aid of (20),

$$\frac{1}{\Sigma_a}\exp\left[(1+\nu)\Sigma_a + 2\epsilon_{Pa}\right] = \frac{1}{\Sigma_b}\exp\left[(1+\nu)\Sigma_b + 2\epsilon_{Pb}\right] \tag{29}$$

where (ϵ_{Pa}, ϵ_{Pb}) denote the respective boundary values of ϵ_P at (a, b). Each pair of solutions (Σ_a, Σ_b) of (29) determines via (21)-(22) the corresponding values of $P_{\max}$ and b/a. This procedure quite easily generates the variation of $P_{\max}$ with the radii ratio as shown in Fig. 2 for the aluminum alloy.

For sufficiently thin tubes it is possible to derive a simple approximate expression for the bursting pressure. Denoting through thickness averages by the subscript o, we get from (21)-(22) the consistent first-order expansions

$$P = F(\Sigma_0)(\Sigma_a - \Sigma_b) \quad \ln\frac{b}{a} = G(\Sigma_0)(\Sigma_a - \Sigma_b). \tag{30}$$

Combining (30) with (20) gives

$$P = \left(\ln\frac{b}{a}\right)\Sigma_0 \exp[-(1+\nu)\Sigma_0 - 2\epsilon_{Po}] \tag{31}$$

where ϵ_{Po} is the through thickness average of ϵ_P. Neglecting the elastic terms and using the power-law relation we can rewrite (31) in the form

$$P = \left(\ln\frac{b}{a}\right)\Sigma_0 \exp(-2K\Sigma_o^n). \tag{32}$$

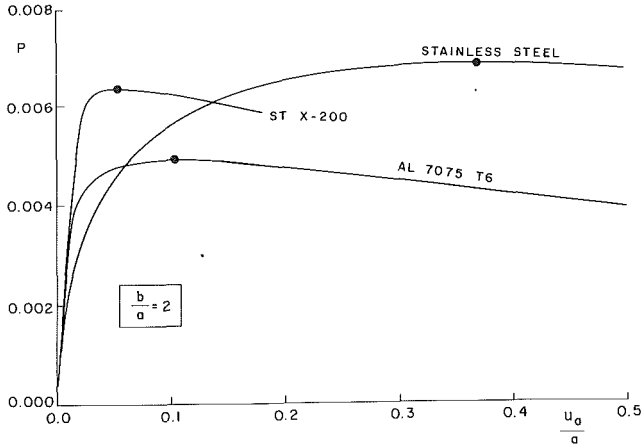

Fig. 1(*a*) Pressure expansion curves for three metals with $b/a = 2$. The bursting pressure is indicated by black circles.

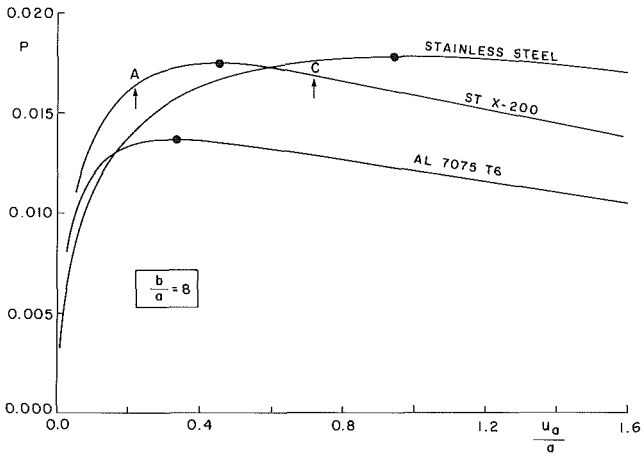

Fig. 1(*b*) Pressure expansion curves for three metals with $b/a = 8$. The bursting pressure is indicated by black circles. The arrows indicate initiation and termination of the second plastic zone for the ST X-200.

Expression (32) has a maximum when

$$\Sigma_o = 2^{-1/n}\Sigma_u \tag{33}$$

where $\Sigma_u = (1/nK)^{1/n}$ is the uniaxial ultimate (necking) stress. It follows that the bursting pressure is given approximately by

$$P_{\max} = (2e)^{-1/n}\left(\ln\frac{b}{a}\right)\Sigma_u. \tag{34}$$

Comparison of (34) with the exact results reveals (Fig. 2) a reasonable agreement even for tubes of moderate thickness.

Within the framework of small strain plasticity and for elastic/linear-hardening response it becomes possible to express integrals (21)-(22) in terms of simple functions. The integrands (19)-(20) are then reduced to the form

$$F(\Sigma) = \frac{(1-\nu^2+\epsilon_P')\Sigma}{2(1-\nu^2)\Sigma + 2\epsilon_P} \tag{35a}$$

$$G(\Sigma) = \frac{F(\Sigma)}{\Sigma} \tag{35b}$$

with

$$\epsilon_P = 0 \quad \text{for } \Sigma \le \frac{Y}{E}$$

$$\epsilon_P = \left(\frac{E}{E_T} - 1\right)\left(\Sigma - \frac{Y}{E}\right) \quad \text{for } \Sigma > \frac{Y}{E} \tag{36}$$

Downloaded 03 May 2010 to 171.66.16.247. Redistribution subject to ASME license or copyright; see http://www.asme.org/terms/Terms_Use.cfm

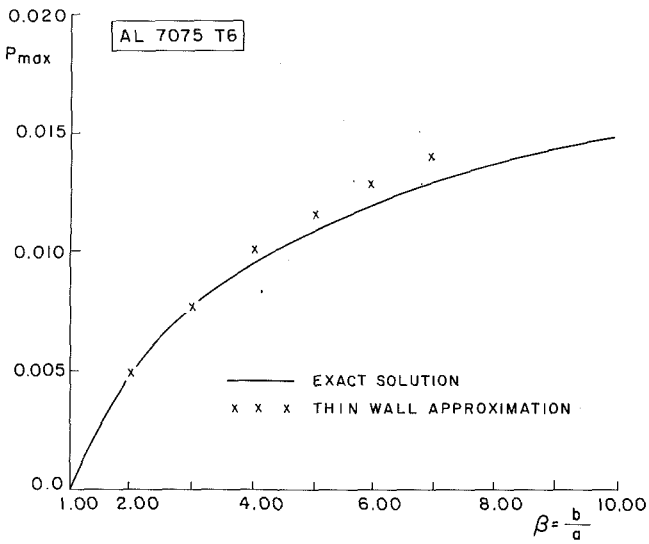

Fig. 2 Variation of bursting pressure P_{max} with radii ratio for AL 7075 T6

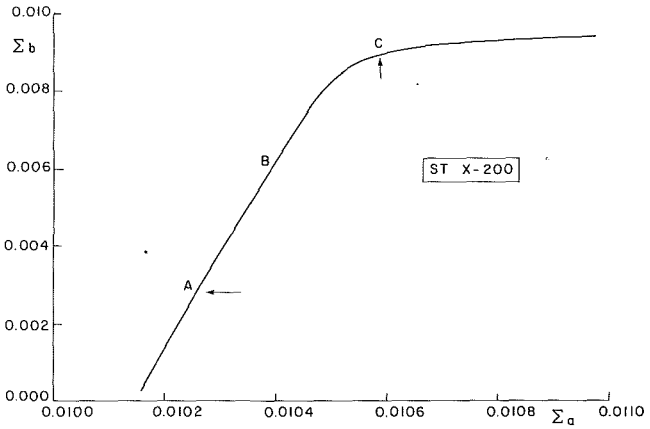

Fig. 3(*a*) Values of effective stress at the boundaries upon initiation of a second plastic zone; ST X-200

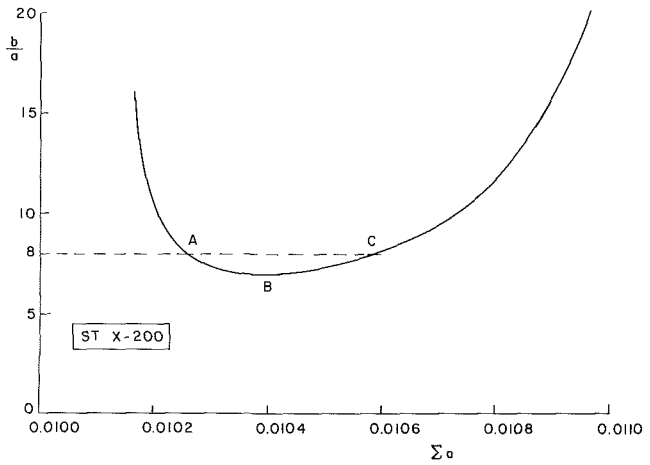

Fig. 3(*b*) Variation of the effective stress at the inner boundary, upon initiation of a second plastic zone, with radii ratio *b/a*. STX-200

where Y is the uniaxial yield stress and E_T is the constant tangent modulus. The integration of (21)–(22) in conjunction with (35)–(36) is essentially due to Bland (1956).

A numerical study over a wide range of geometries and material parameters has indicated that assumption (1) is likely to fail first at the inner boundary when σ_z becomes equal to σ_θ. This happens only for sufficiently thick tubes whose initial radii ratio b/a exceeds a certain critical value. That observation is supported by Koiter's (1953) small strain analysis for elastic/perfectly plastic materials.

Relations (2) and (8) are still valid at the moment where Σ_z $(=\sigma_z/E)$ becomes equal to Σ_θ at $r=a$. It follows that if assumption (1) fails at $r=a$, then the corresponding pressure will be

$$P=\frac{1-\nu}{1-2\nu}\,\Sigma_a. \tag{37}$$

Combining Eqs. (37) with (21)–(22) we find that failure of (1) is determined by the pair (Σ_a, Σ_b) that solves the system

$$\Sigma_a=\frac{1-2\nu}{1-\nu}\int_{\Sigma_b}^{\Sigma_a} F(\Sigma)\,d\Sigma \tag{38a}$$

$$\ln\frac{b}{a}=\int_{\Sigma_b}^{\Sigma_a} G(\Sigma)\,d\Sigma. \tag{38b}$$

Numerical solutions of Eqs. (38) have shown that for given material parameters, there is a critical value of radii ratio b/a below which there is no solution to that system. The exact value of the critical radii ratio can be determined by treating (38*b*) as a minimum problem subjected to the constraint (38*a*). Typical results for the pair (Σ_a, Σ_b) that solves (38*a*) and the corresponding values of b/a from (38*b*) are shown in Figs. 3(*a*)–3(*b*) for the steel X-200. The critical radii ratio for that material is $b/a=6.96$. For smaller radii ratios, assumption (1) remains valid along the entire axisymmetric loading path. With $b/a=8$, assumption (1) will fail when the pair (Σ_a, Σ_b) reaches point A on the curve of Fig. 3(*a*) (see also Fig. 3(*b*)). The corresponding value of the internal pressure, from (37), is shown in Fig. 1(*b*).

The critical radii ratio, below which assumption (1) remains valid along the entire straining path, is highly dependent on material properties, particularly on Poisson's ratio ν. For the aluminum 7075, for example, we get $b/a\approx 43$ for the critical radii ratio. Of course, Eqs. (38) have no solution when the material is incompressible ($\nu = 1/2$) and assumption (1) remains always valid.

4 The Corner Solution

For load levels beyond (37) a new plastic zone will develop and gradually progress outwards from the inner boundary $r = a$ to the current interface $r = r_i$. Our earlier analysis—equations (17)–(18) in particular—is still valid within the outer zone $r_i \le r \le b$, but a different solution is required for the inner zone. That plastic phase is characterized by the corner relations

$$\Sigma_\theta=\Sigma_z \quad \Sigma=\Sigma_\theta-\Sigma_r=\Sigma_z-\Sigma_r \tag{39}$$

so that the normality rule (3) cannot be applied.

The strain rate components may be written in the form,

$$\dot\epsilon_r=\dot\Sigma_r-\nu(\dot\Sigma_\theta+\dot\Sigma_z)+\dot\epsilon_r^P \tag{40a}$$

$$\dot\epsilon_\theta=\dot\Sigma_\theta-\nu(\dot\Sigma_z+\dot\Sigma_r)+\dot\epsilon_\theta^P \tag{40b}$$

$$\dot\epsilon_z=\dot\Sigma_z-\nu(\dot\Sigma_r+\dot\Sigma_\theta)-(\dot\epsilon_r^P+\dot\epsilon_\theta^P) \tag{40c}$$

in view of the plastic incompressibility constraint $\dot\epsilon_r^P + \dot\epsilon_\theta^P + \dot\epsilon_z^P = 0$. Plastic power equivalence (4) together with (39) give here

$$\dot\epsilon_r^P=-\dot\epsilon_P. \tag{41}$$

Downloaded 03 May 2010 to 171.66.16.247. Redistribution subject to ASME license or copyright; see http://www.asme.org/terms/Terms_Use.cfm

Combining (41) with the plane-strain condition $\dot{\epsilon}_z = 0$ and using the relation $\dot{\Sigma}_\theta = \dot{\Sigma}_z$ from (39), we find that the plane-strain rates (40*a*–*b*) become

$$\dot{\epsilon}_r = \dot{\Sigma}_r - 2\nu\dot{\Sigma}_\theta - \dot{\epsilon}_P \tag{42a}$$

$$\dot{\epsilon}_\theta = 2(1-\nu)\dot{\Sigma}_\theta - 2\nu\dot{\Sigma}_r + \dot{\epsilon}_P. \tag{42b}$$

Equations (42*a*)–(42*b*) can now be integrated along the loading history from the onset of the second plastic zone up to the current state. Thus, with the asterisk denoting initial values,

$$\epsilon_r - \epsilon_r^* = \Sigma_r - \Sigma^* - 2\nu(\Sigma_\theta - \Sigma_\theta^*) - (\epsilon_P - \epsilon_P^*) \tag{43a}$$

$$\epsilon_\theta - \epsilon_\theta^* = 2(1-\nu)(\Sigma_\theta - \Sigma_\theta^*) - 2\nu(\Sigma_r - \Sigma_r^*) + (\epsilon_P - \epsilon_P^*). \tag{43b}$$

However, the initial values in (43) must also obey relations (9) together with condition $\nu\Sigma_r^* = (1-\nu)\Sigma_\theta^*$ which signals failure of assumption (1). It follows that (43*a*)–(43*b*) are reduced to the form

$$\epsilon_r = (1-2\nu)\Sigma_r - 2\nu\Sigma - \epsilon_P \tag{44a}$$

$$\epsilon_\theta = 2(1-2\nu)\Sigma_r + 2(1-\nu)\Sigma + \epsilon_P. \tag{44b}$$

Turning back to the equations of equilibrium (10) and compatibility (13) we obtain, with the aid of (44), the two differential equations

$$r\frac{d\Sigma_r}{dr} = \Sigma \exp(\epsilon_r - \epsilon_\theta) \tag{45}$$

$$r\frac{d\Sigma}{dr} = \frac{[1+2(1-2\nu)\Sigma]\exp(\epsilon_r - \epsilon_\theta) - 1}{2(1-\nu) + \epsilon_P'} \tag{46}$$

where, from (44)

$$\epsilon_r - \epsilon_\theta = -(1-2\nu)\Sigma_r - 2\Sigma - 2\epsilon_P. \tag{47}$$

The behavior of the stresses within the second plastic zone $a \le r \le r_i$ is determined by the solution of Eqs. (45)–(46). Of course, that solution has to be matched, at the interface $r = r_i$, with the integrals of (17)–(18). A simple numerical procedure is to guess first a value for Σ_b and write the solution for the outer zone in the form

$$\Sigma_{ri} = -\int_{\Sigma_b}^{\Sigma_i} F(\Sigma)d\Sigma \quad \ln\frac{b}{r_i} = \int_{\Sigma_b}^{\Sigma_i} G(\Sigma)d\Sigma \tag{48}$$

where Σ_{ri} and Σ_i are the interface values of Σ_r and Σ. Also, at the interface a relation of type (37) must hold, namely

$$\Sigma_{ri} = -\frac{1-\nu}{1-2\nu}\Sigma_i. \tag{49}$$

Now, for a given value of Σ_b it is a matter of ease to find from (48)–(49) the corresponding interface values of (Σ_{ri}, Σ_i, r_i). The latter are then used as initial conditions for a numerical integration of (45)–(46) from the interface up to the inner boundary. This will determine the load level P that corresponds to the initial guess of Σ_b. The whole procedure is then repeated for a new value of Σ_b. The stress and strain fields within the entire body follow without difficulty. The inner boundary expansion, for example, can be evaluated directly from (44*b*) by

$$\frac{u_a}{a} = \exp[2(1-\nu)\Sigma_a - 2(1-2\nu)P + \epsilon_{Pa}]. \tag{50}$$

This agrees with (26) at the onset of the second plastic phase.

The solution of Eqs. (48)–(49) will obviously coincide with curves of the type shown in Figs. 3(*a*)–3(*b*), but with the transformation

$$\Sigma_a \to \Sigma_i \quad \frac{b}{a} \to \frac{b}{r_i}. \tag{51}$$

Consider, for example, the specific case of a steel X-200 tube with a radii ratio $b/a = 8$. The second plastic phase is initiated when Σ_a reaches the value of point A in Figs. 3(*a*)–3(*b*). With further loading, the interface values move along these curves from A to B which marks the maximum extent of the interface.

A question now arises in regard to continuous deformation beyond point B where r_i attains its highest possible value $(r_i)_{\max}$. The pattern suggested here, based on a few numerical investigations, is that the interface begins to move back towards the inner boundary. Denoting by r_{ii} the current location of the interface, during its movement back towards $r = a$, we have to consider the behavior within a third plastic zone bounded by $r_{ii} \le r \le (r_i)_{\max}$. We have found that assumption (1) is again valid for the third zone so that the effective stress is again given by (2) and the strain rates are exactly those of (6).

Integrating (6*a*–*b*) and using the plane-strain constraint $\dot{\Sigma}_z = \nu(\dot{\Sigma}_r + \dot{\Sigma}_\theta)$ from (6*c*), gives

$$\epsilon_r - \epsilon_r^{**} = (1-\nu^2)(\Sigma_r - \Sigma_r^{**}) - \nu(1+\nu)(\Sigma_\theta - \Sigma_\theta^{**}) - (\epsilon_P - \epsilon_P^{**}) \tag{52a}$$

$$\epsilon_\theta - \epsilon_\theta^{**} = (1-\nu^2)(\Sigma_\theta - \Sigma_\theta^{**}) - \nu(1+\nu)(\Sigma_r - \Sigma_r^{**}) + (\epsilon_P - \epsilon_P^{**}) \tag{52b}$$

where a double asterisk stands for the initial values. The latter, however, must also obey relations (44*a*–*b*) as well as the condition $\nu\Sigma_r^{**} = (1-\nu)\Sigma_\theta^{**}$ which signals renewal of the validity of assumption (1). It follows that the strains (52) within the third zone are

$$\epsilon_r = (1-\nu^2)\Sigma_r - \nu(1+\nu)\Sigma_\theta - \epsilon_P \tag{53a}$$

$$\epsilon_\theta = (1-\nu^2)\Sigma_\theta - \nu(1+\nu)\Sigma_r + \epsilon_P. \tag{53b}$$

Equations (53) are identical with the single zone relations (9*a*)–(9*b*). Thus, the first and third zones are described by the same equations over the range $r_{ii} \le r \le b$. The inward movement at $r = r_{ii}$ is along the curves BC in Figs. 3(*a*)–3(*b*). Beyond point C the behavior is again governed by the single zone Eqs. (17)–(18). However, the bursting pressure is located before the interface r_{ii} reaches the inner boundary (see the ST X-200 curve in Fig. 1(*b*)).

5 The Elastic/Perfectly Plastic Model

A useful idealization of the uniaxial stress-strain relation is described by the elastic/plastic model where $\epsilon_P = 0$ for $\Sigma \le \Sigma_Y = Y/E$, and $\Sigma \equiv \Sigma_Y$ at higher strain levels. The basic differential relations (17)–(18) now take separate forms in the elastic and plastic regions. Thus, within the elastic phase

$$F(\Sigma) = \frac{(1-\nu^2)\Sigma}{\exp[(1+\nu)\Sigma] + (1-2\nu)(1+\nu)\Sigma - 1} \tag{54}$$

$$G(\Sigma) = \frac{F(\Sigma)}{\Sigma}\exp[(1+\nu)\Sigma] \tag{55}$$

is in agreement, except for a notational change, with Durban's (1988a) analysis for elastically nonlinear tubes. For common metals, $\Sigma_Y \ll 1$ and (54)–(55) may be approximated by

$$F(\Sigma) = \frac{1}{2}\quad G(\Sigma) = \frac{1}{2\Sigma}. \tag{56}$$

Within the plastic phase Σ remains constant and equal to Σ_Y so that $d\Sigma = 0$ but $\epsilon_P' d\Sigma \to d\epsilon_P$. Relations (17)–(18) are therefore reduced to the form

$$d\Sigma_r = -f(\epsilon_P)d\epsilon_P \tag{57}$$

$$\frac{dr}{r} = -g(\epsilon_P)d\epsilon_P \tag{58}$$

where

$$f(\epsilon_P) = \frac{\Sigma_Y}{\exp[(1+\nu)\Sigma_Y + 2\epsilon_P] + (1-2\nu)(1+\nu)\Sigma_Y - 1} \tag{59}$$

$$g(\epsilon_P) = \frac{f(\epsilon_P)}{\Sigma_Y}\exp[(1+\nu)\Sigma_Y + 2\epsilon_P]. \tag{60}$$

Downloaded 03 May 2010 to 171.66.16.247. Redistribution subject to ASME license or copyright; see http://www.asme.org/terms/Terms_Use.cfm

However, for $\Sigma_Y \ll 1$ we can replace (59)–(60) by the two approximate equations

$$f(\epsilon_P) = \frac{\Sigma_Y}{\exp(2\epsilon_P) - 1 + \Delta} \tag{61}$$

$$g(\epsilon_P) = \frac{\exp(2\epsilon_P)}{\exp(2\epsilon_P) - 1 + \Delta} \tag{62}$$

where

$$\Delta = 2(1-\nu^2)\Sigma_Y. \tag{63}$$

Now integrating relations (17)–(18) with (56) over the elastic phase, and relations (57)–(58) with (61)–(62) over the plastic phase, results in the two equations

$$P = \frac{1}{2}(\Sigma_Y - \Sigma_b) + \frac{1}{2}\Sigma_Y \ln \frac{Z - 1 + \Delta}{\Delta Z} \tag{64}$$

$$\left(\frac{b}{a}\right)^2 = \frac{Z - 1 + \Delta}{2(1-\nu^2)\Sigma_b} \tag{65}$$

where

$$Z = \exp(2\epsilon_{Pa}) \tag{66}$$

and ϵ_{Pa} is the value of the effective plastic strain at the inner boundary $r = a$. Note that at the elastic/plastic interface, $\Sigma = \Sigma_Y$ and $\epsilon_P = 0$. The location of that interface, denoted by the material coordinate $r = c$, follows from (18) and the first of (56) in the form

$$\left(\frac{b}{c}\right)^2 = \frac{\Sigma_Y}{\Sigma_b}. \tag{67}$$

Of course, in the purely elastic state, where $\Sigma_a < \Sigma_Y$, Eqs. (64)–(65) are replaced by

$$P = \frac{1}{2} \qquad (\Sigma_a - \Sigma_b)\left(\frac{b}{a}\right)^2 = \frac{\Sigma_a}{\Sigma_b} \tag{68}$$

as obtained directly from (17)–(18) with (56). Relations (68) may be conjoined to give, with $\Sigma_a = \Sigma_Y$, the standard expression for the pressure at the onset of yielding, namely

$$P = \left[1 - \left(\frac{a}{b}\right)^2\right]\frac{\Sigma_Y}{2}. \tag{69}$$

For load levels above (69), the plastic zone will spread outward from the inner radius to the current elasto/plastic interface $r = c$. Eventually, the internal pressure will reach a maximum value which can be evaluated from (64)–(65); substituting Σ_b from (65) in (64) gives

$$P = \frac{\Sigma_Y}{2}\left[1 - \frac{(a/b)^2}{\Delta}(Z - 1 + \Delta) + \ln \frac{Z - 1 + \Delta}{\Delta Z}\right]. \tag{70}$$

Since Z is a monotonically increasing parameter, we equate the derivative dP/dZ to zero when P attains its highest value. The leads to the quadratic equation

$$Z^2 - (1-\Delta)Z - \Delta(1-\Delta)\left(\frac{b}{a}\right)^2 = 0 \tag{71}$$

with the solution

$$Z = \frac{1}{2}\left[1 - \Delta + \sqrt{(1-\Delta)^2 + 4\Delta(1-\Delta)(b/a)^2}\right]. \tag{72}$$

Inserting (72) back in (70) gives the maximum pressure $P_{\max}$. If the parameter $\Delta(b/a)^2$ is much smaller than 1, we may replace (72) by the approximation

$$Z = 1 + \Delta[(b/a)^2 - 1] \tag{73}$$

with the maximum pressure

$$P_{\max} = \frac{\Sigma_Y}{2} \ln \frac{(b/a)^2}{1 + \Delta[(b/a)^2 - 1]}. \tag{74}$$

For sufficiently thin tubes, relation (74) is reduced to $P_{\max} = \Sigma_Y \ln(b/a)$ in agreement with the limit of (34) as $n \to \infty$.

At complete plastification, $\Sigma_b = \Sigma_Y$ and the corresponding plastic strain at the inner boundary is, by (65),

$$Z = 1 - \Delta + \Delta(b/a)^2. \tag{75}$$

Simple algebraic considerations show that this value of Z is always higher than the maximum pressure value (72). It follows that the bursting pressure will be attained while an external elastic zone is still active near the outer boundary.

The results derived so far in this section are valid only as long as σ_z remains the intermediate stress component. Assumption (1) will fail here when, from (37), the inner pressure reaches the value

$$P = \frac{1-\nu}{1-2\nu}\Sigma_Y. \tag{76}$$

Combining condition (76) with (70) gives

$$\left(\frac{a}{b}\right)^2 = \frac{\Delta}{Z - 1 + \Delta}\left(\ln \frac{Z - 1 + \Delta}{\Delta Z} - \frac{1}{1-2\nu}\right). \tag{77}$$

This equation determines the onset of a second plastic phase. Typical curves, evaluated from (77), show in Fig. 4 the corresponding values of Z for given material properties and geometry. Note that for the limiting case of a cylindrical cavity embedded in an infinite medium, we have from (77) with $a/b \to 0$,

$$Z = \frac{1-\Delta}{1 - \Delta \exp\left(\dfrac{1}{1-2\nu}\right)}. \tag{78}$$

The value of Z that corresponds to the minimum radii ratio for which (77) has a solution can be determined by equating to zero the derivative of (77) with respect to Z. For small Δ this essentially gives

$$Z = 1 + \Delta\left[\exp \frac{2(1-\nu)}{1-2\nu} - 1\right], \tag{79}$$

and the critical radii ratio follows as

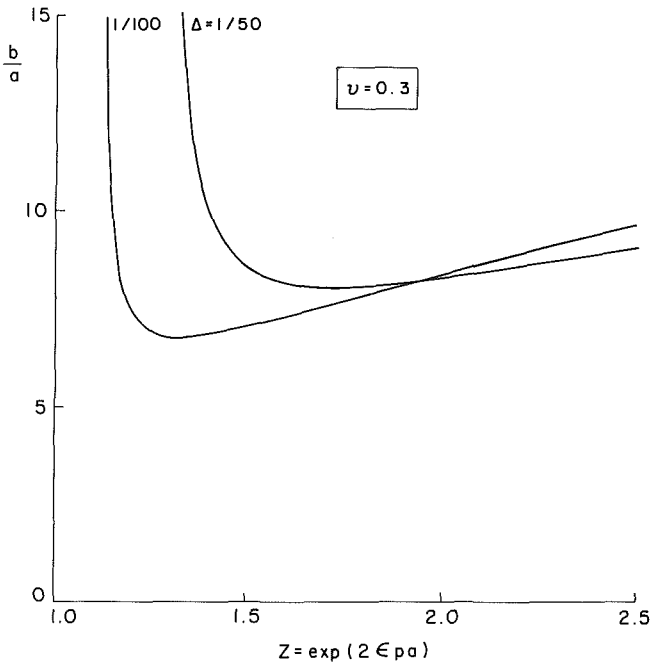

Fig. 4 Values of the effective plastic strain at the inner boundary, upon initiation of a second plastic zone, for elastic/perfectly plastic solids; $\Delta = 2(1-\nu^2)\Sigma_Y$

Downloaded 03 May 2010 to 171.66.16.247. Redistribution subject to ASME license or copyright; see http://www.asme.org/terms/Terms_Use.cfm

$$\frac{b}{a}=\exp\frac{1-\nu}{1-2\nu}+\frac{\Delta}{2}\exp\frac{3(1-\nu)}{1-2\nu}. \tag{80}$$

Equation (80) agrees at the limit of $\Delta\to 0$ with Koiter's (1953) result for the small strain model.

Turning to the second plastic phase, bounded by $a \le r \le r_i$, we have Eqs. (45)–(47) for the elastic/perfectly plastic model in the form

$$r\frac{d\Sigma_r}{dr}=\Sigma_Y\exp(\epsilon_r-\epsilon_\theta) \tag{81}$$

$$r\frac{d\epsilon_P}{dr}=[1+2(1-2\nu)\Sigma_Y]\exp(\epsilon_r-\epsilon_\theta)-1 \tag{82}$$

with

$$\epsilon_r-\epsilon_\theta=-(1-2\nu)\Sigma_r-2\Sigma_Y-2\epsilon_P. \tag{83}$$

Substituting the exponential terms from (81) in (82) and integrating gives the plastic strain

$$\epsilon_P=\epsilon_{Pa}+\frac{1+2(1-2\nu)\Sigma_Y}{\Sigma_Y}(\Sigma_r+P)-\ln\frac{r}{a}. \tag{84}$$

A further substitution of (84) into (83) leads to the solution of (81) in the form

$$\exp(k\Sigma_r)-\exp(-kP)=\frac{1}{2}kC\Sigma_Y\left(\frac{r^2}{a^2}-1\right) \tag{85}$$

where

$$k=\frac{2+5(1-2\nu)\Sigma_Y}{\Sigma_Y}$$

$$C=\exp\left[-2\left(\epsilon_{Pa}+\Sigma_Y+\frac{1+2(1-2\nu)\Sigma_Y}{\Sigma_Y}P\right)\right]. \tag{86}$$

Relations (84)–(86) describe the behavior of the second plastic phase and can be used, together with the single phase solution, to trace the entire loading history of the tube.

As a simple application of this analysis, consider the pressurized cylindrical cavity embedded in an infinite medium. Here, $b\to\infty$ and relation (65) gives — with the inner radius (a) replaced by r_i — that $\Sigma_b=0$. Thus, from (64) with P replaced by $(-\Sigma_{ri})$,

$$-\Sigma_{ri}=\frac{1}{2}\Sigma_Y+\frac{1}{2}\Sigma_Y\ln\frac{Z_i-1+\Delta}{\Delta Z_i}, \tag{87}$$

where $Z_i=\exp(2\epsilon_{Pi})$ is the interface value of Z. Recalling, however, that at the interface, by (76)

$$\Sigma_{ri}=-\frac{1-\nu}{1-2\nu}\Sigma_Y, \tag{88}$$

we find that

$$\epsilon_{Pi}=\frac{1}{2}\ln\frac{1-\Delta}{1-\Delta\exp\left(\frac{1}{1-2\nu}\right)} \tag{89}$$

For the second plastic phase we have, from (84)–(85)

$$\epsilon_{Pi}=\epsilon_{Pa}+\frac{1+2(1-2\nu)\Sigma_Y}{\Sigma_Y}(\Sigma_{ri}+P)-\ln\frac{r_i}{a} \tag{90}$$

$$\exp(k\Sigma_{ri})-\exp(-kP)=\frac{1}{2}kC\Sigma_Y\left(\frac{r_i^2}{a^2}-1\right). \tag{91}$$

Inserting the interface radial stress from (88) in (90)–(91) and using (89) we arrive at a relation between P and r_i/a. This gives, at the limit of $r_i\to\infty$, the asymptotic pressure sustained by a cylindrical cavity (except a few minor terms which have been neglected for the sake of simplicity)

$$P_{\text{asympt}}=\frac{\Sigma_Y}{2}\left[1-\ln\frac{\Sigma_Y}{2}-\ln\left(4(1-\nu^2)\times\left(1-\exp\left(-\frac{1}{1-2\nu}\right)\right)\right)\right]. \tag{92}$$

For an incompressible material ($\nu=1/2$), expression (92) is reduced to

$$P_{\text{asympt}}=\frac{\Sigma_Y}{2}\left(1-\ln\frac{3}{2}\Sigma_Y\right), \tag{93}$$

which is in agreement with (64) at the limit of $\Sigma_b\to 0$, $Z\to\infty$, $\nu=1/2$.

It is interesting to note that (92) has a similar structure to Hill's (1950) result for a Mises solid (for an independent deformation theory derivation see Durban (1988b))

$$P_{\text{asympt}}=\frac{\Sigma_Y}{\sqrt{3}}\left[1-\ln\frac{\Sigma_Y}{\sqrt{3}}-\ln(5-4\nu)\right]. \tag{94}$$

For common metals, the relative decrease in the asymptotic pressure due to elastic compressibility is negligible for both the Tresca (92) and the Mises (94) solids. The essential difference between the two results is just due to the scaling factor $2/\sqrt{3}$ of Σ_Y.

References

Bland, D. R., 1956, "Elastoplastic Thick-Walled Tubes of Work-Hardening Material Subject to Internal and External Pressures and to Temperature Gradients," *J. Mech. Phys. Solids*, Vol. 4, pp. 209–229.

Durban, D., 1979, "Large Strain Solution for Pressurized Elasto/Plastic Tubes," ASME JOURNAL OF APPLIED MECHANICS, Vol. 46, pp. 228–230.

Durban, D., 1988a, "A Finite Strain Axially-Symmetric Solution for Elastic Tubes," *Int. J. Solids Struc.*, Vol. 24, pp. 675–682.

Durban, D., 1988b, "Finite Straining of Pressurized Compressible Elasto-Plastic Tubes," *Int. J. Engng. Sci.*, Vol. 26, pp. 939–950.

Durban, D., and Kubi, M., 1990, "Large Strain Analysis for Plastic-Orthotropic Tubes," *Int. J. Solids Struc.*, Vol. 26, pp. 483–495.

Hill, R., 1950, *The Mathematical Theory of Plasticity*, Clarendon Press, Oxford, U.K.

Koiter, W. T., 1953, "On Partially Plastic Thick-Walled Tubes," *Biezeno Anniv. Vol., H. Stain*, Haarlem-Antwerpen, pp. 232–251.

Downloaded 03 May 2010 to 171.66.16.247. Redistribution subject to ASME license or copyright; see http://www.asme.org/terms/Terms_Use.cfm

Modeling of Creep of Misaligned Short-Fiber Reinforced Ceramic Composites

John R. Pachalis
Assoc. Mem. ASME

Tsu-Wei Chou
Mem. ASME

Center for Composite Materials and
Department of Mechanical Engineering,
University of Delaware,
Newark, DE 19716

A model is developed to predict the steady-state creep behavior of misaligned short-fiber-reinforced ceramic matrix composites. The approach is based on an advanced shear-lag model and uses the multiaxial creep law for the fibers and matrix. The analysis incorporates some unique characteristics of ceramic matrix composites, such as the fiber/matrix interface sliding effect, shear and axial loads carried by the matrix, and the fact that both the fibers and matrix creep at elevated temperatures. Several parameters are varied to determine their effect on the creep behavior.

1 Introduction

Ceramics are emerging as attractive engineering materials; however, their main disadvantage is the low fracture toughness or resistance to crack propagation. Reinforcement of brittle ceramics with continuous or discontinuous fibers is intended to remedy this situation (Chou et al., 1986). Although considerable success has been achieved in enhancing the performance of ceramic matrix composites, their properties at elevated temperature are much less understood. The present paper examines one aspect of these problems, namely, the creep behavior of a misaligned short-fiber-reinforced ceramic composite.

Several analyses have been reported (Kelly and Street, 1972; Mileiko, 1970; McLean, 1972; Lilholt, 1985; de Silva, 1968; McLean, 1985; Min and Crossman, 1982; Mangat and Azari, 1985; Tang, 1970; Hong et al., 1988; Lou and Schapery, 1971; Schapery, 1969) for modeling the steady-state creep deformation of fiber-reinforced composites. Most of these works are concerned with polymer and metal matrix composites. Many analyses assume that there is a perfect bond at the fiber/matrix interface (Mileiko, 1970; McLean, 1972; Lilholt, 1985; de Silva, 1968; Min and Crossman, 1982; Tang, 1970; Hong et al., 1988; Lou and Schapery, 1971; Schapery, 1969). However, in ceramic matrix composites, it is often desirable to minimize the chemical bonds at the fiber/matrix interface in order to improve the composite toughness (Marshall and Evans, 1985). Thus, sliding will occur along the interface. Next, the fibers are often assumed to be rigid and do not creep (Mileiko, 1970; McLean, 1972; McLean, 1985; Min and Crossman, 1982; Hong et al., 1988). Other researchers assume that there is a fiber creeping length where the fiber and matrix are creeping at the same constant rate. Outside of this length, the fiber is assumed to be rigid (Kelly and Street, 1972). Also, the existing analyses in the literature often assume that the matrix does not carry the applied load; the function of the matrix is merely for transferring the load to the fibers through its stress relaxation due to creep (Mileiko, 1970; Lilholt, 1985; Sambell et al., 1972). The purpose of this paper is, therefore, to expand on the new approach first initiated by Kim (1987), Pachalis and Chou (1990, 1989), and Wang and Chou (1990) for the better understanding of the creep behavior of ceramic matrix composites.

The basic approach used here is based on an advanced shear-lag model (Fukuda and Chou, 1981). This model assumes that both the fibers and matrix can creep. It takes into account that there could be a fiber creeping length, over which both the fiber and matrix are creeping at the same rate. The matrix is assumed to be capable of carrying axial loads, as well as shear loads. It is also assumed that there is sliding along the fiber/matrix interface. Next, different geometrical arrangements for the same volume fraction are taken into account. Lastly, both the fibers and matrix are assumed to be elastically rigid; therefore, elastic deformations are ignored in the analysis.

2 Analysis

The stress-strain rate behavior of materials under uniaxial creep conditions can be approximated by many different mathematical forms. The form used here is the power law, which has been shown to match experimental data very well (Carter and Davis, 1984). This relation is given by

$$\dot{\epsilon} = A(\sigma/G)^n \exp(-Q/RT) \tag{1}$$

where A and n are constants, Q is the activation energy, R is the gas constant, T is the absolute temperature, G is the shear modulus, $\dot{\epsilon}$ is the strain rate, and σ is the applied stress. For a given temperature, the above constants can be combined to give, for the fiber and matrix,

$$\dot{\epsilon}_f = (\sigma_f/C_f)^{n_f} \tag{2}$$

$$\dot{\epsilon}_m = (\sigma_m/C_m)^{n_m} \tag{3}$$

Contributed by the Applied Mechanics Division of THE AMERICAN SOCIETY OF MECHANICAL ENGINEERS for publication in the JOURNAL OF APPLIED MECHANICS.

Discussion on this paper should be addressed to the Technical Editor, Prof. Leon M. Keer, The Technological Institute, Northwestern University, Evanston, IL 60208, and will be accepted until two months after final publication of the paper itself in the JOURNAL OF APPLIED MECHANICS. Manuscript received by the ASME Applied Mechanics Division, Apr. 5, 1990; final revision, Aug. 22, 1990.

Copyright © 1992 by ASME
Downloaded 03 May 2010 to 171.66.16.247. Redistribution subject to ASME license or copyright; see http://www.asme.org/terms/Terms_Use.cfm

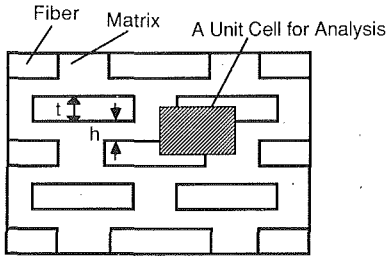

Fig. 1 Schematic of a composite system

where C_f, C_m, n_f, and n_m are constants, and the subscripts f and m denote, respectively, fiber and matrix.

The equations relating stress and strain rate for a material under a multiaxial state of stress depend on the equation used for the case of uniaxial stress. The multiaxial creep law corresponding to the power law is given as (Odquist, 1974; Hult, 1966; Boyle and Spence, 1983; Finnie and Heller, 1959)

$$\dot{\epsilon}_{ij} = \frac{3}{2}\left(\frac{\sigma_e}{C}\right)^{n-1}\frac{S_{ij}}{C} \tag{4}$$

where S_{ij} is the stress deviation tensor, C is either C_f or C_m given in Eqs. (2) and (3), and σ_e is the effective stress.

In ceramic matrix composites, the bond between the fiber and matrix is more of a frictional one than a chemical one. Therefore, sliding can occur along the interface. The relationship between the shear stress, τ, and the normal pressure, P, at the fiber/matrix interface is (Halliday and Resnick, 1981)

$$\tau = -\mu P \tag{5}$$

where μ is the coefficient of sliding friction, and the negative sign is present because the numerical value of P is negative. In order to calculate this pressure, the contractions in the radial direction at the interface must be taken into account. Consider a fiber embedded in a matrix. Due to the presence of the fiber, the matrix will not creep as much in the radial direction as it would if the fiber were absent, and due to the matrix, the fiber will creep more in the radial direction than it would if the matrix was absent. Due to the fact that the matrix wants to creep more than the fiber will let it, a pressure, P, is built up at the fiber/matrix interface. Thus, P has to be solved for such that the creep rates of the fiber and matrix in the radial direction are equal. Using Eq. (4), the equality of strain rates for the fiber and the matrix gives

$$\frac{3}{2}\left(\sigma_f^2 + P^2 - \sigma_f P + 3(\mu P)^2\right)^{(n_f-1)/2}\left(\frac{-\frac{1}{3}\sigma_f + \frac{2}{3}P}{C_f^{n_f}}\right)$$
$$= \frac{3}{2}\left(\sigma_m^2 + P^2 + \sigma_m P + 3(\mu P)^2\right)^{(n_m-1)/2}\left(\frac{-\frac{1}{3}\sigma_m - \frac{2}{3}P}{C_m^{n_m}}\right). \tag{6}$$

This equation is an implicit equation in P, and can be solved numerically.

The two-dimensional schematic of a unidirectional short-fiber composite is shown in Fig. 1. For the analysis of the composite, a unit cell is used, which is the smallest repeating unit of the composite. The unit cell cuts through the middle of two fibers, each of thickness t, and the distance between the sides of the neighboring fibers is given as h. For a given volume fraction, there are two different possible fiber arrangements: one in which the fibers overlap (Model A), and one in which the fibers don't overlap (Model B), as shown in Fig. 2(*a*).

2.1 Model A. In this model, the fibers overlap. Due to symmetry, only half of the unit cell needs to be considered. It is necessary to devise a way to handle the matrix in front of

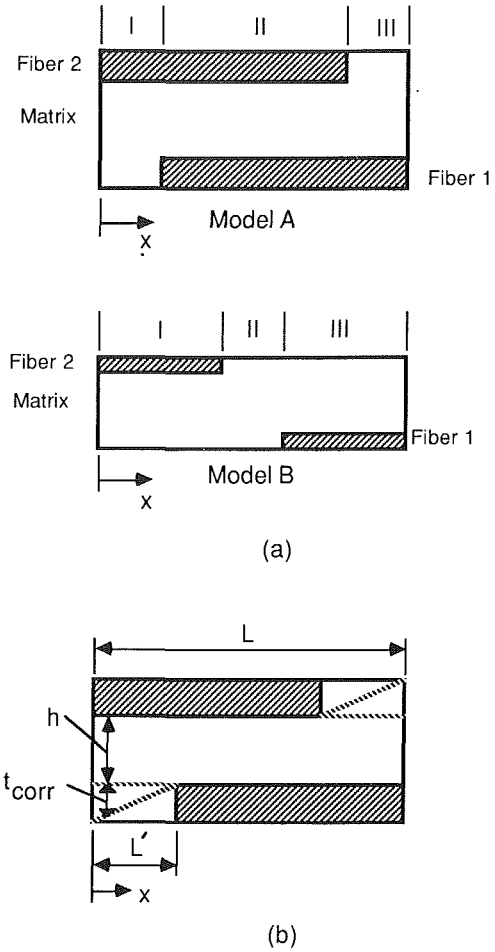

Fig. 2 (*a*) Different models for the same volume fraction; (*b*) the correction factor for Domain I of Model A.

the fiber ends. It is assumed here that there is no stress transfer from the matrix to the fiber at the fiber end surface, so there will be zero stress in the matrix and fiber at this end surface. However, away from the fiber ends, the matrix should be able to carry part of the applied tensile load. Thus, an effective area is defined over which the matrix between fiber ends can carry the load, as shown in Fig. 2(*b*). The width of this additional matrix area that is assumed to carry the load is given by t_{corr},

$$t_{corr} = (t/2)(1 - x/L') \tag{7}$$

where L' is the distance from the beginning of the unit cell to the fiber-1 tip.

Using a free-body diagram for elements in Domain I, the equilibrium equations are

$$\frac{d\sigma_2}{dx}\left(\frac{t}{2}\right) + \tau_2 = 0$$
$$\frac{d\sigma_m}{dx}t_m + \frac{dt_m}{dx}\sigma_m - \tau_2 = 0 \tag{8}$$

where $t_m = h + t_{corr}$, $\tau_2 = -\mu P_2$, $P_2 = P_2(\sigma_2, \sigma_m)$, and higher-order terms with respect to dx in the equations have been neglected. (P_2 is obtained from Eq. (6).)

2.2 Solution Procedure. The fourth-order Runge-Kutta method (Greenberg, 1978) is chosen to solve the above equations. In this method, the equations under consideration have to be of the form

$$y' = f(x, \bar{y}) \tag{9}$$

Downloaded 03 May 2010 to 171.66.16.247. Redistribution subject to ASME license or copyright; see http://www.asme.org/terms/Terms_Use.cfm

where y' is the derivative of the dependent variable y with respect to x, and $\bar{y}$ can be one or more dependent variables. From Eq. (8), the set of equations that are in the Runge-Kutta form for Domain I are

$$\sigma_2' = f_1(\sigma_2, \sigma_m) = \frac{2\mu P_2}{t}$$
$$\sigma_m' = g_1(x, \sigma_2, \sigma_m) = \left(\frac{t}{2L'}\,\sigma_m - \mu P_2\right)\left(\frac{2L'}{2L'h + tL' - tx}\right). \tag{10}$$

Since the Runge-Kutta method is a solution technique for initial value problems, and the present problem is a boundary value one, it is necessary to guess at some of the initial conditions until the boundary conditions are satisfied. The initial value for σ_2 is guessed at, and the value for σ_m is obtained from a force balance:

$$\sigma_c(h + t) = \sigma_2\left(\frac{t}{2}\right) + \sigma_m\left(h + \frac{t}{2}\right) \tag{11}$$

where σ_c is the applied stress to the composite. Domain I is broken down into a number of nodes, and the solution follows the standard Runge-Kutta procedure.

The set of equations that are in the Runge-Kutta form for Domain II can be obtained in a similar manner. The initial conditions for this domain are that σ_2 and σ_m are known from the end of Domain I, and $\sigma_1 = 0$ at the fiber tip. Domain II is broken down into a number of nodes and the solution is similar to that for Domain I. The initial guess for σ_2 in Domain I is iterated over until the symmetry condition at the center of the unit cell is matched.

2.3 Fiber Creeping Length. Under a given loading situation, material properties, and geometric parameters, there exists the possibility of a fiber creeping length, defined here as the length over which the fiber and matrix are creeping at the same (but not necessarily constant) rate. For the case where, in Domain II, there is a region where fiber 2 and the matrix are creeping at the same rate, and fiber 1 is creeping at a different rate, a new set of governing equations is needed. These governing equations are

$$\frac{d\sigma_s}{dx}\left(h + \frac{t}{2}\right) + \tau_1 = 0$$
$$\frac{d\sigma_1}{dx}\left(\frac{t}{2}\right) - \tau_1 = 0. \tag{12}$$

The stress on the fiber 2/matrix system is

$$\sigma_s = F_s/(h + t/2) \tag{13}$$

where F_s, the force acting on this system, is

$$F_s = \sigma_2\left(\frac{t}{2}\right) + \sigma_m(h). \tag{14}$$

Since this region is in the fiber creeping length, $P_2 = 0$, and $\dot{\epsilon}_2 = \dot{\epsilon}_m = \dot{\epsilon}_s$. Substituting the appropriate quantities into Eq. (12), the system of equations in the Runge-Kutta form becomes

$$\dot{\epsilon}_s' = f_s(\sigma_m, \sigma_1) = \mu P_1 \Big/ \left(\frac{hC_m}{n_m}(\dot{\epsilon}_s)^{(1/n_m - 1)} + \frac{tC_f}{2n_f}(\dot{\epsilon}_s)^{(1/n_f - 1)}\right)$$
$$\sigma_1' = g_s(\sigma_m, \sigma_1) = \frac{-2\mu P_1}{t} \tag{15}$$

where, because this is in the fiber creeping length.

$$\dot{\epsilon}_s = (\sigma_m/C_m)^{n_m}. \tag{16}$$

The initial conditions are that $\dot{\epsilon}_s$ is known from Domain I and $\sigma_1 = 0$.

2.4 Model B. In Model B, shown in Fig. 2(*a*), the fibers do not overlap. The solution procedure for the stress distribution, and therefore the strain rates, is similar to that of Model A.

In both Models A and B, the average strain rate of the composite is taken to be the average strain rate of the unit cell, and is found from

$$\dot{\epsilon}_c = \frac{2}{L}\int_0^{L/2} \dot{\epsilon}_m(x)\,dx \tag{17}$$

where L is the length of the unit cell. This equation does not explicitly use $\dot{\epsilon}_f$ because, due to the sliding at the fiber/matrix interface, the matrix is the only continuous phase in the unit cell. The effect of the fibers is implicit in the composite creep rate since the calculation of $\dot{\epsilon}_m$ depends in part on the fiber properties.

3 Off-Axis Fibers

Consider a model of a composite with misaligned fibers in which all of the fibers lie in the x-y plane at an angle θ to the x-axis. The x_1-direction is parallel to the fiber axis, and the x_2-direction is perpendicular to the fibers. The applied stress on the composite is σ_x. For a uniaxial stress in the x-direction, the stresses relating to the x_1, x_2 axes can be obtained by a stress transformation from the x, y axes (Beer and Johnston, 1981). The problem is now broken down into three components: the unit cell subjected to the three applied stresses separately. The case with the normal stress σ_{x_1} applied along the axis of the fibers is solved the same way as in the aligned case, described in the first part of this paper. For the problem with an applied shear stress $\tau_{x_1x_2}$, a constant state of shear stress is assumed inside the unit cell.

The case of the normal stress σ_{x_2} being applied perpendicular to the fibers is solved by using a "spring" model, where the fibers and matrix in each domain are represented by springs in the x_2-direction. The strain rate of the unit cell in the x_2-direction is assumed to be the same at any x_1-location. The determination of the stresses for Models A and B is described as follows.

In Model A, since the cross-sectional areas which support the x_2-direction load in any domain are the same for the fiber and matrix, the stresess in the fiber(s) and matrix in each domain will be the same. Due to symmetry, the stress in Domain I equals the stress in Domain III. Denoting the x_2-direction stress in Domain I as σ_a and the stress in Domain II as σ_b, the force balance equation becomes

$$\sigma_{x_2}L = 2\sigma_a(L - L_f) + \sigma_b(2L_f - L) \tag{18}$$

where L_f is the length of a fiber in the unit cell. The strain rates in each domain are equal, so

$$\left(\frac{\sigma_a}{C_f}\right)^{n_f}\frac{t}{2} + \left(\frac{\sigma_a}{C_m}\right)^{n_m}\left(h + \frac{t}{2}\right) = \left(\frac{\sigma_b}{C_f}\right)^{n_f}t + \left(\frac{\sigma_b}{C_m}\right)^{n_m}h. \tag{19}$$

Solving Eq. (18) for σ_b and putting this into Eq. (19), yields an equation where σ_a can be solved for numerically. The solution for the stresses in Model B can be found using a similar analysis.

At each node in the fibers and matrix, the values of $\sigma_{x_1}(N)$, $\sigma_{x_2}(N)$, and $\tau_{x_1x_2}(N)$ are found from the three previous problems, and the three strain rates, $\dot{\epsilon}_{x_1}(N)$, $\dot{\epsilon}_{x_2}(N)$, and $\dot{\epsilon}_{x_1x_2}(N)$ are found from the three stresses using the multiaxial creep law. The area weighted average of the strain rates of the respective computational nodes in the unit cell are calculated, and the average strain rate of the unit cell in the direction of the applied load, and thus the strain rate of the composite, is given as (Beer and Johnston, 1981)

$$\dot{\epsilon}_c = \dot{\epsilon}_{x_1}^{\text{ave}}\cos^2\theta + \dot{\epsilon}_{x_2}^{\text{ave}}\sin^2\theta - 2\dot{\epsilon}_{x_1x_2}^{\text{ave}}\sin\theta\cos\theta. \tag{20}$$

3.1 Random Fibers. For composites with fibers at dif-

Downloaded 03 May 2010 to 171.66.16.247. Redistribution subject to ASME license or copyright; see http://www.asme.org/terms/Terms_Use.cfm

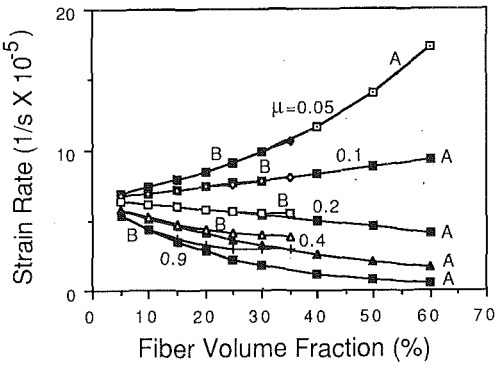

Fig. 3 Effect of the coefficient of sliding friction and volume fraction on the creep rate (Models A and B); L/D = 30, σ_{app} = 100 MPa

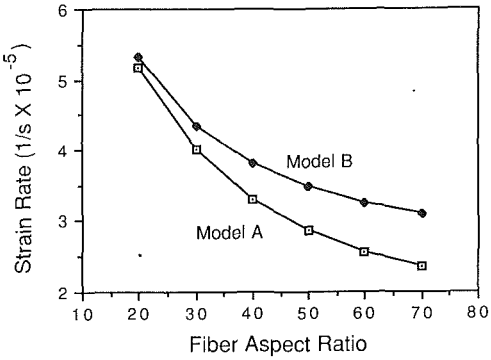

Fig. 5 The effect of the aspect ratio on the composite creep rate: V_f = 25 percent, μ = 0.34, σ_{app} = 100 MPa

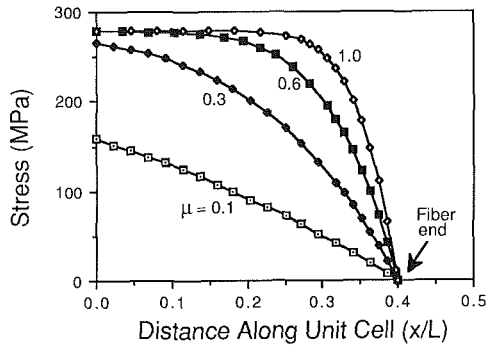

Fig. 4 The effect of the coefficient of sliding friction on the stress distribution; L/D = 30, V_f = 25 percent, σ_{app} = 100 MPa

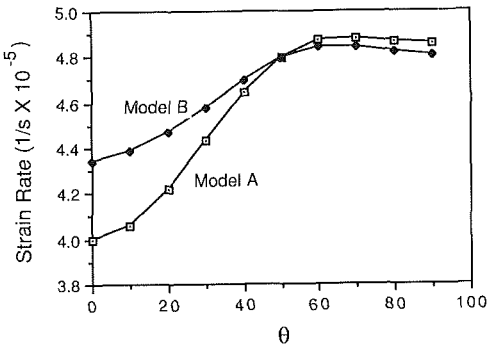

Fig. 6 The effect of the misorientation angle on the composite creep rate; V_f = 25 percent, L/D = 30, μ = 0.34, σ_{app} = 100 MPa

ferent angles, the average creep rate of the composite depends on the fiber orientation distribution, and, for a two-dimensional distribution, is given by (Chou and Nomura, 1980–81)

$$\dot{\epsilon}_c = \int_0^{\pi/2} n(\theta)\, \dot{\epsilon}_c(\theta)\, d\theta \tag{21}$$

where $n(\theta)$ is the probability density function of fiber orientation, and

$$\int_0^{\pi/2} n(\theta)\, d\theta = 1. \tag{22}$$

For completely random fibers, $n(\theta) = 2/\pi$.

4 Material Properties

An SiC whisker-reinforced Al_2O_3 composite has been selected as the model system of this study. There has been a wide range of data reported for the creep properties of SiC and Al_2O_3 (Chokshi and Porter, 1985; Carter and Davis, 1984; Chokshi and Porter, 1986; El-Aiat et al., 1981; Carter et al., 1984; Jou et al., 1986). The alumina used in the work of Chokshi and Porter (1985) exhibited a stress exponent (n_m) of 1.6, and a value of 41,295 MPa $- s^{1/n_m}$ for C_m was obtained from a graph of stress versus strain rate for the alumina. Carter and Davis (1984) reported a stress exponent of 5.7 for SiC. This value was used for n_f here, and a value of 2428 MPa $- s^{1/n_f}$ for C_f was calculated from the creep data of the same SiC.

5 Numerical Results

Numerical calculations have been performed using the material properties discussed above. No comparison was made between theoretical predictions and experiments because of the lack of tensile creep data. The values of several parameters were varied to show their effect on the creep rate. The combined effects of the coefficient of sliding friction and fiber volume fraction are shown in Fig. 3. At low frictional values, the reinforcing effect of the fibers diminishes, and the composite starts to behave like a matrix with holes in it. As the fiber volume fraction increases, and thus the volume fraction of these "holes," the creep rate increases because the available matrix for carrying the load is decreasing. As the coefficient of friction varies from 0.1 to 0.2, the load transfer to the fibers increases to the point where the fibers contribute to the strengthening of the composite (as the fiber volume fraction increases, the creep rate decreases). As the coefficient of sliding friction increases, its effect on the creep rate decreases. It is also seen that Models A and B match each other very well at low frictional values, but start to deviate at higher frictional values as the volume fraction increases.

Figure 4 shows the stress distribution in a fiber from Model B for a range of friction values. If the coefficient of friction is very low, the fiber is not carrying much of the load, but as the friction increases, a larger portion of the fiber is carrying a greater amount of the applied load. The limiting value of the creep rate occurs as the length of the fiber that is carrying the maximum load approaches the fiber length. Next, as can be seen in Fig. 5, the fiber aspect ratio affects the creep rate more for low values of the ratio than for larger ones.

Figure 6 shows the effect that the angle of misorientation of the fibers has on the creep rate of unidirectional short-fiber composites. For both models, as the angle increases, so does the creep rate, up to about 60 degrees. After this point, the creep rate decreases by a small amount, but stays relatively constant. The creep rate doesn't increase beyond 60 degrees, probably because the model overestimates the fiber role in the strain rate when a stress is applied in the x_2-direction.

Downloaded 03 May 2010 to 171.66.16.247. Redistribution subject to ASME license or copyright; see http://www.asme.org/terms/Terms_Use.cfm

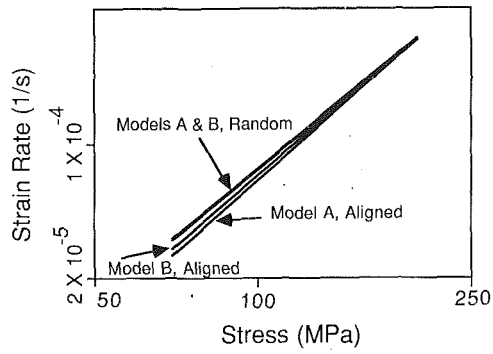

Fig. 7 Comparison of Models A and B: aligned and random; V_f = 20 percent; L/D = 30, μ = 0.34

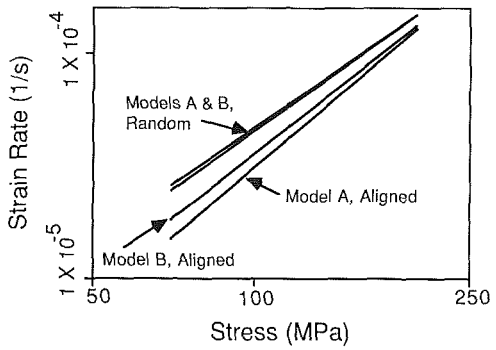

Fig. 8 Comparison of Models A and B: aligned and random; V_f = 20 percent, L/D = 30, μ = 0.7

Figure 7 shows the creep curves for Models A and B with both aligned and random fibers. Models A and B with aligned fibers predict basically the same creep rate, with a slope of 1.7. Models A and B with random fibers also predict the same creep rate, with a slope of 1.6, just slightly less than the aligned case. Figure 8 again shows the creep curves for both models, only at a higher coefficient of sliding friction (0.7 compared with 0.34). From this graph, it is seen that there is more of a difference between Models A and B with aligned fibers, and also between the aligned and random fiber cases. For aligned fibers, the predicted slope for Model A is 2.1, and for Model B is 1.9. The slope for Models A and B with random fibers is 1.7.

6 Conclusions and Discussions

An analysis based on an advanced shear-lag model has been performed on the creep behavior of short-fiber-reinforced ceramic composites. This analysis makes several major assumptions:

1 Both the fibers and matrix are assumed to creep, with the matrix being able to carry both the shear and axial loads.

2 The shear stress at the fiber/matrix interface is due to friction and the differences in contraction of the fiber and matrix.

3 Different fiber arrangements in the unit cell for the same volume fraction have been examined.

4 The possibility of a fiber creeping length is taken into account.

The effect on the creep rate of the fiber volume fraction, fiber aspect ratio, the coefficient of sliding friction, and the misorientation angle has been shown. It is seen that the creep rate is most sensitive to low values of the coefficient of sliding friction, fiber volume fraction, and fiber aspect ratio, and from misorientation angles from 10 deg–60 deg. The results were not compared with experimental data for several reasons. First, this analysis assumes that the composite is under pure tension, whereas the experimental data are from bending tests, in which both tension and compression are present. Also, this work assumes that the matrix and fibers are perfect and have no damage, and thus neglects matrix flaws at elevated temperature. Other uncertainties in this analysis are the correct fiber geometric parameters to use, as well as the material properties, of which a wide range has been reported in the literature.

Acknowledgments

The authors wish to thank the support of the Center for Composite Materials of the University of Delaware (J.R.P.) and the Air Force Office of Scientific Research (TWC; Contract No. AFOSR-87-0383, Dr. L. J. Schioler is the Program Manager).

References

Beer, F. P., and Johnston, E. R., Jr., 1981, *Mechanics of Materials*, McGraw-Hill, New York, pp. 289–340.

Boyle, J. T., and Spence, J., 1983, *Stress Analysis for Creep*, Butterworths, London.

Carter, C. H., Jr., and Davis, R. F., 1984, "Kinetics and Mechanisms of High Temperature Creep in Silicon Carbide: I—Reaction-Bonded," *Journal of the American Ceramic Society*, Vol. 67, pp. 409–417.

Carter, C. H., Jr., Davis, R. F., and Bentley, J., 1984, "Kinetics and Mechanisms of High-Temperature Creep in Silicon Carbide: II—Chemically Vapor Deposited," *Journal of the American Ceramic Society*, Vol. 67, pp. 732–740.

Chokshi, A. H., and Porter, J. R., 1985, "Creep Deformation of an Alumina Matrix Composite Reinforced with Silicon Carbide Whiskers," *Journal of the American Ceramic Society*, Vol. 68, pp. C-144–C-145.

Chokshi, A. H., and Porter, J. R., 1986, "Analysis of Concurrent Grain Growth During Creep of Polycrystalline Alumina," *Journal of the American Ceramic Society*, Vol. 69, pp. C-37–C-39.

Chou, T.-W., and Nomura, S., 1980–81, "Fibre Orientation Effects on the Thermoelastic Properties of Short-Fibre Composites," *Fibre Science and Technology*, Vol. 14, pp. 279–291.

Chou, T.-W., McCullough, R. L., and Pipes, R. B., 1986, "Composites," *Scientific American*, Vol. 254, pp. 192–203.

de Silva, A. R. T., 1968, "A Theoretical Analysis of Creep in Fiber Reinforced Composites," *Journal of the Mechanics and Physics of Solids*, Vol. 16, pp. 169–186.

El-Aiat, M. M., et al., 1981, "High-Temperature Conductivity and Creep of Polycrystalline Al_2O_3 Doped with Fe and/or Ti," *Journal of the American Ceramic Society*, Vol. 64, pp. 174–182.

Finnie, I., and Heller, W. R., 1959, *Creep of Engineering Materials*, McGraw-Hill, New York.

Fukuda, H., and Chou, T.-W., 1981, "An Advanced Shear-Lag Model Applicable to Discontinuous Fiber Composites," *Journal of Composite Materials*, Vol. 15, pp. 79–91.

Greenberg, M. D., 1978, *Foundations of Applied Mathematics*, Prentice-Hall, Englewood Cliffs, N.J., pp. 477–485.

Halliday, D., and Resnick, R., 1981, *Fundamentals of Physics*, John Wiley and Sons, New York, pp. 79–82.

Hong, S. H., et al., 1988, "Internal Stress Superplasticity in 2024 Al-SiC Whisker Reinforced Composites," *Journal of Composite Materials*, Vol. 22, pp. 102–123.

Hult, J. A. H., 1966, *Creep in Engineering Structures*, Blaisdell Publ. Co., Waltham, Mass.

Jou, Z. C., Kuo, S.-Y., and Virkar, A. V., 1986, "Elevated-Temperature Creep of Silicon Carbide—Aluminum Nitride Ceramics: Role of Grain Size," *Journal of the American Ceramic Society*, Vol. 69, pp. C-279–C-281.

Kelly, A., and Street, K. N., 1972, "Creep of Discontinuous Fiber Composites: II—Theory for the Steady State," *Proceedings of the Royal Society, London*, Vol. A328, pp. 283–293.

Kim, J., 1987, "Thermo-Mechanical Behavior of High Temperature Fiber Composites," Ph.D. Dissertation, University of Delaware, Newark, Del.

Lilholt, H., 1985, "Creep of Fibrous Composite Materials," *Composites Science and Technology*, Vol. 22, pp. 277–294.

Lou, Y. C., and Schapery, R. A., 1971, "Viscoelastic Characterization of a Nonlinear Fiber-Reinforced Plastic," *Journal of Composite Materials*, Vol. 5, pp. 208–234.

Mangat, P. S., and Azari, M. M., 1985, "A Theory for the Creep of Steel Fibre Reinforced Cement Matrices Under Compression," *Journal of Material Science*, Vol. 20, pp. 1119–1133.

Marshall, D. B., and Evans, A. G., 1985, "Failure Mechanism in Ceramic-Fiber/Ceramic-Matrix Composites," *Journal of the American Ceramic Society*, Vol. 68, pp. 225–231.

McLean, D., 1972, "Viscous Flow of Aligned Composites," *Journal of Material Science*, Vol. 7, pp. 98–104.

Downloaded 03 May 2010 to 171.66.16.247. Redistribution subject to ASME license or copyright; see http://www.asme.org/terms/Terms_Use.cfm

McLean, M., 1985, "Modeling of Creep Deformation in Metal Matrix Composites," *Proceedings of the Fifth International Conference on Composite Materials* (ICCM-V), pp. 37–51.

Mileiko, S. T., 1970, "Steady State Creep of a Composite Material with Short Fibres," *Journal of Material Science*, Vol. 5, pp. 254–261.

Min, B. K., and Crossman, F. W., 1982, "Analysis of Creep for Metal Matrix Composites," *Journal of Composite Materials*, Vol. 16, pp. 188–203.

Odquist, F. K. G., 1974, *Mathematical Theory of Creep and Creep Rupture*, Clarendon Press, Oxford, U.K.

Pachalis, J. R., Kim, J., and Chou, T.-W., 1990, "Modeling of Creep of Aligned Short Fiber Reinforced Ceramic Composites," *Composites Science and Technology*, Vol. 37, pp. 329–346.

Pachalis, J. R., and Chou, T.-W., 1989, "Creep Behavior of Short Fiber Reinforced Ceramic Matrix Composites," *Proceedings of the Seventh International Conference on Composite Materials* (ICCM-VII), in press.

Sambell, R. A. J., Bowen, D. H., and Phillips, D. C., 1972, "Carbon Fibre Composites with Ceramic and Glass Matrices: Part I—Discontinuous Fibers," *Journal of Material Science*, Vol. 7, pp. 663–675.

Schapery, R. A., 1969, "On the Characterization of Nonlinear Viscoelastic Materials," *Polymer Engineering Science*, Vol. 9, pp. 295–310.

Tang, S., 1970, "Steady State Creep in Laminated Beams," *Journal of Composite Materials*, Vol. 4, pp. 138–143.

Wang, Y. R., and Chou, T.-W., 1990, "Creep Analysis of Short Fiber Reinforced Ceramic Composites," submitted for publication.

Downloaded 03 May 2010 to 171.66.16.247. Redistribution subject to ASME license or copyright; see http://www.asme.org/terms/Terms_Use.cfm

The Optimal Mode and an Approximate Expression of Final Displacement in Dynamic Plastic Response of Structures

Zhu-ping Huang
Department of Mechanics,
Peking University,
Beijing 100871, China

Li-zhi Sun
Laboratory of Fatigue and
Fracture of Materials,
Institute of Metal Research,
Academia Sinica,
Shen-yang 110015, China

The paper is concerned with the dynamic response of impulsively loaded rigid-perfectly plastic structures. By combining the mode approximation technique with the upper and the lower bound theorems, we have derived a set of sequential inequalities on the final displacement of the structure. This can be applied to give a reasonable explanation for the criterion of choosing an optimal mode proposed by Symonds (1980). In addition, an approximate expression of the final displacement of the structure is suggested in cases where the "mode approximation" apparently works poorly. Finally, the suggested expression is also illustrated by examples.

1 Introduction

The dynamic plastic response of structures is a subject which has both practical and theoretical importance. As many problems of practical interest are intractable, it is often preferable to develop some approximate methods for preliminary design purposes. There are mainly two useful approximate methods for estimating the final displacement of a structure under dynamic load:

(1) The bounding method deals with the upper and/or lower displacement bounds which, in ideal circumstances, provide estimates closely bracketing the exact value. An upper displacement bound theorem for impulsively loaded plastic structures was first established by Martin (1964), and a lower displacement bound theorem was given by Morales and Nevill (1970). These theorems have since been extended to cover more general situations. Recently a new lower displacement bound theorem was proposed by Huang (1985), which can be used for any arbitrary "kinematically admissible field." However, when seeking information about the approximate final displacement distribution, all these bound theorems are not convenient to apply.

(2) Mode approximation technique proposed by Martin and Symonds (1966) yields an approximate solution which satisfies all field equations but not the precise initial conditions. Although there are many contributions devoted to developing this technique (e.g., see review article by Huang and Wang, 1985) and to look for the optimal mode (Symonds, 1980; Slutsky et al., 1982), further study on the criterion of choosing "the best" mode according to different initial conditions is still appropriate.

In this paper, we shall combine the mode approximation technique with the bounding theorems to yield a set of sequential inequalities on the final displacement of a structure. They not only can be applied to give a reasonable explanation on the criterion of choosing an optimal mode proposed by Symonds (1980) but they also provide a suggested approximate expression on the final displacement distribution of a structure when the "mode approximation" technique apparently works poorly. The validity of the suggested expression is also examined by two examples.

2 Basic Properties of the Mode Form Solution

In the mode approximation technique, the velocity field of a structure may be written as

$$\dot{u}_i^*(\mathbf{x},t) = \dot{r}(t)\phi_i^*(\mathbf{x}) \tag{1}$$

where $\phi_i^*(\mathbf{x})$, $(i = 1, 2, 3)$ is a vector "shape function" (for a permanent mode-form solution, it is time independent), and the scalar $\dot{r} = \dot{r}(t)$ is the corresponding "rate of amplitude growth" with $\dot{r} \geq 0$. The permanent mode-form solution satisfies all field equations and boundary conditions with the exception of initial conditions. It has been proved, using infinitesimal analysis, that such a solution does exist if a rigid-perfectly plastic structure is subjected to constant loading (cf. Huang and Wang, 1985). For the case when the structure is subjected to impulsive loading, the aforementioned mode-form solutions can be obtained from the functional $\Pi(\phi_i)$ (see Eq. (15) of next section) by minimizing $\Pi(\phi_i)$ or by taking $\Pi(\phi_i)$ to be a stationary extremum. As was discussed by Lee (1972), the former is termed "principal mode" and the latter is termed "higher mode." Examples may be found in the articles of Jones et al. (1976, 1978) for beam problems. Apart from very

Contributed by the Applied Mechanics Division of THE AMERICAN SOCIETY OF MECHANICAL ENGINEERS for publication in the JOURNAL OF APPLIED MECHANICS.

Discussion on this paper should be addressed to the Technical Editor, Prof. Leon M. Keer, The Technological Institute, Northwestern University, Evanston, IL 60208, and will be accepted until two months after final publication of the paper itself in the JOURNAL OF APPLIED MECHANICS. Manuscript received by the ASME Applied Mechanics Division, Nov. 9, 1989; final revision, Mar. 4, 1991.

Copyright © 1992 by ASME
Downloaded 03 May 2010 to 171.66.16.247. Redistribution subject to ASME license or copyright; see http://www.asme.org/terms/Terms_Use.cfm

limited velocity fields which converge onto the higher mode, most of the initial velocity fields will finally converge to the one corresponding to the principal mode form. Thus, for obtaining "the best" approximate final displacement of the structure, we sometimes have to choose and/or make use of higher mode form which depends on the initial velocity distribution. This brings up the question of optimal mode choice (Symonds, 1980; Slutsky et al., 1982) which will be discussed in the next section.

Let us now consider, in general, the mode-form solution for an impulsively loaded plastic structure. The kinetic energy of its mode-form solution can be expressed as

$$K^*(t)=\frac{1}{2}\left(\int_v \rho\phi_i^*\phi_i^* dv\right)(\dot{r})^2=(\dot{r})^2 L_* \tag{2}$$

where ρ is the density and $L_* = \frac{1}{2}\int_v \rho\phi_i^*\phi_i^* dv$. For a rigid-perfectly plastic structure, the rate of dissipated internal energy corresponding to the mode-form solution, $\dot{u}_i^*$, can be written as $D(\dot{\epsilon}_{ij}^*) = \dot{r}D(\eta_{ij}^*)$ where $\dot{\epsilon}_{ij}^* = \dot{r}\eta_{ij}^* = \frac{1}{2}\dot{r}(\phi_{i,j}^* + \phi_{j,i}^*)$.

Suppose the specified displacement on the boundary S_u equals zero, then from

$$\frac{dK^*}{dt}=-D(\dot{\epsilon}_{ij}^*)=-(K^*/L_*)^{1/2}D(\eta_{ij}^*) \tag{3}$$

we have

$$K^*(t)=[(K_0^*)^{1/2}-D(\eta_{ij}^*)t/(2L_*^{1/2})]^2 \tag{4}$$

$$\dot{r}(t)=(K_0^*/L_*)^{1/2}-D(\eta_{ij}^*)t/(2L_*) \tag{5}$$

where $K_0^* = K^*(0)$ is the initial kinetic energy of the mode-form solution $\dot{u}_i^*$. The dynamic response time for the mode-form solution can be easily obtained from Eq. (5) as

$$t_m=2(L_*K_0^*)^{1/2}/D(\eta_{ij}^*). \tag{6}$$

It can be seen from the foregoing that for an impulsively loaded plastic structure, the mode-form solution Eq. (1) may be determined by the proper choice of the mode form $\phi_i^*(\mathbf{x})$ and the initial kinetic energy K_0^* or $\dot{r}^0 = \dot{r}(0) = (K_0^*/L_*)^{1/2}$. The problem of choosing $\phi_i^*(\mathbf{x})$ will be left to the next section. The problem of choosing $\dot{r}^0$ is usually suggested by minimizing the functional

$$\Delta_0=\frac{1}{2}\int_v \rho(\dot{u}_i^0-\dot{r}^0\phi_i^*)(\dot{u}_i^0-\dot{r}^0\phi_i^*)dv \tag{7}$$

when the actual initial velocity distribution $\dot{u}_i^0$ is given.

Thus,

$$\dot{r}^o=\left(\int_v \rho\dot{u}_i^0\phi_i^* dv\right)/(2L_*) \tag{8}$$

and the initial kinetic energy of the mode-form solution is

$$K_0^*=\left(\int_v \rho\dot{u}_i^0\phi_i^* dv\right)^2/(4L_*) \tag{9}$$

which is not larger than the actual initial kinetic energy of the structure K_0. Substituting (9) into (6), we get the response time of the mode-form solution

$$t_f^*=\left(\int_v \rho\dot{u}_i^0\phi_i^* dv\right)/D(\eta_{kl}^*). \tag{10}$$

This is a lower bound on the actual response time t_f. The final displacement of the mode-form solution is

$$u_i^*(\mathbf{x},t_f^*)=\left(\int_v \rho\dot{u}_j^0\phi_j^* dv\right)^2\phi_i^*(\mathbf{x})/[4L_*D(\eta_{kl}^*)]. \tag{11}$$

3 Basic Inequalities and the Optimal Mode Choice

Let us consider an impulsively loaded rigid-perfectly plastic structure. The traction on the boundary S_T and the displacement on the boundary S_u are supposed to be zero. The final displacement of the structure u_i^f may be bounded from below as (Huang, 1985)

$$t_f^0\left[\int_v \rho\dot{u}_i^0\phi_i dv-\frac{1}{2}t_f^0 D(\eta_{ij})\right]\le\int_v \rho\phi_i(\mathbf{x})u_i^f dv \tag{12}$$

where $t_f^0 = 2(\hat{L}K_0)^{1/2}/D(\bar{\eta}_{ij})$ is an upper bound on response time t_f, and $\bar{\eta}_{ij} = \frac{1}{2}(\bar{\phi}_{i,j} + \bar{\phi}_{j,i})$ is the strain field associated with the principal mode $\bar{\phi}_i = \phi_i^{(1)}$. (Here, only one principal mode is assumed; the case for several principal modes can be discussed similarly.) $D(\bar{\eta}_{ij}) = \bar{D}$ and $D(\eta_{ij})$ are the dissipated internal energies corresponding to $\bar{\eta}_{ij}$ and $\eta_{ij} = \frac{1}{2}(\phi_{i,j} + \phi_{j,i})$, respectively, and $\hat{L} = \frac{1}{2}\int_v \rho\bar{\phi}_i\bar{\phi}_i dv$. It may be emphasized that the inequality (12) can be applied to an arbitrary kinematically admissible field $\phi_i(\mathbf{x})$, but in the following, $\phi_i(\mathbf{x})$ will only be taken to be the nth-order mode form $\phi_i^{(n)}(\mathbf{x})$ $(n = 1, 2, 3, \ldots)$. (For a one-dimensional problem, $\phi^{(n)}(x)$ may change sign.)

On the other hand, for a dynamically admissible acceleration field $\ddot{u}_i^{**}(\mathbf{x}, t)$, the following inequality can be established (cf. Martin, 1972)

$$-\int_v \rho\ddot{u}_i^{**}\dot{u}_i dv\le-\int_v \rho\ddot{u}_i\dot{u}_i dv=-\frac{dK}{dt} \tag{13}$$

where $\dot{u}_i$ and K are actual velocity and kinetic energy, respectively. Since the mode-form solution satisfies all field equations, the acceleration field $-D(\eta_{kl}^*)\phi_i^*(\mathbf{x})/(2L_*)$ derived from (1) and (5) is certainly dynamically admissible. So (13) can be written as

$$\left(\int_v \rho\phi_i^*\dot{u}_i dv\right)D(\eta_{KL}^*)/(2L_*)\le-\frac{dK}{dt}.$$

Integrating the above inequality over the interval of time $t = 0$ to $t = t_f$, it follows that

$$\int_v \rho\phi_i^* u_i^f dv\le 2L_*K_0/D(\eta_{ij}^*). \tag{14}$$

In the following, $\phi_i(\mathbf{x})$ in (12) and $\phi_i^*(\mathbf{x})$ in (14) will be taken to be the nth-order mode form $\phi_i^{(n)}(\mathbf{x})$, $(n = 1, 2, 3, \ldots)$. They correspond to the local minimum or the stationary extremum value of the functional (see Appendix)

$$\Pi(\phi_i)=D(\eta_{ij})/L^{1/2} \tag{15}$$

with $L = \frac{1}{2}\int_v \rho\phi_i\phi_i dv$.

Letting

$$\eta_{ij}^{(n)}=\frac{1}{2}(\phi_{i,j}^{(n)}+\phi_{j,i}^{(n)}),\ D_{(n)}=D(\eta_{ij}^{(n)})$$

and

$$L_{(n)}=\frac{1}{2}\int_v \rho\phi_i^{(n)}\phi_i^{(n)}dv,$$

basic sequential inequalities can be obtained as

$$t_f^0\left[\int_v \rho\dot{u}_i^0\phi_i^{(n)}dv-\frac{1}{2}t_f^0 D_{(n)}\right]\le\int_v \rho\phi_i^{(n)}u_i^f dv\le 2L_{(n)}K_0/D_{(n)} \tag{16}$$

or, simply,

Downloaded 03 May 2010 to 171.66.16.247. Redistribution subject to ASME license or copyright; see http://www.asme.org/terms/Terms_Use.cfm

$$C^L_{(n)} \le \left(\int_v \rho \phi_i^{(n)} u_i^f dv \right) / L^{1/2}_{(n)} \le C^U_{(n)} \tag{17}$$

where

$$C^U_{(n)} = 2L^{1/2}_{(n)} K_0 / D_{(n)}$$

$$C^L_{(n)} = 4 \left[(\hat{L} K_0 K_0^{(n)})^{1/2} - \frac{1}{2} \hat{L} D_{(n)} K_0 / (L^{1/2}_{(n)} \overline{D}) \right] / \overline{D}. \tag{18}$$

Generally, the higher mode forms $\phi_i^{(n)}$ ($n \ge 2$) are unstable modes in the sense that when disturbed, they will eventually converge to the principal mode (Lepik, 1980). However, if the initial velocity distribution of the structure is quite close to one of the higher modes corresponding to the stationary extrema of Eq. (15), this mode should be used to provide "the best approximation" for the final displacement. Naturally, there exists the problem on the choice of optimal mode (Symonds, 1980; Slutsky et al., 1982).

The functions $\phi_i^{(n)}/L^{1/2}_{(n)}$ ($n = 1, 2, 3, \ldots$) in the inequalities (17) may be called "base functions" in the $\{\phi_i^{(1)}, \phi_i^{(2)}, \ldots, \phi_i^{(n)}, \ldots\}$ space, then

$$X_{(n)} = \left(\int_v \rho \phi_i^{(n)} u_i^f dv \right) / L^{1/2}_{(n)} \tag{19}$$

can be regarded as the "projections" of the final displacement $u_i^f(\mathbf{x})$ on these "base functions", and (17) can be reduced to

$$C^L_{(n)} \le X_{(n)} \le C^U_{(n)}, \quad (n = 1, 2, \ldots).$$

The values of $X_{(n)}$ are unknown since $u_i^f(\mathbf{x})$ is unknown. But inqualities (17) do give the upper and the lower bounds on $X_{(n)}$. When values of $C^L_{(q)}$ and $C^U_{(q)}$ corresponding to the qth mode $\phi_i^{(q)}(\mathbf{x})$ are much greater than those corresponding to all other possible modes, surely $\phi_i^{(q)}(\mathbf{x})$ may be considered as the optimal mode. Unfortunately, in practical calculations, the difference between $C^U_{(n)}$ and $C^L_{(n)}$ sometimes is quite large. So an approximate estimate for $X_{(n)}$, denoted by $\overline{C}_{(n)}$, is needed which can serve as a criterion for the optimal mode choice.

In the following, the quantity $\overline{C}_{(n)}$ will be taken as

$$\overline{C}_{(n)} = \left(\int_v \rho \dot{u}_i^0 \phi_i^{(n)} dv \right)^2 / (2L^{1/2}_{(n)} D_{(n)}) = 2L^{1/2}_{(n)} K_0^{(n)} / D_{(n)}. \tag{20}$$

Since the initial kinetic energy of the mode form solution is not larger than the actual initial kinetic energy; i.e., $K_0^{(n)} \le K_0$, we have $\overline{C}_{(n)} \le C^U_{(n)}$. On the other hand from

$$\{[2L_{(n)} K_0^{(n)} / D_{(n)}]^{1/2} - [2\hat{L} D_{(n)} K_0]^{1/2} / \overline{D}\}^2 \ge 0$$

we obtain

$$t_f^0 \left[\int_v \rho \dot{u}_i^0 \phi_i^{(n)} dv - \frac{1}{2} t_f^0 D_{(n)} \right] \le \frac{1}{2} \left[\int_v \rho \dot{u}_i^0 \phi_i^{(n)} dv \right]^2 / D_{(n)}$$

or, equivalently, $C^L_{(n)} \le \overline{C}_{(n)}$. This means the new lower bound of Huang (1985) is not larger than that of Morales and Nevill (1970). So the following sequential inequalities are obtained:

$$C^L_{(n)} \le \overline{C}_{(n)} \le C^U_{(n)} \quad (n = 1, 2, \ldots). \tag{21}$$

Taking $\max_{(n)} \{\overline{C}_{(n)}\}$ as a criterion for the optimal mode choice was first suggested by Symonds (Eq. (8*a*), 1980). Although this criterion has not been rigorously proved, the above discussion may be thought of as a reasonable explanation of Symonds' work.

4 A Suggested Approximate Expression on the Final Displacement

In general, the orthogonal conditions for different modes do not exist, namely the quantity

$$A_{pn} = \int_v \rho \phi_i^{(p)} \phi_i^{(n)} dv$$

is not neccessarily equal to zero when $p \ne n$. However, we may still expand the final displacement in the family of modes $\phi_i^{(n)}(\mathbf{x})/L^{1/2}_{(n)}$ ($n = 1, 2, 3, \ldots$)

$$u_i^f(\mathbf{x}) = \kappa_1 \phi_i^{(1)} / L^{1/2}_{(1)} + \kappa_2 \phi_i^{(2)} / L^{1/2}_{(2)} + \ldots + \kappa_n \phi_i^{(n)} / L^{1/2}_{(n)} + \ldots \tag{22}$$

Substituting Eq. (22) into (19), we have

$$X_{(n)} = L^{-1/2}_{(n)} (A_{1n} L^{-1/2}_{(1)} \kappa_1 + A_{2n} L^{-1/2}_{(2)} \kappa_2 + \ldots + A_{nn} L^{-1/2}_{(n)} \kappa_n + \ldots). \tag{23}$$

If the first r terms (corresponding to the first r largest values of $\overline{C}_{(n)}$) are considered only and $X_{(n)}$ is approximately replaced by $\overline{C}_{(n)}$, a system of linear algebraic equations for κ_n ($n = 1, 2, \ldots, r$) can be obtained

$$\sum_{p=1}^{r} B_{pn} \kappa_p = \overline{C}_{(n)} \quad (n = 1, 2, \ldots, r) \tag{24}$$

where

$$B_{pn} = A_{pn} / (L_{(p)} L_{(n)})^{1/2}.$$

Thus, the approximate expression for the final displacement may be given as

$$u_i^f(\mathbf{x}) \doteq \sum_{p=1}^{r} \kappa_p \phi_i^{(p)}(\mathbf{x}) / L^{1/2}_{(p)} \tag{25}$$

so long as κ_p ($p = 1, 2, \ldots r$) are determined from (24). For some practical problems the effect of certain higher modes may be very important, and in that case, especially when $\overline{C}_{(1)}$, $\overline{C}_{(2)}, \ldots, \overline{C}_{(n)}$ are almost the same, expression (25) may be better than that in which only one mode is used; e.g., by Eq. (11).

5 Examples

(1) As the first example, let us consider a two-degree-of-freedom model which was used by many authors (e.g., Symonds, 1980). A simply-supported, rigid-perfectly plastic massless beam with a plastic moment M_0 is shown in Fig. 1. The initial velocities of particles 1 and 2 with mass G are specified to be $\dot{u}_1^0$ and $\dot{u}_2^0$, respectively. The functional of Eq. (15) now reduces to

$$\Pi = \frac{M_0}{\sqrt{(2G)}\, l} \{|3\phi_1 - \phi_2| + |3\phi_2 - \phi_1|\} / (\phi_1^2 + \phi_2^2)^{1/2}. \tag{26}$$

It can be easily verified that the principal mode corresponding to the minimum of Π is $(\phi_1 : \phi_2) = (1:3)$ or $(1:1/3)$ with $\Pi = \frac{4M_0}{\sqrt{5Gl}}$, and the higher (unstable) mode corresponding to the extremum stationary value of Π is $(\phi_1 : \phi_2) = (1:1)$, or $(1:-1)$

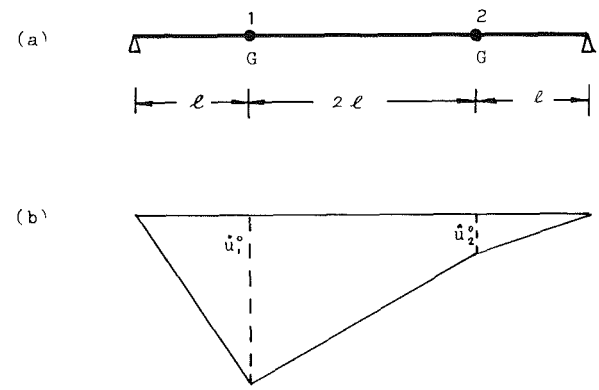

Fig. 1 (*a*) A two-degree-of-freedom model; (*b*) initial velocities at particles 1 and 2

Downloaded 03 May 2010 to 171.66.16.247. Redistribution subject to ASME license or copyright; see http://www.asme.org/terms/Terms_Use.cfm

with $\Pi = \frac{2M_0}{\sqrt{Gl}}$, or $\Pi = \frac{4M_0}{\sqrt{Gl}}$.

Suppose the initial velocities $(\dot{u}_1^0, \dot{u}_2^0)$ satisfy

$$\begin{cases} \dot{u}_1^0 - 3\dot{u}_2^0 \geq 0 \\ \dot{u}_1^0 + \dot{u}_2^0 \geq 0 \end{cases} \tag{27}$$

Then, the accelerations are $\ddot{u}_1 = -\ddot{u}_2 = \frac{2M_0}{Gl}$ in the first phase, and $\ddot{u}_1 = 3\ddot{u}_2 = -\frac{6M_0}{Gl}$ in the second phase. This means the motion will finally converge onto the first (principal) mode $(\phi_1^{(1)}, \phi_2^{(1)}) = (1, 1/3)$, except when $\dot{u}_1^0 = -\dot{u}_2^0$ that corresponds to the higher mode $(\phi_1^{(2)}, \phi_2^{(2)}) = (1, -1)$. Integrating the above equations, we obtain the final displacements

$$\begin{cases} u_1^f = (11\dot{u}_1^{02} + 6\dot{u}_1^0\dot{u}_2^0 + 3\dot{u}_2^{02}) \frac{Gl}{32M_0} \\ u_2^f = (3\dot{u}_1^{02} + 6\dot{u}_1^0\dot{u}_2^0 - 5\dot{u}_2^{02}) \frac{Gl}{32M_0} \end{cases} \tag{28}$$

According to the discussion of Section 3, values of $\bar{C}_{(1)}$ and $\bar{C}_{(2)}$ can be easily calculated from the initial velocities, the larger one of which will correspond to the optimal mode. However, when $\bar{C}_{(1)} = \bar{C}_{(2)}$, neither $(\phi_1^{(1)}, \phi_2^{(1)})$ nor $(\phi_1^{(2)}, \phi_2^{(2)})$ will provide a good approximation on the final displacements. Now consider a specially assumed initial velocities $(\dot{u}_1^0, \dot{u}_2^0) = (1, -0.603)V_0$ which correspond to $\bar{C}_{(1)} = \bar{C}_{(2)}$. The above expression (28) then leads to

$$(u_1^f, u_2^f) = (8.473, -2.436) \frac{GlV_0^2}{32M_0}. \tag{29}$$

From Eq. (11), with the same assumed initial velocities, the final displacements corresponding to first mode and second mode are

$$(u_1^f, u_2^f)_{(1)} = (6.895, 2.298) \frac{GlV_0^2}{32M_0} \tag{30}$$

and

$$(u_1^f, u_2^f)_{(2)} = (5.139, -5.139) \frac{GlV_0^2}{32M_0}, \tag{31}$$

respectively.

Now let us consider the approximate final displacements suggested by the present method. Equation (22) may be written as

$$\bar{u}_i^f = y_1\phi_i^{(1)} + y_2\phi_i^{(2)}, \ (i = 1,2) \tag{32}$$

with $y_1 = \kappa_1/L_{(1)}^{1/2}$, $y_2 = \kappa_2/L_{(2)}^{1/2}$.

Values of y_i can be calculated from

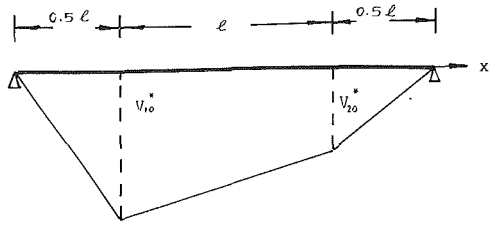

Fig. 2 A rigid plastic, simply-supported beam with piecewise linear initial velocity field

$$\bar{C}_{(1)} = \bar{C}_{(2)} = 0.3212 \frac{G^{3/2}lV_0^2}{M_0}$$

$$B_{11} = B_{22} = 2, \ B_{12} = B_{21} = 2/\sqrt{5},$$

and Eq. (24) which gives

$$y_1 = 4.764 \frac{GlV_0^2}{32M_0}$$

$$y_2 = 3.551 \frac{GlV_0^2}{32M_0}.$$

Thus, Eq. (32) becomes

$$(\bar{u}_1^f, \bar{u}_2^f) = (8.315, -1.963) \frac{GlV_0^2}{32M_0}. \tag{33}$$

Comparing Eq. (29) with Eqs. (30), (31), and (33), we may find that (33) is a better approximation of the final displacements.

(2) The second example is taken from the article by Lepik (1980). A rigid plastic simply-supported beam of length $2l$ is subjected to a piecewise linear initial impulsive velocity (Fig. 2). In the following, we will use the dimensionless quantities as

$$\xi = x/l, \ \tau = t/\beta, \ \beta^2 = ml^3/(6M_0), \ V_{10} = V_{10}^*\beta/l, \ V_{20} = V_{20}^*\beta/l \tag{34}$$

where V_{10}^* and V_{20}^* are initial velocities at $x = 0.5l$ and $x = 1.5l$, respectively. M_0 is the limit moment and m is the mass of the beam per unit length.

For the specified initial velocity field

$$\dot{u}^0(\xi) = \begin{cases} 2V_{10}\xi, & \text{for } \xi \in [0.0, 0.5] \\ V_{10} + (V_{20} - V_{10})(\xi - 0.5), & \text{for } \xi \in [0.5, 1.5] \\ 2V_{20}(2 - \xi), & \text{for } \xi \in [1.5, 2.0], \end{cases} \tag{35}$$

the analytic solution of the final displacement can be expressed as

$$u^f(\xi) = \begin{cases} \frac{1}{64}(59V_{10}^2 + 27V_{20}^2 + 54V_{10}V_{20})\xi, & \text{for } \xi \in [0.0, 0.5] \\ -\frac{9}{8}(V_{10} + V_{20})^2\xi^2 + \frac{1}{64}(111V_{10}^2 + 111V_{20}^2 + 254V_{10}V_{20})\xi \\ \quad -\frac{1}{8}(V_{10}^2 + 3V_{20}^2 + 8V_{10}V_{20}), & \text{for } \xi \in [0.5, 1.0] \\ -\frac{1}{64}(33V_{10}^2 + 33V_{20}^2 + 34V_{10}V_{20})\xi \\ \quad +\frac{1}{4}(4V_{10}^2 + 3V_{20}^2 + 5V_{10}V_{20}), & \text{for } \xi \in [1.0, 1.5] \\ \frac{1}{64}(29V_{10}^2 - 3V_{20}^2 + 58V_{10}V_{20})(2 - \xi), & \text{for } \xi \in [1.5, 2.0]. \end{cases} \tag{36}$$

Downloaded 03 May 2010 to 171.66.16.247. Redistribution subject to ASME license or copyright; see http://www.asme.org/terms/Terms_Use.cfm

From Eq. (11) the dimensionless final displacement corresponding to the first mode can be immediately obtained as

$$u^f_{(1)}(\xi) = 0.4727(V_{10} + V_{20})^2 \phi^{(1)}(\xi) \tag{37}$$

where

$$\phi^{(1)}(\xi) = \begin{cases} \xi, & \text{for } \xi \in [0,1] \\ 2-\xi, & \text{for } \xi \in [1,2]. \end{cases} \tag{38}$$

Similarly, the dimensionless final displacement of the second mode is

$$u^f_{(2)}(\xi) = 0.1250(V_{10} - V_{20})^2 \phi^{(2)}(\xi) \tag{39}$$

with

$$\phi^{(2)}(\xi) = \begin{cases} \xi, & \text{for } \xi \in [0.0,0.5] \\ 1-\xi, & \text{for } \xi \in [0.5,1.5] \\ \xi-2, & \text{for } \xi \in [1.5,2.0]. \end{cases} \tag{40}$$

In the following, only the first two modes $\phi^{(1)}(\xi)$ and $\phi^{(2)}(\xi)$ are taken into consideration. It is seen that these two modes are orthogonal. So, from Eq. (24), the suggested approximate final displacement can be written as

$$u^f_{(1,2)}(\xi) = u^f_{(1)}(\xi) + u^f_{(2)}(\xi). \tag{41}$$

Now, with the same reason following Eq. (28), let us consider a specially assumed initial velocity field (corresponding to $\overline{C}_{(1)} = \overline{C}_{(2)}$):

$$V_{10} = 0.5, \; V_{20} = -0.235. \tag{42}$$

Values of $C^L_{(n)}$, $\overline{C}_{(n)}$, $X_{(n)}$, and $C^U_{(n)}$ $(n = 1, 2)$ calculated from Eq. (18)–(20) are listed in Table 1. From Eq. (42) and these values, the final displacements corresponding to Eq. (36), (37), (39), and (41) can be easily obtained and are plotted in Fig. 3. The deviation of the present result from the analytic one (Lepik, 1980) may be due to the underestimate of $X_{(1)}$. Still, the result of the present paper is better than those of the mode approximation technique.

Table 1 Values of $C^L_{(n)}$, $\overline{C}_{(n)}$, $X_{(n)}$, $C^U_{(n)}$ $(n = 1, 2)$ for initial velocities $V_{10} = 0.5$, $V_{20} = -0.235$

	$C^L_{(n)}$	$\overline{C}_{(n)}$	$X_{(n)}$	$C^U_{(n)}$
n=1	-0.02274	0.03890	0.07240	0.1965
n=2	-0.1089	0.03896	0.04483	0.04912

6 Concluding Remarks

The aim of present paper is to provide an approximate expression of final displacement u^f_i for an impulsively loaded, rigid plastic structure. This can be accomplished by the following procedures:

(1) to calculate the nth-order mode form $\phi^{(n)}_i(\mathbf{x})$ from Eq. (15).
(2) to evaluate unknown $X_{(n)}$ in Eq. (19). This can be done by taking a certain kind of average from the lower bound and the upper bound of $X_{(n)}$, which is approximately evaluated by $\overline{C}_{(n)}$ in Eq. (20).
(3) The $\max_{(n)}\{\overline{C}_{(n)}\}(=\overline{C}_{(q)})$ is chosen to give $\phi^{(q)}_i(\mathbf{x})$ as an optimal mode form. The ordinary mode form solution will then be used. However, when the two (or more) maxima of $\overline{C}_{(n)}$ are approximately the same, the corresponding two (or more) mode forms should be taken into account simultaneously. In this case, a suggested expression on the final displacement (Eq. (25)) will be used.

Acknowledgments

The authors wish to acknowledge the support of the National Natural Science Foundation of China and the helpful discussion with Professors Ren Wang and P. S. Symonds.

References

Huang Zhu-ping, 1985, "Revised Lower Displacement Bounds of Impulsively-Loaded Rigid-Plastic Structures," *Mech. Res. Comm.*, Vol. 12, pp. 257–264.

Huang, Zhu-ping, and Wang Ren, 1985, "The Mode Approximation Technique in Dynamic Plastic Response of Structures," *Advances in Mechanics*, Vol. 15, pp. 1–20, (in Chinese).

Jones, N., and Soares, C. G., 1978, "Higher Modal Dynamic Plastic Behavior of Beams Loaded Impulsively," *Int. J. Mech. Sci.*, Vol. 20, pp. 135–147.

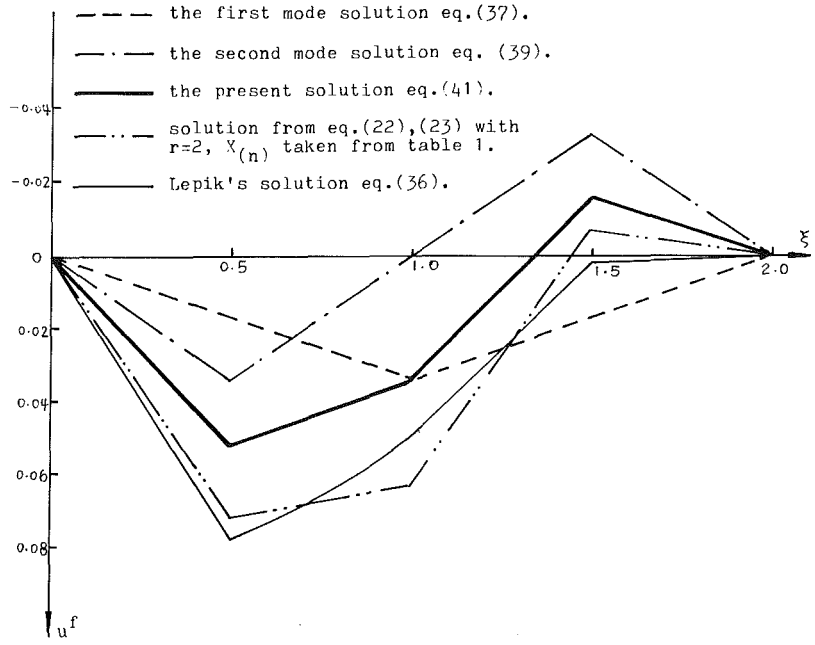

Fig. 3 Final displacements for initial velocities $V_{10} = 0.5$, $V_{20} = -0.235$

Downloaded 03 May 2010 to 171.66.16.247. Redistribution subject to ASME license or copyright; see http://www.asme.org/terms/Terms_Use.cfm

Jones, N., and Wierzbicki, T., 1976, "A Study of the Higher Modal Dynamic Plastic Response of Beams," *Int. J. Mech. Sci.*, Vol. 18, pp. 533-542.

Lee, L. S. S., 1972, "Mode Response of Dynamically Loaded Structures," ASME JOURNAL OF APPLIED MECHANICS, Vol. 39, pp. 904-910.

Lepik, U., 1980, "On the Dynamic Response of Rigid-Plastic Beams," *J. Struct. Mech.*, Vol. 8, pp. 227-235.

Martin, J. B., 1964, "Impulsive Loading Theorems for Rigid-Plastic Continua," *J. Eng. Mech. Div., Proc. ASCE.*, Vol. 90, No. EM5, pp. 27-42.

Martin, J. B., 1972, "Extremum Principles for a Class of Dynamic Rigid-Plastic Problems," *Int. J. Solids. Struct.*, Vol. 8, pp. 1185-1204.

Martin, J. B., and Symonds, P. S., 1966, "Mode Approximations for Impulsively-Loaded Rigid-Plastic Structures," *J. Eng. Mech. Div., Proc. ASCE.*, Vol. 92, No. EM5, pp. 43-66.

Morales, W. J., and Nevill, G. E., 1970, "Lower Bounds on Deformations of Dynamically Loaded Rigid-Plastic Continua," *AIAA. Journal*, Vol. 8, pp. 2043-2046.

Slutsky, S., Chon, C. T., and Yeung, K. S., 1982, "On the *Best* Mode Form in the Mode Approximation Technique Using the Finite Element Method," *J. Struct. Mech.*, Vol. 10, pp. 117-131.

Symonds, P. S., 1980, "The Optimal Mode in the Mode Approximation Technique," *Mech. Res. Comm.*, Vol. 7, pp. 1-6.

Symonds, P. S., and Wierzbicki, T., 1975, "On an Extremum Principle for Mode Form Solutions in Plastic Structural Dynamics," ASME JOURNAL OF APPLIED MECHANICS, Vol. 42, pp. 630-640.

APPENDIX

Suppose the surface traction T_i (specified on the boundary S_T) and the body force F_i are time independent and the displacement on the boundary S_u equals zero, then from the mode form solution Eq. (1) and

$$\int_v \rho \ddot{u}_i^* \dot{u}_i^* dv = \int_v F_i \dot{u}_i^* dv + \int_{s_T} T_i \dot{u}_i^* ds - \int_v \sigma_{ij}^* \dot{\epsilon}_{ij}^* dv, \quad \text{(A1)}$$

we have

$$\ddot{r} = \left[\int_v F_i \phi_i^* dv + \int_{s_T} T_i \phi_i^* ds - D(\eta_{ij}^*) \right] / (2L_*), \quad \text{(A2)}$$

where σ_{ij}^* is the mode form stress field and $D(\eta_{ij}^*) = \int_v \sigma_{ij}^* \eta_{ij}^* dv$. Obviously, when the structure cannot be sustained statically (i.e., the dynamic loading exceeds the static limit load), we have $\ddot{r} > 0$. And when the structure can be sustained statically, we have $\ddot{r} < 0$.

For an arbitrary kinematically admissible acceleration field, consider the following functional of $\ddot{u}_i$

$$J(\ddot{u}_i) = \frac{1}{2} \int_v \rho \ddot{u}_i \ddot{u}_i dv + \int_v \sigma_{ij} \ddot{\epsilon}_{ij} dv - \int_v F_i \ddot{u}_i dv - \int_{s_T} T_i \ddot{u}_i ds. \quad \text{(A3)}$$

(Here, the functional $J(\ddot{u}_i)$ is different from that of Tamuzh's theorem since the actual velocity field is not known in advance).

As was pointed out by Martin (1972) and Symonds and Wierzbicki (1975), if

(1) the dynamic loading exceeds the limit load, then σ_{ij} in Eq. (A3) should be determined by $\dot{\epsilon}_{ij}$ via the flow rule, and $J(\ddot{u}_i)$ is rendered global minimum by the mode form acceleration field $\ddot{r}\phi_i^*(\mathbf{x})$.

(2) the dynamic loading does not exceed the limit load, then σ_{ij} in Eq. (A3) should be determined by $(-\ddot{\epsilon}_{ij})$ via the flow rule, and $J(\ddot{u}_i)$ is rendered local maximum or stationary extremum by the mode form acceleration field $\ddot{r}\phi_i^*(\mathbf{x})$.

Now let us consider a special kind of kinematically admissible acceleration fields

$$\ddot{\bar{u}}_i = \Lambda \phi_i(\mathbf{x}) \quad \text{(A4)}$$

with

$$\Lambda = \left[\int_v F_i \phi_i dv + \int_{s_T} T_i \phi_i ds - D(\eta_{ij}) \right] \Big/ \left(\int_v \rho \phi_i \phi_i dv \right) \quad \text{(A5)}$$

if $\phi_i(\mathbf{x})$ is a small deviation from the mode form solution $\phi_i^*(\mathbf{x})$, then Λ has the same sign with $\ddot{r}$. Since the set expressed by Eq. (A4) is a subset of all possible acceleration fields, the conclusion made by Martin (1972) and Symonds and Wierzbicki (1975) is also valid for the following functional:

$$J(\Lambda\phi_i) = \Lambda^2 \int_v \frac{1}{2} \rho \phi_i \phi_i dv + \Lambda \left[D(\eta_{ij}) - \int_v F_i \phi_i dv - \int_{s_T} T_i \phi_i ds \right]$$

$$= -\frac{1}{2} \left[D(\eta_{ij}) - \int_v F_i \phi_i dv - \int_{s_T} T_i \phi_i ds \right]^2 \Big/ \int \rho \phi_i \phi_i dv. \quad \text{(A6)}$$

Particularly, under impulsive loading ($F_i = 0$ in V; $T_i = 0$ on S_T), the functional (A6) can be written as

$$J(\Lambda\phi_i) = -\frac{1}{4} \{\Pi(\phi_i)\}^2 \quad \text{(A7)}$$

where $\Pi(\phi_i)$ is obtained from Eq. (15). This means the mode form solution renders $\Pi(\phi_i)$ local minimum or stationary extremum.

Downloaded 03 May 2010 to 171.66.16.247. Redistribution subject to ASME license or copyright; see http://www.asme.org/terms/Terms_Use.cfm

Three-Dimensional Effective Moduli of Orthotropic and Symmetric Laminates

Ajit K. Roy
University of Dayton Research Institute,
Dayton, OH 45469-0168
Mem. ASME

Stephen W. Tsai
Department of Aeronautics and Astronautics,
Stanford University,
Stanford, CA 94305-4035
Fellow ASME

A simple and accurate method for estimating the three-dimensional effective moduli of symmetric and orthotropic laminated composites is presented. The method is based on obtaining the exact displacement field of three boundary value problems of laminated composites using the Airy stress function solution technique. The effective moduli are estimated by matching the boundary displacements of the equivalent homogeneous system with those of the laminated system. Among the estimated effective moduli, those associated with the interlaminar direction are of special interest. It is found that the effective interlaminar normal stiffness in extensional deformation is independent of laminae stacking sequence which is consistent with the finding of Pagano (1974). However, the laminate interlaminar shear stiffness is dependent on stacking sequence, and it is shown that the rule of mixtures can not predict the interlaminar shear stiffness accurately.

Introduction

The macroscopic performance of a laminate composed of anisotropic layers can be characterized by its response as a unit body. Thus, in mechanics of composite materials, an aspect of the analysis of composite laminates is related to the studies of its macroscopic behavior where the response of the constituent layers is averaged over the whole laminate. In this type of analysis, one is concerned with the relationship between the applied loads and the deformations which these forces produce. These relations in the literature are termed the *effective* laminate constitutive relations since they define the geometric response caused by loads exerted on the laminate. Once the effective constitutive law is formulated, tools for laminate stress analysis can be developed based on considering the laminate as a unit. The use of effective constitutive relation also reduces the size of a problem for stress analysis, especially for laminates with a large number of laminae. Further, if a particular boundary value problem is solved based on the effective constitutive law, one can determine the approximate detailed layer-by-layer stress and strain distributions from the laminate stress and strains distributions by using the constitutive relations of each layer.

In general, the effective moduli of a laminated body depend on the stacking sequence of its laminae as well as on the deformation mode. There is a number of methods reported in the literature for predicting the effective moduli of a laminate. Some of these methods are based on higher-order plate deformation theory, namely, Whitney and Pagano (1970), and Reddy (1986). However, these theories are based on assuming the deformation in the thickness direction (or interlaminar direction) of the laminate. An assumed deformation shape does not always predict accurate values of the effective moduli for laminated composites, especially for thick composites. Pagano (1974), Chou and Carleone (1972), and recently Sun and Li (1988) have given closed-form expressions for the three-dimensional effective moduli of laminated composites subject to such assumptions. Pagano's (1974) approach is more general than that of Chou and Carleone (1972) and Sun and Li (1988); in fact, Pagano's work unifies the work of Chou and Carleone and Sun and Li. However, in the above three papers, the distributions of interlaminar shear stress is assumed to be constant throughout the thickness of the laminate. Thus, the expressions given by Pagano (1974), Chou and Carleone (1972), and Sun and Li (1988) for the effective interlaminar shear stiffness are independent of stacking sequence of the constituent laminae. By contrast, it is observed experimentally that the effective interlaminar shear stiffness of a laminate depends, in general, on the stacking sequence of the constituent laminae, Roy and Kim (1989). Nevertheless, when a laminate is constructed with repeated sublaminates, as the number of sublaminates increases, the influence of the stacking sequence of the constituent laminae on the values of the effective interlaminar shear stiffness decreases, and eventually the stacking sequence effect is expected to be negligible. Thus, one of the objectives of the present work is to define conditions when and what should be the minimum number of sublaminates to be present in a laminate so that the expressions of Pagano (1974), Chou and Carleone (1972), or Sun and Li (1988) be applicable especially for predicting the effective interlaminar shear stiffnesses.

Contributed by the Applied Mechanics Division of THE AMERICAN SOCIETY OF MECHANICAL ENGINEERS for presentation at the Winter Annual Meeting, Atlanta, Ga., Dec. 1-6, 1991.

Discussion on this paper should be addressed to the Technical Editor, Prof. Leon M. Keer, The Technological Institute, Northwestern University, Evanston, IL 60208, and will be accepted until two months after final publication of the paper itself in the JOURNAL OF APPLIED MECHANICS. Manuscript received by the ASME Applied Mechanics Division, Oct. 18, 1988; final revision, Mar. 15, 1991.

Paper No. 91-WA/APM-12.

Copyright © 1992 by ASME
Downloaded 03 May 2010 to 171.66.16.247. Redistribution subject to ASME license or copyright; see http://www.asme.org/terms/Terms_Use.cfm

The present method for predicting the effective moduli is based on the actual deformation field in a laminate by using linear elasticity. The method is capable of correctly predicting the influence of stacking sequence effect and addresses two deformation modes: extension and bending with shear. The method is, at present, limited to orthotropic and symmetric laminates; however, it is not limited to any number of laminae if the fiber axes of the laminae are aligned parallel or perpendicular to the longitudinal axis of the laminate. Incidentally, among all components of the three-dimensional effective moduli, the components associated with the lamination plane (x-y plane) are easily determined from the classical laminate plate theory. Thus, determination of the interlaminar components (associated with x-z or y-z plane) of effective moduli will be emphasized in this paper. In the following sections the present analytical approach and predicted results are discussed.

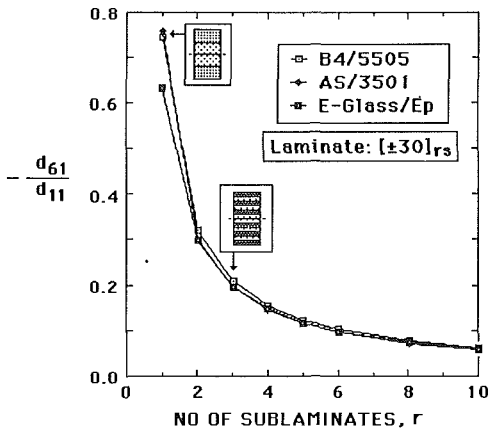

Fig. 1 Plot of twisting to bending couples versus increasing number o sublaminates

Approach

This analysis is presented for in-plane extension (or compression) and bending with shear deformation only. In order to eliminate twisting from bending or extension modes of deformation, a laminate is considered to be composed of homogenous and orthotropic layers stacked symmetrically with respect to the middepth of the laminate. The effective moduli of such laminates are predicted by three separate but interrelated boundary value problems which have exact elasticity solutions. These problems are: (1) a circular ring under equal external and internal pressures, (2) a cantilever beam under a concentrated transverse end load, and (3) a cantilever beam under uniformly distributed loads on the top and bottom surfaces of the beam. By matching the boundary displacements of equivalent homogeneous bodies under identical boundary conditions, we are able to predict all the effective elastic constants of an orthotropic medium as functions of lamina orthotropy and stacking sequence. The three boundary value problems above are chosen for the following reasons: For a large radius to thickness ratio (at least greater than 10), the deformation of the ring due to hydrostatic pressure closely represent the extensional deformation of a laminate. Thus, from the ring problem we will be able to predict the extensional effective moduli. From the cantilever beam problem with end transverse load we will be able to predict the effective module due to bending and interlaminar shear. Similarly, for unequal load intensities on the top and bottom surfaces of the third problem of deformation is similar to that of the second problem; then the prediction of the effective moduli from the third problem can be compared with that from the second problem. On the other hand, when the load intensities on the top and bottom surfaces of the third problem become equal, the beam is in extension with no bending; then the predictions from the third problem can be compared with that of the ring problem. Thus, these three problems are expected to serve as the basic boundary value problems for predicting the effective elastic constants for extension and bending modes of deformation.

The estimates of the values of the effective moduli, as stated before, are obtained by replacing the laminate with a homogenous body of the same geometry and boundary tractions as that of the laminated system and then by matching the boundary displacements of the homogenous body with those of the laminate. The stress and displacement fields of the above three boundary value problems are obtained by considering a state of plane stress in the x-z or y-z plane, with the lamination planes being parallel to the x-y plane. Here, the planes of orthotropic symmetry are the x-y-z planes. This method of predicting the effective moduli is at present limited to orthotropic and symmetric laminates, however, the method is not limited to any number of laminae if the fiber axes of the laminae are aligned parallel or perpendicular to the longitudinal axis (x-axis) of the laminate. When the fiber axis of a lamina is at an angle ϕ ($\phi \neq 0$ deg, 90 deg) with the laminate longitudinal axis, the laminate is assumed to contain adjacent ($\pm\phi$) laminae, and these adjacent ($\pm\phi$) laminae together are assumed to behave as orthotropic layers. If a laminate is made up with a large number of symmetrically stacked thin layers of adjacent ($\pm\phi$) laminae, then the twisting to bending coupling will be negligible, and the above orthotropy assumption is then reasonably accurate.

Figure 1 illustrates the consequence of the orthotropy assumption: Here, the ratio of d_{61}/d_{11} is plotted versus the number of sublaminates, r, for $[+30\text{ deg}/-30\text{ deg}]_{rs}$ laminates. The d_{ij} $(i,j=1,6)$ are the elements of the $[d]$ matrix; $[d]=[D]^{-1}$. The matrices $[D]$ and $[d]$ are, respectively, the flexural stiffness and compliance matrices of a laminates as defined by Tsai (1988, Section 8). The $[+30\text{ deg}/-30\text{ deg}]_{rs}$ laminate is chosen because the value of the ratio of d_{61}/d_{11} attains its maximum at about $+30$ deg/-30 deg orientations for all currently available organic matrix composites. Thus, for any $[\pm\phi]_{rs}$ laminates, the value of the ratio d_{61}/d_{11} will be less than what is shown in Fig. 1. The absolute value of this ratio decreases rapidly as the number of sublaminates, r, increases. For $r=6$, the value of the ratio d_{61}/d_{11} is about 0.1. In other words, if the laminate $[\pm\phi]_{rs}$ is grouped into 6 or more ($\pm\phi$) sublaminates, the twisting deformation due to bending would be less than 10 percent of the bending deformation so that the laminate $[\pm\phi]_{rs}$ can be considered to behave practically as an orthotropic one.

Boundary Value Problems

The three boundary value problems chosen for predicting the effective moduli for extension and bending with interlaminar shear are: (1) a ring subjected to hydrostatic pressures on inner and outer surfaces, (2) a cantilever beam subjected to an end transverse load, and (3) a cantilever beam subjected to uniformly distributed loads on the top and bottom surfaces. The method of predicting the effective moduli from each of these three problems are discussed as follows.

Problem 1: Ring Subjected to Hydrostatic Pressures. The laminated ring and its equivalent homogeneous ring are subjected to equal hydrostatic pressure on both inner and outer surface, p, as shown in Fig. 2. This problem is used to predict the interlaminar effective moduli of symmetric and orthotropic laminates for extensional deformation (no bending). For a large value of the radius-to-thickness ratio, r/t (r: radius, t: thickness), the deformation of the ring approximately represents the extensional deformation. The inner and outer displacements of the homogeneous ring are matched with those of the laminated ring to obtain effective moduli of the laminate of the ring. The interlaminar effective elastic constants ob-

Downloaded 03 May 2010 to 171.66.16.247. Redistribution subject to ASME license or copyright; see http://www.asme.org/terms/Terms_Use.cfm

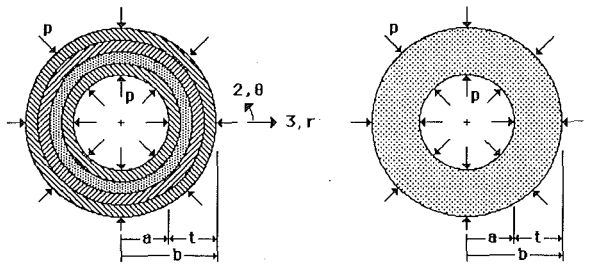

Fig. 2 Configuration of the laminated and its equivalent quasi-homogeneous ring subjected to equal hydrostatic pressure on the inner and outer surface

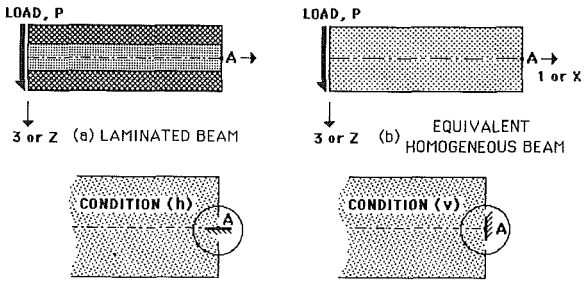

Fig. 3 Configuration of the laminated beam and its equivalent quasi-homogeneous beam under end transverse load

tained from this problem are $\bar{E}_3^o$, $\bar{\nu}_{31}^o$, and $\bar{\nu}_{32}^o$, where ν_{ij} is the Poisson's ratio for ϵ_i under σ_j. The superscript "o" is used to indicate that the elastic constants are associated with the extensional deformation.

The method of obtaining the radial displacement of the laminated composite ring, $u^i(r)$, (Fig. 2(a)) is given by Lekhnitskii (1968). The subscript "i" indicates the ith layer of the laminated ring. We do not find the necessity of repeating the procedure for obtaining the expression of $u^i(r)$ in this paper. The expression for the radial displacement of the equivalent homogeneous ring (whose effective moduli are to be determined, Fig. 2(b)) is similar to that of any layer of the laminated ring; that is

$$u(r)=\frac{p}{1-m^{2k}}S_{23}\left\{(m^{k+1}-1)\left(\frac{r}{b}\right)^{k-1}-(1-m^{k-1})m^{k+1}\left(\frac{b}{r}\right)^{k+1}\right\}r+\frac{p}{1-m^{2k}}S_{22}\left\{(m^{k+1}-1)k\left(\frac{r}{b}\right)^{k-1}+(1-m^{k-1})km^{k+1}\left(\frac{b}{r}\right)^{k+1}\right\}r \quad (1)$$

where $m=\frac{a}{b}$, $k=\sqrt{\frac{S_{33}}{S_{22}}}$, a: inner radius, b: outer radius, and S_{ij} $(i,j=2,3)$ are the elements of the effective compliance matrix.

By equating the inner and outer displacements of the homogeneous ring with those of the laminated ring we get two nonlinear equations in k, S_{22}, and S_{23} as follows:

$$\frac{ap}{1-m^{2k}}[S_{22}k(1+m^{2k}-2m^{k-1})-S_{23}(1-m^{2k})]-u^1(a)=0, \quad (\text{for } r=a,\ i=1) \quad (2)$$

$$\frac{bp}{1-m^{2k}}[S_{22}k(2m^{k+1}-m^{2k}-1)-S_{23}(1-m^{2k})]-u^n(b)=0, \quad (\text{for } r=b,\ i=n). \quad (3)$$

The laminated ring is assumed to have n layers in Eq. (3). Here S_{22} is considered to be known from the laminated plate theory, which seems to be a reasonable assumption. Then S_{23}, k, and hence S_{33} are determined from Eqs. (2) and (3) by the Newton-Raphson's technique. The laminate effective properties in terms of S_{22}, S_{23}, and S_{33} are

$$\bar{E}_3^o=\frac{1}{S_{33}},\quad \bar{\nu}_{32}^o=-\frac{S_{23}}{S_{22}}. \quad (4)$$

The quantity $\bar{\nu}_{31}^o$ can similarly be obtained by rotating the laminate by 90 deg about the r-axis of the ring (a 90-deg rotation brings the 1-axis of the laminate in line with the θ-direction of the ring).

Problem 2: Beam With Transverse End Load. The laminated cantilever beam is subjected to a transverse end load, P, modeled as transverse shear load. The displacement field of the laminated beam is obtained by considering the beam in the state of plane stress either in the 1-3 or in 2-3 plane. The plane of lamination, however, is the 1-2 plane in both cases. From this problem the effective properties, $\bar{G}_{13}^f$, $\bar{G}_{23}^f$, $\bar{\nu}_{32}^f$ are estimated. The superscript "f" is used to indicate that the properties are associated with bending (or flexure) as the dominant mode of deformation.

The expressions for the displacement field can easily be obtained by starting with an Airy stress function appropriate to this problem. Since the end transverse load, P, is modeled as the transverse shear load, (see Fig. 3), thus it is logical to assume that σ_z is zero everywhere in the beam. The Airy stress function, $F_j(x,z)$, for a constituent orthotropic lamina of the above problem for stresses in the (x-z or 1-3) plane has the form

$$F_j(x,z)=A_jxz+B_jz^2+C_jxz^2+D_jz^3+E_jxz^3 \quad (5)$$

where the constants, A_j, B_j,...,E_j are associated with the properties of the jth lamina. After using the linear stress-strain relations and the expressions for stresses in terms of the stress function, $F_j(x,z)$, the displacement fields of the laminated beam, $u_j^c(x,z)$ and $w_j^c(x,z)$, along the x and z directions, respectively, are

$$u_j^c(x,z)=B_j\left[-S_{11}^{(j)}\frac{x^2}{2}+(S_{55}^{(j)}+S_{13}^{(j)})z^2\right]+C_j[-S_{11}^{(j)}x^2z+(S_{55}^{(j)}+S_{13}^{(j)})z^3]+D_jS_{11}^{(j)}xz+E_jS_{11}^{(j)}x+Q_jz+R_j \quad (6)$$

$$w_j^c(x,z)=A_jS_{55}^{(j)}x-B_jS_{13}^{(j)}xz+C_j\left[S_{11}^{(j)}\frac{x^3}{3}+S_{13}^{(j)}xz^2\right]+\frac{1}{2}D_j[S_{13}^{(j)}z^2-S_{11}^{(j)}x^2]+E_jS_{13}^{(j)}z-Q_jx+M_j. \quad (7)$$

The constants A_j, B_j,...,E_j, M_j, Q_j, R_j, for the jth lamina, are determined from the continuity conditions at the interfaces of each lamina, boundary force P, and the boundary conditions at the support end, $x=L$, Here, $S_{ik}^{(j)}$ $(i,k=1,3,5)$ are the elements of the compliance matrix of the jth lamina.

The boundary conditions at the support (i.e., at point A in Fig. 3) are normally modeled in two ways, (Timoshenko, 1934)

$$\text{condition } (h):\quad u(L,0)=w(L,0)=\frac{\partial w}{\partial x}(L,0)=0 \quad (8)$$

$$\text{condition } (v):\quad u(L,0)=w(L,0)=\frac{\partial u}{\partial z}(L,0)=0. \quad (9)$$

Both of these boundary conditions will later be considered to compare the predicted effective moduli with the experimental results.

After following a similar procedure as for Eqs. (6) and (7), the expressions for the displacement fields for the equivalent homogeneous beam, $u^h(x,z)$ and $w^h(x,z)$, (see Fig. 3(b)) for plane stress in the 1-3 (or x-z) plane after satisfying the boundary condition (8) are

Downloaded 03 May 2010 to 171.66.16.247. Redistribution subject to ASME license or copyright; see http://www.asme.org/terms/Terms_Use.cfm

$$u^h(x,z)=\frac{P}{bh^3}\left[6S_{11}(L^2-x^2)z+2S_{13}z^3+S_{55}\left(2z^3-\frac{3}{2}h^2z\right)\right] \tag{10}$$

$$w^h(x,z)=\frac{P}{bh^3}[2S_{11}(x^3-3L^2x+2L^3)-6S_{13}xz^2] \tag{11}$$

and those for boundary condition given by Eq. (9) are

$$u^h(x,z)=\frac{P}{bh^3}[6S_{11}(L^2-x^2)z+2S_{13}z^3+2S_{55}z^3] \tag{12}$$

$$w^h(x,z)=\frac{P}{bh^3}\left[2S_{11}(x^3-3L^2x+2L^3)-6S_{13}xz^2-\frac{3}{2}S_{55}(x-L)h^2\right] \tag{13}$$

where, L, b, h are the length, width, and depth of both beams, respectively. The effective compliance matrix for the homogeneous beam, S_{ij} $(i,j=1,2,5)$, are to be determined by matching the boundary displacement of the homogeneous beam with that of the laminated beam.

To determine S_{11}, S_{13}, and S_{55} from this problem we need at least three simultaneous equations by matching the displacements of the homogeneous beam with that of the laminated beam at three different points along their boundaries. It was, however, found out that matching of the displacements at only three boundary points, in most cases, did not yield a displacement field in the homogeneous beam that could be considered equivalent to that found in the laminated system. Thus, the boundary displacement fields of the two beams are "matched" at more than three boundary points by minimizing the error, Δ:

$$\Delta=\sum_{i=1}^{n}[\{u^h(x_i,z_i)-u^c(x_i,z_i)\}^2+\{w^h(x_i,z_i)-w^c(x_i,z_i)\}^2] \tag{14}$$

where x_i, z_i are coordinates of the points selected along the boundary of the two beams.

After having estimated the elements of S_{ij} by minimizing Δ in Eq. (14), the effective bending stiffness and interlaminar shear stiffness and Poisson's ratio of an orthotropic and symmetric laminate for bending mode of deformation are, respectively,

$$\bar{E}_1^f=\frac{1}{S_{11}},\quad \bar{G}_{13}^f=\frac{1}{S_{55}},\quad \bar{\nu}_{31}^f=-\frac{S_{13}}{S_{11}}. \tag{15}$$

The stress analysis performed in a similar fashion in the 2-3 plane yields the following additional effective elastic constants

$$\bar{G}_{23}^f=\frac{1}{S_{44}},\quad \bar{\nu}_{32}^f=-\frac{S_{23}}{S_{22}}. \tag{16}$$

A sensitivity study was performed for the convergence of the values of the effective properties by varying the number of points in Eq. (14), which will be discussed later.

Problem 3: Beam With Uniformly Distributed Load. For this third problem the beam considered is under uniformly distributed load acting on the top and bottom surfaces of the beam of intensity q and p, respectively, Fig. 4. Besides all the effective properties obtained from Problem 2, one more additonal property, the interlaminar effective normal stiffness, $\bar{E}_3^f$, is obtained from this problem.

If the load intensities on the top and bottom surfaces are made equal, the beam is in extensional deformation; then the values of the effective moduli obtained from this problem are compared with those of the Ring Problem. For unequal load intensities, the beam is in bending with interlaminar shear deformation, and thus the results are compared with those of Problem 2. The procedure of estimating the effective moduli from this problem is the same as that decribed in Problem 2. The transverse normal stress, σ_z, in this problem, however, is not zero. The Airy stress function, $F_j(x,z)$, for an orthotropic lamina of this problem for stresses in the (x-z or 1-3) plane has the form

$$F_j(x,z)=A_jx^2+B_jxz+C_jz^2+D_jx^2z+E_jxz^2+F_jz^3+G_j\left(x^2z^2-\frac{1}{6}\alpha_jz^4\right)+H_jxz^3+J_j\left(x^2z^3-\frac{1}{10}\alpha_jz^5\right) \tag{17}$$

where

$$\alpha_j=\frac{2S_{13}^{(j)}+S_{55}^{(j)}}{S_{11}^{(j)}}.$$

The displacement fields in each layer of the laminated beam, $u_j^c(x,z)$ and $w_j^c(x,z)$, along the x and z directions derived from the above stress function are, respectively,

$$\begin{aligned}u_j^c(x,z)=&[2A_jS_{13}^{(j)}+2C_jS_{11}^{(j)}]x+2D_jS_{13}^{(j)}xz\\&+E_j[S_{11}^{(j)}x^2-(S_{55}^{(j)}+S_{13}^{(j)})z^2]+6F_j(S_{11}^{(j)}xz\\&+G_j\left[\frac{2}{3}S_{11}^{(j)}x^3-2(S_{13}^{(j)}+S_{55}^{(j)})xz^2\right]\\&+H_j[3S_{11}^{(j)}x^2z-(S_{13}^{(j)}+S_{55}^{(j)})z^3]\\&+J_j[2S_{11}^{(j)}x^3z-2(S_{13}^{(j)}+S_{55}^{(j)})xz^3]+Q_jz+R_j\end{aligned} \tag{18}$$

$$\begin{aligned}w_j^c(x,z)=&2A_jS_{33}^{(j)}z-B_jS_{55}^{(j)}x+2C_jS_{13}^{(j)}z\\&+D_j[-(S_{13}^{(j)}+S_{55}^{(j)})x^2+S_{33}^{(j)}z^2]+2E_jS_{13}^{(j)}xz\\&+3F_j[-S_{11}^{(j)}x^2+S_{13}^{(j)}z^2]+G_j\left[2S_{13}^{(j)}x^2z+\frac{2}{3}S_{33}^{(j)}z^3\right]\\&+H_j[-S_{11}^{(j)}x^3+3S_{13}^{(j)}xz^2]+J_j\left[-\frac{1}{2}S_{11}^{(j)}x^4+3S_{13}^{(j)}x^2z^2\right.\\&\left.+\left\{\frac{1}{2}S_{33}^{(j)}+\frac{1}{2}\nu_{31}^{(j)}(2S_{13}^{(j)}+S_{55}^{(j)})\right\}z^4\right]-Q_jx+M_j.\end{aligned} \tag{19}$$

The constants A_j, B_j, ..., Q_j, R_j, M_j are determined from the boundary conditions and the continuity conditions of stresses and displacements at each lamina interface.

After applying Eqs. (18) and (19) for a single layer, the expressions for the displacement fields for the equivalent homogeneous beam, Fig. 4(b), for stresses in the 1-3 plane and satisfying the boundary conditions given by Eq. (8), are

$$u^h(x,z)=\frac{p-q}{bh^3}\left[2S_{11}(x^3-L^3)z+S_{13}\left(\frac{9}{10}(L-x)h^2z-2xz^3\right)+S_{55}\left(\frac{3}{10}(x+4L)h^2z-2xz^2\right)\right]-S_{13}\frac{p+q}{2b}(x-L) \tag{20}$$

$$\begin{aligned}w^h(x,z)=&\frac{p-q}{bh^3}\left[\frac{1}{2}S_{11}(4L^3x-3L^4-x^4)\right.\\&+S_{13}\left\{\frac{9}{20}(x^2-2Lx+L^2)h^2-\bar{\nu}_{31}^f\left(\frac{3}{10}h^2z^2-z^4\right)+3x^2z^2\right\}\\&+S_{33}\left(-\frac{3}{4}h^2z^2+\frac{1}{2}z^4\right)+S_{55}\left(\frac{3}{5}(x^2-2Lx+L^2)h^2\right.\\&\left.\left.-\frac{1}{2}\bar{\nu}_{31}^f\left(\frac{3}{10}h^2z^2-z^4\right)\right)\right]-S_{33}\frac{p+q}{2b}z\end{aligned} \tag{21}$$

and those for the boundary conditions given by Eq. (9) are

$$u^h(x,z)=\frac{p-q}{bh^3}\left[2S_{11}(x^3-L^3)z+S_{13}\left(\frac{9}{10}(L-x)h^2z-2xz^3\right)+S_{55}\left(\frac{3}{10}(x-L)h^2z-2xz^3\right)\right]-S_{13}\frac{p+q}{2b}(x-L) \tag{22}$$

Downloaded 03 May 2010 to 171.66.16.247. Redistribution subject to ASME license or copyright; see http://www.asme.org/terms/Terms_Use.cfm

$$w^h(x,z)=\frac{p-q}{bh^3}\left[\frac{1}{2}S_{11}(4L^3x-3L^4-x^4)\right.$$
$$+S_{13}\left\{\frac{9}{20}(x^2-2Lx+L^2)h^2-\bar{\nu}_{31}^f\left(\frac{3}{10}h^2z^2-z^4\right)+3x^2z^2\right\}$$
$$+S_{33}\left(-\frac{3}{4}h^2z^2+\frac{1}{2}z^4\right)+S_{55}\left(\frac{3}{10}(2x^2+Lx-3L^2)h^2\right.$$
$$\left.\left.-\frac{1}{2}\bar{\nu}_{31}^f\left(\frac{3}{10}h^2z^2-z^4\right)\right)\right]-S_{33}\frac{p+q}{2b}z. \quad (23)$$

The method of estimating S_{11}, S_{13}, S_{33}, and S_{55} from this problem is the same as described in Problem 2. The method, however, requires the displacements $u^h(x,z)$ and $w^h(x,z)$ in Eqs. (20)–(23) to be linear functions of S_{ij} $(i,j=1,3,5)$ and $\bar{\nu}_{31}^f$. In Problem 2, the displacements $u^h(x,z)$ and $w^h(x,z)$ are linear functions of S_{ij}, as seen in Eqs. (10)–(13). However, if $\bar{\nu}_{31}^f$ is considered to be unknown in Eqs. (20)–(23), then $u^h(x,z)$ and $w^h(x,z)$ are no longer linear functions of the S_{ij}. Thus, to force $u^h(x,z)$ and $w^h(x,z)$ to be linear in S_{ij}, the value of $\bar{\nu}_{31}^f$ for the laminate obtained from Problem 2 was supplied to either Eqs. (20)–(21) or the Eqs. (22)–(23) as the initial value. After estimating S_{ij} from Problem 3, $\bar{\nu}_{31}^f$ was recalculated and compared with the calculated in Problem 2. In all of our case studies, the difference in these two values of $\bar{\nu}_{31}^f$ was less than two percent. Moreover, a similar convergence study by varying the number of points in Eq. (14) lead to the same conclusion as in Problem 2.

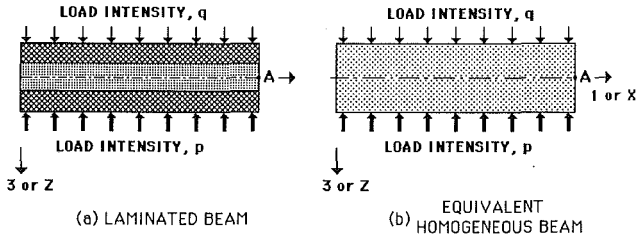

Fig. 4 Configuration of the laminated beam and its equivalent quasi-homogeneous beam under uniformly distributed load on the top and bottom surface

Results

The method described above is capable of determining all nine components of the three-dimensional effective moduli of a symmetric and orthotropic laminate. As a check on the validity of our results, the effective moduli associated with the lamination plane (x-y plane) were compared with the predictions of the classical laminated plate theory. The interlaminar properties predicted by the three boundary value problems were compared among each other. In addition, the predicted interlaminar shear stiffnesses, $\bar{G}_{13}^f$, were compared with the experimental values of several laminates. For the discussion of our

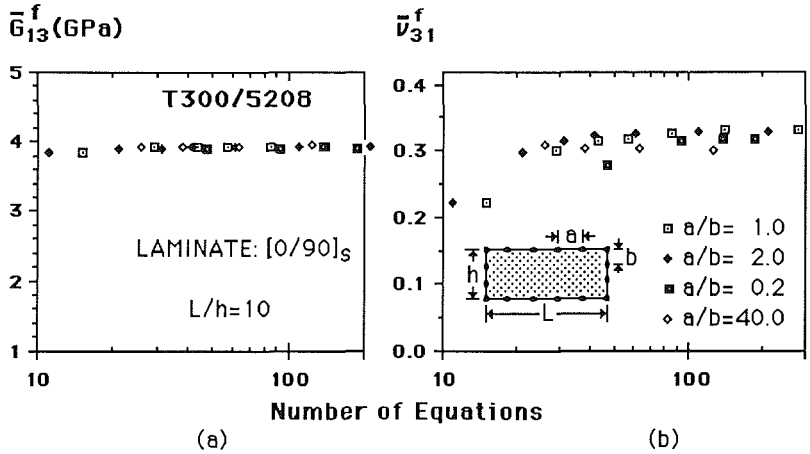

Fig. 5 Convergence of the properties of T300/5208, $[0/90]_s$ laminate for several ratios of horizontal to vertical spacings of the discreet boundary points, a/b; (*a*) for the interlaminar shear stiffness and (*b*) for the interlaminar Poisson's ratio. The abscissa is the number of equations used in Eq. (14).

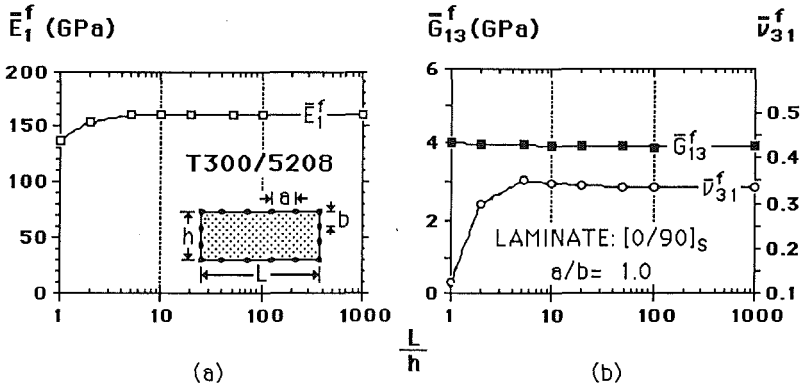

Fig. 6 Convergence of the effective elastic constants of a T300/5208, $[0/90]_s$ laminate for increasing length to depth ratio L/H; (*a*) for the normalized flexural stiffness, E_1^f and (*b*) for the interlaminar shear stiffness and Poisson's ratio

Downloaded 03 May 2010 to 171.66.16.247. Redistribution subject to ASME license or copyright; see http://www.asme.org/terms/Terms_Use.cfm

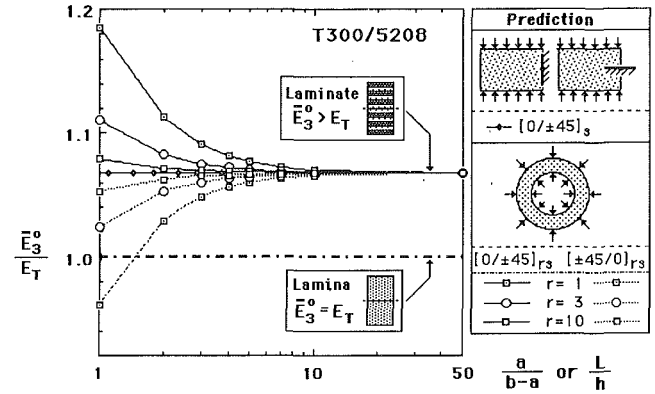

Fig. 7 Convergence of the interlaminar normal stiffness of $[0/\pm45]_{rs}$ and $[\pm45/0]_{rs}$ laminates. As the number of sublaminates r increases, the values of the interlaminar normal stiffness converge faster to its in-plane value.

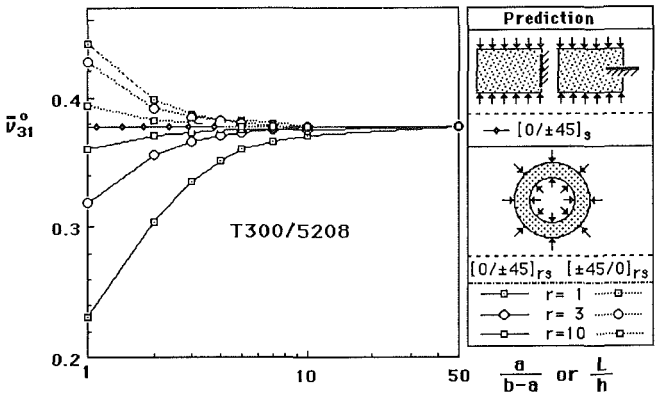

Fig. 8 Convergence of the interlaminar Poisson's ratio of $[0/\pm45]_{rs}$ and $[\pm45/0]_{rs}$ laminates. As the number of sublaminates r increases, the values of the interlaminar Poisson's ratio converge faster to its in-plane value.

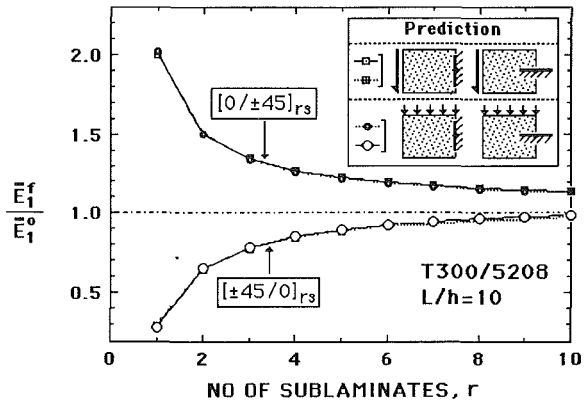

Fig. 9 Convergence of the values of $\bar{E}_1^f$ for $[0/\pm45]_{rs}$ and $[\pm45/0]_{rs}$ laminates. The predictions considering both the boundary conditions are shown.

results, the T300/5208 and AS4/3502 were chosen as two representative composites.

The three-dimensional unidirectional lamina properties were needed as the input data in our calculation. The lamina of a unidirectional graphite-epoxy composite is transversely isotropic. The three-dimensional elastic properties of a transversely isotropic lamina contain five independent constants, four are associated with its in-plane (two-dimensional) properites and the other one can be taken as one of its interlaminar properties, for instance, the transverse-transverse Poisson's ratio, ν_{32} (ν_{TT}). The two-dimensional properties of the two composites considered here are widely known. The authors measured the values of ν_{TT} for AS4/3502 composites, and that for T300/5208 composites was obtained from Knight (1982). The measured value of ν_{32} for both these two composites was found to be 0.52. The two-dimensional properties of these two composites are given in Tsai (1988, Appendix B).

Figures 5–9 are shown to establish the consistency and accuracy of the present method. The effective moduli for in-plane deformation were calculated by matching the outer and inner displacements of the two equivalent rings exactly. However, the effective moduli for the bending mode of deformation were estimated by minimizing the error between the boundary displacements of the two equivalent beams at a discreet number of boundary points. Thus, we need to check the convergence of the values of the effective moduli by varying the spacings of the boundary points and beam geometries (L/h). In Figs. 5 and 6 the results on the convergence of the effective moduli were obtained from Problem 2. Figure 5 shows the values of $\bar{G}_{31}^f$ and $\bar{\nu}_{31}^f$ for several ratios of the horizontal to vertical spacings, a/b, of the boundary points. The abscissa in Fig. 5 is the number of equations used in Eq. (14) for minimizing the error. For n boundary points there were $2n$ number of equations used in Eq. (14). Figure 5(b) reveals that the interlaminar Poisson's ratio, $\bar{\nu}_{31}^f$, was somewhat sensitive to the ratio, a/b, and the number of equations $2n$, however, the scatter was within ten percent. On the other hand, $\bar{E}_1^f$ and $\bar{G}_{31}^f$ were both sensitive to a/b. Several case studies suggested that for a good estimate of $\bar{\nu}_{31}^f$, the spacing of the boundary points in the thickness direction should be less than or equal to the lamina thickness and the value of the ratio a/b should be in the neighborhood of unity.

A similar convergence study is shown in Fig. 6 with increasing beam aspect ratio, L/h. Both Figs. 6(a) and (b) imply that the estimates of the effective moduli are practically constant for $L/h \geq 10$. Thus, we propose this method for estimating the effective moduli for the bending mode of deformation to be applicable for laminate aspect ratio $L/h \geq 10$.

The results from the three boundary value problems will now be presented to discuss the behavior of effective properties of a symmetric laminate under the three types of deformation (in-plane extension, bending, and shear) considered in this paper. For the purpose of discussion, a T300/5208 $[0/\pm45]_{rs}$ was chosen as the representative laminate. The adjacent (±45) laminae of the laminate, as mentioned before, are assumed to behave as orthotropic layers. Figure 7 shows the convergence of the values of $\bar{E}_3^o$ of two $[0/\pm45]_{rs}$ laminates with reversed stacking sequences as obtained from the ring problem. The subscript r, used above in the laminate notation, indicates the number of sublaminates used in the half-laminate. The values of $\bar{E}_3^o$ was normalized by that of the transverse stiffness, E_T, of the constituent lamina. For the ring aspect ratio, $a/(b\text{-}a) \geq 10$, the values of $\bar{E}_3^o$ practically converged to a single value, thus ensuring that the ring was under extensional deformation for $a/(b\text{-}a) \geq 10$. The converged value of $\bar{E}_3^o$ obtained from the ring problem was compared to that obtained from problem 3 with equal load intensities on the top and bottom surfaces. The difference in the values of $\bar{E}_3^o$ obtained from these two problems was found to be within 0.01 percent. Moreover, it was found from several case studies that the value of $\bar{E}_3^o$ of multidirectional laminates made with laminae of the same material was higher than the transverse modulus of a constituent lamina, as was observed by Pagano (1974). Additionally in Fig. 7, with the increasing number of sublaminates r, the effect of stacking sequence on $\bar{E}_3^o$ decreased with decreasing values of the $a/(b\text{-}a)$ ratio. It is also known that if the ring was made with homogeneous material, its $\bar{E}_3^o$ value would have been the same for all values of $a/(b\text{-}a)$. Thus, with an increasing number of sublaminates, the laminate haves more and more like a homogeneous material. A sim-

Downloaded 03 May 2010 to 171.66.16.247. Redistribution subject to ASME license or copyright; see http://www.asme.org/terms/Terms_Use.cfm

Table 1 Comparison of the predicted values of the interlaminar shear stiffness for several laminates with the measured values; composite: AS4/3502

LAMINATE	EXPERIMENTAL (Roy and Kim, 1989)		PREDICTED $\bar{G}^f_{13}$ (GPa)
	L/H	$\bar{G}^f_{13}$ (GPa)	(Present Method)
$[0]_T$	8.96-7.17	4.98±4%	$5.17=G_{LT}$
$[90]_T$	5.54-2.22	3.03±2%	$3.07=G_{TT}$
$[0_2/90_2]_{7S}$	6.82-3.41	4.03±2%	3.97
$[90_2/0_2]_{7S}$	6.71-3.35	4.37±4%	4.00
$[0_2/90_2/45_2/-45_2]_{4S}$	5.97-2.98	4.52±2%	4.08
$[90_2/0_2/45_2/-45_2]_{4S}$	5.85-2.92	4.33±5%	4.05
$[(45/-45)_{11}/0_2]_S$	11.86-2.96	4.16±3%	3.96
$[(-45/45)_{11}/90_2]_S$	10.25-3.07	3.27±6%	3.56

ilar result for the interlaminar Poisson's ratio, $\bar{\nu}^o_{31}$, for the $[0/\pm 45]_{rs}$ laminates are shown in Fig. 8.

We now study the effective moduli of laminates for bending and shear deformation. To check the results obtained from the two beam problems, the bending stiffness associated with the lamination plane, $\bar{E}^f_1$, for $[0/\pm 45]_{rs}$ and $[\pm 45/0]_{rs}$ laminates was plotted in Fig. 9, and then was compared with the extensional stiffness $\bar{E}^o_1$ of those two laminates predicted by the classical laminated plate theory. Both $\bar{E}^f_1$ and $\bar{E}^o_1$ were the respective normalized stiffness as defined by Tsai (1988, in its Section 8). As the number of sublaminates, r, increases while keeping the L/h ratio constant, these two laminates become more and more homogenized; hence, the values of $\bar{E}^f_1$ of these two laminates should converge to its homogeneous value. Figure 9 indicates that trend, however, the values of $\bar{E}^f$ of these two laminated converge asymptotically to a value which is somewhat different from that of $\bar{E}^o_1$ of the laminates as $r\to\infty$. We found that this difference was somewhat dependent of the finite L/h ratio and the lamination scheme.

Two boundary conditions, defined by Eqs. (8) and (9), were considered for estimating the effective stiffnesses for bending and transverse shear deformations. Both boundary conditions predicted practically the same bending stiffness, $\bar{E}^f_1$, as was shown in Fig. 9. However, the predictions of the effective interlaminar shear stiffness, $\bar{G}^f_{13}$, and Poisson's ratio, $\bar{\nu}^f_{31}$, were very sensitive to the difference in the boundary conditions. Figures 10(*a*) and 10(*b*) show the values of $\bar{G}^f_{13}$ predicted by the two boundary conditions. In these two figures the value of $\bar{G}^f_{13}$ was normalized by that of the lamina in-plane shear stiffness, G_{LT}. As in Fig. 9, as the number of sublaminates r increases, the stacking sequence effect of these two laminates, $[0/\pm 45]_{rs}$ and $[\pm 45/0]_{rs}$, influences the value of $\bar{G}^f_{13}$ and is expected to gradually diminish; eventually, as $r\to\infty$ the value of $\bar{G}^f_{13}$ for these two laminates should converge to a single value. Figure 10(*a*) shows this trend whereas Fig. 10(*b*) does not. In Fig. 10(*a*) the values of $\bar{G}^f_{13}$ were predicted by using the boundary condition (*h*) given by Eq. (8). Thus the boundary condition (*h*) was chosen for comparing the predicted values of $\bar{G}^f_{13}$ with the experimental results in the next paragraph. Incidentally, in Fig. 10(*a*) there was some difference (less than four percent for $r=10$) in the values of $\bar{G}^f_{13}$ predicted by the two beam problems. Moreover, the deviation of the predicted values of $\bar{G}^f_{13}$ for any linear combinations of the boundary conditions of Problem 2 and 3 is found to be within four percent of its average value obtained separately from Problems 2 and 3 and for $r=10$. If four percent scatter in the values of $\bar{G}^f_{13}$ is considered to be acceptable, then the values of $\bar{G}^f_{13}$ predicted by averaging the results for the boundary conditions of these two problems indicate to the authors that the present method yields acceptable predictions of $\bar{G}^f_{13}$ for orthotropic

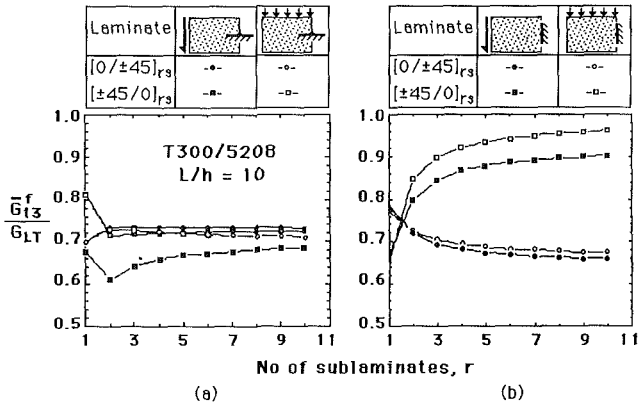

Fig. 10 Convergence of the values of the interlaminar shear stiffness for $[0/\pm 45]_{rs}$ and $[\pm 45/0]_{rs}$ laminates with increasing number of sublaminates; (*a*) for boundary condition (*h*), (*b*) for boundary condition (*v*).

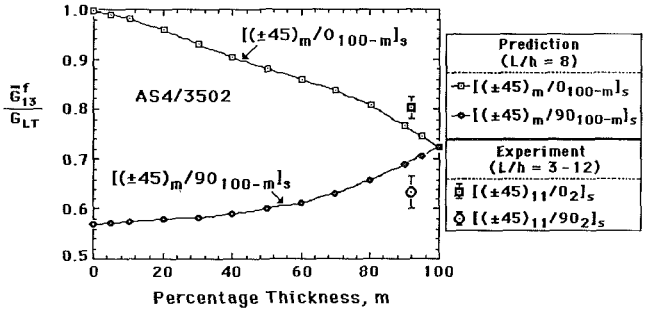

Fig. 11 Comparison of the predicted interlaminar shear stiffness with measured values for two laminates each containing a very thin lamina at midplane. The measured values are from Table 1.

and symmetric laminates in bending with the shear mode of deformation.

Besides comparing our predicted data among the three boundary value problems, we also compared the predicted values of $\bar{G}^f_{13}$ with the experimental data in Table 1. The experimental data of $\bar{G}^f_{13}$ presented in Table 1 are reported by Roy and Kim (1989). The values of $\bar{G}^f_{13}$ were measured by the three-point bend test of beams of rectangular cross-section. The configuration of a beam in the three-point bend test can be modeled as two inverted cantilever beams of the Problem 2, configured symmetrically about the loading point. Between the two boundary conditions (*h*) and (*v*), given by Eqs. (8) and (9), respectively, it was observed in Fig. 10 that condition (*h*) yields a reliable prediction of $\bar{G}^f_{13}$. Thus, the values of $\bar{G}^f_{13}$ predicted by using boundary condition (*h*) were only shown in Table 1. Considering the amount of scatter in the experimental data, the predicted values seemed to be in good agreement with the experimental data.

Except for the laminates, $[(\pm 45)_{11}/0_2]_s$ and $[(\pm 45)_{11}/90_2]_s$, all the laminates shown in Table 1 are made of sublaminates. The two laminates, $[(\pm 45)_{11}/0_2]_s$ and $[(\pm 45)_{11}/90_2]_s$, have very thin (8.3 percent of laminate thickness) layers of 0-deg and 90-deg lamina, respectively. The reason of choosing these two laminates was to critically test the validity of our predictions. Thus, in Fig. 11, the experimental values of the laminates, $[(\pm 45)_{11}/0_2]_s$ and $[(\pm 45)_{11}/90_2]_s$, were compared graphically with the predicted values. The predicted values of $\bar{G}_{f3}$ for these two laminates were, respectively, within five and eight percent of the measured values. The experimental values, however, had three and six percent scatter, respectively. Considering the amount of scatter, the predicted values appeared to be in good agreement with the experimental values.

Figures 7–11 and Table 1 had been used to establish the validity and accuracy of our method. It was also shown above

Downloaded 03 May 2010 to 171.66.16.247. Redistribution subject to ASME license or copyright; see http://www.asme.org/terms/Terms_Use.cfm

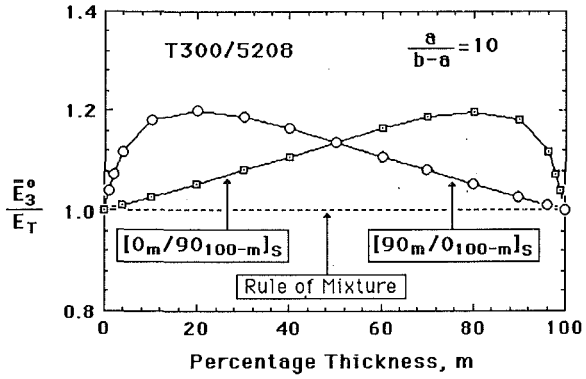

Fig. 12 Variation of the interlaminar normal stiffness with changing lamina thickness ratio of two cross-ply laminates for in-plane deformation

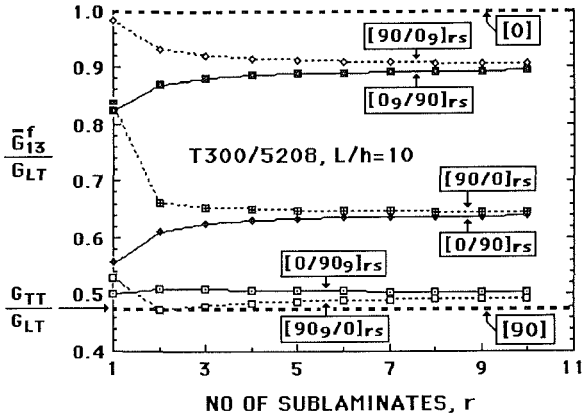

Fig. 13 The interlaminar shear stiffness of several cross-ply laminates of different relative lamina thickness

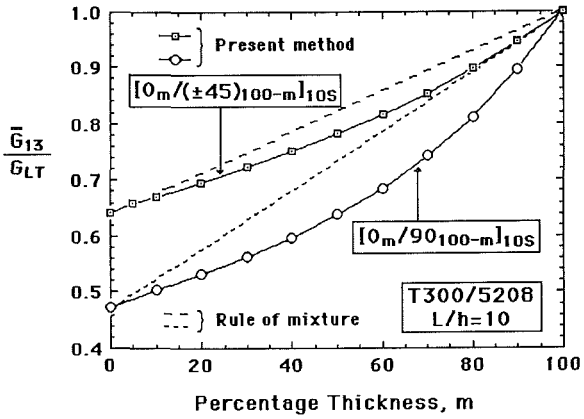

Fig. 14 The interlaminar shear stiffness of two highly homogenized laminates of varying relative lamina thickness. These two laminates are composed of 20 sublaminates.

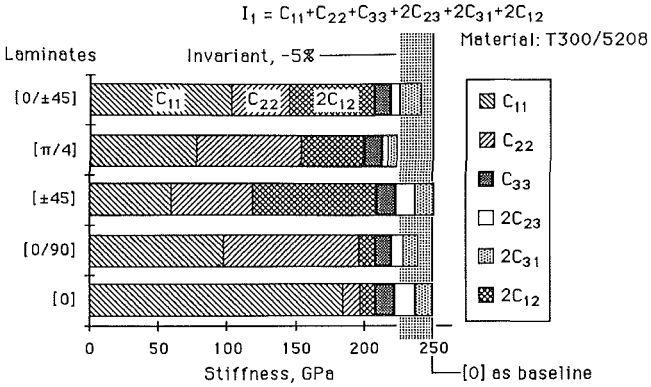

Fig. 15 The first linear invariants of the stiffness constants for various typical laminates are compared with that of the [0] thick laminate

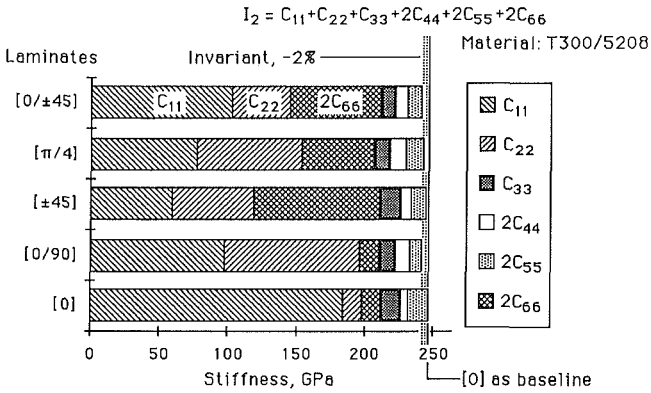

Fig. 16 The second linear invariants of the stiffness constants for various typical laminates are compared with that of the [0] thick laminate

that boundary condition (h) seemed to be the acceptable boundary condition over condition (v) for predicting the values of the effective moduli. Having done so, in the following figures we made a few case studies taking only the boundary condition (h). The effect of relative lamina thickness on the values of effective moduli of laminates was studied in Figs. 12–14. The values of the effective interlaminar normal stiffness, $\bar{E}_3^o$, in extension, for two cross-ply laminates of varying lamina thickness were plotted in Fig. 12. The values of $\bar{E}_3^o$ in this figure were normalized by that of the transverse stiffness, E_T, of the constituent unidirectional lamina. The values of $\bar{E}_3^o$ for these two laminates, $[0_m/90_{100\text{-}m}]_s$ and $[90_m/0_{100\text{-}m}]_s$, were symmetric, m being equal to 50 percent. Thus, $\bar{E}_3^o$ is not dependent on stacking sequence. Moreover, the value of $\bar{E}_3^o$ in extension is independent of any degree of homogenization (i.e., any number sublaminates used in the laminate), because the strain level is the same for all laminae of the laminate for in-plane extension.

The effect of the number of sublaminates and the relative lamina thickness on the shear stiffness, $\bar{G}_{13}^f$, were shown in Figs. 13 and 14. In Fig. 13 the values of $\bar{G}_{13}^f$ were plotted for cross-ply laminates of reversed stacking sequence and with an increasing number of sublaminates. For a large number of sublaminates (for example, $r=10$ or higher), the values of $\bar{G}_{13}^f$ for these laminates of reversed stacking sequence almost converge to the same value. Similar results were also observed in the case of $\bar{\nu}_{31}^f$. Thus, for a symmetric laminate made of 20 or more sublaminates, its effective properties become almost independent of stacking sequence; hence, the prediction by Pagano (1974), Sun (1988), and Chou (1972) for such laminates will be fairly accurate.

In Fig. 14 the values of $\bar{G}_{13}$ of two symmetric laminates consisting of 20 sublaminates, $[0_m/90_{100\text{-}m}]_{10s}$ and $[0_m/(\pm 45)_{100-m}]_{10s}$, were plotted with varying relative thickness of the constituent laminae. Since for laminates with a large number of sublaminates the values of the effective moduli are practically independent of mode of deformation, the superscript "f" and "o" were omitted from the notations of the effective elastic constants in this figure. Frequently, the stiffness rule of mixtures is used in the literature for predicting $\bar{G}_{13}$, Post et al. (1989). Thus, the present predictions of $\bar{G}_{13}$ were compared with that predicted by the stiffness rule of mixture in Fig. 14. The predictions by the rule of mixture for laminates $[0_m/90_{100-m}]_{10s}$ differed from the present ones by as much as 15 percent for $m=60$ percent. As a result, for multidirectional laminates, the rule of mixture gives an inaccurate

Downloaded 03 May 2010 to 171.66.16.247. Redistribution subject to ASME license or copyright; see http://www.asme.org/terms/Terms_Use.cfm

prediction of $\bar{G}_{13}$, whereas it was observed that for $\bar{\nu}_{31}$, the present predictions were the same as that by the rule of mixture.

In two dimensions there exists two linear invariant relations for stiffness; one is related to the areal invariant (a measure of the change in area); the other is the trace. The similar invariant constraints were imposed in the three dimension with effective properties predicted here. For thick laminates of various common-ply orientations, we have shown the degree of invariance of the laminate stiffnesses was compared. The two linear invariants are the hydrostatic invariant, in Fig. 15, and the trace in Fig. 16. Unlike in two dimension, a deviation in the invariance values was observed among various laminates in these two figures. A source of the deviation may be explained in terms of the approximations in the prediction of the interlaminar constants, such as that shown in Fig. 8. Another source of deviation may be attributed to the exact microstructure of the composites. In fact, the invariance of the in-plane (the lamination plane) components reveals more a parallel connected structure than that of the interlaminar components. But as a whole, the deviation is not as great as that for the compliance matrix of our three-dimensional composite. For example, the numerical value of the trace of the stiffness $[C]$ of the laminates shown in Fig. 16 varied from 243 to 248, while the trace of compliance $[S]$ of the same laminates varied from 300 to 485. Thus, suffice it to say that the microstructure of the laminates are more parallel connected than series connected. A check on the invariance is helpful in revealing the nature of the construction of a laminated composite.

In summary, the present method can predict all the effective elastic constants for orthotropic and symmetric laminates for extension and bending with the shear mode of deformations. Among the nine elastic constants, four are associated with the lamination plane (x-y or 1-2 plane), and the rest are associated with the interlaminar planes (x-z, -z; or 1-3 or 2-3 planes). The effective elastic constants associated with the lamination plane are easily predicted by the classical lamination theory. The prediction of effective elastic constants associated with the interlaminar planes were emphasized in this paper. The results of the interlaminar effective elastic constants presented above were for the x-z or 1-3 plane. Similar results associated with the y-z or 2-3 plane could be obtained by rotating the laminate about the z-axis by 90 deg.

Conclusion

A simple method of predicting the three-dimensional effective moduli of orthotropic and symmetric laminates is presented. The effective moduli for the two modes of deformation addressed here are in-plane extension and bending with shear. The effective moduli are estimated by matching the boundary displacements of the laminated system with that of an equivalent homogeneous system. The method is found to be accurate for length-to-depth ratios, $L/h \geq 10$. The values of the interlaminar shear stiffnesses predicted by this method are found to be in good agreement with the experimental results. It is also found that the effect of stacking sequence on the interlaminar shear stiffnesses almost disappears if a symmetric laminate is composed of 20 or more number of sublaminates.

The effective elastic constants are predicted by three separate but interrelated boundary value problems. The predictions of elastic constants obtained by mixing the surface tractions among these three boundary value problems indicate that the scatter in the predicted effective elastic constants are practically negligible, and thus the predicted values can be used as the representative effective elastic constants of a laminate. With the three-dimensional effective elastic constants, the stress analysis for effective response of laminated composites can be much simplified, because the lamina-by-lamina modeling will, in this case, be replaced by modeling the laminate as one equivalent homogeneous body. The method of predicting the effective elastic constants presented here can be used as a preprocessor to any three-dimensional stress analysis of laminated composites.

Acknowledgment

One of the authors (AKR) wishes to acknowledge the financial support for this work from the Air Force Materials Laboratory under contract F33615-87-C-5239. The authors have greatly benefited from several technical discussions with Dr. N. J. Pagano, Material Laboratory, Wright Research and Development Center.

References

Chou, P. C., and Carleone, J., 1972, "Elastic Constants of Layered Media," *Journal of Composite Materials*, Vol. 6, pp. 80–93.

Knight, M., 1982, "Three-Dimensional Elastic Moduli of Graphite/Epoxy Composites," *Journal of Composite Materials*, Vol. 16, pp. 153–159.

Lekhnitskii, S. G., 1968, *Anisotropic Plates*, translated by S. W. Tsai and T. Cheron, Gordon and Breach Science Publishers, pp. 110–114.

Pagano, N. J., 1974, *Exact Moduli of Anisotropic Laminates: Mechanics of Composite Materials*, Vol. 2, G. P. Sendeckyj, ed., Academic Press.

Reddy, J. N., 1986, "A Refined Shear Deformation Theory for the Analysis of Laminated Plates," NASA-CR-3955.

Roy, A. K., and Kim, R. Y., 1989, "Experimental Determination of Transverse Shear Stiffness of a Thick Laminate," 1989 SEM Spring Conference on Experimental Mechanics, May 29–June 1, 1989, Cambridge, Mass.

Sun, C. T., and Li, S., 1988, "Three-Dimensional Effective Elastic Constants for Thick Laminates," *Journal of Composite Materials*, Vol. 22, No. 7, pp. 629–639.

Timoshenko, S. P., and Goodier, J. N., 1934, *Theory of Elasticity*, 3rd ed., McGraw-Hill, New York, Art. 21, pp. 41–46.

Tsai, S. W., 1988, *Composites Design*, 4th ed., Think Composites, Dayton, OH.

Whitney, J. M., and Pagano, N. J., 1970, "Shear Deformation in Heterogeneous Anisotropic Plates," ASME JOURNAL OF APPLIED MECHANICS, Vol. 92, Series E, pp. 1031–1036.

Post, D., Dai, F. L., Guo, Y., and Ifju, P., 1989, "Interlaminar Shear Moduli of Cross-Ply Laminates: An Experimental Analysis," *Journal of Composite Materials*, Vol. 23, pp. 264–279.

Downloaded 03 May 2010 to 171.66.16.247. Redistribution subject to ASME license or copyright; see http://www.asme.org/terms/Terms_Use.cfm

M. Ortiz
Division of Engineering,
Brown University,
Providence, RI 02912

A. Molinari
Laboratoire de Physique et Mecanique
des Materiaux,
Faculte des Sciences,
Ile du Saulcy,
Universite de Metz,
57000 Metz, France

Effect of Strain Hardening and Rate Sensitivity on the Dynamic Growth of a Void in a Plastic Material

The problem studied in this paper concerns the dynamic expansion of a spherical void in an unbounded solid under the action of remote hydrostatic tension. The void is assumed to remain spherical throughout the deformation and the matrix to be incompressible. The effects of inertia, strain hardening, and rate sensitivity on the short and long-term behavior of the void, as well as on its response to ramp loading, are investigated in detail.

1 Introduction

The problem studied in this paper concerns the dynamic expansion of a spherical void in a unbounded rate-dependent solid under the action of rapidly varying remote hydrostatic tension. Conditions such as those investigated here are prevalent in the vicinity of a crack running through a ductile metal, in porous solids subjected to blast loading, and in other situations of practical interest. In particular, void growth and coalescence is known to be a principal micromechanism of fracture in ductile metals. In dynamic crack growth, the microinertia associated with the rapid growth of the voids may influence, in ways as yet not fully understood, the conditions under which a ductile mode of fracture becomes possible.

Whereas much attention has been given to void growth under static conditions, the dynamic problem has remained relatively unexplored. Carroll and Holt (1972) investigated the static and dynamic collapse of voids using a hollow sphere model. The solid was assumed to be rate insensitive and ideally plastic. A notable outcome of their analysis is the small effect of elastic compressibility on the solution. Johnson (1981) applied Carroll's approach to voids expanding in a viscoplastic solid described by a simple linear overstress model. Glennie (1972) sought to extend the analysis of Rice and Johnson (1970) for a void growing in the vicinity of a blunted crack tip in a plastic material, by taking dynamic effects into consideration. However, his analysis is restricted to ideally plastic behavior and linear viscosity. More recently, Klöcker and Montheillet (1988) have conducted numerical calculations for a dynamically growing void in a plastic solid obeying a linear stress-strain rate law. Their results exhibit the potentially stabilizing effect of inertia at the microscale.

The purpose of this investigation is to develop an understanding of the effect of inertia, strain hardening, and rate dependence on void growth in porous metals under conditions of rapid loading. To simplify the analysis, it is assumed that the material is incompressible and the void remains spherical at all times. These assumptions determine the velocity field throughout the body once the rate of expansion of the void is specified. Thus, the problem is reduced to the integration in time of an ODE for the void radius. Whereas a small compressibility is always introduced by the elastic response of the solid, Carroll and Holt's work (1972) suggests that this effect is negligible in cases where the plastic response dominates. The solid is assumed to obey J_2-flow theory of plasticity with power hardening and the elastic response is neglected. Rate sensitivity is introduced into the formulation through a standard power-law viscoplastic model. The details of the formulation of the constitutive model are given in Section 2.

The equations governing the expansion of a void are formulated in Section 3 for various constitutive assumptions. Although the majority of these equations cannot be solved in closed form, the short and long-term solutions can be obtained analytically with some generality. These solutions reveal useful insights into the behavior of the void as determined by the various constitutive descriptions. Finally, full numerical calculations are presented in Section 5 which confirm the short and long-term solutions and exhibit the nature of the intermediate transients.

2 Constitutive Model

Throughout the analysis, we shall assume that the matrix surrounding the void responds to monotonic stressing as a rigid-viscoplastic solid with flow rule

$$d_{ij} = \dot{\epsilon}_e \frac{3s_{ij}}{2\sigma_e} = \frac{\partial \phi(\mathbf{s})}{\partial s_{ij}} \tag{1}$$

Contributed by the Applied Mechanics Division of THE AMERICAN SOCIETY OF MECHANICAL ENGINEERS for publication in the JOURNAL OF APPLIED MECHANICS.

Discussion on this paper should be addressed to the Technical Editor, Prof. Leon M. Keer, The Technological Institute, Northwestern University, Evanston, IL 60208, and will be accepted until two months after final publication of the paper itself in the JOURNAL OF APPLIED MECHANICS. Manuscript received by the ASME Applied Mechanics Division, Apr. 6, 1989.

Copyright © 1992 by ASME
Downloaded 03 May 2010 to 171.66.16.247. Redistribution subject to ASME license or copyright; see http://www.asme.org/terms/Terms_Use.cfm

where

$$\sigma_e = \sqrt{(3/2)s_{ij}s_{ij}} \tag{2}$$

$$s_{ij} = \sigma_{ij} - p\delta_{ij}, \quad p = \sigma_{kk}/3 \tag{3}$$

$$\dot{\epsilon}_e = \dot{\epsilon}_0 \left(\frac{\sigma_e}{\sigma_0}\right)^m \tag{4}$$

$$\phi(\mathbf{s}) = \frac{\sigma_0 \dot{\epsilon}_0}{m+1} \left(\frac{\sigma_e}{\sigma_0}\right)^{m+1}. \tag{5}$$

Here, σ_{ij} is the stress tensor, s_{ij} the deviatoric stresses, p the hydrostatic pressure, d_{ij} is the rate of deformation tensor, σ_e and ϵ_e the effective Mises stress and strain, respectively, σ_0 is a flow stress, and $\dot{\epsilon}_0$ and m are material constants. The flow stress is assumed to obey the hardening law

$$\sigma_0 = \sigma_y \left(\frac{\epsilon_e}{\epsilon_y}\right)^{1/n} \tag{6}$$

where σ_y, ϵ_y and n are material constants.

The rate-independent limit of the aforementioned model is attained by letting $m \to \infty$, whereupon the viscosity law (4) reduces to the condition

$$\sigma_e = \sigma_0. \tag{7}$$

The perfectly plastic limit, on the other hand, is attained by letting $n \to \infty$ in Eq. (4), which thus reduces to the identity

$$\sigma_0 = \sigma_y. \tag{8}$$

The inverse stress-strain relations are readily computed to be

$$s_{ij} = \sigma_e \frac{2d_{ij}}{3\dot{\epsilon}_e} = \frac{\partial \psi(\mathbf{d})}{\partial d_{ij}} \tag{9}$$

where

$$\dot{\epsilon}_e = \sqrt{(2/3)d_{ij}d_{ij}} \tag{10}$$

$$\sigma_e = \sigma_0 \left(\frac{\dot{\epsilon}_e}{\dot{\epsilon}_0}\right)^{1/m} \tag{11}$$

$$\psi(\mathbf{d}) = \frac{m\sigma_0\dot{\epsilon}_0}{m+1} \left(\frac{\dot{\epsilon}_e}{\dot{\epsilon}_0}\right)^{(m+1)/m} = s_{ij}d_{ij} - \phi(\mathbf{s}). \tag{12}$$

For use in subsequent developments, we note that the rate of plastic work per unit volume corresponding to the foregoing model is

$$\dot{w}^p = s_{ij}d_{ij} = \sigma_e\dot{\epsilon}_e = \sigma_0\dot{\epsilon}_0 \left(\frac{\dot{\epsilon}_e}{\dot{\epsilon}_0}\right)^{(m+1)/m} \tag{13}$$

and that, in the rate-independent limit, the dissipated plastic work per unit volume is given by

$$w^p = \int_0^{\epsilon_e} \sigma_e d\epsilon_e = \frac{n\sigma_y\epsilon_y}{n+1} \left(\frac{\epsilon_e}{\epsilon_y}\right)^{(n+1)/n}. \tag{14}$$

3 Governing Equations

Next, consider a spherical void of radius a in an infinite body subjected to remote pressure p. Assume that the void remains spherical throughout the deformation. Then, it follows from the volume constraint that

$$\frac{d}{dt}\frac{4\pi}{3}(r^3 - a^3) = 0 \tag{15}$$

where r is the radius of a material sphere deforming with the solid. This condition uniquely determines the velocity field over the current configuration, with the result that

$$\dot{r} = v_r = \frac{a^2}{r^2}\dot{a}. \tag{16}$$

The corresponding rate of effective Mises strain is computed to be

$$\dot{\epsilon}_e = |\partial v_r/\partial r| = \frac{2a^2}{r^3}|\dot{a}|. \tag{17}$$

Using again the volume constraint one finds

$$r^3 = a^3 + R^3 - a_0^3 \tag{18}$$

where R is the undeformed radius of points currently at r. Inserting (18) in (17) we find

$$\dot{\epsilon}_e = \frac{2a^2}{a^3 + R^3 - a_0^3}|\dot{a}| \tag{19}$$

which gives the effective strain rate as a function of position on the undeformed configuration. This expression is readily integrated to yield

$$\epsilon_e = \frac{2}{3}\log\left(1 + \frac{a^3 - a_0^3}{R^3}\right) = \frac{2}{3}\log\left(1 + \frac{a^3 - a_0^3}{r^3 - (a^3 - a_0^3)}\right) \tag{20}$$

where use has been made once more of the deformation mapping (18).

From (16), the kinetic energy of the body is computed to be

$$K = \int_a^\infty \frac{1}{2}\rho v_r^2 4\pi r^2 dr = \frac{3}{2}\rho\dot{a}^2\frac{4\pi a^3}{3}. \tag{21}$$

The rate of plastic work, on the other hand, follows by integration of (13) over the body, which together with (19) yields

$$\dot{W}^p = \int_a^\infty \sigma_y \left(\frac{\epsilon_e}{\epsilon_y}\right)^{1/n} \dot{\epsilon}_0 \left(\frac{\dot{\epsilon}_e}{\dot{\epsilon}_0}\right)^{(m+1)/m} 4\pi r^2 dr$$

$$= \sigma_y\dot{\epsilon}_0 \left(\frac{2}{3\epsilon_y}\right)^{1/n} \left(\frac{2\dot{a}}{\dot{\epsilon}_0 a}\right)^{(m+1)/m} f(a/a_0, m, n)\frac{4\pi a^3}{3} \tag{22}$$

where

$$f(a/a_0, m, n) = \int_1^\infty \left[\log\left(\frac{x}{x - 1 + a_0^3/a^3}\right)\right]^{1/n} x^{-(m+1)/m} dx. \tag{23}$$

In the perfectly plastic case, one has $f = m$ and (22) reduces to

$$\dot{W}^p = m\sigma_y\dot{\epsilon}_0 \left(\frac{2\dot{a}}{\dot{\epsilon}_0 a}\right)^{(m+1)/m} \frac{4\pi a^3}{3}. \tag{24}$$

In the rate-independent limit, it is possible to compute directly the dissipated plastic work from (14) and (20). Straightforward manipulations give

$$W^p = \int_a^\infty \frac{n\sigma_y\epsilon_y}{n+1} \left(\frac{\sigma_e}{\epsilon_y}\right)^{(n+1)/n} 4\pi r^2 dr \tag{25}$$

$$= \frac{n\sigma_y\epsilon_y}{n+1} \left(\frac{2}{3\epsilon_y}\right)^{(n+1)/n} g(a/a_0, n)\frac{4\pi a^3}{3} \tag{25}$$

where

$$g(a/a_0, n) = \int_1^\infty \left[\log\left(\frac{x}{x - 1 + a_0^3/a^3}\right)\right]^{(n+1)/n} dx. \tag{26}$$

Finally, the external power input into the system by the remotely applied pressure is

$$\dot{W} = 3p\frac{\dot{a}}{a}\frac{4\pi a^3}{3}. \tag{27}$$

If, for instance, the pressure history is of the type

$$p(t) = pH(t), \tag{28}$$

then Eq. (27) can be integrated to give

$$W = p\frac{a^3 - a_0^3}{a^3}\frac{4\pi a^3}{3}. \tag{29}$$

Downloaded 03 May 2010 to 171.66.16.247. Redistribution subject to ASME license or copyright; see http://www.asme.org/terms/Terms_Use.cfm

More generally, if p derives from a potential U through a relation of the type

$$p = U'(\Delta V) \tag{30}$$

where $\Delta V = 4\pi(a^3 - a_0^3)/3$ is the increase in volume of the void, then (29) generalizes to

$$W = U(4\pi(a^3 - a_0^3)/3). \tag{31}$$

The governing equation for a follows simply from the principle of conservation of energy, which in the present context states

$$\dot{W} = \dot{K} + \dot{W}^p. \tag{32}$$

Using (21), (22), and (27), Eq. (32) may be recast as

$$\frac{d}{dt}\left(\frac{3}{2}\rho\dot{a}^2\frac{4\pi a^3}{3}\right) + \sigma_y\dot{\epsilon}_0\left(\frac{2}{3\epsilon_y}\right)^{1/n}\left(\frac{2\dot{a}}{\dot{\epsilon}_0 a}\right)^{(m+1)/m} \times f(a/a_0,m,n)\frac{4\pi a^3}{3} = 3p\frac{\dot{a}}{a}\frac{4\pi a^3}{3} \tag{33}$$

which defines a second-order, nonlinear ODE for $a(t)$, subject to the initial conditions

$$a(0) = a_0. \tag{34}$$

In addition, plastic irreversibility requires that the constraint

$$\dot{a} \geq 0 \tag{35}$$

be satisfied at all times.

In the rate-independent case with p deriving from a potential as in (30), a first integral of (33) can be obtained by recourse to the principle of conservation of energy in its form

$$W = K + W^p. \tag{36}$$

Using (21), (25), and (31), Eq. (36) becomes

$$\frac{3}{2}\rho\dot{a}^2\frac{4\pi a^3}{3} + \frac{n\sigma_y\epsilon_y}{n+1}\left(\frac{2}{3\epsilon_y}\right)^{(n+1)/n} g(a/a_0,n)\frac{4\pi a^3}{3} = U(4\pi(a^3 - a_0^3)/3). \tag{37}$$

This is a first-order ODE in the unknown a.

In subsequent developments it proves advantageous to use governing equations expressed in dimensionless form. To this end, introduce the material constant

$$k = \sigma_y\epsilon_y^{-1/n}\dot{\epsilon}_0^{-1/m}, \tag{38}$$

whereupon Eq. (4) becomes

$$\sigma_e = k\epsilon_e^{1/n}\dot{\epsilon}_e^{1/m}. \tag{39}$$

The scaling of the strain rates and stresses is effected by means of a suitably chosen reference strain rate $\dot{\epsilon}_{\text{ref}}$ and the associated reference stress

$$\sigma_{\text{ref}} = k(\dot{\epsilon}_{\text{ref}})^{1/m}. \tag{40}$$

The proper choice of $\dot{\epsilon}_{\text{ref}}$ depends on the problem under consideration. Dimensionless time $\tilde{t}$, radius $\tilde{a}$, velocity $\tilde{b}$, and pressure $\tilde{p}$ may be defined as

$$\begin{aligned} \tilde{t} &= \dot{\epsilon}_{\text{ref}}t \\ \tilde{a} &= a/a_0 \\ \tilde{b} &= d\tilde{a}/d\tilde{t} \\ \tilde{p} &= p/\sigma_{\text{ref}}. \end{aligned} \tag{41}$$

Using these definitions, the governing Eq. (33) may be reduced to the dimensionless form

$$\frac{d\tilde{b}}{dt} = -\frac{3}{2}\frac{\tilde{b}^2}{\tilde{a}} - \frac{C}{D}\frac{f(\tilde{a})}{\tilde{a}}\left(\frac{\tilde{b}}{\tilde{a}}\right)^{1-m} + \frac{1}{D}\frac{\tilde{p}}{\tilde{a}} \tag{42}$$

where f is given by Eq. (23) with the dependence on m and n omitted for simplicity of notation. The constants C and D are defined as

$$\begin{aligned} C &= 3^{-1-1/n}2^{1+1/n+1/m} \\ D &= \frac{\rho a_0^2\dot{\epsilon}_{\text{ref}}^2}{\sigma_{\text{ref}}} = \frac{\rho a_0^2}{k}\dot{\epsilon}_{\text{ref}}^{2-1/m}. \end{aligned} \tag{43}$$

Of particular interest here is the constant D. It is noted that D is proportional to the mass density ρ, and thus may be thought of as a measure of the effective inertia of the system. In particular, dynamic effects are absent when ρ and, hence, D vanish. It is also revealing that D increases with the initial void size a_0. Consequently, inertia effects may be expected to be more pronounced for large voids. Dynamic effects are also accentuated at higher strain rates $\dot{\epsilon}_{\text{ref}}$.

It is interesting to note that the constant D may be expressed as $D = (a_0/l)^2$, where

$$l = \frac{1}{\dot{\epsilon}_{\text{ref}}}\left[\frac{\sigma_y\epsilon_y^{-1/n}}{\rho}\left(\frac{\dot{\epsilon}_{\text{ref}}}{\dot{\epsilon}_0}\right)^{1/m}\right]^{1/2} \tag{44}$$

which has the dimensions of length. As already stated, dynamic effects may be anticipated to be important when $a_0 \gg l$. Note, however, that l is defined in terms of the reference rate of strain $\dot{\epsilon}_{\text{ref}}$ and, hence, does not define a characteristic length of the solid. In fact, the sole length scale of the problem is set by the initial void radius a_0.

Equation (42) is the most general governing equation considered here. Several particular cases merit special attention. In the quasi-static limit $D \to 0$, Eq. (42) reduces to

$$\frac{d\tilde{a}}{d\tilde{t}} = \tilde{a}\left(\frac{\tilde{p}}{Cf(\tilde{a})}\right)^m. \tag{45}$$

This equation is separable and can therefore be solved by one simple quadrature, with the result

$$\int_1^{\tilde{a}} f^m(\tilde{a})\frac{d\tilde{a}}{\tilde{a}} = \int_0^{\tilde{t}} (\tilde{p}/C)^m d\tilde{t} \tag{46}$$

which implicitly determines $\tilde{a}$ as a function of $\tilde{t}$.

If, on the other hand, the perfectly plastic limit $n \to \infty$ is approached, f reduces to m and (42) becomes

$$\frac{d\tilde{b}}{d\tilde{t}} = -\frac{3}{2}\frac{\tilde{b}^2}{\tilde{a}} - \frac{C}{D}\frac{m}{\tilde{a}}\left(\frac{\tilde{b}}{\tilde{a}}\right)^{1/m} + \frac{1}{D}\frac{\tilde{p}}{\tilde{a}} \tag{47}$$

whereas Eq. (45) governing quasi-static processes further simplifies to

$$\frac{d\tilde{a}}{d\tilde{t}} = \tilde{a}\left(\frac{\tilde{p}}{Cm}\right)^m. \tag{48}$$

This equation governs the expansion of a void in an ideally viscous matrix under quasi-static conditions. In this case, solution (46) specializes to

$$\tilde{a} = \exp\left[\int_0^{\tilde{t}} [\tilde{p}(\tilde{t})/Cm]^m d\tilde{t}\right]. \tag{49}$$

The rate-independent case is also noteworthy. Using normalization (41), Eq. (37) reduces to

$$\left(\frac{d\tilde{a}}{d\tilde{t}}\right)^2 + \frac{n}{n+1}\frac{2C}{3D}g(\tilde{a}) = \frac{2\tilde{p}}{3D}\left(1 - \frac{1}{\tilde{a}^3}\right) \tag{50}$$

where g is given by Eq. (26), with its dependence on n suppressed for simplicity, and the constant C follows from (43a) by taking $m \to \infty$, with the result

$$C = 3^{-1-1/n}2^{1+1/n}. \tag{51}$$

Equation (50) is written for constant pressure, so that the potential U is given by (29). Other pressure potentials can be handled similarly.

As a final special case, we consider the quasi-static rate-independent problem. The equation governing this case may be obtained from (50) by taking the limit $D \to 0$, which yields

Downloaded 03 May 2010 to 171.66.16.247. Redistribution subject to ASME license or copyright; see http://www.asme.org/terms/Terms_Use.cfm

$$g(\tilde{a}) = \frac{n+1}{n}\frac{\tilde{p}}{C}\left(1-\frac{1}{\tilde{a}^3}\right). \tag{52}$$

For monotonic loading, this establishes a one-to-one relation between the pressure $\tilde{p}$ and the radius of the void $\tilde{a}$.

4 Short and Long-Term Behavior

In general, neither Eq. (32) nor its rate-independent specialization (50) can be solved analytically in closed form. However, the short and long-term character of the solutions can be established with some generality. We start by investigating the short-term behavior of the solutions in the general case of a strain hardening, rate sensitive solid under dynamic loading. This case is governed by Eq. (42). For values of $\tilde{a}$ close to 1, a minor computation shows that the function $f(\tilde{a})$ behaves as

$$f(\tilde{a}) \sim \frac{mn}{m+n}\, 3^{1/n}(\tilde{a}-1)^{1/n} + O((\tilde{a}-1)^{1+1/n}). \tag{53}$$

Using this approximation and setting $\tilde{a} \approx 1$, Eq. (42) reduces to

$$\frac{d\tilde{b}}{d\tilde{t}} = -\frac{3}{2}\tilde{b}^2 - \frac{C}{D}\frac{mn}{m+n}\, 3^{1/n}(\tilde{a}-1)^{1/n}\tilde{b}^{1/m} + \frac{\tilde{p}}{D}. \tag{54}$$

Assume that $\tilde{p}$ grows as $\tilde{t}^{\gamma}$ for small $\tilde{t}$, with $\gamma > 0$, and that, as a result, $\tilde{a} - 1$ grows as $\tilde{t}^{\alpha}$, for some α to be determined. Then, the first term of (54) grows as $\tilde{t}^{\alpha-2}$, the second as $\tilde{t}^{2\alpha-2}$, the third as $\tilde{t}^{\alpha/n+(\alpha-1)/m}$, and the fourth as $\tilde{t}^{\gamma}$. Evidently, the third term in (54) dominates the first two provided that

$$\alpha - 2 > \alpha/n + (\alpha-1)/m. \tag{55}$$

Then, the inertia terms in (54) are negligible and the short-term response is dominated by strain hardening and the rate sensitivity of the material. If condition (55) is satisfied, then from the third and fourth terms of (54) one computes

$$\alpha = \frac{(m\gamma+1)n}{n+m}. \tag{56}$$

Using this relation, (55) becomes

$$\gamma > \frac{2m+n}{mn-m-n} \tag{57}$$

This condition places restrictions on the rate of growth of $\tilde{p}$ for the inertia terms to be negligible. If, for instance, we take $n = 10$ and $m = 100$, values which are of an order of magnitude commonly found in metals, then (57) necessitates $\gamma > 0.236$. However, this type of behavior is arguably unphysical since it requires the applied pressure to grow at an infinite rate initially.

Assume that (57) is indeed satisfied and that, consequently, the inertia terms are negligible for small times. Then Eq. (54) reduces to

$$(\tilde{a}-1)^{1/n}\left(\frac{d\tilde{a}}{d\tilde{t}}\right)^{1/m} = \frac{\tilde{p}}{A}, \quad A = \frac{mn}{m+n}\, 3^{1/n}C \tag{58}$$

valid for small $\tilde{t}$. This equation is separable and its general solution is

$$\tilde{a} \sim 1 + \left[\frac{m+n}{n}\int_0^{\tilde{t}} (\tilde{p}/A)^m d\tilde{t}\right]^{n/(m+n)}. \tag{59}$$

The rate-independent limit of (58) requires special handling. In the limit $m \to \infty$, (58) reduces to an algebraic relation. This can be solved for $\tilde{a}$ with the result

$$\tilde{a} \sim 1 + \frac{1}{3}\left(\frac{\tilde{p}}{Cn}\right)^n \tag{60}$$

valid for small times.

It is possible to derive an estimate of the time interval within which the short-term solution (59) dominates. Recall that (59) is obtained by neglecting the inertia terms in the governing Eq. (54). Consequently, solution (59) ceases to be valid when the inertia terms become of the same order as the viscous term. As discussed earlier, the inertia term which grows fastest is $d\tilde{b}/d\tilde{t}$. Thus, the range of dominance of (59) may be estimated from the condition that

$$\left(\frac{d\tilde{b}}{d\tilde{t}}\right) \Big/ \left(\frac{C}{D}\frac{mn}{m+n}\, 3^{1/n}(\tilde{a}-1)^{1/n}\tilde{b}^{1/m}\right) \sim 1 \tag{61}$$

where the left-hand side is evaluated directly from (59). In the particular case in which the pressure history is of the form $\tilde{p} = P\tilde{t}^{\gamma}$, condition (61) reduces to

$$\tilde{t} \sim \left[\frac{D}{A}\left(\gamma\frac{mn}{m+n}+1\right)^{1/n} \times \left(\frac{n}{m+n}\right)^{(2m+n)/(m^2+mn)}\right]^{1/\{\gamma[1-mn/(m+n)]+(1+n)/n\}} \tag{62}$$

The interval of dominance of the rate-independent solution (60) follows simply as the limit of (62) as $m \to \infty$.

We next turn our attention to the long-term behavior of the solutions. For values of $\tilde{a} \gg 1$, the function $f(\tilde{a})$ behaves as

$$f \sim \int_1^{\infty}\left[\log\left(\frac{x}{x-1}\right)\right]^{1/n} x^{-(m+1)/m} dx \equiv f_{\infty}(m,n) \tag{63}$$

Using this approximation, Eq. (42) becomes

$$\frac{d\tilde{b}}{d\tilde{t}} = -\frac{3}{2}\frac{\tilde{b}^2}{\tilde{a}} - \frac{C}{D}\frac{f_{\infty}}{\tilde{a}}\left(\frac{\tilde{b}}{\tilde{a}}\right)^{1/m} + \frac{1}{D}\frac{\tilde{p}}{\tilde{a}}. \tag{64}$$

Next we proceed to establish the order of the terms involved in this equation. To this end, assume that $\tilde{p} \sim \tilde{t}^{\gamma}$ and $\tilde{a} \sim \tilde{t}^{\alpha}$ for large $\tilde{t}$. Then the first two terms in Eq. (64) go as $\tilde{t}^{\alpha-2}$, the third as $\tilde{t}^{-\alpha-1/m}$, and the fourth as $\tilde{t}^{\gamma-\alpha}$. Of the first two groups of terms, it is clear that the first dominates provided that

$$\alpha - 2 > -\alpha - 1/m. \tag{65}$$

Under these conditions, the dissipative term in (64) is negligible and the long-term response is dominated by inertia. Then, matching the dominant terms in Eq. (64), one finds

$$\alpha = 1 + \gamma/2. \tag{66}$$

Using this result, condition (65) becomes

$$\gamma > -1/m \tag{67}$$

If attention is restricted to nondecreasing pressure histories, for which $\gamma \geq 0$, then (67) is satisfied for all finite values of $m > 0$. Under these conditions, one concludes that the long-term response of the void is dominated by inertia.

Note, however, that inequality (67) is violated if $m \to \infty$ and $\gamma = 0$, i.e., for a rate-insensitive solid subjected to constant pressure. Then, all terms in (64) are of the same order in $\tilde{t}$. This case needs to be handled separately from those satisfying restriction (67). Start by noting that, for large $\tilde{a}$, the function $g(\tilde{a})$ behaves as

$$\lim_{\tilde{a}\to\infty} g(\tilde{a}) = \int_1^{\infty}\left[\log\left(\frac{x}{x-1}\right)\right]^{(n+1)/n} dx \equiv g_{\infty}. \tag{68}$$

Inserting this approximation into Eq. (50) specialized to the case $\tilde{a} \to \infty$, one finds

$$\left(\frac{d\tilde{a}}{d\tilde{t}}\right)^2 = \frac{2}{3D}(\tilde{p} - \tilde{p}_{cr}) \tag{69}$$

where the critical pressure $\tilde{p}$ is defined as

$$\tilde{p}_{cr} = \frac{n}{n+1} C g_{\infty}. \tag{70}$$

Assume for now that the pressure is supercritical, i.e., $\tilde{p} \geq \tilde{p}_{cr}$. Then, solutions of (70) exist and are given by

Downloaded 03 May 2010 to 171.66.16.247. Redistribution subject to ASME license or copyright; see http://www.asme.org/terms/Terms_Use.cfm

$$\tilde{a} \sim \left[\frac{2}{3D}(\tilde{p}-\tilde{p}_{cr})\right]^{1/2}\tilde{t}. \tag{71}$$

It is observed that the growth of the void radius is linear in time. In particular, the void grows unboundedly under the effect of a supercritical pressure. The rate of growth becomes increasingly smaller as $\tilde{p} \to \tilde{p}_{cr}$. Beyond this limit, the plastic irreversibility constraint (35) is activated to prevent shrinkage of the void. Thus, for undercritical pressures $\tilde{p} < \tilde{p}_{cr}$, the void undergoes bounded growth, eventually attaining a stationary configuration.

Next, consider the case in which restriction (67) is satisfied. Eliminating the negligibly small dissipative term from (64), the equation governing the long-term behavior of the void is found to be

$$\frac{d\tilde{b}}{d\tilde{t}} = -\frac{3}{2}\frac{\tilde{b}^2}{\tilde{a}} + \frac{1}{D}\frac{\tilde{p}}{\tilde{a}}. \tag{72}$$

Define an effective time τ as

$$\tau = \int_0^{\tilde{t}} \sqrt{\tilde{p}}\, d\tilde{t}. \tag{73}$$

With the aid of this definition, Eq. (72) may be expressed as

$$\frac{d^2\tilde{a}}{d\tau^2} = -\frac{3}{2\tilde{a}}\left(\frac{d\tilde{a}}{d\tau}\right)^2 + \frac{1}{D\tilde{a}}. \tag{74}$$

A first integral of this equation is found to be

$$\left(\frac{d\tilde{a}}{d\tau}\right)^2 = \frac{2}{3D}\left(1-\frac{1}{\tilde{a}^3}\right). \tag{75}$$

Specializing this expression to the case $\tilde{a} \to \infty$, it reduces to

$$\frac{d\tilde{a}}{d\tau} = \sqrt{\frac{2}{3D}} \tag{76}$$

which integrates to

$$\tilde{a} \sim \tau\sqrt{\frac{2}{3D}} = \sqrt{\frac{2}{3D}}\int_0^{\tilde{t}} \sqrt{\tilde{p}}\, d\tilde{t}. \tag{77}$$

Thus, the long-term growth of the void is linear in the effective time τ.

The result (77) ceases to apply in the quasi-static limit, i.e., when the constant $D \to 0$. The long-term behavior for this case, however, may be deduced directly from the exact solution (46). Replacing f by the long-term approximation f_∞ defined by (63), solution (46) reduces to

$$\tilde{a} \sim \exp\left[\int (\tilde{p}/Cf_\infty)^m d\tilde{t}\right]. \tag{78}$$

If, for instance, we take the pressure $\tilde{p}$ to be constant, then the long-term behavior of the void is one of exponential growth.

As in the short-term analysis, it is possible to estimate the time beyond which the long-term solutions start to dominate. Particularly revealing is the estimate for solution (77). This solution pertains to the dynamic rate-dependent case and is obtained by neglecting the viscous term in (64). Consequently, a lower bound for the range of validity of (77) may be derived by estimating the time at which inertia and viscous terms are of the same order, i.e.,

$$\left(\frac{d\tilde{b}}{d\tilde{t}} + \frac{3}{2}\frac{\tilde{b}^2}{\tilde{a}}\right) \Big/ \left[\frac{C}{D}\frac{f_\infty}{\tilde{a}}\left(\frac{\tilde{b}}{\tilde{a}}\right)^{1/m}\right] \sim 1 \tag{79}$$

where the left-hand side is evaluated from (77). Setting, for simplicity, $\tilde{p} = P\tilde{t}^\gamma$, condition (79) reduces to

$$\tilde{t} \sim \left[\frac{3C}{2P}\frac{(\gamma+1)^{(m+1)/m}}{\gamma+3(\gamma+1)/2}\right]^{1/(2\gamma+1/m)} \tag{80}$$

For the case of constant pressure, $\gamma = 0$, estimate (80) specializes to

$$\tilde{t} \sim \left(\frac{Cf_\infty}{P}\right)^m \tag{81}$$

This estimate has some revealing consequences. For n large, f_∞ is well approximated by the ideally plastic limit $f_\infty \approx m$. Inserting this approximation into (81), we obtain

$$\tilde{t} \sim \left(\frac{Cm}{P}\right)^m \tag{82}$$

Consider further the case of a body whose behavior is nearly rate independent, i.e., for which m is large. As m is increased, the right-hand side of (82) grows as m^m and soon becomes extremely large. Under these conditions, the long-term solution (77) may fail to become dominant within any physically reasonable time scale. Instead, following the initial transients, the response of the void may be expected to be close to that predicted by the *rate-independent* long-term solution (71). This supposition is indeed born out by the numerical simulations presented in the next section.

5 Response to Impulse Loading

In this section, we present full numerical solutions which confirm the trends revealed by the preceding short and long-term analyses, and provide useful insights into the nature of the intermediate transients. We consider a ramp variation in time of the applied pressure of the form

$$p(t) = \begin{cases} 0, & \text{if } t \le 0; \\ p_\infty t/t_1, & \text{if } 0 \le t \le t_1; \\ p_\infty, & \text{if } t_1 \le t. \end{cases} \tag{83}$$

Thus, the remote pressure is assumed to increase linearly from $p = 0$ at $t = 0$ to a final value of p_∞ at t_1 and to remain constant thereafter.

The calculations are carried out for the following choice of material constants: $\rho = 7800$ kg/m^3, $k = 10^8$ SI, $m = 100$, $n = 10$, and $a_0 = 10$ μm. These parameters are roughly representative of some types of steels. The terminal pressure is taken to be $p_\infty = 750$ MPa and the rise time $t_1 = 10^{-2}$ μs. If we set the reference strain rate $\dot{\epsilon}_{\text{ref}} = 1/t_1$, then the effective inertia constant (43b) takes the value $D = 64.88$, whereas the characteristic length (44) becomes $l = 1.24$ μm. Since $a_0 \gg l$, inertia effects are expected to be significant. Also note that the critical pressure is in this case $p_{cr} = 705$ MPa. Thus, the applied terminal pressure p_∞ is supercritical and unbounded void growth takes place.

Time histories of void expansion are shown in Figs. 1 and 2 for the following cases: (i) dynamic rate dependent, (ii) quasi-static rate dependent, and (iii) dynamic rate independent. This comparison brings out differences between the effects of inertia and rate dependence. Thus, in the quasi-static rate-dependent case, inertia is neglected altogether, which brings rate dependency effects to the forefront. In the dynamic rate-independent analysis, the individual effect of inertia is singled out. Finally, the dynamic rate-dependent solution exhibits the combined effect of inertia and rate dependence.

The computed short-term solutions are depicted in Fig. 1. In the dynamic rate-dependent case, the short-term response is given by Eq. (59). For the present choice of parameters, this reduces to

$$\tilde{a} \sim 1 + 0.531\tilde{t}^{9.18}. \tag{84}$$

The interval of dominance of this solution as estimated from (62) is $\tilde{t} \sim 0.701$, or, in absolute time, $t \sim 0.701 \times 10^{-2}$ μs. In the quasi-static rate-dependent case, the short-term response is also given by (84). The short-term dynamic rate-independent solution, on the other hand, is given by Eq. (60). For the values of the parameters adopted in the calculations, (60) specializes to

Downloaded 03 May 2010 to 171.66.16.247. Redistribution subject to ASME license or copyright; see http://www.asme.org/terms/Terms_Use.cfm

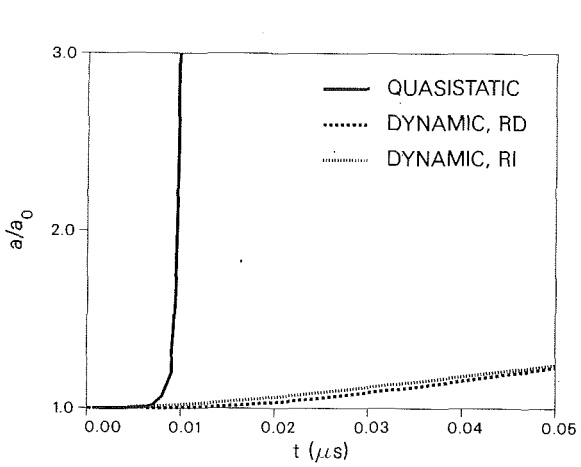

Fig. 1 Initial stages of the numerical solutions for ramp loading and the following choice of parameters: $\rho = 7800$ kg/m^3, $k = 10^8$ SI, $m = 100$, $n = 10$, and $a_0 = 10\ \mu$m, $p_\infty \approx 750$ MPa, and $t_1 = 10^{-2}\ \mu$s. The critical pressure corresponding to these material constants is $p_{cr} \approx 705$ MPa. Solutions are obtained for the following cases: (a) quasi-static, rate dependent, (b) dynamic, rate dependent, and (c) dynamic, rate independent.

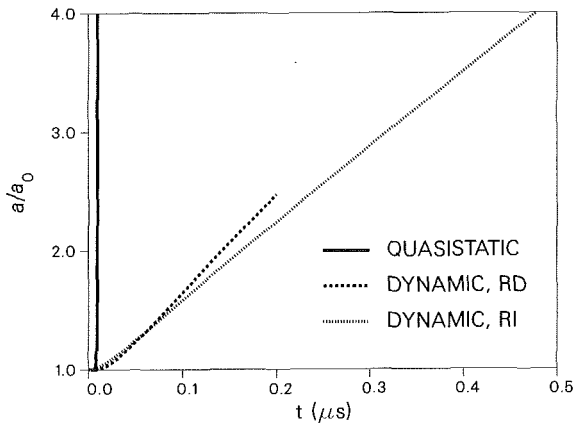

Fig. 2 Long-term solutions for the problem of Fig. 1.

$$\tilde{a} \sim 1 + 1.62\tilde{t}^{10} \tag{85}$$

which, according to estimate (62), dominates up to $\tilde{t} \sim 0.744$, or, in absolute time, $t \sim 0.744 \times 10^{-2}\ \mu$s.

Solutions (84) and (85) have a crossover point at $\tilde{t} = 0.255$. Prior to this time, the void radius is larger in the rate-dependent solution. Beyond the crossover time, the rate-independent solution gives the larger expansion, Fig. 1. Thus, as expected, the rate sensitivity of the material has the effect of retarding the expansion of the void.

Figure 2 shows the long-term behavior of the void. The long term response for the dynamic rate-dependent case is given by Eq. (77), which here reduces to

$$\tilde{a} \sim 0.253\tilde{t}. \tag{86}$$

However, estimate (82) gives $\tilde{t} \sim 22 \times 10^{100}$ as the onset of dominance of (86). Not surprisingly, the computed slope $d\tilde{a}/d\tilde{t} \approx 0.085$ does not match the analytical value of 0.253 derived from (86). Instead, as surmised in the preceding section, the computed growth rate is closer to that predicted by the long-term rate-independent solution (71), which for the present example particularizes to

$$\tilde{a} \sim 0.0620\tilde{t}. \tag{87}$$

The computed growth rate for the actual rate-independent case, $d\tilde{a}/d\tilde{t} \approx 0.0625$, closely matches the analytical solution (87).

Both the rate-dependent and rate-independent dynamic solutions exhibit linear growth following the initial transient, Fig. 2. Here, however, we encounter the seemingly paradoxical situation that the rate-dependent solution grows faster than the rate-independent one. This behavior is counterintuitive, since one would reasonably expect the presence of rate sensitivity to retard the growth of the void relative to the rate insensitive solution.

Finally, the long-term behavior of the quasi-static rate-dependent solution is given by (78), and corresponds to a exponential growth of the void. Indeed, the numerical solution exhibits a sharp upturn as the critical pressure is exceeded, Fig. 2, in contrast with the slower growth rate predicted by the dynamic solutions. This comparison underscores the potentially stabilizing effect of microinertia on void growth, both in rate sensitive and rate insensitive solids.

6 Discussion

A striking feature of the solutions presented above is the widely varying predictions which are obtained depending on the level of description adopted in the analysis. Both inertia, strain hardening, and rate sensitivity have a marked influence on the short and long-term solutions, as well as on the intermediate transients, sometimes with counterintuitive consequences. For instance, under dynamic conditions, a rate-dependent description of the solid may sometimes result in faster void growth than predicted by the corresponding rate independent solution.

While the equations governing the expansion of a void cannot be generally solved in closed form, even with the simplifying assumption adopted in the present analysis, a good deal of progress can be made toward characterizing the short and long term responses. Our analysis shows that microinertia effects are particularly significant for voids which are larger than a characteristic dimension which depends on both the mechanical properties of the solid and the rate of expansion. We have also shown that, whereas the early stages of deformation are dominated by viscous effects, inertia tends to dominate the long-term response of the void. This sets limits on the applicability of phenomenological theories of voided elastic-plastic solids which neglect microinertia. The solutions given here provide possible avenues for extending these theories so as to include material inertia on the physical scale of the ductile void growth mechanism.

Acknowledgments

M. O. gratefully acknowledges the support from the Brown University NSF Materials Research Group through grant DMR-8714665.

References

Carroll, M. M., and Holt, A. C., 1972, "Static and Dynamic Pore-Collapse Relations for Ductile Porous Materials," *J. Appl. Phys.*, Vol. 43, pp. 1626–1636.

Glennie, E. B., 1972, "The Dynamic Growth of a Void in a Plastic Material and an Application to Fracture," *J. Mech. Phys. Solids*, Vol. 20, pp. 415–429.

Johnson, J. N., 1981, "Dynamic Fracture and Spallation in Ductile Solids," *J. Appl. Phys.*, Vol. 52, pp. 2812–2825.

Klöcker, H., and Montheillet, F., 1988, "Modeling the Ductile Growth of Voids at High Strain Rates," *J. de Physique*, Vol. 49, pp. C3-313-C3-318.

Rice, J. R., and Johnson, M. A., 1970, "The Role of Large Crack Tip Geometry Changes in Plane Strain Fracture," *Inelastic Behavior of Solids*, M. F. Kanninen, ed., McGraw-Hill, pp. 641–672.

Downloaded 03 May 2010 to 171.66.16.247. Redistribution subject to ASME license or copyright; see http://www.asme.org/terms/Terms_Use.cfm

A Complete Acoustic Microscopical Analysis of Multilayered Specimens

T. Kundu
Department of Civil Engineering and Engineering Mechanics, University of Arizona, Tucson, AZ 85721
Mem. ASME

A theoretical analysis is carried out to synthesize the V(z) *curves of multilayered solids immersed in water. Solid layers attenuate ultrasound and change its phase. A liquid layer may be located in between two solid layers. The goal of this analysis is to avoid the three major simplifying assumptions of the presently available techniques, as paraxial approximation, assumption of perfect reflection and ambiguous pupil function or incident field strength variation in the illuminated region. Presently available techniques developed for conventional acoustic microscopes can avoid some but not all of these assumptions for computing the* V(z) *curve. In this paper, the analysis is carried out for a spherical cavity lens with a large aperture angle. The* V(z) *curve for a uniform glass half-space is synthesized analytically and compared with experimental results. Analytical results are also presented for chromium plated glass specimens and biological cells on uniform glass half-space. Such an exact analysis of multilayered specimens is necessary for material science research as well as cell research in biology, because advanced engineering composite materials and biological cells in culture have multiple layers.*

1 Introduction

In the last decade, several efforts have been made on the prediction of the voltage (V) generated by an acoustic microscope during the reflection mode operation. Many such analyses are in good agreement with the experimental results. However, every technique uses its own simplifying assumptions, and as a consequence, many experimental data cannot be properly explained by these theories.

The useful data in the acoustic microscopy experiment are obtained from the variation of V as the specimen is moved along the lens axis of symmetry. For a given frequency, f, the variation of V with z (the distance between the reflecting surface and the focal plane) strongly depends on the material properties of the specimen. A major objective of the experiment is to extract quantitative information on these properties by analyzing the $V(z)$ curve, also know as the acoustic material signature (AMS) of the specimen.

The simplest way of synthesizing the $V(z)$ curve is to follow the ray theory approach developed by Parmon and Bertoni (1979), Weglein (1979), and Quate (1980). It computes the interference pattern considering the specularly reflected acoustic waves at almost normal incidence and leaky waves from the surface skimming waves (e.g., Rayleigh waves) generated by critically incident waves at the fluid-solid interface. From this ray theory one gets the following relationship for the distance T between two successive minima in the $V(z)$ curve.

$$2.T.f = \left\{ \frac{1}{\alpha_f} - \frac{\left(\frac{C_r}{\alpha_f} - \frac{\alpha_f}{C_r}\right)}{\sqrt{(C_r^2 - \alpha_f^2)}} \right\}^{-1} \tag{1}$$

where f is the frequency of the acoustic waves, α_f is acoustic wave speed in the fluid, and C_r is the Rayleigh wave speed in the solid specimen. Equation (1) is found to be satisfactory for many homogeneous specimens.

Later, Weglein (1985) carried out some experimental investigations with copper-coated quartz specimens and found two distinct values for the spacing T in $V(z)$ plots. Ordinary ray theory could not explain this phenomenon. Then, Kundu, Mal, and Weglein (1985) and Kundu and Mal (1986) proposed a new hybrid technique that combined the ray theory and wave number integral techniques to synthesize the $V(z)$ curves. $V(z)$ thus synthesized gave better agreement with the experimental results (Kundu, 1985). However, one disadvantage of this hybrid method is that it assumes that the converging acoustic beam is composed of several bounded acoustic beams striking the reflector at different incident angles. While synthesizing the $V(z)$ curve, only those angles of incidence are considered which are equal to some critical angles. For anisotropic materials, such as composites, these critical angles are not known, hence this technique is not very useful there. Even when the critical angles are known, the beam width factor and the field variation within individual incident beams are unknown and

Contributed by the Applied Mechanics Division of THE AMERICAN SOCIETY OF MECHANICAL ENGINEERS for publication in the JOURNAL OF APPLIED MECHANICS.

Discussion on this paper should be addressed to the Technical Editor, Prof. Leon M. Keer, The Technological Institute, Northwestern University, Evanston, IL 60208, and will be accepted until two months after final publication of the paper itself in the JOURNAL OF APPLIED MECHANICS. Manuscript received by the ASME Applied Mechanics Division, Feb. 13, 1990; final revision, Jan. 18, 1991.

Copyright © 1992 by ASME
Downloaded 03 May 2010 to 171.66.16.247. Redistribution subject to ASME license or copyright; see http://www.asme.org/terms/Terms_Use.cfm

are assumed arbitrarily, giving rise to some ambiguity in the final results.

The angular spectrum approach, proposed by Atalar (1978), considers the entire beam during the analysis and does not discretize it into a number of bounded beams incident at different angles. Thus, this technique can be used also when it is difficult to determine the critical angles of the specimen. However, the major shortcoming of this technique is the paraxial approximation of the lens. For lenses with large aperture angles (half lens angle $>$ 20 deg), Atalar's technique based on the paraxial approximation does not produce good results. Sheppard and Wilson (1981) avoided the paraxial assumption in the lens modeling, however, also in their analysis the pupil function of the lens is an unknown quantity and is chosen arbitrarily.

Bertoni (1984) synthesized $V(z)$ curves of linear elastic and homogeneous specimens by separating the geometrically reflected part and the leaky wave part. The advantage of his approach is that the effects of geometrically reflected waves and leaky waves on $V(z)$ curves can be clearly seen. However, such separations for multilayered specimens will be very cumbersome, if not impossible; no one has been able to do that yet. He constructed the pupil function from the ray optical approach assuming a slowly varying amplitude function. Such simplifying assumptions are omitted in the present analysis.

In this research, the $V(z)$ of glass was experimentally generated at 1 GHz frequency by a Leitz acoustic microscope. It showed approximately 8.7 μm spacing between the first two minima and 6 μm between the next two (see Fig. 7). Most of the presently available theoretical techniques predict uniform spacings in the $V(z)$ curve for a homogeneous specimen, hence an alternative analysis is warranted where many simplifying assumptions are avoided. In this paper, such an alternative analysis is presented.

2 Problem Formulation

The general set-up of an acoustic microscopy experiment is sketched in Fig. 1. The transducer T, mounted on a solid surface, generates longitudinal waves which propagate normal to the transducer surface. L is a spherical cavity which serves to focus the incident longitudinal waves into a converging beam of acoustic waves in the coupling fluid. The lens is coated by a thin film to avoid multiple reflections between the lens surface and the specimen. The acoustic beam is reflected from the solid specimen placed at a distance z from the focus F of the spherical lens and is returned to the transducer through the lens to produce a voltage V. Time gating in the recording device separates the reflected signal from incident beam and other spurious reflections. Θ_0 in Fig. 1 denotes the half lens angle, sometimes also called the lens angle.

From simple ray diagram the focal length, f_1 measured from the center point, E, of the lens can be obtained as

$$f_1 = EF = r\left\{1 + \frac{\mu}{\cos\Theta_f - \mu\cos\Theta_s}\right\} \tag{2}$$

where

$$\mu = \frac{\alpha_f}{\alpha_s} \tag{3}$$

$$\Theta_f = \sin^{-1}(\mu \sin\Theta_s). \tag{4}$$

r is the radius of curvature of the lens, α_f, and α_s are acoustic wave speeds in the coupling fluid and in the lens material, respectively. It should be noted here that f_1 depends on the incident angle Θ_s; so for different rays, f_1 is different. Thus, the entire beam is not focussed at a point, it is focussed over a region. For small lens angles, Eq. (2) is simplified to:

$$f_1 = \frac{r}{(1-\mu)}. \tag{5}$$

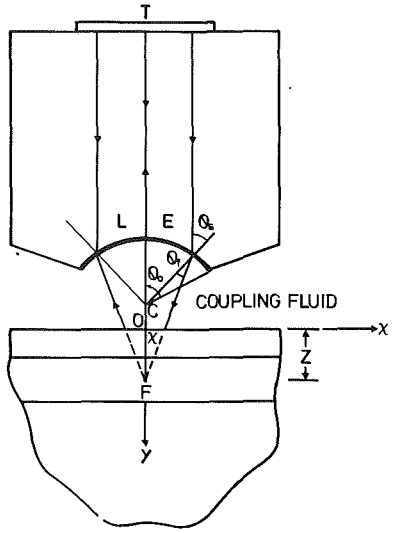

Fig. 1 General set-up of the acoustic microscopy experiment

2.1 Incident Field. To obtain the expression for the incident field potential one can look at a single ray, which after being generated by the transducer, propagates through the lens rod and strike the lens-liquid interface at an incident angle Θ_s. Thus, the incident potential at the specimen surface is obtained:

$$\Phi_i(x,0) = r \cdot T_{sf}(\Theta_s) \cdot \exp\left\{ ik_s r(1-\cos\Theta_s) + \frac{ik_f\left[\dfrac{r}{(\cos\Theta_f - \mu.\cos\Theta_s)} - \sqrt{(x^2+z^2)}\right]}{(\cos\Theta_f - \mu\cdot\cos\Theta_s)\sqrt{(x^2+z^2)}}\right\} \tag{6}$$

where $T_{sf}(\Theta_s)$ is the plane-wave transmission coefficient for waves propagating from the lens to the coupling fluid; its expression is given in Appendix A. The exponential term in Eq. (6) is the wave propagation term in the lens rod and the coupling fluid. Radius of curvature r in the numerator and the entire denominator of Eq. (6) come from the conservation of energy applied to the converging acoustic beam in the coupling fluid. k_s and k_r are longitudinal wave numbers in the lens material and in the coupling fluid, respectively. For an attenuative medium, k_s and k_f are complex:

$$k_s = \frac{\omega}{\alpha_s}\left(1 + \frac{j}{2q_s\alpha_s}\right)$$
$$k_f = \frac{\omega}{\alpha_f}\left(1 + \frac{i}{2q_f\alpha_f}\right) \tag{7}$$

where ω is the circular frequency, α_s and α_f have been defined in Eq. (3), and q_s and q_f are quality factors of the solid and liquid, respectively. A small value of the quality factor of a material means large attentuation in it (Xu and Mal, 1987). Generally, lens materials such as fused quartz and sapphire have negligible attenuation; hence, attenuation in the lens may be neglected.

x, y, and Θ_s of Eq. (6), also shown in Fig. 1, are interrelated. This relation can be obtained from simple geometric considerations: For small lens angles, (Eq. (8)) is simplified to:

$$\frac{x}{z} = \frac{\sin\Theta_s.\cos\Theta_f - \mu.\sin\Theta_s.\cos\Theta_s}{\cos\Theta_s.\cos\Theta_f + \mu.\sin^2\Theta_s} \tag{8}$$

$$\frac{x}{z} = (1-\mu)\sin\Theta_s. \tag{9}$$

Downloaded 03 May 2010 to 171.66.16.247. Redistribution subject to ASME license or copyright; see http://www.asme.org/terms/Terms_Use.cfm

For a given value of x and z, Eq. (8) is first used to obtain Θ_s. If Θ_s is less than the half lens angle Θ_0, then Eq. (6) is used to compute $\Phi_i(x, 0)$, otherwise, the point is beyond the illuminated region and $\Phi_i(x, 0)$ should be zero there.

Fourier inversion of Eq. (6) with respect to x gives:

$$\Phi_i(k,0) = r.\exp(ik_s n) \int_0^{\infty} \frac{f_1(\Theta_s) T_{sf}(\Theta_s)}{\sqrt{(x^2+z^2)}} .\exp\{-ik_s r\cos\Theta_s + ik_f[rf_1(\Theta_s) - \sqrt{(x^2+z^2)}] + ikx\} dx \quad (10)$$

where

$$f_1(\Theta_s) = (\cos\Theta_f - \mu.\cos\Theta_s)^{-1}. \quad (11)$$

Equation (10) can be rewritten in the following form:

$$\Phi_i(k,0) = r.\exp(ik_s r).A(k) \quad (12)$$

where

$$A(k) = \int_0^{\infty} \Gamma(x).\exp\{ik\Phi^R(x)\} dx \quad (13)$$

$$\Gamma(x) = \frac{f_1(\Theta_s) T_{sf}(\Theta_s)}{\sqrt{x^2+z^2}} .\exp\{k_s^I r.\cos\Theta_s - k_f^I[rf_1(\Theta_s) - \sqrt{x^2+z^2}]\} \quad (14)$$

$$\Phi^R(x) = x - \frac{k_s^R.r.\cos\Theta_s}{k} + k_f^R. \frac{rf_1(\Theta_s) - \sqrt{x^2+z^2}}{k} \quad (15)$$

Superscripts R and I in k_s and k_f indicate real and imaginary parts of the wave numbers, respectively.

Integral of Eq. (13) can be computed numerically or by the stationary phase method (Liang et al., 1985; Kundu, 1988). Figure 2 shows the imaginary part of $A(k)$ computed numerically (solid line) and by the stationary phase method (dotted line) at 1.7 GHz frequency, for z = 5 micron and Θ_0 (half lens angle) = 80 deg. In general, the stationary phase method reduces the computation time. However, for this problem, it does not do so. This is because to compute the first and second derivatives of $\Phi^R(x)$ of Eq. (13) during the stationary phase method computation, one needs to evaluate $\frac{d\Theta_s}{dx}$ and $\frac{d^2\Theta_s}{dx^2}$. Closed-form expressions of these two derivatives are not known, so they have to be obtained numerically for Eq. (8). Thus, it requires a considerable amount of computer time. It is more economical to evaluate this integral numerically. However, a comparison between the results from the stationary phase method and from the numerical computation of $A(k)$, as shown in Fig. 2, serves as a good check of the reliability of the numerical computation. Similar good agreement was obtained for the real part of $A(k)$ and for other values of the acoustic wave frequency and lens angles.

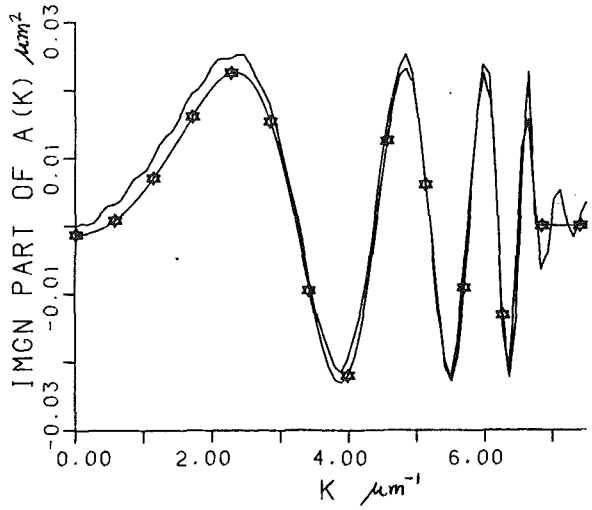

Fig. 2 Imaginary part of $A(k)$ (see Eq. (13)) computed by the numerical integration (solid line without any marker) and by the stationary phase method (line with star markers)

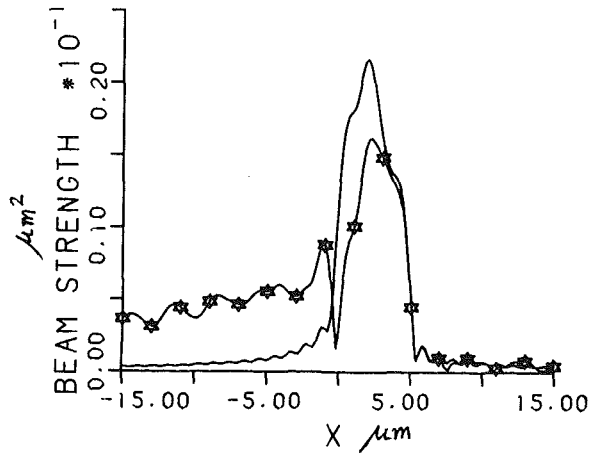

Fig. 3 Incident (line without any marker) and reflected (line with markers) field strength variations at the specimen-coupling fluid interface. The specimen is a glass half-space. The incident beam profile is computed along a radius of the illuminated circle, the reflected beam profile is for the same incident beam.

2.2 Reflected Field. The reflected field at any point (x,y) can be obtained simply by multiplying $\Phi_i(k,0)$ with the plane-wave reflection coefficient $R(k)$ of the reflector specimen and a propagation term $\exp(-ikx - i\delta_f y)$ and then inverting it.

$$\Phi_R(x,y) = \left(\frac{1}{2\pi}\right) \int_{-\infty}^{+\infty} R(k)\Phi_i(k,0)\exp(-ikx - i\delta_f y) dk \quad (16)$$

where

$$\delta_f = \sqrt{\left(\frac{\omega^2}{\alpha_f^2} - k^2\right)} \left\{1 + \frac{i\left(\frac{\omega}{\alpha_f}\right)^2}{2q_f\alpha_f\left(\frac{\omega^2}{\alpha_f^2} - k^2\right)}\right\}. \quad (17)$$

Although Eq. (16) has an infinite integral, one needs to evaluate it numerically between the limits k_0 and k_1 which are minimum and maximum values of the stationary points. Beyond these limits the integrand is very small.

In Eq. (16), if the term $R(k)$ is omitted and $\exp(-i\delta_f y)$ is replaced by $\exp(i\delta_f y)$, then the incident field potential would be obtained instead of the reflected field potential. Incident and reflected field strengths, thus computed for a glass half-space, are shown in Fig. 3. Strong leaky waves in the region $-15 < x < 0$ should be noted here. Note that to obtain the reflected field and leaky waves in it, it was not necessary to know the critical angle of the reflector.

2.3 Reflection Coefficient R(k). Clearly, $R(k)$ has to be computed correctly before $\Phi_R(x, y)$ or $V(z)$ can be obtained. In this paper, special attention is given for accurate computation of $R(k)$. Multilayered solids with and without liquid layers in them are considered. The reflector geometry is shown in Fig. 4. The plane wave is incident at an angle Θ_i; its potential is then given by:

$$\Phi_i(x,y) = \exp(ikx + i\delta_f y) \quad (18)$$

and the reflected field is given by

$$\Phi_R(x,y) = R.\exp(ikx - i\delta_f y). \quad (19)$$

After satisfaction of boundary conditions, continuity condi-

Downloaded 03 May 2010 to 171.66.16.247. Redistribution subject to ASME license or copyright; see http://www.asme.org/terms/Terms_Use.cfm

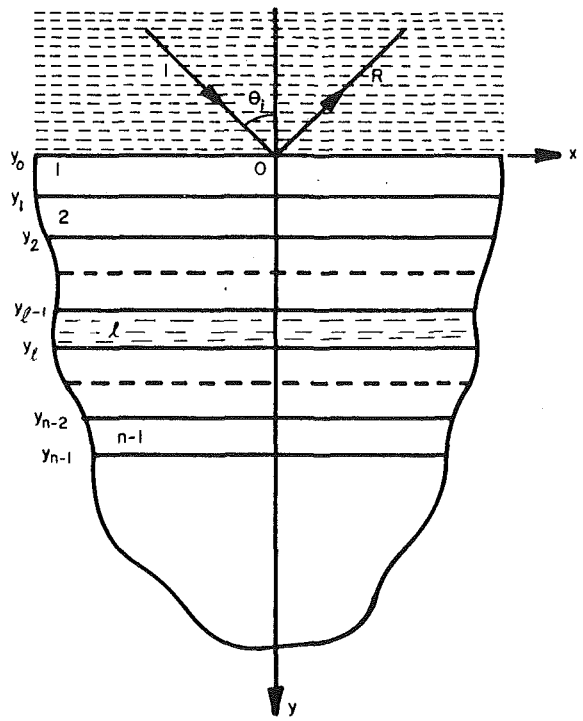

Fig. 4 A multilayered reflector immersed in the coupling fluid. A liquid layer l may be present in between any two solid layers.

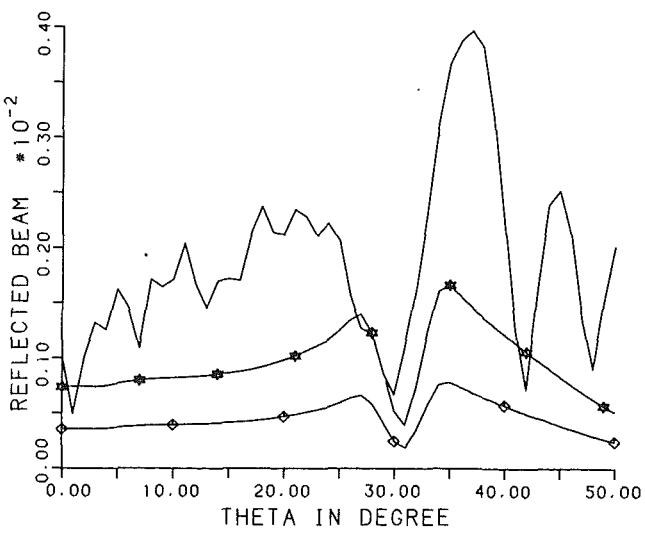

Fig. 5 Reflected beam strength variation (line without any marker) at the lens-coupling fluid interface. Critically reflected part at the same interface is shown by the line with star markers. The critically transmitted beam strength variation inside the lens is shown by the line with square markers.

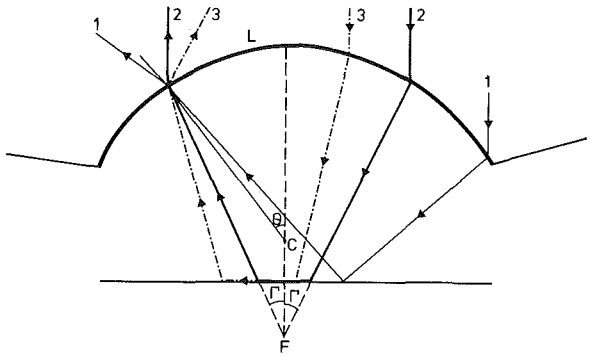

Fig. 6 Ray diagram to show that only a fraction of the total reflected field at the lens-liquid interface can reach the receiver. Among three rays drawn here only ray 2 can reach the receiver.

tions, and regularity conditions by the Thomson-Haskell matrix method (Thomson, 1950; Haskell, 1953; Kundu and Mal, 1985), the reflection coefficient R for a multilayered solid specimen can be obtained in the following form:

$$R=\frac{i\delta_f J_{12}^{12}-\sigma_f\omega^2 J_{13}^{12}}{i\delta_f J_{12}^{12}+\sigma_f\omega^2 J_{13}^{12}} \tag{20}$$

where

$$J_{ki}^{ij}=J_{ik}J_{jl}-J_{il}J_{jk} \tag{21}$$

$$J=E_n^{-1}.A_{n-1}.A_{n-2}\ldots A_2.A_1. \tag{22}$$

If the multilayered reflector contains a liquid layer, let the lth layer be the liquid layer, then the continuity conditions across the interface between the lth and $l+1$st layers and between the lth and $l-1$st layers change, giving rise to a new expression of R.

$$R=\frac{i\delta_f S-\sigma_f\omega^2 U}{i\delta_f S+\sigma_f\omega^2 U} \tag{23}$$

where

$$S=M_{12}^{24}(N_{12}^{12}.A_{l11}+N_{13}^{12}.A_{l21})+M_{12}^{34}(N_{12}^{12}.A_{l12}+N_{13}^{12}.A_{l22}) \tag{24a}$$

$$U=M_{13}^{24}(N_{12}^{12}.A_{l11}+N_{13}^{12}.A_{l21})+M_{13}^{34}(N_{12}^{12}.A_{l12}+N_{13}^{12}.A_{l22}) \tag{24b}$$

$$M=A_{l-1}.A_{l-2}\ldots A_2.A_1 \tag{25a}$$

$$N=E_n^{-1}.A_{n-1}.A_{n-2}\ldots A_{l+1}. \tag{25b}$$

E_n^{-1} and A_m are 4 × 4 matrices similar to those in Eq. (22), and A_l is a 2 × 2 liquid layer matrix and is given in Appendix B.

It is well known that the straightforward numerical computation of R form Eqs. (20) and (23) gives rise to the loss of precision problem. Therefore, delta matrix modification (Kundu and Mal, 1985) is adopted to compute J_{kl}^{ij}, and M_{kl}^{ij} and N_{kl}^{ij} to avoid the precision problem at high frequencies and large layer thicknesses.

2.4 Reflected Field at Receiver. Equation (16) describes the reflected field at any point in the coupling fluid. Thus, the reflected field at the lens-liquid interface can be computed. The solid line without markers in Fig. 5 shows the variation in the reflected field at the lens-liquid surface. Lens position Θ along the horizontal axis is measured from the center of curvature of the lens (see Fig. 6). Θ is zero at the lens center. A simple ray diagram, Fig. 6, can clearly show that the entire reflected beam cannot reach the receiver after it is transmitted into the lens from the coupling fluid. Ray 1, which strikes the lens after being specularly reflected by the specimen, goes away from the lens axis and cannot reach the receiver. Ray 3, after being nonspecularly reflected by the specimen, also fails to reach the receiver. The only ray which can reach the receiver is ray 2. For this ray path, the incident and reflected rays are symmetric about the central axis of the lens. Thus, for each point at the lens-liquid interface, there is a narrow band of beam with an angle of reflection between ($\Gamma - \delta\Gamma$) and ($\Gamma + \delta\Gamma$), which can reach the receiver, where $\delta\Gamma$ has some small value. This part of the reflected beam can be called the critically reflected beam, since only this part is able to reach the receiver. One can obtain the critically reflected beam strength simply by changing the upper and lower limits of integration of Eq. (16)(from $\pm\infty$ to $k_f^R.\sin(\Gamma \pm \delta\Gamma)$, where k_f^R is the real part of k_f.

The line with star markers in Fig. 5 shows the critically reflected beam strength plotted against the lens position Θ measured from the center of curvature of the lens. Multiplying

Downloaded 03 May 2010 to 171.66.16.247. Redistribution subject to ASME license or copyright; see http://www.asme.org/terms/Terms_Use.cfm

Table 1 Material Properties of Different Materials Used in This Analysis

MATERIAL	DENSITY gm/cc (σ)	P-WAVE SPEED km/sec (α)	S-WAVE SPEED km/sec (β)	QUALITY FACTOR (q)
Water	1.0	1.52	0.0	57.8
Glass	2.47	5.87	3.70	10^9
Sapphire	4.0	11.1	6.25	10^9
Chromium	7.2	6.97	3.72	10^9
Homog. cell	1.06	1.66	0.08	38.6
Cell cortex	1.1	1.80	0.16	19.3
Cell interior	1.0	1.52	0.0	57.8

it by the plane-wave transmission coefficient $T_{fs}(\Theta_f)$ for wave transmission from the coupling fluid to the lens, one gets the critically transmitted field. Expression of $T_{fs}(\Theta_f)$ is given in Appendix A. The critically transmitted field (the line with square markers) is also shown in Fig. 5.

Finally, the field reaching the receiver can be obtained by multiplying the critically transmitted field with the propagation term in the lens rod. Thus, the potential field reaching the receiver is obtained as:

$$\Phi_T = \Phi_R^c . T_{fs}(\Theta_f) . \exp\{ik_s r(1-\cos\Theta_s)\} \tag{26}$$

where Φ_R^c is the critically reflected field.

To obtain the voltage produced by the transducer, one needs to integrate Φ_T over the transducer. It is carried out by the Gauss-Legendre formula.

Equation (26) describes the field at the receiver generated by the acoustic waves incident with some inclination along any radius of the illuminated region. In addition to it, the center of the illuminated region is struck by normally incident acoustic waves which strike the receiver after being normally reflected by the specimen. Potential field generated by this normally reflected beam is given by:

$$\Phi_{TO} = \frac{r}{z(1-\mu)} . T_{fs}(0) . T_{sf}(0) . R(0) . \exp\left\{2ik_f \left[\frac{r}{(1-\mu)} - z\right]\right\}. \tag{27}$$

Superimposing Eqs. (26) and (27), and then integrating over the transducer, the transducer motion can be obtained. The voltage produced by the transducer is proportional to this value. The proportionality constant is obtained by matching the first peak values of the AMS produced by the instrument and by this analysis.

3 Numerical Results

Numerical results are given in this section for uniform glass, chromium plated glass, and biological cells on glass. Water is taken as the coupling fluid, the lens is made of sapphire. Material properties associated with different materials are given in Table 1. Cell properties are taken from Hildebrad and Rugar (1984) and Litniewski and Bereiter-Hahn (1990). The sapphire lens has a half lens angle of 50 deg and the acoustic wave frequency is 1 GHz.

Figure 7 shows $V(z)$ curve for the uniform glass half-space. High oscillations near the end of the $V(z)$ curve result from the second reflection of the central beam by the specimen. When the lens-specimen distance becomes small, the central beam can reach the receiver after being reflected twice by the specimen. Stars in Fig. 7 are obtained experimentally.

For the glass properties shown in Table 1, a simplified model (Parmon and Bertoni, 1979; Weglein, 1979; Kundu, Mal, and Weglein, 1985) gives uniform spacings equal to 7 μm between two successive minima, thus matching between experimental and theoretical results are significantly improved by the present analysis.

Figure 8 shows $V(z)$ of glass half-space (solid line, second reflection of the central beam is neglected here), 2 μm-thick

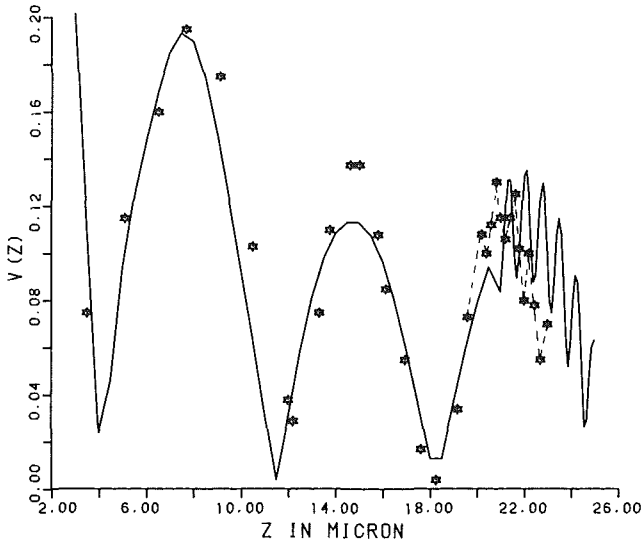

Fig. 7 *V(z)* **of glass half-space. The solid line is obtained from the present analysis and stars are the experimental values. See Table 1 for material properties.**

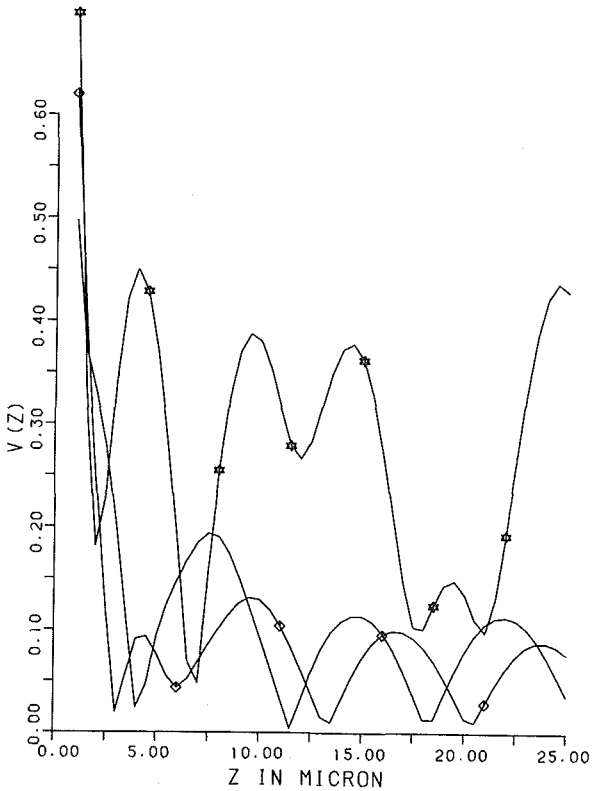

Fig. 8 *V(z)* **for glass half-space (solid line without any marker) and, a two-micron thick homogeneous cell on glass (line with square markers) and a two-micron thick layered cell on glass (line with star markers). See Table 1 for cell and glass properties.**

Downloaded 03 May 2010 to 171.66.16.247. Redistribution subject to ASME license or copyright; see http://www.asme.org/terms/Terms_Use.cfm

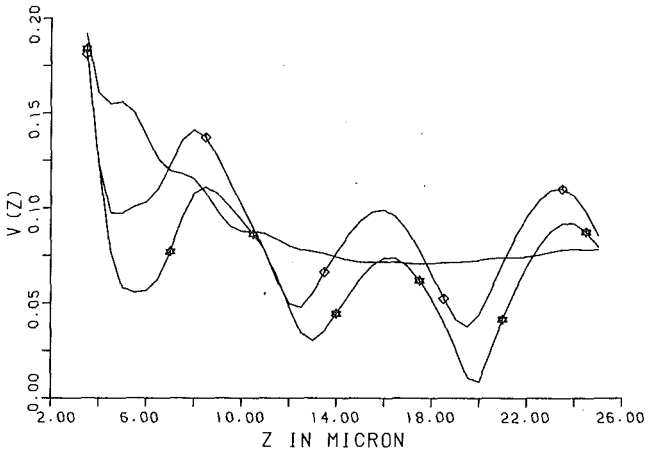

Fig. 9 ***V(z)*** **of chromium half-space (line with square markers) and chromium-plated glass specimens. The line with no marker is for 1-micron thick plating and the line with star markers is for 10-micron thick plating. See Table 1 for chromium properties.**

homogeneous cell on glass (line with square markers), and 2-μm thick layered cell on glass (line with star markers). In the layered cell model, the cell cortex forms the 0.3-μm thick top layer and the cell interior forms the 1.7-μm thick liquid layer in between the cell cortex and the glass half-space. The cell interior has material properties identical to that of water, as shown in Table 1. For the layered cell model, Eq. (23) is used to compute the reflection coefficient. It is interesting to note here that the differences between the $V(z)$ curves of the glass half-space and of the two-micron thick homogeneous cell on glass are not much, but as soon as the cell model is changed from a homogeneous cell to a layered cell, there is a significant change in the $V(z)$ curve.

Finally, Fig. 9 shows $V(z)$ curves for a 10-μm thick chromium layer on glass (line with star markers) and 1-μm thick chromium layer on glass (line with no markers). $V(z)$ of a chromium half-space (line with square markers) is also plotted here for comparison. Significant differences between the $V(z)$ curves for 1-μm and 10-μm thick chromium layered glasses should be noted here. One can also see in this figure that the $V(z)$ of the 10-μm thick chromium layered glass is similar to that of the chromium half-space. This is expected, since very thick chromium layer (several wave lengths thick) should be sensed like a chromium half-space by an acoustic microscope.

4 Concluding Remarks

A complete theoretical analysis is carried out in this paper to compute the $V(z)$ curves of homogeneous and layered solids. Material attenuation has been incorporated in the analysis simply by making the wave numbers complex. Lenses with high aperture angles are considered. The entire converging beam is analyzed without discretizing it, thus prior knowledge about the critical angles of the specimen is not required for the $V(z)$ computation. Variation of the field strength in the illuminated region is obtained by tracing the ray paths; properly considering its transmission, energy absorption during the wave propagation in the attenuative medium and the strength magnification due to focusing. Thus, in this analysis, it is not necessary to assume an arbitrary pupil function for the $V(z)$ computation. In addition to the multilayered solids, multilayered specimens with internal liquid layers are also analyzed here because cell interior behaves more like a liquid layer than a solid layer. Thus, the fundamental problem solved here is applicable to the research related to both engineering and biology.

$V(z)$ curves contain information about elastic properties and thickness of layers. However, extracting this information by inverting the $V(z)$ curve is not easy for multilayered specimens. This inversion technique is currently under investigation.

Acknowledgment

The author would like to express his gratitude to Alexander von Humboldt Stiftung of Germany and the National Science Foundation of the U.S.A. (Contract Number DMC-8807661) for partially funding this research. The authors is grateful to Prof. J. Bereiter-Hahn for providing the experimental facility and reviewing the manuscript, he is also thankful to Mr. K. Hillmann and Mr. H. Lüers for their help during the experimental investigation.

References

Atalar, A., 1978, "An Angular Spectrum Approach to Contrast in Reflection Acoustic Microscopy," *Journal of Applied Physics*, Vol. 49, pp. 5130–5139.

Bertoni, H. L., 1984, "Ray-Optical Evaluation of $V(z)$ in the Reflection Acoustic Microscope," *IEEE Transactions on Sonics and Ultrasonics*, Vol. SU-31, pp. 105–116.

Haskell, N. A., 1953, "The Dispersion of Surface Waves on Multilayered Media," *Bulletin of the Seismological Society of America*, Vol. 43, pp. 17–34.

Hildebrand, J., and Rugar, D., 1984, "Measurement of Cellular Elastic Properties by Acoustic Microscopy," *Journal of Microscopy*, Vol. 134, pp. 245–260.

Kundu, T., 1985, "On Some Aspects of Acoustic Material Signature," *Multiple Scattering of Waves in Random Media and Random Rough Surfaces*, V. K. Varadan and V. V. Varadan, eds., Kurtz Brothers Publ., Pennsylvania State University, pp. 832–844.

Kundu, T., 1988, "A Theoretical Analysis of Acoustic Microscopy with Converging Acoustic Beams," *Applied Physics*, Vol. B46, pp. 325–331.

Kundu, T., and Mal, A. K., 1985, "Elastic Waves in a Multilayered Solid due to a Dislocation Source," *Wave Motion*, Vol. 7, pp. 459–471.

Kundu, T., and Mal, A. K., 1986, "Acoustic Material Signature of a Layered Plate," *International Journal of Engineering Science*, Vol. 24, pp. 1819–1829.

Kundu, T., Mal, A. K., and Weglein, R. D., 1985, "Calculation of the Acoustic Material Signature of a Layered Solid," *Journal of the Acoustical Society of America*, Vol. 77, pp. 353–361.

Liang, K. K., Kino, G. S., and Khuri-Yakub, B. T., 1985, "Material Characterization by the Inversion of $V(z)$," *IEEE Transactions on Sonics and Ultrasonics*, Vol. SU-32, pp. 213–224.

Litniewski, J., and Bereiter-Hahn, J., 1990, "Measurements of Cells in Culture by Scanning Acoustic Microscopy," *Journal of Microscopy*, Vol. 158, pp. 95–107.

Parmon, W., and Bertoni, H. L., 1979, "Ray Interpretation of the Material Signature in the Acoustic Microscope," *Electron. Letters*, Vol. 15, pp. 684–686.

Quate, C. F., 1980, "Microwaves, Acoustics, and Scanning Microscopy," *Scanned Imaging and Microscopy*, E. A. Ash, ed., Academic Press, London, pp. 23–55.

Sheppard, C. J. R., and Wilson, T., 1981, "Effects of High Angles of Convergence on $V(z)$ in the Scanning Acoustic Microscope," *Applied Physics Letters*, Vol. 38, pp. 858–859.

Thomson, W. T., 1950, "Transmission of Elastic Waves Through a Stratified Solid Medium," *Journal of Applied Physics*, Vol. 21, pp. 89–93.

Weglein, R. D., 1979, "A Model for Predicting Acoustic Material Signatures," *Applied Physics Letter*, Vol. 34, pp. 179–181.

Xu, P.-C., and Mal, A. K., 1987, "Calculation of Green's Functions for a Layered Viscoelastic Solid," *Bulletin of the Seismological Society of America*, Vol. 77, pp. 1823–1837.

APPENDIX A

Expressions for the plane-wave transmission coefficients T_{sf} and T_{fs} of Eqs. (6) and (24) are given in this Appendix.

$$T_{sf}=\frac{-2(2k^2-k_\beta^2)}{\dfrac{\sigma_f\omega^2}{\mu_s}+\delta_f\dfrac{(2k^2-k_\beta^2)^2+4k^2\epsilon_s\delta_s}{\delta_s k_\beta^2}}$$

$$T_{fs}=\frac{-2(2k^2-k_\beta^2)}{\dfrac{\delta_s k_\beta^2}{\delta_f}+\dfrac{\mu_s\{(2k^2-k_\beta^2)^2+4k^2\epsilon_s\delta_s\}}{(\sigma_f\omega^2)}}$$

where

Downloaded 03 May 2010 to 171.66.16.247. Redistribution subject to ASME license or copyright; see http://www.asme.org/terms/Terms_Use.cfm

$$\delta_s = \left(\frac{\omega^2}{\alpha_s^2} - k^2\right)^{1/2} \frac{1 + i\left(\frac{\omega}{\alpha_s}\right)^2}{2q_s\alpha_s\left(\frac{\omega^2}{\alpha_s^2} - k^2\right)}$$

$$\epsilon_s = \left(\frac{\omega^2}{\beta_s^2} - k^2\right)^{1/2} \frac{1 + i\left(\frac{\omega}{\beta_s}\right)^2}{2q_s\beta_s\left(\frac{\omega^2}{\beta_s^2} - k^2\right)}.$$

α_s, β_s, μ_s, and k_β are longitudinal wave speed, shear wave speed, shear modulus, and shear wave number, respectively, of the solid. σ_s and σ_f are densities of solid and fluid, respectively; δ_f is defined in Eq. (17).

APPENDIX B

Elements of A_m, E_n^{-1} and A_l, matrices, which appeared in Eqs. (22) and (25), are given in this Appendix. Notations a_{ij}, σ_{ij}, and l_{ij} are used to denote the ij-element of A_m, and E_n^{-1} and A_l matrices, respectively.

$$a_{11} = a_{44} = \Gamma_m C_{pm} - \Sigma_m C_{qm}$$

$$a_{12} = a_{34} = -\frac{-i\Sigma_m k S_{pm}}{\delta_m} - \frac{i\Gamma_m \epsilon_m S_{qm}}{k}$$

$$a_{13} = a_{24} = \frac{ik(-C_{pm} + C_{qm})}{\cap_m}$$

$$a_{14} = \frac{\left(\frac{k^2 S_{pm}}{\delta_m} + \epsilon_m S_{qm}\right)}{\cap_m}$$

$$a_{21} = a_{43} = \frac{i\Gamma_m \delta_m S_{pm}}{k} + \frac{i\Sigma_m k S_{qm}}{\epsilon_m}$$

$$a_{22} = a_{33} = -\Sigma_m C_{pm} + \Gamma_m C_{qm}$$

$$a_{23} = \frac{\left(\delta_m S_{pm} + \frac{k^2 S_{qm}}{\epsilon_m}\right)}{\cap_m}$$

$$a_{31} = a_{42} = 2ik\mu_m\Sigma_m(-C_{pm} + C_{qm})$$

$$a_{32} = \frac{-\cap_m \Sigma_m^2 S_{pm}}{\delta_m} - 2\Gamma_m\mu_m\epsilon_m S_{qm}$$

$$a_{41} = -2\Gamma_m\mu_m\delta_m S_{pm} - \frac{\cap_m \Sigma_m^2 S_{qm}}{\epsilon_m}$$

where

$$\Gamma_m = 2\left(\frac{k}{k_{\beta m}}\right)^2$$

$$\Sigma_m = \Gamma_m - 1$$

$$\cap_m = \mu_m k_{\beta m}^2$$

$$C_{pm} = \cos(\delta_m h_m)$$

$$C_{qm} = \cos(\epsilon_m h_m)$$

$$S_{pm} = \sin(\delta_m h_m)$$

$$S_{qm} = \sin(\epsilon_m h_m)$$

$$k_{\beta m} = \frac{\omega}{\beta_m}\left\{1 + \frac{i}{(2q_m\beta_m)}\right\}$$

$$\delta_m = \left(\frac{\omega^2}{\alpha_m^2} - k^2\right)^{1/2}\left\{1 + \frac{i\left(\frac{\omega}{\alpha_m}\right)^2}{\left[2q_m\alpha_m\left(\frac{\omega^2}{\alpha_m^2} - k^2\right)\right]}\right\}$$

$$\epsilon_m = \left(\frac{\omega^2}{\beta_m^2} - k^2\right)^{1/2}\left\{1 + \frac{i\left(\frac{\omega}{\beta_m}\right)^2}{\left[2q_m\beta_m\left(\frac{\omega^2}{\beta_m^2} - k^2\right)\right]}\right\}.$$

μ_m, h_m, α_m, β_m, and q_m are shear modulus, thickness, longitudinal wave velocity, shear wave velocity, and quality factor, respectively, of the mth layer.

$$-\Theta_{11} = \Theta_{22} = -\Theta_{31} = \Theta_{42} = \frac{ik}{k_{\beta m}^2}$$

$$-\Theta_{12} = \Theta_{32} = \frac{i\Sigma_m}{(2\delta_m)}$$

$$-\Theta_{21} = \Theta_{41} = \frac{i\Sigma_m}{(2\epsilon_m)}$$

$$\Theta_{13} = \Theta_{33} = \Theta_{24} = \Theta_{44} = -\frac{1}{(2\cap_m)}$$

$$-\Theta_{34} = \Theta_{14} = \frac{k}{(2\delta_m\cap_m)}$$

$$-\Theta_{23} = \Theta_{43} = \frac{k}{(2\epsilon_m\cap_m)}$$

and

$$l_{11} = l_{22} = C_{pl}$$

$$l_{12} = \frac{\delta_l S_{pl}}{(\sigma_l\omega^2)}$$

$$l_{21} = \frac{-\sigma_l\omega^2 S_{pl}}{\delta_l}.$$

Expressions of C_{pl}, S_{pl}, and δ_l are similar to those of C_{pm}, S_{pm}, and δ_m which are defined earlier. The only difference is that the subscript m there is replaced by the subscript l here to represent the liquid layer properties.

Downloaded 03 May 2010 to 171.66.16.247. Redistribution subject to ASME license or copyright; see http://www.asme.org/terms/Terms_Use.cfm

Corner Singularities of Three-Dimensional Planar Interface Cracks

F. Ghahremani

C. F. Shih
Mem. ASME.

Division of Engineering,
Brown University,
Providence, RI 02912

Very high stresses develop near the intersection of a planar interfacial crack with the free surface of joined materials with large mismatch of elastic moduli. The so-called corner singularity is more singular than the $1/\sqrt{}$distance singularity of the interior fields. The eigenvalues corresponding to the most singular state, and for which the strain energy of a finite cone is bounded, are in general complex. For a wide selection of material pairs, our calculations show that the eigenvalue of the dominant singularity, $0(r^{-s})$, is real and s increases from 0.5 to about 0.75 as the moduli mismatch increases. Values of s are reported for a broad range of material combinations. A class of anisotropic materials and bicrystals is also investigated.

1 Introduction

Surface cracks are likely to develop on the bonding planes of joined materials with large mismatch of elastic moduli. Such cracks are also likely to be exposed to the environment which can be deleterious to interfacial strength and fracture toughness. The high stresses working in concert with the environment can initiate the process of failure, e.g., delamination of layered materials or peeling of thin films. Thus, the performance of advanced material systems can be controlled by such highly stressed sites.

The three-dimensional asymptotic fields at such sites can be studied by considering a cracked solid-hemisphere as shown in Fig. 1; the xz-plane is the interface. Near the intersection of the crack front with the free surface, referred as the vertex, the state of stress is three dimensional. The asymptotic series for the stress is composed of terms of the following form:

$$r^{-s}\tilde{\sigma}(\theta,\varphi;s), \tag{1}$$

where r is the radial distance from the vertex, θ and φ are the spherical coordinates, and $\tilde{\sigma}(\theta,\varphi;s)$ is the tensor of angular functions defined on a spherical shell of unit radius which surrounds the vertex ($r\to 0$). The order of the singularity, s, can be real or complex. Corner signularities for homogenous materials have been investigated by Benthem (1977), Bazant and Estenssoro (1979), and Ghahremani (1991), for these cases, the eigenvalues, s, are real.

In a typical ductile material, the crack front of a through-thickness crack tunnels and the trailing crack edge near the free surface fails by shear lip formation. The reverse of this process, where by fracture initiates near the intersection of a straight crack front with a free surface, has been observed in a brittle material. Near the crack front intersecting the free surface, the highly stressed elastic state can be more singular than $1\sqrt{r}$ since

$$\sigma = K_A O(r^{-s_1}) + K_S O(r^{-s_2}) + \text{ higher order terms} \tag{2}$$

where $s_1 > 0.5 > s_2$ (Benthem, 1977; Bazant and Estenssoro, 1979; Nakamura and Parks, 1989). The leading term in the series corresponds to the antisymmetric mode with amplitude K_A (field producing in-plane and out-of-plane sliding displacement jumps across the crack faces), while the second term corresponds to the symmetric mode with amplitude K_S (field producing only opening displacement jumps across the crack faces). If $K_A \neq 0$ the stresses near the vertex are more singular than the $1/\sqrt{r}$ singularity of the interior stress field, and the vertex is the likely site of fracture initiation. More typically, the crack is loaded in tension so that $K_A = 0$, or $K_A L^{-s_1}/K_S L^{-s_2} << 1$ (L is a characteristic dimension of the crack geometry)—therefore stresses over any length scale of physical relevance are less singular than $1/\sqrt{r}$ because $s_2 < 0.5$. In this case, the stresses in the interior, which are dominated by the $1/\sqrt{r}$ singularity, are larger.

The three-dimensional corner singularity of an elastic body bonded to a rigid substrate has been investigated by Barsoum (1990) and Barsoum and Chen (1990). Their analysis, which is limited to the leading singularity, showed that the order of the singularity is stronger than $1/\sqrt{r}$, i.e., $\mathrm{Re}(s) > 0.5$ where Re denotes the real part. Some information on the stress and strain fields are provided in their paper; however, the eigenfunction is not easily extractable from their results.

In this paper, a fairly complete discussion of the fields near the vertex formed by two dissimilar elastic bodies is presented. We elucidate upon the structure of the series in Eq. (1) including the two leading eigenvalues and their eigenfunctions. For typical material pairs, the eigenvalues of the first two terms in the asymptotic series are real so that the structure of the fields near the bimaterial vertex is similar to that for the homogeneous material. However, there are important differences. For

Contributed by the ASME Applied Mechanics Division of The American Society of Mechanical Engineers for publication in the Journal of Applied Mechanics.

Discussion on this paper should be addressed to the Technical Editor, Prof. Leon M. Keer, The Technological Institute, Northwestern University, Evanston, IL 60208, and will be accepted until two months after final publication of the paper itself in the Journal of Applied Mechanics. Manuscript received by the ASME Applied Mechanics Division, Mar. 15, 1990; final revision, Aug. 8, 1990.

Copyright © 1992 by ASME
Downloaded 03 May 2010 to 171.66.16.247. Redistribution subject to ASME license or copyright; see http://www.asme.org/terms/Terms_Use.cfm

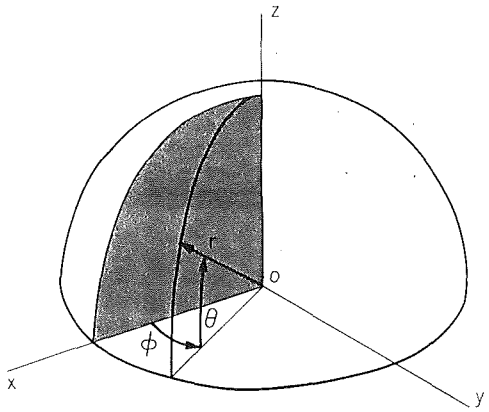

Fig. 1 Spherical coordinates centered at intersection of crack front with free surface. The crack is shaded *xz*-plane is the interface and *xy*-plane is the free surface.

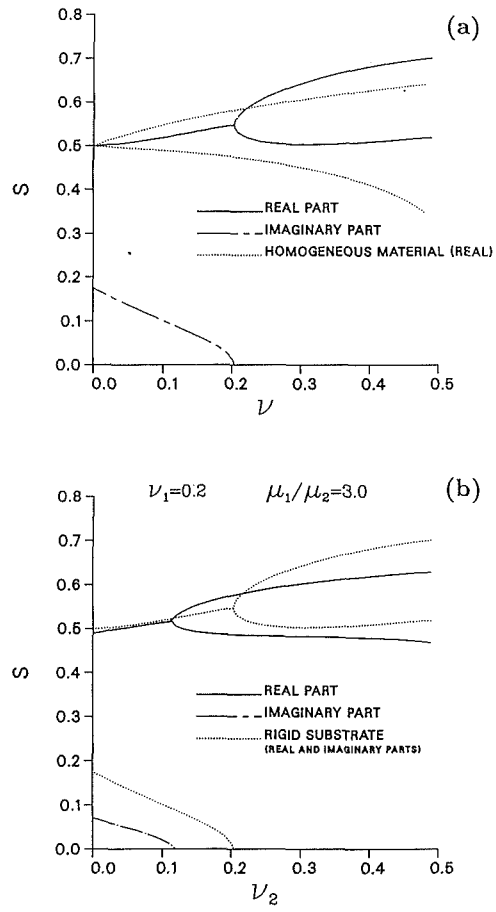

Fig. 2 The order of the corner singularity for an interface crack. (*a*) rigid substrate (homogeneous material included for comparison); (*b*) elastic substrate, $\nu_1 = 0.2$ and $\mu_1/\mu_2 = 3$ (rigid substrate included for comparison).

the bimaterial vertex, the stronger singularity, s_1, is dominated by the antisymmetric mode whereas the weaker singularity, s_2, is dominated by the symmetric mode, i.e., no purely antisymmetric or symmetric modes exists. We have studied a wide selection of material pairs and found that $0.5 \le s_1 < 0.75$, and $0.3 < s_2 < 0.55$. Since an interfacial crack is almost always subject to mixed-mode loading, $K_A \neq 0$, and therefore the stresses near the vertex are generally more singular than $1/\sqrt{r}$. In other words, the vertex is the site of largest stresses! In addition, experimental measurements to date have shown that interfacial fracture toughness can be considerably lower than the toughness of the constituent material. The combination of high stresses and low interfacial toughness simply means that the vertex region is the most likely site for initiation of fracture. We make use of the first two eigenvalues and associated eigenfunctions to interprete some recent experimental observations on interface crack profiles. These aspects are taken up in Section 4.

2 Problem Formulation and Results

We consider a planar interface crack between two adhering linear elastic materials. The crack front perpendicularly intersects the free surface as shown in Fig. 1. The *xy*-plane is the free surface and the *xz*-plane is the interface between the two materials. The crack front is along the *z*-axis and the crack is shaded. Near the vertex, the state of stress is three dimensional. The asymptotic series for the displacement vector and the stress tensor are composed of terms of the following form:

$$\sigma = r^{-s}\tilde{\sigma}(\theta\varphi;s) \tag{3}$$

$$\mathbf{u} = r^{1-s}\tilde{\mathbf{u}}(\theta\varphi;s). \tag{4}$$

Here, r is the radial distance from the vertex, θ and φ are the spherical coordinates, and $\tilde{\sigma}(\theta\varphi;s)$ and $\tilde{\mathbf{u}}(\theta,\varphi,s)$ are the tensor of angular functions of the stresses and displacements pertaining to an infinitesimally thin spherical shell of unit radius surrounding the vertex. The order of the singularity, s, can be real or complex.

The method used to calculate the eigenvalues s and their associated eigenfunctions is described in detail by Ghahremani (1991). Briefly, a weak variational principle in the form of principle of virtual work is formulated for an infinitesimally thin spherical shell of unit radius. The sphere is divided into six-node spherical triangles. The shape functions of a six-node triangle are complete quadratic polynomials with each node having three degrees-of-freedom. Different mesh designs and mesh refinements for an elastic body on a rigid substrate were tested; we chose a mesh with about 500 degrees-of-freedom. About twice as many degrees-of-freedom is required for the mesh for two dissimilar elastic bodies. The Galerkin method is used to obtain an approximate quadratic eigenvalue problem in which the eigenvalue is s and the eigenvector is the displacements of the points on the unit shell. The finite element eigenvalue problem is solved by inverse treppen iteration. The method was applied to crack problems with known solutions and the comparison indicates that our calculations are accurate to two significant digits—approaching the exact values from below, so that s is slightly underestimated.

In general, there is an infinite number of terms in the series (1). However, we restrict our attention to singular states for which the strain energies of a finite cone are bounded, i.e., the search for s is confined to the range $0 < \mathrm{Re}(s) < 3/2$. Furthermore, our discussion is focussed on the two most singular (admissible) eigenvalues and the corresponding modes. Higher order terms of the form in (3), (4) have been obtained, but these as well as the rigid body modes will not be discussed.

Consider a crack lying on the interface between an elastic body and a rigid body. This case is representative of bimaterial pairs like cork/alumina and polymer/alumina. The values of s as a function of Poisson's ratio, ν, are shown in Fig. 2(*a*). For $\nu = 0$, the traction-free surface boundary conditions and the field equation are satisfied by the plane-strain solution (as well as the plane-stress solution) which is therefore a solution to the present problem. The plane-strain solution is $\mathrm{Re}(s) = 0.5$ and $\mathrm{Im}(s) = 0.175$. (e.g., Rice, 1988). To three significant figures our calculated values are $\mathrm{Re}(s) = 0.499$ and $\mathrm{Im}(s) = 0.174$, i.e., our solutions are accurate to two significant digits. As Poisson's ratio is increased, the $\mathrm{Re}(s)$ increases and the $\mathrm{Im}(s)$ decreases, and at $\nu \approx 0.2$, $\mathrm{Im}(s)$ vanishes altogether. For ν greater than about 0.2, the complex eigenvalue and its conjugate are replaced by two real eigenvalues. The larger (real)

Downloaded 03 May 2010 to 171.66.16.247. Redistribution subject to ASME license or copyright; see http://www.asme.org/terms/Terms_Use.cfm

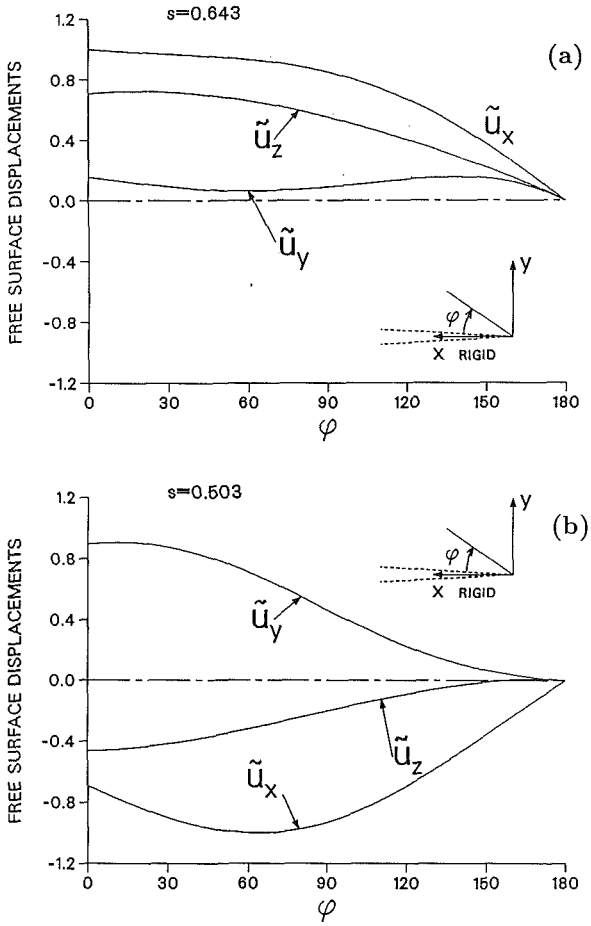

Fig. 3 Eigenfunctions for elastic body (ν = 0.3) on rigid substrate; (*a*) for the larger eigenvalue, (*b*) for the smaller eigenvalue

eigenvalue increases steadily as ν increases while the smaller (real) eigenvalue decreases and then increases. We have carried out many calculations and have observed that the transition from a pair of complex eigenvalues to two real eigenvalues always takes place in a smooth manner, i.e., if the average value of the two eigenvalues is plotted against ν, a smooth curve (with continuous slope) is obtained. (When the eigenvalues are complex, the average value is simply the real part of the complex pair).

The next term in the asymptotic expansion is also of the form in (3), (4). For $0<\nu<0.20$, the eigenvalue is real and decreases from 0.3 to 0. Beyond ν greater than about 0.23, the eigenvalue becomes complex with a positive real part i.e., the associated stresses are bounded. We conclude that for $\nu>0.23$, only two singular modes exist: the most singular mode given by s_1, and the weaker mode given by s_2.

For comparison purposes, the eigenvalues for a homogeneous material and obtained by the same numerical method is included in Fig. 2(*a*); the eigenvalues are real and are indicated by dotted lines (Ghahremani, 1991). In the case of the homogeneous material, the division into two branches begins at $\nu=0$; in contrast, such a separation occurs at a nonzero value of ν when the crack is on a bimaterial interface. It is noteworthy that the calculated eigenvalues for the homogeneous material are typically within one percent of those values obtained by Benthem (1977) and Bazant and Estenssoro (1979). This provides an indication of the accuracy of the present solutions.

Barsoum and Chen (1990) have carried out a limited study of an interface crack in which the second material is rigid. The eigenvalue s was obtained by using a finite element iterative method (FEIM). Unlike the numerical method used in the present study, the FEIM does not take full advantage of the assumed form of the three-dimensional fields in (3), (4) so that their calculations are fairly involved. They obtained a curve similar to our curve for the larger eigenvalue shown in Fig. 2(*a*) of this paper. Their values for $\mathrm{Re}(s)$ are similar to the present values; however, there are some differences for $\mathrm{Im}(s)$. Their calculations suggest that $\mathrm{Im}(s)$ vanishes for $\nu>0.3$, whereas our results indicate that this occurs for $\nu>0.2$. They provide no results for the next eigenvalue.

As another material combination for study, we take the upper and lower halves to be elastic bodies with Poisson's ratio and shear modulus denoted by ν_1, μ_1, and ν_2, μ_2 respectively. Figure 2*b* shows the variation of s with ν_2 for $\nu_1=0.2$ and $\mu_1/\mu_2=3$. The result for a rigid substrate considered previously is also included. It can be seen that reducing the severity of the mismatch of elastic moduli results in the eigenvalues being real over a larger range of values of Poisson's ratio. At $\nu_1=0$, $\mathrm{Re}(s)\neq 0.5$, and this is not unexpected since plane-strain conditions do not exist at the free surface for $\nu_1\neq\nu_2$.

The displacements for the elastic body (with $\nu=0.3$) bonded to a rigid substrate are examined next. The displacements at the free-surface ($z=0$) at radial distance $r=1$, corresponding to the more singular eigenvalue, is shown in Fig. 3(*a*); the displacements corresponding to the smaller eigenvalue is shown in Fig. 3(*b*). The dimensionless displacement functions $\tilde{\mathbf{u}}(\theta,\varphi;s)$ are rendered unique by requiring the maximum dimensionless displacement component on the unit sphere, $r=1$, to equal unity. The undetermined normalizing factor can be obtained from the solution to the actual crack problem. The values of $\tilde{u}_y$, $\tilde{u}_x$, and $\tilde{u}_z$ at $\varphi=0$ are the normal opening and the in-plane and out-of-plane sliding displacements, respectively. As can be seen, the displacement jumps associated with the larger eigenvalue are dominated by the shearing mode (Fig. 3(a), while the displacements of the smaller eigenvalue have larger opening displacements (Fig. 3(*b*)). These displacement patterns are rather similar to those obtained by Ghahremani (1991) for the homogeneous material. However, there is an important difference—in the homogeneous case, the eigenfunction of the stronger singularity corresponds precisely to the antisymmetric mode (producing in-plane and out-of-plane sliding displacement jumps) while the eigenfunction of the smaller eigenvalue corresponds to the symmetric mode (producing only opening displacement jumps). In contrast, the eigenfunctions for the bimaterial are not purely anti-symmetric (see Fig. 3(*a*)) or purely symmetric (see Fig. 3(*b*)).

These displacement patterns are easily recognized by comparing the crack profiles. The displacement jumps across the crack associated with the antisymmetric mode (larger eigenvalue) of the homogeneous material with $\nu=0.3$ are shown in Fig. 4(*a*). In the figure, $[\tilde{u}_x]$ designate the jumps $\tilde{u}_x^+-\tilde{u}_x^-$, where $+$ denotes the value from the side $y>0$ and $-$ from $y<0$, and similarly for the other bracketed quantities. The jumps at the free surface, $z=0$, and at an interior plane, $z=1$, are shown. It can be seen that the displacement jumps of the stronger singularity correspond to the antisymmetric mode (involving only in-plane and out-of-plane sliding). The displacement jumps given by the stronger singularity of the bimaterial, $\nu_1=0.2$, $\nu_2=0.3$ and $\mu_1/\mu_2=3$ are shown in Fig. 4(*b*). Again, the sliding displacement jumps dominate, and the similarity to the displacements in Fig. 4(*a*) can be seen. Nevertheless, the interface crack has a small opening ($[\tilde{u}_y]>0$) so that if the applied stresses are reversed, the crack faces will come into contact. In contrast, the opening displacement of the homogeneous material vanishes identically so that the antisymmetric mode will not produce crack face contract should the applied stresses be reversed.

The crack profiles associated with the smaller eigenvalue of the homogeneous material and of the bimaterial are shown in Fig. 4(*c*) and 4(*d*), respectively. In Fig. 4(*c*) the opening displacement is the only nonvanishing displacement jump, i.e.,

Downloaded 03 May 2010 to 171.66.16.247. Redistribution subject to ASME license or copyright; see http://www.asme.org/terms/Terms_Use.cfm

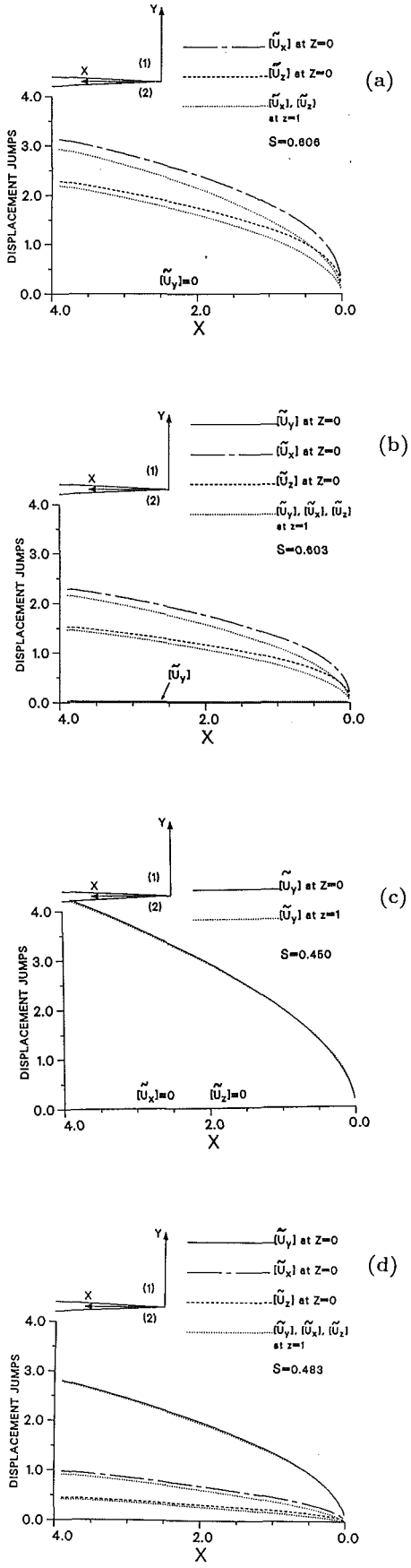

Fig. 4 Crack profiles for homogeneous material with $\nu = 0.3$ and bimaterial with $\nu_1 = 0.2$, $\nu_2 = 0.3$ and $\mu_1/\mu_2 = 3$; material 1 is placed in the region $y > 0$, (*a*) larger eigenvalue, homogeneous material, (*b*) larger eigenvalue, bimaterial, (*c*) smaller eigenvalue, homogeneous material, (*d*) smaller eigenvalue, bimaterial

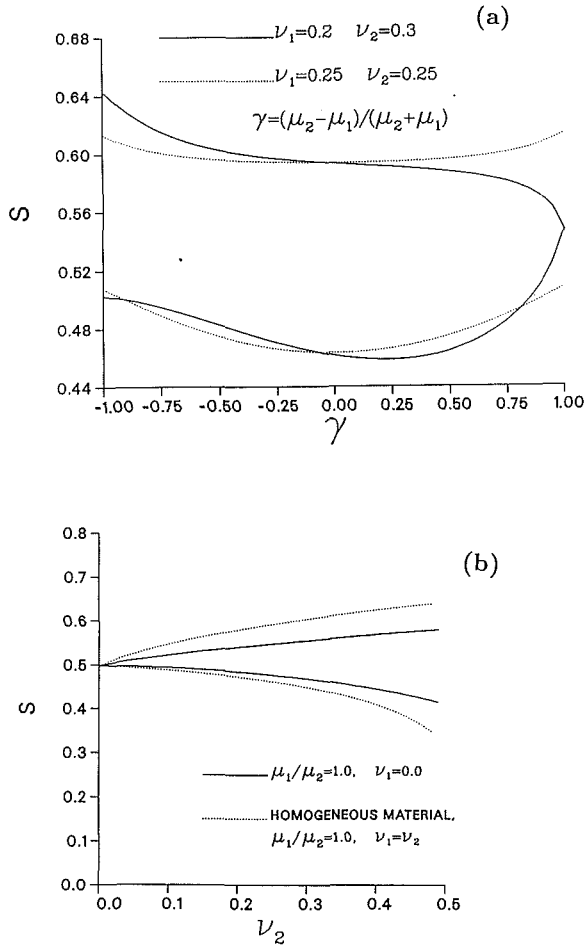

Fig. 5 (*a*) Dependence of s on μ_1/μ_2 for $\nu_1 = 0.3$, $\nu_2 = 0.2$, and for $\nu_1 = \nu_2 = 0.25$, (*b*) dependence of s on ν_2 for $\nu_1 = 0$ and $\mu_1/\mu_2 = 1$; homogeneous material included for comparison

the fields associated with the weaker singularity correspond to the symmetric mode. The displacement jumps in Fig. 4(*d*) consist primarily of opening displacement with smaller contributions from the shearing displacements.

The stresses in bonded dissimilar isotropic bodies must, in general, depend on all four elastic moduli. Since the four moduli can be reduced to three dimensionless moduli, s must, in general, depend on three nondimensional parameters, ν_1, ν_2, and the ratio μ_1/μ_2, or three other convenient nondimensional combinations of ν_1, ν_2, μ_1, and μ_2. Some results on how s depends on moduli are presented. In one case we take $\nu_1 = 0.2$, $\nu_2 = 0.3$ and vary the ratio μ_1/μ_2, and in the other case we take $\nu_1 = \nu_2 = 0.25$ and vary μ_1/μ_2. We calculate the two most singular eigenvalues and these are plotted against the ratio $\gamma = (\mu_2 - \mu_1)/(\mu_2 + \mu_1)$ in Fig. 5(*a*). Note that γ equal to -1, 0, and 1 correspond to μ_1/μ_2 equal to 0, 1 and ∞. For $\nu_1 = 0.2$ and $\nu_2 = 0.3$ and $\gamma = 1$, the larger and smaller eigenvalues coalesce to one complex eigenvalue (and its conjugate). As another example, we take $\mu_1/\mu_2 = 1$, $\nu_1 = 0$, and calculate the eigenvalues for $0 \le \nu \le 0.5$. The values are plotted in Fig. 5(*b*). For these values of the moduli, s is always real; $s = 0.5$ for $\nu_2 = \nu_1 = 0$, and from this point emanate two branches of real eigenvalues for $\nu_2 > 0$. These two branches are bounded by the eigenvalues for the homogeneous material. The results in Fig. 5 show that s depends on all three dimensionless material moduli. Moreover, the most singular state for every material combination under consideration is more singular than $1/\sqrt{r}$.

The fields of plane problems of interface cracks depend only on two combinations of elastic constants, α and β (Dundurs, 1969). For plane strain,

Downloaded 03 May 2010 to 171.66.16.247. Redistribution subject to ASME license or copyright; see http://www.asme.org/terms/Terms_Use.cfm

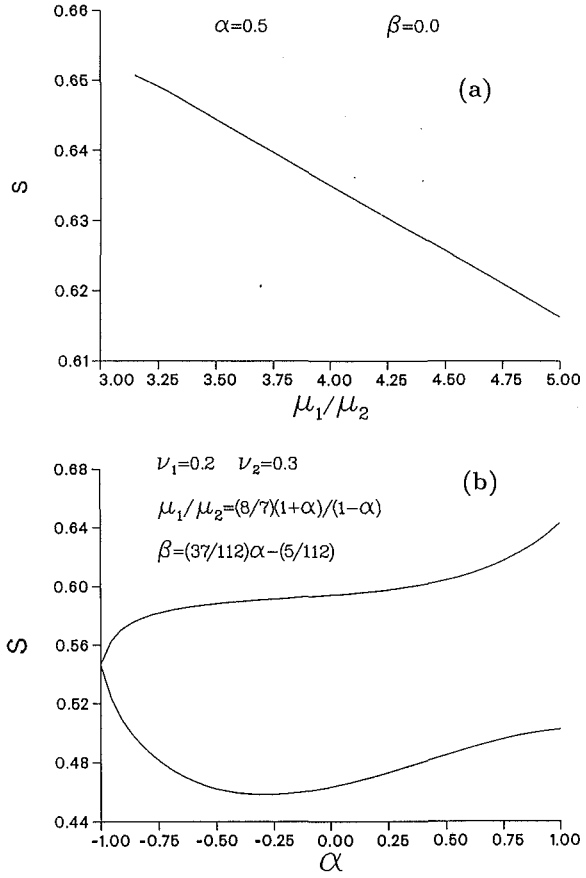

Fig. 6 (*a*) Dependence s on μ_1/μ_2 when α and β are kept constant, (*b*) dependence of s on α for $\nu_1 = 0.2$, $\nu_2 = 0.3$, and $0 < \mu_1/\mu_2 < \infty$

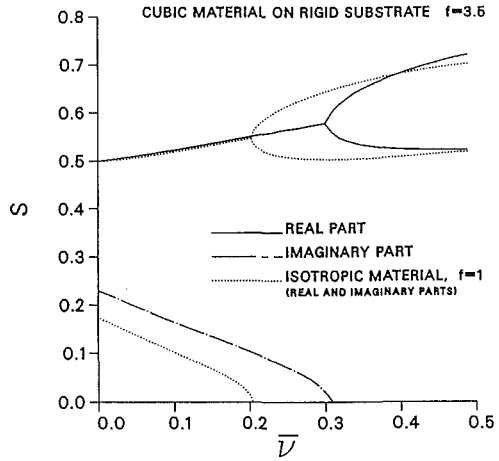

Fig. 7 The order of corner singularity versus $\bar{\nu} \equiv C_{12}/(C_{11} + C_{12})$; $f \equiv 2C_{44}/(C_{11} - C_{12})$ is the anisotropy factor. Isotropic material is included for comparison; for isotropic material $\bar{\nu}$ is Poisson's ratio.

$$\alpha = \left(\frac{1-\nu_2}{\mu_2} - \frac{1-\nu_1}{\mu_1}\right) \Big/ \left(\frac{1-\nu_1}{\mu_2} + \frac{1-\nu_1}{\mu_1}\right),$$

$$\beta = \frac{1}{2}\left(\frac{1-2\nu_2}{\mu_2} - \frac{1-2\nu_1}{\mu_1}\right) \Big/ \left(\frac{1-\nu_2}{\mu_2} + \frac{1-\nu_1}{\mu_1}\right). \tag{5}$$

Since most data on material pairs are characterized in this manner, we present some of our results in terms of Dundurs' parameters α and β. For $\alpha = 0.5$ and $\beta = 0$, the variation of the largest eigenvalue with μ_1/μ_2 is shown in Fig. 6(*a*). For this particular case, s depends nearly linearly on μ_1/μ_2. The range of μ_1/μ_2 in Fig. 6(*a*) corresponds to $0 \le \nu \le 0.5$.

Table 1 Order of corner singularities of interface cracks for some common metals on rigid substrate

Metal	$\bar{\nu}$	f	s_1	s_2
Pb	.461	4.00	.712	.524
Cu	.419	3.21	.692	.523
Ni	.390	2.63	.678	.521
Fe	.373	2.42	.670	.520
Al	.365	1.22	.670	.508

Table 2 For Al_2O_3, Young's modulus = 390.0 GPa and Poisson's ratio = 0.22. For Cu, C_{11} = 168.4 GPa, C_{12} = 121.4 GPa, C_{44} = 75.4 GPa

Crack plane	Crack front	Cu/Al_2O_3 s_1	Cu/Al_2O_3 s_2	Cu/rigid s_1	Cu/rigid s_2
$(2\bar{2}1)$	[110]	.651	.467	.718	.466
(001)	[110]	.552	.485	.600	.548

When any two of the parameters ν_1, ν_2 and μ_1/μ_2 are kept constant and the third is varied, a segment of a straight line is generated in the $\alpha\beta$-plane (Dundurs, 1969). From the above relations for α and β, it is easily shown that for $\nu_1 = 0.2$ and $\nu_2 = 0.3$, the equation of the line is $(\beta = 37/112)\alpha - (5/112)$. This line passes through most of the data representative of material pairs tabulated by Suga et. al. (1989). For material pairs parameterized by this material line, Fig. 6(*b*) shows the two most singular eigenvalues as functions of α. The eigenvalues are real, but they merge into a complex conjugate pair near $\alpha = -1$. According to Suga et al.'s tabulation, $|\beta| < 0.25$ for most material pairs. For β in this range, our calculations show that the eigenvalues are generally real and that the associated eigenfunctions are similar to those shown in Figs. 3 and 4.

To gain some understanding as to how the eigenvalue s is affected by anisotropy, we consider a crack at the interface of a cubic single crystal and a rigid substrate. The geometry of the crack is the same as that in Fig. 1. For the example calculations, we align the crystal so that the (001) plane coincide with the crack plane and [010] direction with the crack front, the z-axis. Cubic materials are described by two non-dimensional constants, the anisotropy factor $f \equiv 2C_{44}/(C_{11} - C_{12})$ and $\bar{\nu} \equiv C_{12}/(C_{11} + C_{12})$ where the coefficients C_{ij} are the elastic moduli (e.g., see Cottrell, 1981). The range of f is $(0,\infty)$. When $f = 1$, the material is isotropic in which case ν corresponds to the usual Poisson's ratio.

Figure 7 shows the plot of s versus $\bar{\nu}$ for $f = 3.5$; the results for an isotropic material bonded to a rigid substrate is included (from Fig. 2(*a*)). While the trends of both material pairs are similar at a given value of $\bar{\nu}$, the singularity of the anisotropic material is stronger; it is also complex for a wider range of $\bar{\nu}$. The value of f and $\bar{\nu}$ for several common metals are tabulated in Table 1 (Cottrell, 1981). We calculated s of material pairs involving these metals and a rigid substrate, and for the orientation described above. The two largest eigenvalues are real—they are given in Table 1. Needless to say, the eigenvalues depend on the crystal orientation. For example, if the (111) plane of copper is the crack plane and [T10] is the crack front, $s_1 = 0.717$ and $s_2 = 0.471$. We should mention that if a finite stiffness is assigned to the substrate, the eigenvalues are smaller than those reported above.

By considering the competition of dislocation emission and atomic decohesion at the crack tip, Rice, Suo, and Wang (1989) have developed a theory for predicting the circumstances whereby the interface of a ductile single crystal with a brittle ceramic is intrinsically cleavable. They have illustrated their theory by analyzing Cu/Al_2O_3 interface for certain orientations of copper single crystals. As another example, we have calculated the order of corner singularity for these cases. The results are summarized in Table 2. If instead of sapphire (Al_2O_3)

Downloaded 03 May 2010 to 171.66.16.247. Redistribution subject to ASME license or copyright; see http://www.asme.org/terms/Terms_Use.cfm

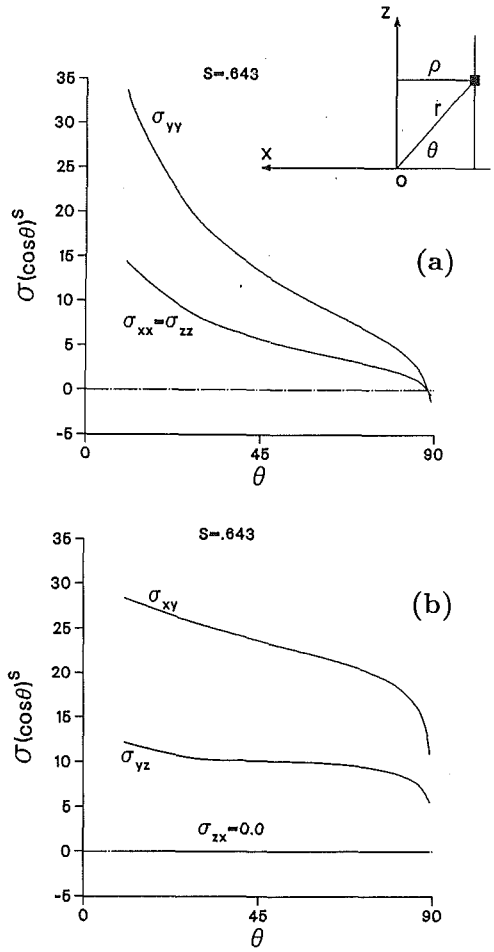

Fig. 8 Elastic body, ν = 0.3, on rigid substrate. Behavior of stresses, corresponding to the larger eigenvalue, at the bonding plane at unit distance ahead of the crack front; (*a*) normal stresses, (*b*) shear stresses.

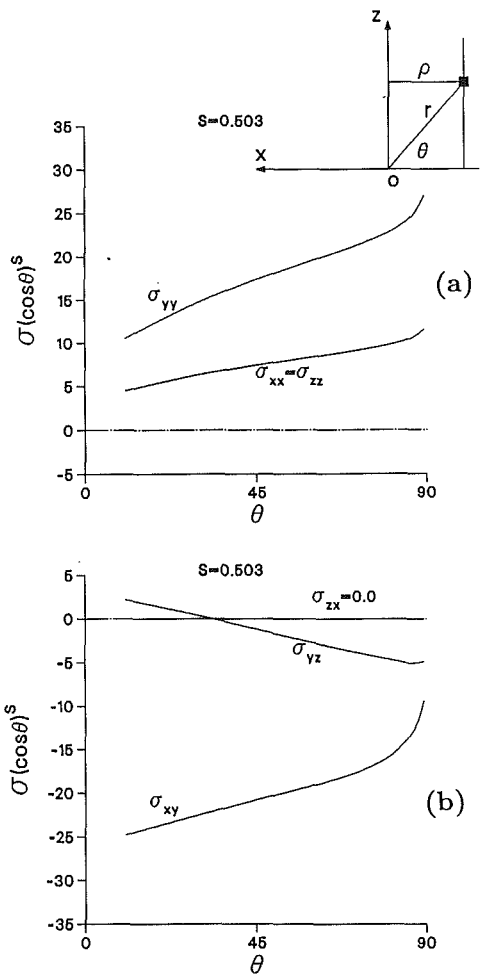

Fig. 9 Elastic body, ν = 0.3, on rigid substrate. Behavior of stresses, corresponding to the weaker eigenvalue, at the bonding plane at unit distance ahead of the crack front; (*a*) normal stresses, (*b*) shear stresses.

the substrate is taken as rigid, the numbers given under Cu/rigid are obtained. In all these cases, the eigenfunctions of s_1 are dominated by the shearing mode while the eigenfunctions of s_2 are dominated by opening mode, much like the displacement patterns of the isotropic bimaterials discussed previously.

3 Stresses Near the Interface

Stresses near the vertex are of interest since it is the likely site of fracture initiation. To assess the accuracy of our stress calculations, we computed the stresses on free surface ($z=0$) of a cracked homogeneous elastic body; these stresses agreed remarkably well with the stress distributions for the corner singularity case presented in Fig. 4 of Benthem (1977).

We begin by examining the stresses on the bonding plane ($y=0$, or $\varphi=\pi$) corresponding to the largest eigenvalue of an elastic body (with $\nu=0.3$) bonded to a rigid substrate. Figure 8(a) shows the behavior of the normal stresses along a line at unit distance ($x=1$) ahead of the crack front. The curves of $(\cos\theta)^s\hat{\sigma}(\theta,\varphi)$ versus θ depict the variation of the normalized stresses as distance from the free surface is increased. For example, $\theta=0$ deg, 45 deg, and 63.4 deg, correspond to points at distances $z=0$, 1, and 2 on the line $x=-1$. Every stress component is scaled by the same normalization factor; the latter follows immediately from the way the displacements are scaled. Recall that the displacements are rendered definite by requiring the maximum displacement component on the unit sphere to equal unity. The stresses are calculated from these displacements by setting the Young's modulus equal to 100; therefore the numbers are the percentages of Young's modulus.

Of course, any multiple of the stresses shown is also an acceptable distribution. It can be seen that the normal stresses decrease rapidly as the distance away from the free surface is increased.

Since the substrate is rigid, $\epsilon_{xx}=\epsilon_{zz}=0$ on the bonding plane $y=0$. Using Hooke's law, it can easily be shown that $\sigma_{xx}=\sigma_{zz}$ and $\sigma_{yy}=\sigma_{zz}(1-\nu)/\nu$. For $\nu=0.3$ this gives $\sigma_{yy}=(7/3)\sigma_{zz}$. That these conditions are fulfilled can be seen in Figs. 8(a) and 9(a). At the free surface ($\theta=0$), σ_{zz} must vanish. It follows that σ_{xx} and σ_{yy} must also vanish at the free surface, i.e. σ_{zz}, σ_{xx}, σ_{yy}, $\to 0$ as $\theta\to 0$. It is clear that such details near the free edge are not resolved by the meshes employed in our calculations. The behavior of the shear stresses corresponding to the strongest singularity is shown in Fig. 8(b). The stresses decrease slowly as the distance away from the free surface increases; this pattern contrasts sharply from that of the normal stresses (compare Figs. 8(a), and 8(b)). At $\theta=0$, σ_{yz} must vanish; this detail is not reproduced by the calculations[1].

The behavior of the normal and shear stresses corresponding to the weaker singularity are shown in Figs. 9(a) and 9(b), respectively. The normal stresses increase as the distance moves away from the free surface; this pattern stands in contrast to that seen in Fig. 8(a). The magnitude of the dominant shear stress decreases as the distance from the surface is increased.

[1]It should be noted that the corner bimaterial interface crack involves two singularity lines: The crack front is one-line singularity, the intersection of the interface with the free surface—i.e., the negative z-axis—is the other line singularity.

Downloaded 03 May 2010 to 171.66.16.247. Redistribution subject to ASME license or copyright; see http://www.asme.org/terms/Terms_Use.cfm

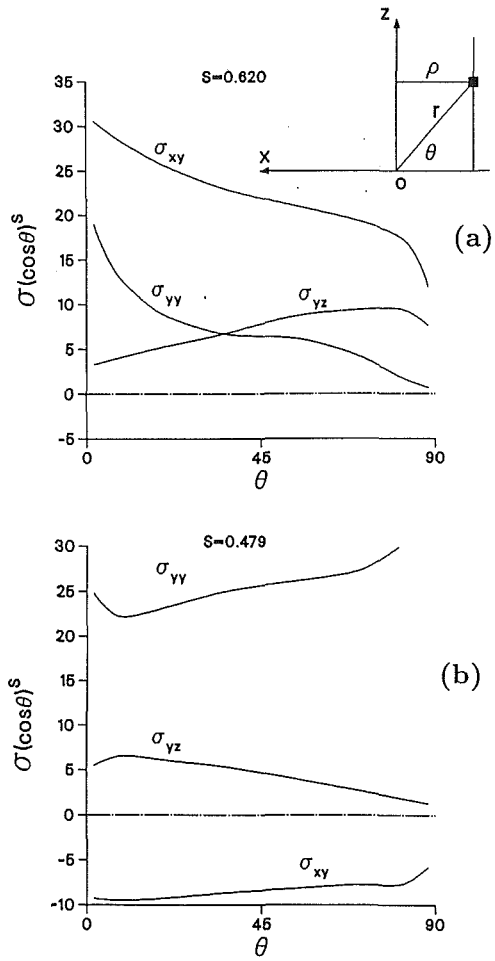

Fig. 10 Dissimilar elastic bodies, $\nu_1 = 0.2$, $\nu_2 = 0.4$, and $\mu_1/\mu_2 = 3$. Behavior of tractions at the bonding plane at unit distance ahead of the crack front; (*a*) larger eigenvalue, (*b*) weaker eigenvalue.

Two dissimilar elastic bodies characterized by $\nu_1 = 0.2$, $\nu_2 = 0.4$ and $\mu_1/\mu_2 = 3$ are considered next. For this material pair, $\beta = 0$ and the plane-strain singularity along this crack from is nonoscillatory. The behavior of the interfacial tractions corresponding to the stronger singularity is shown in Fig. 10(*a*). Here the stresses are computed from the appropriately scaled displacements by setting $E_2 = 100$; therefore the numbers are percentages of Young's modulus E_2. It can be seen that the shear traction σ_{xy} is the dominant component. The interfacial transactions for the weaker singularity are shown in Fig. 10(*b*). In this case, the normal traction dominates.

4 Discussion

For every realistic material pair that we have considered the leading two eigenvalues of the corner singularity are real, and the associated stress states are strongly singular. Lessening the mismatch of the elastic moduli has a mitigating effect on the severity of the singularity. The stress state associated with the larger eigenvalue is nearly antisymmetric and is more singular than $1/\sqrt{r}$.

On the other hand, the state associated with the smaller eigenvalue is nearly symmetric and can be slightly stronger or weaker than $1/\sqrt{r}$. In this regard, it is pertinent to raise the question as to which mode dominates the fields near the vertex, defined as intersection of the crack front with the free surface.

As $r \to 0$, the antisymmetric mode (associated with the larger eigenvalue) must dominate the crack-tip state. However, this is not necessarily the case if a finite distance comparable to a relevant microstructural length is considered, since the amplitude factors of the stronger and weaker singularities can have rather different values. To make this point, consider an example in which the amplitude of the weaker singularity K_S (the subscript S identifies the associated eigenfunction as dominated by the symmetric mode) is considerably larger than the amplitude of the stronger singularity K_A (the subscript A identifies the associated eigenfunction as dominated by the antisymmetric mode). Then it is possible that at a relevant microstructural distance from the vertex, the stresses associated with the weaker singularity are larger than those associated with the stronger singularity.

To develop our argument, a length scale must be introduced. First consider s is complex, and let $s = a + ib$. It is helpful to write the stresses in the following form:

$$\tilde{\sigma}(r,\theta,\varphi) = \frac{1}{r^a}\Big[\,\mathrm{Im}\{Kr^{ib}\}\tilde{\sigma}^A(\theta,\varphi;s) + \mathrm{Re}\{Kr^{ib}\}\tilde{\sigma}^S(\theta,\varphi;s)\Big] \quad \text{for } r << L \tag{6}$$

where $K = K_S + iK_A$ and K_S and K_A are the stress concentration factors which depend on the crack geometry and linearly on the applied loads, and $\tilde{\sigma}^S$ and $\tilde{\sigma}^A$ are the universal dimensionless angular functions which depend on s. L is a characteristic crack dimension which is the shortest of the uncracked ligament thickness or width, crack length, film (layer) thickness, or the distance between the vertex and the point of load application. Note that $|r^{ib}| = 1$. It is convenient to require the components $\tilde{\sigma}^S_{yy}(\theta = 0, \varphi = \pi)$ and $\tilde{\sigma}^A_{xy}(\theta = 0, \varphi = \pi)$ to equal unity, since the stress concentration factors are then uniquely defined. (Note that this is different from the normalization used in the Figs. 8–10, but is inconsequential to this discussion.) Similarly, the near-tip displacement has the form,

$$\mathbf{u}(r,\theta,\varphi) = \mathbf{u}^0 + r^{1-a}\Big[\,C_A\mathrm{Im}\{Kr^{-ib}\}\,\tilde{\mathbf{u}}^A(\theta,\varphi;s) + C_S\mathrm{Re}\{Kr^{-ib}\}\tilde{\mathbf{u}}^S(\theta,\varphi;s)\Big] \quad \text{for } r << L \tag{7}$$

where C_A and C_S are coefficients which depend on the moduli of the material pair, and $\tilde{\mathbf{u}}^A$ and $\tilde{\mathbf{u}}^s$ are the universal dimensionless angular functions which depend on s, and $\mathbf{u}^0$ are rigid body motions. The displacements $\mathbf{u}$ involve all three displacement components.

We have noted that s is almost always real for many material pairs of interest. For real s, the fields take the form,

$$\sigma(r,\theta,\sigma) \approx \frac{K_A}{r^{s_1}}\tilde{\sigma}^A(\theta,\varphi;s_1) + \frac{K_S}{r^{s_2}}\tilde{\sigma}^S(\theta,\varphi;s_2) \text{ for } r << L \tag{8}$$

$$\mathbf{u}(r,\theta,\varphi) \approx \mathbf{u}^0 + C_A K_A r^{1-s_1}\tilde{\mathbf{u}}^A(\theta,\varphi;s_1) + C_S K_S r^{1-s_2}\tilde{\mathbf{u}}^S(\theta,\varphi;s_2) \text{ for } r \ll L, \tag{9}$$

where $s_1 > s_2$. The angular functions $\tilde{\mathbf{u}}^A$ and $\tilde{\mathbf{u}}^S$ for one material pair are shown in Fig. 3; the displacement jumps across the crack faces are shown in Fig. 4. These displacement angular functions are scaled by requiring the maximum displacement component on the unit sphere, $r = 1$, to equal unity. It may be noted that form in (8) is similar to the form in (2) which pertains to a homogeneous material.

As an example calculation, we consider the first material pair in Table 2, namely, copper bonded to alumina for which $s_1 = 0.651$ and $s_2 = 0.467$. Along the radial line defined by $\theta = 0$ and $\varphi = \pi$,

$$\sigma_{xy} \approx \frac{K_A}{r^{s_1}}, \qquad \sigma_{yy} \approx \frac{K_S}{r^{s_2}}.$$

Suppose that $K_A = 0.1\sigma^\infty L^{s_1}$ and $K_S = \sigma^\infty L^{s_2}$ where σ^∞ is the magnitude of the remotely applied stress and L is the characteristic geometric length. At the microstructural distance $\hat{L}$ from the vertex, the stresses are

$$\sigma_{xy} \approx 0.1\sigma^\infty\left(\frac{L}{\hat{L}}\right)^{s_1}, \quad \sigma_{yy} \approx \sigma^\infty\left(\frac{L}{\hat{L}}\right)^{s_2}.$$

Downloaded 03 May 2010 to 171.66.16.247. Redistribution subject to ASME license or copyright; see http://www.asme.org/terms/Terms_Use.cfm

Further suppose that L is 1cm, and the relevant microstructural distance, $\hat{L}$, is 10μm. Then the ratio of the shear to normal transactions across the interface is $0.1 \times 1000^{0.651}/1000^{0.467} = 0.36$. Thus, the normal traction across the interface at distance $\hat{L}$ is larger than the shear traction. The example demonstrates that the question as to which eigenvalue or mode controls the fields near the vertex can only be addressed through analysis taking into account the actual crack geometry, the applied loads and a relevant microstructural length of the material pair[2]. This notwithstanding, it is a fair assumption the interface crack is subject to mixed-mode loading that in a typical situation produce $K_A L^{-s_1}$ that is comparable to $K_S L^{-s_2}$. For these cases, the antisymmetric mode dominates the stress field near the vertex.

The matching of the fields of the three-dimensional corner singularity to the interior two-dimensional fields remains a difficult issue. Recall that the leading two eigenvalues of the three-dimensional corner singularity are generally real. In contrast, the leading eigenvalue of the interior two-dimensional singularity is complex so that the interior singularity is oscillatory (e.g., Rice, 1988). The different nature of the asymptotic fields does not permit a direct application of matching procedures for estimating the zone of dominance of corner singularities. This difficulty can be avoided by considering material pairs where the second Dundurs' parameter β vanishes and for which the interior fields possess the usual $1/\sqrt{r}$ singularity.

Nakamura and Parks (1989) have examined the dominance of the antisymmetric and symmetric corner singularities of a homogeneous material and have shown by detailed finite element calculations that these corner singularity fields adequately characterizes the state in a region bounded by a spherical radius of about $0.03L$ measured from the vertex. The latter estimate should also be applicable to the corner singularity of a bimaterial in which the mismatch of elastic moduli is not overly severe. Finally, we note that plastic flow in one material or both materials can relieve the high stresses and thus change the nature of the three-dimensional corner fields.

Liechti and Chai (1990) have extensively tested strips of polymer bonded to a ceramic substrate using a special experimental setup which allows them to control the mode mixity of the interior plane-strain crack-tip fields. For tests in which the near-tip states have a strong asymmetric component, they observed that the crack front leads at the free surface (i.e., the reverse of the thumbnail profile). Their observations can be interpreted by our results. We have shown that the antisymmetric part of the three-dimensional singularity near the free edge is considerably stronger than the $1/\sqrt{r}$ singularity of the two-dimensional interior field. The mixed-mode loading of the above tests induces a large value of K_A (the amplitude of the antisymmetric part of the three-dimensional field) so that the stresses near the vertex are considerably larger than those within the interior; therefore, the crack front at the free edge can be expected to lead. We have not investigated how the order of the corner singularity depends on the angle of intersection between the crack-front tangent and the free surface. However, a crack-front shape, which is concave in the direction of propagation (as has been measured by Liechti and Chai, 1990), could be consistent with a $1/\sqrt{r}$ field everywhere along the crack front.

[2]The shear stress σ_{xy} (scaled by K_A) is a maximum at $\theta = 0$ (see Fig. 10(a)), whereas the normal stresses σ_{yy} (scaled by K_S) is a maximum at a finite distance away from the free surface σ_{yy} (see Fig. 10(b)). Furthermore, a typical interface can usually support larger shear tractions than normal tractions. Thus, the issue is more involved than that given above.

Acknowledgments

This investigation is supported by the Office of Naval Research through ONR Grant "Mechanics of Interfacial Fracture." The computations were carried out at the Computational Mechanics Research Facility within the Division of Engineering of Brown University.

Notes

Since the preparation of this manuscript, Nakamura (1990) has completed out a fairly thorough three-dimensional finite element analysis of a crack bimaterial plate. For $\beta = 0$, he showed that the zone of dominance of the corner singularity is smaller than one percent of the plate thickness. More importantly, he found that the stress state near the vertex region is strongly mixed mode.

References

Barsoum, R. S., 1990, "Asymptotic Fields at Interfaces Using the Finite Element Iterative Method," *Computers and Structures*, Vol. 35, pp. 285–292.

Barsoum, R. S., and Chen, T. K., 1990, "Three Dimensional Surface Singularity of an Interface Crack," *International Journal of Fracture*, to appear.

Bazant, Z. P., and Estenssoro, L. F., 1979, "Surface Singularity and Crack Propagation," *International Journal of Solids and Structures*, Vol. 15, pp. 405–426. (See also erratum, 1983, Vol. 19, p. 661).

Benthem, J. P., 1977, "State of Stress at the Vertex of a Quarter-Infinite Crack in a Half-Space," *International Journal of Solids and Structures*, Vol. 13, pp. 479–492.

Cottrell, A. H., 1981, *The Mechanical Properties of Matter*, Robert E. Krieger Publishing Company, Huntington, New York.

Dundurs, J., 1969, "Edge-Bonded Dissimilar Orthogonal Elastic Wedges Under Normal and Shear Loading," ASME Journal of Applied Mechanics, Vol. 36, pp. 650–652.

Ghahremani, F., 1991, "A Numerical Variational Method for Extracting 3D Singularities," *International Journal of Solids and Structures*, Vol. 27, pp. 1371–1386.

Liechti, K. M., and Chai, Y.-S., 1990, "Three Dimensional Effects in Interfacial Crack Growth," *Mechanics USA 1990, Proceedings of the 11th US National Congress of Applied Mechanics*, pp. 271–275.

Nakamura, T., 1991, "Three-Dimensional Stress Fields of Elastic Interface Cracks," ASME Journal of Applied Mechanics, Vol. 58, pp. 939–946.

Nakamura, T., and Parks, D. M., 1989, "Antisymmetrical 3-D Stress Field Near the Crack Front at a Thin Elastic Plate," *International Journal of Solids and Structures*, Vol. 25, pp. 1411–1426.

Rice, J. R., 1988, "Elastic Fracture Mechanics Concepts for Interfacial Cracks," ASME Journal of Applied Mechanics, Vol. 55, pp. 98–103.

Rice, J. R., Suo, Z., and Wang, J. S., 1990, "Mechanics and Thermodynamics of Brittle Interfacial Failure in Bimaterial Systems," *Metal-Ceramic Interfaces* (Acta-Scripta Metallurgica Proceedings Series), Vol. 4, pp. 269–294.

Suga, T., Elssner, E., and Schmauder, S., 1988, "Composite Parameters and Mechanical Compatibility of Material Joints," *Journal of Composite Materials*, Vol. 22, pp. 917–934.

Downloaded 03 May 2010 to 171.66.16.247. Redistribution subject to ASME license or copyright; see http://www.asme.org/terms/Terms_Use.cfm

Static Axisymmetric End Problems in Semi-infinite and Finite Solid Cylinders

Yoon Young Kim
Assistant Professor,
Department of Mechanical Design and Production Engineering,
Seoul National University,
Seoul, Korea
Assoc. Mem. ASME

Charles R. Steele
Professor,
Division of Applied Mechanics,
Stanford University,
Stanford, CA 94305
Fellow ASME.

Our earlier technique for a semi-infinite strip (Kim and Steele, 1990) is extended to study general end problems and corner singularities for semi-infinite and finite solid cylinders with free walls. For handling general end conditions, we expand the displacement and stress in term of the Dini series which are the solutions of the cylinders with mixed wall conditions. The relation between the harmonic coefficients of the end displacement and stress is then formed, which we call the end stiffness matrix. One advantage of the end stiffness matrix approach is that the procedure for finite cylinders can be easily built up from that of semi-infinite cylinders. For some end conditions which may yield singular stresses, the nature of the singularity is investigated by the asymptotic analysis of the Dini series coefficients of the stresses. The problems studied by Benthem and Minderhoud (1972) and Robert and Keer (1987) are solved with the present approach.

1 Introduction

The boundary value problem in a linear isotropic elastic solid cylinder with a traction-free lateral surface has been studied by numerous investigators over last few decades due to various practical applications in engineering. However, it appears that unified approaches applicable for both general end problems and corner singularities, with potential extensions to cylinders with axial multiple layers, have not been proposed.

Available approaches[1] for general end conditions include those by Fama (1972), Little and Childs (1967), Power and Childs (1971), Gerhardt and Cheng (1981), Mayes (1983), and Robert and Keer (1987). These approaches, which utilize the bi-orthogonality or optimal weighting functions, are most efficient for smooth end conditions, not for rapidly varying end conditions.

To analyze singular stress fields near the corner of a finite cylinder, Robert and Keer (1987) use the technique of Benthem and Minderhoud (1972) who suggested the use of a function describing the corner singularity. As pointed out by these authors, their approach does not guarantee the convergence of the solution due to the overcompleteness of the expansion sets. Gupta (1974) formulates an integral equation to analyze the corner singularity, but his formulation appears to involve substantial numerical work.

Recently, we have presented for semi-infinite strips an approach different from those mentioned earlier (Kim and Steele, 1990). As its natural extension to cylinders, either semi-infinite or finite, the first part of the present paper summarizes a systematic solution approach for general end problems of semi-infinite cylinders. The procedure for finite cylinders, with possible extensions to axially multiply-layered cylinders, then follows. In this approach, the displacement and stress are expanded in terms of the Dini series that are the solutions of cylinders with mixed lateral wall conditions. By forming the harmonic coefficient relation of the end displacement and stress, we develop an efficient, numerically stable technique.

Lastly, we focus on a technique to handle the corner singularity. We demonstrate that it is possible to extract the nature of the singularity by the asymptotic analysis of the coefficients of the present complete series expansions of the end stress. Numerical results indicate that this technique virtually suppresses local oscillations of the solutions.

2 Cylinders With Free-Wall Conditions

The general axisymmetric solution for self-equilibrated end conditions in a semi-infinite solid cylinder occupying the region $0 \le r \le 1$ and $0 \le z < \infty$ with a traction-free cylindrical surface can be written as

$$\Psi(r,z) = 2\Re\left[\sum_{p=1}^{\infty} E^p \tilde{\Psi}^p(r)\exp(-\lambda^p z)\right] \tag{1}$$

where

$$[\Psi(r,z),\ \tilde{\Psi}^p(r)] \in \{[u_r,\tilde{u}_r^p(r)],\ [u_z,\tilde{u}_z^p(r)],\ [\sigma_{rz},\tilde{\sigma}_{rz}^p(r)],\ [\sigma_{zz},\tilde{\sigma}_{zz}^p(r)],\ [\sigma_{rr},\ \tilde{\sigma}_{rr}^p(r)][\sigma_{\theta\theta},\tilde{\sigma}_{\theta\theta}^p(r)]\}.$$

[1] For the survey of the existing techniques and the limitations of those, refer to Benthem and Minderhoud (1972) and Gerhardt and Cheng (1981), for instance.

Contributed by the Applied Mechanics Division of THE AMERICAN SOCIETY OF MECHANICAL ENGINEERS for presentation at the Winter Annual Meeting, Atlanta, Ga., Dec. 1-6, 1991.

Discussion on this paper should be addressed to the Technical Editor, Prof. Leon M. Keer, The Technological Institute, Northwestern University, Evanston, IL 60208, and will be accepted until two months after final publication of the paper itself in the JOURNAL OF APPLIED MECHANICS. Manuscript received by the ASME Applied Mechanics Division, June 29, 1989; final revision, Oct. 16, 1990.
Paper No. 91-WA/APM-13.

Copyright © 1992 by ASME
Downloaded 03 May 2010 to 171.66.16.247. Redistribution subject to ASME license or copyright; see http://www.asme.org/terms/Terms_Use.cfm

The stress σ_{ij} and displacement u_i are referred to $2G$, twice the shear modulus and a, the radius of the cylinder, respectively, and the dimensionless radial and axial coordinates r and z are normalized by a. The complex-valued expansion coefficient E in Eq. (1) is to be determined from end conditions. The equation for the eigenvalues λ^p and the components of the eigenfunctions are given in terms of the Bessel functions. (See, e.g., Robert and Keer, 1987.) Note that in (1), the eigenvalues with positive real and imaginary parts are only used.

The bi-orthogonality relation of the eigenfunction is written (Fama, 1972; Gregory, 1983), which will be frequently utilized in the present analysis:

$$\int_0^1 [\tilde{\sigma}^p_{zz}(r)\tilde{u}^q_z(r) - \tilde{u}^p_r(r)\tilde{\sigma}^q_{rz}(r)]rdr = 0 \quad \text{for} \quad \lambda^p \neq \lambda^q \tag{2}$$

and for $\lambda^p = \lambda^q$ we define

$$D^p = \int_0^1 [\tilde{\sigma}^p_{zz}(r)\tilde{u}^p_z(r) - \tilde{u}^p_r(r)\tilde{\sigma}^p_{rz}(r)]rdr$$
$$= 2(1-\nu)(\lambda^p)^2 J_1^2(\lambda^p)[2J_0(\lambda^p)\{(1-\nu)J_1(\lambda^p) - \lambda^p J_0(\lambda^p)\} - \lambda^p J_1^2(\lambda^p)] \tag{3}$$

where ν is Poisson's ratio and J_n is the Bessel function of the first kind of order n. This bi-orthogonality is most useful for mixed end conditions ($z = 0$) for which the expansion coefficients are easily determined as:

$$E^p = \int_0^1 [\sigma_{zz}(r,0)\tilde{u}^p_z(r) - u_r(r,0)\tilde{\sigma}^p_{rz}(r)]rdr/D^p \tag{4a}$$

or

$$E^p = \int_0^1 [\tilde{\sigma}^p_{zz}(r)u_z(r,0) - \tilde{u}^p_r(r)\sigma_{rz}(r,0)]rdr/D^p. \tag{4b}$$

3 Special Mixed Lateral Wall Conditions

Kim (1989) shows that special mixed cylindrical surface conditions lead to uncoupled wave motion between dilation and shear in a cylinder. We use exactly the same wall conditions to find simple solutions which will provide asymptotic solutions to the end problems of cylinders with free walls.

For a semi-infinite solid cylinder with the following wall conditions

$$u_r|_{r=1} = 0; \quad \sigma_{rz}|_{r=1} = 0 \tag{5}$$

$$\sigma_{rr}|_{r=1} + u_r|_{r=1} = 0; \quad u_z|_{r=1} = 0, \tag{6}$$

we can obtain the simple series solutions

$$u_r(r) = \sum_{i=1}^{\infty} J_1(\xi_i r)[A_i - 2(1-\nu)B_i + B_i\xi_i z]\exp(-\xi_i z)$$

$$u_z(r) = \sum_{i=0}^{\infty} J_0(\xi_i r)[A_i + (1-2\nu)B_i + B_i\xi_i z]\exp(-\xi_i z)$$

$$\sigma_{rz}(r) = -\sum_{i=1}^{\infty} \xi_i J_1(\xi_i r)(A_i - B_i + B_i\xi_i z)\exp(-\xi_i z)$$

$$\sigma_{zz}(r) = -\sum_{i=0}^{\infty} \xi_i J_0(\xi_i r)(A_i + B_i\xi_i z)\exp(-\xi_i z) \tag{7}$$

where A and B are unknowns. If ξ's are zeros of $J'_0(\xi)[\xi \equiv \beta]$, the solution (7) satisfies (5), and if ξ's are zeros of $J_0(\xi)$ or equivalently zeros of $J_1(\xi) + \xi J'_1(\xi)[\xi \equiv \gamma]$, (7) satisfies (6).

If we rewrite (7) as

$$u_r(r,z) = \sum_{i=1}^{\infty} \frac{U_i(z)}{\tau_i} J_1(\xi_i r)$$

$$u_z(r,z) = \sum_{i=0}^{\infty} \frac{W_i(z)}{\tau_i} J_0(\xi_i r) \tag{8a,b}$$

$$\sigma_{rz}(r,z) = \sum_{i=1}^{\infty} \frac{R_i(z)}{\tau_i} J_1(\xi_i r)$$

$$\sigma_{zz}(r,z) = \sum_{i=0}^{\infty} \frac{Z_i(z)}{\tau_i} J_0(\xi_i r), \tag{8c,d}$$

with

$$\tau_i = \left(\frac{J_0^2(\beta_i)}{2}\right)^{1/2} (\equiv \tau_i^\beta) \text{ for } \xi = \beta$$
$$\tau_i = \left(\frac{J_1^2(\gamma_i)}{2}\right)^{1/2} (\equiv \tau_i^\gamma) \text{ for } \xi = \gamma,$$

the series coefficients W_i, etc., can be determined from the orthogonality of the Dini series. (See, e.g., Watson, 1966.)

Particularly at the end ($z = 0$), we introduce a matrix $\mathbf{K}$, which we call the end stiffness matrix:

$$\begin{Bmatrix} \mathbf{Z}(0) \\ \mathbf{R}(0) \end{Bmatrix} = [\mathbf{K}] \begin{Bmatrix} \mathbf{W}(0) \\ \mathbf{U}(0) \end{Bmatrix} = \begin{bmatrix} \mathbf{K11} & \mathbf{K12} \\ \mathbf{K21} & \mathbf{K22} \end{bmatrix} \begin{Bmatrix} \mathbf{W}(0) \\ \mathbf{U}(0) \end{Bmatrix},$$

in which we define[2]

$$\mathbf{W}(z) = \begin{Bmatrix} W_1(z) \\ W_2(z) \\ \vdots \end{Bmatrix}; \quad \mathbf{U}(z) = \begin{Bmatrix} U_1(z) \\ U_2(z) \\ \vdots \end{Bmatrix}$$

$$\mathbf{Z}(z) = \begin{Bmatrix} Z_1(z) \\ Z_2(z) \\ \vdots \end{Bmatrix}; \quad \mathbf{R}(z) = \begin{Bmatrix} R_1(z) \\ R_2(z) \\ \vdots \end{Bmatrix}.$$

The only nonzero components in $\mathbf{K}$ are easily shown to be

$$\mathbf{K11}_{i,i} = \mathbf{K22}_{i,i} = \frac{-(2-2\nu)\xi_i}{3-4\nu}$$

$$\mathbf{K12}_{i,i} = \mathbf{K21}_{i,i} = \frac{-(1-2\nu)\xi_i}{3-4\nu}.$$

4 Semi-Infinite Cylinder

The end stiffness matrix approach, proposed by Kim and Steele (1990), will be employed here as an effective means to solve static boundary value problems in a cylinder with the traction-free cylindrical condition. A systematic summary of the procedure is presented in this section.

First, we expand the eigenfunctions in terms of the series solutions (7):

$$\tilde{u}^p_r(r) = \sum_{i=1}^{n_h} \frac{U^p_i}{\tau^\gamma_i} J_1(\gamma_i r); \quad \tilde{u}^p_z(r) = \sum_{i=0}^{n_h} \frac{W^p_i}{\tau^\beta_i} J_0(\beta_i r) \tag{9a,b}$$

$$\tilde{\sigma}^p_{rz}(r) = \sum_{i=1}^{n_h} \frac{R^p_i}{\tau^\gamma_i} J_1(\gamma_i r); \quad \tilde{\sigma}^p_{zz}(r) = \sum_{i=0}^{n_h} \frac{Z^p_i}{\tau^\beta_i} J_0(\beta_i r), \tag{9c,d}$$

where n_h is the highest term in the series expansion. The definition of W^p_i in (9), for instance, is

$$W^p_i = \frac{1}{\tau^\beta_i} \int_0^1 J_0(\beta_i r)\tilde{u}^p_z(r)rdr. \tag{10}$$

[2]Since the nondecaying solution uncouples with the decaying solution in a semi-infinite cylinder, we neglect $W_0(z)$ and $Z_0(z)$ in the definition of $\mathbf{W}(z)$ and $\mathbf{Z}(z)$.

Downloaded 03 May 2010 to 171.66.16.247. Redistribution subject to ASME license or copyright; see http://www.asme.org/terms/Terms_Use.cfm

The closed-form expressions of U_i^p, W_i^p, R_i^p, and Z_i^p are possible using the orthogonality of the Dini series, some formulas containing the Bessel functions (Watson, 1966), and the formula (which apparently has not been previously been given explicitly)

$$a(a^2-b^2)\int_0^1 J_{n+1}(ar)J_n(br)r^2dr$$
$$= -\left\{n+\frac{2a^2}{a^2-b^2}\right\}\{aJ_n(b)J_n'(a)-bJ_n(a)J_n'(b)\}$$
$$+\{(n^2-a^2)J_n(a)J_n(b)-abJ_n'(a)J_n'(b)\}\Big] \quad (\text{for } a\neq b).$$

It is easily seen that Z_0^p is identically zero. We remark that the series used in (9) do allow nonzero values at $r = 1$ due to the use of two sets of parameters, β (zeros of J_1) and γ (zeros of J_0).

The next step is to construct the end stiffness matrix **S** of the cylinder with the free wall:

$$\begin{Bmatrix}\mathbf{Z}(0)\\ \mathbf{R}(0)\end{Bmatrix}=[\mathbf{S}]\begin{Bmatrix}\mathbf{W}(0)\\ \mathbf{U}(0)\end{Bmatrix}=\begin{bmatrix}\mathbf{S11} & \mathbf{S12}\\ \mathbf{S21} & \mathbf{S22}\end{bmatrix}\begin{Bmatrix}\mathbf{W}(0)\\ \mathbf{U}(0)\end{Bmatrix}. \tag{11}$$

To this end, we compute **A11** and **B22** defined in

$$\begin{Bmatrix}\mathbf{W}(0)\\ \mathbf{R}(0)\end{Bmatrix}=\begin{bmatrix}\mathbf{A11} & \mathbf{A12}\\ \mathbf{A21} & \mathbf{A22}\end{bmatrix}\begin{Bmatrix}\mathbf{Z}(0)\\ \mathbf{U}(0)\end{Bmatrix};$$
$$\begin{Bmatrix}\mathbf{Z}(0)\\ \mathbf{U}(0)\end{Bmatrix}=\begin{bmatrix}\mathbf{B11} & \mathbf{B12}\\ \mathbf{B21} & \mathbf{B22}\end{bmatrix}\begin{Bmatrix}\mathbf{W}(0)\\ \mathbf{R}(0)\end{Bmatrix}.$$

Using the bi-orthogonality (2)–(4) and the expansions (9), we obtain

$$\mathbf{A11}_{i,j}=\sum_{p=1}^{n_e}\frac{W_i^pW_j^p}{D^p};\quad \mathbf{B22}_{i,j}=\sum_{p=1}^{n_e}\frac{U_i^pU_j^p}{D^p}$$

where n_e is the number of the exact eigenfunctions to be used in the analysis. The expressions for the symmetric submatrices **S11** and **S22** are simply

$$\mathbf{S11}=\mathbf{A11}^{-1};\ \mathbf{S22}=\mathbf{B22}^{-1},$$

and will compute **S12** and **S21** later when necessary. Unless the right scale factors τ^γ and τ^β were used in (9), **S11** and **S22** would not be symmetric.

It should be mentioned that **S11** and **S22** are asymptotically equivalent to **K11** and **K22** for large harmonic indices. As indicated by Kim and Steele (1990) in a strip problem, the asymptotic behavior of **S11** and **S22** can be utilized to reduce substantially the amount of numerical computation. This behavior is also useful in the matrix inversion of **A11** and **B22** due to the strongly diagonal nature of the matrices. (See Kim and Steele (1990) for more discussion.)

Now we proceed to solve the boundary value problem. When a displacement end condition [**W**(0), **U**(0)] is given at $z = 0$, we split it into two sets of end conditions, [**W**(0) $\neq$ **0**, **U**(0) = **0**] and [**W**(0) = **0**, **U**(0) $\neq$ **0**].

For the first set of the end conditions, we compute **Z**(0) using only **S11**. Then we apply the bi-orthogonality condition (4*b*) to determine the expansion coefficients E^p from **U**(0) = **0** and **Z**(0) just computed:

$$D^pE^p=\int_0^1[\sigma_{zz}(r,z=0)\tilde{u}_z^p(r)-\underbrace{u_r(r,z=0)}_{=0}\tilde{\sigma}_{rz}^p(r)]rdr$$
$$=\int_0^1\sum_{i=1}^{n_h}\frac{Z_i(0)}{\tau_i^\beta}J_0(\beta_ir)\tilde{u}_z^p(r)rdr$$
$$=\sum_{i=1}^{n_h}Z_i(0)W_i^p$$
$$=\sum_{i=1}^{n_h}\left[\sum_{j=1}^{n_h}\mathbf{S11}_{i,j}W_j(0)\right]W_i^p.$$

In the expression above, we used Eq. (8*d*) for the second line, the definition (10) of W_i^p for the third line, and Eq. (11) with **U**(0) = **0** for the last line. By repeating the same procedure for the second set, the complete expression for E^p is then provided by

$$D^pE^p=\sum_{i=1}^{n_h}\left[\sum_{j=1}^{n_h}\mathbf{S11}_{i,j}W_j(0)\right]W_i^p-\sum_{i=1}^{n_h}\left[\sum_{j=1}^{n_h}\mathbf{S22}_{i,j}U_j(0)\right]U_i^p.$$

Since E^p has been determined, we can now express the series coefficients $U_i(z)$:

$$U_i(z)=\sum_{p=1}^{n_e}E^p\exp(-\lambda^pz)U_i^p, \tag{12}$$

and $W_i(z)$, $R_i(z)$, and $Z_i(z)$ are similarly obtained. To obtain $U_i(z)$, we used

$$u_r(r,z)=\sum_{p=1}^{n_c}E^p\exp(-\lambda^pz)\tilde{u}_r^p(r)$$
$$=\sum_{i=1}^{n_h}\sum_{p=1}^{n_e}E^p\exp(-\lambda^pz)U_i^p\frac{J_1(\gamma_ir)}{\tau_i^\gamma}.$$

It may be also useful to relate directly the series coefficients of the stress and displacement at any z with the end conditions at $z = 0$ by the elimination of E^p in (12). This approach, which will be utilized in finite cylinders, leads to the introduction of two matrices **DM**(z), and **FM**(z) such that

$$\begin{Bmatrix}\mathbf{W}(z)\\ \mathbf{U}(z)\end{Bmatrix}=[\mathbf{DM}(z)]\begin{Bmatrix}\mathbf{W}(0)\\ \mathbf{U}(0)\end{Bmatrix}$$
$$=\begin{bmatrix}\mathbf{DM11}(z) & \mathbf{DM12}(z)\\ \mathbf{DM21}(z) & \mathbf{DM22}(z)\end{bmatrix}\begin{Bmatrix}\mathbf{W}(0)\\ \mathbf{U}(0)\end{Bmatrix}$$
$$\begin{Bmatrix}\mathbf{Z}(z)\\ \mathbf{R}(z)\end{Bmatrix}=[\mathbf{FM}(z)]\begin{Bmatrix}\mathbf{W}(0)\\ \mathbf{U}(0)\end{Bmatrix}$$
$$=\begin{bmatrix}\mathbf{FM11}(z) & \mathbf{FM12}(z)\\ \mathbf{FM21}(z) & \mathbf{FM22}(z)\end{bmatrix}\begin{Bmatrix}\mathbf{W}(0)\\ \mathbf{U}(0)\end{Bmatrix}$$

where

$$\mathbf{DM11}_{i,j}(z)=\sum_{p=1}^{n_e}\frac{\exp(-\lambda^pz)}{D^p}W_i^p\left(\sum_{m=1}^{n_h}\mathbf{S11}_{m,j}W_m^p\right)$$
$$\mathbf{DM21}_{i,j}(z)=\sum_{p=1}^{n_e}\frac{\exp(-\lambda^pz)}{D^p}U_i^p\left(\sum_{m=1}^{n_h}\mathbf{S11}_{m,j}W_m^p\right)$$
$$\mathbf{DM12}_{i,j}(z)=\sum_{p=1}^{n_e}\frac{\exp(-\lambda^pz)}{D^p}W_i^p\left(-\sum_{m=1}^{n_h}\mathbf{S22}_{m,j}U_m^p\right)$$
$$\mathbf{DM22}_{i,j}(z)=\sum_{p=1}^{n_e}\frac{\exp(-\lambda^pz)}{D^p}U_i^p\left(-\sum_{m=1}^{n_h}\mathbf{S22}_{m,j}U_m^p\right)$$
$$\mathbf{FM11}_{i,j}(z)=\sum_{p=1}^{n_e}\frac{\exp(-\lambda^pz)}{D^p}Z_i^p\left(\sum_{m=1}^{n_h}\mathbf{S11}_{m,j}W_m^p\right)$$
$$\mathbf{FM21}_{i,j}(z)=\sum_{p=1}^{n_e}\frac{\exp(-\lambda^pz)}{D^p}R_i^p\left(\sum_{m=1}^{n_h}\mathbf{S11}_{m,j}W_m^p\right)$$
$$\mathbf{FM12}_{i,j}(z)=\sum_{p=1}^{n_e}\frac{\exp(-\lambda^pz)}{D^p}Z_i^p\left(-\sum_{m=1}^{n_h}\mathbf{S22}_{m,j}U_m^p\right)$$
$$\mathbf{FM22}_{i,j}(z)=\sum_{p=1}^{n_e}\frac{\exp(-\lambda^pz)}{D^p}R_i^p\left(-\sum_{m=1}^{n_h}\mathbf{S22}_{m,j}U_m^p\right).$$

Downloaded 03 May 2010 to 171.66.16.247. Redistribution subject to ASME license or copyright; see http://www.asme.org/terms/Terms_Use.cfm

At $z = 0$, we can see that $\mathbf{DM}(0) = \mathbf{I}$, and $\mathbf{FM}(0) = \mathbf{S}$. Before we discuss the procedure for finite cylinders, we point out that although the end-effect solutions do produce constant axial displacement at $z = 0$, the displacement can be neglected in the analysis for semi-infinite cylinders. However, we do consider this displacement in a finite cylinder since nonzero relative constant axial displacement of one end to another produces stresses.

5 Finite Cylinder

One advantage of the present stiffness matrix approach is that the solution procedure for a finite cylinder can be easily formulated once the technique handling a semi-infinite cylinder is developed. Furthermore, the approach for a cylinder with axially varying material properties (and/or possibly different radii) can be established.

In this section we discuss a procedure of superposing the solutions of two semi-infinite cylinders in which the previously constructed $\mathbf{DM}(z)$ and $\mathbf{FM}(z)$ for a semi-infinite cylinder are used. Since only self-equilibrated solutions are worked out for semi-infinite cylinders, uniform solutions (nondecaying) also need to be taken into account for a finite cylinder.

Assuming that the finite cylinder occupies the region defined by $0 \le z \le d$ and $0 \le r \le 1$, we can write the general solutions for any z in terms of the expansion coefficients

$$\mathbf{D}(z) = \mathbf{DM}^+(z)\mathbf{D}^+ + \mathbf{DM}^-(z)\mathbf{D}^-$$
$$\mathbf{F}(z) = \mathbf{FM}^+(z)\mathbf{D}^+ + \mathbf{FM}^-(z)\mathbf{D}^- \qquad (13)$$

with

$$\mathbf{DM}^{\pm} = \begin{bmatrix} \mathbf{DM11}^{+} & \mathbf{DM12}^{\pm} \\ (0{:}n_h \times 0{:}n_h) & (0{:}n_h \times n_h) \\ \mathbf{DM21}^{\pm} & \mathbf{DM22}^{\pm} \\ (n_h \times 0{:}n_h) & (n_h \times n_h) \end{bmatrix}; \quad \mathbf{FM}^{\pm} = \begin{bmatrix} \mathbf{FM11}^{\pm} & \mathbf{FM12}^{\pm} \\ (0{:}n_h \times 0{:}n_h) & (0{:}n_h \times n_h) \\ \mathbf{FM21}^{\pm} & \mathbf{FM22}^{\pm} \\ (n_h \times 0{:}n_h) & (n_h \times n_h) \end{bmatrix}.$$

The size of the submatrices in $\mathbf{DM}^{\pm}$ and $\mathbf{FM}^{\pm}$ is so adjusted to take into account the non-decaying solutions. In (13), we introduce

$$\mathbf{D}(z) \equiv \{\mathbf{W}(z), \mathbf{U}(z)\}^T; \quad \mathbf{F}(z) \equiv \{\mathbf{Z}(z), \mathbf{R}(z)\}^T,$$

and $W_0(z)$ and $Z_0(z)$ are included in the definition of $\mathbf{W}(z)$ and $\mathbf{Z}(z)$ for the finite cylinder. We also introduce $\mathbf{D}^+$ and $\mathbf{D}^-$ such that

$$\mathbf{D}^+ \equiv \begin{Bmatrix} C^+ \\ W_1^+ \\ W_2^+ \\ \vdots \\ W_{n_h}^+ \\ U_1^+ \\ U_2^+ \\ \vdots \\ U_{n_h}^+ \end{Bmatrix}; \quad \mathbf{D}^- \equiv \begin{Bmatrix} C^- \\ W_1^- \\ W_2^- \\ \vdots \\ W_{n_h}^- \\ U_1^- \\ U_2^- \\ \vdots \\ U_{n_h}^- \end{Bmatrix}.$$

Physically, $\{W_1^+, W_2^+, \ldots W_{n_h}^+\}^T$ and $\{U_1^+, U_2^+, \ldots U_{n_h}^+\}^T$ represent the series coefficients of the end condition at $z = 0$ in a semi-infinite cylinder ($z \ge 0$) associated with end-effect solutions.[3] The constant C^+ is associated with a uniform solution:

$$u_r(r,z) = -\frac{C^+\nu}{1+\nu} r; \quad u_z(r,z) = \frac{C^+}{1+\nu} z$$
$$\sigma_{zz}(r,z) = C^+; \quad \sigma_{rr}(r,z) = \sigma_{rz}(r,z) = 0.$$

[3] The same interpretation is applied to quantities with the superscript $^-$.

Once $\mathbf{D}^+$ and $\mathbf{D}^-$ are known, we apply the procedure for semi-infinite cylinders to obtain decaying parts of solutions and add nondecaying solutions associated with C^+ and C^- to get the total solution.

The nonzero elements of submatrices of $\mathbf{DM}^+$ and $\mathbf{FM}^+$ can be shown to be for $i, j \ge 1$:

$$\mathbf{DMIJ}_{i,j}^{+} = \mathbf{DMIJ}_{i,j}, \ \mathbf{FMIJ}_{i,j}^{+} = \mathbf{FMIJ}_{i,j} \text{ for } \mathbf{I},\mathbf{J} = 1,2$$

and

$$\mathbf{DM11}_{0,j}^{+} = \mathbf{DM11}_{0,j}, \ \mathbf{DM11}_{0,0}^{+} = \frac{z}{\sqrt{2}(1+\nu)}$$
$$\mathbf{DM12}_{0,j}^{+} = \mathbf{DM12}_{0,j}, \ \mathbf{DM21}_{i,0}^{+} = -\frac{\nu}{1+\nu}\frac{(-1)^{i+1}2^{3/2}}{\gamma_i^2}$$
$$\mathbf{FM11}_{0,0}^{+} = \frac{1}{\sqrt{2}}.$$

Since it can be shown that

$$\mathbf{DM}(z)^- = \begin{bmatrix} -\mathbf{DM11}^+(d-z) & -\mathbf{DM12}^+(d-z) \\ \mathbf{DM21}^+(d-z) & \mathbf{DM22}^+(d-z) \end{bmatrix}$$
$$\mathbf{FM}(z)^- = \begin{bmatrix} \mathbf{FM11}^+(d-z) & \mathbf{FM12}^+(d-z) \\ -\mathbf{FM21}^+(d-z) & -\mathbf{FM22}^+(d-z), \end{bmatrix}$$

substantial savings in computation are apparent.

If the displacements at the ends are prescribed, for example, the unknown constants $\mathbf{D}^{\pm}$ can be computed directly from

$$\mathbf{D}(0) = \mathbf{DM}^+(0)\mathbf{D}^+ + \mathbf{DM}^-(0)\mathbf{D}^-$$
$$\mathbf{D}(d) = \mathbf{DM}^+(d)\mathbf{D}^+ + \mathbf{DM}^-(d)\mathbf{D}^-.$$

An alternative procedure is the serial calculation procedure (see e.g., Steele, 1989), which is related to invariant imbedding (see, e.g., Casti and Kalaba, 1973). This procedure, very useful for cylinders with piecewise axial variations of material properties, needs the stiffness matrix $\mathbf{S}_d$ such that

$$\mathbf{F}(d) = \mathbf{S}^d\mathbf{D}(d) + \mathbf{F}_p^d$$

with

$$\mathbf{S}_d = \mathbf{FM}^+(d)\mathbf{H}_d + \mathbf{FM}^-(d)\mathbf{G}_d$$
$$\mathbf{F}_d = [\mathbf{FM}^+(d)\mathbf{H}_0 + \mathbf{FM}^-(d)\mathbf{G}_0]\mathbf{D}(0),$$

and

$$\mathbf{G}_d = [\mathbf{I} - \mathbf{DM}^+(d)\mathbf{DM}^-(0)]^{-1}; \quad \mathbf{G}_0 = -\mathbf{G}_d\mathbf{DM}^+(d)$$
$$\mathbf{H}_d = -\mathbf{DM}^-(0)\mathbf{G}_d; \quad \mathbf{H}_0 = \mathbf{I} - \mathbf{DM}^-(0)\mathbf{G}_0.$$

Refer to Steele (1989) for the complete description and applications of the serial calculation procedure.

6 Asymptotic Analysis of Corner Singularity

In this section, we extend our earlier technique of handling the corner singularity in strips (Kim and Steele, 1990) to that of solid cylinders. The singular stress fields are typical in cracks and clamped-free corners.

The essence of the present technique is to extract the nature of singularities from the series coefficients discussed earlier by means of the asymptotic analysis. For the subsequent analysis, we assume that near $r = 1$

$$\sigma_{rz} \sim c_r(1-r)^{-\rho}; \quad \sigma_{zz} \sim c_z(1-r)^{-\rho},$$

where ρ and (c_r, c_z) are called the order and strength of the singularity. Benthem and Minderhoud (1972) present analytic solutions for ρ and c_z/c_r for the clamped-free corners.

First, consider the expansion

$$h(r) = \sum_{m=1}^{\infty} \frac{h_m}{\tau_m^{\gamma}} J_1(\gamma_m r) \quad \text{for} \quad 0 < r < 1 \qquad (14)$$

where

Downloaded 03 May 2010 to 171.66.16.247. Redistribution subject to ASME license or copyright; see http://www.asme.org/terms/Terms_Use.cfm

Table 1 Order and strength of shear stress σ_{rz} at the corner

	$n_h = 10$	$n_h = 20$	$n_h = 40$	$n_h = 80$	Benthem and Minderhoud (1972)
ρ	−0.0426	0.136	0.220	0.251	0.255 (Exact)
c_r	−2.74	0.456	0.194	0.144	0.138

Table 2 Order and strength of normal stress σ_{zz} at the corner

	$n_y = 10$	$n_h = 20$	$n_h = 40$	$n_h = 80$	Benthem and Minderhoud (1972)
ρ	0.464	0.352	0.298	0.274	0.255 (Exact)
c_z	−0.115	−0.241	−0.364	−0.451	−0.537

Table 3 Strength of corner singularity using exact order

	$n_h = 10$	$n_h = 20$	$n_h = 40$	$n_h = 80$	Benthem and Minderhoud (1972)
c_r	0.172	0.148	0.141	0.138	0.138
c_z	−0.462	−0.507	−0.529	−0.538	−0.537

$$h(r) = c[(1-r)^{-\rho} - 1] \quad \text{with} \quad 0 < \rho < 1. \tag{15}$$

The asymptotic form of the coefficient h_m can be written as (see Appendix)

$$h_m \sim \sqrt{\frac{\pi}{2}} c \left[\frac{(-1)^{m+1}\Gamma(1-\rho)\sin\frac{\pi\rho}{2}}{\gamma_m^{\frac{5}{2}-\rho}} \right]. \tag{16}$$

Now we propose the following operations $h_m^{(1)}$ and $h_m^{(2)}$ such that

$$h_m^{(1)} \equiv \gamma_m^3 h_m - \gamma_{m-1}^3 h_{m-1}, \tag{17}$$

$$h_m^{(2)} \equiv \frac{h_m^{(1)}}{h_{m-1}^{(1)}}. \tag{18}$$

For large m,

$$\rho \sim -\frac{1}{2} - \frac{(4m-5)(1+h_m^{(2)})}{2(1-h_m^{(2)})},$$

$$c \sim \sqrt{\frac{\pi}{2}} \frac{(-1)^{m+1} h_m^{(1)}}{\Gamma(1-\rho)(\gamma_m^{\rho+1/2} + \gamma_{m-1}^{\rho+1/2})\sin\frac{\rho\pi}{2}}.$$

By utilizing the foregoing asymptotic analysis, it is possible to split a series expansion into a smooth part and a singular part of the type (15) (if any). Consequently, for an expansion

$$f(r) = \sum_{m=1}^{\infty} \frac{f_m}{\tau_m^{\gamma}} J_1(\gamma_m r),$$

we can approximate $f(r)$ as

$$f(r) \approx \sum_{m=1}^{\infty} \frac{f_m - h_m}{\tau_m^{\gamma}} J_1(\gamma_m r) + c[(1-r)^{-\rho} - 1]. \tag{19}$$

Similarly, we can also estimate the order ρ and strength c of the singularity from the expansion

$$h(r) = \sum_{m=1}^{\infty} \frac{h_m}{\tau_m^{\beta}} J_0(\beta_m r) \quad \text{for} \quad 0 < r < 1$$

where

$$h(r) = c\left[(1-r)^{-\rho} - \frac{1}{(1-\rho)(2-\rho)} \right].$$

Using the operations given in (17) and (18) with γ_m replaced by β_m, it can be shown

$$\rho \sim -\frac{1}{2} - \frac{(4m-3)(1+h_m^{(2)})}{2(1-h_m^{(2)})},$$

$$c \sim \sqrt{\frac{\pi}{2}} \frac{(-1)^{m} h_m^{(1)}}{\Gamma(1-\rho)(\beta_m^{\rho+1/2} + \beta_{m-1}^{\rho+1/2})\sin\frac{\rho\pi}{2}}.$$

7 Numerical Examples

As a numerical example, consider the problem studied by Benthem and Minderhoud (1972) for $\nu = 0.25$

$$\sigma_{zz} = -1, \quad \sigma_{rz} = 0 \quad \text{at} \quad z = \infty$$
$$u_z = 0, \quad u_r = 0 \quad \text{at} \quad z = 0$$
$$\sigma_{rz} = 0, \quad \sigma_{rr} = 0 \quad \text{at} \quad r = 1.$$

Using the present method for a semi-infinite cylinder (the non-decaying part of the solution is trivial), we can obtain the results shown in Tables 1 and 2 for the strength c_r of $\sigma_{rz}|_{z=0}$ and c_z of $\sigma_{zz}|_{z=0}$ near the corner ($r = 1$, $z = 0$).[4] Although we know the order ρ of singularity by analytical means for the present problem ($\rho = 0.255$), we try to extract ρ in addition to the strength of singularity—see Tables 1 and 2.

As may be anticipated, the use of the exact order improves substantially the rate of convergence. In Table 3, only the strength is extracted while the exact order ρ is used rather than estimated from the analysis.

Tables 1 through 3 indicate that converging solutions are obtained as n_h, the number of the expansion terms, increases. More accurate results were obtained for the shear stress than for the normal stress. The reason, explained in the earlier paper (Kim and Steele, 1990), is that the present stiffness matrix approach yields a very accurate **FM22**(0) = **S22** with good asymptotic behavior, but a less accurate **FM12**(0) = **S12** without any asymptotic behavior. This is related to the fact that for the construction of **S12**, two sets of expansion parameters γ and β are combined.

It is apparent from Table 3 that the use of the known order of the singularity accelerates substantially the convergence of the solutions. The purpose of presenting the results in Tables 1, 2 is to demonstrate that the present technique is potentially useful even when the order of the singularity is not known or difficult to determine analytically.

As the next example, consider the finite cylinder with the prescribed end displacements worked out by Robert and Keer (1987). The end conditions are

$$u_r(r,0) = -\alpha r; \quad u_z(r,0) = \delta$$
$$u_r(r,d) = \alpha r; \quad u_z(r,d) = -\delta$$

where α = 8E-3, δ = 2E-2, and d = 1.2. Following the procedure described in Sections 5–6 yields the results shown in Table 4 for the strength of the corner singularities.

Figure 1 compares the present results with the results by Robert and Keer (1987) for the shear and normal stresses at $z = 0$ and $z = d$. The present results, which are obtained after

[4] For stepwise procedures, see Kim and Steele (1990).

Downloaded 03 May 2010 to 171.66.16.247. Redistribution subject to ASME license or copyright; see http://www.asme.org/terms/Terms_Use.cfm

Table 4 Strength of corner singularity using exact order

	$n_h = 10$	$n_h = 20$	$n_h = 40$	$n_h = 80$	Robert and Keer (1987)
$c_r\|_{z=0}$	0.0146	0.0132	0.0128	0.0128	0.0128
$c_z\|_{z=0}$	−0.0341	−0.0372	−0.0385	−0.0389	−0.0384
$c_r\|_{z=d}$	−0.00239	−0.00245	−0.00255	−0.00262	−0.00253
$c_z\|_{z=d}$	−0.00735	−0.00801	−0.00813	−0.00808	−0.00762

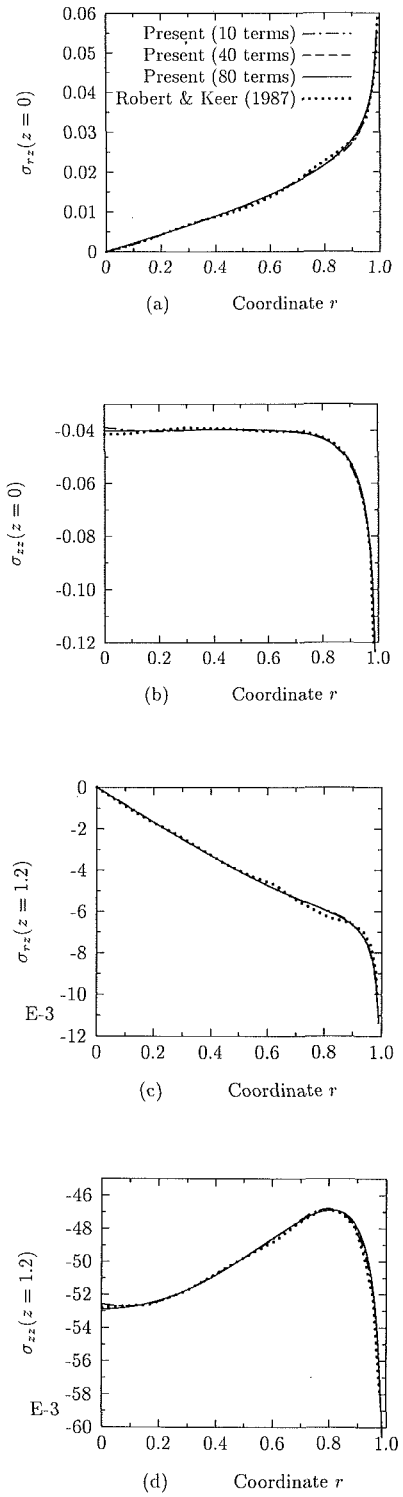

Fig. 1 The stress in a traction-free finite cylinder. The present results obtained with n_h = 10 (dashed), n_h = 40 (long-dashed) and n_h = 80 (solid) are compared with the results (thick solid) by Robert and Keer (1987); for (*a*) shear stress at $z=0$, (*b*) normal stress at $z=0$, (*c*) shear stress at $z=1.2$, (*d*) normal stress at $z=1.2$

applying the technique described in Section 6[5], converge very rapidly. However, the results by Robert and Keer (1987) exhibit somewhat unexpected local variation which appears due to the insufficient number of unknowns. In their approach, the number of unknowns was limited because of the overcompleteness of the expansion sets. Figure 1 also indicates that good curves can be obtained with only few terms.

8 Conclusions

An effective alternative to solve end problems and handle corner singularities is presented for semi-infinite and finite cylinders with traction-free lateral walls. It was demonstrated that the present approach effectively handles end problems. The corner singularity was also effectively treated by means of the present procedure based on the asymptotic analysis. The procedure, which virtually suppress local oscillations, yielded converging results. It was found that only few terms are required for good curves of the stress distributions.

References

Benthem, J. P., and Minderhoud, P., 1972, "The Problem of the Solid Cylinder Compressed between Rough Rigid Stamps," Vol. 8, pp. 1027–1042.

Bleistein, N., and Handelsman, R. A., 1986, *Asymptotic Expansions of Integrals*, Dover Publications, New York.

Casti, J., and Kalaba, R., 1973, *Imbedding Methods in Applied Mathematics*, Addison-Wesley Pub. Co., Reading.

Erdélyi, A., 1956, *Asymptotic Expansions*, Dover Publications, New York.

Fama, M. E. D., 1972, "Radial Eigenfunctions for the Elastic Circular Cylinder," *Quart. J. Mech. Appl. Mech.*, Vol. 15, pp. 479–495.

Gerhardt, T. D., and Cheng, S., 1981, "A Diagonally Dominant Solution for the Cylinder End Problem," ASME JOURNAL OF APPLIED MECHANICS, Vol. 48, pp. 876–880.

Gregory, R. D., 1983, "A Note on Bi-Orthogonality Relations for Elastic Cylinders of General Cross Section," *J. Elasticity*, Vol. 13, pp. 351–355.

Gupta, G. D., 1974, "The Analysis of the Semi-Infinite Cylinder Problem," *Int. J. Solids Structures*, Vol. 10, pp. 137–148.

Kim, Y. Y., 1989, "Uncoupled Wave Systems and Dispersion in an Infinite Solid Cylinder," ASME JOURNAL OF APPLIED MECHANICS, Vol. 56, pp. 347–355.

Kim, Y. Y., and Steele, C. R., 1990, "Modification of Series Expansions for General End Conditions and Corner Singularities on the Semi-Infinite Strip," ASME JOURNAL OF APPLIED MECHANICS, Vol. 57, pp. 581–588.

Little, R. W. M., and Childs, S. B., 1967, "Elastostatic Boundary Region Problem in Solid Cylinders," *Quart. J. Appl. Mech.*, Vol. 25, pp. 261–274.

Mayes, P. J. D., 1983, "End Stress Calculations on Elastic Cylinders," *Int. J. Solids Structures*, Vol. 19, pp. 895–906.

Power, L. D., and Childs, S. B., 1971, "Axisymmetric Stresses and Displacements in a Finite Circular Bar," *Int. J. Eng. Sci.*, Vol. 9, pp. 241–255.

Robert, M., and Keer, L. M., 1987, "An Elastic Circular Cylinder with Displacement Prescribed at the Ends-Axially Symmetric Case," *Quart. J. Mech. Appl. Mech.*, Vol. 40, pp. 339–363.

Steele, C. R., 1989, *Theory of Thin Shells* (Lecture Notes), Stanford University.

Watson, G. N., 1966, *A Treatise on the Theory of Bessel Functions*, Cambridge University Press.

APPENDIX

An asymptotic expansion of the integral

$$L(k)=\int_0^1 J_\nu(kx)x(1-x)^{\lambda-1}dx \quad 0<\lambda\le 1$$

will be derived for large k in this Appendix. To facilitate the derivation, we utilize the neutralizer η (see Erdélyi, 1956) defined as

$$\frac{d^n\eta(x)}{dx^n}=0 \quad \text{at } x=0,1 \quad \text{for } n=1, 2, \ldots$$

$$\eta(0)=1, \quad \eta(1)=0,$$

and rewrite $L(k)$ as

[5]Kim and Steele (1990) demonstrate that local oscillations are virtually suppresed by the step similar to (19).

Downloaded 03 May 2010 to 171.66.16.247. Redistribution subject to ASME license or copyright; see http://www.asme.org/terms/Terms_Use.cfm

$$L(k)=\int_0^1 J_\nu(kx)x(1-x)^{\lambda-1}\eta(x)dx$$

$$+\int_0^1 J_\nu(kx)x(1-x)^{\lambda-1}[1-\eta(x)]dx\equiv L_1(k)+L_2(k).$$

Note that the contributions of the end points $x = 0$ and $x = 1$ to the integral $L(k)$ are represented by $L_1(k)$ and $L_2(k)$, respectively.

For the asymptotic expansion of $L_1(k)$, we expand $x(1 - x)^{\lambda-1}$ in a Taylor series at $x = 0$ and rewrite $L_1(k)$ as:

$$L_1(k)=\int_0^1 h(x)\eta(x)dx$$

with the definition

$$h(x)=J_\nu(kx)\left[\sum_{m=0}^{\infty}\frac{\Gamma(m+1-\lambda)}{\Gamma(m+1)\Gamma(1-\lambda)}x^{m+1}\right].$$

Integrating $L_1(k)$ by parts yields

$$L_1(k)=[h_{-1}(x)\eta(x)]_0^1-\int_0^1 h_{-1}(x)\eta_1(x)dx$$

$$=-h_{-1}(0)-\int_0^1 h_{-1}(x)\eta_1(x)dx,$$

where we define

$$\eta_1(x)=\frac{d\eta(x)}{dx},$$

$$h_{-1}(t)=\int_c^t h(x)dx \quad (c=\text{any constant})$$

$$=\int_\infty^t h(x)dx \quad (\text{choosing } c=\infty).$$

To evaluate

$$h_{-1}(0)=\int_\infty^0 J_\nu(kx)\sum_{m=0}^{\infty}\frac{\Gamma(m+1-\lambda)}{\Gamma(m+1)\Gamma(1-\lambda)}x^{m+1}dx,$$

we use the expression (Bleistein and Handelsman, 1986)

$$\int_0^\infty x^\mu J_\nu(kx)dx=\frac{2^\mu\Gamma\left(\frac{1+\mu+\nu}{2}\right)}{k^{\mu+1}\Gamma\left(\frac{1-\mu+\nu}{2}\right)}.$$

Although the strip of analyticity of the integral given above is limited by $-\nu - 1 < \mu < 1/2$, Bleistein and Handelsman (1986) show that the expression can be analytically continued beyond the strip of analyticity. Since $\eta(x)$ may be such a function that makes $\int_0^1 h_{-1}(x)\eta_1(x)dx$ vanishingly small, the asymptotic expansions of $L_1(k)$ can be given by

$$L_1(k)\sim\sum_{m=0,1,2,\ldots}^{\infty}\frac{\Gamma(m+1-\lambda)}{2\Gamma(m+1)\Gamma(1-\lambda)}\times\frac{\Gamma\left(\frac{2+m+\nu}{2}\right)}{\Gamma\left(\frac{\nu-m}{2}\right)}\left(\frac{k}{2}\right)^{-m-2}.$$

For the asymptotic expansion of $L_2(k)$ for *real* k, first we note that

$$L_2(k)=\Re\int_0^1 H_\nu^{(1)}(kx)x(1-x)^{\lambda-1}[1-\eta(x)]dx,$$

where $H_\nu^{(1)}$ is the Hankel function of the first kind.

Using the asymptotic expansion of the Hankel function (Watson, 1966)[6] and integrating by parts, we express L_2 as

$$L_2(k)=\Re\int_0^1 g(x)[1-\eta(x)]dx$$

$$=\Re\left[g_{-1}(1)+\int_0^1 g_{-1}(x)\eta_1(x)dx\right],$$

with the definition

$$g(x)=\left(\frac{2}{\pi}\right)^{\frac{1}{2}}\exp\left[-i\left(kx-\frac{\nu\pi}{2}-\frac{\pi}{4}\right)\right]\times\sum_{m=0}^{\infty}\frac{(\nu,m)}{(-2i)^m}(kx)^{-m-\frac{1}{2}}x(1-x)^{\lambda-1},$$

$$(\nu,m)=\frac{\Gamma(\nu+m+1/2)}{\Gamma(m+1)\Gamma(\nu-m+1/2)}.$$

As before, the contribution of $\int_0^1 g_{-1}(x)\eta_1(x)dx$ can be made negligible. The expression of $g_{-1}(t)$ is given by

$$g_{-1}(t)=\int_c^t g(x)dx \quad (c=\text{any constant})$$

$$=\int_\infty^t g(x)dx \quad (c=\infty)$$

$$=\int_{t+i\infty}^t g(x)dx. \tag{A1}$$

Note that the Cauchy's integral theorem is used to obtain (A1).

To obtain the asymptotic expansion of $g_{-1}(1)$, we change the variables from x to σ such that

$$x=1+i\sigma,$$

[6]The asymptotic expansion of the Hankel function is valid on $-\pi < \arg(kx) < 2\pi$.

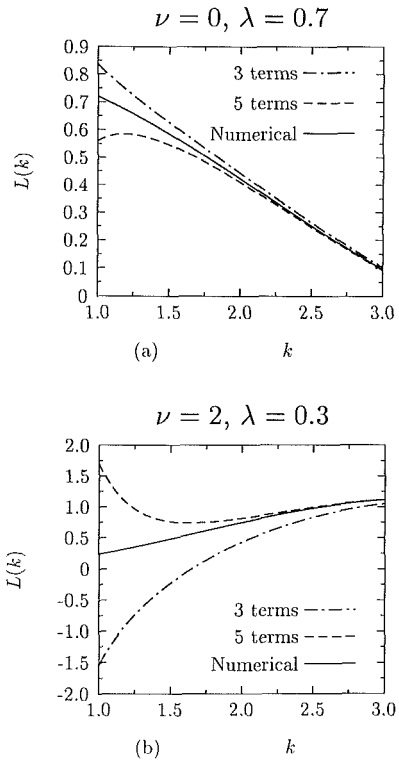

Fig. 2 The three-term and five-term asymptotic expansions of the integral $L(k) = \int_0^1 J_\nu(kx)x(1 - x)^{\lambda-1}dx$ are compared with the results from direct numerical integration for (a) $\nu = 0$, $\lambda = 0.7$ and (b) $\nu = 2$, $\lambda = 0.3$

Downloaded 03 May 2010 to 171.66.16.247. Redistribution subject to ASME license or copyright; see http://www.asme.org/terms/Terms_Use.cfm

expand $g(1 + i\sigma)$ at $\sigma = 0$, and integrate term by term. The result is

$$L_2(k) \sim \left(\frac{2}{\pi}\right)^{1/2} \sum_{l=0}^{\infty} \sum_{m=0}^{\infty} \frac{\Gamma(\lambda+l)}{\Gamma(l+1)} \frac{(\nu,m)}{2^m} \frac{\Gamma\left(m+\frac{1}{2}+l\right)}{\Gamma\left(m+\frac{1}{2}\right)} \times [\cos\varphi_{l,m} k^{-(\lambda+1/2+l+m)} + \sin\varphi_{l,m} k^{-(\lambda+3/2+l+m)}]$$

where

$$\varphi_{l,m} = \varphi - \frac{(l-m)\pi}{2}; \quad \varphi = k - \frac{\nu\pi}{2} - \frac{\pi}{4} - \frac{\lambda\pi}{2}.$$

The first few terms in the asymptotic expressions of $L_1(k)$ and $L_2(k)$ are given explicitly:

$$L_1(k) \sim \nu k^{-2} + (1-\lambda)(\nu^2-1)k^{-3} + \frac{(2-\lambda)(1-\lambda)\nu(\nu^2-4)}{2} k^{-4},$$

$$L_2(k) \sim \left(\frac{2}{\pi}\right)^{1/2} \Gamma(\lambda) \left[\cos\varphi k^{-(\lambda+1/2)} - \sin\varphi \frac{4\nu^2-1+4\lambda}{8} k^{-(\lambda+3/2)} - \cos\varphi \frac{(4\nu^2-1)(4\nu^2-9)-8\lambda(4\nu^2-1)-16\lambda(\lambda+1)}{128} k^{-(\lambda+5/2)} \right]$$

In Fig. 2, we compare the three-term and five-term expansions with the value from direct numerical integration for varying k. The results for ($\nu = 0$, $\lambda = 0.7$) and ($\nu = 2$, $\lambda = 0.3$) are shown in Fig. 2(*a*) and Fig. 2(*b*), respectively. The comparison confirms that the expansion is valid for moderate values of ν as k becomes large.

Downloaded 03 May 2010 to 171.66.16.247. Redistribution subject to ASME license or copyright; see http://www.asme.org/terms/Terms_Use.cfm

Norio Hasebe
Department of Civil Engineering,
Nagoya Institute of Technology,
Gokisocho, Showaku, Nagoya 466, Japan

Mikiya Okumura
Tokyu Construction Co., Ltd.,
Sibuya 1-16-14, Sibuyaku,
Tokyo 150, Japan

Takuji Nakamura
Department of Civil Engineering,
Nagoya Institute of Technology
Gokisocho, Showaku, Nagoya 466, Japan

Bonded Bi-material Half-Planes With Semi-elliptical Notch Under Tension Along the Interface

A problem of two bonded, dissimilar half-planes containing an elliptical hole on the interface is solved. The external load is uniform tension parallel to the interface. A rational mapping function and complex stress functions are used and an analytical solution is obtained. Stress distributions are shown. Stress concentration factors are also obtained for arbitrary lengths of debonding and for several material constants. In addition, an approximate expression of the stress concentration factor is given for elliptical holes and the accuracy is investigated.

Introduction

Dissimilar material interfaces can be found in many materials and structural bonds such as composite materials, welded parts, inclusions in matrix, bond between metallic and ceramic materials, and so forth. Many researchers have turned their attention to the mechanical behavior of this interface. In particular, problems of two bonded dissimilar materials have been mostly analyzed as a basic model. The research of cracks on and near the interface were summarized by Sih (1972), Cherepanov (1979), Sih and Chen (1981), and Murakami et al. (1987). The study of interfacial crack was described by Rice (1988).

The problems of bonded dissimilar materials have been analyzed with many methods such as an expansion of eigenfunction (Williams, 1959; Rice and Sih, 1965), an analytic solution of complex stress function which is reduced to a Riemann-Hilbert problem (Erdogan, 1963, 1965; England, 1965), an expansion of Fourier series for displacements (Chou and Hirth, 1970), and the weight function method (Sham and Bueckner, 1988). For a solution for a singular integral equation many numerical methods have been used: Erdogan's method (1978) for singular integral equation obtained by Fourier transformation (Erdogan and Guputa, 1971), Mellin transformation (Hein and Erdogan, 1971; Cook and Erdogan, 1972); a collocation method (Sawyer and Anderson, 1972); the superposition of a semi-infinite strip and a half-plane (Bogy, 1975), and an expansion in Tchebycheff's polynomial of an infinitesimal dislocation (Tamate and Iwasaka, 1976). Furthermore, many numerical procedures have been developed such as a finite element method (Lin and Mar, 1976), the body force method (Isida and Noguchi, 1983), the finite element method of conservation integral (Yau and Wang, 1984), and the boundary element method using the Hetényi and Dundurs (1962) basic solution (Yuuki et al., 1987).

Problems of two bonded dissimilar half-planes containing partial flaws on and near the interface and subjected to uniform tension parallel to the interface at infinity were analyzed by Rice and Sih (1965), Erdogan (1972), Erdogan and Biricikoglu (1973), Goree and Venezia (1977a,b), Piva and Viola (1980), Viola and Piva (1981), Isida and Noguchi (1983), Chen (1986), and Shih and Asaro (1988). However, the analysis for an elliptical hole on the interface seems to have not been carried out.

The primary purpose of the present paper is to derive the complex stress functions by using a rational mapping function of a sum of fractional expressions. Since the mapping function is expressed as a generalized form, the stress function for a different shape is given by changing the coefficients of the mapping function. Therefore, the analysis for relatively arbitrary shapes becomes possible. Complex stress functions are obtained as a closed form. Using the stress functions, the stress distributions, the stress concentration factors, stress intensity factors at the crack tip, the complex stress intensity factors, and the energy release rates for the interfacial crack can be easily obtained. Moreover, any length of the interfacial crack can be obtained by changing coordinates of the tip of the interface. Secondly, using the stress functions, a problem of an infinite plane bonded by two half-planes with semi-elliptical notches is analyzed. The external force is uniform tension parallel to the interface. In the problem of bonded dissimilar materials, the analysis of strength for interfacial crack is an important subject. However, the defect on the interface is not only a crack but also a circular or elliptical hole. One extreme limit of the elliptical hole is a crack penetrating through the interface. In the present paper, the stress distributions and the stress concentration factors for an elliptical hole are calculated. The elliptical hole with the interfacial crack at either or both

Contributed by the Applied Mechanics Division of THE AMERICAN SOCIETY OF MECHANICAL ENGINEERS for publication in the JOURNAL OF APPLIED MECHANICS.

Discussion on this paper should be addressed to the Technical Editor, Prof. Leon M. Keer, The Technological Institute, Northwestern University, Evanston, IL 60208, and will be accepted until two months after final publication of the paper itself in the JOURNAL OF APPLIED MECHANICS. Manuscript received by the ASME Applied Mechanics Division, Sept. 21, 1989; final revision, Aug. 20, 1990.

Copyright © 1992 by ASME
Downloaded 03 May 2010 to 171.66.16.247. Redistribution subject to ASME license or copyright; see http://www.asme.org/terms/Terms_Use.cfm

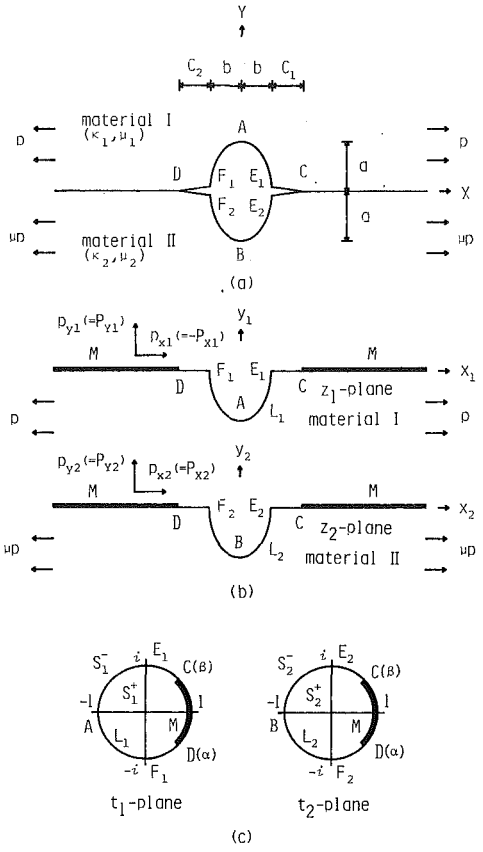

Fig. 1 *(a)* **An elliptic hole with debondings embedded in the interface of bonded bi-material half-planes;** *(b)* **half-plane I with semi-elliptical notch obtained by rotational transformation about the *X*-axis, and half-plane II with semi-elliptical notch;** *(c)* **unit circles for half-planes I and II**

sides is analyzed. An approximate expression of the stress concentration factor is obtained and the accuracy is investigated.

Expressions for Boundary Condition

Two bonded dissimilar half-planes containing an elliptical hole with two debondings (interfacial cracks) of lengths C_1 and C_2 along the interface are considered (see Fig. 1(*a*)). The interface is in the X-axis and coincides with one of the principal axes of the hole. Hence, the shape is symmetric with respect to the X-axis. The half-plane I occupies region $Y \geq 0$, and the half-plane II occupies region $Y \leq 0$. The shape of I is the same as that of II by the rotational transformation about the X-axis (Fig. 1(*b*)). Therefore, the same mapping function can be used to map I and II in Fig. 1(*b*) into the unit circles in t_1 and t_2-planes in Fig. 1(*c*), respectively. Capital letters refer to subscripts of the components of stress or the like in Fig. 1(*a*) and small letters refer to those in Fig. 1(*b*). The boundary of the interface is denoted by M and the boundary conditions are the continuity of stress and displacement. On the boundary shown by L_j ($j = 1, 2$), two components of external force are given on L_1 and L_2, respectively. The points $Z_1 = Z_2$ on M in Fig. 1(*a*) correspond to $t_1 = t_2$ in Fig. 1(*c*). Since the boundary conditions are expressed by the same variable, the distinction of t_1 and t_2 are not required on M. Hereafter, t_j on the boundary is denoted by σ and the relation $\bar{\sigma} = 1/\sigma$ holds since $\sigma = e^{i\epsilon}$. External forces, stresses, and displacements in Figs. 1(*a*) and 1(*b*) are related by

$$P_{X1} = -p_{x1},\ P_{Y1} = p_{y1},\ P_{X2} = p_{x2},\ P_{Y2} = p_{y2}$$
$$\sigma_{X1} = \sigma_{x1},\ \sigma_{Y1} = \sigma_{y1},\ \tau_{XY1} = -\tau_{xy1},$$
$$\sigma_{X2} = \sigma_{x2},\ \sigma_{Y2} = \sigma_{y2},\ \tau_{XY2} = \tau_{xy2},$$
$$U_1 = u_1,\ V_1 = -v_1,\ U_2 = u_2,\ V_2 = v_2. \quad (1)$$

The stress functions for I and II in Fig. 1(*b*), which are expressed by t_j in Fig. 1(*c*), are derived. Components of stress and displacement in Fig. 1(*b*) are given by the stress functions and then components in Fig. 1(*a*) are obtained by Eq. (1).

The mapping function which maps a half-plane with a semi-elliptical notch in Fig. 1(*b*) into the unit circle in Fig. 1(*c*) is expressed as follows:

$$z_j = \frac{E_o}{1-t_j} + \sum_{k=1}^{N} \frac{E_k}{\zeta_k - t_j} + E_c \equiv \omega(t_j) \quad (2)$$

where $N = 24$ is used in the present paper (Hasebe et al., 1988; Hasebe, 1972).

It is convenient to use the Dundurs' constants, α_D and β_D, for the stress analysis (Dundurs, 1967, 1969)

$$\alpha_D = \frac{(\kappa_1+1)\Gamma - (\kappa_2+1)}{(\kappa_1+1)\Gamma + (\kappa_2+1)},\ \beta_D = \frac{(\kappa_1-1)\Gamma - (\kappa_2-1)}{(\kappa_1+1)\Gamma + (\kappa_2+1)},\ \Gamma = \frac{\mu_2}{\mu_1} \quad (3)$$

where μ_j is the shear modulus and $\kappa_j = 3 - 4\nu_j$ for plane strain, and $\kappa_j = (3 - \nu_j)/(1 + \nu_j)$ for generalized plane stress, ν_j being the Poisson's ratio. Desired complex stress functions, $\phi_j(t_j)$ and $\psi_j(t_j)$, are regular in the unit circles in the t_j-plane. Uniform tension at infinity in the x-direction is considered, and then the stress functions are expressed as follows:

$$\phi_j(t_j) = \phi_j^A(t_j) + \phi_j^B(t_j),\ \psi_j(t_j) = \psi_j^A(t_j) + \psi_j^B(t_j) \quad (4)$$

where

$$\phi_1^A(t_1) = \frac{p}{4}\omega(t_1), \quad \psi_1^A(t_1) = -\frac{p}{2}\omega(t_1)$$

$$\phi_2^A(t_2) = \frac{\mu p}{4}\omega(t_2), \quad \psi_2^A(t_2) = -\frac{\mu p}{2}\omega(t_2) \quad (5)$$

and

$$\mu = \frac{\mu_2(\kappa_1+1)}{\mu_1(\kappa_2+1)} = \frac{1+\alpha_D}{1-\alpha_D}. \quad (6)$$

When the uniform tension p applies to I, the uniform tension μp must apply to II to equalize strains ϵ_{x2} with ϵ_{x1} on the interface, where ϵ_{x1} and ϵ_{x2} are strains for I and II in the x-direction, respectively (Rice and Sih, 1965). The functions $\psi_j(t_j)$ are given by analytic continuation for traction-free boundary (Muskhelishvili, 1963),

$$\psi_j(t_j) = -\bar{\phi}_j\left(\frac{1}{t_j}\right) - \frac{\bar{\omega}\left(\frac{1}{t_j}\right)}{\omega'(t_j)}\phi_j'(t_j) \quad (7)$$

Then the boundary conditions for the external force and displacement are expressed by using (7) as follows:

$$\phi_j(\sigma) + \frac{\omega(\sigma)}{\overline{\omega'(\sigma)}}\overline{\phi_j'(\sigma)} + \overline{\psi_j(\sigma)} = \phi_j^+(\sigma) - \phi_j^-(\sigma) = i\int (p_{jx} + ip_{jy})ds \quad (8)$$

$$\frac{1}{\mu_j}\left[\phi_j(\sigma) - \frac{\omega(\sigma)}{\overline{\omega'(\sigma)}}\overline{\phi_j'(\sigma)} - \overline{\psi_j(\sigma)}\right] = \frac{1}{\mu_j}[\kappa_j\phi_j^+(\sigma) + \phi_j^-(\sigma)] = 2(u_j + iv_j) \quad (9)$$

where superscripts $^+$ and $^-$ refer to the values of the function on the boundary as approached from regions S_j^+ and S_j^-, respectively (see Fig. 1(*c*)). If the components of the external force, p_{jx} and p_{jy}, apply to L_j, then the boundary condition is obtained by substituting (4) and (5) into (8)

$$\phi_j^{B+}(\sigma) - \phi_j^{B-}(\sigma) = i\int_{L_j} (p_{jx} + ip_{jy})ds \equiv h_{Lj}(\sigma) \quad (10)$$

where

Downloaded 03 May 2010 to 171.66.16.247. Redistribution subject to ASME license or copyright; see http://www.asme.org/terms/Terms_Use.cfm

$$\phi_j^{A+}(\sigma)=\phi_j^{A-}(\sigma). \tag{11}$$

In the present case, $h_{Lj}(\sigma) = 0$, because $p_{jx} = p_{jy} = 0$ on L_j. The boundary condition on M is expressed by the continuity condition of stress using (1) and (8) as follows:

$$\phi_1^+(\sigma)-\phi_1^-(\sigma)=\overline{\phi_2^+(\sigma)}-\overline{\phi_2^-(\sigma)} \tag{12}$$

and using (1)and (9) for the continuity condition of displacement

$$\frac{1}{\mu_1}[\kappa_1\phi_1^+(\sigma)+\phi_1^-(\sigma)]=\frac{1}{\mu_2}[\kappa_2\overline{\phi_2^+(\sigma)}+\overline{\phi_2^-(\sigma)}]. \tag{13}$$

From (4), (5), (11), (12), and (13), similar conditions can be written as follows:

$$\phi_1^{B+}(\sigma)-\phi_1^{B-}(\sigma)=\overline{\phi_2^{B+}(\sigma)}-\overline{\phi_2^{B-}(\sigma)} \tag{14}$$

$$\frac{1}{\mu_1}[\kappa_1\phi_1^{B+}(\sigma)+\phi_1^{B-}(\sigma)]=\frac{1}{\mu_2}[\kappa_2\overline{\phi_2^{B+}(\sigma)}+\overline{\phi_2^{B-}(\sigma)}]+D_1(\sigma) \tag{15}$$

$$D_1(\sigma)=\frac{p(\kappa_1+1)}{4\mu_1}[\overline{\omega(\sigma)}-\omega(\sigma)] \tag{16}$$

where $D_1(\sigma)$ is the term of displacement due to $\phi^A{}_j(\sigma)$. Since the boundary M is in the x-axis and $\bar{\sigma} = 1/\sigma$ holds,

$$\omega(\sigma)=\overline{\omega(\sigma)}=\bar{\omega}\left(\frac{1}{\sigma}\right). \tag{17}$$

Hence, $D_1(\sigma) = 0$ in the present analysis. Equation (14) is arranged as follows:

$$\left[\phi_1^{B+}(\sigma)+\overline{\phi_2^{B-}\left(\frac{1}{\bar{\sigma}}\right)}\right]-\left[\phi_1^{B-}(\sigma)+\overline{\phi_2^{B+}\left(\frac{1}{\bar{\sigma}}\right)}\right]=0. \tag{18}$$

A general solution of (18) is given by an arbitrary rational function $g_1(t_1)$ (Muskhelishvili, 1963)

$$\phi_1^B(t_1)+\overline{\phi_2^B\left(\frac{1}{\bar{t}_1}\right)}=g_1(t_1). \tag{19}$$

Since $g_1^+(\sigma) = g_1^-(\sigma) \equiv g_1(\sigma)$ on the boundary,

$$\overline{\phi_2^{B+}(\sigma)}=-\phi_1^{B-}(\sigma)+g_1(\sigma)$$

$$\overline{\sigma_2^{B-}(\sigma)}=-\phi_1^{B+}(\sigma)+g_1(\sigma). \tag{20}$$

Substituting (20) into (15) and arranging, the boundary condition on M finally becomes

$$\phi_1^{B+}(\sigma)+\lambda_1\phi_1^{B-}(\sigma)=\gamma_1 g_1(\sigma)+\frac{\mu_2\gamma_1}{\kappa_2+1}D_1(\sigma)\equiv\gamma_1 g_1(\sigma)+h_{M_1}(\sigma) \tag{21}$$

$$\lambda_1=\frac{\kappa_2\mu_1+\mu_2}{\kappa_1\mu_2+\mu_1}=\frac{1-\beta_D}{1+\beta_D},\ \gamma_1=\frac{\mu_1(\kappa_2+1)}{\kappa_1\mu_2+\mu_1}=\frac{1-\alpha_D}{1+\beta_D}. \tag{22}$$

As mentioned previously, the problem of obtaining $\phi_1^B(t_1)$ is reduced to a Riemann-Hilbert problem given by (10) on L_1 and by (21) on M. Similarly, the problem of obtaining $\phi_2^B(t_2)$ is given by interchanging subscripts 1 and 2 in the foregoing process. The coefficients corresponding to (22) are written

$$\lambda_2=\frac{1}{\lambda_1},\ \gamma_2=\frac{\mu_2(\kappa_1+1)}{\kappa_2\mu_1+\mu_2}=\frac{1+\alpha_D}{1-\beta_D}. \tag{23}$$

Derivation of Solution

First, $\phi_1^B(t_1)$ is derived. $g_1(t_1)$ is expressed as a sum of two irregular terms in S_1^- and S_1^+, respectively, i.e.,

$$g_1(t_1)=\sum_n\frac{a_n}{\xi_n-t_1}+\sum_n\frac{b_n}{\eta_n-t_1} \tag{24}$$

where $|\xi_n| > 1$, $|\eta_n| < 1$, and a_n and b_n are undetermined complex constants. Since terms for the poles higher than second order and for the positive power in $g_1(t_1)$ finally become zero, $g_1(t_1)$ is set in the form of (24) (see (38)). A solution of the Riemann-Hilbert problem for (10) and (21) is obtained as follows:

$$\phi_1^B(t_1)=H_1(t_1)+P_1(t_1)\chi_1(t_1)+\frac{\gamma_1\chi_1(t_1)}{2\pi i}\int_M\frac{g_1(\sigma)}{\chi_1(\sigma)(\sigma-t_1)}d\sigma \tag{25}$$

$$H_1(t_1)=\frac{\chi_1(t_1)}{2\pi i}\int_{L_1}\frac{h_{L_1}(\sigma)}{\chi_1(\sigma)(\sigma-t_1)}d\sigma+\frac{\chi_1(t_1)}{2\pi i}\int_M\frac{h_{M_1}(\sigma)}{\chi_1(\sigma)(\sigma-t_1)}d\sigma. \tag{26}$$

In the present analysis, since $h_{L_1}(\sigma) = 0$ and $h_{M_1}(\sigma) = 0$, $H_1(t_1) = 0$—except the integration constants. $P_1(t_1)$ is an arbitrary rational function and $\chi_1(t_1)$ is the Plemelj function as

$$\chi_1(t_1)=(t_1-\alpha)^{m_1}(t_1-\beta)^{1-m_1},\ m_1=0.5+i\frac{\ln\lambda_1}{2\pi}. \tag{27}$$

The coordinates α and β correspond to the junctures D and E of the boundaries M and L_j (see Fig. 1(c)). Since $\chi_1(t_1)$ is a multivalued function, the branch $\chi_1(t_1)/t_1 \to 1$ is chosen for $t_1 \to \infty$. $\chi_1(t_1)$ on the boundary has the relation $\chi_1^+(\sigma) = -\lambda_1\chi_1^-(\sigma)$ on M and $\chi_1^+(\sigma) = \chi_1^-(\sigma)$ on L_1. Using the residue theorem, the integral of the third term in (25) is

$$\frac{\gamma_1\chi_1(t_1)}{2\pi i}\int_M\frac{g_1(\sigma)d\sigma}{\chi_1(\sigma)(\sigma-t_1)}=\frac{\gamma_1\chi_1(t_1)}{(1+\lambda_1)2\pi i}\oint_M\frac{g_1(\sigma)d\sigma}{\chi_1(\sigma)(\sigma-t_1)}=\frac{\gamma_1}{1+\lambda_1}\left\{\sum_n\left[1-\frac{\chi_1(t_1)}{\chi_1(\xi_n)}\right]\frac{a_n}{\xi_n-t_1}+\sum_n\left[1-\frac{\chi_1(t_1)}{\chi_1(\eta_n)}\right]\frac{b_n}{\eta_n-t_1}\right\}. \tag{28}$$

Next, $P_1(t_1)$ is determined by the regular condition for $\psi_1^B(t_1)$. Substituting (4) and (5) into (7),

$$\psi_1^B(t_1)=-\overline{\phi_1^B}\left(\frac{1}{t_1}\right)-\frac{\bar{\omega}\left(\frac{1}{t_1}\right)}{\omega'(t_1)}\phi_1^{B\prime}(t_1)+\frac{p}{2}\left[\omega(t_1)-\bar{\omega}\left(\frac{1}{t_1}\right)\right]. \tag{29}$$

The second term of the right-hand side of (29) is expanded in a Laurent's series around $t_1 = 1/\bar{\zeta}_k \equiv \zeta_k'$;

$$\frac{\bar{\omega}\left(\frac{1}{t_1}\right)}{\omega'(t_1)}\phi_1^{B\prime}(t_1)=-\sum_{k=1}^N\frac{A_{1k}\overline{B}_k\zeta_k'^2}{\zeta_k'-t_1}+\text{ regular terms in } S_1^+ \tag{30}$$

where $A_{1k}=\phi_1^{B\prime}(\zeta_k')$ and $B_k \equiv E_k/\overline{\omega'(\zeta_k')}$. On the right-hand side in (29), the first term is expressed by (25) and (28), and the third term is done by (2). Noting the terms with the poles in S_1^+ as a matter of form, $\psi_1^B(t_1)$ is given as follows:

$$\psi_1^B(t_1)=\frac{\gamma_1}{1+\lambda_1}\sum_n\left[1-\frac{\overline{\chi_1}\left(\frac{1}{t_1}\right)}{\overline{\chi_1(\xi_n)}}\right]\frac{\overline{a_n}\xi_n'}{\xi_n'-t_1}-\overline{P_1}\left(\frac{1}{t_1}\right)\overline{\chi_1}\left(\frac{1}{t_1}\right)+\sum_{k=1}^N\frac{A_{1k}\overline{B}_k\zeta_k'^2}{\zeta_k'-t_1}+\frac{p}{2}\sum_{k=1}^N\frac{\overline{E}_k\zeta_k'^2}{\zeta_k'-t_1}+\text{ regular terms in } S_1^+ \tag{31}$$

Downloaded 03 May 2010 to 171.66.16.247. Redistribution subject to ASME license or copyright; see http://www.asme.org/terms/Terms_Use.cfm

where $\xi_n' = 1/\overline{\xi_n}$. On the right-hand side of (31), the first term is regular at $t_1 = \xi_n'$ and the third and fourth terms have the poles at $t_1 = \zeta_k'$. Since $\psi_1^B(t_1)$ is regular in S_1^+, the irregular terms in S_1^+ (the second, third, and fourth terms) must cancel out. Thus, expanding the second term in a Laurent's series for $t_1 = \zeta_k'$ and canceling out the third and fourth terms, $P_1(t_1)$ is finally given as follows:

$$P_1(t_1) = -\sum_{k=1}^{N} \frac{\overline{A_{1k}} B_k + \frac{pE_k}{2}}{\chi_1(\zeta_k)(\zeta_k - t_1)}. \tag{32}$$

The function $\phi_2^B(t_2)$ is obtained as well as $\phi_1^B(t_1)$. From the conjugation of (14) and the interchange of subscripts 1 and 2 in (19),

$$\phi_2^B(t_2) + \overline{\phi_1^B\left(\frac{1}{t_2}\right)} = g_2(t_2). \tag{33}$$

From (14), (19), and (33), $g_2(t_2)$ may be written as

$$g_2(t_2) = \overline{g_1\left(\frac{1}{t_2}\right)} = -\sum_n \frac{\overline{a_n}\xi_n'^2}{\xi_n' - t_2} - \sum_n \frac{\overline{b_n}\eta_n'^2}{\eta_n' - t_2} \tag{34}$$

where $\xi_n' = 1/\overline{\xi_n}$ and $\eta_n' = 1/\overline{\eta_n}$. $P_2(t_2)$, corresponding to $P_1(t_1)$ in (25), is given as

$$P_2(t_2) = -\sum_{k=1}^{N} \frac{\overline{A_{2k}} B_k + \frac{\mu p E_k}{2}}{\chi_2(\zeta_k)(\zeta_k - t_2)}. \tag{35}$$

Next, $g_1(t_1)$ is determined. The term $\chi_2(1/\overline{t_1})$ contained in $\phi_2^B(1/\overline{t_1})$ is expressed by $\chi_1(t_1)$ as

$$\frac{\overline{\chi_2(1/\overline{t_1})}}{\chi_2(\xi_n)} = \frac{\xi_n' \chi_1(t_2)}{t_1 \chi_1(\xi_n')}, \quad \frac{\overline{\chi_2(1/\overline{t_1})}}{\chi_2(\eta_n)} = \frac{\eta_n' \chi_1(t_1)}{t_1 \chi_1(\eta_n')}, \quad \frac{\overline{\chi_2(1/\overline{t_1})}}{\chi_2(\zeta_k)} = \frac{\zeta_k' \chi_1(t_1)}{t_1 \chi_1(\zeta_k')} \tag{36}$$

where $m_2 = \overline{m_1}$. Thus, $g_1(t_1)$ is given by (19) as follows:

$$\begin{aligned}
&\phi_1^B(t_1) + \overline{\phi_2^B\left(\frac{1}{t_1}\right)} \\
&= \sum_n \left[1 - \frac{\chi_1(t_1)}{\chi_1(\xi_n)}\right] \frac{a_n}{\xi_n - t_1} + \sum_n \left[1 - \frac{\chi_1(t_1)}{\chi_1(\eta_n)}\right] \frac{b_n}{\eta_n - t_1} \\
&\quad - \sum_{k=1}^{N} \frac{\chi_1(t_1)\left(\overline{A_{1k}} B_k + \frac{pE_k}{2}\right)}{\chi_1(\zeta_k)(\zeta_k - t_1)} \\
&\quad + \sum_{k=1}^{N} \frac{\chi_1(t_1)\left(A_{2k}\overline{B_k} + \frac{\mu p \overline{E_k}}{2}\right)\zeta_k'^2}{\chi_1(\zeta_k')(\zeta_k' - t_1)}.
\end{aligned} \tag{37}$$

The function $g_1(t_1)$, given by (24) and (37), must be identically equal. Therefore, their poles must be the same and the coefficients in two terms, which either include or exclude the Plemelj functions, must also be equal at each pole in S_1^+ and S_1^-. Comparing the coefficients in those terms, $g_1(t_1)$ is determined as follows:

$$g_1(t_1) = -\sum_{k=1}^{N} \frac{\overline{A_{1k}} B_k + \frac{pE_k}{2}}{\zeta_k - t_1} + \sum_{k=1}^{N} \frac{\left(\overline{A_{2k}} B_k + \frac{\mu p \overline{E_k}}{2}\right)\zeta_k'^2}{\zeta_k - t_1}. \tag{38}$$

Finally, $\phi_1^B(t_1)$ is obtained through (25), (28), (32), and (38),

$$\begin{aligned}
\phi_1^B(t_1) = \frac{1}{1+\mu} \Bigg\{ &-\sum_{k=1}^{N} \left[1 + \mu \frac{\chi_1(t_1)}{\chi_1(\zeta_k)}\right] \frac{\overline{A_{1k}} B_k + \frac{pE_k}{2}}{\zeta_k - t_1} \\
&+ \sum_{k=1}^{N} \left[1 - \frac{\chi_1(t_1)}{\chi_1(\zeta_k')}\right] \frac{\left(A_{2k}\overline{B_k} + \frac{\mu p \overline{E_k}}{2}\right)\zeta_k'^2}{\zeta_k' - t_1}.
\end{aligned} \tag{39}$$

Using (34) and (35) and interchanging subscripts 1 and 2 and μ in (39) to $1/\mu$ (see(6)), $\phi_2^B(t_2)$ is obtained as

$$\begin{aligned}
\phi_2^B(t_2) = \frac{\mu}{1+\mu} \Bigg\{ &-\sum_{k=1}^{N} \left[1 + \frac{\chi_2(t_2)}{\mu \chi_2(\zeta_k)}\right] \frac{\overline{A_{2k}} B_k + \frac{\mu p E_k}{2}}{\zeta_k - t_2} \\
&+ \sum_{k=1}^{N} \left[1 - \frac{\chi_2(t_2)}{\chi_2(\zeta_k')}\right] \frac{\left(A_{1k}\overline{B_k} + \frac{p\overline{E_k}}{2}\right)\zeta_k'^2}{\zeta_k' - t_2}.
\end{aligned} \tag{40}$$

However, the integration constants in $\phi_j^B(t_j)$ were omitted because they represent the rigid displacements. It is confirmed that the solutions (39) and (40) also satisfy (33). The undetermined complex constants A_{1k} and A_{2k} are determined by using $A_{1k} = \phi_B'(\zeta_k')$ and $A_{2k} = \phi_2^{B\prime}(\zeta_k')$, $(k = 1, 2, \ldots N)$, (see (30)), and solving $4N$ simultaneous equations with respect to the real and imaginary parts of A_{1k} and A_{2k}. It is noted from (6), (22), and (23) that all material constants in (39) and (40) are expressed by Dundurs' constants in (3). Thus, the components of stress are dependent on Dundurs' constants.

$\chi_j(t_j)$ in (27) has the singularity at the smooth juncture with the 180 degree angle for bonded dissimilar materials. However, in the present analysis, before a debonding occurrence ($C_1 = 0$ or $C_2 = 0$), the juncture is an edge with the corner angle 90 deg. In this case, the singularity at the tip of the juncture is expressed by the combination of $\omega(t_1)$ and $\chi_1(t)$. However, this singularity does not appear explicitly in the stress function.

Constants of Material

Table 1 contains elastic constants of some materials: iron, nickel, aluminum, copper, lead, epoxy resin, tungusten, Al_2O_3, and Si_3N_4. Figure 2 shows the values of α_D and β_D for these elastic constants. Since the symmetric shape (with respect to M) is considered, it is sufficient to pay attention to $\alpha_D \leq 0$. When $\Gamma = 0$ ($\alpha_d = -1$) and $\mu_2 = 0$, $\phi_1(t_1)$ coincides with the stress function for the problem of half-plane with a semi-elliptical notch under uniform tension (Hasebe (1972)—hereafter we denote this problem as "problem A"). Then, from (5) and (40), $\phi_2(t_2) = 0$ for the whole t_2 – plane, and the stress and displacement do not arise in II. For the homogeneous case ($\alpha_D = 0$) without a debonding ($C_1 = C_2 = 0$), the problem reduces to that of the infinite plane with an elliptical hole (hereafter we denote this problem as "problem B").

Table 1 Elastic properties for some materials

Material	Shear modulus μ_j (GPa)	Poisson's ratio ν_j
Fe	81.10	0.30
Ni	73.20	0.36
Al	26.70	0.32
Cu	48.20	0.34
Pb	6.83	0.22
Epoxy resin	1.09	0.35
W	204.00	0.18
Al_20_3	114.00	0.40
Al_20_3	148.00	0.22
Si_3N_4	120.00	0.27

Downloaded 03 May 2010 to 171.66.16.247. Redistribution subject to ASME license or copyright; see http://www.asme.org/terms/Terms_Use.cfm

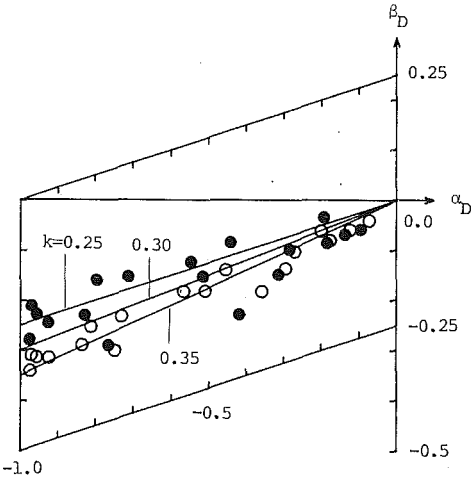

Fig. 2 Dundurs' constants for the combination of some materials, for plane stress (○) and plane strain (●)

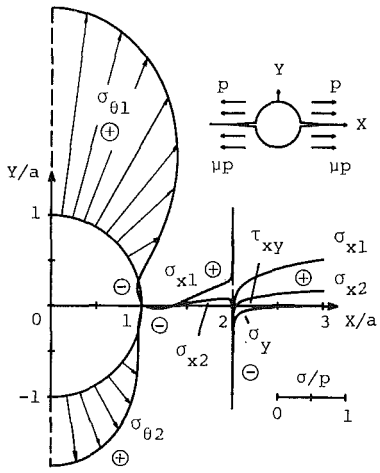

Fig. 3 Stress distribution on the boundary and the interface; b/a = 1.0, $\alpha_D = -0.5$, $\beta_D = -0.15$, and $C_1 = C_2$

Stress Distribution

Figure 3 shows the stress distribution for a circular hole ($b/a = 1$) with symmetric debondings along M ($C_1 = C_2 = a$). The material constants $\alpha_D = -0.5$ and $\beta_D = -0.15$ nearly correspond to the combination of steel and aluminum. Since the shape is symmetric with respect to the Y-axis, the figure for $X \geq 0$ is shown. The stress components on the interface are

$$\sigma_{x_2} = \mu\sigma_{x_1} + \gamma\sigma_y, \tag{41}$$

the shearing stress on M, $\tau_{xy} \doteqdot 0$ except the neighborhood of the debonding tip. The stress diverges infinitely at point C and $\sigma_y < 0$ near C on M. Thus, the debonding does not propagate for the tensile load but may propagate for the compressive load.

Stress Concentration Factor

The stress concentration factor (SCF) at points A and B is investigated for various elliptical holes. SCF is defined as follows:

$$S_A = \frac{\sigma_{x1}^A}{p}, \quad S_B = \frac{\sigma_{x2}^B}{\mu p} \tag{42}$$

where σ_{x1}^A and σ_{x2}^B refer to the stress components at A and B, respectively, in the x-direction. Although S_B is not defined for $\mu = 0$, $\sigma_{x2}^B = 0$ in the present case. The states of stress for $C_1 = C_2$ and for long debondings become approximately equal to the stresses for problem A subjected to the load p in I and μp in II.

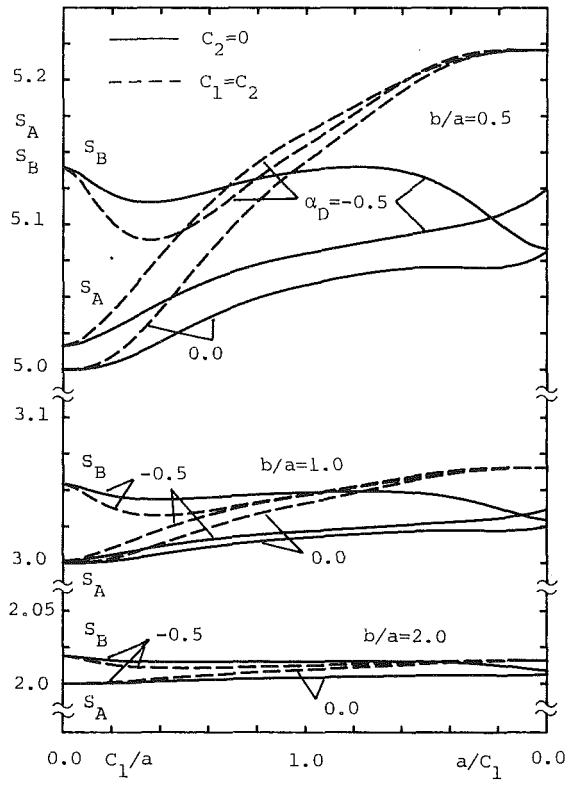

Fig. 4 Stress concentration factors; b/a = 0.5, 1.0, 2.0, and (α_D, β_D) = (0, 0), (−0.5, −0.15)

Figure 4 shows S_A and S_B versus C_1/a for $\alpha_D = -0.5$ and 0.0. The dashed lines show the values for the symmetric debonding ($C_1 = C_2$) and the solid lines show the debonding at only one side ($C_1 \neq 0$, $C_2 = 0$). For $C_1 = C_2$, S_A is minimum at $C_1/a = 0$ and maximum at $a/C_1 = 0$. S_B is maximum at $C_1/a = 0$ and minimum at a certain length of debonding in $0 < C_1/a < 1$. For $C_2 = 0$, the maximum and minimum values of S_A and S_B are at either $C_1/a = 0$ or $a/C_1 = 0$.

Next, the effect of an elliptical hole on S_A and S_B is examined. As b/a becomes large, the ellipse becomes flat and approaches to an interfacial crack. Therefore, the effect of the bonded length becomes small in both debonding cases. For $b/a = 2$, the difference between the values of S_A and S_B at an arbitrary C_1/a and those of problem A is less than 1 percent. Thus, those of problem A may be used in practical application. For b/a = 1 and 0.5, the difference is less than 2.2 percent and 4.4 percent, respectively.

Figure 5 shows the ratio S_A/S_{EH} and S_B/S_{EH} versus b/a for $C_1 = C_2 = 0$, where S_{EH} is SCF for problem B defined as follows:

$$S_{EH} = \frac{\sigma_{\max}}{p} = 1 + 2\sqrt{\frac{a}{\rho}}. \tag{43}$$

Normalizing SCF by S_{EH}, the effect of material constant can be known well, and SCF, which becomes infinite for small b/a, can easily be expressed. Moreover, SIF is related to SCF at points A and B by

$$K_1^A = \lim_{\rho \to 0} \frac{\sqrt{\pi\rho}\ \sigma_{x1}^A}{2}, \quad K_1^B = \lim_{\rho \to 0} \frac{\sqrt{\pi\rho}\ \sigma_{x2}^B}{2}. \tag{44}$$

An extreme state of $b/a \to 0$ becomes a through crack on the interface and SIF is expressed as follows: $S_A/S_{EH} \to K_1^A$

Downloaded 03 May 2010 to 171.66.16.247. Redistribution subject to ASME license or copyright; see http://www.asme.org/terms/Terms_Use.cfm

$/(p\sqrt{\pi a})$ and $S_B/S_{EH} \to K_1^B/(\mu p\sqrt{\pi a})$. Noting $\sigma_{x1}^A > \sigma_{x2}^B$, $S_A/S_{EH} < S_B/S_{EH}$ holds true for arbitrary shape. For $\alpha_D = -0.25$, $S_A/S_{EH} < 1$ for arbitrary shapes and comparing with problem B, the stress concentration is slightly relaxed. However, besides $\alpha_D = -0.25$, $S_A/S_{EH} > 1$ and $S_B/S_{EH} > 1$—and so the ratio becomes larger than those for problem B.

In general, SCF at the notch tip is expressed by using the radius of curvature ρ at the tip (Hasebe, 1971):

$$\sigma = \sum_{j=1}^{\infty} k_j \rho^{n_j} \tag{45}$$

where n_j are the roots of the characteristic equation determined by the corner angle and the boundary conditions and k_j are constants determined by the shape and the boundary conditions. In the present paper, the first three terms in (45) are

$$S_A \text{ or } S_B = k_1 \sqrt{\frac{a}{\rho}} + k_2 + k_3 \sqrt{\frac{\rho}{a}} \tag{46}$$

were $\rho = b^2/a$ and $n_1 = -0.5$, $n_2 = 0$ and $n_3 = 0.5$ owing to the geometry of the ellipse. Since the effect of debonding is small, S_A and S_B are considered for $C_1 = C_2 = 0$. For various material constants, k_1, k_2, and k_3 are obtained by a least squares method using the analytical results and were shown in Table 2. The used 21 data for each S_A or S_B are those for $b/a = 0.001$, 0.005, and ranges from $b/a = 0.01$ to 0.1 at every increment 0.01 and from $b/a = 0.1$ to 1 at every increment 0.1. Table 2 also contains the nondimensional stress intensity factors $F_1^A = K_1^A/(p\sqrt{\pi a})$ and $F_1^B = K_1^B/(\mu p\sqrt{\pi a})$ for the through crack without a debonding. Using (44) and (45), $k_1 = 2K_1^A/(p\sqrt{\pi a}) = 2F_1^A$ in I and $k_1 = 2K_1^B/(\mu p\sqrt{\pi a}) = 2F_1^B$ in II hold true. The difference between the values of k_1 obtained from (46) and the value of F_1 is in one-thousandth place. The stress function for $\alpha_D = -1$ is equal to that for problem A regardless of β_D. Therefore, the stress functions are not distinguished by β_D in Table 2. Table 3 contains S_A for $\alpha_D = -0.5$, $\beta_D = -0.15$, and the approximate values obtained from (46). It is noted that the stress concentration values can be expressed with sufficient accuracy because the errors are less than 0.8 percent.

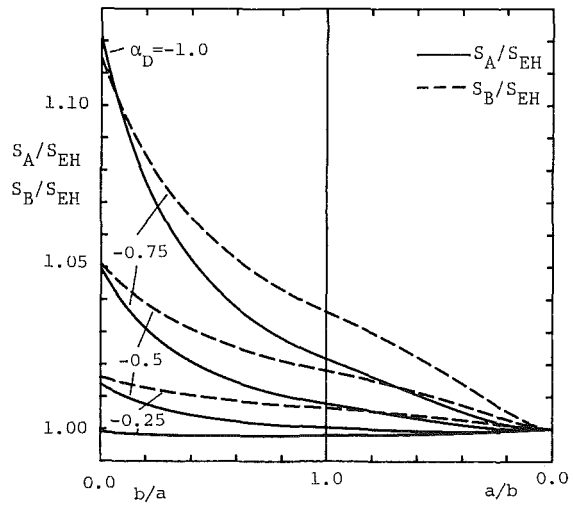

Fig. 5 Stress concentration factors standardized by S_{EH}; $C_1 = C_2 = 0$ and $\beta_D = 0.3\ \alpha_D$

Conclusions

Using the rational mapping function in (2), the complex stress functions are given by (39), (40), and (7) for the uniform tension parallel to the interface at infinity. The deriving process of $\phi_j(t_j)$ is somewhat complicated, but the obtained functions (39) and (40) have very simple forms. If the mapping function is changed, other shapes can be analyzed. For example, using the mapping function for a half-plane with a triangular notch (Hasebe and Iida, 1978), the solution for a rhombic hole on the interface can be obtained. Using the mapping function of a half-plane with an oblique edge crack (Hasebe and Inohara, 1980), the solution for a V-shaped crack on the interface can also be obtained. If the coordinates of the juncture is changed, then the analysis for an arbitrary debonded length can be carried out. By using the same approach as the present analysis, a solution of the bond problem for other loading conditions and for other shapes than a half-plane can also be obtained.

The stress distributions were shown for a circular hole with the debondings. The stress concentration factors S_A and S_B of the elliptical holes were obtained for various material constants, for various shapes of an elliptical hole, and for arbitrary debonded length. The debonded length does not affect S_A and S_B, and the effect increases as b/a decreases. For $b/a = 2$, $\alpha_D = -0.5$, $\beta_D = -0.15$, and arbitrary debonded length, the difference among the values of S_A, S_B, and the stress concentration factors for the half-plane with a semi-elliptical notch was less than one percent. Thus, in practical application, the stress concentration factors of problem A can be used. For $\rho/a < 1$, the stress concentration factors are expressed by (46)

Table 3 Stress concentration factors, approximate values and errors of Eq. (48), $\alpha_D = -0.50$, $\beta_D = -0.15$, $C_1 = C_2 = 0$, $\mu = 1/3$

ρ/b	S_A (1)	Eq. (48) (2)	Error (percent) $\frac{(1)-(2)}{(1)} \times 100$
0.001	2027.000	2027.000	0.00
0.005	406.400	406.200	0.05
0.010	203.700	203.600	0.05
0.020	102.300	102.300	0.00
0.040	51.630	51.650	−0.04
0.060	34.730	34.760	−0.09
0.080	26.280	26.320	−0.15
0.100	21.220	21.260	−0.19
0.200	11.090	11.120	−0.27
0.400	6.026	6.046	−0.33
0.600	4.344	4.348	−0.10
0.800	3.504	3.495	0.27
1.000	3.001	2.979	0.75

Table 2 Comparison of dimensionless stress intensity factors, $\nu_1 = \nu_2 = 0.3$, plane stress condition

			Isida		Our results	
Γ	α_D	β_D	F_I^A	F_I^B	F_I^A	F_I^B
0.1	−0.818	−0.286	1.062	1.153	1.062	1.154
0.2	−0.667	−0.233	1.032	1.097	1.032	1.098
0.3	−0.538	−0.188	1.015	1.064	1.015	1.065
0.4	−0.429	−0.150	1.006	1.043	1.005	1.043
0.5	−0.333	0.117	1.000	1.028	1.000	1.028
0.6	−0.250	−0.088	0.998	1.019	0.998	1.018
0.8	−0.111	−0.039	0.997	1.006	0.997	1.006
1.0	0.000	0.000	1.000	1.000	1.000	1.000

Downloaded 03 May 2010 to 171.66.16.247. Redistribution subject to ASME license or copyright; see http://www.asme.org/terms/Terms_Use.cfm

with good accuracy. An analysis for uniform tension in the Y-direction and for the debonding strength and energy release rate at the debonded tip will be reported in another paper.

References

Bogy, D. B., 1975, "The Plane Solution for Joined Dissimilar Elastic Semistrips under Tension," ASME JOUNRAL OF APPLIED MECHANICS, Vol. 42, pp. 93-98.

Chen, Y. Z., 1986, "Multiple Crack Problems for Two Bonded Half Planes in Plane and Antiplane Elasticity," *Engineering Fracture Mechanics*, Vol. 25, pp. 1-9.

Cherepanov, G. P., 1979, "Piecewise-homogeneous Bodies" (Chapter 3.8) and "Fracture Mechanics of Composite Materials" (Chapter 9), *Mechanics of Brittle Fracture*, McGraw-Hill, New York.

Chou, T. W., and Hirth, J. P., 1970, "Stress Distribution in a Bimaterial Plate under Uniform External Loadings," *Journal of Composite Materials*, Vol. 4, pp. 102-112.

Cook, T. S., and Erdogan, F., 1972, "Stress in Bonded Materials with a Crack perpendicular to the Interface," *International Journal of Engineering Science*, Vol. 10, pp. 677-697.

Dundurs, J., 1967, "Effect of Elastic Constants on Stress in Composite under Plane Deformation," *Journal of Composite Materials*, Vol. 1, pp. 310-322.

Dundurs, J., 1969, "Discussion: Edge-Bonded Dissimilar Orthogonal Elastic Wedges under Normal and Shear Loading," ASME JOURNAL OF APPLIED MECHANICS, Vol. 36, pp. 650-652.

England, A. H., 1965, "A Crack between Dissimilar Media," ASME JOURNAL OF APPLIED MECHANICS, Vol. 32, pp. 400-402.

Erdogan, F., 1963, "Stress Distribution in a Nonhomogeneous Elastic Plane with Cracks," ASME JOURNAL OF APPLIED MECHANICS, Vol. 30, pp. 232-236.

Erdogan, F, 1965, "Stress Distribution in Bonded Dissimilar Materials with Cracks," ASME JOURNAL OF APPLIED MECHANICS, Vol. 32, pp. 403-410.

Erdogan, F., and Guputa, G, 1971, "The Stress Analysis of Multilayered Composites with a Flaw," *International Journal of Solids and Structure*, Vol. 7, pp. 39-61.

Erdogan, F., 1972, "Fracture Problems in Composite Materials," *Engineering Fracture Mechanics*, Vol. 4, pp. 811-840.

Erdogan, F., and Biricikoglu, V., 1973, "Two Bonded Half Planes with a Crack Going through the Interface," *International Journal of Engineering Science*, Vol. 11, pp. 745-766.

Erdogan, F., 1978, "Mixed Boundary-Value Problems in Mechanics," *Mechanics Today*, Vol. 4, S. Nemat-Nasser, ed., Pergamon Press, U.K., Chapter 1.

Goree, J. D., and Venezia, W. A., 1977a, "Bonded Elastic Half-planes with an Interface Crack and a Perpendicular Intersecting Crack That Extends into the Adjacent Material-I," *International Journal of Engineering Science*, Vol. 15, pp. 1-17.

Goree, J. D., and Venezia, W. A., 1977b, "Bonded Elastic Half-planes with an Interface Crack and a Perpendicular Intersecting Crack That Extends into the Adjacent Material-II," *International Journal of Engineering Science*, Vol. 15, pp. 19-27.

Hasebe, N., 1971, "Stress Analyses of a Semi-infinite Plate with a Triangular Notch or Mound," *Proceedings of Japan Society of Civil Engineers*, No. 194, pp. 29-40, (in Japanese).

Hasebe, N., 1972, "Stress Analysis of a Semi-infinite Plate with a Semi-elliptic Notch," *Bulletin of the Nagoya Institute of Technology*, Vol. 24, pp. 295-301, (in Japanese).

Hasebe, N., 1979, "Uniform Tension of a Semi-infinite Plate with a Crack at an End of a Stiffened Edge," *Ingenieur-Archiv*, Vol. 48, pp. 129-141.

Hasebe, N., and Iida, J., 1978, "A Crack Originating from a Triangular Notch on a Rim of a Semi-infinite Plate," *Engineering Fracture Mechanics*, Vol. 10, pp. 773-782.

Hasebe, N., and Inohara, S., 1980, "Stress Analysis of a Semi-infinite Plate with an Oblique Edge Crack," *Ingenieur-Archiv*, Vol. 49, pp. 51-62.

Hasebe, N., and Ueda, M., 1980, "Crack Originating from a Corner of a Square Hole," *Engineering Fracture Mechanics*, Vol. 13, No. 4, pp. 913-923.

Hasebe, N., 1983, "Mixed Boundary Value Problem of Plate with Crack," *ASCE Journal of Engineering Mechanics*, Vol. 110, pp. 37-48.

Hasebe, N., Tsutsui, S., and Nakamura, T., 1988, "Debondings at a Semi-elliptic Rigid Inclusion on the Rim of a Half Plane," ASME JOURNAL OF APPLIED MECHANICS, Vol. 55, pp. 574-579.

Hein, V. L., and Erdogan, F., 1971, "Stress Singularities in a Two-Material Wedge," *International Journal of Fracture Mechanics*, Vol. 7, No. 3, pp. 317-330.

Hetényi, M., and Dundurs, J., 1962, "The Elastic Plane with a Circular Insert, Loaded by a Tangentially Directed Force," ASME JOURNAL OF APPLIED MECHANICS, Vol. 29, pp. 362-368.

Isida, M., and Noguchi, H., 1983, "Plane Problems of Arbitrarily Oriented Cracks in Bonded Dissimilar Materials," *Transactions of the Japan Society of Mechanical Engineers*, Vol. 49, pp. 36-45, (in Japanese).

Lin, K. Y., and Mar, J. W., 1976, "Finite Element Analysis of Stress Intensity Factors for Cracks at a Bi-material Interface," *International Journal of Fracture*, Vol. 12, pp. 521-531.

Murakami, Y., et al., eds., 1987, "Crack in Inhomogeneous Materials," *Stress Intensity Factors Handbook*, Pergamon Press, Oxford, U.K., Chapter 8.

Muskhelishvili, N. I., 1963, *Some Basic Problems of the Mathematical Theory of Elasticity*, Noordhoff, Groningen.

Piva, A., and Viola, E., 1980, "Biaxial Load Effects on a Crack between Dissimilar Media," *Engineering Fracture Mechanics*, Vol. 13, pp. 143-174.

Rice, J. R., and Sih, G. C., 1965, "Plane Problems in Dissimilar Media," ASME JOURNAL OF APPLIED MECHANICS, Vol. 32, pp. 418-423.

Rice, J. R., 1988, "Elastic Fracture Mechanics Concepts for Interfacial Cracks," ASME JOURNAL OF APPLIED MECHANICS, Vol. 55, pp. 98-103.

Sawyer, S. G., and Anderson, R. B., 1972, "Collocated Interfacial Stress Intensity Factors for Finite Bi-material Plates," *Engineering Fracture Mechanics*, Vol. 4, pp. 605-616.

Sham, T. L., and Bueckner, H. F., 1988, "The Weight-function Theory for Piecewise Homogeneous Isotropic Notches in Antiplane Strain," ASME JOURNAL OF APPLIED MECHANICS, Vol. 55, pp. 596-603.

Shih, C. F., and Asaro, R. J., 1988, "Elastic-plastic Analysis of Cracks of Bimaterial Interfaces: Part I—Small Scale Yielding," ASME JOURNAL OF APPLIED MECHANICS, Vol. 55, pp. 299-316.

Sih, G. C., 1972, *Handbook of Stress Intensity Factors*, Institute of Fracture and Solid Mechanics, Lehigh University, Pa.

Sih, G. C., and Chen, E. P., 1981, *Cracks in Composite Materials, Mechanics of Fracture*, Vol. 6, Martinus Nijhoff Publishers, The Hague.

Tamate, O., and Iwasaka, N., 1976, "International of a Bimetallic Interface with a Line Crack in a Composite Body under Tension," *Transactions of the Japan Society of Mechanical Engineers*, Vol. 42, No. 353, pp. 23-30, (in Japanese).

Viola, E., and Piva, A., 1981, "Plane Strain Interfacial Fracture Analysis of a Bimaterial Incompressible Body," *Engineering Fracture Mechanics*, Vol. 15, pp. 131-142.

Williams, M. L., 1959, "The Stress around a Fault or Crack in Dissimilar Media," *Bulletin of the Seismological Society of America*, Vol. 49, pp. 199-204.

Yau, J. F., and Wang, S. S., 1984, "An Analysis of Interface Cracks between Dissimilar Isotropic Materials using Conservation Integrals in Elasticity," *Engineering Fracture Mechanics*, Vol. 20, pp. 423-432.

Yuuki, R., Cho, S. B., Matsumoto, T., and Kisu, H., 1987, "Efficient Boundary Element Elastostatic Analysis using Hetényi's Fundamental Solution," *Transactions of the Japan Society of Mechanical Engineers*, Vol. 53, pp. 1581-1589.

Downloaded 03 May 2010 to 171.66.16.247. Redistribution subject to ASME license or copyright; see http://www.asme.org/terms/Terms_Use.cfm

R. Mohan[1]

M. Ortiz
Mem. ASME

C. F. Shih
Mem. ASME

Division of Engineering,
Brown University,
Providence, RI 02912

Influence of Cracking Direction on Interfacial Fracture in Bicrystals With Symmetric Tilt Boundary

Recent experiments by Wang (1990) on copper bicrystals with a [110] symmetric tilt of 38.9 degrees have shown that the mode of fracture of these bicrystals, i.e., whether fracture is of a ductile or brittle nature, depends on the direction of cracking. An analysis of this effect within the framework of continuum crystal plasticity is presented. The formulation accounts for finite deformations and finite lattice rotations, as well as for the full three-dimensional collection of slip systems in FCC crystals. Our results indicate that, whereas the level of stress ahead of the crack tip is similar for the ductile and brittle cracking directions, the sizes of the plastic regions differ significantly in the two cases.

1 Introduction

The fracture properties of grain boundaries in polycrystalline metals strongly influence the behavior of the bulk material (McLean, 1957; Hirth, 1972; Watanabe, 1988; Randle and Ralph, 1988). Bicrystals constitute a convenient model system for developing an understanding of the mechanics of crystalline interfaces, and have been extensively studied in the past (Livingston and Chalmers, 1957; Hook and Hirth, 1967; Miura and Saeki, 1978; Chuang and Margolin, 1973; Rey and Zaoui, 1980). Wang and Anderson (1991) has recently conducted experiments on Cu-bicrystals with symmetric and asymmetric tilt boundaries, and found that the mode of fracture depends upon such factors as the type of interface, the amount of impurity segregation, and the direction of cracking. The directional dependence, which is the main focus of this paper, was observed in bicrystals with a [110] symmetric tilt of 38.9 deg, the interface being a $(2\bar{2}1)$ lattice plane. This tilt boundary is commonly denoted $\Sigma 9[110]/(2\bar{2}1)$. In essence, an intergranular brittle fracture surface with cleavage tongues is observed for cracking in the $[1\bar{1}4]$ direction (Fig. 7 of Wang and Anderson (1991)). By way of contrast, transgranular ductile fracture occurs for cracking in the opposite direction (Fig. 8 of Wang and Anderson, 1991).

A theoretical explanation of this effect has been attempted by Wang and Anderson (1990) and by Rice, Suo, and Wang (1990) with the aid of a modified Rice and Thomson (1975) model. In this model, the type of fracture is predicted on the basis of an analysis of the competition between cleavage and blunting by dislocation emission, with fracture presumed to be brittle when the energy release rate associated with cleavage is less than that required for dislocation emission from the tip, and ductile otherwise. Saaedvafa and Rice (1990) have carried out small-strain continuum plasticity calculations and concluded that, whereas the deformation pattern varies depending on direction, the stress levels are ostensibly identical.

In this paper we endeavor to determine whether continuum plasticity provides any indication as to the type of fracture in Wang and Anderson's Σ9 experiment. We adopt a geometrically rigorous formulation accounting for finite deformation and finite lattice rotations, as well as the full three-dimensional geometry of the crystals. The crack is considered to be mathematically sharp in its initial configuration. We have computed crack-tip fields for two different hardening laws proposed by Peirce, Asaro, and Needleman (1981) and by Bassani and Wu (1991). Our results are consistent with Saaedvafa and Rice's (1990) observation that the levels of stress ahead of the tip are quite insensitive to the direction of cracking. However, we find that the plastic zone sizes, as defined by the isocontours of slip activity, vary substantially between directions, with the larger zones arising in the ductile case. Thus, based on this limited evidence, there appears to be some correlation between the plastic zone sizes predicted by the continuum theory and the mode of fracture. The calculated plastic zone sizes are found to vary widely depending on the choice of hardening law, with Bassani and Wu's (1991) model giving the largest differences between the ductile and brittle directions. A detailed account of the results of the calculations is given in Section 3.

2 Theory and Solution Procedure

Consider a crystal lattice being deformed from its initial undeformed configuration $\mathcal{B}_0$ to its current configuration $\mathcal{B}_t$ at time t. The deformation gradient $\mathbf{F}$ fully describes the local deformations of the crystal. We assume that two different

[1]Presently at the Department of Mechanical Engineering, University of Pennsylvania.

Contributed by the Applied Mechanics Division of THE AMERICAN SOCIETY OF MECHANICAL ENGINEERS for publication in the JOURNAL OF APPLIED MECHANICS.

Discussion on this paper should be addressed to the Technical Editor, Prof. Leon M. Keer. The Technological Institute, Northwestern University, Evanston, IL 60208, and will be accepted until two months after final publication of the paper itself in the JOURNAL OF APPLIED MECHANICS. Manuscript received by the ASME Applied Mechanics Division, Sept. 18, 1990; final revision, Mar. 15, 1991.

Copyright © 1992 by ASME
Downloaded 03 May 2010 to 171.66.16.247. Redistribution subject to ASME license or copyright; see http://www.asme.org/terms/Terms_Use.cfm

deformation mechanisms contribute to $\mathbf{F}$: plastic flow of the lattice due to shearing on the slip systems, which leaves the lattice invariant, and distortion of the lattice. Following Lee (1969) and others (e.g., Teodosiu, 1970; Mandel, 1972; Hill and Rice, 1972; Havner, 1973; Asaro and Rice, 1977), this suggests a multiplicative decomposition

$$\mathbf{F} = \mathbf{F}^e\mathbf{F}^p \tag{1}$$

or $\mathbf{F}$ into an elastic and plastic parts, $\mathbf{F}^e$ and $\mathbf{F}^p$, respectively. The collection of plastically deformed local configurations, defined by $\mathbf{F}^p$, are collectively referred to as the intermediate configuration $\bar{\mathfrak{B}}_t$. The plastic rate of deformation relative to the crystal lattice is given by (Rice, 1971)

$$\dot{\mathbf{F}}^p\mathbf{F}^{p-1} = \sum_\alpha \dot{\gamma}^\alpha \mathbf{s}^\alpha \otimes \mathbf{m}^\alpha \tag{2}$$

where $\dot{\gamma}^\alpha$ is the shear strain rate on slip system α and $\mathbf{s}^\alpha$ and $\mathbf{m}^\alpha$ are the slip direction and slip plane normal. The sum ranges over all active slip systems.

The slip rate on system α, $\dot{\gamma}^\alpha$, is assumed to depend on stress only through the corresponding resolved shear stress

$$\tau^\alpha = \mathbf{s}^\alpha \cdot (\mathbf{F}^{eT}\tau\mathbf{F}^{e-T}) \cdot \mathbf{m}^\alpha \tag{3}$$

where τ is the Kirchhoff stress on $\mathfrak{B}_t$. In our calculations we have adopted the power law

$$\dot{\gamma}^\alpha = \dot{\gamma}_0 \operatorname{sgn}(\tau^\alpha)\left(\frac{|\tau^\alpha|}{g^\alpha}\right)^{1/m} \tag{4}$$

where $\dot{\gamma}_0^\alpha$ is the reference shear strain rate, g^α is the current shear flow stress on slip system α, and m is the rate sensitivity exponent. For multiple slip, the evolution of the flow stresses is taken to be governed by a hardening law of the form

$$\dot{g}^\alpha = \sum_\beta h_{\alpha\beta}|\dot{\gamma}^\beta| \tag{5}$$

for some hardening moduli $h_{\alpha\beta}$. In calculations, we consider two different forms of $h_{\alpha\beta}$. In the first, henceforth referred to as the 'PAN' model for ease of reference, the moduli are assumed to be of the form proposed by Peirce, Asaro, and Needleman (1983)

$$h_{\alpha\beta} = h(\gamma)\,(q + (1-q)\delta^{\alpha\beta}) \tag{6}$$

where $\gamma = \Sigma_\alpha\gamma_\alpha$ is the sum of the accumulated slip strains on all slip systems and q characterizes the hardening behavior. The value $q = 1$, which corresponds to isotropic or Taylor hardening, has been used in our calculations. Based on the experiments of Chang and Asaro (1981), Peirce, Asaro, and Needleman (1983) proposed the expression

$$h(\gamma) = h_0 \operatorname{sech}^2\left(\frac{h_0\gamma}{\tau_s - \tau_0}\right) \tag{7}$$

as appropriate to Al-Cu alloy crystals. Here, h_0 is the initial hardening rate, τ_0 is the critical resolved shear stress, and τ_s is the saturation strength.

Based on carefully controlled latent hardening experiments in Cu single crystals (Wu, Bassani, and Laird, 1991), Bassani and Wu (1991) have recently proposed a model of hardening in single crystals, henceforth referred to as the 'BW' model, in which the hardening moduli are taken to be of the form

$$h_{\alpha\alpha} = \left[(h_0 - h_s)\operatorname{sech}^2\left(\frac{(h_0 - h_s)\gamma_\alpha}{\tau_I - \tau_0}\right) + h_s\right] \times \left(1 + \sum_{\substack{\beta \\ \beta \neq \alpha}} f_{\alpha\beta}\tanh\left(\frac{\gamma_\beta}{\gamma_0}\right)\right) \tag{8}$$

$$h_{\alpha\beta} = \epsilon h_{\alpha\alpha}$$

where τ_I is the stage I stress, i.e., the breakthrough stress where large plastic flow initiates, h_0 and h_s define the hardening slope just after initial yield and during easy glide, respectively, and ϵ is a small parameter which defines the off-diagonal terms. The functions $f\alpha\beta$ are the amplitude factors which depend on the type of dislocation junction formed between α and β slip systems. They are classified into five groups and are represented by five constants. The paper by Bassani and Wu (1991) may be consulted for details on these amplitude factors. In our calculations, we have taken $\epsilon = 0$ which corresponds to a diagonal form of the hardening moduli.

For metals, the elastic relations may be assumed to be of the simple form

$$\bar{\mathbf{S}} = \bar{\mathfrak{L}}^e\bar{\mathbf{E}}^e, \quad \bar{\mathbf{E}}^e = (\mathbf{C}^e - \mathbf{I})/2, \quad \mathbf{C}^e = \mathbf{F}^{eT}\mathbf{F}^e \tag{9}$$

without much loss of generality. Here, $\bar{\mathbf{S}} = \bar{\mathbf{F}}^{e-1}\tau\mathbf{F}^{e-T}$ is a second Piola-Kirchhoff stress tensor relative to $\bar{\mathfrak{B}}_t$, and $\bar{\mathbf{E}}^e$ and $\bar{\mathbf{C}}^e$ are the Green strain tensor and the right Cauchy-Green deformation tensor on $\bar{\mathfrak{B}}_t$, respectively. To a first approximation, the elastic moduli $\bar{\mathfrak{L}}^e$ for the crystals under study may be taken to be isotropic, i.e., of the form

$$\mathfrak{L}^e_{ijkl} = \lambda\delta_{ij}\delta_{kl} + \mu(\delta_{ik}\delta_{jl} + \delta_{il}\delta_{jk}) \tag{10}$$

where λ and μ are the elastic Lamé constants.

We adopt the method of solution advanced by Moran, Ortiz, and Shih (1990) in the context of flow theories of plasticity. Here, the method is generalized to handle several simultaneously active slip systems. The constitutive update is based on an *implicit* treatment of the elastic-plastic kinematics and the elastic response, defined by Eqs. (1)–(4) and (9), combined with an *explicit* treatment of the hardening laws (7) and (8), whereby the hardening moduli (6) and (8) is sampled at the start of the time step. This method of discretization results in the following algebraic equations defining the state update:

$$\begin{aligned}
&\mathbf{F}_{n+1} = \mathbf{F}^e_{n+1}\mathbf{F}^p_{n+1}, \quad \mathbf{C}^e_{n+1} = \mathbf{F}^{eT}_{n+1}\mathbf{F}^e_{n+1}\\
&(\mathbf{F}^p_{n+1} - \mathbf{F}^p_n)\mathbf{F}^{p-1}_n = \sum_\alpha \Delta\gamma^\alpha \mathbf{s}^\alpha \otimes \mathbf{m}^\alpha\\
&\Delta\gamma^\alpha = \Delta t\dot{\gamma}_0 \operatorname{sgn}(\tau^\alpha_{n+1})\left(\frac{|\tau^\alpha_{n+1}|}{g^\alpha_{n+1}}\right)^{1/m}\\
&\tau^\alpha_{n+1} = \mathbf{s}^\alpha \cdot (\mathbf{C}^e_{n+1}\bar{\mathbf{S}}_{n+1}) \cdot \mathbf{m}^\alpha\\
&g^\alpha_{n+1} = g^\alpha_n + \sum_\beta h(\gamma_n)\,(q + (1-q)\delta_{\alpha\beta})\,|\Delta\gamma^\beta|\\
&\bar{\mathbf{S}}_{n+1} = \mathfrak{L}^e : (\mathbf{C}^e_{n+1} - \mathbf{I})/2
\end{aligned} \tag{11}$$

where the subindeces $(\ )_n$ and $(\ )_{n+1}$ refer to the initial and updated values of the state variables, respectively, $\Delta\gamma^\alpha$ are the incremental slip strains, and Δt is the time increment. In (11), the final deformation gradients $\mathbf{F}_{n+1}$ are to be regarded as given. It is of interest to note that, since the hardening modulus h is treated explicitly, (11) can be reduced to a system of nonlinear equations for the incremental shear strains $\Delta\gamma^\alpha$ (for details, see Mohan, Ortiz, and Shih, 1990). In the present analysis, this system is solved by means of a local Newton-Raphson iteration with line searches. With the determination of $\Delta\gamma^\alpha$, the remaining state variables follow immediately from (11). Owing to the implicit treatment of the constitutive equations and the inclusion of the elastic response, the updated state is always unique even in the rate-independent limit, provided that the elastic domain is convex. The integration of the equilibrium equations is performed *explicitly*, by the forward-gradient method of the type proposed by Peirce, Shih, and Needleman (1984).

The finite element mesh is composed of 8-noded isoparametric brick elements. In order to prevent locking due to near incompressibility under conditions of fully developed plastic flow, we employ an assumed strain method developed by Moran, Ortiz, and Shih (1990). The method generalizes the mean-dilatation approach of Nagtegaal, Parks, and Rice (1974) to finite deformations, and consists of postulating a constant deformation Jacobian $\det(\mathbf{F})$ over each element, the value of

Downloaded 03 May 2010 to 171.66.16.247. Redistribution subject to ASME license or copyright; see http://www.asme.org/terms/Terms_Use.cfm

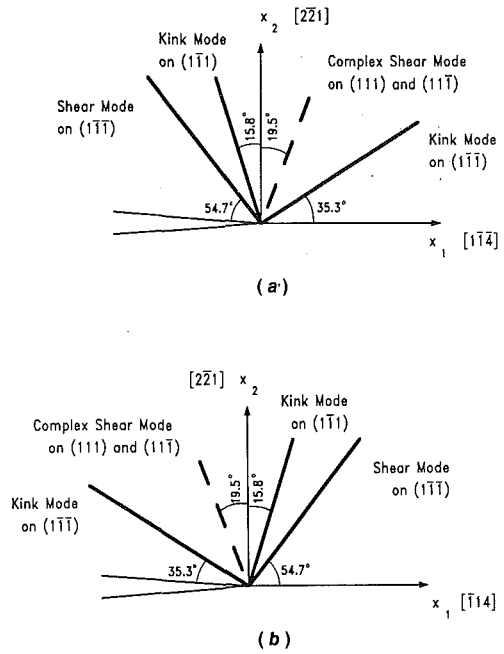

Fig. 1 The orientations of the discontinuities in the vicinity of the crack tip, based on Rice's (1987) small-strain solution, for the (*a*) [1$\bar{1}$4] (brittle) and (*b*) [$\bar{1}$14] (ductile) cracking directions

which is sampled at the centroid. The generalized plane condition is enforced by meshing a slice of the solid perpendicular to the crack front by a single layer of elements and constraining the three displacement components to be equal on both surfaces of the slice.

In the present analysis, a fan-like mesh with exponential grading in the radial direction and uniform grading in the circumferential direction is used. The ratio of the innermost to the outermost element sizes is of the order of 10^{-5}. The angular resolution of the mesh is 12 deg, and the total number of degrees-of-freedom is 5784. Tractions consistent with the linear elastic asymptotic Mode I field are distributed over the outer boundary, and increased at increments such that essentially one new ring of elements is plastified at each step. The rate of application of the loads is chosen such that the maximum strain rates in the vicinity of the crack tip are of the order of the reference strain rate $\dot{\gamma}_0$. This results in modest or negligible amounts of overstress due to rate dependency. The values of the material constants used in the calculations are: $\lambda = 576.92\tau_0$, $\mu = 384.62\tau_0$, $\dot{\gamma}_0 = 10^{-3}$, $m = 0.005$. In addition, the parameters used in describing the PAN hardening moduli are $q = 1$, $h_0 = 8.9\tau_0$, $\tau_s = 1.89\tau_0$. These values are typical of Al-Cu alloys (Chang and Asaro, 1981). For the BW hardening moduli, the parameters chosen are (Bassani and Wu, 1991): $\gamma_0 = 10^{-3}$, $h_0 = 90\tau_0$, $h_s = 1.5\tau_0$, and $\tau_I = 1.3\tau_0$. The amplitude factors $f_{\alpha\beta}$ are determined from five parameters, i.e., $a_1 = a_2 = a_3 = 8$, $a_4 = 15$ and $a_5 = 20$, (see Table 2 of Bassani and Wu, 1991).

3 Results

For the crystal orientations considered, the small-strain theory (Saeedvafa and Rice, 1990) predicts slip activity to be restricted to the six systems. For slip systems whose effective slip direction and normal lie in-plane, plastic shearing can occur either parallel or perpendicular to the slip plane. These two modes of deformation will be termed shear and kink modes, respectively. In addition, pairs of slip systems symmetrically disposed about the plane of the analysis combine to give an in-plane complex shearing mode of deformation. In Rice's theory (Rice, 1987), a set of potentially active slip systems

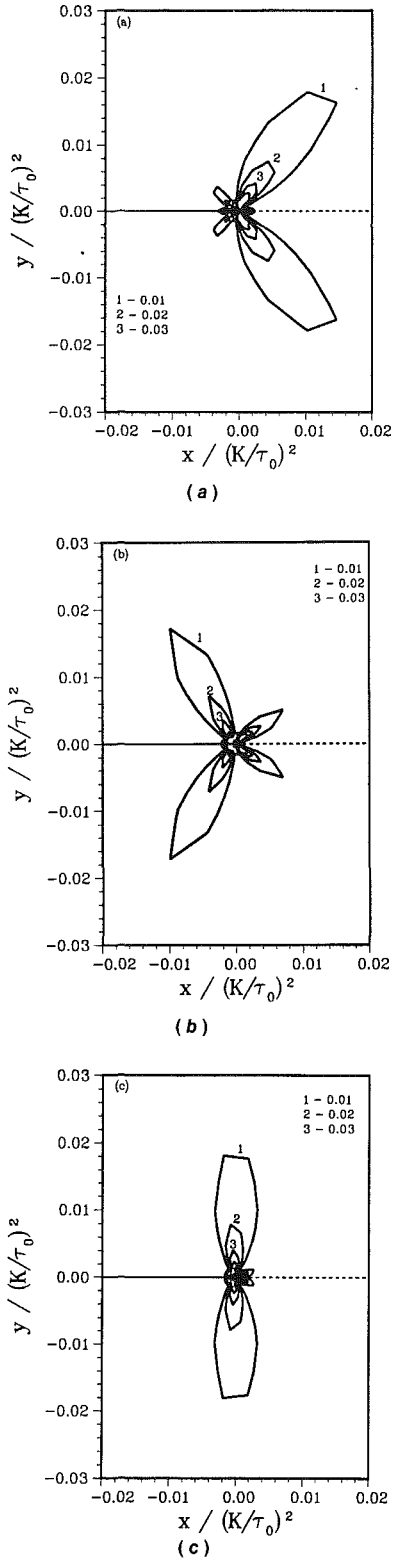

Fig. 2 Contours of slip activity, for the brittle cracking direction, on systems (*a*) (1$\bar{1}$1) [101] and (111)[011], (*b*) (111) [101] and (1$\bar{1}$1) [011], and (*c*) (111) [1$\bar{1}$0] and (11$\bar{1}$) [1$\bar{1}$0]. The results correspond to PAN hardening law.

involves the (1$\bar{1}\bar{1}$) or (1$\bar{1}$1) planes and effective slip in the [1$\bar{1}$2] or [$\bar{1}$12] directions due to equal and simultaneous slip along [101] and [0$\bar{1}$1] or [$\bar{1}$01], and [011], respectively. Another type of slip system involves the [1$\bar{1}$0] direction and the (111) and (11$\bar{1}$) planes. Within the framework of Rice's analysis, stress and shear displacement discontinuities arise in the vicinity of

Downloaded 03 May 2010 to 171.66.16.247. Redistribution subject to ASME license or copyright; see http://www.asme.org/terms/Terms_Use.cfm

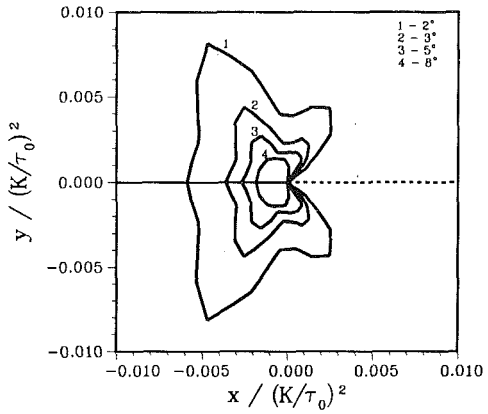

Fig. 3 Contours of lattice rotation for the brittle cracking direction predicted by PAN hardening law

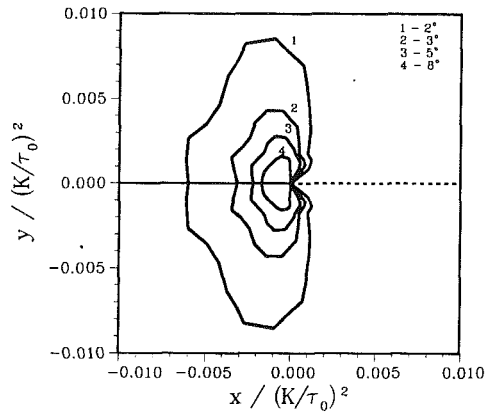

Fig. 5 Contours of lattice rotation for the ductile cracking direction predicted by PAN hardening law

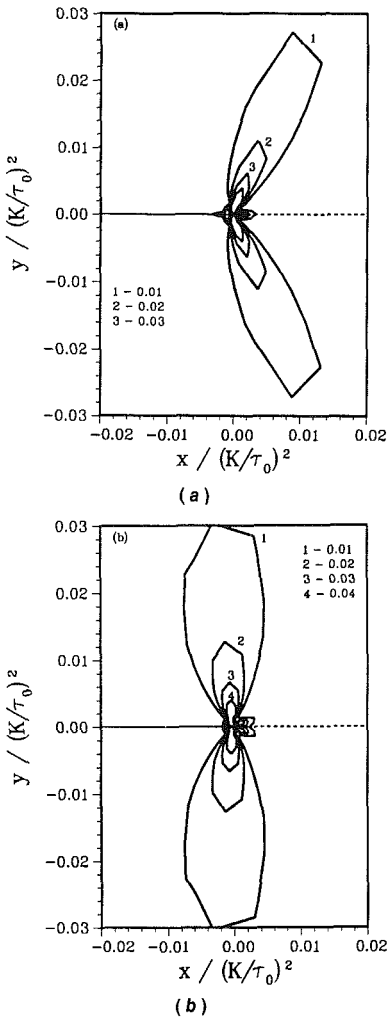

Fig. 4 Contours of slip activity, for the ductile cracking direction, on systems (*a*) $(1\bar{1}1)$ [101] and $(11\bar{1})[01\bar{1}]$, and (*b*) $(\bar{1}11)$ [101] and $(\bar{1}\bar{1}1)$ [011]. The results correspond to PAN hardening law.

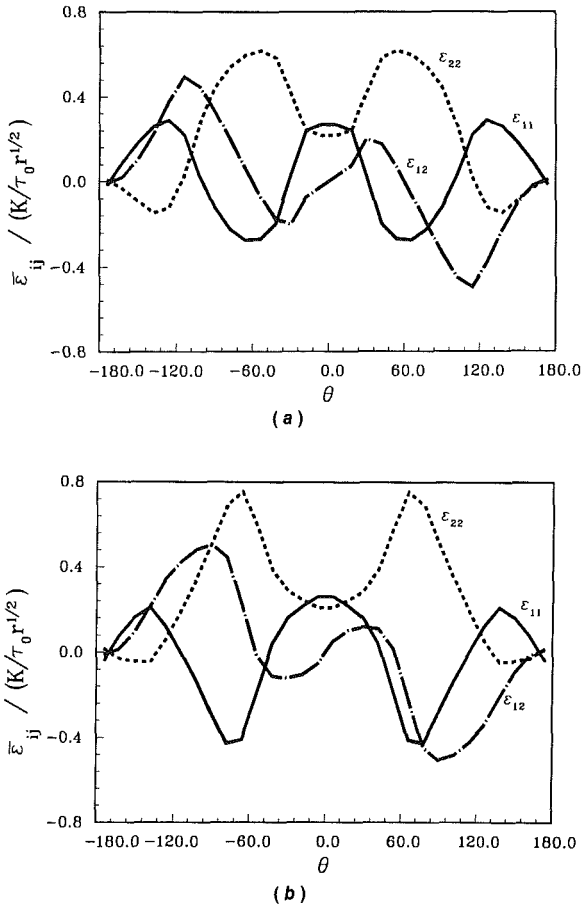

Fig. 6 Angular variation of the Almansi strain components normalized by $(K/\tau_0)r^{-1/2}$ for the (*a*) brittle, and (*b*) ductile cracking directions. The results correspond to PAN hardening law.

the crack tip which are either parallel to the active slip plane, in the shear modes, or perpendicular to it, in the kink modes. These lines of discontinuity separate sectors of constant stress.

For the specific geometry under consideration, the various sectors which define Rice's solution in the brittle and ductile cases are the reflection of each other about the $[2\bar{2}1]$ direction. A shear mode and a kink mode are predicted to arise from the $(1\bar{1}\bar{1})$-type systems. In addition, the $(1\bar{1}1)$-type systems contribute a kink mode. Complex shear involving the $[\bar{1}10]$ direction and the (111) and $(11\bar{1})$ planes introduces an additional shear mode. The orientations of the resulting discontinuities are shown in Figs. 1 (*a*) and (*b*), for the ductile and brittle crack directions, respectively.

3.1 PAN Hardening Law. Contours of slip activity for the dominant slip systems when the crack is oriented along $[1\bar{1}4]$ (brittle) direction are shown in Figs. 2(*a*)–(*c*). The equal and simultaneous slip activity on the $(1\bar{1}\bar{1})$ [101] and $(1\bar{1}\bar{1})[0\bar{1}1]$

Downloaded 03 May 2010 to 171.66.16.247. Redistribution subject to ASME license or copyright; see http://www.asme.org/terms/Terms_Use.cfm

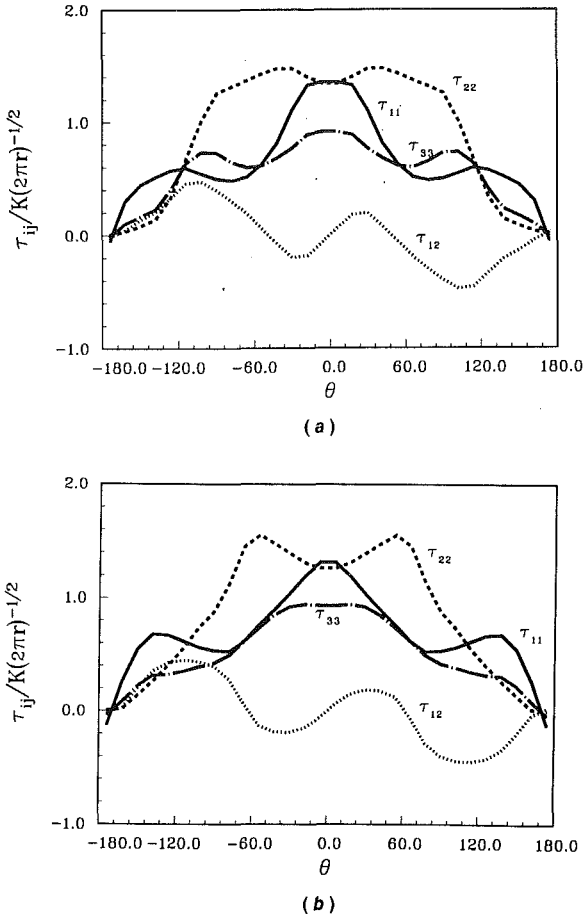

Fig. 7 Angular variation of the Kirchhoff stress components normalized by $K/\sqrt{2\pi r}$ for the (*a*) brittle and (*b*) ductile cracking directions. The results correspond to PAN hardening law.

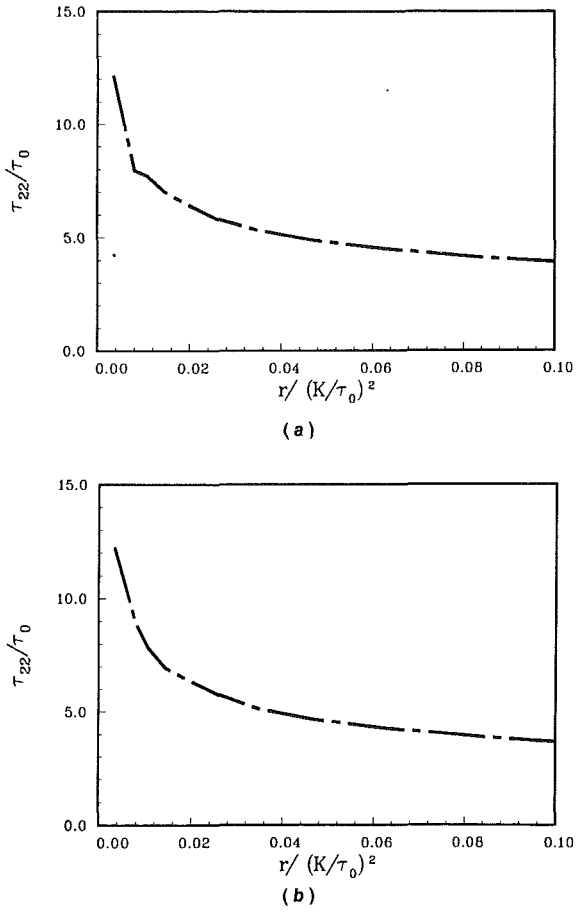

Fig. 8 Radial variation (θ = 6 deg) of the opening stress component, τ_{22}, normalized by $K/\sqrt{2\pi r}$ for the (*a*) brittle, and (*b*) ductile cracking directions. The results correspond to PAN hardening law.

systems, Fig. 2(*a*), reveals a strong kink mode at 54 deg and a weak shear mode at 144 deg. Here and subsequently, the angles subtended by the various modes are measured from the line of the crack and are determined from the corresponding maxima in the angular variations of slip strain. Slip activity on the $(1\bar{1}1)$ $[\bar{1}01]$ and $(1\bar{1}1)$ [011] systems reveals a strong kink mode at 120 deg and a relatively weak shear mode at 30 deg, Fig. 2(*b*). Figure 2(*c*) shows the contours of slip strain on the (111) $[1\bar{1}0]$ and $(11\bar{1})$ $[1\bar{1}0]$ systems. A complex shear mode at 90 deg is evident from the figure.

Some differences between the results of our calculations and Rice's (1987) asymptotic small-strain solution are noteworthy. For instance, the computed shear mode about the $(1\bar{1}1)$ plane is absent in the asymptotic solution. The reverse situation is found as regards the shear mode on $(1\bar{1}\bar{1})$: While this mode is almost absent in our computations, it does figure in Rice's solution. In addition to these differences, there are also discrepancies between the orientations of the modes which do appear in both solutions. Some of these discrepancies can be partly attributed to the intervening effect of the large lattice rotations which develop near the crack tip. Contours of lattice rotation for the brittle cracking direction are shown in Fig. 3. Interestingly, the largest rotations are observed to arise along directions which are nearly aligned with the kink modes in the solution.

For the ductile cracking direction, it is found that the complex shearing mode on slip systems (111) $[\bar{1}10]$ and $(11\bar{1})$ $[\bar{1}10]$ is nearly absent. By contrast, the contours of slip activity on the $(1\bar{1}1)$ [101] $(11\bar{1})$ $[0\bar{1}1]$ systems reveal a strong shear mode at 60 deg, Fig. 4(*a*). A kink mode predicted by Rice's asymptotic solution is not observed in our calculations. The slip activity on the $(1\bar{1}1)$ $[\bar{1}01]$ and $(1\bar{1}1)$ [011] systems reveals a kink mode at 90 deg, Fig. 4(*b*). Contours of the lattice rotation are shown in Fig. 5. As before, rotations are largest at 90 deg, i.e., in the direction of the kink mode. A significant difference between the two cracking directions is that the isocontours of slip activity associated with each of the operative slip systems are up to 50 percent larger in the ductile than in the brittle direction.

The angular variation of the Almansi strain components normalized by $(K/\tau_0)r^{-1/2}$ is shown in Figs. 6(*a*) and (*b*), corresponding to the brittle and ductile cracking directions, respectively. For the ductile direction, ϵ_{22} reaches a sharp peak at about 60 deg. This peak is somewhat smeared for the brittle direction. This difference is mainly due to more extensive shearing on $(1\bar{1}\bar{1})$ [101] and $(11\bar{1})$ $[0\bar{1}1]$ in the ductile case. The in-plane shear component ϵ_{12} has well defined peaks at 30 deg and 120 deg for the brittle cracking direction, whereas a smoother variation of this component is observed for the ductile cracking direction. Differences in slip activity of the $(1\bar{1}1)$ $[10\bar{1}]$ system account for these features.

The angular variation of the Kirchhoff stress components is shown in Figs. 7(*a*) and (*b*) for the brittle and ductile cracking directions. Of special interest is the variation of the opening stress component τ_{22} along the interface, since a high level of stress therein facilitates crack growth by cleavage. In Figs. 8(*a*) and (*b*), τ_{22} is plotted versus the distance to the crack tip at θ = 6 deg, for the ductile and brittle cracking directions. In-

Downloaded 03 May 2010 to 171.66.16.247. Redistribution subject to ASME license or copyright; see http://www.asme.org/terms/Terms_Use.cfm

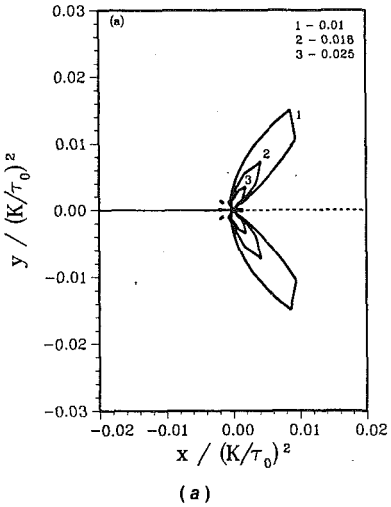

(a)

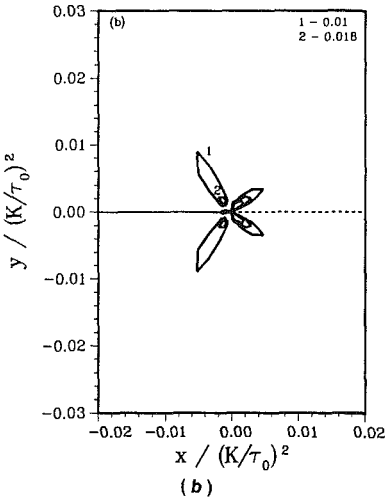

(b)

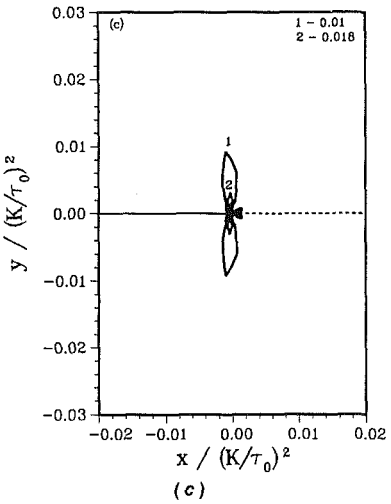

(c)

Fig. 9 Contours of slip activity, for the brittle cracking direction, on systems (*a*) (1$\bar{1}$1) [101] and (11$\bar{1}$)[011], (*b*) (1$\bar{1}$1) [101] and (1$\bar{1}$1) [011], and (*c*) (111) [1$\bar{1}$0] and (111) [11$\bar{0}$]. **The results correspond to BW hardening law.**

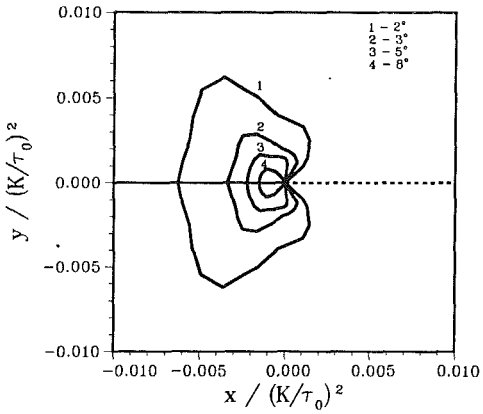

Fig. 10 Contours of lattice rotation for the brittle cracking direction predicted by BW hardening law

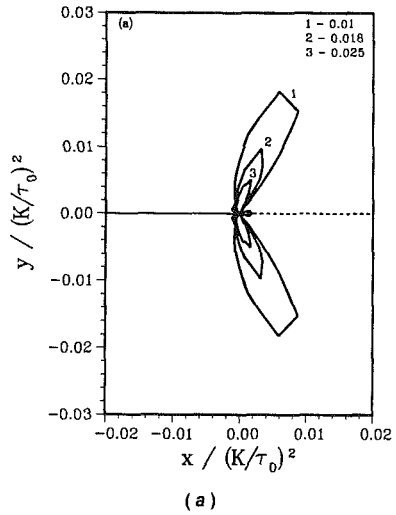

(a)

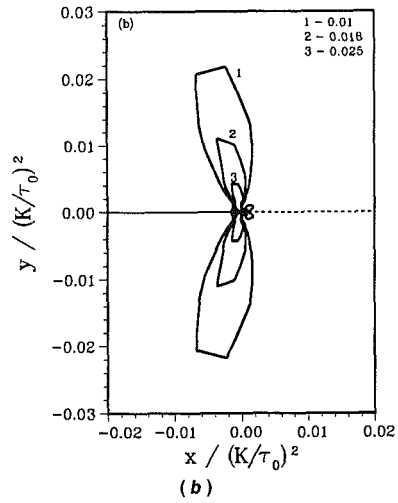

(b)

Fig. 11 Cointours of slip activity, for the ductile cracking direction, on systems (*a*) (1$\bar{1}$1) [101] and (1$\bar{1}$1)[011] and (*b*) (1$\bar{1}$1) [101] and (111) [011]. **The results correspond to BW hardening law.**

terestingly, the levels of stress attained are quite similar in both cases. A factor contributing to this similarity may be the presence of a substantial elastic sector ahead of the tip in both cracking directions.

3.2 BW Hardening Law. Contours of slip activity on the (1$\bar{1}$1) [101] and (1$\bar{1}$1) [0$\bar{1}$1] systems for the cracking direction parallel to [1$\bar{1}$4], i.e., for the brittle case, are shown in Fig. 9(*a*). In contrast to the predictions of the PAN hardening law, only a kink mode at 54 deg is observed in this case. The slip systems (1$\bar{1}$1) [10$\bar{1}$] and (1$\bar{1}$1) [011] give rise to both kink and shear modes, Fig. 9(*b*), of which the former is the more intense one. The slip strain contours for systems (111) [1$\bar{1}$0] and (11$\bar{1}$) [1$\bar{1}$0] reveal a complex mode at 90 deg, Fig. 9(*c*). Contours of lattice rotation for the brittle cracking direction

Downloaded 03 May 2010 to 171.66.16.247. Redistribution subject to ASME license or copyright; see http://www.asme.org/terms/Terms_Use.cfm

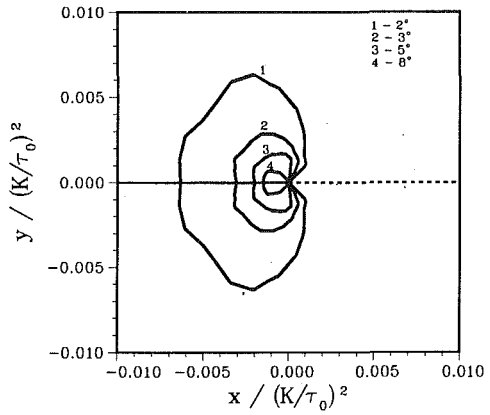

Fig. 12 Contours of lattice rotation for the ductile cracking direction predicted by BW hardening law

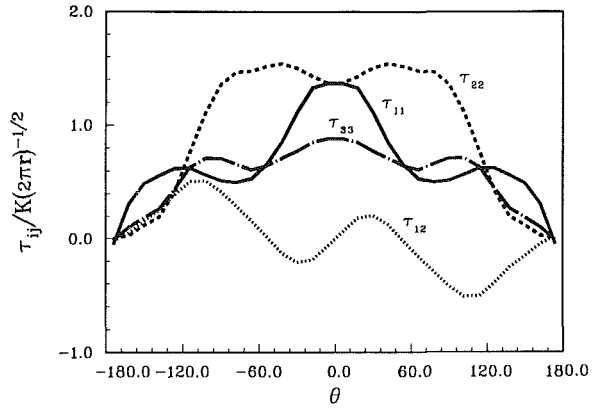

(a)

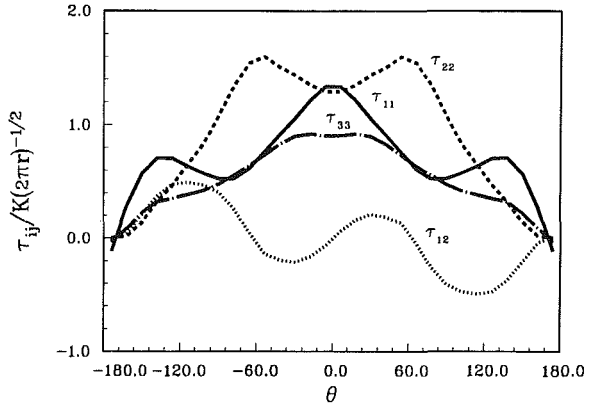

(b)

Fig. 13 Angular variation of the Kirchhoff stress components normalized by $K/\sqrt{2\pi r}$ for the (*a*) brittle and (*b*) ductile cracking directions. The results correspond to BW hardening law.

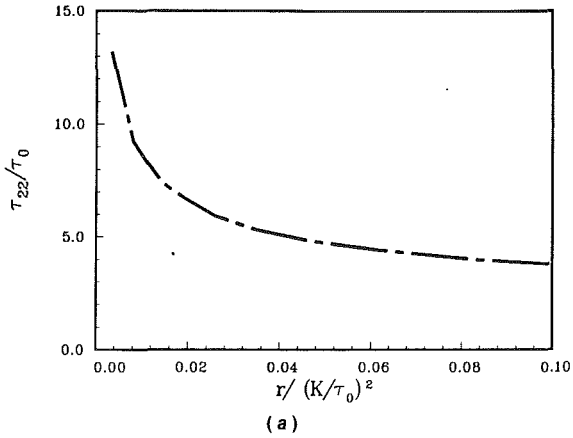

(a)

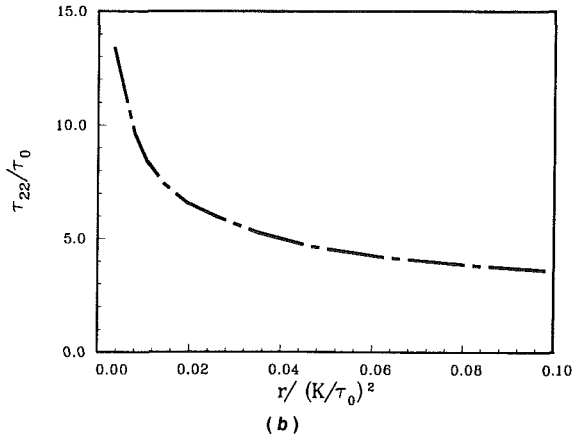

(b)

Fig. 14 Radial variation (θ = 6 deg) of the opening stress component, τ_{22}, normalized by $K/\sqrt{2\pi r}$ for the (*a*) brittle and (*b*) ductile cracking directions. The results correspond to BW hardening law.

are shown in Fig. 10. As in all the preceding cases, rotations tend to be focused in the direction of the kink mode.

For the ductile cracking direction, the complex shearing mode on slip systems (111) $[\bar{1}10]$ and $(11\bar{1})$ $[\bar{1}10]$ is nearly absent. The contours of slip activity on $(1\bar{1}\bar{1})$ [101] and $(1\bar{1}\bar{1})$ $[0\bar{1}1]$ are indicative of a strong shear mode at 60 deg, Fig. 11(*a*). In addition, a kink mode is afforded by slip systems $(1\bar{1}1)$ $[10\bar{1}]$ and $(1\bar{1}1)$ [011], Fig. 11(*b*). The influence of the kink mode on lattice rotations is also evident in this case, Fig. 12. It is quite remarkable that the sizes of the isocontours of slip activity predicted by the BW model in the ductile case are up to twice the size of the corresponding regions in the brittle case. It therefore follows that the BW model differentiates between the ductile and brittle directions more sharply than the PAN model.

The angular variation of Kirchhoff stress components are shown in Figs. 13(*a*) and (*b*) for the brittle and ductile cracking directions. The variations are much the same as those computed from the PAN model. Likewise, the radial dependence of τ_{22} in the ductile and brittle directions, Figs. 14(*a*) and (*b*), is in close correspondence with that predicted by the PAN model. In particular, it is seen that nearly identical levels of stress are attained ahead of the tip for both the brittle and ductile directions.

4 Conclusions

We have carried out numerical simulations of recent experiments by Wang and Anderson (1991) on copper bicrystals with a [110] symmetric tilt of 38.9 deg within the framework of continuum crystal plasticity. Wang and Anderson's (1991) observations suggest that the mode of fracture of these bicrystals, i.e., whether fracture is of a ductile or brittle nature, depends on the direction of cracking. Our results show that the levels of stress which are attained ahead of the crack tip are quite insensitive to the direction of cracking, in agreement with the small-strain calculations of Saaedvafa and Rice (1990). By contrast, the plastic activity patterns are considerably more discriminating. Depending on the model of hardening adopted in the calculation the sizes of the isocontours of slip activity

Downloaded 03 May 2010 to 171.66.16.247. Redistribution subject to ASME license or copyright; see http://www.asme.org/terms/Terms_Use.cfm

for the ductile direction can be up to 50 percent (PAN model) or 100 percent (BW model) larger than those for the brittle direction. This increase in plastic activity may partially account for the transgranular and ductile character of crack growth for cracks pointing in the [$\bar{1}$14] direction.

There is not enough experimental evidence at this point to permit a clear assessment of the role of continuum plasticity effects in determining the ductile versus brittle character of cracking along bicrystal interfaces. However, our results seem to suggest that some correlation may exist between plastic zone size and fracture mode. The fact that plastic zone size predictions are so sensitive to the hardening model points to the need to develop physically based and accurate hardening laws before calculations can be made more predictive.

Acknowledgments

The support of the National Science Foundation through the Materials Research Group at Brown University, Grant DMR-9002994, is gratefully acknowledged. We are also indebted to J. R. Rice and M. Saeedvafa for making available to us the results of their computations.

References

Asaro, R. J., 1983, "Micromechanics of Crystals and Polycrystals," *Advances in Applied Mechanics*, Vol. 23, pp. 1–115.

Asaro, R. J., and Rice, J. R., 1977, "Strain Localization in Ductile Single Crystals," *Journal of the Mechanics and Physics of Solids*, Vol. 25, pp. 309–338.

Bassani, J. L., and Wu, T.-Y., 1991, "Latent Hardening in Single Crystals: Part 2, Analytical Characterization and Predictions," *Proceedings of Royal Society of London*, Vol. A435, pp. 21–41.

Bilby, B. A., Cottrell, A. H., and Swinden, K. H., 1963, "The Spread of Plastic Yield from a Notch," *Proceedings of the Royal Society, London*, Vol. A272, pp. 304–314.

Chang, Y. W., and Asaro, R. J., 1981, "An Experimental Study of Shear Localization in Aluminum-Copper Single Crystals," *Acta Metallurgica*, Vol. 29, pp. 241–257.

Chaung, Y.-D., and Margolin, H., 1973, "Brass Bicrystal Stress-Strain Relations," *Metallurgical Transactions*, Vol. 4, pp. 1905–1917.

Havner, K. S., 1973, "On the Mechanics of Crystalline Solids," *Journal of the Mechanics and Physics of Solids*, Vol. 21, pp. 383–394.

Hill, R., and Rice, J. R., 1972, "Constitutive Analysis of Elastic-Plastic Crystals at Arbitrary Strain," *Journal of the Mechanics and Physics of Solids*, Vol. 20, pp. 401–413.

Hirth, J. P., 1972, "The Influence of Grain Boundaries on Mechanical Properties," *Metallurgical Transactions*, Vol. 3, pp. 3047–3067.

Hook, R. E., and Hirth, J. P., 1967, "The Deformation Behaviour of Isoaxial Bicrystals of Fe-3% Si," *Acta Metallurgica*, Vol. 15, pp. 535–551.

Kelly, A., Tyson, W. R., and Cottrell, A. H., 1967, "Ductile and Brittle Crystals," *Philosophical Magazine*, Vol. 15, pp. 567–586.

Lee, E. H., "Elastic-Plastic Deformation at Finite Strains," ASME JOURNAL OF APPLIED MECHANICS, Vol. 36, pp. 1–6.

Livingston, J. D., and Chalmers, B., 1957, "Multiple Slip in Bicrystal Deformation," *Acta Metallurgica*, Vol. 5, pp. 322–327.

McLean, D., 1957, *Grain Boundaries in Metals*, Oxford University Press, Oxford, U.K.

Mandel, J., 1972, *Plasticité Classique et Viscoplasticité*, Course given at Int. Centre for Mech. Sci., Udine 1971, Springer, Berlin.

Miura, S., and Saeki, Y., 1978, "Plastic Deformation of Aluminum Bicrystals ⟨100⟩ Oriented," *Acta Metallurgica*, Vol. 26, pp. 93–101.

Mohan, R., Ortiz, M., and Shih, C. F., 1990, "An Analysis of Cracks in Ductile Single Crystals: Part I—Anti-Plane Shear," *Journal of Mechanics and Physics of Solids*, to appear.

Moran, B., Ortiz, M., and Shih, C. F., 1990, "Formulation of Implicit Finite Element Methods for Multiplicative Finite Deformation Plasticity," *International Journal for Numerical Methods in Engineering*, Vol. 29, pp. 483–514.

Nagtegaal, J. D., Parks, D. M., and Rice, J. R., 1974, "On Numerically Accurate Finite Element Solutions in the Fully Plastic Range," *Computer Methods in Applied Mechanics and Engineering*, Vol. 4, pp. 153–177.

Peirce, D., Asaro, R. J., and Needleman, A., 1983, "Material Rate Dependence and Localized Deformation in Crystalline Solids," *Acta Metallurgica*, Vol. 31, pp. 1951–1976.

Peirce, D., Shih, C. F., and Needleman, A., 1984, "A Tangent Modulus Method for Rate Independent Solids," *Computers and Structures*, Vol. 18, pp. 875–887.

Randle, V., and Ralph, B., 1988, "Applications of Grain Boundary Engineering to Anamolous Grain Growth," *Interfacial Structure, Properties and Design*, Vol. 122, M. H. Yoo et al., eds., MRS, Pittsburgh, pp. 419–424.

Rey, C., and Zaoui, A., 1980, "Slip Heterogeneities in Deformed Aluminum Bicrystals," *Acta Metallurgica*, Vol. 28, pp. 687–697.

Rice, J. R., 1971, "Inelastic Constitutive Relations for Solids: An Internal-Variable Theory and Its Application to Metal Plasticity," *Journal of the Mechanics and Physics of Solids*, Vol. 19, pp. 443–455.

Rice, J. R., 1987, "Tensile Crack Tip Fields in Elastic-Ideally Plastic Crystals," *Mechanics of Materials*, Vol. 6, pp. 317–335.

Rice, J. R., Suo, Z., and Wang, J.-S., 1990, "Mechanics and Thermodynamics of Brittle Interfacial Failure in Bimaterial Systems," *Proceedings of Acta/Scripta Metallurgical Conference on Bonding, Structure and Mechanical Properties of Metal/Ceramic Interfaces*, M. Ruhle et al., eds., Pergamon Press, New York, pp. 269–294.

Rice, J. R., and Thomson, R., 1974, "Ductile Versus Brittle Behaviour of Crystals," *Philosophical Magazine*, Vol. 29, pp. 73–97.

Saeedvafa, M., and Rice, J. R., 1990, work in progress, Harvard University.

Teodosiu, C., 1970, "A Dynamic Theory of Dislocations and its Applications to the Theory of Elastic-Plastic Continuum," *Fundamental Aspects of Dislocation Theory*, Vol. II, J. A. Simmons et al., eds., U.S. National Bureau of Standards U.S. Special Publication, pp. 837–876.

Wang, J.-S., and Anderson, P., 1991, "Fracture Behaviour of Embrittled F.C.C. Metal Bicrystals," *Acta Metallurgica*, Vol. 39, pp. 779–792.

Watanabe, T., 1988, "The Importance of Grain Boundary Character Distribution to Grain Boundary Design," *Interfacial Structure, Properties and Design*, Vol. 122, M. H. Yoo et al., eds., MRS, Pittsburgh, pp. 443–454.

Wu, T.-Y., Bassani, J. L., and Laird, C., 1991, "Latent Hardening in Single Crystals: Part 1, Experimental Characterization," *Proceedings of Royal Society of London*, Vol. A435, pp. 1–19.

Downloaded 03 May 2010 to 171.66.16.247. Redistribution subject to ASME license or copyright; see http://www.asme.org/terms/Terms_Use.cfm

K.-C. Wu
Institute of Applied Mechanics,
National Taiwan University,
Taipei, Taiwan 10764

On the Contact Zone Model for Interface Cracks

1 Introduction

Comninou (1977, 1978, 1979) proposed a model in which frictionless contact zones are admitted near the tips of an interface crack in an isotropic bimaterial. It was found that the stress field exhibits a square root singularity close to the crack tips. Recently, Gautesen and Dundurs (1988) showed the integral equation formulated by Comninou could be solved exactly. Gautesen and Dundurs (1988) noted that the values of the stress intensity factors they obtained agree well with the numerical results given by Comninou (1979) for the crack tip associated with large contact zones. The agreement is poor, however, for the crack tip with very small contact zones. The model proposed by Comninou (1977) was applied to the anisotropic interface crack by Wang and Choi (1983a, 1983b). Their numerical result indicated similar features as those observed for isotropic interface cracks.

In this paper we examine the stress and displacement fields near the tip of an interface crack in an anisotropic bimaterial. We show that accurate approximations for the stress intensity factors can be derived for the class of bimaterials in which the in-plane shear deformation and antiplane shear deformation are uncoupled.

2 Crack-Tip Fields

Consider a semi-infinite interface crack between materials I and II in an infinite body as shown in Fig. 1. The boundary conditions on the crack faces are described by

$$\frac{\partial \Delta u_2}{\partial x_1} = 0$$

$$T_1 = T_3 = 0. \tag{1}$$

In the following discussions, a complex matrix $\mathbf{N}$ plays an important role. The matrix $\mathbf{N}$ is related to the elastic constants for both the upper and the lower materials and can be expressed as (Wu, 1990)

$$\mathbf{N} = \tilde{\mathbf{W}} + i\tilde{\mathbf{D}} \tag{2}$$

where $\tilde{\mathbf{W}}$ is antisymmetric and $\tilde{\mathbf{D}}$ is symmetric. Using the Stroh formalism (1958) with the technique of continuation of analytic functions (Clements, 1971), one can show that the stresses and displacements along the crack line can be obtained from those for a plane-strain traction-free interface crack problem considered by Wu (1990) by changing the index 2 to 3.

Ahead of the crack, the stress $\mathbf{s} = (\sigma_{12}, \sigma_{32})$ is given by

$$\mathbf{s} = \frac{1}{\sqrt{2\pi r}} \hat{\mathbf{R}} \left[\left(\frac{r}{l} \right)^{i\hat{\gamma}} \right] \hat{\mathbf{K}} \tag{3}$$

where the matrix $\hat{\mathbf{R}}$ is given by

$$\hat{\mathbf{R}}[c] = \Re[c]\mathbf{I} + \Im[c]\hat{\mathbf{P}} \tag{4}$$

in which

$$\hat{\mathbf{P}} = \frac{1}{\sqrt{\tilde{D}_{11}\tilde{D}_{33} - \tilde{D}_{13}^2}} \begin{pmatrix} -\tilde{D}_{13} & \tilde{D}_{11} \\ -\tilde{D}_{33} & \tilde{D}_{13} \end{pmatrix}, \tag{5}$$

and $\Re$, $\Im$ denote the real and the imaginary part, respectively. The bimaterial constant $\hat{\gamma}$ in Eq. (3) is given by

$$\hat{\gamma} = \frac{1}{2\pi} \log \frac{1+\hat{\beta}}{1-\hat{\beta}} \tag{6}$$

$$\hat{\beta} = \frac{\tilde{W}_{31}}{\sqrt{\tilde{D}_{11}\tilde{D}_{33} - \tilde{D}_{13}^2}}. \tag{7}$$

From Eq. (3) it is seen that for general anisotropic interface cracks, although the crack faces would not overlap, the oscillatory behavior of the stresses is still present in the contact zone model. The inclusion of a contact zone would yield a

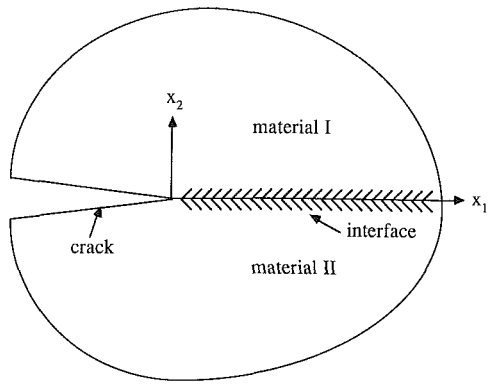

Fig. 1 Semi-infinite interfacial crack between infinite dissimilar anisotropic materials

Contributed by the Applied Mechanics Division of THE AMERICAN SOCIETY OF MECHANICAL ENGINEERS for publication in the JOURNAL OF APPLIED MECHANICS.

Discussion on this paper should be addressed to the Technical Editor, Prof. Leon M. Keer, The Technological Institute, Northwestern University, Evanston, IL 60208, and will be accepted until final publication of the paper itself in the JOURNAL OF APPLIED MECHANICS. Manuscript received by the ASME Applied Mechanics Division, Apr. 1, 1989; final revision, Apr. 16, 1990.

Copyright © 1992 by ASME
Downloaded 03 May 2010 to 171.66.16.247. Redistribution subject to ASME license or copyright; see http://www.asme.org/terms/Terms_Use.cfm

square root stress singularity only for the class of bimaterial systems whose $\hat{\gamma}$ or $\tilde{W}_{31} = 0$. Isotropic bimaterials and fiber-reinforced composites are two examples. The length scale l is required in Eq. (3) to make the argument of $\hat{\mathbf{R}}$ dimensionless. The parameters $\hat{\mathbf{K}}$ are real-valued and have the same dimension of stress times square root of length as the usual stress intensity factors for homogeneous cracks. The parameters, therefore, can be identified as the stress intensity factors for the contact zone model. Note that $\hat{\mathbf{K}}$ contains only two independent parameters, $\hat{K}_{II}$ and $\hat{K}_{III}$, related to in-plane and antiplane shear stresses ahead of the crack. In the contact zone, the relative displacement $\Delta\hat{\mathbf{u}} = (\Delta u_1, \Delta u_3)^T$ is given by

$$\Delta\hat{\mathbf{u}} = \sqrt{\frac{2r}{\pi}}\,\tilde{\mathbf{d}}^{-1}\hat{\mathbf{R}}\left[\frac{\cosh(\pi\hat{\gamma})}{1+2i\hat{\gamma}}\left(\frac{r}{l}\right)^{i\hat{\gamma}}\right]\hat{\mathbf{K}} \tag{8}$$

where $\tilde{\mathbf{d}}$ is the matrix obtained by deleting the second row and column of $\tilde{\mathbf{D}}$. From Eqs. (3) and (8) the energy release rate can be derived as

$$\mathcal{G} = \frac{1}{4}\,\hat{\mathbf{K}}^T\tilde{\mathbf{d}}^{-1}\hat{\mathbf{K}}. \tag{9}$$

3 Approximate Stress Intensity Factors

In problems where tensile loading is dominant, the sizes of contact zones are usually very small compared to the crack length. In these problems, it is expected that the crack-tip fields derived under traction-free conditions are still valid at distances large compared with the size of the contact zone, but small with respect to the crack length. The concept similar to that of small-scale yielding in inelastic fracture mechanics can be applied in the present case. The concept implies that the energy release rate of the traction-free crack-tip fields and that for the contact zone model must be the same. Thus,

$$\mathcal{G} = \frac{1}{4}\,\hat{\mathbf{K}}^T\tilde{\mathbf{d}}^{-1}\hat{\mathbf{K}} = \frac{1}{4}\,\mathbf{K}^T\tilde{\mathbf{D}}^{-1}\mathbf{K} \tag{10}$$

where $\mathbf{K}$ is the stress intensity factor for traction-free interface cracks introduced by Wu (1990). If the in-plane shear deformation and the antiplane shear deformation are uncoupled, $\hat{K}_{II}$ and $\hat{K}_{III}$ can be separately determined by Eq. (10). The concept discussed above has been applied by Park and Earmme (1986) for isotropic interface cracks in a tension field. The energy release rate for traction-free interface cracks in an uniform stress field can be found in (Wu, 1990).

If the interface crack is in a compression-dominant field, existing results (Comninou, 1979; Gautesen and Dundurs, 1988; Wang and Choi, 1983) show that contact zones of the sizes comparable to the crack length are present behind one crack tip accompanied by extremely small contact zones at the other tip. For the tip associated with large contact zones, we can assume that the crack is completely closed. The corresponding stress intensity factors $\hat{K}_{II}$ and $\hat{K}_{III}$ for uniform loading can be shown to be $\sqrt{\pi a}T_1$ and $\sqrt{\pi a}T_3$, respectively, with a being the half crack length.

4 Comparison

Some results obtained by Eq. (10) for an interface crack with length $2a$ under uniform loading are compared to existing results in this section. Before the comparison is made, we first note that the absolute values of the stress intensity factors $\hat{K}_{II}$ or $\hat{K}_{III}$ associated with either crack tip are the same regardless of the sizes of the contact zones and the modes of loading. The fact can be seen by applying the J-integral of Rice (1968) over the contour enclosing the crack. Calculation of the J-integral leads to

$$\mathcal{G}^+ = \mathcal{G}^- \tag{11}$$

where $\mathcal{G}^+$ and $\mathcal{G}^-$ are the energy release rates associated with the right and left tips, respectively. As for the materials considered here, $\hat{K}_{II}$ and $\hat{K}_{III}$ can exist separately. The above equation implies that except for the sign difference, the values of the stress intensity factors are the same for either crack tip. One only needs, therefore, to focus on the right crack tip.

For isotropic bimaterials with $\beta = 0.5$, the values of $\hat{K}_{II}$ scaled by the factor $T_1\sqrt{\pi a}$ are 1.059, 1.080, 1.141, respectively, for $T_2/T_1 = 0$, 0.2, 0.4. The corresponding values obtained by Comninou and Schmueser (1979) and Gautesen and Dundurs (1988) are 1.032, 1.071, and 1.138. Comparison between the approximated values and the exact values shows that the approximation is extremely accurate even for the worst case $T_2 = 0$ where the size of contact zone is $0.658a$. The relative error in that case is about three percent. The fact that approximate values are very close to the exact values suggests that $\hat{K}_{II}$ is a weak function of the size of the contact zone. For the left crack tip, the values of $\hat{K}_{II}/T_1\sqrt{\pi a}$ in the Comninou and Schmueser paper are -0.445, -0.6, and -0.785 for $T_2/T_1 = 0$, 0.2, 0.4, respectively. The corresponding values given by Gautesen and Dundurs are -1.032, -1.070, and -1.136. As discussed previously, aside from the sign, the values of the stress intensity should be the same as those for the right crack tip. It appears that the values obtained by Comninou and Schmueser are erroneous and the correct results are given by Gautesen and Dundurs. For loading with compressive component, the results of Gautesen and Dundurs show that the sizes of the contact zones for compression-shear loading are greater than a in general for the right tip. Thus, for such loading, the large contact zone approximation can be used to yield approximate values for the stress intensity factors. The values of $\hat{K}_{II}/T_1\sqrt{\pi a}$ for $T_2/T_1 = -0.4$, -0.2, 0, and $\beta = 0.5$ in Gautesen and Dundurs paper are 1.008, 1.015, and 1.032. The agreement between the exact values and the approximate value, 1, is close.

We next compare our approximations to the numerical results given by Wang and Choi (1983a, 1983b) for a ± 45-deg anisotropic composite. The corresponding value of γ is 0.03434. In the case of pure tension, the energy release rate for the traction-free interface crack is $1.4(T_2^2 a/E)$. The value agrees with that given by Wang and Choi (1983a). The approximate value of the stress intensity factor $\hat{K}_{III}/\sqrt{\pi a}T_2$ is calculated to be 1.151. However, the value given in the Wang and Choi paper is 0.4163. It is believed that the value obtained by Wang and Choi is questionable. For combinations of T_2 and T_3, the stress intensity factor is

$$\frac{\hat{K}_{III}}{T_3\sqrt{\pi a}} = \sqrt{(1+4\gamma^2)\left[1+1.318\left(\frac{T_2}{T_3}\right)^2\right]} \tag{12}$$

for $T_2 > 0$. For $T_2 < 0$, the approximate stress intensity factor is given by $T_3\sqrt{\pi a}$. The values calculated using the above equations are in close agreement with numerical values obtained by Wang and Choi (1983b) for the right crack tip over the range of T_2/T_3 ratios shown in Fig. 5 in their paper.

References

Clements, D. L., 1971, "A Crack between Dissimilar Anisotropic Media," *Int. J. Eng. Sci.*, Vol. 9, pp. 257–265.

Comninou, M., 1977, "The Interface Crack," ASME JOURNAL OF APPLIED MECHANICS, Vol. 44, pp. 631–636.

Comninou, M., 1978, "The Interface Crack in a Shear Field," ASME JOURNAL OF APPLIED MECHANICS, Vol. 45, pp. 287–290.

Comninou, M., and Schmueser, D., 1979, "The Interface Crack in a Combined Tension-compression and Shear Field," ASME JOURNAL OF APPLIED MECHANICS, Vol. 46, pp. 345–358.

Gautesen, A. K., and Dundurs, J., 1988, "The Interface Crack Under Combined Loading," ASME JOURNAL OF APPLIED MECHANICS, Vol. 55, pp. 580–586.

Downloaded 03 May 2010 to 171.66.16.247. Redistribution subject to ASME license or copyright; see http://www.asme.org/terms/Terms_Use.cfm

Park, J. H., and Earmme, Y. Y., 1986, "Application of Conservation Integrals to Interfacial Crack Problems," *Mechanics of Materials*, Vol. 5, pp. 261–276.

Rice, J. R., 1968, "A Path Independent Integral and the Approximate Analysis of Strain Concentration by Notches and Cracks," ASME JOURNAL OF APPLIED MECHANICS, Vol. 35, p. 379.

Stroh, A. N., 1958, "Dislocations and Cracks in Anisotropic Elasticity," *Philos. Mag.*, Vol. 7, pp. 625–646.

Wang, S. S., and Choi, I., 1983a, "The Interface Crack between Dissimilar Anisotropic Materials," ASME JOURNAL OF APPLIED MECHANICS, Vol. 50, pp. 169–178.

Wang, S. S., and Choi, I., 1983b, "The Interface Crack Behavior in Dissimilar Anisotropic Composites Under Mixed Loading," ASME JOURNAL OF APPLIED MECHANICS, Vol. 50, pp. 179–183.

Wu, K. C., 1990, "Stress Intensity Factor and Energy Release Rate for Interfacial Cracks Between Dissimilar Anisotropic Materials," ASME JOURNAL OF APPLIED MECHANICS, Vol. 57, pp. 882–886.

Downloaded 03 May 2010 to 171.66.16.247. Redistribution subject to ASME license or copyright; see http://www.asme.org/terms/Terms_Use.cfm

Crack-Tip Stress and Deformation Fields in Strain-Softening Nonlinearly Viscoelastic Materials

B. Moran
Department of Civil Engineering,
Northwestern University,
Evanston, IL 60208
Assoc. Mem. ASME

W. G. Knauss
Graduate Aeronautical Laboratories,
California Institute of Technology,
Pasadena, CA 91125
Fellow ASME

In some polymers, stress-induced changes in molecular mobility give rise to a strain-softening effect. The influence of this effect on the stress and deformation fields near a crack tip are examined using the finite element method. A phenomenological nonlinearly viscoelastic constitutive model (based on the concept of free volume) is used in the calculations. When a load is suddenly applied to a cracked specimen, the instantaneous response of the material is linearly elastic. However, strain-induced softening in the crack-tip region leads to a relaxation in the stress and time variation of the region over which the singular field prevails. For realistic material parameters, this region may become extremely small. In addition, a zone of strain-softened material emanantes from the crack tip and extends along the crack line. This process zone can promote conditions which are favorable for the nucleation and growth of microvoids and the formation of crazes.

1 Introduction

The increasing use of polymers in engineering design is largely due to their high strength to weight ratio and to their corrosion resistance. While polymers offer these advantages over traditional metallic materials, their characteristic time-dependent behavior may lead to excessive creep and/or failure. Thus, the long-term strength of a polymeric component is influenced by its nonlinearly viscoelastic response and the accompanying time-dependent crack growth. Analytical and numerical studies on the fracture behavior of polymers are limited. The time-dependent aspects of fracture in polymers are discussed in the reviews by Knauss (1973, 1989). Much of the work has been confined to the cases of linearly viscoelastic material despite the fact that many polymers exhibit highly nonlinear behavior and may undergo considerable strain softening in the presence of stress or strain concentrations. The role of strain softening in the mechanical behavior of polymers has been recognized by Gent (1960) who proposed a mechanism for craze formation in glassy polymers on the basis of a stress-activated devitrifaction of the material in the vicinity of a nick of a flaw. Argon and Salama (1977), discuss the role of a Taylor-type instability associated with viscous flow of the material in the formation of crazes. Recently, Robertson et al. (1989) refer to the phenomenon of liquefaction and its influence on crack growth patterns in polymeric materials.

In this paper, the near crack-tip stress and deformation fields have been investigated for a class of nonlinearly viscoelastic materials that exhibit strain softening in regions of stress concentration. The class of materials considered may be loosely referred to as *rheologically simple* whereby stress-induced changes in molecular mobility are modeled using the free volume concept discussed by Knauss and Emri (1981, 1987). These materials are highly nonlinear and exhibit a so-called *yield phenomenon* and a strain-softening response. Possible consequences of strain softening are the localization of deformation (shear bands), the nucleation and growth of voids and the onset of crazing. It is important, therefore, to gain an understanding of the nature of the crack-tip stress and deformation fields in these materials as a precursor to failure.

In the present analysis, we examine the crack-tip fields for such a nonlinear but rheologically simple material. The finite element method is used to simulate the time-dependent response of a center crack panel under step-loading conditions. We first consider a simple standard nonlinear solid constitutive model and then a model which simulates the behavior of polyvinyl acetate (PVAc). The time dependence of the crack-tip stress fields is illustrated and shown to depend on the strain-softening behavior of the material. In addition, a thin zone of strain-softened material emanates from the crack tip. The stress state in this zone is shown to be hydrostatic, which may promote the nucleation and growth of microvoids or the initiation of crazes.

2 Constitutive Model

Based on experimental studies, Knauss and Emri (1981, 1987) proposed a constitutive model for nonlinearly viscoelastic materials based on the concept of free volume. The material nonlinearity enters the constitutive description through the

Contributed by the Applied Mechanics Division of THE AMERICAN SOCIETY OF MECHANICAL ENGINEERS for publication in the JOURNAL OF APPLIED MECHANICS.

Discussion on this paper should be addressed to the Technical Editor, Professor Leon M. Keer, The Technological Institute, Northwestern University, Evanston, IL 60208, and will be accepted until two months after final publication of the paper itself in the JOURNAL OF APPLIED MECHANICS. Manuscript received by the ASME Applied Mechanics Division, Dec. 28, 1989; final revision, Mar. 4, 1991.

Copyright © 1992 by ASME
Downloaded 03 May 2010 to 171.66.16.247. Redistribution subject to ASME license or copyright; see http://www.asme.org/terms/Terms_Use.cfm

time shift factor, ϕ, which is a function of the free volume expressed in terms of the Doolittle-type equation (Ferry, 1980)

$$\log_{10}\phi = \frac{b}{2.303}\left(\frac{1}{f}-\frac{1}{f_0}\right) \tag{1}$$

where f is the (fractional) free volume, f_0 is the free volume at some suitably chosen reference state, and b is a material parameter. The free-volume concept provides a unifying basis for incorporation of the effects of temperature, solvent concentration, and mechanical dilatation on the time-dependent response of many polymers (Knauss and Emri, 1987). In the present analysis, only the influence of mechanically induced aging is considered and an expression for the free volume is written as

$$f = f_0 + \delta\epsilon_{kk} \tag{2}$$

where δ is a material parameter which may be taken to be unity for the materials under consideration here (Knauss and Emri, 1981) and ϵ_{kk} is the volumetric strain. The summation convention is employed for repeated indices.

Based on the approach introduced by Morland and Lee (1960), the time-shift factor is used to define an internal (also referred to as reduced or intrinsic) time, $\zeta(t)$, as follows:

$$d\zeta(t) = \frac{dt}{\phi(\epsilon_{kk}(t))} \quad \text{and} \quad \zeta(t) = \int_0^t \frac{dt'}{\phi(\epsilon_{kk}(t'))}. \tag{3}$$

The stress may then be represented as a convolution integral of the form

$$s_{ij} = 2\int_{-\infty}^{t} \mu(\zeta(t)-\zeta(t'))\frac{\partial e_{ij}(t')}{\partial t'}\,dt'$$

$$\sigma_{kk} = 3\int_{-\infty}^{t} k(\zeta(t)-\zeta(t'))\frac{\partial \epsilon_{kk}(t')}{\partial t'}\,dt' \tag{4}$$

where $s_{ij} = \sigma_{ij} - (\sigma_{kk}/3)\delta_{ij}$ is the deviatoric stress, $\sigma_{kk}/3$ is the hydrostatic stress and $e_{ij} = \epsilon_{ij} - (\epsilon_{kk}/3)\delta_{ij}$ is the deviatoric strain. It is noted that the expressions (4) differ from their linearly viscoelastic counterparts through the dependence of the kernels μ and k on the internal rather than the actual (laboratory) time. In (4) the material has been taken to be isotropic and μ and k may be identified with the shear and bulk relaxation moduli, respectively. In many polymers, the relaxation moduli may be represented by a finite Dirichlet series of exponential relaxation functions (generalized Maxwell model) i.e.,

$$k(t) = \sum_{i=1}^{N_b} k^i \exp(-t/\tau_i^b)$$

$$\mu(t) = \sum_{i=1}^{N_s} \mu^i \exp(-t/\tau_i^s) \tag{5}$$

where k_i and μ_i are the bulk and shear moduli of the elements in the series and τ_i^b and τ_i^s are the corresponding relaxation times. The number of elements in the series representations of the bulk and shear moduli are denoted by N_b and N_s, respectively. For a crosslinked polymer (viscoelastic *solid*), one of the relaxation times will be infinite in each of the series above.

A solution procedure for the thermomechanical analysis of nonlinearly viscoelastic solids using constitutive relations of the form (1)–(4) has been discussed by Taylor, Pister, and Goudreau (1970). The finite element formulation used in the present analysis is based upon a modified version of this procedure. Details of the method, along with some numerical examples, are given in the report by Moran and Knauss (1989).

3 Crack-Tip Fields

To examine the crack-tip behavior, we consider a center-cracked panel under plane-strain conditions, subjected to a step loading (see Fig. 1). Let the origin of a rectangular cartesian coordinate system be at the center of the crack with the crack oriented along the x-axis. Note that $a/b = 0.01$, where a is the half crack length and b is the half width of the specimen. The smallest element has a dimension of the order $a/100$ and for a crack dimension of $a = 1$ mm, say, the smallest element is approximately 10 μm in length. From symmetry, only one quarter of the panel needs to be analyzed. The applied traction is specified as

$$T_y(x,b) = \sigma_0 H(t), \quad 0 \le x \le b \tag{6}$$

where $H(t)$ is the heaviside operator. The initial response is therefore characterized by the elastic state $(u_i^0, \epsilon_{ij}^0, \sigma_{ij}^0)$ (Gurtin and Sternberg, 1962). At time $t = 0^+$, the crack-tip stress field is written as

$$\sigma_{ij}^0 \sim \frac{K_I}{\sqrt{2\pi r}}\tilde{\sigma}_{ij}(\theta) \quad \text{as } r \to 0 \tag{7}$$

where r and θ are polar coordinates centered at the crack tip and K_I is the mode I stress intensity factor.

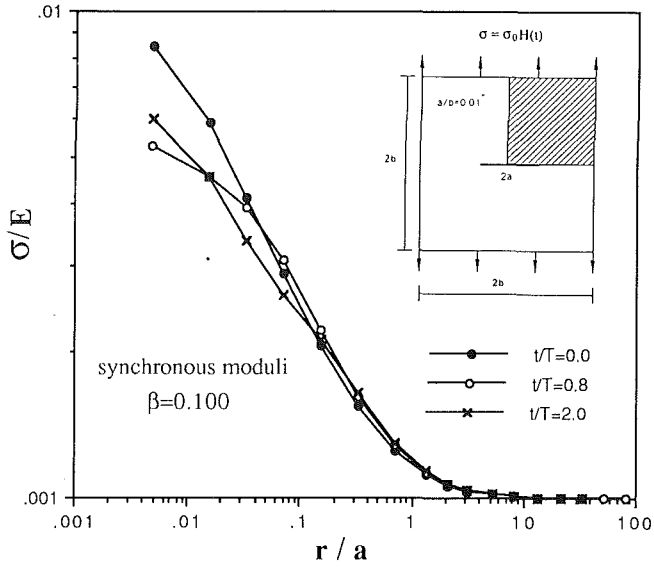

Fig. 1(*a*)

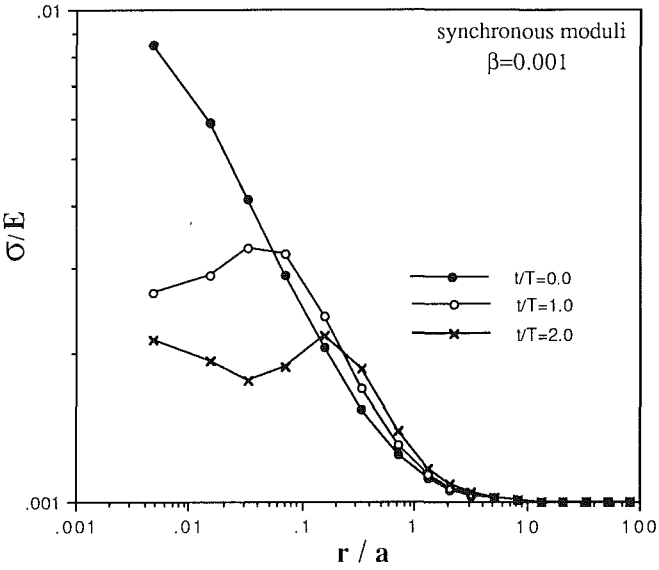

Fig. 1(*b*)

Fig. 1 Normalized opening stress, σ_{yy}/E at different times—two-element model, (*a*) $\beta = 0.1$, (*b*) $\beta = 0.001$

Downloaded 03 May 2010 to 171.66.16.247. Redistribution subject to ASME license or copyright; see http://www.asme.org/terms/Terms_Use.cfm

If the material were linearly viscoelastic, a well-known result in viscoelasticity theory shows that the stress and strain fields at subsequent times are given by

$$\sigma_{ij}(x,y,t)=\sigma^0_{ij}(x,y), \quad \epsilon_{ij}(x,y,t)=s_{ij}*dJ_1+\frac{1}{3}\sigma_{kk}\delta_{ij}*dJ_2 \qquad (8)$$

where * denotes convolution and J_1 and J_2 are the deviatoric and bulk creep compliances, respectively. Thus, under these loading conditions, the crack-tip stress field is completely characterized by the stress intensity factor K_I and the strains evolve according to the creep compliances. If K_I is time dependent, it can be computed using a path-independent integral in the Laplace transformed domain (Nilsson, 1973). An alternative representation in the time domain has been given by Jiang (1986).

In this analysis, the material is nonlinearly viscoelastic. The instantaneous response of the material to a step is linearly elastic, however, and the initial stress distribution is given by (7). The nonlinearity enters through the time-shift factor ϕ which depends on the free volume, f. The initial elastic state thus determines the initial spatial distribution of the free volume. Furthermore, the material in the crack-tip region attains a rubbery state immediately upon loading since the crack-tip strains are infinite and the time-shift factor reduces to the constant value

$$\bar{\phi}=\exp(-b/f_0). \qquad (9)$$

The material in the crack-tip region thus behaves as a linearly viscoelastic material with reduced relaxation times, $\bar{\phi}\tau_i$, in Eq. (5), although the surrounding material is nonlinear. The crack-tip stress field is thus expected to take the form (7) with a time-varying stress intensity factor, K_I. A question of some significance is whether the singular field prevails over a physically meaningful distance. If the computed stress fields agree with the analytic form (7) (to within a few percent) and if this characterization extends over a physically meaningful distance from the crack, we say that the crack-tip fields are K dominated. For the center crack panel, the initial region of K-dominance is about $a/10$. Thus, for a half-crack length of $a=1$ mm, say, the region of K-dominance would be approximately 100 μm.

The strain-softening at the crack tip leads to an immediate relaxation of the crack-tip stresses with an associated reduction in the stress intensity factor, K_I. Thus,

$$\sigma_{ij}\sim\frac{K_I(t)}{\sqrt{2\pi r}}\tilde{\sigma}_{ij}(\theta)$$

$$\epsilon_{ij}\sim s_{ij}*d\bar{J}_2+\frac{1}{3}\sigma_{kk}\delta_{ij}*d\bar{J}_2 \quad \text{as } r\to 0 \qquad (10)$$

where now $\bar{J}_1$ and $\bar{J}_2$ are the creep compliances evaluated using the reduced relaxation times, $\bar{\phi}\tau_i$. At long times, for a cross-linked polymer, the relaxation moduli approach their rubbery limits throughout the specimen and thus

$$\sigma_{ij}(x,y,\infty)\to\sigma^0_{ij}(x,y). \qquad (11)$$

Between the short and long-time extremes, the time dependence of the crack-tip stress fields is influenced strongly by the strain-softening characteristics of the material. This will be discussed further in Sections 3.1 and 3.2.

The behavior here differs from that observed in power-law creeping materials (e.g., Reidel and Rice, 1980) where creep strain rates dominate at the crack tip and an HRR field, characterized by the time-dependent creep integral $C(t)$ develops. We note that Schapery (1990) discusses a path-independent integral, J_v, for a class of nonlinearly viscoelastic materials which can be described by a single herediatary integral. By limiting the dependence of the time-shift factor on the stress or by choosing specific power-law forms for the constitutive response, Schapery shows that J_v is path independent for materials with constitutive equations based on a reduced time, and is a candidate parameter for the characterization of the crack-tip fields. Since the constitutive model used here does not fall into this category, we have not attempted to employ the J_v-integral.

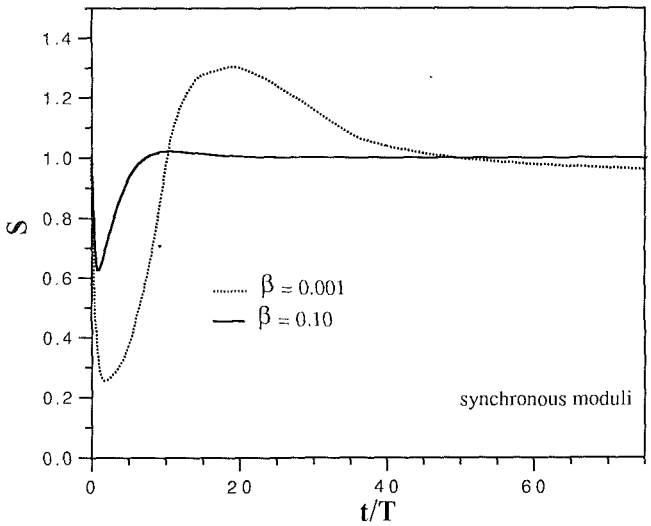

Fig. 2 Time variation of normalized stress, $S=\sigma_{yy}(t)/\sigma_{yy}(0)$, in crack-tip element, $r/a=0.005$—two-element model

3.1 Numerical Results: Standard Nonlinear Solid. Initially, we consider a simple constitutive model given by a two-term representation of the generalized Maxwell model (5), which we refer to as a standard nonlinear solid. The relaxation moduli are given by

$$k(t)=k_\infty+k_1\exp(-t/\tau_1^b)$$
$$\mu(t)=\mu_\infty+\mu_1\exp(-t/\tau_1^s). \qquad (12)$$

We choose the ratio of the long-time to initial moduli of the material to be equivalent in bulk and shear and introduce the parameter $\beta=k_\infty/(k_\infty+k_1)=\mu_\infty/(\mu_\infty+\mu_1)$. Note that $\beta=0$ corresponds to a Maxwell element while $\beta=1$ represents an elastic solid. The time-shift parameters are chosen as $f_0=0.01$ and $b=0.05$. The normalized applied stress has a value of $\sigma_0/E=10f_0$ where E is the initial (glassy) Young's modulus. These parameters were chosen for illustrative purposes and are representative of a moderately strain-softening polymer. While the standard nonlinear solid is a very simple constitutive model, it does provide some insight into the time dependence of the crack-tip stress field.

The normalized mode I opening stress σ_{yy}/E along the crack line, $y=0$, is plotted in Fig. 1(a), for the case $\beta=0.1$ and for synchronous moduli; i.e., $\tau_1^s=\tau_1^b=T$. The same quantities are plotted in Fig. 1(b) for the case $\beta=0.001$ whereby the response of the standard nonlinear solid approximates that of a nonlinear Maxwell model. In Fig. 2, the normalized stress, $S=\sigma_{yy}(t)/\sigma_{yy}(0)$, in the near-tip element ($r/a=0.005$) is plotted against normalized time, t/T, for both $\beta=0.1$ and $\beta=0.001$.

The transient nature of the stresses evident in these figures is explained as follows: At $t/T=0$, the stress field takes the singular form (7). The instantaneous reduction in the viscosity or relaxation times (see Eq. (9)) of the material in the crack-tip region and the constraint from the surrounding more viscous material causes relaxation of the crack-tip stresses as illustrated in Figs. 1(a) and 1(b). Since overall equilibrium must be satisfied, the stress drop at the crack tip must be equilibrated elsewhere and a "travelling stress hump" develops which travels away from the crack tip with a speed dependent upon the relaxation times of the material (see also Knauss,

Downloaded 03 May 2010 to 171.66.16.247. Redistribution subject to ASME license or copyright; see http://www.asme.org/terms/Terms_Use.cfm

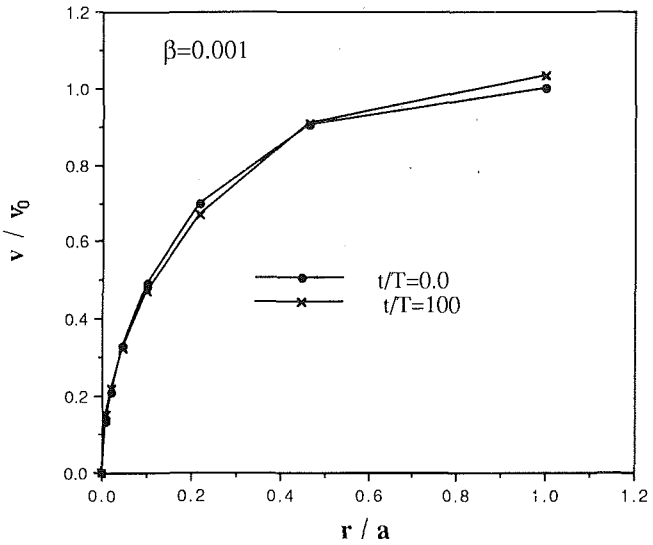

Fig. 3 Normalized crack-opening profiles for $\beta = 0.1$ and $\beta = 0.001$—two-element model

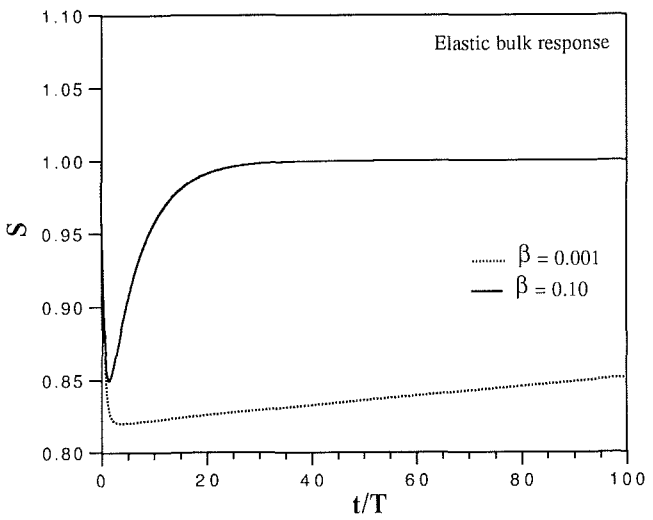

Fig. 4 Time variation of opening stress in crack-tip element ($r/a = 0.005$)—two-element model with elastic bulk modulus

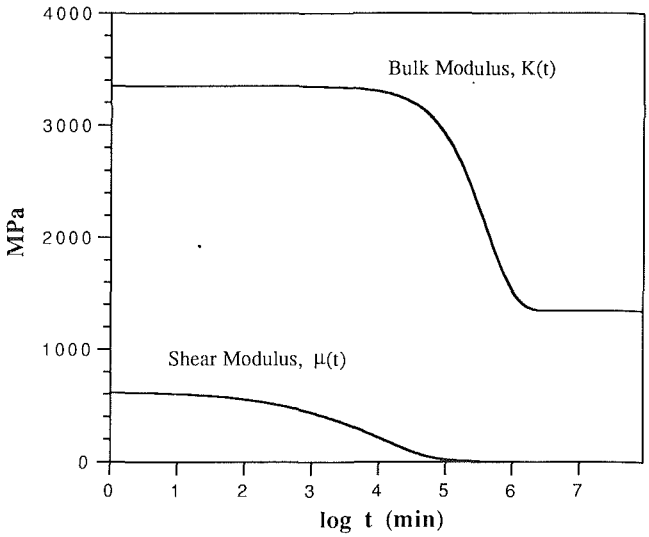

Fig. 5 Bulk and shear relaxation moduli for PVAc

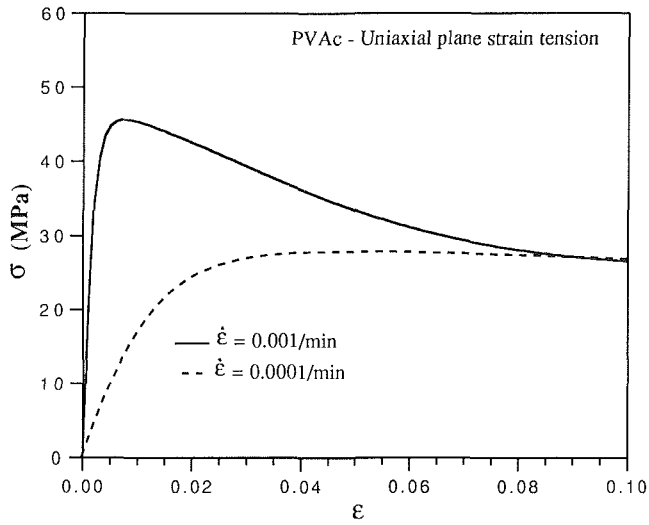

Fig. 6 Stress-strain curves for PVAc—uniaxial plane-strain tension

1989). When this "stress hump" reaches the edge of the specimen, a further stress redistribution occurs producing a rise in the crack-tip stresses. Depending upon the material properties, this stress rise may be accompanied by an overshoot. This is most evident in Fig. 2, where, for $\beta = 0.001$, an overshoot of approximately 30 percent follows the initial stress relaxation.

It can be seen from Fig. 1 that the time-dependent region of dominance of the singular fields (or so-called region of K-dominance) is significantly different for the two cases considered. For $\beta = 0.1$, the extent of the region of K-dominance does not vary much from the initial value of approximately $r/a = 0.1$—which is well resolved by our finite element mesh. The time variation of the stress intensity factor thus approximately follows the time variation of the crack-tip stress as given by the solid line in Fig. 2.[1] For $\beta = 0.001$, however, the region of K-dominance is not resolved by the mesh and can be said to be smaller than $r/a = 0.005$. (Note that it is certainly possible to resolve the near-tip field in this latter case by refining the near-tip mesh. A different choice of β may require additional refinement and so on. Our aim here is to illustrate that for small values of β the region of K-dominance is small compared to the crack length.)

The crack opening profile is shown in Fig. 3 for the case $\beta = 0.001$ and for two times, $t/T = 0.0$ and $t/T = 100$. The opening displacement v has been normalized with respect to the quantity v_0, where v_0 is the crack-opening displacement at the center of the panel, for $t/T = 0$, and β^{-1} times this quantity for $t/T = 100$. The normalized profiles are virtually conicident, which illustrates that at long times, the response approaches that of a linearly elastic solid with moduli k_∞ and μ_∞. A time step of $\Delta t = 0.2T$ was used in the above calculations.

To illustrate the influence of the bulk modulus on the nonlinear response, calculations for a two-element model of the form (12) with $\tau_1^b = \infty$ (elastic bulk modulus) were carried out. The normalized stress $S = \sigma_{yy}(t)/\sigma_{yy}(0)$ in the crack-tip element ($r/a = 0.005$) is plotted for the two values of β. The stress recovery for $\beta = 0.001$ takes place much more slowly than for the analogous case with synchronous moduli. In addition, the stress overshoot, evident in Fig. 2, for $\beta = 0.001$, where the bulk modulus is nonlinearly viscoelastic, is not present.

3.2 Numerical Results: Material Model Simulating PVAc. The constitutive model used to simulate the response of polyvinyl acetate (PVAc), an uncrosslinked polymer, is given

[1]Calculations for small-scale creep, not shown here, confirm that the initial time variation of K_I is well approximated by the time variation of the near-tip stress field.

Downloaded 03 May 2010 to 171.66.16.247. Redistribution subject to ASME license or copyright; see http://www.asme.org/terms/Terms_Use.cfm

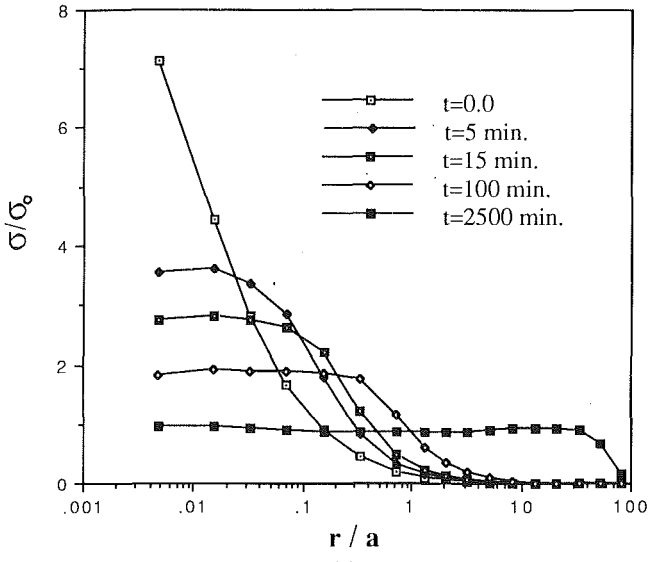

Fig. 7(*a*)

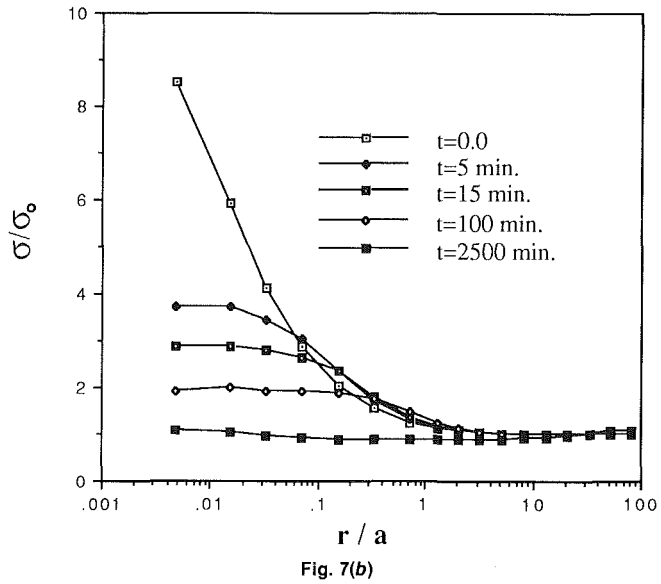

Fig. 7(*b*)

Fig. 7 Stress acting on crack line at different times—PVAc material model, (*a*) σ_{xx}, (*b*) σ_{yy}

by Knauss and Emri (1981). The bulk and shear relaxation moduli for the reference temperature of 26.5°C are shown in Fig. 5. Note that the glass transition temperature is approximately 28°C for PVAc. The time-shift parameters are given by $f_0 = 0.01$ and $b = 0.16$ (Knauss and Emri, 1981). A time step of $\Delta t = 1.0$ min was used in the calculations. Stress-strain curves for uniaxial plane-strain tension are shown in Fig. 6, illustrating the strain softening response of the material and the so-called *yield phenomenon*.

In Figs. 7(*a*) and 7(*b*), the stresses σ_{xx} and σ_{yy} are plotted as a function of distance from the crack tip for times $t = 0$, 5, 15, 100, and 2500 min. Note that a significant stress relaxation in the crack-tip region is evident in each of these figures and that the stress field approaches a hydrostatic state ($\sigma_{xx} = \sigma_{yy}$) as time progresses and that at $t = 2500$ min, the stress is nearly constant along the crack line to a distance of approximately $r/a = 40$. As will be seen, the evolution of this stress distribution corresponds to the development of a thin zone of strain-softened material ahead of the crack. Apart from the initial elastic response, no region of K-dominance is evident here for the times considered and thus the singular crack-tip stress fields prevail over a distance which is significantly less than $r/a = 0.005$ (the size of the near-tip element). For realistic values of crack length a, the region of K-dominance will be of submicron dimension and smaller than the expected size of the process zone and the zone of finite strains. This would appear to rule out a stress-intensity-based characterization of fracture initiation for this material.

Contour plots of normalized effective stress, $\bar{\sigma}/\sigma_0$, where $\bar{\sigma} = [3 S_{ij} S_{ij}/2]^{1/2}$, and σ_0 is the applied stress of 20 MPa, are shown in Fig. 8, for times $t = 5$, 100, and 2500 min. In these figures, a lobe or thin band of strain-softened material, where $\bar{\sigma}/\sigma_0 < 1$, is evident. Within this lobe, and close to the crack, the effective stress has all but vanished. Thus, the stress state is virtually hydrostatic which can promote the cavitation and subsequent growth of microvoids and the development of a "primordial craze." Note that Gent (1960) proposes that "crazing is the inevitable consequence of thin-band softening." At time $t = 2500$ min, the lobe has extended across the entire specimen.

At $t = 100$ min, creep strains in the crack-tip region are some 50 times larger than the original elastic strains. It is to be expected that some micromechanical failure process would become operative at large strains and that finite strains should be accounted for in future work. There is no tendency for stress recovery at these times for this material model and thus, given the strain magnitudes, the stress recovery and overshoot phenomenon encountered with the two-element model would appear to play no role in a creep failure initiation process for a PVAc-like material. A normalized crack-opening profile is shown in Fig. 9. Apart from a slight peak in the profile close to the crack, the crack-opening displacement is virtually constant along the entire crack length, which is a manifestation of the intense blunting accompanying the crack-tip deformation.

The evolution of the damage (or softening) zone can be estimated by considering the distribution of internal time ζ as a function of real-time t. The internal time profile along the crack line is shown in Fig. 10 for different times t. We arbitrarily define the extent of the softening zone as the length of the region ahead of the crack tip over which the internal time exceeds the bulk relaxation time $\tau_1^b = 4.0 \times 10^5$ min (Knauss and Emri, 1981). These distances are read from Fig. 10 (dashed line) and plotted against real time t in Fig. 11. It is noted that the points fall on a nearly straight line on a log-log plot with slope close to unity, indicating that the evolution of the softening zone is approximately steady state. The mesh employed in these calculations is rather coarse outside of the immediate crack-tip region and Fig. 9 is intended to give only a representative view of the growth of the softening zone.

4 Discussion and Conclusions

An attempt has been made to gain an understanding of the nature of the crack-tip stress and deformation fields in strain-softening nonlinearly viscoelastic solids. We have considered an idealized two-element model and a physically representative material model for polyvinyl acetate. We have argued that the asymptotic behavior at the crack tip is that of a linearly viscoelastic material with a viscosity reduced from that of the bulk material. The near-tip behavior is thus expected to have the form (7) with a time-dependent stress-intensity factor. The time variation of the region of so-called K-dominance is greatly influenced by the material properties and for the PVAc material model, it is reduced to several orders of magnitude below the crack size and well below the expected size of a process zone and the zone of finite strains. This rules out a stress-intensity-based characterization of the fracture initiation process.

Some general conclusions regarding the fracture behavior

Downloaded 03 May 2010 to 171.66.16.247. Redistribution subject to ASME license or copyright; see http://www.asme.org/terms/Terms_Use.cfm

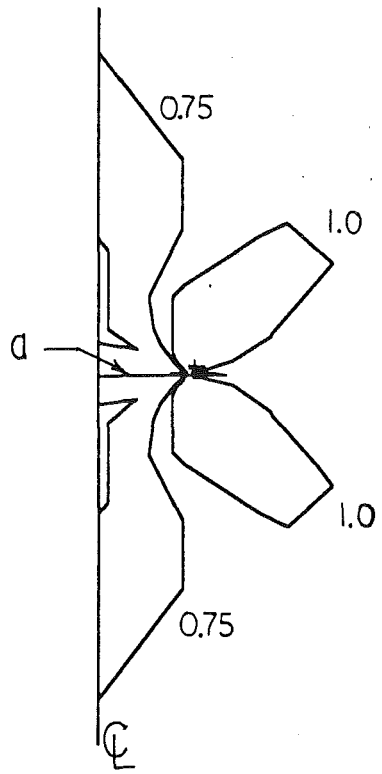

Fig. 8(*a*)

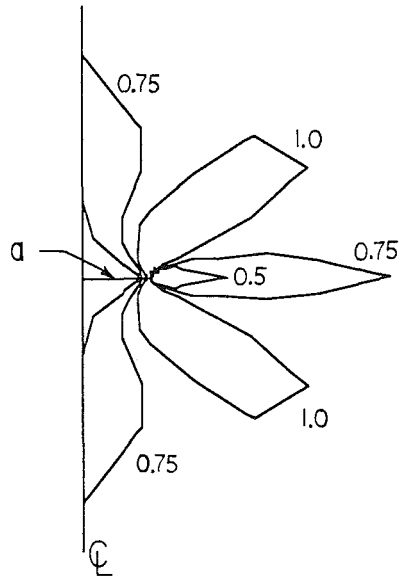

Fig. 8(*b*)

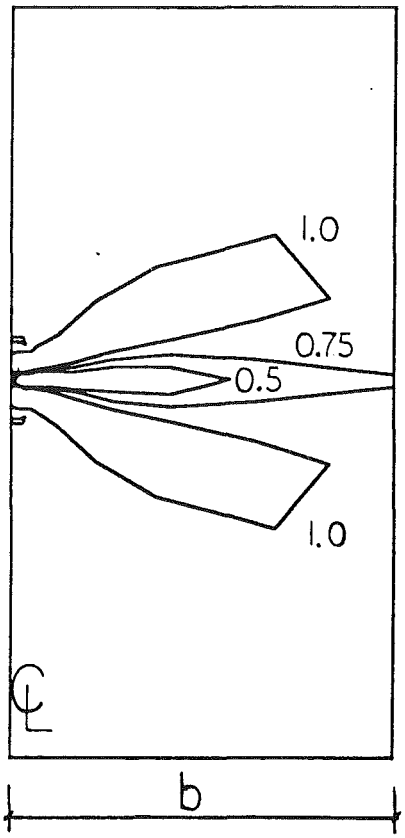

Fig. 8(*c*)

Fig. 8 Contour plots of normalized effective stress, $\bar{\sigma}/\sigma_0$ at (*a*) $t = 5$ min, (*b*) $t = 100$ min, and (*c*) $t = 2500$ min—PVAc

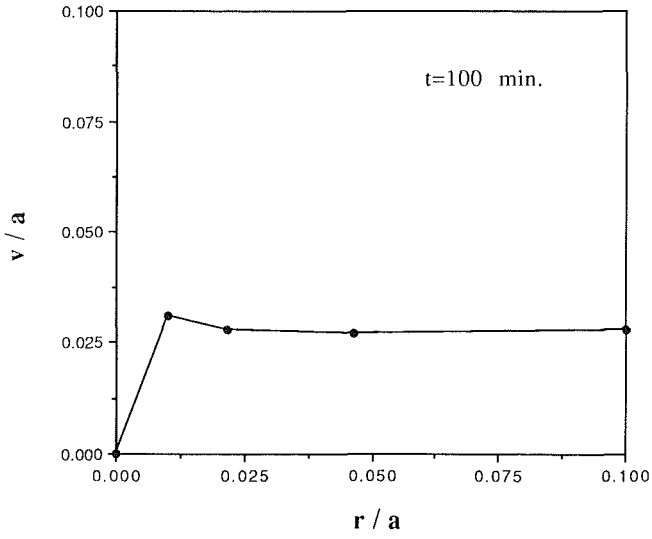

Fig. 9 Normalized crack-opening profile, $t = 100$ min—PVAc

of these materials can be drawn from these calculations. We note that the importance of strain-softening at stress or strain concentrations in glassy polymers has been emphasized by Gent (1960). The numerical results presented in this paper indicate the development of a thin zone of strain-softened material associated with the devitrification of the material ahead of the crack. In Gent's analysis, such a zone of strain-softened material forms the basis for craze formation via the formation of microvoids. The effect of strain softening is to relieve the stress concentration at the crack tip. The stress fields tend towards a uniform state ahead of the crack in a zone of strain-softening material. Intense inelastic deformation takes place within this process zone, which may lead to strain localization or the formation of crazes associated with microvoid nucleation and growth. A curious stress-overshoot phenomenon occurs for the standard nonlinear solid but not for the more realistic PVAc model.

Our analysis has been carried out within the framework of small deformations, although the results indicate that the effects of large deformation are likely to be significant. For example, the influence of finite strains, leading to crack blunting, and treatment of microscopic damage processes, such as void nucleation and growth (and the development of crazing), may have a significant effect on the material behavior in the

Downloaded 03 May 2010 to 171.66.16.247. Redistribution subject to ASME license or copyright; see http://www.asme.org/terms/Terms_Use.cfm

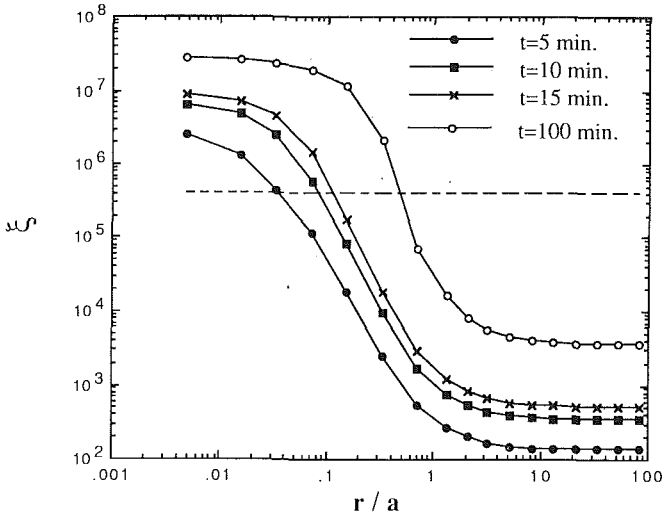

Fig. 10 Internal time profiles along crack line—PVAc

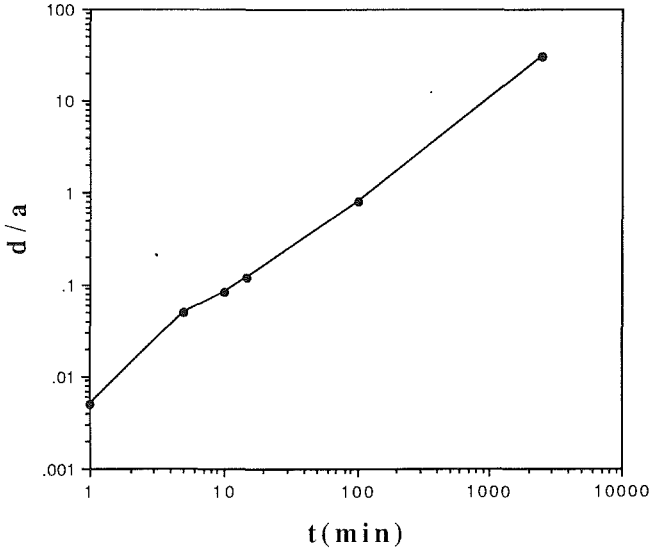

Fig. 11 Evolution of the strain-softening zone—PVAc

process zone. The investigation of instabilities associated with strain softening and so-called "liquefaction" of the material (Robertson, 1989; Argon and Salama, 1977) appears warranted. It is proposed to address these issues in future work. In this regard, we note that the validity of the constitutive model presented in Section 2 has been questioned at finite strains (Knauss and Emri, 1987). At large strains, orientation or alignment of molecular chains may change the nature of molecular motions and the suitability of the free-volume description of molecular mobility should be re-examined.

Acknowledgments

The authors would like to acknowledge helpful discussions with Prof. G. Ravichandran and Dr. Giancarlo Losi, Caltech. B. M. is grateful for the support of an IBM Research Fellowship at Caltech. W. G. K. is grateful for the support, in part, of Caltech's Program in Advanced Technologies, which is sponsored by Aerojet General, General Motors, and TRW. Finally, this work was made possible largely through an NSF grant making the facilities of the Supercomputer Center at the University of California at San Diego available to us.

References

Argon, A. S., and Salama, M. M., "Growth of Crazes in Glassy Polymers," *Philosophical Magazine*, Vol. 36, No. 5, pp. 1217–1234.

Ferry, J. D., 1980, *Viscoelastic Properties of Polymers*, John Wiley and Sons, New York.

Gent, A., 1970, "Hypothetical Mechanism of Crazing in Glassy Plastics," *Journal of Material Science*, Vol. 5, pp. 925–932.

Gurtin, M. E., and Sternberg, E., 1962, "On the Linear Theory of Viscoelasticity," *Archives for Rational Mechanics and Analysis*, Vol. 2, pp. 291–356.

Jiang, Q., 1986, "Conservation Laws in Linear Viscoelastodynamics," *Journal of Elasticity*, Vol. 16, pp. 213–219.

Knauss, W. G., 1973, "The Mechanics of Polymer Fracture," *Applied Mechanics Reviews*, ASME, New York, Vol. 26, pp. 1–17.

Knauss, W. G., 1989, "Time Dependent Fracture of Polymers," *Proceedings of the Seventh International Conference on Fracture*," Vol. ICF7, Houston, Texas.

Knauss, W. G., and Emri, I., 1981, "Non-Linear Viscoelasticity Based on Free Volume Considerations," *Computers and Structures*, Vol. 13, pp. 123–128.

Knauss, W. G., and Emri, I., 1987, "Volume Change and the Nonlinearly Thermo-Viscoelastic Constitution of Polymers," *Polymer Engineering and Science*, Vol. 27, pp. 86–100.

Moran, B., and Knauss, W. G., 1989, "Crack Tip Stress and Deformation Fields in Strain-Softening Nonlinearly Viscoelastic Materials," Caltech Report SM-89.

Morland, M. L., and Lee, E. H., 1960, "Stress Analysis for Linear Viscoelastic Materials with Temperature Variation," *Transactions of the Society of Rheology*, Vol. 8, pp 233–263.

Nilsson, F., 1973, "A Path-Independent Integral for Transient Crack Problems," *International Journal of Solids and Structures*, Vol. 9, pp. 1107–1115.

Riedel, H., and Rice, J. R., 1980, "Tensile Cracks in Creeping Solids," in *Fracture Mechanics: Twelfth Conference*, ASTM-STP-700, American Society for Testing and Materials, Philadelphia, PA, pp. 112–130.

Robertson, R. E., Sporer, M. G., Pan, P.-Y., and Mindrouri, V. E., 1989, "Plasticity of Brittle Epoxy Resins During Debonding Failure," to appear in the *Journal of Materials Science*.

Schapery, R. A., 1990, "On Some Path-Independent Integrals and Their Use in Fracture of Nonlinear Viscoelastic Media," *International Journal of Fracture*, Vol. 42, pp. 189–207.

Taylor, R. L., Pister, K., and Goudreau, G., 1970, "Thermomechanical Analysis of Viscoelastic Solids," *International Journal for Numerical Methods in Engineering*, Vol. 2, pp. 45–59.

Downloaded 03 May 2010 to 171.66.16.247. Redistribution subject to ASME license or copyright; see http://www.asme.org/terms/Terms_Use.cfm

Reflection and Transmission of a Plane Wave by an Array of Cavities in the Interface of Two Solids

Yonglin Xu
Department of Civil Engineering,
Northwestern University,
Evanston, IL 60208

The reflection and transmission of a plane wave by a distribution of cavities in the interface of two solids of different mechanical properties are investigated. For the calculation of the reflection and transmission coefficients by a distribution of cavities, six auxiliary wave states are used in conjunction with the reciprocal identity. Specific results are presented for scattering by a doubly periodic array of cavities in the interface of solids of different elastic moduli and mass densities. For a typical cell, the boundary integral equations for scattering by a cavity at the interface of two solids are derived on the basis of continuity of displacements and tractions across the interface and by taking advantage of the geometrical periodicity. Solutions to the system of singular integral equations have been obtained by the boundary element method. Numerical results are presented as functions of the frequency for two angles of incidence.

1 Introduction

In diffusion bonding, two pieces of different materials are joined together across a bond plane. It does, however, frequently happen that the bonding process is imperfect, and that the bond plane contains defects and impurities which reduce its strength. Defects, when they do occur, are generally distributed in the plane of bond, and they affect the reflection of ultrasonic wave motion by the interface.

In this paper, the reflection and transmission by a planar doubly periodic array of one kind of defects, namely voids or cavities in the interface of two solids, is studied. The centers of the cavities are located in a single plane at positions $x_1 = ma$, $x_2 = nb$ (m, $n = 0, \pm 1, \pm 2, \pm 3 \ldots$) as shown in Fig. 1. The reflected and transmitted waves (L wave, TV wave, TH wave) will be investigated for an incident wave of arbitrary angle of incidence. The reflected and transmitted wave motions may be expressed as superpositions of an infinite number of wave modes, each with its own cutoff frequency. At the cutoff frequency, a mode converts from a standing wave mode into a propagating wave mode. At small frequencies only the lowest-order modes of longitudinal and transverse wave motion are propagating. The reflection and transmission coefficients have been defined in terms of coefficients of the zeroth-order scattered waves. Six auxiliary wave states will be used to calculate these six coefficients of reflection and transmission.

In recent years a number of elastodynamic applications of the boundary element method have been published. The general approach has been discussed by Kitahara (1985). For various geometrical configurations, frequency domain applications of the boundary element method have been presented by Rizzo et al. (1985); Kitahara and Nakagawa (1985); Zhang and Achenbach (1986); Budreck and Achenbach (1988). Some typical difficulties that may develop at higher frequencies have been discussed by Rezayat et al. (1986). The problem of reflection and transmission by a periodic array of cavities in a homogeneous solid has been studied by Achenbach and Kitahara (1986) and the corresponding problem for an array of cracks has been solved by Angel and Achenbach (1984), (1985).

In a recent work on interface scattering, problems of elastic

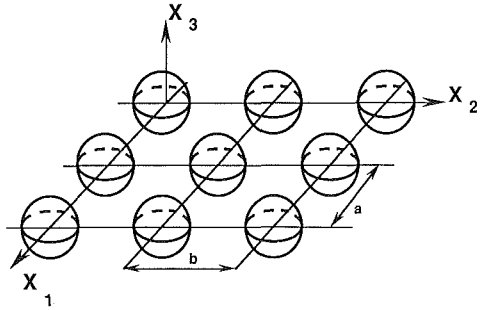

Fig. 1 Array of spherical cavities with centers in x_1x_2-plane

Contributed by the ASME Applied Mechanics Division of THE AMERICAN SOCIETY OF MECHANICAL ENGINEERS for presentation at the Winter Annual Meeting, Atlanta, GA., Dec. 1-6, 1991.

Discussion on this paper should be addressed to the Technical Editor, Prof. Leon M. Keer, The Technological Institute, Northwestern University, Evanston, IL 60208, and will be accepted until two months after final publication of the paper itself in the JOURNAL OF APPLIED MECHANICS. Manuscript received by the ASME Applied Mechanics Division, Aug. 21, 1990; final revision, Dec. 15, 1990.

Paper No. 91-WA/APM-16.

Copyright © 1992 by ASME
Downloaded 03 May 2010 to 171.66.16.247. Redistribution subject to ASME license or copyright; see http://www.asme.org/terms/Terms_Use.cfm

wave scattering by a crack at the interface between a layer and a half-space have been formulated and solved by Yang and Bogy (1985), and Gracewski and Bogy (1986). The solutions of these problems led to a set of coupled singular integral equations for the jump in displacements across the crack. For three-dimensional configurations, scattering by a flaw at an interface has been studied by Xu and Achenbach (1989), and in deriving the system of singular integral equations, it was decided to use the Green's functions for the unbounded regions of two materials, rather than the single Green's function for the space of the joined half spaces. The boundary integral equations derived from that study will be expanded to the problem of a periodic distribution of cavities in the interface of two solids.

2 Problem Formulation

A plane time-harmonic wave denoted by $u^i(\mathbf{x})\exp(-i\omega t)$ is incident on a doubly periodic array of cavities in the interface of two solids. The geometry is shown in Fig. 1. The surfaces of the cavities are free of surface tractions, i.e., $t_i(\mathbf{x}) = 0$, $\mathbf{x} \in S^{mn}$. Where S^{mn} is defined by

$$(x_1 - ma)^2 + (x_2 - nb)^2 + x_3^2 = d^2. \tag{1}$$

The scattered field is induced by an incident longitudinal wave of the form

$$u^{in}(\mathbf{x}) = \exp(ik_L \mathbf{p}\cdot\mathbf{x}). \tag{2}$$

Here, $\mathbf{p} = (\cos\gamma_1^L, \cos\gamma_2^L, \cos\gamma_3^L)$. The total displacement field is written as

$$\mathbf{u}(\mathbf{x}) = \mathbf{u}^g(\mathbf{x}) + \mathbf{u}^s(\mathbf{x}). \tag{3}$$

The geometrical fields are

$$\mathbf{u}^g(\mathbf{x}) = \mathbf{u}^{in}(\mathbf{x}) + \mathbf{u}^L(\mathbf{x}) + \mathbf{u}^T(\mathbf{x}).$$

A scattered field is sought which has the term $\exp[ik_L(x_1\cos\gamma_1^L + x_2\cos\gamma_2^L)]$ in common with the incident wave.

$$\mathbf{u}^s(\mathbf{x}) = \bar{\mathbf{u}}^s \exp[ik_L(x_1\cos\gamma_1^L + x_2\cos\gamma_2^L)] \tag{4}$$

and

$$\bar{\mathbf{u}}^s(x_1 + a, x_2 + b, x_3) = \bar{\mathbf{u}}^s(x_1, x_2, x_3). \tag{5}$$

The periodical form of $\bar{\mathbf{u}}^s(\mathbf{x})$ can be represented by an exponential Fourier series. To write down a general form of this series representation it is convenient to employ the usual displacement decomposition of the original $\mathbf{u}^s$ in terms of a scalar potential $\Phi(\mathbf{x})$ and a vector potential $\Psi(\mathbf{x})$

$$\mathbf{u}^s(\mathbf{x}) = \nabla\Phi + \nabla\times\Psi \tag{6}$$

and

$$\Psi(\mathbf{x}) = (\Psi_1, \Psi_2, \Psi_3), \tag{7}$$

where $\Phi(\mathbf{x})$ and $\Psi(\mathbf{x})$ satisfy reduced wave equations with wave numbers k_L and k_T, respectively. Suitable expressions for $\Phi(\mathbf{x})$ and $\Psi(\mathbf{x})$ for the lower half-space and the upper half-space are

$x_3 \le 0$

$$\Phi(\mathbf{x}) = \sum_p\sum_q \Phi_{pq}\exp\, i(\alpha_p^L x_1 + \beta_q^L x_2 - \gamma_{pq}^L x_3) \tag{8}$$

$$\Psi(\mathbf{x}) = \sum_p\sum_q \Psi_{pq}\exp\, i(\alpha_p^T x_1 + \beta_q^T x_2 - \gamma_{pq}^T x_3) \tag{9}$$

$x_3 \ge 0$

$$\bar{\Phi}(\mathbf{x}) = \sum_p\sum_q \bar{\Phi}_{pq}\exp\, i(\bar{\alpha}_p^L x_1 + \bar{\beta}_q^L x_2 + \bar{\gamma}_{pq}^L x_3) \tag{10}$$

$$\bar{\Psi}(\mathbf{x}) = \sum_p\sum_q \bar{\Psi}_{pq}\exp\, i(\bar{\alpha}_p^T x_1 + \bar{\beta}_q^T x_2 + \bar{\gamma}_{pq}^T x_3), \tag{11}$$

where $\Psi_{pq} = (\Psi_1, \Psi_2, \Psi_3)_{pq}$. Only two components of Ψ_{pq} are independent because of the condition $\nabla\cdot\Psi(\mathbf{x}) = 0$. Also,

$$\alpha_p^L = k_L\cos\gamma_1^L + \frac{2p\pi}{a}, \quad \alpha_P^T = k_T\cos\gamma_1^T + \frac{2p\pi}{a} \tag{12a, b}$$

$$\beta_p^L = k_L\cos\gamma_2^L + \frac{2q\pi}{b}, \quad \beta_q^T = k_T\cos\gamma_2^T + \frac{2q\pi}{b} \tag{13a, b}$$

and

$$\gamma_{pq}^L = \sqrt{(k_L)^2 - (\alpha_p^L)^2 - (\beta_q^L)^2} \tag{14}$$

$$\gamma_{pq}^T = \sqrt{(k_T)^2 - (\alpha_p^T)^2 - (\beta_q^T)^2}. \tag{15}$$

In Eqs. (8)–(11), $\mathrm{Im}\,\gamma_{pq}^L > 0$ and $\mathrm{Im}\,\gamma_{pq}^T > 0$, as well as $\mathrm{Im}\,\bar{\gamma}_{pq}^L > 0$ and $\mathrm{Im}\,\bar{\gamma}_{pq}^T > 0$. An analogous formulation can be obtained from (12) to (15) for the upper half-space.

In Eqs. (8)–(11), the following relations, in terms of Snell's law, hold

$$k_L(\cos\gamma_1^L x_1 + \cos\gamma_2^L x_2) = k_T(\cos\gamma_1^T x_1 + \cos\gamma_2^T x_2)$$
$$= \bar{k}_L(\cos\bar{\gamma}_1^L x_1 + \cos\bar{\gamma}_2^L x_2) = \bar{k}_T(\cos\bar{\gamma}_1^T x_1 + \cos\bar{\gamma}_2^T x_2). \tag{16}$$

The exponentials with $\bar{\gamma}_{pq}^L x_3$ and $\bar{\gamma}_{pq}^T x_3$ denote transmitted waves while the ones with $-\gamma_{pq}^L x_3$ and $-\gamma_{pq}^T x_3$ denote reflected waves. For $p = q = 0$ and small values of the frequency ($\omega < \tilde{\omega}$), only zeroth-order modes are propagating. All the other modes decay with increasing $|x_3|$; $\tilde{\omega}$ is the cutoff frequency.

3 The Calculation of the Cutoff Frequency

The cutoff frequency $\tilde{\omega}$ is a function of the distance between neighboring cavities (a and b) and the propagation vector. It can be calculated as follows for either the longitudinal or the transverse wave. If the propagation vector $\mathbf{p} = (\cos\gamma_1, \cos\gamma_2, \cos\gamma_3)$, and

$$\alpha_p = k\cos\gamma_1 + \frac{2p\pi}{a}, \quad \beta_q = k\cos\gamma_2 + \frac{2q\pi}{b}, \tag{17a, b}$$

then, from Eq. (14) and (15),

$$\gamma_{pq} = \sqrt{(k^2 - \alpha_p^2 - \beta_q^2)}$$
$$= \sqrt{k^2\cos^2\gamma_3 - 2k(\cos\gamma_1 A_p + \cos\gamma_2 B_q) - (A_p^2 + B_q^2)}, \tag{18}$$

where $A_p = 2p\pi/\alpha$ and $B_q = 2q\pi/\beta$ are constants. The equation

$$k^2\cos^2\gamma_3 - 2k(\cos\gamma_1 A_p + \cos\gamma_2 B_q) - (A_p^2 + B_q^2) = 0 \tag{19}$$

has two roots for k. It is easily seen that one root is negative and that the other root is positive. Let k_{pq} be the positive root. Hence,

$$k_{pq} = (\cos\gamma_1 A_p + \cos\gamma_2 B_q +$$
$$\sqrt{(\cos\gamma_1 A_p + \cos\gamma_2 B_q)^2 + \cos^2\gamma_3(A_p^2 + B_q^2)})/\cos^2\gamma_3 \tag{20}$$

where $k_{pq} = \omega_{pq}/c$ defines the frequency of the pq wave mode. At the cutoff frequency, the pq wave mode will convert from a standing mode to a propagating mode. This frequency follows from

$$\tilde{k} = \min\,(k_{pq}). \tag{21}$$

Here, Eq. (21) is considered only for the cases of $p = 0$, $q = 1$ or $p = 1$ or $q = 0$. Hence,

$$\tilde{k} = \frac{2\pi e}{\cos^2\gamma_3} \quad \text{or} \quad \tilde{\omega} = c\,\frac{2\pi e}{\cos^2\gamma_3} \tag{22a, b}$$

where

$$e = \min\left(\frac{\cos\gamma_1 + \sqrt{\cos^2\gamma_1 + \cos^2\gamma_3}}{a}, \right.$$
$$\left. \frac{\cos\gamma_2 + \sqrt{\cos^2\gamma_2 + \cos^2\gamma_3}}{b}\right). \tag{23}$$

By comparing the wave numbers of longitudinal waves and transverse waves to Eq. (22a, b), we have

Downloaded 03 May 2010 to 171.66.16.247. Redistribution subject to ASME license or copyright; see http://www.asme.org/terms/Terms_Use.cfm

$$\tilde{\omega} = c_T \frac{2\pi e^T}{\cos^2 \gamma_3^T} \tag{24}$$

where

$$e^T = \min\left(\frac{\cos\gamma_1^T + \sqrt{\cos^2\gamma_1^T + \cos^2\gamma_3^T}}{a}, \frac{\cos\gamma_2^T + \sqrt{\cos^2\gamma_2^T + \cos^2\gamma_3^T}}{b}\right). \tag{25}$$

For two special cases, the cutoff frequency can be expressed as follows:

(1) normal incidence

$$\tilde{\omega} = c_T \frac{2\pi}{\max(a,b)} \quad \text{or} \quad \tilde{k}_T = \frac{2\pi}{\max(a,b)}. \tag{26a, b}$$

(2) incident vector in the $x_1 - x_3$ plane, $b \geq a$,

$$\tilde{\omega} = c_T \frac{2\pi}{b \cos\gamma_3^T}. \tag{27}$$

When the frequency of the incident wave is less than the cutoff frequency $\tilde{\omega}$, only the zeroth-order modes propagate.

4 Zeroth-Order Modes ($p = q = 0$)

The displacements of the zeroth-order modes involve both longitudinal and transverse wave components.

$$\mathbf{u}^s(\mathbf{x}) = \nabla\Phi + \nabla\times\Psi$$

Hence, for the zeroth-order modes,

$$\mathbf{u}^s(\mathbf{x}) = \nabla\Phi^{00}\exp(ik_L\mathbf{p}\cdot\mathbf{x}) + \nabla\times\Psi^{00}\exp(ik_T\mathbf{p}\cdot\mathbf{x})$$
$$= ik_L\Phi^{00}\mathbf{p}\exp(ik_L\mathbf{p}\cdot\mathbf{x}) + ik_T\mathbf{p}\times\Psi^{00}\exp(ik_T\mathbf{p}\cdot\mathbf{x}). \tag{28}$$

Since the vector $\mathbf{p}\times\Psi^{00}$ is normal to $\mathbf{p}$, we have

$$\mathbf{p}\times\Psi^{00} = ((\mathbf{p}\times\Psi^{00})\cdot\mathbf{d})\mathbf{d} + ((\mathbf{p}\times\Psi^{00})\cdot\mathbf{D})\mathbf{D} \tag{29}$$

where $\mathbf{d}$ is the transverse unit vector in the plane spanned by the x_3 axis and the propagation vector, and $\mathbf{D}$ is normal to that plane:

$$\mathbf{d} = d(\mathbf{p}) = \frac{(\mathbf{p}\times\mathbf{i}_3)\times\mathbf{p}}{|(\mathbf{p}\times\mathbf{i}_3)\times\mathbf{p}|} \tag{30}$$

$$\mathbf{D} = D(\mathbf{p}) = \frac{\mathbf{p}\times\mathbf{i}_3}{|\mathbf{p}\times\mathbf{i}_3|}. \tag{31}$$

Here,

$$(\mathbf{p}\times\mathbf{i}_3\times\mathbf{p}) = (-\cos\gamma_1\cos\gamma_3, -\cos\gamma_2\cos\gamma_3, \cos^2\gamma_1 + \cos^2\gamma_2) \tag{32}$$

$$(\mathbf{p}\times\mathbf{i}_3) = (\cos\gamma_2, \cos\gamma_1, 0) \tag{33}$$

$$|(\mathbf{p}\times\mathbf{i}_3)\times\mathbf{p}| = |\mathbf{p}\times\mathbf{i}_3| = \cos^2\gamma_1 + \cos^2\gamma_2. \tag{34}$$

Equation (28) can be rewritten as follows:

$$\mathbf{u}^s(\mathbf{x}) = ik_L\Phi^{00}\mathbf{p}\exp(ik_L\mathbf{p}\cdot\mathbf{x}) + ik_T\Psi_V\mathbf{d}\exp(ik_T\mathbf{p}\cdot\mathbf{x}) + ik_T\Psi_H\mathbf{D}\exp(ik_T\mathbf{p}\cdot\mathbf{x}) \tag{35}$$

where $\Psi_V = (\mathbf{p}\times\Psi)\cdot\mathbf{d}$, $\Psi_H = (\mathbf{p}\times\Psi)\cdot\mathbf{D}$ and $\Psi = (\Psi_1, \Psi_2, \Psi_3)$. Only two of the three components Ψ_1, Ψ_2, Ψ_3 are independent since $\nabla\cdot\Psi = 0$. Hence, Ψ_V and Ψ_H can be expressed in terms of two components of Ψ. The reflected waves and transmitted waves then are as follows:

$x_3 \leq 0$:

$$\mathbf{u}^L = \mathbf{p}\exp(ik_L\mathbf{p}\mathbf{x}) + A_1\mathbf{p}_1\exp(ik_L\mathbf{p}_1\mathbf{x}) + ik_L\Phi^{00}\mathbf{p}_1\exp(ik_L\mathbf{p}_1\mathbf{x}) \tag{36}$$

$$\mathbf{u}^T = A_2\mathbf{d}_1\exp(ik_T\mathbf{p}_2\mathbf{x}) + ik_T\Psi_V^{00}\mathbf{d}_1\exp(ik_T\mathbf{p}_2\mathbf{x}) \tag{37}$$

$$\mathbf{u}^H = ik_T\Psi_H^{00}\mathbf{D}_1\exp(ik_T\mathbf{p}_2\mathbf{x}) \tag{38}$$

$x_3 \geq 0$:

$$\bar{\mathbf{u}}^L = A_3\mathbf{p}_3\exp(i\bar{k}_L\mathbf{p}_3\mathbf{x}) + i\bar{k}_L\bar{\Phi}^{00}\mathbf{p}_3\exp(i\bar{k}_L\mathbf{p}_3\mathbf{x}) \tag{39}$$

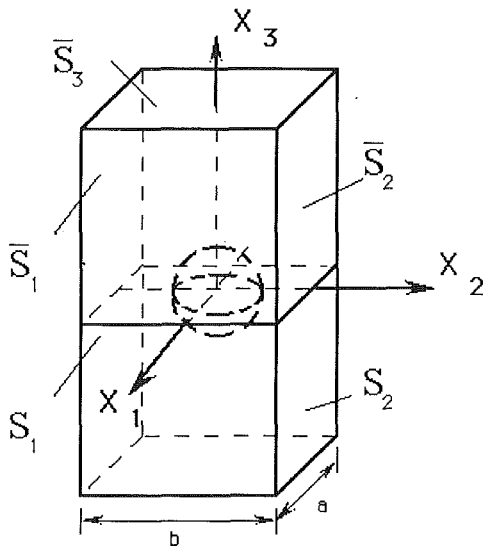

Fig. 2 Unit cell for application of reciprocal identity

$$\mathbf{u}^T = A_4\mathbf{d}_2\exp(i\bar{k}_T\mathbf{p}_4\mathbf{x}) + i\bar{k}_T\bar{\Psi}_V^{00}\mathbf{d}_2\exp(i\bar{k}_T\mathbf{p}_4\mathbf{x}) \tag{40}$$

$$\mathbf{u}^H = i\bar{k}_T\bar{\Psi}_H^{00}\mathbf{D}_2\exp(i\bar{k}_T\mathbf{p}_4\mathbf{x}), \tag{41}$$

where

$$\mathbf{p} = (\cos\gamma_1^L, \cos\gamma_2^L, \cos\gamma_3^L) \tag{42}$$

$$\mathbf{p}_1 = (\cos\gamma_1^L, \cos\gamma_2^L, -\cos\gamma_3^L) \tag{43}$$

$$\mathbf{p}_2 = (\cos\gamma_1^T, \cos\gamma_2^T, -\cos\gamma_3^T) \tag{44}$$

$$\mathbf{p}_3 = (\cos\bar{\gamma}_1^L, \cos\bar{\gamma}_2^L, \cos\bar{\gamma}_3^L) \tag{45}$$

$$\mathbf{p}_4 = (\cos\bar{\gamma}_1^T, \cos\bar{\gamma}_2^T, -\cos\bar{\gamma}_3^T) \tag{46}$$

and

$$\mathbf{d}_1 = d(\mathbf{p}_2), \quad \mathbf{d}_2 = d(\mathbf{p}_4) \tag{47a, b}$$

$$\mathbf{D}_1 = D(\mathbf{p}_2), \quad \mathbf{D}_2 = D(\mathbf{p}_4). \tag{48a, b}$$

Here, the vectors $\mathbf{p}$ and $\mathbf{p}_j$ ($j = 1, 4$) are as shown in Fig. 3. The coefficients of reflection A_1 (longitudinal wave), A_2 (transverse wave), and the coefficient of transmission A_3 (longitudinal wave), A_4 (transverse wave) can be calculated as discussed in Achenbach (1973). The calculation is also given in Appendix (B1).

5 The Calculation of Reflection and Transmission Coefficients

The reciprocal identity can be used to determine the coefficients in Eq. (36)-(41). For a volume V with boundary S, two states A and B are related by

$$\int_V (f_i^B u_i^A - f_i^A u_i^B)\,dv = \int_S (u_i^B t_i^A - u_i^A t_i^B)\,ds \tag{49}$$

where f_i and t_i are components of body forces and surface tractions, respectively.

Application of the reciprocal identity to the unit cell, $|x_1| < a/2$, $|x_2| < b/2$, $-\infty < x_3 < \infty$, (see Fig. 2), yields

$$\int_S (u_i^B t_i^A - u_i^A t_i^B)\,ds = 0 \tag{50}$$

where $s = s_1^{\pm} + s_2^{\pm} + s_3^{\pm} + s^{00}$. For $[u_i^A, t_i^A]$ the actual state corresponding to Eq. (50) is chosen and for $[u_i^B, t_i^B]$, an auxiliary wave state is selected. Six auxiliary wave states are required, and these states are opposite in phase and propagate in directions opposite to the zeroth-order reflected and transmitted longitudinal and transverse waves. The six auxiliary wave states are

(1) $\mathbf{u}_{Ri}^{BL} = -\mathbf{p}_1\exp(-ik_L\mathbf{p}_1\mathbf{x})$.

Downloaded 03 May 2010 to 171.66.16.247. Redistribution subject to ASME license or copyright; see http://www.asme.org/terms/Terms_Use.cfm

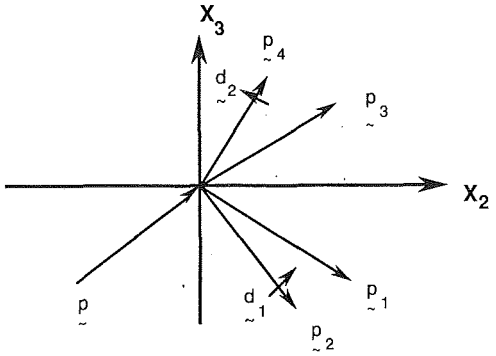

Fig. 3 Propagation vector of plane waves reflected and transmitted by interface

The corresponding reflection and transmission coefficients in the absence of the cavities can be calculated from Eq. (B2), (see Appendix B). The geometrical field $\mathbf{u}_R^{BL}$ due to the incident wave $\mathbf{u}_{Ri}^{BL}$ then immediately follows.

(2) $\mathbf{u}_{Ti}^{BL} = -\mathbf{p}_3 \exp(-i\bar{k}_L \mathbf{p}_3 \mathbf{x})$

The geometrical fields $\mathbf{u}_T^{BL}$ can be calculated from Eq. (B3).

(3) $\mathbf{u}_{Ri}^{BT} = -\mathbf{d}_1 \exp(-ik_T \mathbf{p}_2 \mathbf{x})$

The geometrical fields $\mathbf{u}_T^{BT}$ can be calculated from Eq. (B4).

(4) $\mathbf{u}_{Ti}^{BT} = -\mathbf{d}_2 \exp(-i\bar{k}_L \mathbf{p}_4 \mathbf{x})$

The geometrical fields $\mathbf{u}_T^{BT}$ can be calculated from Eq. (B5).

(5) $\mathbf{u}_{Ri}^{BH} = -\mathbf{D}_1 \exp(-ik_T \mathbf{p}_2 \mathbf{x})$

The geometrical fields $\mathbf{u}_R^{BH}$ can be calculated as follows:

$$\mathbf{u}_R^{BH} = A_5 \mathbf{D}_1 \exp(ik_T \mathbf{p}_2 \mathbf{x}) + A_6 \mathbf{D}_2 \exp(i\bar{k}_T \mathbf{p}_4 \mathbf{x}). \tag{51}$$

Here,

$$A_5 = \frac{\mu \bar{c}_T \cos \bar{\gamma}_3^T - \bar{\mu} c_T \cos \gamma_3^T}{\mu \bar{c}_T \cos \gamma_3^T + \bar{\mu} c_T \cos \bar{\gamma}_3^T} \tag{52}$$

$$A_6 = \frac{2\mu \bar{c}_T \cos \gamma_3^T}{\mu \bar{c}_T \cos \gamma_3^T + \bar{\mu} c_T \cos \bar{\gamma}_3^T} \tag{53}$$

(6) $\mathbf{u}_{Ti}^{BH} = -\mathbf{D}_2 \exp(-ik_T \mathbf{p}_4 \mathbf{x})$

The geometrical fields $\mathbf{u}_R^{BH}$ can be expressed as

$$\mathbf{u}_R^{BH} = B_5 \mathbf{D}_2 \exp(i\bar{k}_T \mathbf{p}_4 \mathbf{x}) + B_6 \mathbf{D}_1 \exp(ik_T \mathbf{p}_2 \mathbf{x}). \tag{54}$$

Here,

$$B_5 = \frac{\bar{\mu} c_T \cos \gamma_3^T - \mu \bar{c}_T \cos \bar{\gamma}_3^T}{\mu \bar{c}_T \cos \gamma_3^T + \bar{\mu} c_T \cos \bar{\gamma}_3^T} \tag{55}$$

$$B_6 = \frac{2\bar{\mu} c_T \cos \bar{\gamma}_3^T}{\mu \bar{c}_T \cos \theta_1 + \bar{\mu} c_T \cos \bar{\gamma}_3^T}. \tag{56}$$

Substituting Eqs. (36)–(41) into Eq. (50) for state A and the auxiliary wave state (1), $\mathbf{u}_R^{BL}$, for state B yields

$$-2(ik_L)^2 \Phi^{00}(2\mu + 1)\cos \gamma_3^L ab - \int_{s_0} \mathbf{u}^A \mathbf{t}_R^{BL} ds = 0. \tag{57}$$

Since

$$R^L = A_1 + ik_L F^{00} \tag{58}$$

it follows from Eq. (57) that

$$R^L = A_1 - F_{L1} \int_{s_0} \mathbf{u}^A \mathbf{t}_R^{BL} ds,$$

$$F_{L1} = (2ik_L(2\mu + \lambda)ab \cos \gamma_3^L)^{-1}. \tag{59a, b}$$

Similarly, for the in-plane reflected transverse wave, we obtain

$$R^T = A_2 + ik_T \Psi_V^{00} \tag{60}$$

$$R^T = A_2 - F_{T1} \int_{s_0} \mathbf{u}^A \mathbf{t}_R^{BT} ds, \quad F_{T1} = (2ik_T \mu ab \cos \gamma_3^T)^{-1}. \tag{61a, b}$$

For the transmitted longitudinal wave we find

$$T^L = A_3 + i\bar{k}_L \bar{\Phi}^{00} \tag{62}$$

and

$$T^L = A_3 - F_{L2} \int_{s_0} \mathbf{u}^A \mathbf{t}_T^{BL} ds, \quad F_{L2} = (2i\bar{k}_L(2\bar{\mu} + \bar{\lambda})ab \cos \bar{\gamma}_3^L)^{-1}, \tag{63a, b}$$

while for the transmitted in-plane transverse wave we obtain

$$T^T = A_4 + i\bar{k}_T \bar{\Psi}_V^{00} \tag{64}$$

$$T^T = A_4 - F_{T2} \int_{s_0} \mathbf{u}^A \mathbf{t}_T^{BT} ds, \quad F_{T2} = (2i\bar{k}_T \bar{\mu} ab \cos \bar{\gamma}_3^T)^{-1}. \tag{65}$$

The coefficient for the reflected antiplane transverse wave is

$$R^H = ik_T \Psi_H^{00} \tag{66}$$

$$R^H = -F_{H1} \int_{s_0} \mathbf{u}^A \mathbf{t}_R^{BH} ds, \quad F_{H1} = (2ik_T \mu ab \cos \gamma_3^T)^{-1}. \tag{67a, b}$$

For the transmitted antiplane transverse wave we finally find

$$T^H = i\bar{k}_T \bar{\Psi}_H^{00} \tag{68}$$

$$T^H = -F_{T2} \int_{s_0} \mathbf{u}^A \mathbf{t}_T^{BH} ds, \quad F_{T1} = (2i\bar{k}_T \bar{\mu}_2 ab \cos \bar{\gamma}_3^T)^{-1}. \tag{69a, b}$$

6 Boundary Integral Equation

The boundary integral equation for one cavity in the interface of two solids has been derived by Xu and Achenbach (1989). For the case of periodically distributed cavities, the equation is

$$\begin{aligned} Cu_i(\mathbf{x}) = &- \sum_m \sum_n \int_{S^{mn}} T_{ij} u_j dS(\mathbf{y}) - \sum_m \sum_n \int_{\bar{S}^{mn}} \bar{T}_{ij} u_j dS(\mathbf{y}) \\ &+ \sum_m \sum_n \int_{\Gamma^{mn}} [(U_{ij} - \bar{U}_{ij}) t_j - (T_{ij} - \bar{T}_{ij}) u_j] dS(\mathbf{y}) \\ &- \sum_m \sum_n \int_{\Gamma^{mn} + \Gamma_0^{mn}} [(U_{ij} - \bar{U}_{ij}) t_j^g - (T_{ij} - \bar{T}_{ij}) u_j^g] dS(\mathbf{y}) + u_i^g(\mathbf{x}) \end{aligned} \tag{70}$$

where the summation over the integers m and n is from $-\infty$ to ∞. The position $\mathbf{x}$ in cell (m, n) and $\mathbf{x}^0$ in the reference cell (0,0) are related by

$$x_1 = x_1^0 + ma, \quad x_2 = x_2^0 + nb, \quad x_3 = x_3^0. \tag{71}$$

By the use of this transformation the incident field, the total field for this problem can be expressed as

$$\mathbf{u}(\mathbf{x}) = \mathbf{u}(\mathbf{x}^0) \exp(ik_L(ma \cos \gamma_1 + nb \cos \gamma_2) \tag{72}$$

and

$$\mathbf{t}(\mathbf{x}) = \mathbf{t}(\mathbf{x}^0) \exp(ik_L(ma \cos \gamma_1 + nb \cos \gamma_2). \tag{73}$$

The formulation can then be reduced to an integration over a single surface, namely the surface s^0 of the sphere in the reference cell. The resulting boundary integral equations then have the same form as (70):

$$Cu_i = \int_{S^0} \tilde{T}_{ij} u_j dS(\mathbf{y}) - \int_{\bar{S}^0} \tilde{\bar{T}}_{ij} u_j dS(\mathbf{y})$$

Downloaded 03 May 2010 to 171.66.16.247. Redistribution subject to ASME license or copyright; see http://www.asme.org/terms/Terms_Use.cfm

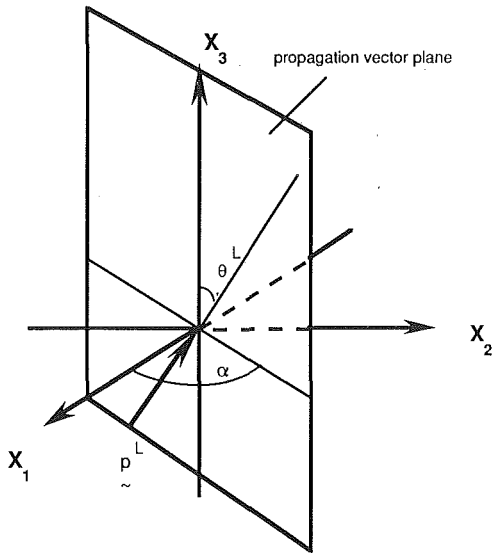

Fig. 4 Propagation vector in spherical coordinate system

$$+\int_{\Gamma^0}[(\tilde{U}_{ij}-\tilde{\tilde{U}}_{ij})t_j-(\tilde{T}_{ij}-\tilde{\tilde{T}}_{ij})u_j]dS(\mathbf{y})$$

$$-\int_{\Gamma^0+\Gamma_0^0}[(\tilde{U}_{ij}-\tilde{\tilde{U}}_{ij})t_j^g-(\tilde{T}_{ij}-\tilde{\tilde{T}}_{ij})u_j^g]dS(\mathbf{y})+u_i^g. \quad (74)$$

Here,

$$\tilde{U}_{ij}=\sum_m\sum_n U_{ij}(\mathbf{x}^0;\mathbf{y}^0;\mathbf{r}_{mn})\exp(ik_L(ma\cos\gamma_1+nb\cos\gamma_2)) \quad (75)$$

$$\tilde{T}_{ij}=\sum_m\sum_n T_{ij}(\mathbf{x}^0;\mathbf{y}^0;\mathbf{r}_{mn})\exp(ik_L(ma\cos\gamma_1+nb\cos\gamma_2)) \quad (76)$$

and

$$r_{mn}^2=(x_1^0-y_1^0-ma)^2+(x_2^0-y_2^0-nb)^2+(x_3^0-y_3^0)^2. \quad (77)$$

The expressions for the Green's functions $\tilde{\tilde{U}}_{ij}$ and $\tilde{\tilde{T}}_{ij}$ of the upper half-space are of the same forms as (75) and (76). Since both displacements and tractions are unknowns over the interface, equations

$$\frac{1}{2}u_i=-\int_{S^0}\tilde{T}_{ij}u_j dS(\mathbf{y})+\int_{\Gamma^0}[(\tilde{U}_{ij}t_j-\tilde{T}_{ij}u_j]dS(\mathbf{y})$$

$$-\int_{\Gamma^0+\Gamma_0^0}[(\tilde{U}_{ij}t_j^g-\tilde{T}_{ij}u_j^g]dS(\mathbf{y})+\frac{1}{2}u_i^g \quad (78)$$

and

$$\frac{1}{2}u_i=-\int_{\bar{S}^0}\tilde{\tilde{T}}_{ij}u_j dS(\mathbf{y})+\int_{\bar{\Gamma}^0}[(\tilde{\tilde{U}}_{ij}t_j-\tilde{\tilde{T}}_{ij}u_j]dS(\mathbf{y})$$

$$-\int_{\bar{\Gamma}^0+\bar{\Gamma}_0^0}[(\tilde{\tilde{U}}_{ij}t_j^g-\tilde{\tilde{T}}_{ij}u_j^g]dS(\mathbf{y})+\frac{1}{2}u_i^g \quad (79)$$

should be added. Equation (74) for $\mathbf{x}$ on S and $\bar{S}$, while Eqs. (78) and (79) are used for $\mathbf{x}\in\Gamma$ and $\mathbf{x}\in\bar{\Gamma}$.

The singular parts of the integrands have been dealt with as described by Kitahara and Nakagawa (1985). Thus, the Green's function tractions have been split in singular and nonsingular parts. The singular parts are just the same as the displacements and tractions corresponding to static loading, and they are computed as in the boundary element method for static problems. The dynamic deviations are not singular, and they may be expanded in a series. Usually a small number of terms in the expansions suffice for satisfactory results.

7 Numerical Results and the Power Balance Equation

For the case of spherical cavities for radius d, the elements

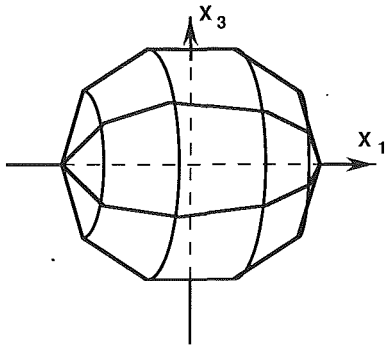

Fig. 5(*a*) Elements on the surface of the sphere

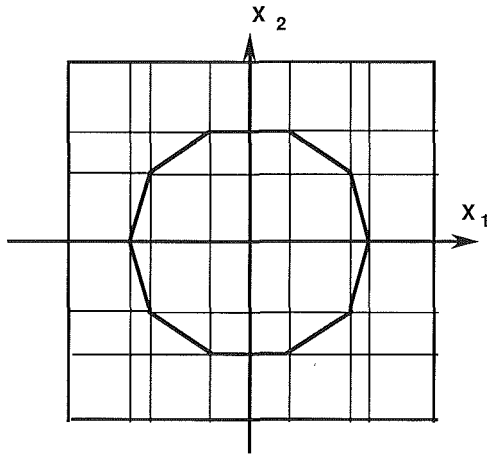

Fig. 5(*b*) Elements in the interface for the periodic distribution of spherical cavity

on the surface of a cavity are as shown in Fig. 5(*a*). For the elements in the interface, we take rectangular and triangular elements as shown in Fig. 5(*b*). For $k_L d < 0.3$, we take 18 elements in the interface. For $k_L d > 0.3$, we use 30 elements on the surface of the sphere and 34 elements in the interface.

The method to deal with the singular parts of the integrands differs very little from the one for the single cavity problem. The fundamental solution $\tilde{T}_{ij}$ given by Eq. (76) is singular only when $m = 0$ and $n = 0$ in the term $T_{ij}(\mathbf{x}^0; \mathbf{y}^0; \mathbf{r}_{mn})$. This term can be separated into a static term (singular term) and a dynamic term (regular part). Then the singular part is evaluated.

Specific results have been checked by the power balance equation. This equation may be written as follows:

$$|R^L|^2+|T^L|^2a_1+(|R^T|^2+|R^H|^2)a_2$$
$$+(|T^T|^2+|T^H|^2)a_3=0. \quad (80)$$

Here

$$a_1=\frac{(\bar{\lambda}+2\bar{\mu})c_L\cos\bar{\gamma}_3^L}{(\lambda+2\mu)\bar{c}_L\cos\gamma_3^L} \quad (81)$$

$$a_2=\frac{\mu c_L\cos\gamma_3^T}{(\lambda+2\mu)c_T\cos\gamma_3^L} \quad (82)$$

$$a_3=\frac{\bar{\mu}c_L\cos\bar{\gamma}_3^T}{(\lambda+2\mu)\bar{c}_T\cos\gamma_3^L}. \quad (83)$$

If the two materials are identical, Eqs. (81) to (83) reduce to $a_1 = 1$, and $a_2 = a_3$

$$=\frac{\sqrt{1-(\sin\gamma_3^L/\kappa)^2}}{\kappa\cos\gamma_3^L}. \quad (84)$$

The coefficients a_1, a_2 and a_3 then are the same as those given in Achenbach and Kitahara (1986).

Downloaded 03 May 2010 to 171.66.16.247. Redistribution subject to ASME license or copyright; see http://www.asme.org/terms/Terms_Use.cfm

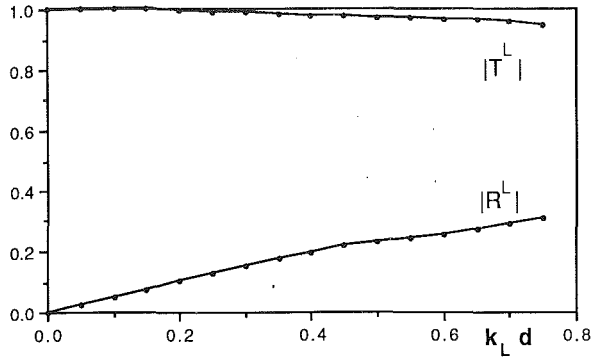

Fig. 6 Absolute values of reflection and transmission coefficients for normal incident wave

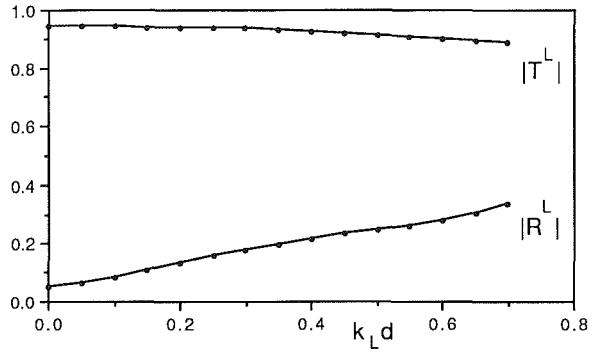

Fig. 7 Absolute value of reflection and transmission for normal incident wave

Calculations have been carried out for three combinations of the material properties of the two half-spaces.

The first case and the second case considered concern normal materials properties are given by

$$\nu = 0.25, \quad \bar{\nu} = 0.25, \quad \bar{\rho}/\rho = 0.8, \quad \bar{c}_L/c_L = 1.25,$$

and

$$\nu = 0.25, \quad \bar{\nu} = 0.25, \quad \bar{\rho}/\rho = 1.25, \quad \bar{c}_L/c_L = 1.1,$$

with $a/d = b/d = 3$ and normal incidence. Figures 6 and 7 show the absolute value of reflection and transmission coefficients R^L and T^L, versus the dimensionless longitudinal wave number $k_L d$. For these cases there are no reflected and transmitted transverse wave modes of zero order, i.e., $|R^T| = |T^T| = 0$, while the coefficients of reflection and transmission in these cases are different at $k_L d = 0$ due to the different ratios of impedances. The first case can be characterized as identical media at very low frequency since the ratio of the impedance equals one.

For the third case, the incident angle is 30 deg. The material properties are

$$\nu = 0.25, \quad \bar{\nu} = 0.23, \quad \bar{\rho}/\rho = 0.83, \quad \bar{c}_L/c_L = 1.13.$$

Figure 8 shows the absolute values of the reflection and transmission coefficients as the functions of $k_L d$. It is noted that $|R^T| > |R^L|$ and $|T^T|$ varies very smoothly at low frequency.

In the BEM formulation, the inhomogeneities in an interface between two solids of different mechanical properties presents some additional complications with regard to the evaluation of the integrals in the interface, the choice of the Green's function to deal with two different media, and the calculation of the singular boundary integrals in the different media. The system of equations become much larger due to the presence of the elements in the interface. Therefore, the supercomputers have to be used for more computer memory and higher running speed. In the calculations presented in Figs. 5 to 7, the power balance given by Eq. (80) is satisfied with a maximum error of 3 percent.

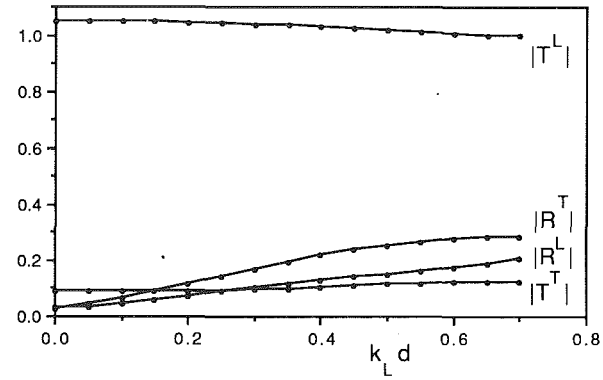

Fig. 8 Absolute value of reflection and transmission coefficients for $\theta = 30$ deg

Acknowledgment

This work was carried out in the course of Research Sponsored by the Office of Naval Research. The author is grateful to Prof. J. D. Achenbach for his help in the preparation of this paper. A Grant from Cray Research, Inc. for access to the Pittsburgh Supercomputing Center is also gratefully acknowledged.

References

Achenbach, J. D., 1973, *Wave Propagation in Elastic Solids*, North-Holland Publishing Company, New York.

Achenbach, J. D., and Kitahara, M., 1986, "Reflection and Transmission of an Obliquely Incident Wave by an Array of Spherical Cavities," *J. Acoust. Soc. Am.*, pp. 1209–1214.

Achenbach, J. D., and Kitahara, M., 1987, "Harmonic Waves in a Solid with a Periodic Distribution of Spherical Cavities," *J. Acoust. Soc. Am.*, Vol. 81, pp. 595–598.

Angel, Y. C., and Achenbach, J. D., 1984, "Reflection and Transmission of Obliquely Incident Rayleigh Waves by a Surface-Breaking Crack," *J. Acoust. Soc. Am.*, Vol. 75, pp. 313–319.

Angel, Y. C., and Achenbach, J. D., 1985, "Reflection and Transmission of Elastic Waves by a Periodic Array of Cracks: Oblique Incidence," *Wave Motion*, Vol. 7, pp. 375–397.

Budreck, D. E., and Achenbach, J. D., 1988, "Scattering from Three Dimensional Planar Cracks by the Boundary Integral Equation Method," ASME JOURNAL OF APPLIED MECHANICS, Vol. 55, pp. 405–412.

Gracewski, S. M., and Body, D. B., 1986, "Elastic Waves Scattering from an Interface Crack in a Layered Half-Space Submerged in Water: Part 1: Applied Tractions at the Liquid-Solid Interface," ASME JOURNAL OF APPLIED MECHANICS, Vol. 53, pp. 326–332.

Gracewski, S. M., and Body, D. B., 1986, "Elastic Waves Scattering from an Interface Crack in a Layered Half Space Submerged in Water: Part 2: Incident Plane Waves and Bounded Beams," ASME JOURNAL OF APPLIED MECHANICS, Vol. 53, pp. 333–338.

Kitahara, M., 1985, *Boundary Integral Equation Methods in Eigenvalue Problems of Elastodynamics and Thin Plates*, Elsevier, Amsterdam.

Kitahara, M., and Nakagawa, K., 1985, "Boundary Integral Equation Methods in Three Dimensional Elastodynamics," *Proceedings of the 7th International Conference*, C. A. Brebbia and G. Maier, eds., Villa Olmo, Lake Como, Italy.

Rezayat, M., Shippy, D. J., and Rizzo, F. J., 1986, "On Time-Harmonic Elastic-Wave Analysis by the Boundary Element Method for Moderate to High Frequencies," *Comput. Meths. Appl. Mech. Engrg.*, Vol. 55, pp. 349–367.

Rizzo, F. J., and Shippy, D. J., Rezayat, M., 1985, "A Boundary Integral Equation Method for Radiation and Scattering of Elastic Waves in Three Dimensions," *Int. J. Numer. Methods Eng.*, Vol. 21, pp. 115–129.

Xu, Y., and Achenbach, J. D., 1989, "Numerical Analysis of Scattering by Interface Flaws," *Review of Progress in Quantitative Nondestructive Evaluation*, D. O. Thompson and D. E. Chimenti, eds., Plenum Press.

Yang, H. J., and Bogy, D. B., 1985, "Elastic Waves Scattering from an Interface Crack in a Layered Half Space," ASME JOURNAL OF APPLIED MECHANICS, Vol. 52, pp. 42–50.

Zhang, Ch., and Achenbach, J. D., 1988, "Scattering by Multiple Crack Configurations," ASME JOURNAL OF APPLIED MECHANICS, Vol. 55, pp. 104–110.

APPENDIX A

Basic Singular Solution

The basic singular elastodynamic solution (the Green's func-

Downloaded 03 May 2010 to 171.66.16.247. Redistribution subject to ASME license or copyright; see http://www.asme.org/terms/Terms_Use.cfm

tion) $U_{ij}(\mathbf{x}, \mathbf{y})$ and the corresponding $T_{ij}(\mathbf{x}, \mathbf{y})$ were used in the following forms:

$$U_{ij}(\mathbf{x},\mathbf{y})=\frac{1}{4\pi\mu}\left\{\delta_{ij}\left[\frac{e^{ik_T r}}{r}+\frac{1}{k_T^2 r}\left(a_1(k_T,r)-a_1(k_L,r)\right)\right]+\frac{r}{k_T^2}\left(a_2(k_T,r)-a_2(k_L,r)\right)r_{,i}r_{,j}\right\} \quad \text{(A1)}$$

$$T_{ij}(\mathbf{x},\mathbf{y})=\frac{-1}{4\pi\mu}\left\{\delta_{ij}\left[\mu a_1(k_T,r)+\frac{2\mu}{k_T^2}\left[(a_2(k_T,r)-a_2(k_L,r))\right]r_{,k}n_k+\left[\lambda\frac{k_L^2}{k_T^2}a_1(k_L,r)+\frac{2\mu}{k_T^2}\left(a_2(k_T,r)-a_2(k_L,r)\right)\right]r_{,i}n_j+\left[\mu a_1(k_T,r)+\frac{2\mu}{k_T^2}\left(a_2(k_T,r)-a_2(k_L,r)\right)\right]r_{,j}n_i+\frac{2\mu r^2}{k_T^2}\left[(a_3(k_T,r)-a_3(k_L,r)\right]r_{,i}r_{,j}r_{,k}n_k\right\} \quad \text{(A2)}$$

where

$$r=|\mathbf{x}-\mathbf{y}| \quad \text{(A3)}$$

$$a_1(k,r)=\left(\frac{ik}{r}-\frac{1}{r^2}\right)e^{ikr} \quad \text{(A4)}$$

$$a_2(k,r)=\left(-\frac{k^2}{r^2}-\frac{3ik}{r^3}+\frac{3}{r^4}\right)e^{ikr} \quad \text{(A5)}$$

$$a_3(k,r)=\left(-\frac{ik^3}{r^3}+\frac{6k^2}{r^4}+\frac{15ik}{r^5}-\frac{15}{r^6}\right)e^{ikr}. \quad \text{(A6)}$$

APPENDIX B

The Coefficients of Reflection and Transmission

For six auxiliary wave states the coefficients of reflection and transmission can be calculated in terms of the continuation of displacement and stress in the interface. Here we use A_1, A_2, A_3, A_4 to represent coefficients R^L, R^T, T^L, T^T, and θ_1, θ_2, θ_3, θ_4 to represent angle θ^L, θ^T, $\bar{\theta}^L$, $\bar{\theta}^T$, respectively.

For the incident wave $\mathbf{u}^i = \mathbf{p}\exp(ik_L\mathbf{px})$, the coefficients of reflection and transmission can be given by the equation

$$\begin{pmatrix} -\sin\theta_1 & -\cos\theta_2 & \sin\theta_3 & -\cos\theta_4 \\ \cos\theta_1 & -\sin\theta_2 & \cos\theta_3 & \sin\theta_4 \\ \sin 2\theta_1 & \kappa\cos 2\theta_2 & m_1\sin 2\theta_3 & -m_2\cos 2\theta_4 \\ -\kappa^2\cos 2\theta_2 & \kappa\sin 2\theta_2 & m_3\cos 2\theta_4 & m_2\sin 2\theta_4 \end{pmatrix}\begin{pmatrix} A_1 \\ A_2 \\ A_3 \\ A_4 \end{pmatrix} = \begin{pmatrix} \sin\theta_1 \\ \cos\theta_1 \\ \sin 2\theta_1 \\ \kappa^2\cos 2\theta_2 \end{pmatrix}. \quad \text{(B1)}$$

For the auxiliary wave (1) $\mathbf{u}_{Ri}^{BL} = -\mathbf{p}_1\exp(-ik_L\mathbf{p}_1\mathbf{x})$, the equation is

$$\begin{pmatrix} \sin\theta_1 & -\cos\theta_2 & -\sin\theta_3 & -\cos\theta_4 \\ \cos\theta_1 & \sin\theta_2 & \cos\theta_3 & -\sin\theta_4 \\ -\sin 2\theta_1 & \kappa\cos 2\theta_2 & -m_1\sin 2\theta_3 & -m_2\cos 2\theta_4 \\ -\kappa^2\cos 2\theta_2 & -\kappa\sin 2\theta_2 & m_3\cos 2\theta_4 & -m_2\sin 2\theta_4 \end{pmatrix}\times\begin{pmatrix} A_1 \\ A_2 \\ A_3 \\ A_4 \end{pmatrix} = \begin{pmatrix} \sin\theta_1 \\ \cos\theta_1 \\ \sin 2\theta_1 \\ \kappa^2\cos 2\theta_2 \end{pmatrix}. \quad \text{(B2)}$$

Here,

$$m_1=\frac{\bar{\mu}c_L}{\mu\bar{c}_L}, \quad m_2=\frac{\bar{\mu}c_L}{\mu\bar{c}_T}, \quad m_3=\frac{\bar{\mu}c_L}{\mu\bar{c}_L}\bar{\kappa}^2$$

and

$$\kappa=\frac{c_L}{c_T}, \quad \bar{\kappa}=\frac{\bar{c}_L}{\bar{c}_T}.$$

For the auxiliary wave (2) $\mathbf{u}_{Ti}^{BL} = -\mathbf{p}_3\exp(-i\bar{k}_L\mathbf{p}_3\mathbf{x})$, the equation is

$$\begin{pmatrix} -\sin\theta_3 & -\cos\theta_4 & \sin\theta_1 & -\cos\theta_2 \\ \cos\theta_3 & -\sin\theta_4 & \cos\theta_1 & \sin\theta_2 \\ \sin 2\theta_3 & \bar{\kappa}\cos 2\theta_4 & n_1\sin 2\theta_1 & -n_2\cos 2\theta_2 \\ -\bar{\kappa}^2\cos 2\theta_2 & \bar{\kappa}\sin 2\theta_4 & n_3\cos 2\theta_4 & n_2\sin 2\theta_2 \end{pmatrix}\begin{pmatrix} A_1 \\ A_2 \\ A_3 \\ A_4 \end{pmatrix} = \begin{pmatrix} \sin\theta_3 \\ \cos\theta_3 \\ \sin 2\theta_3 \\ \bar{\kappa}^2\cos 2\theta_4 \end{pmatrix}. \quad \text{(B3)}$$

Here

$$n_1=\frac{\mu\bar{c}_L}{\bar{\mu}c_L}, \quad n_2=\frac{\mu\bar{c}_L}{\bar{\mu}c_T}, \quad n_3=\frac{\mu\bar{c}_L}{\bar{\mu}c_L}\kappa^2.$$

For the auxiliary wave (3) $\mathbf{u}_{Ri}^{BT} = -\mathbf{d}_1\exp(-ik_T\mathbf{p}_2\mathbf{x})$, the equation is

$$\begin{pmatrix} -\sin\theta_1 & \cos\theta_2 & \sin\theta_3 & \cos\theta_4 \\ -\cos\theta_1 & -\sin\theta_2 & -\cos\theta_3 & \sin\theta_4 \\ \kappa^{-1}\sin 2\theta_1 & -\cos 2\theta_2 & s_1\sin 2\theta_3 & s_2\cos 2\theta_4 \\ \kappa\cos 2\theta_2 & \sin 2\theta_2 & -s_3\cos 2\theta_4 & s_2\sin 2\theta_4 \end{pmatrix}\begin{pmatrix} A_1 \\ A_2 \\ A_3 \\ A_4 \end{pmatrix} = \begin{pmatrix} \cos\theta_2 \\ \sin\theta_2 \\ \cos 2\theta_2 \\ \sin 2\theta_2 \end{pmatrix}. \quad \text{(B4)}$$

Here

$$s_1=\frac{\bar{\mu}c_T}{\mu\bar{c}_L}, \quad s_2=\frac{\bar{\mu}c_T}{\mu\bar{c}_T}, \quad s_3=\frac{\bar{\mu}c_T}{\mu\bar{c}_L}\bar{k}^2.$$

For the auxiliary wave (4) $\mathbf{u}_{Ti}^{BT} = -\mathbf{d}_2\exp(-i\bar{k}_L\mathbf{p}_4\mathbf{x})$, the equation is

$$\begin{pmatrix} \sin\theta_3 & \cos\theta_4 & -\sin\theta_1 & \cos\theta_2 \\ \cos\theta_3 & -\sin\theta_4 & \cos\theta_1 & \sin\theta_2 \\ -\bar{\kappa}^{-1}\sin 2\theta_3 & -\cos 2\theta_4 & -t_1\sin 2\theta_1 & t_2\cos 2\theta_2 \\ -\bar{\kappa}\cos 2\theta_2 & \sin 2\theta_4 & t_3\cos 2\theta_4 & t_2\sin 2\theta_2 \end{pmatrix}\begin{pmatrix} A_1 \\ A_2 \\ A_3 \\ A_4 \end{pmatrix} = \begin{pmatrix} \cos\theta_4 \\ \sin\theta_4 \\ \cos 2\theta_4 \\ \sin 2\theta_4 \end{pmatrix}. \quad \text{(B5)}$$

Here

$$t_1=\frac{\mu\bar{c}_T}{\bar{\mu}c_L}, \quad t_2=\frac{\mu\bar{c}_T}{\bar{\mu}c_T}, \quad t_3=\frac{\mu\bar{c}_T}{\bar{\mu}c_L}\kappa^2.$$

Downloaded 03 May 2010 to 171.66.16.247. Redistribution subject to ASME license or copyright; see http://www.asme.org/terms/Terms_Use.cfm

Analysis of the Fully Developed Chute Flow of Granular Materials

Hojin Ahn
Assoc. Mem. ASME

Christopher E. Brennen
Mem. ASME.

Rolf H. Sabersky
Mem. ASME.

California Institute of Technology,
Pasadena, CA 91125

Existing constitutive relations and governing equations have been used to solve for fully developed chute flows of granular materials. In particular, the results of Lun et al. (1984) have been employed and the boundary value problem has been formulated with two parameters (the coefficient of restitution between particles, and the chute inclination), and three boundary values at the chute base wall, namely the values of solid fraction, granular temperature, and mean velocity at the wall. The boundary value problem has been numerically solved by the "shooting method." The results show the significant role played by granular conduction in determining the profiles of granular temperature, solid fraction, and mean velocity in chute flows. These analytical results are also compared with experimental measurements of velocity fluctuation, solid fraction, and mean velocity made by Ahn et al. (1989), and with the computer simulations by Campbell and Brennen (1985b).

1 Introduction

The rapid flow of granular materials is characterized by high deformation rates, and this rapid shearing motion of the flow causes collisions between particles, generating random motion of those particles. The random motions constitute a so-called granular temperature which is a measure of the fluctuation energy in the granular material. Just like the normal thermodynamic temperature, granular temperature is conducted if there is any temperature gradient. That is, fluctuation energy flows from a region of high fluctuation energy to a region of low fluctuation energy by the process of granular conduction.

Though many studies on granular materials draw the analogy with the kinetic theory of gases, there are differences between granular materials and gas molecules. One of the major differences is that the collisions between granular particles are inelastic. This implies that energy dissipation due to inelastic collisions plays an important role in fluctuation energy balance. Therefore, the question of how the flow creates a balance between the generation of fluctuation energy due to shear motions, its dissipation, and granular conducion becomes an important issue to be explored (see Haff (1983, 1986)).

Our knowledge of the rheological behavior of rapidly flowing granular materials has been advanced by several theoretical works. For example, Ogawa et al. (1980), Savage and Jeffrey (1981), Jenkins and Savage (1983), and Lun et al. (1984) have provided constitutive relations which lead to a comprehension of how stresses are associated with solid fraction, shear rate, and granular temperature, and how energy flux is related to granular temperature, solid fraction, and their gradients. These theoretical results have been applied to a simple shear flow. Especially in the work of Lun et al., the ratio of the characteristic mean shear velocity to the granular temperature, and the ratio of shear stress to normal stress, are given as functions of solid fraction and the coefficient of restitution. In application to chute flows, however, theoretical works have faced difficulties due to lack of knowledge of appropriate boundary conditions at the solid wall (for example, see Hui et al. (1984) and Richman and Marciniec (1988)). Furthermore, the nonuniformity of velocity gradient, granular temperature, and solid fraction over the depth of flow complicate the solution of the equations for chute flows.

Computer simulations of Couette flows (for example, Campbell and Brennen (1985a), Walton and Braun (1986a,b), Campbell and Gong (1986), and Campbell (1989)) have added considerably to our knowledge of the rheology of granular material flows. For example, anisotropy of the granular temperature has been found in most computer simulations while most theoretical works assume the temperature to be isotropic. Relatively little work has been done on the computer simulation of gravity flows. Campbell and Brennen (1985b) simulated chute flows with two-dimensional disks, presenting profiles of velocity, solid fraction, and granular temperature over the depth of flow. Walton et al. (1988) have used three-dimensional spheres to simulate gravity flow of particles through arrays of cylindrical horizontal rods and down inclined chutes. Both have employed periodic boundaries which imply steady, fully developed flow.

On the other hand, progress in experimental methods for granular materials has been very limited, being hindered by obvious difficulties involved in making point measurements of velocity, solid fraction, and granular temperature in the interior of granular flows. For example, the granular temperature, in spite of its importance, had not been experimentally measured until Ahn et al. (1988) used fiber-optic displacement probes to measure one component of the granular temperature. The present state of the experimental information on granular flows consists of a number of Couette flow studies (e.g., Savage

Contributed by the Applied Mechanics Division of THE AMERICAN SOCIETY OF MECHANICAL ENGINEERS for publication in the JOURNAL OF APPLIED MECHANICS.

Discussion on this paper should be addressed to the Technical Editor, Prof. Leon M. Keer, The Technological Institute, Northwestern University, Evanston, IL 60208, and will be accepted until two months after final publication of the paper itself in the JOURNAL OF APPLIED MECHANICS. Manuscript received by the ASME Applied Mechanics Division, Apr. 17, 1989; final revision, Nov. 29, 1990.

Copyright © 1992 by ASME
Downloaded 03 May 2010 to 171.66.16.247. Redistribution subject to ASME license or copyright; see http://www.asme.org/terms/Terms_Use.cfm

and McKeown (1983), Savage and Sayed (1984), Hanes and Inman (1985), Craig et al. (1986)) and several studies of flows down inclined chutes (e.g., Bailard (1978), Augenstein and Hogg (1978), Savage (1979), Sayed and Savage (1983), and Ahn et al. (1988, 1989)). The understandable initial objective of some of the Couette flow experiments, such as those of Savage and McKeown, was to produce a simple shear flow with uniform velocity gradient, uniform solid fraction, and hopefully, uniform granular temperature. To this end the surfaces of the solid walls were roughened to create a no-slip condition at the wall though practical engineering applications usually involve smooth walls.

Only recently has the numerical analysis of the flow of granular materials been attempted, partly because the constitutive relations have been unclear and partly because the boundary conditions remain still uncertain. For rapid granular flow, Hui et al. (1984) developed boundary conditions which were derived from the nature of individual grain-wall collisions. Johnson and Jackson (1987) proposed constitutive relations in which frictional and collisional-translational mechanisms are combined for stress transmission. Furthermore, they developed boundary conditions at the wall which relate friction force and slip velocity at the wall with the large-scale roughness of the surface and relate the wall-particle coefficient of restitution and fluctuation energy flux at the wall. Both relations were described in terms of local density and granular temperature. Using these boundary conditions, Johnson and Jackson (1988) attempted to solve numerically the chute flow of granular materials.

Clearly, the limitations involved in an analytical approach to granular material flows lie in the postulated constitutive relations and boundary conditions, and in the assumption that a continuum approach has validity. Therefore, without thorough understanding of constitutive relations and boundary conditions, the analytical results will be of limited value. Furthermore, the continuum assumption implies that the analysis will become of dubious validity when the depth of the flow becomes less than several particle diameters.

2 Analysis of Chute Flows

2.1 The Governing Equations and the Constitutive Equations. In the present analysis of fully developed chute flow, the constitutive equations of Lun et al. (1984) for granular materials are used along with the basic equations of motions. The continuity equation, the momentum equations, and the translational fluctuation energy equation are as follows:

$$\frac{d\rho}{dt} = -\rho \nabla \cdot \mathbf{u} \tag{1}$$

$$\rho \frac{d\mathbf{u}}{dt} = \rho \mathbf{b} - \nabla \cdot \mathbf{P} \tag{2}$$

$$\frac{3}{2}\rho \frac{dT}{dt} = -\mathbf{P}: \nabla \mathbf{u} - \nabla \cdot \mathbf{q} - \gamma. \tag{3}$$

In these equations, $\rho = \rho_p \nu$ represents the bulk density, where ρ_p is the particle density and ν is the solid fraction. The bulk velocity and the body force per unit mass are represented by $\mathbf{u}$ and $\mathbf{b}$, respectively, and $\mathbf{P}$ is the stress tensor. The granular temperature, T, is defined by $(1/3)(\langle u'^2 \rangle + \langle v'^2 \rangle + \langle w'^2 \rangle)$ where u', v', and w' are the three velocity fluctuation components. Finally, $\mathbf{q}$ is the flux of fluctuation energy, and γ is the rate of the dissipation of fluctuation energy per unit volume. In the translational fluctuation energy equation, the term $-\mathbf{P}: \nabla \mathbf{u}$ indicates the work done to the system by the stresses, and the so-called conduction term, $-\nabla \cdot \mathbf{q}$, represents the conduction of the fluctuation energy within the system.

The recent studies of the rheological behavior of rapidly flowing granular materials have provided explicit constitutive expressions most of which have been derived using methodologies from the kinetic theory of gases. Most of them, however, are not applicable over the entire range of solid fraction. For example, the expressions of Jenkins and Savage (1983) fail at the boundary of the free surface of the chute flow. Only the results presented by Lun et al. (1984) seem to be satisfactory for application to chute flows. Following Lun et al., the total stress tensor is written as

$$\mathbf{P} = \left\{ \rho_p g_1(\nu, e_p) T - \rho_p d \frac{8\sqrt{\pi}}{3} \eta \nu^2 g_0 T^{1/2} \nabla \cdot \mathbf{u} \right\} \times \mathbf{I} - 2\rho_p d g_2(\nu, e_p) T^{1/2} \mathbf{S}, \tag{4}$$

where $\mathbf{I}$ is the identity matrix and $\mathbf{S}$ is given as $\mathbf{S} = (1/2)(u_{i,j} + u_{j,i}) - 1/3 u_{k,k}\delta_{ij}$. The particle diameter is d, and $\eta = (1 + e_p)/2$ where e_p is the coefficient of restitution for collisions between particles. The flux vector of fluctuation energy is

$$\mathbf{q} = -\rho_p d (g_3(\nu, e_p) T^{1/2} \nabla T + g_4(\nu, e_p) T^{3/2} \nabla \nu), \tag{5}$$

and the rate of dissipation per unit volume is

$$\gamma = \frac{\rho_p}{d} g_5(\nu, e_p) T^{3/2}. \tag{6}$$

Here, $g_1(\nu, e_p)$, $g_2(\nu, e_p)$, $g_3(\nu, e_p)$, $g_4(\nu, e_p)$, and $g_5(\nu, e_p)$ are the functions of ν and e_p as follows:

$$g_1(\nu, e_p) = \nu + 4\eta \nu^2 g_0,$$

$$g_2(\nu, e_p) = \frac{5\sqrt{\pi}}{96}\left(\frac{1}{\eta(2-\eta)} \frac{1}{g_0} + \frac{8}{5} \frac{3\eta - 1}{2 - \eta} \nu + \frac{64}{25} \eta \left(\frac{3\eta - 2}{2 - \eta} + \frac{12}{\pi} \right) \nu^2 g_0 \right),$$

$$g_3(\nu, e_p) = \frac{25\sqrt{\pi}}{16\eta(41 - 33\eta)}\left(\frac{1}{g_0} + \frac{12}{5} \eta \{1 + \eta(4\eta - 3)\} \nu + \frac{16}{25} \eta^2 \left\{ 9\eta(4\eta - 3) + \frac{4}{\pi}(41 - 33\eta) \right\} \nu^2 g_0 \right),$$

$$g_4(\nu, e_p) = \frac{15\sqrt{\pi}}{4} \frac{(2\eta - 1)(\eta - 1)}{41 - 33\eta}\left(\frac{1}{\nu g_0} + \frac{12}{5} \eta \right) \frac{d}{d\nu}(\nu^2 g_0),$$

$$g_5(\nu, e_p) = \frac{48}{\sqrt{\pi}} \eta(1 - \eta) \nu^2 g_0.$$

And g_0, the radial distribution function, is chosen as suggested by Lun and Savage (1986), as follows:

$$g_0 = \left(1 - \frac{\nu}{\nu^*} \right)^{-2.5\nu^*},$$

where ν^* is the maximum shearable solid fraction for spherical particles; a value of $\nu^* = 0.62$ is used in this analysis. It should be noted that g_1, g_2, g_3, and g_5 are positive quantities for all ν and e_p while g_4 is always negative. Furthermore, g_1 and g_5 vanish as $\nu \to 0$ while g_0, g_2, g_3, g_4, and all the derivatives of g_0, g_1, g_2, g_3, g_4, with respect to ν, do not vanish as $\nu \to 0$.

2.2 The Formulation of the Boundary Value Problem. We shall now apply these governing equations by Lun et al. (1984) to two-dimensional fully developed flow down an inclined plane. In such a flow the derivatives parallel to the plane are zero and the continuity Eq. (1) is automatically satisfied. The momentum Eqs. (2) in the flow direction (x-direction) and in the direction normal to the chute base (y-direction) become

$$\frac{\partial P_{yy}}{\partial y} = -\rho_p \nu g \cos\theta, \tag{7}$$

$$\frac{\partial P_{yx}}{\partial y} = \rho_p \nu g \sin\theta, \tag{8}$$

Downloaded 03 May 2010 to 171.66.16.247. Redistribution subject to ASME license or copyright; see http://www.asme.org/terms/Terms_Use.cfm

where θ is the angle of the chute inclination, and g is the gravitational acceleration. Note that for the fully developed chute flow, $-P_{yx}/P_{yy}=\tan\theta$. The energy equation simplifies to

$$0=-P_{yx}\frac{\partial u}{\partial y}-\frac{\partial q_y}{\partial y}-\gamma. \tag{9}$$

The constitutive Eqs. (4) and (5) also simplify. Since $\nabla\cdot\mathbf{u}=0$, the normal and shear stresses become

$$P_{yy}=\rho_p g_1 T, \tag{10}$$

$$P_{yx}=-\rho_p d g_2\frac{\partial u}{\partial y}T^{1/2}, \tag{11}$$

and the y-component of fluctuation energy flux is given as

$$q_y=-\rho_p d\left(g_3 T^{1/2}\frac{\partial T}{\partial y}+g_4 T^{3/2}\frac{\partial \nu}{\partial y}\right). \tag{12}$$

Here the temperature gradient term has no known physical significance. For the sake of comparison, we retain all the terms of Lun et al.

Equations (7)–(9) with (6) and (10)–(12), after nondimensionalization, can be written in the following form:

$$\frac{\partial \nu}{\partial y^*}=-\frac{1}{g_1' T^*}\left(\nu+g_1\frac{\partial T^*}{\partial y^*}\right), \tag{13}$$

$$\frac{\partial^2 T^*}{\partial y^{*2}}=\frac{1}{g_1'^2(g_1g_4-g_1'g_3)}\left[T^* g_1'^3\left\{\frac{g_1^2}{g_2}\tan^2\theta-g_5\right\}+\frac{1}{T^*}\left(\frac{\partial T^*}{\partial y^*}\right)^2\times\left\{\frac{1}{2}g_1'^3 g_3-g_1 g_1'^2 g_3'+\frac{1}{2}g_1 g_1'^2 g_4+g_1^2 g_1' g_4'-g_1^2 g_1'' g_4\right\}+\frac{1}{T^*}\frac{\partial T^*}{\partial y^*}\left\{g_1 g_1' g_4+\left(2g_1 g_1' g_4'-2g_1 g_1'' g_4-g_1'^2 g_3+\frac{1}{2}g_1'^2 g_4\right)\nu\right\}+\frac{1}{T^*}\{g_1' g_4\nu+(g_1' g_4'-g_1'' g_4)\nu^2\}\right], \tag{14}$$

$$\frac{\partial u^*}{\partial y^*}=\frac{g_1}{g_2}T^{*1/2}\tan\theta. \tag{15}$$

Here the dimensionless spatial coordinate y^*, granular temperature T^*, and mean velocity u^* are defined by

$$y^*=\frac{y}{d},\qquad T^*=\frac{T}{gd\cos\theta},\qquad u^*=\frac{u}{\sqrt{gd\cos\theta}}.$$

And in g_1', g_3', g_4', and g_1'', the dashes denote differentiation with respect to ν. These differential equations are nonlinear, and must be solved simultaneously. Equations (13) and (14) can be solved for ν and T^*; u^* follows from Eq. (15). It is important to note that ν and T^* have solutions independent of u^*.

The above system of differential Eqs. (13)–(15) requires boundary conditions both at the wall of the chute base and at the free surface. At the free surface, the stresses and the energy flux, q_y, must vanish. It is clear that all the conditions are satisfied if and only if $\partial T^*/\partial y^*$ vanishes at the free surface. In Eq. (13), when this gradient of the granular temperature tends to zero at the free surface, the gradient of solid fraction is always negative, and thus the solid fraction vanishes in an approximately exponential manner. Since the solid fraction vanishes at the free surface, the gradient of the solid fraction tends to zero. Therefore, the energy flux vanishes because both gradients of granular temperature and solid fraction vanish at the free surface. Note that the gradient of mean velocity also vanishes, since the solid fraction tends to zero at the free surface. Therefore, all the stresses and their derivatives vanish as ν goes to zero, satisfying the momentum equations at the free surface. The energy equation is also satisfied since all three terms in Eq. (9) vanish independently at the free surface.

It transpires that $T=0$ also satisfies all the boundary conditions at the free surface. However, if $T=0$, $\partial q_y/\partial y$ should be zero from the energy Eq. (9). The condition of $\partial q_y/\partial y=0$ at the free surface with $T=0$ yields $\partial T/\partial y=0$ at the free surface. (This can be shown by differentiating Eq. (12) with respect to y.) Therefore, the condition $\partial T/\partial y=0$ is sufficient and necessary to satisfy all the boundary conditions at the free surface.

Hence, the boundary value problem is formulated as follows: The differential Eqs. (13), (14), and (15), are to be solved with three boundary values at the wall (ν, T^*, and u^* at $y^*=0$) and one boundary condition at the free surface ($\partial T^*/\partial y^*=0$). A "shooting method" has been chosen to solve this boundary value problem. That is, for given ν, T^*, and u^* at the wall, a guess is made for the value of $\partial T^*/\partial y^*$ at $y^*=0$. With these four values, the above differential equations are integrated from $y^*=0$ to $y^*=\infty$. If $\partial T^*/\partial y^*$ at $y^*=\infty$ is not zero after integration, another $\partial T^*/\partial y^*$ at $y^*=0$ is tried. This iterative procedure is continued until $\partial T^*/\partial y^*$ at $y^*=\infty$ becomes zero. In practice, as the equations are integrated from 0 to ∞, a finite y_s^* is found at which $\partial T^*/\partial y^*$ is sufficiently small to say that y_s^* is the location of the free surface. Iterations were done until the ratio of the temperature gradient at the free surface to that at the wall became about 10^{-6}, and the differential equations were, for most of cases, integrated up to $y^*=10\sim100$. A fourth-order Runge-Kutta method was employed, and no convergence problems were encountered.

It is noteworthy that the location of the free surface is automatically determined in the present analysis. In other literature, there have been efforts to locate the free surface using various techniques. For example, Johnson and Jackson (1988) have attempted a numerical analysis similar to the present one. In their analysis, the spatial coordinate Y was normalized by h, the depth of flow. Since h is not well defined because often ν vanishes slowly, it was necessary to define a small layer adjacent to the free surface. The location of this layer was then defined as h, and a boundary value problem was solved between $Y=0$ and $Y=h$. Later, the results near $Y=h$ were matched to asymptotic low density solutions in the neighborhood of the free surface. The asymptotic solutions were obtained by demanding that the solid fraction and the derivatives of velocity and granular temperature vanish as $Y\to\infty$.

3 Results of Analysis and Comparisons

3.1 Results of Analysis. As described earlier, the flow properties, ν, T^*, and u^*, were obtained as functions of y^*—the distance from the chute base normalized by the particle diameter. Each result was specified by the two parameters, e_p and $\tan\theta$, and three boundary values at the wall, ν_w, T_w^*, and u_w^*. The results for $\sqrt{T^*}$ and u^* were normalized by $\sqrt{T_w^*}$ and u_w^*, respectively.

Though two parameters and three boundary values created numerous variations, the results could be classified into two distinct types and a transitional type according to the form of the granular temperature profile. The first type is illustrated by the solution shown in Fig. 1 for which $e_p=0.95$, $\tan\theta=0.4$, $T^*=2$, $\nu_w=0.2$, and $u^*=10$. Note that granular temperature increases with distance from the wall. The profile of solid fraction exhibits a monotonic decrease from the wall to the free surface, and it is clear that solid fraction vanishes at the free surface. The profile of mean velocity appears to be roughly parabolic. Near the wall the profile is fairly linear, and the velocity gradient tends to zero at the free surface. The physical location of the free surface, h, is ill-defined in view of the solid fraction profile. One might reach different conclusions about

Downloaded 03 May 2010 to 171.66.16.247. Redistribution subject to ASME license or copyright; see http://www.asme.org/terms/Terms_Use.cfm

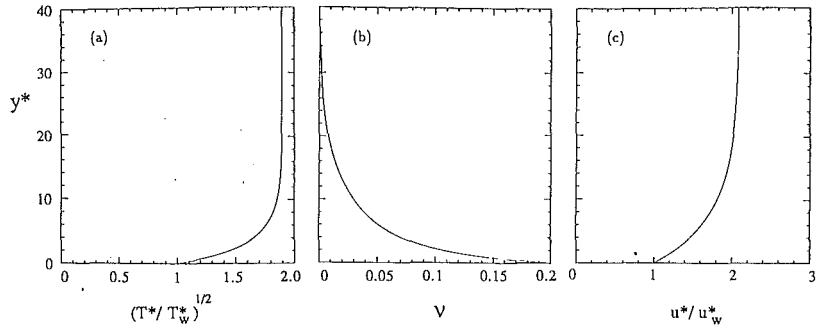

Fig. 1(*a*) Nondimensionalized square root of granular temperature, $(T^*/T_w^*)^{1/2}$, (*b*) solid fraction, ν, and (*c*) nondimensionalized mean velocity, u^*/u_w^*, against nondimensionalized distance from the chute base, y^*. Parameters: $e_p = 0.95$ and $\tan\theta = 0.4$. Boundary values at the wall: $T_w^* = 2$, $\nu_w = 0.2$, and $u_w^* = 10$.

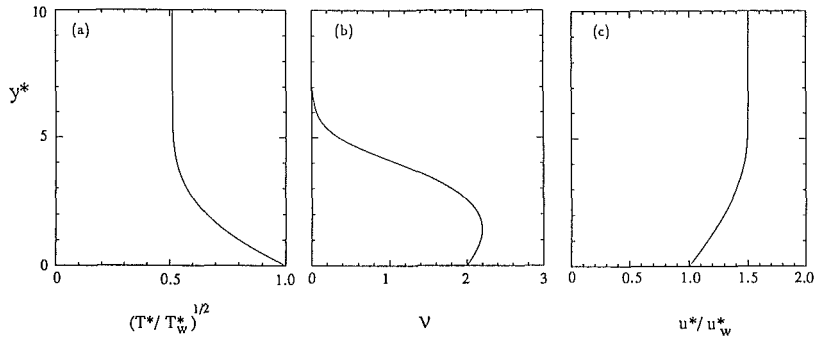

Fig. 2(*a*) Nondimensionalized square root of granular temperature, $(T^*/T_w^*)^{1/2}$, (*b*) solid fraction, ν, and (*c*) nondimensionalized mean velocity, u^*/u_w^*, against nondimensionalized distance from the chute base, y^*. Parameters: $e_p = 0.6$ and $\tan\theta = 0.4$. Boundary values at the wall: $T_w^* = 2$, $\nu_w = 0.2$, and $u_w^* = 10$.

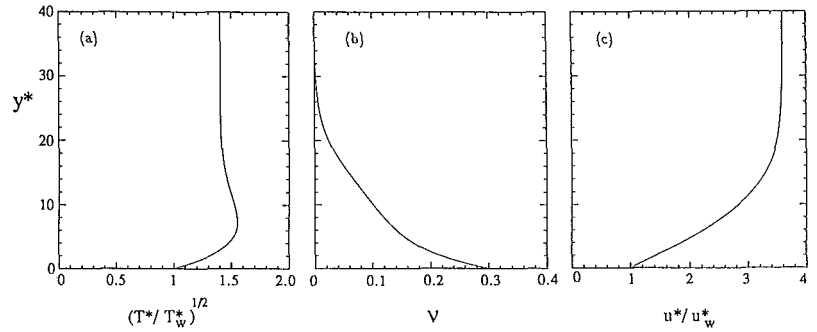

Fig. 3(*a*) Nondimensionalized square root of granular temperature, $(T^*/T_w^*)^{1/2}$, (*b*) solid fraction, ν, and (*c*) nondimensionalized mean velocity, u^*/u_w^*, against nondimensionalized distance from the chute base, y^*. Parameters: $e_p = 0.9$ and $\tan\theta = 0.4$. Boundary values at the wall: $T_w^* = 2$, $\nu_w = 0.3$, and $u_w^* = 10$.

the value of h, depending on whether the granular temperature or the velocity profile is being examined.

Obvious differences in the profile of the granular temperature occur for the second type illustrated in Fig. 2 for which $e_p = 0.6$ and the other values remain unchanged. First of all, the temperature gradient is now negative. The variation of the magnitude of the temperature with distance from the chute based is substantial. The different choice of the value of the coefficient of restitution also results in a particular type of solid fraction profile, where the maximum solid fraction is achieved in the center of the flow and lower densities occur both at the wall and at the free surface. In this case, the free surface is more clearly defined.

Finally, a transitional type, which contains features of both the first and second types, is illustrated in Fig. 3. Note that $e_p = 0.8$ and $\nu_w = 0.3$ while the other parameter and boundary values are not changed. The granular temperature first increases with distance from the wall boundary, then decreases at larger distances from the wall, and then becomes uniform near the free surface. The profile of solid fraction is similar to that of the first type.

The question of when each of these types of the granular temperature profiles occurs will be discussed later. In this presentation, the first, second, and last types will be referred to as Type I, Type II, and Type III, respectively.

The effect of the variation of the parameter $\tan\theta$ is investigated in Fig. 4. The results show that higher gradients of granular temperature and velocity arise from a higher angle of chute inclination, and the depth of flow also increases. This is consistent with a physical understanding of the chute flow.

Downloaded 03 May 2010 to 171.66.16.247. Redistribution subject to ASME license or copyright; see http://www.asme.org/terms/Terms_Use.cfm

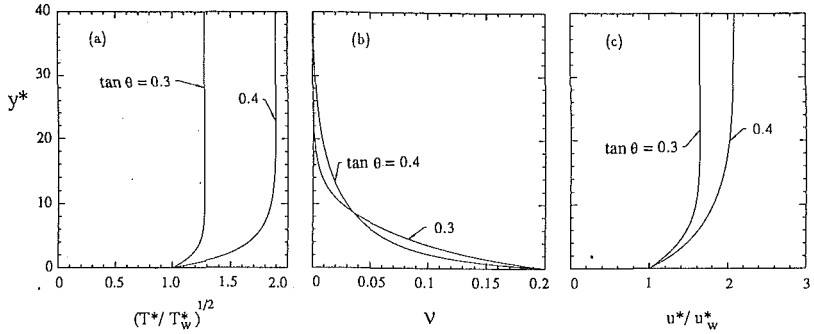

Fig. 4 The effect of the variation of the chute inclination angle. (*a*) Nondimensionalized square root of granular temperature, $(T^*/T_w^*)^{1/2}$, (*b*) solid fraction, ν, and (*c*) nondimensionalized mean velocity, u^*/u_w^*, against nondimensionalized distance from the chute base, y^*. Parameters: $e_p = 0.95$, $\tan\theta = 0.3$, and 0.4. Boundary values at the wall: $T_w^* = 2$, $\nu_w = 0.2$, and $u_w^* = 10$.

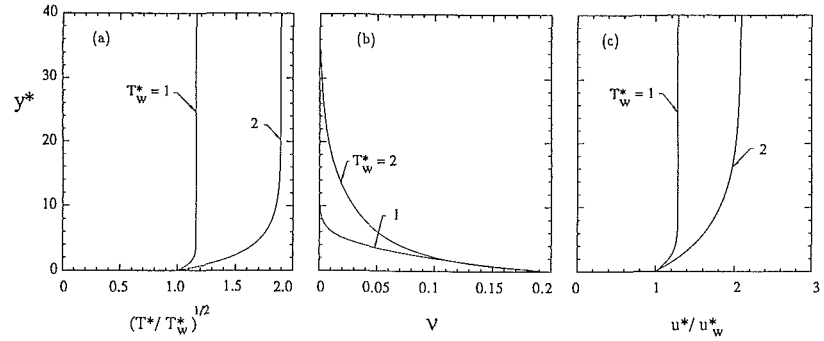

Fig. 5 The effect of the variation of granular temperature at the wall. (*a*) Nondimensionalized square root of granular temperature, $(T^*/T_w^*)^{1/2}$, (*b*) solid fraction, ν, and (*c*) nondimensionalized mean velocity, u^*/u_w^*, against nondimensionalized distance from the chute base, y^*. Parameters: $e_p = 0.95$ and $\tan\theta = 0.4$. Boundary values at the wall: $T_w^* = 1$ and 2, $\nu_w = 0.2$, and $u_w^* = 10$.

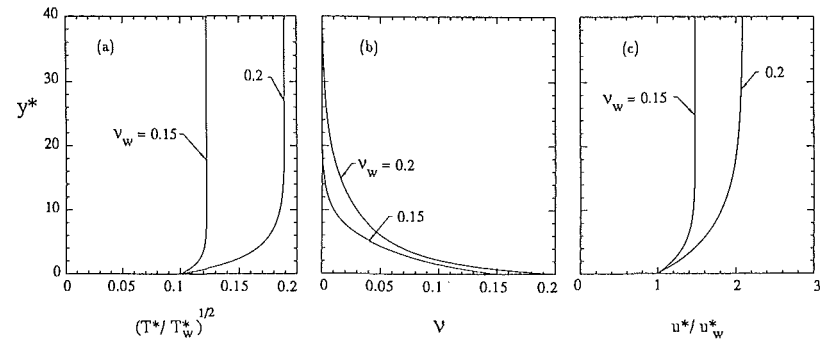

Fig. 6 The effect of the variation of solid fraction at the wall. (*a*) Nondimensionalized square root of granular temperature, $(T^*/T_w^*)^{1/2}$, (*b*) solid fraction, ν, and (*c*) nondimensionalized mean velocity, u^*/u_w^*, against nondimensionalized distance from the chute base, y^*. Parameters: $e_p = 0.95$ and $\tan\theta = 0.4$. Boundary values at the wall: $T_w^* = 2$, $\nu_w = 0.15$ and 0.2, and $u_w^* = 10$.

That is, for a higher inclination angle, particles move faster and collide with greater impact, resulting in the increase of granular temperature and velocity gradient. The increase of the overall granular temperature causes dilatation near the wall which is accompanied by an increase in the depth of flow. As a result, the solid fraction for the higher chute inclination is lower near the wall, but higher at a distance from the wall.

The effect of the variation of boundary values at the wall is examined in Figs. 5 and 6. Comparison shows that a larger value of granular temperature at the wall results in an increase in the granular temperature gradient and thus the overall granular temperature as shown in Fig. 5. As a consequence, (see Eq. (15)), the gradient of mean velocity also increases. The increase of granular temperature is also accompanied by an increase in the depth of flow. These results are consistent with the experimental observations of Ahn et al. (1989). On the surface where higher temperature is created, higher gradients of temperature and velocity are observed, and the depth of flow is increased.

The effect of the variation of solid fraction at the wall is examined in Fig. 6. When a larger solid fraction is prescribed at the wall, the granular temperature, the depth of flow, and

Downloaded 03 May 2010 to 171.66.16.247. Redistribution subject to ASME license or copyright; see http://www.asme.org/terms/Terms_Use.cfm

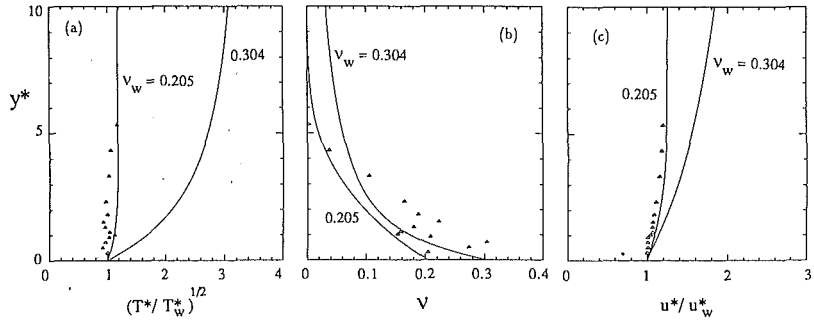

Fig. 7 Comparison with the experimental data of Ahn et al. (1989). The smooth aluminum surface used for the chute base and $d = 1.26$ mm Δ, data from the experiment. Solid line results of the present analysis. (*a*) Nondimensionalized square root of granular temperature, $(T^*/T_w^*)^{1/2}$, (*b*) solid fraction, ν, and (*c*) nondimensionalized mean velocity, u^*/u_w^*, against nondimensionalized distance from the chute base, y^*. Parameters: $e_p = 0.95$ and $\tan\theta = 0.418$. Boundary values at the wall: $T_w^* = 0.935$, $\nu_w = 0.205$ and 0.304, and $u_w^* = 11.3$.

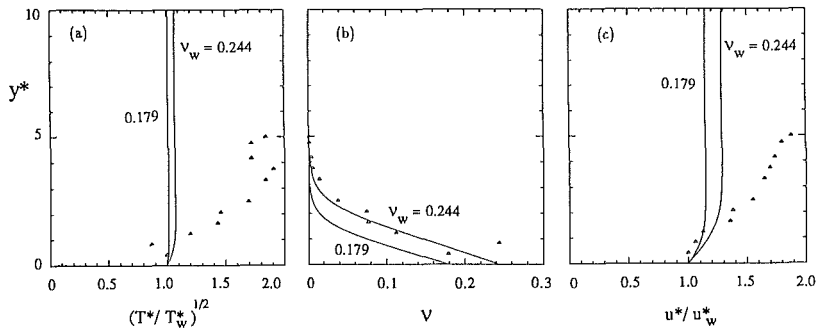

Fig. 8 Comparison with the experimental data of Ahn et al. (1989). The rubber-coated surface used for the chute base and $d = 3.04$ mm Δ, data from the experiment. Solid line results of the present analysis. (*a*) Nondimensionalized square root of granular temperature, $(T^*/T_w^*)^{1/2}$, (*b*) solid fraction, ν, and (*c*) nondimensionalized mean velocity, u^*/u_w^*, against nondimensionalized distance from the chute base, y^*. Parameters: $e_p = 0.95$ and $\tan\theta = 0.418$. Boundary values at the wall: $T_w^* = 0.440$, $\nu_w = 0.179$ and 0.244, and $u_w^* = 4.39$.

the mean velocity all increase significantly. These results agree with the experimental observations. In order to have a high solid fraction at a given chute inclination, the mass flow rate needs to be large and this implies a deeper flow.

3.2 Comparison with Experimental Results. Few experimental data are available for comparison with these analytical results. In particular, there are almost no measurements of granular temperature. Furthermore, the wall boundary conditions are not sufficiently well understood to allow us to estimate the values of T^*, ν, and u^* at the wall. The experiments of Ahn et al. (1989) represent an attempt to acquire the necessary data. In measurements through the sidewalls, the profiles of one component of granular temperature, mean velocity, and linear concentration were obtained. For comparison with the present results, granular temperature and solid fraction are obtained from one component of granular temperature, $\langle u'^2 \rangle$, and linear concentration, ν_{1D}, by taking $T = \langle u'^2 \rangle$ and $\nu = \pi\nu_{1D}^3/6$. Furthermore, the value of $e_p = 0.95$ is appropriate for the glass beads used in the experiments (see Lun and Savage (1986)) and this value of e_p is employed in all the results presented.

In a strict sense the solid fraction goes to zero at the wall since the particles are spherical. As a result, the appropriate wall solid fraction to be used in the corresponding continuum model is rather unclear. Therefore, two candidate choices are employed in the comparisons which follow. One is the solid fraction which was obtained at the measurement location closest to the wall. The other is the maximum solid fraction which was usually obtained at between a half and one-particle diameter distance from the wall.

Experimental data for 1.26-mm diameter glass beads flowing down a chute with a smooth aluminum surface are compared with the present analysis in Fig. 7. The chute inclination angle θ was 22.7 deg, and the boundary values at the wall, $T_w^* = 0.935$ and $u_w^* = 11.3$ are taken from the experiments. Two wall solid fractions are used as described above, namely, 0.205 and 0.304. The profile of granular temperature from the experiments shows a general increase of temperature with distance from the wall. This increasing feature is predicted by the present analysis. With $\nu_w = 0.205$, the magnitude of granular temperature is also well predicted. Moreover, the monotonic decrease of solid fraction with distance from the wall is consistent with the experiments. Near the wall, the result for the case of $\nu_w = 0.304$ shows better agreement with the experiments, but at the free surface, the present analytical result deviates from the experiments. For $\nu_w = 0.205$, the depth of flow of the analysis is consistent with that of the experiments while there is slight discrepancy near the wall. In addition, good agreement is observed between the profiles of mean velocity for the case of $\nu_w = 0.205$.

For the second comparison, experimental data with a rubber-coated chute base are presented in Fig. 8. This rubber-coated surface created quite different boundary conditions. Compared to a smooth aluminum surface, the depth of flow was high, mean velocity was usually low, and both the gradients of mean velocity and granular temperature were high. In the

Downloaded 03 May 2010 to 171.66.16.247. Redistribution subject to ASME license or copyright; see http://www.asme.org/terms/Terms_Use.cfm

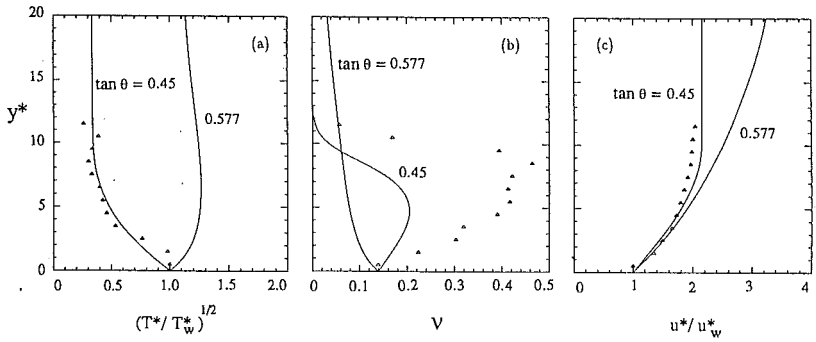

Fig. 9 Comparison with the computer simulations by Campbell and Brennen (1985b). Δ, data from the computer simulations. Type A simulation with $\theta = 30$ deg, $e_p = 0.6$, and $e_w = 0.8$. Solid line, results of the present analysis. Parameters: $e_p = 0.6$, and $\tan\theta = 0.577$ and 0.45. Boundary values at the wall: $T_w^* = 7.00$, $\nu_w = 0.140$, and $u_w^* = 14.0$. (*a*) Nondimensionalized square root of granular temperature, $(T^*/T_w^*)^{1/2}$, (*b*) solid fraction, ν, and (*c*) nondimensionalized mean velocity, u^*/u_w^*, against nondimensionalized distance from the chute base, y^*.

experiments, the 3.04-mm glass beads were used, and the chute inclination angle was 22.7 deg. Boundary values at the wall, $T_w^* = 0.44$ and $u_w^* = 4.388$ are taken from the experiments, and $\nu_w = 0.179$ and $\nu_w = 0.244$ are chosen as alternative solid fractions at the wall. Considerable discrepancy is observed between the profiles of granular temperature. The present analysis yields almost uniform granular temperature while the experimental data display significant granular conduction from the free surface to the wall. On the other hand, a remarkable agreement is found in the profiles of solid fraction, especially in the case of $\nu_w = 0.244$. The depth of flow as well as the general shape of solid fraction profile is well predicted in the present analysis. In the profiles of mean velocity, a deviation of the analysis from the experimental data is found. The discrepancies found in the profiles of granular temperature and mean velocity could be a result of the experimental flow not being fully developed. One might surmise that this flow would obtain a higher granular temperature as it becomes fully developed. If a large value of T_w^* were used in the present analysis, considerable increases of granular temperature and mean velocity would result (as shown in Fig. 5).

3.3 Comparison with Computer Simulation. Comparison of the present analysis can also be made with the computer simulations of Campbell and Brennen (1985b). The results of Campbell and Brennen for $\theta = 30$ deg or $\tan\theta = 0.557$, $e_p = 0.6$, and $e_w = 0.8$ and their Type A boundary condition are presented in Fig. 9. The results, with two-dimensional disks, were converted into three-dimensional values by taking $\nu_{3D} = 4\nu_{2D}^{3/2}/3\sqrt{\pi}$ and $T = (1/2)(\langle u'^2\rangle + \langle v'^2\rangle)$. The boundary values were $T_w^* = 7$, $u_w^* = 14$, and $\nu_w = 0.14$. The results of the present analysis with these parameters and boundary values are shown in Fig. 9. When $\tan\theta = 0.577$ is used as a parameter in the analysis, a fundamental difference is found. The results of Campbell and Brennen are of Type II, while the present analysis yields a Type III flow. However, when $\tan\theta = 0.45$ is used for the analysis, comparison shows excellent agreement between the analysis and the computer simulation. Both profiles of granular temperature have negative gradients, and their magnitudes are also in good agreement. The profiles of solid fraction are qualitatively similar, and the depth of flow is also well predicted. A discrepancy in the magnitude of solid fraction may arise from the fact that the computer simulations were done with two-dimensional disks. In the case of $\tan\theta = 0.45$, the mean velocity profiles also show good agreement between the computer simulation and the present analysis.

In short, good agreement is achieved in the case of $\tan\theta = 0.45$, which is slightly different from the value of the computer simulation. This may imply that the present analysis confirms the possibility of the existence of Type II flow but does not accurately predict when that type of flow takes place.

The results of Campbell and Brennen's computer simulations at the small chute angle of $\theta = 20$ deg could not be reproduced by the present analysis. The analysis yielded a Type II temperature profile, while the computer simulations produced a type of plug flow. That is, the minimum granular temperature was achieved in the center of the flow and higher temperature occurred both at the wall and at the free surface. The solid fraction profile of the analysis was similar to Type I while the computer simulation result had the profile of Type II.

Comparisons of the present analysis with experiments and computer simulations lead to the following conclusions: The experimental data are similar to Type I flow in which a positive temperature gradient and monotonically decreasing solid fraction are observed. The present analysis also produces the results of Type I as long as the boundary values are properly chosen. The general profiles of flow properties are well predicted, though some discrepancies in their magnitudes are observed. On the other hand, the computer simulations have Type II flows for sufficiently high chute inclinations. The granular temperature decreases with distance from the wall, and the solid fraction increases near the wall and decreases with further distance from the wall. These results can also be produced by the present analysis when a slight change in the parameter $\tan\theta$ is made.

The fundamental difference between the experimental results and the computer simulations is the value of the coefficient of restitution ($e_p = 0.95$ for the experiments and $e_p = 0.6$ for the computer simulations). The different values of e_p result in Type I flow for the experiments and Type II flow for the computer simulations. This will be discussed further in the next section.

4 The Nature of Granular Conduction

For fully developed chute flows, the translational fluctuation energy Eq. (9) may be written as follows:

$$W + Q - \gamma = 0$$

where W is the rate of the work done by stresses to the system per unit volume, Q is the rate of conduction of the fluctuation energy within the system, and γ is the dissipation rate per unit volume. For a simple shear flow, the conduction term disappears from the energy equation. But for chute flows, the role of the conduction term, or its magnitude compared to the other two terms, has been unclear. Haff (1986) emphasized the importance of grain inelasticity during a discussion of the

Downloaded 03 May 2010 to 171.66.16.247. Redistribution subject to ASME license or copyright; see http://www.asme.org/terms/Terms_Use.cfm

conduction and damping length scales. In this section, the fundamental nature of the conduction term will be discussed.

For fully developed chute flow, the ratio of shear stress to normal stress is a constant, given by $\tan\theta$. Using the constitutive equations for the stresses presented in Eqs. (10) and (11), the ratio of the characteristic velocity gradient to the granular temperature, often known as S or R in the literature, is given as follows:

$$S=\frac{d\dfrac{du}{dy}}{T^{1/2}}=\frac{\dfrac{du^*}{dy^*}}{T^{*1/2}}=\frac{g_1}{g_2}\tan\theta.$$

Recall that g_1 and g_2 are functions only of e_p and ν. Therefore, S is a function not only of e_p and ν but also of $\tan\theta$, while for Couette flows it is a function only of e_p and ν. Note S vanishes at the free surface since g_1 tends to zero as $\nu\to 0$.

The explicit form of S makes it possible to evaluate the work done by shear stress, and thus all the terms in the fluctuation energy equation are given as follows:

$$W^*=\frac{g_1^2}{g_2}T^{*3/2}\tan^2\theta,$$

$$\gamma=g_5T^{*3/2}$$

$$Q^*=\gamma^*-W^*,$$

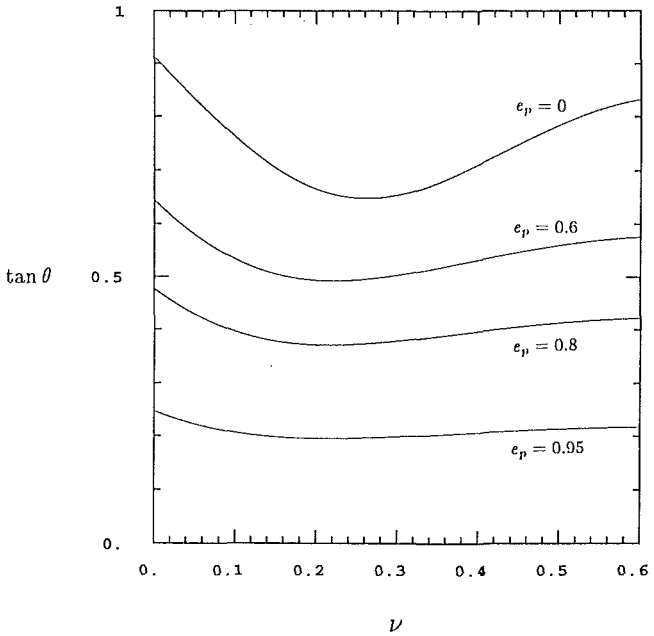

Fig. 10 Zeros of the granular conduction term for various e_p.

where W^*, γ^*, and Q^* are shear work term, dissipation term, and granular conduction term nondimensionalized by $\rho_p(gd\cos\theta)^{3/2}/d$. Furthermore, it is recalled that

$$Q^*=-\frac{\partial q^*}{\partial y^*},$$

where q^*, the fluctuation energy flux nondimensionalized by $\rho_p(gd\cos\theta)^{3/2}$, is given as

$$q^*=-\left(g_3T^{*1/2}\frac{\partial T^*}{\partial y^*}+g_4T^{*3/2}\frac{\partial \nu}{\partial y^*}\right).$$

It can be noted from the constitutive equations that γ^* is quite sensitive to the value of e_p while W^* is less sensitive, and that γ^* vanishes as e_p approaches 1. Therefore, for large e_p (e.g. 0.95), W^* is larger than γ^*, and this results in a negative value of Q^*. The opposite is true for small e_p such as 0.6. For a positive Q^*, the gradient of q^* is negative, and a positive gradient of q^* is achieved for negative Q^*. But the boundary condition at the free surface requires that $q^*\to 0$ as $y^*\to\infty$. Consequently, for a fixed ν, a negative value of q^* is obtained for all y^* in the case of a positive gradient of q^*, and a positive value of q^* in the case of a negative gradient of q^*. In other words, for a sufficiently large e_p, a negative energy flux, q^*, is achieved along with a negative granular conduction term Q^*. And for a sufficiently small e_p, a positive Q^* results in a positive energy flux.

As ν varies over the depth of the flow, however, the above argument may need modification. The effects of ν and $\tan\theta$ on the conduction term can be examined along with the effect of e_p as follows: The zero of Q^* is found by examining the following equation for Q^*

$$Q^*=\left(g_5-\frac{g_1^2}{g^2}\tan^2\theta\right)T^{*3/2}=0.$$

This is solved as shown in Fig. 10. Each curve represents zeros of Q^* for a given e_p. If $\tan\theta$ is greater than the value on the curve for a given ν, negative values of Q^* are obtained, and if $\tan\theta$ is smaller, then $Q^*>0$. For example, for $\tan\theta=0.4$, negative values of Q^* result for all ν in the case of $e_p=0.95$, but positive values result in the case of $e_p=0.6$.

The effects of e_p, ν, and $\tan\theta$ on the conduction term were examined in detail for solutions of Type I, Type II, and Type III flows. The energy flux, q^*, and the conduction term, Q^*, are plotted in Fig. 11(*a*), (*b*), and (*c*) with the same parameters and boundary values as given in Figs. 1, 2, and 3, respectively. As expected from the results of Fig. 10 in the case of $e_p=0.95$ and $\tan\theta=0.4$, negative Q^* is achieved in Fig. 11(*a*) and thus negative q^*. But for $e_p=0.6$ and $\tan\theta=0.4$ in Fig. 11(*b*), positive Q^* and q^* emerge, which are in accordance with the results of Fig. 10. When q^* is negative at the wall boundary it means that the wall absorbs the fluctuation energy. For this

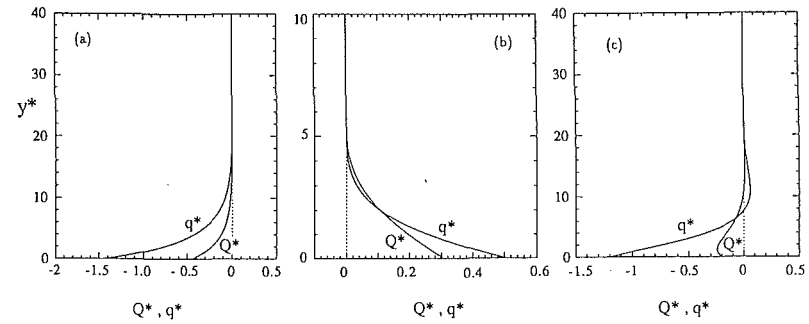

Fig. 11 Nondimensionalized granular conduction, Q^*, and fluctuation energy flux, q^*, against nondimensionalized distance from the chute base, y^*. Parameters and boundary values at the wall; (*a*) as in Fig. 1, (*b*) as in Fig. 2, and (*c*) as in Fig. 3.

Downloaded 03 May 2010 to 171.66.16.247. Redistribution subject to ASME license or copyright; see http://www.asme.org/terms/Terms_Use.cfm

case, the granular temperature is expected to be low near the wall while high temperature is exhibited at the free surface, and thus the fluctuation energy is conducted from the free surface to the wall. The generation of fluctuation energy through shear motion feeds fluctuation energy into the bulk, where it is partly absorbed at the wall boundary and partly dissipated away. On the other hand, positive fluctuation energy flux at the wall implies that the wall should supply energy to the flow. Unless energy is provided to granular materials through the wall (for example, by vibrating the chute base), there can be no such positive fluctuation energy flux and therefore no such flow. (Note that changes to granular material flows wrought by vibration are well known in industrial practice.) In the experiments of Ahn et al. (1989) when the angle of the chute inclination was less than about 12 deg, there was no flow unless the chute was agitated. This is consistent with the results of Fig. 10 in which the zero of Q^* for $e_p = 0.95$ is achieved at $\tan\theta \simeq 0.22$.

With this idea in mind, it is interesting to study a hypothetical experiment in which there is no shear motion but granular materials are allowed to have granular temperature which might be supplied by wall vibration. Then fluctuation energy will be conducted from the wall and should all be dissipated inside the bulk. Now examine such a state using the present analysis. The mean velocity and its gradient are zero, and $\tan\theta = 0$. From Fig. 10 it is expected that the conduction term will be positive for all values of the coefficient of restitution. The solutions are illustrated in Fig. 12 in which $e_p = 0.9$ and 0.95, $\tan\theta = 0$, $\nu_w = 0.2$, and $T_w^* = 5$. As expected, the solutions are of Type II because of a positive conduction term. Temperature decreases with distance from the wall, and solid fraction increases near the wall but decreases with further distance from the wall. Comparison between the results for different values of e_p show

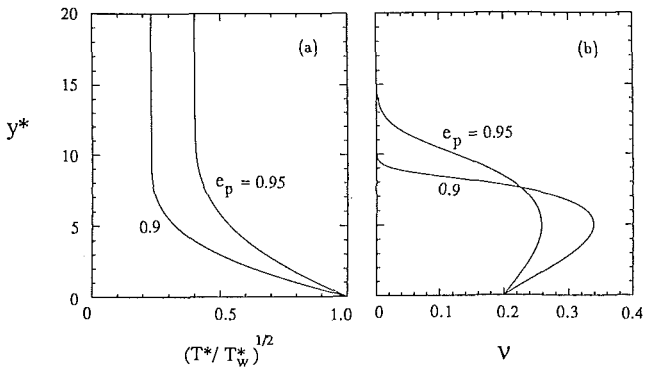

Fig. 12 The study of the case in which no shear motion and mean velocity exist. (*a*) Nondimensionalized square root of granular temperature, $(T^*/T_w^*)^{1/2}$, and (*b*) solid fraction, ν, against nondimensionalized distance from the chute base, y^*. Parameters: $e_p = 0.9$ and 0.95, and $\tan\theta = 0$. Boundary values at the wall: $T_w^* = 5$ $\nu_w = 0.2$.

as expected that for low e_p, the fluctuation energy dissipates faster than for high e_p. Therefore, the case of the lower e_p results in a lower temperature at the free surface.

At this point, it is necessary to study how solid fraction varies with granular temperature. Physically, it is clear that it is difficult for particles to stay close in the presence of high temperature. Therefore, when the temperature is high, the solid fraction is low. The variation of solid fraction with granular temperature can be explained in more detail by using Eq. (13):

$$\frac{\partial \nu}{\partial y^*} = -\frac{1}{g_1' T^*}\left(\nu + g_1 \frac{\partial T^*}{\partial y^*}\right).$$

When the temperature gradient is negative, the solid fraction gradient can be positive since both g_1 and g_1' are always positive. Therefore, when the temperature decreases significantly with distance from the wall, the solid fraction increases near the wall as shown in Figs. 2 and 12. Furthermore, when the temperature is lower, the magnitude of the solid fraction gradient is higher. Hence, the solid fraction for $e_p = 0.9$ increases more than for $e_p = 0.95$ as shown in Fig. 12. Equation (13) also explains the variation of solid fraction near the free surface. Near the free surface g_1' tends to 1, g_1 is the same order as ν, and the temperature gradient is negligible. Therefore, ν decreases approximately as e^{-y^*/T^*}. When the temperature is low at the free surface, a rapid decrease of solid fraction occurs. Therefore, the free surface is clearly defined as shown in Fig. 2. On the other hand, when the temperature is high near the free surface, the solid fraction decreases slowly with distance, resulting in the case of Fig. 1.

Figure 11(*c*) is an interesting case for which q^* and Q^* start with negative values but become positive and tend to zero as the free surface is approached. The boundary values at the wall ($\nu = 0.3$) and the two parameters ($e_p = 0.8$ and $\tan\theta = 0.4$) give a negative value of Q^* from Fig. 10. As ν decreases from the wall to the free surface, a positive Q^* is to be obtained from Fig. 10. This particular profile of energy flux over the depth gives rise to the particular shape of temperature profile in Fig. 3. Note from Fig. 11(*c*) that a local maximum of q^* is achieved when $Q^* = 0$.

The fundamental question of the magnitude of the conduction term in the chute flow is answered in Fig. 13 where the ratio of the conduction term to the dissipation term is plotted against y^*. Figures 13(*a*), (*b*), and (*c*) are the results from cases of Figs. 1, 2, and 3, respectively. In none of Figs. 13(*a*) and (*b*) is the conduction term insignificant relative to the dissipation term. In an transitional case such as Fig. 13(*c*), the conduction term is relatively smaller than the dissipation term. In fact, the ratio of the conduction term to the dissipation term is given as follows:

$$\frac{Q^*}{\gamma^*} = 1 - \frac{g_1^2}{g_2 g_5}\tan^2\theta.$$

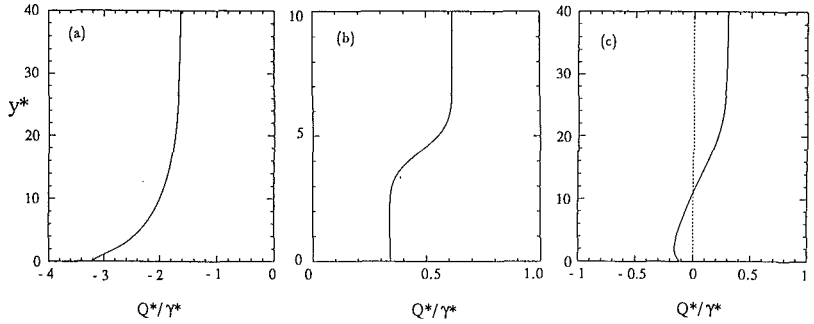

Fig. 13 The ratio of granular conduction to dissipation, Q^*/γ^*, against nondimensional distance from the chute base, y^*. Parameters and boundary values at the wall: (*a*) as in Fig. 1, (*b*) as in Fig. 2, and (*c*) as in Fig. 3.

Downloaded 03 May 2010 to 171.66.16.247. Redistribution subject to ASME license or copyright; see http://www.asme.org/terms/Terms_Use.cfm

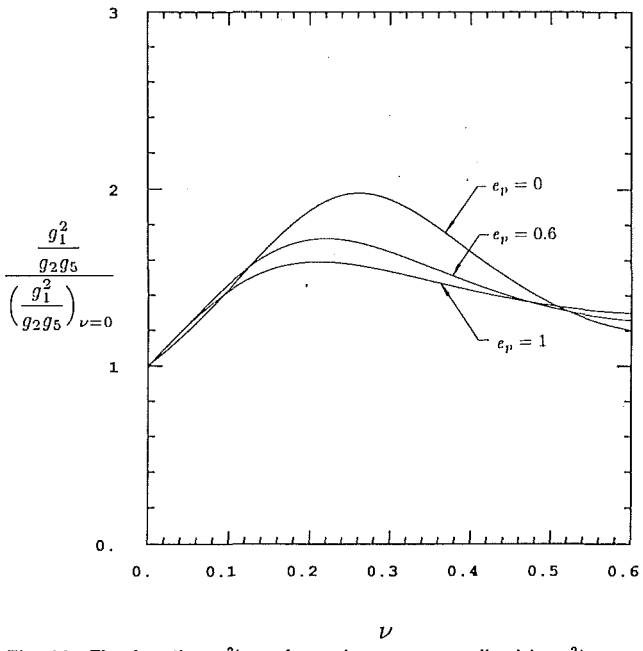

Fig. 14 The function g_1^2/g_2g_5 for various e_p, normalized by g_1^2/g_2g_5 at $\nu=0$

In Fig. 14, g_1^2/g_2g_5, normalized by the value at $\nu=0$, is plotted as a function of ν and e_p. Note that g_1^2/g_2g_5 at $\nu=0$ is given as follows:

$$\left(\frac{g_1^2}{g_2g_5}\right)_{\nu=0}=\frac{2}{5}\left(\frac{3-e_p}{1-e_p}\right).$$

Therefore, Q^*/γ^* varies from 1(when $\theta=0$) to $-\infty$ (when $e_p=1$), and conduction is always important. In general, the magnitude of the ratio is large for large e_p and small for small e_p. When negative conduction exists, a higher chute inclination yields a larger value for the ratio. That is, for a higher chute inclination, the conduction term plays a more important role relative to the dissipation term than for a lower chute inclination. When the conduction is positive, the opposite is true.

Since $W^*/\gamma^*=1-Q^*/\gamma^*$, the shear work term is small compared to the dissipation term when the conduction term is positive. When the conduction term is negative, W^*/γ^* is relatively large. (Note the comparison between Figs. 13(*a*) and (*b*)). When W^*/γ^* is small (such as the case of Fig. 13(*b*)) granular temperature is low, because fluctuation energy is slowly generated by the shear work. Furthermore, the flow dissipates well because of a low coefficient of restitution. As a result, the high density at the center of the flow is not dilated (see Fig. 2).

5 Conclusion

The governing equations and the constitutive relations presented by Lun et al. (1984) have been used in the present analysis of fully developed chute flow. The boundary value problem has been formulated with two parameters (e_p and $\tan\theta$). Three boundary values at the wall (ν_w, T_w, and u_w) are required for the solution. It is found that all the boundary conditions at the free surface are satisfied if and only if the gradient of temperature vanishes at the free surface. This boundary value problem has been numerically solved by a "shooting method."

The solutions fall into two categories: Only the two parameters (e_p and $\tan\theta$) determine which type of flow will occur, and three boundary values at the wall play no role in determining the type of flow. The first type has a granular temperature which increases from the wall boundary to the free surface. The solid fraction monotonically decreases with distance from the chute base, and the free surface is not well defined. The second type exhibits high temperature near the chute base, and a rapid decrease of the temperature as the free surface is approached. In this type the solid fraction is low at both boundaries but high in the center of the flow, and the free surface is rather clearly defined. A transitional type is also found which exhibits features of both the first and second types of flow; the temperature increases near the wall but decreases thereafter. The solid fraction has a profile similar to the first type.

These profiles are closely connected to the role of the granular conduction term in the fluctuation energy equation. The conduction term, which depends on e_p, $\tan\theta$, and ν, determines the energy flux, and thus the gradients of granular temperature and solid fraction, causing different profiles to occur. The conduction term often appears to be significant in magnitude compared to the dissipation term.

The effect of the variations of the parameter and wall boundary values is also studied. As the chute inclination angle increases, granular temperature, mean velocity, and the depth of flow increase. A higher granular temperature at the wall also causes an overall increase in temperature, mean velocity, and flow depth. An increase in the solid fraction at the wall also yields the same result.

Comparisons with experiments and computer simulations have been made. The experiments of Ahn et al. (1989) correspond to Type I flows. The experimental data show that with distance from the chute base the solid fraction decreases monotonically, and granular temperature increases indicating granular conduction from the free surface to the wall. The results of the present analysis are consistent with those data. The general profiles of flow properties are well predicted, though some discrepancies in their magnitudes are observed. On the other hand, the computer simulations by Campbell and Brennen (1985b) correspond to Type II flows. Granular conduction from the wall to the free surface is observed, and the solid fraction is low at both boundaries but high in the bulk. Good agreement between the present analysis and the computer simulations is found when a slightly different value of the parameter $\tan\theta$ is used as an input. The decrease of granular temperature with distance from the wall is well predicted, and the profile of solid fraction is similar to that of the computer simulations. Some discrepancies may be due to the fact that the computer simulations were conducted with two-dimensional disks.

The different types of flow occurring in the experiments and the computer simulations are the results of the different values of the coefficient of restitution appropriate to those circumstances. A high value of e_p, such as the value of about 0.95 in the experiments, causes the granular temperature to be conducted from the free surface to the wall; and a low value of e_p, such as the value of 0.6 used in the computer simulations, results in granular conduction in the opposite direction.

References

Ahn, H., Brennen, C. E., and Sabersky, R. H., 1988, "Experiments on Chute Flows of Granular Materials," *Micromechanics of Granular Materials*, M. Satake and J. T. Jenkins, eds., Elsevier, Amsterdam, pp. 339–348.

Ahn, H., Brennen, C. E., and Sabersky, R. H., 1989, "Measurements of Velocity, Velocity Fluctuation, Density, and Stresses in Chute Flows of Granular Materials," ASME JOURNAL OF APPLIED MECHANICS, to be published.

Augenstein, D. A., and Hogg, R., 1978, "An Experimental Study of the Flow of Dry Powders on Inclined Surfaces," *Powder Technology*, Vol. 19, pp. 205–215.

Bailard, J., 1978, "An Experimental Study of Granular-Fluid Flow," Ph.D. Thesis, University of California, San Diego.

Campbell, C. S., 1989, "The Stress Tensor for Simple Shear Flows of a Granular Material," *J. Fluid Mech.*, to be published.

Campbell, C. S., and Brennen, C. E., 1985a, "Computer Simulation of Granular Shear Flows," *J. Fluid Mech.*, Vol. 151, pp. 167–188.

Campbell, C. S., and Brennen, C. E., 1985b, "Chute Flows of Granular

Downloaded 03 May 2010 to 171.66.16.247. Redistribution subject to ASME license or copyright; see http://www.asme.org/terms/Terms_Use.cfm

Material: Some Computer Simulations," ASME JOURNAL OF APPLIED MECHANICS, Vol. 52, pp. 172–178.

Campbell, C. S., and Gong, A., 1986, "The Stress Tensor in a Two-Dimensional Granular Shear Flow," *J. Fluid Mech.*, Vol. 164, pp. 107–125.

Craig, K., Buckholz, R. H., and Domoto, G., 1986, "An Experimental Study of the Rapid Flow of Dry Cohesionless Metal Powders," ASME JOURNAL OF APPLIED MECHANICS, Vol. 53, pp. 935–942.

Haff, P. K., 1983, "Grain Flow as a Fluid Mechanical Phenomenon," *J. Fluid Mech.*, Vol. 134, pp. 401–430.

Haff, P. K., 1986, "A Physical Picture of Kinetic Granular Fluids," *J. Rheology*, Vol. 30, No. 5, pp. 931–948.

Hanes, D. M., and Inman, D. L., 1985, "Observations of Rapidly Flowing Granular-Fluid Flow," *J. Fluid Mech.*, Vol. 150, pp. 357–380.

Hui, K., Haff, P. K., Ungar; J. E., and Jackson, R., 1984, "Boundary Conditions for High-Shear Grain Flows," *J. Fluid Mech.*, Vol. 145, pp. 223–233.

Jenkins, J. T., and Savage, S. B., 1983, "A Theory for the Rapid Flow of Identical, Smooth, Nearly Elastic Particles," *J. Fluid Mech.*, Vol. 130, pp. 187–202.

Johnson, P. C., and Jackson, R., 1987, "Frictional-Collisional Constitutive Relations for Granular Materials, With Application to Plane Shearing," *J. Fluid Mech.*, Vol. 176, pp. 67–93.

Johnson, P. C., and Jackson, R., 1988, "Frictional-Collisional Equations of Motion for Particulate Flows and Their Application to Chutes," submitted to *J. Fluid Mech.*

Lun, C. K. K., and Savage, S. B., 1986, "The Effects of an Impact Velocity Dependent Coefficient of Restitution on Stresses Developed by Sheared Granular Materials," *Acta Mechanica*, Vol. 63, pp. 15–44.

Lun, C. K. K., Savage, S. B., Jeffrey, D. J., and Chepurniy, N., 1984, "Kinetic Theories for Granular Flow: Inelastic Particles in Couette Flow and Slightly Inelastic Particles in a General Flowfield," *J. Fluid Mech.*, Vol. 140, pp. 223–256.

Ogawa, S., Umemura, A., and Oshima, N., 1980, "On the Equations of Fully Fluidized Granular Materials," *J. App. Math. Phys.* (*ZAMP*), Vol. 31, pp. 483–493.

Richman, M. W., and Marciniec, R. P., 1988, "Gravity-Driven Granular Flows of Smooth, Inelastic Spheres Down Bumpy Inclines," submitted to ASME JOURNAL OF APPLIED MECHANICS.

Savage, S. B., 1979, "Gravity Flow of Cohesionless Granular Materials in Chutes and Channels," *J. Fluid Mech.*, Vol. 92, pp. 53–96.

Savage, S. B., and Jeffrey, D. J., 1981, "The Stress Tensor in a Granular Flow at High Shear Rates," *J. Fluid Mech.*, Vol. 110, pp. 255–272.

Savage, S. B., and McKeown, S., 1983, "Shear Stress Developed During Rapid Shear of Dense Concentrations of Large Spherical Particles Between Concentric Cylinders," *J. Fluid Mech.*, Vol. 127, pp. 453–472.

Savage, S. B., and Sayed, M., 1984, "Stresses Developed by Dry Cohesionless Granular Materials in an Annular Shear Cell," *J. Fluid Mech.*, Vol. 142, pp. 391–430.

Sayed, M., and Savage, S. B., 1983, "Rapid Gravity Flow of Cohesionless Granular Materials Down Inclined Chutes," *J. Appl. Math. Phys.*, Vol. 34, pp. 84–100.

Walton, O. R., and Braun, R. L., 1986a, "Viscosity, Granular-Temperature, and Stress Calculations for Shearing Assemblies of Inelastic, Frictional Disks," *J. of Rheology*, Vol. 30, No. 5, pp. 949–980.

Walton, O. R., and Braun, R. L., 1986b, "Stress Calculations for Assemblies of Inelastic Spheres in Uniform Shear," *Acta Mechanica*, Vol. 63, pp. 73–86.

Walton, O. R., Braun, R. L., Mallon, R. G., and Cervelli, D. M., 1988, "Particle-Dynamics Calculations of Gravity Flow of Inelastic, Frictional Spheres," *Micromechanics of Granular Materials*, M. Satake and J. T. Jenkins, eds., Elsevier, Amsterdam, pp. 153–162.

Downloaded 03 May 2010 to 171.66.16.247. Redistribution subject to ASME license or copyright; see http://www.asme.org/terms/Terms_Use.cfm

Boundary Conditions for Rapid Granular Flow: Flat, Frictional Walls

J. T. Jenkins
Department of Theoretical and Applied Mechanics,
Cornell University,
Ithaca, NY 14853-1503
Mem. ASME

We employ Coulomb friction and both tangential and normal restitution in a model for a collision between a homogeneous sphere and a flat wall. We calculate the impulse and change in kinetic energy in typical collisions and use a particularly simple velocity distribution function to obtain the rates at which momenta and energy are supplied to the flow over a unit area of the wall. From these, we determine boundary conditions that relate the shear stress and energy flux in the flow at the wall to the normal stress, slip velocity, and fluctuation energy and to the parameters that characterize a collision.

Introduction

Rapid granular flows are often driven and inevitably influenced by the surfaces that bound them. Because the thickness of a granular flow is often limited to tens of particles, their influence can be extremely pervasive. An indication of the importance of the boundaries in determining the characteristics of the flow is provided by experiments on the rapid shearing of glass spheres carried out by Savage and Sayed (1984) and Hanes and Inman (1985). To roughen their boundaries, Savage and Sayed covered them with sandpaper, while Hanes and Inman cemented glass spheres to theirs. At the same shear rate and density, the shear stresses of the latter were about three times those of the former. An insight into the mechanisms responsible for this is provided by the numerical simulations of steady plane shearing of circular disks carried out, for example, by Campbell and Gong (1987). These show how the profiles of the density, velocity, and energy of the flow across the thickness of the gap vary as the size and spacing of the boundary disks are changed. The shear and normal stress, transmitted across the gap, change with the profiles.

Boundary conditions for flows of smooth spheres and disks have been determined by Jenkins and Richman (1986), Jenkins (1987), and Richman (1988) who calculate Maxwellian and near-Maxwellian averages of the momentum and energy transferred in collisions between flow particles and a bumpy, frictionless wall. A simpler method of averaging, of importance to the present paper, was employed for the same purposes by Pasquarell and Ackermann (1989). In these approaches, the boundary condition, associated with the balance of momentum normal to the wall, resulted in a overly restrictive condition on the density at the wall. Hanes, Jenkins, and Richman (1988) relax this condition in a way that is roughly consistent with numerical simulations carried out by Snook and Henderson (1978) and Henderson and Van Swol (1984). In general, slip occurs at the boundary and, because of it, the boundary may supply fluctuation energy to the flow. Such a term was omitted in the boundary conditions earlier derived by Hui, Haff, Unger, and Jackson (1984) using heuristic arguments, but it was later included by Johnson and Jackson (1987). The possibility that fluctuation energy may be supplied to the flow at a boundary appears to be critical to the understanding of many granular flows.

Boundaries internal to the granular material are also important. Internal boundaries separate regions that are being rapidly sheared from regions that are not deforming. Johnson and Jackson (1987) assume that, at such an interface, some particles are sliding and some particles are colliding. The tangential and normal tractions of the sliding particles are related by a Coloumb yield condition. In contrast, Jenkins and Askari (1990) explore the situation in which the enduring contacts do not yield and collisions alone are responsible for the transfer of momentum and energy over surfaces separating translating and shearing regions. On these surfaces they assume that the mean velocity vanishes and that, in the translating region, the shear stress results from anisotropy induced in the arrangement of colliding grains. Whether the mechanical behavior of such an interface is determined primarily by the yielding of contacts or by collisional exchanges is likely to depend upon both the nature of the particles and the flow. For example, for given particles in a shear cell, a steady flow may exist corresponding to each mechanism alone.

A similar frictional contribution at an external boundary was also introduced by Johnson and Jackson (1987). They assumed that some of the particles were sliding relative to the boundary, and that the tangential and normal tractions of these were related by Columb's law of friction. In this paper we also focus attention on frictional interactions at an external boundary. However, we again confine our attentions to collisions and incorporate Coulomb friction into the collisional

Contributed by the Applied Mechanics Division of THE AMERICAN SOCIETY OF MECHANICAL ENGINEERS for publication in the JOURNAL OF APPLIED MECHANICS.

Discussion on this paper should be addressed to the Technical Editor, Prof. Leon M. Keer, The Technological Institute, Northwestern University, Evanston, IL 60208, and will be accepted until two months after final publication of the paper itself in the JOURNAL OF APPLIED MECHANICS. Manuscript received by the ASME Applied Mechanics Division, May 10, 1990; final revision, Nov. 20, 1990.

Copyright © 1992 by ASME
Downloaded 03 May 2010 to 171.66.16.247. Redistribution subject to ASME license or copyright; see http://www.asme.org/terms/Terms_Use.cfm

exchanges at a flat wall. Difficulties arise because not every collision involves an impulse with a sufficiently large tangential component, relative to its normal component, to insure that sliding of the point of contact occurs. A second complication results from the fact that energy stored in the particle during a collision may be returned to the component of the contact velocity tangential to the wall. In this case, the sliding of the contact relative to the wall may change its direction during a collision.

The integrations of the collisional impulse and change in energy over all possible collisions are extremely complicated. We carry them out analytically only for the simplest of velocity distribution functions. In the limiting case in which the coefficient of friction is so large that there is no sliding, the results are very close to those based upon a Maxwellian velocity distribution. In the limit in which the friction coefficient is so small that all collisions involve sliding, the ratio of shear to normal tractions is, essentially, equal to the coefficient of friction. Near these two limits we provide expressions for the stress ratio and energy flux that permit the evaluation of the relatively simple limiting forms and provide alternatives to them.

Flat Frictional Walls

We consider the collisional exchange of momentum and energy between a flow of identical, homogeneous, inelastic, frictional spheres and a flat frictional wall. During a collision, energy is stored in elastic deformations associated with both the normal and tangential displacements of the contact point relative to the center of a sphere. Because of the release of this energy may have a significant effect on its rebound (Maw, Barber, and Fawcett, 1976; 1981), we follow Walton (1988) and introduce coefficients of restitution associated with both the normal and tangential components of the velocity of the point of contact.

Collisions. The flat, frictional wall has a unit normal $\mathbf{n}$ pointing into the flow and supplies an impulse $\mathbf{J}$ to a sphere during a collision. A single homogeneous sphere has a moment of inertia I about its center, given in terms of its mass and diameter by $I=m\sigma^2/10$. Prior to a collision, it has translational velocity $\mathbf{c}$ and angular velocity ω; the corresponding post-collisional velocities are denoted by primes. The velocities before and after a collision are related by

$$m(\mathbf{c}'-\mathbf{c})=\mathbf{J}, \tag{1}$$

and

$$(m\sigma^2/10)(\omega'-\omega)=-(\sigma/2)\mathbf{n}\times\mathbf{J}. \tag{2}$$

In order to completely determine the impulse $\mathbf{J}$, we introduce the velocity $\mathbf{g}$ of the point of contact,

$$\mathbf{g}=\mathbf{c}-(\sigma/2)\omega\times\mathbf{n}, \tag{3}$$

and note that $\mathbf{n}\cdot\mathbf{g}=\mathbf{n}\cdot\mathbf{c}$.

We assume that the normal components of $\mathbf{g}$ before and after a collision are related by the usual coefficient of restitution e:

$$(\mathbf{n}\cdot\mathbf{g}')=-e(\mathbf{n}\cdot\mathbf{g}), \tag{4}$$

where $0\le e\le 1$. In a collision in which there is no sliding of the contact point relative to the wall, the tangential components of $\mathbf{g}$ are assumed to be related by a tangential coefficient of restitution β_0:

$$(\mathbf{n}\times\mathbf{g}')=-\beta_0(\mathbf{n}\times\mathbf{g}), \tag{5}$$

where $0\le\beta_0\le 1$. In collisions that involve sliding, the sliding is assumed to be resisted by Coulomb friction and the tangential and normal components of the impulse are related by the coefficient of friction μ:

$$|\mathbf{n}\times\mathbf{J}|=\mu(\mathbf{n}\cdot\mathbf{J}), \tag{6}$$

where $\mu\ge 0$.

It is convenient to write the impulse $\mathbf{J}$ in terms of the normal and tangential components of $\mathbf{g}$,

$$\mathbf{J}=A(\mathbf{n}\cdot\mathbf{g})\mathbf{n}+B[\mathbf{g}-(\mathbf{n}\cdot\mathbf{g})\mathbf{n}], \tag{7}$$

where A and B are to be determined. Then using Eqs. (1), (2), and (3), the contact velocities before and after a collision are related by

$$m(\mathbf{g}'-\mathbf{g})=A(\mathbf{n}\cdot\mathbf{g})\mathbf{n}+(7/2)B[\mathbf{g}-(\mathbf{n}\cdot\mathbf{g})\mathbf{n}]. \tag{8}$$

In order to distinguish between the two types of collisions, we first assume that sliding occurs and determine the impulse $\mathbf{J}^{(1)}$ in this case. The normal component of (8) used with (4) fixes the normal component of $\mathbf{J}^{(1)}$, after which (6) provides its tangential component. As a result,

$$\mathbf{J}^{(1)}=-m(1+e)(\mathbf{n}\cdot\mathbf{g})\mathbf{n}+\mu m(1+e)\cot\gamma[\mathbf{g}-(\mathbf{n}\cdot\mathbf{g})\mathbf{n}], \tag{9}$$

where

$$\cot\gamma\equiv(\mathbf{n}\cdot\mathbf{g})/|\mathbf{n}\times\mathbf{g}|. \tag{10}$$

For an impending collision, the angle γ between $\mathbf{g}$ and $\mathbf{n}$ is between $\pi/2$ and π, so the cotangent is negative. The relation between the velocities of the point of contact before and after a collision may be obtained from (8):

$$\mathbf{g}'=\mathbf{g}-(1+e)(\mathbf{n}\cdot\mathbf{g})\mathbf{n}+\mu_0\cot\gamma[\mathbf{g}-(\mathbf{n}\cdot\mathbf{g})\mathbf{n}], \tag{11}$$

where

$$\mu_0\equiv(7/2)(1+e)\mu. \tag{12}$$

Sliding stops when $(\mathbf{n}\times\mathbf{g}')=-\beta_0(\mathbf{n}\times\mathbf{g})$ or, equivalently, at a value γ_0 of the collision angle given by

$$1+\mu_0\cot\gamma_0=-\beta_0. \tag{13}$$

For collisions involving larger values of γ, there is no sliding and the normal and tangential components of the impulse $\mathbf{J}^{(2)}$ are obtained by employing (4) and (5) in (8). In this case,

$$\mathbf{J}^{(2)}=-m(1+e)(\mathbf{n}\cdot\mathbf{g})\mathbf{n}-(2m/7)(1+\beta_0)[\mathbf{g}-(\mathbf{n}\cdot\mathbf{g})\mathbf{n}]. \tag{14}$$

The total kinetic energy of a sphere, $K\equiv(m/2)c^2+(m\sigma^2/20)\omega^2$, experiences the change $\Delta K=K'-K$ in a collision. Using (1), (2), and (3), ΔK is given by

$$\Delta K=\mathbf{g}\cdot\mathbf{J}+(7/4m)\mathbf{J}^2-(5/4m)(\mathbf{n}\cdot\mathbf{J})^2. \tag{15}$$

In a sliding collision, the change $\Delta K^{(1)}$ in energy may be obtained by employing $\mathbf{J}^{(1)}$, given by (9), in (15):

$$\Delta K^{(1)}=-(m/7)(1-\beta^2)[g^2-(\mathbf{n}\cdot\mathbf{g})^2]-(m/2)(1-e^2)(\mathbf{n}\cdot\mathbf{g})^2, \tag{16}$$

where

$$\beta\equiv-(1+\mu_0\cot\gamma). \tag{17}$$

In a collision that does not involve sliding, the change $\Delta K^{(2)}$ in energy follows from using $\mathbf{J}^{(2)}$, given by (14), in (15):

$$\Delta K^{(2)}=-(m/7)(1-\beta_0^2)[g^2-(\mathbf{n}\cdot\mathbf{g})^2]-(m/2)(1-e^2)(\mathbf{n}\cdot\mathbf{g})^2. \tag{18}$$

The distinction between sliding and nonsliding collisions is clearly central to this study. One consequence of this is that the friction coefficient μ often enters the analysis through a parameter $\bar{\mu}_0$ given by

$$\bar{\mu}_0\equiv-\cot\gamma_0=\mu_0/(1+\beta_0)=(7/2)\mu(1+e)/(1+\beta_0). \tag{19}$$

Averages. In general, averages are calculated using a velocity distribution function $f(\mathbf{c}, \omega, \mathbf{r}, t)$ defined so that the number density n of particles at position $\mathbf{r}$ and time t is given as the integral of f over all values of velocity $\mathbf{c}$ and angular velocity ω,

Downloaded 03 May 2010 to 171.66.16.247. Redistribution subject to ASME license or copyright; see http://www.asme.org/terms/Terms_Use.cfm

$$n(\mathbf{r}, t) = \int\int f(\mathbf{c}, \omega, \mathbf{r}, t) d\mathbf{c}\, d\omega. \quad (20)$$

Given a particle property ψ that is a function of $\mathbf{c}$ and ω, its average $\langle\psi\rangle$ is defined by

$$\langle\psi\rangle = \frac{1}{n}\int\int \psi(\mathbf{c}, \omega) f(\mathbf{c}, \omega) d\mathbf{c}\, d\omega, \quad (21)$$

where the integration is over all $\mathbf{c}$ and ω and the dependence on $\mathbf{r}$ and t is to be understood. The mean velocity $\mathbf{u}$, fluctuation velocity $\mathbf{C}$, and granular temperature T are then

$$\mathbf{u} \equiv \langle \mathbf{c} \rangle, \ \mathbf{C} \equiv \mathbf{c} - \mathbf{u}, \text{ and } T \equiv (1/3)\langle C^2 \rangle, \quad (22)$$

respectively; while the mean angular velocity $\mathbf{w}$, the spin fluctuation velocity $\boldsymbol{\Omega}$, and the spin temperature τ are

$$\mathbf{w} = \langle \omega \rangle, \ \boldsymbol{\Omega} \equiv (\sigma/\sqrt{10})(\omega - \mathbf{w}), \text{ and } \tau \equiv (1/3)\langle \Omega^2 \rangle. \quad (23)$$

Collisional Fluxes. We take the wall to be at rest and denote the average velocity of the flow at the wall by $\mathbf{v}$. This slip velocity does not, in general, vanish; however, the wall is impenetrable, so $\mathbf{v}\cdot\mathbf{n} = 0$. In the same way, the mean angular velocity of the flow at the wall is not, in general, zero. Typically, these quantities must be determined as part of a solution to a boundary value problem in which boundary conditions are determined by considering the collisional exchange of linear momentum, angular momentum, and energy at the wall.

A particle will collide with an area element dA of the wall in a time interval dt if it is traveling towards the wall, $\mathbf{c}\cdot\mathbf{n} \le 0$, and has its center in the volume element $d\mathbf{r} = -\mathbf{c}\cdot\mathbf{n}\, dA dt$. In a collision, the particle property changes from ψ to ψ'. At the wall, we suppose that the number of particles per unit volume is $n\chi$, where χ is a factor that takes into account the presence of the wall on the spatial distribution of the particles. Then the collisional rate of change $\mathbf{C}(\psi)$ of ψ per unit area of the wall is the integral of the change in ψ in a single collision over the rate of collisions per unit area:

$$\mathbf{C}(\psi) = -\chi\int\int (\psi' - \psi) f(\mathbf{c}, \omega) \mathbf{c}\cdot\mathbf{n}\, d\mathbf{c}\, d\omega, \quad (24)$$

where the integration is to be taken over all ω and over all values of $\mathbf{c}$ for which $\mathbf{c}\cdot\mathbf{n} \le 0$. The particle properties of interest are its linear momentum

$$\psi = m\mathbf{c}, \text{ with } \psi' - \psi = \mathbf{J}, \text{ and } \mathbf{M} \equiv \mathbf{C}(m\mathbf{c}); \quad (25)$$

angular momentum

$$\psi = I\omega, \text{ with } \psi' - \psi = -(\sigma/2)\mathbf{n}\times\mathbf{J}, \text{ and } \mathbf{L} \equiv \mathbf{C}(I\omega); \quad (26)$$

and total energy

$$\psi = (1/2)mc^2 + (1/2)I\omega^2, \text{ with } \psi' - \psi = \Delta K, \text{ and}$$
$$-D \equiv \mathbf{C}(mc^2/2 + I\omega^2/2). \quad (27)$$

The quantities $\mathbf{M}$ and $\mathbf{L}$ are, respectively, the rates of supply of linear and angular momentum per unit area of the wall, while D is the rate of dissipation of energy per unit area.

Boundary Conditions. Boundary conditions are obtained by considering an infinitesimal volume in the flow in the shape of a pillbox with one face fixed on the wall. If $\mathbf{t}$ is the stress tensor in the flow, then, as the faces of the pillbox approach each other, the force per unit area $\mathbf{t}\cdot\mathbf{n}$ applied to the pillbox by the flow and the rate $\mathbf{M}$ of momentum supplied per unit area of the wall must sum to zero, so

$$-\mathbf{t}\cdot\mathbf{n} = \mathbf{M}. \quad (28)$$

If, next, $\mathbf{m}$ is the couple stress in the flow, the balance of angular momentum about the origin requires that, in the limit

$$\mathbf{r}\times(\mathbf{t}\cdot\mathbf{n}) + \mathbf{m}\cdot\mathbf{n} + \mathbf{r}\times\mathbf{M} + \mathbf{L} = 0, \quad (29)$$

or, with (28),

$$-\mathbf{m}\cdot\mathbf{n} = \mathbf{L}. \quad (30)$$

Finally, if $\mathbf{q}$ is the energy flux in the flow, the balance of total energy for the pillbox is, in the limit,

$$\mathbf{v}\cdot\mathbf{t}\cdot\mathbf{n} + \mathbf{w}\cdot\mathbf{m}\cdot\mathbf{n} - \mathbf{q}\cdot\mathbf{n} - D = 0, \quad (31)$$

or, with (28) and (30),

$$-\mathbf{v}\cdot\mathbf{M} - \mathbf{w}\cdot\mathbf{L} - D = \mathbf{q}\cdot\mathbf{n}. \quad (32)$$

We introduce the contact slip velocity $\mathbf{g}_0$, the mean velocity of the contact point relative to the boundary,

$$\mathbf{g}_0 \equiv \mathbf{v} + (\sigma/2)\mathbf{n}\times\mathbf{w}, \quad (33)$$

and note that as a consequence of $(25)_2$ and $(26)_2$, $\mathbf{L} = -(\sigma/2)\mathbf{n}\times\mathbf{M}$. Then, (32) can be written in terms of $\mathbf{M}$ and $\mathbf{g}_0$ as

$$-\mathbf{g}_0\cdot\mathbf{M} - D = \mathbf{q}\cdot\mathbf{n}. \quad (34)$$

Fluctuation energy is provided to the flow when the working of the boundary traction $\mathbf{M}$ through its velocity $-\mathbf{g}_0$ relative to the contact point exceeds the dissipation D.

Integrations. In order to carry out the integrations for $\mathbf{M}$ and D, we make several simplifying assumptions. These facilitate the calculation while, we anticipate, they retain the essential physics.

In the absence of a reliable flow theory for frictional spheres, the mean spin at the wall cannot be predicted. Consequently, in order to produce boundary conditions that can be applied to existing theories for spheres, we first assume that, at the wall, the mean angular velocity of the spheres is equal to the angular velocity of the mean flow:

$$\mathbf{w} = (1/2)\nabla\times\mathbf{u}. \quad (35)$$

This is the relation between these quantities in a steady, simple shear with uniform velocity gradient, number density, and temperatures (e.g., Campbell, 1989). The extent to which this assumption fails near a flat frictional wall can be seen in the numerical simulations of Campbell and Gong (1987).

Second, we ignore the fluctuations in angular velocity. Calculations valid for small coefficients of friction (Jenkins and Richman, 1985; Lun and Savage, 1987) indicate that the ratio of rotational to translational fluctuation energies is proportional to the friction coefficient. On the other hand, numerical simulations of the steady simple shear of very frictional spheres show that the energy of the angular velocity fluctuations may be as large as 60 percent of that associated with the translational velocity fluctuations (Campbell, 1990). At this point, we accept the error associated with their neglect and employ a distribution function $F(\mathbf{C})$ with the property that

$$n = \int F(\mathbf{C}) d\mathbf{C}, \quad (36)$$

with the integration taken over all velocity fluctuations.

Third, we assume that $F(\mathbf{C})$ is a function only of C^2. Numerical simulations (Campbell and Gong, 1986; Walton and Braun, 1986a,b) and calculations (Jenkins and Richman, 1988; Richman, 1989) that involve the steady simple shear of smooth, inelastic disks or spheres indicate that, at a given number density, deviations from such an isotropic velocity distribution function become increasingly pronounced as the collisions become less elastic. For smooth inelastic particles, the stresses differ by as much as a factor of two from those based on an isotropic distribution function as the coefficient of restitution decreases. The presence of the additional dissipation associated with friction is expected to further increase this anisotropy, so our predictions for very inelastic and/or very frictional collisions are likely to contain an error associated with this assumption.

Finally, we assume that the magnitudes of the fluctuation velocities are equal to their root mean square, or $C^2 = 3T$. Phrased in terms of the velocity distribution function, that is

Downloaded 03 May 2010 to 171.66.16.247. Redistribution subject to ASME license or copyright; see http://www.asme.org/terms/Terms_Use.cfm

$$F(C^2)=\frac{n}{4\pi(3T)}\delta(C^2-3T), \tag{37}$$

where $\delta(\cdot)$ is the delta function. Such a simple form of the velocity distribution functions was first introduced by Ogawa, Umemura, and Oshima (1980) and has been employed by Ackermann and Shen (1982) and others. Pasquarell, Ackermann, Shen, and Hopkins (1989) and Pasquarell and Babic (1989) provide corrected versions of the earlier constitutive relations based on it and make comparisons with the results of more elaborate systems of averaging. They find that for smooth, nearly elastic spheres, the stresses derived from it differ by no more than 20 percent from those resulting from a distribution function generated by the Chapman-Enskog procedure.

With these assumptions, the expression (24) for the rate of collisional production of a property ψ per unit area of the wall may be written as

$$\mathbf{C}(\psi)=-\chi\int(\psi'-\psi)F(C^2)\mathbf{C}\cdot\mathbf{n}d\mathbf{C}, \tag{38}$$

where $F(C^2)$ is given by (37) and the integration is over all values of $\mathbf{C}$ for which $\mathbf{C}\cdot\mathbf{n}\le 0$.

We carry out the integrations in (38) in a spherical polar coordinate system in velocity space that is based on $\mathbf{n}$ and $\mathbf{g}_0$. The coordinate system is sketched in Fig. 1. In terms of these coordinates,

$$\mathbf{C}(\psi)=\chi\int_0^{\pi/2}\int_{-\pi}^{\pi}\int_0^{\infty}(\psi'-\psi)F(C^2)\sin\phi\cos\phi C^3 dC\,d\theta\,d\phi, \tag{39}$$

where $\psi=\psi(\mathbf{g})$ and $\mathbf{g}=\mathbf{g}_0+\mathbf{C}$. When $\mathbf{g}$ is inside the friction cone shown in Fig. 1,

$$\frac{C\cos\phi}{(g_0^2+2g_0C\sin\phi\cos\theta+C^2\sin^2\phi)^{1/2}}\ge\frac{1}{\bar{\mu}_0}, \tag{40}$$

and the collision involves no sliding.

To distinguish the various types of integrals that arise, we first take into account the fact that the delta function fixes the magnitude of $\mathbf{C}$ at $(3T)^{1/2}$, normalize all velocities by this factor, and write $r=g_0/(3T)^{1/2}$. Next, in order to avoid more complicated integrations involving the apex of the cone, we restrict attention to $r\ge 1$. We anticipate that normalized contact slip speeds less than one are exceptional. Then, depending on the value γ_0, there are two cases of interest: small friction and large friction.

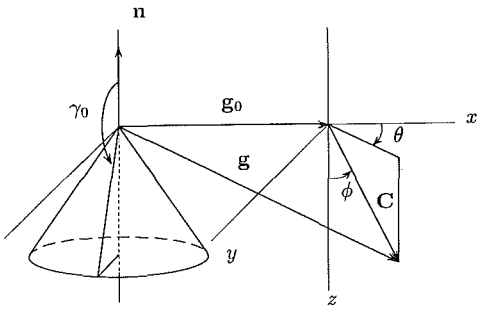

Fig. 1 The coordinate system

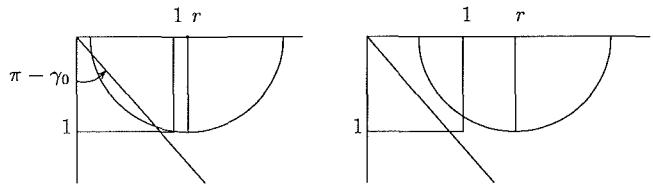

Fig. 2 Small friction; (*a*) large sliding, (*b*) all sliding

Small friction is defined to be when $-\cot\gamma_0<1$ or, from (19), when $\bar{\mu}_0\equiv\mu_0/(1+\beta_0)<1$. There are two possibilities: large sliding, for $1\le r^2\le 1+\bar{\mu}_0^2$; and all sliding, for $1+\bar{\mu}_0^2\le r^2$. These are illustrated in Fig. 2 by showing the intersections of the unit hemisphere and the normalized x-z plane.

For large friction, $\bar{\mu}_0>1$, there are three possibilities: small sliding, for $1\le r^2\le\bar{\mu}_0^2$; large sliding, for $\bar{\mu}_0^2\le r^2\le 1+\bar{\mu}_0^2$; and all sliding, for $1+\bar{\mu}_0^2\le r^2$. These are illustrated in Fig. 3.

We first use (39) to calculate the rates of momentum supply $\mathbf{M}$ and dissipation D for the limiting cases of large friction/no sliding and small friction/all sliding. We then provide a more complete analysis for large friction. We note that because of the presence of the factor 7/2 in the definition (12) of μ_0, the case of large friction may include coefficients μ as small as 0.14.

Large Friction/No Sliding. No sliding occurs for all values of $\mathbf{g}$ in the limit of infinite friction. In this case, the impulse and the change in energy are

$$\mathbf{J}^{(2)}=m(1+e)C\cos\phi\mathbf{n}-(2/7)m(1+\beta_0)[(g_0+C\sin\phi\cos\theta)\mathbf{i}+C\sin\phi\sin\theta\mathbf{j}] \tag{41}$$

and

$$\Delta K^{(2)}=-(1/7)m(1-\beta_0^2)(g_0^2+2g_0C\sin\phi\cos\theta+C^2\sin^2\phi)-(1/2)m(1-e^2)C^2\cos^2\phi, \tag{42}$$

respectively.

The integrations for $\mathbf{M}$ and D are straightforward. Upon carrying them out, we obtain

$$\mathbf{M}=(1/2)\rho\chi(1+e)T\mathbf{n}-(1/14)\rho\chi(1+\beta_0)(3T)^{1/2}g_0\mathbf{i} \tag{43}$$

and

$$D=(1/16)\rho\chi(1-e^2)(3T)^{3/2}+(1/56)\rho\chi(1-\beta_0^2)(3T)^{1/2}(2g_0^2+3T). \tag{44}$$

We note that if we employ the Maxwellian velocity distribution

$$F(C^2)=\frac{n}{(2\pi T)^{3/2}}\exp\left(\frac{-C^2}{2T}\right) \tag{45}$$

rather than (37) in calculating $\mathbf{M}$ and D, we obtain

$$\mathbf{M}=(1/2)\rho\chi(1+e)T\mathbf{n}-(1/7)(2/3\pi)^{1/2}\rho\chi(1+\beta_0)(3T)^{1/2}g_0\mathbf{i} \tag{46}$$

and

$$D=(1/54\pi)^{1/2}\rho\chi(1-e^2)(3T)^{3/2}+(1/28)(2/3\pi)^{1/2}\rho\chi(1-\beta_0^2)(3T)^{1/2}(2g_0^2+4T). \tag{47}$$

Corresponding terms in the two expressions for $\mathbf{M}$ differ by less than ten percent, while the greatest difference in corresponding terms of the two expressions for D is slightly greater than 20 percent.

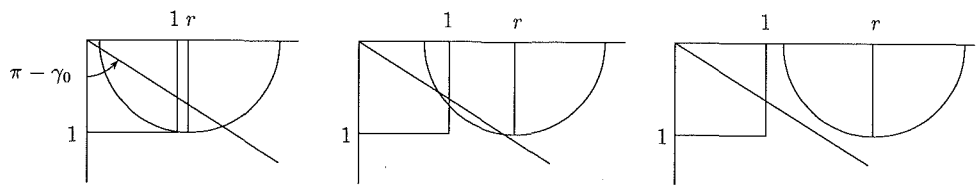

Fig. 3 Large friction; (*a*) small sliding, (*b*) large sliding, (*c*) all sliding

Downloaded 03 May 2010 to 171.66.16.247. Redistribution subject to ASME license or copyright; see http://www.asme.org/terms/Terms_Use.cfm

From (43), the magnitudes N and S of the normal and tangential components of the force per unit area applied by the wall to the flow are, respectively,

$$N=(1/2)\rho\chi+(1+e)T \tag{48}$$

and

$$S=(3/14)\rho\chi(1+\beta_0)Tr, \tag{49}$$

where, we recall that $r=g_0/(3T)^{1/2}$. Consequently,

$$S=\frac{3}{7}N\frac{(1+\beta_0)}{(1+e)}r. \tag{50}$$

Also, from (34), (43), and (44), the rate $Q=\mathbf{q}\cdot\mathbf{n}$ at which fluctuation energy is provided to the flow per unit area of the wall is

$$Q=\frac{3}{28}\frac{N}{(1+e)}(3T)^{1/2}[2(1+\beta_0)^2r^2-(1-\beta_0^2)] -\frac{3}{8}N(1-e)(3T)^{1/2}. \tag{51}$$

In this limit the "dynamic friction coefficient" S/N is a linear function of r and, by virtue of the working of the shear stress through its velocity relative to the contact, the flux of energy to the flow may be positive.

Small Friction/All Sliding. Sliding occurs for almost all values of $\mathbf{g}$ in the limit of small friction. For these values, the impulse and the change of energy are

$$\mathbf{J}^{(1)}=-m(1+e)C\cos\phi\mathbf{n}-\frac{(2/7)m\mu_0C\cos\phi}{(g_0^2+2g_0C\sin\phi\cos\theta+C^2\sin^2\phi)^{1/2}} \times[(g_0+C\sin\phi\cos\theta)\mathbf{i}+C\sin\phi\sin\theta\mathbf{j})] \tag{52}$$

and

$$\Delta K^{(1)}=-(1/2)m(1-e^2)C^2\cos^2\phi-(1/7)m(1-\beta^2) \times(g_0^2+2g_0C\sin\phi\cos\theta+C^2\sin^2\phi), \tag{53}$$

where

$$(1-\beta^2)=\frac{2\mu_0C\cos\phi}{(g_0^2+2g_0C\sin\phi\cos\theta+C^2\sin^2\phi)^{1/2}} -\frac{\mu_0^2C^2\cos^2\phi}{g_0^2+2g_0C\sin\phi\cos\theta+C^2\sin^2\phi}. \tag{54}$$

In calculating $\mathbf{M}$ and D, we first integrate over C; then, with $u\equiv\sin\phi$ and $r=g_0/(3T)^{1/2}$, we introduce the expansions

$$\frac{1}{(r^2+ru\cos\theta+u^2)^{1/2}}=\frac{1}{r}\left[1-\cos\theta\frac{u}{r} +\frac{1}{2}(3\cos^2\theta-1)\left(\frac{u}{r}\right)^2+\cdots\right] \tag{55}$$

and

$$\frac{1}{r^2+2ru\cos\theta+u^2}=\frac{1}{r^2}\left[1-2\cos\theta\frac{u}{r}+(4\cos^2\theta-1)\left(\frac{u}{r}\right)^2+\cdots\right]. \tag{56}$$

We integrate the resulting terms, first over u from 0 to 1, then over θ from 0 to 2π, to obtain

$$N=(1/2)\rho\chi(1+e)T, \tag{57}$$

$$S=\mu N\left(1-\frac{1}{10}\frac{1}{r^2}\right)+O\left(\frac{1}{r^4}\right), \tag{58}$$

and

$$D=\mu N(3T)^{1/2}\left(r-\frac{3}{8}\mu_0+\frac{1}{10}\frac{1}{r}\right) +\frac{3}{8}(1-e)N(3T)^{1/2}+O\left(\frac{1}{r^3}\right). \tag{59}$$

So,

$$Q=\frac{3}{8}N(3T)^{1/2}\left[\mu\mu_0-\frac{8}{15}\mu\frac{1}{r}-(1-e)\right]+O\left(\frac{1}{r^3}\right). \tag{60}$$

Here, because all collisions involve sliding, the ratio of the shear to the normal stress is, essentially, the coefficient of friction μ.

In the two limiting cases, the resulting forms of the tractions, dissipation, and energy flux are relatively simple. In one case, the integrations can be carried out using more complicated distribution functions without much difficulty. The question is, to what extent are the limiting cases typical? We attempt to answer this question by using the elementary distribution function (37) to determine expressions for $\mathbf{M}$, D, and Q that are valid for all values of $\bar{\mu}_0$ greater than one. Because of the difficulty of the resulting integrations, we are only partially successful. We obtain results in intervals of r that, for a given value of $\bar{\mu}_0$, are near the limiting cases. Piecewise analytic expressions for the stress ratio and the energy flux that are based upon the limiting cases are presented in the final section of the paper. They are placed in the context of the more complicated calculations in Figs. 4 and 5.

Large Friction/Small Sliding. We first consider approximate evaluations of the integrals for $\mathbf{M}$ and D that are valid near the large friction/no sliding limit. In this case we restrict our attention to values of r between 1 and $\bar{\mu}_0$, with $\bar{\mu}_0>1$. The situation is illustrated for a typical value of r in Fig. 3(*a*). The largest and smallest values of $\sin\phi$ for which sliding takes place may be obtained by solving the equality in (40) for $\sin\phi$ and setting θ equal to π and 0, respectively:

$$\sin\phi_M=[1-\epsilon(1+r^2)+\epsilon^2r^2]^{1/2}+\epsilon r \tag{61}$$

and

$$\sin\phi_m=[1-\epsilon(1+r^2)+\epsilon^2r^2]^{1/2}-\epsilon r, \tag{62}$$

where

$$\epsilon\equiv 1/(1+\bar{\mu}_0^2). \tag{63}$$

We write $u=\sin\phi$, $u_M=\sin\phi_M$, and $u_m=\sin\phi_m$ and note that $u_M-u_m=2\epsilon r$ exactly.

For points on the hemisphere that are within the friction

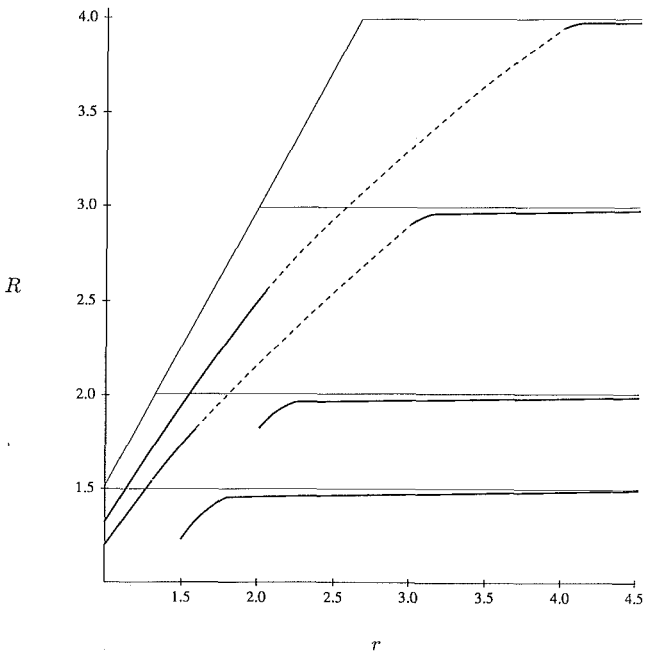

Fig. 4 Normalized stress ratio versus nondimensional contact slip speed

Downloaded 03 May 2010 to 171.66.16.247. Redistribution subject to ASME license or copyright; see http://www.asme.org/terms/Terms_Use.cfm

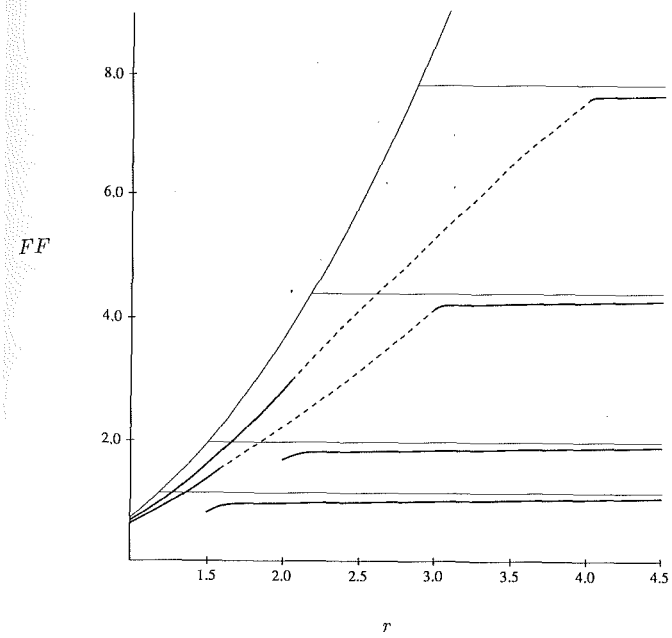

Fig. 5 Normalized frictional energy flux versus nondimensional contact slip speed

cone, there is no sliding and the integrals for **M** and D involve $\mathbf{J}^{(2)}$ and $\Delta K^{(2)}$ given in (41) and (42), respectively. For points on the hemisphere that are outside the friction cone, sliding occurs and the integrations involve $\mathbf{J}^{(1)}$ and $\Delta K^{(1)}$ given in (52), (53), and (54). The integrals inside and outside of the friction cone may each be divided into a part that is symmetric about the z-axis and a part that is not. In the symmetric part that integration over θ is between $-\pi$ and π. In the other part, the limits on the integration over θ depend upon u through the equality in (40):

$$\cos\theta = [\bar{\mu}_0^2 - r^2 - (1+\bar{\mu}_0^2)u^2]/2ru, \tag{64}$$

where $u_m \le u \le u_M$.

In each of the four parts of an integral, we integrate first over C using the delta function and then carry out the θ integrations exactly. To do this where sliding occurs, we make use of tabulated integrals (Byrd and Friedman, 1971). We carry out the integrations over u in an approximate way in all but the axisymmetric nonsliding part of each integral. To do this, we first suppose that both $u_M - u_m$ and $1 - u_M$ are small and of an order no greater than $\epsilon^{1/2}$. Then, to evaluate the integrals on the intervals u_m to u_M and u_M to 1, we use the trapazoidal rule with $\theta(u_m) = 0$ and $\theta(u_M) = \pi$. On the interval 0 to u_m, we integrate exactly. The results are expressed in terms of complete elliptic integrals of the first and second kind, $K(k)$ and $E(k)$, respectively, with

$$k^2 \equiv 4ru/(r+u)^2. \tag{65}$$

We find that the magnitude of the normal component of **M** is again given by (57); $M_y = 0$;

$$M_x = -\frac{6}{7\pi}\frac{N}{(1+e)}\mu_0\frac{(1-u_M^2)^{1/2}}{r+u_M}\left\{ru_M K_M + \left(\frac{u_M}{k_M}\right)^2[(k_M^2-2)K_M + 2E_M]\right\}(1-u_m+2r\epsilon) - \frac{3}{7}N\frac{(1+\beta_0)}{(1+e)}ru_m(u_m+2r\epsilon), \tag{66}$$

up to an error of order $(r\epsilon)^3$, where

$$k_M^2 \equiv 4ru_M/(r+u_M)^2, \tag{67}$$

$K_M \equiv K(k_M)$, and $E_M = E(k_M)$; and

$$D = \frac{6}{7\pi}\frac{N}{(1+e)}(3T)^{1/2}\mu_0\frac{(1-u_M^2)^{1/2}}{r+u_M}\left\{(r^2+u_M^2)u_M K_M + 2r\left(\frac{u_M}{k_M}\right)^2[(k_M^2-2)K_M + 2E_M]\right\}(1-u_M+2r\epsilon) - \frac{3}{14}\frac{N}{(1+e)}(3T)^{1/2}\mu_0^2\frac{(1-u_M^2)u_M}{(r^2-u_M^2)(r+u_M)^2} \times \{r^2+u_M^2+(r^2-u_M^2-1)(r+u_M)^2\}(1-u_M+2r\epsilon) + \frac{3}{14}\frac{N}{(1+e)}(3T)^{1/2}(1-\beta_0^2)u_m \times \left[r^2(u_m+2r\epsilon) + u_m^2\left(\frac{1}{2}u_m + 2r\epsilon\right)\right] + \frac{3}{7}\frac{N}{(1+e)}(3T)^{1/2}(1+\beta_0)r^2u_m(u_m+2r\epsilon) + \frac{3}{8}N(3T)^{1/2}(1-e), \tag{68}$$

up to an error of order of $(r\epsilon)^3$. Consequently,

$$Q = -\frac{6}{7\pi}\frac{N}{(1+e)}(3T)^{1/2}\mu_0\frac{(1-u_M^2)^{1/2}}{r+u_M}\left\{u_M^3 K_M + r\left(\frac{u_M}{k_M}\right)^2[(k_M^2-2)K_M + 2E_M]\right\}(1-u_M+2r\epsilon) + \frac{3}{14}\frac{N}{(1+e)}(3T)^{1/2}\mu_0^2\frac{(1-u_M^2)u_M}{(r^2-u_M^2)(r+u_M)^2} \times \{r^2+u_M^2+(r^2-u_M^2-1)(r+u_M)^2\}(1-u_M+2r\epsilon) - \frac{3}{14}\frac{N}{(1+e)}(3T)^{1/2}(1-\beta_0^2)u_m \times \left[r^2(u_m+2r\epsilon) - u_m^2\left(\frac{1}{2}u_m + 2r\epsilon\right)\right] + \frac{3}{7}\frac{N}{(1+e)}(3T)^{1/2}(1+\beta_0)r^2u_m(u_m+2r\epsilon) - \frac{3}{8}N(3T)^{1/2}(1-e) \tag{69}$$

up to error of order $r^4\epsilon^3$, where $1 \le r \le \bar{\mu}_0$.

As the coefficient of friction increases, these expressions for **M**, D, and Q reduce to those calculated in the large friction/no sliding limit.

Large Friction/Large Sliding. We next consider the situation in which $1 \le \bar{\mu}_0^2 \le r^2 \le 1 + \mu_0^2$. In this range of r, sliding occurs for all but a small fraction of the collisions. A typical example is shown in Fig. 3(*b*). As r decreases from large values outside of this interval, sliding first stops at $r^2 = 1 + \bar{\mu}_0^2$ for those velocity fluctuations with orientations in the neighborhood of $\theta = \pi$ and $\phi = \phi_0$, where

$$\sin\phi_0 \equiv 1/(1+\bar{\mu}_0^2)^{1/2} = \epsilon^{1/2}. \tag{70}$$

As r is further decreased, the orientations for which sliding does not occur lie within the curve of intersection of the velocity hemisphere and the friction cone. The relationship between ϕ and θ on this curve may be obtained by first squaring both sides of the equality in (40):

$$(1+\bar{\mu}_0^2)\sin^2\phi - 2r\cos\theta'\sin\phi + r^2 - \bar{\mu}_0^2 = 0, \tag{71}$$

where $\theta' \equiv \pi - \theta$, and from this determining the solutions for $\sin\phi$ that are appropriate for values of θ' between $-\pi/2$ and $\pi/2$.

$$\sin\phi = \epsilon r\cos\theta' \pm r\left[\epsilon^2\cos^2\theta' - \epsilon\left(1 - \frac{\bar{\mu}_0^2}{r^2}\right)\right]^{1/2} \tag{72}$$

Downloaded 03 May 2010 to 171.66.16.247. Redistribution subject to ASME license or copyright; see http://www.asme.org/terms/Terms_Use.cfm

We use (71) to relate the increments in θ' and ϕ on the curve and find that extreme values of θ' occur when

$$r\cos\theta' = (1+\bar{\mu}_0^2)\sin\phi. \tag{73}$$

Employing this in (72), we find that the largest value θ'_M satisfies

$$\cos^2\theta'_M = (1+\bar{\mu}_0^2)\left(1-\frac{\bar{\mu}_0^2}{r^2}\right). \tag{74}$$

We note that θ'_M varies from 0 to $\pi/2$ as r^2 decreases from $1+\bar{\mu}_0^2$ to $\bar{\mu}_0^2$. Because $1-(\bar{\mu}_0/r)^2$ varies from ϵ to 0 as r^2 decreases from $1+\bar{\mu}_0^2$ to $\bar{\mu}_0^2$, both terms in Eq. (72) are, at most, of order $\epsilon^{1/2}$.

We calculate a correction to the expressions (58) and (59) for S and D in the interval $\bar{\mu}_0 \le r \le (1+\bar{\mu}_0^2)^{1/2}$ by employing $J_x^{(2)} - J_x^{(1)}$ and $\Delta K^{(2)} - \Delta K^{(1)}$ in the collisional production integral (39) for that part of the collision hemisphere within the friction cone. To evaluate the resulting integrals we use the expansions (55) and (56) and integrate term by term, first over $u = \sin\phi$ from

$$u_1 = \epsilon r\cos\theta' - r\epsilon(A^2 - \sin^2\theta')^{1/2}, \tag{75}$$

where

$$A^2 \equiv 1-(1+\bar{\mu}_0^2)\left(1-\frac{\bar{\mu}_0^2}{r^2}\right) = \sin^2\theta'_M, \tag{76}$$

to

$$u_2 = \epsilon r\cos\theta' + r\epsilon(A^2 - \sin^2\theta')^{1/2}, \tag{77}$$

and then over θ' from $-\theta'_M$ to θ'_M. We discard terms of order greater than $\epsilon^{3/2}$ in the correction ΔS to S and order greater than ϵ in the correction ΔD to D.

The results are

$$\Delta S = -\frac{3}{7}\frac{N}{(1+e)} r^2\epsilon^2 A^2\left[\mu_0 - (1+\beta_0)r\left\{1-\epsilon\left(1-\frac{1}{4}A^2\right) - \frac{8\epsilon}{3\pi}[E(A)-(1-A^2)K(A)] - \frac{8\epsilon}{9\pi}\left[2\left(\frac{1}{A^2}-1\right)K(A) - \left(\frac{2}{A^2}-1\right)E(A)\right]\right\}\right] \tag{78}$$

up to an error of order ϵ^2, and

$$\Delta D = -\frac{3}{14}\frac{N}{(1+e)}(3T)^{1/2} r^2\epsilon^2 A^2\left\{2\mu_0 r - \mu_0^2 - (1-\beta_0^2)r^2\left[1-2\epsilon\left(1+\frac{1}{4}A^2\right)\right]\right\} \tag{79}$$

up to an error of order $\epsilon^{3/2}$.

The correction ΔQ to the energy flux may be obtained up to an error of $\epsilon^{3/2}$ by multiplying ΔS by g_0 and subtracting ΔD.

Results and Discussion

The results of the various calculations of S/N are presented in Fig. 4. Here, a normalized stress ratio

$$R \equiv \frac{7}{2}\frac{(1+e)}{(1+\beta_0)}\frac{S}{N} \tag{80}$$

is plotted versus the nondimensional contact slip speed r.

The light, straight lines are the lowest order approximation to the behavior of the stress ratio with contact slip speed at a given value of $\bar{\mu}_0$. It is a piecewise linear approximation based on the two limiting cases:

$$R = \begin{cases} \dfrac{3}{2}r, & 1 \le r \le \dfrac{2}{3}\bar{\mu}_0; \\ \bar{\mu}_0, & \dfrac{2}{3}\bar{\mu}_0 \le r \le \infty. \end{cases} \tag{81}$$

It is shown for values of $\bar{\mu}_0$ equal to 1.5, 2.0, 3.0, and 4.0.

The bold lines are the results of the more elaborate calculations for each value of $\bar{\mu}_0$ over the range of r of their validity. The small sliding curves for $\bar{\mu}_0$ equal to 3.0 and 4.0 have been terminated at $r = 1.58$ and 2.04, respectively. At these values of r, $2r\epsilon$ is equal to $\epsilon^{1/2}$ and the assumptions on which the calculations are based are certainly satisfied. The dashed lines are suggested connections between the small sliding and large sliding branches of the curves for $\bar{\mu}_0 = 3.0$ and 4.0.

The results of the calculations of the energy flux are provided in Fig. 5. Here, a normalized frictional flux

$$FF \equiv \frac{7}{2}\frac{(1+e)}{(1+\beta_0)}\left[\frac{Q}{N(3T)^{1/2}} + \frac{3}{8}(1-e)\right] \tag{82}$$

is plotted versus r. Again, the light lines are the lowest order approximation to the limiting behavior:

$$FF = \begin{cases} \dfrac{3}{8}[2(1+\beta_0)r^2 - (1-\beta_0)], & 1 \le r^2 \le \dfrac{1}{2}\left[\bar{\mu}_0^2 + \dfrac{(1-\beta_0)}{(1+\beta_0)}\right], \\ \dfrac{3}{8}(1+\beta_0)\bar{\mu}_0^2, & \dfrac{1}{2}\left[\bar{\mu}_0^2 + \dfrac{(1-\beta_0)}{(1+\beta_0)}\right] \le r^2 \le \infty. \end{cases} \tag{83}$$

There are shown for $\beta_0 = 0.3$ and $\bar{\mu}_0 = 1.5$, 2.0, 3.0, and 4.0, with $\bar{\mu}_0$ increasing from the bottom to the top. The bold lines are the results of the more elaborate calculations. The small sliding branches of the curves for $\bar{\mu}_0 = 3.0$ and 4.0 are terminated as before, and the dashed lines are suggested connections between their small sliding and large sliding branches.

Based on the curves in Figs. 4 and 5, one can make a judgement on whether to employ the simple approximate forms for the stress ratio and energy flux that apply in the limits, to adopt the more exact forms calculated here over the limited ranges of their applicability, or to improve upon these calculations. If the last course is chosen, we hope that this paper provides a context in which to formulate the improvements and an indication of the nature of the difficulties involved.

Acknowledgments

This research has been supported by the U.S. Army Research Office through the Mathematical Sciences Institute at Cornell University. The author is indebted to Nondas Mastorakos and Wendy Nelson for their assistance in generating the figures.

References

Ackermann, N. L., and Shen, H., 1982, "Stresses in Rapidly Sheared Fluid—Solid Mixtures," *ASCE Journal of Engineering Mechanics*, Vol. 108, pp. 95–113.

Byrd, P. F., and Friedman, M. D., 1971, *Handbook of Elliptic Integrals for Engineers and Scientists*, 2nd ed., Springer-Verlag, New York.

Campbell, C. S., 1989, "The Stress Tensor for Simple Shear Flows of a Granular Material," *Journal of Fluid Mechanics*, Vol. 203, pp. 449–473.

Campbell, C. S., 1990, private communication.

Campbell, C. S., and Gong, A., 1986, "The Stress Tensor in a Two-Dimensional Granular Shear Flow," *Journal of Fluid Mechanics*, Vol. 164, pp. 107–125.

Campbell, C. S., and Gong, A., 1987, "Boundary Conditions for Two Dimensional Granular Flows," *Proceedings of the Sino-U.S. Symposium on Multiphase Flow*, Vol. 1, Zhejiang University Press, Hangzhou, pp. 278–283.

Hanes, D. M., and Inman, D. L., 1985, "Observations of Rapidly Flowing Granular-Fluid Materials," *Journal of Fluid Mechanics*, Vol. 150, pp. 357–380.

Hanes, D. M., Jenkins, J. T., and Richman, M. W., 1988, "The Thickness of Steady Plane Shear Flows of Circular Disks Driven by Identical Boundaries," ASME Journal of Applied Mechanics, Vol. 55, pp. 969–974.

Henderson, J. R., and van Swol, F., 1984, "On the Interface Between a Fluid and a Planar Wall. Theory and Simulations of a Hard Sphere Fluid at a Hard Wall," *Molecular Physics*, Vol. 51, pp. 991–1010.

Hui, K., Haff, P. K., Ungar, J. E., and Jackson, R., 1984, "Boundary Conditions for High-Shear Grain Flows," *Journal of Fluid Mechanics*, Vol. 145, pp. 223–233.

Downloaded 03 May 2010 to 171.66.16.247. Redistribution subject to ASME license or copyright; see http://www.asme.org/terms/Terms_Use.cfm

Jenkins, J. T., 1987, "Rapid Flows of Granular Materials," *Non-Classical Continuum Mechanics*, R. J. Knops and A. A. Lacey, eds., Cambridge University Press, pp. 213–225.

Jenkins, J. T., and Askari, E., 1990, "Boundary Conditions for Rapid Granular Flow: Phase Interfaces," *Journal of Fluid Mechanics*, Vol. 223, pp. 497–508.

Jenkins, J. T., and Richman, M. W., 1985, "Kinetic Theory for Plane Flows of a Dense Gas of Identical, Rough, Inelastic, Circular Disks," *Physics of Fluids*, Vol. 28, pp.3485–3495.

Jenkins, J. T., and Richman, M. W., 1986, "Boundary Conditions for Plane Flows of Smooth, Nearly Elastic, Circular Disks," *Journal of Fluid Mechanics*, Vol. 171, pp. 53–69.

Jenkins, J. T., and Richman, M. W., 1988, "Plane Simple Shear of Smooth Inelastic Circular Disks: The Anisotropy of the Second Moment in the Dilute and Dense Limits," *Journal of Fluid Mechanics*, Vol. 192, pp. 313–328.

Johnson, P. C., and Jackson, R., 1987, "Frictional-Collisional Constitutive Relations for Granular Materials with Applications to Plane Shearing," *Journal of Fluid Mechanics*, Vol. 176, pp. 67–93.

Lun, C. K. K., and Savage, S. B., 1987, "A Simple Kinetic Theory for Granular Flow of Rough, Inelastic, Spherical Particles," ASME JOURNAL OF APPLIED MECHANICS, Vol. 54, pp. 47–53.

Maw, N., Barber, J. R., and Fawcett, J. N., 1976, "The Oblique Impact of Elastic Spheres," *Wear*, Vol. 38, pp. 101–114.

Maw, N., Barber, J. R., and Fawcett, J. N., 1981, "The Role of Elastic Tangential Compliance in Oblique Impact," *Journal of Lubrication Technology*, Vol. 103, pp. 74–80.

Ogawa, S., Umemura, A., and Oshima, N., 1980, "On the Equations of Fully Fluidized Granular Materials," *Journal of Applied Mathematics and Physics (ZAMP)*, Vol 31, pp. 483–493.

Pasquarell, G. C., and Ackermann, N. L., 1989, "Boundary Conditions for Planar Granular Flows," *ASCE Journal of Engineering Mechanics*, Vol. 115, pp. 1283–1302.

Pasquarell, G. C., Ackermann, N. L., Shen, H. H., and Hopkins, M. A., 1989, "Collisional Stress in Granular Flows: Bagnold Revisited," *ASCE Journal of Engineering Mechanics*, Vol. 114, pp. 49–64.

Pasquarell, G. C.,and Babić, M., 1989, "On the Form of the Velocity Distribution Function for Rapid Granular Flows," *ASCE Journal of Engineering Mechanics*, Vol. 116, pp. 1261–1275.

Richman, M. W., 1988, "Boundary Conditions Based Upon a Modified Maxwellian Velocity Distibution Function for Flows of Identical, Smooth, Nearly Elastic Spheres," *Acta Mechanica*, Vol. 75, pp. 227–240.

Richman, M. W., 1989, "The Source of Second Moment in Dilute Granular Flows of Highly Inelastic Spheres," *Journal of Rheology*, Vol. 33, pp. 1293–1306.

Savage, S. B., and Sayed, M., 1984, "Stresses Developed by Dry Cohesionless Granular Materials Sheared in an Annular Shear Cell," *Journal of Fluid Mechanics*, Vol. 142, pp. 391–430.

Snook, I. K., and Henderson, D., 1978, "Monte Carlo Study of Hard-Sphere Fluid Near a Hard Wall," *Journal of Chemical Physics*, Vol. 68, pp. 2134–2139.

Walton, O. R., 1988, "Granular Solids Flow Project, Quarterly Report, January–March 1988, UCID-20297-88-1," Lawrence Livermore National Laboratory.

Walton, O. R., and Braun R. L., 1986a, "Viscosity, Granular-Temperature, and Stress Calculations for Shearing Assemblies of Inelastic, Frictional Disks," *Journal of Rheology*, Vol. 30, pp. 949–980.

Walton, O. R., and Braun, R. L., 1986b, "Stress Calculations for Assemblies of Inelastic Spheres in Uniform Shear," *Acta Mechanica*, Vol. 63, pp. 73–86.

Downloaded 03 May 2010 to 171.66.16.247. Redistribution subject to ASME license or copyright; see http://www.asme.org/terms/Terms_Use.cfm

A Viscoelastic Model for the Dynamic Behavior of Saturated Poroelastic Soils

J. P. Bardet
Associate Professor,
Civil Engineering Department,
University of Southern California,
Los Angeles, CA 90089-2531

A viscoelastic model is proposed to describe the dynamic response of the saturated poroelastic materials that obey the Biot theory (1956). The viscoelastic model is defined from the velocity and attenuation of dilatational and distortional waves in poroelastic materials. Its material properties are defined in terms of the elastic moduli, porosity, specific gravity, degree of saturation, and permeability of the soils. The proposed model is tested by comparing its response with the one of poroelastic materials in the case of axial and lateral harmonic loadings of one-dimensional columns. The viscoelastic model is simpler to use than poroelastic materials but yields similar results for a wide range of soils and dynamic loadings.

1 Introduction

The two-phase formulation of Biot (1956) is a powerful approach to analyze the dynamic response of saturated soils. Unfortunately, it is difficult to use when solving practical problems. Substantial effort has been devoted to develop analytical solutions for poroelastic materials (e.g., Simon, Zienkiewicz, and Paul, 1984) and to implement the Biot theory into finite element methods (Zienkiewicz et al., 1980; Ghaboussi and Wilson, 1972; Prevost, 1985).

The present paper proposes a viscoelastic model to describe the dynamic response of saturated soils. This approach is reminiscent but different from the viscoelastic modeling that Hardin (1965) and Richart et al. 1970) applied to account for the hysteretic and elastoplastic energy dissipation of dry soils. In addition to material irreversibility, water diffusion dissipates a significant amount of energy during the dynamic loadings of saturated soils. This phenomenon was shown for the propagation of dilatational waves (Bardet and Sayed, 1990a) and the longitudinal vibration of soil columns (Bardet and Sayed, 1990b).

The viscoelastic character of poroelastic materials has long been appreciated (Biot, 1962, and Wijesinghe and Kingsbury, 1979), but surprisingly has received little attention in solid mechanics and geomechanics. Simon, Zienkiewicz, and Paul 1984) briefly mentioned that poroelastic and viscoelastic materials had similar transient responses. It is only recently that Okuno and Kingsbury (1989) calculated viscous moduli during the dynamic compression and bending of poroelastic fluid-filled foams.

Following the Introduction, the second section of the paper reviews the two-phases formulation of Biot (1956) and gives approximate expressions for the velocity and attenuation of dilatational and distortional waves. The third section provides similar expressions for viscoelastic materials and defines the properties of the viscoelastic model in terms of soil properties. The fourth and fifth sections assess the validity of the proposed approach by comparing the longitudinal and lateral responses of columns made by poroelastic material and the viscoelastic model.

2 Two-Phases Poroelastic Soils

From now on, the Biot formulation (1956) is used to describe the dynamic behavior of nearly saturated soils. Vardoulakis and Beskos (1986) showed that it is similar to the theories of Bowen (1976), Ghaboussi and Wilson (1972), Mei and Foda (1981), Van der Kogel (1977), and Prevost (1985).

2.1 Basic Definitions. Nearly saturated soils are two-phases media but consist of a porous assemblage of solid grains having a porosity n:

$$n=\frac{V_v}{V_t} \tag{1}$$

where V_v is the volume of the pores and V_t the total volume of the medium. The pore volume V_v is partially filled with fluid and gas; the degree of saturation is S:

$$S=\frac{V_f}{V_v} \tag{2}$$

where V_f is the volume of fluid. From now on, S is assumed to be between 0.95 and 1. The fluid-gas mixture is homogeneous. Its bulk modulus D_f depends on S (Verruijt, 1969):

$$D_f=\frac{1}{\beta_f+\dfrac{1-S}{p}} \tag{3}$$

where p is the absolute fluid pressure and β_f is the compressibility of the fluid alone ($1/\beta_f=2140.$ MPa). The unit mass of

Contributed by the Applied Mechanics Division of THE AMERICAN SOCIETY OF MECHANICAL ENGINEERS for publication in the JOURNAL OF APPLIED MECHANICS.

Discussion on this paper should be addressed to the Technical Editor, Prof. Leon M. Keer, The Technological Institute, Northwestern University, Evanston, IL 60208, and will be accepted until two months after final publication of the paper itself in the JOURNAL OF APPLIED MECHANICS. Manuscript received by the ASME Applied Mechanics Division, June 29, 1990; final revision, Oct. 25, 1990.

Copyright © 1992 by ASME
Downloaded 03 May 2010 to 171.66.16.247. Redistribution subject to ASME license or copyright; see http://www.asme.org/terms/Terms_Use.cfm

the fluid ρ_f is equal to the unit mass of water $\rho_w = 1$ g/cm^3. The unit mass of the solid, ρ_s, is constant; it is defined by the specific gravity:

$$G_s = \frac{\rho_s}{\rho_f}. \tag{4}$$

For isotropic and linearly poroelastic materials, the effective stress σ'_{ij} acting on the solid skeleton is (Verruijt, 1969)

$$\sigma'_{ij} = \lambda(\epsilon_{kk})\delta_{ij} + 2\mu\,\epsilon_{ij} \tag{5}$$

where λ is the elastic Lamé modulus and μ is the elastic shear modulus. The strain ϵ_{ij} is related to the displacement of the solid constituent $\mathbf{u} = (u_1, u_2, u_3)$ through

$$\epsilon_{ij} = \frac{1}{2}\left(\frac{\partial u_i}{\partial x_j} + \frac{\partial u_j}{\partial x_i}\right). \tag{6}$$

δ_{ij} is Kronecker's symbol

$$\delta_{ij} = \begin{cases} 1 & i = j \\ 0 & i \neq j. \end{cases} \tag{7}$$

2.2 Governing Equations. In the absence of the additional fluid mass ρ_{12}, Biot (1956) showed that the solid displacement $\mathbf{u}$ and the average displacement of interstitial water $\mathbf{U} = (U_1, U_2, U_3)$ obey the following equation:

$$\begin{cases} \mu\,\nabla^2\mathbf{u} + \mathbf{grad}\,((A+\mu)\epsilon_v + Q\epsilon_f) \\ \qquad = \dfrac{\partial^2}{\partial t^2}\,((1-n)\rho_s\mathbf{u}) + b\dfrac{\partial}{\partial t}\,(\mathbf{u}-\mathbf{U}) \\ \mathbf{grad}(Q\epsilon_v + R\epsilon_f) = \dfrac{\partial^2}{\partial t^2}\,(n\rho_f\mathbf{U}) - b\dfrac{\partial}{\partial t}\,(\mathbf{u}-\mathbf{U}) \end{cases} \tag{8}$$

where ϵ_v and ϵ_f are the volumetric strain of the solid and fluid, respectively,

$$\begin{cases} \epsilon_v = \dfrac{\partial u_i}{\partial x_i} \\ \epsilon_f = \dfrac{\partial U_i}{\partial x_i}. \end{cases} \tag{9}$$

The coefficient b is related to fluid viscosity μ_f and Darcy's coefficient of permeability k_B through

$$b = \frac{\mu_f n^2}{k_B} \tag{10}$$

where k_B is different from the permeability coefficient k that is used in soil mechanics

$$k_B = k\frac{\mu_f}{g\rho_f}. \tag{11}$$

The earth acceleration is $g = 9.81$ ms^{-2}. When the grains are made of material much more incompressible than the interstitial fluid and the grain skeleton, the coefficients Q, R, and A are (Biot and Willis, 1957)

$$\begin{cases} Q = (1-n)D_f \\ R = nD_f \\ A = \lambda + \dfrac{(n-1)^2}{n}D_f. \end{cases} \tag{12}$$

After using Eqs. (10), (11), and (12), Eq. (8) becomes

$$\begin{cases} \mu\,\nabla^2\mathbf{u} + (\lambda+\mu)\mathbf{grad}(\epsilon_v) - (1-n)\mathbf{grad}(\Delta p) \\ \qquad = (1-n)\rho_s\dfrac{\partial^2\mathbf{u}}{\partial t^2} + b\dfrac{\partial}{\partial t}\,(\mathbf{u}-\mathbf{U}) \\ -n\,\mathbf{grad}(\Delta p) = n\rho_f\dfrac{\partial^2\mathbf{U}}{\partial t^2} - b\dfrac{\partial}{\partial t}\,(\mathbf{u}-\mathbf{U}). \end{cases} \tag{13}$$

The change Δp of fluid pressure depends on the volumetric strains ϵ_v and ϵ_f

$$\Delta p = -D_f\left(\frac{1-n}{n}\epsilon_v + \epsilon_f\right). \tag{14}$$

2.3 Dilatational and Distortional Waves in Poroelastic Solids. The dilatational waves propagating in the x-direction have the following expression:

$$\begin{cases} u(x,t) = A\,e^{-\frac{\omega x}{\delta}}\,e^{i\omega\left(t-\frac{x}{c}\right)} \\ U(x,t) = B\,e^{-\frac{\omega x}{\delta}}\,e^{i\omega\left(t-\frac{x}{c}\right)} \end{cases} \tag{15}$$

where $i = \sqrt{-1}$ and ω is the circular frequency of the harmonic signal. The wave (phase) velocity c and the absorption coefficient δ are:

$$\begin{cases} c = -\dfrac{c_w}{\Im\{\psi\}} \\ \delta = -\dfrac{c_w}{\Re\{\psi\}} \end{cases} \tag{16}$$

where $\Re\{\psi\}$ and $\Im\{\psi\}$ are the real and imaginary parts of ψ

$$\psi = -\frac{c_w}{\delta} - i\frac{c_w}{c} \tag{17}$$

and where c_w is the wave velocity in the fluid

$$c_w = \sqrt{\frac{D_f}{\rho_f}}. \tag{18}$$

The complex ψ is the solution of the following characteristic equation

$$\frac{\chi}{n}\psi^4 + a\psi^2 + a' = 0 \tag{19}$$

where a and a' are

$$\begin{cases} a = \left(\chi + \dfrac{1}{n}\right)\dfrac{1}{n} + \dfrac{1}{n\beta} - \dfrac{2}{n} - i\dfrac{g}{k\omega}\,(1+\chi) \\ a' = \dfrac{1}{n\beta} - 1 - i\dfrac{g}{k\omega}\dfrac{1}{\beta} \end{cases} \tag{20}$$

and where D, χ, and β are

$$\begin{cases} D = \lambda + 2\mu \\ \chi = \dfrac{D}{D_f} \\ \beta = \dfrac{1}{n + (1-n)G_s}. \end{cases} \tag{21}$$

Equation (19) has four complex roots

$$\begin{cases} \psi_{1,3} = \pm\sqrt{\dfrac{-an - \sqrt{n^2a^2 - 4a'n\chi}}{2\chi}} \\ \psi_{2,4} = \pm\sqrt{\dfrac{-an + \sqrt{n^2a^2 - 4a'n\chi}}{2\chi}}. \end{cases} \tag{22}$$

Therefore, there are two waves that have for velocity $\pm c_1$ and $\pm c_2$, and for amplitude decay $\pm\delta_1$ and $\pm\delta_2$

$$\begin{cases} c_{1,2} = \pm\dfrac{c_w}{|\Im\{\psi_{1,2}\}|} \\ \delta_{1,2} = \pm\dfrac{c_w}{|\Re\{\psi_{1,2}\}|}. \end{cases} \tag{23}$$

Downloaded 03 May 2010 to 171.66.16.247. Redistribution subject to ASME license or copyright; see http://www.asme.org/terms/Terms_Use.cfm

In the case of soils, the wave of the second type is much slower and more attenuated than the one of the first type (Bardet and Sayed, 1990a). Its dynamic contribution is therefore expected to be much smaller than the first type of waves. When the dimensionless coefficient $k\omega/g$ is $\ll 1$, the velocity and attenuation of the waves of the first type are approximated as follows:

$$\begin{cases} c_1 \approx c_o = c_w \sqrt{\beta\left(\chi + \dfrac{1}{n}\right)} \\ \delta_1 \approx \dfrac{g}{k\omega}\dfrac{2c_o}{\beta}\left(\dfrac{\chi+\dfrac{1}{n}}{\chi-\chi_u}\right)^2 \end{cases} \tag{24}$$

where

$$\chi_u = \left(\frac{1}{n} - 1\right)(G_s - 1). \tag{25}$$

For rotational waves propagating in the x-direction, the rotations of solid and fluid in the z-direction are:

$$\begin{cases} \Omega_s(x, t) = A\, e^{-\frac{\omega x}{\delta}} e^{i\omega\left(t-\frac{x}{c}\right)} \\ \Omega_f(x, t) = B\, e^{-\frac{\omega x}{\delta}} e^{i\omega\left(t-\frac{x}{c}\right)}. \end{cases} \tag{26}$$

Biot (1956) found that

$$\begin{cases} c = \sqrt{\dfrac{\mu\beta}{\rho_f}}\dfrac{\sqrt{2}}{\sqrt{\sqrt{E_r^2+E_i^2}+E_r}} \\ \delta = \sqrt{\dfrac{\mu\beta}{\rho_f}}\dfrac{\sqrt{2}}{\sqrt{\sqrt{E_r^2+E_i^2}-E_r}} \end{cases} \tag{27}$$

where

$$\begin{cases} E_r = \dfrac{1+(1-n)\beta G_s\left(\dfrac{k\omega}{ng}\right)^2}{1+\left(\dfrac{k\omega}{ng}\right)^2} \\ E_i = \dfrac{k\omega}{g}\dfrac{\beta}{1+\left(\dfrac{k\omega}{ng}\right)^2}. \end{cases} \tag{28}$$

When $k\omega/ng$ is $\ll 1$, the velocity and attenuation of Eq. (27) are approximated as follows:

$$\begin{cases} c \approx d_o = \sqrt{\dfrac{\mu\beta}{\rho_f}} \\ \delta \approx \dfrac{g}{k\omega}\dfrac{2d_o}{\beta}. \end{cases} \tag{29}$$

2.4 Typical Variation of Soil Parameters. The soil properties are characterized by five parameters: n, G_s, k, λ, and μ, and the water properties by two parameters: S and p.

The bulk modulus of the interstitial fluid D_f strongly depends on the degree of saturation S as specified in Eq. (3). D_f is 2,140 MPa for pure water ($S = 100$ percent) and 2 MPa for $S = 95$ percent. Therefore, a decrease of S from 1 to 0.95 multiplies the dimensionless coefficient ψ by 10^3. The effect of S on D_f is reduced by increasing the absolute pressure p.

Table 1 Approximate values for parameters of typical soils

Soil type	porosity n	G_s	k (m/s)	D (MPa)	χ S=1.0	χ S=0.95
Gravel	0.12-0.46	2.6-2.7	10^{-2}	200	9×10^{-2}	10^{2}
Dense sand	0.17-0.55	2.6-2.7	10^{-4}	50	2×10^{-2}	2×10^{1}
Loose sand			10^{-6}	5	2×10^{-3}	2
Silt	0.29-0.52	2.5-2.7	10^{-8}	2	9×10^{-4}	1
Clay	0.30-0.75	2.2-3.2	10^{-10}	0.05	2×10^{-5}	2×10^{-2}

Pure water: $\rho_f = 1.0$ g/cm^3, $1/\beta_f = 2140$. MPa and $c_w = 1460$ m/s

Atmospheric pressure: p=100 kPa.

Table 1 summarizes the typical range of variation for the soil parameters. Typically, n varies between 0.12 and 0.55 for sands, gravels, and silts and between 0.3 and 0.75 for clays (Lambe and Whitman, 1979). The specific gravity of soil grains G_s has 2.2 and 3.2 for extreme values. β varies between 0.42 and 0.77 for all soils. The coefficient of permeability k has a very large range of variation. It varies from 0.01 m/s for gravel to 10^{-10} m/s for clay. Therefore, the condition $k\omega/g \ll 1$ applies to all soils provided that the circular frequency ω is smaller than 100 c.p.s., a maximum value that encompasses most practical applications in soil dynamics and earthquake engineering. According to Scott (1963), the modulus D of soil skeleton varies typically between 0.05 and 200 MPa. Typical values for λ and μ may be calculated from D by assuming a Poisson's ratio ν between 0.2 and 0.3. For $\nu = 0.25$, $\mu = D/3$, which gives the well-known result $c_o = \sqrt{3}\, d_o$. According to the range of variation for D and D_f, χ varies from 2×10^{-5} for saturated clays to 10^2 for nearly saturated gravels.

3 Viscoelastic Solids

3.1 Linear Viscoelastic Solid. In linear Kelvin-Voigt materials, the stress σ_{ij} is (Eringen, 1980)

$$\sigma_{ij} = \lambda_e(\epsilon_{kk})\delta_{ij} + 2\mu_e\epsilon_{ij} + \lambda_v\frac{\partial\epsilon_{kk}}{\partial t}\delta_{ij} + 2\mu_v\frac{\partial\epsilon_{ij}}{\partial t} \tag{30}$$

where λ_e and μ_e are Lame elastic moduli and λ_v and μ_v the viscous moduli. Without body forces, the field equations are

$$(\lambda_e+\mu_e)\frac{\partial^2 u_j}{\partial x_i\partial x_j} + \mu_e\frac{\partial^2 u_i}{\partial x_j\partial x_j} + (\lambda_v+\mu_v)\frac{\partial^3 u_j}{\partial t\partial x_i\partial x_j} + \mu_v\frac{\partial^3 u_i}{\partial t\partial x_j\partial x_j} - \rho_v\frac{\partial^2 u_i}{\partial t^2} = 0 \tag{31}$$

where ρ_v is the unit mass of the viscoelastic material.

3.2 Dilatational and Distortional Waves in Viscoelastic Solids. Eringen (1980) showed that the irrotational waves propagating in the x-direction are

$$u(x, t) = A\, e^{-\alpha_d x} e^{i\omega\left(t-\frac{x}{c_d}\right)} \tag{32}$$

where

Downloaded 03 May 2010 to 171.66.16.247. Redistribution subject to ASME license or copyright; see http://www.asme.org/terms/Terms_Use.cfm

$$\begin{cases} c_d = \sqrt{\dfrac{|D_e + i\omega D_v|}{\rho_v}} \sec\left(\dfrac{\Delta_d}{2}\right) \\ \alpha_d = \dfrac{\omega}{c_d} \tan\left(\dfrac{\Delta_d}{2}\right) \\ \tan(\Delta_d) = k_d \omega \\ k_d = \dfrac{D_v}{D_e} \\ D_e = \lambda_e + 2\mu_e \\ D_v = \lambda_v + 2\mu_v. \end{cases} \tag{33}$$

It is appropriate to rewrite c_d and α_d as follows:

$$\begin{cases} c_d = \sqrt{2} \sqrt{\dfrac{D_e}{\rho_v}} \dfrac{\sqrt{1 + k_d^2 \omega^2}}{\sqrt{1 + \sqrt{1 + k_d^2 \omega^2}}} \\ \alpha_d = \dfrac{\sqrt{1 + k_d^2 \omega^2} - 1}{k^k d c_d}. \end{cases} \tag{34}$$

From the comparison of Eqs. (15) and (32), the attenuation coefficient δ_d is

$$\delta_d = \frac{\omega}{\alpha_d}. \tag{35}$$

When $k_d \omega \ll 1$, Eq. (34) becomes

$$\begin{cases} c_d \approx \sqrt{\dfrac{D_e}{\rho_v}} \\ \delta_d \approx \dfrac{2 c_d}{k_d \omega}. \end{cases} \tag{36}$$

For the distortional waves propagating in the x-direction, Eringen (1980) showed that the rotation is

$$\Omega_x(x, t) = B e^{-\alpha_s x} e^{i\omega\left[t - \frac{x}{c_s}\right]} \tag{37}$$

where

$$\begin{cases} c_s = \sqrt{\dfrac{|\mu_e + i\omega\mu_v|}{\rho_v}} \sec\left(\dfrac{\Delta_d}{2}\right) \\ \alpha_s = \dfrac{\omega}{c_s} \tan\left(\dfrac{\Delta_s}{2}\right) \\ \tan(\Delta_s) = \mathrm{k}_s \omega \\ k_s = \dfrac{\mu_v}{\mu_e}. \end{cases} \tag{38}$$

Equation (38) may be rewritten as follows:

$$\begin{cases} c_s = \sqrt{2} \sqrt{\dfrac{\mu_e}{\rho_v}} \dfrac{\sqrt{1 + k_s^2 \omega^2}}{\sqrt{1 + \sqrt{1 + k_s^2 \omega^2}}} \\ \alpha_s = \dfrac{\sqrt{1 + k_s^2 \omega^2} - 1}{k_s c_s}. \end{cases} \tag{39}$$

When $k_d \omega \ll 1$, Eq. (39) becomes

$$\begin{cases} c_s \approx \sqrt{\dfrac{\mu_e}{\rho_v}} \\ \delta_s = \dfrac{\omega}{\alpha_s} \approx \dfrac{2 c_s}{k_s \omega}. \end{cases} \tag{40}$$

3.3 Viscoelastic Models of Poroelastic Materials. The comparison of Eqs. (24), (29), (36), and (40) indicates that poroelastic materials and Kelvin-Voight materials have similar expressions for the velocity and attenuation of dilatational and distortional waves, provided that the following conditions are met

$$\begin{cases} \dfrac{k\omega}{ng} \ll 1 \\ k_s \omega \ll 1 \\ k_d \omega \ll 1. \end{cases} \tag{41}$$

Therefore, a viscoelastic model of poroelastic materials is defined by equating the velocity and attenuation of dilatational and distortional waves

$$\begin{cases} \rho_v = n\rho_f + (1-n)\rho_s \\ \mu_e = \mu \\ \mu_v = \dfrac{\beta k}{g} \mu \\ \lambda_e = \lambda + \dfrac{D_f}{n} = D_f\left(\chi + \dfrac{1}{n}\right) - 2\mu \\ \lambda_v = \dfrac{\beta k}{g}\left(\dfrac{(\chi - \chi_u)^2}{\chi + \dfrac{1}{n}} D_f - 2\mu\right). \end{cases} \tag{42}$$

By using Eq. (42), it is shown that

$$\begin{cases} k_s = \dfrac{\beta k}{g} \\ k_d = \dfrac{\beta k}{g}\left(\dfrac{\chi - \chi_u}{\chi + \dfrac{1}{n}}\right)^2. \end{cases} \tag{43}$$

After noticing that the ratio dependent on χ in Eq. (43) is maximum and equal to $(1-n)(G_s - 1)^2$ at $\chi = 0$, it is concluded that the inequalities $k_s \omega \ll 1$ and $k_d \omega \ll 1$ are satisfied for viscoelastic models, provided that $k\omega/ng << 1$.

Poroelastic materials and viscoelastic models have identical shear modulus but different bulk modulus. The modulus $D_e = \lambda_e + 2\mu_e$ depends on the degree of saturation, porosity, and specific gravity. The viscous moduli λ_v and μ_v are proportional to the permeability k. The modulus $D_v = \lambda_v + 2\mu_v$ becomes zero when $\chi = \chi_u$, i.e., for a particular degree of saturation. This corresponds to the unattenuated propagation of dilatational waves within nearly saturated poroelastic solids (Bardet and Sayed, 1990a).

4 Axial Vibrations of Soil Columns

4.1 Poroelastic Solution. In the one-dimensional case, u and U denote the solid and fluid displacement in the x_1-direction that is referred to as the x-direction from now on

$$\begin{cases} u = u_1, \quad u_2 = u_3 = 0 \\ U = U_1, \; U_2 = U_3 = 0. \end{cases} \tag{44}$$

Equation (13) becomes

$$\begin{cases} \left(D + \dfrac{1-n}{n} D_f\right) \dfrac{\partial^2 u}{\partial x^2} + D_f \dfrac{\partial^2 U}{\partial x^2} = (1-n)\rho_s \dfrac{\partial^2 u}{\partial t^2} + n\rho_f \dfrac{\partial^2 U}{\partial t^2} \\ D_f\left(\dfrac{1-n}{n} \dfrac{\partial^2 u}{\partial x^2} + \dfrac{\partial^2 U}{\partial x^2}\right) = \rho_f \dfrac{\partial^2 U}{\partial t^2} + \dfrac{n\rho_f g}{k}\left(\dfrac{\partial U}{\partial t} - \dfrac{\partial u}{\partial t}\right). \end{cases} \tag{45}$$

As shown in Fig. 1(*a*), the column is clamped and undrained at $x = L$. At $x = 0$, it is free to displace and is drained. Also,

Downloaded 03 May 2010 to 171.66.16.247. Redistribution subject to ASME license or copyright; see http://www.asme.org/terms/Terms_Use.cfm

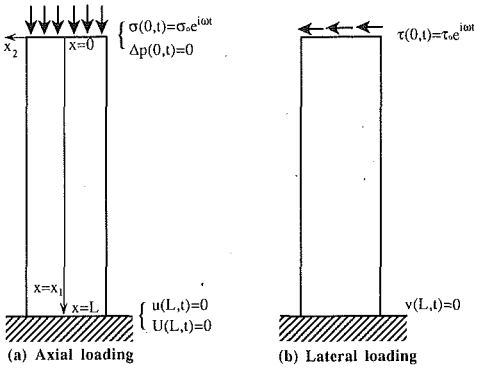

Fig. 1 Geometry and boundary conditions of soil columns subjected to axial and lateral loadings

at $x=0$, its solid part is subjected to a normal stress with a frequency ω and amplitude σ_0:

$$\begin{cases} \Delta\sigma(0,\ t)=\sigma_o\, e^{i\omega t} \\ \Delta p(0,\ t)=0 \\ u(L,\ t)=0 \\ U(L,\ t)=0. \end{cases} \tag{46}$$

The harmonic solution is

$$\begin{cases} u(x,\ t)=u_o(x)e^{i\omega t} \\ U(x,\ t)=U_o(x)e^{i\omega t} \end{cases} \tag{47}$$

where $u_o(x)$ and $U_o(x)$ are

$$\begin{cases} u_o(x)=A\, e^{\zeta x} \\ U_o(x)=B\, e^{\zeta x} \end{cases} \tag{48}$$

and where ζ is related to the complex ψ of Eq. (22) through

$$\psi=\frac{c_w\,\zeta}{\omega}. \tag{49}$$

The amplitude $u_o(x)$ is obtained by superposing the four harmonic waves of Eq. (22) and by enforcing the boundary conditions of Eq. (46) (Bardet and Sayed, 1990b)

$$u_o(x)=\frac{L\sigma_o}{D}\,\frac{1}{K_2-K_1}\left(\frac{(K_2+1)\sinh[\zeta_1(x-L)]}{\zeta_1 L\cosh[\zeta_1 L]}\right.$$
$$\left.-\frac{(K_1+1)\sinh[\zeta_2(x-L)]}{\zeta_2 L\cosh[\zeta_2 L]}\right) \tag{50}$$

where the complex constants K_1 and K_2 are

$$\begin{cases} K_1=-\dfrac{\psi_1^2(1+n\chi)+\dfrac{n}{\beta}}{\psi_1^2+n} \\ K_2=-\dfrac{\psi_2^2(1+n\chi)+\dfrac{n}{\beta}}{\psi_2^2+n}. \end{cases} \tag{51}$$

The amplitude $u_o(0)$ at $x=0$ is:

$$u_o(0)=\frac{L\sigma_o}{D}G(\Omega) \tag{52}$$

where $G(\Omega)$ is

$$G(\Omega)=\frac{1}{K_2-K_1}\left((K_2+1)\frac{\tanh\zeta_1 L}{\zeta_1 L}-(K_1+1)\frac{\tanh\zeta_2 L}{\zeta_2 L}\right) \tag{53}$$

and where the dimensionless circular frequency Ω is

$$\Omega=\frac{\omega L}{c_o}. \tag{54}$$

$L\sigma_o/D$ is the deformation of the column under a drained ($k=\infty$) and static ($\Omega=0$) loading. As Ω tends towards 0, $G(\Omega)$ tends towards 1 and $u_o(0)$ tends towards the drained static deformation $L\sigma_o/D$. The phase angle ϕ is defined as

$$\phi=\tan^{-1}\left(\frac{\Im\{G(\Omega)\}}{\Re\{G(\Omega)\}}\right). \tag{55}$$

4.2 Viscoelastic Solution. In the one-dimensional case, Eq. (31) becomes

$$D_e\frac{\partial^2 u}{\partial x^2}+D_v\frac{\partial^3 u}{\partial t\partial x^2}-\rho_v\frac{\partial^2 u}{\partial t^2}=0. \tag{56}$$

The harmonic solution is

$$u(x,\ t)=A\, e^{\zeta x}e^{i\omega t} \tag{57}$$

where

$$\zeta=\pm\frac{i\omega}{\sqrt{\dfrac{D_e}{\rho_v}+i\omega\dfrac{D_v}{\rho_v}}}. \tag{58}$$

The boundary conditions of Fig. 1(*b*) are

$$\begin{cases} \Delta\sigma(0,\ t)=\sigma_o\, e^{i\omega t} \\ u(L,\ t)=0. \end{cases} \tag{59}$$

The amplitude $u_o(x)$ is

$$u_o(x)=\frac{L\sigma_o}{D_e}\,\frac{\sinh[\zeta(x-L)]}{\zeta L\cosh[\zeta L]}. \tag{60}$$

For the viscoelastic model, i.e., $c_o=\sqrt{D_e/\rho_v}$, $u_o(x)$ at $x=0$ is

$$u_o(0)=\frac{L\sigma_o}{D_e}G_v(\Omega) \tag{61}$$

where

$$\begin{cases} G_v(\Omega)=\dfrac{\tanh[\zeta L]}{\zeta L} \\ \zeta L=\dfrac{i\Omega}{\sqrt{1+i\Omega\dfrac{k_d c_o}{L}}}. \end{cases} \tag{62}$$

$u_o(0)$ is equal to $L\sigma_o/D_e=(L\sigma_o/D)[\chi/(\chi+1/n)]$ when $\Omega=0$. The viscoelastic model does not account for the static drained deformation of the column.

4.3 Comparison of Poroelastic and Viscoelastic Solutions. The poroelastic solution of Eq. (53) depends on seven parameters: n, G_s, D, S, p, k, and L. Bardet and Sayed (1990b) showed that the poroelastic response varies from undamped in all soils when $\chi=\chi_u$ to overcritically damped in fully saturated gravels.

Hereafter, the validity of the viscoelastic model is only investigated for two particular but typical soils. The porosity n and the specific gravity G_s are arbitrarily fixed to typical values for soils: $n=0.3$ and $G_s=2.65$. The column length L is fixed to 10 m. The absolute water pressure is equal to the atmospheric pressure: $p=100$ kPa. Given a value of S, D_f is determined from Eq. (3).

Figures 2 and 3 show the variation of $|G(\Omega)|$ and ϕ versus Ω for a column made of fully saturated silts ($S=1$, $D=2$ MPa, $k=10^{-8}$ m/s, $\chi=9.4\times10^{-4}$). The poroelastic response is amplified dynamically. $|G(\Omega)|$ has very sharp peaks when Ω is about equal to $(2j-1)\pi/2$ where j is a positive integer. As shown in Fig. 2, the static response $|G(0)|$ of the poroelastic material is equal to 1, whereas the one of the viscoelastic model $|G_v(0)|$ is equal to 2.8×10^{-4} ($|G_v(0)|=\chi/[\chi+(1/n)]$). The

Downloaded 03 May 2010 to 171.66.16.247. Redistribution subject to ASME license or copyright; see http://www.asme.org/terms/Terms_Use.cfm

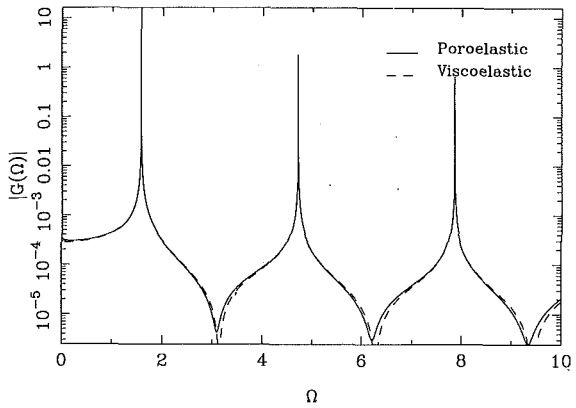

Fig. 2 Variation of amplification factor $|G(\Omega)|$ of poroelastic material and viscoelastic model in the case of fully saturated silts ($k=10^{-8}$ m/s, $S=1$, and $D=2$ MPa)

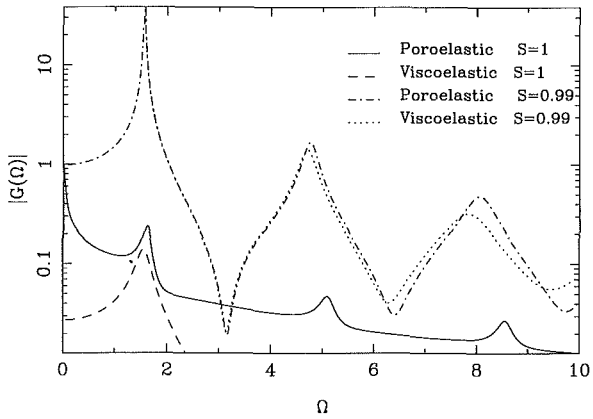

Fig. 4 Variation of amplification factor $|G(\Omega)|$ of poroelastic material and viscoelastic model in the case of gravel ($k=10^{-2}$ m/s and $D=200$ MPa) with two different degrees of saturation

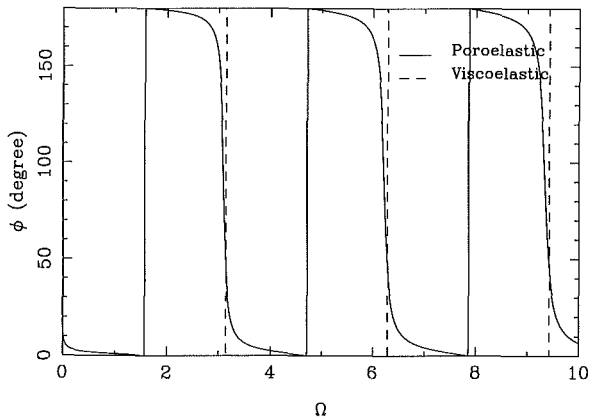

Fig. 3 Variation of phase angle ϕ of the poroelastic material and viscoelastic model in the case of fully saturated silts ($k=10^{-8}$ m/s, $S=1$, and $D=2$ MPa)

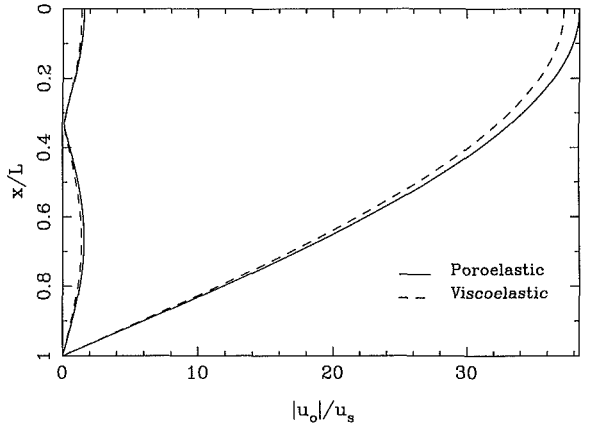

Fig. 5 Distribution of solid displacement within a column for poroelastic material and viscoelastic model at the first and second peaks of Fig. 4 ($S=0.99$)

viscoelastic model does not account for the drained static deformation of poroelastic materials; it only describes the dynamic response of saturated soil masses that have a consolidation time scale much larger than their fundamental period of vibration. However, both poroelastic and viscoelastic solutions merge rapidly when ω increases. The slight discrepancy when $|G(\Omega)|<10^{-5}$ is negligible; it is exacerbated by the logarithmic representation. As shown in Fig. 3, the poroelastic and viscoelastic phase angles ϕ are similar. ϕ decreases smoothly from 180 deg to 0 deg for poroelastic materials while it varies abruptly in square pulses for the viscoelastic model.

Figures 2 and 3 demonstrate that the viscoelastic model simulates the natural frequencies and damping properties of poroelastic materials with a small permeability. This result was expected, since the condition $k\omega/g \ll 1$ is satisfied for a large range of harmonic loading. When k decreases further (e.g., for clays), the viscoelastic and poroelastic responses become indistinguishable.

Figure 4 shows the variation of $|G(\Omega)|$ versus Ω for a column made of gravels ($D=200$ MPa) having a very large permeability ($k=10^{-2}$ m/s) and two different degrees of saturation ($S=1$ and 0.99). The amplitude of the fully saturated ($S=1$) response is attenuated compared to Fig. 2. The static response $|G(0)|$ of poroelastic materials is equal to 1, while the one of the viscoelastic model, $|G_v(0)|$, is equal to 2.7×10^{-2}. The viscoelastic model simulates the amplitude and frequency of the first peak but overestimates the damping properties of poroelastic materials. The viscoelastic model has limitations when applied to fully saturated poroelastic soils with an extremely large permeability.

However, the viscoelastic model is capable of describing the decrease of damping properties as the degree of saturation decreases from 1 to 0.99. When $S=0.99$, χ is equal to 20 and $\chi/(\chi+1/n)$ approaches 1. As shown in Fig. 4, the static and dynamic responses of poroelastic and viscoelastic materials coincide when S is smaller than one.

Figure 5 shows the distribution of solid displacement normalized by the static displacement $u_s=L\sigma_o/D$ within the column. The modes correspond to the first and second peak of Fig. 4 for $S=0.99$. The viscoelastic model performs as well in the interior as on the surface of the column.

5 Lateral Vibrations of Soil Columns

5.1 Poroelastic Solution. The soil column is assumed to deform as a shear beam. The displacement of the fluid and soil are all zero except for the v and V components that are only functions of x

$$\begin{cases} v=u_2, & u_1=u_3=0 \\ V=U_2, & U_1=U_3=0. \end{cases} \tag{63}$$

Equation (13) becomes

Downloaded 03 May 2010 to 171.66.16.247. Redistribution subject to ASME license or copyright; see http://www.asme.org/terms/Terms_Use.cfm

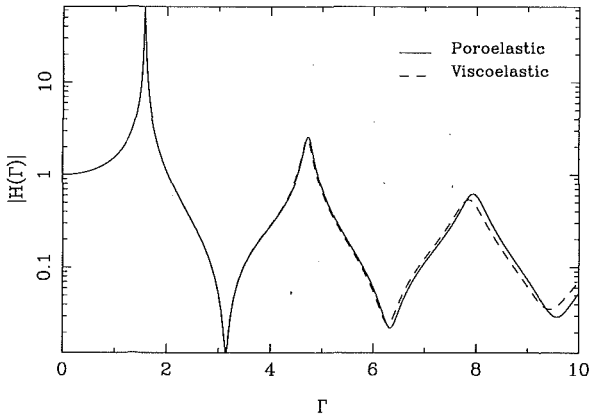

Fig. 6 Variation of the amplification factor $|H(\Gamma)|$ of poroelastic material and viscoelastic model in the case of gravels ($k=10^{-2}$ m/s, $S=1$, and $\mu=60$ MPa)

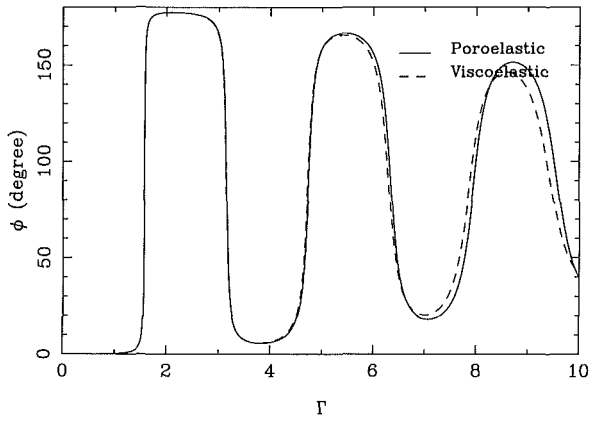

Fig. 7 Variation of phase angle ϕ of poroelastic material and viscoelastic model in the case of gravels ($k=10^{-2}$ m/s, $S=1$, and $\mu=60$ MPa)

$$\begin{cases} \mu\dfrac{\partial^2 v}{\partial x^2}=(1-n)\rho_s\dfrac{\partial^2 v}{\partial t^2}+\dfrac{n\rho_f g}{k}\left(\dfrac{\partial v}{\partial t}-\dfrac{\partial V}{\partial t}\right) \\ n\rho_f\dfrac{\partial^2 V}{\partial t^2}=\dfrac{n\rho_f g}{k}\left(\dfrac{\partial v}{\partial t}-\dfrac{\partial V}{\partial t}\right). \end{cases} \tag{64}$$

The porepressure remains equal to zero since the deformation is isochoric.

As shown in Fig. 1(*b*), the column is clamped at the base ($x=L$) and its solid part at the top ($x=0$) is subjected to a harmonic shear stress with a frequency ω and amplitude τ_o

$$\begin{cases} \Delta\tau(0,\ t)=\tau_o e^{i\omega t} \\ v(L,\ t)=0. \end{cases} \tag{65}$$

The harmonic solutions are

$$\begin{cases} v(y,\ t)=A\,e^{-\zeta x}e^{i\omega t} \\ V(y,\ t)=B\,e^{-\zeta x}e^{i\omega t} \end{cases} \tag{66}$$

where ζ is related to c and δ in Eq. (27) through

$$\zeta=\frac{\omega}{\delta}+i\frac{\omega}{c}. \tag{67}$$

The solid displacement is

$$v(x,\ t)=v_o(x)e^{i\omega t}=\frac{\tau_o L}{\mu}\frac{\sinh[\zeta(x-L)]}{\zeta L\cosh[\zeta L]}e^{i\omega t}. \tag{68}$$

It is independent from the boundary conditions on the fluid constituent. The amplitude $v_o(x)$ at $x=0$ is

$$v_o(0)=-\frac{L\tau_o}{\mu}H(\Gamma) \tag{69}$$

where

$$\begin{cases} H(\Gamma)=\dfrac{\tanh[\zeta L]}{\zeta L} \\ \Gamma=\dfrac{\omega L}{d_o}. \end{cases} \tag{70}$$

The term $L\tau_o/\mu$ is the lateral displacement at $x=0$ of the column subjected to a static load. When $k\omega/ng\ll 1$, Eq. (67) becomes

$$\zeta L=\pm\Gamma\left(\frac{k\omega\beta}{2g}+i\right). \tag{71}$$

5.2 Viscoelastic Solution. In the case of the shear beam of Fig. 1(*b*), Eq. (31) becomes

$$\mu_e\frac{\partial^2 v}{\partial x^2}+\mu_v\frac{\partial^3 v}{\partial t\partial x^2}-\rho_v\frac{\partial^2 v}{\partial t^2}=0. \tag{72}$$

The boundary conditions of Fig. 1(*b*) are the same as Eq. (65). By analogy to the longitudinal vibration problem, the harmonic displacement $v(x,\ t)$ is

$$v(x,\ t)=v_o(x)\,e^{i\omega t}=\frac{L\tau_o}{\mu_e}\frac{\sinh[\zeta(x-L)]}{\zeta L\cosh[\zeta L]}e^{i\omega t} \tag{73}$$

where

$$\zeta=\pm\frac{i\omega}{\sqrt{\dfrac{\mu_e}{\rho_v}+i\dfrac{\omega\mu_v}{\rho_v}}}. \tag{74}$$

For the viscoelastic model, i.e., $d_o=\sqrt{\mu_e/\rho_v}$, the amplitude $v_o(x)$ at $x=0$ is

$$v_o(0)=\frac{L\tau_o}{\mu_e}H_v(\Gamma) \tag{75}$$

where

$$H_v(\Gamma)=\frac{\tanh[\zeta L]}{\zeta L} \tag{76}$$

When $k_s\omega\ll 1$, Eq. (74) becomes:

$$\zeta L=\pm\Gamma\left(\frac{\omega k_s}{2}+i\right). \tag{77}$$

Equations (71) and (77) coincide for poroelastic materials and viscoelastic models. Therefore, their harmonic responses (Eqs. (69) and (75)) are identical when $k\omega/ng\ll 1$.

5.3 Comparison of Poroelastic and Viscoelastic Solutions. Figures 6 and 7 show the variation of $|H(\Gamma)|$ and ϕ versus Γ for a column made of gravels ($\mu=60$ MPa, and $k=10^{-2}$ m/s). In contrast to the axial solution, the lateral response is not influenced by the degree of saturation. The poroelastic and viscoelastic responses have an identical static response. They have practically identical amplitude and phase angle when $\Gamma>0$. The slight difference increases with Γ, which is expected since the ratio $k\omega/g$ increases.

Figure 8 shows the distribution of solid displacement for the poroelastic and viscoelastic materials within the column at the first and second peaks of Fig. 6. The amplitude v_o is normalized by the static displacement $v_s=L\tau_o/\mu$. It is concluded that the

Downloaded 03 May 2010 to 171.66.16.247. Redistribution subject to ASME license or copyright; see http://www.asme.org/terms/Terms_Use.cfm

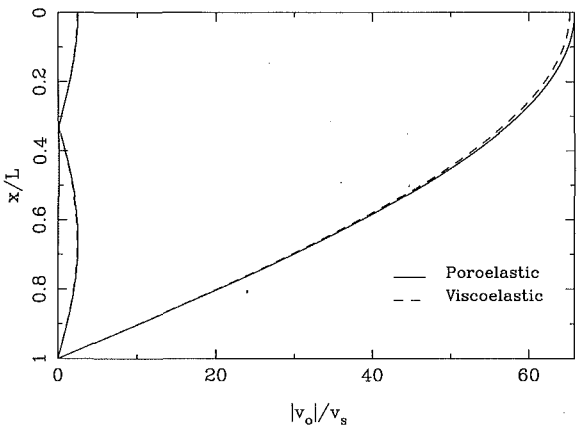

Fig. 8 Distribution of solid displacement within the column for poroelastic material and viscoelastic model at the first and second peaks of Fig. 6

viscoelastic model is also capable of simulating the modes of deformation inside the column.

6 Discussion

The proposed viscoelastic model is not claimed to replace poroelastic materials. It is an approximate model that is much simpler to use than poroelastic materials when solving dynamic problems. It is useful to assess the changes of stiffness and damping that arise from water diffusion. However, it has limitations. The viscoelastic materials does not account for the drainage conditions applied to the water constituent. It becomes inaccurate when the time scale of consolidation and dynamic loading become similar.

The viscoelastic model is calibrated for poroelastic soils. It assumes that soils behave elastically and does not account for hysteretic behavior and energy dissipation caused by the frictional slippage between soil particles. It predicts a constant velocity, whereas irreversible behavior generates an equivalent viscosity inversely proportional to frequency (Hardin, 1965). The model is also limited to nearly saturated materials and excludes the influence of capillary tension.

7 Conclusion

A viscoelastic model has been proposed to describe the dynamic response of saturated poroelastic materials that obeys the two-phases formulation of Biot. The viscoelastic model has been defined from the velocity and attenuation of the dilatational and distortional waves in poroelastic materials. Its material properties are defined in terms of the elastic modulus, specific gravity, degree of saturation, and permeability of soils. It is much simpler to use than poroelastic materials but yields similar results for a wide range of soils and dynamics loadings.

Acknowledgment

The financial support of the National Foundation is acknowledged (Grants CEES-8800735 and MSM-8657999).

References

Bardet, J. P., and Sayed, H., 1990a, "An Analysis of the Velocity and Attenuation of Compression Waves in Nearly Saturated Soils," *J. of Engineering Mechanics*, submitted for publication.

Bardet, J. P., and Sayed, H., 1990b, "An Analysis of the Damping Properties of Nearly Saturated Poroelastic Soils," *J. of Earthquake Engineering and Structural Dynamics*, submitted for publication.

Biot, M., 1956, "Theory of Propagation of Elastic Waves in a Fluid-Saturated Porous Solid," *J. of Acoustical Society of America*, Vol. 28, No. 4, pp. 168–191.

Biot, M., and Willis, D. G., 1957, "The Elastic Coefficient of the Theory of Consolidation," ASME JOURNAL OF APPLIED MECHANICS, Vol. 24, pp. 594–601.

Biot, M., 1962, "Mechanics of Deformation and Acoustic Propagation in Porous Media," *J. of Applied Physics*, Vol. 33, No. 4, pp. 1482–1498.

Bowen, R. M., 1982, "Compressible Porous Media Models by Use of the Theory of Mixtures," *Int. J. Engng. Sci.*, Vol. 20, No. 6, pp. 697–735.

Eringen, A. C., 1980, *Mechanics of Continua*, R. E. Krieger, Huntington, N.Y., pp. 385–406.

Ghaboussi, J., and Wilson, E. L., 1972, "Variational Formulation of Dynamics of Fluid-Saturated Porous Elastic Solids," *J. Engineering Mechanics*, EM.4, pp. 947–963.

Hardin, B. O., 1965, "The Nature of Damping in Sands," *J. of the Soil Mechanics and Foundation Engineering Division*, ASCE, Vol. 91, No. SM1, pp. 63–97.

Lambe, T. W., and Whitman, R. V., 1979, *Soil Mechanics: SI Version*, John Wiley and Sons, New York, pp. 281–294.

Mei, C. C., and Foda, M. A., 1981, "Wave-Induced Responses in a Fluid-Filled Poro-Elastic Solid with a Free Surface—A Boundary Layer Theory," *Geophys. J. R. Astr. Soc.*, Vol. 66, pp. 597–631.

Okuno, A., and Kingsbury, H. B., 1989, "Dynamic Modulus of Poroelastic Materials," ASME JOURNAL OF APPLIED MECHANICS, Vol. 56, pp. 535–540.

Prevost, J. H., 1985, "Wave Propagation in Fluid-Saturated Porous Media: An Efficient Finite Element Procedure," *Soil Dynamics and Earthquake Eng.*, Vol. 4, No. 4, pp. 183–202.

Richart, F. E., Jr., Woods, R. D., and Hall, J. R., 1970, *Vibrations of Soils and Foundations*, Prentice-Hall, Englewood Cliffs, N.J., pp. 129–190.

Scott, R. F., 1963, *Principles of Soil Mechanics*, Addison-Wesley Co., p. 180.

Simon, B. R., Zienkiewicz, O. C., and Paul, D. K., 1984, "An Analytical Solution for the Transient Response of Saturated Porous Elastic Solids," *International Journal for Numerical and Analytical Methods in Geomechanics*, Vol. 8, pp. 381–398.

Van der Kogel, H., 1977, "Wave Propagation in Saturated Porous Media," Thesis in partial fulfillment of the requirement for Ph.D. degree, California Institute of Technology, Pasadena, Calif.

Vardoulakis, I., and Beskos, D. E., 1986, "Dynamic Behavior of Nearly Saturated Porous Media," *Mechanics of Materials*, Vol. 5, pp. 87–108.

Verruijt, A., 1969, "Elastic Storage of Aquifers," *Flow Through Porous Media*, R. J. M. De Weist, Academic Press, London.

Wijesinghe, and Kingsbury, H. B., 1979, "On the Dynamic Behavior of Poroelastic Materials," *J. of Acoustical Society of America*, Vol. 65, No. 1, pp. 90–95.

Zienkiewicz, O. C., Chang, C. T., and Bettes, P., 1980, "Drained, Undrained, Consolidating and Dynamic Behaviour Assumptions in Soils," *Geotechnique*, Vol. 30, No. 4, pp. 385–395.

Downloaded 03 May 2010 to 171.66.16.247. Redistribution subject to ASME license or copyright; see http://www.asme.org/terms/Terms_Use.cfm

Frequency-Dependent Element Mass Matrices

N. J. Fergusson
Graduate Student.

W. D. Pilkey
Morse Professor of Engineering,
Fellow ASME.

Department of Mechanical
and Aerospace Engineering,
The University of Virginia,
Charlottesville, VA 22901

This paper considers some of the theoretical aspects of the formulation of frequency-dependent structural matrices. Two types of mass matrices are examined, the consistent mass matrix found by integrating frequency-dependent shape functions, and the mixed mass matrix found by integrating a frequency-dependent shape function against a static shape function. The coefficients in the power series expansion for the consistent mass matrix are found to be determinable from those in the expansion for the mixed mass matrix by multiplication by the appropriate constant. Both of the mass matrices are related in a similar manner to the coefficients in the frequency-dependent stiffness matrix expansion. A formulation is derived which allows one to calculate, using a shape function truncated at a given order, the mass matrix expansion truncated at twice that order. That is the terms for either of the two mass matrix expansions of order 2n *are shown to be expressible using shape functions terms of order* n. *Finally, the terms in the matrix expansions are given by formulas which depend only on the values of the shape function terms at the boundary.*

1 Introduction

The advantages of the use of frequency-dependent structural matrixes have been demonstrated by Przemieniecki (1968), who included frequency dependence in the stiffness matrix as well as the mass matrix. The same dynamic stiffness matrix has been considered by Paz and Dung (1975), Downs (1980, 1986), and Melosh and Smith (1989), but each author has grouped all the density containing terms into the mass matrix, resulting in a frequency-independent (static) stiffness matrix. This approach involves a mixed mass matrix which is constructed by integrating a frequency-dependent shape function against a static shape function. The approach of Przemieniecki employs a consistent mass matrix obtained by integrating only frequency-dependent shape functions.

In the present work, the power series terms for the two mass matrices are shown to be related in the sense that the terms are multiples of one another. The same sort of relationship is shown for the mass and stiffness matrices, and proves to be a power series equivalent of a differential relationship developed by Richards and Leung (1977) stating that the mass matrix of Przemieniecki can be found by differentiating the dynamic stiffness matrix with respect to the frequency squared.

The equations derived in this paper are presented in a general notation for frequency-dependent structural elements. The frequency-dependent matrices considered are calculated using shape functions which appear as exact solutions to a boundary value problem which specifies nodal values for the boundary values. The nodes used, therefore, must be boundary inclusive, such as the endpoints of a beam or nodal circles of an annular plate or shell of revolution element. The scope is therefore limited to linelike elements, and the integrals will reduce to one-dimensional integrals over a real interval.

More general two-dimensional elements with frequency dependence have been computed by Gupta (1978, 1979, 1984) but are not exact in the sense that the shape functions do not satisfy the boundary values.

2 Formulation

The governing equations for a continuous linear elastic structural member in the absence of body forces can be summarized as

$$\boldsymbol{\epsilon} = \mathbf{D}_u \mathbf{u} \tag{1}$$

$$\mathbf{s} = \mathbf{E}\boldsymbol{\epsilon} \tag{2}$$

$$\mathbf{D}_s^T \mathbf{s} - \boldsymbol{\rho}\ddot{\mathbf{u}} = \mathbf{0} \tag{3}$$

or the displacement form

$$\mathbf{D}_s^T \mathbf{E}\, \mathbf{D}_u\, \mathbf{U} - \boldsymbol{\rho}\ddot{\mathbf{u}} = \mathbf{0} \tag{4}$$

in addition to initial and boundary conditions where $\boldsymbol{\epsilon}$ is the columnn of generalized strains, and these may include slopes, curvatures, etc.; $\mathbf{u}$ is the column of generalized displacements, and may include extensions, deflections, rotations, etc.; $\mathbf{s}$ is the column of generalized stresses, and these may include various stress resultants like bending moments, shear forces, etc.; $\boldsymbol{\rho}$ is the generalized density matrix, its components possibly containing radius of gyration terms to account for rotary inertia; the differential operators $\mathbf{D}_u$ and $\mathbf{D}_s^T$ are generalized forms of the gradient and divergence operators, respectively, as applied in the case of general elasticity. The divergence of the three-dimensional Cauchy stress tensor $\mathbf{T}$, for example, can be written as $\mathbf{D}_s^T\mathbf{s}$ when $\mathbf{s}$ is a 6×1 column containing the

Contributed by the ASME Applied Mechanics Division of THE AMERICAN SOCIETY OF MECHANICAL ENGINEERS for publication in the JOURNAL OF APPLIED MECHANICS.

Discussion on this paper should be addressed to the Technical Editor, Prof. Leon M. Keer, The Technological Institute, Northwestern University, Evanston, IL 60208, and will be accepted until two months after final publication of the paper itself in the JOURNAL OF APPLIED MECHANICS. Manuscript received by the ASME Applied Mechanics Division, May 10, 1990; final revision, Jan. 18, 1991.

Copyright © 1992 by ASME
Downloaded 03 May 2010 to 171.66.16.247. Redistribution subject to ASME license or copyright; see http://www.asme.org/terms/Terms_Use.cfm

six symmetric components of $\mathbf{T}$. In light of this fact, the operators $\mathbf{D}_u$ and $\mathbf{D}_s^T$ satisfy a certain formal adjoint relationship

$$\int_V \mathbf{u}^T {}_u\mathbf{D}^T \mathbf{s}\, dV = \oint_{\partial V} \mathbf{u}^T \mathbf{A}^T \mathbf{s}\, dS - \int_V \mathbf{u}^T \mathbf{D}_s^T \mathbf{s}\, dV \tag{5}$$

where $\mathbf{u}$ and $\mathbf{s}$ are arbitrary vector columns smooth enough for the integrals to make sense, and $\mathbf{A}^T$ is a direction cosine matrix which describes the relationship between the traction $\mathbf{p}$ on an oblique surface in a body and the generalized stress components

$$\mathbf{p} = \mathbf{A}^T \mathbf{s}. \tag{6}$$

Note that the symbols ${}_u\mathbf{D}^T$ and ${}_s\mathbf{D}$ represent $\mathbf{D}_u$ and $\mathbf{D}_s^T$ transposed, and act on the vector to their left.

The above adjoint relationship is a form of the divergence theorem commonly written

$$\int_V \nabla \mathbf{v} \cdot \mathbf{T} dV = \oint_{\partial V} \mathbf{v} \cdot \mathbf{S}\mathbf{n} dS - \int_V \mathbf{v} \cdot \mathrm{div}\mathbf{T} d\mathbf{V}. \tag{7}$$

Finally, for an arbitrary virtual displacement, $\delta\mathbf{u}$, consistent with the geometric constraints, the displacement field $\mathbf{u}$ satisfies the Principle of Virtual Work

$$\int_V \delta\mathbf{u}^T {}_u\mathbf{D}^T \mathbf{E}\, \mathbf{D}_u \mathbf{u}\, dV + \int_V \delta\mathbf{u}^T \boldsymbol{\rho}\, \ddot{\mathbf{u}}\, dV = \mathbf{0}. \tag{8}$$

3 Discrete Equations of Motion

A finite element analysis proceeds with the selection of a shape function $\mathbf{N}$ used to interpolate the displacement field between a fixed number of nodes in the body

$$\mathbf{u}(\mathbf{x},t) = \mathbf{N}(\mathbf{x})\mathbf{v}(t) \tag{9}$$

where $\mathbf{x}$ represents a spatial coordinate in the body, t represents time, and $\mathbf{v}$ signifies the column of nodal displacements. The symbol $\mathbf{N}$ is used here for the global shape function, whose components are constructed to vanish over part of the body. This allows one to write this global shape function in terms of local or element shape functions.

In the interest of computing natural frequencies and mode shapes, the displacement field is assumed as a harmonic form

$$\mathbf{u}(\mathbf{x},t) = \mathbf{u}(\mathbf{x})e^{i\omega t} \tag{10}$$

as is the nodal column

$$\mathbf{v}(t) = \mathbf{v}e^{i\omega t}, \tag{11}$$

where ω will be found as an eigenvalue representing one of the natural frequencies.

This paper concerns itself with shape functions which interpolate the displacement magnitude $\mathbf{u}$ exactly; that is, the shape function $\mathbf{N}$ is such that $\mathbf{u}$ satisfies the displacement form of the time-independent equilibrium equation. The shape function can be constructed so that $\mathbf{u}$ satisfies the static form of the displacement equation

$$\mathbf{D}_s^T \mathbf{E}\, \mathbf{D}_u\, \mathbf{u} = \mathbf{0} \tag{12}$$

or alternatively, so that $\mathbf{u}$ satisfies the dynamic displacement equation

$$\mathbf{D}_s^T \mathbf{E}\, \mathbf{D}_u \mathbf{u} + \rho\, \omega^2 \mathbf{u} = \mathbf{0}. \tag{13}$$

This second option leads to a shape function that is frequency dependent.

The introduction of the harmonic form of Eq. (10) and the interpolation relationship

$$\mathbf{u}(\mathbf{x}) = \mathbf{N}(\mathbf{x},\omega)\mathbf{v} \tag{14}$$

for the displacement amplitude, into the principle of virtual work, provides a nonlinear eigenvalue problem of the form

$$[\mathbf{K}(\omega) - \omega^2 \mathbf{M}(\omega)]\mathbf{v} = \mathbf{0} \tag{15}$$

for the natural frequencies and mode shapes, where $\mathbf{M}$ is the global mass matrix, and $\mathbf{K}$ is the global stiffness matrix. The global matrices are assembled by a summation process using element matrices defined over subregions.

Definition 1.

The static element shape function $\mathbf{N}_0$ is defined as the solution to the boundary value problem

$$\mathbf{D}_s^T \mathbf{E}\, \mathbf{D}_u\, \mathbf{N}_0 = \mathbf{0} \tag{16}$$

subject to Boolean (zeros and ones)-type boundary conditions dictated by the form of the nodal column $\mathbf{v}$.

Definition 2.

The frequency-dependent element shape function $\mathbf{N}$ is defined as the solution to the boundary value problem

$$\mathbf{D}_s^T \mathbf{E}\, \mathbf{D}_u \mathbf{N} + \rho\omega^2 \mathbf{N} = \mathbf{0} \tag{17}$$

subject to the same Boolean boundary conditions as the static shape function $\mathbf{N}_0$.

The boundary conditions for $\mathbf{N}_0$ and $\mathbf{N}$ are seen to be the same by considering the fact that the nodal column $\mathbf{v}$ contains values of the displacement $\mathbf{u}$ at the boundaries, but is not dependent on the frequency.

Definition 3.

The (frequency-dependent) element consistent mass matrix is given by

$$\mathbf{m} = \int_V \mathbf{N}^T \boldsymbol{\rho}\, \mathbf{N}\, dV. \tag{18}$$

Definition 4.

The (frequency-dependent) element stiffness matrix is given by

$$\mathbf{k} = \int_V \mathbf{N}_u^T \mathbf{D}^T \mathbf{E}\, \mathbf{D}_u\, \mathbf{N}\, dV. \tag{19}$$

The vanishing of the determinant of the coefficient matrix in Eq. (15) is necessary for the existence of an eigenpair ($\mathbf{v}$, ω), which motivates the following.

Definition 5.

The element dynamic stiffness matrix is given by

$$\mathbf{d} = \mathbf{k} - \omega^2 \mathbf{m}. \tag{20}$$

The traditional definition of stiffness parameters describes k_{ij} as the displacement at node i due to a force at node j. This description is formalized in the following.

Theorem 1.

The dynamic stiffness matrix can be written in terms of boundary values of the shape functions as

$$\mathbf{d} = \oint_{\partial V} \mathbf{N}_0^T \mathbf{A}^T\, \mathbf{E}\, \mathbf{D}_u \mathbf{N}\, dS. \tag{21}$$

Proof: Apply the adjoint relationship (5) to Eq. (20) and make use of Definition 1 to arrive at

$$\mathbf{d} = \int_{\partial V} \mathbf{N}^T \mathbf{A}^T \mathbf{E}\, \mathbf{D}_u\, \mathbf{N} dS \tag{22}$$

The boundary conditions for $\mathbf{N}_0$, however, are the same as those for $\mathbf{N}$, so that the undifferentiated shape function $\mathbf{N}$ in this expression may be replaced by $\mathbf{N}_0$.

The reports of Downs (1980, 1986), and Melosh and Smith (1989) construct a "mixed" mass matrix as follows.

Downloaded 03 May 2010 to 171.66.16.247. Redistribution subject to ASME license or copyright; see http://www.asme.org/terms/Terms_Use.cfm

Definition 6. *The element mixed mass matrix* $\tilde{\mathbf{m}}$ *is defined by*

$$\tilde{\mathbf{m}} = \int_V \mathbf{N}_0^T \boldsymbol{\rho} \mathbf{N} dV. \tag{23}$$

The mixed mass matrix allows the calculation of modes using just the static stiffness matrix as evidenced by the following result.

Theorem 2. *The dynamic stiffness matrix of Definition 5 can be written as*

$$\mathbf{d} = \mathbf{k}_0 - \omega^2 \tilde{\mathbf{m}}. \tag{24}$$

Proof: First it will be demonstrated that the "mixed" stiffness matrix

$$\tilde{\mathbf{k}} = \int_V \mathbf{N}_0^T {}_{\mathrm{u}}\mathbf{D}^T \mathbf{E}\, \mathbf{D}_{\mathrm{u}}\, \mathbf{N} dV \tag{25}$$

is the same as the static stiffness matrix $\mathbf{k}_0$. Upon application of the transpose of Eq. (5) with the use of Definition 1 it appears that

$$\tilde{\mathbf{k}} = \oint_{\partial V} \mathbf{N}_0^T {}_{\mathrm{u}}\mathbf{D}^T\, \mathbf{E}\, \mathbf{A}\, \mathbf{N}\, dS \tag{26}$$

Since $\mathbf{N}$ satisfies the same boundary conditions as $\mathbf{N}_0$, $\mathbf{N}$ can be replaced by $\mathbf{N}_0$. Then

$$\tilde{\mathbf{k}} = \oint_{\partial V} \mathbf{N}_0^T {}_{\mathrm{u}}\mathbf{D}^T\, \mathbf{E}\, \mathbf{A}\, \mathbf{N}_0\, dS \tag{27}$$

which can be shown to be equal to $\mathbf{k}_0$. Applying Eq. (5) and Definition 2 to $\tilde{\mathbf{k}} - \omega^2 \tilde{\mathbf{m}}$, results in

$$\tilde{\mathbf{k}} = \int_{\partial V} \mathbf{N}_0^T \mathbf{A}^T \mathbf{E}\, \mathbf{D}_{\mathrm{u}}\, \mathbf{N}\, dS \tag{28}$$

which equals $\mathbf{d}$ by Theorem 1.

This mixed mass matrix is the same as the mass matrix used by Paz and Dung (1975), who defined the mass matrix according to Eq. (24). They obtained it by computing the dynamic stiffness directly according to the definition of the stiffness coefficients as the displacements at one node due to unit forces at the other nodes, then expanding in a Taylor series.

For the sake of tractability, the shape function, mass matrix, and stiffness matrix are expanded in a Taylor series in powers of the frequency squared. This leads to the following definition.

Definition 7. *The shape function, consistent mass, mixed mass, and stiffness terms are defined as the coefficient matrices in the respective Taylor expansions for* $\mathbf{N}$, $\mathbf{m}$, $\tilde{\mathbf{m}}$, *and* $\mathbf{k}$

$$\mathbf{N} = \sum_{n=0}^{\infty} \mathbf{N}_n \omega^{2n} \tag{29}$$

$$\mathbf{m} = \sum_{n=0}^{\infty} \mathbf{m}_n \omega^{2n} \tag{30}$$

$$\tilde{\mathbf{m}} = \sum_{n=0}^{\infty} \tilde{\mathbf{m}}_n \omega^{2n} \tag{31}$$

$$\mathbf{k} = \sum_{n=0}^{\infty} \mathbf{k}_n \omega^{2n}. \tag{32}$$

Note that the terms $\mathbf{N}_n$ are calculated according to Eq. (17) by solving the recursive system of differential equations

$$\mathbf{D}_s^T\, \mathbf{E}\, \mathbf{D}_{\mathrm{u}}\, \mathbf{N}_0 = \mathbf{0} \tag{33}$$

$$\mathbf{D}_s^T\, \mathbf{E}\, \mathbf{D}_{\mathrm{u}}\, \mathbf{N}_n + \boldsymbol{\rho} \mathbf{N}_{n-1} = \mathbf{0},\ n \geq 1 \tag{34}$$

which shows that the leading term $\mathbf{N}_0$ is the static shape function. When the shape function expansion is inserted into the various matrices, the terms in the matrix expansions are found as

$$\mathbf{k}_n = \sum_{j=0}^{n} \int_V \mathbf{N}_j^T {}_{\mathrm{u}}\mathbf{D}^T\, \mathbf{E}\, \mathbf{D}_{\mathrm{u}}\, \mathbf{N}_{n-j}\, dV \tag{35}$$

$$\mathbf{m}_n = \sum_{j=0}^{n} \int_V \mathbf{N}_j^T \boldsymbol{\rho} \mathbf{N}_{n-j}\, dV \tag{36}$$

$$\tilde{\mathbf{m}}_n = \int_V \mathbf{N}_0^T \rho \mathbf{N}_n dV \tag{37}$$

$$\mathbf{d}_0 = \mathbf{k}_0 \tag{38}$$

$$\mathbf{d}_n = \mathbf{k}_n - \mathbf{m}_{n-1},\ n \geq 1. \tag{39}$$

It should be noted, however, that the sums in Eqs. (35) and (36) contain terms that equate. All the terms in the mass sum are equal, as are those in the stiffness sum, save the first and last, which vanish. As a result of this, the coefficient matrices can be written as single terms multiplied by the appropriate integer. This is stated precisely in the following theorem.

Theorem 3. The mass and stiffness terms m_n and k_n are given by

$$\mathbf{m}_n = (n+1) \int_0 \mathbf{N}_j^T \boldsymbol{\rho} \mathbf{N}_{n-j}\, dV,\ n \geq 0 \tag{40}$$

where j *is an integer between 0 and* n *inclusive, and*

$$\mathbf{k}_n = (n-1) \int_V \mathbf{N}_i^T {}_{\mathrm{u}}\mathbf{D}^T\, \mathbf{E}\, \mathbf{D}_{\mathrm{u}}\, \mathbf{N}_{n-i}\, dV,\quad n \geq 2 \tag{41}$$

where i is any integer between 1 and n − *1 inclusive. The term* $\mathbf{k}_0$ *is expressed using Eq. (35), while the term* $\mathbf{k}_1$ *vanishes identically.*

Proof: The special cases for $\mathbf{k}_0$ and $\mathbf{k}_1$ are proved using arguments similar to the ones in the following: Consider the formula (35) for the nth stiffness term. Using Eq. (5) and Definition 1 along the fact that $\mathbf{N}_n$ satisfies homogeneous boundary conditions, it follows that the first and last terms in the sum vanish. Consider any other term

$$\int_V \mathbf{N}_j^T {}_{\mathrm{u}}\mathbf{D}^T\, \mathbf{E}\, \mathbf{D}_{\mathrm{u}}\, \mathbf{N}_{n-j}\, dV \tag{42}$$

for some j between 1 and n-1 inclusive. In light of Eq. (17) the adjoint relation (5) can be applied, or its transpose can be applied resulting in two different expressions

$$\omega^2 \int_V \mathbf{N}_{j-1}^T\, \boldsymbol{\rho} \mathbf{N}_{n-j}\, dV \text{ or } \omega^2 \int_V \mathbf{N}_j^T \boldsymbol{\rho} \mathbf{N}_{n-j-1} dV. \tag{43}$$

This proves that the consecutive terms in the sum for $\mathbf{m}_n$ are equal. Since j runs from 1 to $n-1$, the above formula for $\mathbf{m}_n$ follows. Similarly, the first expression in Eq. (43) can be shown to equal consecutive terms in the stiffness sum, and the result follows.

The power of these formulas lies in their description of the $(2j)$th-order mass term $\mathbf{m}_{2j}$ as a function of the jth-order shape function term $\mathbf{N}_j$. The computation of $\mathbf{N}_2$, for example, allows the calculation of $\mathbf{m}_4$ using

$$\mathbf{m}_4 = 5 \int_V \mathbf{N}_2^T \boldsymbol{\rho} \mathbf{N}_2 dV. \tag{44}$$

Theorem 4, however, will show that $\mathbf{k}_5$ can be found also.

An interesting fact regarding the frequency-dependent structural matrices is the interdependence of their respective nonleading terms. The evaluation of one leads to expressions for the other three:

Theorem 4: *For any* n ≥ *1*

$$(n+1)\mathbf{k}_{n+1} = n\mathbf{m}_n = n(n+1)\tilde{\mathbf{m}}_n = -n(n+1)\mathbf{d}_{n+1} \tag{45}$$

Downloaded 03 May 2010 to 171.66.16.247. Redistribution subject to ASME license or copyright; see http://www.asme.org/terms/Terms_Use.cfm

along with the special cases for the leading coefficients $\mathbf{d}_0 = \mathbf{k}_0$, $\mathbf{d}_1 = -\mathbf{m}_0$, $\mathbf{k}_0 = \mathbf{0}$, $m_0 = \tilde{\mathbf{m}}_0$.

Proof: The special cases follow by using procedures similar to the ones used in the following arguments. Assume $n \geq 1$. To prove the second equality, insert Eq. (29) into (23) and compare to the statement of Theorem 3 with $j = 0$. The first equality follows by applying the adjoint relationship to the formula for $\mathbf{k}_{n+1}$ in Theorem 3. Since $\mathbf{N}_j$ vanishes on the boundary ∂V for $j \geq 1$, and $\mathbf{N}_0$ and $\mathbf{N}$ satisfy the same boundary conditions, the boundary term vanishes. The use of Eq. (34) produces an integral which is equal to $n\mathbf{m}_n/(n+1)$ by theorem 3. Finally, the fact that $\mathbf{d}_{n+1}$ can be related to either $\mathbf{m}_n$ or $\mathbf{k}_{n+1}$ is proved by using Eq. (39) and the first equality in Theorem 4.

The previous formula is shown to be equivalent (within the radius of convergence) to the following differential relationship between the mass and the dynamic stiffness matrices.

Theorem 5 (Richards, Leung, 1977).

$$\mathbf{m} = -\frac{\partial \mathbf{d}}{\partial(\omega^2)} \tag{46}$$

This equivalence is quite easily demonstrated by inserting the appropriate power series into Theorem 5 and collecting like terms, and using the adjoint relationship.

The previous formula, when used in tandem with Eq. (45), provides boundary formulas for the mass and stiffness terms also.

4 Conclusion

The consistent mass matrix and the mixed mass matrix have been shown to be equivalent in the sense that the terms in their respective Taylor expansions are proportional to one another, and that they both lead to the same dynamic stiffness matrix when used with the appropriate stiffness matrix. Furthermore, the calculation of the $2j$th-order term for either of these can be accomplished with the knowledge of the jth-order shape function term. In addition, proportionality is shown between the mass and stiffness terms, as is the dependence of each of the terms of each of the terms for any of the four matrices $\mathbf{m}$, $\tilde{\mathbf{m}}$, $\mathbf{k}$, and $\mathbf{d}$, on the boundary values of the shape functions.

Dedication

This work is dedicated to Prof. Walter Wunderlich on the occasion of his 60th birthday.

References

Downs, B., 1980, "Vibration Analysis of Continuous Systems by Dynamic Discretization," ASME JOURNAL OF MECHANICAL DESIGN, Vol. 102, pp. 391–398.

Downs, B., 1986, "An Equivalent Inertia Matrix for a Segment of a Uniform Timoshenko Beam of Any Geometry and Material," *J Sound Vib.*, Vol. 105, No. 1, pp. 109–120.

Gupta, K. K., 1978, "Development of a Finite Dynamic Element for Free Vibration Analysis of Two-Dimensional Structures," *Int. J. Num. Meth.*, Vol. 12, No. 8, pp. 1311–1327.

Gupta, K. K., 1979, "Finite Dynamic Element Formulation for a Plane Triangular Element," *Int. J. Num. Meth.*, Vol. 14, No. 10, pp. 1431–1448.

Gupta, K. K., 1984, "Numerical Formulation for a Higher Order Plane Dynamic Element," *Int. J. Num. M.*, Vol. 20, No. 8, pp. 1407–1414.

Melosh, R. J., and Smith, H. A., 1989, "New Formulation for Vibration Analysis," *J. Eng. Mech.*, ASCE, Vol. 115, No. 3, pp. 543–554.

Paz, M., and Dung, L., 1975, "Power Series Expansion of the General Stiffness Matrix for Beam Elements," *Int. J. Num. M.*, Vol. 9, pp. 449–459.

Przemieniecki, J. S., 1968, *Theory of Matrix Structural Analysis*, McGraw-Hill, New York.

Richards, T. H., and Leung, Y. T., 1977, "An Accurate Method in Structural Vibration Analysis," *J. Sound Vib.*, Vol. 55, No. 3, pp. 363–376.

Downloaded 03 May 2010 to 171.66.16.247. Redistribution subject to ASME license or copyright; see http://www.asme.org/terms/Terms_Use.cfm

P. Yu

A. H. Shah

N. Popplewell

Faculty of Engineering,
The University of Manitoba,
Winnipeg, Manitoba R3T 2N2, Canada

Inertially Coupled Galloping of Iced Conductors

This paper is concerned with the galloping of iced conductors modeled as a two-degrees-of-freedom system. It is assumed that a realistic cross-section of a conductor has eccentricity; that is, its center of mass and elastic axis do not coincide. Bifurcation theory leads to explicit asymptotic solutions not only for the periodic solutions but also for the nonresonant, quasi-periodic motions. Critical boundaries, where bifurcations occur, are described explicitly for the first time. It is shown that an interesting mixed-mode phenomenon, which cannot happen in cocentric cases, may exist even for nonresonance.

1 Introduction

Developments in galloping technology have encompassed a wide spectrum of engineering and practical approaches since Den Hartog (1932) gave the classical stability criterion for the large amplitude, low-frequency plunge motions of an iced transmission conductor. Indeed, the cocentric case of a conductor without ice has been studied in fair detail (e.g., Blevins, 1974; Blevins and Iwan, 1974). A cocentric model does not predict, however, the complicated coupled motions observed normally in the field. Very little has been done, especially theoretically, on the more complex eccentric case where ice has accumulated on a conductor although several authors (e.g., Richardson, 1981) have investigated a few special practical cases. The aim of this paper is to give a general picture of the effect of eccentricity in terms of stability diagrams for the equilibrium solution and the nonresonant periodic motions.

The present analysis is based on the two-degrees-of-freedom autonomous model of Blevins (1974). It is well known that such a model may exhibit various forms of dynamic behavior corresponding to equilibrium solutions; self-excited, periodic (Hopf bifurcation) solutions; quasi-periodic motions lying on an invariant torus; and even a more complicated chaotic behavior. However, researchers who have previously considered galloping have used largely classical methods of mechanics (e.g., see Desai et al., 1989). Bifurcation theory is applied here, on the other hand, because it provides a more complete analysis of the stability and catastrophic motions of nonlinear dynamical systems. It is shown that mixed-mode or quasi-periodic motions, which do not exist in the corresponding cocentric case, may occur, under certain conditions, even for the nonresonant case. Furthermore, criteria to determine when a system will exhibit periodic motions or quasi-periodic motions (lying on a two-dimensional torus) are discussed. All the asymptotic solutions and the critical bifurcation boundaries are derived explicitly, for the first time, in terms of coefficients of the system.

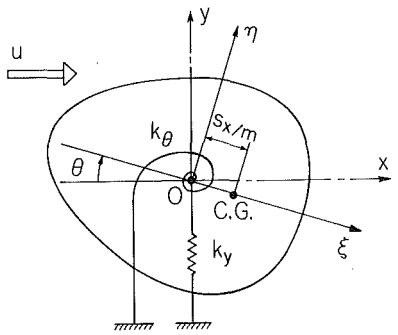

Fig. 1 Elastically supported two-degrees-of-freedom model

2 Mathematical Formulation

The basic two-degree-of-freedom oscillator developed by Blevins (1974) is illustrated in Fig. 1. Its equations of motion are described by

$$m\ddot{y} + c_y\dot{y} - s_x\ddot{\theta} + k_y y = F_y,$$
$$I\ddot{\theta} + c_\theta\dot{\theta} - s_x\ddot{y} + k_\theta\theta = F_M, \quad (1)$$

where y is the vertical or plunge displacement, θ is the angle of twist, and a dot superscript denotes differentiation with respect to time. The k_y and k_θ represent the stiffness in plunge and torsion, respectively, and the c_y and c_θ are the corresponding viscous dampers (which are not shown in Fig. 1). Furthermore, m and I are the mass and the moment of inertia of the iced conductor's cross-section, A, about its center of rotation, O. They are defined by

$$m = \int_A \mu\, d\xi\, d\eta, \quad I = \int_A (\xi^2 + \eta^2)\mu\, d\xi\, d\eta. \quad (2)$$

The s_x in Eq. (1) indicates the eccentricity of the system. It is given by

$$s_x = \int_A \xi\, \mu\, d\xi\, d\eta, \quad (3)$$

Contributed by the Applied Mechanics Division of THE AMERICAN SOCIETY OF MECHANICAL ENGINEERS for publication in the JOURNAL OF APPLIED MECHANICS.

Discussion on this paper should be addressed to the Technical Editor, Prof. Leon M. Keer, The Technological Institute, Northwestern University, Evanston, IL 60208, and will be accepted until two months after final publication of the paper itself in the JOURNAL OF APPLIED MECHANICS. Manuscript received by the ASME Applied Mechanics Division, June 4, 1990; final revision, Jan. 18, 1991.

Copyright © 1992 by ASME
Downloaded 03 May 2010 to 171.66.16.247. Redistribution subject to ASME license or copyright; see http://www.asme.org/terms/Terms_Use.cfm

where μ is the generalized mass density over A and s_x/m is the lateral position of the center of gravity measured from O.

If the maximum velocity of the structure, $\dot{y}$, is much less than the wind's free-stream velocity U, the angle of attack, α, is approximately

$$\alpha \cong \theta - \frac{R_1}{U}\dot{\theta} - \frac{1}{U}\dot{y}, \tag{4}$$

where R_1 is the characteristic radius of the section (Blevins and Iwan, 1974). Then the aerodynamic force and moment acting on A, F_y, and F_M, respectively, can be expressed by

$$F_y = -\frac{1}{2}\rho U^2 d C_y(\alpha),$$

and

$$F_M = -\frac{1}{2}\rho U^2 d^2 C_M(\alpha), \tag{5}$$

where ρ is the density of air. The d is a characteristic structural length which is usually taken as the maximum width of the cross-section normal to the free stream. Coefficients C_y and C_M are relatively smooth, continuous functions of α which may be expressed as experimentally determined polynomials in this variable. The representation of C_y and C_M gives rise to the nature of the nonlinearity in the system (and the complexity of the subsequent analysis). In fact, polynomials up to 25th order of α have been used (Slater, 1969). Although the complexities introduced by a higher-order polynomial may increase accuracy, such complexities cause a loss of physical understanding of the effect of various parameters. Furthermore, a simple cubic approximation was shown to capture many of the qualitative features of the galloping of a symmetrically iced conductor (Blevins and Iwan, 1974). Consequently, a cubic polynomial will be used so that

$$\begin{aligned} C_y &= a_1\alpha + a_3\alpha^3, \\ C_M &= b_1\alpha + b_3\alpha^3, \end{aligned} \tag{6}$$

where a_1, a_3, b_1, and b_3 are "best fit" coefficients.

A combination of Eqs. (1), (5), and (6) produces

$$\begin{aligned} \ddot{Y} - e_x\ddot{\theta} + Y &= -2\xi_y\dot{Y} - \eta_y U_y^2(a_1\alpha + a_3\alpha^3) \\ \ddot{\theta} - \eta e_x\ddot{Y} + \omega^2\theta &= -2\xi\omega\dot{\theta} - \eta_\theta U_y^2(b_1\alpha + b_3\alpha^3) \end{aligned} \tag{7}$$

where

$$\begin{gathered} Y = \frac{y}{d},\ e_x = \frac{s_x}{md},\ \omega_y^2 = \frac{k_y}{m},\ \omega_\theta^2 = \frac{k_\theta}{I},\ \omega = \frac{\omega_\theta}{\omega_y} \\ \xi_y = \frac{c_y}{2m\,\omega_y},\ \xi_\theta = \frac{c_\theta}{2I\omega_\theta},\ U_y = \frac{U}{\omega_y d}, \\ \eta_y = \frac{\rho d^2}{2m},\ \eta_\theta = \frac{\rho d^4}{2I},\ \eta = \frac{\eta_\theta}{\eta_y} \end{gathered} \tag{8}$$

and α is rewritten in the form

$$\alpha = \theta - \frac{r_1}{U_y}\dot{\theta} - \frac{1}{U_y}\dot{Y}, \tag{9}$$

where $r_1 = R_1/d$. A dot superscript now indicates a derivative with respect to the nondimensionalized time $\tau = \omega_y t$. It can be seen easily from Eqs. (7) and (9) that $Y = \dot{Y} = \theta = \dot{\theta} = 0$ is an equilibrium solution. Suppose the system is initially in stable equilibrium but a parameter changes (e.g., the steady wind speed, U, increases) so that the initial equilibrium becomes unstable. The aim here is to investigate which subsequent periodic and quasi-periodic motions are possible and to explicitly find the asymptotic motions as well as the instability conditions, when the damping and aerodynamic forces are small compared to the forces arising from the conductor's stiffnesses. Then the terms on the right of Eq. (7) are of order ϵ a positive small parameter, and, furthermore, $\epsilon = 0$ denotes a critical point of system (7).

Many authors (e.g., Blevins, 1974) have considered galloping and vibration phenomena by using the approximation of Bogoliubov and Mitropolsky (1961) and the principal coordinate approach (Meirovitch, 1971). Here, bifurcation theory and a perturbation method—the multiple-scale intrinsic harmonic balancing and unification technique (Huseyin and Yu, 1988)—will be employed because the conditions when system (7) jumps from one state to another can be elucidated more clearly. The characteristic polynomial of the homogeneous system (7), $G(\omega_c^2)$ can be obtained at the critical point, c, by employing $Y = A_y\cos\omega t$, and $\theta = A_\theta\cos\omega t$. Then

$$G(\omega_c^2) = (1-\eta e_x^2)\omega_c^4 - (1+\omega^2)\omega_c^2 + \omega^2, \tag{10}$$

which in turn yields the two characteristic frequencies

$$\omega_{(1,2)c}^2 = \frac{1}{2(1-\eta e_x^2)} \cdot \left[(1+\omega^2) \pm \sqrt{(1+\omega^2)^2 - 4(1-\eta e_x^2)\omega^2}\right]. \tag{11}$$

Subscript c indicates values associated with the critical point c. From Eqs. (2) and (3), it can be shown, by using the Schwartz Inequality (Rudin, 1987), that

$$s_x^2 < mI, \quad \text{i.e.,}\ 1 - \eta e_x^2 > 0 \tag{12}$$

which guarantees $\omega_{(1,2)c} > 0$. Furthermore, it can be observed from Eq. (11) that $\omega_{1c} = \omega_{2c}$ at the critical point if and only if $\omega = 1$ and $e_x = 0$ ($s_x = 0$). These last two conditions give rise to a 1:1 resonance vibration which is not considered here.

For definiteness, that is, for the case $e_x = 0$, $\omega_{1c} = 1$ and $\omega_{2c} = \omega$, the positive and negative square root in (11) correspond to ω_{1c}^2 and ω_{2c}^2, respectively, when $\omega < 1$. The reverse situation holds when $\omega > 1$. Next, the linear transformation

$$\begin{bmatrix} Y \\ \dot{Y} \\ \theta \\ \dot{\theta} \end{bmatrix} = \begin{bmatrix} 1 & 0 & K_2 & 0 \\ 0 & \omega_{1c} & 0 & K_2\omega_{2c} \\ K_1 & 0 & 1 & 0 \\ 0 & K_1\omega_{1c} & 0 & \omega_{2c} \end{bmatrix} \begin{bmatrix} x_1 \\ x_2 \\ x_3 \\ x_4 \end{bmatrix}, \tag{13}$$

where

$$K_1 = \frac{\omega_{1c}^2}{\omega_{1c}^2 - \omega^2}\eta e_x \qquad K_2 = \frac{\omega_{2c}^2}{\omega_{2c}^2 - 1}e_x, \tag{14}$$

is introduced into Eq. (7) to obtain

$$\{\dot{x}\} = [D]\{x\} + \{N\} \tag{15}$$

in which $\{x\}^t = [x_1, x_2, x_3, x_4]$ and superscript t denotes a transpose. The $[D]$ is a 4×4 matrix whose nonvanishing components are given in the Appendix. The nonlinear components of $\{N\}$ are

$$\{N\}^T = E_1[-K_1U_yx_1 + \omega_{1c}(1+K_1r_1)x_2 - U_yx_3 + \omega_{2c}(K_2+r_4)x_4]^3\ \{N_1\}^t,$$

where

$$\{N_1\}^t = \left[0,\ \omega_{1c}\eta_y(a_3+K_1b_3),\ 0,\ \frac{\omega_{2c}}{\omega^2}\eta_\theta(K_2a_3+b_3)\right], \tag{16}$$

and

$$E_1 = \frac{1}{(1-K_1K_2)U_y}. \tag{17}$$

The Jacobian matrix of (15), evaluated at the critical point for the initial equilibrium solution, $\{x\} = \{0\}$, now takes the canonical form

$$J_c = \begin{bmatrix} 0 & \omega_{1c} & 0 & 0 \\ -\omega_{1c} & 0 & 0 & 0 \\ 0 & 0 & 0 & \omega_{2c} \\ 0 & 0 & -\omega_{2c} & 0 \end{bmatrix}. \tag{18}$$

Downloaded 03 May 2010 to 171.66.16.247. Redistribution subject to ASME license or copyright; see http://www.asme.org/terms/Terms_Use.cfm

Only the nonresonant case (where the ratio $\omega_{1c}/\omega_{2c} \neq m/n$, m and n integers) is considered. The periodic and quasi-periodic solutions and the associated stability conditions can be derived from Eq. (15). This is accomplished by first assuming that the quasi-periodic, as well as the periodic solutions are described in the vicinity of the critical point (where $\epsilon = 0$) by the two-time scale Fourier series

$$x_j(\tau_1, \tau_2, \epsilon) = \sum_{\substack{m=0 \\ (m_1+m_2=0)}}^{M} [p_{j,m_1m_2}(\epsilon)\cos(m_1\tau_1 + m_2\tau_2) + r_{j,m_1m_2}(\epsilon)\sin(m_1\tau_1 + m_2\tau_2)]. \quad (19)$$

Here $j = 1, 2, 3, 4$; and m, m_1 and m_2 are integers (but $m \geq 0$) whereas M is an arbitrary positive integer. Furthermore,

$$\tau_1 = \omega_1(\epsilon)\tau, \quad \tau_2 = \omega_2(\epsilon)\tau. \quad (20)$$

The ω_1, ω_2, p_{j,m_1m_2} and r_{j,m_1m_2} are functions of the system's parameters which are associated with the symbolic small parameter, ϵ. They are determined through a perturbation procedure (Huseyin and Yu, 1988).

Based on Eqs. (15) and (19), the multiple-scale intrinsic harmonic balancing and unification technique can be applied to obtain the rate equations, from which steady-state (periodic and quasi-periodic) solutions and their stability conditions can be derived. These relations are expressed most advantageously in terms of the system's coefficients. The approach can be summarized as follows: First, assume that the solutions are in the parametric form $x_j = x_j(\epsilon)$. By successively differentiating Eq. (15) with respect to ϵ, the first, second, and higher-order perturbation equations can be determined systematically. Then, by substituting Eq. (19) into these perturbation equations and setting the coefficients of the circular functions to zero (harmonic balancing), algebraic equations are derived for each step of the perturbation procedure. Finally, the unification technique is applied to the algebraic equations to find the rate equations in terms of the amplitudes (A_y, A_θ) and phases (ϕ_y, ϕ_θ) of the variables (x_1, x_3). These equations can by written, by retaining terms up to third order, as

$$\dot{A}_y = E_1 U_y \omega_{1c}^2 \eta_y A_y \left[B_1 + E_2(B_3 A_y^2 + 2B_4 A_\theta^2) \right],$$

$$\dot{A}_\theta = E_1 U_y \left(\frac{\omega_{2c}}{\omega}\right)^2 \eta_\theta A_\theta \left[B_2 + E_3(2B_3 A_y^2 + B_4 A_\theta^2) \right], \quad (21a)$$

and

$$\dot{\phi}_y = \omega_{1c}\left\{1 + K_1 E_1 U_y^2 \eta_y \left[\frac{1}{2} U_y(a_1 + K_1 b_1) + (a_3 + K_1 b_3)(B_3 A_y^2 + 2B_4 A_\theta^2)\right]\right\},$$

$$\dot{\phi}_\theta = \omega_{2c}\left\{1 + E_1\left(\frac{U_y}{\omega}\right)^2 \eta_\theta \left[\frac{1}{2} U_y(K_2 a_1 + b_1) + (K_2 a_3 + b_3)(2B_3 A_y^2 + B_4 A_\theta^2)\right]\right\}, \quad (21b)$$

where

$$B_1 = \frac{1}{2} U_y(1 + K_1 r_1)(a_1 + K_1 b_1) - \left[\frac{\xi_y}{\eta_y} + K_1^2 \frac{\omega \xi_\theta}{\eta_\theta}\right],$$

$$B_2 = \frac{1}{2} U_y(K_2 + r_1)(K_2 a_1 + b_1) - \left[K_2^2 \frac{\xi_y}{\eta_y} + \frac{\omega \xi_\theta}{\eta_\theta}\right],$$

$$B_3 = \frac{3}{8U_y}\left[K_1^2 U_y^2 + (1 + K_1 r_1)^2 \omega_{1c}^2\right] (>0),$$

$$B_4 = \frac{3}{8U_y}\left[U_y^2 + (K_2 + r_1)^2 \omega_{2c}^2\right] (>0),$$

$$E_2 = (1 + K_1 r_1)(a_3 + K_1 b_3),$$

$$E_3 = (K_2 + r_1)(K_2 a_3 + b_3). \quad (22)$$

Setting $\dot{A}_y = \dot{A}_\theta = 0$ yields the steady-state solutions $\overline{A}_y$ and $\overline{A}_\theta$ which are the amplitudes of the periodic solutions having frequencies $\omega_1(\epsilon) = \dot{\phi}_y$ and $\omega_2(\epsilon) = \dot{\phi}_\theta$, respectively. The degenerate case of a cocentric cross-section, which was studied by Blevins and Iwan (1974), can be obtained by setting $e_x = 0$ (i.e., $K_1 = K_2 = 0$) in Eqs. (21) and (22).

3 Periodic and Quasi-Periodic Solutions

Steady-state solutions can be obtained easily from Eq. (21a) by setting $\dot{A}_y = \dot{A}_\theta = 0$. First, it may be noted that

$$A_y = A_\theta = 0 \quad (23)$$

is a solution which, indeed, represents the initial equilibrium solution. Second, there are two distinct families of limit cycles for the periodic solutions which bifurcate from the initial equilibrium solution. These limit cycles are described by

$$A_y^2 = -\frac{1}{E_2} \cdot \frac{B_1}{B_3}, \quad A_\theta^2 = 0, \quad (24)$$

and

$$A_y^2 = 0, \quad A_\theta^2 = -\frac{1}{E_3} \cdot \frac{B_2}{B_4}. \quad (25)$$

Solution (24) represents a purely plunge vibration having a frequency

$$\omega_1 = \dot{\phi}_y = \omega_{1c}\left[1 + \frac{K_1\left(\xi_y + K_1^2 \frac{\omega \xi_\theta}{\eta}\right) E_1 U_y^2}{(1 + K_1 r_1)}\right] \quad (26)$$

whereas (25) corresponds to a solely torsional vibration with frequency

$$\omega_2 = \dot{\phi}_\theta = \omega_{2c}\left[1 + \frac{\left(\xi_\theta + K_2^2 \frac{\eta \xi_y}{\omega}\right) E_1 U_y^2}{\omega(K_2 + r_1)}\right]. \quad (27)$$

From Eqs. (11) and (14), it can be demonstrated that

$$\frac{K_1}{K_2} = -\frac{\eta}{\omega^2} \text{ and, therefore, } K_1 K_2 < 0 \quad (28)$$

(which implies that $E_1 > 0$). It can be also shown that $K_1 > 0$ (so that $K_2 < 0$) if and only if $\omega < 1$, and that $K_1 < 0$ ($K_2 > 0$) if and only if $\omega > 1$.

A more interesting coupled plunge-torsion steady-state solution can be determined from Eq. (21a) as

$$A_y^2 = \frac{1}{3B_3}\left(\frac{B_1}{E_2} - \frac{2B_2}{E_3}\right),$$

$$A_\theta^2 = \frac{1}{3B_4}\left(\frac{B_2}{E_3} - \frac{2B_1}{E_2}\right), \quad (29)$$

if $E_2 E_3 \neq 0$. Relation (29) represents two distinct amplitudes of a family of quasi-periodic motions which lie on an invariant torus. Such motions, although observed commonly in the galloping of conductors, are not possible for the cocentric, $e_x = 0$, case. The quasi-periodic motions have frequencies ω_1 and ω_2 which can be found from Eq. (21b). These frequencies are surprisingly identical to those of the uncoupled periodic solutions given by (26) and (27), respectively. First-order asymptotic expressions for the family of two-dimensional tori are expressed by

$$x_1 = A_y \cos\omega_1 \tau, \quad x_2 = -A_y \sin\omega_1 \tau,$$

$$x_3 = A_\theta \cos\omega_2 \tau, \quad x_4 = -A_\theta \sin\omega_2 \tau. \quad (30)$$

(More accurate third-order approximations, which may not be found by using a conventional averaging approach, can be obtained from Huseyin and Yi (1988).)

Downloaded 03 May 2010 to 171.66.16.247. Redistribution subject to ASME license or copyright; see http://www.asme.org/terms/Terms_Use.cfm

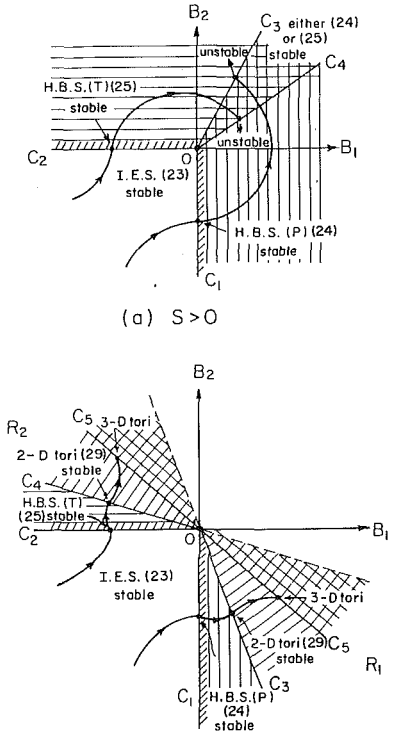

Fig. 2 *Bifurcation and stability diagrams; (a) $S>0$ and (b) $S<0$*

4 The Initiation of Galloping and Stability Analysis

The stability of the four steady-state solutions derived previously will be considered next. In particular, conditions will be sought for the initiation of galloping (i.e., the instability of the initial equilibrium solution (23)) and the instabilities of the three steady-state solutions (24), (25), and (29). In other words, critical stability boundaries will be found where a steady-state solution becomes unstable and jumps to a new state. Stability conditions may be determined on the basis of the Jacobian of (21*a*), that is

$$J(A_y, A_\theta; \epsilon) = E_1 U_y \begin{bmatrix} J_{11} & J_{12} \\ J_{21} & J_{22} \end{bmatrix}, \tag{31}$$

where

$$J_{11} = \omega_{1c}^2 \eta_y \left[B_1 + E_2 (3B_3 A_y^2 + 2B_4 A_\theta^2) \right],$$
$$J_{12} = 4\omega_{1c}^2 \eta_y E_2 B_4 A_y A_\theta,$$
$$J_{21} = 4\left(\frac{\omega_{2c}}{\omega}\right)^2 \eta_\theta E_3 B_3 A_y A_\theta,$$
$$J_{22} = \left(\frac{\omega_{2c}}{\omega}\right)^2 \eta_\theta \left[B_2 + E_3 (2B_3 A_y^2 + 3B_4 A_\theta^2) \right]. \tag{32}$$

The resulting bifurcation diagram, having B_1 and B_2 as its coordinates, and the associated stability regions are illustrated in Fig. 2. In this figure, I.E.S., H.B.S. (P), and H.B.S. (T) represent the initial equilibrium solution, the Hopf bifurcation solution for a periodic plunge vibration, and the Hopf bifurcation solution for a periodic torsional vibration, respectively. These solutions will be detailed next.

4.1 Initial Equilibrium Solution and Periodic Solutions. Substituting Eq. (23) or (24) or (25) into (31) results in $J_{12} = J_{21} = 0$. Thus, the initial equilibrium solution (I.E.S.) or the plunge periodic motion (H.B.S. (P)) or the torsional periodic motion (H.B.S. (T)) is stable if $J_{11} < 0$ and $J_{22} < 0$. These conditions yield critical boundaries where a new state may bifurcate from the previous steady-state solutions. These results are summarized in Table 1. It can be observed from the I.E.S. stability condition that the initial equilibrium soltuion and the plunge (torsional) motion exchange their stability on the critical boundary $C_1 (C_2)$.

Table 1 Stability conditions and critical boundaries for the initial equilibrium and periodic solutions

Solution	I. E. S. (23)		H. B. S. (P) (24), (26)	H. B. S. (T) (25), (27)
Existence Condition			$\frac{B_1}{E_2} < 0$	$\frac{B_2}{E_3} < 0$
Stability Condition	$B_1 < 0$, $B_2 < 0$		$B_1 > 0$, $B_2 - \frac{2E_3}{E_2} B_1 < 0$	$B_1 - \frac{2E_2}{E_3} B_2 < 0$, $B_2 > 0$
Critical Boundary	C_1: $B_1 = 0$	C_2: $B_2 = 0$	C_3: $B_2 - \frac{2E_3}{E_2} B_1 = 0$	C_4: $B_1 - \frac{2E_2}{E_3} B_2 = 0$
Bifurcation Solution	H.B.S.(P) (24), (26)	H.B.S.(T) (25), (27)	Quasi-periodic Motion (26), (27), (29)	

It has been observed in the field that a larger steady wind speed (Edwards and Madeyski, 1956) is an important factor in causing instability or the initiation of galloping. This is clear from (22) which indicates that at least one of B_1 and B_2 grow when U_y increases. Table 1 suggests that the possibility of the instability of the corresponding initial equilibrium solution also increases, as expected.

4.2 Quasi-periodic Motion. The stability of the quasi-periodic motions are found by first substituting (29) into the Jacobian (31) to produce

$$J_{(IV)}(A_y, A_\theta; \epsilon) = E_1 U_y \begin{bmatrix} 2\omega_{1c}^2 \eta_y E_2 B_3 A_y^2 & 4\omega_{1c}^2 \eta_y E_2 B_4 A_y A_\theta \\ 4\left(\frac{\omega_{2c}}{\omega}\right)^2 \eta_\theta E_3 B_3 A_y A_\theta & 2\left(\frac{\omega_{2c}}{\omega}\right)^2 \eta_\theta E_3 B_4 A_\theta^2 \end{bmatrix}. \tag{33}$$

The A_y and A_θ, of course, are given by solution (29). Stability conditions for this family of two-dimensional tori are determined by the trace and determinant of $J_{(IV)}$, that is, trace $J_{(IV)} < 0$ and $\det J_{(IV)} > 0$ for which the eigenvalues of the characteristic polynomial of $J_{(IV)}$ have negative real parts. More specifically,

$$\text{trace } J_{(IV)} = 2E_1 U_y \left[\omega_{1c}^2 \eta_y E_2 B_3 A_y^2 + \left(\frac{\omega_{2c}}{\omega}\right)^2 \eta_\theta E_3 B_4 A_\theta^2 \right], \tag{34}$$

and

$$\det J_{(IV)} = -12 \left(E_1 U_y \omega_{1c} \frac{\omega_{2c}}{\omega} \right)^2 \eta_y \eta_\theta E_2 E_3 B_3 B_4 A_y^2 A_\theta^2. \tag{35}$$

Substituting (29) into (34) results in the stability condition

$$\left[\omega_{1c}^2 - \frac{2E_3}{E_2} \left(\frac{\omega_{2c}}{\omega}\right)^2 \eta \right] B_1 + \left[\left(\frac{\omega_{2c}}{\omega}\right)^2 \eta - \frac{2E_3}{E_2} \omega_{1c}^2 \right] B_2 < 0, \tag{36}$$

and

$$E_2 E_3 < 0. \tag{37}$$

Recalling the generic condition $E_2 E_3 \neq 0$, it should be noted that the solution of the two-dimensional torus and its stability (see (37)) cannot be determined if $E_2 E_3 = 0$. Both the coefficients of B_1 and B_2 in (36), on the other hand, are positive due to condition (37). Thus, at least one of B_1 and B_2 must be negative to satisfy condition (36)—otherwise the family of two-dimensional tori is unstable. Of course, the existence conditions for the family of two-dimensionl tori have to be considered. These conditions can be determined readily from Eq. (29) by requiring $A_y^2 > 0$ and $A_\theta^2 > 0$ so that

Downloaded 03 May 2010 to 171.66.16.247. Redistribution subject to ASME license or copyright; see http://www.asme.org/terms/Terms_Use.cfm

$$\frac{B_1}{E_2}-\frac{2B_2}{E_3}>0 \quad \text{and} \quad \frac{B_2}{E_3}-\frac{2B_1}{E_2}>0. \tag{38}$$

It is not difficult to see that conditions (36) through (38) are compatible. In other words, a region does occur in which stable quasi-periodic solutions, represented by (29), exist.

Condition (36) imples that another stability boundary (see Fig. 2(*b*))

$$C_5: \left[\omega_{1c}^2-2\left(\frac{\omega_{2c}}{\omega}\right)^2\eta\frac{E_3}{E_2}\right]B_1-\left[2\omega_{1c}^2\frac{E_2}{E_3}-\left(\frac{\omega_{2c}}{\omega}\right)^2\eta\right]B_2=0 \tag{39}$$

arises when the quasi-periodic solution becomes unstable and may bifurcate into a three-dimensional torus or chaotic motion. In fact, at the critical boundary defined by (39), the Jacobian (31) has a pair of complex conjugate eigenvalues on the imaginary axis. This phenomenon gives rise to the well-known, classical Hopf bifurcation. Such a bifurcation will create a new amplitude and a third frequency, corresponding to a new family of limit cycles, for the family of two-dimensional tori (29). If this new amplitude is independent of the amplitudes of the two-dimensional torus and the third frequency is well separated from the ω_1 and ω_2 of the two-dimensional torus, the combined motion will lie on an invariant three-dimensional torus. However, the critical boundary, C_5, should be shown to be located in the region where the quasi-periodic solution (29) exists.

For simplicity, let

$$S=\frac{E_3}{E_2}. \tag{40}$$

The S must be negative for the existence of the stable family of two-dimensional tori (29) due to condition (37). With this constraint placed on S, the region defined by (38) can be rewritten as either

$$\mathfrak{R}_1=\begin{cases}B_2-2SB_1>0\\ B_2-\dfrac{S}{2}B_1<0\end{cases} \quad (\text{for } E_3>0), \tag{41}$$

or

$$\mathfrak{R}_2=\begin{cases}B_2-2SB_1<0\\ B_2-\dfrac{S}{2}B_1>0\end{cases} \quad (\text{for } E_3<0). \tag{42}$$

Equation (39) then takes the form

$$B_2-\frac{\omega_1^2-\left(\dfrac{\omega_{2c}}{\omega}\right)^2\eta(2S)}{\omega_{1c}^2\left(\dfrac{2}{S}\right)-\left(\dfrac{\omega_{2c}}{\omega}\right)^2\eta}B_1=0. \tag{43}$$

Furthermore, it can be shown straightforwardly that

$$2S<\frac{\omega_{1c}^2-\left(\dfrac{\omega_{2c}}{\omega}\right)^2\eta(2S)}{\omega_{1c}^2\left(\dfrac{2}{S}\right)-\left(\dfrac{\omega_{2c}}{\omega}\right)^2\eta}<\frac{1}{2}S \quad \forall\, S<0. \tag{44}$$

Thus, it it easy to verify that C_5 is located in $\mathfrak{R}_1$ for $B_1>0$ and $B_2<0$ whereas C_5 is in $\mathfrak{R}_2$ for $B_1<0$ and $B_2>0$. Therefore it is possible for a stable family of two-dimensional tori to lose stability and bifurcate into a family of three-dimensional tori when the critical boundary C_5 is intersected.

It should be noted from Fig. 2(*a*), which requires $S>0$, that the stable region in this figure is similar to that for the cocentric case (e.g., see Blevins and Iwan, 1974). Also, it is worthy to note that parameter S plays a significant role in determining the system's behavior. No mixed mode exists if $S>0$. When $S<0$, on the other hand, Fig. 2(*b*) suggests that quasi-periodic motions (a mixed mode), which lie on a two-dimensional or even a three-dimensional torus, are possible.

5 Numerical Illustration

The theory has been applied to a 24-Kcm test span of Ontario Hydro having a single "Drake", 795-Mcm conductor (Nigol and Clarke, 1974). The spanwise properties of this transmisison line and a simulated ice accretion are reported by Ip et al. (1991). A procedure to calculate the numerical properties of an equivalent oscillator is also given. By following this procedure, values of the properties appearing in Eqs. (6) and (8) are:

$a_1=261.9478,\ 274.4842;$ $\quad a_3=-34.2889,\ -52.1284,$
$b_1=28.2562,\ 29.8533;$ $\quad b_3=-3.1132,\ -2.9278,$
$\omega_y=1.9312,\ 3.4312;$ $\quad \omega_\theta=15.2413,\ 21.2343,$
$\xi_y=1.0031\times10^{-2},\ 0.5646\times10^{-2};$ $\quad \xi_\theta=0.7936\times10^{-2},\ 1.1393\times10^{-2}$
$\eta_y=0.2312\times10^{-5},\ 0.2323\times10^{-5};$ $\quad \eta_\theta=1.3849\times10^{-5},\ 1.5522\times10^{-5}$
$e_x=0.2823\times10^{-1},\ 0.5099\times10^{-1};$ $\quad U_y=38.9597,\ 20.7119,$
$r_1=0.5293,\ 0.50.$

A parameter's first value corresponds to a limit cycle of a one loop per span oscillation whereas the second is the analogous two loops per span case. The corresponding B_1 and B_2 obtained from Eq. (22) are:

$B_1=755.04,\ 395.90;$ $\quad B_2=-4137.30,\ -4296.16.$

Both these points lie in the fourth quadrant of Fig. 2(*a*).

6 Conclusions

A considerably general and complete study is given, for the first time, of the galloping of an eccentrically iced conductor. It has been found that such a conductor may exhibit more complicated dynamic behavior than that which is possible in the cocentric case. This additional feature is associated with a mixed-mode motion which has two or three characteristic radii corresponding to a two-dimensional or a three-dimensional torus, respectively. Each of the radii is associated with a distinct frequency. If these frequencies are not resonant or, more generally, if the frequencies are irrational with each other, quasi-periodic motions do not repeat a given orbit. In other words, the torus is covered by the quasi-periodic orbits.

From a practical viewpoint, the results presented in this paper, especially the critical boundaries where bifurcations occur, can be used to assess instability trends with respect to a system's parameters. In particular, the effects of eccentricity may be found and the feasibility of vibration control devices like dampers may be assessed.

Acknowledgments

The authors gratefully acknowledge the financial support of the Canadian Electrical Association (CEA Project No. 321 T 672) through the auspices of Manitoba Hydro. Partial support was also received from the Natural Sciences and Engineering Research Council of Canada.

References

Blevins, R. D., 1974, "Flow Induced Vibration," Ph.D. Thesis, California Institute of Technology, Pasadena, Calif.

Blevins, R. D., and Iwan, W. D., 1974, "The Galloping Response of a Two-Degree-of-Freedom System," ASME Journal of Applied Mechanics, Vol. 41, pp. 1113-1118.

Bogoliubov, N. N., and Mitropolsky, Y. A., 1961, *Asymptotic Methods in the Theory of Non-Linear Oscillations*, Hindustan Publishing Corporation, (INDIA), Delhi.

Downloaded 03 May 2010 to 171.66.16.247. Redistribution subject to ASME license or copyright; see http://www.asme.org/terms/Terms_Use.cfm

Den Hartog, J. P., 1932, "Transmission Line Vibration Due to Slit," *Trans. AIEE*, Vol. 51, Part 4, pp. 1074–1086.

Desai, Y. M., Popplewell, N., Shah, A. H., and Chan, J. K., 1989, "Static and Dynamic Behaviour of Mechanical Components Associated with Electrical Transmission Lines—III: Part A—Theoretical Perspective," *Shock and Vib. Dig.*, Vol. 21, pp. 3–8.

Edwards, A. T., and Madeyski, A., 1956, "Progress Report on the Investigation of Galloping of Transmission Line Conductors," *Trans. AIEE*, Vol. 75, pp. 666–686.

Huseyin, K., and Yu, P., 1988, "On Bifurcations into Non-Resonant Quasi-Periodic Motions," *Appl. Math. Modelling*, Vol. 12, pp. 189–201.

Ip, C. Y., Desai, Y. M., Yu, P., Shah, A. H., and Popplewell, N., 1991, "An Oscillator Model for the Galloping of an Electrical Transmission Line," *Proceedings of the 4th International Conference on Recent Advances in Structural Dynamics*, pp. 801–810.

Meirovitch, L., 1971, *Analytical Methods in Vibrations*, Macmillan, New York.

Nigol, O., and Clarke, G. J., 1974, "Conductor Galloping and Control Based on Torsional Mechanism," presented at IEEE Power Engineering Society Meeting, New York.

Richardson, A. S., 1981, "Dynamic Analysis of Lightly Iced Conductor Galloping in Two Degrees of Freedom," *IEEE Proc.*, Vol. 128, Part C, No. 4, pp. 211–218.

Rudin, W., 1987, *Real and Complex Analysis*, 3rd ed., McGraw-Hill, New York.

Slater, J. E., 1969, "Aeroelastic Instability of a Structural Angle Section," Ph.D. Thesis, University of British Columbia, Canada.

APPENDIX

The nonvanishing components of the 4×4 matrix $[D]$ associated with Eq. (15) are given as follows:

$$D_{12}=\omega_{1c},\quad D_{21}=-\omega_{1c}-E_1\omega_{1c}K_1\eta_y U_y^3(a_1+K_1b_1)$$

$$D_{22}=-E_1U_y\omega_{1c}^2\left[2\xi_y+2K_1^2\frac{\omega}{\eta}\xi_\theta-\eta_yU_y(1+K_1r_1)(a_1+K_1b_1)\right],$$

$$D_{23}=-E_1\omega_{1c}\eta_yU_y^3(a_1+K_1b_1),$$

$$D_{24}=-E_1U_y\omega_{1c}\omega_{2c}\left[2K_2\xi_y+2K_1\frac{\omega}{\eta}\xi_\theta-\eta_yU_y(K_2+r_1)(a_1+K_1b_1)\right],$$

$$D_{34}=\omega_{2c},\quad D_{41}=-E_1\frac{\omega_{2c}}{\omega^2}K_1\eta_\theta U_y^3(K_2a_1+b_1),$$

$$D_{42}=-E_1U_y\frac{\omega_{1c}\omega_{2c}}{\omega^2}\left[2K_2\eta\xi_y+2K_1\omega\xi_\theta-\eta_\theta U_y(1+K_1r_1)(K_2a_1+b_1)\right],$$

$$D_{43}=-\omega_{2c}-E_1U_y\frac{\omega_{2c}}{\omega_2}\eta_\theta U_y^3(K_2a_1+b_1),$$

$$D_{44}=-E_1U_y\left(\frac{\omega_{2c}}{\omega}\right)^2\left[2K_2^2\eta\xi_y+2\omega\xi_\theta-\eta_\theta U_y(K_2+r_1)(K_2a_1+b_1)\right]. \quad \text{(A1)}$$

Downloaded 03 May 2010 to 171.66.16.247. Redistribution subject to ASME license or copyright; see http://www.asme.org/terms/Terms_Use.cfm

On the Behavior of Pretwisted Beams With Irregular Cross-Sections

J. B. Kosmatka
Department of Applied Mechanics and Engineering Science, University of California, San Diego, La Jolla, CA 92093
Mem. ASME

An analytical model is developed to study the extension-bending-torsion coupling behavior of an initially twisted elastic beam with an irregular cross-section. The determination of the complete displacement field requires solving a coupled two dimensional boundary value problem in a curvilinear coordinate system for the local deformations in the section plane and warping out of the section plane. The principle of minimum potential energy is applied to a discretized representation of the cross-section (Ritz method) to calculate solutions to this problem. Numerical results illustrate the pronounced effects pretwist, initial twist axis location, and in-plane deformation have on the behavior of solid and single and multi-celled sections, including airfoil sections.

Introduction

The complex behavior of a pretwisted blade can be studied by representing the blade as a general elastic beam with initial or built-in twist. The beam, which is composed of a homogeneous isotropic material, is defined by rotating a cambered airfoil (or an arbitrary) section about an initial twist axis. Generally, this axis is not coincident with the section centroid so that the blade has a helical line of centroids. The internal geometry of the section can be highly irregular, having spars and varying wall thickness. Thus, applying an axial force to the pretwisted blade will produce extension combined with bending and either untwisting or further twisting.

Previous investigators have studied the behavior of pretwisted bars with simple (doubly symmetric) solid cross-sections. Okubo (1951, 1954) derived the governing equations in a two-dimensional elasticity form for the extension-torsion behavior of a bar with initial twist and for spiral (helical) rods. Goodier and Griffin (1969) developed a series solution for the bending of pretwisted bars and showed for thin sections that pretwist significantly reduces the bending stiffness in the stiff plane while the reduction in the flexible plane is negligible. Shield (1982) extended Okubo's (1954) work using a displacement formulation where each section undergoes identical local deformations that includes in-plane distortions and out-of-plane warping. His results for elliptical cross-sections show an extension force will untwist the bar if the initial twist axis and centroidal axis are coincident, but if the initial twist axis and centroid are not coincident, then the bar may either untwist or further twist depending upon the initial twist axis location, cross-section shape, and Poisson's ratio.

In addition to the previous elasticity approaches, numerous technical beam theories have been developed which try to capture this behavior in an approximate manner (initial twist defined about the elastic or centroidal axis, in-plane deformations including Poisson contractions have been neglected). Chu (1951) has shown, analytically and experimentally, that torsional rigidity increases as a result of pretwist. Downs (1979) investigated the effects of pretwist on the torsion and bending stiffness of thin elliptical sections with camber. Other authors (for example: Hodges, 1980; Krenk, 1983; Rosen, 1980, 1983) have developed models that illustrate the fundamental characteristics (increased torsional stiffness and extension-torsion coupling) using a curvilinear coordinate system, the Saint-Venant torsion warping function, and a variational approach.

The objective of this paper is to develop an analytical model to study the elastic behavior of a helical beam with an arbitrary cross-section. This model has direct applications to rotating blades where the section has an irregular outer definition and a complex internal structure. Displacement solutions are written in terms of derivable functions that represent extension, bending, and twisting and general functions for the local deformations in the section plane and out-of-plane warping. These general functions, which depend upon the section planform, Poisson's ratio, pretwist level, and initial twist axis location, are determined by solving a coupled two-dimensional boundary value problem. Solutions are calculated by applying the principle of minimum potential energy to a discretized representation of the cross-section (Ritz method). The extension-bend-twist coupling effects and the pretwist dependent section stiffness are calculated by making use of the section equations of equilibrium.

The use of the Ritz method to determine the coupled in-plane and out-of-plane section deformations for a helical beam with an arbitrary cross-section is believed to be unique and

Contributed by the Applied Mechanics Division of THE AMERICAN SOCIETY OF MECHANICAL ENGINEERS for publication in the JOURNAL OF APPLIED MECHANICS.

Discussion on this paper should be addressed to the Technical Editor, Prof. Leon M. Keer, The Technological Institute, Northwestern University, Evanston, IL 60208, and will be accepted until two months after final publication of the paper itself in the JOURNAL OF APPLIED MECHANICS. Manuscript received by the ASME Applied Mechanics Division, Sept. 15, 1989; final revision, Apr. 30, 1990.

Copyright © 1992 by ASME
Downloaded 03 May 2010 to 171.66.16.247. Redistribution subject to ASME license or copyright; see http://www.asme.org/terms/Terms_Use.cfm

has not previously appeared in the literature. The current model will be useful to analysts of highly pretwisted blades, who must understand the behavior of the blade in order to assess its performance capabilities. For example, extension-blade-twist coupling could be specifically designed into variable speed rotors (for example, tilt rotors) so that the blade deforms into the optimum aerodynamic shape for a given operating condition (hover, cruise) by simply changing the rotor speed (centrifugal force distribution). Numerical results are presented that validate this model and illustrate the pronounced effects pretwist and initial twist axis location have on the behavior of solid and single and multi-cell sections (NACA-0012) airfoils.

Theoretical Derivation

Consider a long elastic bar of length l where the shape is defined by rotating a uniform cross-section about an initial twist axis (z-axis). (See Fig. 1.) The line of centroids can be, in general, a helix, since it is not required to be coincident with the initial twist axis. A space-fixed orthonormal vector set (x, y, z) and a curvilinear coordinate system (ξ, η, z) are used to define and analyze the bar where ξ and η align with the x and y axes at the bar root ($z=0$), but rotate with the section about the initial twist axis. Displacements in the curvilinear system are defined as (u, v, w), respectively. The two systems are related using

$$\begin{Bmatrix} \xi \\ \eta \end{Bmatrix} = \begin{bmatrix} \cos(\alpha z) & \sin(\alpha z) \\ -\sin(\alpha z) & \cos(\alpha z) \end{bmatrix} \begin{Bmatrix} x \\ y \end{Bmatrix}, \tag{1}$$

where α is the initial twist per unit length. The lateral surface of the bar is defined by an equation of the form

$$f(\xi, \eta) = 0. \tag{2}$$

The following relations between the (x, y, z) set and the (ξ, η, z) system hold

$$\begin{aligned} \xi_{,z} &= \alpha\eta, \\ \eta_{,z} &= -\alpha\xi, \\ z_{,\xi} &= z_{,\eta} = 0. \end{aligned} \tag{3a-c}$$

A linear elastic isotropic material is used that obeys Hooke's law

$$\{\sigma\} = [C]\{\epsilon\}, \tag{4a}$$

where $[C]$ is the material stiffness defined by

$$\begin{aligned} C_{11} &= C_{22} = C_{33} = (\lambda + 2\mu), \\ C_{12} &= C_{13} = C_{23} = \lambda, \\ C_{44} &= C_{55} = C_{66} = \mu, \end{aligned} \tag{4b}$$

the stress and strain vectors are given as

$$\{\sigma\}^T = \{\sigma_{\xi\xi}, \sigma_{\eta\eta}, \sigma_{zz}, \tau_{\eta z}, \tau_{\xi z}, \tau_{\xi\eta}\} \tag{4c}$$

$$\{\epsilon\}^T = \{\epsilon_{\xi\xi}, \epsilon_{\eta\eta}, \epsilon_{zz}, \gamma_{\eta z}, \gamma_{\xi z}, \gamma_{\xi\eta}\}, \tag{4d}$$

and λ and μ are Lame's constants.

The applied stress distribution on the ends of the bar ($z=0$, l) is statically equivalent to an applied extensional force P that acts along the initial twist axis and a couple with components M_x, M_y, and M_z about the x, y, and z axes, respectively. The ends of the bar are free to warp so that the twist is uniform along the length. Assuming that the body forces are negligible in comparison to the applied stress distribution, the stress equations of equilibrium can be written in the curvilinear system as

$$\sigma_{\xi\xi,\xi} + \tau_{\xi\eta,\eta} + \tau_{\xi z,z} + \alpha D\,\tau_{\xi z} - \alpha\tau_{\eta z} = 0, \tag{5a}$$

$$\tau_{\xi\eta,\xi} + \sigma_{\eta\eta,\eta} + \tau_{\eta z,z} + \alpha D\,\tau_{\eta z} + \alpha\tau_{\xi z} = 0, \tag{5b}$$

$$\tau_{\xi z,\xi} + \tau_{\eta z,\eta} + \sigma_{zz,z} + \alpha D\,\sigma_{zz} = 0, \tag{5c}$$

where the symbol D is an operator defined as

$$D = \eta\frac{\partial}{\partial\xi} - \xi\frac{\partial}{\partial\eta}. \tag{6}$$

The boundary conditions include a stress-free lateral surface given by

$$(\sigma_{\xi\xi} + \alpha\eta\tau_{\xi z})n_\xi + (\tau_{\xi\eta} - \alpha\xi\tau_{\xi z})n_\eta = 0, \tag{7a}$$

$$(\tau_{\xi\eta} + \alpha\eta\tau_{\eta z})n_\xi + (\sigma_{\eta\eta} - \alpha\xi\tau_{\eta z})n_\eta = 0, \tag{7b}$$

$$(\tau_{\xi z} + \alpha\eta\sigma_{zz})n_\xi + (\tau_{\eta z} - \alpha\xi\sigma_{zz})n_\eta = 0, \tag{7c}$$

where n_ξ and n_η are equal to $f_{,\xi}$ and $f_{,\eta}$, respectively. The stresses within the cross-section must satisfy the following equations of equilibrium:

$$\begin{aligned} \int_A \sigma_{zz}dA &= P, & \int_A \eta\sigma_{zz}dA &= M_\xi, \\ \int_A (\xi\tau_{\eta z} - \eta\tau_{\xi z})dA &= M_z, & \int_A \xi\sigma_{zz}dA &= -M_\eta, \end{aligned} \tag{8a-d}$$

where A is the cross-sectional area of the bar and M_ξ and M_η are the components of the applied couple about the ξ and η axes, respectively. The displacement distributions are given as

$$u = -\theta\eta z - \frac{\kappa_\xi}{\alpha^2}\{1 - \cos(\alpha z) - (\alpha z)\sin(\alpha z)\} + \frac{\kappa_\eta}{\alpha^2}\{(\alpha z)\cos(\alpha z) - \sin(\alpha z)\} + \psi_\xi, \tag{9a}$$

$$v = \theta\xi z + \frac{\kappa_\eta}{\alpha^2}\{1 - \cos(\alpha z) - (\alpha z)\sin(\alpha z)\} + \frac{\kappa_\xi}{\alpha^2}\{(\alpha z)\cos(\alpha z) - \sin(\alpha z)\} + \psi_\eta, \tag{9b}$$

$$w = ez + \frac{\kappa_\xi}{\alpha}\{\eta\{1 - \cos(\alpha z)\} - \xi\sin(\alpha z)\} + \frac{\kappa_\eta}{\alpha}\{\xi(1 - \cos(\alpha z)\} + \eta\sin(\alpha z)\} + \psi_z, \tag{9c}$$

where, e, θ, κ_ξ, and κ_η represent the extension, the elastic twist per unit length, and the bending curvatures of the bar in the ξ-z and $\eta - z$ planes, respectively, ψ_ξ and ψ_η are local deformations in the section plane (including Poisson contractions), and ψ_z describes out-of-plane warping. ψ_ξ, ψ_η, and ψ_z are dependent upon ξ and η only. The approximate bending relations were selected so that: (1) the axial strain component ϵ_{zz} is periodic in αz, (2) the remaining strains are independent of z, and (3) in the limiting case as αz approaches zero (untwisted bar), the strain field reduces to uniform bending. The extension and torsion terms of (9a–c) agree with Shield (1982) except for the Poisson contractions which are implicitly defined in the current model and the bending terms agree with the terms of the power series developed by Goodier and Griffin (1969).

The strain components in the ξ, η, z system are found using the above displacement relations (9a–c)

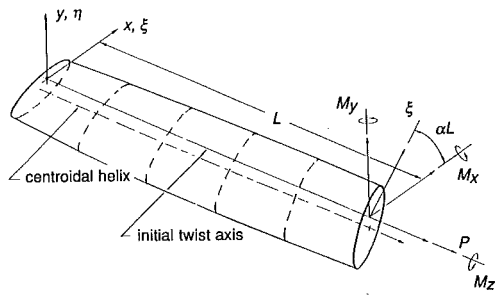

Fig. 1 Initially twisted elastic beam with spaced-fixed (x, y, z) and curvilinear (ξ, η, z) coordinate systems and applied extension (P), bending (M_x, M_y) and torsion (M_z) loads

Downloaded 03 May 2010 to 171.66.16.247. Redistribution subject to ASME license or copyright; see http://www.asme.org/terms/Terms_Use.cfm

$$\epsilon_{\xi\xi} = \psi_{\xi,\xi} \quad \epsilon_{\eta\eta} = \psi_{\eta,\eta},$$

$$\epsilon_{zz} = \underline{e + \eta\kappa_\eta - \xi\kappa_\xi + \alpha D\psi_z},$$

$$\gamma_{\eta z} = \underline{\theta\xi + \psi_{z,\eta}} + \alpha(\psi_\xi + D\psi_\eta),$$

$$\gamma_{\xi z} = \underline{-\theta\eta + \psi_{z,\xi}} - \alpha(\psi_\eta - D\psi_\xi),$$

$$\gamma_{\xi\eta} = \psi_{\xi,\eta} + \psi_{\eta,\xi}. \qquad (10a\text{–}f)$$

Technical beam theories for pretwisted bars are developed using only the underlined terms in (10*a–f*) and a Saint-Venant torsion function for ψ_z.

The total potential energy of the system is given as

$$\Pi = \frac{1}{2}\int_0^l \int_A \{\sigma\}^T\{\epsilon\}\,dA\,dz - PLe - M_z l\theta - \frac{1}{\alpha}\{M_\eta\kappa_\xi + M_\xi\kappa_\eta\}\sin(\alpha L) - \frac{1}{\alpha}\{M_\xi\kappa_\xi - M_\eta\kappa_\eta\}(1-\cos(\alpha L)). \qquad (11)$$

Substituting (4) and (10) into (11) results in

$$\Pi = \frac{1}{2}\int_0^l \int_A \lambda\{\psi_{\xi,\xi} + \psi_{\eta,\eta} + \{e + \eta\kappa_\eta - \xi\kappa_\xi + \alpha D\psi_z\}\}^2 + \mu\{\theta\xi + \psi_{z,\eta} + \alpha\{\psi_\xi + D\psi_\eta\}\}^2 + \mu\{-\theta\eta + \psi_{z,\xi} - \alpha\{\psi_\eta - D\psi_\xi\}\}^2 + 2\mu\{\psi_{\xi,\xi}^2 + \psi_{\eta,\eta}^2 + \{e + \eta\kappa_\eta - \xi\kappa_\xi + \alpha D\psi_z\}^2\} + \mu\{\psi_{\xi,\eta} + \psi_{\eta,\xi}\}^2 dA\,dz - Ple - M_z l\theta - \frac{1}{\alpha}\{M_\eta\kappa_\xi + M_\xi\kappa_\eta\}\sin(\alpha L) - \frac{1}{\alpha}\{M_\xi\kappa_\xi - M_\eta\kappa_\eta\}(1-\cos(\alpha L)) \qquad (12)$$

where the correct solutions for ψ_ξ, ψ_η, and ψ_z are admissible functions that minimize the total potential energy for a given set of applied loads.

The pretwist dependent section stiffnesses and coupling effects can be studied by making use of the section equations of equilibrium (Eq. (8*a–d*), where the stresses (including ψ_ξ, ψ_η, and ψ_z) are defined in terms of an applied extension (e), bending curvatures (κ_ξ, κ_η), and twist rate (θ). Thus,

$$\begin{bmatrix} k_{11} & k_{12} & k_{13} & k_{14} \\ k_{21} & k_{22} & k_{23} & k_{24} \\ k_{31} & k_{32} & k_{33} & k_{34} \\ k_{41} & k_{42} & k_{43} & k_{44} \end{bmatrix} \begin{Bmatrix} e \\ \kappa_\xi \\ \kappa_\eta \\ \theta \end{Bmatrix} = \begin{Bmatrix} P \\ M_\eta \\ M_\xi \\ M_z \end{Bmatrix} \qquad (13)$$

where the matrix $[k]$ is symmetric based upon reciprocity. For an untwisted bar, the twist is independent of extension and bending ($k_{14} = k_{24} = k_{34} = 0$), the diagonal terms equal the nominal extensional stiffness ($k_{11} = EA_o$), bending stiffness ($k_{22} = EI_{\eta\eta o}$, $k_{33} = EI_{\xi\xi o}$), and torsion stiffness ($k_{44} = GJ_o$). The remaining off-diagonal terms, which couple extension and bending, are the first and second moments of inertia that result when the local axes (ξ, η) are not coincident with the principal axes of the section ($k_{13} = EA_{\eta o}$, $k_{12} = -EA_{\xi o}$, $k_{23} = -EI_{\xi\eta o}$). These last three terms can be used to locate the centroid and principal axes of the section. Equation (13) is used to study the behavior of "constrained" pretwisted beams. For example, to place a pretwisted bar in pure twist with no extension of bending ($\theta \neq 0$, $e = \kappa_\xi = \kappa_\eta = 0$), one must apply an axial force and a general couple with bending moment components that satisfy

$$\frac{P}{M_z} = \frac{k_{14}}{k_{44}}, \quad \frac{M_\xi}{M_z} = \frac{k_{34}}{k_{44}}, \quad \frac{M_\eta}{M_z} = \frac{k_{24}}{k_{44}}. \qquad (14a\text{–}c)$$

Positive (negative) ratios of (14*a*) are associated with the application of an extension force to keep the bar from contracting (extending), whereas nonzero terms of (14*b*,*c*) signify that the general couple is acting about a vector that is skew (not perpendicular) to the cross-section. Multiplying (13) by the inverse of $[k]$, results in a flexibility relationship that can be used to study the behavior of "unconstrained" pretwisted beams. For example, applying an axial force (P) produces extension as well as bending and twisting that satisfies the following ratios

$$\frac{\kappa_\xi}{e} = \frac{a_{21}}{a_{11}}, \quad \frac{\kappa_\eta}{e} = \frac{a_{31}}{a_{11}}, \quad \frac{\theta}{e} = \frac{a_{41}}{a_{11}}, \qquad (15a\text{–}c)$$

where a_{ij} are the components of the flexibility matrix $[a]\,(=[k]^{-1})$. The extension-bending coupling ratios (15*a*,*b*) are associated with the axial force not acting through the centroid. Similarly, applying a torsion moment (M_z) results in extension, bending, and twisting ratios of the form

$$\frac{e}{\theta} = \frac{a_{14}}{a_{44}}, \quad \frac{\kappa_\xi}{\theta} = \frac{a_{24}}{a_{44}}, \quad \frac{\kappa_\eta}{\theta} = \frac{a_{34}}{a_{44}}. \qquad (16a\text{–}c)$$

Negative (or positive) ratios of (15*c*) and (16*a*) correspond to untwisting (or further twisting) of the beam as a result of an applied extension, and contraction (or extension) from an applied twist moment, respectively.

Method of Solution

Solutions for the local cross-section deformations (ψ_ξ, ψ_η, ψ_z) exist for simple (doubly symmetric) solid cross-sections (see Shield, 1982). For an irregular section, the determination of a solution can, in general, be intractable. Alternatively, approximate solutions for irregular cross-sections can be calculated by casting the problem as an extremum problem, based upon the principle of minimum potential energy, and solving for the local deformation field that produces a relative minimum value of the total potential energy (12). This is an application of the Ritz method were the trial function family is the displacement field associated with a finite element based representation of the cross-section.

The cross-section of the bar is approximated with quadrilateral subregions where ψ_ξ, ψ_η, and ψ_z are represented within each subregion using an isoparametric formulation with biquadratic interpolation functions. These functions were selected over the computationally simpler bi-linear functions because of their improved convergence characteristics and their ability to model curved boundaries. Within the ith subregion, the displacement functions for ψ_ξ, ψ_η, and ψ_z can be written as

$$\psi_\xi = [N(\xi,\eta)]\{\Psi_{\xi_i}\}, \quad \psi_\eta = [N(\xi,\eta)]\{\Psi_{\eta_i}\}, \quad \psi_z = [N(\xi,\eta)]\{\Psi_{z_i}\}, \qquad (17a\text{–}c)$$

where $[N(\xi,\eta)]$ is the interpolation function and $\{\Psi_{\xi_i}\}$, $\{\Psi_{\eta_i}\}$, and $\{\Psi_{z_i}\}$ are nodal displacements on the ith subregion boundary in the ξ, η, and z directions, respectively.

The total potential energy of the bar (11) can be written as

$$\Pi = \sum_{i=1}^{n} U_i - Ple - M_z l\theta - \frac{1}{\alpha}\{M_\eta\kappa_\xi + M_\xi\kappa_\eta\}\sin(\alpha L) - \frac{1}{\alpha}\{M_\xi\kappa_\xi - M_\eta\kappa_\eta\}(1-\cos(\alpha L)) \qquad (18)$$

where n is the number of subregions and U_i is the strain energy of the ith subregion given by

$$U_i = \frac{1}{2}\int_0^L \int_{A_i} \{\epsilon_i\}^T[C]\{\epsilon_i\}\,dA_i\,dz. \qquad (19)$$

Here, $\{\epsilon_i\}$ are the strain components in the ith subregion (4*d*), $[C]$ is the material stiffness matrix (4*b*), and A_i is the area of the ith subregion. Substituting (4), (10), (17), and (19) into (18), performing the appropriate integration, and setting the variation of Π with respect to $\{\{\psi_\xi\}, \{\psi_\eta\}, \{\psi_z\}\}$ equal to zero will result in following set of linear algebraic equations

Downloaded 03 May 2010 to 171.66.16.247. Redistribution subject to ASME license or copyright; see http://www.asme.org/terms/Terms_Use.cfm

$$\sum_{i=1}^{n} [K_i]\{\Psi_i\} + [F_i]\{b\} = \{0\} \tag{20}$$

where the ith stiffness, force, and displacement arrays are defined as

$$[K_i] = \int_{A_i} [B_i]^T [C][B_i] dA_i, \tag{21a}$$

$$[F_i] = \int_{A_i} [B_i]^T [C][f_i] dA_i, \tag{21b}$$

$$\{\Psi_i\}^T = \{\{\Psi_{\xi_i}\}, \{\Psi_{\eta_i}\}, \{\Psi_{z_i}\}\} \tag{21c}$$

$$\{b\}^T = \{e, \kappa_\xi, \kappa_\eta, \theta\} \tag{21d}$$

$$[B_i] = \begin{bmatrix} N(\xi,\eta),_\xi & 0 & 0 \\ 0 & N(\xi,\eta),_\eta & 0 \\ 0 & 0 & \alpha DN(\xi,\eta) \\ \alpha N(\xi,\eta) & \alpha DN(\xi,\eta) & N(\xi,\eta),_\eta \\ \alpha DN(\xi,\eta) & -\alpha N(\xi,\eta) & N(\xi,\eta),_\xi \\ N(\xi,\eta),_\eta & N(\xi,\eta),_\xi & 0 \end{bmatrix} \tag{21e}$$

and

$$[f_i]^T = \begin{bmatrix} 0 & 0 & 1 & 0 & 0 & 0 \\ 0 & 0 & -\xi & 0 & 0 & 0 \\ 0 & 0 & \eta & 0 & 0 & 0 \\ 0 & 0 & 0 & \xi & -\eta & 0 \end{bmatrix}. \tag{21f}$$

The matrix equations (18) are assembled into a complete model of a cross-section using standard finite element procedures. A set of "unit" cross-sectional deformation functions (ψ_ξ, ψ_η, ψ_z) can be calculated for each of the four cases (e, θ, κ_ξ, κ_η) by setting the appropriate value to unity and the remaining three to zero. Displacement and stress distributions defined in terms of the four cases (e, θ, κ_ξ, κ_η) are determined by substituting the calculated deformation functions into (9), (10), and (4a), respectively. The stiffness relationships of Eq. (13) is calculated numerically using Gaussian quadrature where the stresses are evaluated at the element Gauss points. Finally, the displacement and stress distributions defined in terms of the applied loads (P, M_ξ, M_η, M_z) are calculated by, first, solving for (e, θ, κ_ξ, κ_η) in terms of the applied loads (i.e., take inverse of Eq. (13)), and then substituting this flexibility relation into (9) and (4a), respectively.

A two-dimensional finite element computer program was written where the cross-section is discretized using 8-node quadrilateral isoparametric elements (24 degrees-of-freedom/element). The cross-section is defined in a local system (ξ_e, η_e) that can be arbitrarily positioned relative to the curvilinear reference frame (ξ, η, z) using offsets (ξ_a, η_a) (see Fig. 2).

Results and Discussion

Two sets of numerical results are presented. First, the current approach is verified using previously published results for pretwisted bars with centered and off-centered elliptical sections. The second set involves studying the extension-torsion coupling behavior of a NACA-0012 airfoil for a variety of cross-section definitions (solid, single and multi-cell), pretwist levels, and initial twist axis locations.

Verification Studies. A pretwisted elastic bar having a thin elliptical cross-section with semi-axes a,b ($a/b = 10$) and material properties given by $E = 1.0$ and $\nu = .30$ was analyzed. The cross-section is defined in a local system (ξ_e, η_e) offset from the initial twist axis (ξ_a, η_a) and modeled using 180 elements (see Fig. 2). The calculated section deformation distributions (ψ_ξ, ψ_η, ψ_z) for an untwisted bar ($\alpha = 0$) subjected to the four cases (e, κ_ξ, κ_η, θ) are presented in Fig. 3. The first three loadings

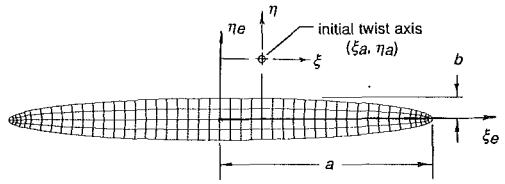

Fig. 2 Thin elliptical section ($a/b = 10$) defined in a local system (ξ_e, η_e) offset from the initial twist axis by an amount (ξ_a, η_a)

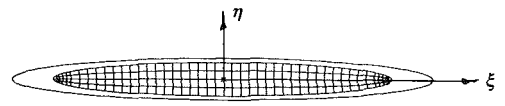

a.) Poisson-type contractions for applied extension ($\psi z = 0$).

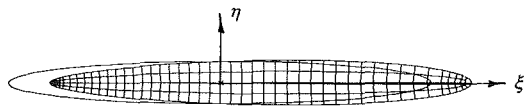

b.) Anticlastic surface for uniform bending about the η axis ($\psi z = 0$).

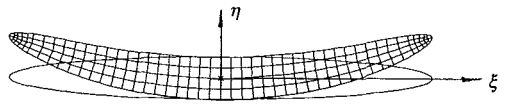

c.) Anticlastic surface for uniform bending about the ξ axis ($\psi z = 0$).

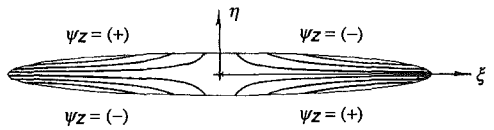

d.) Torsion-type warping for applied twist rotation ($\psi\xi = \psi\eta = 0$).

Fig. 3 Cross-section deformation distributions (ψ_ξ, ψ_η, ψ_z) for an untwisted elliptical beam subjected to a unit extension, curvature, and twist

produce deformations in the section plane that are characterized by extension produced Poisson contractions (see Fig. 3a), an anticlastic surface associated with uniform bending ($\kappa\xi$) where σ_{zz} is in tension on the $-\xi$ side and in compression on the $+\xi$ side (Fig. 3(c)), and an anticlastic surface from uniform bending (κ_η) with the upper side in tension and the lower in compression (Fig. 3(b)). Applying a unit twist (θ) produces torsion-type warping only (contour lines are presented in Fig. 3(d)). All four solutions are in exact agreement with Love (1944). In addition, the untwisted torsion stiffness was calculated ($GJ_o = .01194a^4$) using the current torsion warping solution along with (8d) and the result was within .2 percent of the closed-form solution (Love, 1944).

For centered pretwisted bars ($\xi_a = \eta_a = 0$), the local section deformation due to extension or twist describes a complex surface composed of Poisson-type contraction (ψ_ξ, ψ_η) coupled with out-of-plane warping (ψ_z). For off-centered pretwisted bars (helical bars with ξ_a, $\eta_a \neq 0$), the local section deformation is composed of in-plane deformations (ψ_ξ, ψ_η) decribed by Poisson contractions combined with an anticlastic surface coupled to out-of-plane warping (ψ_z).

The variation in section stiffnesses and extension-torsion couplings as a function of pretwist level ($2\alpha a$) for a centered elliptical bar ($\xi_a = \eta_a = 0$) are presented in Figs. 4 through 6, where EA, $EI_{\eta\eta}$, $EI_{\xi\xi}$ and GJ are equal to $1/a_{11}$, $1/a_{22}$, $1/a_{33}$, and $1/a_{44}$, respectively. Negative values of the ratios θ/e ($= a_{41}/a_{11}$) and e/θ ($= a_{14}/a_{44}$) are associated with bar untwist for

Downloaded 03 May 2010 to 171.66.16.247. Redistribution subject to ASME license or copyright; see http://www.asme.org/terms/Terms_Use.cfm

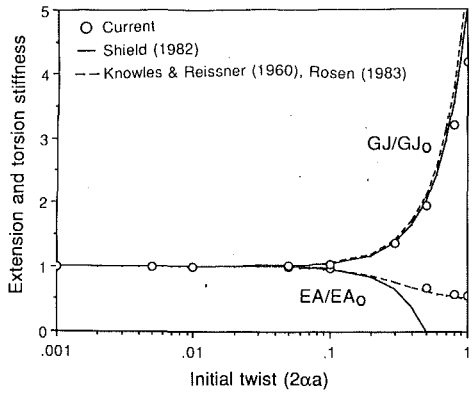

Fig. 4 Extension and torsion stiffness of a pretwisted elliptical bar ($\xi_a = \eta_a = 0$)

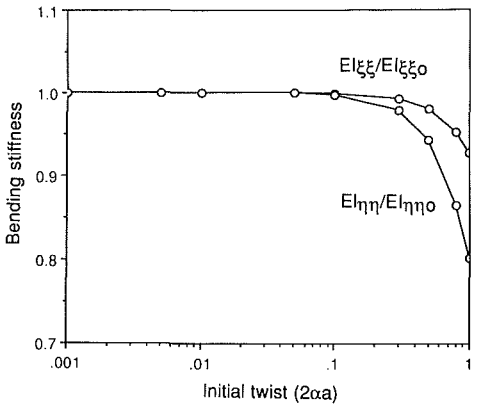

Fig. 5 Bending stiffnesses of a pretwisted elliptical bar ($\xi_a = \eta_a = 0$)

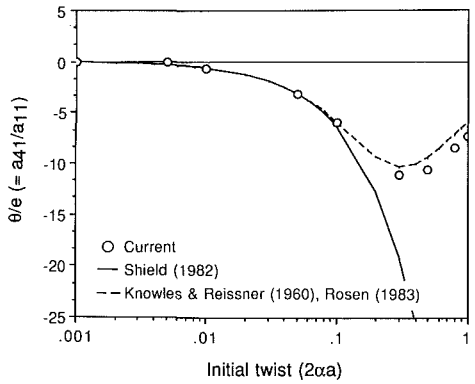

Fig. 6 Extension-torsion coupling of a pretwisted elliptical bar ($\xi_a = \eta_a = 0$)

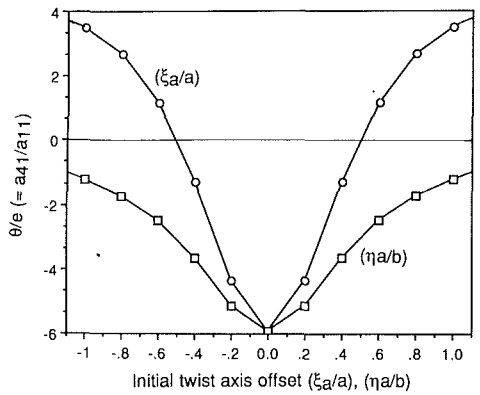

Fig. 7 Extension-torsion coupling of a helical elliptical bar ($2\alpha a = .100$) with the initial twist axis offset along the major axis (ξ_a/a) or the minor axis (η_a/b)

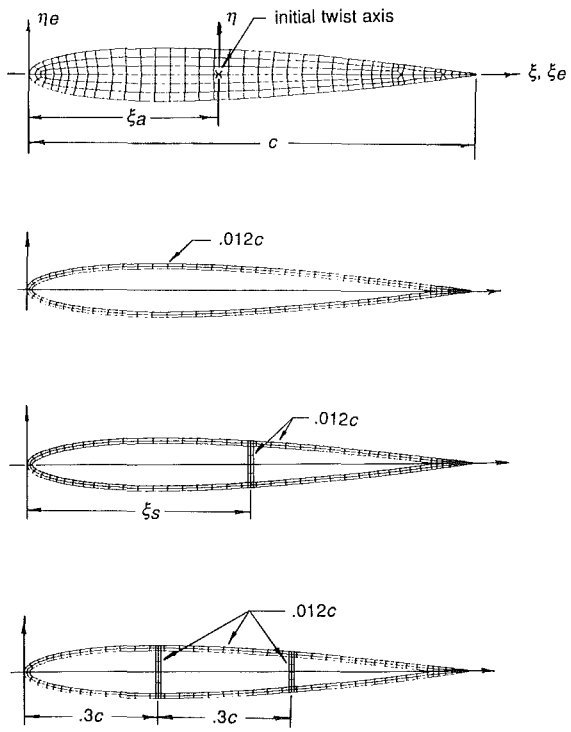

Fig. 8 Discretization of four sections (NACA-0012 airfoils) with the wall and spar thickness equal to 0.12c; (*a*) solid section, (*b*) single-cell, (*c*) double-cell, and (*d*) triple-cell

applied extension (P) and bar contraction of applied torsion (M_t), respectively, where the maximum a_{41}/a_{11} coupling occurs with $\alpha = .30$. The current extension-torsion results (Figs. 4 and 6) are in excellent agreement with Shield (1982), Knowles and Reissner (1960), and Rosen (1983) for low pretwist levels ($\alpha < .1$). Small discrepancies with Knowles and Reissner (1960) and Rosen (1983) are associated with their use of a thin rectangular section and neglecting in-plane deformations. The divergence of the extensional stiffness from Shield's (1982) results above $\alpha > 1$ can be traced to the ordering scheme used for α. The bending stiffness reductions (Fig. 5) in the stiff plane ($EI_{\eta\eta}$) are less than those predicted by Goodier and Griffin (1969), but are better than Downs predictions (1979). The discrepancy with Goodier and Griffin's results (1969) occurs because the current model contains only the fundamental terms of the power series solution.

The variation in the extension-torsion coupling (a_{41}/a_{11}) of a helical beam ($2\alpha a = .100$) as a function of the elliptical section offset from the initial twist axis was studied (Fig. 7). As the initial twist axis is offset from the section centroid along the major axis (ξ), the coupling changes sign from negative to positive, thus the bar undergoes further twisting instead of untwisting for applied extension (P). The critical location for zero coupling is $\xi_a/a = .506$, which is in agreement with previous predictions of $\xi_a/a = .500$, for thin elliptical sections (Shield, 1982) and $\xi_a/a = 1/\sqrt{3}$ for thin rectangular sections (Reissner and Wan, 1968). Movement of the initial twist axis along the minor axis (η) results in a gradual decrease in coupling that approaches zero for $\eta_a \gg b$.

Airfoil Sections. Four pretwisted rotating blades were analyzed where the outer planform is a NACA-0012 airfoil section and internal section geometries include: (a) solid section having 210 elements, (b) a single-cell section with 160 elements, (c) a double-cell section having 180 elements, and (d) a triple-cell

Downloaded 03 May 2010 to 171.66.16.247. Redistribution subject to ASME license or copyright; see http://www.asme.org/terms/Terms_Use.cfm

Table 1 Section properties of untwisted NACA-0012 airfoils ($E=1$, $\nu=.333$). All wall and spar thicknesses are equal to 0.12c.

		Current Solutions					Thin-Wall Estimate (Love)
Type	Spar ξ_s/c	Centroid ξ_o/c	EA_o/c^2 (10^{-3})	$EI_{\xi\xi_o}/c^4$ (10^{-5})	$EI_{\eta\eta_o}/c^4$ (10^{-3})	GJ_o/c^4 (10^{-5})	GJ_o/c^4 (10^{-5})
Solid	-	0.4206	82.15	6.796	4.533	9.97	-
1-cell	-	0.4802	23.37	3.694	1.839	4.75	4.58
2-cell	.50	0.4810	24.35	3.747	1.836	4.97	4.88
3-cell	.30,.60	0.4758	25.33	3.811	1.884	5.08	5.01

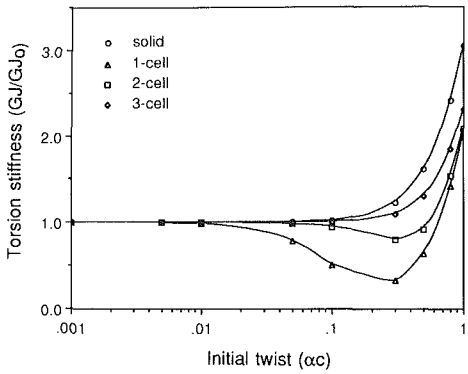

Fig. 9 Torsional stiffness of pretwisted NACA-0012 airfoil sections with the initial twist axis located at the section centroid

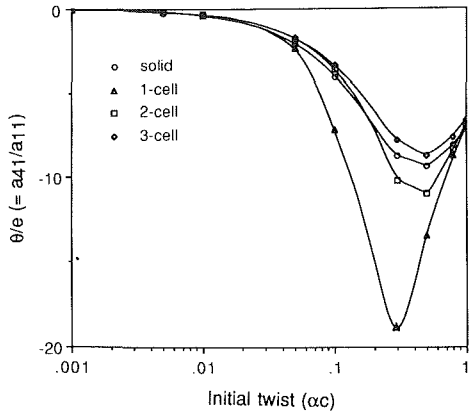

Fig. 10 Extension-torsion coupling of pretwisted NACA-0012 airfoils with the initial twist axis located at the section centroid

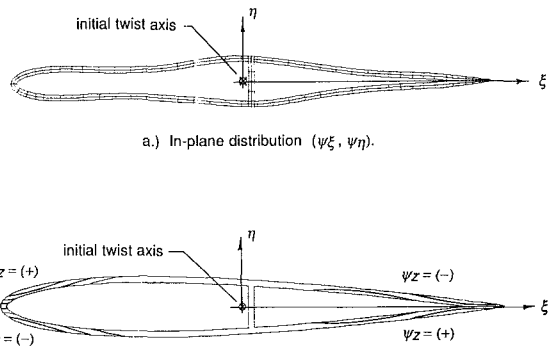

Fig. 11 Cross-section deformation of a pretwisted 2-cell NACA-0012 airfoil section ($\alpha c=.30$, $\xi_s=.5c$) subjected to an applied twist (θ). Initial twist axis is at section centroid.

section with 200 elements. The discretization of the four sections is presented in Fig. 8, where c is the chord, ξ_a is the distance from the leading edge to the initial twist axis location, ξ_s is the spar location for the double-cell section ($\xi_s=.50c$ unless otherwise stated), and all wall/spar thicknesses are equal to 10 percent of the maximum airfoil thickness. The material properties are $E=1.0$ and $\nu=.333$. The airfoil section properties without pretwist are presented in Table 1, where the current value of GJ_o are slightly higher than the thin-wall approximation (Love, 1944) because the current approach accounts for nonuniform shear stress over the wall thickness and the increasing effective wall thickness at the trailing edge.

The variation of the torsional stiffness and extension-torsion coupling (a_{41}/a_{11}) as a function of initial twist (αc) with the initial twist axis coincident with the centroidal axis are presented in Figs. 9 and 10, respectively. This range of initial twist encompasses most rotor blade applications from helicopters and wind turbines (0.005–0.01) to aviation propellers and tilt-rotors (0.1–0.3) to ducted turbofans (0.2–0.5). Overall, the trends are similar to those of the elliptical sections (Figs. 4 and 6). However, the influence of pretwist is strongest in thin-walled sections, where the torsional stiffness is single and double-cell sections decreases for moderate pretwist levels before increasing for high pretwist levels. This reduction in torsional stiffness (instead of the expected increase) in the single and double-cell sections can be understood by observing that the application of a unit twist can produce measurable deformations in the section plane that reduce the section profile in addition to the torsion-type warping (Fig. 11).

The variation in the extension-torsion coupling as a function of initial twist axis location along the chord (ξ_a/c) for four propeller or tilt-rotor blades ($\alpha c=.30$) was studied (Fig. 12). Locating the initial twist axis close to the centroidal axis will maximize the negative extension-torsion coupling, thus producing large blade untwisting from applied extension (centrifugal) force. Negligible extension-torsion coupling can be produced by locating the initial twist near the quarter or three-quarter chord positions for these initial twist axis outside of this region will result in positive coupling that produce further blade twisting from an applied extension. Thus, rotor blade analysts must know the position of the centroid relative to the initial twist in order to fully understand the extension-torsion coupling behavior.

The effects of varying the spar location ($.2c<\xi_s<.6c$) on the couplings of a double-cell airfoil with fixed pretwist parameters ($\alpha c=.30$, $\xi_a=.25c$) was investigated. In order to produce a significant movement in the centroid location (ξ_c/c), the material stiffness of the spar was defined to be ten times greater than the wall stiffness ($E_s/E_w=10.0$). The variations in the centroid location and extension-torsion coupling are presented in Fig. 13 where two spar locations exist that result in zero extension-torsion coupling ($\xi_s=0.32c$, $0.51c$). Locating the spar near the leading edge positions the centroid near the initial twist axis, and produces measurable negative extension-torsion couplings. Locating the spar near the center of the airfoil moves the centroid away from the initial twist axis, thus producing positive coupling. Finally, locating the spar near the aft portion of the airfoil results in a negative coupling.

Conclusions

An analytical model for studying the behavior of pretwisted bars having irregular cross-sections has been presented. The solutions are developed using functions which represent the general behavior of the bar and functions characterizing the local section deformation that are determined using the principle of minimum potential energy along with a discretized representation of the cross-section (Ritz method). The local

Downloaded 03 May 2010 to 171.66.16.247. Redistribution subject to ASME license or copyright; see http://www.asme.org/terms/Terms_Use.cfm

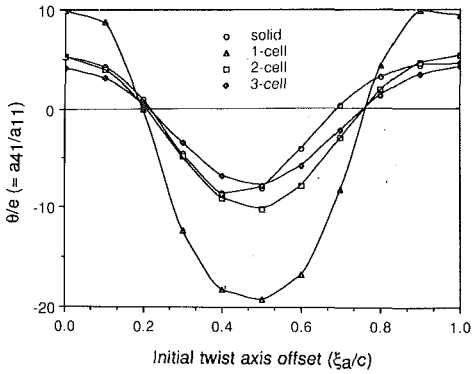

Fig. 12 Extension-torsion coupling of a NACA-0012 airfoil section ($\alpha c = .30$) with initial twist axis offset along the chord-wise axis (ξ_a/c)

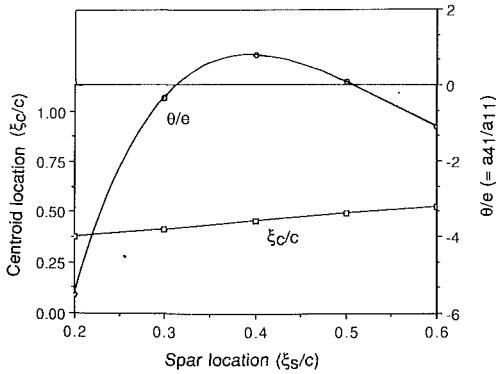

Fig. 13 Variation in the centroid location and couplings of a 2-cell NACA-0012 airfoil section as a function of spar location ($.2 < \xi_s < .6$) with $\alpha c = .30$ and $\xi_a = .25c$

section deformation for applied extension or torsion is a complex surface composed of out-of-plane warping coupled with in-plane Poisson-type contractions (centered bar) or Poisson contractions and anticlastic behavior (off-centered bar). Numerical results are presented that completely validate the current approach with previously published results for centered and off-centered sections and demonstrate the importance of including the deformations in the section plane. In addition, solid and thin-walled multi-cell sections (NACA-0012 airfoils) were analyzed to illustrate the pronounced effects that pretwist, initial twist axis location, and spar location have on coupled behavior. For moderate levels of pretwist, a solid section has increased torsional stiffness and decreased extensional stiffness, whereas certain single and multi-cell configurations undergo a reduction in both extensional and torsional stiffness due to deformations in the section plane that reduce the section planform. Locating the initial twist axis at the centroid maximizes the negative extension-torsion coupling, whereas location the axis near the quarter or three-quarter chord eliminates the coupling for the four section profiles. However, locating the initial twist axis outside of this region introduces positive coupling. Varying the spar location of a pretwisted double-cell section, significantly alters the magnitude and the sign of the extension-torsion coupling terms where two spar locations exist that result in zero extension-torsion coupling.

Acknowledgments

The support of this research by the National Science Foundation through grant MSM-8809132 is gratefully acknowledged.

References

Chu, C., 1951, "The Effect of Initial Twist on the Torsional Rigidity of Thin Prismatical Bars and Tubular Members," *Proceedings of the First U.S. National Congress on Applied Mechanics*, Chicago, pp. 265–269.

Downs, B., 1979, "The Effect of Substantial Pretwist on the Stiffness Properties of Thin Beams of Cambered Section," ASME JOURNAL OF APPLIED MECHANICS, Vol. 46, pp. 341–344.

Goodier, J. N., and Griffin, D. S., 1969, "Elastic Bending of Pretwisted Bars," *International Journal of Solids and Structures*, Vol. 5, pp. 1231–1245.

Hodges, D. H., 1980, "Torsion of Pretwisted Beams Due to Axial Loading," ASME JOURNAL OF APPLIED MECHANICS, Vol. 47, pp. 393–397.

Knowles, J. K., and Reissner, E., 1960, "Torsion and Extension of Helicoidal Shells," *Quarterly of Applied Mathematics*, Vol. 27, No. 4, pp. 409–422.

Krenk, S., 1983, "A Linear Theory for Pretwisted Elastic Beams," ASME JOURNAL OF APPLIED MECHANICS, Vol. 50, pp. 137–142.

Love, A. E. H., 1944, *A Treatise on the Mathematical Theory of Elasticity*, Dover Publications, New York.

Okubo, H., 1951, "The Torsion and Stretching of Spiral Rods I," *Quarterly of Applied Mathematics*, Vol. 9, pp. 263–272.

Okubo, H., 1954, "The Torsion and Stretching of Spiral Rods II," *Quarterly of Applied Mathematics*, Vol. 11, pp. 488–495.

Reissner, E., and Wan, F. Y. M., 1968, "On Axial Extension and Torsion of Helicoidal Shells," *Journal of Mathematics and Physics*, Vol. 47, pp. 1–31.

Rosen, A., 1980, "The Effect of Initial Twist on the Torsional Rigidity of Beams—Another Point of View," ASME JOURNAL OF APPLIED MECHANICS, Vol. 47, pp. 389–392.

Rosen, A., 1983, "Theoretical and Experimental Investigation of the Nonlinear Torsion and Extension of Initially Twisted Bars," ASME JOURNAL OF APPLIED MECHANICS, Vol. 50, pp. 321–326.

Shield, R. T., 1982, "Extension and Torsion of Elastic Bars with Initial Twist," ASME JOURNAL OF APPLIED MECHANICS, Vol. 49, pp. 779–786.

Downloaded 03 May 2010 to 171.66.16.247. Redistribution subject to ASME license or copyright; see http://www.asme.org/terms/Terms_Use.cfm

S. L. Lau
Senior Lecturer,
Mem. ASME.

W.-S. Zhang[1]
Research Assistant.

Department of Civil and Structural Engineering,
Hong Kong Polytechnic,
Kowloon, Hong Kong

Nonlinear Vibrations of Piecewise-Linear Systems by Incremental Harmonic Balance Method

The incremental harmonic balance (IHB) method is extended to analyze the periodic vibrations of systems with a general form of piecewise-linear stiffness characteristics. An explicit formulation has been worked out. This development is of significance as many structural and mechanical systems of practical interest possess a piecewise-linear stiffness. Typical examples show that the IHB method is very effective for analyzing this kind of systems under steady-state vibrations.

I Introduction

Many structural systems of practical interest possess a piecewise-linear stiffness such as structures with different tension and compression moduli, supports with motion-limiting stops, and mechanical systems having clearances or snubbers, etc. Recently nonlinear elements have been widely used to obtain better performance in vibration controls. Many of these elements may be modeled as possessing piecewise-linear or piecewise-nonlinear characteristics.

The free vibrations of simple piecewise-linear systems can be solved exactly, as introduced in some classical textbooks (e.g., Timoshenko, 1974). However, even for such a simple system, it is not easy to obtain a closed-form solution for a forced steady-state vibration (Galhond et al., 1987).

As is well known, a common solution procedure for strongly nonlinear vibration problems is the numerical time integration. This approach can give both transient and steady-state responses for given initial conditions and specified frequencies. However, there are some drawbacks to this approach. For example, it is very expensive and difficult to obtain the frequency responses, especially in parameter regions where the response is multivalued; and it is impossible to obtain unstable solutions which are definitely necessary for gaining an insight into the system behavior.

Another widely used approach is the harmonic balance (HB) method. Maezawa et al. (1973, 1980) applied this method successfully to symmetric and unsymmetric piecewise-linear single degree-of-freedom oscillators. Recently, Choi and Noah (1988) analyzed a similar problem by this method using the FFT algorithm. Watanabe and Sato (1988) developed a nonlinear building block approach for treating structural systems using a describing function for the piecewise-linear elements.

In this paper, the incremental harmonic balance (IHB) method is extended to solve systems with a general piecewise-linear stiffness. All formulae have been worked out in explicit form by using the step function which may yield higher computational efficiency.

The IHB method was initially proposed in a series of papers for treating nonlinear periodic and quasi-periodic vibrations of continuous systems (e.g., Lau and Cheung (1981) and Lau et al. (1982)). Recently, this method has been extended to analyze the steady-state response of systems with dry friction by Pierre et al. (1985). This extension is of great significance, as vibration control devices using dry friction are increasingly employed.

Another frequency-domain analysis procedure for nonlinear systems is the so-called Galerkin/Newton-Raphson (GNR) method (see Ferri and Dowell, (1988), for example). In fact, this method is exactly equivalent to the IHB method. Ferri (1986) has made a detailed comparison. The GNR method differs from IHB only in the order in which the Galerkin (or harmonic balance) method and the Newton-Raphson procedure are applied.

The notable developments of analysis procedures made by Ling and Wu (Fast Galerkin method, 1987) and by Cameron and Griffin (AFT method, 1989) essentially consist in a substitution of the harmonic balance step by a FFT algorithm. These developments can be considered as generalizations of the IHB method. The authors share the same thought with Wei and Pierre (1989), that it is essentially an efficient implementation of the IHB (or GNR) method.

According to our own experience, the use of FFT replacing the HB step can reduce the amount of algebraic manipulation and programming work. In general, it may be more efficient than the conventional IHB method, especially for those cases in which the nonlinearity is rather complicated, and a considerable number of harmonic terms is required in the solution. However, for the present piecewise-linear problems as well as for most practical structural vibrations, as long as explicit formulae for integrals arisen in the Galerkin procedure are

[1]Permanent address: Research Institute of Engineering Mechanics, Dalian University of Technology, Dalian, People's Republic of China.

Contributed by the Applied Mechanics Division of THE AMERICAN SOCIETY OF MECHANICAL ENGINEERS for publication in the JOURNAL OF APPLIED MECHANICS.

Discussion of this paper should be addressed to the Technical Editor, Prof. Leon M. Keer, The Technological Institute, Northwestern University, Evanston, IL 60208, and will be accepted until two months after final publication of the paper itself in the JOURNAL OF APPLIED MECHANICS. Manuscript received by the ASME Applied Mechanics Division, May 2, 1989; final revision, July 27, 1990.

Copyright © 1992 by ASME
Downloaded 03 May 2010 to 171.66.16.247. Redistribution subject to ASME license or copyright; see http://www.asme.org/terms/Terms_Use.cfm

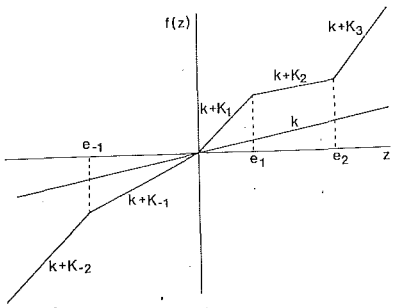

Fig. 1 Restoring force versus displacement relationship of the general piecewise-linear spring

available or only a small number of harmonic terms is sufficient to give satisfactory results, the conventional IHB method is still more effective than that of using FFT algorithm.

In the present work, the extended IHB method is applied to single degree-of-freedom (DOF) systems to demonstrate its effectiveness. Two examples of practical significance in some mechanical devices are considered. The convergence of the solution sought is examined by increasing the number of harmonic terms. It is shown that only a few harmonic terms are sufficient to obtain satisfactory results.

The technique presented in this paper can easily be extended to multiple DOF systems with piecewise-linear stiffness and piecewise-linear damping.

II Equation of Motion

Consider the single DOF system consisting of a mass, a viscous damper, and a piecewise-linear spring of general form. The equation of motion can be written as

$$m\frac{d^2z}{dt^2}+c\frac{dz}{dt}+f(z)=q(t) \tag{1}$$

where

$$f(z)=kz+G(z) \tag{2}$$

and m, c, k, t, and z denote the mass, viscous damping coefficient, linear spring constant, time, and displacement, respectively. The nonlinear restoring force $G(z)$, which has a general piecewise-linear characteristic, is shown in Fig. 1 and can be expressed as follows:

$$\begin{aligned} &G(0)=0, \quad e_0=0, \quad e_{-p}=-\infty, \quad e_q=\infty \\ &G(z)=K_{-i}(z-e_{-(i-1)})+G(e_{-(i-1)}), \quad e_{-i}\le z\le e_{-(i-1)} \\ &\qquad\qquad (i=1,2,\ldots,p) \\ &G(z)=K_i(z-e_{i-1})+G(e_{i-1}), \quad e_{i-1}\le z\le e_i \\ &\qquad\qquad (i=1,2,\ldots,q) \end{aligned} \tag{3}$$

where the $k + K_i$ ($i = -p, -(p-1), \ldots, -2, -1, 1, 2, \ldots, (q-1), q$) are spring constants (Fig. 1), and $|k|$ is assumed to be greater than zero.

The exciting force $q(t)$ can be represented by a general periodic function:

$$q(t)=\sum_{n=0}^{N} q_n=f_0/2+\sum_{n=0}^{N}(f_n\cos n\omega t+g_n\sin n\omega t) \tag{4}$$

where f_0, f_n, and g_n ($n = 1, 2, .. N$) are force component amplitudes of the corresponding harmonic terms.

For convenience, we introduce a phase angle θ given by

$$\theta=\omega t \tag{5}$$

and change the independent variable to θ from t. Equation (1) is transformed into

$$\Omega^2\frac{d^2z}{d\theta^2}+2\zeta\Omega\frac{dz}{d\theta}+z+\frac{1}{k}G(z)=\frac{1}{k}q(\theta) \tag{6}$$

where

$$\Omega=\frac{\omega}{\sqrt{k/m}}, \quad \text{and} \quad \zeta=\frac{c}{2\sqrt{mk}} \tag{7}$$

are the frequency ratio and the damping ratio, respectively.

III IHB Analysis

Since the IHB method has been well expounded in a number of papers (Lau and Cheung (1981), Lau et al. (1982), Pierre et al. (1985), Pierre and Dowell (1985), for example), the required formulation will be briefly stated here.

Assuming that the current state of vibration corresponding to the excitation parameters Ω_0 and q_0 is denoted by $z_0(\theta)$, a neighboring state can be expressed by adding the corresponding increments as follows:

$$\begin{aligned} z(\theta)&=z_0(\theta)+\Delta z(\theta) \\ q(\theta)&=q_0(\theta)+\Delta q(\theta) \\ \Omega&=\Omega_0+\Delta\Omega. \end{aligned} \tag{8}$$

For a small increment Δz, the function $G(z)$ may be written formally as

$$G(z)=G(z_0)+G'(z_0)\Delta z \tag{9}$$

where $G'(z_0)$ represents the value of the first derivative with respect to z at z_0 which can be expressed with the step function. Following the procedure in Lau et al. (1982), a linearized incremental equation is obtained in the form

$$\Omega_0^2\frac{d^2\Delta z}{d\theta^2}+2\zeta\Omega_0\frac{d\Delta z}{d\theta}+\Delta z+\frac{1}{k}G'(z)\Delta z=R+\Delta\Omega F+\Delta Q \tag{10}$$

where

$$R=-\left[\Omega_0^2\frac{d^2z_0}{d\theta^2}+2\zeta\Omega_0\frac{dz_0}{d\theta}+z_0+\frac{1}{k}G(z_0)-\frac{1}{k}q_0\right] \tag{11}$$

$$F=-2\Omega_0\frac{d^2z_0}{d\theta^2}-2\zeta\frac{dz_0}{d\theta} \tag{12}$$

$$\Delta Q=\Delta q/k. \tag{13}$$

R is the corrective term and F is the unbalanced force term due to unit frequency shifting.

An approximate periodic solution may be expressed as

$$z_0=\sum_{n=0}^{N} z_{0n}=a_0/2+\sum_{n=1}^{N}(a_n\cos n\theta+b_n\sin n\theta) \tag{14}$$

and, accordingly,

$$\Delta z=\sum_{n=0}^{N}\Delta z_n=\Delta a_0/2+\sum_{n=1}^{N}(\Delta a_n\cos n\theta+\Delta b_n\sin n\theta) \tag{15}$$

where N = the number of harmonic terms taken.

The Galerkin procedure is carried out with the Δa_n's and Δb_n's as the generalized coordinates:

$$\begin{aligned} &\int_0^{2\pi}\left[\Omega_0^2\frac{d^2\Delta z}{d\theta^2}+2\zeta\Omega_0\frac{d\Delta z}{d\theta}+\Delta z+\frac{1}{k}G'(z)\Delta z\right]\delta(\Delta z)\,d\theta \\ &\qquad=\int_0^{2\pi}(R+\Delta\Omega F+\Delta Q)\,\delta(\Delta z)\,d\theta. \end{aligned} \tag{16}$$

Denoting the amplitude vector and its incremental vector by

$$\mathbf{a}=[a_0,a_1..a_N,b_1,b_2..b_N]^T \tag{17}$$

$$\Delta\mathbf{a}=[\Delta a_0,\Delta a_1..\Delta a_N,\Delta b_1,\Delta b_2..\Delta b_N]^T, \tag{18}$$

respectively, a system of $2N + 1$ linearized equations in terms of the increments Δa_n's and Δb_n's is obtained from Eq. (16) in the form of

$$\mathbf{C}\Delta\mathbf{a}=\mathbf{R}+\Delta\Omega\mathbf{F}+\Delta\mathbf{Q} \tag{19}$$

$$\mathbf{C}=\begin{bmatrix}[\mathbf{C}_1] & [\mathbf{C}_{12}]\\ [\mathbf{C}_{21}] & [\mathbf{C}_2]\end{bmatrix} \tag{20}$$

Downloaded 03 May 2010 to 171.66.16.247. Redistribution subject to ASME license or copyright; see http://www.asme.org/terms/Terms_Use.cfm

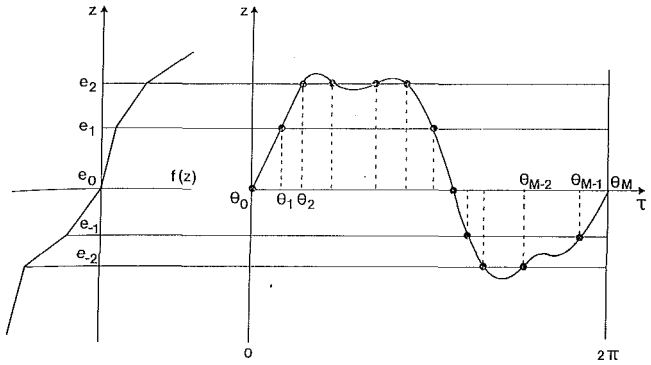

Fig. 2 Zeros of equations $z = e_n (n = -p, -p+1, \ldots, -2, -1, 0, 1, 2, \ldots, q-1, q)$

$$\mathbf{R} = \begin{bmatrix} \mathbf{R}_1 \\ \mathbf{R}_2 \end{bmatrix} \tag{21}$$

$$\mathbf{F} = \begin{bmatrix} \mathbf{F}_1 \\ \mathbf{F}_2 \end{bmatrix} \tag{22}$$

$$\Delta\mathbf{Q} = \begin{bmatrix} \Delta\mathbf{Q}_1 \\ \Delta\mathbf{Q}_2 \end{bmatrix}. \tag{23}$$

The explicit expressions for $\mathbf{C}$, $\mathbf{R}$, $\mathbf{F}$, and $\Delta\mathbf{Q}$ have been worked out as follows:

(1) Elements of the matrix $\mathbf{C}$:

$$[\mathbf{C}_1]_{ij} = \alpha_j \delta_{ij} \pi (1 - j^2 \Omega_0^2) + [\mathbf{C}_1]_{ij}^{NL}, \quad (i = 0,1,\ldots,N,\ j = 0,1,\ldots,N) \tag{24}$$

$$[\mathbf{C}_{12}]_{ij} = 2\delta_{ij} \pi \zeta j \Omega_0 + [\mathbf{C}_{12}]_{ij}^{NL}, \quad (i = 0,1,\ldots,N,\ j = 1,\ldots,N) \tag{25}$$

$$[\mathbf{C}_{21}]_{ij} = -2\delta_{ij} \pi \zeta j \Omega_0 + [\mathbf{C}_{21}]_{ij}^{NL}, \quad (i = 1,2,\ldots,N,\ j = 0,1,\ldots,N) \tag{26}$$

$$[\mathbf{C}_2]_{ij} = \delta_{ij} \pi (1 - j^2 \Omega_0^2) + [\mathbf{C}_2]_{ij}^{NL}, \quad (i = 1,2,\ldots,N,\ j = 1,\ldots,N) \tag{27}$$

where

$$\alpha_n = \begin{cases} 1 & \text{for } n \neq 0 \\ 1/2 & \text{for } n = 0 \end{cases}$$

δ_{ij} is the Kronecker's notation.

(2) Elements of vectors $\mathbf{R}$, $\mathbf{F}$, and $\Delta\mathbf{Q}$:

$$\mathbf{R}_{1i} = -\alpha_i \left[(1 - i^2 \Omega_0^2) a_i + 2\zeta i \Omega_0 b_i - \frac{f_i}{k} \right] \pi + \mathbf{R}_{1i}^{NL}, \quad (i = 0,1,\ldots,N) \tag{28}$$

$$\mathbf{R}_{2i} = -\left[(1 - i^2 \Omega_0^2) b_i - 2\zeta i \Omega_0 a_i - \frac{g_i}{k} \right] \pi + \mathbf{R}_{2i}^{NL}, \quad (i = 1,2,\ldots,N) \tag{29}$$

$$\mathbf{F}_{1i} = 2\pi i (i\Omega_0 a_i - \zeta b_i), \quad (i = 0,1,\ldots,N) \tag{30}$$

$$\mathbf{F}_{2i} = 2\pi i (i\Omega_0 b_i + \zeta a_i), \quad (i = 1,2,\ldots,N) \tag{31}$$

$$\Delta\mathbf{Q}_{1i} = \frac{1}{k} \alpha_i \pi \Delta f_i, \quad (i = 0,1,\ldots,N) \tag{32}$$

$$\Delta\mathbf{Q}_{2i} = \frac{1}{k} \pi \Delta g_i, \quad (i = 1,\ldots,N). \tag{33}$$

The nonlinear part of the elements of $\mathbf{C}$ and of the components of $\mathbf{R}$ are expressed by:

$$[\mathbf{C}_1]_{ij}^{NL} = \frac{\alpha_i \alpha_j}{k} \int_0^{2\pi} G'(z_0) \cos i\theta \cos j\theta \, d\theta \tag{34}$$

$$[\mathbf{C}_{12}]_{ij}^{NL} = \frac{\alpha_i}{k} \int_0^{2\pi} G'(z_0) \cos i\theta \sin j\theta \, d\theta \tag{35}$$

$$[\mathbf{C}_{21}]_{ij}^{NL} = \frac{\alpha_j}{k} \int_0^{2\pi} G'(z_0) \sin i\theta \cos j\theta \, d\theta \tag{36}$$

$$[\mathbf{C}_2]_{ij}^{NL} = \frac{1}{k} \int_0^{2\pi} G'(z_0) \sin i\theta \sin j\theta \, d\theta \tag{37}$$

$$\mathbf{R}_{1i}^{NL} = -\frac{\alpha_i}{k} \int_0^{2\pi} G(z_0) \cos i\theta \, d\theta \tag{38}$$

$$\mathbf{R}_{2i}^{NL} = -\frac{1}{k} \int_0^{2\pi} G(z_0) \sin i\theta \, d\theta \tag{39}$$

where $G'(z_0)$ can be expressed by the use of the step function.

The evaluation of the integrals (34)–(39) requires a knowledge of the zeros of the equations $z = e_n$ $(n = -(p-1), \ldots, -2, -1, 0, 1, 2, \ldots, q-1)$. In the computer program, this is achieved at each iteration through a procedure which uses bisection and interpolation methods on the trigonometric equation $z = e_n$. Let $\theta_1, \theta_2, \ldots, \theta_M$ $(\theta_1 < \theta_2 < \ldots < \theta_M)$ be the M zeros of $z = e_{-(p-1)}$, $z = e_{-(p-2)}$, $\ldots$, $z = e_{-1}$, $z = e_0$, $z = e_1$, $\ldots$, $z = e_{q-1}$ and $s_{1,n}, s_{2,n}, \ldots, s_{M+1,n}$ be the value of the sign function of $z - e_n$ $(n = -p, \ldots, -1, 0, 1, \ldots, q)$, respectively, in the intervals $[\theta_0, \theta_1] \ldots [\theta_M, \theta_{M+1}]$, with $\theta_0 = 0$ and $\theta_{M+1} = 2\pi$, and denote the step function by

$$H(x,y) = \begin{cases} 1 & \text{if } x \cdot y < 0 \\ 0 & \text{if } x \cdot y > 0. \end{cases} \tag{40}$$

The integrals (34)–(39) can then be expressed explicitly in terms of θ_u and $S_{u,v}$:

$$[\mathbf{C}_1]_{ij}^{NL} = \frac{\alpha_i \alpha_j}{k} \sum_{u=0}^{M} \left\{ \sum_{v=-p}^{-1} H(s_{u+1,v}, s_{u+1,v+1}) K_v(A_{ij}(\theta_{u+1}) - A_{ij}(\theta_u)) + \sum_{v=1}^{q} H(s_{u+1,v-1}, s_{u+1,v}) K_v(A_{ij}(\theta_{u+1}) - A_{ij}(\theta_u)) \right\} \tag{41}$$

$$[\mathbf{C}_{12}]_{ij}^{NL} = \frac{\alpha_i}{k} \sum_{u=0}^{M} \left\{ \sum_{v=-p}^{-1} H(s_{u+1,v}, s_{u+1,v+1}) K_v(B_{ij}(\theta_{u+1}) - B_{ij}(\theta_u)) + \sum_{v=1}^{q} H(s_{u+1,v-1}, s_{u+1,v}) K_v(B_{ij}(\theta_{u+1}) - B_{ij}(\theta_u)) \right\} \tag{42}$$

$$[\mathbf{C}_{21}]_{ij}^{NL} = \frac{\alpha_j}{k} \sum_{u=0}^{M} \left\{ \sum_{v=-p}^{-1} H(s_{u+1,v}, s_{u+1,v+1}) K_v(C_{ij}(\theta_{u+1}) - C_{ij}(\theta_u)) + \sum_{v=1}^{q} H(s_{u+1,v-1}, s_{u+1,v}) K_v(C_{ij}(\theta_{u+1}) - C_{ij}(\theta_u)) \right\} \tag{43}$$

$$[\mathbf{C}_2]_{ij}^{NL} = \frac{1}{k} \sum_{u=0}^{M} \left\{ \sum_{v=-p}^{-1} H(s_{u+1,v}, s_{u+1,v+1}) K_v(D_{ij}(\theta_{u+1}) - D_{ij}(\theta_u)) + \sum_{v=1}^{q} H(s_{u+1,v-1}, s_{u+1,v}) K_v(D_{ij}(\theta_{u+1}) - D_{ij}(\theta_u)) \right\} \tag{44}$$

$$\mathbf{R}_{1i}^{NL} = -\frac{\alpha_i}{k} \sum_{u=0}^{M} \left\{ \sum_{v=-p}^{-1} H(s_{u+1,v}, s_{u+1,v+1}) \right.$$

Downloaded 03 May 2010 to 171.66.16.247. Redistribution subject to ASME license or copyright; see http://www.asme.org/terms/Terms_Use.cfm

$$\times\left(K_v\sum_{j=0}^{N}\alpha_j[a_j[A_{ij}(\theta_{u+1})-A_{ij}(\theta_u)]+b_j[B_{ij}(\theta_{u+1})-B_{ij}(\theta_u)]]+\kappa_v[E_i(\theta_{u+1})-E_i(\theta_u)]\right)$$

$$+\sum_{v=1}^{q}H(s_{u+1,v-1},s_{u+1,v})\left(K_v\sum_{j=0}^{N}\alpha_j\left[a_j[A_{ij}(\theta_{u+1})-A_{ij}(\theta_u)]+b_j[B_{ij}(\theta_{u+1})-B_{ij}(\theta_u)]\right]+\kappa_v[E_i(\theta_{u+1})-E_i(\theta_u)]\right)\Bigg\} \quad (45)$$

$$\mathbf{R}_{2i}^{NL}=-\frac{1}{k}\sum_{u=0}^{M}\Bigg\{\sum_{v=-p}^{-1}H(s_{u+1,v},s_{u+1,v+1})\times\left(K_v\sum_{j=0}^{N}\alpha_j[a_j[C_{ij}(\theta_{u+1})-C_{ij}(\theta_u)]+b_j[D_{ij}(\theta_{u+1})-D_{ij}(\theta_u)]]+\kappa_v[F_i(\theta_{u+1})-F_i(\theta_u)]\right)$$

$$+\sum_{v=1}^{q}H(s_{u+1,v-1},s_{u+1,v})\left(K_v\sum_{j=0}^{N}\alpha_j[a_j[C_{ij}(\theta_{u+1})-C_{ij}(\theta_u)]+b_j[D_{ij}(\theta_{u+1})-D_{ij}(\theta_u)]]+\kappa_v[F_i(\theta_{u+1})-F_i(\theta_u)]\right)\Bigg\} \quad (46)$$

where

$$\left.\begin{aligned}\kappa_{-r}&=(K_{-1}-K_{-2})e_{-1}+(K_{-2}-K_{-3})e_{-2}+\ldots\\&\qquad+(K_{r+1}-K_{-r})e_{-r+1}\\\kappa_r&=(K_1-K_2)e_1+(K_2-K_3)e_2+\ldots+(K_{r-1}-K_r)e_{r-1}\end{aligned}\right\} \quad (47)$$

$$A_{ij}(\theta)=\frac{\theta}{2}\left[\frac{\sin(i-j)\theta}{(i-j)\theta}+\frac{\sin(i+j)\theta}{(i+j)\theta}\right] \quad (48)$$

$$B_{ij}(\theta)=\begin{cases}\dfrac{\theta}{2}\left[\dfrac{\cos(i-j)\theta}{(i-j)\theta}-\dfrac{\cos(i+j)\theta}{(i+j)\theta}\right] & (i\neq j)\\[2ex] -\dfrac{\theta}{2}\left[\dfrac{\cos 2i\theta}{2i\theta}\right] & (i=j)\end{cases} \quad (49)$$

$$C_{ij}(\theta)=B_{ji}(\theta) \quad (50)$$

$$D_{ij}(\theta)=\frac{\theta}{2}\left[\frac{\sin(i-j)\theta}{(i-j)\theta}-\frac{\sin(i+j)\theta}{(i+j)\theta}\right] \quad (51)$$

$$E_i(\theta)=\theta\frac{\sin i\theta}{i\theta} \quad (52)$$

$$F_i(\theta)=-\theta\frac{\cos i\theta}{i\theta}. \quad (53)$$

In expressions (48)–(53), the limiting values should be taken if both the numerator and denominator become zero.

IV Numerical Examples

To obtain a frequency response curve of a system, an initial state should first be given. This state need not be a solution, but an assumed vibration state will do as long as the initialization process can converge to a required solution (e.g., super/subresonance, fundamental resonance, etc.). The incrementation procedure for tracing the frequency responses (usually one of the their branches) for a constant force level is similar to that described in Lau et al. (1982). There are two options in this procedure. One is the Ω-incrementation option; i.e., the frequency increment is prescribed and $\Delta\Omega$ is kept to be zero in the subsequent iteration process. At every increment, one has to iterate with the following equations,

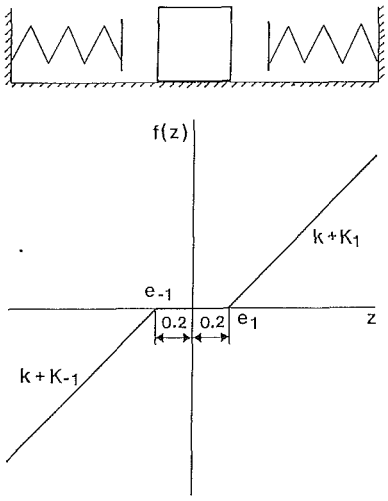

Fig. 3 A single DOF system with clearance, $m = 1$, $k = 1$, $e_{-1} = -0.2$, $e_1 = 0.2$, $K_1 = K_{-1} = -k$, $K_2 = K_{-2} = 0$, $\zeta = c/\sqrt{4mk} = 0.01$, $q(t) = \cos\omega t$

$$\mathbf{C}^{(i)}\Delta\mathbf{a}^{(i+1)}=\mathbf{R}^{(i)} \quad (54)$$

$$\mathbf{a}^{(i+1)}=\mathbf{a}^{(i)}+\Delta\mathbf{a}^{(i+1)} \quad (55)$$

and the updated matrices $\mathbf{C}^{i+1}$, $\mathbf{R}^{(i+1)}$ are then evaluated from Eqs. (24)–(29) in terms of the $(i+1)$th amplitude vector $\mathbf{a}^{(i+1)}$.

The other option is by A-incrementation; i.e., a properly chosen amplitude component increment Δa_k or Δb_k (usually the one that is in resonance and varies faster) is prescribed, and in the subsequent iteration process this Δa_k (or Δb_k) is kept equal to zero. In this case, one has to iterate with the following equations,

$$\mathbf{C}^{(i)}\Delta\mathbf{a}^{(i+1)}=\mathbf{R}^{(i)}+\Delta\Omega^{(i+1)}\mathbf{F}^{(i)} \quad (56)$$

$$\mathbf{a}^{(i+1)}=\mathbf{a}^{(i)}+\Delta\mathbf{a}^{(i+1)} \quad (57)$$

$$\Omega^{(i+1)}=\Omega^{(i)}+\Delta\Omega^{(i+1)}. \quad (58)$$

The updated matrices $\mathbf{C}^{(i+1)}$, $\mathbf{R}^{(i+1)}$ are evaluated from Eqs. (24)–(29) in terms of the $(i+1)$th vector $\mathbf{a}^{(i+1)}$ and $\Omega^{(i+1)}$ for the next iteration.

Depending on the local relative slope of the response curve, one of the incrementation options is used. To obtain the next point of solution the iteration process proceeds until the criterion

$$\max\left|\frac{\Delta a_i}{a_{\text{ref}}}\right|\leq\epsilon \quad (59)$$

is satisfied, where ϵ is the permissible error depending on the accuracy required, Δa_i represents the ith component of the most recently computed increment, and a_{ref} stands for the largest component of the vector $\mathbf{a}$.

In general, the number of iterative steps required for convergence is problem dependent. Nevertheless, the required number can be reduced by using an extrapolation procedure to obtain a prediction for the next solution point from the known ones before the iteration process is started.

The required number of iterations to converge is obviously dependent on the magnitude of the increments in an incremental step as well. The smaller the increment, the fewer the iterative steps required. In our computer program, the desired number of iterative steps to converge can be set by the user, and the program will adjust automatically the arc length of the extrapolated increment step by step, so as to retain the preset number of iterations as close as possible during the incrementation process. In the following examples, the desired number of iteration for convergence is set to be four.

Downloaded 03 May 2010 to 171.66.16.247. Redistribution subject to ASME license or copyright; see http://www.asme.org/terms/Terms_Use.cfm

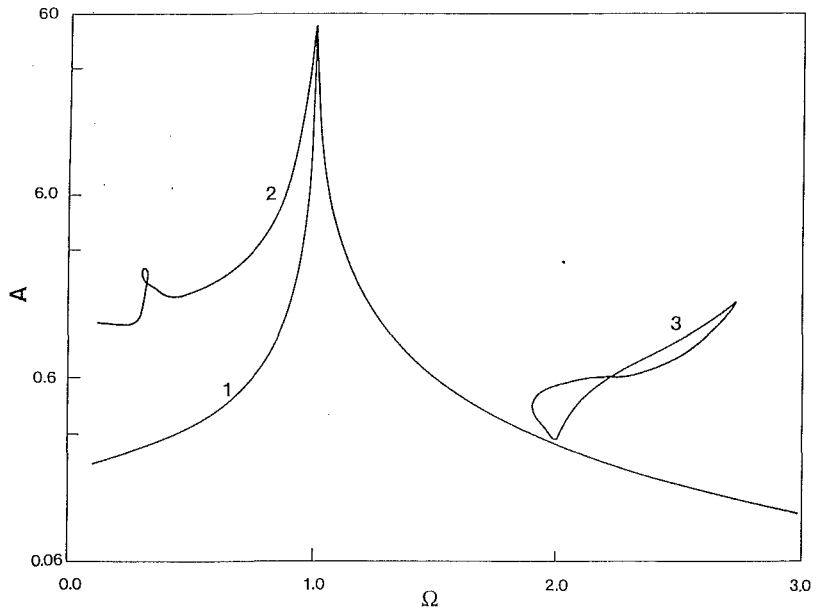

Fig. 4 Maximum amplitude versus frequency; curve 1: free vibration backbone; curve 2: superharmonic/fundamental response; curve 3: subharmonic response. $A = (z_{max} - z_{min})/2$.

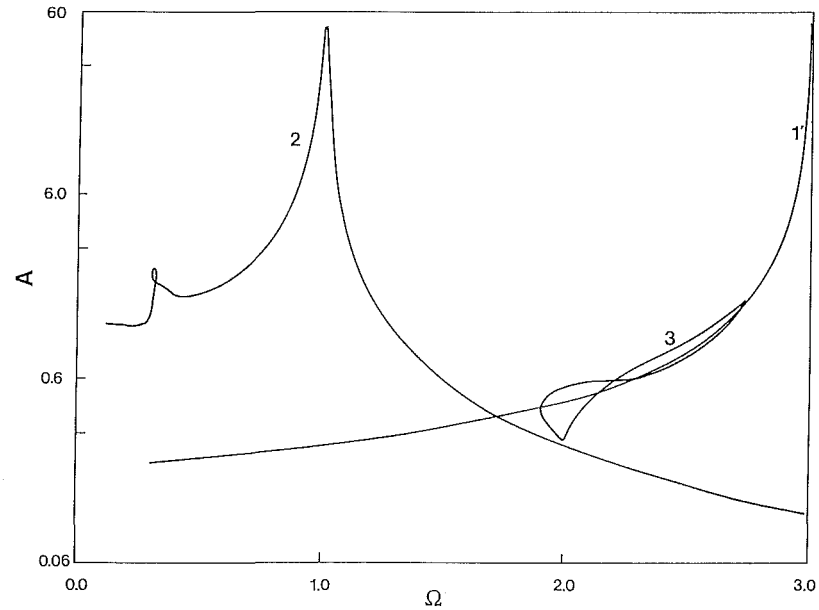

Fig. 5 Maximum amplitude versus frequency; curve 1: shifted free vibration backbone; curve 2: superharmonic/fundamental response; curve 3: subharmonic response. $A = (z_{max} - z_{min})/2$.

Example 1: Single DOF System With Clearance. The mathematical model of this problem and its related parameters are shown in Fig. 3. In the analysis, two odd sine terms and cosine terms are adopted. The computed maximum amplitude versus frequency responses are shown in Fig. 4. Curve 1 represents the free vibration backbone curve; the frequency approaches 1.0 with increase of amplitude and reduces to zero when the amplitude decreases at the clearance boundary. Although the clearance does not cause much effect on the fundamental resonance (curve 2), this kind of nonlinearity gives rise to superharmonic and subharmonic resonances (see curves 2 and 3, respectively). However, the existence of damping, even when this is of a rather small magnitude, causes both the super and subharmonic resonances to be greatly suppressed, in comparison with the fundamental resonance. If we shift the free vibration backbone curve by multiplying the frequency by three, it is found that the subharmonic resonance response is located in the neighborhood of the shifted backbone curve (see Fig. 5, curve 1′). A similar phenomenon is observed for the superharmonic resonance by shifting the backbone curve to the left side with the frequency divided by three. These interesting facts reveal the free vibration response, which relates to the inherent characteristics of the system, affects the behavior of various kinds of resonances.

In the case of no damping, the subharmonic response extends to infinity at both positive (in-phase solution) and negative (out-of-phase solution) branches. The sub-harmonic response shrinks into complicated closed curves in the presence of damping as shown in Fig. 6, where $a_{1/3}$, $b_{1/3}$, a_1, and b_1, are the amplitudes for the $\cos(\omega t/3)$, $\sin(\omega t/3)$, $\cos(\omega t)$ and $\sin(\omega t)$

Downloaded 03 May 2010 to 171.66.16.247. Redistribution subject to ASME license or copyright; see http://www.asme.org/terms/Terms_Use.cfm

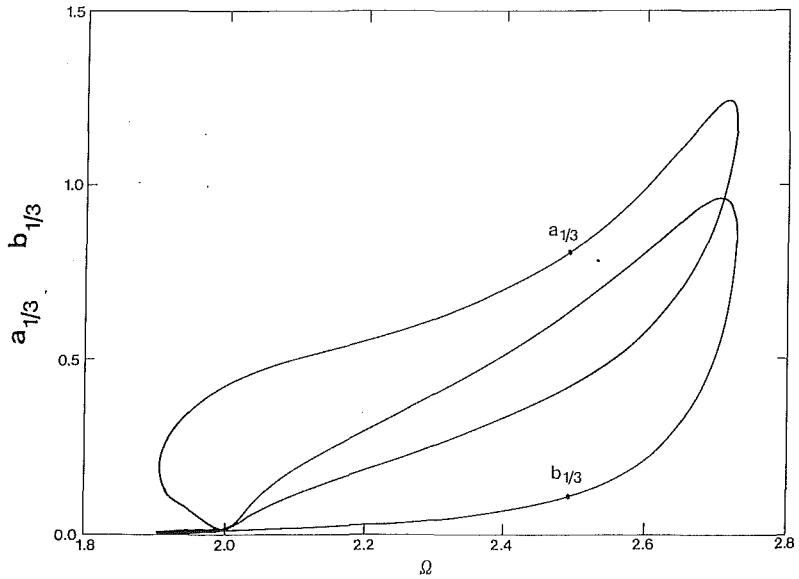

Fig. 6(*a*) Amplitudes $a_{1/3}$, $b_{1/3}$ versus frequency Ω

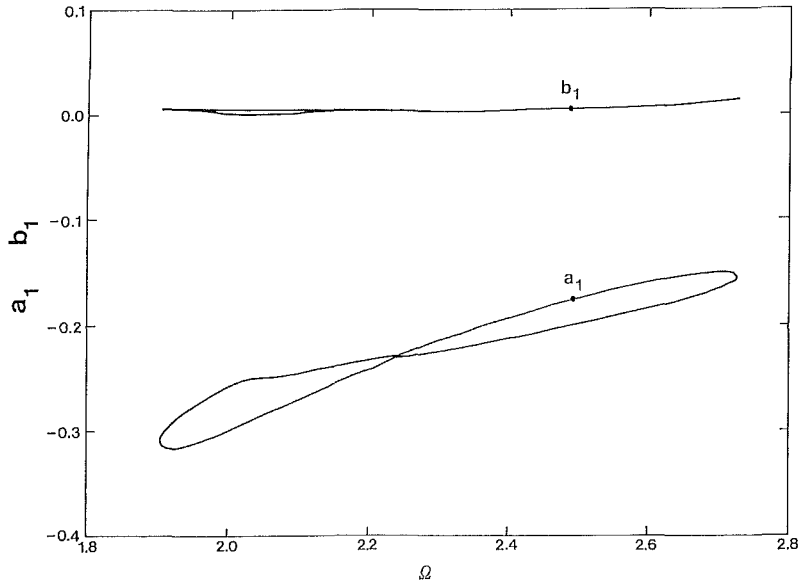

Fig. 6(*b*) Amplitudes a_1, b_1, versus frequency Ω

Fig. 6 Subharmonic response amplitudes, $z(t) = a_{1/3}\cos(\omega t/3) + b_{1/3}\sin(\omega t/3) + a_1\cos(\omega t) + b_1\sin(\omega t)$

terms, respectively. In either case, the subharmonic response is separated from the superharmonic/fundamental response solution.

It should be noted that in order to obtain the third-order subharmonic resonance without modifying the above formulation, the exciting force $q(t)$ in Eq. (4) should be taken to be $q(t) = \cos 3\,\omega t$. After the computation, the subharmonic response is obtained by shifting with the frequency divided by three. For the separate subharmonic resonance, a starting guessed state may be obtained by referring to the corresponding shifted free vibration backbone curve, such as the one shown in Fig. 5.

Example 2: Single DOF System With Symmetric Piecewise-Linear Stiffness. The mathematical model and its parameters are shown in Fig. 7. The computed results with two odd sine terms and cosine terms under a single harmonic excitation are plotted in Fig. 8. The third harmonic response curves appear to be quite complicated. This is basically due to a rotation of

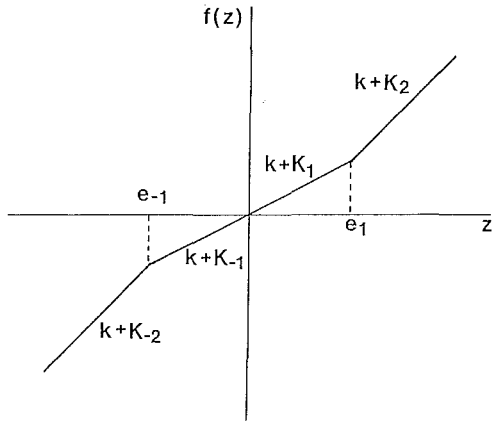

Fig. 7 A single DOF system with symmetric piecewise stiffness, $m = 1$, $k = 1$, $K_1 = K_{-1} = 0$, $_2 = K_{-2} = 1$, $e_{-1} = -0.5$, $e_1 = 0.5$, $\zeta = c/\sqrt{4mk} = 0.01$, $q(t) = \cos\omega t$

Downloaded 03 May 2010 to 171.66.16.247. Redistribution subject to ASME license or copyright; see http://www.asme.org/terms/Terms_Use.cfm

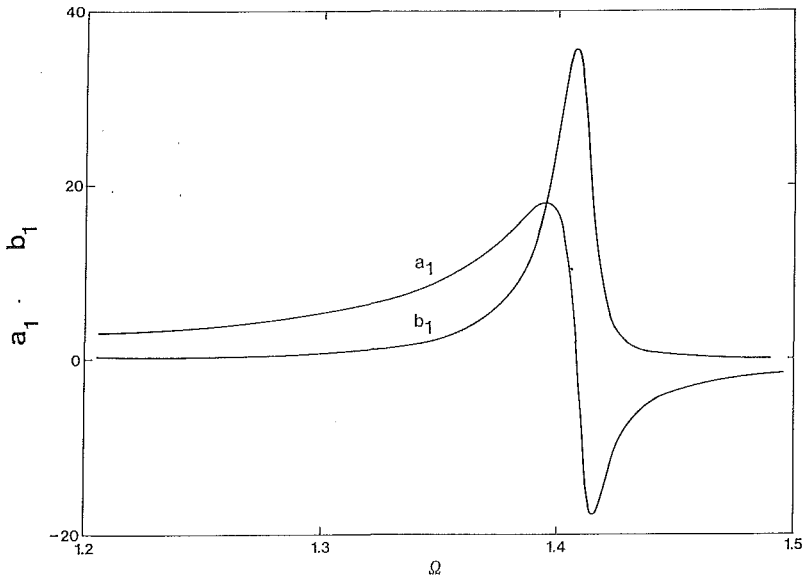

Fig. 8(*a*) Amplitudes a_1, b_1 versus frequency Ω

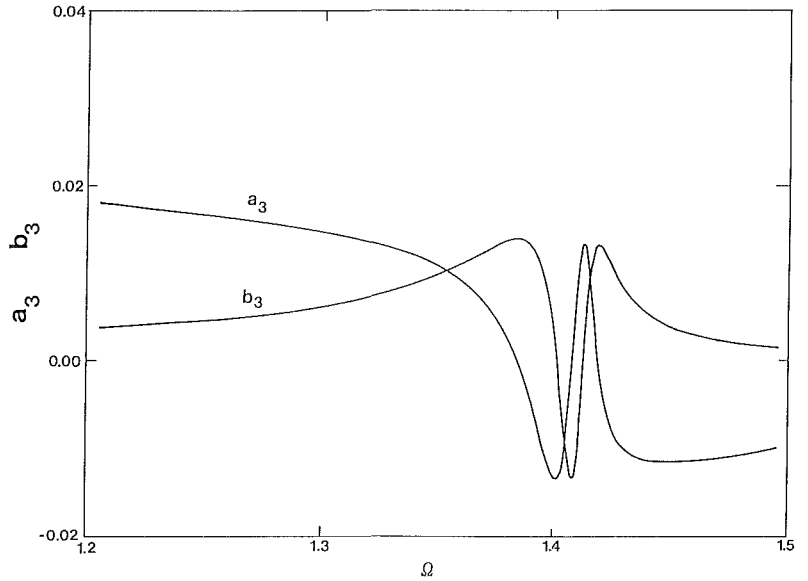

Fig. 8(*b*) Amplitudes a_3, b_3 versus frequency Ω

Fig. 8 Fundamental responses of symmetric piecewise linear system, $z(t) = a_1\cos\omega t + b_1\sin\omega t + a_3\cos 3\omega t + b_3\sin 3\omega t$

more than 2π in the phase angle. The subharmonic resonance is also separate under the present excitation level, and has a similar response to that of example 1. When K_2, K_{-2} are large in comparison with k, this model represents a system having a massless snubber which is widely used in some vibration control devices. Figure 9 shows the total amplitude response of such a system in which the snubber stiffness is ten times that of the spring stiffness. The results are obtained with three odd sine and cosine terms. It can be seen that for a given frequency, the amplitude is much less than that of the linear counterpart. Note that the right portion of the response curve above $A = 5$ represents unstable solutions.

To show the convergence of the obtained solutions, this problem has been also computed with five and again eight harmonic terms (i.e., up to $\cos(15\omega t)$ and $\sin(15\omega t)$). The time histories (z versus θ) obtained for $\omega = 1$ and 2 are listed in Table 1 and Table 2, respectively. We can see that very good results are obtained by using only three harmonic terms for these cases. Of course, to analyze higher-order super/subharmonic responses, the corresponding harmonic terms should be included.

Table 1 Time histories for $\omega = 1$ obtained with different number of harmonic terms (NH)

NH	θ	0	$\pi/6$	$\pi/3$	$\pi/2$	$2\pi/3$	$5\pi/6$	π
3		5.352	4.813	2.980	0.534	−2.048	−4.176	−5.352
5		5.359	4.793	2.985	0.529	−2.041	−4.172	−5.359
8		5.360	4.793	2.985	0.529	−2.043	−4.173	−5.360

Table 2 Time histories for $\omega = 2$ obtained with different number of harmonic terms (NH)

NH	θ	0	$\pi/6$	$\pi/3$	$\pi/2$	$2\pi/3$	$5\pi/6$	π
3		8.607	9.330	6.971	3.018	−1.160	−5.303	−8.607
5		8.613	9.325	6.974	3.022	−1.169	−5.293	−8.613
8		8.612	9.325	6.975	3.024	−1.168	−5.291	−8.612

V Concluding Remarks

The IHB method has been extended to the analysis of systems

Downloaded 03 May 2010 to 171.66.16.247. Redistribution subject to ASME license or copyright; see http://www.asme.org/terms/Terms_Use.cfm

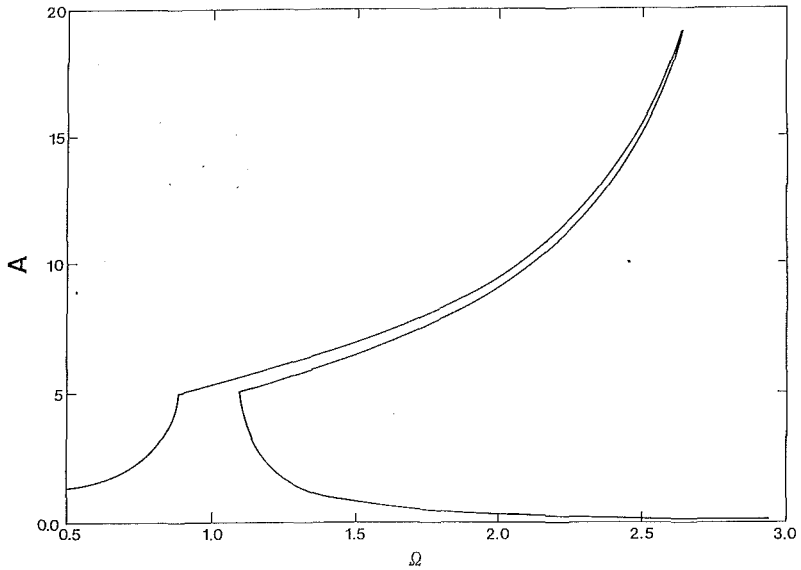

Fig. 9 Maximum amplitude versus frequency for the system shown in Fig. 7 with parameters: $m = 1$, $k = 1$, $K_1 = K_{-1} = 0$, $K_2 = K_{-2} = 9$, $e_{-1} = -5$, $e_1 = 5$, $\zeta = 0.01$, $q = \cos\omega t$. $A = (z_{max} - z_{min})/2$.

with a piecewise-linear stiffness of general characteristics. All formulae have been worked out in explicit form. This method can be further extended to treat multiple-DOF systems with piecewise-linear stiffness as well as piecewise-linear damping. Moreover, the present technique can be applied to the so-called ramp function used in modeling dry friction dampers (Ferri and Dowell, 1988). The explicit formulation used here yields higher computational efficiency.

In contrast to the time-step integration method, both the stable and the unstable vibration states are obtained by the IHB method. The stability analysis can be performed by the use of Hsu's method (Hsu, 1972, 1973, Friedmann, 1977) on the corresponding variational equations. It is worth pointing out that the variational equations are identical to the incremental equations (with the right-hand side term set to zero) used in the IHB method.

The subharmonic resonances are closely related to the occurrence of chaos, which has become a prominent topic over the past few years in engineering and applied science. Some interesting problems involving piecewise-linear systems with a single change in stiffness have been dealt with by Thompson (1983) and Shaw and Holmes (1983) associated with the existence of chaotic motions. The IHB method can be applied to systems of this kind for seeking subharmonic resonances.

Recently, Dowell and Pierre (1984) in a review paper suggested the IHB method could be used for studying the self-excited, chaotic oscillation of autonomous systems. We are looking forward to seeing such a development in the near future.

Acknowledgment

This work has been supported by a Research Grant from the Hong Kong Polytechnic. The authors wish to thank Prof. M. Anson and the reviewers for their comments which were very helpful in the revision of this paper.

References

Choi, Y. S., and Noah, S. T., 1988, "Forced periodic vibration of unsymmetric piecewise-linear systems," *J. Sound and Vibration*, Vol. 121, No. 1, pp. 117–126.

Cameron, T. M., and Griffin, J. H., 1989, "An Alternating Frequency/Time Domain Method for Calculating the Steady-State Response of Nonlinear Dynamic Systems," ASME JOURNAL OF APPLIED MECHANICS, Vol. 56, pp. 149–154.

Dowell, E. H., and Pierre, C., 1984, "Chaotic oscillations in mechanical systems," *Chaos in Nonlinear Dynamic Systems*, J. Chandra, ed., SIAM.

Ferri, A. A., 1986, "On the Equivalence of the Incremental Harmonic Balance Method and the Harmonic Balance—Newton Raphson Method," ASME JOURNAL OF APPLIED MECHANICS, Vol. 53, pp. 455–456.

Ferri, A. A., and Dowell, E. H., 1988, "Frequency domain solutions to multi-degree-of-freedom, dry friction damped systems," *J. Sound and Vibration*, Vol. 124, No. 2, pp. 207–224.

Friedmann, P., Hammond, C. E., and Woo, T. H., 1977, "Efficient numerical treatment of periodic systems with application to stability problems," *Int. J. Num. Math. Engg.*, Vol. 11, pp. 1117–1136.

Galhoud, L. E., Masri, S. F., and Anderson, J. C., 1987, "Transfer Function of a Class of Nonlinear Multidegree of Freedom Oscillators," ASME JOURNAL OF APPLIED MECHANICS, Vol. 54, pp. 215–225.

Hsu, C. S., 1972, "Impulsive Parametric Excitation: Theory," ASME JOURNAL OF APPLIED MECHANICS, Vol. 39, pp. 551–558.

Hsu, C. S., 1973, "Applications of the theory of impulsive parametric excitation and new treatments of general parametric excitation problems," ASME JOURNAL OF APPLIED MECHANICS, Vol. 40, pp. 78–86.

Lau, S. L., and Cheung, Y. K., 1981, "Amplitude Incremental Variational Principal for Nonlinear Vibration of Elastic System," ASME JOURNAL OF APPLIED MECHANICS, Vol. 48, pp. 959–964.

Lau, S. L., Cheung, Y. K., and Wu, S. Y., 1982, "Variable Parameter Incrementation Method for Dynamic Instability of Linear and Nonlinear System," ASME JOURNAL OF APPLIED MECHANICS, Vol. 49, pp. 849–853.

Lau, S. L., Cheung, Y. K., and Wu, S. Y., 1983, "Incremental Harmonic Balance Method With Multiple Time Scales for Nonlinear Aperiodic Vibrations," ASME JOURNAL OF APPLIED MECHANICS, Vol. 50, pp. 871–876.

Lau, S. L., Cheung, Y. K., and Wu, S. Y., 1984, "Nonlinear Vibration of Thin Elastic Plates: Part II Internal Resonance," ASME JOURNAL OF APPLIED MECHANICS, Vol. 51, pp. 845–851.

Ling, F. H., and Wu, X. X., 1987, "Fast Galerkin method and its application to determine periodic solutions of non-linear oscillators," *Int. J. Nonlinear Mechanics*, Vol. 22, pp. 89-98.

Maezawa, S., and Furukawa, S., 1973, "Superharmonic resonance in piecewise-linear system," *Bulletion of the JSME*, Vol. 16, pp. 931–941.

Maezawa, S., Kumano, H., and Minakuchi, Y., 1980, "Forced vibrations in an unsymmetric piecewise-linear system excited by general periodic force functions," *Bulletin of the JSME*, Vol. 23, pp. 68–75.

Pierre, C., and Dowell, E. H., 1985, "A Study of Dynamic Instability of Plates by an Extended Incremental Harmonic Balance Method," ASME JOURNAL OF APPLIED MECHANICS, Vol. 52, pp. 693–697.

Pierre, C., Ferri, A. A., and Dowell, E. H., 1985, "Multi-harmonic Analysis of Dry Friction Damped Systems Using an Incremental Harmonic Balance Method," ASME JOURNAL OF APPLIED MECHANICS, Vol. 52, pp. 958–964.

Shaw, S. W., and Holmes, P. J., 1983, "A periodically forced piecewise linear oscillator," *J. Sound and Vibration*, Vol. 90, No. 1, pp. 129–155.

Thompson, J. M. T., 1983, "Complex dynamics of compliant offshore structures," *Proc. R. Soc., London*, Vol. A387, pp. 407–427.

Timoshenko, S. P., Young, D. H., and Weaver, W., Jr., 1974, *Vibration Problems in Engineering*, 4th ed., John Wiley and Sons, New York.

Watanabe, K., and Sato, H., 1988, "Development of Nonlinear Building Block Approach," ASME *Journal of Vibration, Acoustics, Stress, Reliability in Design*, Vol. 110, pp. 36–41.

Wei, S. T., and Pierre, C., 1989, "Effects of dry friction damping on the occurrence of localized forced vibrations in nearly cyclic structures," *J. Sound and Vibration*, Vol. 129, No. 3, pp. 397–416.

Downloaded 03 May 2010 to 171.66.16.247. Redistribution subject to ASME license or copyright; see http://www.asme.org/terms/Terms_Use.cfm

Chaotic Dynamics of a Quasi-Periodically Forced Beam

K. Yagasaki
Department of Mechanical Engineering,
Tamagawa University,
Machida, Tokyo, 194, Japan

A straight beam with fixed ends, forced with two frequencies is considered. By using Galerkin's method, the equation of motion of the beam is reduced to a finite degree-of-freedom system. The resulting equation is transformed into a multi-frequency system and the averaging method is applied. It is shown, by using Melnikov's method, that there exist transverse homoclinic orbits in the averaged system associated with the first-mode equation. This implies that chaotic motions may occur in the single-mode equation. Furthermore, the effect of higher modes and the implications of this result for the full beam motions are described.

1 Introduction

In this paper, we study chaotic vibrations of a straight beam with fixed ends, excited by the quasi-periodic motion of its supporting base. The beam is initially tensioned by a small external load, N_0, and subjected to the gravitational force. The length and the thickness of the beam are denoted by l and h, respectively (see Fig. 1). The equation of motion of the beam is given by

$$EI\frac{\partial^4 u}{\partial x^4}-\frac{\partial}{\partial x}\left(\left[\frac{EA}{2l}\int_0^l\left(\frac{\partial u}{\partial x}\right)^2 dx+N_0\right]\frac{\partial u}{\partial x}\right) = -m\frac{\partial^2}{\partial t^2}\{u+z(t)\}-c\frac{\partial u}{\partial t}-mg, \quad (1)$$

where u is the transverse displacement of the beam relative to the base and $z(t)$ is the base motion. In Eq. (1), m is the mass per unit length, c is the damping constant, E is Young's modulus, I is the moment of inertia, A is the cross-section for the beam, and g is the acceleration of gravity. Boundary conditions are given by

$$u=\frac{\partial u}{\partial x}=0 \text{ at } x=0 \text{ and } l. \quad (2)$$

The quasi-periodic base motion is assumed to be of the form

$$z(t)=z_1\cos\bar{\nu}_1 t+z_2\cos\bar{\nu}_2 t. \quad (3)$$

The nonlinear vibrations of beams subjected to periodic excitation have been extensively studied (see Nayfeh and Mook, 1979, and references therein). In particular, Tseng and Dugundji (1970) experimentally and analytically studied harmonic, subharmonic, and superharmonic motions in a straight beam with fixed ends, such as is shown in Fig. 1. Furthermore, Tseng and Dugundji (1971) studied a buckled beam and found "chaotic snap-through" motions in numerical simulations and experiments. Subsequently, Holmes and Marsden (1981) generalized Melnikov's method (cf., Guckenheimer and Holmes, 1983) to a class of partial differential equations, and showed that the equation of motion of the buckled beam has transverse homoclinic orbits which are responsible for such chaotic motions. Moon and Holmes (1979) found similar chaotic motions in experiments with an elastic, ferromagnetic beam and obtained a criterion for the existence of chaotic motions in a single-mode Galerkin approximation using the standard Melnikov method. (See also Moon (1980) and Guckenheimer and Holmes (1983) for the last example.)

However, there has been little attention given to nonlinear vibrations of quasi-periodically forced beams. Moon and Holmes (1985) experimentally studied chaotic dynamics of a buckled beam forced with two frequencies. They utilized a double Poincaré section to expose the fractal nature of the strange attractor. Wiggins (1987) and Ide and Wiggins (1989) applied a version of Melnikov's method by Wiggins (1988) and showed that there exist transverse homoclinic tori yielding chaotic motions in a single-mode Galerkin approximation for the quasi-periodically forced buckled beam. To the author's knowledge, chaotic dynamics of periodically or quasi-periodically forced straight beams have not been reported.

This paper is organized as follows: In Section 2, the equation of motion (1) is reduced to a finite degree-of-freedom system by using Galerkin's method. The resulting equation is transformed into the form of multidimensional systems forced with multi-frequencies and the averaging method is applied. A necessary version of the averaging theorem is reviewed in Appendix A. In Section 3, chaotic dynamics of the single-mode equation is studied. The standard Melnikov method is applied to the associated averaged system and the existence of trans-

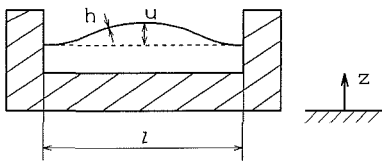

Fig. 1 The forced straight beam

Contributed by the Applied Mechanics Division of THE AMERICAN SOCIETY OF MECHANICAL ENGINEERS for publication in the JOURNAL OF APPLIED MECHANICS.

Discussion on this paper should be addressed to the Technical Editor, Prof. Leon M. Keer, The Technological Institute, Northwestern University, Evanston, IL 60208, and will be accepted until two months after final publication of the paper itself in the JOURNAL OF APPLIED MECHANICS. Manuscript received by the ASME Applied Mechanics Division, Apr. 3, 1990; final revision, Jan. 18, 1991.

Copyright © 1992 by ASME
Downloaded 03 May 2010 to 171.66.16.247. Redistribution subject to ASME license or copyright; see http://www.asme.org/terms/Terms_Use.cfm

verse homoclinic points is detected, as in Yagasaki et al. (1990) and Yagasaki (1990, 1991). Such points in the averaged system correspond to transverse homoclinic tori in the full system, which yield chaotic dynamics in the single-mode equation. Section 4 contains discussions of the effect of higher modes and the dynamics of the full beam equation when there exist transverse homoclinic orbits in the averaged system for the single-mode equation. A summary and some comments are given in Section 5.

2 The Modal Equations and Averaging

2.1 Galerkin's Method. We apply Galerkin's method to (1). The solution of the partial differential Eq. (1) is assumed to be of the form

$$u(x,\,t)=\sum_{i=1}^{N}\bar{a}_i(t)\phi_i\left(\frac{x}{l}\right), \tag{4}$$

where $\phi_i(\xi)$ is the ith normal modes of the associated linear problem without external tension and given by

$$\phi_i(\xi)=\frac{\cos\lambda_i-\cosh\lambda_i}{\sin\lambda_i-\sinh\lambda_i}\{\sin(\lambda_i\xi)-\sinh(\lambda_i\xi)\}-\{\cos(\lambda_i\xi)-\cosh(\lambda_i\xi)\}, \tag{5}$$

and $\lambda_i>0$ is the ith positive root of the transcendental equation $\cos\lambda\cosh\lambda-1=0$. Note that $\phi_i(\xi)$, $i=1,\,2,\,\cdots$, satisfy the orthonormal conditions

$$\int_0^1\phi_i(\xi)\phi_j(\xi)d\xi=\delta_{ij}, \tag{6}$$

where δ_{ij} is the Kronecker delta. Since the external tension load N_0 is assumed to be small, we used the zero tension modal functions in (4).

Substituting (4) into (1) and taking the inner product with $\phi_n(x/l)$, $n=1,\,2,\,\cdots,\,N$, one obtains a finite set of second-order ordinary differential equations for the modal amplitudes $\bar{a}_n(t)$, $n=1,\,2,\,\cdots,\,N$, as follows:

$$\ddot{\bar{a}}_n+\bar{\delta}\,\dot{\bar{a}}_n+\bar{\omega}_n^2\bar{a}_n+\sum_{k,i,j=1}^{N}\bar{A}_{ijkn}\bar{a}_i\bar{a}_j\bar{a}_k+\sum_{k\neq n}^{N}\bar{B}_{kn}\bar{a}_k=\bar{\gamma}_n\cos\bar{\nu}_1t+\bar{\beta}_n\cos\bar{\nu}_2t-\bar{\eta}_n,\ n=1,\,2,\,\cdots,\,N, \tag{7}$$

where

$$\bar{\delta}=c/m,\ \bar{\omega}_n^2=\frac{EI}{m}\left(\frac{\lambda_n}{l}\right)^4+\bar{B}_{nn}, \tag{8a}$$

$$\bar{\gamma}_n=\bar{\nu}_1^2z_1\Phi_n,\ \bar{\beta}_n=\bar{\nu}_2^2z_2\Phi_n,\ \bar{\eta}_n=g\Phi_n, \tag{8b}$$

$$\bar{A}_{ijkn}=\frac{EA}{2ml^4}\Psi_{ij}\Psi_{kn},\ \bar{B}_{kn}=\frac{N_0}{ml^2}\Psi_{kn}, \tag{8c}$$

$$\Phi_n=\int_0^1\phi_n(\xi)d\xi, \tag{9a}$$

$$\Psi_{kn}=\int_0^1\phi_k'(\xi)\phi_n'(\xi)d\xi=-\int_0^1\phi_k''(\xi)\phi_n(\xi)d\xi. \tag{9b}$$

Note that $\bar{B}_{kn}$, $k,\,n=1,\,\cdots,\,N$, are small parameters since N_0 is small.

2.2 Averaging. As in Yagasaki et al. (1990) and Yagasaki (1991), we introduced two small parameters ϵ and μ, such that $0<\epsilon\ll\mu\ll1$. We consider the case in which the base motion $z(t)$ is small. Hence, the modal amplitudes $\bar{a}_n(t)$, $n=1,\,\cdots,\,N$, are also small. Moreover, it is assumed that the effects of gravitation, tension, and damping are small, and the forcing amplitude z_1 at the frequency $\bar{\nu}_1$ is greater than the forcing amplitude z_2 at the frequency $\bar{\nu}_2$. Specifically, we assume that

$$\frac{\bar{a}_n(t)}{h}=O(\sqrt{\epsilon}),\ \frac{z_1}{h}=O(\epsilon^{3/2}),\ \frac{z_2}{h}=O(\epsilon^{3/2}\mu),\ \frac{g}{h\bar{\omega}_1^2}=O(\epsilon^{3/2}),\ \frac{N_0}{ml\bar{\omega}_1^2}=O(\epsilon),\ \frac{\bar{\delta}}{\bar{\omega}_1}=O(\epsilon\mu), \tag{10}$$

and set

$$\sqrt{\epsilon}a_n(t)=\frac{\bar{\omega}_0}{\bar{\omega}_1}\frac{\bar{a}_n(t)}{h},\ \epsilon^{3/2}\gamma_n=\frac{\bar{\omega}_0}{\bar{\omega}_1^3}\frac{\bar{\gamma}_n}{h},\ \mu\epsilon^{3/2}\beta_n=\frac{\bar{\omega}_0}{\bar{\omega}_1^3}\frac{\bar{\beta}_n}{h},\ \epsilon^{3/2}\eta_n=\frac{\bar{\omega}_0}{\bar{\omega}_1^3}\frac{\bar{\eta}_n}{h},\ \epsilon B_{kn}=\frac{\bar{B}_{kn}}{\bar{\omega}_1^2},\ \epsilon\mu\delta=\frac{\bar{\delta}}{\bar{\omega}_1}, \tag{11}$$

with $\bar{\omega}_0^2=(EI/m)\cdot(\lambda_1/l)^4$.

By rescaling the time variable as $t\to\bar{\omega}_1t$, Eq. (7) becomes

$$\ddot{a}_1+a_1=\epsilon\left\{\left(\gamma_1\cos\nu_1t-\eta_1-\sum_{k,i,j=1}^{N}A_{ijk1}a_ia_ja_k-\sum_{k\neq1}^{N}B_{k1}a_k\right)+\mu(\beta_1\cos\nu_2t-\delta\dot{a}_1)\right\}, \tag{12a}$$

$$\ddot{a}_n+\omega_n^2a_n=\epsilon\left\{\left(\gamma_n\cos\nu_1t-\eta_n-\sum_{k,i,j=1}^{N}A_{ijkn}a_ia_ja_k-\sum_{k\neq n}^{N}B_{kn}a_k\right)+\mu(\beta_n\cos\nu_2t-\delta\dot{a}_n)\right\},\ n=2,\,\cdots,\,N, \tag{12b}$$

where $\omega_n=\bar{\omega}_n/\bar{\omega}_1$, $n=2,\,\cdots,\,N$, $\nu_i=\bar{\nu}_i/\bar{\omega}_1$, $i=1,\,2$, and

$$A_{ijkn}=\left(\frac{h}{\bar{\omega}_0}\right)^2\bar{A}_{ijkn}=\frac{6\Psi_{ij}\Psi_{kn}}{\lambda_1^4}. \tag{13}$$

Henceforth, we denote $\omega_1=\nu_1$ for simplicity of notations.

We assume the resonance relationship $\nu_1\approx\nu_2\approx1$ so that

$$\nu_1^2-1=\epsilon\Omega,\ \nu_2-\nu_1=\epsilon\nu,\ \Omega,\ \nu=O(1). \tag{14}$$

This implies that the forcing frequencies $\bar{\nu}_1$, $\bar{\nu}_2$ are close to the first-mode frequency $\bar{\omega}_1$. It is also assumed that the higher modes are nonresonant and

$$|\omega_i-\omega_j|,\ |\omega_i-3\omega_j|,\ |\omega_i\pm\omega_j\pm2\omega_k|,\ |\omega_i\pm\omega_j\pm\omega_k\pm\omega_n|=O(1), \tag{15}$$

for all $i,\,j,\,k,\,n$ $(=1,\,\cdots,\,N)$ which are different from each other.

Using the transformation

$$J_n=\frac{\omega_n}{2}\left\{a_n^2+\left(\frac{\dot{a}_n}{\omega_n}\right)^2\right\},\ \psi_n=-\tan^{-1}\left(\frac{\dot{a}_n}{\omega_na_n}\right)-\omega_nt,\ n=1,\,\cdots,\,N, \tag{16}$$

or

$$a_n=\sqrt{2J_n/\omega_n}\cos(\omega_nt+\psi_n),\ \dot{a}_n=-\sqrt{2\omega_nJ_n}\sin(\omega_nt+\psi_n),\ n=1,\,\cdots,\,N, \tag{17}$$

and introducing the new state variable $\tau=\epsilon\nu t$, we obtain

$$\dot{J}_n=-\epsilon\{f_n(J_1,\,\cdots,\,J_N,\,\psi_1,\,\cdots,\,\psi_N,\,\omega_1t,\,\cdots,\,\omega_Nt)+\mu g_n(J_1,\,\cdots,\,J_N,\,\psi_1,\,\cdots,\,\psi_N,\,\omega_1t,\,\cdots,\,\omega_Nt,\,\tau)\}\times\sqrt{2J_n/\omega_n}\sin(\omega_nt+\psi_n), \tag{18a}$$

$$\dot{\psi}_n=-\epsilon\{f_n(J_1,\,\cdots,\,J_N,\,\psi_1,\,\cdots,\,\psi_N,\,\omega_1t,\,\cdots,\,\omega_Nt)+\mu g_n(J_1,\,\cdots,\,J_N,\,\psi_1,\,\cdots,\,\psi_N,\,\omega_1t,\,\cdots,\,\omega_Nt,\,\tau)\}\times\frac{1}{\sqrt{2\omega_nJ_n}}\cos(\omega_nt+\psi_n),\ n=1,\,\cdots,\,N, \tag{18b}$$

$$\dot{\tau}=\epsilon\nu, \tag{18c}$$

where

Downloaded 03 May 2010 to 171.66.16.247. Redistribution subject to ASME license or copyright; see http://www.asme.org/terms/Terms_Use.cfm

$$f_n(J_1, \cdots, J_N, \psi_1, \cdots, \psi_N, \omega_1 t, \cdots, \omega_N t)$$
$$= \delta_{1n}\Omega\sqrt{2J_n/\omega_n}\cos(\omega_n t + \psi_n) + \gamma_n \cos\omega_1 t - \eta_n$$
$$- 2\sqrt{2}\sum_{i,j,k=1}^{N} A_{ijkn}\left(\frac{J_i J_j J_k}{\omega_i\omega_j\omega_k}\right)^{1/2}\cos(\omega_i t + \psi_i)$$
$$\times \cos(\omega_j t + \psi_j)\cos(\omega_k t + \psi_k)$$
$$- \sum_{k\neq n}^{N} B_{kn}\sqrt{2J_k/\omega_k}\cos(\omega_k t + \psi_k), \quad (19a)$$

$$g_n(J_1, \cdots, J_N, \psi_1, \cdots, \psi_N, \omega_1 t, \cdots, \omega_N t, \tau)$$
$$= \beta_n(\cos\omega_1 t\cos\tau - \sin\omega_1 t\sin\tau) + \delta\sqrt{2\omega_n J_n}\sin(\omega_n t + \psi_n). \quad (19b)$$

Equation (18) is a $(2N+1)$-dimensional system forced with N nonresonant $O(1)$ frequencies. Holmes (1986) obtained a system similar to (18) for an N degree-of-freedom model of surface waves but overlooked the quasi-periodicity of the system.

We now apply a version of the averaging method for multi-frequency systems to (18). In Appendix A, we outline the method in the present context. (See Arnold et al. (1988), and Lochak and Meunier (1988) for the details on this version of the averaging theorem.)

Carrying out the averaging for (18), we obtain

$$\dot{J}_1 = \frac{\epsilon}{2}\{-\gamma_1\sqrt{2J_1}\sin\psi_1 + \mu[-2\delta J_1 + \beta_1\sqrt{2J_1}\sin(\tau - \psi_1)]\}, \quad (20a)$$

$$\dot{J}_n = \frac{\epsilon\mu}{2\omega_n}(-2\delta\omega_n J_n), \quad (20b)$$

$$\dot{\psi}_1 = \frac{\epsilon}{2}\left\{\left[-\Omega + \frac{3}{4}\sum_{k=1}^{N}\alpha_{1k}\left(\frac{2J_k}{\omega_k}\right) - \frac{\gamma_1\cos\psi_1}{\sqrt{2J_1}}\right] + \mu\left[-\frac{\beta_1}{\sqrt{2J_1}}\cos(\tau - \psi_1)\right]\right\}, \quad (20c)$$

$$\dot{\psi}_n = \frac{\epsilon}{2\omega_n}\left\{\frac{3}{4}\sum_{k=1}^{N}\alpha_{nk}\left(\frac{2J_k}{\omega_k}\right)\right\}, \quad n = 2, \cdots, N, \quad (20d)$$

$$\dot{\tau} = \epsilon\nu, \quad (20e)$$

where

$$\alpha_{nk} = \begin{cases} A_{nnnn}; & n = k, \\ \frac{4}{3}(A_{nkkn} + A_{knkn} + A_{kknn}); & n \neq k. \end{cases} \quad (21)$$

Here we used the relation $\omega_1 = \nu_1 = 1 + O(\epsilon)$ and neglected higher order terms of $O(\epsilon^2)$.

The averaging theorem (cf., Theorem A1 of Appendix A) implies that solutions of (18) are well approximated by solutions of (20). This fact plays an important role in the following sections.

3 Single-Mode Dynamics

In this section we study the chaotic dynamics of the single-mode equation. By setting $N=1$, Eq. (12) becomes

$$\ddot{a} + a = \epsilon\{(\gamma\cos\nu_1 t - \eta - \alpha^3) + \mu(\beta\cos\nu_2 t - \delta\dot{a}\}, \quad (22)$$

and the corresponding averaged system (18) becomes

$$\dot{J} = \frac{\epsilon}{2}\{-\gamma\sqrt{2J}\sin\psi + \mu[\beta\sqrt{2J}(\cos\psi\sin\tau - \sin\psi\cos\tau) - 2\delta J]\}, \quad (23a)$$

$$\dot{\psi} = \frac{\epsilon}{2}\left\{\left[-\Omega + \frac{3}{2}\alpha J - \frac{\gamma\cos\psi}{\sqrt{2J}}\right] + \mu\left[-\frac{\beta}{\sqrt{2J}}(\cos\psi\cos\tau + \sin\psi\sin\tau)\right], \quad (23b)$$

$$\dot{\tau} = \epsilon\nu. \quad (23c)$$

Here we abbreviated the subscripts of a_1, J_1, ψ_1, α_{11}, β_1, γ_1, and η_1. From (13) we see that the value of α is about 1.814 and the value used in Tseng and Dugundji (1970), which is $\alpha = 1.652$ in our notation, is incorrect.

Changing time variable $t \to \epsilon t/2$ in (23), we obtain

$$\dot{J} = \gamma\sqrt{2J}\sin\psi + \mu[\beta\sqrt{2J}(\cos\psi\sin\tau - \sin\psi\cos\tau) - 2\delta J], \quad (24a)$$

$$\dot{\psi} = \left[-\Omega + \frac{3}{2}\alpha J - \frac{\gamma\cos\psi}{\sqrt{2J}}\right] + \mu\left[-\frac{\beta}{\sqrt{2J}}(\cos\psi\cos\tau + \sin\psi\sin\tau)\right], \quad (24b)$$

$$\dot{\tau} = \nu_0, \quad (24c)$$

where $\nu_0 = 2\nu$. Let $\Sigma_a = \{(J, \psi, \tau) \mid \tau = 0\} \subset \mathbf{R}\times S^1 \times S^1$ be a global cross-section, where $S^1 = \mathbf{R}/2\pi$ is the circle of length 2π. Then, the Poincaré map generated by the flow of (24) is given by

$$F_\mu : \Sigma_a \to \Sigma_a, \ (J(0), \psi(0)) \to (J(T/2), \psi(T/2)), \quad (25)$$

where $(J(t), \psi(t))$ is a solution of system (24) and $T = 2\pi/\nu$ $(T/2 = 2\pi/\nu_0)$.

When $\mu = 0$, the (J,ψ) component of (24) becomes a completely integrable Hamiltonian system

$$\dot{J} = -\gamma\sqrt{2J}\sin\psi, \quad (26a)$$

$$\dot{\psi} = \left[-\Omega + \frac{3}{2}\alpha J - \frac{\gamma\cos\psi}{\sqrt{2J}}\right], \quad (26b)$$

with Hamiltonian

$$H(J, \psi) = -\Omega J + \frac{3}{4}\alpha J^2 - \gamma\sqrt{2J}\cos\psi. \quad (27)$$

If $\alpha > 0$, $\Omega > 0$, and $0 < \gamma < (4/9)(\Omega^3/\alpha)^{1/2}$, then there exist two centers $(J, \psi) = (j_1, \pi)$, $(j_3, 0)$ and a hyperbolic saddle (j_2, π), where $0 < j_1 < j_2 < j_3$ are roots of the cubic equation

$$x^3 - 2\left(\frac{2\Omega}{3\alpha}\right)x^2 + \left(\frac{2\Omega}{3\alpha}\right)^2 x - 2\left(\frac{\gamma}{3\alpha}\right)^2 = 0. \quad (28)$$

We denote these fixed points (j_1, π), (j_2, π), $(j_3, 0)$ by $\mathbf{p}_i$, $i = 1, 2, 3$. The level set

$$H(J, \psi) = H(j_2, \pi) \equiv H_0, \quad (29)$$

is composed of the fixed point $\mathbf{p}_2$ and two homoclinic orbits $\Gamma_\pm = (J_\pm(t), \psi_\pm(t))$ given by

$$J_\pm(t) = \pm\frac{2r_+ r_-}{(r_+ - r_-)\cosh at \pm (r_+ + r_-)} + j_2, \quad (30a)$$

$$\psi_\pm(t) = -\arcsin\left(\frac{\dot{J}_\pm(t)}{\gamma\sqrt{2J_\pm(t)}}\right), \quad (30b)$$

where $a = 3\alpha\sqrt{-r_+ r_-}/4$, $r_\pm = 2(\kappa \pm \sqrt{2\kappa j_2})$, and $\kappa = 2\Omega/3\alpha - j_2$. The phase portraits are shown in Fig. 2. Note that the phase space (J, ψ) is $\mathbf{R}\times S^1$, where $S^1 = \mathbf{R}/2\pi$ is the circle of length 2π. Thus, the unperturbed Poincaré map F_0 has a hyperbolic fixed point $\mathbf{p}_2$ whose stable and unstable manifolds $W^s(\mathbf{p}_2)$, $W^u(\mathbf{p}_2)$ are coincident.

For sufficiently small μ, F_μ still has a hyperbolic fixed point $\mathbf{p}_2^\mu = \mathbf{p}_2 + O(\mu)$, which corresponds to a hyperbolic periodic orbit of the averaged system (24). Moreover, its stable and unstable manifolds $W^s(\mathbf{p}_2^\mu)$, $W^u(\mathbf{p}_2^\mu)$ may intersect transversely. Using Melnikov's method, we compute the separation of these manifolds. The readers should consult Guckenheimer and Holmes (1983) and Wiggins (1988) for details and generalizations of the Melnikov method.

The distance between $W^s(\mathbf{p}_2^\mu)$ and $W^u(\mathbf{p}_2^\mu)$ near $(J_\pm(t_0), \psi_\pm(t_0))$ can be written as

$$d_\pm(t_0) = \mu K_\pm(t_0)^{-1} M_\pm(t_0) + O(\mu^2), \quad (31)$$

where the subscripts + and − indicate, respectively, the lower and upper branches of these invariant manifolds, $M_\pm(t_0)$ are

Downloaded 03 May 2010 to 171.66.16.247. Redistribution subject to ASME license or copyright; see http://www.asme.org/terms/Terms_Use.cfm

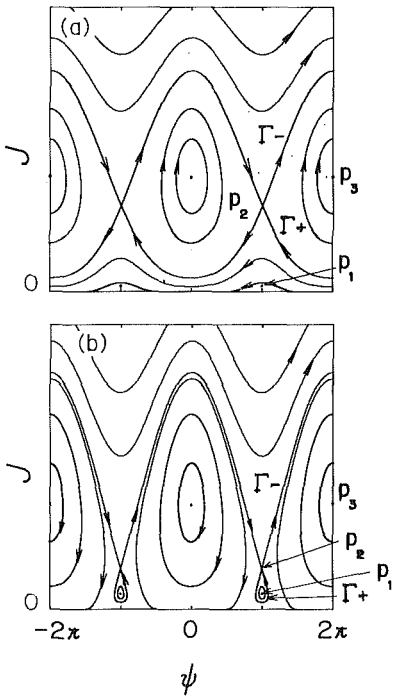

Fig. 2 Phase portraits of Eq. (26); (a) $0<\gamma<\frac{2}{9}\sqrt{\frac{2\Omega^3}{\alpha}}$, (b) $\frac{2}{9}\sqrt{\frac{2\Omega^3}{\alpha}}<\gamma<\frac{4}{9}\sqrt{\frac{\Omega^3}{\alpha}}$.

the Melnikov functions, and $K_\pm(t_0)$ are nonzero $O(1)$ quantities. In this case the Melnikov functions $M_\pm(t_0)$ are given by

$$M_\pm(t_0)=\int_{-\infty}^{\infty}\Bigg\{(-\gamma\sqrt{2J_\pm(t)}\sin\psi_\pm(t))\times\left(-\frac{\beta}{\sqrt{2J_\pm(t)}}\cos[\nu_0(t-t_0)-\psi_\pm(t)]\right)-\left[-\Omega+\frac{3}{2}\alpha J_\pm(t)-\frac{\gamma\cos\psi_\pm(t)}{\sqrt{2J_\pm(t)}}\right]\times(\beta\sqrt{2J_\pm(t)}\sin[\nu_0(t-t_0)-\psi_\pm(t)]-2\delta J_\pm(t))\Bigg\}dt. \quad (32)$$

Substituting (30) into (32) and evaluating the integrals, we obtain

$$M_\pm(\theta)=\beta A_\pm(\alpha,\gamma,\Omega,\nu_0)\sin\nu_0\theta\mp\delta B_\pm(\alpha,\gamma,\Omega), \quad (33)$$

where

$$A_\pm(\alpha,\gamma,\Omega,\nu_0)=\operatorname{cosech}\frac{4\pi\nu_0}{3\rho\alpha}\Bigg\{\mp\left(\frac{8\pi}{3\alpha\gamma}\nu_0^2+\frac{2\pi}{3\alpha\gamma}[3\rho\alpha\cot\theta_0-2(2\Omega-3\alpha j_2)]\nu_0+\frac{\pi}{6\alpha\gamma}[27\rho^2\alpha^2\cot^2\theta_0-18\rho\alpha(2\Omega-3\alpha j_2)\cot\theta_0-4(9\alpha\gamma\sqrt{2j_2}-2\Omega[2\Omega-3\alpha j_2])+9\rho^2\alpha^2]\right)\sinh\left(\frac{4}{3\rho\alpha}\nu_0\theta_0^\pm\right)+\left(\frac{8\pi}{3\alpha\gamma}\nu_0^2+\left[\frac{2\pi}{\alpha\gamma}(3\rho\alpha\cot\theta_0-2[2\Omega-3\alpha j_2])\right]\nu_0\right)\cosh\left(\frac{4}{3\rho\alpha}\nu_0\theta_0^\pm\right)\Bigg\}, \quad (34a)$$

$$B_\pm(\alpha,\gamma,\Omega)=\frac{16}{3\alpha}\left(\Omega\theta_0^\pm\mp\frac{9}{8}\rho\alpha\right), \quad (34b)$$

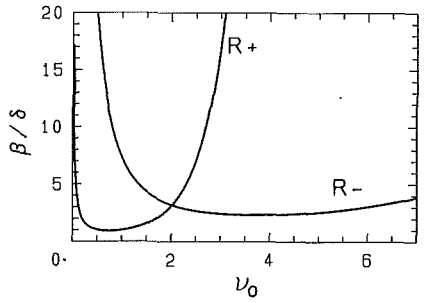

Fig. 3 Homoclinic bifurcation curves, $\alpha=1.814$, $\gamma=1.5$, $\Omega=3$

with

$$\theta_0=\arccos\left(\frac{r_++r_-}{r_+-r_-}\right),\ \theta_0^+=\theta_0,\ \theta_0^-=\pi-\theta_0,\qquad \rho=\sqrt{-r_+r_-}. \quad (35)$$

(See Appendix B for this calculation.) We note that θ_0, $\theta_0^\pm$, and ρ depend only on α, γ, and Ω.

It follows from (31) that if $M_\pm(t_0)$ have simple zeros, i.e.,

$$\frac{\beta}{\delta}>\left|\frac{B_\pm(\alpha,\gamma,\Omega)}{A_\pm(\alpha,\gamma,\Omega,\nu_0)}\right|\equiv R_\pm(\alpha,\gamma,\Omega,\nu_0), \quad (36)$$

then the lower and upper branches of $W^s(\mathbf{p}_2^\mu)$ and $W^u(\mathbf{p}_2^\mu)$ intersect transversely and there exist transverse homoclinic orbits which are homoclinic to $\mathbf{p}_2^\mu$. By the Smale-Birkhoff homoclinic theorem (cf., Guckenheimer and Holmes, 1983), the existence of such orbits implies that F_μ has an invariant set with a Cantor-type structure on which orbits correspond to realizations of a completely random process—coin tossing. Hence, if (36) is satisfied, then chaotic motions may exist in the averaged system (24). Figure 3 shows the homoclinic bifurcation curves $\beta/\delta=R_\pm(\alpha,\gamma,\Omega,\nu_0)$ in $\beta/\delta-\nu_0$ space for $\alpha=1.814$, $\gamma=1.5$, and $\Omega=3$.

As described in Yagasaki (1991), the existence of transverse homoclinic orbits in the averaged system also implies that chaotic motions may exist in the full system. This follows from the fact that solutions of the full system are well approximated by solutions of the averaged system. Also, the chaotic motions in the full system result from the existence of transverse homoclinic tori which correspond to transverse homoclinic points in the averaged system. Thus, condition (36) gives a criterion for the existence of chaotic motions in the full system (18) for $N=1$. Moreover, from (16) we see that $J(t)$ and $\psi(t)$ represent the slowly varying amplitude and phase. Hence, if condition (36) is satisfied, then the response of the single-mode system (22) indicates chaotic motions with randomlike modulations of the amplitude and phase (Yagasaki, 1991). (See also Yagasaki et al. (1990) and Yagasaki (1990).)

In the next section we describe the dynamical implications of the existence of transverse homoclinic orbits in the averaged system (23) for the multi-mode system (12) and the full beam equation (1).

4 Multi-Mode Dynamics and Full Beam Motions

We first discuss the dynamics of the multi-mode system (12). To this end, we define the Poincaré maps $\Phi_{\epsilon,\mu}$, $\bar{\Phi}_\mu$ associated with (18) and (20). The phase space is extended to $\mathbf{R}^N\times T^{2N+1}$, so that the systems (18) and (20) are, respectively, rewritten as

$$\dot{J}_n=-\epsilon\{f_n(J_1,\cdots,J_N,\psi_1,\cdots,\psi_N,\theta_1,\cdots,\theta_N)+\mu g_n(J_1,\cdots,J_N,\psi_1,\cdots,\psi_N,\theta_1,\cdots,\theta_N,\tau)\}\times\sqrt{2J_n/\omega_n}\sin(\omega_nt+\psi_n),\ n=1,\cdots,N. \quad (37a)$$

Downloaded 03 May 2010 to 171.66.16.247. Redistribution subject to ASME license or copyright; see http://www.asme.org/terms/Terms_Use.cfm

$$\dot{\psi}_n = -\epsilon\{f_n(J_1, \cdots, J_N, \psi_1, \cdots, \psi_N, \theta_1, \cdots, \theta_N) + \mu g_n(J_1, \cdots, J_N, \psi_1, \cdots, \psi_N, \theta_1, \cdots, \theta_N, \tau)\} \times \frac{1}{\sqrt{2\omega_n J_n}}\cos(\omega_n t + \psi_n),\ n=1, \cdots, N, \quad (37b)$$

$$\dot{\theta}_n = \omega_n,\ n=1, \cdots, N, \quad (37c)$$

$$\dot{\tau} = \epsilon\nu, \quad (37d)$$

and

$$\dot{J}_1 = \frac{\epsilon}{2}\{-\gamma_1\sqrt{2J_1}\sin\psi_1 + \mu[-2\delta J_1 + \beta_1\sqrt{2J_1}\sin(\psi_1 - \tau)]\}, \quad (38a)$$

$$\dot{J}_n = \frac{\epsilon\mu}{2\omega_n}(-2\delta\omega_n J_n),\ n=2, \cdots, N, \quad (38b)$$

$$\dot{\psi}_1 = \frac{\epsilon}{2}\left\{\left[-\Omega + \frac{3}{4}\sum_{k=1}^{N}\alpha_{1k}\left(\frac{2J_k}{\omega_k}\right) - \frac{\gamma_1\cos\psi_1}{\sqrt{2J_1}}\right] + \mu\left[-\frac{\beta_1}{\sqrt{2J_1}}\cos(\psi_1 - \tau)\right]\right., \quad (38c)$$

$$\dot{\psi}_n = \frac{\epsilon}{2\omega_n}\left\{\frac{3}{4}\sum_{k=1}^{N}\alpha_{nk}\left(\frac{2J_k}{\omega_k}\right)\right\},\ n=2, \cdots, N, \quad (38d)$$

$$\theta_n = \omega_n,\ n=1, \cdots, N, \quad (38e)$$

$$\dot{\tau} = \epsilon\nu, \quad (38f)$$

where $T^{2N+1} = S^1 \times \cdots \times S^1$ is a $2N+1$-dimensional torus. We define the global cross-section as

$$\Sigma = \{(J_1, \cdots, J_N, \psi_1, \cdots, \psi_N, \theta_1, \cdots, \theta_N, \tau) \in \mathbf{R}^N \times T^{2N+1} | \tau = 0\}. \quad (39)$$

The Poincaré maps $\Phi_{\epsilon,\mu}, \overline{\Phi}_\mu : \Sigma \to \Sigma$ for the flows of (37) and (38) are then given by

$$\Phi_{\epsilon,\mu}, \overline{\Phi}_\mu;\ (J_1(0), \cdots, J_N(0), \psi_1(0), \cdots, \psi_N(0), \theta_1, \cdots, \theta_N) \to (J_1(T/\epsilon), \cdots, J_N(T/\epsilon), \psi_1(T/\epsilon), \cdots, \psi_N(T/\epsilon), \theta_1 + \omega_1 T/\epsilon, \cdots, \theta_N + \omega_N T/\epsilon), \quad (40)$$

where $(J_n(t), \psi_n(t))$, $n=1, \cdots, N$, represents a solution of (18) or (20). It follows from the averaging theorem that $\Phi_{\epsilon,\mu}$ is well approximated by $\overline{\Phi}_\mu$ as

$$\Phi_{\epsilon,\mu} = \overline{\Phi}_\mu + O(\epsilon), \quad (41)$$

(see Eq. (A7) in Appendix A).

Suppose condition (36) is met and the stable and unstable manifolds $W^s(\mathbf{p}_2^\mu)$, $W^u(\mathbf{p}_2^\mu)$ of the hyperbolic fixed point $\mathbf{p}_2^\mu$ for the Poincaré map F_μ of (24) intersect transversely, that is, there exist transverse homoclinic orbits in the averaged system (23) for the single-mode Eq. (22). By denoting $\mathbf{p}_2^\mu = (J_0^\mu, \psi_0^\mu)$, the $(2N-1)$-dimensional torus

$$\overline{T}_\mu = \{(J_1, J_2, \cdots, J_N, \psi_1, \cdots, \psi_N, \theta_1, \cdots, \theta_N) | J_1 = J_0^\mu, \psi_1 = \psi_0^\mu, J_i = 0, i=2, \cdots, N\}, = (J_0^\mu, 0, \cdots, 0, \psi_0^\mu) \times T^{2N-1}, \quad (42)$$

is invariant by the Poincaré map $\overline{\Phi}_\mu$ of (38). This invariant torus $\overline{T}_\mu$ is normally hyperbolic since the linearized map $D\overline{\Phi}_\mu$ at $\overline{T}_\mu$ expands or contracts vectors normal to $\overline{T}_\mu$ but does not expand nor contract vectors tangent to $\overline{T}_\mu$. Moreover, $\overline{T}_\mu$ has a $(3N-1)$-dimensional stable manifold $W^s(\overline{T}_\mu)$ and a $2N$-dimensional unstable manifold $W^u(\overline{T}_\mu)$ that intersect transversely in a torus and there exist transverse homoclinic tori. (See Fig. 4.)

In this situation it is shown by the invariant manifolds theorem (Hirsch et al., 1977) that the Poincaré map $\Phi_{\epsilon,\mu} = \overline{\Phi}_\mu + O(\epsilon)$ of (37) has a $(2N-1)$-dimensional normally hyperbolic invariant torus $T_{\epsilon,\mu}$ near $\overline{T}_\mu$. Moreover, the $(3N-1)$-dimensional stable manifold $W^s(T_{\epsilon,\mu})$ and the $2N$-dimensional unstable manifold $W^u(T_{\epsilon,\mu})$ of $T_{\epsilon,\mu}$ intersect transversely in a torus since they are $O(\epsilon)$ close to $W^s(\overline{T}_\mu)$ and $W^u(\overline{T}_\mu)$ and the splitting distance between $W^s(\overline{T}_\mu)$ and $W^u(\overline{T}_\mu)$ is $O(\mu)$. Hence, there exist transverse homoclinic tori, and by a generalization of the Smale-Birkhoff homoclinic theorem due to Wiggins (1988), $\Phi_{\epsilon,\mu}$ has an invariant Cantor set of tori on which the dynamics of $\Phi_{\epsilon,\mu}$ is "Smale horseshoe-like" and chaotic. Thus, chaotic dynamics may occur in the system (18). It follows from the transformation (17) that chaotic motions with slowly but randomly varying amplitudes and phases may exist in the multi-mode system (12).

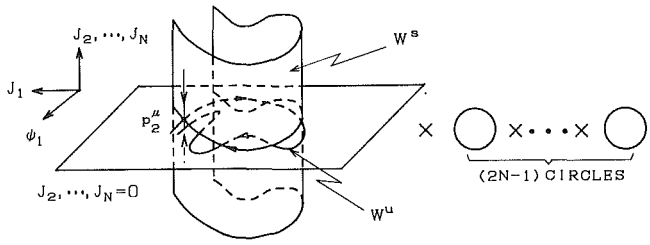

Fig. 4 Manifold structure in the space $(J_1, \cdots, J_N, \psi_1, \cdots, \psi_N, \theta_1, \cdots, \theta_N)$

We now turn to the full beam dynamics. The above result holds for arbitrary N. Furthermore, solutions of the Galerkin approximations (7) converge to solutions of the full partial differential Eq. (1) (cf., Proposition 2.13 of Holmes and Marsden, 1978). Hence, Eq. (36) also gives a criterion for the existence of chaotic dynamics in the beam motion. In particular, since all modes but the first remain small owing to the presence of the damping terms $-\epsilon\mu\delta J_n$ in (20b), chaotic motions of the beam are dominated by the first-mode dynamics. The precise description of chaotic dynamics of the beam requires more delicate treatments similar to those of Holmes and Marsden (1981).

5 Conclusions

Chaotic vibrations of a straight beam forced with two frequencies has been studied. It was shown, by using the averaging method and Melnikov's technique, that chaos may occur in both the single and multi-mode Galerkin approximations. These chaotic motions result from the presence of orbits homoclinic to normally hyperbolic invariant tori. It also followed from this result that there may exist chaotic motions of the beam which involve primarily the first mode.

Chaotic dynamics can occur not only in strongly nonlinear systems, but also weakly nonlinear systems. Holmes (1986) showed that there exist chaotic motions of the Smale horseshoe type in a weakly nonlinear model of surface waves in vertically excited containers. (See Simonelli and Gollub (1989) and references therein for other theoretical and experimental works of this example.) Johnson and Bajaj (1989) also observed chaotic motions in numerical integrations of a two degree-of-freedom system associated with a periodically forced, stretched string. The model considered here provides another example of physical systems with weak nonlinearity in which chaotic motions may occur. In the forthcoming paper we will report experimental results for chaotic dynamics of this model.

References

Arnold, V. I., Kozlov, V. V., and Neishtadt, A. I., 1988, "Mathematical Aspects of Classical and Celestial Mechanics," *Dynamical Systems III*, V. I. Arnold, ed., Springer-Verlag, Berlin.

Guckenheimer, J., and Holmes, P. J., 1983, *Nonlinear Oscillations, Dynamical Systems, and Bifurcations of Vector Fields*, Springer-Verlag, New York.

Hirsch, M. W., Pugh, C. C., and Shub, M., 1977, *Invariant Manifolds*, (Lecture Notes in Mathematics, No. 583), Springer-Verlag, New York.

Holmes, P. J., 1986, "Chaotic Motions in a Weakly Nonlinear Model for Surface Waves," *Journal of Fluid Mechanics*, Vol. 162, pp. 365-388.

Downloaded 03 May 2010 to 171.66.16.247. Redistribution subject to ASME license or copyright; see http://www.asme.org/terms/Terms_Use.cfm

Holmes, P. J., and Marsden, J., 1978, "Bifurcation to Divergence and Flutter in Flow-induced Oscillations: An Infinite Dimensional Analysis," *Automatica*, Vol. 14, pp. 367–384.

Holmes, P. J., and Marsden, J., 1981, "A Partial Differential Equation with Infinitely Many Periodic Orbits: Chaotic Oscillations of a Forced Beam," *Archives for Rational Mechanics and Analysis*, Vol. 76, pp. 135–165.

Ide, K., and Wiggins, S., 1989, "The Bifurcation to Homoclinic Tori in the Quasiperiodically Forced Duffing Oscillator," *Physica D*, Vol. 34, pp. 169–182.

Johnson, J. M., and Bajaj, A. K., 1989, "Amplitude Modulated and Chaotic Dynamics in Resonant Motion of Strings," *Journal of Sound and Vibration*, Vol. 128, pp. 87–107.

Lochak, P., and Meunier, C., 1988, *Multiphase Averaging for Classical Systems, With Applications to Adiabatic Theorems*, Springer-Verlag, New York.

Moon, F. C., 1980, "Experiments on Chaotic Motions of a Forced Nonlinear Oscillator: Strange Attractors," ASME JOURNAL OF APPLIED MECHANICS, Vol. 47, pp. 638–644.

Moon, F. C., and Holmes, P. J., 1979, "A Magnetoelastic Strange Attractor," *Journal of Sound and Vibration*, Vol. 65, pp. 275–296.

Moon, F., and Holmes, W. T., 1985, "Double Poincaré Sections of a Quasiperiodically Forced, Chaotic Attractor," *Physics Letters A*, Vol. 111, pp. 157–160.

Nayfeh, A. H., and Mook, D. T., 1979, *Nonlinear Oscillations*, John Wiley and Sons, New York.

Simonelli, F., and Gollub, J. P., 1989, "Surface Wave Mode Interactions: Effects of Symmetry and Degeneracy," *Journal of Fluid Mechanics*, Vol. 199, pp. 471–494.

Tseng, W. Y., and Dugundji, J., 1970, "Nonlinear Vibrations of a Beam Under Harmonic Excitation," ASME JOURNAL OF APPLIED MECHANICS, Vol. 37, pp. 292–297.

Tseng, W. Y., and Dugundji, J., 1971, "Nonlinear Vibrations of a Buckled Beam Under Harmonic Excitation," ASME JOURNAL OF APPLIED MECHANICS, Vol. 38, pp. 467–476.

Wiggins, S., 1987, "Chaos in the Quasiperiodically Forced Duffing Oscillator," *Physics Letters A*, Vol. 124, pp. 138–142.

Wiggins, S., 1988, *Global Bifurcations and Chaos—Analytical Methods*, Springer-Verlag, New York.

Yagasaki, K., 1990, "Second-order Averaging and Chaos in Quasiperiodically Forced Weakly Nonlinear Oscillators," *Physica D*, Vol. 44, pp. 445–458.

Yagasaki, K., 1991, "Chaos is a Weakly Nonlinear Oscillator With Parametric and External Resonances," ASME JOURNAL OF APPLIED MECHANICS, Vol. 58, pp. 244–250.

Yagasaki, K., Sakata, M., and Kimura, K., 1990, "Dynamics of a Weakly Nonlinear System Subjected to Combined Parametric and External Excitation," ASME JOURNAL OF APPLIED MECHANICS, Vol. 57, pp. 209–217.

APPENDIX A

The Averaging Theorem for Multi-Frequency Systems

We consider systems of the form

$$\dot{\mathbf{x}} = \epsilon \mathbf{f}(\mathbf{x}, \omega_1 t, \cdots, \omega_N t), \ \mathbf{x} \in \mathbf{R}^n, \ 0 < \epsilon \ll 1, \tag{A1}$$

where $\mathbf{f}(\mathbf{x}, \theta_1, \cdots, \theta_N) \in \mathbf{R}^n$ is 2π-periodic in each of θ_i, $i = 1, \cdots, N$, and analytic in all the arguments. The associated averaged system is defined as

$$\dot{\mathbf{y}} = \epsilon \bar{\mathbf{f}}(\mathbf{y}), \tag{A2}$$

where

$$\bar{\mathbf{f}}(\mathbf{y}) = \frac{1}{(2\pi)^N} \int_0^{2\pi} \cdots \int_0^{2\pi} \mathbf{f}(\mathbf{y}, \theta_1, \cdots, \theta_N) d\theta_1 \cdots d\theta_N. \tag{A3}$$

In this situation we have:

Theorem A1. Suppose the components of the frequency vectors $\omega = (\omega_1, \cdots, \omega_N)$ are strongly incommensurable, i.e., the following inequality holds for all vectors $\mathbf{k} = (k_1, \cdots, k_N) \neq 0$ with integer components:

$$|(\mathbf{k}, \omega)| > c^{-1} |\mathbf{k}|^{-\nu}, \tag{A4}$$

where $(\mathbf{k}, \omega) = k_1\omega_1 + \cdots + k_N\omega_N$ is an inner product of $\mathbf{k}$ and ω, $|\mathbf{k}| = \sqrt{(\mathbf{k}, \mathbf{k})}$, and c and ν are positive constants. Then, there exists a change of coordinates

$$\mathbf{x} = \mathbf{y} + \epsilon \mathbf{w}(\mathbf{y}, \omega_1 t, \cdots, \omega_N t), \tag{A5}$$

under which Eq. (A1) becomes

$$\dot{\mathbf{y}} = \epsilon \bar{\mathbf{f}}(\mathbf{y}) + O(\epsilon^2), \tag{A6}$$

where the $O(\epsilon^2)$ remainder term is quasi-periodic in t with N frequencies $\omega_1, \cdots, \omega_N$. Moreover, if $\mathbf{x}(t)$ and $\mathbf{y}(t)$ are, respectively, solutions of (A1) and (A2) with $\mathbf{x}(0) = \mathbf{y}(0) + O(\epsilon)$, then

$$|\mathbf{x}(t) - \mathbf{y}(t)| = O(\epsilon), \tag{A7}$$

on a time scale $t \sim 1/\epsilon$.

Sketch of Proof. Expanding $\mathbf{f}$ and $\mathbf{w}$ in Fourier series

$$\mathbf{f}(\mathbf{y}, \omega t) = \bar{\mathbf{f}}(\mathbf{y}) + \sum_{\mathbf{k} \neq 0} \mathbf{f}_{\mathbf{k}}(\mathbf{y}) e^{i(\mathbf{k}, \omega)t}, \tag{A8}$$

$$\mathbf{w}(\mathbf{y}, \omega t) = \sum_{\mathbf{k} \neq 0} \mathbf{w}_{\mathbf{k}}(\mathbf{y}) e^{i(\mathbf{k}, \omega)t}, \tag{A9}$$

and substituting (A8) and (A9) into (A1), we have

$$\dot{\mathbf{y}} = \epsilon \{ \bar{\mathbf{f}}(\mathbf{y}) + \sum_{\mathbf{k} \neq 0} [\mathbf{f}_{\mathbf{k}}(\mathbf{y}) - i(\mathbf{k}, \omega) \mathbf{w}_{\mathbf{k}}(\mathbf{y})] e^{i(\mathbf{k}, \omega)t} \} + O(\epsilon^2). \tag{A10}$$

By setting

$$\mathbf{w}_{\mathbf{k}}(\mathbf{y}) = \frac{1}{i(\mathbf{k}, \omega)} \mathbf{f}_{\mathbf{k}}(\mathbf{y}), \tag{A11}$$

Eq. (A6) is obtained. Here the strong incommensurability condition (A4) for frequencies was required in order that the Fourier series (A9) converges. Furthermore, the estimation (A7) is obtained by using Gronwall's lemma (cf. Guckenheimer and Holmes, 1983). (See Arnold et al. (1988) for the details of the proof.)

For some applications, the Fourier series (A8) for $\mathbf{f}(\mathbf{y}, \omega t)$ is finite, i.e.,

$$\mathbf{f}(\mathbf{y}, \omega t) = \bar{\mathbf{f}}(\mathbf{y}) + \sum_{j=1}^{m} \mathbf{f}_{k_j}(\mathbf{y}) e^{i(k_j, \omega)t}. \tag{A12}$$

Equation (18) gives such an example. In these cases, condition (A4) can be written as follows: The frequency vector ω satisfies

$$(\mathbf{k}_j, \omega) = O(1), \text{ for } j = 1, \cdots, m. \tag{A13}$$

Equation (15) represents condition (A13) for (18).

APPENDIX B

Calculation of the Melnikov Functions

By using the fact that $J_\pm(t)$, $\cos\psi_\pm(t)$ and $\cos\nu_0 t$ are even, and $\sin\psi_\pm(t)$ and $\sin\nu_0 t$ are odd, Eq. (32) becomes

$$\begin{aligned} M_\pm(t_0) = \beta \sin\nu_0 t_0 \Bigg\{ & \int_{-\infty}^{\infty} \Bigg[-\Omega \sqrt{2J_\pm(t)} \cos\psi_\pm(t) \\ & + \frac{3}{4} \alpha (2J_\pm(t))^{3/2} \cos\psi_\pm(t) - \gamma \Bigg] \cos\nu_0 t dt \\ & - \Omega \int_{-\infty}^{\infty} \sqrt{2J_\pm(t)} \sin\psi_\pm(t) \sin\nu_0 t dt \\ & + \frac{3}{4} \alpha \int_{-\infty}^{\infty} (2J_\pm(t))^{3/2} \sin\psi_\pm(t) \sin\nu_0 t dt \Bigg\} \\ \mp \delta \Bigg\{ \mp \int_{-\infty}^{\infty} 2 & \Bigg[-\Omega + \frac{3}{2} \alpha J_\pm(t) - \frac{\gamma \cos\psi_\pm(t)}{\sqrt{2J_\pm(t)}} \Bigg] J_\pm(t) dt \Bigg\} \\ & \equiv \beta \sin\nu_0 t_0 \cdot A_\pm \mp \delta B_\pm. \end{aligned} \tag{B1}$$

Since $H(j_2, \pi) = H(J_\pm(t), \psi_\pm(t)) = H_0$,

$$-\Omega j_2 + \frac{3\alpha}{4} j_2^2 + \gamma \sqrt{2j_2} = H_0, \tag{B2}$$

$$\cos\psi_\pm(t) = \frac{1}{\gamma \sqrt{2J_\pm(t)}} \left(-\Omega J_\pm(t) + \frac{3}{4} \alpha [J_\pm(t)]^2 - H_0 \right). \tag{B3}$$

Letting

Downloaded 03 May 2010 to 171.66.16.247. Redistribution subject to ASME license or copyright; see http://www.asme.org/terms/Terms_Use.cfm

$$I_{\pm}(t)=J_{\pm}(t)-j_2=\pm\frac{2r_+r_-}{(r_+-r_-)\cosh at\pm(r_++r_-)}, \quad \text{(B4)}$$

and using (B2) and (B3), we have

$$-\Omega\sqrt{2J_{\pm}(t)}\cos\psi_{\pm}(t)+\frac{3}{4}\alpha(2J_{\pm}(t))^{3/2}\cos\psi_{\pm}(t)-\gamma$$
$$=\frac{9\alpha^2}{8\gamma}[I_{\pm}(t)]^3-\frac{9\alpha}{8\gamma}(2\Omega-3\alpha j_2)[I_{\pm}(t)]^2$$
$$-\frac{1}{4\gamma}[9\alpha\gamma\sqrt{2j_2}-2\Omega(2\Omega-3\alpha j_2)]I_{\pm}(t). \quad \text{(B5)}$$

Using (B4) and (B5) and noting that $\dot{J}_{\pm}(t)=-\gamma\sqrt{2J_{\pm}(t)}\sin\psi_{\pm}(t)$, we obtain

$$A_{\pm}=\frac{9\alpha^2}{8\gamma}K_3^{\pm}-\frac{9\alpha}{8\gamma}(2\Omega-3\alpha j_2)K_2^{\pm}-\frac{1}{4\gamma}[9\alpha\gamma\sqrt{2j_2}$$
$$-2\Omega(2\Omega-3\alpha j_2)]K_1^{\pm}-\frac{3\alpha}{2\gamma}L_1^{\pm}+\frac{1}{2\gamma}(2\Omega-3\alpha j_2)L_0^{\pm}, \quad \text{(B6)}$$

where

$$K_n^{\pm}=\int_{-\infty}^{\infty}[I_{\pm}(t)]^n\cos\nu_0 t\,dt, \quad \text{(B7}a\text{)}$$

$$L_n^{\pm}=\int_{-\infty}^{\infty}[I_{\pm}(t)]^n\cdot\dot{I}_{\pm}(t)\sin\nu_0 t\,dt. \quad \text{(B7}b\text{)}$$

By substituting (B4) into (B7) and using the method of residues, the integrals $K_n^{\pm}$, $n=1, 2, 3$, and $L_n^{\pm}$, $n=0, 1$, are evaluated as follows:

$$K_1^{\pm}=\mp\frac{8\pi\sinh\nu_0'\theta_0^{\pm}}{3\alpha\sinh\pi\nu_0'}, \quad \text{(B8}a\text{)}$$

$$K_2^{\pm}=\frac{8\pi\rho}{3\alpha}\cdot\frac{\nu_0'\cosh\nu_0'\theta_0^{\pm}\mp\cot\theta_0\sinh\nu_0'\theta_0^{\pm}}{\sinh\pi\nu_0'}, \quad \text{(B8}b\text{)}$$

$$K_3^{\pm}=\mp\frac{4\pi\rho^2}{3\alpha}$$
$$\times\frac{(\nu_0'^2+3\cot^2\theta_0+1)\sinh\nu_0'\theta_0^{\pm}\mp3\nu_0'\cot\theta_0\cosh\nu_0'\theta_0^{\pm}}{\sinh\pi\nu_0'}, \quad \text{(B8}c\text{)}$$

$$L_0^{\pm}=\pm\frac{8\pi\nu_0\sinh\nu_0'\theta_0^{\pm}}{3\alpha\sinh\pi\nu_0'}, \quad \text{(B8}d\text{)}$$

$$L_1^{\pm}=-\frac{4\pi\rho\nu_0}{3\alpha}\cdot\frac{\nu_0'\cosh\nu_0'\theta_0^{\pm}\mp\cot\theta_0\sinh\nu_0'\theta_0^{\pm}}{\sinh\pi\nu_0'}, \quad \text{(B8}e\text{)}$$

where $\nu_0'=4\nu_0/3\rho\alpha$.

Substitution of (B8) into (B6) yields (34*a*).

To estimate $B_{\pm}$ in (B1), we change the variable from t to $I=J-j_2$ in the integral. By setting $I=I_{\pm}(t)$, $J=J_{\pm}(t)$ and $\psi=\psi_{\pm}(t)$, and using (B2) and (B3),

$$2\left[-\Omega+\frac{3}{2}\alpha J-\frac{\gamma\cos\psi}{\sqrt{2J}}\right]J=-\Omega J+\frac{9}{4}\alpha J^2+H_0$$
$$=-\Omega(I+j_2)+\frac{9}{4}(I+j_2)^2+(-\Omega j_2+\frac{3}{4}\alpha j_2^2+\gamma\sqrt{2j_2})$$
$$=\frac{9}{4}\alpha I^2+\left(\frac{9}{2}\alpha j_2-\Omega\right)I, \quad \text{(B9)}$$

$$\frac{dI}{dt}=\frac{dJ}{dt}=-\gamma\sqrt{2J}\sin\psi$$
$$=-\gamma\sqrt{2J}\cdot(\pm\sqrt{1-\cos^2\psi})$$
$$=\mp\sqrt{\gamma^2\cdot2J-\left(-\Omega J+\frac{3}{4}\alpha J^2-H_0\right)^2}$$
$$=\mp\frac{3}{4}\alpha|I|\sqrt{-(I-r_-)(I-r_+)}. \quad \text{(B10)}$$

Here we note that $dI_+/dt<0$ and $dI_-/dt>0$ when $t<0$; and $dI_+/dt>0$ and $dI_-/dt<0$ when $t>0$. Since $I_+<0$ and $I_->0$, we have

$$B_{\pm}=\pm\frac{4}{3\alpha}\left\{\frac{9}{4}\alpha\cdot2\int_{r_{\mp}}^{0}\frac{I\,dI}{\sqrt{-(I-r_-)(I-r_+)}}\right.$$
$$\left.+\left(\frac{9}{2}\alpha j_2-\Omega\right)\cdot2\int_{r_{\mp}}^{0}\frac{dI}{\sqrt{-(I-r_-)(I-r_+)}}\right\}. \quad \text{(B11)}$$

Evaluating the integrals in (B11), we can obtain (34*b*).

Downloaded 03 May 2010 to 171.66.16.247. Redistribution subject to ASME license or copyright; see http://www.asme.org/terms/Terms_Use.cfm

The Pseudo-Shakedown of Beams and Plates When Subjected to Repeated Dynamic Loads[1]

Wei Qin Shen[2]

Norman Jones
Fellow ASME.

Impact Research Centre,
Department of Mechanical Engineering,
The University of Liverpool,
Liverpool L69 3BX, U.K.

A conjecture is derived in this paper for the pseudo-shakedown phenomenon of beams and plates which strengthen with finite displacements when subjected to repeated dynamic transverse loads causing material plastic flow and permanent deflections. This behavior is illustrated for a fully clamped, rigid, perfectly plastic beam which is subjected to a repeatedly applied, rectangular-shaped pressure-time history at the midspan. It transpires that a curve divides the dynamic load magnitude-pulse duration time area into two regions where pseudo-shakedown may or may not occur. Another curve in the region where pseudo-shakedown does not occur identifies when the dynamic problem may be studied with a static analysis.

1 Introduction

The simplifying assumption of infinitesimal displacements is used in the classical shakedown theorems for quasi-static variable loads (Koiter, 1960), and in the shakedown theorems which include inertia and damping forces for variable repeated loadings applied rapidly to elastic-plastic structures (Ceradini, 1980 and Polizzotto, 1984). This assumption produces linear equilibrium and compatibility equations. The shakedown theorems for infinitesimal displacements and an elastic-plastic material use a "first-order" theory (Konig and Maier, 1981), in contrast to a "second-order" theory with geometric effects which has been used, for example, by Maier (1972) for quasi-static loads and by Corradi and De Donato (1975) for the dynamic case. However, linear equilibrium equations and strain-displacement relations are still used in the "second-order" theory for the moderate displacements of elastic-plastic structures. An extended version of Melan's theorem for small strains accompanied by finite displacements has been presented by Weichert (1984) for static loads.

In this paper, a special class of rigid, perfectly plastic structure is examined in which the end fixing of beams and the edge fixing of plates cause the structural stiffness to increase with an increase in the transverse displacements. This class of structure is subjected to a repeated load having a high intensity with a short duration which produces a response with moderate transverse displacements. The global collapse of the rigid, perfectly plastic structure occurs at the onset of loading and finite displacements are developed and grow for subsequent loadings so that the strain-displacement relations are nonlinear and the equilibrium equations are also nonlinear due to the increase of the membrane forces with transverse displacements. The deformation of a rigid, perfectly plastic structure always tends towards a permanent state. In some cases, to be defined later in this article, the final transverse displacement is reached after the first pressure pulse, and the structure then remains rigid for subsequent loading cycles. However, for other cases, the transverse displacements grow with each pressure pulse and tend towards a permanent state. This phenomenon is defined as pseudo-shakedown in this article and was introduced by Jones (1973) for this class of structure. Pseudo-shakedown has been observed in practice and good agreement between the theoretical rigid, perfectly plastic predictions (Jones, 1973) and the corresponding experimental results (Jones, 1977) was obtained for the repeated wave impact of ship bows, as shown in Fig. 1, where η is the dimensionless external load and $\overline{W}$ denotes the dimensionless maximum transverse displacement of the test models.

It is well known that finite displacements, or geometry changes, dominate the behavior of many structures when subjected to external loads which are larger than the associated static plastic collapse load for infinitesimal displacements (Jones, 1989a). This change in geometry leads to the development of in-plane membrane forces in initially flat plates and initially straight beams. In this circumstance, plastic flow is controlled by a yield condition which relates the influence of bending moments and membrane forces when assuming that plastic yield is not affected by transverse shear forces.

A unique pulse characteristic time τ^* associated with the pseudo-shakedown phenomenon is identified in this paper for

---

[1]A similar version of this paper was presented at the ASME Winter Annual Meeting, San Francisco, Dec. 1989, and published in *Recent Advances in Impact Dynamics of Engineering Structures*—1989, D. Hui and N. Jones, eds., AMD Vol. 105/AD Vol. 17, ASME, pp. 47–56.

[2]Royal Society Postdoctoral Visiting Scholar, Associate Professor, Shanghai Jiao Tong University, China.

Contributed by the Applied Mechanics Division of THE AMERICAN SOCIETY OF MECHANICAL ENGINEERS for publication in the JOURNAL OF APPLIED MECHANICS.

Discussion on this paper should be addressed to the technical Editor, Prof. Leon M. Keer, The Technological Institute, Northwestern University, Evanston, IL 60208, and will be accepted until two months after final publication of the paper itself in the JOURNAL OF APPLIED MECHANICS. Manuscript received by the ASME Applied Mechanics Division, Feb. 26, 1990; final revision, Oct. 10, 1990.

Copyright © 1992 by ASME
Downloaded 03 May 2010 to 171.66.16.247. Redistribution subject to ASME license or copyright; see http://www.asme.org/terms/Terms_Use.cfm

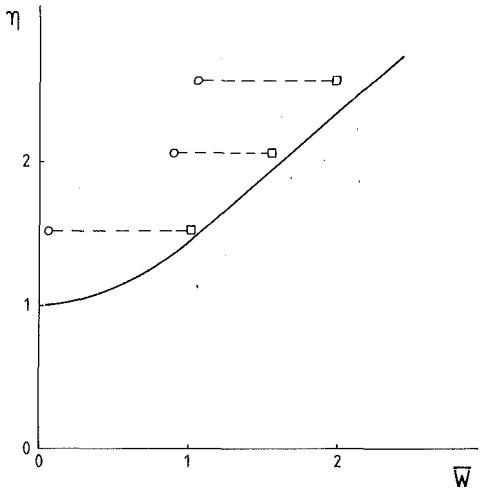

Fig. 1 Damage of ship bow rectangular plate models; ○: after first impact (Jones, 1977 and Yuhara, 1975); □: after sufficient number of identical repeated impacts (Jones, 1977 and Yuhara, 1975) (saturated or pseudo-shakedown condition); ———: quasi-static analysis for a rigid, perfectly plastic rectangular plate (Jones, 1977)

a given structure[3] and type of pressure loading. For pulse characteristic times $\tau < \tau^*$, the transverse deflection acquired by a structure during the first pressure loading-unloading cycle is smaller than that predicted by an analysis with the same peak pressure applied statically[4]. Thus, the transverse deflections of the structure increase during subsequent identical pressure loading cycles and tend towards the corresponding quasi-static value. This phenomenon is defined as pseudo-shakedown (Jones, 1973).

For pulse characteristic times $\tau \geq \tau^*$, the transverse deflection produced during the first pressure loading cycle is equal to, or larger than, that predicted by a quasi-static analysis which retains finite-displacement effects. Thus, the final deformed shape of a structure is reached during the initial dynamic pressure loading cycle. No further plastic deformations occur for subsequent repetitions of the same dynamic pressure loading cycle, provided reversed plastic yielding does not occur.

For convenience, the approximate rigid, perfectly plastic theoretical procedure, developed by Sawczuk (1964), Jones (1971), and Jones and Walters (1971) for the static and dynamic finite-displacement behavior of beams and plates, is summarized and discussed in the next section. The observations on the behavior of beams and plates are then used in Section 3 to obtain a conjecture on the pseudo-shakedown behavior of structures, while bound curves for pseudo-shakedown are introduced in Section 4.

2 Plastic Behavior of Beams and Plates Subjected to Static Transverse Loads

A rigid, perfectly plastic material is used in this section in order to simplify the analyses and clarify the main features of the pseudo-shakedown phenomenon.

It was shown (Jones, 1989a; Sawczuk, 1964; Jones, 1971; Jones and Walters, 1971) for a statically loaded, initially flat, rigid perfectly plastic plate, which deforms into a number of rigid regions separated by n straight line plastic hinges, each of length l_m, that

[3]The pseudo-shakedown phenomenon is examined only for beams and plates in this paper.

[4]It is assumed that the transverse displacement profiles in both cases are the same.

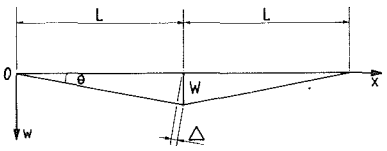

Fig. 2 Transverse displacement profile

$$\int_A^{\cdot} p\dot{w}dA = \sum_{m=1}^{n} \int_{l_m} (M+Nw)\dot{\theta}_m dl_m, \tag{1}$$

where p, w, $\dot{w}$, $\dot{\theta}_m$, M, and N are the external pressure, transverse displacement, transverse velocity, angular velocity, bending moment and membrane force (per unit length for plates), respectively. Equation (1) is simply a statement of energy conservation and a physical derivation of Eq. (1) is presented by Jones (1989a), while Taya and Mura (1974) have recovered this equation using a variational method.

The yield condition relating the bending moment M and the membrane force N in Eq. (1) for the plastic deformation of a rectangular-shaped cross-section is taken as

$$\frac{M}{M_o} + \left(\frac{N}{N_o}\right)^2 = 1, \tag{2}$$

where M_o and N_o are the fully plastic bending moment and membrane force, respectively. It may be shown, for a simply-supported beam, that

$$\theta \cong \frac{W}{L} \tag{3a}$$

and

$$\Delta \cong \frac{W^2}{2L} \tag{3b}$$

when using the transverse displacement profile shown in Fig. 2, and neglecting all the higher order terms for moderate deformations, where W and L are maximum transverse displacement and half length of a beam or plate, θ and Δ denote angular rotation of a beam with respect to a support and change in half-length of beam centreline, as shown in Fig. 2, respectively.

It is straightforward to show, when using the normality relation of plasticity for generalized stresses and generalized strain rates, that

$$\frac{N}{N_o} = 2\overline{W}, \qquad \overline{W} \leqq \frac{1}{2} \tag{4a}$$

$$\frac{N}{N_o} = 1, \qquad \overline{W} > \frac{1}{2}, \tag{4b}$$

where $\overline{W} = W/H$ and H is the thickness of a beam or plate, for a rigid, perfectly plastic beam with simply-supported boundary conditions. Similarly, using $\Delta \cong W^2/4L$, gives

$$\frac{N}{N_o} = \overline{W}, \qquad \overline{W} \leqq 1 \tag{5a}$$

and

$$\frac{N}{N_o} = 1, \qquad \overline{W} > 1 \tag{5b}$$

for fully clamped boundary conditions at the supports.

Equations (1), (2), and (4), together with $w = Wx/L$ for $0 \leqq x \leqq L$ from Fig. 2, give the static load displacement relations

$$\eta_s = 1 + 4\overline{W}_s^2, \qquad \overline{W}_s \leqq \frac{1}{2} \tag{6a}$$

and

$$\eta_s = 4\overline{W}_s \qquad \overline{W}_s > \frac{1}{2} \tag{6b}$$

Downloaded 03 May 2010 to 171.66.16.247. Redistribution subject to ASME license or copyright; see http://www.asme.org/terms/Terms_Use.cfm

for simply-supported beams subjected to either a concentrated load at the midspan with a static plastic collapse load $P_c = 2M_o/L$ or a pressure distributed uniformly over the entire span with a static plastic collapse pressure $p_c = 2M_o/L^2$, where $\eta_s = P_s/P_c$ (or $\eta_s = p_s/p_c$), $M_o = \sigma_o BH^2/4$, B is the width of a beam or half width of a rectangular plate, and σ_o denotes the uniaxial yield stress. Similarly, for beams which are fully clamped at both supports, then

$$\eta_s = 1 + \overline{W}_s^2, \qquad \overline{W}_s \leqq 1 \tag{7a}$$

and

$$\eta_s = 2\overline{W}_s, \qquad \overline{W}_s > 1, \tag{7b}$$

where $P_c = 4\,M_o/L$ for a concentrated load at the midspan and $p_c = 4M_o/L^2$ for a uniform pressure.

It may be shown that Eq. (1), for a simply-supported rectangular plate when subjected to a uniformly distributed pressure, which is assumed to produce a roof-shaped transverse displacement profile (see Fig. 7.13 (Jones, 1989a)), gives

$$\eta_s = 1 + 4\{\zeta_o + (3-2\zeta_o)^2\}\overline{W}_s^2/3(3-\zeta_o), \quad \overline{W}_s \leqq \frac{1}{2} \tag{8a}$$

and

$$\eta_s = 4\overline{W}_s\{1 + \zeta_o(2-\zeta_o)(1/12\overline{W}_s^2 - 1)/(3-\zeta_o)\}, \quad \overline{W}_s > \frac{1}{2} \tag{8b}$$

where

$$p_c = 6M_o/(B^2\tan^2\phi),$$
$$\zeta_o = \beta\tan\phi, \qquad \beta = B/L,$$
$$\tan\phi = \sqrt{3+\beta^2} - \beta \text{ and } M_o = \sigma_o H^2/4.$$

The same theoretical procedure using Eq. (1) for a fully clamped rectangular plate subjected to a uniformly distributed pressure predicts that

$$\eta_s = 1 + \{\zeta_o + (3-2\zeta_o)^2\}\,\overline{W}_s^2/3(3-\zeta_o), \quad \overline{W}_s \leqq 1 \tag{9a}$$

and

$$\eta_s = 2\overline{W}_s\{1 + \zeta_o(2-\zeta_o)(1/3\overline{W}_s^2 - 1)/(3-\zeta_o)\}, \quad \overline{W}_s > 1 \tag{9b}$$

where $p_c = 12M_o/(B^2\tan^2\phi)$. In the case of a circular plate, an additional integral for continuous deformation fields must be included on the right-hand side of Eq. (1), as noted by Jones (1989a). Equation (1) then gives

$$\eta_s = 1 + 4\overline{W}_s^2/3, \qquad \overline{W}_s \leqq \frac{1}{2} \tag{10a}$$

and

$$\eta_s = 2\overline{W}_s + 1/6\overline{W}_s, \qquad \overline{W}_s > \frac{1}{2} \tag{10b}$$

where $p_c = 6M_o/\{b^2(3-2b/R)\}$ for simply-supported circular plates of radius R without radial restraint under a pressure distributed uniformly within a central circular zone of radius b, which is assumed to produce a conical-shaped transverse displacement profile (see Fig. 7.11(b) (Jones, 1989a)).

It should be noted that the theoretical procedure used to obtain Eqs. (6)–(10) is an approximate method of analysis, as discussed by Jones (1971), Jones (1989a), and Jones and Walters (1971). However, the method has been used to predict the finite-deflection behavior of many beam and plate problems subjected to static or dynamic loads, and good agreement has been obtained with experimental results (Jones, 1975; Jones, 1976). It may be shown that the generalized stresses M and N, associated with Eqs. (6) and (7) for a beam subjected to a concentrated load, lie everywhere on or within the exact yield surface. Thus, the theoretical solutions are both kinematically admissible and statically admissible, and, therefore, are exact for this particular loading.

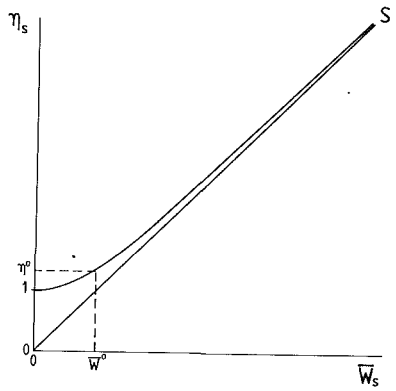

Fig. 3 η_S versus $\overline{W}_S$ and the asymptote OS

Equations (6) to (10) have the common dimensionless load-transverse displacement characteristics in Fig. 3, where $\overline{W}^o = 1/2$ and $\overline{W}^o = 1$ for the simply-supported and fully clamped cases, respectively, and where η^o and $\overline{W}^o$ relate to the transition from combined bending-tension behavior to pure membrane deformations.

Two common features emerge from Eqs. (6) to (10) and Fig. 3. One is the convexity of the curves, or

$$\frac{d^2\eta_s}{d\overline{W}_s^2} \geqq 0, \qquad \overline{W}_s \geqq 0. \tag{11}$$

The other is the existence of an asymptotic line OS which passes through the origin. The first expresses the strengthening effect of geometry changes for this class of structures, while the second corresponds to the membrane solution which disregards all bending effects.

3 A Conjecture on the Pseudo-Shakedown of Rigid, Perfectly Plastic Beams and Plates When Subjected to Repeated Dynamic Pressure Pulses

3.1 Statement of a Conjecture on Pseudo-Shakedown. Now, define $\overline{W}_1$ as the dimensionless maximum permanent transverse displacement of a beam or plate after the first impact event and $\overline{W}_{sm}$ as the corresponding value for the same peak pressure applied statically. Thus, by conjecture, $\overline{W}_1 < \overline{W}_{sm}$ is a necessary and sufficient condition for the pseudo-shakedown of rigid, perfectly plastic structures which strengthen with finite displacements when subjected to repeated dynamic pressure pulses. The cycle time for the repeated dynamic pressure pulse is assumed to be larger than or equal to the dynamic response time so that the structure is stationary when struck by a subsequent dynamic pressure pulse.

3.2 Proof of the Sufficient Condition. It is required to prove that when $\overline{W}_1 < \overline{W}_{sm}$, there exist $\overline{W}_i < \overline{W}_{sm}$ ($i = 2, 3, \ldots, \infty$) with $\lim_{i\to\infty} \overline{W}_i = \overline{W}_{sm}$. Figure 4 is an illustration of the sufficiency condition, which shows the structural response of an identical external dynamic loading cycle which is repeated indefinitely. If a rectangular-shaped pressure-time pulse with a peak value η_m is applied repeatedly to a structure, then $\overline{W}_1$ ($\overline{W}_1 < \overline{W}_{sm}$) is produced after the first impact so that the permanently deformed structure has been strengthened with an associated enhanced static collapse pressure $\eta_1 (1 < \eta_1 < \eta_m)$. Now, because $\eta_m > \eta_1$, the second impact causes a permanent displacement $\overline{W}_2 > \overline{W}_1$ with $\overline{W}_2 < \overline{W}_{sm}$, which gives an increased structural strength $\eta_2 > \eta_1$ and $\eta_2 < \eta_m$. The sufficiency condition implies that this process continues indefinitely with $\overline{W}_i < \overline{W}_{sm}$ and $\eta_i < \eta_m$, provided $\overline{W}_1 < \overline{W}_{sm}$.

If the influence of transverse inertia is retained in the gov-

Downloaded 03 May 2010 to 171.66.16.247. Redistribution subject to ASME license or copyright; see http://www.asme.org/terms/Terms_Use.cfm

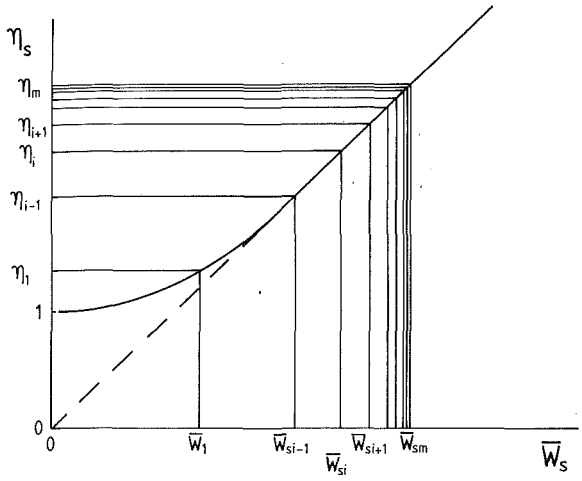

Fig. 4 Demonstration of the sufficiency condition

erning equations for beams and plates, then Eq. (1) becomes (Jones, 1971)

$$\int_A p\dot{w}dA - \int \mu\ddot{w}\dot{w}dA = \sum_{m=1}^{n} \int_{lm} (M+Nw)\dot{\theta}_m dl_m, \quad (12)^5$$

where μ is the mass per unit area of a plate and $\ddot{w}$ denotes transverse acceleration.

For a given pulse duration τ and a dimensionless peak pressure η_m, a rectangular-shaped pressure pulse will cause larger structural deformations than any other pressure pulse. In other words, $\overline{W}_1$ produced by a rectangular-shaped pressure-time history will be the largest among all values of $\overline{W}_1$ which would be produced by any other pressure pulse having the same duration τ and dimensionless peak value η_m. Thus, only a rectangular-shaped pressure-time history is considered in this paper. A rectangular-shaped pressure-time history can be written in the form

$$\eta = \eta_m, \qquad 0 \leqq t \leqq \tau \qquad (13a)$$

and

$$\eta = 0, \qquad t > \tau. \qquad (13b)$$

Equations (12) and (13*a*) give the following three kinds of differential equations:

$$\ddot{\overline{W}} + k_1\overline{W}^2 = k_2\eta - k_2, \quad \text{for} \quad \overline{W} \leqq \overline{W}^o \qquad (14a)$$

and

$$\ddot{\overline{W}} + k_3\overline{W} = k_4\eta, \quad \text{for} \quad \overline{W} > \overline{W}^o \qquad (14b)$$

or

$$\ddot{\overline{W}} + k_5\overline{W} + k_6/\overline{W} = k_7\eta, \quad \text{for} \quad \overline{W} > \overline{W}^o \qquad (14c)$$

which govern the response of initially flat plates and beams with $\eta = \eta_m$ when $0 \leqq t \leqq \tau$, and $\eta = 0$ for $t > \tau$, and where the constant coefficients $k_i > 0$ ($i = 1, 2, \ldots, 7$) are reported by Jones (1989a). Equations (6) to (10) may be recovered from Eqs. (14) when $\overline{W} = 0$ which allows k_i to be identified for the various cases.

Now, Eq. (14*b*) with $\ddot{\overline{W}} = 0$ gives

$$\eta_s = k_3\overline{W}_s/k_4, \qquad \overline{W}_s \geqq \overline{W}^o \qquad (15a)$$

for the dimensionless static pressure carrying capacity associated with a dimensionless permanent transverse displacement $\overline{W}_s$, which, for example, might have arisen from a dynamic pressure pulse. Similarly,

$$\overline{W}_{sm} = k_4\eta_m/k_3, \qquad \overline{W}_{sm} \geq \overline{W}^o \qquad (15b)$$

for the dimensionless permanent transverse displacement $\overline{W}_{sm}$ associated with the peak value of the dynamic pressure pulse η_m when applied statically.

Consider a structure with a dimensionless maximum permanent transverse displacement $\overline{W}_{i-1} \geqq W^o$ and $\overline{W}_{i-1} < \overline{W}_{sm}$ due to the $i-1$th dynamic pressure pulse loading which is characterized by Eqs. (13). The deformed structure requires a dimensionless pressure $\eta \geqq k_3\overline{W}_{i-1}/k_4$ in order to produce further plastic deformation according to Eq. (15*a*) when $\eta \leq \eta_m$. The structure with the initial conditions $\overline{W} = \overline{W}_{i-1}$ and $\dot{\overline{W}} = 0$ is then subjected to the ith dynamic pressure pulse described by Eq. (13*a*), so that Eq. (14*b*) with $\overline{W} \neq 0$ gives

$$\overline{W} = (\overline{W}_{i-1} - \overline{W}_{sm}) \cos\sqrt{k_3}t + \overline{W}_{sm}, \qquad 0 \leqq t \leqq \tau \qquad (16)$$

when using Eq. (15*b*). Equation (16), with time $t = \tau$, predicts the dimensionless transverse displacement

$$\overline{W}_{\tau i} = (\overline{W}_{i-1} - \overline{W}_{sm}) \cos\sqrt{k_3}\,\tau + \overline{W}_{sm}, \qquad (17a)$$

which can be recast in the form

$$\overline{W}_{\tau i} - \overline{W}_{i-1} = (\overline{W}_{sm} - \overline{W}_{i-1})(1 - \cos\sqrt{k_3}\,\tau). \qquad (17b)$$

The dimensionless external work of the dynamic pressure pulse having a constant dimensionless value η_m with a duration τ is

$$\eta_m(\overline{W}_{\tau i} - \overline{W}_{i-1}).$$

The dimensionless internal plastic energy dissipated in the same structure when subjected to a static loading having the same spatial distribution, which produces an identical time-independent transverse displacement profile, is

$$\int_{\overline{W}_{si-1}}^{\overline{W}_{si}} \eta_s d\overline{W}_s,$$

where $\overline{W}_{si-1} = \overline{W}_{i-1}$ and $\overline{W}_{si} = \overline{W}_i$. The variation of η_s with $\overline{W}_s$ is shown in Fig. 4, and $\overline{W}_i$ is the dimensionless permanent transverse displacement when motion ceases after the ith pressure loading. Thus, equating these two energies gives

$$\eta_m(\overline{W}_{\tau i} - \overline{W}_{i-1}) = \frac{k_3}{2k_4}(\overline{W}_i^2 - \overline{W}_{i-1}^2), \quad i = 2, \ldots, \infty, \qquad (18)$$

when using Eq. (15*a*).

Equations (17*b*) and (18) predict that

$$\frac{\overline{W}_i - \overline{W}_{i-1}}{\overline{W}_{sm} - \overline{W}_{i-1}} = \frac{2k_4\eta_m}{k_3}\frac{(1 - \cos\sqrt{k_3}\,\tau)}{(\overline{W}_i + \overline{W}_{i-1})}. \qquad (19a)$$

Similarly,

$$\frac{\overline{W}_{i+1} - \overline{W}_i}{\overline{W}_{sm} - \overline{W}_i} = \frac{2k_4\eta_m}{k_3}\frac{(1 - \cos\sqrt{k_3}\,\tau)}{(\overline{W}_{i+1} + \overline{W}_i)} \qquad (19b)$$

when

$$\overline{W}_i > \overline{W}^o \text{ and } \overline{W}_i < \overline{W}_{sm}.$$

Now, it has been assumed in the foregoing analysis that $\overline{W}^o \leqq \overline{W}_{i-1} < \overline{W}_{sm}$, $\overline{W}^o < \overline{W}_i < \overline{W}_{sm}$ and $\tau > 0$, so that Eqs. (17*b*) and (18) give

$$\overline{W}_{\tau i} > \overline{W}_{i-1}, \qquad \overline{W}_i > \overline{W}_{i-1},$$
$$\overline{W}_{\tau i+1} > \overline{W}_i, \quad \text{and} \quad \overline{W}_{i+1} > \overline{W}_i \qquad (20a\text{-}d)$$

and, therefore,

$$\overline{W}_i + \overline{W}_{i-1} < \overline{W}_{i+1} + \overline{W}_i. \qquad (20e)$$

Thus, Eqs. (19) predict

$$\frac{\overline{W}_i - \overline{W}_{i-1}}{\overline{W}_{sm} - \overline{W}_{i-1}} > \frac{\overline{W}_{i+1} - \overline{W}_i}{\overline{W}_{sm} - \overline{W}_i} \qquad (21)$$

[5]This equation gives an approximate solution when the static admissible requirement is not satisfied. In the case of a circular plate, an additional integral for continuous deformation fields must be included on the right-hand side of this equation.

Downloaded 03 May 2010 to 171.66.16.247. Redistribution subject to ASME license or copyright; see http://www.asme.org/terms/Terms_Use.cfm

Table 1 Calculations for fully clamped beams subjected to repeated concentrated loads at the midspan

$r_i = (\overline{W}_i - \overline{W}_{i-1})/(\overline{W}_{sm} - \overline{W}_{i-1})$

(1) Case 1 with $\eta_m = 1.6$ and $\tau = 30$ μsec

i	$\overline{W}_i$	r_i
1	0.01727	0.023059
5	0.08591	0.024137
10	0.16873	0.026005
15	0.24584	0.027364
20	0.31569	0.028260
25	0.37767	0.028794
30	0.43194	0.029070
35	0.47905	0.029176
36	0.48767	0.0291827
37	0.49604	0.0291859*
38	0.50417	0.0291857
40	0.51973	0.029177
45	0.55476	0.029116
50	0.58490	0.029022
55	0.61082	0.028914
60	0.63312	0.028801
65	0.65231	0.028691
70	0.66884	0.028587
75	0.68309	0.028492
80	0.69538	0.028405
85	0.70560	0.028326
90	0.71516	0.028257
95	0.72309	0.028195
100	0.72994	0.028140
105	0.73588	0.028092
110	0.74101	0.028050
115	0.74546	0.028013
120	0.74932	0.027981
125	0.75266	0.027953
130	0.75556	0.027928
135	0.75807	0.027907
140	0.76025	0.027893
145	0.76214	0.027873
150	0.76378	0.027860
155	0.76521	0.027849
160	0.76644	0.027840
165	0.76752	0.027832
170	0.76845	0.027826
175	0.76926	0.027821
180	0.76996	0.027817
185	0.77057	0.027814
190	0.77110	0.027813

Table 1 (continued)

(2) Case 2 with $\eta_m = 2$ and $\tau = 30$ μsec

i	$\overline{W}_i$	r_i
1	0.035984	0.035984
5	0.17670	0.040065
10	0.33487	0.042542
13	0.41677	0.042943
14	0.44182	0.042956*
15	0.46578	0.042925
20	0.57032	0.042343
25	0.65297	0.041465
30	0.71840	0.040577
35	0.77050	0.039781
40	0.81225	0.039099
45	0.84592	0.038529
50	0.87321	0.038056
55	0.89543	0.037665
60	0.91361	0.037343
65	0.92852	0.037077
70	0.94078	0.036858
75	0.95089	0.036677
80	0.95924	0.036527
85	0.96615	0.036404
90	0.97187	0.036302
95	0.97661	0.036218
100	0.98055	0.036149
105	0.98381	0.036092
110	0.98653	0.036046
115	0.98878	0.036009
120	0.99066	0.035980
125	0.99222	0.035957
130	0.99353	0.035940
135	0.99461	0.035928
140	0.99551	0.035921
145	0.99626	0.035918

which, with $\overline{W}_i < \overline{W}_{sm}$ requires

$$\overline{W}_{i+1} < \overline{W}_{sm} \tag{22}$$

and, therefore,

$$\eta_{i+1} < \eta_m, \tag{23}$$

according to Eq. (15*a*). Finally, the inequalities (20*d*) and (22) lead to

$$\lim_{i \to \infty} \overline{W}_i = \overline{W}_{sm}. \tag{24}$$

It was necessary to assume that $\overline{W}^o \leqq \overline{W}_{i-1} < \overline{W}_{sm}$ and $\overline{W}^o < \overline{W}_i < \overline{W}_{sm}$ in order to arrive at Eq. (22). Now it is shown that this requirement may be relaxed. It is evident that if $\overline{W}_1 \to \overline{W}_{sm}$ ($\overline{W}_1 < \overline{W}_{sm}$), then Eq. (17*b*) shows that $\overline{W}_{\tau 2} \to \overline{W}_1$, while Eq. (18) gives $\overline{W}_2 \to \overline{W}_1$, and, therefore, $\overline{W}_2 \to \overline{W}_{sm}$. Furthermore, if a pulse with a given peak value is repeated twice on a given structure, the shorter the duration time, the smaller the transverse displacement. These two observations imply that if $\overline{W}_1 < \overline{W}_{sm}$, then $\overline{W}_2 < \overline{W}_{sm}$. Thus, the sufficiency condition has been proved[6] for the case of $\eta_m > \eta^o$, i.e., $\overline{W}_{sm} > \overline{W}^o$, and either $\overline{W}_1 \geqq \overline{W}^o$ or $\overline{W}_1 < \overline{W}^o$.

Equation (14*a*) for small pressure pulses $\eta_m \leqq \eta^o$, which give $\overline{W}_{sm} \leqq \overline{W}^o$, is a nonlinear differential equation which requires a numerical solution. Table 1 and Fig. 5(*a*) contain the results for the particular case of a fully clamped beam with $a = 1.5\ \sigma_o/\rho L^2 = 40 \times 10^6\ \text{sec}^{-2}$ where ρ is the density of the material when subjected to a repeated concentrated load having a rectangular-shaped load-time history with a peak value $\eta_m \leqq \eta^o$ at the midspan. Two curves for $\eta_m > \eta^o$ and $\overline{W}_1 < 1$ are shown in Fig. 5(*b*).

The differential Eq. (14*b*) leads to inequality (21) from which the pseudo-shakedown condition (24) is obtained. Thus, the inequality (21) is required for the pseudo-shakedown of structures controlled by Eq. (14*b*) and, therefore, is examined in Table 1 for the numerical solution of Eq. (14*a*).

The numerical results in Table 1 show, for practical examples, that inequality (21) is satisfied when $i \geqq 37$ for case (1) and $i \geqq 14$ for case (2). Thus, the pseudo-shakedown phenomenon occurs as long as there is a finite integer i^* beyond which inequality (21) is satisfied. In fact, a number of other calculated results also show that a finite integer i^* always exists when $\overline{W} < \overline{W}^o$. It is evident from Fig. 5(*a*) that the pseudo-shakedown phenomenon occurs when $\overline{W} < \overline{W}^o$, as long as the inequality $\overline{W}_1 < \overline{W}_{sm}$ is satisfied. Thus, on the basis of these calculated results, it is suggested, tentatively, that the pseudo-shakedown phenomenon occurs for this class of structures when $\eta_m < \eta^o$ and $\overline{W}_1 < \overline{W}_{sm}$ and that inequality (21) may be used as a shakedown criterion.

3.3 Proof of the Necessary Condition. If the pressure-time history is applied repeatedly to a rigid, perfectly plastic structure which reaches, eventually, a pseudo-shakedown state, i.e.,

$$\overline{W}_i < \overline{W}_{sm}\ (i = 2, 3, \ldots, \infty),$$

and

$$\lim_{i \to \infty} \overline{W}_i = \overline{W}_{sm},$$

then the inequality $\overline{W}_1 < \overline{W}_{sm}$ is required.

It is obvious that $\overline{W}_1 \leqq \overline{W}_2$, which leads to $\overline{W}_1 < \overline{W}_{sm}$ because $\overline{W}_2 < \overline{W}_{sm}$.

3.4 Estimate of the Number of Repeated Loadings to Reach Pseudo-Shakedown. An estimate is made in this section of

[6] It should be noted that sufficiency has been proved only for Eq. (14*b*). However, Fig. 3 shows that Eqs. (14*a*) and (14*c*) give a convex curve which is close to the straight line OS when $\overline{W} > \overline{W}^o$. This suggests that the sufficiency condition might also be valid for Eq. (14*c*).

Downloaded 03 May 2010 to 171.66.16.247. Redistribution subject to ASME license or copyright; see http://www.asme.org/terms/Terms_Use.cfm

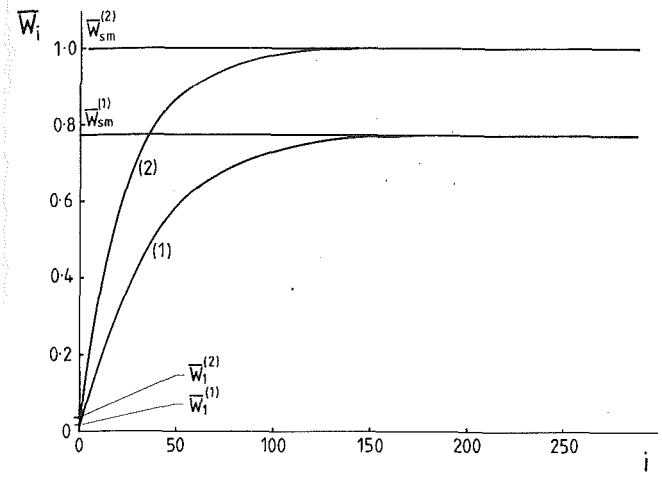

Fig. 5(*a*) (1): $\eta_m = 1.6$ and $\tau = 30$ μsec (2): $\eta_m = 2$ and $\tau = 30$ μsec

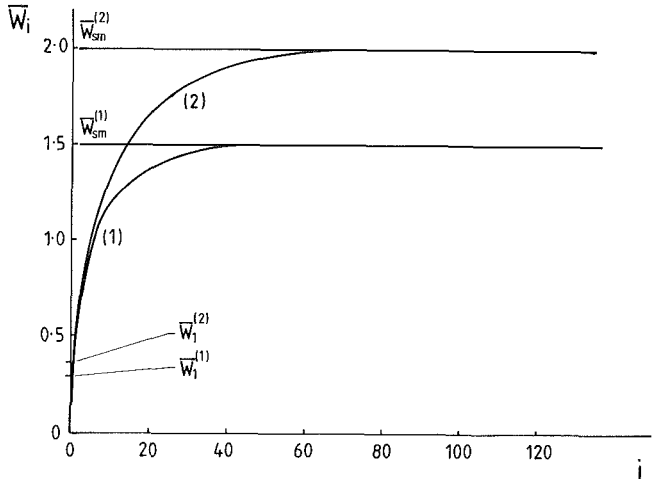

Fig. 5(*b*) (1): $\eta_m = 3$ and $\tau = 50$ μsec (2): $\eta_m = 4$ and $\tau = 40$ μsec

Fig. 5 The dimensionless transverse displacement $\overline{W}_i$ versus the number of repeated impacts for fully clamped beams with $a = 40 \times 10^6$ sec^{-2} subjected to concentrated loads at the midspan

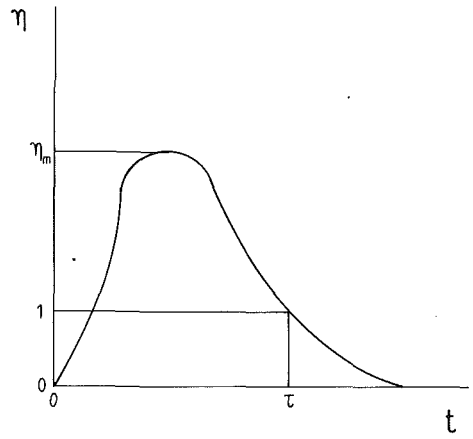

Fig. 6 Dynamic pressure-time history

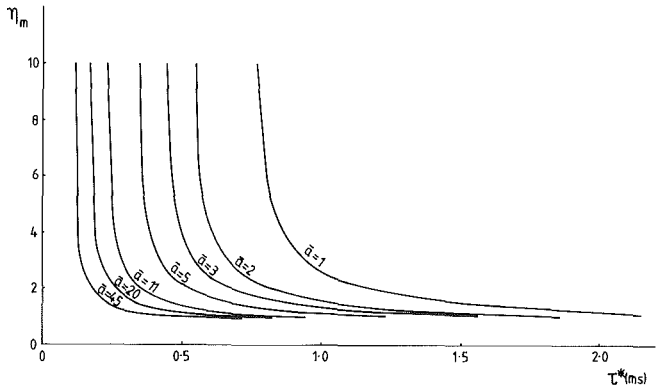

Fig. 7 Pseudo-shakedown bound curves for fully clamped beams when subjected to a concentrated load at the midspan having a rectangular shaped force-time history, where $\bar{a} = a/10^6$.

the number of repeated identical loading cycles required for the transverse displacements $\overline{W}_i$ to almost reach $\overline{W}_{sm}$. From a practical viewpoint, the required number of cycles i_o may be defined by the relation

$$\overline{W}_{sm} - \overline{W}_i < \overline{W}_{sm}/10^4 \tag{25}$$

when $i > i_o$.

The value of i_o depends on r_i which is determined by the pulse characteristics according to Eq. (19*a*). Thus, $i_o = 0$ if η_m or τ is large enough (e.g., $\tau \to \tau^*$). It is also evident that $i_o \to \infty$ when $\eta_m \to 1$ ($\eta_m > 1$) and $\tau \to 0$. $r_i > r_{i+1}$ according to Eq. (21) although the numerical results in Table 1 show that r_i changes only slightly when $i > i^*$.

The value of i_o may be estimated when r_i is constant. Now taking $r_i = r$, then

$$\overline{W}_i = \overline{W}_{i-1} + r(\overline{W}_{sm} - \overline{W}_{i-1}) \tag{26}$$

which may be recast in the form

$$\overline{W}_i = \{1 - (1-r)^i\}\overline{W}_{sm}, \tag{27}$$

or

$$\overline{W}_{sm} - \overline{W}_i = (1-r)^i \overline{W}_{sm}. \tag{28}$$

Substituting Eq. (28) into inequality (25) yields

$$\{1/(1-r)\}^i > 10^4$$

which gives

$$i > -4/\log_{10}(1-r), \tag{29}$$

and, therefore,

$$i_o = -4/\log_{10}(1-r). \tag{30}$$

Equation (30) predicts that $i_o = 13$ when $r = 0.5$, $i_o \to 0$ when $r \to 1$ and $i_o = 921029$ if $r = 0.00001$.

The nonlinear form of the governing equations causes r_i to vary with $\overline{W}_i$ and

$$r_i > r_{i+1} \tag{31}$$

according to Eq. (21). In this case, it may be shown that the actual value of i_o is larger than that predicted by Eq. (30) with $r = r^*$.

4 Bound Curves for Pseudo-Shakedown

Consider a given structure which is subjected repeatedly to the same pressure-time history having a peak value η_m and a characteristic time duration τ, as defined in Fig. 6. It is evident that there is a unique value of the time τ^* which is identified with the condition $\overline{W}_1 = \overline{W}_{sm}$. In other words, pseudo-shakedown occurs for $\tau < \tau^*$, but not for $\tau \geqq \tau^*$, according to the pseudo-shakedown conjecture in Section 3. Therefore, for every value of $\eta_m > 1$, there is an associated value of τ^*, so that the set (η_m, τ^*) form a curve, as shown in Fig. 7.

The pseudo-shakedown bound curves presented in Fig. 7 were calculated for several fully clamped, rigid, perfectly plastic beams when subjected to a rectangular-shaped load-time history producing $\overline{W}_1 = \overline{W}_{sm}$.

Downloaded 03 May 2010 to 171.66.16.247. Redistribution subject to ASME license or copyright; see http://www.asme.org/terms/Terms_Use.cfm

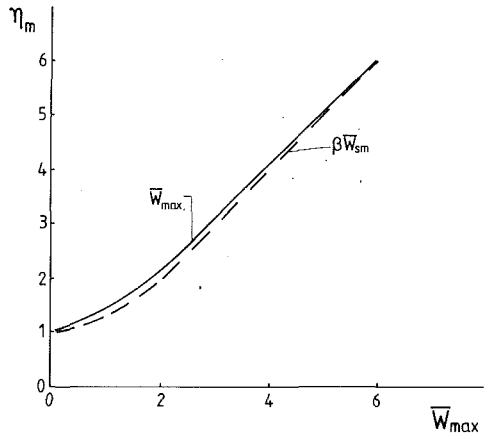

Fig. 8 The maximum transverse deflection $\eta_m - \overline{W}_{max}$ curves for a fully clamped, rigid, perfectly plastic beam subjected to a rectangular load-time history at the midspan. $a = 40 \times 10^6$ sec^{-2}. ———: dynamic solution; ---: quasi-static solution with $\beta = 2$.

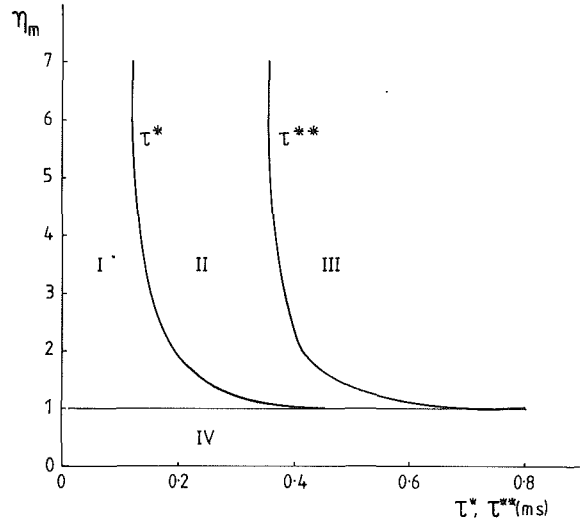

Fig. 9 Bound curves for the pseudo-shakedown $\eta_m - \tau^*$ and the maximum transverse deflection $\eta_m - \tau^{**}$ of a fully clamped, rigid, perfectly plastic beam subjected to a rectangular load-time history at the midspan. $a = 40 \times 10^6$ sec^{-2}.

5 Discussion

It was shown in Sections 3 and 4 that beams and plates, which strengthen with increase in finite transverse displacements, may exhibit a pseudo-shakedown phenomenon. This phenomenon is associated with dynamic loads having "relatively short" durations, as shown in Fig. 7 for beams. However, there is another limitation on pressure pulses having a "relatively long" duration.

Numerical calculations using the exact yield curve, as well as the theoretical results for a simplified yield curve show that, for a given structure, there is another bound curve in $\eta_m - \tau$ space which is related to a pulse duration τ^{**}. The dimensionless permanent transverse displacement $\overline{W}$ reaches a maximum value $\overline{W}_{\max}$ when $t = \tau^{**}$ for pressure pulses having $\tau \geqq \tau^{**}$. This maximum value is close to $\beta\overline{W}_{sm}$, where β is a constant for a given shape of pressure-time history. The difference between $\overline{W}_{\max}$ and $\beta\overline{W}_{sm}$ decreases as η_m increases, as shown in Fig. 8. It is straightforward to show that $\beta = 2$ for the rectangular-shaped pressure-time history characterized by Eqs. (13). Thus, under dynamic loads having a relatively long duration, i.e., $\tau \geqq \tau^{**}$, the dimensionless permanent transverse displacements of structures are close to those for a static load with a dimensionless magnitude $\gamma\eta_m$, where $1 < \gamma \leqq \beta$.

Figure 9 shows the pseudo-shakedown boundary $\eta_m - \tau^*$ and the maximum permanent deflection boundary $\eta_m - \tau^{**}$ for a fully clamped beam subjected to a concentrated load at the midspan having a rectangular load-time history.

It is evident that Fig. 9 may be divided into four regions having different kinds of response. The maximum dimensionless permanent transverse displacements in region I, for beams with relatively short duration pulses, would be smaller than the corresponding static deflections associated with pressure pulses having the same peak values. Thus, the phenomenon of pseudo-shakedown would occur in beams having pressure pulses with the characteristics lying in region I, provided the cycle time of the repeated pressure pulses is larger than, or equal to, the dynamic response time, so that the beam is stationary when struck by a subsequent pressure pulse. The maximum permanent transverse displacement would increase with each repeated impact and tend towards the associated static value.

Pseudo-shakedown would not occur in beams with pressure pulse characteristics lying within region II. The maximum dimensionless permanent transverse displacements in this region would occur during the first loading cycle and lie within the range $\overline{W}_{sm} < \overline{W} < \beta\overline{W}_{sm}$.

The beam has a type of quasi-static response in the region labelled III, but with the dimensionless maximum permanent transverse displacement equal to a constant value which is close to βW_{sm}.

Rigid, perfectly plastic beams would remain rigid for pressure pulses having the characteristics lying in region IV.

Figure 8 shows the curve of the maximum permanent transverse deflection when $\tau \geqq \tau^{**}$ for the beam examined in Fig. 9.

The transverse displacement profile for the actual dynamic plastic response of structures which satisfies the requirements of static admissibility is, for many problems, different from that associated with static or quasi-static loadings having similar spatial characteristics. In particular, travelling plastic hinges may arise during the early period of motion for certain dynamic loadings. A modified conjecture is suggested for this class of problems: It is a necessary and sufficient condition for the pseudo-shakedown of rigid, perfectly plastic structures which strengthen with finite displacements when subjected to repeated dynamic pressure pulses that the static plastic collapse load of the deformed structure after the first loading cycle is smaller than η_m.

6 Conclusions

The approximate theoretical method characterized by Eqs. (1) and (12) has been found adequate for predicting the behavior of many beams, circular and rectangular plates subjected to static, or dynamic loads which cause finite transverse displacements. This procedure has been used in this paper to clarify the pseudo-shakedown phenomenon which may occur when a structure is subjected to repeated identical pressure pulses. The general observations have been applied to the particular case of a fully clamped beam. It is found that the transverse displacements associated with pseudo-shakedown tend towards the value which is predicted by a static analysis using the peak value of the pressure pulses. It is also evident that the maximum permanent transverse displacement for long duration pressure pulses will be smaller than a certain value which is close to βW_{sm} predicted by a static analysis using the peak value of the pulse multiplied by γ, i.e., $\gamma\eta_m$, where $1 < \gamma \leqq \beta$. Thus, a dynamic problem may be studied using a static analysis, which is a significant simplification for a designer.

No consideration is given in this paper to low-cycle fatigue

Downloaded 03 May 2010 to 171.66.16.247. Redistribution subject to ASME license or copyright; see http://www.asme.org/terms/Terms_Use.cfm

failures, or to tensile tearing or transverse shear failures (Jones, 1989b) which, in practice, could prevent the achievement of a pseudo-shakedown state. The influences of material strain-rates sensitivity and strain hardening are also disregarded.

Acknowledgments

One of the authors (WQS) wishes to thank the Royal Society for their partial support of this study through the Sino-British Fellowship Trust.

The authors are also indebted to the Impact Research Centre at the University of Liverpool and, in particular, to Dr. R. S. Birch, to Mrs. M. White for her secretarial assistance, and to Mr. H. Parker for assistance with the tracings.

Thanks are also due to Shanghai Jiao Tong University and Prof. T. Y. Chen for their interest and support.

References

Ceradini, G., 1980, "Dynamic Shakedown in Elastic-Plastic Bodies," *Journal of the Engineering Mechanics Division*, ASCE, Vol. 106, EM3, pp. 481–499.

Corradi, L., and De Donato, O., 1975, "Dynamic Shakedown Theory Allowing for Second Order Geometric Effects," *Meccanica*, Vol. 10, No. 2, pp. 93–106.

Jones, N., 1971, "A Theoretical Study of the Dynamic Plastic Behaviour of Beams and Plates with Finite-Deflections," *International Journal of Solids and Structures*, Vol. 7, pp. 1007–1029.

Jones, N., 1973, "Slamming Damage," *Journal of Ship Research*, Vol. 17, No. 2, pp. 80–86.

Jones, N., 1975, "A Literature Review of the Dynamic Plastic Response of Structures," *The Shock and Vibration Digest*, Vol. 7, No. 8, pp. 89–105.

Jones, N., 1976, "Plastic Behaviour of Ship Structures," *Transactions, Society of Naval Architects and Marine Engineers*, Vol. 84, pp. 115–145.

Jones, N., 1977, "Damage Estimates for Plating of Ships and Marine Vehicles," International Symposium on Practical Design in Shipbuilding (PRADS), Society of Naval Architects of Japan, Tokyo, pp. 121–128.

Jones, N., 1989a, *Structural Impact*, Cambridge University Press, Cambridge, U.K., pp. 276–332.

Jones, N., 1989b, "On the Dynamic Inelastic Failure of Beams," *Structural Failure*, T. Wierzbicki and N. Jones, eds., John Wiley and Sons, New York, pp. 133–159.

Jones, N., and Walters, R. M., 1971, "Large Deflections of Rectangular Plates," *Journal of Ship Research*, Vol. 15, pp. 164–171, 288.

Koiter, W. T., 1960, "General Theorems for Elastic-Plastic Solids," *Progress in Solid Mechanics*, North-Holland, Amsterdam, pp. 165–221.

Konig, J. A., and Maier, G., 1981, "Shakedown Analysis of Elasto-Plastic Structures: A Review of Recent Developments," *Nuclear Engineering and Design*, Vol. 66, pp. 81–95.

Maier, G., 1972, "A Shakedown Matrix Theory Allowing for Workhardening and Second Order Geometric Effects," *Proceedings of Symposium on Foundations of Plasticity*, Warsaw, pp. 417–432.

Polizzotto, C., 1984, "Dynamic Shakedown of Elastic-Plastic Solids for a Set of Alternative Loading Histories," *International Journal of Nonlinear Mechanics*, Vol. 19, No. 4, pp. 363–371.

Sawczuk, A., 1964, "Large Deflections of Rigid-Plastic Plates," *Proceedings of the 11th International Congress of Applied Mechanics*, pp. 224–228.

Taya, M., and Mura, T., 1974, "Dynamic Plastic Behaviour of Structures Under Impact Loading Investigated by the Extended Hamilton's Principle," *International Journal of Solids and Structures*, Vol. 10, pp. 197–209.

Weichert, D., 1984, "Shakedown at Finite Displacements; A Note on Melan's Theorem," *Mechanics Research Communications*, Vol. 11, No. 2, pp. 121–127.

Yuhara, T., 1975, "Fundamental Study of Wave Impact Loads on Ship Bow," *Journal of the Society of Naval Architects of Japan*, Vol. 137, pp. 240–245.

Downloaded 03 May 2010 to 171.66.16.247. Redistribution subject to ASME license or copyright; see http://www.asme.org/terms/Terms_Use.cfm

Overdamped and Gyroscopic Vibrating Systems[1]

Lawrence Barkwell

Peter Lancaster

Department of Mathematics and Statistics,
University of Calgary,
Calgary, Alberta T2N 1N4
Canada

Some linear vibrating systems give rise to differential equations of the form $\mathrm{I}\ddot{x}(\mathrm{t})+\mathrm{B}\dot{x}(\mathrm{t})+\mathrm{C}x(\mathrm{t})=0$, *where* B *and* C *are square matrices. Stability criteria involving only the matrix coefficients* I, B, C, *and a single parameter are obtained for some special cases. Thus, if* $\mathrm{B}^*=\mathrm{B}>0$, $\mathrm{C}^*=\mathrm{C}>0$ *and* $\mathrm{B}>\mathrm{kI}+\mathrm{k}^{-1}\mathrm{C}$, *then the system will be overdamped (and hence stable). Gyroscopic systems also have the above form where* B *is real and skew symmetric. The case where* $\mathrm{C}>0$ *is well understood and for the case* $-\mathrm{C}>0$ *we show the condition* $\mathrm{B}_{\mathrm{abs}}>\mathrm{kI}-\mathrm{k}^{-1}\mathrm{C}$ *for some* $\mathrm{k}>0$ *will ensure stability. In fact, this condition can be generalized to systems with* $\mathrm{B}^*=\mathrm{B}$, $\mathrm{C}>0$.

1 Introduction and Preliminaries

Linear elastic vibrating systems oscillating about an equilibrium position, with no external applied forces, give rise to systems of constant coefficient differential equations which take the matrix-vector form

$$A\ddot{\mathbf{x}}(t)+B\dot{\mathbf{x}}(t)+C\mathbf{x}(t)=\mathbf{0}, \tag{1}$$

where A, B, C, are real $n\times n$ matrices. The leading coefficient A is positive definite (denoted by $A>0$) and (in mechanical engineering) is generally the matrix of the quadratic form determining the kinetic energy of the system. We consider two fundamentally different classes of problems of this type.

1 *Viscously damped systems* in which $C>0$, signifying oscillations about a position of stable equilibrium, and also $B>0$, being the matrix of a viscous energy dissipation function (see Lancaster (1966) and Meirovitch (1980), for example).

2 *Gyroscopic systems* in which B is real and skew symmetric, representing the effect of gyroscopic internal forces, and either $C>0$ or $-C>0$, when oscillations may be about stable or unstable equilibrium positions, respectively.

Whatever the hypotheses on B and C may be, it is well known that the solutions of the system (1) are completely determined by *algebraic* properties of the quadratic matrix polynomial

$$\lambda^2A+\lambda B+C \tag{2}$$

(see Lancaster (1966) and Meirovitch (1980)). In particular, the solutions can be expressed in terms of the eigenvalues, eigenvectors, and generalized eigenvectors of (2). The eigenvalues and eigenvectors are the numbers λ_0 and (constant) vectors $\mathbf{x}\neq\mathbf{0}$ for which

$$(\lambda_0^2A+\lambda_0B+C)\mathbf{x}=\mathbf{0}.$$

In general, eigenvalues and eigenvectors may be real or complex, and multiple eigenvalues are not uncommon. In the latter case, there may be a deficiency of eigenvectors (in other words, the eigenvalues have nonlinear elementary divisors), or the number of linearly independent eigenvectors may match the algebraic multiplicity of the eigenvalue (the case when the eigenvalue has only linear elementary divisors). For ease of reference we shall say that, in the latter case, the eigenvalue is *semi-simple*.

Let us focus on viscously damped system first of all. In this case the system (1) is said to be asymptotically stable if $\|\mathbf{x}(t)\|\to 0$ as $t\to\infty$ for all solutions $\mathbf{x}(t)$. In terms of the matrix polynomial of (2) this occurs if and only if all the eigenvalues have negative real parts. There is a well-known criterion which ensures not only this, but also that all eigenvalues are real and negative (and even semi-simple), thus guaranteeing asymptotic stability of the system. This is the *overdamping* condition of R. J. Duffin (see Duffin (1955) and Gohberg et al. (1982), for example) namely, that for all nonzero complex n-vectors $\mathbf{x}$ (more briefly, for all $\mathbf{x}\in\mathbb{C}^n$), we have

$$(\mathbf{x}^*B\mathbf{x})^2>4(\mathbf{x}^*A\mathbf{x})(\mathbf{x}^*C\mathbf{x}). \tag{3}$$

It is important to recognize that this is a *sufficient* condition for (2) to have real and negative eigenvalues (when $B>0$ and $C>0$), and is not necessary. Furthermore, condition (3) is not easy to verify numerically. Consequently, in the literature on mechanical engineering, some attention has been paid to the formulation of more easily verified criteria to guarantee that all eigenvalues of (2) are real and negative, and hence that (1) is asymptotically stable. A conjecture that has been made in this connection will be disproved here and another criterion is proposed in Theorem 1.

It is well known, and easily verified, that gyroscopic systems cannot be asymptotically stable. However, stability in the sense of Lyapunov may still occur, i.e., when $\|\mathbf{x}(t)\|$ is uniformly bounded for all $t\geq 0$ and all solutions $\mathbf{x}(t)$. This admits pure imaginary eigenvalues for (2), and hence harmonic motion for (1). However, the pure imaginary eigenvalues of (2) must be

[1] Research supported in part by a grant from the Natural Sciences and Engineering Research Council.

Contributed by the Applied Mechanics Division of THE AMERICAN SOCIETY OF MECHANICAL ENGINEERS for publication in the JOURNAL OF APPLIED MECHANICS.

Discussion on this paper should be addressed to the Technical Editor, Prof. Leon M. Keer, The Technological Institute, Northwestern University, Evanston, IL 60208, and will be accepted until two months after final publication of the paper itself in the JOURNAL OF APPLIED MECHANICS. Manuscript received by the ASME Applied Mechanics Division, July 13, 1989; final revision, Sept. 14, 1990.

Copyright © 1992 by ASME
Downloaded 03 May 2010 to 171.66.16.247. Redistribution subject to ASME license or copyright; see http://www.asme.org/terms/Terms_Use.cfm

semi-simple, otherwise a harmonic solution of the form $\mathbf{a}e^{i\omega t}$ may be multiplied by a polynomial in t, thus producing instability.

Gyroscopic systems in motion about a stable equilibrium position (with $C>0$) are well understood and all nonzero eigenvalues of (2) are necessarily pure imaginary and semi-simple (see Duffin (1960), Lancaster (1966), Greenlee (1975), Huseyin (1976), and Plaut (1976)) and will be briefly discussed in Section 4 below.

Gyroscopic systems in motion about an unstable equilibrium position (with $-C>0$) have also been investigated (see Hagedorn (1975), Plaut (1976), and Huseyin et al. (1983)) and, as for viscously damped systems, there is demand for a simple criterion to ensure that all eigenvalues of (2) are pure imaginary and semi-simple, thus guaranteeing stability. Such a criterion will be given in Theorem 5. The proof of this result is technical and will be presented in the mathematical literature (see Barkwell et al. (1991)).

A proper understanding of this paper requires some knowledge of the property of an eigenvalue-eigenvector pair $(\lambda_0, \mathbf{x})$ (with λ_0 real) known as its "type" (either positive or negative, see below). Despite the early work of Duffin (1960), this is a notion that has not made a convincing entrance onto the scene of mechanical engineering. It is an issue that is avoided in Section 6.7 of the text by Meirovitch (1980), for example, by the use of complex-symmetric congruence transformations, (rather than inertia-preserving congruence transformations). However, important information is lost in this way—information that is required for a complete understanding of this paper. The necessary ideas are briefly presented here.

If $L(\lambda)$ is a hermitian (or real-symmetric) analytic matrix-valued function of the real parameter λ with $\det L(\lambda) \not\equiv 0$ then λ_0 is an eigenvalue with corresponding eigenvector $\mathbf{x}$ if $\mathbf{x}\neq\mathbf{0}$ and $L(\lambda_0)\mathbf{x}=\mathbf{0}$. Let $L^{(1)}(\lambda)$ denote the matrix function obtained by differentiating $L(\lambda)$ with respect to λ. If λ_0 is real the eigenpair $(\lambda_0,\mathbf{x})$ is said to be of *positive* or *negative type* if

$$\mathbf{x}^*L^{(1)}(\lambda_0)\mathbf{x}>0, \quad \text{or} \quad \mathbf{x}^*L^{(1)}(\lambda_0)\mathbf{x}<0, \tag{4}$$

respectively. For a fixed eigenvalue λ_0, if all eigenpairs $(\lambda_0,\mathbf{x})$ are of one type, then we say that λ_0 is of that type. In particular, if λ_0 is an unrepeated eigenvalue it has a uniquely defined type. If an eigenvalue λ_0 is not semisimple there is always an eigenvector $\mathbf{x}$ for which $\mathbf{x}^*L^{(1)}(\lambda_0)\mathbf{x}=0$ and (using this definition) λ_0 itself does not have a well-defined type. If λ_0 is semi-simple and is not of positive or negative type, it may be described as having "mixed" type.

When $L(\lambda)=\lambda M+N$, a first-degree polynomial in λ, then condition (4) is simply

$$\mathbf{x}^*M\mathbf{x}>0, \quad \text{or} \quad \mathbf{x}^*M\mathbf{x}<0, \tag{5}$$

respectively, and we note that both cases may occur if M is not a definite matrix.

If $L(\lambda)=\lambda^2A+\lambda B+C$ as in (2) with $A>0$, then conditions (4) take the form

$$2\lambda_0>-\frac{\mathbf{x}_0^*B\mathbf{x}_0}{\mathbf{x}_0^*A\mathbf{x}_0}, \quad \text{or} \quad 2\lambda_0<-\frac{\mathbf{x}_0^*B\mathbf{x}}{\mathbf{x}_0^*A\mathbf{x}}. \tag{6}$$

This quadratic matrix polynomial is frequently analyzed via the hermitian linearization (see Gohberg et al. (1982) for precise definitions) $\lambda M+N$ where

$$M=\begin{bmatrix} B & A \\ A & 0 \end{bmatrix}, \quad N=\begin{bmatrix} C & 0 \\ 0 & -A \end{bmatrix}. \tag{7}$$

The eigenvalue types obtained using (5) and (7) or using (6) are easily seen to be consistent.

2 Introduction to Overdamped Systems

The classical model of a single-degree-of-freedom damped linear system with no external forces leads to the equation $a\ddot{x}(t)+b\dot{x}(t)+cx(t)=0$ where a, b, and c are positive. Such a system is said to be overdamped if $b>2(ac)^{1/2}$, which guarantees that the associated eigenvalues of the system are real, negative, and distinct, and hence all solutions $x(t)$ of the differential equation approach zero with time.

This leads to generalizations of the concept of overdamping for systems of the form

$$A\ddot{\mathbf{x}}(t)+B\dot{\mathbf{x}}(t)+C\mathbf{x}(t)=0 \tag{8}$$

where $A>0$, $B>0$, and $C>0$. One wants a criterion that will guarantee that the corresponding matrix polynomial has all of its eigenvalues with negative real parts and, consequently, asymptotic stability for the system (8).

As $A>0$, one can utilize the positive definite square root in a familiar way to reduce the system to the form

$$I\ddot{\mathbf{x}}(t)+B\dot{\mathbf{x}}(t)+C\mathbf{x}(t)=0 \tag{9}$$

where $B>0$ and $C>0$. As remarked above, all solutions of this equation are determined by the structure of eigenvalues and (generalized) eigenvectors of the quadratic matrix polynomial

$$L(\lambda)=\lambda^2I+\lambda B+C.$$

Let λ_0 be an eigenvalue of $L(\lambda)$ with corresponding unit eigenvector $\mathbf{u}$, that is $L(\lambda_0)\mathbf{u}=\mathbf{0}$, $\|\mathbf{u}\|=1$. Then $\mathbf{u}^*L(\lambda_0)\mathbf{u}=\lambda_0^2+\lambda_0(\mathbf{u}^*B\mathbf{u})+\mathbf{u}^*C\mathbf{u}=0$ so that

$$2\lambda_0=-\mathbf{u}^*B\mathbf{u}\pm\sqrt{(\mathbf{u}^*B\mathbf{u})^2-4\mathbf{u}^*C\mathbf{u}}. \tag{10}$$

It will be convenient to write $b_{\mathbf{u}}=\mathbf{u}^*B\mathbf{u}$, $c_{\mathbf{u}}=\mathbf{u}^*C\mathbf{u}$, etc. Thus, in this notation,

$$b_{\mathbf{u}}^2>4c_{\mathbf{u}}. \tag{11}$$

For *every* unit vector $\mathbf{u}$ will guarantee negative semi-simple real eigenvalues and, in fact, considerably more, as we will clarify in the next section. The condition (11) or the equivalent inequality (3) is the classical definition of overdamped systems first used by Duffin (1955), and the one that is adopted in this paper.

The computations involved in checking criterion (11) are substantial, so some efforts have been made to obtain a simpler criterion. In 1980, and in subsequent works, Inman and Andry proposed the definition

$$B>2C^{1/2} \tag{12}$$

(see Inman and Andry Jr. (1980) and Inman (1989)). This condition turns out not to guarantee real eigenvalues as the following example illustrates.

Example 1. Consider $L(\lambda)=\lambda^2I+\lambda B+C$ where

$$B=\begin{pmatrix} 7/4 & 0 \\ 0 & 21/2 \end{pmatrix} \text{ and } C=\begin{pmatrix} 1/2 & 1 \\ 1 & 7 \end{pmatrix}.$$

Then it is easily verified that $B>0$, $C>0$, and $B^2-4C>0$, which implies $B>2C^{1/2}$. But direct calculation shows that the spectrum of $L(\lambda)$ contains the complex pair $-1.1355\pm .1858\,i$. □

The Cauchy-Schwartz inequality gives $(\mathbf{u}^*B\mathbf{u})^2\le\mathbf{u}^*B^2\mathbf{u}$ for any unit vector $\mathbf{u}$ and hence Duffin's overdamping condition (11) implies that $B^2-4C>0$. However, the reverse implication does not hold.

It is instructive to appreciate why the criterion (12) has been favored for a number of years, at least until such a counter-example was discovered. We give three possible reasons for this:

1 The reverse inequality $B<2C^{1/2}$ does ensure that all eigenvalues are nonreal. To see this observe that $B<2C^{1/2}$ means that for any $\mathbf{x}$ with $\|\mathbf{x}\|=1$ $(B\mathbf{x},\,\mathbf{x})<2(C^{1/2}\mathbf{x},\,\mathbf{x})$. Using the Cauchy Schwartz inequality, again we obtain

$$(B\mathbf{x},\,\mathbf{x})^2<4(C^{1/2}\mathbf{x},\,\mathbf{x}))^2\le 4\|C^{1/2}\mathbf{x}\|^2\|\mathbf{x}\|^2=4(C\mathbf{x},\,\mathbf{x}).$$

Downloaded 03 May 2010 to 171.66.16.247. Redistribution subject to ASME license or copyright; see http://www.asme.org/terms/Terms_Use.cfm

Thus, the discriminant of (10) is always negative and all eigenvalues must be nonreal. This phenomenon may lead to the (vain) hope that, conversely, $B>2C^{1/2}$ implies that all eigenvalues are real.

2 It is easily seen that $B>2C^{1/2}$ is equivalent to condition (11) when B and C commute and, in particular, in the case of "proportional damping."

3 In an appropriate sense $B>2C^{1/2}$ is a local overdamping criterion but not globally so. To make this precise let $B=2C^{1/2}+\epsilon B_0$ where $\epsilon\geq 0$ and $B_0>0$. Then

$$\lambda^2 I+\lambda B+C=(\lambda I+C^{1/2})^2+\lambda\epsilon B_0.$$

An interesting application of Theorem 5.1 of Gohberg et al. (1985) shows that for *sufficiently small* $\epsilon>0$, the system has real and negative eigenvalues (although it is not generally overdamped). The extent to which ϵ can be increased and the real eigenvalues of $L(\lambda)$ are retained depends on the separation of the eigenvalues of C and, of course, on B_0.

The problem here lies in the plausible but false idea that if $\lambda^2 I+\lambda B+C$ has all real and negative eigenvalues, then so does any quadratic polynomial $\lambda^2 I+\lambda B_1+C$ with $B_1>B$. This fallacy has been demonstrated, by example, in Gohberg et al. (1986), and the numerical example above is drawn from Example 6.1 of that paper. On the other hand, if $\lambda^2 I+\lambda B+C$ is already overdamped and $B_1>B$, then clearly $\lambda^2 I+\lambda B_1+C$ is also overdamped.

3 A Criterion for Overdamped and Hyperbolic Systems

Note first that condition (11) makes sense without assuming that B and/or C is positive, although it certainly requires that B is nonsingular. We therefore make no such hypotheses in establishing the main mathematical result. But if B is not positive, it is not appropriate to describe B as a "damping" matrix or to describe $L(\lambda)$ as "overdamped." So we revert to the mathematical terminology and say that the matrix polynomial

$$L(\lambda)=A\lambda^2+B\lambda+C$$

with $A>0$ and $B^*=B$, $C^*=C$ is *hyperbolic* if $b_{\mathbf{x}}^2>4a_{\mathbf{x}}c_{\mathbf{x}}$ for all $\mathbf{x}\neq\mathbf{0}$. In Duffin (1960) such systems are called "relative overdamped."

We indicate a proof of the next theorem that uses Duffin's approach, but must point out that the theorem is a special case of a more general theory of "hyperbolic" operator polynomials (see Theorem 31.7 and Lemma 31.23 of Markus (1988), for example).

Theorem 1. The matrix polynomial

$$L(\lambda)=A\lambda^2+B\lambda+C \tag{13}$$

where $A>0$, $B^*=B$, *and* $C^*=C$ *is hyperbolic if and only if* $L(k)<0$ *for some* $k\in\mathbb{R}$.

Proof. First, if $k\in\mathbb{R}$ and $L(k)<0$, then for any $\mathbf{u}\neq\mathbf{0}$, we have

$$a_{\mathbf{u}}k^2+b_{\mathbf{u}}k+c_{\mathbf{u}}<0,$$

and this implies $b_{\mathbf{u}}^2>4a_{\mathbf{u}}c_{\mathbf{u}}$. Thus, $L(\lambda)$ is hyperbolic.

Conversely, let $L(\lambda)$ be hyperbolic. The symmetric polynomial of first degree

$$\begin{bmatrix} B & A \\ A & 0 \end{bmatrix}\lambda-\begin{bmatrix} -C & 0 \\ 0 & A \end{bmatrix} \tag{14}$$

is a linearization of $L(\lambda)$ (as defined in Gohberg et al. (1982) or Lancaster and Tismenetsky (1985)). The proof of Theorem 13.1 of Gohberg et al. (1982) (originating mainly with Duffin) when applied shows that $L(\lambda)$, and hence the linearization (14), have all real and semi-simple eigenvalues—each with a well-defined type (i.e., either positive or negative). (The hypotheses $A=I$, $B>0$ and $C>0$ used in Gohberg et al. (1982) are easily seen to be unnecessary for our conclusions.) Furthermore, there are n eigenvalues of negative type which are strictly less than n eigenvalues of positive type.

It then follows from Theorem 1.2 of Lancaster and Ye (1989) that (14) is a *definite pencil*. That is, there exist $\alpha,\beta\in\mathbb{R}$ with $\beta>0$, such that

$$\alpha\begin{bmatrix} B & A \\ A & 0 \end{bmatrix}+\beta\begin{bmatrix} -C & 0 \\ 0 & A \end{bmatrix}=\begin{bmatrix} \alpha B-\beta C & \alpha A \\ \alpha A & \beta A \end{bmatrix}>0.$$

But we have the congruence

$$\begin{bmatrix} \alpha B-\beta C & \alpha A \\ \alpha A & \beta A \end{bmatrix}$$

$$=\begin{bmatrix} I & \frac{\alpha}{\beta}I \\ 0 & I \end{bmatrix}\begin{bmatrix} \alpha B-\beta C-\frac{\alpha^2}{\beta}A & 0 \\ 0 & \beta A \end{bmatrix}\begin{bmatrix} I & 0 \\ \frac{\alpha}{\beta}I & I \end{bmatrix}.$$

Hence, $\frac{\alpha^2}{\beta}A-\alpha B+\beta C<0$. Putting $k=-\alpha/\beta$, we obtain $L(k)<0$ as required. □

Corollary 2. The matrix polynomial $L(\lambda)$ *of (13) with* $A>0$, $B>0$ *and* $C>0$ *is overdamped if and only if*

$$B>Ak_0+Ck_0^{-1} \tag{15}$$

for some $k_0>0$.

Proof. The theorem implies overdamping if and only if

$$Ak^2+Bk+C<0.$$

This can only be satisfied if $k<0$. The result is obtained on multiplying by k^{-1} and setting $k_0=-k$. □

The Corollary suggests that condition (15) is an alternative to (11) as a computational criterion for overdamping. It is not as simple as (12), of course, but it does depend on only one scalar parameter, and in some cases will give an easily verified sufficient condition for overdamping. It is certainly much easier to use than the defining property (3) or (11).

If $A>0$, $B>0$, and $C>0$ are already given and it is asked whether condition (15) is satisfied, we can at present suggest no better procedure than trial and error. The design of a systematic algorithm for verifying this condition (or otherwise) is an open question of some interest. However, there is a strong *sufficient* condition for validity of (15) which is reminiscent of (12).

Theorem 3. Let $A>0$, $B>0$, *and* $C>0$ *be given and let* β_1 *and* γ_n *be minimal and maximal eigenvalues of* $A^{-1}B$ *and* $A^{-1}C$, *respectively. If* $\beta_1>2\gamma_n^{1/2}$, *then* $L(\lambda)=A\lambda^2+B\lambda+C$ *is overdamped and (15) is satisfied with* $k_0=\gamma_n^{1/2}$.

Proof. This follows immediately from the criterion (11) after reduction to the case $A=I$. □

Introduction to Gyroscopic Systems. For a gyroscopic system described by n generalized coordinates x_i, the set of governing differential equations leads to the real matrix differential equation

$$I\ddot{\mathbf{x}}(t)+G\dot{\mathbf{x}}(t)+K\mathbf{x}(t)=\mathbf{0} \tag{16}$$

where $G^T=-G$ and $K^T=K$ (see Inman, 1989, for example).

This leads to the study of the algebraic properties of the quadratic matrix polynomial

$$\mu^2 I+\mu G+K. \tag{17}$$

In the following, it is convenient to consider the Hermitian matrix polynomial whose eigenvalues are those of (17) rotated through a right angle in the complex plane. That is, we substitute $\mu=-i\lambda$ in (17) and consider

Downloaded 03 May 2010 to 171.66.16.247. Redistribution subject to ASME license or copyright; see http://www.asme.org/terms/Terms_Use.cfm

$$L(\lambda) := \lambda^2 I + \lambda i G + C \tag{18}$$

where $G^T = -G$, $C^T = C = -K$. Hence, as described in the introduction, (16) will be stable only when all eigenvalues of (18) are real and semi-simple.

It is well known that if $C < 0$, the system (18) is stable (Duffin (1960), Lancaster (1966). (See also Huseyin, 1976.) Greenlee (1975) showed that if $C \leq 0$, then stability will result if and only if $N(PG/_{N(C)}) = \{\mathbf{0}\}$ where N stands for the nullspace and P is the orthogonal projection onto $N(C)$.

Our concern is with the case $C > 0$. Physically, this corresponds to a system where there is oscillation about an equilibrium point which is unstable (in the absence of gyroscopic forces). For example, in Whittaker (1937) the classic analysis of the motion of a "sleeping" top leads, after linearization, to a system of this kind with two degrees-of-freedom.

In the case $C > 0$ there have been attempts to find a stability criterion using the Hermitian form $4C + G^2$ (note that $G^T = -G$ implies $-G^2 > 0$). Hagedorn (1975) showed that $4C + G^2 > 0$ implies instability. However,

$$4C + G^2 < 0 \tag{19}$$

does not guarantee stability (unless $n = 2$); neither is it necessary for stability. The following examples illustrate these points.

Example 2.

$$\text{Let } G = \begin{bmatrix} 0 & \frac{7}{4} & 0 & 0 \\ -\frac{7}{4} & 0 & 0 & 0 \\ 0 & 0 & 0 & \frac{21}{2} \\ 0 & 0 & -\frac{21}{2} & 0 \end{bmatrix} \text{ and}$$

$$C = \begin{bmatrix} \frac{1}{2} & 0 & 1 & 0 \\ 0 & \frac{1}{2} & 0 & 1 \\ 1 & 0 & 7 & 0 \\ 0 & 1 & 0 & 7 \end{bmatrix}.$$

Then $-G^2 - 4C > 0$, but the spectrum of the corresponding matrix polynomial (18) is found to contain nonreal eigenvalues so that the system (16) is unstable. □

Example 3.

$$\text{Let } G = \begin{bmatrix} 0 & 2 & 2 & 2 \\ -2 & 0 & 3 & 0 \\ -2 & -3 & 0 & 2 \\ -2 & 0 & -2 & 0 \end{bmatrix}, \quad C = \begin{bmatrix} 0.5 & 0 & 0 & 0 \\ 0 & 1.0 & 0 & 0 \\ 0 & 0 & 1.5 & 0 \\ 0 & 0 & 0 & 1.25 \end{bmatrix}.$$

Then $L(\lambda)$ of (18) has eight distinct real eigenvalues so that the corresponding system (16) is stable. However, $-G^2 - 4C$ has three positive and one negative eigenvalue. □

In the next section we present a criterion in terms of the coefficients G and C which will guarantee semi-simple real eigenvalues for (18)—hence semi-simple purely imaginary eigenvalues for (17), and hence stability for Eq. (16).

4 A Criterion for Gyroscopic Systems

The criterion to be obtained is in the spirit of Corollary 2. Indeed, that result plays a vital part in our proof. We give some comments on the proof to show how this comes about but reserve the technical arguments for a subsequent paper (see Barkwell et al., 1991). We also state a more general result (Theorem 7) which can be seen as a generalization of the result for both overdamped and gyroscopic systems (with $C > 0$).

To begin with we state, without proof, some properties of skew-symmetric matrices (see Lancaster and Tismenetsky (1985) or Yakubovich and Starzhinski (1975).

Lemma 4. Let G *be a real nonsingular skew-symmetric* n × n *matrix. Then* n *is even and there are positive numbers* $\gamma_1, \gamma_2, \ldots, \gamma_{n/2}$ *such that* $\sigma(iG) = \{\pm\gamma_1, \pm\gamma_2, \ldots, \pm\gamma_{n/2}\}$. *Furthermore, there is a (complex) unitary matrix* U *with the partitioned form* $U = [X, \overline{X}]$ *such that if* $\Gamma = diag[\gamma_1, \ldots, \gamma_{n/2}]$, *then*

$$iG = U \begin{bmatrix} \Gamma & 0 \\ 0 & -\Gamma \end{bmatrix} U^*.$$

From the last equation we also see that

$$-G^2 = U \begin{bmatrix} \Gamma^2 & 0 \\ 0 & \Gamma^2 \end{bmatrix} U^* > 0.$$

We make the following definition

$$G_{\text{abs}} := U \begin{bmatrix} \Gamma & 0 \\ 0 & \Gamma \end{bmatrix} U^* > 0. \tag{20}$$

Then $(G_{\text{abs}})^2 = -G^2$ so G_{abs} is the unique positive definite square root of $-G^2$ (see Section 5.4 of Lancaster and Tismenetsky, 1985, for example).

It can be shown that if

$$G_{\text{abs}} > kI + k^{-1}C \tag{21}$$

for some $k > 0$ or, in particular, if

$$-G^2 > (kI + k^{-1}C)^2 \tag{22}$$

for some $k > 0$, then all eigenvalues of $L(\lambda)$ (of Eq. (18)) are real.

Theorem 5. If G *is a real skew symmetric nonsingular matrix, and* $C > 0$ *and is real, then the matrix polynomial*

$$L(\lambda) := \lambda^2 I + \lambda i G + C$$

has all real eigenvalues whenever

$$G_{\text{abs}} \geq kI + k^{-1}C \tag{23}$$

for some $k > 0$. *Furthermore, when* (21) *holds, all the eigenvalues of* $L(\lambda)$ *are real and have either positive or negative type (and are hence semi-simple).*

The proof begins in the following way. Let λ be an eigenvalue of $L(\lambda)$ with eigenvector $\mathbf{x} \neq 0$; that is $L(\lambda)\mathbf{x} = \mathbf{0}$. Using the unitary matrix $U = [X, \overline{X}]$ of the previous lemma we get $U^* L(\lambda) U\mathbf{y} = \mathbf{0}$ where $\mathbf{y} = U^*\mathbf{x}$ or, in terms of partitioned matrices,

$$\left[\lambda^2 I + \lambda \begin{bmatrix} \Gamma & 0 \\ 0 & -\Gamma \end{bmatrix} + \begin{bmatrix} C_{11} & C_{12} \\ C_{12}^* & C_{22} \end{bmatrix}\right] \mathbf{y} = \mathbf{0} \tag{24}$$

where $C_{11} = X^* C X$, $C_{12} = X^* C \overline{X}$ and $C_{22} = \overline{X}^* C \overline{X} = \overline{C}_{11}$.

Suppose that we have the strict inequality (21), then

$$\begin{bmatrix} \Gamma & 0 \\ 0 & \Gamma \end{bmatrix} > kI + k^{-1} \begin{bmatrix} C_{11} & C_{12} \\ C_{12}^* & C_{22} \end{bmatrix}. \tag{25}$$

In particular, we deduce that

$$\left.\begin{aligned} \Gamma &> kI + k^{-1}C_{11} \\ \Gamma &> kI + k^{-1}C_{22} \end{aligned}\right\}. \tag{27}$$

Using Corollary 2 we see that the quadratic bundles $L_1(\lambda) := \lambda^2 I + \lambda\Gamma + C_{11}$ and $L_2(-\lambda) = \lambda^2 I + \lambda\Gamma + C_{22}$ are overdamped with $L_1(\lambda)$ having only negative eigenvalues and $L_2(\lambda)$ having only positive eigenvalues. Using the fact that these subsystems have real eigenvalues and the fact that C is positive definite (so that the coupling term C_{12} in (24) cannot be too big), the first pair of the theorem can be established. The second requires more technical ideas about matrix polynomials.

Downloaded 03 May 2010 to 171.66.16.247. Redistribution subject to ASME license or copyright; see http://www.asme.org/terms/Terms_Use.cfm

We remark that the stronger sufficient condition (22) for stability of the gyroscopic system is equivalent to the overdamping condition (15) applied to the polynomial

$$I\lambda^2 + (-G^2 - 2C)\lambda + C^2.$$

The reader will easily verify this statement.

The next example shows that condition (23) does not ensure stability.

Example 4. Let $C = 2I$ and

$$G = \begin{pmatrix} 0 & 2\sqrt{2} \\ -2\sqrt{2} & 0 \end{pmatrix}.$$

Then it is found that $\det L(\lambda) = (\lambda^2 - 2)^2$. Thus, the eigenvalues of $L(\lambda)$ are $\sqrt{2}$ and $-\sqrt{2}$ each with algebraic multiplicity two. However, $L(\sqrt{2})$ and $L(-\sqrt{2})$ each have a one-dimensional nullspace and it follows that neither eigenvalue is semi-simple. Thus, the corresponding system (16) (with $K = -C$) is unstable.

A little calculation shows that $-G^2 = 8I$ and for all $k > 0$

$$G_{\text{abs}} \le kI + k^{-1}C$$

with equality for $k = \sqrt{2}$. Thus, (23) holds but not (21). □

Example 5. Using the matrices G and C of Example 3 we obtain a stable system. However, numerical experiments show that there is no $k > 0$ for which (21) holds. Thus, (21) may be sufficient for stability but is not necessary. □

A strong sufficient condition for (22) to hold can be formulated which is an analog of Theorem 3.

Theorem 6. Let G *be a real skew-symmetric nonsingular matrix and* $C > 0$ *be real. Let* γ_n *be a maximal eigenvalue of* C *and* β_1 *be an eigenvalue of* iG *of least absolute value. Then if* $|\beta_1| > 2\gamma_n^{1/2}$, *condition* (21) *is satisfied with* $k = \gamma_n^{1/2}$.

Proof. For an $\mathbf{x}$ with $\|\mathbf{x}\| = 1$, and with $k = \gamma_n^{1/2}$, we have $\mathbf{x}^*(kI + k^{-1}C)\mathbf{x} = \gamma_n^{1/2} + \gamma_n^{-1/2}\ \mathbf{x}^*C\mathbf{x} \le 2\gamma^{1/2} < |\beta_1| \le \mathbf{x}^*G_{\text{abs}}\mathbf{x}$, and hence condition (21). □

In contrast to the separation of real eigenvalue types that appears with overdamped systems and is described in the proof of Theorem 1, the real eigenvalues for gyroscopic systems under the strict inequality (21) appear in four different "separate" subsets, each with a uniform eigenvalue type. First, the real eigenvalues are symmetric about the imaginary axis. For the n negative eigenvalues, $n/2$ eigenvalues (n is necessarily even) are of negative type, and the $n/2$ negative eigenvalues closest to the origin are of positive type. The reflections of these eigenvalues are of course positive, and all have their types reversed.

6 More General Systems

It turns out that the arguments used in the proof of Theorem 5 can be extended to the following more general result (see Barkwell et al., 1991 for the proof). The hypotheses of the next theorem admit more general mixing of the eigenvalue types. Furthermore, it is easily seen that Corollary 2 and Theorem 5 are both included in this more general statement (which also extends further to a general Hilbert space context).

Theorem 7. Let $B^* = B$, C *be positive definite* (B *and* C *are not necessarily real), and* $L(\lambda) = I\lambda^2 + B\lambda + C$. *If*

$$B_{\text{abs}} \ge kI + k^{-1}C \tag{27}$$

for some $k > 0$, *then all eigenvalues of* $L(\lambda)$ *are real. If strict inequality holds in* (27), *then all eigenvalues have positive or negative type* (*and are hence semi-simple*).

Here, B_{abs} denotes the positive definite square root of B^2. Corollary 2 is a special case in which B has all eigenvalues positive. In this case, (27) with strict inequality implies (15). For the gyroscopic systems, $B(=iG)$ has $n/2$ positive eigenvalues and $n/2$ negative eigenvalues. But Theorem 7 admits coefficients B with any division between the positive and negative eigenvalues, thus producing more complicated mixing of the eigenvalue types for $L(\lambda)$.

7 Concluding Remarks

Criteria have been formulated for the stability of systems of the form (1) when:

(a) the system is viscously damped, and motion is about a stable equilibrium position,
(b) the system is gyroscopic, and motion is about an unstable equilibrium position, and
(c) the system is of a more general kind including (a) and (b).

In all cases the criteria involve a single real parameter connecting the coefficients A, B, and C. In case (a) with A, B, C all positive definite, the criterion proposed in Corollary 2 is equivalent to Duffin's overdamping condition but is easier to apply. With A, B, and C merely positive definite it is *possible* that all eigenvalues of the system are real but it is *not* overdamped. This case is not considered, and we conjecture that there is no simple sufficient condition connecting positive definite A, B, and C which will cover this case.

In case (b) the corresponding symmetric system (see Eq. (18)) can never be hyperbolic (i.e., overdamped). Nevertheless, all eigenvalues may be real and semi-simple, thus ensuring stability. A criterion guaranteeing these properties is presented in Theorem 5. In Theorem 7 a more general result is stated which unifies and extends cases (a) and (b).

Acknowledgment

The authors are grateful to A. S. Markus for assistance in completion of the proofs of Theorems 5 and 7.

References

Barkwell, L., Lancaster, P., and Markus, A. S., 1991, "Gyroscopically Stabilized Systems: A Class of Quadratic Eigenvalue Problems with Real Spectrum," *Canadian Journal of Mathematics*, to appear.

Duffin, R. J., 1955, "A Minimax Theory for Overdamped Networks," *Journal of Rational Mechanics and Analysis*, Vol. 4, pp. 221–233.

Duffin, R. J., 1960, "The Rayleigh-Ritz Method for Dissipative or Gyroscopic Systems," *Quarterly of Applied Mathematics*, Vol. 18, pp. 215–221.

Gohberg, I., Lancaster, P., and Rodman, L., 1982, *Matrix Polynomials*, Academic Press, New York.

Gohberg, I., Lancaster, P., and Rodman, L., 1983, *Matrices and Indefinite Scalar Products*, Birkhäuser Verlag, Basel.

Gohberg, I., Lancaster, P., and Rodman, L., 1985, "Perturbation of Analytic Hermitian Matrix Functions," *Applicable Analysis*, Vol. 20, pp. 23–48.

Gohberg, I., Lancaster, P., and Rodman, L., 1986, "Quadratic Matrix Polynomials with a Parameter," *Advances in Applied Mathematics*, Vol. 7, pp. 253–281.

Greenlee, W. M., 1975, "Lyapunov Stability of Linear Gyroscopic Systems," *Utilitas Mathematics*, Vol. 8, pp. 225–231.

Hagedorn, P., 1975, "Über die Instabilität Konservativer Systeme mit gyroskopischen Kräften," *Archive for Rational Mechanics and Analysis*, Vol. 58, No. 1, pp. 1–9.

Huseyin, K., 1976, "Standard Forms of the Eigenvalue Problems Associated with Gyroscopic Systems," *Journal of Sound and Vibration*, Vol. 45, No. 1, pp. 29–37.

Huseyin, K., Hagedorn, P., and Tescher, W., 1983, "On the Stability of Linear Conservative Gyroscopic Systems," *Journal of Applied Mathematics and Physics*, Vol. 34, Nov., pp. 807–815.

Inman, D. J., and Andry, Jr., A. N., 1980, "Some Results on the Nature of Eigenvalues of Discrete Damped Linear Systems," ASME JOURNAL OF APPLIED MECHANICS, Vol. 47, pp. 927–930.

Inman, D. J., 1988, "A Sufficient Condition for the Stability of Conservative Gyroscopic Systems," ASME JOURNAL OF APPLIED MECHANICS, Dec., pp. 895–898.

Inman, D. J., 1989, *Vibration with Control, Measurement and Stability*, Prentice-Hall, Englewood Cliffs, New Jersey.

Downloaded 03 May 2010 to 171.66.16.247. Redistribution subject to ASME license or copyright; see http://www.asme.org/terms/Terms_Use.cfm

Lancaster, P., 1966, *Lamda-Matrices and Vibrating Systems*, Pergamon Press, Oxford, U.K.

Lancaster, P., and Tismenetsky, M., 1985, *The Theory of Matrices*, 2nd ed., Academic Press, New York.

Lancaster, P., and Ye, Q., 1989, "Variational Properties and Rayleigh Quotient Algorithms for Symmetric Matrix Pencils," *Operator Theory: Advances and Applications*, Vol. 40, pp. 247–278.

Markus, A. S., 1988, *Introduction to the Spectral Theory of Polynomial Operator Pencils*, American Mathematical Society, Providence.

Meirovitch, L., 1980, *Computational Methods in Structural Dynamics*, Sijthoft and Noordhoff, Rockville, MD.

Plaut, R. H., 1976, "Alternative Formulations for Discrete Gyroscopic Eigenvalue Problems," *American Institute of Aeronautics and Astronautics*, Vol. 14, No. 4, pp. 431–435.

Whittaker, E. T., 1937, *Analytical Dynamics*, 4th ed., Macmillan, Cambridge, U.K.

Yakubovich, V. A., and Starzhinski, V. M., 1975, *Linear Differential Equations with Periodic Coefficients*, Vol. 1, John Wiley and Sons, New York.

Downloaded 03 May 2010 to 171.66.16.247. Redistribution subject to ASME license or copyright; see http://www.asme.org/terms/Terms_Use.cfm

A Boundary Element Method Formulation for Design Sensitivities in Steady-State Conduction-Convection Problems

Abhijit Chandra
Assoc. Professor,
Mem. ASME.

Cho Lik Chan
Asst. Professor,
Assoc. Mem. ASME.

Department of Aerospace and Mechanical Engineering,
The University of Arizona,
Tucson, AZ 85721

A Boundary Element Method (BEM) formulation for the determination of design sensitivities of temperature distributions to various shape and process parameters in steady-state convection-diffusion problems is presented in this paper. The present formulation is valid for constant or piecewise-constant convective velocities. This approach is based on direct differentiation (DDA) of the relevant BEM formulation of the problem. It retains the advantages of the BEM regarding accuracy and efficiency while avoiding strongly singular kernels. The BEM formulation is also observed to avoid any false diffusion. This approach provides a new avenue toward efficient optimization of steady-state convection-diffusion problems and may be easily adapted to investigate the thermal aspects of various machining processes.

Introduction

The heat transfer phenomenon in various manufacturing processes, such as metal cutting, metal forming, etc., may be modeled as steady-state convection-diffusion problems. In many cases, the convective velocity may also be assumed to be piecewise constant. In metal cutting, for example, the velocities of the workpiece, the chip, and the tool are different, but the convective velocity may be assumed to be constant in each of these zones with respect to appropriate coordinate systems.

There are various analytical (e.g., Carslaw and Jaeger, 1986; Shaw, 1984; Bhattacharyya, 1984), finite element (e.g., Tay et al., 1974; Stevenson et al., 1983; Dawson and Malkin, 1984), and boundary element (Tanaka et al., 1986; Chan and Chandra, 1991) analyses of steady-state convection-diffusion problems. Several researchers have used such analyses to investigate the thermal aspects of metal cutting operations. Chan and Chandra (1991) have paid particular attention to the interface conditions at the tool-workpiece, tool-chip, and chip-workpiece interfaces. They obtained a complete heat transfer model of steady-state turning by matching the boundary conditions across the interfaces.

These analyses provide crucial insights into this class of convection-diffusion problems. On the one hand, numerical situations may be used to gain insight into the physics of various aspects of the problem and, on the other hand, computational methods may be used by the designers to predict the characteristics of alternative designs for heat transfer. Assuming that one has the ability to analyze the problem at hand, the question then arises of how to modify the design to improve the performance.

This brings us to the all important question that arises again and again in design, "What if . . . ?" In fact, the design process is not complete until all such pertinent questions have been asked and satisfactorily answered. One way of answering these questions entails perturbing each independent variable in turn, recalculating the characteristics, and evaluating the sensitivities with a finite difference technique. Optimal designs of heat transfer processes are typically carried out by nonlinear programming methods. Such algorithms require repeated iterations on the design variables, which may contain shape parameters, process parameters, and material parameters. Even for a simple heat transfer problem, such a procedure involving repeated analyses can become extremely computer intensive. Also of great importance is the fact that it may be inaccurate to the point of producing meaningless results, as the effect of small perturbations in the independent variable may drown in the noise of iterative solutions of the system. For more realistic problems such as machining, the design task becomes even more complicated. Muraka et al. (1979) demonstrate the importance of the variations in process parameters on the temperature distributions in orthogonal machining processes. A crucial ingredient for obtaining successful and economical solutions to such design optimization problems is the accurate and efficient determination of design sensitivities.

Accordingly, accurate and efficient determination of design sensitivities is the main thrust of our research in this area. As

Contributed by the Applied Mechanics Division of THE AMERICAN SOCIETY OF MECHANICAL ENGINEERS for publication in the JOURNAL OF APPLIED MECHANICS.

Discussion on this paper should be addressed to the Technical Editor, Prof. Leon M. Keer, The Technological Institute, Northwestern University, Evanston, IL 60208, and will be accepted until two months after final publication of the paper itself in the JOURNAL OF APPLIED MECHANICS. Manuscript received by the ASME Applied Mechanics Division, Dec. 18, 1989; final revision, Nov. 23, 1990.

Copyright © 1992 by ASME
Downloaded 03 May 2010 to 171.66.16.247. Redistribution subject to ASME license or copyright; see http://www.asme.org/terms/Terms_Use.cfm

a first attempt, only steady-state convection-diffusion problems are considered, and a boundary element formulation for determining the design sensitivities of temperature distributions is presented in this paper. Of concern here are situations where the shape of the heat transfer domain, as well as other process parameters (e.g., Peclet number) and material parameters (e.g., diffusivity), are design variables of interest.

A large amount of literature exists on evaluation of design sensitivity coefficients (DSC's) in linear problems of solid mechanics. Prager and Taylor (1968) have investigated the various issues in optimal structural design. Fleury (1979) has introduced dual methods for convex programming. Haftka (1982) has obtained second-order sensitivities in elastic structural optimization problems. Braibant and Fleury (1984) have also used B-splines for shape optimal design. In a paper such as this, it is very difficult to acknowledge all the worthwhile contributions in this field. A recent book by Haug et al. (1986) provides a review of the work in this area. A review article by Haftka and Gandhi (1986) and another recent book by Mota Soares (1987) also provide excellent overviews of the work in this field. Recently, Suzuki and Kikuchi (1990) have also introduced homogenization for shape and topology optimization for linear elastic structures. Very recently, Tsay and Arora (1988) have used finite element method (FEM) analyses to obtain design sensitivities in nonlinear structures with history-dependent effects, and Mukherjee and Chandra (1989, 1991) have obtained boundary element method (BEM) formulations for design sensitivities in problems involving material as well as geometric nonlinearities.

In general, two methods emerge as the most powerful ones for the determination of design sensitivities. These are the direct differentiation approach (DDA) and the adjoint structure approach (ASA). In the DDA, the governing equation is directly differentiated with respect to the design variables and the resulting equations are solved to obtain the sensitivities. The ASA, on the other hand, defines adjoint structures whose solutions permit explicit evaluation of the sensitivity coefficients.

The DDA, in conjunction with the BEM, provides an extremely elegant approach toward the determination of design sensitivities. The differentiation procedures developed by Barone and Yang (1988) and by Mukherjee and Chandra (1989, 1991) do not increase the singularities of the relevant kernels. Thus, while one usually starts with kernels that are ln r and $1/r$ singular, respectively, for two-dimensional problems (r being the distance between a source point and a field point), the differentiated kernels are regular and $1/r$ singular, respectively. Using an alternative strategy, Saigal and Chandra (1989) have also discretized the BEM equations first. Appropriate modes are then used on the discretized version to avoid direct numerical evaluation of kernels with $1/r$ singularity. The discretized BEM equations are then used for indirect evaluation of singular kernels arising in the sensitivity equations. Zabaras et al. (1988) have also used the DDA in inverse transient diffusion problems.

In the present work, the approaches of Mukherjee and Chandra (1989a,b) are followed. Appropriate models are first used to modify the BEM equations (Rice and Mukherjee, 1989), and the modified BEM equations for steady-state convection-diffusion are then differentiated with respect to design variables. This paper begins with a BEM formulation for obtaining design sensitivities in steady-state convection-diffusion problems. The integral equations are then discretized, and the BEM formulation for the determination of DSC's is applied to two-dimensional example problems.

Numerical results for the DSC's with respect to several design variables are obtained for four different cases. For the case of uniform compression, the BEM sensitivity results are compared to analytical solutions. For the case of parabolic bulging, the results obtained by the BEM sensitivity algorithm are also compared to those obtained by differencing the solutions of two successive regular BEM analyses. Design sensitivities are also obtained for parabolic variations of shear planes and gradual nose wear of cutting tools in machining problems.

Boundary Element Formulation

The governing equation for a steady-state convection-diffusion problem may be expressed as

$$-\kappa \frac{\partial^2 T}{\partial x_i^2} + v_i^{(s)} \frac{\partial T}{\partial x_i} = 0 \quad \text{in } B. \tag{1}$$

Here, $v_i^{(s)}$ is the convective velocity and $\kappa = k/\rho c$ is the thermal diffusivity. It is assumed that thermal conductivity, specific heat, and density remain constant in the domain B. For situations involving spatial variations of κ, the domain B may be divided into several zones and the thermal diffusivity, κ, may be assumed to be piecewise constant over each of these zones.

The boundary conditions for a steady-state convection-diffusion problem may be written as

$$T = \overline{T} \qquad \text{on } \partial B_T \tag{2a}$$

and

$$k \frac{\partial T}{\partial x_i} n_i = \overline{q} \qquad \text{on } \partial B_q \tag{2b}$$

or

$$k \frac{\partial T}{\partial x_i} n_i = -h(T - T_\infty) \qquad \text{on } \partial B_h. \tag{2c}$$

Here, T represents the temperature field, q represents the flux, k is the thermal conductivity of the material, h is the convection coefficient, T_∞ represents the ambient temperature, x_i represents the spatial coordinates, and n_i's are the components of the outward normal on the boundary of the domain. Equation (1) applies to an Eulerian reference frame that remains spatially fixed while the material flows through it. The convective term represents the energy transported by the material as it moves through the reference frame. Following Tanaka et al. (1986) and Chan and Chandra (1991), an integral equation for an internal point may be written as

$$T(p) = \int_{\partial B} \left\{ \left[\frac{\partial G(p,Q)}{\partial n_Q} + G(p,Q) v_i^{(s)} n_i(Q) \right] \times T(Q) - G(p,Q) \frac{\partial T(Q)}{\partial n_Q} \right\} ds(Q) \tag{3a}$$

when

$$v_{i,i}^{(s)} = 0. \tag{3b}$$

Here, a comma (,) denotes field point differentiation; p and q represent a source point and a field point, respectively, in the domain; and P and Q represent a source point and a field point on the boundary. $G(p, q)$ is the Green's function for the steady-state conduction-convection Eq. (1). The fundamental solution $G(p, q)$ may be expressed as (Carslaw and Jaeger, 1986)

$$G(p,q) = \frac{1}{4\pi k r} \exp\left\{ -\frac{vr - v_i^{(s)}[x_i(q) - x_i(p)]}{2\kappa} \right\} \quad \text{in 3D} \tag{3c}$$

and

$$G(p,q) = \frac{1}{2\pi k} \exp\left\{ \frac{v_i^{(s)}[x_i(q) - x_i(p)]}{2\kappa} \right\} K_0\left(\frac{vr}{2\kappa}\right) \quad \text{in 2D} \tag{3d}$$

where v is the magnitude of the scanning velocity vector $v_i^{(s)}$,

Downloaded 03 May 2010 to 171.66.16.247. Redistribution subject to ASME license or copyright; see http://www.asme.org/terms/Terms_Use.cfm

r is the distance between the source and the field point, and K_0 is the modified Bessel function of the second kind of order zero. In the present work, the numerical implementations of the BEM formulation are done in two-dimensional situations only. Hence, two-dimensional versions of equations are presented in this section. The BEM formulation, however, is also valid for three-dimensional situations. For two or three-dimensional applications, appropriate versions of the fundamental solution $G(p, q)$ should, of course, be used.

A boundary integral equation for the steady-state convection-diffusion problem may now be obtained as $p \to P$ (Chan and Chandra, 1991). This gives

$$C(P)T(P) = \int_{\partial B} \left\{ \left[\frac{\partial G(P,Q)}{\partial n_Q} + G(P,Q) v_i^{(s)} n_i(Q) \right] \times T(Q) - G(P,Q) \frac{\partial T(Q)}{\partial n_Q} \right\} ds(Q). \quad (4)$$

The coefficient $C(P)$, called the "corner tensor," depends on the local geometry at P. If the boundary is locally smooth at P, $C = 1/2$. Otherwise, it may be evaluated indirectly using a uniform potential mode (Chan and Chandra, 1991; Tanaka et al., 1986).

By applying a unit temperature field all over the boundary of the body, it may be shown that

$$C(P) = \int_{\partial B} \left[\frac{\partial G(P,Q)}{\partial n_Q} + G(P,Q) v_i^{(s)} n_i(Q) \right] ds(Q). \quad (5)$$

Substituting Eq. (5) in Eq. (4), we get

$$0 = \int_{\partial B} \left\{ \left[\frac{\partial G(P,Q)}{\partial n_Q} + G(P,Q) v_i^{(s)} n_i(Q) \right] [T(Q) - T(P)] - G(P,Q) \frac{\partial T(Q)}{\partial n_Q} \right\} ds(Q). \quad (6)$$

In order to determine the design sensitivities of temperature and flux with respect to any design parameter, Eq. (6) may be differentiated with respect to the particular parameter of interest. Barone and Yang (1988) and Mukherjee and Chandra (1989a,b) have investigated shape optimization and assumed at this stage that the shape of a body is determined by a finite dimensional vector with components b_i and that the shape changes occur continuously. The design parameter b_i, however, need not be restricted to shape variables. Process parameters like the convective velocity, material parameters like thermal diffusivity, or a combined parameter like the Peclet number may also be chosen as the design parameter of interest. It is also possible to choose the specified boundary conditions as design parameters. Differentiating Eq. (6) with respect to a typical b_i (designated here as b), we get

$$0 = \int_{\partial B} \left\{ \left[\frac{\partial G(b,P,Q)}{\partial n_Q} + G(b,P,Q) v_i^{(s)}(b) n_i(b,Q) \right] [\overset{*}{T}(b,Q) - \overset{*}{T}(b,P)] - G(b,P,Q) \frac{\partial \overset{*}{T}(b,Q)}{\partial n_Q} \right\} ds(b,Q)$$
$$+ \int_{\partial B} \left\{ \left[\frac{\partial \overset{*}{G}(b,P,Q)}{\partial n_Q} + \overset{*}{G}(b,P,Q) v_i^{(s)}(b) n_i(b,Q) + G(b,P,Q) \overset{*}{v}_i^{(s)}(b) n_i(b,Q) + G(b,P,Q) v_i^{(s)}(b) \overset{*}{n}_i(b,Q) \right] \times [T(b,Q) - T(b,P)] - \overset{*}{G}(b,P,Q) \frac{\partial T(b,Q)}{\partial n_Q} \right\} ds(b,Q)$$
$$+ \int_{\partial B} \left\{ \left[\frac{\partial G(b,P,Q)}{\partial n_Q} + G(b,P,Q) v_i^{(s)}(b) n_i(b,Q) \right] [T(b,Q) - T(b,P)] - G(b,P,Q) \frac{\partial T(b,Q)}{\partial n_Q} \right\} d\overset{*}{s}(b,Q), \quad (7)$$

where a superposed asterisk (*) denotes a derivative with respect to b. It should be pointed out that, depending on the particular choice of b, several terms in Eq. (7) may become zero. If b is a shape variable, $\overset{*}{v}_i^{(s)}$ is equal to zero; $\overset{*}{n}_i$ becomes zero if b is identified to be the Peclet number. If b represents the specified boundary conditions, $\overset{*}{G}$, $\partial \overset{*}{G}/\partial n_Q$, $\overset{*}{v}_i^{(s)}$, $\overset{*}{n}_i$, and $d\overset{*}{s}$ are equal to zero.

The kernels $\overset{*}{G}(b, P, Q)$ and $[\partial \overset{*}{G}(b, P, Q)]/\partial n_Q$ may be expressed as

$$\overset{*}{G}(b,P,Q) = G_{,k}(b,P,Q)[\overset{*}{x}_k(Q) - \overset{*}{x}_k(P)] \quad (8)$$

$$\frac{\partial \overset{*}{G}(b,P,Q)}{\partial n_Q} = \frac{\partial G_{,k}(b,P,Q)}{\partial n_Q} [\overset{*}{x}_k(Q) - \overset{*}{x}_k(P)] + \overset{*}{n}_k(Q) G_{,k}(b,P,Q) \quad (9)$$

and

$$d\overset{*}{s}(b,Q) = \left\{ \frac{\dfrac{\partial}{\partial b}\left(\left| \dfrac{\partial}{\partial \eta}(x_k e_k) \right| \right)}{\left| \dfrac{\partial}{\partial \eta}(x_k e_k) \right|} \right\} ds(b,Q), \quad (10)$$

where b is a shape parameter and e_k represents a component of unit vector. The quantity $[\overset{*}{x}_k(Q) - \overset{*}{x}_k(P)] \sim O(r)$. Hence, when b is a shape parameter, $\overset{*}{G}$ and $\partial \overset{*}{G}/\partial n_Q$ are regular and $1/r$ singular, respectively, for two-dimensional applications. When b is not a shape parameter, $d\overset{*}{s}$ is zero. It can be seen also that differentiation with respect to a nonspatial variable does not affect the order of singularity in either G or $\partial G/\partial n_Q$. More details about $\overset{*}{n}_k(Q)$ and $d\overset{*}{s}(b, Q)$ are given in Appendix A. An example for a wedge problem (Case 4 in the "Numerical Results" section) is shown in Appendix B.

Once the regular BEM analysis is performed, the temperature $T(b, Q)$ and the flux $[\partial T(b, Q)]/\partial n_Q$ are known everywhere on the boundary. From the given boundary conditions, half of the quantities of $\overset{*}{T}(b, Q)$ and $[\partial \overset{*}{T}(b, Q)]/\partial n_Q$ are known for a well-posed problem. Hence, Eqs. (7)–(10) may be used to solve for the unknown temperature sensitivities and flux sensitivities on the boundary in terms of the known ones.

A sensitivity equation for an internal point may now be obtained by differentiating Eq. (3a) with respect to b. This gives

$$\overset{*}{T}(b,p) = \int_{\partial B} \left\{ \left[\frac{\partial G(b,p,Q)}{\partial n_Q} + \mathrm{G(b,}p\mathrm{,}Q) v_i^{(s)}(b) n_i(b,Q) \right] \overset{*}{T}(b,Q) - G(b,p,Q) \frac{\partial \overset{*}{T}(b,Q)}{\partial n_Q} \right\} ds(b,Q)$$
$$+ \int_{\partial B} \left\{ \left[\frac{\partial \overset{*}{G}(b,p,Q)}{\partial n_Q} + \overset{*}{G}(b,p,Q) v_i^{(s)}(b) n_i(b,Q) + G(b,p,Q) \overset{*}{v}_i^{(s)}(b) n_i(b,Q) + G(b,p,Q) v_i^{(s)}(b) \overset{*}{n}_i(b,Q) \right] \times T(b,Q) - \overset{*}{G}(b,p,Q) \frac{\partial T(b,Q)}{\partial n_Q} \right\} ds(b,Q)$$

Downloaded 03 May 2010 to 171.66.16.247. Redistribution subject to ASME license or copyright; see http://www.asme.org/terms/Terms_Use.cfm

$$+\int_{\partial B}\left\{\left[\frac{\partial G(b,p,Q)}{\partial n_Q}+G(b,p,Q)v_i^{(s)}(b)n_i(b,Q)\right]\right.$$

$$\left.\times T(b,Q)-G(b,p,Q)\frac{\partial T(b,Q)}{\partial N_Q}\right\}d\overset{*}{s}(b,Q). \quad (11)$$

It should be noted here that Eq. (11) requires only algebraic evaluations for the determination of design sensitivities in convection-diffusion problems. The kernels, in this case, do not become singular since Q lies on the boundary while p is strictly an internal point.

Numerical Implementation

Discretization of Equations. Numerical implementation of the BEM Eqs. (7)–(10) for determination of design sensitivities in conduction-convection problems is discussed in this section. In the present work, two-dimensional problems are considered.

The first step is the discretization of the boundary of the two-dimensional domain into boundary elements. A discretized version of the boundary integral Eq. (7) may be written as (Chan and Chandra, 1991)

$$0=\sum_{i=1}^{N_s}\int_{\Delta s_i}\left\{\left[\frac{\partial G(b,P_M,Q)}{\partial n_Q}+G(b,P_M,Q)v_\ell^{(s)}(b,Q)n_\ell(b,Q)\right]\right.$$

$$\times[\overset{*}{T}(b,Q)-\overset{*}{T}(b,P_M)]-G(b,P_M,Q)\left.\frac{\partial \overset{*}{T}(b,Q)}{\partial n_Q}\right\}ds(Q)$$

$$+\sum_{i=1}^{N_s}\int_{\Delta s_i}\left\{\left[\frac{\partial \overset{*}{G}(b,P_M,Q)}{\partial n_Q}+\overset{*}{G}(b,P_M,Q)v_\ell^{(s)}(b)n_\ell(b,Q)\right.\right.$$

$$\left.+G(b,P_M,Q)\overset{*}{v}_\ell^{(s)}(b)n_\ell(b,Q)+G(b,P_M,Q)v_\ell^{(s)}(b)\overset{*}{n}_\ell(b,Q)\right]$$

$$\times[T(b,Q)-T(b,P)]-\overset{*}{G}(b,P_M,Q)\left.\frac{\partial T(b,Q)}{\partial n_Q}\right\}ds(b,Q)$$

$$+\sum_{i=1}^{N_s}\int_{\Delta s_i}\left\{\left[\frac{\partial G(b,P_M,Q)}{\partial n_Q}+G(b,P_M,Q)v_\ell^{(s)}(b)n_\ell(b,Q)\right]\right.$$

$$\times[T(b,Q-T(b,P_M)]$$

$$\left.-G(b,P_M,Q)\frac{\partial T(b,Q)}{\partial n_Q}\right\}d\overset{*}{s}(b,Q), \quad (12)$$

where the boundary of the domain ∂B is divided into N_s boundary segments and $T(P_M)$ represents temperature at a point P that coincides with node M.

Suitable shape functions must now be chosen for the variation of temperature, temperature sensitivity, flux, and flux sensitivity over each boundary element Δs_i. In the present work, each of the above quantities is assumed to vary linearly over individual elements. It is clear from Eq. (12) that the regular BEM problem for $T(P_M)$ and $[\partial T(P_M)]/\partial n_Q$ should be solved first. Details of such an analysis may be found in Chan and Chandra (1991). Once temperature and flux are known everywhere on the boundary, Eq. (12) may be cast in the form (Rice and Mukherjee, 1989)

$$\sum_{j=1}^{N_s}A_{ij}\overset{*}{T}_j+\sum_{j=1}^{N_s}B_{ij}\overset{*}{q}_j^{(n)}=F_i. \quad (13)$$

Here, $q_j^{(n)}=\partial T_j/\partial n_Q$ and therefore $\overset{*}{q}_j^{(n)}=\partial \overset{*}{T}_j/\partial n_Q$.

It should be noted that the coefficient matrices A_{ij} and B_{ij} appearing in Eq. (13) are exactly the same as those in the regular BEM analysis. The vector F_i contains the contributions of the last two boundary integrals appearing in Eq. (12).

At each location over the entire boundary of the domain, either $\overset{*}{T}$ or $\overset{*}{q}^{(n)}$ (or a combination of the two) is prescribed for a well-posed problem. Equation (13) may now solved for the unknown $\overset{*}{T}$ and $\overset{*}{q}^{(n)}$ in terms of the known ones. Typically, the temperature or the flux sensitivity is zero when the temperature or the flux is specified respectively at any particular point on the boundary. It should be noted that the BEM sensitivity formulation can also accommodate any arbitrarily specified $\overset{*}{T}$ or $\overset{*}{q}^{(n)}$ on any portion of the boundary. Once $\overset{*}{T}$ and $\overset{*}{q}^{(n)}$ have been obtained over the entire boundary, the internal Eq. (11) may be used to obtain the temperature sensitivity at any internal point. A derivative form of Eq. (11) may also be used to determine the flux sensitivity at any internal point.

It is also important to note here that the matrices A_{ij} and B_{ij} in Eq. (13) depend on the reference configuration only and do not depend on the choice of the design parameter b. All the effects for a particular choice of b are incorporated through the right-hand-side vector F_i in Eq. (13). This makes the BEM formulation very efficient when sensitivities with respect to a large number of design variables are sought for a particular reference configuration. For the slight increase in additional costs due to additional evaluations of the right-hand side, sensitivities with respect to several design variables may be obtained. Using parallel processing features, such design sensitivities may also be tracked simultaneously.

Numerical Results

It is assumed here that the boundary ∂B of a simply connected region may be decomposed as

$$\partial B=\partial B_{\text{no-opt}}\cup\partial B_{\text{opt}}, \quad (14)$$

where ∂B_{opt} is the portion of the boundary being optimized.

Case 1—Uniform Compression of an Initially Square Domain. In this section, the BEM sensitivity algorithm is first verified against an analytical solution for the case of a one-dimensional uniform compression (or stretching) problem. The one-dimensional convection equation is

$$\frac{d^2T}{dx^2}-\text{Pe}\frac{dT}{dx}=0; \qquad 0\le x\le \ell \quad (15)$$

subject to the boundary conditions

$$T(0)=1.0 \quad \text{and} \quad T(\ell)=0. \quad (16)$$

The solution of Eq. (15) subject to the boundary conditions (16) is

$$T(x)=\frac{e^{-\text{Pe}x}-e^{-\text{Pe}\ell}}{1-e^{-\text{Pe}\ell}}. \quad (17)$$

The uniform compression can be represented by the parameterization,

$$x=\eta(1-b); \qquad 0\le\eta\le 1$$
$$\ell=1-b, \quad (18)$$

where b is the design parameter representing the amount of compression. The temperature sensitivity can now be calculated as

$$\overset{*}{T}=\frac{\text{Pe}[(1-\eta)e^{-\text{Pe}(1-b)(1+\eta)}+\eta e^{-\text{Pe}(1-b)\eta}-e^{-\text{Pe}(1-b)}]}{[1-e^{-\text{Pe}(1-b)}]^2} \quad (19)$$

The flux sensitivity at $x=0$ and ℓ are the same and may be expressed as

$$\left(\frac{dT}{dx}\right)^*_{\eta=0}=\left(\frac{dT}{dx}\right)^*_{\eta=1}=\frac{-\text{Pe}^2e^{-\text{Pe}(1-b)}}{[1-e^{-\text{Pe}(1-b)}]^2}. \quad (20)$$

The two-dimensional BEM formulation is applied to a square domain as shown in Fig. 1. The boundary conditions are

Downloaded 03 May 2010 to 171.66.16.247. Redistribution subject to ASME license or copyright; see http://www.asme.org/terms/Terms_Use.cfm

between successive specified nodes
uniform boundary elements are defined

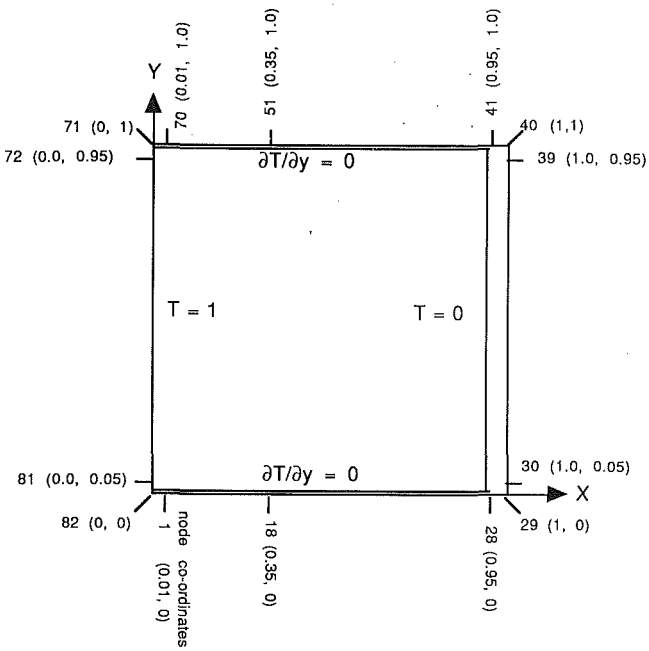

Fig. 1 Schematic diagram for the uniform compression problem

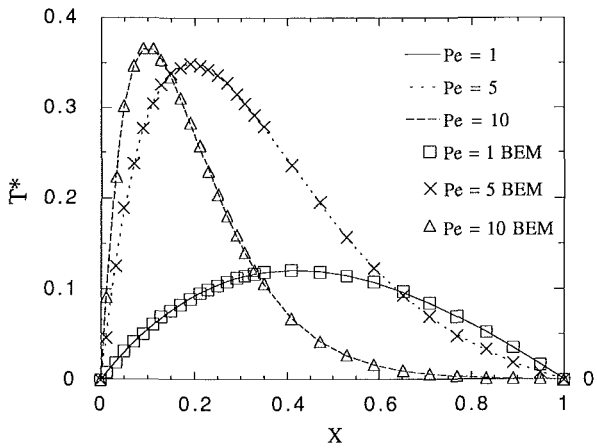

Fig. 2 Comparison of temperature sensitivities for the uniform compression problem

$$x=0; \quad T=1$$
$$x=1; \quad T=0$$
$$y=0; \quad \partial T/\partial y=0$$
$$y=1; \quad \partial T/\partial y=0. \tag{21}$$

These boundary conditions give rise to a one-dimensional problem which is identical to the analytical problem posed in Eqs. (15)–(16). The uniform compression is simulated as follows:

Along the horizontal boundaries at $y = 0$ and $y = 1$,

$$x=\eta(1-b)$$
$$y=0; \quad 0\le\eta\le 1, \tag{22}$$

and along the vertical boundary at $x = 1$,

$$x=-b,$$
$$y=\eta; \quad 0\le\eta\le 1. \tag{23}$$

The results from the analytical solution and those obtained from the BEM formulation are compared in Fig. 2. The temperature sensitivities as a function of x for three different Pe numbers are plotted in Fig. 2. The analytical and BEM results are almost identical. It is interesting to note that the temperature sensitivities have a very steep gradient near $x = 0$ for high Peclet number. Accordingly, a very fine grid is needed to properly capture the rapid change in the temperature sensitivities and the flux sensitivities at $x = 0$.

between successive specified nodes
uniform boundary elements are defined

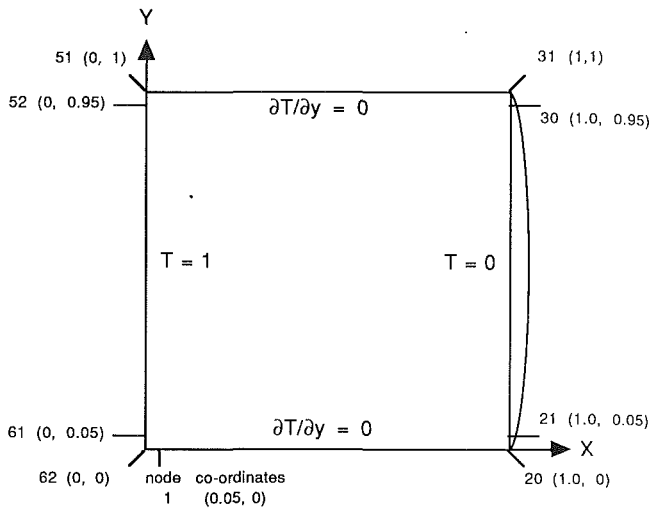

Fig. 3 Schematic diagram for the parabolic bulging problem

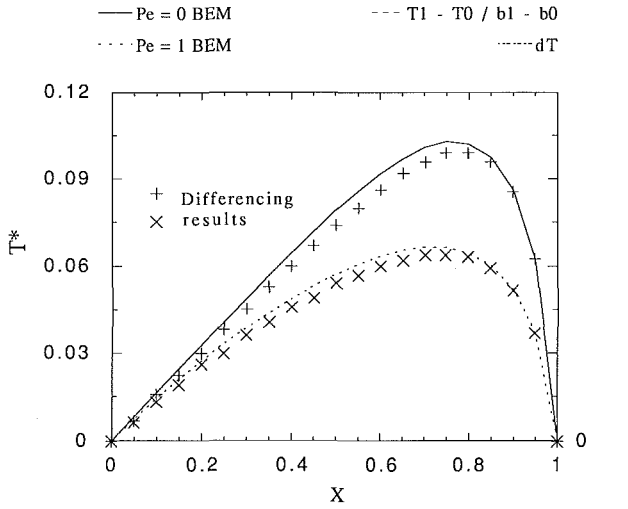

Fig. 4 Comparison of temperature sensitivities for the parabolic bulging problem

Case 2—Parabolic Bulging of an Initially Square Domain. As shown in Fig. 3, the parabolic bulging of an initially square domain is considered next. The boundary conditions are

$$x=0; \quad T=1$$
$$x=1; \quad T=0$$
$$y=0; \quad \partial T/\partial y=0$$
$$y=1; \quad \partial T/\partial y=0. \tag{24}$$

The two horizontal boundaries and the vertical boundary at $x = 0$ are kept unchanged. The shape of the vertical boundary at $x = 1$ is varied as a family of parabolae,

Downloaded 03 May 2010 to 171.66.16.247. Redistribution subject to ASME license or copyright; see http://www.asme.org/terms/Terms_Use.cfm

$$x' = \eta$$

$$y' = -b(\eta - 0.5)(\eta + 0.5); \qquad -0.5 \le \eta \le 0.5, \qquad (25)$$

where x' and y' are the local tangential and normal coordinates, respectively, and b is the design parameter representing the amount of the bulge.

The temperature sensitivities and the flux sensitivities for different Peclet numbers are presented in Figs. 4 and 5, respectively. Estimates of the sensitivities are also evaluated by differencing the temperature and flux fields obtained from two successive regular BEM analyses with $b = 0$ and $b = 0.01$. The numerical results obtained from the BEM sensitivity analysis are also compared to these estimates. Figure 4 shows the temperature sensitivities obtained by the BEM algorithm and those obtained by the differencing scheme for Pe = 0 and Pe = 1. The two results compare very well with errors less than five percent. It can also be observed from Fig. 5 that the two flux sensitivity results compare just as well with errors less than five percent.

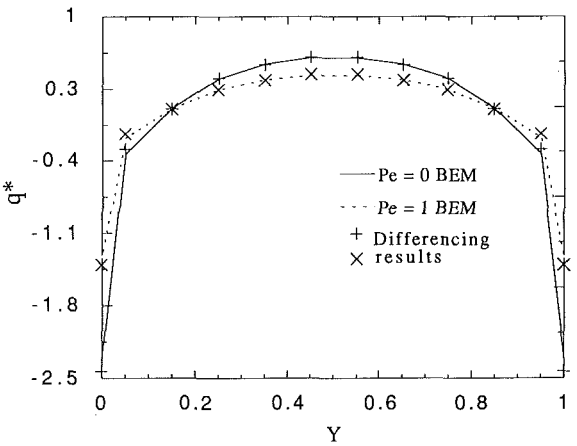

Fig. 5 Comparison of flux sensitivities for the parabolic bulging problem

Case 3—Parabolic Variation of Shear Plane in Machining Problems. In metal cutting processes, the chip thickness is typically assumed to be uniform. In many situations (Trent, 1984), however, the chip thickness is not uniform. Hence, the shear angle may vary across the depth of cut, and the shear plane will also be curved. Similar situations also arise in plunge grinding. To investigate the implications of uniform chip thickness assumption, the shear plane geometry is varied as a parabola (see Fig. 6) represented as

$$x' = \eta$$

$$y' = b(\eta - 0.5)(\eta + 0.5); \qquad -0.5 \le \eta \le 0.5, \qquad (26)$$

where x' and y' are local tangential and normal coordinates, respectively, at the shear plane.

The nominal configuration is a straight line ($b = 0$). Figure 7 shows the temperature and its sensitivity along a shear plane (in the nominal configuration) for Pe = 10 and 30 at a shear angle of 45 degrees. The abscissa is the dimensionless distance along the shear plane (see Fig. 6) measured from $A(x = 0)$ to $B(x = 1)$. The sensitivity of the temperature decreases with the Peclet number and, as Pe goes from 10 to 30, the maximum temperature sensitivity goes from -0.06 to -0.025. The position of the maximum also shifts toward point A (in Fig. 7).

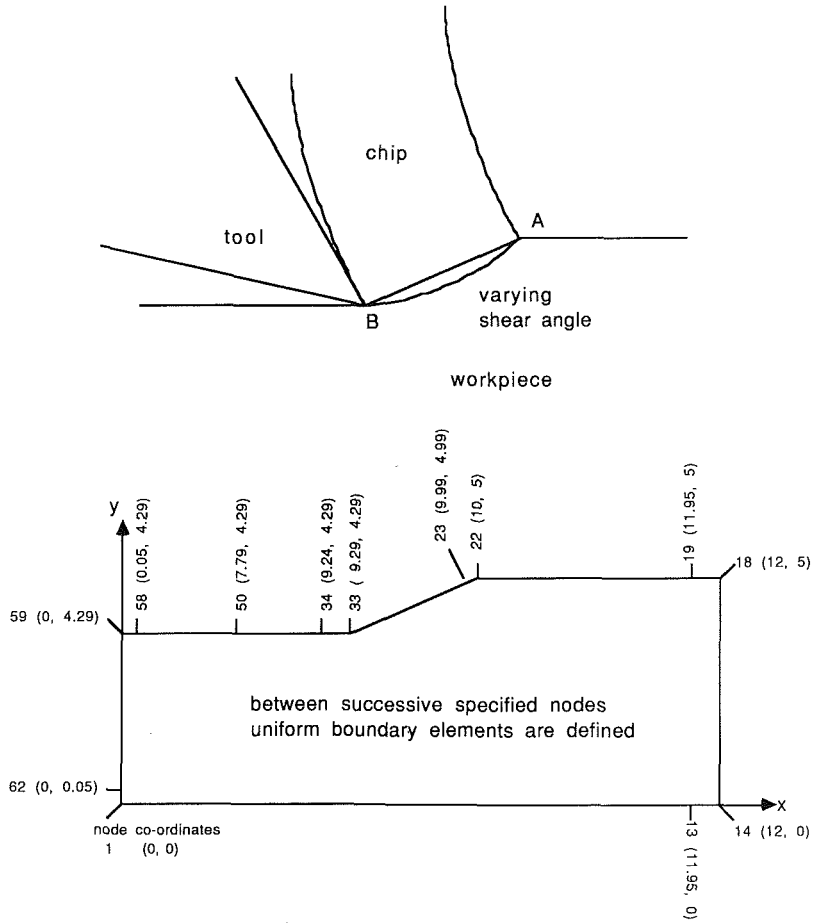

Fig. 6 Schematic diagram for varying shear angle in machining problems

Downloaded 03 May 2010 to 171.66.16.247. Redistribution subject to ASME license or copyright; see http://www.asme.org/terms/Terms_Use.cfm

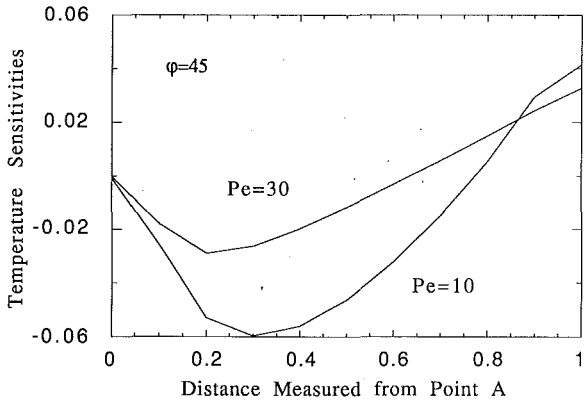

Fig. 7 Temperature sensitivities along the shear plane due to shear angle variations

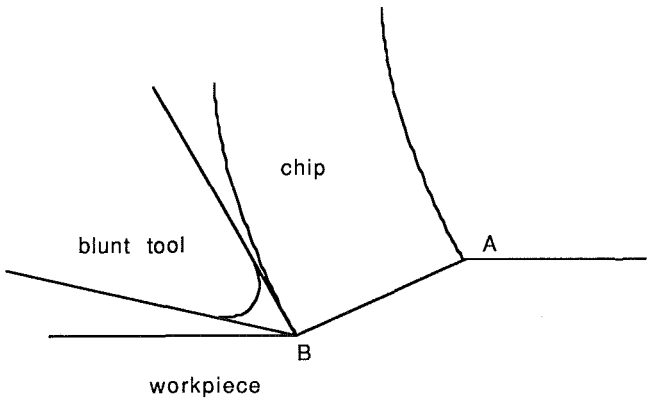

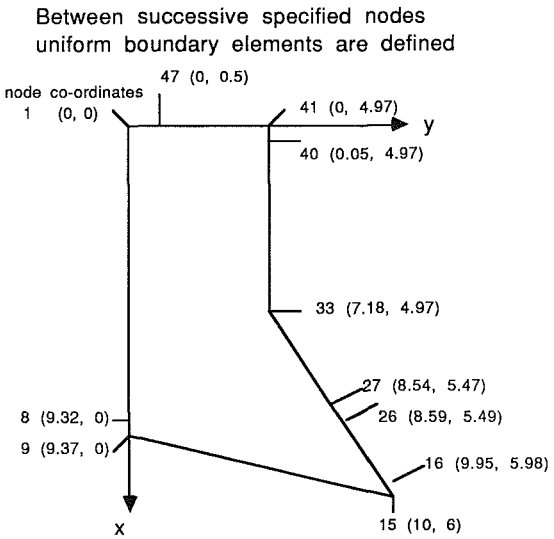

Fig. 8 Schematic diagram for gradual nose wear of a cutting tool in machining problems

Case 4—Gradual Nose Wear of a Cutting Tool. The wear of the tool nose with machining is considered next. The nose curve is parameterized as

$$x' = \eta$$

$$y' = a\left[\frac{1}{b}\exp(-b|\eta|) + |\eta|\right]; \qquad -1.0 \le \eta \le 1.0, \quad (27)$$

where x' and y' are the local tangential and normal coordinates, respectively, at the tool nose. The parameter a is the cotangent of half of the included angle in the tool wedge, and

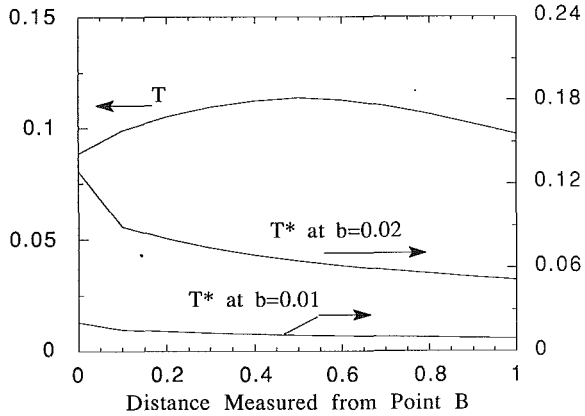

Fig. 9 Temperature sensitivities along the chip-tool interface due to gradual nose wear

b represents the amount of blunting of the tool nose. A perfectly sharp tool is represented by setting $b = 0$, and the blunting of the nose is repeated by increasing b. Figure 8 shows a schematic diagram of the tool wear. Detailed calculations for $\overset{*}{x}_k$, $\overset{*}{n}_k$, and $d\overset{*}{s}$ are given in Appendix B. Figure 9 shows the temperature sensitivity along the chip-tool interface. The abscissa is the distance measured from point B in Fig. 8. In this case, the nominal configuration is of crucial importance. The temperature sensitivity increases significantly as the tool wears out. The maximum temperature sensitivity occurs at point B and goes from 0.021 to 0.129 as b goes from 0.01 to 0.02. This also corroborates the physical observations in real-life machining operations.

Conclusions

A boundary element method (BEM) formulation for the determination of design sensitivities in steady-state conduction-convection problems is developed through a direct differentiation approach (DDA). This does not increase the singularity of the kernels and does retain the accuracy advantages of the BEM. The BEM formulation is based on the fundamental solution of the full adjoint equation. Accordingly, the convection term is modeled with higher precision than that obtained by upwinding in finite difference. Consequently, the BEM solution is stable regardless of the Peclet number and does not show any false diffusion. Irregular boundaries may be easily handled by BEM. It also has the advantage of using a smaller amount of core memory since only the boundary of the domain needs to be discretized. It is also important to note that the matrices of A and B in Eq. (13) depend on the reference configuration only and do not depend on the choice of design parameter b. All the effects for a particular choice of b are incorporated through the right-hand-side vector. Accordingly, for the slight increase in additional cost due to evaluation of right-hand-side vectors, sensitivities with respect to several design variables may be obtained simultaneously. This makes the BEM sensitivities algorithm very efficient. The BEM formulation is applicable to two-dimensional as well as three-dimensional problems.

Numerical results are presented for four two-dimensional problems. For the uniform compression problem, an analytical solution is also obtained. The results obtained from the BEM formulation are almost identical to the analytical solution. For the parabolic bulging case, the results obtained by the BEM sensitivity algorithm compare very well with those obtained by the "differencing scheme." The DDA in conjunction with the BEM can also be used to determine the design sensitivities in many real-life manufacturing processes. Two example problems involving variations of shear plane geometry and gradual

Downloaded 03 May 2010 to 171.66.16.247. Redistribution subject to ASME license or copyright; see http://www.asme.org/terms/Terms_Use.cfm

nose wear of cutting tools in machining problems are also presented in this paper.

Acknowledgments

A. Chandra's contribution to this research has been supported by Grant No. DMC-8657345 of the U.S. National Science Foundation and by Hughes Aircraft Company. C. L. Chan's contribution to this research is supported by Engineering Foundation Grant No. RI-A-88-7.

References

Barone, M. R., and Yang, R.-J., 1988, "Boundary Integral Equations for Recovery of Design Sensitivities in Shape Optimization," *AIAA J.*, Vol. 26, pp. 589–594.

Bhattacharyya, A., 1984, *Metal Cutting Theory and Practice*, Central Book Publisher, Calcutta.

Braibant, V., and Fleury, C., 1984, "Shape Optimal Design Using B-Splines," *Comp. Meth. Appl. Mech. Eng.*, Vol. 44, pp. 247–267.

Carslaw, H. S., and Jaeger, J. C., 1986, *Conduction of Heat in Solids*, 2nd ed., Clarendon Press, Oxford.

Chan, C. L., and Chandra, A., 1991, "A Boundary Element Analysis of the Thermal Aspects of Metal Cutting Processes," ASME *Journal of Engineering for Industry*, Vol. 113, p. 311.

Dawson, P. R., and Malkin, S., 1984, "Inclined Moving Heat Source Model for Calculating Metal Cutting Temperatures," *ASME J. Eng. Ind.*, Vol. 106, pp. 179–186.

Fleury, C., 1979, "Structural Weight Optimization by Dual Methods of Convex Programming," *Int. J. Num. Meth. Eng.*, Vol. 14, pp. 1761–1783.

Haftka, R. T., 1982, "Second Order Sensitivity Derivatives in Structural Optimization," *AIAA J.*, Vol. 20, pp. 1765–1766.

Haftka, R. T., and Gandhi, R. V., 1986, "Structural Shape Optimization—A Survey," *Comp. Meth. Appl. Mech. Eng.*, Vol. 57, pp. 91–106.

Haug, E. J., Choi, K. K., and Komkov, V., 1986, *Design Sensitivity Analysis of Structural Systems*, Academic Press, New York.

Mota Soares, C. A., ed., 1987, *Computer Aided Optimal Design: Structural and Mechanical Systems*, Springer-Verlag, Berlin.

Mukherjee, S., and Chandra, A., 1989, "A Boundary Element Formulation for Design Sensitivities in Materially Nonlinear Problems," *Acta Mechanica*, Vol. 78, pp. 243–253.

Mukherjee, S., and Chandra, A., 1991, "A Boundary Element Formulation for Design Sensitivities in Problems Involving Both Geometric and Material Nonlinearities," *Mathematical and Computer Modelling*, Vol. 15, pp. 81–92.

Muraka, P. D., Barrow, G., and Hinduja, S., 1979, "Influence of the Process Variables on the Temperature Distribution in Orthogonal Machining Using the Finite Element Method," *Int. J. Mech. Sci.*, Vol. 21, pp. 445–456.

Prager, W., and Taylor, J. E., 1968, "Problems of Optimal Structural Design," ASME JOURNAL OF APPLIED MECHANICS, Vol. 35, pp. 102–106.

Rice, J. R., and Mukherjee, S., 1990, "Design Sensitivity Coefficients for Axisymmetric Elasticity Problems by Boundary Element Methods," *Engineering Analysis*, Vol. 7, pp. 13–20.

Saigal, S., and Chandra, A., 1989, "Shape Sensitivities and Optimal Configurations for Heat Diffusion Problems: A BEM Approach," ASME *Journal of Heat Transfer*, Vol. 113, pp. 287–295.

Shaw, M. C., 1984, *Metal Cutting Principles*, Clarendon Press, Oxford.

Stevenson, M. G., Wright, P. K., and Chow, J. G., 1983, "Further Developments in Applying the Finite Element Method to the Calculation of Temperature Distributions in Machining and Comparisons With Experiment," *ASME J. Eng. Ind.*, Vol. 105, pp. 149–154.

Suzuki, K., and Kikuchi, N., 1990, "Shape and Topology Optimization by a Homogenization Method," *Sensitivity Analysis and Optimization with Numerical Methods*, ASME-AMD Vol. 115, pp. 15–30.

Tanaka, Y., Honma, T., and Kaji, I., 1986, "On Mixed Element Solutions of Convection-Diffusion Problems in Three Dimensions," *Appl. Math. Modelling*, Vol. 10, pp. 170–175.

Tay, A. E., Stevenson, M. G., and DeVahl Davis, G., 1974, "Using the Finite Element Method to Determine Temperature Distributions in Orthogonal Machining," *Proceedings Inst. Mech. Engrs.*, Vol. 188, pp. 627–638.

Trent, E. M., 1984, *Metal Cutting*, Butterworths, London.

Tsay, J.-J., and Arora, J. S., 1988, "Design Sensitivity Analysis of Nonlinear Structures With History Dependent Effects," Tech. Rept. ODL-88.4, Optimal Design Laboratory, College of Engineering, University of Iowa, Iowa City.

Zabaras, N., Mukherjee, S., and Richmond, O., 1988, "An Analysis of Inverse Heat Transfer Problems With Phase Changes Using an Integral Method," *ASME J. Heat Transfer*, Vol. 110, pp. 554–561.

APPENDIX A

Determination of $\overset{*}{n}_k(Q)$ in Eq. (9) for Two-Dimensional Cases

Let the parametric representation for the curve be given as

$$x_1 = f(\eta; b) \tag{A1}$$

$$x_2 = g(\eta; b). \tag{A2}$$

The outward normal vector to this curve at any point may be expressed as

$$\mathbf{n} = \frac{\dfrac{\partial x_2}{\partial \eta}\hat{i} - \dfrac{\partial x_1}{\partial \eta}\hat{j}}{\sqrt{\left(\dfrac{\partial x_1}{\partial \eta}\right)^2 + \left(\dfrac{\partial x_2}{\partial \eta}\right)^2}}. \tag{A3}$$

Defining $\overset{*}{n}_k$ as $d(n_k)/db$, when b is the design parameter of interest, we get (for a two-dimensional situation)

$$\overset{*}{n}_1 = -\frac{\dfrac{\partial x_2}{\partial \eta}\left[\dfrac{\partial x_1}{\partial \eta}\dfrac{\partial}{\partial b}\left(\dfrac{\partial x_1}{\partial \eta}\right) + \dfrac{\partial x_2}{\partial \eta}\dfrac{\partial}{\partial b}\left(\dfrac{\partial x_2}{\partial \eta}\right)\right] - \dfrac{\partial}{\partial b}\dfrac{\partial x_2}{\partial \eta}\left[\left(\dfrac{\partial x_1}{\partial \eta}\right)^2 + \left(\dfrac{\partial x_2}{\partial \eta}\right)^2\right]}{\left[\left(\dfrac{\partial x_1}{\partial \eta}\right)^2 + \left(\dfrac{\partial x_2}{\partial \eta}\right)^2\right]^{3/2}} \tag{A4}$$

and

$$\overset{*}{n}_2 = \frac{\dfrac{\partial x_1}{\partial \eta}\left[\dfrac{\partial x_1}{\partial \eta}\dfrac{\partial}{\partial b}\left(\dfrac{\partial x_1}{\partial \eta}\right) + \dfrac{\partial x_2}{\partial \eta}\dfrac{\partial}{\partial b}\left(\dfrac{\partial x_2}{\partial \eta}\right)\right] - \dfrac{\partial}{\partial b}\dfrac{\partial x_1}{\partial \eta}\left[\left(\dfrac{\partial x_1}{\partial \eta}\right)^2 + \left(\dfrac{\partial x_2}{\partial \eta}\right)^2\right]}{\left[\left(\dfrac{\partial x_1}{\partial \eta}\right)^2 + \left(\dfrac{\partial x_2}{\partial \eta}\right)^2\right]^{3/2}}. \tag{A5}$$

The quantities $\partial/\partial b(\partial x_1/\partial \eta)$ and $\partial/\partial b(\partial x_2/\partial \eta)$ depend on the particular choice of the design parameter b. An example is shown in Appendix B.

Determination of $d\overset{*}{s}(b, Q)$ in Eq. (10) for Two-Dimensional Cases

The arc length is

$$s = \int_0^{\eta}\left[\left(\frac{dx_1}{d\eta}\right)^2 + \left(\frac{dx_2}{d\eta}\right)^2\right]^{1/2} d\eta. \tag{A6}$$

Hence,

$$ds = \left[\left(\frac{dx_1}{d\eta}\right)^2 + \left(\frac{dx_2}{d\eta}\right)^2\right]^{1/2} d\eta. \tag{A7}$$

Denoting, $\dfrac{\partial}{\partial b}\left(\dfrac{\partial x_i}{\partial \eta}\right) \equiv \left(\dfrac{\partial x_i}{\partial \eta}\right)^*$,

$$d\overset{*}{s} = \frac{\dfrac{dx_1}{d\eta}\left(\dfrac{dx_1}{d\eta}\right)^* + \dfrac{dx_2}{d\eta}\left(\dfrac{dx_2}{d\eta}\right)^*}{\left[\left(\dfrac{dx_1}{d\eta}\right)^2 + \left(\dfrac{dx_2}{d\eta}\right)^2\right]} ds \tag{A8}$$

or

Downloaded 03 May 2010 to 171.66.16.247. Redistribution subject to ASME license or copyright; see http://www.asme.org/terms/Terms_Use.cfm

$$d\overset{*}{s}=\frac{1}{2}\left\{\frac{\frac{dx_1}{d\eta}\left(\frac{dx_1}{d\eta}\right)^{*}+\frac{dx_1}{d\eta}\left(\frac{dx_1}{d\eta}\right)^{*}+\frac{dx_2}{d\eta}\left(\frac{dx_2}{d\eta}\right)^{*}+\frac{dx_2}{d\eta}\left(\frac{dx_2}{d\eta}\right)^{*}}{\left[\left(\frac{dx_1}{d\eta}\right)^{2}+\left(\frac{dx_2}{d\eta}\right)^{2}\right]}\right\}ds \quad \text{(A9)}$$

or

$$d\overset{*}{s}=\frac{1}{2}\left\{n_2^2\frac{\left(\frac{dx_1}{d\eta}\right)^{*}}{\left(\frac{dx_1}{d\eta}\right)}+n_1^2\frac{\left(\frac{dx_2}{d\eta}\right)^{*}}{\left(\frac{dx_2}{d\eta}\right)}-n_1n_2\left[\frac{\left(\frac{dx_1}{d\eta}\right)^{*}}{\left(\frac{dx_2}{d\eta}\right)}+\frac{\left(\frac{dx_2}{d\eta}\right)^{*}}{\left(\frac{dx_1}{d\eta}\right)}\right]\right\}dx. \quad \text{(A10)}$$

APPENDIX B

Example Calculations of $\partial/\partial b(x_k)$ and $\partial/\partial b(\partial x_k/\partial\eta)$ for a Wedge

Let the family of curves of interest be expressed as

$$x_1'=\eta \quad \text{(B1)}$$

and

$$x_2'=a\left[\frac{1}{b}\exp(-b|\eta|)+|\eta|\right] \quad \text{(B2)}$$

while

$$x_1=x_1'\cos\theta-x_2'\sin\theta \quad \text{(B3)}$$

and

$$x_2=x_1'\sin\theta+x_2'\cos\theta. \quad \text{(B4)}$$

Let "b" be the design parameter of interest. In this case, increasing η_0 increases the radius of curvature of the nose curve of the wedge and θ defines the orientation of the wedge. Then,

$$\overset{*}{x}_1'=\frac{\partial}{\partial b}(x_1')=0 \quad \text{(B5)}$$

and

$$\overset{*}{x}_2'=\frac{\partial}{\partial b}(x_2')=\frac{a}{b}(-|\eta|)\exp(-b|\eta|)-\frac{a}{b^2}\exp(-b|\eta|). \quad \text{(B6)}$$

This gives

$$\overset{*}{x}_1=\frac{\partial x_1}{\partial b}=\frac{a}{b}\exp(-b|\eta|)\left[\frac{1}{b}+|\eta|\right]\sin\theta \quad \text{(B7)}$$

and

$$\overset{*}{x}_2=\frac{\partial x_2}{\partial b}=-\frac{a}{b}\exp(-b|\eta|)\left[\frac{1}{b}+|\eta|\right]\cos\theta. \quad \text{(B8)}$$

Differentiating x_1' and x_2' with respect to η, we get

$$\frac{\partial x_1'}{\partial\eta}=1 \quad \text{(B9)}$$

and

$$\frac{\partial x_2'}{\partial\eta}=a\left[-\exp(-b|\eta|)\frac{\eta}{|\eta|}+\frac{\eta}{|\eta|}\right]. \quad \text{(B10)}$$

This gives

$$\frac{\partial x_1}{\partial\eta}=-a\left[-\exp(-b|\eta|)\frac{\eta}{|\eta|}+\frac{\eta}{|\eta|}\right]\sin\theta \quad \text{(B11)}$$

and

$$\frac{\partial x_2}{\partial\eta}=a\left[-\exp(-b|\eta|)\frac{\eta}{|\eta|}+\frac{\eta}{|\eta|}\right]\cos\theta. \quad \text{(B12)}$$

Finally,

$$\frac{\partial}{\partial b}\left(\frac{\partial x_1}{\partial\eta}\right)=-\eta a\sin\theta\exp(-b|\eta|) \quad \text{(B13)}$$

and

$$\frac{\partial}{\partial b}\left(\frac{\partial x_2}{\partial\eta}\right)=\eta a\cos\theta\exp(-b|\eta|). \quad \text{(B14)}$$

Equations (B11)–(B14) may now be used to calculate $\overset{*}{n}_k$ and $d\overset{*}{s}$, respectively.

Downloaded 03 May 2010 to 171.66.16.247. Redistribution subject to ASME license or copyright; see http://www.asme.org/terms/Terms_Use.cfm

Response of a Liquid Bridge With Rotationally Excited Bottom

Helmut F. Bauer
Univ. Professor,
Institut für Raumfahrttechnik,
Universität der Bundeswehr Munchen,
Werner-Heisenberg-Weg 39,
8014 Neubiberg, Germany

The response of a cylindrical liquid column consisting of an incompressible and frictionless liquid has been investigated for a pitching bridge bottom. The response of the free surface and velocity distribution has been determined and numerically evaluated. In addition, the transient behavior of the column has been treated. Since for nonviscous liquid the response exhibits at the resonances singularity, a semi-empirical damping was introduced in the resonance terms. Its magnitude has to be determined by experiments.

1 Introduction

Cylindrical liquid bridges play an important role in many areas of manufacturing in space. Since they are easily susceptible to oscillations, which are in most cases detrimental to the production processes and its product, the knowledge of the dynamic behavior of such liquid columns has recently gained quite some interest. The vibrational response of the free liquid surface, which in zero or microgravity is in its cylindrical form held together by surface tension, shall therefore be investigated. The knowledge of the magnitude of the natural frequencies of the liquid column and the response of the liquid to harmonic excitations and the transient due to the change of excitation, i.e., change of forcing frequency and excitation amplitude, is of quite some interest to the experimenter. For this reason an experiment on the second German D-2-Spacelab-Mission will be performed under the title "Liquid Columns Resonances" (LICORE), in order to establish experimentally the natural frequencies, the oscillatory liquid behavior, and the response of the liquid to various excitations. To support these experiments the necessary theoretical knowledge of the liquid behavior of a liquid column and pilot experiments on the ground have to be investigated before flight experiments in order to guarantee and receive useful, efficient, and conclusive results from the experiments in orbit. Linearized theory has been performed in numerous investigations for some geometries, as well as for frictionless, viscous, and even viscoelastic liquids (Rayleigh, 1879, 1945; Lamb, 1932; Bauer, 1983, 1984, 1986). The emphasis of these studies centered around the determination of the natural and damped frequencies as well as the stability of the liquid column. Natural frequencies for inviscid liquid are presented for various configurations of immiscible liquids in (Bauer, 1982). Recently, the nonlinear liquid behavior of a frictionless liquid (Eidel and Bauer, 1988) was determined and it was found that for large liquid surface amplitudes, the natural frequencies may deviate considerably from the results of linearized theory if the aspect ratio h/a is small and if its ratio approaches the *Rayleigh instability* in the axisymmetric mode $m=0$. It was also found that higher modes exhibit a larger softening behavior than the lower modes. Linear harmonic axial excitation was investigated (Bauer, 1988) and showed a sharply tuned first-mode response, which could easily be missed by a sweeping experiment. In case the excitation is not completely axial and the test set-up performs (in addition) a rotational component of excitation, other natural frequencies shall appear. For this reason the response of a harmonic rotational excitation is treated here in order to be able to identify these natural frequencies. For various axial excitations such as counter-directional, top and bottom excitation (Bauer, 1989a), one-sided axial excitation (Bauer, 1989b), or unequal excitation of top and bottom wall (Bauer, 1989c), the response was given previously. If the top and liquid bridge bottom walls are excited, both in phase and pitching motion, the response and transient behavior may be found in Bauer (1989d).

2 Basic Equations

A cylindrical liquid column of length h and radius a is placed between two plates of which the lower one (Fig. 1) is harmonically oscillated with $\theta_o e^{i\Omega t}$ about an axis through $\varphi=\frac{\pi}{2}$. The liquid is considered incompressible and frictionless. θ_o is the angular excitation amplitude and Ω the forced excitation frequency. The response of the liquid, which is held together by *surface tension*, shall be investigated, i.e., its velocity distribution and its free surface displacement above the equilibrium position $r=a$. Assuming the liquid flow to be irrotational, the velocity $\mathbf{v}=u\mathbf{e}_r+v\mathbf{e}_\varphi+w\mathbf{k}$ can be represented as the gradient of a velocity potential $\Phi(r, \varphi, z, t)$. Satisfying the continuity equation div $\mathbf{v}=0$ yields the Laplace equation

$$\Delta\Phi=0 \tag{1}$$

where

Contributed by the Applied Mechanics Division of THE AMERICAN SOCIETY OF MECHANICAL ENGINEERS for publication in the JOURNAL OF APPLIED MECHANICS.

Discussion on this paper should be addressed to the Technical Editor, Prof. Leon M. Keer, The Technological Institute, Northwestern University, Evanston, IL 60208, and will be accepted until two months after final publication of the paper itself in the JOURNAL OF APPLIED MECHANICS. Manuscript received by the ASME Applied Mechanics Division, July 24, 1989; final revision, Jan. 18, 1991.

Copyright © 1992 by ASME
Downloaded 03 May 2010 to 171.66.16.247. Redistribution subject to ASME license or copyright; see http://www.asme.org/terms/Terms_Use.cfm

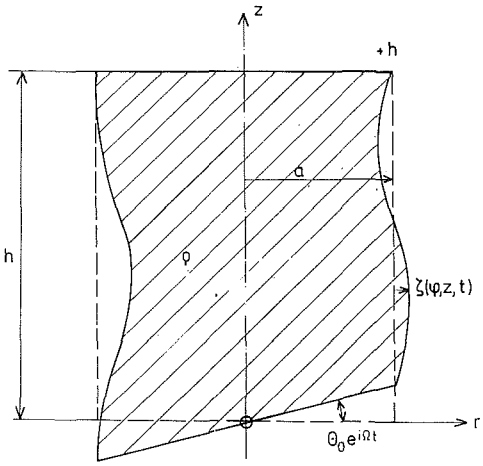

Fig. 1 Geometry of liquid bridge and rotational excitation

$$\Delta \equiv \frac{\partial^2}{\partial r^2}+\frac{1}{r}\frac{\partial}{\partial r}+\frac{1}{r^2}\frac{\partial^2}{\partial \varphi^2}+\frac{\partial^2}{\partial z^2},$$

and which has to be solved with the boundary conditions

$$\frac{\partial \Phi}{\partial z}=\begin{Bmatrix} i\theta_o \Omega e^{i\Omega t} r\cos\varphi & \text{for } z=0 \\ 0 & \text{for } z=h \end{Bmatrix} \tag{2}$$

and the free surface conditions, i.e., the kinematic condition

$$\frac{\partial \Phi}{\partial r}=\frac{\partial \zeta}{\partial t} \text{ at } r=a \tag{3a}$$

and the dynamic condition

$$\frac{\partial \Phi}{\partial t}-\frac{\sigma}{\rho a^2}\left[\zeta+\frac{\partial^2 \zeta}{\partial \varphi^2}+a^2\frac{\partial^2 \zeta}{\partial z^2}\right]=\frac{-\sigma}{\rho a} \text{ at } r=a \tag{3b}$$

where σ is the surface tension, ρ the density of the liquid, and $\zeta(\varphi, z, t)$ is the free surface displacement above $r=a$.

Combining Eqs. (3*a*) and (3*b*) yields

$$\frac{\partial^2 \Phi}{\partial t^2}-\frac{\sigma}{\rho a^2}\left[\frac{\partial \Phi}{\partial r}+\frac{\partial^3 \Phi}{\partial r \partial \varphi^2}+a^2\frac{\partial^3 \Phi}{\partial r \partial z^2}\right]=0 \text{ at } r=a. \tag{4}$$

To obtain the velocity potential Φ, we have to solve the Laplace Eq. (1) with Eqs. (2) and (4).

3 Method of Solution

For the solution of the Laplace equation (1), we transform with

$$\Phi(r,\varphi,z,t)=e^{i\Omega t}\left[\Psi(r,z)-i\Omega\theta_o\frac{r(z-h)^2}{2h}\right]\cos\varphi, \tag{5}$$

thus obtaining the Poisson equation

$$\frac{\partial^2 \Psi}{\partial r^2}+\frac{1}{r}\frac{\partial \Psi}{\partial r}-\frac{\Psi}{r^2}+\frac{\partial^2 \Psi}{\partial z^2}=i\Omega\theta_o r/h \tag{6}$$

which has to be solved with the boundary conditions

$$\frac{\partial \Psi}{\partial z}=0 \text{ for } z=0,\ h. \tag{7}$$

Assuming a solution of the form

$$\Psi(r,z)=A_o(r)+\sum_{n=1}^{\infty}A_n(r)\cos\left(\frac{n\pi z}{h}\right)$$

yields the velocity potential

$$\Phi(r,\varphi,z)=i\Omega\theta_o e^{i\Omega t}ah\cos\varphi\left\{\left(\frac{1}{6}-\frac{1}{8(h^2/a^2)}+\frac{\sigma}{\rho a\Omega^2}\frac{1}{h^2}\right)\left(\frac{r}{a}\right)+\frac{1}{8(h^2/a^2)}\left(\frac{r}{a}\right)^3-\left(\frac{r}{a}\right)\frac{(z-h)^2}{2h^2}-\frac{2\Omega^2}{\pi^2}\sum_{n=1}^{\infty}\frac{I_1\left(\frac{n\pi r}{h}\right)\cos\left(\frac{n\pi z}{h}\right)}{n^2 I_1\left(\frac{n\pi a}{h}\right)(\omega_{1n}^2-\Omega^2)}\right\}, \tag{8}$$

where ω_{1n} are the natural frequencies, i.e.,

$$\omega_{1n}^2=\frac{\sigma}{\rho a^3}\left(\frac{n\pi a}{h}\right)^3\frac{I_1'\left(\frac{n\pi a}{h}\right)}{I_1\left(\frac{n\pi a}{h}\right)},\quad n=1,2,\ldots$$

and where I_1 is the modified Bessel function. From this velocity potential all mechanical values of interest may be obtained by differentiations and integrations. The velocity distribution in the radial direction is

$$u(r,\varphi,z,t)=\frac{\partial \Phi}{\partial r}=i\Omega\theta_o e^{i\Omega t}h\cos\varphi\left\{\left(\frac{1}{6}-\frac{1}{8(h^2/a^2)}+\frac{\sigma}{\rho a\Omega^2 h^2}\right)+\frac{3}{8(h^2/a^2)}\left(\frac{r}{a}\right)^2-\frac{(z-h)^2}{2h^2}-\frac{2\Omega^2}{\pi\left(\frac{h}{a}\right)}\sum_{n=1}^{\infty}\frac{I_1'\left(\frac{n\pi r}{h}\right)\cos\left(\frac{n\pi z}{h}\right)}{nI_1\left(\frac{n\pi a}{h}\right)(\omega_{1n}^2-\Omega^2)}\right\}, \tag{9}$$

in the angular direction

Nomenclature

a = radius of liquid column
h = length of column
I_1 = modified Bessel function of first kind and first order
r,φ,z = cylindrical coordinates
t = time
u,v,w = velocity distribution in radial, circumferential, and axial direction, respectively
ζ = free-surface displacement
$\bar{\zeta}$ = damping factor
Φ = velocity potential
θ_o = rotational excitation angle
Ω = forcing frequency
ω_{1n} = natural frequencies
σ = surface tension
ρ = density of liquid

Downloaded 03 May 2010 to 171.66.16.247. Redistribution subject to ASME license or copyright; see http://www.asme.org/terms/Terms_Use.cfm

$$v(r,\varphi,z,t)=\frac{1}{r}\frac{\partial\Phi}{\partial\varphi}=i\Omega\theta_o e^{i\Omega t}h\sin\varphi\left\{\left(\frac{1}{6}-\frac{1}{8(h^2/a^2)}+\frac{\sigma}{\rho a\Omega^2h^2}\right)\right.$$

$$+\frac{1}{8(h^2/a^2)}\left(\frac{r}{a}\right)^2-\frac{(z-h)^2}{2h^2}$$

$$\left.-\frac{2\Omega^2}{\pi^2}\sum_{n=1}^{\infty}\frac{I_1\left(\frac{n\pi r}{h}\right)\cos\left(\frac{n\pi z}{h}\right)}{n^2I_1\left(\frac{n\pi a}{h}\right)\left(\frac{r}{a}\right)(\omega_{1n}^2-\Omega^2)}\right\}\quad(10)$$

and in the axial direction

$$w(r,\varphi,z,t)=\frac{\partial\Phi}{\partial z}=-i\Omega\theta_o e^{i\Omega t}a\cos\varphi\left\{\frac{(z-h)}{h}\left(\frac{r}{a}\right)\right.$$

$$\left.-\frac{2\Omega^2}{\pi}\sum_{n=1}^{\infty}\frac{I_1\left(\frac{n\pi r}{h}\right)\sin\left(\frac{n\pi z}{h}\right)}{nI_1\left(\frac{n\pi a}{h}\right)(\omega_{1n}^2-\Omega^2)}\right\}.\quad(11)$$

From the free surface condition (3*a*) we obtain,

$$u=\frac{\partial\zeta}{\partial t}\text{ at }r=a$$

for the free surface elevation the expression

$$\zeta(\varphi,z,t)=\theta_o e^{i\Omega t}h\cos\varphi\left\{\left(\frac{1}{6}+\frac{1}{4(h^2/a^2)}+\frac{\sigma}{\rho a^3(h^2/a^2)\Omega^2}\right)\right.$$

$$\left.-\frac{1}{2}\left(\frac{z}{h}-1\right)^2-\frac{2\Omega^2}{\pi}\frac{h}{a}\sum_{n=1}^{\infty}\frac{I_1'\left(\frac{n\pi a}{h}\right)\cos\left(\frac{n\pi z}{h}\right)}{nI_1\left(\frac{n\pi a}{h}\right)(\omega_{1n}^2-\Omega^2)}\right\}.\quad(12)$$

4 Transient Response

If for the time regime $t\leqq 0$ the liquid column is in a steady-state excitation through the rotation of the bottom with $\theta_o e^{i\Omega_o t}$, and is at $t=0$ subjected to a new angular excitation amplitude θ_2 and forcing frequency Ω_2, the system will perform a transient motion, which, in the case of dissipation, results in the steady-state condition with $\theta_2 e^{i\Omega_2 t}$ for $t\to\infty$. To determine the transient liquid behavior, we have to solve the Laplace equations

$$\Delta\Phi_o=0\text{ for }t\leqq 0\text{ and }\Delta\Phi_2=0\text{ for }t\geqq 0\quad(13)$$

with the boundary condition

$$\frac{\partial\Phi_\lambda}{\partial z}=\begin{Bmatrix}i\theta_\lambda\Omega_\lambda e^{i\Omega_\lambda t}r\cos\varphi & \text{for } z=0\\ 0 & \text{for } z=h\end{Bmatrix}\text{ for }\begin{Bmatrix}t\leqq 0\ \lambda=0\\ t\geqq 0\ \lambda=2\end{Bmatrix}\quad(14)$$

together with the free liquid surface condition (4) for $j=0,2$. The velocity potential Φ_2 is the superposition of the final potential Φ_2^* and the transient potential $\tilde{\Phi}$, i.e.,

$$\Phi_1(r,\varphi,z,t)=\Phi_2^*(r,\varphi,z,t)+\sum_{n=1}\tilde{\Phi}_n(r,\varphi,z)e^{i\omega_{1n}t},\quad(15)$$

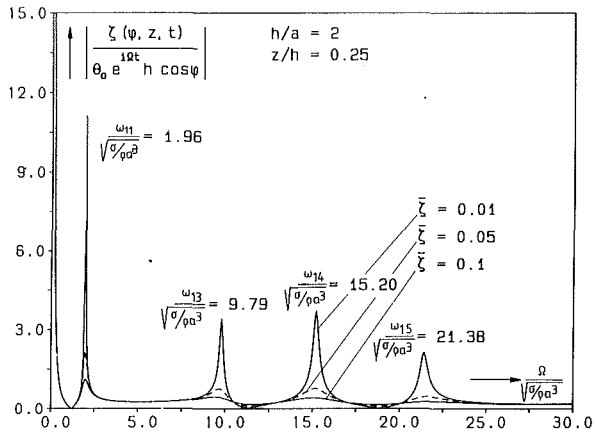

Fig. 2(*a*)

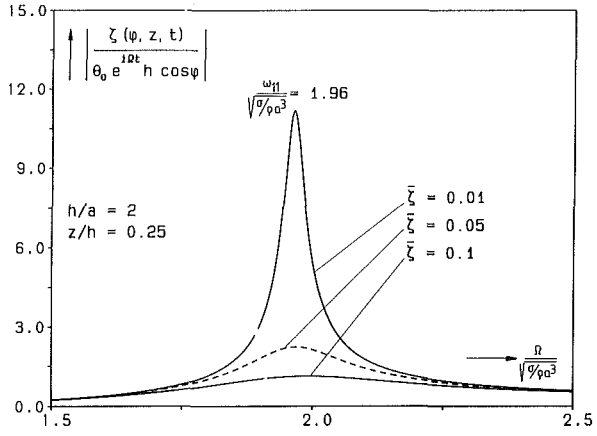

Fig. 2(*b*)

Fig. 2 Response of free-liquid-surface displacement, ζ, at the location $z=h/4$

where we notice that the transient response is (due to the application of frictionless liquid) not damped out. The introduction of damping will later make this transient motion disappear as the time $t\to\infty$. The velocity potential Φ_o for $t\leqq 0$ is given by Eq. (8) for subscript "0", while Φ_2^* yields a similar expression (8) for subscript "2". The transient solution, according to Eqs. (13), (14), and the free surface condition, is obtained from

$$\Delta\tilde{\Phi}=0\text{ and }\frac{\partial\tilde{\Phi}}{\partial z}=0\text{ at }z=0,h.\quad(16)$$

It is

$$\tilde{\Phi}(r,\varphi,z,t)=\sum_{n=1}^{\infty}iC_nI_1\left(\frac{n\pi r}{h}\right)\cos\left(\frac{n\pi z}{h}\right)e^{i\omega_{1n}t}\cos\varphi,\quad(17)$$

with

$$C_n=-\frac{2ah}{\pi^2n^2}\frac{\omega_{1n}}{I_1\left(\frac{n\pi a}{h}\right)}\left[\frac{\theta_o\Omega_o^2}{(\omega_{1n}^2-\Omega_o^2)}-\frac{\theta_2\Omega_2^2}{(\omega_{1n}^2-\Omega_2^2)}\right].\quad(18)$$

The free-surface displacement is obtained for the various time regimes from Eq. (12), while the corresponding velocity and pressure distribution may be easily obtained by differentiations of the velocity potential.

5 Introduction of Damping

Since the response of nonviscous liquid exhibits singularities at the resonances, and since we are particularly interested in

Downloaded 03 May 2010 to 171.66.16.247. Redistribution subject to ASME license or copyright; see http://www.asme.org/terms/Terms_Use.cfm

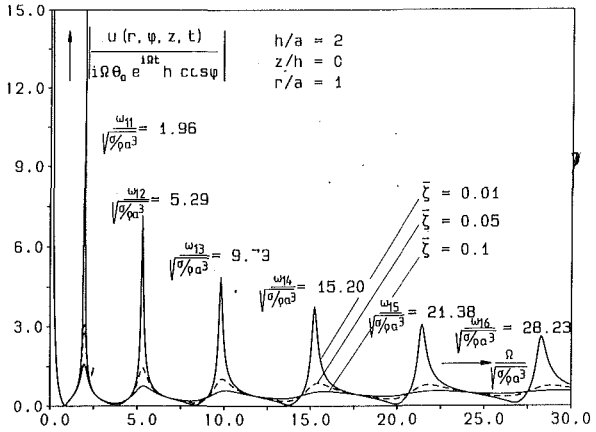

Fig. 3(*a*)

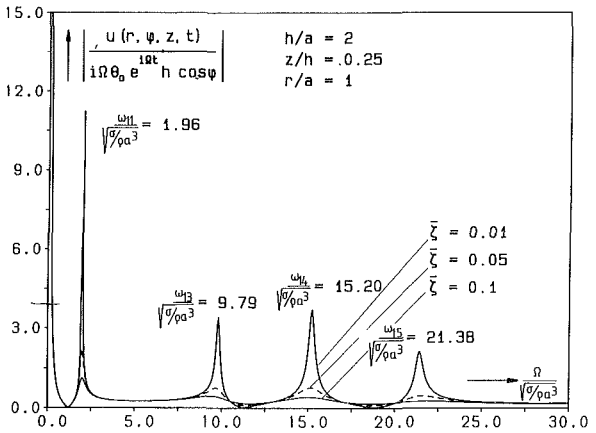

Fig. 3(*b*)

Fig. 3 Response of radial velocity *u* at locations $z=0$, $0.25h$, and $r=a$

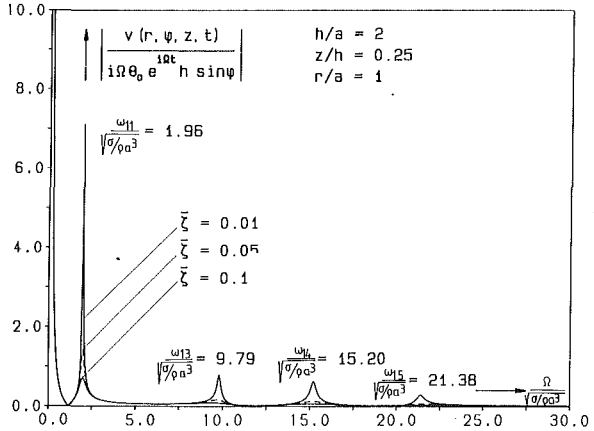

Fig. 4(*a*)

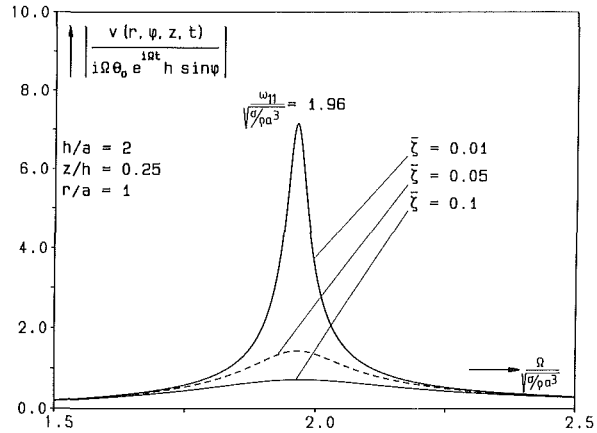

Fig. 4(*b*)

Fig. 4 Response of circumferential velocity *v* at location $z=0.25h$ and $r=a$

those response amplitudes as in the largest ones, we introduce damping in a semi-empirical way by writing for the resonance terms $(\omega_{1n}^2-\Omega^2)$, the expression $(\omega_{1n}^2-\Omega^2+2i\bar{\zeta}_n\omega_{1n}\Omega)$, where the damping factors $\bar{\zeta}_n$ have to be measured in experiments performed with the liquid bridge. Therefore, the free-surface displacement (12) may be written in its damped version in the form

$$\zeta(\varphi,z,t)=\theta_o e^{i\Omega t}h\cos\varphi\left\{\left(\frac{1}{6}+\frac{1}{4(h^2/a^2)}+\frac{\sigma}{\rho a^3(h^2/a^2)\Omega^2}\right)-\frac{1}{2}\left(\frac{z}{h}-1\right)^2-\frac{2\Omega^2}{\pi\left(\frac{h}{a}\right)}\sum_{n=1}^{\infty}\frac{I_1'\left(\frac{n\pi a}{h}\right)\cos\left(\frac{n\pi z}{h}\right)}{n\,I_1\left(\frac{n\pi a}{h}\right)(\omega_{1n}^2-\Omega^2+2i\bar{\zeta}_n\omega_{1n}\Omega)}\right\}. \quad (19)$$

In the case of a transient motion as presented above, the transient part $\tilde{\zeta}$ will decay as

$$e^{-\bar{\zeta}_n\omega_{1n}t+i\omega_{1n}\sqrt{1-\bar{\zeta}_n^2}t}$$

for subcritical damping $\bar{\zeta}_n<1$. Therefore, the free-surface displacement is given by Eq. (12) for subscript "0" and

$$\zeta_2(\varphi,z,t)=\theta_2 e^{i\Omega_2 t}h\cos\varphi\left[\left(\frac{1}{6}+\frac{1}{4(h^2/a^2)}+\frac{\sigma}{\rho a^3(h^2/a^2)\Omega_2^2}\right)-\frac{1}{2}\left(\frac{z}{h}-1\right)^2\right]-\frac{2a}{\pi}\cos\varphi\sum_{n=1}^{\infty}\frac{I_1'\left(\frac{n\pi a}{h}\right)\cos\left(\frac{n\pi z}{h}\right)}{n\,I_1\left(\frac{n\pi a}{h}\right)}\cdot\left\{\frac{\theta_2\Omega_2^2}{(\omega_{1n}^2-\Omega_2^2+2i\bar{\zeta}_n\omega_{1n}\Omega_2)}\cdot\left[e^{i\Omega_2 t}-e^{-\bar{\zeta}_n\omega_{1n}t+i\omega_{1n}\sqrt{1-\bar{\zeta}_n^2}t}\right]+\frac{\theta_o\Omega_o^2}{(\omega_{1n}^2-\Omega_o^2+2i\bar{\zeta}_n\omega_{1n}\Omega_o)}\cdot e^{-\bar{\zeta}_n\omega_{1n}t+i\omega_{1n}\sqrt{1-\bar{\zeta}_n^2}t}\right\}. \quad (20)$$

The velocity distribution for transient motion may be determined in a similar fashion.

6 Numerical Evaluation

Some of the previously obtained analytical results have been evaluated numerically for some special parameters of the system. The aspect ratio of the liquid bridge was chosen to be $h/a=2$. The response has been evaluated at the location $z=h/4$ and $r=a$ for various damping factors $\bar{\zeta}_n=0.01$, 0.05, and 0.1. Before, however, proceeding to the results of the response,

Downloaded 03 May 2010 to 171.66.16.247. Redistribution subject to ASME license or copyright; see http://www.asme.org/terms/Terms_Use.cfm

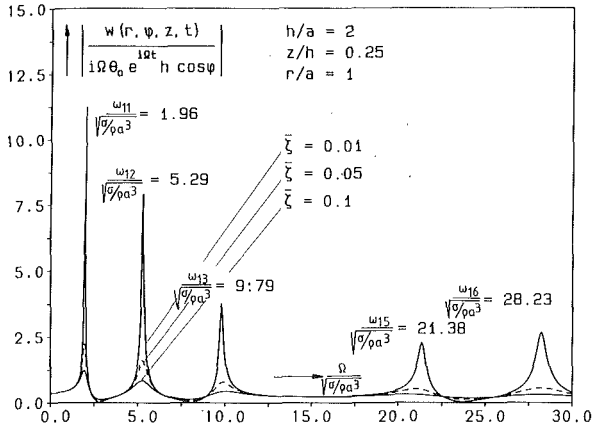

Fig. 5(*a*)

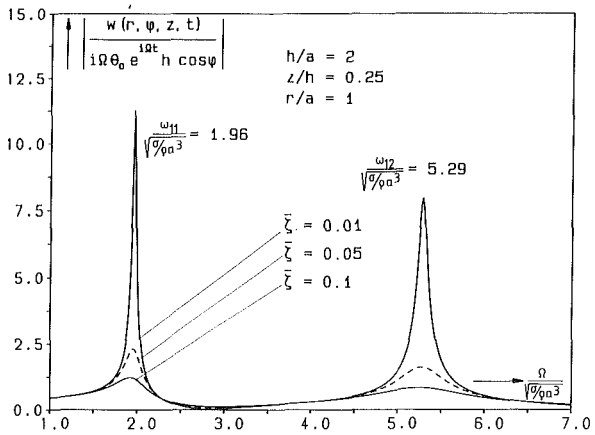

Fig. 5(*b*)

Fig. 5 Response of axial velocity w at location $z=0.25h$ and $r=a$

the term proportional to Ω^{-2} in the foregoing results (9), (10), and (12) calls for some further discussion. As the forcing frequency $\Omega \to 0$ approaches zero value we notice, in the free-surface displacement of the radial and circumferential velocity, a singularity. This is due to the slipping of the liquid at the walls. Since the curvatures of the liquid surface are different at different locations, the pressure is in agreement with the law of Laplace-Young which is larger at the side of the inclined wall surfaces. This yields a motion of the slipping liquid into the converging direction of the inclined walls. The foregoing analytical results have been evaluated numerically after a semi-empirical damping was introduced in the resonance terms. In Figs. 2(*a*) and 2(*b*), the response of the free surface elevation was presented for the height ratio $h/a=2$ at the location $z=h/4$. The damping factor $\bar{\zeta}$ was chosen to be $\bar{\zeta}=0.01$, 0.05, and 0.1 and shows with increasing magnitude, quite a rapid decrease of the resonance amplitudes. The enlarged presentation of the free-surface displacement $|\zeta/\theta_o h e^{i\Omega t}\cos\varphi|$ is shown in Fig. 2(*b*) for only the first resonance at ω_{11}. The radial velocity distribution $|u/i\Omega\theta_o e^{i\Omega t}h\cos\varphi|$ is presented at $z=0$, $h/4$, and $r=a$. While, at $z=h/4$, only the odd resonances at ω_{12n-1} appear, all resonances are present in the response at $z=0$; and only the even ones, ω_{12n}, at the location $z=h/2$. Again, we notice the decrease of resonance amplitudes with increasing mode number and increasing damping factor $\bar{\zeta}$ (Figs. 3(*a*) and 3(*b*)). The circumferential velocity $|v/i\Omega\theta_o e^{i\Omega t}h\sin\varphi|$ is shown in Figs. 4(*a*) and 4(*b*) at $z=h/4$ and $r=a$. The amplitudes at resonances decrease rapidly to very small values after the first mode (ω_{11}). Finally, the axial velocity $|w/i\Omega\theta_o e^{i\Omega t}h\cos\varphi|$ is presented for $z=h/4$ and $r=a$ in Figs. 5(*a*) and 5(*b*), where Fig. 5(*b*) is again an enlarged version around the lower resonances at ω_{11} and ω_{12}. It should be noted that in ζ, u, and v, certain resonances are missing according to $\cos\left(\frac{n\pi}{4}\right)$, while for the axial velocity, w, all resonances ω_{14}, ω_{18}, ... are missing, because $\sin\frac{n\pi}{4}$ yields zero for $n=4,8,\ldots$ ($n=0$ mod (4)).

References

Bauer, H. F., 1982, "Coupled Oscillations of a Solidly Rotating Liquid Bridge," *Acta Astronautica*, Vol. 9, pp. 547–563.

Bauer, H. F., 1983, "Natural Damped Frequencies of an Infinitely Long Column of Immiscible Viscous Liquids," *Forsch. Ing. West.*, Vol. 49, pp. 117–126.

Bauer, H. F., 1984, "Natural Damped Frequencies of an Infinitely Long Column of Immiscible Viscous Liquids," *Zeitschr. Angew. Math. u. Mech.*, Vol. 64, pp. 475–490.

Bauer, H. F., 1986, "Free Surface and Interface Oscillations of an Infinitely Long Viscous-Elastic Liquid Column," *Acta Astronautica*, Vol. 13, pp. 9–22.

Bauer, H. F., 1988, "Axial Response, Transient and Pulse Behavior of a Cylindrical Liquid Column in Zero-Gravity, Part I," Forschungsbericht Universitat der Bundeswehr München, LRT-WE-9-FB-9.

Bauer, H. F., 1989a, "Response of a Liquid Column to Counder-Directional Excitation Under Zero-Gravity," Forschungsbericht der Universitat der Bundeswehr München, LRT-WE-9-FB-6.

Bauer, H. F., 1989b, "Response of a Liquid Column to One-Sided Axial Excitation in Zero-Gravity," Forschungsbericht der Universitat der Bundeswehr München, LRT-WE-9-FB-3.

Bauer, H. F., 1989c, "Response of a Liquid Column to Unequal Counter-directional Excitation Under Zero-Gravity," Forschungsbericht der Universitat der Bundeswehr München, LRT-WE-9-FB-7.

Bauer, H. F., 1989d, "Response of a Liquid Column With Respect to Oscillatory Rotational Top and Bottom Excitation," Forschungsbericht der Universitat der Bundeswehr München, LRT-WE-9-FB-8.

Eidel, W., and Bauer, H. F., 1988, "Nonlinear Oscillations of an Inviscid Liquid Column Under Zero-Gravity," *Ing. Arch.*, Vol. 58, pp. 276–284.

Lamb, H.l, 1982, *Hydrodynamics*, Cambridge University Press, Cambridge, U.K.

Rayleigh, Lord, 1879, "On the Capillary Phenomenon of Jets," *Proc. Royal Society, London*, Vol. 29, pp 71–79.

Rayleigh, Lord, 1945, *Theory of Sound*, Dover, New York.

Downloaded 03 May 2010 to 171.66.16.247. Redistribution subject to ASME license or copyright; see http://www.asme.org/terms/Terms_Use.cfm

M. P. Païdoussis[1]
Department of Mechanical Engineering,
McGill University,
Montreal, Quebec, H3A 2K6, Canada
Fellow ASME

J. P. Cusumano
Department of Engineering
Science and Mechanics,
Pennsylvania State University,
University Park, PA 16802
Mem. ASME

G. S. Copeland
Department of Theoretical
and Applied Mechanics,
Cornell University,
Ithaca, NY 14853

Low-Dimensional Chaos in a Flexible Tube Conveying Fluid

This paper describes the observed dynamical behavior of a cantilevered pipe conveying fluid, an autonomous nonconservative (circulatory) dynamical system, limit-cycle motions of which, upon loss of stability via a Hopf bifurcation, interact with nonlinear motion-limiting constraints. This system was found to become chaotic at sufficiently high flow rates. Motions of the system, sensed by an optical tracking system, were analyzed by Fast Fourier Transform, autocorrelation, Poincaré map, and delay embedding techniques, and the fractal dimension of the system, d_c, was calculated. Values of d_c = 1.03, 1.53, and 3.20 were obtained in the period-1, "fuzzy" period-2 and chaotic regimes of oscillation of the system. Based on these calculations, a four-dimensional analytical model was constructed, which was found to capture the essential dynamical features of observed behavior quite well.

1 Introduction

It is well known that a cantilevered pipe conveying fluid, an autonomous nonconservative system, loses stability by flutter at sufficiently high flow velocity (Païdoussis, 1987), via a Hopf bifurcation leading to a stable limit-cycle oscillation—as elucidated by several theoretical and experimental studies of the problem, e.g., by Benjamin (1961), Gregory and Païdoussis (1966), Herrmann and Nemat-Nasser (1967), Paıdoussis (1970), Païdoussis and Issid (1976), Holmes (1977), Sethna and Shapiro (1977), Bejaj, Sethna, and Lundgren (1980), Rousselet and Herrmann (1981), to mention but a few.

With the recent interest in chaotic motions of nonlinear mechanical systems (Guckenheimer and Holmes, 1983; Moon, 1987), it seemed natural to investigate whether regions of chaotic oscillations could exist in the parameter space of a modified version of the fluid-conveying cantilever system, in which limit-cycle motions interact with motion-limiting constraints; these constraints provide a source of strong nonlinearity of the type shown in the past, for forced vibration of slender beams, to give rise to interesting dynamics and chaos (Moon and Shaw, 1983; Shaw and Holmes, 1983; Shaw, 1985).

To assuage possible fears that the system to be investigated may be too particular, some words may be appropriate. First, the fluid-conveying cantilevered pipe has become a classical problem for the study of all autonomous nonconservative dynamical systems (Païdoussis, 1987) because of the simplicity with which it can be modelled analytically and the relative ease with which reliable experiments may be conducted—thus affording theoretical and experimental investigations in parallel and comparison of one to the other; see, e.g., Païdoussis (1970). Second, although a pipe conveying fluid is perhaps one of the simplest conceivable systems involving fluid-structure interaction, yet it displays a surprisingly rich kaleidoscope of dynamical behavior and may be considered a paradigm for a very broad class of problems in aero-hydro-elasticity (Dowell, 1975; Tang and Dowell, 1988; Chen, 1987; Blevins, 1977). Finally, the motion-limiting constraints being considered are inspired from the real physical world, in which limit-cycle motions often interact with purposely or unintentionally present restraints; see, e.g., Axisa et al. (1988), Païdoussis and Li (1991), and Tung and Shaw (1988). The first two of these references are of particular importance here, since they deal with another self-excited fluid-elastic system interacting with motion limiting constraints: namely, the flow-induced chaotic oscillations of heat-exchanger tubes impacting on the baffle plates, a technologically important problem.

The experimental system of a pipe conveying fluid with motion-limiting constraints was investigated first. These experiments will be described briefly in Section 2, whereas a fuller description is given by Païdoussis and Moon (1988). The main emphasis of this paper is in the analysis of the experimental data, the central question being the determination of the fractal dimension of the system, which, among other things, indicates the lowest dimension that an analytical model should have if it is to capture the essential dynamics of the experimental system.

2 The Experiments

The experiments were conducted with an elastomer cantilevered pipe hanging vertically, with the lower end free as

[1]This work was initiated while on sabbatic leave at the Department of Theoretical and Applied Mechanics, Cornell University, Aug. 1987–May 1988.

Contributed by the ASME Applied Mechanics Division of THE AMERICAN SOCIETY OF MECHANICAL ENGINEERS for presentation at the Winter Annual Meeting, Atlanta, Ga., Dec. 1–6, 1991.

Discussion on this paper should be addressed to the Technical Editor, Prof. Leon M. Keer, The Technological Institute, Northwestern University, Evanston, IL 60208, and will be accepted until two months after final publication of the paper itself in the JOURNAL OF APPLIED MECHANICS. Manuscript received by the ASME Applied Mechanics Division, Aug. 2, 1989; final revision, May 3, 1991.
Paper No. 91-WA/APM-17.

Copyright © 1992 by ASME
Downloaded 03 May 2010 to 171.66.16.247. Redistribution subject to ASME license or copyright; see http://www.asme.org/terms/Terms_Use.cfm

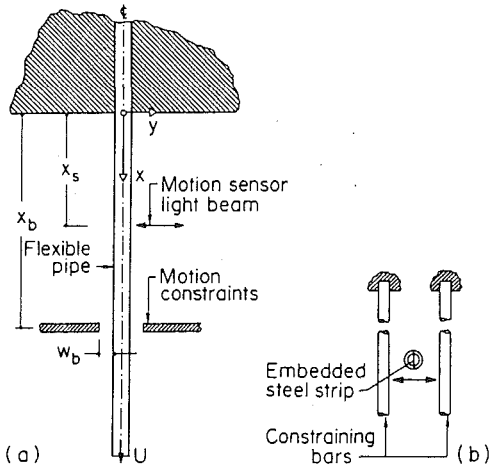

Fig. 1(*a*) Schematic of the experimental system; (*b*) scheme for achieving planar motions with steel strip embedded in the pipe, also showing motion-constraining bars

shown in Fig. 1(*a*). The pipe was molded specially, to ensure uniformity and straightness. In order to make the dynamics as simple as possible, lateral motions were confined to a plane; this was achieved by incorporating a thin metal strip, integrally molded with the pipe, in a diametral plane of the pipe all along its length, Fig. 1(*b*).

The fluid utilized was water, provided by a closed-loop supply-collection system via a centrifugal pump. The pump discharged the water into a large, partially air-filled tank, upstream of the flexible pipe, so that the flow rate delivered to the pipe was acceptably steady. The flow rate was varied through a set of valves and a bypass loop to the test-pipe circuit. Care was taken to ensure that the flow entering the flexible pipe was uniform and swirl-free, through the use of screens and a long straight run of piping just upstream, of much larger diameter than that of the flexible pipe, leading to a smooth contraction with a 36:1 area ratio.

The motion constraints in the experiments to be described were two polycarbonate-plastic horizontal bars (Fig. 1(*b*)) on either side of the flexible pipe, each of which acted as a beam, and thus had some flexibility when impacted upon at its midpoint by the pipe. The location of the constraints x_b and the gap w_b (Fig. 1) were varied, but in these experiments they were constant.

The motion was sensed by an optical tracking system (Optron 806A) at a location x_s, typically 0.2 L, where L is the flexible pipe length; at appreciably larger x_s the amplitude was generally too large for the tracking system to follow linearly and reliably. The signal could be analyzed directly on a FFT signal analyzer or stored on disk via a Nicolet 2090 digital storage oscilloscope; the disks could then be loaded onto a minicomputer for analysis.

The mass flow rate, the main variable in the experiments, was monitored continuously from the readout of weighing scales, on which rested a large tank collecting the water discharging from the pipe; the out-flow from the tank could be interrupted quickly by closing a ball valve, and the amount of water collected in a given time measured.

Experiments were conducted with several pipes, and qualitatively all gave similar results. Only one set of experiments will be presented here and analyzed in depth, where the system parameters for the pipe were as follows: internal and external diameters D_i = 7.94 mm, D_o = 15.88 mm, length L = 441 mm, mass per unit length (empty) m = 0.182 kg/m, flexural rigidity EI = 7.28 × 10^{-3} N m^2, and logarithmic decrement for material damping in the empty pipe δ_1 = 0.028, δ_2 = 0.081, in the first and second mode, respectively. For the constraints, x_b/L = 0.65 and w_b/D_o = 1.52; the stiffness at the point of impact by the flexible pipe was measured to be 740 N/m (4.23 lb/in.), but the effective stiffness was smaller, as the pipe wall also is flexible.

The general behavior of the system was as follows: With increasing flow, the effective damping of the system increased gradually, to the point where the system became overdamped, as ascertained by perturbing the system with a small push (cf., Gregory and Païdoussis, 1966; Païdoussis, 1970). Increasing the flow further eventually resulted in a rapid decrease in effective damping, to the point where it eventually became negative, leading to a Hopf bifurcation and limit-cycle motion of the pipe. The amplitude of the limit cycle at $x = x_b$ was sufficiently small for impacting on the motion constraints not to occur; however, as the flow rate was augmented further, the amplitude increased, and impacting with the constraints began to take place. At light impacting levels the vibration was periodic, with progressively richer harmonic content. Then, at higher flow rates, the subharmonic content increased very appreciably and the motion became erratic, as will be described in Section 4.

3 Data Analysis

In analyzing data from nonlinear systems, it is necessary to use several different techniques which can then be checked against each other to arrive at a full picture of the dynamical state which generated the data. Two of the techniques used in this paper, the Fast Fourier Transform (FFT) and autocorrelation, come from the domain of traditional signal analysis and need not be discussed here. The other techniques, the delay-embedding method and the computation of what are generically called fractal dimensions, are recent developments in dynamical systems theory. A full introduction to these and other methods can be found in Moon's (1987) book, which contains many examples of applications as well as an extensive bibliography. An excellent review paper from a more theoretical point of view is that of Eckmann and Ruelle (1985).

The basic assumption underlying our approach is that the dynamical steady state being analyzed is evolving on a low-dimensional manifold in the full phase space (which itself can have many, possibly infinite dimensions). One would like to characterize different attracting states and to track changes in the states as system parameters are varied. In addition, knowledge of the dimensions of attractors over the operating range of a system yields a firm estimate of the number of degrees of freedom needed to model observed dynamics.

In this paper we use the *correlation dimension* developed by Grassberger and Proccacia (1983a,b). The correlation dimension has been the most widely applied dimension measure, largely because of the ease with which it can be computed. Malraison et al. (1983) and Brandstäter et al. (1983) have used the correlation dimension to study low-dimensional chaos in fluid systems. Recently, Cusumano and Moon (1990) have successfully applied this technique to the study of a flexible solid-mechanical system.

To define the correlation dimension, let $\mathbf{x}(t)$ denote the steady-state solution under consideration: Following our basic assumptions, we assume $\mathbf{x}(t)$ to be a finite-dimensional state vector. We sample the data at a fixed time-step Δt and obtain a data record

$$\{\mathbf{x}_1, \mathbf{x}_2, \mathbf{x}_3, \ldots, \mathbf{x}_N\},$$

where $\mathbf{x}_i \triangleq \mathbf{x}(\Delta t i)$ and the time origin is taken to be zero. To measure the dimension of this set, Grassberger and Proccacia define the *correlation integral* $C(r)$ as

$$C(r) = \lim_{N\to\infty} \frac{1}{N^2} \sum_{i=1}^{N} \sum_{\substack{j=1 \\ j\neq i}}^{N} H(r - \|\mathbf{x}_i - \mathbf{x}_j\|)$$

$$\simeq \frac{1}{N_{\text{pairs}}} \sum_{i=1}^{N} \sum_{j>i} H(r - \|\mathbf{x}_i - \mathbf{x}_j\|), \quad (1)$$

Downloaded 03 May 2010 to 171.66.16.247. Redistribution subject to ASME license or copyright; see http://www.asme.org/terms/Terms_Use.cfm

where H is the Heaviside step function, r is a scalar length scale and $N_{\text{pairs}} = 1/2(N^2 - N)$. Note that in the limit as $N \to \infty$, the two expressions (1) become equal. $C(r)$ is the cumulative distribution of length scales on the attractor; this statistical interpretation is important for efficient computation. Grassberger and Proccacia defined the correlation dimension d_c by

$$\lim_{r\to 0} \frac{\ln C(r)}{\ln r} = d_c. \tag{2}$$

The main problem that must be addressed in applying Eqs. (1) and (2) to experimental data is that the data record (which in our case is sampled output from the optical tracking system) is of the form

$$\{x_1, x_2, \ldots, x_N\} \quad (x_i = x(\Delta t i)), \tag{3}$$

where the x_i are now simply *scalar* quantities. Using the delay embedding procedure, however, one can reconstruct the phase space of the underlying system. This technique was first used by Packard et al. (1980) and put on a sound mathematical foundation by Takens (1980). To construct vectors $\mathbf{x}_i \in \mathbb{R}^m$ from the scalar series $\{x_i\}_{i=1}^N$ for some fixed m, one simply forms m-tuples from the scalar series by defining

$$\begin{aligned}\mathbf{x}_i &\triangleq (x(\Delta t i), x(\Delta t(i+d)), \ldots, x(\Delta t(i+(m-1)d))) \\ &= (x_i, x_{i+d}, \ldots, x_{i+(m-1)d}),\end{aligned} \tag{4}$$

where $d \in \mathbb{N}$ and $(\Delta t)d$ is called the *delay*. The set of all vectors so constructed are called *pseudovectors* and the dimension m used in their construction is called the *embedding dimension*. For m sufficiently large, this procedure leaves the topological type and dimension of the underlying attractor invariant. Thus, one can use the collection of pseudovectors to obtain an estimate for d_c. Note, however, that one must pick m and d to implement the method.

Selection of a delay is a subtle issue and the reader is referred to papers by Broomehead and King (1986) and Fraser and Swinney (1986) for examples of how the idea of "optimality" in d might be approached. In this work, suitable delays were found by plotting (x_i, x_{i+d}) and choosing values for d that expanded the pseudo-orbit as much as possible with respect to the noise amplitude in the system while maintaining a deterministic orbit structure. Nearby values for d were then used to check that consistent results are obtained. We opted for a simple trial-and-error approach to finding delays, as originally used by Malraison et al. (1983), because at the time of writing the jury was still out on competing, more sophisticated methods.

The overall strategy for finding the dimension of the attractor is to pick m, construct the m-dimensional pseudovectors, and compute $d_c = d_c(m)$; m is then incremented and the procedure is repeated. For a deterministic signal, d_c will level out at some critical value of m; whereas for a random signal d_c will grow indefinitely, and in the limit of an infinite number of data points, $d_c(m) = m$.

The statistical nature of $C(r)$ was used to efficiently compute d_c. For a given embedding dimension, all pseudo-vectors are constructed and stored; then, a random subset thereof (with N_{subs} elements) is selected from the total population of approximately N pseudo-vectors ($N \gg N_{\text{subs}}$). All distances in the subset are computed, sorted, normalized so that the largest distance is equal to 1, and stored in a one-dimensional array with N_{pairs} elements, where $N_{\text{pairs}} = 1/2\,(N_{\text{subs}}^2 - N_{\text{subs}})$. This array is used to obtain an approximate cumulative distribution $C_j(r_i)$ evaluated at 500 values of r_i which are equally spaced on a logarithmic scale. Another subset is chosen and the procedure is repeated N_{avg} times for the same embedding dimension. Then the average $C_j(r_i)$ is obtained:

$$\overline{C}_i \triangleq \overline{C}(r_i) = \frac{1}{N_{\text{avg}}} \sum_{j=1}^{N_{\text{avg}}} C_j(r_i) \simeq C(r_i). \tag{5}$$

This algorithm is repeated for each embedding dimension, giving an entire family of $\ln \overline{C}(r)$ versus $\ln r$ curves (a typical set of such curves being shown in Fig. 2(d)). The scaling regions in the $\ln \overline{C}(r)$ versus $\ln r$ curves were identified, and a least-squares fit used to obtain an estimate of $d_c(m)$ for each m. Error estimates for d_c were obtained using standard methods (Bevington, 1969); an alternative approach that yields significantly larger estimates has been proposed by Holzfuss and Mayer-Kress (1987). First, one has the formula for the variance of the mean:

$$\sigma^2_{\overline{C}(r_i)} = \frac{1}{N_{\text{avg}}(N_{\text{avg}}-1)} \sum_{j=1}^{N_{\text{avg}}} (C_j(r_i) - \overline{C}(r_i))^2; \tag{6}$$

then from the least-squares fit formula for the slope,

$$d_c \simeq \frac{\Sigma u_i \Sigma v_i - N_{\text{scale}} \Sigma u_i v_i}{\Delta}, \tag{7}$$

where N_{scale} is the number of points in the scaling region, $\Delta = (\Sigma u_i)^2 - N_{\text{scale}} \Sigma u_i^2$, $u_i = \ln r_i$ and $v_i = \ln \overline{C}_i$. Thus, the measurement error in d_c is

$$\delta d_c \le \sum_{i=1}^{N_{\text{scale}}} \left|\frac{\partial d_c}{\partial v_i}\right| \delta v_i = \sum_{i=1}^{N_{\text{scale}}} \left|\frac{\partial d_c}{\partial v_i}\right| \frac{\sigma_{\overline{C}_i}}{\overline{C}_i}. \tag{8}$$

Note that we use 68 percent confidence limits for all error estimates. The "quadrature" or root mean-square estimate for error was not used, since it is not reasonable to assume that variations in the v_i's are statistically independent. We also point out that it is generally difficult to get a good estimate of *systematic* errors in estimates for d_c.

4 Experimental Results

We now turn to the results of this paper. By applying the techniques of Section 3, a bifurcation sequence for the fluid-tube system is followed by using the water mass flow rate W as the bifurcation parameter; W was controllable to 0.005 kg/s over the range of the experiment. All data is the output of an optical tracking system, as presented in Section 2. In the analysis, 32,000-point records sampled at 50 Hz were used in each case. In all cases, the data was low-pass filtered by a Butterworth filter with a knee frequency of 25 Hz. All FFTs were taken with a signal analyzer, utilizing a Hanning window.

The results for a mass flow rate $W = 0.335$ kg/s are shown in Fig. 2. The FFT of Fig. 2(a) shows a nominally periodic signal with a fundamental frequency at 2.7 Hz. In this and subsequent figures, the FFT can be seen to have two components: one comprised of a series of approximate delta functions, and the other a "noisy" broad-band component. In the FFT of Fig. 2(a) the noisy component has a maximum level of 50 dB below the peak of the fundamental. The accompanying autocorrelation $R(s)$ of Fig. 2(b) shows that the effect of noise (deterministic or otherwise) is not appreciable, since strong correlation is apparent for time scales associated with many fundamental periods of the motion. A delay reconstruction of the orbit (Fig. 2(c)) confirms that to the visual limit of system noise the motion is periodic: A fuzzy closed orbit is the result.[2] Finally, Fig. 2(d, e) shows the results of correlation dimension calculations for the data: d_c saturates above $m = 2$ to a value of about 1.030 with an estimated measurement error of ± 0.004 and a scaling region in r of about $e^{2.7}$, or a factor of 14. Note that the $\ln \overline{C}$ versus $\ln r$ curves have a "knee" at $\ln r \simeq -3.8$. This phenomenon is well known and is caused by the random noise component of the signal (see, for example, Eckmann and Ruelle, 1985): Slopes below the knee will increase monotonically, and given enough data will approach the embedding dimen-

[2]The plane Σ defining the Poincaré section of Figs. 2(c), 3(c), and 4(c) is given by $\Sigma = [(x(n), x(n+d), x(n+2d)) | x(n) = 0, x(n+d) > 0]$.

Downloaded 03 May 2010 to 171.66.16.247. Redistribution subject to ASME license or copyright; see http://www.asme.org/terms/Terms_Use.cfm

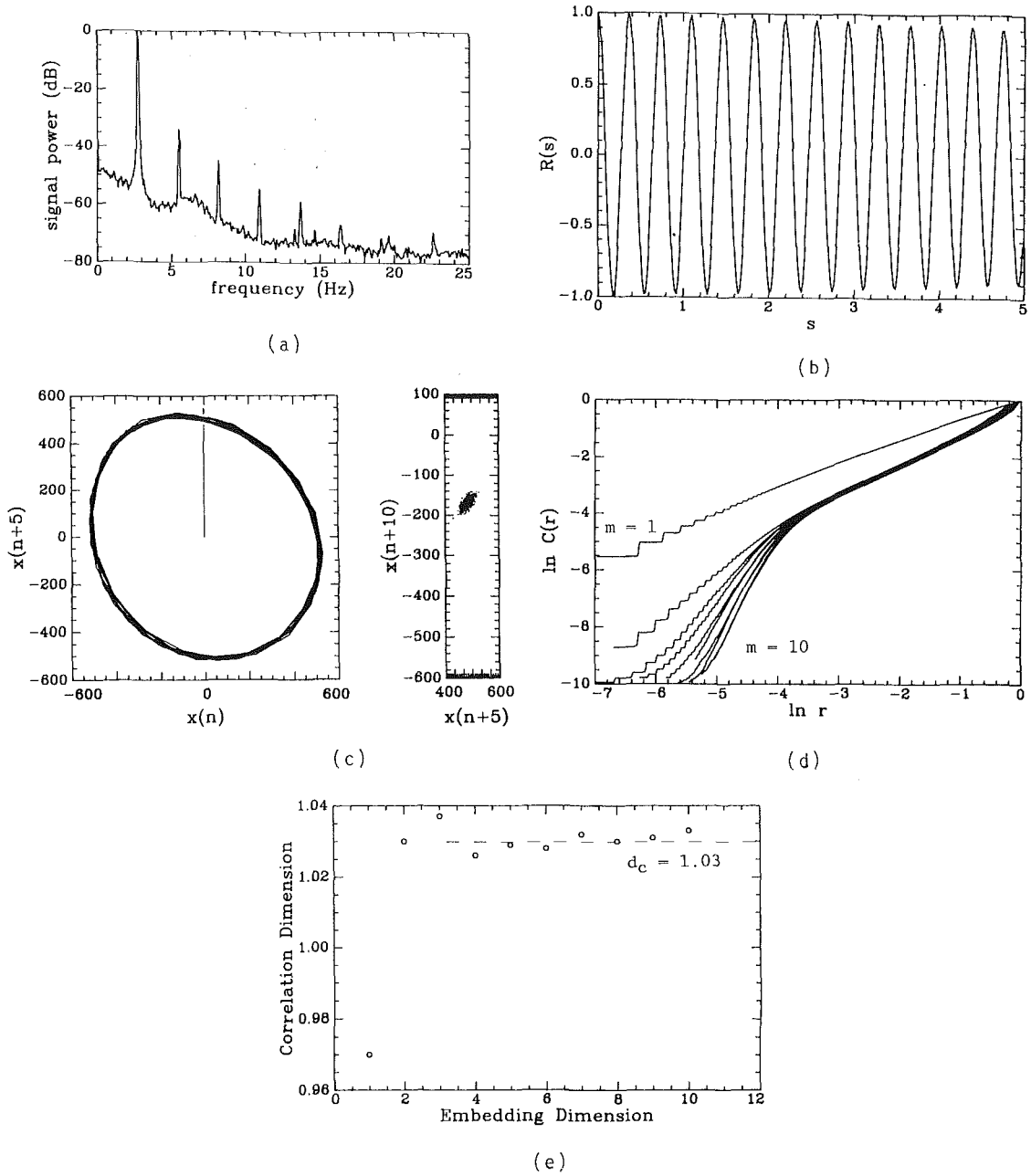

Fig. 2(*a*) Power spectrum; (*b*) normalized autocorrelation; (*c*) delay reconstruction of the orbit and a corresponding Poincaré section; (*d*) correlation integral $C(r)$ versus length scale r for embedding dimensions $m = 1 - 10$; (*e*) correlation dimension d_c versus embedding dimension m; all from the displacement signal from the optical tracking system at $W = 0.335$ kg/s. In (*c*), the output from the optical device is unscaled (arbitrary units), and the vertical line marks location of the section $[x(n) = 0; x(n + 5) > 0]$. In (*d*), $d = 5$, $N_{subs} = 300$, $N_{avg} = 50$. In (*e*), the measurement error (68 percent confidence limit) for convergent $m(\geq 4)$ was 0.004.

sion. The knee gives an estimate of the relative noise amplitude: $r_{noise} \simeq \exp(-3.8) \simeq 0.02$, which compares favorably to the estimate one obtains by measuring directly from the pseudo-orbit the ratio of the noisy "thickness" of the orbit to its maximum diameter.

The dimension results confirm the essentially periodic nature of the motion. The fact that the estimate of d_c overshoots by about 3 percent the value of 1 theoretically expected for a periodic orbit is believed to result from the random noisy component of the dynamics, and is consistent with similar observations made elsewhere (Abraham et al., 1986). This result suggests that true errors may be an order of magnitude larger than the mean-square errors obtained here, cf. Caswell and Yorke (1986), who suggest that all dimension estimates be accompanied by the scaling range used for the computation.

Figure 3 shows the results for the system with W increased to 0.360 kg/s. The FFT shows that the fundamental (peak) frequency of the response has increased slightly to 3.1 Hz. In addition, a period-two subharmonic bifurcation has occurred, and the broad-band component of the spectrum has increased to a maximum value of about 35 dB below the peak. The autocorrelation still shows a large periodic component, but the

Downloaded 03 May 2010 to 171.66.16.247. Redistribution subject to ASME license or copyright; see http://www.asme.org/terms/Terms_Use.cfm

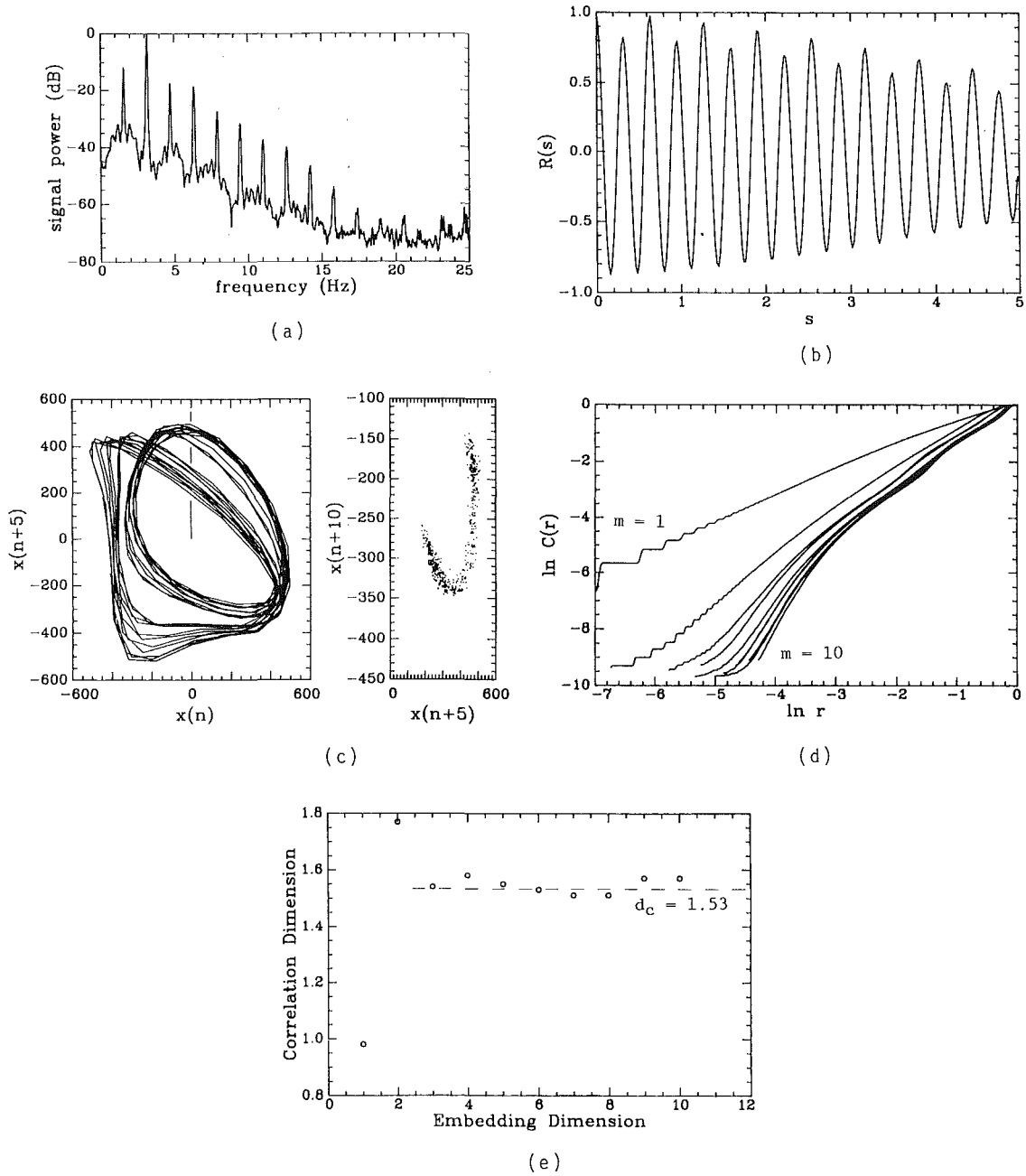

Fig. 3(*a*) Power spectrum; (*b*) normalized autocorrelation; (*c*) delay reconstruction of orbit and Poincaré section; (*d*) correlation integral $C(r)$ for embedding dimensions $m = 1 - 10$; (*e*) correlation dimension d_c versus m; for $W = 0.360$ kg/s

signal becomes significantly uncorrelated after only 15 or 20 fundamental periods. The delay reconstruction of the orbit shows an attractor with the topology of a thick Möbius strip. The edge of the attractor is the most often visited, which is consistent with the nominally period-two character of the motion, since period-two subharmonic orbits can be viewed geometrically as the edge of a Möbius strip. That the attractor is indeed near a two-dimensional manifold can be seen in the Poincaré section of Fig. 3 which shows that a section through the attractor can be well fitted by a curve. However, the probability of visiting points along the curve is not uniform due to the strong subharmonic component of the motion. Hence, one expects a dimension for this attractor between 1 and 2, and the results in Fig. 3(*d*, *e*) show that this is indeed the case since d_c saturates at a value of about 1.53 with a measurement error of ± 0.03.[3] This result is problematic in that the attractor lies in a fuzzy band near a Möbius strip which is a two-dimensional nonorientable manifold. It is known from Peixoto's Theorem (Chillingsworth, 1977) that the only *structurally stable* dynamical systems on two-dimensional manifolds are those whose attracting sets are either fixed points or periodic orbits (assuming certain reasonable hypotheses), and thus one should expect an orbit lying in a Möbius strip to have at most $d_c = 1$ (within measurement error). We hypothesize that the orbit is indeed chaotic, but that the additional degrees-of-freedom required are hidden in the system noise. This hypothesis is

[3]In Fig. 3(*d*) the scaling region is $(-2.8, -1.8)$ on the ln r axis, or $r_{max}/r_{min} = 2.7$.

Downloaded 03 May 2010 to 171.66.16.247. Redistribution subject to ASME license or copyright; see http://www.asme.org/terms/Terms_Use.cfm

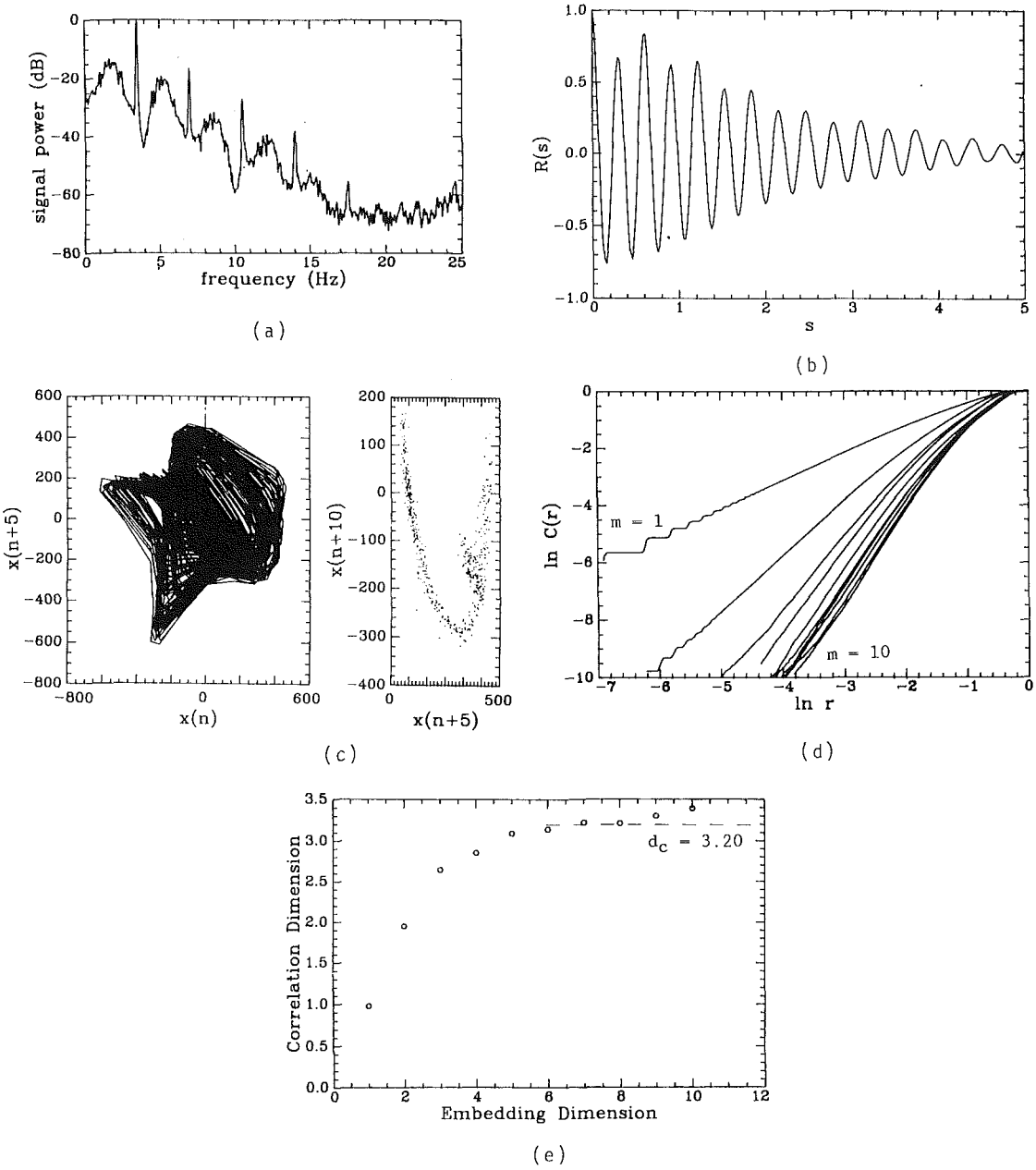

Fig. 4 Same as caption for Fig. 3, but for W = 0.370 kg/s

supported by the modeling and numerical work presented in Section 5.

The final set of experimental results are shown in Fig. 4, which were obtained for W = 0.370 kg/s. The fundamental harmonic components of the signal has moved up to 3.5 Hz and the broad-band signal component has a maximum value of only 15 dB below the peak. The subharmonic portion of the signal appears to be buried under a low-frequency noisy modulation. While the motion still has a strong harmonic component, the autocorrelation shows that the signal is substantially uncorrelated after only seven fundamental periods. The delay reconstruction of the orbit shows that the motion has become more complex and is not readily displayed in two or three dimensions, although a significant amount of structure is apparent. The computation of the correlation dimension converges nicely and an estimate for d_c of 3.20 ± 0.07 is obtained.[4]

[4]In Fig. 4(*d*) the scaling region is (−3, −2) on the ln r axis, or r_{max}/r_{min} = 2.7.

The results show that as the mass flow rate is increased, the correlation dimension of the attracting orbits for the tube-fluid system increased from about 1 to about 3.2. One can use these results to put bounds on the number of state variables needed to model the observed dynamics. A lower bound is easy to obtain. The delay-embedding procedure results in having an image of the attractor suspended in a linear vector space with m state variables: To contain a fractal object of dimension d_c, one needs to have m be *at least* the next greatest integer to d_c. For an upper bound, a theorem due to Mañé (1981) is needed which states that one can always parametrize the surface containing the attractor by m variables if $m > 2d_k + 1$, where d_k is the *capacity dimension*. If the orbit covers the attractor uniformly, $d_c = d_k$; in general, however, $d_c \leq d_k$ (for example, for the results of Fig. 3, $d_k \simeq 2$ but $d_c \simeq 1.5$ because the orbit is more dense at the edges). Nevertheless, one obtains a reasonable estimate for the upper bound by assuming that for the chaotic system $d_c \simeq d_k$ and thus m is bounded by

$$d_c \leq m \leq 2d_c + 2. \tag{9}$$

Downloaded 03 May 2010 to 171.66.16.247. Redistribution subject to ASME license or copyright; see http://www.asme.org/terms/Terms_Use.cfm

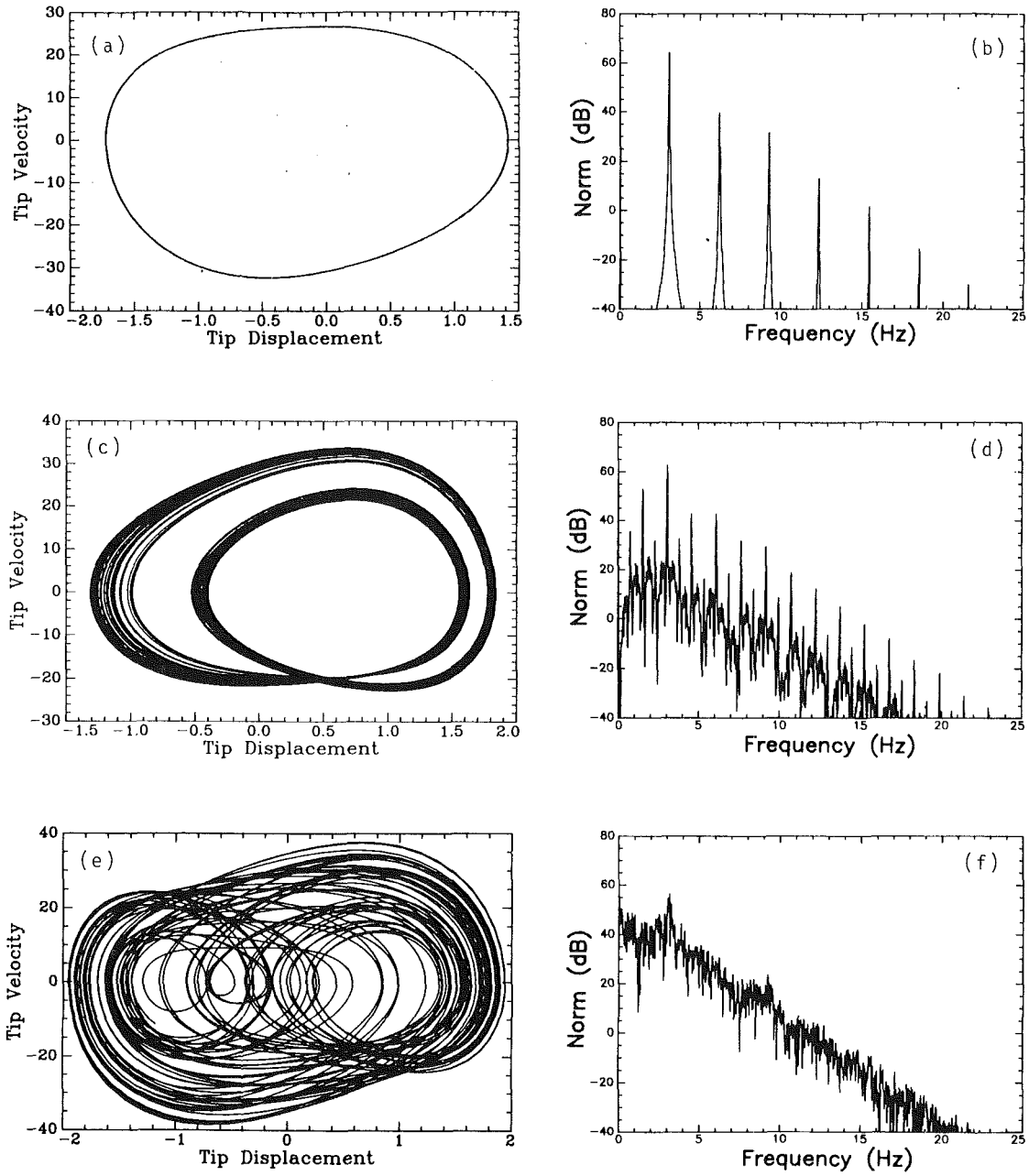

Fig. 5 Theoretical phase-plane portraits and corresponding power spectra for the dimensionless tip displacement $\eta(1, \tau)$: (*a*), (*b*) for W = 0.395 kg/s (u = 9.12); (*c*), (*d*) for W = 0.436 kg/s (u = 10.06), (*e*), (*f*) for W = 0.450 kg/s (u = 10.4126)

In our case, the maximum value of d_c is about 3.2, so

$$3.2 \leq m \leq 8.4.$$

In other words, our data leads to the estimate that one needs between two and four degrees-of-freedom to model the dynamics of the system.

5 The Analytical Model and Simulation Results

5.1 The Model. A four-dimensional (two degree-of-freedom) analytical model was constructed, based on the linear equations of motion of the unconstrained system and with the motion limiting constraints modeled by a cubic spring (Païdoussis, 1970; Païdoussis and Moon, 1988); the nondimensional motion is given by

$$\frac{\partial^4\eta}{\partial\xi^4} + u^2\frac{\partial^2\eta}{\partial\xi^2} - \frac{\partial}{\partial\xi}\left[\gamma(1-\xi)\frac{\partial\eta}{\partial\xi}\right] + 2\beta^{1/2}u\frac{\partial^2\eta}{\partial\xi\partial\tau} + c_r\frac{\partial\eta}{\partial\tau} + \kappa\eta^3\delta(\xi-\xi_b) + \frac{\partial^2\eta}{\partial\tau^2} = 0. \quad (10)$$

For a pipe of flexural rigidity EI, length L and mass per unit length m, mass of the conveyed fluid per unit length M, flow velocity U, cubic spring stiffness k, modal damping c_r, and lateral pipe displacement $w(x, t)$, x being the axial location along the pipe and t the time, the dimensionless quantities in (9) are defined by

$$\eta = w/L, \quad \xi = x/L, \quad \tau = [EI/(M+m)]^{1/2}t/L^2,$$
$$u = [M/EI]^{1/2}UL, \quad \beta = M/(M+m),$$
$$\gamma = (M+m)gL^3/EI, \quad \kappa = kL^5/EI, \quad (11)$$

Downloaded 03 May 2010 to 171.66.16.247. Redistribution subject to ASME license or copyright; see http://www.asme.org/terms/Terms_Use.cfm

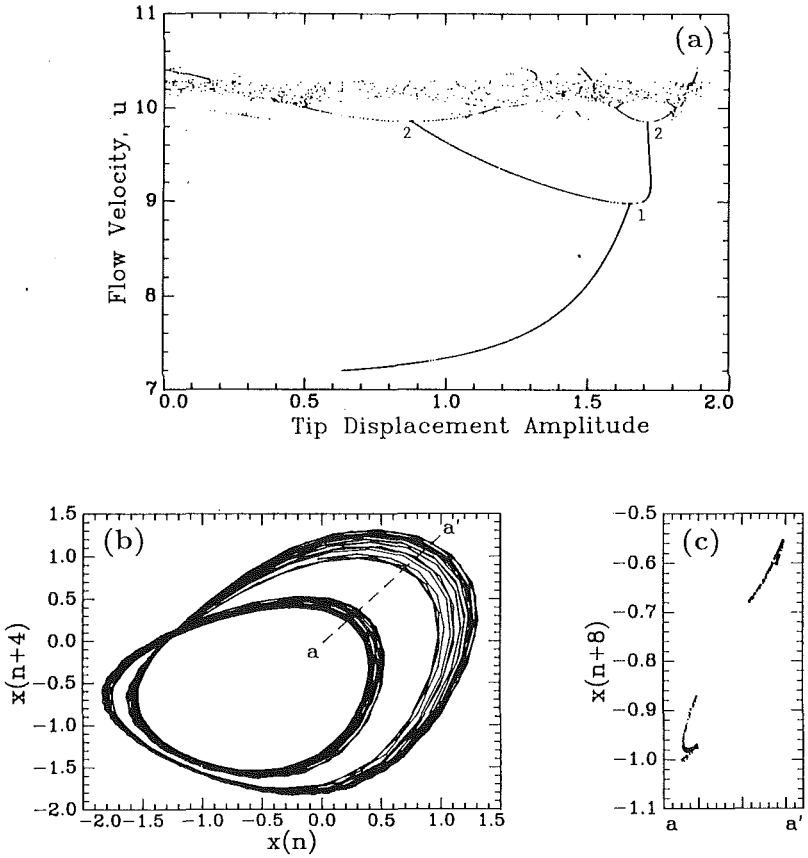

Fig. 6(*a*) The bifurcation diagram of the amplitude of the tip displacement, $\eta(1, \tau)$, with the dimensionless flow velocity, u, as bifurcation parameter; 1. transcritical-like pitchfork bifurcation, 2. first period-doubling bifurcation; (*b*) theoretical delay-reconstructed orbit, and (*c*) Poincaré map for $W = 0.436$ kg/s, just beyond the onset of chaos, where the Poincaré section plane Σ is as shown by the dashed line in (*b*) of this figure

ξ_b is the location of the cubic spring (see Fig. 1) and δ is the Dirac delta function. Thus, the seven terms in (10) may be identified as (i) the flexural restoring force, (ii) the flow-induced centrifugal force, (iii) the gravity-induced tension force, (iv) the flow-induced Coriolis force, (v) the damping force, (vi) the cubic-spring force, and (vii) the inertia force. In contrast to previous work (Païdoussis and Moon, 1988), here a more realistic, equivalent viscous-damping model is used employing the measured modal logarithmic decrements δ_r and the corresponding zero-flow eigenfrequencies ω_r, $r = 1, 2$, so that $c_r = (\delta_r/\pi)\omega_r$ in the discretized system.

Utilizing Galerkin's method, with the cantilever-beam eigenfunctions as a base, the infinite-dimensional system of Eq. (10) is reduced to a two degree-of-freedom discrete system, and thence to a four-dimensional first-order system:

$$\{\dot{y}\} = [A]\{y\} + \{f(y)\}, \quad \{y\} = \{q_1, \dot{q}_1, q_2, \dot{q}_2\}^T, \qquad (12)$$

where the elements of the 4×4 matrix $[A]$ are functions of the dimensionless flow velocity u, reduced mass β, gravimetric parameter γ, and dissipative constants c_1 and c_2 for the first and second mode, respectively; the elements of $\{f(y)\}$ are functions of the dimensionless spring constant κ and the beam eigenfunctions at the point of the constraint, $\phi_r(\xi_b)$, $r = 1, 2$, and are cubic functions of the q_r.

5.2 Results. Solutions of Eq. (12) were obtained using a fourth-order Runge-Kutta integration algorithm with a step size of 0.005. The results presented in Figs. 5 and 6 were computed with the parameters $\beta = 0.21$, $\gamma = 27$, $\xi_b = 0.75$, $\kappa = 100$, $c_1 = 0.045$, $c_2 = 0.640$. They are those of the experimental system, except for ξ_b which was slightly larger (cf. Section 2), and κ which is much smaller, the experimental value being of $\mathcal{O}(10^4)$. Calculations with $\xi_b = 0.65$ and $\kappa \sim \mathcal{O}(10^4)$ led to numerical difficulties, in the case of ξ_b at least reflecting weaknesses in the four-dimensional modeling of the system. Concerning the value of κ, it was found that varying it from 10 to 10^4 caused insignificant changes in the critical values of u in the bifurcation diagram; indeed, the principal effect of the value of κ was in the size of the limit cycle and, in the case of chaotic motion, the corresponding basin of attraction of the strange attractor: The larger the value of κ, the smaller were the motions (Païdoussis et al., 1988, 1991). Hence, for computational ease the value of $\kappa = 100$ was retained throughout, since the general character of the solutions was not affected.

The "tip displacement" and "tip velocity" in Figs. 5 and 6 represent the reconstituted two-dimensional approximation of the dimensionless free-end displacement, $\eta(1, \tau) = \phi_1(1)q_1(\tau) + \phi_2(1)q_2(\tau)$ and the corresponding velocity $\dot{\eta}(1, \tau)$.

The bifurcation diagram of Fig. 6(*a*) shows $\eta(1, \tau)$ at τ when $\dot{\eta}(1, \tau)$ crosses zero from the positive side, with the dimensionless flow velocity u as the bifurcation parameter; the conversion for u in these experiments is W(kg/s) = 0.0433 u.

Figure 6(*a*) shows the bifurcations beyond the Hopf bifurcation, which occurs at $u = 7.15$, for initial values of $\{y\} = \{0, \pm 0.1, 0, \pm 0.1\}^T$ and $\{\pm 0.10, 0, \pm 0.1, 0\}^T$. The first bifurcation observed is at $u = 8.95$; it is a transcritical-type pitchfork bifurcation, whereupon the symmetry of the limit-cycle is destroyed, as shown in the phase-plane diagram of Fig. 5(*a*). The two branches of the pitchfork have been obtained

Downloaded 03 May 2010 to 171.66.16.247. Redistribution subject to ASME license or copyright; see http://www.asme.org/terms/Terms_Use.cfm

with different initial conditions (the ± signs above). At u = 9.90, a sequence of period-doubling bifurcations begins, leading to chaos at $u = u_{chaos} = 10.06$. The phase-plane diagrams and power spectra of Fig. 5(*c*, *d*) and 5(*e*, *f*) correspond, respectively, to the weakly chaotic region just after transition and to a more strongly chaotic region at higher u.

5.3 Comparison With Analyzed Experimental Data. The phase-plane portraits and power spectra of Fig. 5 correspond to W = 0.395, 0.436, and 0.450 kg/s, each about 20 percent higher than the experimental values of W in Figs. 2, 3, 4, respectively. Apart from that, however, the qualitative and quantitative similarities between experiment and simulation are remarkable. Thus, for the lowest W in the set, Fig. 2 shows an asymmetric periodic orbit, with a power spectrum showing several harmonics; so do the analytical results of Fig. 5(*a*, *b*). The principal frequency f_{pr} in Fig. 2 is 2.7 Hz, whereas in Fig. 5(*b*) f_{pr} = 3.0 Hz.

For the intermediate value of W, the power spectrum of Fig. 5(*d*) shows a nominally period-two motion. However, there is a broad-band component to the signal with a maximum level about 40 dB below the peak. The overall shape of the power spectrum is similar to that Fig. 3(*a*). Since the numerical data is virtually free of random noise, the broad-band spectrum suggests that the system is chaotic. The tip-displacement phase-plane plot of Fig. 5(*c*) shows that the orbit has a shape close to a Möbius strip, similar to the attractor observed in the experimental orbit of Fig. 3(*c*). Thus, similarly to Fig. 3(*c*), the orbit visits the edge of the attractor most often; in fact, in the simulation attractor of Fig. 5(*c*), there is no probability for the orbit to visit a band close to the middle of the attractor. Thus, Fig. 5(*c*, *d*) displays a chaotically modulated period-two motion, very similar to the experimentally observed state of Fig. 3. We remark for completeness that a second attractor coexists with this one, which is identical up to a rotation about the origin by 180 deg.

Since the phase trajectory of Fig. 5(*c*) crosses itself, it is clear that the motion requires at least three phase-space dimensions. To explore this further, we performed a delay reconstruction in $\mathbb{R}^3$ of the numerical tip coordinate, η, just as was done for the experimental data of Figs. 2–4(*c*), and is shown in Fig. 6(*b*). The reconstructed data was then used to obtain a Poincaré section of the orbit, again just as was done for experimental data; the result is shown in Fig. 6(*c*). The Poincaré map shows that the attractor is indeed close to a two-dimensional manifold. Across the thickness of the numerically obtained attractor, folding regions are clearly visible, and such folding regions are known to be associated with chaotic attractors (Crutchfield, 1982). This confirms that the orbit is chaotic and that the attractor can be embedded in $\mathbb{R}^3$. The result supports the hypothesis that the experimentally observed motion of Fig. 3(*c*) is evolving on a strange attractor of dimension greater than two, but that random noise in the system is sufficiently large to swamp the thin fractal direction of the attractor.

Finally, for the highest W, the results of Figs. 4 and 5 show strongly chaotic behavior. The corresponding spectra show the presence of a strong principal frequency, f_{pr} = 3.5 and 3.1 – 3.3 Hz, respectively, in Figs. 4(*c*) and 5(*f*). There are some clear qualitative differences between the experimental data and the simulation data in this case. First, the experimental power spectrum has strong harmonic components visible, even though the broad-band component of the spectrum is only about 15 dB below the peak, whereas in the simulation the broad-band components are dominant. Second, the simulation attractor has regained some of the symmetry lost in the original pitchfork bifurcation; it is symmetric with respect to rotations by 180 deg in the tip-displacement phase plane. No such symmetry is apparent in the corresponding experimental data. In fact, the simulation attractor of Fig. 5(*e*) appears to recombine the two separate, but symmetrically related, attractors that coexist for u below 10.06 ($W < 0.436$ kg/s).

6 Conclusion

In this paper, the delay embedding method and computation of fractal dimension are briefly introduced and then applied to the specific problem at hand. The remarkable feature of these techniques is that, starting from a set of time series representing a single measurement (the displacement time history of a particular point of the pipe), a set of calculations may be performed from which the dynamical behavior of the system may be assessed in some detail without even knowing the system or having an analytical model at one's disposal. This paper demonstrates that this can be done even with less than perfect, noisy (i.e., typical) experimental data. The delay-reconstruction orbits of Figs. 2, 3, 4(*c*) are closely similar to experimental phase-plane plots (velocity versus displacement) obtained from on-line direct processing of the optical tracking signal (Païdoussis and Moon, 1988).

Furthermore, the fractal dimension determination via correlation dimension calculations showed clearly that the complex dynamics of an essentially infinite-dimensional system may in practice be projected onto a low-dimensional manifold, which nevertheless retains the essence of the dynamics of the system. The minimum correlation dimension found ranged from approximately 1 for periodic motion, to 3.2 for chaotic motion. This suggests that an analytical model with reasonable prospects of reproducing the dynamics of the system (including chaos) should at the very least be four-dimensional, i.e., of two degrees-of-freedom. Moreover, as discussed in Section 4, this minimum is not necessarily sufficient, and the model may have to be as high as eight dimensional (four degrees-of-freedom); in fact, more degrees-of-freedom than that may be needed in practice, since dimension theory does not indicate appropriate configuration variables. This study shows that dimension calculations are sensitive to noise. Further development of these methods must directly address the effects of noise in the system and in the measurement apparatus.

In this paper the results for a considerably idealized, two degree-of-freedom model are presented and compared to the analyzed experimental results. The remarkable thing is that the model not only is capable of capturing the essentials of both observed and delay-reconstructed dynamical behavior—cf. the spectra of Figs. 3(*a*) and 5(*d*), and the delay reconstruction maps and Poincaré sections of Figs. 3(*c*) and 6(*b*, *c*), for instance—but can do so within reasonable quantitative margins. The model works especially well in the flow-velocity range following from the Hopf bifurcation to the weakly chaotic (i.e., lower-dimensional) state of Fig. 3. The model begins to diverge from the experimental results for the more strongly chaotic (i.e., higher-dimensional) state of Fig. 4.

Thus, despite excellent qualitative agreement, quantitative agreement between experiments and the two degree-of-freedom model is only of $\mathcal{O}$(20 percent). For better agreement, a higher-dimensional model is required, with more realistic modeling of impact dynamics. Such a model has recently been constructed (Païdoussis et al., 1991). It was shown that convergence, in terms of the critical flows for period-doubling and chaotic oscillations, could be obtained as the number of degrees-of-freedom was increased to 4 or 5. With four degrees-of-freedom, agreement of about 12 percent could be obtained, with only a slight improvement for five degrees-of-freedom. This is in good agreement with the prediction of Eq. (9) and *a posteriori* further validates these dimension calculations (conducted some two years earlier). Hence, both the lowest and minimum highest fractal dimensions were estimated by the methods of this paper with high accuracy.

Downloaded 03 May 2010 to 171.66.16.247. Redistribution subject to ASME license or copyright; see http://www.asme.org/terms/Terms_Use.cfm

Acknowledgments

The authors are very grateful to Prof. F. C. Moon for making available to them all facilities, experimental and computational, of his laboratories at Cornell, where this work was carried out, and to Dr. G.-X. Li for assistance with some of the simulation results.

References

Abraham, N. B., Albano, A. M., Das, B., De Guzman, G., Yong, S., Gioggia, R. S., Puccioni, G. P., and Tredicce, J. R., 1986, "Calculating the Dimension of Attractors from Small Data Sets," *Physics Letters*, Vol. 114A, pp. 217–221.

Axisa, F., Antunes, J., and Villard, B., 1988, "Overview of Numerical Methods for Predicting Flow-Induced Vibration," *ASME Journal of Pressure Vessel Technology*, Vol. 110, pp. 6–14.

Bajaj, A. K., Sethna, P. R., and Lundgren, T. S., 1980, "Hopf Bifurcation Phenomena in Tubes Carrying Fluid," *SIAM Journal of Applied Mathematics*, Vol. 39, pp. 213–230.

Benjamin, T. B., 1961, "Dynamics of a System of Articulated Pipes Conveying Fluid. I. Theory; II. Experiments," *Proceedings of the Royal Society, London*, Vol. A261, pp. 457–486, 487–499.

Bevington, P. R., 1969, *Data Reduction and Error Analysis for the Physical Sciences*, McGraw-Hill, New York.

Blevins, R. D., 1977, *Flow-Induced Vibration*, Van Nostrand Reinhold, New York.

Brandstäter, A., Swift, J., Swinney, H., Wolf, A., Farmer, J. D., Jen, E., and Crutchfield, J. P., 1983, "Low-Dimensional Chaos in a Hydrodynamic System," *Physical Review Letters*, Vol. 51, pp. 1442–1445.

Broomhead, D. S., and King, G. P., 1986, "Extracting Qualitative Dynamics from Experimental Data," *Physica*, Vol. 20D, pp. 217–236.

Caswell, W. E., and Yorke, J. A., 1986, "Invisible Errors in Dimension Calculations: Geometric and Systematic Effects," *Dimensions and Entropies in Chaotic Systems*, G. Mayer-Kress, ed., Springer-Verlag, Berlin.

Chen, S. S., 1987, *Flow-Induced Vibration of Circular Cylindrical Structures*, Hemisphere, Washington, D.C.

Chillingsworth, D. R. J., 1976, *Differential Topology With a View to Application*, Pitman, London.

Crutchfield, J. P., 1982, "Chaotic Attractors of Driven Oscillators," *Chaotica I*, (video tape available from Aerial Press, Santa Cruz, Calif.).

Cusumano, J. P., and Moon, F. C., 1990, "Chaotic Nonplanar Vibrations of a Forced Elastica. I. Experimental Observation of Planar Instability and Computation of Fractal Dimensions," submitted for publication.

Dowell, E. H., 1975, *Aeroelasticity of Plates and Shells*, Noordhoff, Leyden.

Eckmann, J.-P., and Ruelle, D., 1985, "Ergodic Theory of Chaos and Strange Attractors," *Reviews of Modern Physics*, Vol. 57, pp. 617–656.

Fraser, A. M., and Swinney, H. L., 1986, "Independent Coordinates for Strange Attractors from Mutual Information," *Physical Review*, Vol. 33A, pp. 1134–1140.

Grassberger, P., and Proccacia, I., 1983a, "Measuring the Strangeness of Strange Attractors," *Physica*, Vol. 9D, pp. 189–208.

Grassberger, P., and Proccacia, I., 1983b, "Characterization of Strange Attractors," *Physical Review Letters*, Vol. 50, pp. 346–349.

Gregory, R. W., and Païdoussis, M. P., 1966, "Unstable Oscillation of Tubular Cantilevers Conveying Fluid. I. Theory; II. Experiments," *Proceedings of the Royal Society, London*, Vol. A293, pp. 512–527, 528–542.

Guckenheimer, J., and Holmes, P. J., 1983, *Nonlinear Oscillations, Dynamical Systems and Bifurcation of Vector Fields*, Springer, New York.

Herrmann, G., and Nemat-Nasser, S., 1967, "Instability Modes of Cantilevered Bars Induced by Fluid Flow through Attached Pipes," *International Journal of Solids and Structures*, Vol. 3, pp. 39–52.

Holmes, P. J., 1977, "Bifurcations to Divergence and Flutter in Flow-Induced Oscillations: A Finite-Dimensional Analysis," *Journal of Sound and Vibration*, Vol. 53, pp. 471–503.

Holzfuss, J., and Mayer-Kress, G., 1986, "An Approach to Error Estimation in the Application of Dimension Algorithms," *Dimensions and Entropies in Chaotic Systems*, G. Mayer-Kress, ed., Springer-Verlag, Berlin.

Malraison, G., Atten, P., Bergé, P., and Dubois, M., 1983, "Dimension of Strange Attractors: An Experimental Determination of the Chaotic Regime of Two Convective Systems," *Journal of Physics Letters*, Vol. 44, pp. 897–902.

Mañé, R., 1981, "On the Dimension of the Compact Invariant Sets of Certain Non-Linear Maps," *Dynamical Systems and Turbulence* (Springer Lecture Notes in Mathematics), Vol. 898, D. A. Rand and L.-S. Young, eds., New York: Springer-Verlag, New York, pp. 230–242.

Moon, F. C., 1987, *Chaotic Vibrations: An Introduction for Applied Scientists and Engineers*, John Wiley and Sons, New York.

Moon, F. C., and Shaw, S. W., 1983, "Chaotic Vibrations of a Beam With Non-Linear Boundary Conditions," *International Journal of Non-Linear Mechanics*, Vol. 18, pp. 465–477.

Packard, N. H., Crutchfield, J. P., Farmer, J. D., and Shaw, R. S., 1980, "Geometry from a Time Series," *Physical Review Letters*, Vol. 45, pp. 712–716.

Païdoussis, M. P., 1970, "Dynamics of Tubular Cantilevers Conveying Fluid," *Journal of Mechanical Engineering Science*, Vol. 12, pp. 85–103.

Païdoussis, M. P., 1987, "Flow-Induced Instabilities of Cylindrical Structures," *Applied Mechanics Reviews*, Vol. 40, pp. 163–175.

Païdoussis, M. P., and Issid, N. T., 1974, "Dynamic Stability of Pipes Conveying Fluid," *Journal of Sound and Vibration*, Vol. 33, pp. 267–294.

Païdoussis, M. P., and Li, G. X., 1991, "Dynamics of Cross-Flow-Induced Vibrations of Heat-Exchanger Tubes Impacting on Loose Supports," *Journal of Sound and Vibration*, in press.

Païdoussis, M. P., Li, G. X., and Rand, R. H., 1991, "Chaotic Motions of a Constrained Pipe Conveying Fluid: Comparison between Simulation, Analysis and Experiment," ASME JOURNAL OF APPLIED MECHANICS, Vol. 58, pp. 559–565.

Païdoussis, M. P., and Moon, F. C., 1988, "Nonlinear and Chaotic Fluidelastic Vibrations of a Flexible Pipe Conveying Fluid," *Journal of Fluids and Structures*, Vol. 2, pp. 567–591.

Rousselet, J., and Herrmann, G., 1981, "Dynamic Behavior of Continuous Cantilevered Pipes Conveying Fluid near Critical Velocities," ASME JOURNAL OF APPLIED MECHANICS, Vol. 48, pp. 943–947.

Sethna, P. R., and Shapiro, S. M., 1977, "Nonlinear Behavior of Flutter in Unstable Dynamical Systems with Gyroscopic and Circulatory Forces," ASME JOURNAL OF APPLIED MECHANICS, Vol. 44, pp. 755–762.

Shaw, S. W., 1985, "The Dynamics of a Harmonically Excited System having Rigid Amplitude Constraints. Part I: Subharmonic Motions and Local Bifurcations; Part II: Chaotic Motions and Global Bifurcations," ASME JOURNAL OF APPLIED MECHANICS, Vol. 52, pp. 453–458, 459–469.

Shaw, S. W., and Holmes, P. J., 1983, "A Periodically Forced Piecewise Linear Oscillator," *Journal of Sound and Vibration*, Vol. 90, pp. 129–155.

Takens, F., 1980, "Detecting Strange Attractors in Turbulence," *Dynamical Systems and Turbulence*, (Springer Lecture Notes in Mathematics, Vol. 898, D. A. Rand and L.-S. Young, eds.), Springer-Verlag, New York, pp. 366–381.

Tang, D. M., and Dowell, E. H., 1988, "Chaotic Oscillations of a Cantilevered Pipe Conveying Fluid," *Journal of Fluids and Structures*, Vol. 2, pp. 263–283.

Tung, P. C., and Shaw, S. W., 1988, "The Dynamics of an Impact Print Hammer," ASME *Journal of Vibration, Acoustics, Stress and Reliability in Design*, Vol. 110, pp. 193–200.

Downloaded 03 May 2010 to 171.66.16.247. Redistribution subject to ASME license or copyright; see http://www.asme.org/terms/Terms_Use.cfm

Symmetry Reduction of Reynolds Equation and Applications to Film Lubrication

M. L. Abell[1]

W. F. Ames[2]

School of Mathematics,
Georgia Institute of Technology,
Atlanta, GA 30332

A symmetry reduction using a one-parameter spiral group is performed on a Reynolds equation in order to analyze this equation arising in the study of film lubrication. Approximate solutions are found for the time-independent case—both numerically and by the method of perturbation. Solutions to the time-dependent equation are found by using the invariance in the time and angular variables only. These solutions, called semi-invariant solutions, are determined through separation of variables.

1 Introduction

Group analysis is employed to study Reynolds equation, a nonlinear equation encountered in the study of film lubrication, which describes the pressure, p, at every point in a lubricant film. We study Reynolds equation in polar coordinates (r, θ) for a slider bearing in which gas is used as a lubricant (Gross, 1962):

$$\frac{\partial}{\partial r}\left(\frac{rh^3}{\mu}\frac{\partial(p^{(1/n)+1})}{\partial r}\right)+\frac{1}{r}\frac{\partial}{\partial\theta}\left(\frac{h^3\partial(p^{(1/n)+1})}{\mu\ \partial\theta}\right)$$
$$=\frac{n+1}{n}\left(6r\hat{\omega}\frac{\partial(p^{(1/n)}h)}{\partial\theta}+12r\frac{\partial(p^{(1/n)}h)}{\partial t}\right) \tag{1}$$

where n is the gas expansion exponent, $\hat{\omega}$ is the angular velocity of the bearing, and h and μ are given functions describing film thickness and viscosity, respectively.

A symmetry reduction, using a one-parameter spiral group, is performed on both the time-independent and time-dependent cases of the equation. Solutions of the time-dependent cases are found by using the translational invariance in the variables t and θ only. These solutions, called semi-invariant solutions, are determined through separation of variables techniques. Exact and approximate solutions are found for the time-independent case.

2 Symmetry Reduction

The first step in our analysis of Reynolds equation is to perform a symmetry reduction through the use of a one-parameter transformation group. A full group analysis of Reynolds equation has not been attempted because of the presence of the arbitrary functions for film thickness, h, and viscosity, μ. Nonetheless, we can find a group consisting of scaling and translation under which Reynolds equation remains invariant. This one-parameter spiral group, with identity $a=1$, is defined as follows:

$$\begin{aligned} r&=a^{\alpha}\hat{r}\\ \theta&=\hat{\theta}+\beta\ln a\\ t&=\hat{t}+\gamma\ln a\\ h&=a^{\epsilon}\hat{h}\\ \mu&=a^{\sigma}\hat{\mu}\\ p&=a^{\lambda}\hat{p}. \end{aligned} \tag{2}$$

Since Reynolds equation is invariant under the spiral group, we are able to perform a symmetry reduction. The foundations and applications of this procedure can be found in Ames (1972) and other works.

First, the invariance condition is determined by substituting Eqs. (2) into Reynolds equation (1). This condition is found to be

$$3\epsilon-\alpha-\sigma+\left(\frac{1}{n}+1\right)\lambda=\alpha+\epsilon+\frac{1}{n}\lambda. \tag{3}$$

We therefore must impose the restriction that

$$\frac{\lambda}{\alpha}=\frac{\sigma}{\alpha}-\frac{2\epsilon}{\alpha}+2 \tag{4}$$

in determining the group invariants applicable to Reynolds equation.

By making use of Eqs. (2)–(4) as well as elementary techniques (Ames, 1972), we find the invariants applicable to Reynolds equation to be

$$\psi=r\exp\left(\frac{-\alpha\theta}{\beta}\right) \tag{5}$$

$$\eta=r\exp\left(\frac{-\alpha t}{\gamma}\right) \tag{6}$$

[1] Permanent Address: Department of Mathematics and Computer Science, Georgia Southern University, Statesboro, GA 30460-8093.

[2] Also at the School of Mechanical Engineering, Georgia Institute of Technology, Atlanta, GA 30332.

Contributed by the Applied Mechanics Division of THE AMERICAN SOCIETY OF MECHANICAL ENGINEERS for publication in the JOURNAL OF APPLIED MECHANICS.

Discussion on this paper should be addressed to the Technical Editor, Prof. Leon M. Keer, The Technological Institute, Northwestern University, Evanston, IL 60208, and will be accepted until two months after final publication of the paper itself in the JOURNAL OF APPLIED MECHANICS. Manuscript received by the ASME Applied Mechanics Division, Nov. 21, 1989; final revision, Sept. 24, 1990.

Copyright © 1992 by ASME

Downloaded 03 May 2010 to 171.66.16.247. Redistribution subject to ASME license or copyright; see http://www.asme.org/terms/Terms_Use.cfm

$$h = r^{\epsilon/\alpha} f(\eta, \psi) \tag{7}$$

$$\mu = r^{\sigma/\alpha} m(\eta, \psi) \tag{8}$$

$$p = r^{\lambda/\alpha} g(\eta, \psi) \tag{9}$$

where λ/α is given in Eq. (4).

By performing a symmetry reduction, we reduce the number of independent variables (r, θ, t) which appear in Reynolds equation (1) to two independent variables (η, ψ). This is accomplished through the use of invariants given in Eqs. (5)–(9) and the Chain Rule. The equation in the symmetry variables ψ and η obtained through this reduction is

$$\left(\psi\frac{\partial}{\partial\psi}+\eta\frac{\partial}{\partial\eta}\right)\left(\frac{f^3}{m}\left(\psi\frac{\partial(g^{(1/n)+1})}{\partial\psi}+\eta\frac{\partial(g^{(1/n)+1})}{\partial\eta}\right)\right)+\frac{\alpha^2}{\beta^2}\psi\frac{\partial}{\partial\psi}\left(\frac{\psi f^3}{m}\frac{\partial(g^{(1/n)+1})}{\partial\psi}\right)=-6\alpha\left(\frac{n+1}{n}\right)\left(\frac{\psi}{\beta}\frac{\partial(g^{(1/n)}f)}{\partial\psi}+\frac{2\eta}{\gamma}\frac{\partial(g^{(1/n)}f)}{\partial\eta}\right). \tag{10}$$

If the steady case of Reynolds equation in which there is no dependence on time is considered, we find from Eqs. (2) that

$$\epsilon = \sigma = 0 \tag{11}$$

in order that the steady case of Reynolds equation remain invariant under the spiral group. Therefore, the invariants for the time-independent equation become

$$\psi = r\exp\left(\frac{-\alpha\theta}{\beta}\right) \tag{12}$$

provided the specified functions

$$h = f(\psi) \tag{13}$$

$$\mu = m(\psi) \tag{14}$$

and then

$$p = r^2 g(\psi). \tag{15}$$

Therefore, through symmetry reduction, we obtain the following ordinary differential equation corresponding to the steady case of Reynolds equation:

$$\hat{C}\frac{d}{d\psi}\left(\frac{\psi f^3}{m}\frac{d}{d\psi}(\psi^2 g)^{(1/n)+1}\right)=\psi^2\frac{d}{d\psi}((\psi^2 g)^{(1/n)}f), \tag{16}$$

where

$$\hat{C} = -\frac{1}{6}\frac{\beta n}{\alpha\hat{\omega}(n+1)}\left(1+\frac{\alpha^2}{\beta^2}\right) \tag{17}$$

and α/β is arbitrary.

3 Semi-Invariant Solutions to Reynolds Equation

We return to the original form of Reynolds equation for gas films given in Eq. (1). In determining the invariants applicable to Reynolds equation, Eqs. (5)–(9), we made use of the Lagrange equations. In doing so, we have the equation

$$\frac{d\theta}{\beta}=\frac{dt}{\gamma}$$

in the variables θ and t. This equation has the solution

$$\theta-\frac{\beta}{\gamma}t=\text{constant}.$$

By letting $\lambda=\beta/\gamma$ and by defining the new variable as

$$\omega=\theta-\lambda t,$$

we can seek solutions of Eq. (1) of the form

$$p(r, \theta, t) = R(r)W(\omega)$$

by substituting this product into Eq. (1). This leads to the equation

$$\frac{\partial}{\partial r}\left(\frac{rh^3}{\mu}\frac{\partial((RW)^{(1/n)+1})}{\partial r}\right)+\frac{1}{r}\frac{\partial}{\partial\omega}\left(\frac{h^3}{\mu}\frac{\partial(RW)^{(1/n)+1}}{\partial\omega}\right)=\frac{n+1}{n}(6r)(\hat{\omega}-2\lambda)\frac{\partial((RW)^{(1/n)}h)}{\partial\omega}. \tag{18}$$

Clearly, in Eq. (18) if the angular velocity of the bearing, $\hat{\omega}$, is twice the wave parameter, λ, then the right-hand side of Eq. (18) is eliminated. Therefore, Eq. (18) becomes the homogeneous equation:

$$W^{(1/n)+1}\frac{\partial}{\partial r}\left(\frac{rh^3}{\mu}\frac{d(R^{(1/n)+1})}{dr}\right)+\frac{R^{(1/n)+1}}{r}\frac{\partial}{\partial\omega}\left(\frac{h^3}{\mu}\frac{d(W^{(1/n)+1})}{d\omega}\right)=0. \tag{19}$$

Equation (19) can be solved for the functions $R^{(1/n)+1}(r)$ and $W^{(1/n)+1}(\omega)$ through separation of variables techniques when the given functions for film thickness, h, and viscosity, μ, are specified. This method is applicable if the given functions h and μ are solely functions of either the variable r or of the variable ω, or if these functions can be expressed as a product of a function of r and a function of ω.

As an illustration of this technique, let us consider the problem in which film thickness and viscosity are both constant. Making substitutions into Eq. (19) and separating variables, we acquire the following equations for $R^{(1/n)+1}(r)$ and $W^{(1/n)+1}(\omega)$

$$r^2\frac{d^2(R^{(1/n)+1})}{dr^2}+r\frac{d(R^{(1/n)+1})}{dr}-\sigma^2R^{(1/n)+1}=0 \tag{20}$$

$$\frac{d^2(W^{(1/n)+1})}{d\omega^2}+\sigma^2W^{(1/n)+1}=0 \tag{21}$$

whre σ^2 is a separation constant.

The solution to Eq. (20) is found to be (Kamke, 1945):

$$R^{(1/n)+1}(r) = Cr^{\sigma}+Dr^{-\sigma} \tag{22}$$

where C and D are arbitrary constants. Clearly, the solution to Eq. (21) is

$$W^{(1/n)+1}(\omega) = E\cos(\sigma\omega)+F\sin(\sigma\omega)$$

where E and F are arbitrary constants. Hence, in terms of the original variables, we have

$$W^{(1/n)+1}(\theta-\lambda t) = E\cos\sigma(\theta-\lambda t)+F\sin\sigma(\theta-\lambda t). \tag{23}$$

Therefore, if the film thickness and viscosity are constant, then we have the following solution to Eq. (18):

$$p(r, \theta, t) = ((Cr^{\sigma}+Dr^{-\sigma})(E\cos\sigma(\theta-\lambda t)+F\sin\sigma(\theta-\lambda t)))^{n/(n+1)}$$

where $\lambda=\hat{\omega}/2$.

As another example of this technique, let us consider the case in which $h=h(r)$ and $\mu=\mu(\omega)$. In particular, suppose that

$$h(r) = r^m \quad \left(m\neq-\frac{1}{3}\right) \tag{24}$$

and

$$\mu(\omega) = \omega^k. \tag{25}$$

After substituting Eqs. (24)–(28) in Eq. (19) and separating variables, we have the following differential equations for $R^{(1/n)+1}(r)$ and $W^{(1/n)+1}(\omega)$

$$r^2\frac{d^2(R^{(1/n)+1})}{dr^2}+(3m+1)r\frac{d(R^{(1/n)+1})}{dr}-\sigma^2R^{(1/n)+1}=0 \tag{26}$$

$$\omega^2\frac{d^2(W^{(1/n)+1})}{d\omega^2}-k\omega\frac{d(W^{(1/n)+1})}{d\omega}+\sigma^2\omega^2W^{(1/n)+1}=0 \tag{27}$$

where, again, σ^2 is a separation constant.

Downloaded 03 May 2010 to 171.66.16.247. Redistribution subject to ASME license or copyright; see http://www.asme.org/terms/Terms_Use.cfm

The solution to Eq. (26) is found by solving the equations $\alpha+\beta=1-a$ and $\alpha\beta=b$ for α and β, where $a=3m+1$ and $b=-\sigma^2$ (Kamke, 1945). In this case,

$$\alpha=\frac{3m\pm(9m^2+4\sigma^2)^{1/2}}{2} \tag{28}$$

and

$$\beta=\frac{3m\mp(9m^2+4\sigma^2)^{1/2}}{2}. \tag{29}$$

Therefore, the solution to Eq. (26) is

$$R^{(1/n)+1}(r)=\begin{cases} Cr^{\alpha}+Dr^{\beta} & \alpha\neq\beta \\ r^{\sigma}(C+D\ln r) & \alpha=\beta \end{cases}$$

if α and β are real numbers, or

$$R^{(1/n)+1}(r)=r^{b}(C\cos(s\ln r)+D\sin(s\ln r))$$

if α, $\beta=b\pm is$ where C, D are arbitrary constants and α, β are given in Eqs. (28)–(29).

Equation (27) has the Bessel function solution (Lebedev, 1972)

$$W^{(1/n)+1}(\omega)=\omega^{(k+1)/2}(EJ_{(k+1)/2}(\sigma\omega)+FY_{(k+1)/2}(\sigma\omega))$$

where E, F are arbitrary constants and the functions J and Y are Bessel functions of the first and second kinds, respectively (Lebedev, 1972).

By taking the $\left(\frac{n+1}{n}\right)^{\text{th}}$ root of the product of the functions $R^{(1/n)+1}(r)$ and $W^{(1/n)+1}(\omega)$, we obtain the solution to Reynolds equations for the case in which $h(r)=r^m$ $(m\neq -1/3)$ and $\mu(\omega)=\omega^k$.

4 Solutions to the Steady Case of Reynolds Equation

4.1 Exact Solutions. Let us recall the ordinary differential equation which was obtained through symmetry reduction for the steady case of Reynolds equation found in Eqs. (16)–(17). If, in this reduced equation, we make the substitution

$$M(\psi)=(\psi^2 g(\psi))^{(1/n)}, \tag{30}$$

then the equation for the steady case becomes

$$\hat{C}\frac{d}{d\psi}\left(\frac{\psi f^3}{m}\frac{d(M^{n+1})}{d\psi}\right)=\psi^2\frac{d}{d\psi}(Mf) \tag{31}$$

where $\hat{C}$ is the constant given in Eq. (17). We must remember that $f(\psi)$ and $m(\psi)$ are given functions which correspond to film thickness and viscosity, respectively. Therefore, our objective is to solve Eq. (31) for the function $M(\psi)$. This task can be accomplished by defining the functions $f(\psi)$ and $m(\psi)$ and searching for the solution $M(\psi)$ of a certain form.

As an example of this procedure, consider the problem in which $f(\psi)=K$ and $m(\psi)=b^{-1}\psi^{-s}$ where b and K are positive constants. We search for a solution of the form

$$M(\psi)=d\psi^{q} \tag{32}$$

(where d and q are constants, $d\neq 0$) by substituting Eq. (32) into Eq. (31) and determining the values of d and q. In this case, we find that

$$q=\frac{2-s}{n},\ n\neq 0$$

and

$$d=(K^2\hat{C}b(n+1)(s+(n+1)q))^{-(1/n)},\ n\neq 0.$$

Therefore, in the original variables, we have the solution

$$p(r,\theta)=\frac{nr^{2-s}}{K^2\hat{C}b(n+1)(2n+1-s)}\exp\left(\frac{\alpha s\theta}{\beta}\right),\ s\neq 2n+1,\ K\neq 0$$

where α/β is arbitrary.

4.2 Numerical Solutions. In order to obtain numerical results for the steady case of Reynolds equation, we will rely on the ordinary differential equation achieved through symmetry reduction. If we consider the form of Reynolds equation in which viscosity is constant, then we have the following reduced equation corresponding to the time-independent case of Reynolds equation.

$$C\frac{d}{d\psi}\left(\psi f^3\frac{d}{d\psi}((\psi^2 g)^{(1/n)+1})\right)=\psi^2\frac{d}{d\psi}((\psi^2 g)^{(1/n)}f) \tag{33}$$

where

$$C=\frac{-\beta n}{6\alpha\mu\hat{\omega}(n+1)}\left(1+\frac{\alpha^2}{\beta^2}\right). \tag{34}$$

We now propose to transform the second-order differential equation given in Eq. (33) into a system of two first-order ordinary differential equations by using elementary techniques (Jordan and Smith, 1987). This system is obtained by letting

$$u(\psi)=(\psi^2 g)^{(n+1)/n} \tag{35}$$

and

$$\frac{du}{d\psi}=v. \tag{36}$$

By using Eqs. (33), (35), and (36) we convert Eq. (33) into the system:

$$\frac{du}{d\psi}=v$$

$$\frac{dv}{d\psi}=\frac{\psi}{Cf^2(n+1)}u^{-n/(n+1)}v+\frac{\psi}{Cf^3}u^{1/(n+1)}\frac{df}{d\psi}-\frac{v}{\psi}+\frac{3vf'}{f}. \tag{37}$$

By making use of a computer program based on the Runge-Kutta Method (Atkinson, 1978) which solves systems of ordinary differential equations, we can solve Eqs. (37) for various choices of the function, f, for film thickness. We graphically show the numerical results for the following given data in Fig. 1:

$$f(\psi)=2+\cos\psi,\ 1.0\leq\psi\leq 4.0$$
$$n=\mu=\hat{\omega}=1$$
$$\frac{\alpha}{\beta}=-.10$$
$$u(1.0)=.6$$
$$u(4.0)=.3.$$

4.3 Perturbation Analysis. In an attempt to obtain a functional form of solutions to Reynolds equation, we turn to the method of perturbation. This method involves solving a nonlinear partial differential equation in powers of a parameter which either appears in the original problem or is introduced in some manner (Ames, 1972). If we once again recall the ordinary differential equation obtained in the symmetry reduction of the steady case of Reynolds equation in which viscosity is constant,

$$\frac{d}{d\psi}\left(\psi f^3\frac{d}{d\psi}((\psi^2 g)^{(1/n)+1})\right)=\frac{1}{C}\psi^2\frac{d}{d\psi}(f(\psi^2 g)^{(1/n)}) \tag{38}$$

where

$$C=\frac{-\beta n}{6\alpha\mu\hat{\omega}(n+1)}\left(1+\frac{\alpha^2}{\beta^2}\right), \tag{39}$$

we see that we can employ the arbitrary constant $1/C$ as the parameter in which to expand our solution. Therefore, by appropriately selecting α/β, we can let

$$\epsilon=\frac{1}{C}\ll 1. \tag{40}$$

Downloaded 03 May 2010 to 171.66.16.247. Redistribution subject to ASME license or copyright; see http://www.asme.org/terms/Terms_Use.cfm

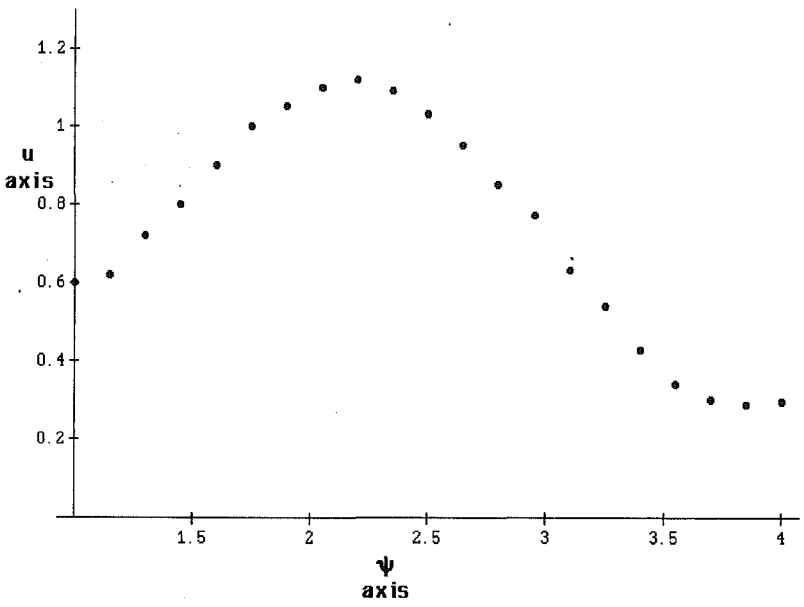

Fig. 1

We also make the substitution

$$G(\psi) = (\psi^2 g)^{(1/n)+1}. \tag{41}$$

Hence, Eq. (38) becomes

$$\frac{d}{d\psi}\left(\psi f^3 \frac{dG}{d\psi}\right) = \epsilon \psi^2 \frac{d}{d\psi}(fG^{1/(n+1)}). \tag{42}$$

We now expand the function $G(\psi)$ in powers of ϵ (Jordan and Smith, 1987):

$$G(\psi, \epsilon) = G_0(\psi) + \epsilon G_1(\psi) + \epsilon^2 G(\psi) + \cdots. \tag{43}$$

Substitution of Eq. (43) into Eq. (42) yields

$$\frac{d}{d\psi}\left(\psi f^3 \left(\frac{dG_0}{d\psi} + \epsilon \frac{dG_1}{d\psi} + \cdots\right)\right)$$

$$= \epsilon \psi^2 \frac{d}{d\psi}\left(f\left(G_0{}^{1/(n+1)} + \frac{\epsilon}{n+1} G_0{}^{-n/(n+1)} G_1 + \cdots\right)\right) \tag{44}$$

where $G^{1/(n+1)}(\psi)$ is obtained by a Taylor series expansion in the parameter.

By equating terms of equal order of ϵ in Eq. (44), we obtain a sequence of equations of the following form (Jordan and Smith, 1987):

Order "0":

$$\frac{d}{d\psi}\left(\psi f^3 \frac{dG_0}{d\psi}\right) = 0. \tag{45}$$

Order "ϵ":

$$\frac{d}{d\psi}\left(\psi f^3 \frac{dG_1}{d\psi}\right) = \psi^2 \frac{d}{d\psi}(fG_0{}^{1/(n+1)}). \tag{46}$$

Order "ϵ^2":

$$\frac{d}{d\psi}\left(\psi f^3 \frac{dG_2}{d\psi}\right) = \psi^2 \frac{d}{d\psi}\left(\frac{1}{n+1} f G_0{}^{-n/(n+1)} G_1\right). \tag{47}$$

Equations of order ϵ^k, $k \geq 3$, are obtained in a similar fashion.

The solution of Eq. (45) is easily found to be

$$G_0(\psi) = \int_{\psi_0}^{\psi} \frac{\hat{K}}{\tau f^3(\tau)} d\tau \tag{48}$$

where $\hat{K}$ is constant. This solution is substituted into Eq. (46) in order to solve for $G_1(\psi)$. Of course, the solution for $G_1(\psi)$ in most cases will be more difficult to obtain than that of $G_0(\psi)$ and may require a numerical method. Once found, however, $G_1(\psi)$ and $G_0(\psi)$ are substituted into Eq. (47) resulting in an equation for $G_2(\psi)$, and this process continues.

Clearly, the determination of the functions $G_0(\psi)$, $G_1(\psi)$, $G_2(\psi)$, ... depends largely on the function for film thickness. Under most circumstances, a functional form of the solution will not be possible past the equation of order zero. However, for very small ϵ, the solution for $G_0(\psi)$ given in Eq. (48) will be a good approximation to the desired solution $G(\psi)$.

As an example of this method in which several terms of the expansion of $G(\psi)$ can be found, let us consider Eq. (42) with

$$f(\psi) = \psi,$$

and let us impose the conditions

$$G(\psi_0) = K \quad \text{and} \quad \frac{dG}{d\psi}(\psi_0) = 0.$$

Through the method of perturbation, we find that

$$G(\psi, \epsilon) = K + \frac{\epsilon K^{1/(n+1)}}{3}\left(\ln\left(\frac{\psi}{\psi_0}\right) + \frac{1}{3}\left(\frac{\psi^3}{\psi_0{}^3} - 1\right)\right)$$

$$+ \frac{\epsilon^2 K^{(1-n)/(n+1)}}{3(n+1)} \hat{G}_2(\psi) + \cdots$$

where

$$\hat{G}_2(\psi) = \ln\left(\frac{\psi}{\psi_0}\right)\left(\frac{1}{4} + \frac{2}{3}\frac{\psi_0{}^3}{\psi^3} - \frac{1}{3}\right) + \frac{1}{9}\frac{\psi_0{}^3}{\psi^3}$$

$$+ \frac{\psi_0{}^3}{\psi^2}\left(\frac{\psi_0}{16\psi} - \frac{1}{6}\right) - \frac{19\psi}{48} + \frac{\psi_0}{2} - \frac{1}{9}.$$

Downloaded 03 May 2010 to 171.66.16.247. Redistribution subject to ASME license or copyright; see http://www.asme.org/terms/Terms_Use.cfm

References

Abell, M. L., 1989, "Symmetry Reduction of Reynolds Equation and Applications to Film Lubrication," Ph.D. Thesis, Georgia Institute of Technology, Atlanta.

Ames, W. F., 1972, *Nonlinear Partial Differential Equations in Engineering*, Vol. II, Academic Press, New York, pp. 87–145.

Atkinson, K. E., 1978, *An Introduction to Numerical Analysis*, John Wiley and Sons, New York, pp. 366–380.

Birkhoff, G., 1960, *Hydrodynamics*, 2nd ed., Princeton University Press, Princeton, N.J.

Gross, W. A., 1962, *Gas Film Lubrication*, John Wiley and Sons, New York.

Herman, Robert, 1975, *Sophus Lie's 1880 Transformation Group Paper*, Math. Sci. Press, Brookline, Mass., (in part a translation by Michael Ackerman of "Theorie der Transformationsgruppen" by S. Lie, *Mathematische Annalen*, Vol. 16, 1880, pp. 441–528.)

Herman, Robert, 1976, *Sophus Lie's 1884 Differential Invariant Paper*, Math. Sci. Press, Brookline, Mass., (in part a translation by Michael Ackerman of "On Differential Invariants" by S. Lie, *Mathematische Annalen*, Vol. 24, 1884, pp. 537–578).

Jordan, D. W., and Smith, P., 1987, *Nonlinear Ordinary Differential Equations*, 2nd ed., Clarendon Press, Oxford, pp. 1–64, 120–145.

Kamke, E., 1945, *Differentialgleichungun*, J. W. Edwards, Publ.

Lebebev, N. N., 1972, *Special Functions and Their Applications*, (Translated and edited by R. A. Silverman), Dover Publications, New York.

Downloaded 03 May 2010 to 171.66.16.247. Redistribution subject to ASME license or copyright; see http://www.asme.org/terms/Terms_Use.cfm

Journal of Applied Mechanics

Brief Notes

A Brief Note is a short paper that presents a specific solution of technical interest in mechanics but which does not necessarily contain new general methods or results. A Brief Note should not exceed 1500 words *or equivalent* (a typical one-column figure or table is equivalent to 250 words; a one line equation to 30 words). Brief Notes will be subject to the usual review procedures prior to publication. After approval such Notes will be published as soon as possible. The Notes should be submitted to the Technical Editor of the JOURNAL OF APPLIED MECHANICS. Discussions on the Brief Notes should be addressed to the Editorial Department, ASME, United Engineering Center, 345 East 47th Street, New York, N. Y. 10017, or to the Technical Editor of the JOURNAL OF APPLIED MECHANICS. Discussions on Brief Notes appearing in this issue will be accepted until two months after publication. Readers who need more time to prepare a Discussion should request an extension of the deadline from the Editorial Department.

Laminated Plates Under Uniformly Distributed and Concentrated Loads

S. Savithri[1] and T. K. Varadan[2]

Introduction

Refined theories accounting for shear deformations of generally laminated plates are generally assessed by comparison with the three-dimensional elasticity solutions (Pagano, 1969, 1970). These solutions are available for sinusoidal transverse loading for orthotropic laminates. In a recent paper (Simmonds, 1990), it has been stated that a higher order theory, which performs better than the classical plate theory at the low end of the frequency spectrum, may be actually worse in the presence of concentrated loads. In this context, a refined plate theory should be assessed for its accuracy at both ends of the frequency spectrum, that is for loads corresponding to a single half-wave and a concentrated load.

Three-dimensional elasticity solutions for an infinite strip under a uniformly distributed and concentrated loads are given by Pagano and Wang (1971) but are not available for the more general case of finite laminates. Such solutions are the objective of the present work. Specifically, the problem of a square orthotropic laminated plate simply supported at the boundaries and subjected to concentrated load/u.d.l on the top surface has been solved, and deflections and stresses at different locations are presented. These solutions, besides Pagano's (1970), are necessary for a more complete assessment of a new plate theory.

Analysis and Results

We consider a laminate of N orthotropic layers such that the various axes of elastic symmetry are parallel to the in-plane axes x and y, and transverse axis z. The geometric midplane is the reference plane, and z is positive when measured upwards. The plate is simply supported on all edges and is subjected to a load $q_o(x,y)$ applied on the top surface while the lower surface is traction-free. The simple-support edge conditions are taken as

$$\text{At } x=0,a: \quad \sigma_x = v = w = 0$$

$$\text{At } y=0,a: \quad \sigma_y = u = w = 0.$$

The procedure for the three-dimensional elasticity solution is the same as that given by Pagano (1970), and hence it is not repeated here. The exact solution satisfies the three equilibrium equations written in terms of displacements within each layer, the boundary conditions at the simple supports and plate top and bottom surfaces, and the interface $(6N-1)$ continuity conditions for three displacements, one normal stress and two shear stresses in the plane represented by the outward normal z, in adjacent layers at each interface.

The laminate under consideration is subjected to two types of transverse loads (a) uniformly distributed load q_o and (b) concentrated load P. The concentrated load is simulated by a small patch load shown in Fig. 1. The loading functions are expanded in Fourier series as

$$q_o(x,y) = \sum_{m=1,9..} \sum_{n=1,9..} q_{mn} \sin px \sin qy \qquad (1)$$

where

$$q_{mn} = \begin{cases} 16q_o/mn\pi^2 & \text{for the u.d.l } q_o \\ [(m+n)/2]-1 & \\ (-1)\ 16P \sin(pr/2) \sin(qr/2)/(mn\pi^2 r^2) & \text{for the concentrated load } P. \end{cases}$$

Numerical examples considered are (i) unidirectional laminate with fiber orientation in x-direction and (ii) symmetric three-ply laminate with layers of equal thicknesses where the

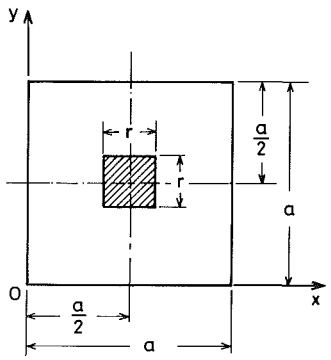

Fig. 1 Patch load

[1]Research Scholar, Department of Mathematics, Indian Institute of Technology, Madras-600 036, India.

[2]Professor, Department of Aerospace Engineering, Indian Institute of Technology, Madras-600 036, India.

Contributed by the Applied Mechanics Division of THE AMERICAN SOCIETY OF MECHANICAL ENGINEERS. Manuscript received by the ASME Applied Mechanics Division, Feb. 5, 1990; final revision, Jan. 18, 1991.

Copyright © 1992 by ASME
Downloaded 03 May 2010 to 171.66.16.247. Redistribution subject to ASME license or copyright; see http://www.asme.org/terms/Terms_Use.cfm

Table 1 Displacements and stresses for various values of *(a/h)*

a/h	Parameter	Unidirctional		(0/90/0)	
		u.d.l	conc.load	u.d.l.	conc.load
4	$\bar{w}(a/2,a/2,0)$	2.3590	11.7921	3.0445	12.8742
	$\bar{\sigma}_x(a/2,a/2,\bar{z})$*	-0.9643	-5.5615	-0.2869 , 0.0068	-12.4207 , 0.7656
	$\bar{\sigma}_y(a/2,a/2,\bar{z})$	-0.0788	-0.9410	0.0385 , 0.7604	1.3493 , 6.8405
	$\bar{\tau}_{xy}(0,0,\bar{z})$	0.0786	0.1266	-0.0075 ,-0.0075	-0.0224 ,-0.0224
	$\bar{\tau}_{xz}(0,a/2,0)$	0.6161	1.3618	0.4435	0.8949
	$\bar{\tau}_{yz}(a/2,0,0)$	0.2084	0.0120	0.4875	0.2821
10	$\bar{w}(a/2,a/2,0)$	0.9478	4.4452	1.1541	4.7121
	$\bar{\sigma}_x(a/2,a/2,\bar{z})$	-0.8213	-0.6790	0.1402 , 0.0108	-11.6118 , 0.7870
	$\bar{\sigma}_y(a/2,a/2,\bar{z})$	-0.0363	-1.1675	0.0173 , 0.3580	1.3681 , 7.5652
	$\bar{\tau}_{xy}(0,0,\bar{z})$	0.0507	0.0704	-0.0123 ,-0.0123	-0.0236 ,-0.0236
	$\bar{\tau}_{xz}(0,a/2,0)$	0.7312	1.4603	0.6284	1.1575
	$\bar{\tau}_{yz}(a/2,0,0)$	0.1885	-0.0854	0.4018	-0.1717
20	$\bar{w}(a/2,a/2,0)$	0.7255	2.9643	0.7951	2.9239
	$\bar{\sigma}_x(a/2,a/2,\bar{z})$	-0.7958	-7.7350	0.2352 , 0.0121	-10.7538 , 0.7624
	$\bar{\sigma}_y(a/2,a/2,\bar{z})$	-0.0276	-1.1354	0.0122 , 0.2381	1.3382 , 8.2486
	$\bar{\tau}_{xy}(0,0,\bar{z})$	0.0442	0.0585	-0.0128 ,-0.0128	-0.0222 ,-0.0222
	$\bar{\tau}_{xz}(0,a/2,0)$	0.7639	1.3929	0.6877	1.1423
	$\bar{\tau}_{yz}(a/2,0,0)$	0.1891	-0.0976	0.3880	-0.2213
CPT	$\bar{w}(a/2,a/2,0)$	0.6497	2.3238	0.6660	2.1302
	$\bar{\sigma}_x(a/2,a/2,\bar{z})$	-0.7867	-8.4186	0.2692 , 0.0126	-2.5503 , 0.1704
	$\bar{\sigma}_y(a/2,a/2,\bar{z})$	-0.0245	-1.3591	0.0102 , 0.1914	0.3096 , 7.1442
	$\bar{\tau}_{xy}(0,0,\bar{z})$	0.0465	0.0409	-0.0142 ,-0.0142	-0.0186 ,-0.0186

$$* \bar{z} = \begin{cases} h/6 & \text{for (0/90/0) laminate} \\ -h/2 & \text{for unidirectional laminate} \end{cases}$$

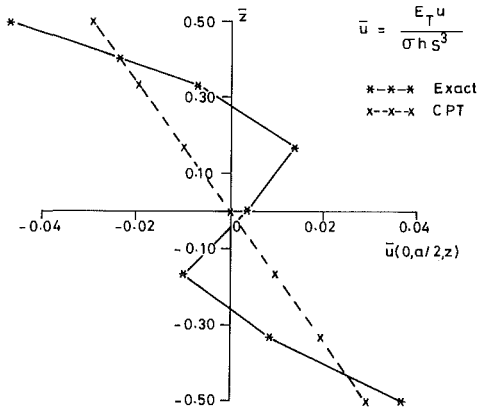

Fig. 2 Thickness distribution of $\bar{u}$ for conc.load; $N = 3$, $S = 4$

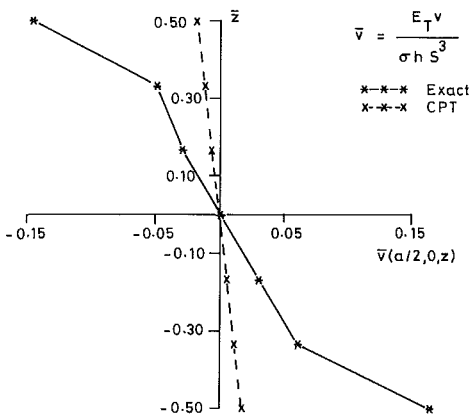

Fig. 3 Thickness distribution of $\bar{v}$ for conc.load; $N = 3$, $S = 4$

fibers coincide with the x-axis in the outer layers and the fibers are oriented in the transverse direction in the central layer. The layer material constants are (Pagano, 1970) $E_L = 25 \times 10^6$ psi, $E_T = 10^6$ psi, $G_{LT} = 0.5 \times 10^6$ psi, $G_{TT} = 0.2 \times 10^6$ psi, $\upsilon_{LT} = \upsilon_{TT} = 0.25$ where L is the direction parallel to the fibers and T is the transverse direction. (r/a) is taken as 0.005. The following nondimensional displacement and stresses are used:

$$\bar{w} = (100\, E_T w/\sigma h S^4),\ (\bar{\sigma}_x, \bar{\sigma}_y, \bar{\tau}_{xy}) = (\sigma_x, \sigma_y, \tau_{xy})/\sigma S^2$$
$$(\bar{u},\ \bar{v}) = (u, v) E_T/\sigma h S^3$$
$$(\bar{\tau}_{xz}, \bar{\tau}_{yz}) = (\tau_{xz}, \tau_{yz})/\sigma S \qquad (2)$$

where $S = a/h$, $\sigma = q_o$ or P/a^2 depending upon the applied load considered and h is the thickness of the laminate.

The convergence study for the series corresponding to Eq. (1) is to be established for the loads before proceeding to the detailed investigation. A major problem, for the reasons indicated below, is encountered. The argument of cosh and sinh functions which appear in the z-dependent function of the displacements u, v, and w, is $m_j z$, (see Eqs. (19) and (20) of Pagano, 1970). m_j are the roots of the sixth-degree algebraic equation obtained by making the determinant of the three equilibrium equations for the assumed displacement functions vanish. This $m_j z$ is written in the nondimensional form as $m_j(z/$

Downloaded 03 May 2010 to 171.66.16.247. Redistribution subject to ASME license or copyright; see http://www.asme.org/terms/Terms_Use.cfm

Table 2 Displacements and stresses at different points; $a/h = 4$

x/a	y/a	Parameter	Unidirectional		(0/90/0)	
			u.d.l.	conc.load	u.d.l.	conc.load
0.3	0.5	$\bar{w}(x/a, y/a, 0)$	1.9618	6.1999	2.5386	6.7897
		$\bar{\sigma}_x(x/a, y/a, \bar{z})$	-0.8335	-1.9026	0.0053	0.0858
		$\bar{\sigma}_y(x/a, y/a, \bar{z})$	-0.0647	-0.4706	0.6235	2.3109
		$\bar{\tau}_{xz}(x/a, y/a, 0)$	0.2786	1.8052	0.2054	1.0907
		$\bar{\tau}_{yz}(x/a, y/a, 0)$	0.0000	0.0000	0.0000	0.0000
0.4	0.5	$\bar{w}(x/a, y/a, 0)$	2.2591	9.0744	2.9176	9.8092
		$\bar{\sigma}_x(x/a, y/a, \bar{z})$	-0.9323	-3.8146	0.0064	0.2455
		$\bar{\sigma}_y(x/a, y/a, \bar{z})$	-0.0752	-0.7520	0.7257	3.8122
		$\bar{\tau}_{xz}(x/a, y/a, 0)$	0.1401	2.7021	0.1034	1.4100
		$\bar{\tau}_{yz}(x/a, y/a, 0)$	0.0000	0.0000	0.0000	0.0000
0.5	0.3	$\bar{w}(x/a, y/a, 0)$	2.0739	4.3469	2.5813	6.1682
		$\bar{\sigma}_x(x/a, y/a, \bar{z})$	-0.8366	-2.0680	0.0083	-0.0344
		$\bar{\sigma}_y(x/a, y/a, \bar{z})$	-0.0859	0.0095	0.7017	0.9597
		$\bar{\tau}_{xz}(x/a, y/a, 0)$	0.0000	0.0000	0.0000	0.0000
		$\bar{\tau}_{yz}(x/a, y/a, 0)$	0.0202	0.5094	0.1155	1.2902
0.5	0.4	$\bar{w}(x/a, y/a, 0)$	2.2916	7.4318	2.9303	9.3092
		$\bar{\sigma}_x(x/a, y/a, \bar{z})$	-0.9339	-3.7691	0.0072	-0.0731
		$\bar{\sigma}_y(x/a, y/a, \bar{z})$	-0.0811	-0.3155	0.7481	2.2338
		$\bar{\tau}_{xz}(x/a, y/a, 0)$	0.0000	0.0000	0.0000	0.0000
		$\bar{\tau}_{yz}(x/a, y/a, 0)$	0.0049	1.2829	0.0482	2.6499
0.5	0.5	$\bar{w}(x/a, y/a, 0)$	2.3590	11.7921	3.0445	12.8742
		$\bar{\sigma}_x(x/a, y/a, \bar{z})$	-0.9643	-5.5615	0.0088	0.7656
		$\bar{\sigma}_y(x/a, y/a, \bar{z})$	-0.0788	-0.9410	0.7604	6.8405
		$\bar{\tau}_{xz}(x/a, y/a, 0)$	0.0000	0.0000	0.0000	0.0000
		$\bar{\tau}_{yz}(a/2, y/a, 0)$	0.0000	0.0000	0.0000	0.0000

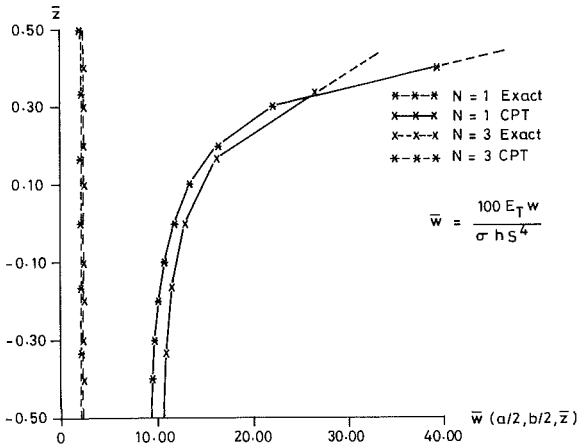

Fig. 4 Thickness distribution of $\bar{w}$ for conc.load; $S = 4$

$h)(h/a)$, that is, $m_j\bar{z}\ (h/a)$. This factor becomes larger and larger as m and n increase, resulting equal values for $\cosh(m_j\bar{z}h/a)$ and $\sin h(m_j\bar{z}h/a)$. So, for higher harmonics the two rows of the coefficient matrix for determining the constants F_{jk} and G_{jk} of the displacements u, v, and w become equal making the matrix singular. The constants F_{jk} and G_{jk} for any kth layer are determined by using the interface continuity conditions for displacements (u, v, w) and stresses (σ_z, τ_{xz}, τ_{yz}). This difficulty in convergence of the series is overcome by adopting the local coordinate system instead of the global coordinate system. The local coordinate system x_i, y_i is taken on the center line of the ith layer at the end $x = 0$. The thickness of the ith layer is designated as h_i.

The convergence is faster in the case of uniformly distributed load and it is rather slow for concentrated load. The maximum deflection $\bar{w}$ converges faster than the corresponding in-plane stresses. Also, the convergence for deflection and stresses is slower for a thin plate compared to a thick plate. The number of terms taken for m and n in Eq. (1) has been progressively increased from 9 in steps of 30 to a such a value that the results are the same up to the fourth decimal by addition of 30 more terms for each m and n. For $(a/h) = 4$, 10, 20, the values of N for the unidirectional laminate for the case of u.d.l. are 39, 69, and 99 and for concentrated load 99, 129, and 189. Similarly, for the (0/90/0) laminate, they are 69, 99, and 129 for the u.d.l. case and 99, 189, and 259 for the concentrated load case.

Results for transverse displacement and stresses are presented in Tables 1 and 2 for various values of (a/h) and at different points of the central plane of the plate. The values of τ_{xy} are not reported in Table 2 as they will be zero when $(x/a) = 0.5$ or $(y/a) = 0.5$. The variation of the in-plane and transverse displacements through the thickness of the three-ply laminate under concentrated load for $(a/h) = 4$ is given in Figs. 2 to 4, and the results obtained by CPT solution are also presented therein.

Conclusions

Deflections and stresses for a square orthotropic laminate under transverse uniformly distributed load/concentrated load

Downloaded 03 May 2010 to 171.66.16.247. Redistribution subject to ASME license or copyright; see http://www.asme.org/terms/Terms_Use.cfm

based on three-dimensional elasticity are presented here. Along with the corresponding results for sinusoidal loading (Pagano, 1970), these serve to assess the new plate theories.

Acknowledgment

Suggestion of this problem by Mr. K. Bhaskar of the Department of Aerospace Engineering is gratefully acknowledged.

References

Pagano, N. J., 1969, "Exact Solutions for Composite Laminates in Cylindrical Bending," *Journal of Composite Materials*, Vol. 3, pp. 398-411.

Pagano, N. J., 1970, "Exact Solutions for Rectangular Bidirectional Composites and Sandwich Plates," *Journal of Composite Materials*, Vol. 4, pp. 20-34.

Pagano, N. J., and Wang, A. S. D., 1971, "Further Study of Composite Laminates Under Cylindrical Bending," *Journal of Composite Materials*, Vol. 5, pp. 521-528.

Simmonds, J. G., 1991, "Pointwise Errors in the classical and in Reissner's Linear Theory of Plates, Especially for Concentrated Loads," to appear in *Journal of Elasticity*.

On the Invariance of Flow in a Narrow Channel of Varying Gap

R. Usha[3]

1 Introduction

An exact similarity solution for squeeze film flow between disks of long plates has been obtained by Wang (1976) if the dimensionless film thickness varies as $H(t) = (a + bt)^{1/2}$ and it has been confirmed by Phan-Thien (1980) using the group theory method that the plane squeeze flow problem admits a similarity solution if the film thickness is proportional to $(a + bt)^{1/2}$. Tichy and Bourgin (1986) and Bourgin and Tichy (1985) have found Wang's paper valuable as a test case of inertia approximations for the simple squeeze film bearing. They have also noted the lack of a comparable test for the presumably simpler case of the steady slider bearing. In this Note, we show that a similarity solution exists using the group theory method for steady thin film flows where the film thickness variation is $G(x) = (a + bx)^m$, and a, b, and m are constants. In this case, the thin film lubrication assumptions are used. The present solution is exact for the limiting case of a narrow channel far downstream of the inlet.

2 Invariant Group

We consider the steady, two-dimensional laminar incompressible flow of a Newtonian fluid in a long, narrow channel of slowly varying height $G(x)$. All symbols represent dimensionless variables. The coordinates x and y are scaled to a reference film thickness, and the velocities u and v are scaled to a reference sliding speed, thus we have $x \gg 1$, $y \simeq 1$, $u \simeq 1$, $v \ll 1$. Under these conditions, the Navier-Stokes equations can be written in terms of the stream function ψ as

$$R(\psi_y \quad \psi_{xyy} - \psi_x \quad \psi_{yyy}) = \psi_{yyyy} \tag{1}$$

where R, the Reynolds number, is the reference sliding velocity times the film thickness divided by the kinematic viscosity.

Consider a one-parameter (ϵ) Lie group of transformation (Bluman and Cole, 1974) written in an infinitesimal manner.

$$\begin{aligned} \bar{x} &= x + \epsilon\zeta(x, y, \psi) + 0(\epsilon^2) \\ \bar{y} &= y + \epsilon\rho(x, y, \psi) + 0(\epsilon^2) \\ \bar{\psi} &= \psi + \epsilon\eta(x, y, \psi) + 0(\epsilon^2) \end{aligned} \tag{2}$$

where $\bar{x}$, $\bar{y}$, $\bar{\psi}$ are the new variables.

Equation (1) is said to be invariant under the group of transformations (2) if it remains unchanged in the new variables, namely

$$R[(\bar{\psi}_{\bar{y}}\ \bar{\psi}_{\bar{x}\bar{y}\bar{y}}) - (\bar{\psi}_{\bar{x}}\ \bar{\psi}_{\bar{y}\bar{y}\bar{y}})] = \bar{\psi}_{\bar{y}\bar{y}\bar{y}\bar{y}} \tag{3}$$

must be satisfied. Using the mathematics of invariance of a partial differential equation involving a single dependent variable and two independent variables presented in Bluman and Cole (1974), we obtain the following determining equations for the infinitesimals ζ, ρ, and η.

$$\zeta_y = \zeta_\psi = \rho_\psi = \rho_{yx} = \rho_{yy} = \eta_x = \eta_y = 0, \quad \eta_\psi + \rho_y - \zeta_x = 0 \tag{4}$$

which gives

$$\begin{aligned} \zeta &= Bx + D \\ \rho &= Ay + f(x) \\ \eta &= \psi(B - A) + C. \end{aligned} \tag{5}$$

This represents a five-parameter group of transformations; four are explicit (A, B, C, D) and one is implicitly contained in $f(x)$.

For any function F that remains invariant under (5), it must satisfy the invariant surface condition (5)

$$\zeta F_x + \rho F_y + \eta F_\psi = 0$$

which can be solved by the characteristic method:

$$\frac{dx}{\zeta} = \frac{dy}{\rho} = \frac{d\psi}{\eta}. \tag{6}$$

Similarity variables can be generated by (6). We illustrate its application by taking the flow of a viscous incompressible fluid in a narrow channel of varying gap.

3 Flow in a Narrow Channel of Varying Gap

The flow of a viscous incompressible fluid in a narrow channel of varying height $G(x)$ which is adequately described by (1), under the thin film lubrication assumptions is considered. The lower surface may slide along its length at varying speed and there may be spatially varying suction or injection at either surface. The channel arbitrarily begins at $x = 0$, but we are concerned with the region $x \gg 1$ and $G(x) > 0$.

The boundary conditions are

$$y = 0: \quad u = U_o(x) \tag{7}$$

$$y = 0: \quad v = V_o(x) \tag{8}$$

$$y = G(x): \quad u = 0 \tag{9}$$

$$y = G(x): \quad v = V_1(x) \tag{10}$$

where $u = \psi_y$, $v = -\psi_x$. Now, we select a subgroup of (6) that also preserves the boundary conditions (7)-(10). Invariance of the boundary curve $y = 0$ requires that $\bar{y} = 0$ which leads to $f(x) = 0$. Invariance of $y = G(x)$ requires that

$$\bar{y} = G(\bar{x}) \tag{11}$$

which implies

$$AG(x) = (Bx + D)G'(x). \tag{12}$$

We obtain from (12)

$$G(x) = C_1(Bx + D)^{A/B} \tag{13}$$

where C_1 is an arbitrary constant of integration. Invariance of boundary conditions (7) and (8) on $y = 0$ imply that

$$\bar{u} = U_o(\bar{x}), \ \bar{v} = V_o(\bar{x}) \text{ on } y = 0 \tag{14}$$

which gives

$$U_o(x) = C_2(Bx + D)^{(B-2A)/B} \tag{15}$$

[3]Department of Mathematics, Anna University, Guindy 600 025, India.

Contributed by the Applied Mechanics Division of THE AMERICAN SOCIETY OF MECHANICAL ENGINEERS. Manuscript received by the ASME Applied Mechanics Division, Sept. 5, 1989; final revision, Mar. 4, 1991.

Downloaded 03 May 2010 to 171.66.16.247. Redistribution subject to ASME license or copyright; see http://www.asme.org/terms/Terms_Use.cfm

based on three-dimensional elasticity are presented here. Along with the corresponding results for sinusoidal loading (Pagano, 1970), these serve to assess the new plate theories.

Acknowledgment

Suggestion of this problem by Mr. K. Bhaskar of the Department of Aerospace Engineering is gratefully acknowledged.

References

Pagano, N. J., 1969, "Exact Solutions for Composite Laminates in Cylindrical Bending," *Journal of Composite Materials*, Vol. 3, pp. 398-411.

Pagano, N. J., 1970, "Exact Solutions for Rectangular Bidirectional Composites and Sandwich Plates," *Journal of Composite Materials*, Vol. 4, pp. 20-34.

Pagano, N. J., and Wang, A. S. D., 1971, "Further Study of Composite Laminates Under Cylindrical Bending," *Journal of Composite Materials*, Vol. 5, pp. 521-528.

Simmonds, J. G., 1991, "Pointwise Errors in the classical and in Reissner's Linear Theory of Plates, Especially for Concentrated Loads," to appear in *Journal of Elasticity*.

On the Invariance of Flow in a Narrow Channel of Varying Gap

R. Usha[3]

1 Introduction

An exact similarity solution for squeeze film flow between disks of long plates has been obtained by Wang (1976) if the dimensionless film thickness varies as $H(t) = (a + bt)^{1/2}$ and it has been confirmed by Phan-Thien (1980) using the group theory method that the plane squeeze flow problem admits a similarity solution if the film thickness is proportional to $(a + bt)^{1/2}$. Tichy and Bourgin (1986) and Bourgin and Tichy (1985) have found Wang's paper valuable as a test case of inertia approximations for the simple squeeze film bearing. They have also noted the lack of a comparable test for the presumably simpler case of the steady slider bearing. In this Note, we show that a similarity solution exists using the group theory method for steady thin film flows where the film thickness variation is $G(x) = (a + bx)^m$, and a, b, and m are constants. In this case, the thin film lubrication assumptions are used. The present solution is exact for the limiting case of a narrow channel far downstream of the inlet.

2 Invariant Group

We consider the steady, two-dimensional laminar incompressible flow of a Newtonian fluid in a long, narrow channel of slowly varying height $G(x)$. All symbols represent dimensionless variables. The coordinates x and y are scaled to a reference film thickness, and the velocities u and v are scaled to a reference sliding speed, thus we have $x \gg 1$, $y \simeq 1$, $u \simeq 1$, $v \ll 1$. Under these conditions, the Navier-Stokes equations can be written in terms of the stream function ψ as

$$R(\psi_y \quad \psi_{xyy} - \psi_x \quad \psi_{yyy}) = \psi_{yyyy} \tag{1}$$

where R, the Reynolds number, is the reference sliding velocity times the film thickness divided by the kinematic viscosity.

Consider a one-parameter (ϵ) Lie group of transformation (Bluman and Cole, 1974) written in an infinitesimal manner.

$$\begin{aligned} \bar{x} &= x + \epsilon\zeta(x, y, \psi) + 0(\epsilon^2) \\ \bar{y} &= y + \epsilon\rho(x, y, \psi) + 0(\epsilon^2) \\ \bar{\psi} &= \psi + \epsilon\eta(x, y, \psi) + 0(\epsilon^2) \end{aligned} \tag{2}$$

where $\bar{x}$, $\bar{y}$, $\bar{\psi}$ are the new variables.

Equation (1) is said to be invariant under the group of transformations (2) if it remains unchanged in the new variables, namely

$$R[(\bar{\psi}_{\bar{y}}\ \bar{\psi}_{\bar{x}\bar{y}\bar{y}}) - (\bar{\psi}_{\bar{x}}\ \bar{\psi}_{\bar{y}\bar{y}\bar{y}})] = \bar{\psi}_{\bar{y}\bar{y}\bar{y}\bar{y}} \tag{3}$$

must be satisfied. Using the mathematics of invariance of a partial differential equation involving a single dependent variable and two independent variables presented in Bluman and Cole (1974), we obtain the following determining equations for the infinitesimals ζ, ρ, and η.

$$\zeta_y = \zeta_\psi = \rho_\psi = \rho_{yx} = \rho_{yy} = \eta_x = \eta_y = 0, \quad \eta_\psi + \rho_y - \zeta_x = 0 \tag{4}$$

which gives

$$\begin{aligned} \zeta &= Bx + D \\ \rho &= Ay + f(x) \\ \eta &= \psi(B - A) + C. \end{aligned} \tag{5}$$

This represents a five-parameter group of transformations; four are explicit (A, B, C, D) and one is implicitly contained in $f(x)$.

For any function F that remains invariant under (5), it must satisfy the invariant surface condition (5)

$$\zeta F_x + \rho F_y + \eta F_\psi = 0$$

which can be solved by the characteristic method:

$$\frac{dx}{\zeta} = \frac{dy}{\rho} = \frac{d\psi}{\eta}. \tag{6}$$

Similarity variables can be generated by (6). We illustrate its application by taking the flow of a viscous incompressible fluid in a narrow channel of varying gap.

3 Flow in a Narrow Channel of Varying Gap

The flow of a viscous incompressible fluid in a narrow channel of varying height $G(x)$ which is adequately described by (1), under the thin film lubrication assumptions is considered. The lower surface may slide along its length at varying speed and there may be spatially varying suction or injection at either surface. The channel arbitrarily begins at $x = 0$, but we are concerned with the region $x \gg 1$ and $G(x) > 0$.

The boundary conditions are

$$y = 0: \quad u = U_o(x) \tag{7}$$

$$y = 0: \quad v = V_o(x) \tag{8}$$

$$y = G(x): \quad u = 0 \tag{9}$$

$$y = G(x): \quad v = V_1(x) \tag{10}$$

where $u = \psi_y$, $v = -\psi_x$. Now, we select a subgroup of (6) that also preserves the boundary conditions (7)-(10). Invariance of the boundary curve $y = 0$ requires that $\bar{y} = 0$ which leads to $f(x) = 0$. Invariance of $y = G(x)$ requires that

$$\bar{y} = G(\bar{x}) \tag{11}$$

which implies

$$AG(x) = (Bx + D)G'(x). \tag{12}$$

We obtain from (12)

$$G(x) = C_1(Bx + D)^{A/B} \tag{13}$$

where C_1 is an arbitrary constant of integration. Invariance of boundary conditions (7) and (8) on $y = 0$ imply that

$$\bar{u} = U_o(\bar{x}), \ \bar{v} = V_o(\bar{x}) \text{ on } y = 0 \tag{14}$$

which gives

$$U_o(x) = C_2(Bx + D)^{(B-2A)/B} \tag{15}$$

[3]Department of Mathematics, Anna University, Guindy 600 025, India.

Contributed by the Applied Mechanics Division of THE AMERICAN SOCIETY OF MECHANICAL ENGINEERS. Manuscript received by the ASME Applied Mechanics Division, Sept. 5, 1989; final revision, Mar. 4, 1991.

Copyright © 1992 by ASME
Downloaded 03 May 2010 to 171.66.16.247. Redistribution subject to ASME license or copyright; see http://www.asme.org/terms/Terms_Use.cfm

$$V_o(x) = C_3(Bx+D)^{-A/B} \tag{16}$$

where C_2, C_3 are arbitrary constants of integration. Invariance of the boundary condition (9) is automatically satisfied. Invariance of (10) requires that

$$\bar{v} = -\bar{\psi}_{\bar{x}} = V_1(\bar{x}) \text{ on } y = G(x) \tag{17}$$

which implies

$$-AV_1(x) = (Bx+D)V_1'(x) \tag{18}$$

and it gives

$$V_1(x) = C_4(Bx+D)^{-A/B} \tag{19}$$

where C_4 is an arbitrary constant of integration. Therefore, if the film thickness variation is given by (13), the prescribed sliding velocity by (15) and the prescribed spatially varying suction or injection at either surface by (19) and (16), then the flow in a narrow channel of varying gap admits similarity solutions described by the following characteristics:

$$\frac{dx}{Bx+D} = \frac{dy}{Ay} = \frac{dz}{(B-A)\psi + C}. \tag{20}$$

The first equality yields the similarity variable

$$\zeta_1 = y(Bx+D)^{-A/B} \tag{21}$$

from which the stream function for the case $C = 0$ is given by

$$\psi = (Bx+D)^{(B-A)/B}\phi(\zeta_1) \tag{22}$$

where $\phi(\zeta_1)$ can be determined by substituting (22) back in (1). We consider a special case, where

$$A/B = 1/2,\ B = 2\alpha,\ \alpha = GG',\ C_1 = 1,\ C_2 = \bar{U}_o,$$
$$C_3 = -\alpha\bar{V}_o,\ C_4 = -\alpha\bar{V}_1,\ D = 1 \tag{23}$$

so that

$$\begin{aligned} G(x) &= (1+2\,\alpha\,x)^{1/2} \\ U_o(x) &= \bar{U}_o \\ V_o(x) &= -G'(x)\bar{V}_o \\ V_1(x) &= -G'(x)\bar{V}_1 \\ \psi &= (1+2\,\alpha\,x)^{1/2}\,\phi(\zeta_1) \\ \zeta_1 &= y(1+2\,\alpha\,x)^{-1/2}. \end{aligned} \tag{24}$$

Substitution of ψ from (24) into (1) results in an ordinary differential equation given by

$$\phi'''' + \alpha R[\phi\phi''' + \phi'\phi''] = 0 \tag{25}$$

where α is a measure of the slope G' and the parameter αR is analogous to the modified or reduced Reynolds number used in lubrication analysis. This equation has been extensively studied by Tichy and Bourgin (1986) who found that when $G(x)$ is proportional to $(1 + 2\,\alpha\,x)^{1/2}$, a similarity solution for the flow in a narrow channel of varyaing gap is possible.

References

Bluman, G. W., and Cole, J. D., 1974, *Similarity Methods for Differential Equations*, Springer-Verlag, New York.

Bourgin, P., and Tichy, J.A., 1985, "Lubricating Films of a Viscoelastic Fluid Studied by a Linearization Method," *International Journal of Engineering Science*, Vol. 23, pp. 1135–1149.

Phan-Thien, N., 1980, "On the Invariance Group of the Plane Squeezing Flow of a Viscous Fluid," ASME JOURNAL OF APPLIED MECHANICS, Vol. 47, pp. 213–214.

Tichy, J. A., and Bourgin, P., 1986, "A Similarity Solution for Flow in a Narrow Channel of Varying Gap," ASME JOURNAL OF APPLIED MECHANICS, Vol. 53, pp. 943–946.

Tichy, J. A., and Bourgin, P., 1986, "The Effect of Inertia in Lubrication Flow Including Entrance and Initial Conditions," ASME JOURNAL OF APPLIED MECHANICS, Vol. 107, pp. 759–765.

Wang, C. Y., 1976, "The Squeezing of a Fluid Between Two Plates," ASME JOURNAL OF APPLIED MECHANICS, Vol. 43, pp. 579–583.

Interaction Between an Edge Dislocation and a Lamellar Inhomogeneity With a Slipping Interface

L. Stagni[4] and R. Lizzio[4]

The plane elasticity problem of an internal stress source located near a lamellar inhomogeneity is considered. It is assumed that the lamella-matrix interface does not transmit tangential displacements or shear tractions (slipping interface). The elastic field is given in terms of the source bulk field and one parameter formed from the elastic constants. The image force on an edge dislocation near the lamella is calculated and discussed. A dislocation stable-equilibrium position exists in a domain of elastic constants and Burgers vector directions. This result is characteristic of the interaction with a slipping lamellar inhomogeneity having finite thickness.

1 Introduction

The problem of the elastic interaction between a dislocation and a lamellar inhomogeneity is a basic one in the study of the mechanical properties of layered or lamellar composite materials. Chou (1966) treated this problem for a screw dislocation, and Stagni and Lizzio (1987, 1988) analyzed the more complicated interaction between an edge dislocation and a lamella, by assuming a perfect bond between lamella and matrix (*adhering interface*). Nevertheless, in certain real situations this condition may not be fulfilled. In particular, at elevated temperatures the transition zone from an inclusion to the matrix behaves like a viscous liquid layer, loosing its capability of transmitting shear tractions and tangential displacements (*slipping interface*). The importance of studying slipping interface effects is testified by a number of published works (Head, 1953; Dundurs et al., 1966; Dundurs and Gangadharan, 1969; Ghahremani, 1980; Srolovitz et al., 1983). None of these studies, however, deals with inhomogeneities of a lamellar shape.

The problem of a lamellar inhomogeneity with a slipping interface was recently confronted by Stagni and Lizzio (1990), who investigated the behavior of an edge dislocation *inside* the lamella. The present paper continues this investigation by recording the elasticity solution to the problem of a stress source *near* a slipping lamella, in generalized plane-stress or plane-strain conditions. Using this solution, the image force on an edge dislocation near the inhomogeneity is calculated. Dislocation equilibrium is discussed and the results are compared with those found in the adhering-interface case.

2 The Elasticity Solution

Figure 1 shows the problem geometry, having denoted by G and ν the shear modulus and the Poisson's ratio of the matrix (Regions 1 and 3), respectively, and by G_2 and ν_2 the elastic constants of the lamellar inhomogeneity (Region 2). The slipping interface between the matrix and the lamella is characterized by the boundary conditions

$$\begin{aligned} &\sigma_{yy}^{(1)} = \sigma_{yy}^{(2)};\ \sigma_{xy}^{(1)} = \sigma_{xy}^{(2)} = 0;\ u_y^{(1)} = u_y^{(2)} \text{ for } y = a \\ &\sigma_{yy}^{(3)} = \sigma_{yy}^{(2)};\ \sigma_{xy}^{(3)} = \sigma_{xy}^{(2)} = 0;\ u_y^{(3)} = u_y^{(2)} \text{ for } y = -a \end{aligned} \tag{1}$$

where σ_{yy} and σ_{xy} are the components of the interface traction, u_y is the normal displacement, and superscripts specify regions.

[4]Dipartimento di Fisica, Università degli Studi di Roma "La Sapienza," 00185 Roma, Italy; Gruppo Nazionale di Struttura della Materia del C.N.R. and Centro Interuniversitario di Struttura della Materia del M.P.I., Roma, Italy.

Contributed by the Applied Mechanics Division of THE AMERICAN SOCIETY OF MECHANICAL ENGINEERS. Manuscript received by the Applied Mechanics Division, Jan. 15, 1990; final revision, Mar. 4, 1991.

Downloaded 03 May 2010 to 171.66.16.247. Redistribution subject to ASME license or copyright; see http://www.asme.org/terms/Terms_Use.cfm

$$V_o(x) = C_3(Bx+D)^{-A/B} \tag{16}$$

where C_2, C_3 are arbitrary constants of integration. Invariance of the boundary condition (9) is automatically satisfied. Invariance of (10) requires that

$$\bar{v} = -\bar{\psi}_{\bar{x}} = V_1(\bar{x}) \text{ on } y = G(x) \tag{17}$$

which implies

$$-AV_1(x) = (Bx+D)V_1'(x) \tag{18}$$

and it gives

$$V_1(x) = C_4(Bx+D)^{-A/B} \tag{19}$$

where C_4 is an arbitrary constant of integration. Therefore, if the film thickness variation is given by (13), the prescribed sliding velocity by (15) and the prescribed spatially varying suction or injection at either surface by (19) and (16), then the flow in a narrow channel of varying gap admits similarity solutions described by the following characteristics:

$$\frac{dx}{Bx+D} = \frac{dy}{Ay} = \frac{dz}{(B-A)\psi + C}. \tag{20}$$

The first equality yields the similarity variable

$$\zeta_1 = y(Bx+D)^{-A/B} \tag{21}$$

from which the stream function for the case $C = 0$ is given by

$$\psi = (Bx+D)^{(B-A)/B}\phi(\zeta_1) \tag{22}$$

where $\phi(\zeta_1)$ can be determined by substituting (22) back in (1). We consider a special case, where

$$A/B = 1/2,\ B = 2\alpha,\ \alpha = GG',\ C_1 = 1,\ C_2 = \bar{U}_o,$$
$$C_3 = -\alpha\bar{V}_o,\ C_4 = -\alpha\bar{V}_1,\ D = 1 \tag{23}$$

so that

$$\begin{aligned} G(x) &= (1+2\,\alpha\,x)^{1/2} \\ U_o(x) &= \bar{U}_o \\ V_o(x) &= -G'(x)\bar{V}_o \\ V_1(x) &= -G'(x)\bar{V}_1 \\ \psi &= (1+2\,\alpha\,x)^{1/2}\,\phi(\zeta_1) \\ \zeta_1 &= y(1+2\,\alpha\,x)^{-1/2}. \end{aligned} \tag{24}$$

Substitution of ψ from (24) into (1) results in an ordinary differential equation given by

$$\phi'''' + \alpha R[\phi\phi''' + \phi'\phi''] = 0 \tag{25}$$

where α is a measure of the slope G' and the parameter αR is analogous to the modified or reduced Reynolds number used in lubrication analysis. This equation has been extensively studied by Tichy and Bourgin (1986) who found that when $G(x)$ is proportional to $(1 + 2\,\alpha\,x)^{1/2}$, a similarity solution for the flow in a narrow channel of varyaing gap is possible.

References

Bluman, G. W., and Cole, J. D., 1974, *Similarity Methods for Differential Equations*, Springer-Verlag, New York.

Bourgin, P., and Tichy, J.A., 1985, "Lubricating Films of a Viscoelastic Fluid Studied by a Linearization Method," *International Journal of Engineering Science*, Vol. 23, pp. 1135–1149.

Phan-Thien, N., 1980, "On the Invariance Group of the Plane Squeezing Flow of a Viscous Fluid," ASME JOURNAL OF APPLIED MECHANICS, Vol. 47, pp. 213–214.

Tichy, J. A., and Bourgin, P., 1986, "A Similarity Solution for Flow in a Narrow Channel of Varying Gap," ASME JOURNAL OF APPLIED MECHANICS, Vol. 53, pp. 943–946.

Tichy, J. A., and Bourgin, P., 1986, "The Effect of Inertia in Lubrication Flow Including Entrance and Initial Conditions," ASME JOURNAL OF APPLIED MECHANICS, Vol. 107, pp. 759–765.

Wang, C. Y., 1976, "The Squeezing of a Fluid Between Two Plates," ASME JOURNAL OF APPLIED MECHANICS, Vol. 43, pp. 579–583.

Interaction Between an Edge Dislocation and a Lamellar Inhomogeneity With a Slipping Interface

L. Stagni[4] and R. Lizzio[4]

The plane elasticity problem of an internal stress source located near a lamellar inhomogeneity is considered. It is assumed that the lamella-matrix interface does not transmit tangential displacements or shear tractions (slipping interface). The elastic field is given in terms of the source bulk field and one parameter formed from the elastic constants. The image force on an edge dislocation near the lamella is calculated and discussed. A dislocation stable-equilibrium position exists in a domain of elastic constants and Burgers vector directions. This result is characteristic of the interaction with a slipping lamellar inhomogeneity having finite thickness.

1 Introduction

The problem of the elastic interaction between a dislocation and a lamellar inhomogeneity is a basic one in the study of the mechanical properties of layered or lamellar composite materials. Chou (1966) treated this problem for a screw dislocation, and Stagni and Lizzio (1987, 1988) analyzed the more complicated interaction between an edge dislocation and a lamella, by assuming a perfect bond between lamella and matrix (*adhering interface*). Nevertheless, in certain real situations this condition may not be fulfilled. In particular, at elevated temperatures the transition zone from an inclusion to the matrix behaves like a viscous liquid layer, loosing its capability of transmitting shear tractions and tangential displacements (*slipping interface*). The importance of studying slipping interface effects is testified by a number of published works (Head, 1953; Dundurs et al., 1966; Dundurs and Gangadharan, 1969; Ghahremani, 1980; Srolovitz et al., 1983). None of these studies, however, deals with inhomogeneities of a lamellar shape.

The problem of a lamellar inhomogeneity with a slipping interface was recently confronted by Stagni and Lizzio (1990), who investigated the behavior of an edge dislocation *inside* the lamella. The present paper continues this investigation by recording the elasticity solution to the problem of a stress source *near* a slipping lamella, in generalized plane-stress or plane-strain conditions. Using this solution, the image force on an edge dislocation near the inhomogeneity is calculated. Dislocation equilibrium is discussed and the results are compared with those found in the adhering-interface case.

2 The Elasticity Solution

Figure 1 shows the problem geometry, having denoted by G and ν the shear modulus and the Poisson's ratio of the matrix (Regions 1 and 3), respectively, and by G_2 and ν_2 the elastic constants of the lamellar inhomogeneity (Region 2). The slipping interface between the matrix and the lamella is characterized by the boundary conditions

$$\begin{aligned} &\sigma_{yy}^{(1)} = \sigma_{yy}^{(2)};\ \sigma_{xy}^{(1)} = \sigma_{xy}^{(2)} = 0;\ u_y^{(1)} = u_y^{(2)} \text{ for } y = a \\ &\sigma_{yy}^{(3)} = \sigma_{yy}^{(2)};\ \sigma_{xy}^{(3)} = \sigma_{xy}^{(2)} = 0;\ u_y^{(3)} = u_y^{(2)} \text{ for } y = -a \end{aligned} \tag{1}$$

where σ_{yy} and σ_{xy} are the components of the interface traction, u_y is the normal displacement, and superscripts specify regions.

[4]Dipartimento di Fisica, Università degli Studi di Roma "La Sapienza," 00185 Roma, Italy; Gruppo Nazionale di Struttura della Materia del C.N.R. and Centro Interuniversitario di Struttura della Materia del M.P.I., Roma, Italy.

Contributed by the Applied Mechanics Division of THE AMERICAN SOCIETY OF MECHANICAL ENGINEERS. Manuscript received by the Applied Mechanics Division, Jan. 15, 1990; final revision, Mar. 4, 1991.

Copyright © 1992 by ASME
Downloaded 03 May 2010 to 171.66.16.247. Redistribution subject to ASME license or copyright; see http://www.asme.org/terms/Terms_Use.cfm

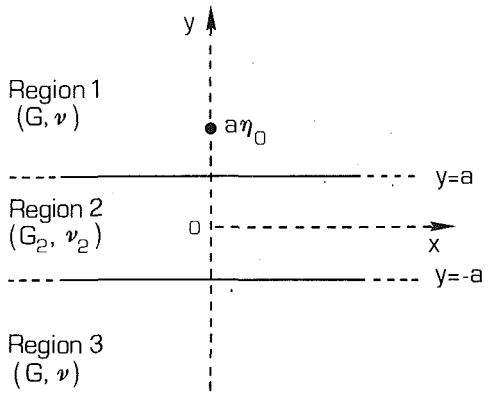

Fig. 1 Source of internal stress near a lamellar inhomogeneity

The elastic fields induced by a source of internal stress located at $y = a\eta_0$ ($\eta_0 \geq 1$) can be obtained with the same procedure used for the adhering-interface case (Stagni and Lizzio, 1987). Therefore, we limit ourselves to record the final formulas. Putting

$$z = x + iy\,(i^2 = -1);\ \zeta = z/a$$

and

$$\zeta_k = \zeta - i\eta_k;\ \eta_k = 2k + (-1)^k\eta_0\ (k = 0, \pm 1, \pm 2, \ldots\ldots),$$

the complex elastic potentials $\varphi(z)$, $\psi(z)$ (Muskhelishvili, 1975) for the three regions are

$$\varphi_1(z) = \varphi_*(z) + a\sum_{n=0}^{\infty}\left(A_{n,0}\ln\zeta_{1-2n} + \sum_{m=1}^{\infty} A_{n,m}\zeta_{1-2n}^{-m}\right)$$

$$\psi_1(z) = \psi_*(z) + a\sum_{n=0}^{\infty}\left(B_{n,0}\ln\zeta_{1-2n} + \sum_{m=1}^{\infty} B_{n,m}\zeta_{1-2n}^{-m}\right)$$

$$\varphi_2(z) = a\sum_{n=0}^{\infty}\left(C_{n,0}\ln\zeta_{2n} + \sum_{m=1}^{\infty} C_{n,m}\zeta_{2n}^{-m}\right) + a\sum_{n=1}^{\infty}\left(C_{-n,0}\ln\zeta_{1-2n} + \sum_{m=1}^{\infty} C_{-n,m}\zeta_{1-2n}^{-m}\right)$$

$$\psi_2(z) = a\sum_{n=0}^{\infty}\left(D_{n,0}\ln\zeta_{2n} + \sum_{m=1}^{\infty} D_{n,m}\zeta_{2n}^{-m}\right) + a\sum_{n=1}^{\infty}\left(D_{-n,0}\ln\zeta_{1-2n} + \sum_{m=1}^{\infty} D_{-n,m}\zeta_{1-2n}^{-m}\right)$$

$$\varphi_3(z) = a\sum_{n=0}^{\infty}\left(E_{n,0}\ln\zeta_{2n} + \sum_{m=1}^{\infty} E_{n,m}\zeta_{2n}^{-m}\right)$$

$$\psi_3(z) = a\sum_{n=0}^{\infty}\left(F_{n,0}\ln\zeta_{2n} + \sum_{m=1}^{\infty} F_{n,m}\zeta_{2n}^{-m}\right)$$

where

$$\varphi_*(z) = a\left(A_0^*\ln\zeta_0 + \sum_{m=1}^{\infty} A_m^*\zeta_0^{-m}\right);\qquad \psi_*(z) = a\left(B_0^*\ln\zeta_0 + \sum_{m=1}^{\infty} B_m^*\zeta_0^{-m}\right)$$

are the bulk potentials.

The boundary conditions (1) are fulfilled by the following set of recursion equations ($n, m = 0, 1, 2, \ldots$.):

$$\begin{aligned}
C_{0,m} &= (\alpha+1)^{-1}[B_m^* - (m-1)A_m^* + i(2-\eta_0)\omega_m A_{m-1}^*]\\
C_{-1,m} &= (\alpha+1)^{-1}[(\alpha-1)\overline{C}_{0,m} - 4i\omega_m\overline{C}_{0,m-1}]\\
C_{n+1,m} &= (\alpha+1)^{-1}[2\alpha\overline{C}_{-1-n,m} + 4i\omega_m\overline{C}_{-1-n,m-1} - (\alpha-1)C_{n,m}]\\
C_{-n-2,m} &= (\alpha+1)^{-1}[2\alpha\overline{C}_{n+1,m} - 4i\omega_m\overline{C}_{n+1,m-1} - (\alpha-1)C_{-1-n,m}] \qquad (2)\\
A_{0,m} &= \overline{A_m^*} - \alpha\overline{C_{0,m}}\\
B_{0,m} &= (m-1)\overline{A_m^*} - (\alpha m-1)\overline{C_{0,m}} - i\eta_0\omega_m A_{0,m-1}\\
D_{0,m} &= (m+1)C_{0,m} - i(2-\eta_0)\omega_m C_{0,m-1}\\
A_{n+1,m} &= \alpha(C_{-1-n,m} - \overline{C}_{n+1,m})\\
B_{n+1,m} &= (m+1)A_{n+1,m} - i(2-\eta_{-1-2n})\omega_m A_{n+1,m-1}\\
D_{-1-n,m} &= (m-\alpha)C_{-1-n,m} + i(2+\eta_{-1-2n})\omega_m C_{-1-n,m-1} + (\alpha-1)\overline{C}_{n,m}\\
D_{n+1,m} &= (m-\alpha)C_{n+1,m} - i(2-\eta_{2n+2})\omega_m C_{n+1,m-1} + (\alpha-1)\overline{C}_{-1-n,m}\\
E_{n,m} &= \alpha(C_{n,m} - \overline{C}_{-1-n,m})\\
F_{n,m} &= (m+1)E_{n,m} + i(2+\eta_{2n})\omega_m E_{n,m-1} \qquad (3)
\end{aligned}$$

where

$$\alpha = \frac{\kappa_2 + 1}{\Gamma(\kappa+1)}; \qquad (4)$$

$\Gamma = G_2/G$; $\kappa = 3 - 4\nu$ for plane strain, $\kappa = (3-\nu)/(1+\nu)$ for plane stress; $A_{n,-1} = C_{k,-1} = E_{n,-1} = 0$; $\omega_m = m - 1 - \delta_{1,m}$, and $\delta_{n,m}$ is the Kronecker symbol.

A remarkable feature of this solution is that it involves one parameter, α, formed from four elastic constants (in the adhering interface case two parameters are required).

If the source of internal stress is an edge dislocation with Burgers vector (b_x, b_y), then the solution is completed by the well-known relationships

$$A_0^* = \gamma,\ B_0^* = \overline{\gamma},\ B_1^* = i\gamma\eta_0,\ B_m^* = 0\ (m \geq 2) \qquad (5)$$

where

$$\gamma = \frac{G(b_y - ib_x)}{a\pi(\kappa+1)}. \qquad (6)$$

3 Image Force

Due to the fact that the strain energy depends on the dislocation distance from the lamella, the unit length of dislocation is subjected to a force directed along the y-axis. In terms of complex potentials this force may be expressed as (Stagni and Lizzio, 1987)

$$F = be^{i\theta}[\overline{z}\varphi_e''(z) + \psi_e'(z)] - be^{-i\theta}[\varphi_e'(z) + \overline{\varphi_e'(z)}] \quad \text{for } z = ia\eta_0 \qquad (7)$$

where

$$b = \sqrt{b_x^2 + b_y^2},\ \theta = \tan^{-1}\frac{b_y}{b_x}$$

and

$$\varphi_e(z) = \varphi_1(z) - \varphi_*(z) = a\sum_{n=0}^{\infty}\left(A_{n,0}\ln\zeta_{1-2n} + \sum_{m=1}^{\infty} A_{n,m}\zeta_{1-2n}^{-m}\right)$$

$$\psi_e(z) = \psi_1(z) - \psi_*(z) = a\sum_{n=0}^{\infty}\left(B_{n,0}\ln\zeta_{1-2n} + \sum_{m=1}^{\infty} B_{n,m}\zeta_{1-2n}^{-m}\right). \qquad (8)$$

Introducing (8) into (7), and exploiting the Eqs. (2)-(6), it may be deduced that

Downloaded 03 May 2010 to 171.66.16.247. Redistribution subject to ASME license or copyright; see http://www.asme.org/terms/Terms_Use.cfm

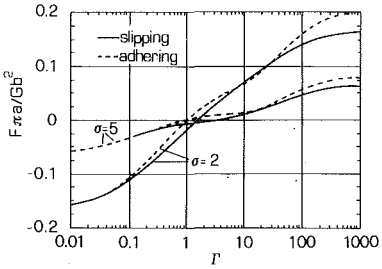

Fig. 2 Image force on dislocation versus relative hardness (plane strain; $\nu = \nu_2 = 0.25$; $\theta = 90$ deg)

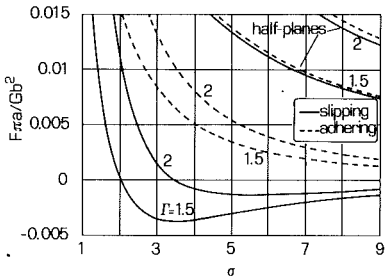

Fig. 3 Image force on dislocation versus distance (plane strain; $\nu = \nu_2 = 0.25$; $\theta = 90$ deg)

$$F = -\frac{Gb^2}{a\pi(\kappa+1)}\frac{\alpha+\cos 2\theta}{\alpha+1}\sigma^{-1} + 2be^{-i\theta}\mathrm{Re}\sum_{n=1}^{\infty}\sum_{m=1}^{2n+2}\frac{(2i)^{-m}\omega_m A_{n,m-1}}{(\sigma+2n)^m} - be^{i\theta}\sigma\sum_{n=1}^{\infty}\sum_{m=1}^{2n+2}\frac{(2i)^{-m}m\omega_m A_{n,m-1}}{(\sigma+2n)^{m+1}} \quad (9)$$

where $\sigma = \eta_0 - 1$ is the dislocation distance from the nearest interface in units of a, and Re denotes the real part.

The first term on the right-hand side of (9) is the force exerted by a slipping lamellar inhomogeneity of infinite thickness (joined half-planes); it will be denoted as the *bimetallic force*.[5] Thus, the remaining terms are the contribution of the inhomogeneity finiteness. Numerical analyses of (9) show that such contribution is always attractive, presenting one negative minimum as a function of σ. On the other hand, the bimetallic force is proportional to σ^{-1} and is repulsive (or zero) for

$$0 \le \alpha \le -\cos 2\theta.$$

It follows that this condition is necessary and sufficient for the existence of an equilibrium position (stable equilibrium). It is worth noting that the *total* force vanishes at the equilibrium distance, meaning that spontaneous dislocation displacements from this position may occur neither by glide nor by climb.

The slipping and adhering-interface forces are now compared. In order to avoid unnecessary complications, only the physically most important situation will be considered, i.e., that of a dislocation with its Burgers vector normal to the lamellar inhomogeneity ($\theta = 90$ deg).

Figure 2 shows the slipping-interface and the adhering-interface force versus the relative hardness Γ, for two dislocation positions and identical Poisson's ratios (numerical analyses for differing Poisson's ratios lead to the same general conclusions). It is seen that distinct zero-points of the slipping-interface curves occur for $\Gamma > 1$, i.e., in this range a dislocation equilibrium position exists for each value of Γ.

On the contrary, all the adhering-interface curves intersect at the point ($\Gamma = 1$, $F = 0$), meaning that, as expected, the force vanishes identically when matrix and lamella are made of the same material. Near an adhering interface the force is attractive for $\Gamma < 1$ (soft lamella), repulsive for $\Gamma > 1$ (hard lamella), and no equilibrium position exists.

Further results are presented in Fig. 3, where the slipping-interface force is plotted against σ for two values of Γ. In the same figure the corresponding curves for adhering interface and for bimetallic interface are shown. It is seen that (i) the intensity of the force, and therefore, the elastic energy stored in the material, is reduced by reducing the inhomogeneity thickness; (ii) relaxation of the interface from adhering to slipping also induces a reduction of the elastic energy; (iii) only the slipping-interface force changes its sign. This means, in particular, that a hard lamella may become a trapping center for dislocations when the adherence of the matrix-lamella interface is lost. In other words, a sort of *debond hardening* of lamellar composites may occur by increasing the temperature beyond a certain point.

[5]Equation (9) shows that for $\theta = 0$, this is the same image force which a traction-free surface would produce.

Acknowledgment

The work reported here was supported by the Ministero della Pubblica Istruzione, Italy.

References

Chou, Y. T., 1966, "Screw Dislocations In and Near Lamellar Inclusions," *Physica Status Solidi*, Vol. 17, pp. 509–516.

Dundurs, J., Fukui, K., and Kukui, T., 1966, "Concentrated Force Near a Smooth Circular Inclusion," ASME JOURNAL OF APPLIED MECHANICS, Vol. 33, pp. 871–876.

Dundurs, J., and Gangadharan, A. C., 1969, "Edge Dislocation Near an Inclusion With a Slipping Interface," *Journal of the Mechanics and Physics of Solids*, Vol. 17, pp. 459–471.

Ghahremani, F., 1980, "Effect of Grain Boundary Sliding on Anelasticity of Polycrystals," *International Journal of Solids & Structures*, Vol. 16, pp. 825–845.

Head, A. K., 1953, "Edge Dislocations in Inhomogeneous Media," *Proceedings of the Physical Society*, Series B, Vol. 66, pp. 793–801.

Muskhelishvili, N. I., 1975, *Some Basic Problems of the Mathematical Theory of Elasticity*, Noordhoff Ltd., Leyden.

Srolovitz, D., Petkovic-Luton, R. A., and Luton, M. J., 1983, "Edge Dislocation—Circular Inclusion Interaction at Elevated Temperatures," *Acta Metallurgica*, Vol. 31, pp. 2151–2159.

Stagni, L., and Lizzio, R., 1987, "Interaction of an Edge Dislocation with a Lamellar Inhomogeneity," *Mechanics of Materials*, Vol. 6, pp. 17–25.

Stagni, L., and Lizzio, R., 1988, "Edge Dislocation Inside a Lamellar Inhomogeneity," *Journal of Applied Physics*, Vol. 64, pp. 1594–1596.

Stagni, L., and Lizzio, R., 1990, "Edge Dislocation in a Lamellar Inhomogeneity with a Slipping Interface," *Journal of Materials Science*, Vol. 25, pp. 1618–1622.

Strain-Hardening Creep Relaxation

P. A. Huneault[6]

Relaxation testing is an important alternative for investigating the creep properties of a material. A solution for the strain-hardening form of the power law is derived and compared to its time-hardening counterpart.

Introduction

This Note relates an explicit analytical expression governing strain-hardening relaxation. Integral forms for relaxation re-

[6]Researcher, Institute for Research in Construction, National Research Council Canada, Ottawa, Ontario K1A 0R6, Canada. Presently at Rousseau, Sauvé, Warren & Associates, Consultants, Montréal, Québec, H2Z 1W7, Canada.

Contributed by the Applied Mechanics Division of THE AMERICAN SOCIETY OF MECHANICAL ENGINEERS. Manuscript received by the ASME Applied Mechanics Division, July 11, 1990; final revision, Nov. 9, 1990.

Downloaded 03 May 2010 to 171.66.16.247. Redistribution subject to ASME license or copyright; see http://www.asme.org/terms/Terms_Use.cfm

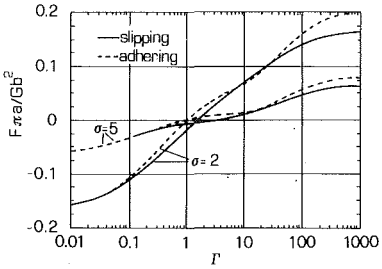

Fig. 2 Image force on dislocation versus relative hardness (plane strain; $\nu = \nu_2 = 0.25$; $\theta = 90$ deg)

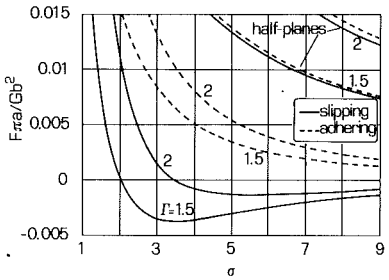

Fig. 3 Image force on dislocation versus distance (plane strain; $\nu = \nu_2 = 0.25$; $\theta = 90$ deg)

$$F = -\frac{Gb^2}{a\pi(\kappa+1)}\frac{\alpha+\cos 2\theta}{\alpha+1}\sigma^{-1} + 2be^{-i\theta}\mathrm{Re}\sum_{n=1}^{\infty}\sum_{m=1}^{2n+2}\frac{(2i)^{-m}\omega_m A_{n,m-1}}{(\sigma+2n)^m} - be^{i\theta}\sigma\sum_{n=1}^{\infty}\sum_{m=1}^{2n+2}\frac{(2i)^{-m}m\omega_m A_{n,m-1}}{(\sigma+2n)^{m+1}} \quad (9)$$

where $\sigma = \eta_0 - 1$ is the dislocation distance from the nearest interface in units of a, and Re denotes the real part.

The first term on the right-hand side of (9) is the force exerted by a slipping lamellar inhomogeneity of infinite thickness (joined half-planes); it will be denoted as the *bimetallic force*.[5] Thus, the remaining terms are the contribution of the inhomogeneity finiteness. Numerical analyses of (9) show that such contribution is always attractive, presenting one negative minimum as a function of σ. On the other hand, the bimetallic force is proportional to σ^{-1} and is repulsive (or zero) for

$$0 \le \alpha \le -\cos 2\theta.$$

It follows that this condition is necessary and sufficient for the existence of an equilibrium position (stable equilibrium). It is worth noting that the *total* force vanishes at the equilibrium distance, meaning that spontaneous dislocation displacements from this position may occur neither by glide nor by climb.

The slipping and adhering-interface forces are now compared. In order to avoid unnecessary complications, only the physically most important situation will be considered, i.e., that of a dislocation with its Burgers vector normal to the lamellar inhomogeneity ($\theta = 90$ deg).

Figure 2 shows the slipping-interface and the adhering-interface force versus the relative hardness Γ, for two dislocation positions and identical Poisson's ratios (numerical analyses for differing Poisson's ratios lead to the same general conclusions). It is seen that distinct zero-points of the slipping-interface curves occur for $\Gamma > 1$, i.e., in this range a dislocation equilibrium position exists for each value of Γ.

On the contrary, all the adhering-interface curves intersect at the point ($\Gamma = 1$, $F = 0$), meaning that, as expected, the force vanishes identically when matrix and lamella are made of the same material. Near an adhering interface the force is attractive for $\Gamma < 1$ (soft lamella), repulsive for $\Gamma > 1$ (hard lamella), and no equilibrium position exists.

Further results are presented in Fig. 3, where the slipping-interface force is plotted against σ for two values of Γ. In the same figure the corresponding curves for adhering interface and for bimetallic interface are shown. It is seen that (i) the intensity of the force, and therefore, the elastic energy stored in the material, is reduced by reducing the inhomogeneity thickness; (ii) relaxation of the interface from adhering to slipping also induces a reduction of the elastic energy; (iii) only the slipping-interface force changes its sign. This means, in particular, that a hard lamella may become a trapping center for dislocations when the adherence of the matrix-lamella interface is lost. In other words, a sort of *debond hardening* of lamellar composites may occur by increasing the temperature beyond a certain point.

[5]Equation (9) shows that for $\theta = 0$, this is the same image force which a traction-free surface would produce.

Acknowledgment

The work reported here was supported by the Ministero della Pubblica Istruzione, Italy.

References

Chou, Y. T., 1966, "Screw Dislocations In and Near Lamellar Inclusions," *Physica Status Solidi*, Vol. 17, pp. 509–516.

Dundurs, J., Fukui, K., and Kukui, T., 1966, "Concentrated Force Near a Smooth Circular Inclusion," ASME JOURNAL OF APPLIED MECHANICS, Vol. 33, pp. 871–876.

Dundurs, J., and Gangadharan, A. C., 1969, "Edge Dislocation Near an Inclusion With a Slipping Interface," *Journal of the Mechanics and Physics of Solids*, Vol. 17, pp. 459–471.

Ghahremani, F., 1980, "Effect of Grain Boundary Sliding on Anelasticity of Polycrystals," *International Journal of Solids & Structures*, Vol. 16, pp. 825–845.

Head, A. K., 1953, "Edge Dislocations in Inhomogeneous Media," *Proceedings of the Physical Society*, Series B, Vol. 66, pp. 793–801.

Muskhelishvili, N. I., 1975, *Some Basic Problems of the Mathematical Theory of Elasticity*, Noordhoff Ltd., Leyden.

Srolovitz, D., Petkovic-Luton, R. A., and Luton, M. J., 1983, "Edge Dislocation—Circular Inclusion Interaction at Elevated Temperatures," *Acta Metallurgica*, Vol. 31, pp. 2151–2159.

Stagni, L., and Lizzio, R., 1987, "Interaction of an Edge Dislocation with a Lamellar Inhomogeneity," *Mechanics of Materials*, Vol. 6, pp. 17–25.

Stagni, L., and Lizzio, R., 1988, "Edge Dislocation Inside a Lamellar Inhomogeneity," *Journal of Applied Physics*, Vol. 64, pp. 1594–1596.

Stagni, L., and Lizzio, R., 1990, "Edge Dislocation in a Lamellar Inhomogeneity with a Slipping Interface," *Journal of Materials Science*, Vol. 25, pp. 1618–1622.

Strain-Hardening Creep Relaxation

P. A. Huneault[6]

Relaxation testing is an important alternative for investigating the creep properties of a material. A solution for the strain-hardening form of the power law is derived and compared to its time-hardening counterpart.

Introduction

This Note relates an explicit analytical expression governing strain-hardening relaxation. Integral forms for relaxation re-

[6]Researcher, Institute for Research in Construction, National Research Council Canada, Ottawa, Ontario K1A 0R6, Canada. Presently at Rousseau, Sauvé, Warren & Associates, Consultants, Montréal, Québec, H2Z 1W7, Canada.

Contributed by the Applied Mechanics Division of THE AMERICAN SOCIETY OF MECHANICAL ENGINEERS. Manuscript received by the ASME Applied Mechanics Division, July 11, 1990; final revision, Nov. 9, 1990.

Copyright © 1992 by ASME
Downloaded 03 May 2010 to 171.66.16.247. Redistribution subject to ASME license or copyright; see http://www.asme.org/terms/Terms_Use.cfm

lated to creep are given in Findley et al. (1976) whereas phenomenological theories are discussed in Rabotnov (1969) and Boyle and Spence (1983). Various experimental aspects of stress relaxation testing are to be found in ASTM (1979).

Relaxation is characterized by a zero total strain-rate $\dot{\epsilon}^{tot}$ over time or

$$\dot{\epsilon}^{tot} = \dot{\epsilon}^{c} + \dot{\epsilon}^{e} = 0 \tag{1}$$

where $\dot{\epsilon}^{c}$ is the creep strain-rate and $\dot{\epsilon}^{e}$ refers to the elastic strain-rate portion

$$\dot{\epsilon}^{e} = \dot{\sigma}/E \tag{2}$$

with E denoting the Young's modulus. Spence and Hult (1973) express the time-hardening relaxation solution for

$$\dot{\epsilon}^{c} = K\sigma^{n} b t^{b-1} \tag{3}$$

,$K > 0$, $n > 1$, $0 < b \leq 1$, in the form

$$\chi(t) = [1 + (n-1)\sigma_o^{n-1} t^*]^{-1/(n-1)} \tag{4}$$

with $\chi(t) = \sigma(t)/\sigma_o$ and t^* denoting the transformed "time" $t^* = EKt^b$ under the boundary condition $(\sigma = \sigma_o)$ @ $(t = 0)$.

The purpose of the following is to define a readily solved analytical expression for the strain-hardening relaxation of a material that creeps according to

$$\dot{\epsilon}^{c} = Q\sigma^{m} (\epsilon^{c})^{p} \tag{5}$$

where, in terms of the parameters given previously, $Q = bK^{1/b} > 0$, $m = n/b > 1$, $p = (b-1)/b \leq 0$. Rabotnov (1969) discusses the relaxation of a strain-hardening law associated with an exponential function of the stress.

Strain-Hardening Relaxation

From Eqs. (1), (2), and (5), strain-hardening relaxation must satisfy

$$Q\sigma^{m} (\epsilon^{c})^{p} + (\dot{\sigma}/E) = 0. \tag{6}$$

Expression (6) is implicit in the stress σ. Noting the Bernouilli differential equation form of Eq. (5), we first obtain for the strain-hardening creep strain ϵ^{c}

$$(\epsilon^{c})^{1-p} = (1-p) \int Q\sigma^{m} dt + C_1 \tag{7}$$

where C_1 is an integration constant. Imposing for virgin specimens the condition $(\epsilon^{c} = 0)$ @ $(t = 0)$, then $(C_1 = 0)$ and

$$\epsilon^{c} = \left[(1-p) \int Q\sigma^{m} dt \right]^{1/(1-p)} \tag{8}$$

which, when combined with Eq. (6), yields

$$\dot{\sigma} + A\sigma^{m} \left[\int \sigma^{m} dt \right]^{B} = 0 \tag{9}$$

with $A = EQ[(1-p)Q]^{B}$, $B = p/(1-p)$.

Expression (9) is the explicit fundamental law for relaxation of a strain-hardening material and may be solved as follows. Denoting $v \equiv \int \sigma^{m} dt$, then $\dot{v} = \sigma^{m}$ and Eq. (9) transforms to

$$\dot{\sigma} = -A\dot{v}v^{B}, \tag{10}$$

the solution of which is

$$\sigma = \frac{-A}{B+1} \left[\int \sigma^{m} dt \right]^{B+1} + C_2 \tag{11}$$

for which, from $(\sigma = \sigma_o)$ @ $(t = o)$, we get $(C_2 = \sigma_0)$. Thereafter

$$\left[\left(\frac{B+1}{A} \right) (\sigma_o - \sigma) \right]^{1/(B+1)} = \int \sigma^{m} dt, \tag{12}$$

and redifferentiating both sides of Eq. (12), with respect to t, and simplifying yields

$$\frac{\dot{\sigma}}{\sigma^{m} (\sigma_o - \sigma)^{p}} = -E^{1-p} Q \tag{13}$$

or

$$\int_{\sigma_o}^{\sigma} \frac{(\sigma_o - \sigma)^{M}}{\sigma^{m}} d\sigma = -E^{1+M} Q \int_0^{t} dt \tag{14}$$

with, $M = -p \geq 0$.

Denoting

$$\emptyset_m^M \equiv \int_{\sigma_o}^{\sigma} \frac{(\sigma_o - \sigma)^{M}}{\sigma^{m}} d\sigma, \tag{15}$$

and recalling the definitions of t^* and constants, Eq. (14) now gives

$$\emptyset_m^M + \frac{(t^*)^{M+1}}{M+1} = 0. \tag{16}$$

Solutions for $\emptyset_m^M$ in Eq. (16) for particular values of M are readily obtained in a recursion form (Gradshteyn and Ryzhik, 1965) and ultimately in an explicit form. A component of the latter can further be reduced to a binominal series in order to finally arrive at the relaxation solution for a strain-hardening material as

$$\left[\sum_{r=0}^{M} \frac{\prod_{k=0}^{M-r} (k-m)}{\prod_{k=0}^{M+1} (k-m)} \sum_{z=0}^{M-r} \frac{(-1)^{2(M-r)-z}}{(M-r-z)!z!} \chi^{1-m+z} \right] + \frac{(t^*)^{M+1}}{(M+1)!\sigma_o^{M+1-m}} - \frac{1}{\prod_{k=1}^{M+1} (k-m)} = 0. \tag{17}$$

Expression (17) is a polynomial of degree $(m-1)$ in $\chi(t) = \sigma(t)/\sigma_o$. The relaxation solution $[\chi(t)]$ is that root bracketed between the values 0 and 1 for particular values of σ_o, t^*, M, and m. The numerical solution of Eq. (17) is straightforward. Newton-Raphson combined with bisection are the methods of choice (Press et al., 1986). The singularity of the root between the values of 0 and 1 and hence of the solution, can easily be verified by further bracketing.

For comparison purposes, the time-hardening relaxation solution, as given in Eq. (4), can be transformed to the notation in Eq. (17) as

$$\chi(t) = \left[1 + \frac{m-(M+1)}{M+1} \sigma_o^{(m-(M+1))/(M+1)} t^* \right]^{(M+1)/(M+1-m)} \tag{18}$$

Equation (17) reduces to Eq. (18) for $(M = -p = 0)$.

Although the relaxation is a function of the initial stress level σ_o as shown in Eqs. (17) and (18), this feature has effectively been subtracted from Figs. (1) and (2) by first isolating from Eq. (18) a value of t^* for a given value of $\chi(t)$ and inserting the same into Eq. (17). Thus, Figs. (1) and (2) are universal curves, independent of σ_o.

Time-hardening and strain-hardening relaxation are equivalent for $(b = 1)$, regardless of the value of n. In Figs. (1) and (2), strain-hardening relaxation is shown to be an altogether slower process. Further, the lower the value of the parameter b, the greater the difference between strain and time-hardening relaxation. The influence of the parameter n in strain-hardening relaxation is more complex: for strain-hardening $\chi(t)$ values greater than about 0.5, the greater the value of n, the slower the process whereas for $\chi(t) < 0.5$, the higher n values lead to an accelerated relaxation.

Figures (1) and (2) imply that:

(i) the time-hardening formulation yields an upper bound to

Downloaded 03 May 2010 to 171.66.16.247. Redistribution subject to ASME license or copyright; see http://www.asme.org/terms/Terms_Use.cfm

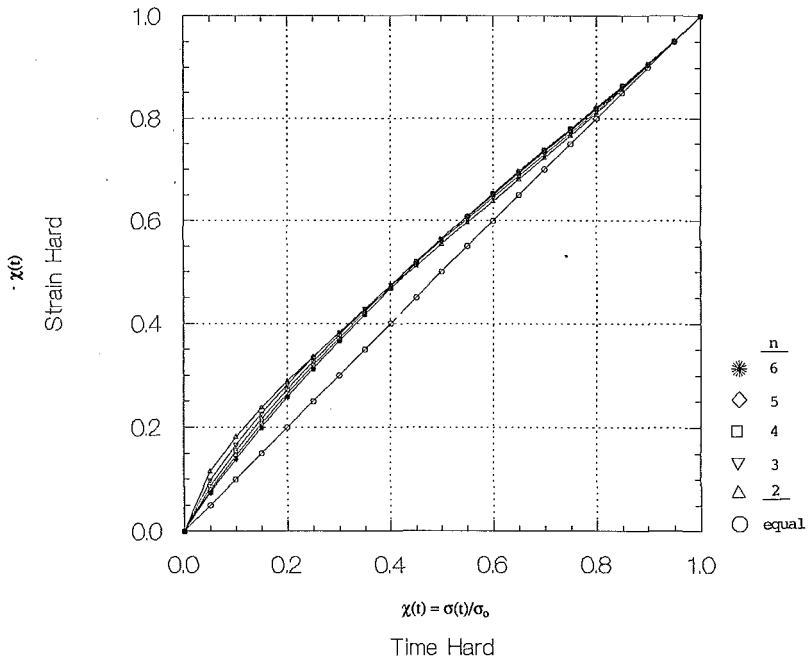

Fig. 1 Time and strain-hardening relaxation, $b = 1/2$

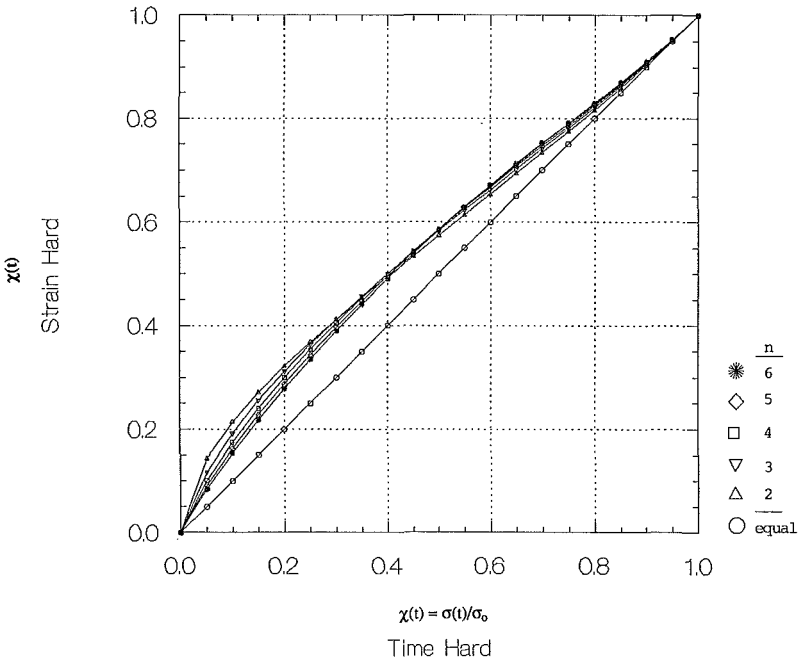

Fig. 2 Time and strain-hardening relaxation, $b = 1/3$

the relaxation process occurring in a strain-hardening material, (ii) relaxation testing has the potential of differentiating between time and strain-hardening creep.

Acknowledgments

The author, formerly research associate, Department of Civil Engineering, Ecole Polytechnique de Montréal, wishes to acknowledge Prof. B. Ladanyi under whom this work was initiated in conjunction with a research grant from the Office of Energy Research Development, Energy, Mines and Resources Canada. The helpful comments from reviewers are also appreciated.

References

ASTM, 1979, *Stress Relaxation Testing* (ASTM STP-676), Alfred Fox, ed., American Society for Testing and Materials.

Boyle, J. T., and Spence, J., 1983, *Stress Analysis for Creep*, Butterworths.

Findley, W. N., Lai, J. S., and Onaran, K., 1976, *Creep and Relaxation of Nonlinear Viscoelastic Materials* (North-Holland Series in Appl. Math. and Mech.), Vol. 18, North-Holland.

Gradshteyn, I. S., and Ryzhik, I. M., 1965, *Tables of Integrals, Series and Products*, 4th ed., Academic Press.

Press, W. H., Flannery, B. P., Teukolsky, S. A., and Wetterling, W. T., 1986, *Numerical Recipes, The Art of Scientific Computing*, Cambridge University Press.

Rabotnov, Y. N., 1969, *Creep Problems in Structural Members* (North-Holland Series in Appl. Math. and Mech.) Vol. 7, North-Holland.

Spence, J., and Hult, J., 1973, "Simple Approximations for Creep Relaxation," *Int. J. Mech. Sci.*, Vol. 15, pp. 741-75.

Downloaded 03 May 2010 to 171.66.16.247. Redistribution subject to ASME license or copyright; see http://www.asme.org/terms/Terms_Use.cfm

A Constitutive Model for Bimodular Materials With an Application to Plate Bending

E. Sacco[7] and J. N. Reddy[8]

1 Introduction

Many engineering materials as well as some biological tissues exhibit different elastic properties when stressed in compression rather than tension, especially fiber-reinforced materials with very soft matrix (e.g., cord-rubber composites). In other words, the Young's modulus is quite different in compression and in tension. Such materials are called bimodular.

Many models have been developed to describe the behavior of bimodular media. The first work on such materials is due to Ambartsumyan (1965), Isabekyan and Khachatryan (1969), and Shapiro (1966) and, more recently, to Jones (1977) and Green and Mkrtichian (1977). In such works the constitutive rule depends on the signs of the principal strains or stresses. Bert (1977) introduced the "macroscopic fiber-governed model," which agrees very closely with experimental data. Here the constitutive relation depends on the sign of the strain in the direction of the fibers.

In this work we present a Green's type approach, i.e., existence of a strain energy density function is insured, to formulate a constitutive law for bimodular materials. We apply the proposed model and the Bert's model to the elastostatic problem for a plate. The finite element formulation with the direct iteration method is given to solve the nonlinear elastostatic problem. Some numerical results are presented as well.

2 Proposed Model

Let us denote, by D, the set of the finite strain tensor obtained as:

$$D=\frac{1}{2}\left(\nabla u+\nabla u^T+\nabla u^T\nabla u\right) \tag{1}$$

where u is the displacement vector. Let us consider the spectral representation of D:

$$D=\lambda_1 e_1\otimes e_1+\lambda_2 e_2\otimes e_2+\lambda_3 e_3\otimes e_3, \tag{2}$$

where λ_1, λ_2, and λ_3 are the finite principal strains, e_1, e_2, and e_3 are the principal directions of D, and the symbol $\otimes$ indicates the diadical product.

Taking into account the signs of λ_i, we can define the tensors D^+ and D^- in the following way:

$$\begin{array}{lll}
1 & \lambda_1\geq\lambda_2\geq\lambda_3\geq 0 & \\
 & D^+=\lambda_1P_1+\lambda_2P_2+\lambda_3P_3=D, & D^-=0\\
2 & \lambda_1\geq\lambda_2\geq 0\geq\lambda_3 & \\
 & D^+=\lambda_1P_1+\lambda_2P_2, & D^-=\lambda_3P_3\\
3 & \lambda_1\geq 0\geq\lambda_2\geq\lambda_3 & \\
 & D^+=\lambda_1P_1, & D^-=\lambda_2P_2+\lambda_3P_3\\
4 & 0\geq\lambda_1\geq\lambda_2\geq\lambda_3 & \\
 & D^+=0, & D^{-1}=\lambda_1P_1+\lambda_2P_2+\lambda_3P_3=D,
\end{array} \tag{3}$$

where $P_i = e_i \otimes e_i$ (no sum on i). It is easy to verify that the tensors D^+ and D^- are positive and negative semidefinite, respectively.

Let us denote by $\mathbf{P}^+$ and $\mathbf{P}^-$ the two operators that define the positive and negative parts of D, respectively:

$$D^+=\mathbf{P}^+D,\quad D^-=\mathbf{P}^-D. \tag{4}$$

The sets of the positive and negative semidefinite finite strain tensors will be denoted as D^+ and D^-:

$$D^+=\{D\epsilon D: D\bullet(n\otimes n)\geq 0 \text{ for any } n\} \tag{5a}$$

$$D^-=\{D\epsilon D: D\bullet(n\otimes n)\leq 0 \text{ for any } n\} \tag{5b}$$

where n denotes the unit vector.

For every $i = 1, 2, 3$, we have:

$$De_i=\lambda_i e_i,$$

and multiplying diadically the first and second member by e_i, we obtain

$$(De_i)\otimes e_i=D(e_i\otimes e_i)=DP_i=\lambda_iP_i \tag{6}$$

and, because of the symmetry of P_i, the relation

$$\lambda_iP_i=\frac{1}{2}\left(DP_i+P_iD\right). \tag{7}$$

Introducing the $\boxtimes$ product in this way:

$$ABC^T=(A\boxtimes C)B$$

where A, B, and C are second-order tensors, and $A \boxtimes C$ is a fourth-order tensor, Eq. (7) can be written as:

$$\lambda_iP_i=\frac{1}{2}\left(I\boxtimes P_i+P_i\boxtimes I\right)D=\mathbf{P}_iD \tag{8}$$

with I being the second-order unit tensor.

The operators defined in (4), related to the cases 1, 2, 3, and 4 in Eq. (3), assume the following form:

$$\begin{array}{lll}
1 & D^+=(\mathbf{P}_1+\mathbf{P}_2+\mathbf{P}_3)D & \mathbf{P}^+=\mathbf{P}_1+\mathbf{P}_2+\mathbf{P}_3\\
 & D^-=0 & \mathbf{P}^-=\mathbf{0}\\
2 & D^+=(\mathbf{P}_1+\mathbf{P}_2)D & \mathbf{P}^+=\mathbf{P}_1+\mathbf{P}_2\\
 & D^-=\mathbf{P}_3D & \mathbf{P}^-=\mathbf{P}_3\\
3 & D^+=\mathbf{P}_1D & \mathbf{P}^+=\mathbf{P}_1\\
 & D^-=(\mathbf{P}_1+\mathbf{P}_2)D & \mathbf{P}^-=\mathbf{P}_1+\mathbf{P}_2\\
4 & D^+=0 & \mathbf{P}^+=\mathbf{0}\\
 & D^-=(\mathbf{P}_1+\mathbf{P}_2+\mathbf{P}_3)D & \mathbf{P}^-=\mathbf{P}_1+\mathbf{P}_2+\mathbf{P}_3.
\end{array} \tag{9}$$

We now consider a bimodular material for which the existence of a strain energy density is ensured; in other words, it is elastic in Green's sense. For such media, we assume that the strain energy density $\sigma(D)$ depends on the positive and the negative parts of the strain tensor in the following form:

$$\sigma(D)=\frac{1}{2}\mathbf{C}^+D^+\bullet D+\frac{1}{2}\mathbf{C}^-D^-\bullet D, \tag{10}$$

where $\mathbf{C}^+$ and $\mathbf{C}^-$ are two fourth-order elasticity tensors. Such strain energy is generally nondifferentiable in the whole D, but we can define its gradient and its one-side gradient, respectively, in the interior and on the boundary of each set defined by Eq. (3). Then it is possible to define the second Piola-Kirchhoff stress tensor S associated with D as:

$$S=\frac{1}{2}\left[\mathbf{C}^+\mathbf{P}^++\mathbf{P}^+\mathbf{C}^++\mathbf{C}^-\mathbf{P}^-+\mathbf{P}^-\mathbf{C}^-\right]D=\mathbf{C}D \tag{11}$$

with

$$\mathbf{C}=\mathrm{Sym}[\mathbf{C}^+\mathbf{P}^++\mathbf{C}^-\mathbf{P}^-]. \tag{12}$$

For the four cases introduced in (9) we have:

$$\begin{array}{ll}
1 & S=\mathbf{C}^+D\\
2 & S=\frac{1}{2}\left[\mathbf{C}^+(\mathbf{P}_1+\mathbf{P}_2)+(\mathbf{P}_1+\mathbf{P}_2)\mathbf{C}^++\mathbf{C}^-\mathbf{P}_3+\mathbf{P}_3\mathbf{C}^-\right]D\\
3 & S=\frac{1}{2}\left[\mathbf{C}^+\mathbf{P}_1+\mathbf{P}_1\mathbf{C}^++\mathbf{C}^-(\mathbf{P}_2+\mathbf{P}_3)+(\mathbf{P}_2+\mathbf{P}_3)\mathbf{C}^-\right]D\\
4 & S=\mathbf{C}^{-1}D.
\end{array} \tag{13}$$

[7]Visiting from the Department of Civil Engineering, University of Rome, Rome, Italy.

[8]Department of Engineering Science and Mechanics, Virginia Polytechnic Institute and State University, Blacksburg, VA 24061. Fellow ASME.

Contributed by the Applied Mechanics Division of The American Society of Mechanical Engineers. Manuscript received by the ASME Applied Mechanics Division, Feb. 5, 1990; final revision, Nov. 30, 1990.

Copyright © 1992 by ASME
Downloaded 03 May 2010 to 171.66.16.247. Redistribution subject to ASME license or copyright; see http://www.asme.org/terms/Terms_Use.cfm

3 Extension of Bert's Model to Finite Elasticity

For fiber composites with very soft matrices (e.g., cord rubber), Bert (1977) introduced the macroscopic fiber-governed model. He assumed the existence of two symmetric tensors $\mathbf{C}^+$ and $\mathbf{C}^-$ so that the second Piola-Kirchhoff stress tensor is obtained by:

$$S=[\alpha\mathbf{C}^+ +(1-\alpha)\mathbf{C}^-]D, \tag{14a}$$

where α is the Heaviside function defined as:

$$\alpha=1 \quad \text{if } D\cdot(n\otimes n)>0$$
$$\alpha=0 \quad \text{if } D\cdot(n\otimes n)\le 0 \tag{14b}$$

and n is the unit vector in fiber direction. Thus, in Bert's model the elasticity constants are set in different ways depending whether the fiber-direction strain is in elongation or shortening. The sets D^+ and D^- are defined analogously to (5), but now in terms of fiber-direction strain.

The symmetry of $\mathbf{C}^+$ and $\mathbf{C}^-$ ensures the existence of a strain energy density, so that this model is also a Green elastic one. It is worth noting that, as in the proposed model, the strain energy is nondifferentiable.

4 Geometrically Linear Theory

When the displacement vector u and its gradient ∇u are small, the finite strain tensor D collapses to the infinitesimal strain tensor E, defined as:

$$E=\frac{1}{2}(\nabla u+\nabla u^T), \tag{15}$$

and the second Piola-Kirchhoff stress tensor S coincides with the Cauchy stress tensor, T. In such a case the set of admissible strain tensors describing a linear space E, and the tensors E^+ and E^-, defined analogously to D^+ and D^-, respectively, represent the projection of E on the closed convex cones $E^+ \subset E$ and $E^- \subset E$ of the positive and negative semidefinite tensors:

$$E^+ : \|E-E^+\| = \min_{F\in E^+} \|E-F\| \tag{16a}$$

$$E^- : \|E-E^-\| = \min_{F\in E^-} \|E-F\|, \tag{16b}$$

where $\|\cdot\|$ denotes the norm in E, such that $E^+ + E^- = E$. The operators $\mathbf{P}^+$ and $\mathbf{P}^-$ are then orthogonal projectors of E on E^+ and E^-, respectively.

The constitutive equation in the proposed model and Bert's model remains formally the same, but now involves linear measures of strain and stress:

(a) proposed model

$$T=\frac{1}{2}[\mathbf{C}^+\mathbf{P}^+ +\mathbf{P}^+\mathbf{C}^+ +\mathbf{C}^-\mathbf{P}^- +\mathbf{P}^-\mathbf{C}^-]E=\mathbf{C}E, \tag{17}$$

(b) Bert's model

$$T=[\alpha\mathbf{C}^+ +(1-\alpha)\mathbf{C}^-]E.$$

The von Karman plate theory is used to analyze laminated bimodular plates. The constitutive relations for a bimodular plate composed of n thin orthotropic layers are:

$$\begin{bmatrix} N_1 & N_{12} \\ N_{12} & N_2 \end{bmatrix} = \mathbf{A}(E^o+K)+\mathbf{B}G,$$
$$\begin{bmatrix} M_1 & M_{12} \\ M_{12} & M_2 \end{bmatrix} = \mathbf{B}(E^o+K)+\mathbf{D}G \tag{18}$$

with $\mathbf{A}$, $\mathbf{B}$, and $\mathbf{D}$ fourth-order tensors with dimensions $2\times 2\times 2\times 2$, defined as:

$$(\mathbf{A},\mathbf{B},\mathbf{D})=\sum_{i=1}^{n}\int_{h_i}\mathbf{C}^{iR}(1,x_3,x_3^2)dx_3, \tag{19}$$

$$D=E+K \tag{20}$$

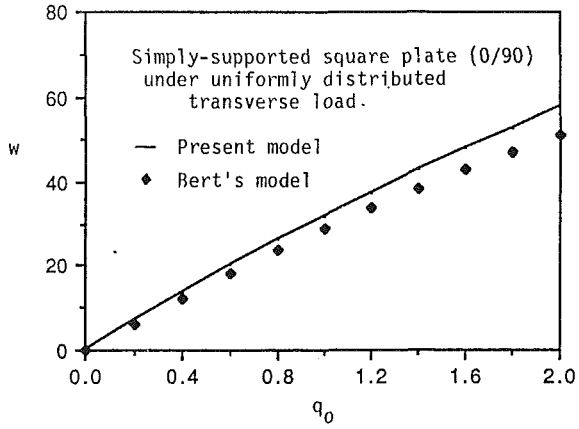

Fig. 1 Center transverse deflection (w) versus intensity (q_o) of uniformly distributed load for two-layer (0/90) plate

where h_i is the thickness of the ith layer of the plate and $\mathbf{C}^{iR}$ the elasticity tensor, previously defined in (11) or (14a) but reduced to dimensions $2\times 2\times 2\times 2$, of the same ith layer, and K is the nonlinear part of the strain tensor.

5 Sample Numerical Results

Numerical results are obtained for a simply-supported square plate made of two layers (0/90), with dimension a, thickness h, and side-to-thickness ratio 100. In all the considered cases, the individual layers are taken to be of equal thickness, and the following material properties are used:

$$E_L^+/E_T^- = 10.0 \quad E_T^+/E_T^- = 1.0 \quad G_{LT}^+/E_T^- = 0.5 \quad \nu_{LT}^+ = 0.25$$
$$E_L^-/E_T^- = 1.0 \quad G_{LT}^-/E_T^- = 0.5 \quad \nu_{LT}^- = 0.25.$$

The finite element method with a 3×3 mesh of nine-node Lagrange quadratic elements was used to obtain the results.

Figure 1 contains a comparison of the center deflection ($w = u_3 a/h^3$) obtained by the present model (solid line) and Bert's model. The load is nondimensionalized as $q_o = qa^3/h^3E_T^-$. The difference between the results obtained using the present model and Bert's model are not negligible.

Acknowledgment

The research reported herein is supported by NATO Science Program (CRG 910001).

References

Ambartsymyan, S. A., 1965, "The Axisymmetric Problem of Circular Cylindrical Shell Made of Materials with Different Stiffness in Tension and in Compression," *Izvestiya Akademiya Nauk SSSR, Mekhanika*, (English translation, NTIS Rept., No. 4, pp. 77–85).

Ambartsymyan, S. A., 1969, "The Basic Equations and Relations of the Different-Modulus Theory of Elasticity of an Anisotropic Body," *Mech. Solids*, Vol. 4, No. 3, pp. 48–56.

Bert, C. W., 1977, "Models for Fibrous Composites with Different Properties in Tension and Compression," *J. Engng. Materials Tech.*, Vol. 99, No. 4, pp. 344–349.

Green, A. E., and Mkrtichian, J. A., 1977, "Elastic Solids with Different Moduli in Tension and Compression," *J. Elasticity*, Vol. 7, No. 4, pp. 369–386.

Isabekyan, N. G., and Khachatryan, A. A., 1969, "On the Multimodulus Theory of Elasticity of Anisotropic Bodies in a Plane Stress State," *Izvestiya Akademiya Nauk SSSR, Mekhanika*, No. 5, pp. 25–34.

Jones, R. M., 1977, "Stress-Strain Relations for Materials with Different Moduli in Tension and Compression," *AIAA J.*, Vol. 15, pp. 16–23.

Reddy, J. N., and Chao, W. C., 1980, "Finite-Element Analysis of Laminated Bimodulus Composite-Material Plates," *Computer & Structures*, Vol. 12, pp. 245–251.

Shapiro, G. S., 1966, "Deformation of Solids with Different Tensile and Compressive Strength," *Mechanics of Solids*, Vol. 1, No. 1, pp. 85–86.

Downloaded 03 May 2010 to 171.66.16.247. Redistribution subject to ASME license or copyright; see http://www.asme.org/terms/Terms_Use.cfm

Elastodynamic Behavior of Relatively Thick, Symmetrically Laminated, Anisotropic Circular Cylindrical Shells

Marco Di Sciuva[9,11] and Erasmo Carrera[10,11]

Introduction

In a previous paper (Di Sciuva, 1987), the first author developed the general linear equations governing the elastodynamic behavior of moderately thick, multilayered anisotropic shells by making use of a displacement field which allows piecewise linear variation of the in-plane displacements u and v, and constant value of the transverse displacement w through the thickness of the laminate (discrete-layer model). The major advantage of the proposed displacement field rests upon the fact that it fulfills *a priori* the static and geometric continuity conditions at the interfaces between the layers and that only five generalized displacements are required to describe the deformation of the laminate, as in first-order shear deformation theories (F.S.D.T.). No numerical results were given. In the present paper the approach developed by Di Sciuva (1987) is applied to the analysis of the elastodynamic behavior of circular cylindrical shells. To avoid geometrical nonlinear effects, that can be present in the unsymmetric laminates even if deflection is in the so-called small deflection range (Sun and Chin, 1988), only symmetric laminates will be considered in the sequel.

Exact solutions for cross-ply lamination schemes are developed. Numerical results show how the various material and geometrical parameters influence the undamped frequencies of cylindrical panels and circular cylindrical shells. To illustrate the accuracy and reliability of the proposed approach, some comparisons with results from the open literature are made.

Governing Equations

Consider a moderately thick, laminated, circular cylindrical shell composed of N generally orthotropic layers, symmetrically located with respect to the midsurface of the shell. The equations of motion can be derived from those given by Di Sciuva (1987). In terms of displacement components these read

$$\sum_{j=1}^{5} L_{ij}U_j = \sum_{j=1}^{5} M_{ij}\ddot{U}_j \qquad i=1,\ 5. \tag{1}$$

For the differential operators L_{ij} the following expressions hold:

$$L_{11}=L_3^A;\ L_{12}=L_4^A;\ L_{13}=-L_1^A/R;\ L_{14}=L_{15}=0;$$
$$L_{22}=L_5^A+L_5^D/R^2;\ L_{23}=(L_4^D/R)_{,x}+(L_5^D/R)_{,y}-L_2^A;$$
$$L_{24}=-(L_4^D+L_4^{Da}+L_5^{Dd})/R;\ L_{25}=-(L_5^D+L_5^{Dd}+L_4^{Dc})/R;$$
$$L_{33}=L_{3,xx}^D+2L_{4,xy}^D+L_{5,yy}^D+A_{22}/R^2$$
$$L_{34}=-[(L_3^D+L_3^{Da}+L_4^{Dd})_{,x}+(L_4^D+L_4^{Da}+L_5^{Dd})_{,y}]$$
$$L_{35}=-[(L_4^D+L_4^{Dd}+L_3^{Dc})_{,x}+(L_5^D+L_5^{Db}+L_4^{Dc})_{,y}]$$
$$L_{44}=L_3^D+2L_3^{Da}+L_3^{Daa}+2L_4^{Dd}+2L_4^{Dad}+L_5^{Ddd}-A_{44}-A_{44}^a-A_{45}^d$$
$$L_{45}=L_4^D+L_3^{Dc}+L_4^{Da}+L_4^{Db}+L_5^{Dd}+L_3^{Dac}+L_4^{Dab}+L_4^{Dcd}+L_5^{Dbd}-A_{45}-A_{45}^a-A_{55}^d$$
$$L_{54}=L_4^D+L_3^{Dc}+L_4^{Da}+L_4^{Db}+L_5^{Dd}+L_3^{Dac}+L_4^{Dab}+L_4^{Dcd}+L_5^{Dbd}-A_{45}-A_{45}^b-A_{44}^c$$
$$L_{55}=L_5^D+2L_4^{Dc}+2L_5^{Db}+L_3^{Dcc}+2L_4^{Dbc}+L_5^{Dbb}-A_{55}-A_{55}^b-A_{45}^c$$

where

$$L_1^\tau=\tau_{12}(\bullet)_{,x}+\tau_{26}(\bullet)_{,y};\ L_3^\tau=\tau_{11}(\bullet)_{,xx}+2\tau_{16}(\bullet)_{,xy}+\tau_{66}(\bullet)_{,yy}$$
$$L_2^\tau=\tau_{26}(\bullet)_{,x}+\tau_{22}(\bullet)_{,y};\ L_5^\tau=\tau_{66}(\bullet)_{,xx}+2\tau_{26}(\bullet)_{,xy}+\tau_{22}(\bullet)_{,yy}$$
$$L_4^\tau=\tau_{16}(\bullet)_{,xx}+(\tau_{12}+\tau_{66})(\bullet)_{,xy}+\tau_{26}(\bullet)_{,yy}$$

and $U_1 = u$; $U_2 = v$; $U_3 = w$; $U_4 = \phi_x$; $U_5 = \phi_y$. Here, u, v, and w denote the displacement components of a point belonging to the shell reference surface; ϕ_x and ϕ_y denote the values of the shear rotations in the (x, z) and (y, z) planes, respectively. R is the curvature radius of the shell reference cylindrical surface; x and y are the orthogonal coordinates on the reference surface (Fig. 1). The symbol $(\bullet)_{,x}$ stands for partial derivative with respect to x; the overdot indicates differentiation with respect to time t.

The differential operators which appear in the expressions for L_{ij} are obtained by replacing τ in L_i with the superscripts which appear in L_{ij}. These superscripts stand for the extensional and bending stiffnesses whose expressions are given below:

$$[A_{ij}\ D_{ij}]=\langle[1\ z^2]Q_{ij}(s)\rangle \text{ for } i,j=1,2,6$$
$$D_{ij}^\delta=\langle zQ_{ij}(s)\delta_k\rangle;\ D_{ij}^\delta=\langle Q_{ij}(s)\delta_k\delta_r\rangle$$
$$A_{ij}=hQ_{ij}(1) \text{ and } A_{ij}^\delta=Q_{ij}(1)\langle\Sigma_k\delta_k\rangle \text{ for } i,j=4,5.$$

In the above definitions, the Q_{ij} are the coefficients of the stiffness matrix of the sth layer; a_k, b_k, c_k, and d_k are known constants depending on the coefficients of the transverse shear stiffness matrix of the constituent layers only (Di Sciuva, 1987). For notational convenience, $\langle..\rangle$ is defined by

$$\langle..\rangle=\sum_{s=1}^{N}\int_{z_{s-1}}^{z_s}(..)dz \text{ and } \Sigma_k \text{ stands for } \sum_{k=1}^{s-1}.$$

For the inertia operators M_{ij}, the following expressions hold

$$M_{11}=M(\bullet);\ M_{12}=M_{13}=M_{14}=M_{15}=0;$$
$$M_{22}=(M+J/R^2)(\bullet);\ M_{23}=(J/R)(\bullet)_{,y};$$
$$M_{24}=-(J^d/R)(\bullet);\ M_{25}=-[(J+J^b)/R](\bullet);$$
$$M_{33}=[-M(\bullet)+J(\bullet)_{,xx}+J(\bullet)_{,yy};$$
$$M_{34}=[-(J+J^a)(\bullet)_{,x}-J^d(\bullet)_{,y}];$$
$$M_{35}=[-J^c(\bullet)_{,x}-(J+J^d)(\bullet)_{,y};$$
$$M_{44}=(J+2J^a+J^{aa}+J^{dd})(\bullet)$$
$$M_{45}=(J^c+J^d+J^{ac}+J^{bd})(\bullet);\ M_{55}=(J+2J^b+J^{bb}+J^{cc})(\bullet)$$

where the following definitions hold:

$$[M\ J]=\langle[1\ z^2]\mu(s)\rangle$$
$$[J^a\ J^b\ J^c\ J^d]=\langle z[A_k\ B_k\ C_k\ D_k]\mu(s)\rangle$$
$$[J^{aa}\ J^{bb}\ J^{cc}\ J^{dd}]=\langle[A_kA_r\ B_kB_r\ C_kC_r\ D_kD_r]\mu(s)\rangle$$

with $(A_k, B_k, C_k, D_k) = \Sigma_k(a_k, b_k, c_k, d_k)(z - z_k)$ and $\mu(s)$ being the material mass density of the sth layer.

Numerical Results and Concluding Remarks

We assume for the spatial variations of the unknown generalized displacements the following expressions:

$$U_i=\sum_{m=1}^{R}\sum_{n=1}^{T}C_{i,mn}F_{i,mn}(x,y) \tag{2}$$

where $C_{i,mn}$ are arbitrary parameters to be determined and $F_{i,mn}$ are a priori chosen functions. The set

$$F_{1,mn}=F_{4,mn}=\cos\alpha_m\sin\beta_n\ F_{2,mn}=F_{5,mn}=\sin\alpha_m\cos\beta_n$$
$$F_{3,mn}=\sin\alpha_m\sin\beta_n\ (\alpha_m=m\pi x/a;\ \beta_n=n\pi y/b)$$

[9]Associate Professor.

[10]Doctoral Research Student.

[11]Department of Aerospace Engineering, Politecnico di Torino, 10129 Turin, Italy.

Contributed by the Applied Mechanics Division of THE AMERICAN SOCIETY OF MECHANICAL ENGINEERS. Manuscript received by the ASME Applied Mechanics Division, Mar. 26, 1990; final revision, July 17, 1990.

Copyright © 1992 by ASME
Downloaded 03 May 2010 to 171.66.16.247. Redistribution subject to ASME license or copyright; see http://www.asme.org/terms/Terms_Use.cfm

Table 1 Comparison of fundamental frequency parameter $\bar{\omega} = \omega a^2(M/E_T h^3)^{1/2}$. Simply-supported cylindrical shells (square panel and complete ring). The HSDT values are from Reddy and Liu (1985). Symmetric cross-ply 0 deg/90 deg/90 deg/0 deg.

R/a	a/h = 10				a/h = 100			
	CLT	FSDT X=5/6	HSDT	ZIG-ZAG	CLT	FSDT X=5/6	HSDT	ZIG-ZAG
square panel m=n=1								
5	15.123	12.265	11.830	11.880	20.396	20.364	20.360	20.356
10	15.107	12.235	11.790	11.847	16.672	16.633	16.630	16.623
20	15.103	12.227	11.780	11.839	15.599	15.555	15.555	15.546
50	15.102	12.225	11.780	11.837	15.284	15.242	15.230	15.231
100	15.101	12.225	11.780	11.837	15.239	15.196	15.190	15.148
Sq.plate	15.101	12.225	11.780	11.837	15.227	15.184	15.170	15.140
complete ring m=1, n in apexes								
5	13.704^{14}	10.958^{14}		10.462^{14}	20.035^{36}	20.000^{36}		19.990^{36}
10	13.499^{18}	10.698^{22}		10.187^{22}	16.544^{56}	16.506^{56}		16.496^{56}
20	13.401^{24}	10.579^{28}		10.063^{28}	14.827^{86}	14.787^{86}		14.776^{86}
50	13.345^{10}	10.496^{16}		9.996^{16}	13.881^{70}	13.840^{70}		13.827^{70}
100	13.336^{4}	10.496^{4}		9.971^{4}	13.600^{200}	13.559^{200}		13.547^{200}
Strip	13.326	10.490		9.971	13.380	13.338		13.326

Table 2 Comparison of fundamental (m = 1) frequency parameter $\bar{\omega} = \omega R^2(M/E_T h^3)^{1/2}$. Simply-supported cylindrical shells. Symmetric cross-ply 0 deg/90 deg/0 deg. * strip; ** beam theory.

a/R	R/h=100			R/h=50			R/h=20		
	CLT	FSDT X=1	ZIG-ZAG	CLT	FSDT X=1	ZIG-ZAG	CLT	FSDT X=1	ZIG-ZAG
0.10	1409.90	1160.00	1075.00	1120.50	815.53	715.25	448.31	384.29	352.93
	1395.00*	1142.00*	1056.00*	1111.70*	808.85*	707.14*	444.69*	382.69*	349.23*
0.25	248.06	240.75	236.20	233.17	205.48	194.86	220.01	132.46	116.98
	223.90*	215.59*	211.53*	223.53*	194.92*	183.81*	177.87*	129.42*	113.94*
0.5	83.45	82.96	82.74	70.07	68.04	67.15	59.24	50.02	46.96
1	38.72	38.69	38.68	27.31	27.18	27.14	18.82	18.15	17.87
2.5	17.52	17.51	17.51	11.49	11.48	11.48	6.55	6.53	6.52
5	9.37	9.37	9.37	6.28	6.28	6.28	3.70	3.70	3.70
10	4.76	4.76	4.76	3.53	3.53	3.53	1.73	1.73	1.73
25	1.74	1.74	1.74	1.27	1.27	1.27	0.74	0.74	0.74
50	1.08	1.08	1.08	0.54	0.54	0.54	0.22	0.22	0.22
	1.18**	1.18**	1.18**	0.59**	0.59**	0.59**	0.24**	0.24**	0.24**
100	0.28	0.28	0.28	0.14	0.14	0.14	0.06	0.06	0.06
	0.30**	0.30**	0.30**	0.15**	0.15**	0.15**	0.06**	0.06**	0.06**

(m and n are the half-waves number in the axial and circumferential direction, respectively) leads to an exact solution for symmetric cross-ply laminates with the following simple-support boundary conditions (hinged edges, free in the in-plane normal direction)

$$x=0,a: \quad N_{xx}=M_{xx}=U_2=U_3=U_5=0$$
$$y=0,b: \quad N_{yy}=M_{yy}=U_1=U_3=U_5=0.$$

Upon substitution of Eq. (2) into Eqs. (1), the required system of linear algebraic equations is obtained. Assuming a time dependence of harmonic type with frequency ω, Eqs. (1) give rise to a classical eigenvalue problem.

To illustrate the accuracy and reliability of the proposed approach, we present exact solutions for cross-ply circular cylindrical shells and compare these with other numerical results from the literature.

The numerical results refer to the following lamina mechanical properties:

$$E_L/E_T=25;\ G_{LT}/E_T=.5;\ G_{TT}/E_T=.2;\ \nu_{LT}=\nu_{TT}=.25;\ \mu=1$$

where E_L and E_T are major and minor Young's moduli in the principal material directions (L, T); ν_{LT} and ν_{TT} are Poisson's ratios, G_{LT} and G_{TT} are the shear moduli.

For purposes of comparison, Table 1 gives some numerical results from ESDT (X is the shear correction factor) and HSDT (third-order shear deformation theory, Reddy and Liu, 1985). In the tables and the figure we will denote present theory as zig zag. Simply-supported circular cylindrical shells (square panel and complete ring) are considered. Notice that the proposed model gives results very close to those obtained by Reddy and Liu, irrespective of the values of the radius-to-length ratio R/a and of the length-to-thickness ratio a/h.

It is very interesting to note that for a complete ring, the CLT fails to predict the fundamental mode. In effect, at low values of a/h and intermediate values of R/a ratios, the fundamental mode predicted by CLT has a number of circumferential half-waves n lower than those predicted by FSDT and by the present study. The limiting values for a square panel and for a complete ring are those relative to the square plate and to strip of infinite length, respectively. Further, the values of the fundamental frequency parameter for a square plate of side length a and for a strip are approached in a different manner for increasing values of R/a, depending on the values of a/h. In particular, moderately thick, symmetrically laminated shells (in the numerical example, a/h = 10) are less sensitive to R/a variations than thin shells (in the numerical example, a/h = 100).

Downloaded 03 May 2010 to 171.66.16.247. Redistribution subject to ASME license or copyright; see http://www.asme.org/terms/Terms_Use.cfm

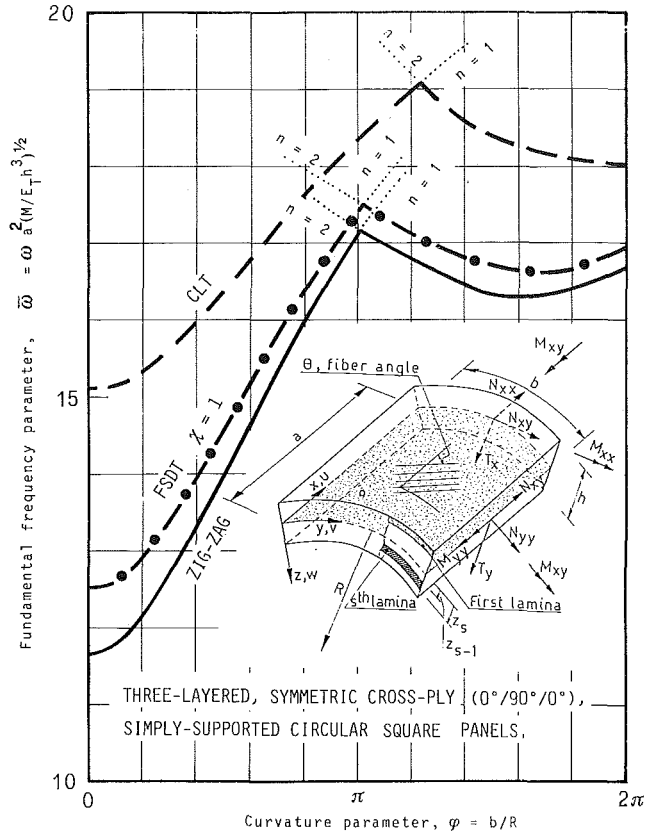

Fig. 1 Influence of the curvature parameter φ on the fundamental frequency parameter; $R/h = 10$, $m = 1$

Table 2 gives the comparison with the results from the CLT and FSDT theories for three different values of the shell radius-to-thickness ratio a/h. The starred and double-starred values are those of the fundamental frequency parameter as given by the strip of infinite length and beam solutions, respectively, for the same value of the ratio a/h. Some remarks should be made about the results given in this table. As before, for the same value of the ratios a/R and R/h, the fundamental mode predicted by the three theories, is not always for the same value of n. Moreover, for decreasing values of R/h, the strip and beam solutions are closer to the corresponding shell solution.

The influence of the curvature is shown in Fig. 1 for three-layered, symmetric cross-ply (0 deg/90 deg/0 deg), simply-supported circular cylindrical square panels. As expected, the results indicate that an increase in the curvature produces an increase in the frequency parameter, thereby countering the effects of the transverse shear deformability terms which tend to reduce the frequency parameter. Notice that the values of the curvature parameter ϕ are obtained by changing R for a fixed value of b. Then, $\phi = 0$ ($R \to \infty$) corresponds to the flat square plate, while $\phi = 2\pi$ corresponds to the circular cylindrical shells.

References

Di Sciuva, M., 1987, "An Improved Shear-Deformation Theory for Moderately Thick Multilayered Shells and Plates," ASME JOURNAL OF APPLIED MECHANICS, Vol. 54, pp. 589–596.

Reddy, J. N., and Liu, C. F., 1985, "A Higher-Order Shear Deformation Theory of Laminated Elastic Shells," *Int. J. Engng. Sci.*, Vol. 23, No. 3, pp. 319–330.

Sun, C. T., and Chin, H., 1988, "On Large Deflection Effects in Unsymmetric Cross-Ply Composite Laminates," *J. Comp. Mat.*, Vol. 22, pp. 1045–1059.

Circumferential Stresses in Curved Beams

Robert D. Cook[12]

We consider circumferential stress σ_θ in the curved beam of Fig. 1. From mechanics of materials approximations, the accepted formula for σ_θ at arbitrary θ, obtained by superposing bending stress and direct stress, is

$$\sigma_\theta = \frac{M(r_n - r)}{Aer} + \frac{N}{A} \tag{1}$$

where A is the area of the cross-section, r_n locates the neutral axis of pure bending, and

$$e = R - r_n \qquad R = \frac{1}{A}\int r\, dA \qquad \frac{1}{r_n} = \frac{1}{A}\int \frac{dA}{r}. \tag{2}$$

The centroid of A is at $r = R$. In Eq. (1), $M = M_o + PR\sin\theta$ and $N = P\sin\theta$. The term that contains M in Eq. (1) is rationally derived from the assumptions that stress σ_θ is uniaxial and that plane cross-sections remain plane under bending. The appended N/A term has almost no rationale: Its form is familiar and it satisfies statics, but it is intended for use with straight bars. If $N = 0$, Eq. (1) is in excellent agreement with exact results from theory of elasticity for rectangular cross-sections (Cook and Young, 1985; Timoshenko and Goodier, 1970). For example, at $r = b$ and with $N = 0$, σ_θ from Eq. (1) is 0.3 percent high for $a/b = 4$ and 5.0 percent high for $a/b = 8$. However, if $N \neq 0$, errors are of greater magnitude, and σ_θ is underestimated rather than overestimated. The offending term, N/A in Eq. (1), should therefore be replaced by a more accurate approximation if its form is simple enough for easy use. Such alternatives for N/A are the subject of the present Note.

Consider a case of tension without bending: In Fig. 1, let $M_0 = -PR$, and examine the cross-section at $\theta = \pi/2$. Exact theory (Timoshenko and Goodier, 1970) and finite element solutions show that strain ϵ_θ on the inner portion of this cross-section varies approximately as c/r, where c is a constant. If it is also assumed that stress σ_θ is uniaxial, as is customary, then $\sigma_\theta = E\epsilon_\theta$, and

$$N = \int \sigma_\theta dA = \int \frac{Ec}{r}\, dA = Ec\frac{A}{r_n}. \tag{3}$$

Hence, $c = Nr_n/AE$. The direct stress term becomes Nr_n/Ar, and Eq. (1) is replaced by

$$\sigma_\theta = \frac{M(r_n - r)}{Aer} + \frac{Nr_n}{Ar}. \tag{4}$$

Unfortunately Eq. (4) places the centroid of the direct stress distribution at $r = r_n$ rather than at $r = R$, and moment equilibrium is not satisfied. A remedy for this inconsistency is to augment the direct stress by a term that varies linearly with distance from the centroid. Thus, the direct stress becomes $[(r_n/r) + \alpha(r - R)]N/A$, where constant α can be determined by equilibrium of moments about point Q in Fig. 1(b) with $\theta = \pi/2$.

$$\int \sigma_\theta (r - R)dA + M_o + PR = 0. \tag{5}$$

Hence, with $I_G = \int (R - r)^2 dA$ the centroidal moment of inertia of A, we obtain $\alpha = Ae/I_G$, and Eq. (4) is replaced by

[12]Department of Engineering Mechanics, University of Wisconsin-Madison, Madison, WI 53706. Mem. ASME.

Contributed by the Applied Mechanics Division of THE AMERICAN SOCIETY OF MECHANICAL ENGINEERS. Manuscript received by the ASME Applied Mechanics Division, May 25, 1990; final revision, Mar. 15, 1991.

Downloaded 03 May 2010 to 171.66.16.247. Redistribution subject to ASME license or copyright; see http://www.asme.org/terms/Terms_Use.cfm

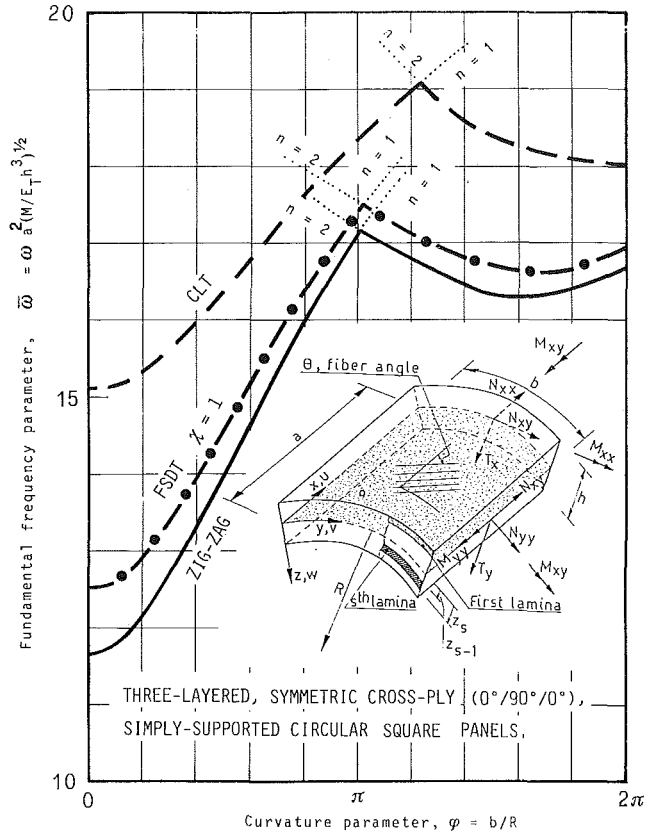

Fig. 1 Influence of the curvature parameter φ on the fundamental frequency parameter; $R/h = 10$, $m = 1$

Table 2 gives the comparison with the results from the CLT and FSDT theories for three different values of the shell radius-to-thickness ratio a/h. The starred and double-starred values are those of the fundamental frequency parameter as given by the strip of infinite length and beam solutions, respectively, for the same value of the ratio a/h. Some remarks should be made about the results given in this table. As before, for the same value of the ratios a/R and R/h, the fundamental mode predicted by the three theories, is not always for the same value of n. Moreover, for decreasing values of R/h, the strip and beam solutions are closer to the corresponding shell solution.

The influence of the curvature is shown in Fig. 1 for three-layered, symmetric cross-ply (0 deg/90 deg/0 deg), simply-supported circular cylindrical square panels. As expected, the results indicate that an increase in the curvature produces an increase in the frequency parameter, thereby countering the effects of the transverse shear deformability terms which tend to reduce the frequency parameter. Notice that the values of the curvature parameter ϕ are obtained by changing R for a fixed value of b. Then, $\phi = 0$ ($R \to \infty$) corresponds to the flat square plate, while $\phi = 2\pi$ corresponds to the circular cylindrical shells.

References

Di Sciuva, M., 1987, "An Improved Shear-Deformation Theory for Moderately Thick Multilayered Shells and Plates," ASME JOURNAL OF APPLIED MECHANICS, Vol. 54, pp. 589–596.

Reddy, J. N., and Liu, C. F., 1985, "A Higher-Order Shear Deformation Theory of Laminated Elastic Shells," *Int. J. Engng. Sci.*, Vol. 23, No. 3, pp. 319–330.

Sun, C. T., and Chin, H., 1988, "On Large Deflection Effects in Unsymmetric Cross-Ply Composite Laminates," *J. Comp. Mat.*, Vol. 22, pp. 1045–1059.

Circumferential Stresses in Curved Beams

Robert D. Cook[12]

We consider circumferential stress σ_θ in the curved beam of Fig. 1. From mechanics of materials approximations, the accepted formula for σ_θ at arbitrary θ, obtained by superposing bending stress and direct stress, is

$$\sigma_\theta = \frac{M(r_n - r)}{Aer} + \frac{N}{A} \tag{1}$$

where A is the area of the cross-section, r_n locates the neutral axis of pure bending, and

$$e = R - r_n \qquad R = \frac{1}{A}\int r\, dA \qquad \frac{1}{r_n} = \frac{1}{A}\int \frac{dA}{r}. \tag{2}$$

The centroid of A is at $r = R$. In Eq. (1), $M = M_o + PR\sin\theta$ and $N = P\sin\theta$. The term that contains M in Eq. (1) is rationally derived from the assumptions that stress σ_θ is uniaxial and that plane cross-sections remain plane under bending. The appended N/A term has almost no rationale: Its form is familiar and it satisfies statics, but it is intended for use with straight bars. If $N = 0$, Eq. (1) is in excellent agreement with exact results from theory of elasticity for rectangular cross-sections (Cook and Young, 1985; Timoshenko and Goodier, 1970). For example, at $r = b$ and with $N = 0$, σ_θ from Eq. (1) is 0.3 percent high for $a/b = 4$ and 5.0 percent high for $a/b = 8$. However, if $N \neq 0$, errors are of greater magnitude, and σ_θ is underestimated rather than overestimated. The offending term, N/A in Eq. (1), should therefore be replaced by a more accurate approximation if its form is simple enough for easy use. Such alternatives for N/A are the subject of the present Note.

Consider a case of tension without bending: In Fig. 1, let $M_0 = -PR$, and examine the cross-section at $\theta = \pi/2$. Exact theory (Timoshenko and Goodier, 1970) and finite element solutions show that strain ϵ_θ on the inner portion of this cross-section varies approximately as c/r, where c is a constant. If it is also assumed that stress σ_θ is uniaxial, as is customary, then $\sigma_\theta = E\epsilon_\theta$, and

$$N = \int \sigma_\theta dA = \int \frac{Ec}{r}\, dA = Ec\frac{A}{r_n}. \tag{3}$$

Hence, $c = Nr_n/AE$. The direct stress term becomes Nr_n/Ar, and Eq. (1) is replaced by

$$\sigma_\theta = \frac{M(r_n - r)}{Aer} + \frac{Nr_n}{Ar}. \tag{4}$$

Unfortunately Eq. (4) places the centroid of the direct stress distribution at $r = r_n$ rather than at $r = R$, and moment equilibrium is not satisfied. A remedy for this inconsistency is to augment the direct stress by a term that varies linearly with distance from the centroid. Thus, the direct stress becomes $[(r_n/r) + \alpha(r - R)]N/A$, where constant α can be determined by equilibrium of moments about point Q in Fig. 1(b) with $\theta = \pi/2$.

$$\int \sigma_\theta (r - R)dA + M_o + PR = 0. \tag{5}$$

Hence, with $I_G = \int (R - r)^2 dA$ the centroidal moment of inertia of A, we obtain $\alpha = Ae/I_G$, and Eq. (4) is replaced by

[12]Department of Engineering Mechanics, University of Wisconsin-Madison, Madison, WI 53706. Mem. ASME.

Contributed by the Applied Mechanics Division of THE AMERICAN SOCIETY OF MECHANICAL ENGINEERS. Manuscript received by the ASME Applied Mechanics Division, May 25, 1990; final revision, Mar. 15, 1991.

Copyright © 1992 by ASME
Downloaded 03 May 2010 to 171.66.16.247. Redistribution subject to ASME license or copyright; see http://www.asme.org/terms/Terms_Use.cfm

Table 1 Stress σ_θ on plane $\theta = \pi/2$ of Fig. 1. The cross-section is rectangular. Results are presented as the ratio to σ_θ from theory of elasticity (Timoshenko and Goodier, 1970).

Geometry a/b	At inside, r = b Bending + tension (P > 0, M_o = 0)				At inside, r = b Tension only (P > 0, M_o = -PR)				At outside, r = a Bending + tension (P > 0, M_o = 0)			
	Eq. 1	Eq. 4	Eq. 6	Eq. 7	Eq. 1	Eq. 4	Eq. 6	Eq. 7	Eq. 1	Eq. 4	Eq. 6	Eq. 7
1.2	0.998	1.001	0.999	0.999	0.959	1.052	0.965	0.965	0.998	1.001	0.998	0.998
2.0	0.977	1.011	0.985	0.986	0.800	1.154	0.879	0.888	0.977	1.020	0.967	0.969
4.0	0.920	1.031	0.967	0.973	0.535	1.157	0.798	0.836	0.920	1.094	0.839	0.866
8.0	0.850	1.044	0.964	0.980	0.305	1.027	0.731	0.790	0.850	1.229	0.593	0.720
16.0	0.785	1.049	0.975	0.996	0.158	0.855	0.660	0.716	0.785	1.419	0.236	0.574

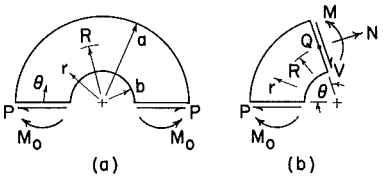

Fig. 1 A curved beam, showing (*a*) force and moment loads on a half-circle bar, and (*b*) internal forces and moment

$$\sigma_\theta = \frac{M(r_n - r)}{Aer} + \frac{N}{A}\left[\frac{r_n}{r} + \frac{Ae}{I_G}(r - R)\right]. \quad (6)$$

Finally, one may introduce an approximation best suited to slender curved beams, namely $e = I_G/RA$ (Cook and Young, 1985). Thus, Eq. (6) becomes

$$\sigma_\theta = \frac{M(r_n - r)}{Aer} + \frac{N}{A}\left[\frac{r_n}{r} + \frac{r}{R} - 1\right]. \quad (7)$$

Equations (1), (4), (6), and (7) are compared by calculating σ_θ on the plane $\theta = \pi/2$ in Fig. 1. Two loadings are considered: shear loading on the ring ($M_o = 0$) and momentless tension on the analysis plane ($M_o = -PR$). The cross-section is rectangular and of unit thickness. Results are reported in Table 1 as the ratio of σ_θ from curved beam formulas to σ_θ from theory of elasticity (Timoshenko and Goodier, 1970). For both types of loading in Table 1, the magnitude of σ_θ is much greater at $r = b$ than at $r = a$. For example, with $a/b = 4$, $\sigma_{\theta b}/\sigma_{\theta a} = -4.0$ for the bending plus tension loading and $\sigma_{\theta b}/\sigma_{\theta a} = 1.9$ for the tension only loading. Clearly, it is almost important that the stress formula be accurate at the inner radius $r = b$. At $r = b$, Table 1 shows that the proposed formulas are considerably more accurate than N/A.

Of the foregoing equations for σ_θ, Eq. (6) is least burdened by approximation and inconsistency. Nevertheless, the writer prefers Eq. (4) for its combination of simplicity and accuracy at $r = b$, where σ_θ has its greatest magnitude. It should be noted that quite accurate formulas for radial stress σ_r and shear stress $\tau_{r\theta}$ are also available (Young and Cook, 1989; Wang, 1967).

References

Cook, R. D., and Young, W. C., 1985, *Advanced Mechanics of Materials*, Macmillian, New York.

Timoshenko, S. P., and Goodier, J. N., 1970, *Theory of Elasticity*, 3rd ed., McGraw-Hill, New York.

Young, W. C., and Cook, R. D., 1989, "Radial Stress Formula for Curved Beams," *ASME Journal of Vibration, Acoustics, Stress, and Reliability in Design*, Vol. 111, pp. 491-492.

Wang, T. S., 1967, "Shear Stresses in Curved Beams," *Machine Design*, Vol. 39, pp. 175-178.

On General Conditions of Rotordynamic Stability Under Combined Axial Forces and Torque

Sunil K. Sinha[13]

1 Introduction

In the author's previous paper (Sinha, 1989) on the related topic, the parametric instability of the viscoelastic rotor-disk system under dynamic axial loads was analyzed. Another important form of dynamic instability in flexible rotors called "whirling instability" is caused by the presence of tangential torque (Cohen and Porat, 1984; Yim, Noah, and Vance, 1986) and hysteretic damping in the system (Ehrich, 1964; Genin and Maybee, 1970; Pedersen, 1973; Vance and Lee, 1974; Crandall, 1980; Bucciarelli, 1982; Hendricks, 1986; Zhang and Ling, 1986; Ota and Mizutani, 1987). Similar to the rotor instability caused by the presence of the well-known "Alford Forces" (Alford, 1965; Vance and Laudadio, 1984) due to varying tip clearance in a turbomachinery, the tangential torque and hysteretic damping in a rotating system introduce the cross-coupled skew-symmetric stiffness terms in the plane of the rotation. In the present technical Note, the global stability of a simply-supported multidisk rotor system under the combined effects of tangential torque, axial forces, and internal structural damping (Plaut, 1977) is considered. In this analysis, we assume that both the tangential torque and axial forces are fully dynamic in nature with a periodic sinusoidal component superimposed on a constant value. In the conclusion, sample numerical results of parametric resonance and whirling instability are presented for some typical cases.

2 Governing Equations

Mathematical derivations are recalled here briefly for clarity and keeping this Note self-contained, but for more detailed background of this topic, the reader should refer to the author's previous work (Sinha, 1989). Similar to the assumptions in that paper, the disks on the shaft are considered relatively thin and rigid with respect to the shaft. The shaft is of uniform circular cross-section with the outer and inner radii as "R" and "r", respectively. There are in all "n" number of disks with the jth disk of mass M_j and diametral mass moment of intertia J_j, mounted on the shaft at discrete locations $z_j (j = 1,$

[13]G. E. Aircraft Engines, General Electric Company, Cincinnati, OH 45215. Mem. ASME.

Contributed by the Applied Mechanics Division of THE AMERICAN SOCIETY OF MECHANICAL ENGINEERS. Manuscript received by the ASME Applied Mechanics Division, June 4, 1990; final revision, Mar. 15, 1991.

Downloaded 03 May 2010 to 171.66.16.247. Redistribution subject to ASME license or copyright; see http://www.asme.org/terms/Terms_Use.cfm

Table 1 Stress σ_θ on plane $\theta = \pi/2$ of Fig. 1. The cross-section is rectangular. Results are presented as the ratio to σ_θ from theory of elasticity (Timoshenko and Goodier, 1970).

Geometry a/b	At inside, r = b Bending + tension (P > 0, M_o = 0)				At inside, r = b Tension only (P > 0, M_o = -PR)				At outside, r = a Bending + tension (P > 0, M_o = 0)			
	Eq. 1	Eq. 4	Eq. 6	Eq. 7	Eq. 1	Eq. 4	Eq. 6	Eq. 7	Eq. 1	Eq. 4	Eq. 6	Eq. 7
1.2	0.998	1.001	0.999	0.999	0.959	1.052	0.965	0.965	0.998	1.001	0.998	0.998
2.0	0.977	1.011	0.985	0.986	0.800	1.154	0.879	0.888	0.977	1.020	0.967	0.969
4.0	0.920	1.031	0.967	0.973	0.535	1.157	0.798	0.836	0.920	1.094	0.839	0.866
8.0	0.850	1.044	0.964	0.980	0.305	1.027	0.731	0.790	0.850	1.229	0.593	0.720
16.0	0.785	1.049	0.975	0.996	0.158	0.855	0.660	0.716	0.785	1.419	0.236	0.574

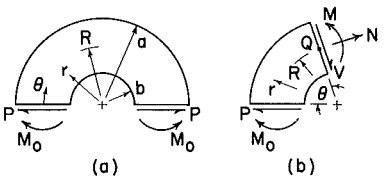

Fig. 1 A curved beam, showing (*a*) force and moment loads on a half-circle bar, and (*b*) internal forces and moment

$$\sigma_\theta = \frac{M(r_n - r)}{Aer} + \frac{N}{A}\left[\frac{r_n}{r} + \frac{Ae}{I_G}(r - R)\right]. \quad (6)$$

Finally, one may introduce an approximation best suited to slender curved beams, namely $e = I_G/RA$ (Cook and Young, 1985). Thus, Eq. (6) becomes

$$\sigma_\theta = \frac{M(r_n - r)}{Aer} + \frac{N}{A}\left[\frac{r_n}{r} + \frac{r}{R} - 1\right]. \quad (7)$$

Equations (1), (4), (6), and (7) are compared by calculating σ_θ on the plane $\theta = \pi/2$ in Fig. 1. Two loadings are considered: shear loading on the ring ($M_o = 0$) and momentless tension on the analysis plane ($M_o = -PR$). The cross-section is rectangular and of unit thickness. Results are reported in Table 1 as the ratio of σ_θ from curved beam formulas to σ_θ from theory of elasticity (Timoshenko and Goodier, 1970). For both types of loading in Table 1, the magnitude of σ_θ is much greater at $r = b$ than at $r = a$. For example, with $a/b = 4$, $\sigma_{\theta b}/\sigma_{\theta a} = -4.0$ for the bending plus tension loading and $\sigma_{\theta b}/\sigma_{\theta a} = 1.9$ for the tension only loading. Clearly, it is almost important that the stress formula be accurate at the inner radius $r = b$. At $r = b$, Table 1 shows that the proposed formulas are considerably more accurate than N/A.

Of the foregoing equations for σ_θ, Eq. (6) is least burdened by approximation and inconsistency. Nevertheless, the writer prefers Eq. (4) for its combination of simplicity and accuracy at $r = b$, where σ_θ has its greatest magnitude. It should be noted that quite accurate formulas for radial stress σ_r and shear stress $\tau_{r\theta}$ are also available (Young and Cook, 1989; Wang, 1967).

References

Cook, R. D., and Young, W. C., 1985, *Advanced Mechanics of Materials*, Macmillian, New York.

Timoshenko, S. P., and Goodier, J. N., 1970, *Theory of Elasticity*, 3rd ed., McGraw-Hill, New York.

Young, W. C., and Cook, R. D., 1989, "Radial Stress Formula for Curved Beams," *ASME Journal of Vibration, Acoustics, Stress, and Reliability in Design*, Vol. 111, pp. 491-492.

Wang, T. S., 1967, "Shear Stresses in Curved Beams," *Machine Design*, Vol. 39, pp. 175-178.

On General Conditions of Rotordynamic Stability Under Combined Axial Forces and Torque

Sunil K. Sinha[13]

1 Introduction

In the author's previous paper (Sinha, 1989) on the related topic, the parametric instability of the viscoelastic rotor-disk system under dynamic axial loads was analyzed. Another important form of dynamic instability in flexible rotors called "whirling instability" is caused by the presence of tangential torque (Cohen and Porat, 1984; Yim, Noah, and Vance, 1986) and hysteretic damping in the system (Ehrich, 1964; Genin and Maybee, 1970; Pedersen, 1973; Vance and Lee, 1974; Crandall, 1980; Bucciarelli, 1982; Hendricks, 1986; Zhang and Ling, 1986; Ota and Mizutani, 1987). Similar to the rotor instability caused by the presence of the well-known "Alford Forces" (Alford, 1965; Vance and Laudadio, 1984) due to varying tip clearance in a turbomachinery, the tangential torque and hysteretic damping in a rotating system introduce the cross-coupled skew-symmetric stiffness terms in the plane of the rotation. In the present technical Note, the global stability of a simply-supported multidisk rotor system under the combined effects of tangential torque, axial forces, and internal structural damping (Plaut, 1977) is considered. In this analysis, we assume that both the tangential torque and axial forces are fully dynamic in nature with a periodic sinusoidal component superimposed on a constant value. In the conclusion, sample numerical results of parametric resonance and whirling instability are presented for some typical cases.

2 Governing Equations

Mathematical derivations are recalled here briefly for clarity and keeping this Note self-contained, but for more detailed background of this topic, the reader should refer to the author's previous work (Sinha, 1989). Similar to the assumptions in that paper, the disks on the shaft are considered relatively thin and rigid with respect to the shaft. The shaft is of uniform circular cross-section with the outer and inner radii as "R" and "r", respectively. There are in all "n" number of disks with the jth disk of mass M_j and diametral mass moment of intertia J_j, mounted on the shaft at discrete locations $z_j (j = 1,$

[13]G. E. Aircraft Engines, General Electric Company, Cincinnati, OH 45215. Mem. ASME.

Contributed by the Applied Mechanics Division of THE AMERICAN SOCIETY OF MECHANICAL ENGINEERS. Manuscript received by the ASME Applied Mechanics Division, June 4, 1990; final revision, Mar. 15, 1991.

Copyright © 1992 by ASME
Downloaded 03 May 2010 to 171.66.16.247. Redistribution subject to ASME license or copyright; see http://www.asme.org/terms/Terms_Use.cfm

2. . .$n-1$, n), which are handled by a Dirac's delta impulse function $\delta(z-z_j) = 0$ for $z \neq z_j$ and, $\int_o^l \delta(z-z_j)dz = 1$.

The corresponding equations of motion in the x–y plane referred to the fixed frame of reference for the lateral deflection (u, v) of this rotor $(0 \le z \le l)$, under combined axial loads P_o and P_t and tangential torques T_o and T_t are written as

$$\mathcal{L}_1(u,v) = \left[EI + 2\zeta H \frac{\partial}{\partial t}\right] u_{,zzzz} + \rho_{eq}A\, u_{,tt} - I_d u_{,zztt} - I_p\Omega_o v_{,zzt} + 2\zeta H\Omega_o v_{,zzzz} + (T_o + T_t\cos\Omega t)v_{,zzz} - (P_o + P_t\cos\Omega t)u_{,zz} = 0 \quad (1)$$

and

$$\mathcal{L}_2(u,v) = \left[EI + 2\zeta H \frac{\partial}{\partial t}\right] v_{,zzzz} + \rho_{eq}A\, v_{,tt} - I_d v_{,zztt} + I_p\Omega_o u_{,zzt} - 2\zeta H\Omega_o u_{,zzzz} - (T_o + T_t\cos\Omega t)u_{,zzz} - (P_o + P_t\cos\Omega t)v_{,zz} = 0 \quad (2)$$

where

- EI = flexural rigidity of the rotor,
- P_o, P_t = constant and periodic axial force components (The sign for steady-state axial load P_o is positive in tension and negative in compression.);
- T_o, T_t = constant and periodic tangential torque components (The sign of steady-state torque T_o is positive for a driving torque and is negative for a load torque, e.g., T_o is positive in a turbine and is negative in a compressor.)
- $\rho_{eq}A$ = equiv. mass per unit length of the shaft = $\rho A + \sum_{j=1}^{n} M_j\delta(z-z_j)$
- I_d = equiv. shaft diametral mass moment of inertia (per unit length) = $\frac{\rho A(R^2+r^2)}{4} + \sum_{j=1}^{n} J_j\delta(z-z_j)$
- I_p = equiv. shaft polar mass moment of inertia (per unit length) = $2I_d$
- H = hysteretic damping parameter in the rotor shaft = $\frac{l^2}{\pi^2}[EI\rho A]^{1/2}$,
- ζ = nondimensional factor for the amount of material internal damping,
- Ω = frequency of axial force P_t and tangential torque T_t (rad./sec.),
- Ω_o = angular velocity of shaft rotation (rad./sec.).

Usually, the value of Ω is an integral multiple of the rotational velocity Ω_o. However, in order to keep this derivation general enough we would treat them as independent quantities. In this discussion, we are considering the example of a rotor with short bearings at the two ends, where the support conditions can be modeled as simply-supported, yielding following boundary conditions for all values of time "t":

$u(z,t)$ and $v(z,t) = 0$, at $z = 0$ and $z = l$; and,
bending moment $(BM) = 0$, at $z = 0$ and $z = l$.

Here, the expressions for the instantaneous bending moments $(BM)_x$ and $(BM)_y$ for any cross-section of the shaft $(0 \le z \le l)$ are written as,

$$(BM)_x = EIu_{,zz} + 2\zeta H\Omega_o v_{,zz} + (T_o + T_t\cos\Omega t)v_{,z} - (P_o + P_t\cos\Omega t)u$$

and,

$$(BM)_y = EIv_{,zz} - 2\zeta H\Omega_o u_{,zz} - (T_o + T_t\cos\Omega t)u_{,z} - (P_o + P_t\cos\Omega t)v.$$

The solution of Eqs. (1) and (2) can be expressed in a product form of functions of time "t" and spatial variable "z." We assume the deformed shape of the shaft in the form of a set of orthogonal sine-function as:

$$u(z,t) = \sum_{k=1}^{\infty} [f_1(t)]_k \sin\left(\frac{k\pi z}{l}\right) \quad (3)$$

$$v(z,t) = \sum_{k=1}^{\infty} [f_2(t)]_k \sin\left(\frac{k\pi z}{l}\right) \quad (4)$$

where f_1 and f_2 are complex functions of time "t", and k represents the buckled mode-shape number. For illustration purposes, we would limit our discussion only to the first mode $(k = 1)$ deformed shape of the shaft. Here it should be noted that each term of the above sinusoidal series satisfies the geometric boundary conditions naturally, however, the bending moments at the ends due to the presence of tangential torque are not fully balanced. With the expressions in Eqs. (3)–(4), and applying the Galerkin's method along with the additional terms to account for the residual end moments, one obtains a set of following equations:

$$\int_o^l \mathcal{L}_1(u,v)\sin\left(\frac{k\pi z}{l}\right)dz + 2(T_o + T_t\cos\Omega t)\frac{\pi^2}{l^2}f_2(t) = 0 \quad (5)$$

$$\int_o^l \mathcal{L}_2(u,v)\sin\left(\frac{k\pi z}{l}\right)dz - 2(T_o + T_t\cos\Omega t)\frac{\pi^2}{l^2}f_1(t) = 0. \quad (6)$$

For brevity, the above set of algebraic equations in a matrix form are written as,

$$\mathbf{M}\{\ddot{f}\} + \mathbf{C}\{\dot{f}\} + (\mathbf{K} - \mathbf{B}\cos\Omega t)\{f\} = \{0\} \quad (7)$$

where, $\{f\}^T = \{f_1\ f_2\}$, and $(\dot{})$ denotes ordinary derivative with respect to time "t." The nonzero terms of the matrices **M**, **C**, **K**, and **B** are

$$M_{1,1} = M_{2,2} = \frac{\rho Al}{2}\left(1 + \frac{\pi^2(R^2+r^2)}{4l^2}\right) + \tfrac{1}{2}\sum_{j=1}^{n}\left(M_j + \frac{\pi^2}{l^2}J_j\right)\left(1 - \cos\frac{2\pi z_j}{l}\right),$$

$$C_{1,1} = C_{2,2} = \zeta H\frac{\pi^4}{l^3}$$

$$C_{1,2} = -C_{2,1} = \Omega_o\frac{\pi^2}{l^2}\left[\frac{\rho Al(R^2+r^2)}{4} + \sum_{j=1}^{n} J_j\left(1 - \cos\frac{2\pi z_j}{l}\right)\right],$$

$$K_{1,1} = K_{2,2} = EI\frac{\pi^4}{2l^3} + P_o\frac{\pi^2}{2l},$$

$$K_{1,2} = -K_{2,1} = 2T_o\frac{\pi^2}{l^2} + \zeta H\Omega_o\frac{\pi^4}{l^3}$$

$$B_{1,1} = B_{2,2} = -P_t\frac{\pi^2}{2l},$$

$$B_{1,2} = -B_{2,1} = -2T_t\frac{\pi^2}{l^2}.$$

In the above relations, J_j and M_j stand for the diametral moment of inertia and mass of the respective disk whereas M, with double subscripts, denotes the elements of the **M** matrix. Here, it should be noted that while **M** is a diagonal matrix, other matrices **C**, **K**, and **B** are combinations of symmetric and skew-symmetric parts. Equation (7) can be identified as a set of modified coupled Mathieu-Hill equations with additional contributions from the velocity-dependent coefficient matrix **C**. It can be seen that the skew-symmetric part of the **K** matrix contains hysteretic damping H and the tangential torque T_o causing instability in the dynamical system. Furthermore, the presence of nonzero **B** matrix creates parametric instability in the rotor. The solution of Eq. (7) is sought in the form of a product of two functions: first, an exponential function with characteristic exponent λ and the second a periodic function in the form of an infinite Fourier series. Sub-

Downloaded 03 May 2010 to 171.66.16.247. Redistribution subject to ASME license or copyright; see http://www.asme.org/terms/Terms_Use.cfm

stitution of the series representation of $\{f(t)\}$, enables us to use the method of harmonic balance (Sinha, 1989), which yields a set of homogeneous algebraic equations in the form:

$$(\mathbf{P}+\lambda\mathbf{Q}+\lambda^2\mathbf{R})\{X\}=\{0\}. \tag{8}$$

Matrix **P**:

$$\begin{bmatrix}
\mathbf{K} & 0 & 0 & 0 & -\mathbf{B} & 0 & 0 & 0 & 0 & \cdots\cdots \\
0 & \left(\mathbf{K}-\frac{1}{4}\Omega^2\mathbf{M}\right) & -\frac{\Omega}{2}\mathbf{C} & 0 & 0 & -\tfrac{1}{2}\mathbf{B} & 0 & 0 & 0 & \cdots\cdots \\
0 & \frac{\Omega}{2}\mathbf{C} & \left(\mathbf{K}-\frac{1}{4}\Omega^2\mathbf{M}\right) & 0 & 0 & 0 & -\tfrac{1}{2}\mathbf{B} & 0 & 0 & \cdots\cdots \\
0 & 0 & 0 & (\mathbf{K}-\Omega^2\mathbf{M}) & -\Omega\mathbf{C} & 0 & 0 & -\tfrac{1}{2}\mathbf{B} & 0 & \cdots\cdots \\
-\tfrac{1}{2}\mathbf{B} & 0 & 0 & \Omega\mathbf{C} & (\mathbf{K}-\Omega^2\mathbf{M}) & 0 & 0 & 0 & -\tfrac{1}{2}\mathbf{B} & \cdots\cdots \\
0 & -\tfrac{1}{2}\mathbf{B} & 0 & 0 & 0 & \left(\mathbf{K}-\frac{9}{4}\Omega^2\mathbf{M}\right) & -\frac{3}{2}\Omega\mathbf{C} & 0 & 0 & \cdots\cdots \\
0 & 0 & -\tfrac{1}{2}\mathbf{B} & 0 & 0 & \frac{3}{2}\Omega\mathbf{C} & \left(\mathbf{K}-\frac{9}{4}\Omega^2\mathbf{M}\right) & 0 & 0 & \cdots\cdots \\
0 & 0 & 0 & -\tfrac{1}{2}\mathbf{B} & 0 & 0 & 0 & (\mathbf{K}-4\Omega^2\mathbf{M}) & -2\Omega\mathbf{C} & \cdots\cdots \\
0 & 0 & 0 & 0 & -\tfrac{1}{2}\mathbf{B} & 0 & 0 & 2\Omega\mathbf{C} & (\mathbf{K}-4\Omega^2\mathbf{M}) & \cdots\cdots \\
\vdots & \vdots & \vdots & \vdots & \vdots & \vdots & \vdots & \vdots & \vdots &
\end{bmatrix}$$

Matrix **Q**:

$$\begin{bmatrix}
\mathbf{C} & 0 & 0 & 0 & 0 & 0 & 0 & 0 & 0 & \cdots\cdots \\
0 & \mathbf{C} & -\Omega\mathbf{M} & 0 & 0 & 0 & 0 & 0 & 0 & \cdots\cdots \\
0 & \Omega\mathbf{M} & \mathbf{C} & 0 & 0 & 0 & 0 & 0 & 0 & \cdots\cdots \\
0 & 0 & 0 & \mathbf{C} & -2\Omega\mathbf{M} & 0 & 0 & 0 & 0 & \cdots\cdots \\
0 & 0 & 0 & 2\Omega\mathbf{M} & \mathbf{C} & 0 & 0 & 0 & 0 & \cdots\cdots \\
0 & 0 & 0 & 0 & 0 & \mathbf{C} & -3\Omega\mathbf{M} & 0 & 0 & \cdots\cdots \\
0 & 0 & 0 & 0 & 0 & 3\Omega\mathbf{M} & \mathbf{C} & 0 & 0 & \cdots\cdots \\
0 & 0 & 0 & 0 & 0 & 0 & 0 & \mathbf{C} & -4\Omega\mathbf{M} & \cdots\cdots \\
0 & 0 & 0 & 0 & 0 & 0 & 0 & 4\Omega\mathbf{M} & \mathbf{C} & \cdots\cdots \\
\vdots & \vdots & \vdots & \vdots & \vdots & \vdots & \vdots & \vdots & \vdots &
\end{bmatrix}$$

Matrix **R**:

Diag. [**M** **M** **M** **M** **M** **M** **M** **M** **M** $\cdots\cdots$]

The column vector $\{X\}$ in the above equation contains unknown Fourier coefficients, and the coefficient matrices **P**, **Q**, and **R** are shown. It can be seen that these matrices are in fact infinite in nature which can be truncated depending upon the number of Fourier expansion terms one is interested in. The general solution of this set of equations results in complex roots of the eigenvalues λ, such that one can write $\lambda = \lambda_r \pm i\lambda_i$, where $i = \sqrt{-1}$. The imaginary part of the eigenvalue λ_i indicates the critical speeds of the rotor, usually denoted by ω_c, which is equal to $|\lambda_i|$. The positive and negative signs of the real part of the eigenvalue (λ_r) indicate the unstable and stable behaviors of the rotating system. Another way to establish stability is to determine the so-called effective logarithmic decrement, defined as $\delta = -2\pi(\lambda_r/\omega_c)$, of the dynamical system. The boundary frequencies (roots of Ω) of the "principal instability region" for the system governed by the Mathieu-Hill Eq. (7) are determined by finding the eigenvalues of the following matrix:

$$\begin{bmatrix}
0 & 0 & \mathbf{I} & 0 \\
0 & 0 & 0 & \mathbf{I} \\
2\mathbf{M}^{-1}(2\mathbf{K}+\mathbf{B}) & 0 & 0 & -2\mathbf{M}^{-1}\mathbf{C} \\
0 & 2\mathbf{M}^{-1}(2\mathbf{K}-\mathbf{B}) & 2\mathbf{M}^{-1}\mathbf{C} & 0
\end{bmatrix}. \tag{9}$$

Since, all the matrices **M**, **C**, **K**, and **B** are fully defined and **I** is the standard unit matrix, the global stability conditions of the rotor, with a known value of internal damping ζ, can easily be determined for any combination of P_o, P_t, and T_o, T_t.

3 Numerical Results and Discussion

Sample numerical results have been generated for a rotor shaft with one disk located at 1/3 of the span. The weight and polar mass moment of inertia of the disk are assumed to be ten and six times than those of the shaft, respectively. The fundamental mode undamped natural frequency ω_n in the nonrotating condition of the rotor is, ω_n = 173.16 Hz. The first mode frequency of this rotor without the disk is 577.29 Hz. All the numerical results are presented in terms of nondimensional parameters. The principal (parametric) instability regions for excitation frequencies Ω in the subcritical ($\Omega_o < \omega_n$) and supercritical ($\Omega_o > \omega_n$) operational ranges of the rotor for changing values of P_t, shown in Fig. 1, indicate that the instability zone increases substantially for higher rotational speeds.

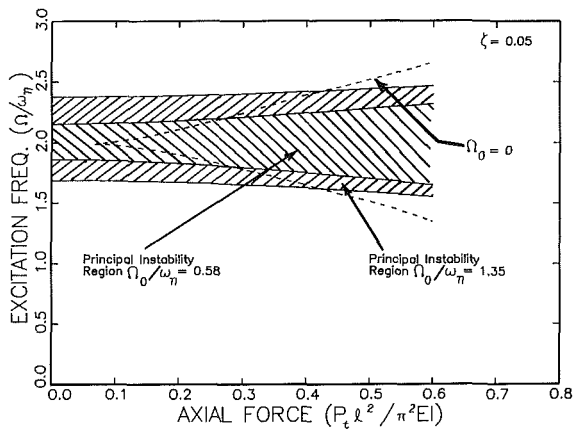

Fig. 1 Principal parametric instability regions for different rotational speeds ($\Omega_o = \Omega_o/\omega_n$ = 0.58, 1.35)

Downloaded 03 May 2010 to 171.66.16.247. Redistribution subject to ASME license or copyright; see http://www.asme.org/terms/Terms_Use.cfm

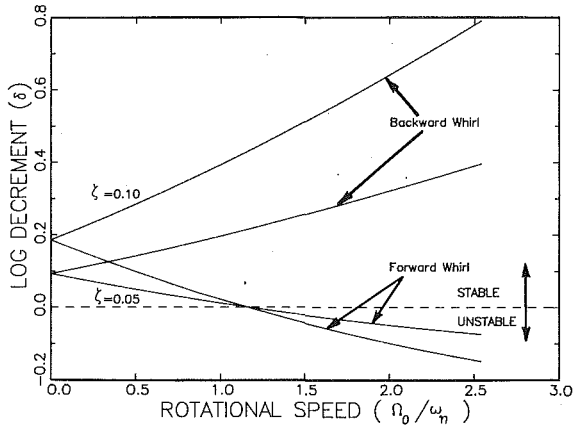

Fig. 2 Rotor stability for two different values of material damping (ζ = 0.05 and 0.1)

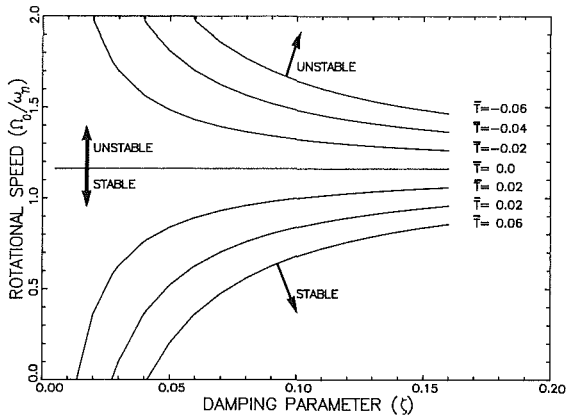

Fig. 3 Stability boundaries for different values of tangential torque; ($\bar{T} = T_o l/EI$) as a function of damping ratio ζ; ($\bar{T} = -0.06, -0.04, -0.02, 0, 0.02, 0.04$, and 0.06)

The parametric instability boundaries for $\Omega_o = 0$ are shown with dotted lines, which highlight the fact that the spinning rotor would go into parametric resonance even for very small values of P_t with excitation frequencies Ω in the range of 1.6 to 2.4 times of ω_n. These plots, generated for $\zeta = 0.05$, show that gyroscopic effects in rotating condition tend to keep the width of unstable region almost same, and do not fan out with increasing values of P_t as it does for $\Omega_o = 0$. The effect of hysteretic damping on the whirling stability of the rotor is shown in Fig. 2. As the damping increases from $\zeta = 0.05$ to 0.1, the rotor becomes more stable in the backward whirl and less stable in the forward whirl, and becomes unstable at $\Omega_o/\omega_n = 1.2$. For this particular rotor, this is the threshold speed above which it is dynamically unstable. Figure 3 shows the combined effects of hysteretic damping ζ and tangential torque in the rotor. The stability boundaries for a family of constant torque curves for $\bar{T} = -0.06, -0.04, -0.02, 0.0$, and 0.02, 0.04, and 0.06, where $\bar{T} = T_o l/EI$, plotted for increasing values of ζ. For a given spinning RPM of the rotor, it becomes less stable with increasing torque and more stable with increasing damping. One of the most interesting observation is that the load torque has much more stabilizing effect at higher speeds on the rotor than a driving torque. As a matter of fact, the rotor becomes stable with the increasing load torque and less stable with the increasing driving torque. Figure 3 also shows that this particular rotor, at zero torque, is unstable above $(\Omega_o/\omega_n) = 1.16$. For a rotor without any disk this value is equal to 1.032, which is close to the Gunter's result for the rigid support, plotted by Vance and Lee (1974). The corresponding Gunter's (1967) result is equal to 1, and the slight increase in the nondimensional rotational speed is due to the lowering of first beam-mode natural frequency of the rotor due to the consideration of rotary inertia of the shaft in the present analysis. The increase in the instability threshold from 1.032 to 1.16 shows that a rotor-disk system will remain stable at relatively higher nondimensional speed.

The numerical results presented in this paper are only for the first buckled mode of a rotor with one disk. However, the equations derived here are general enough that it can easily be extended for higher modes with any number of disks as well.

References

Alford, J. S., 1965, "Protecting Turbomachinery From Self-Excited Rotor Whirl," ASME *Journal of Engineering for Power*, Vol. 87, Series A, pp. 333–344.

Bucciarelli, L. L., 1982, "On the Instability of Rotating Shafts Due to Internal Damping," ASME Journal of Applied Mechanics, Vol. 49, pp. 425–428.

Cohen, R., and Porat, I., 1984, "Influence of Load Torque on Stability of Rotor Driven by Flexible Shaft," *Journal of Sound and Vibration*, Vol. 95, pp. 151–160.

Crandall, S. H., 1980, "Physical Explanations of the Destabilizing Effect of Damping in Rotating Parts," *Rotordynamic Instability Problems in High-Performance Turbomachinery*, NASA CP-2133, May, pp. 369–382.

Ehrich, F. F., 1964, "Shaft Whirl Induced by Rotor Internal Damping," ASME Journal of Applied Mechanics, Vol. 31, pp. 279–282.

Genin, J., and Maybee, J. S., 1970, "Whirling Motion of a Viscoelastic Continuous Shaft," *International Journal of Eng. Science*, Vol. 8, pp. 671–686.

Gunter, E. J., Jr., 1967, "The Influence of Internal Friction on the Stability of High-Speed Rotors," ASME *Journal of Engineering for Industry*, Vol. 89, p. 683–688.

Hendricks, S. L., 1986, "The Effect of Viscoelasticity on the Vibration of a Rotor," ASME Journal of Applied Mechanics, Vol. 53, No. 2, pp. 412–416.

Ota, H., and Mizutani, K., 1987, "Self-Excited Vibrations of a Rotating Shaft With Structural Damping," *Transactions of JSME*, Vol. 53, pp. 1172–1177.

Pedersen, P. T., 1973, "On Self-Excited Whirl of Rotors," *Ingenieur-Archiv*, Vol. 42, pp. 267–284.

Plaut, R. H., 1977, "Stability of Rotating Shafts with Axial Load and Damping," *Proc. 1st ASCE-EMD Speciality Conference on Mechanics in Engineering* R. N. Dubey and N. C. Lind, eds., University of Waterloo Press, Waterloo, Canada, pp. 133–148.

Sinha, S. K., 1989, "Stability of a Viscoelastic Rotor-Disk System Under Dynamic Axial Loads," *AIAA Journal*, Vol. 27, No. 11, pp. 1653–1655.

Vance, J. M., and Laudadio, F. J., 1984, "Experimental Measurement of Alford's Force in an Axial Flow Turbomachinery," ASME Paper No. 84-GT-140, *Journal of Engineering for Gas Turbine and Power*, Vol. 106, No. 3, pp. 585–590.

Vance, J. M., and Lee, J., 1974, "Stability of High-Speed Rotors With Internal Friction," ASME *Journal of Engineering for Industry*, Vol. 96, pp. 960–968.

Yim, K. B., Noah, S. T., and Vance, J. M., 1986, "Effect of Tangential Torque on the Dynamics of Flexible Rotors," ASME Journal of Applied Mechanics, Vol. 53, pp. 711–718.

Zhang, W., and Ling, F. H., 1986, "Dynamic Stability of the Rotating Shaft Made of Boltzmann Viscoelastic Solid," ASME Journal of Applied Mechanics, Vol. 53, No. 2, pp. 424–429.

On the Numerical Evaluation of the Unforced Response of a Duffing Oscillator

G. D. Hahn,[14,17] J. F. Carney III,[15,17] and Malcolm H. Ray[16,17]

A recent study suggested that the use of numerical integration methods would generally lead to the erroneous prediction of chaotic behavior for an unforced Duffing's oscillator. It is shown herein that appropriate implementations of such methods lead to accurate, nonchaotic computations of the associated response.

[14]Assistant Professor of Civil Engineering.

[15]Professor of Civil Engineering.

[16]Research Instructor.

[17]Department of Civil and Environmental Engineering, Vanderbilt University, Nashville, TN 37235.

Contributed by the Applied Mechanics Division of The American Society of Mechanical Engineers. Manuscript received by the ASME Applied Mechanics Division, July 11, 1990; final revision, Nov. 20, 1990.

Downloaded 03 May 2010 to 171.66.16.247. Redistribution subject to ASME license or copyright; see http://www.asme.org/terms/Terms_Use.cfm

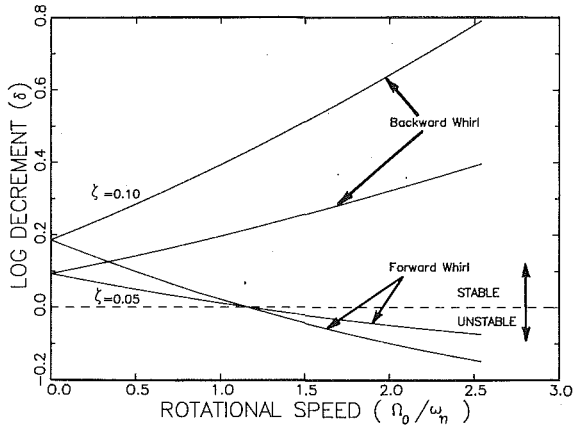

Fig. 2 Rotor stability for two different values of material damping (ζ = 0.05 and 0.1)

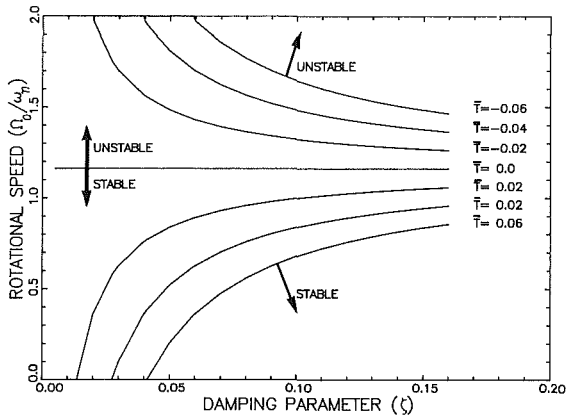

Fig. 3 Stability boundaries for different values of tangential torque; ($\bar{T} = T_o l/EI$) as a function of damping ratio ζ; ($\bar{T} = -0.06, -0.04, -0.02, 0, 0.02, 0.04$, and 0.06)

The parametric instability boundaries for $\Omega_o = 0$ are shown with dotted lines, which highlight the fact that the spinning rotor would go into parametric resonance even for very small values of P_t with excitation frequencies Ω in the range of 1.6 to 2.4 times of ω_n. These plots, generated for $\zeta = 0.05$, show that gyroscopic effects in rotating condition tend to keep the width of unstable region almost same, and do not fan out with increasing values of P_t as it does for $\Omega_o = 0$. The effect of hysteretic damping on the whirling stability of the rotor is shown in Fig. 2. As the damping increases from $\zeta = 0.05$ to 0.1, the rotor becomes more stable in the backward whirl and less stable in the forward whirl, and becomes unstable at $\Omega_o/\omega_n = 1.2$. For this particular rotor, this is the threshold speed above which it is dynamically unstable. Figure 3 shows the combined effects of hysteretic damping ζ and tangential torque in the rotor. The stability boundaries for a family of constant torque curves for $\bar{T} = -0.06, -0.04, -0.02, 0.0$, and 0.02, 0.04, and 0.06, where $\bar{T} = T_o l/EI$, plotted for increasing values of ζ. For a given spinning RPM of the rotor, it becomes less stable with increasing torque and more stable with increasing damping. One of the most interesting observation is that the load torque has much more stabilizing effect at higher speeds on the rotor than a driving torque. As a matter of fact, the rotor becomes stable with the increasing load torque and less stable with the increasing driving torque. Figure 3 also shows that this particular rotor, at zero torque, is unstable above $(\Omega_o/\omega_n) = 1.16$. For a rotor without any disk this value is equal to 1.032, which is close to the Gunter's result for the rigid support, plotted by Vance and Lee (1974). The corresponding Gunter's (1967) result is equal to 1, and the slight increase in the nondimensional rotational speed is due to the lowering of first beam-mode natural frequency of the rotor due to the consideration of rotary inertia of the shaft in the present analysis. The increase in the instability threshold from 1.032 to 1.16 shows that a rotor-disk system will remain stable at relatively higher nondimensional speed.

The numerical results presented in this paper are only for the first buckled mode of a rotor with one disk. However, the equations derived here are general enough that it can easily be extended for higher modes with any number of disks as well.

References

Alford, J. S., 1965, "Protecting Turbomachinery From Self-Excited Rotor Whirl," ASME *Journal of Engineering for Power*, Vol. 87, Series A, pp. 333–344.

Bucciarelli, L. L., 1982, "On the Instability of Rotating Shafts Due to Internal Damping," ASME Journal of Applied Mechanics, Vol. 49, pp. 425–428.

Cohen, R., and Porat, I., 1984, "Influence of Load Torque on Stability of Rotor Driven by Flexible Shaft," *Journal of Sound and Vibration*, Vol. 95, pp. 151–160.

Crandall, S. H., 1980, "Physical Explanations of the Destabilizing Effect of Damping in Rotating Parts," *Rotordynamic Instability Problems in High-Performance Turbomachinery*, NASA CP-2133, May, pp. 369–382.

Ehrich, F. F., 1964, "Shaft Whirl Induced by Rotor Internal Damping," ASME Journal of Applied Mechanics, Vol. 31, pp. 279–282.

Genin, J., and Maybee, J. S., 1970, "Whirling Motion of a Viscoelastic Continuous Shaft," *International Journal of Eng. Science*, Vol. 8, pp. 671–686.

Gunter, E. J., Jr., 1967, "The Influence of Internal Friction on the Stability of High-Speed Rotors," ASME *Journal of Engineering for Industry*, Vol. 89, p. 683–688.

Hendricks, S. L., 1986, "The Effect of Viscoelasticity on the Vibration of a Rotor," ASME Journal of Applied Mechanics, Vol. 53, No. 2, pp. 412–416.

Ota, H., and Mizutani, K., 1987, "Self-Excited Vibrations of a Rotating Shaft With Structural Damping," *Transactions of JSME*, Vol. 53, pp. 1172–1177.

Pedersen, P. T., 1973, "On Self-Excited Whirl of Rotors," *Ingenieur-Archiv*, Vol. 42, pp. 267–284.

Plaut, R. H., 1977, "Stability of Rotating Shafts with Axial Load and Damping," *Proc. 1st ASCE-EMD Speciality Conference on Mechanics in Engineering* R. N. Dubey and N. C. Lind, eds., University of Waterloo Press, Waterloo, Canada, pp. 133–148.

Sinha, S. K., 1989, "Stability of a Viscoelastic Rotor-Disk System Under Dynamic Axial Loads," *AIAA Journal*, Vol. 27, No. 11, pp. 1653–1655.

Vance, J. M., and Laudadio, F. J., 1984, "Experimental Measurement of Alford's Force in an Axial Flow Turbomachinery," ASME Paper No. 84-GT-140, *Journal of Engineering for Gas Turbine and Power*, Vol. 106, No. 3, pp. 585–590.

Vance, J. M., and Lee, J., 1974, "Stability of High-Speed Rotors With Internal Friction," ASME *Journal of Engineering for Industry*, Vol. 96, pp. 960–968.

Yim, K. B., Noah, S. T., and Vance, J. M., 1986, "Effect of Tangential Torque on the Dynamics of Flexible Rotors," ASME Journal of Applied Mechanics, Vol. 53, pp. 711–718.

Zhang, W., and Ling, F. H., 1986, "Dynamic Stability of the Rotating Shaft Made of Boltzmann Viscoelastic Solid," ASME Journal of Applied Mechanics, Vol. 53, No. 2, pp. 424–429.

On the Numerical Evaluation of the Unforced Response of a Duffing Oscillator

G. D. Hahn,[14,17] J. F. Carney III,[15,17] and Malcolm H. Ray[16,17]

A recent study suggested that the use of numerical integration methods would generally lead to the erroneous prediction of chaotic behavior for an unforced Duffing's oscillator. It is shown herein that appropriate implementations of such methods lead to accurate, nonchaotic computations of the associated response.

[14]Assistant Professor of Civil Engineering.

[15]Professor of Civil Engineering.

[16]Research Instructor.

[17]Department of Civil and Environmental Engineering, Vanderbilt University, Nashville, TN 37235.

Contributed by the Applied Mechanics Division of The American Society of Mechanical Engineers. Manuscript received by the ASME Applied Mechanics Division, July 11, 1990; final revision, Nov. 20, 1990.

Copyright © 1992 by ASME
Downloaded 03 May 2010 to 171.66.16.247. Redistribution subject to ASME license or copyright; see http://www.asme.org/terms/Terms_Use.cfm

Introduction

In a recent publication (Reinhall, Caughey, and Storti, 1989), it was suggested that the use of numerical integration techniques will generally lead to the erroneous prediction of chaotic behavior (Thompson and Stewart, 1988) for an unforced Duffing's oscillator. In that publication (Reinhall, Caughey, and Storti, 1989), the Duffing equation was discretized using both the Euler and Newmark methods, and some of the numerical results involved unrealistic characteristics that do not exist in the exact solution to the problem. In this paper, it is shown that these characteristics are not the result of an inherent unsuitability of the Euler and Newmark methods, as the authors (Reinhall, Caughey, and Storti, 1989) contended, but are caused by the specification of inappropriate time steps in the numerical integration process.

Equation of Motion

The differential equation that governs the response of an unforced, undamped Duffing's oscillator may be written as

$$\ddot{x}+\omega^2 x+\frac{\omega^2}{x_r^2}x^3=0 \tag{1}$$

where

$$\omega^2=\frac{k}{m} \tag{2}$$

in which m is the mass of the oscillator; k is a measure of its stiffness; x_r is a parameter with units of length; x represents the resulting displacements; and a dot superscript denotes differentiation with respect to time, t.

The solution of Eq. (1) for an initial displacement, $x(t=0)=x_o$, and zero initial velocity, $\dot{x}(t=0)=0$, is available (Mickens, 1981; Dinca and Teodosiu, 1973), and may be expressed as

$$x=x_o cn(\Omega t,u) \tag{3}$$

in which cn is Jacobi's elliptic cosine function (Mickens, 1981; Dinca and Teodosiu, 1973; Byrd and Friedman, 1971; Davis, 1962; Jahnke-Emde-Losch, 1960) and

$$\Omega=\omega(1+\alpha^2)^{1/2} \tag{4}$$

$$u=\left(\frac{\alpha^2}{2(1+\alpha^2)}\right)^{1/2} \tag{5}$$

$$\alpha=\frac{x_o}{x_r} \tag{6}$$

where $0\le\alpha^2\le\infty$ and $0\le u^2\le 0.5$. The motion defined by Eq. (3) is periodic with a period given by (Mickens, 1981; Dinca and Teodosiu, 1973)

$$T=\frac{4}{\Omega}K(u) \tag{7}$$

in which K is the complete elliptic integral of the first kind (Mickens, 1981; Dinca and Teodosiu, 1973; Byrd and Friedman, 1971; Davis, 1962; Jahnke-Emde-Losch, 1960). It can be easily demonstrated from Eq. (7) that the period T decreases with increasing values of the amplitude of the motion, x_o.

Analysis of a Particular Case

The Duffing oscillator with $x_r=1$ mm and $\omega=2\pi$ rad/sec is analyzed numerically by using the modified Euler method (MEM) as presented by Hahn (1990), and the Newmark beta method (NBM) with beta = 1/4 described by Newmark (1959)

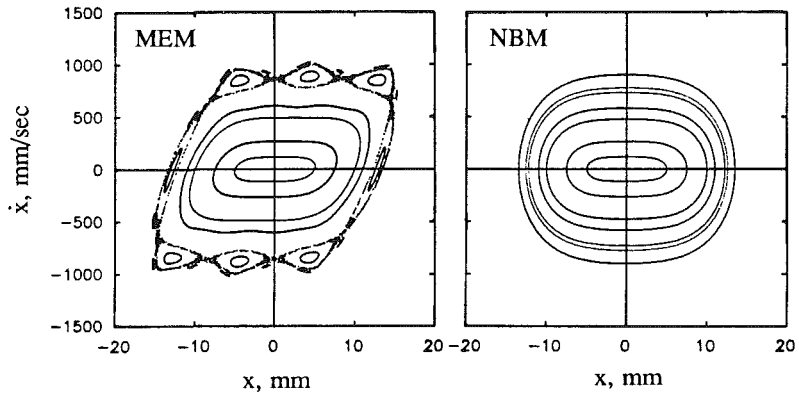

Fig. 1 Responses obtained for a particular case of the Duffing oscillator by the MEM and NBM for $\Delta t=0.01$ sec

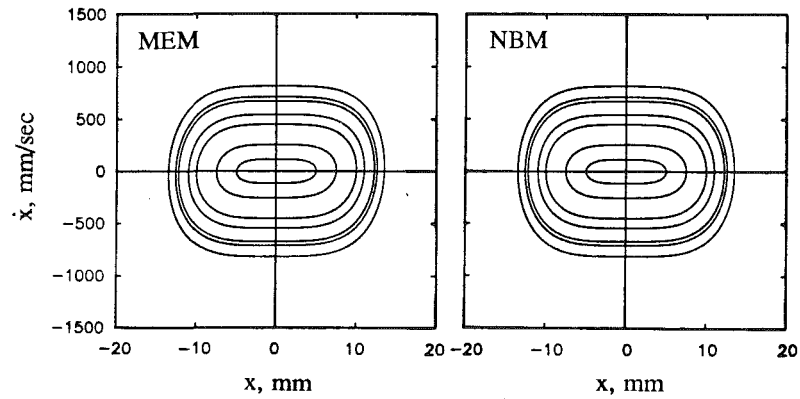

Fig. 2 Responses obtained for a particular case of the Duffing oscillator by the MEM and NBM for $\Delta t/T=0.01$

Downloaded 03 May 2010 to 171.66.16.247. Redistribution subject to ASME license or copyright; see http://www.asme.org/terms/Terms_Use.cfm

and Hughes (1987). Under these conditions, Eq. (1) reduces to

$$\ddot{x} + (2\pi)^2 x + (2\pi)^2 x^3 = 0 \tag{8}$$

in which x and $\ddot{x}$ are measured in mm and mm/sec^2, respectively.

Solutions of Eq. (8) in the phase plane are shown in Figs. 1 and 2 calculated for an initial displacement, x_o, and zero initial velocity. These solutions were obtained by using both the MEM and NBM, for $x_o = 5$, 7.5, 10, 11, 12.25, 12.6, and 13.5 mm.

Figure 1 shows responses computed for a time step $\Delta t = 0.01$ sec. In order to interpret the results of this figure, it is important to realize that the period, T, decreases as x_o increases. The accuracy of the numerical solutions deteriorates as the ratio $\Delta t/T$ increases, and the MEM eventually becomes unstable for relatively large values of $\Delta t/T$. The solution reported in Fig. 1 for the MEM is particularly attractive because of its chaotic appearance. Indeed, Reinhall, Caughey, and Storti (1989) associated such an appearance with chaotic behavior. This appearance, however, is simply the result of a deterioration in solution accuracy due to inappropriate applications of the MEM.

Figure 2 shows solutions corresponding to those presented in Fig. 1 that have been recomputed by using $\Delta t = 0.01T$. It is observed in Fig. 2 that responses obtained for the same x_o by the MEM and NBM are almost indistinguishable from each other. Such responses are essentially the same as the corresponding exact solutions, and this indicates that appropriate implementations of these numerical techniques lead to accurate response evaluations for the Duffing oscillator considered in this study and in the study by Reinhall, Caughey, and Storti (1989).

Conclusion

Numerical solutions for the response of an undamped, unforced Duffing's oscillator have been obtained by applications of two different numerical integration methods, the MEM and NBM. The applications of these methods do not lead to the prediction of chaos for such an oscillator, a conclusion that is in contrast with that reached by Reinhall, Caughey, and Storti (1989). The indiscriminate, inappropriate use of numerical integration approaches can certainly lead to erroneous predictions for the response of the system. However, central to the appropriate implementation of a numerical method is an appropriate appreciation of its limitations. For the case of the Duffing's oscillator studied herein, accurate evaluations of the response are made by both the MEM and NBM if $\Delta t < \approx 0.01T$. The information reported in this paper eliminates the confusion which may have resulted from the publication of the study by Reinhall, Caughey, and Storti (1989).

References

Byrd, P. F., and Friedman, M. D., 1971, *Handbook of Elliptic Integrals for Engineers and Scientists*, Springer-Verlag, New York.

Davis, H. T., 1962, *Introduction to Nonlinear Differential and Integral Equations*, Dover, New York.

Dinca, F., and Teodosiu, C., 1973, *Nonlinear and Random Vibrations*, Academic Press, New York.

Hahn, G. D., 1991, "A Modified Euler Method for Dynamic Analyses," *Journal for Numerical Methods in Engineering*, Vol. 32.

Hughes, T. J. R., 1987, *The Finite Element Method: Linear Static and Dynamic Finite Element Analysis*, Prentice-Hall, Englewood Cliffs, N.J.

JAHNKE-EMDE-LOSCH, 1960, *Tables of Higher Functions*, McGraw-Hill, New York.

Mickens, R. E., 1981, *An Introduction to Nonlinear Oscillations*, Cambridge University Press, New York.

Newmark, N. M., 1959, "A Method of Computation for Structural Dynamics," *Journal of the Engineering Mechanics Division*, Proceedings Paper 2094, ASCE, New York.

Reinhall, P. G., Caughey, T. K., and Storti, D. W., 1989, "Order and Chaos in a Discrete Duffing Oscillator: Implications on Numerical Integration," ASME JOURNAL OF APPLIED MECHANICS, Vol. 56, pp. 162–167.

Thompson, J. M. T., and Stewart, H. B., 1988, *Nonlinear Dynamics and Chaos*, John Wiley and Sons, New York.

The Influence of Two-Dimensional End Effects on the Natural Frequencies of Cantilevered Beams Weak in Shear[18]

J. M. Duva[19,20] and J. G. Simmonds[19,21]

Introduction

This Brief Note is designed to supply further specific evidence to support a thesis that we—and others—have asserted before:

1 In elastically orthotropic beams (that may be either homogeneous or layered), so-called higher-order theories offer, in general, no advantages beyond those resulting from an enlargement of the class of admissible functions in a Rayleigh-Ritz procedure unless two-dimensional end effects are considered.

Moreover,

2 if end effects are considered, then simple, easily computable refinements to elementary theory (properly interpreted and applied) suffice.

It remains to extend these conclusions to higher-order plate and shell theories where further complications await. (See Duva and Simmonds, 1991; Ladevèze, 1985; Simmonds, 1976, for citations to related fundamental studies by Friedrichs and Dressler, Goldenveiser, Gregory and Gladwell, Gregory and Wan, Koiter, Lin and Wan, and van der Heijden, among others.)

Specifically, we apply the linear dynamic equations of plane orthotropic elasticity to a cantilevered rectangular beam of narrow rectangular cross-section. Using formal asymptotic methods, we show that if the beam is weak in shear, in the sense that the ratio of the shear modulus, G, to the geometric mean of the longitudinal and transverse moduli, E_x and E_z, is of the order of the ratio of the depth of the beam, $2H$, to its length, L, then the corrections to the squares of the natural frequencies of vibration predicted by elementary beam theory are of relative order H/L. Although corrections of the same order of magnitude were found by Duva and Simmonds (1991) in the analogous problem for an *isotropic* beam, the corrections there were proportional to Poisson's ratio, ν, while here the corrections arise from a different mechanism and do not vanish with ν.

Finally, we note (and shall show at the end of the paper) that there *is* a value of the elusive shear coefficient k such that Timoshenko beam theory will give the same relative $O(H/L)$ correction to the natural frequencies of elementary theory. *However, this value of* k *depends on an analysis of two-dimensional end effects.* Moreover, if one decides to include end effects, then the more elaborate Timoshenko equations are not needed: Simple additions to the solutions of elementary theory will do.

The Governing Equations

Let the undeformed beam occupy the region $0 \le x \le L$, $|y| \le B$, $|z| \le H$ in an inertial, right-hand Cartesian reference frame, $Oxyz$. Further, let σ_x, τ, σ_z and U, W denote, respectively, the standard components of stress and displacement

[18]This work was supported in part by the National Science Foundation under Grant MSS-8903130 and in part by the Academic Enhancement Program at the University of Virginia.

[19]Department of Applied Mathematics, University of Virginia, Charlottesville, VA 22903.

[20]Assoc. Mem. ASME.

[21]Mem. ASME.

Contributed by the Applied Mechanics Division of THE AMERICAN SOCIETY OF MECHANICAL ENGINEERS. Manuscript received by the ASME Applied Mechanics Division, July 17, 1990; final revision, Mar. 15, 1991.

Downloaded 03 May 2010 to 171.66.16.247. Redistribution subject to ASME license or copyright; see http://www.asme.org/terms/Terms_Use.cfm

and Hughes (1987). Under these conditions, Eq. (1) reduces to

$$\ddot{x} + (2\pi)^2 x + (2\pi)^2 x^3 = 0 \tag{8}$$

in which x and $\ddot{x}$ are measured in mm and mm/sec^2, respectively.

Solutions of Eq. (8) in the phase plane are shown in Figs. 1 and 2 calculated for an initial displacement, x_o, and zero initial velocity. These solutions were obtained by using both the MEM and NBM, for $x_o = 5$, 7.5, 10, 11, 12.25, 12.6, and 13.5 mm.

Figure 1 shows responses computed for a time step $\Delta t = 0.01$ sec. In order to interpret the results of this figure, it is important to realize that the period, T, decreases as x_o increases. The accuracy of the numerical solutions deteriorates as the ratio $\Delta t/T$ increases, and the MEM eventually becomes unstable for relatively large values of $\Delta t/T$. The solution reported in Fig. 1 for the MEM is particularly attractive because of its chaotic appearance. Indeed, Reinhall, Caughey, and Storti (1989) associated such an appearance with chaotic behavior. This appearance, however, is simply the result of a deterioration in solution accuracy due to inappropriate applications of the MEM.

Figure 2 shows solutions corresponding to those presented in Fig. 1 that have been recomputed by using $\Delta t = 0.01T$. It is observed in Fig. 2 that responses obtained for the same x_o by the MEM and NBM are almost indistinguishable from each other. Such responses are essentially the same as the corresponding exact solutions, and this indicates that appropriate implementations of these numerical techniques lead to accurate response evaluations for the Duffing oscillator considered in this study and in the study by Reinhall, Caughey, and Storti (1989).

Conclusion

Numerical solutions for the response of an undamped, unforced Duffing's oscillator have been obtained by applications of two different numerical integration methods, the MEM and NBM. The applications of these methods do not lead to the prediction of chaos for such an oscillator, a conclusion that is in contrast with that reached by Reinhall, Caughey, and Storti (1989). The indiscriminate, inappropriate use of numerical integration approaches can certainly lead to erroneous predictions for the response of the system. However, central to the appropriate implementation of a numerical method is an appropriate appreciation of its limitations. For the case of the Duffing's oscillator studied herein, accurate evaluations of the response are made by both the MEM and NBM if $\Delta t < \approx 0.01T$. The information reported in this paper eliminates the confusion which may have resulted from the publication of the study by Reinhall, Caughey, and Storti (1989).

References

Byrd, P. F., and Friedman, M. D., 1971, *Handbook of Elliptic Integrals for Engineers and Scientists*, Springer-Verlag, New York.

Davis, H. T., 1962, *Introduction to Nonlinear Differential and Integral Equations*, Dover, New York.

Dinca, F., and Teodosiu, C., 1973, *Nonlinear and Random Vibrations*, Academic Press, New York.

Hahn, G. D., 1991, "A Modified Euler Method for Dynamic Analyses," *Journal for Numerical Methods in Engineering*, Vol. 32.

Hughes, T. J. R., 1987, *The Finite Element Method: Linear Static and Dynamic Finite Element Analysis*, Prentice-Hall, Englewood Cliffs, N.J.

JAHNKE-EMDE-LOSCH, 1960, *Tables of Higher Functions*, McGraw-Hill, New York.

Mickens, R. E., 1981, *An Introduction to Nonlinear Oscillations*, Cambridge University Press, New York.

Newmark, N. M., 1959, "A Method of Computation for Structural Dynamics," *Journal of the Engineering Mechanics Division*, Proceedings Paper 2094, ASCE, New York.

Reinhall, P. G., Caughey, T. K., and Storti, D. W., 1989, "Order and Chaos in a Discrete Duffing Oscillator: Implications on Numerical Integration," ASME JOURNAL OF APPLIED MECHANICS, Vol. 56, pp. 162–167.

Thompson, J. M. T., and Stewart, H. B., 1988, *Nonlinear Dynamics and Chaos*, John Wiley and Sons, New York.

The Influence of Two-Dimensional End Effects on the Natural Frequencies of Cantilevered Beams Weak in Shear[18]

J. M. Duva[19,20] and J. G. Simmonds[19,21]

Introduction

This Brief Note is designed to supply further specific evidence to support a thesis that we—and others—have asserted before:

1 In elastically orthotropic beams (that may be either homogeneous or layered), so-called higher-order theories offer, in general, no advantages beyond those resulting from an enlargement of the class of admissible functions in a Rayleigh-Ritz procedure unless two-dimensional end effects are considered.

Moreover,

2 if end effects are considered, then simple, easily computable refinements to elementary theory (properly interpreted and applied) suffice.

It remains to extend these conclusions to higher-order plate and shell theories where further complications await. (See Duva and Simmonds, 1991; Ladevèze, 1985; Simmonds, 1976, for citations to related fundamental studies by Friedrichs and Dressler, Goldenveiser, Gregory and Gladwell, Gregory and Wan, Koiter, Lin and Wan, and van der Heijden, among others.)

Specifically, we apply the linear dynamic equations of plane orthotropic elasticity to a cantilevered rectangular beam of narrow rectangular cross-section. Using formal asymptotic methods, we show that if the beam is weak in shear, in the sense that the ratio of the shear modulus, G, to the geometric mean of the longitudinal and transverse moduli, E_x and E_z, is of the order of the ratio of the depth of the beam, $2H$, to its length, L, then the corrections to the squares of the natural frequencies of vibration predicted by elementary beam theory are of relative order H/L. Although corrections of the same order of magnitude were found by Duva and Simmonds (1991) in the analogous problem for an *isotropic* beam, the corrections there were proportional to Poisson's ratio, ν, while here the corrections arise from a different mechanism and do not vanish with ν.

Finally, we note (and shall show at the end of the paper) that there *is* a value of the elusive shear coefficient k such that Timoshenko beam theory will give the same relative $O(H/L)$ correction to the natural frequencies of elementary theory. *However, this value of* k *depends on an analysis of two-dimensional end effects.* Moreover, if one decides to include end effects, then the more elaborate Timoshenko equations are not needed: Simple additions to the solutions of elementary theory will do.

The Governing Equations

Let the undeformed beam occupy the region $0 \le x \le L$, $|y| \le B$, $|z| \le H$ in an inertial, right-hand Cartesian reference frame, $Oxyz$. Further, let σ_x, τ, σ_z and U, W denote, respectively, the standard components of stress and displacement

[18]This work was supported in part by the National Science Foundation under Grant MSS-8903130 and in part by the Academic Enhancement Program at the University of Virginia.

[19]Department of Applied Mathematics, University of Virginia, Charlottesville, VA 22903.

[20]Assoc. Mem. ASME.

[21]Mem. ASME.

Contributed by the Applied Mechanics Division of THE AMERICAN SOCIETY OF MECHANICAL ENGINEERS. Manuscript received by the ASME Applied Mechanics Division, July 17, 1990; final revision, Mar. 15, 1991.

Copyright © 1992 by ASME
Downloaded 03 May 2010 to 171.66.16.247. Redistribution subject to ASME license or copyright; see http://www.asme.org/terms/Terms_Use.cfm

associated with the x and z-directions. Then the equations of motion and the displacement-stress relations of plane stress theory take the form

$$\sigma_{x,x}+\tau_{,z}=\rho U_{,tt},\quad \tau_{,x}+\sigma_{z,z}=\rho W_{,tt} \tag{1}$$

$$E_x U_{,x}=\sigma_x-\nu(E_x/E_z)\sigma_z,\quad G(U_{,z}+W_{,x})=\tau,\quad E_z W_{,z}=\sigma_z-\nu\sigma_x. \tag{2}$$

Here, a comma followed by a subscript denotes differentiation with respect to that subscript, ρ is the mass per unit volume (taken constant), and t is time.

The boundary conditions for a cantilevered beam are no displacement at the left end,

$$U(0,z,t)=W(0,z,t)=0, \tag{3}$$

no traction on the faces,

$$\sigma_z(x,\pm H,t)=\tau(x,\pm H,t)=0, \tag{4}$$

and no traction on the right end,

$$\sigma_x(L,z,t)=\tau(L,z,t)=0. \tag{5}$$

The Interior Solution

As in Duva and Simmonds (1991), we first seek solutions, harmonic in time, of the form

$$\{U,W\}=W_0\{\epsilon u,w\}e^{i\Omega t},\quad \{\sigma_x,\tau,\sigma_z\}=(W_0E_xH/L^2)\{s_\xi,\epsilon s,\epsilon^2 s_\zeta\}e^{i\Omega t}, \tag{6}$$

where

$$\epsilon=H/L,\quad \xi=x/L,\quad \zeta=z/H. \tag{7}$$

Here, W_0 is a reference amplitude and ϵ is our basic small parameter. We now choose a material that is weak in shear in the sense that

$$(E_x/E_z)^{1/2}(E_z/G-2\nu)=c\epsilon^{-1},\quad c=O(1). \tag{8}$$

(See Horgan and Simmonds, 1991. For the present work, their ϵ^{-1} should be replaced everywhere by $c\epsilon^{-1}$.) Then, introducing the additional dimensionless parameter and frequency,

$$\tilde{E}=E_x/E_z,\quad \omega^2=3\rho L^4\Omega^2/E_xH^2, \tag{9}$$

using $(2)_1$ to write

$$s_\xi=u_{,\xi}+\nu\tilde{E}\epsilon^2 s_\zeta, \tag{10}$$

and rearranging (1) and (2) in the order in which we shall asymptotically integrate them, we have

$$w_{,\zeta}=\epsilon^2\tilde{E}[-\nu u_{,\xi}+\epsilon^2(1-\nu^2\tilde{E})s_\zeta] \tag{11}$$

$$u_{,\zeta}=-w_{,\xi}+\epsilon\tilde{E}^{1/2}(1+2\nu\tilde{E}^{1/2}\epsilon)s \tag{12}$$

$$s_{,\zeta}=-u_{,\xi\xi}-\epsilon^2[(1/3)\omega^2u+\nu\tilde{E}s_{\zeta,\xi}] \tag{13}$$

$$s_{\zeta,\zeta}=-s_{,\xi}-(1/3)\omega^2w. \tag{14}$$

The associated boundary conditions are, from (3)–(10),

$$u(0,\zeta)=w(0,\zeta)=0 \tag{15}$$

$$s_\zeta(\xi,\pm1)=s(\xi,\pm1)=0 \tag{16}$$

$$u_{,\xi}(1,\zeta)+\nu\tilde{E}\epsilon^2 s_\zeta(1,\zeta)=s(1,\zeta)=0. \tag{17}$$

Finally, as we are interested in free *transverse* vibrations,

$$\begin{Bmatrix} w,s \\ u,s_\xi,s_\zeta \end{Bmatrix} \text{ must be } \begin{Bmatrix} \text{even} \\ \text{odd} \end{Bmatrix} \text{ in } \zeta. \tag{18}$$

Elementary beam theory is obtained by setting $\epsilon=0$ in (11)–(17). Denoting the associated solutions by a superscript$^{(0)}$ or a subscript $_0$, as convenient, we obtain, in a straightforward way, as in Duva and Simmonds (1991),

$$w^{(0)}=\nu_0(\xi),\quad u^{(0)}=-\nu_0'(\xi)\zeta \tag{19}$$

$$s^{(0)}=-(1/2)\nu_0'''(\xi)(1-\zeta^2),\quad s_\zeta^{(0)}=(1/6)\omega_0^2\nu_0(\xi)\zeta(1-\zeta^2), \tag{20}$$

where ν_0 and ω_0 satisfy the elementary beam equation,

$$\nu_0''''-\omega_0^2\nu_0=0,\quad 0<\xi<1 \tag{21}$$

and the boundary conditions

$$\nu_0(0)=\nu_0'(0)=\nu_0''(1)=\nu_0'''(1)=0. \tag{22}$$

Note that the elementary beam theory solution satisfies *all* the boundary conditions, (15)–(17), if $\epsilon=0$. (Interesting) problems arise when we attempt to improve elementary theory by including the effects of $O(\epsilon)$-terms.

Corrections to Elementary Beam Theory—Edge Effects

The structure of our governing Eqs., (11)–(18), and especially the appearance of ϵ to the first power in (12), suggests that we seek *tentative* asymptotic solutions of the form

$$f=f^{(0)}(\xi,\zeta)+\epsilon f^{(2)}(\xi,\zeta)+\ \ldots\ +\epsilon^N f^{(2N)}(\xi,\zeta)+O(\epsilon^{N+1}). \tag{23}$$

(The reason for the even superscripts on the f's is that, when we come to consider end effects, we shall see that the boundary condition of no displacement can be satisfied to all orders in ϵ only if f is expanded in powers of $\epsilon^{1/2}$. It also turns out that $f^{(1)}\equiv 0$.) From (11)–(14), (16), and (18)–(21), we obtain

$$w^{(2)}=\nu_2(\xi),\quad u^{(2)}=-\nu_2'(\xi)\zeta-(1/2)\tilde{E}^{1/2}\nu_0'''(\xi)(\zeta-\zeta^3/3). \tag{24}$$

$$s^{(2)}=-(1/2)[\nu_2'''(\xi)+(1/12)\tilde{E}^{1/2}\omega_0^2\nu_0'(\xi)(5-\zeta^2)](1-\zeta^2) \tag{25}$$

$$s_\zeta^{(2)}=(1/6)[\omega_0^2\nu_2(\xi)+\omega_2^2\nu_0(\xi)+(1/20)\tilde{E}^{1/2}\omega_0^2\nu_0''(\xi)(1-\zeta^2)]\zeta(1-\zeta^2), \tag{26}$$

where

$$\nu_2''''-\omega_0^2\nu_2=\omega_2^2\nu_0(\xi)-(2/5)\tilde{E}^{1/2}\omega_0^2\nu_0''(\xi),\quad 0<\xi<1. \tag{27}$$

In (24)–(27) and in the following, functions of ξ only are denoted by a subscript. These expressions represent first-order corrections to elementary beam theory. Note that in obtaining these corrections, we did nothing more than integrate polynomials in ζ. The determination of ω_2 will be discussed presently.

Although the traction-free face conditions (16) are met by (25) and (26), we cannot choose ν_2 to meet the end boundary conditions that follow from $(15)_1$ and (17), namely $u^{(2)}(0,\zeta)=0$ and $u^{(2)}{}_{,\xi}(1,\zeta)=s^{(2)}(1,\zeta)=0$, because the ζ-variations in the ν_0 and ν_2-terms in $(24)_2$ and (25) do not match. The cause of this discrepancy is that we have tacitly assumed that differentiation with respect to ξ does not change orders of magnitude with respect to ϵ. However, near the ends, this is not true.

The Left End Zone. First, let us focus on the left end of the beam to see how to determine a *supplementary, decaying end-zone solution* such that this solution plus the interior solution satisfy the conditions of zero total displacement (at least asymptotically). Guided by the scaling of variables introduced by Horgan and Simmonds (1991) in a *static* analysis of a semi-infinite, elastically orthotropic strip weak in shear where the ratio of the axial to the transverse displacement is $O(\epsilon^{1/2})$[22], we introduce a new dimensionless axial variable, α, and new *supplementary* dimensionless displacements and stresses, denoted by an overbar, by setting

$$x=(c/\epsilon)^{1/2}\tilde{E}^{1/4}H\alpha \tag{28}$$

$$\{U,W\}=W_0[\{\epsilon u,w\}+\epsilon^2\{\bar{u},(c/\epsilon)^{1/2}\tilde{E}^{1/4}\bar{w}\}]e^{i\Omega t} \tag{29}$$

$$\{\sigma_x,\tau,\sigma_z\}=(W_0E_xH/L^2)[\{s_\xi,\epsilon s,\epsilon^2 s_\zeta\}+(\epsilon/c)^{1/2}\tilde{E}^{-1/4}\{\bar{s}_\xi,(\epsilon/c)^{1/2}\tilde{E}^{-1/4}\bar{s},\tilde{E}^{-1/2}\bar{s}_\zeta\}]e^{i\Omega t}. \tag{30}$$

[22] In an elastically *isotropic* strip, the decaying axial and transverse displacements are of the *same* order of magnitude. This is why the present analysis differs from that of Duva and Simmonds (1991).

Downloaded 03 May 2010 to 171.66.16.247. Redistribution subject to ASME license or copyright; see http://www.asme.org/terms/Terms_Use.cfm

From (1), $(9)_5$, and (28)–(30), we conclude that the dimensionless supplemental stresses and displacements satisfy equations of motion of the form

$$\bar{s}_{\xi,\alpha}+\bar{s}_{,\zeta}+(1/3)c\tilde{E}^{1/2}\epsilon^3\omega^2\bar{u}=0,$$
$$(\epsilon/c)\bar{s}_{,\alpha}+\bar{s}_{\zeta,\zeta}+(1/3)c\tilde{E}\epsilon^3\omega^2\bar{w}=0. \quad (31)$$

Thus, as long as $\omega = O(1)$, i.e., for the low natural frequencies of a cantilevered beam, the supplementary fields satisfy static equations to within a relative error of $O(\epsilon^3)$.

The forms of (29) and (30) are chosen so that the supplementary end-zone solutions will decay. This necessitates discarding the tentative interior expansion, (23), and replacing it by

$$f=f^{(0)}(\xi,\zeta)+\epsilon f^{(2)}(\xi,\zeta)+\epsilon^{3/2}f^{(3)}(\xi,\zeta)+\ \ldots\ . \quad (32)$$

Because $f^{(1)}$ is found to be identically zero, we have omitted it from (32). The supplementary variables in the left end zone have expansions of the form

$$\bar{f}=\bar{f}^{(0)}(\alpha,\zeta)+\epsilon^{1/2}\bar{f}^{(1)}(\alpha,\zeta)+\ \ldots\ . \quad (33)$$

In particular, the boundary conditions (15), the interior solutions (24), the total displacement field (29), and the expansions (32) and (33) imply that

$$\nu_2(0)=0, \quad \bar{u}^{(0)}(0,\zeta)=\nu_2'(0)\zeta$$
$$+(1/2)\tilde{E}^{1/2}\nu_0'''(0)(\zeta-\zeta^3/3). \quad (34)$$

Gregory and Wan (1984) and Lin and Wan (1988) have derived necessary conditions on the end data if all stresses and displacements in a semi-infinite elastic strip, traction-free on its sides, are to decay (exponentially) to zero as one moves away from the end of the strip. Horgan and Simmonds (1991) have shown how these conditions may be simplified for a strip weak in shear (i.e., as $\epsilon \to 0$). For the case at hand, the only relevant condition is their Eq. $(6.21)_2$,

$$\int_{-1}^{1}\zeta\bar{u}^{(0)}(0,\zeta)d\zeta=0, \quad (35)$$

which, by $(34)_2$, yields

$$\nu_2'(0)=-(2/5)\tilde{E}^{1/2}\nu_0'''(0). \quad (36)$$

(The other nontrivial necessary condition of Horgan and Simmonds, their Eq. (9.18), affects the choice of ν_3.)

The Right-End Zone. To cancel the tractions produced on the right end of the beam by the interior solutions, we must impose the supplementary dimensionless stresses

$$-s(1,\zeta,\epsilon) \text{ and } -s_\xi(1,\zeta,\epsilon)=-u_{,\xi}(1,\zeta,\epsilon)-\nu\tilde{E}\epsilon^2 s_\zeta(1,\zeta,\epsilon). \quad (37)$$

But if these imposed stresses are to produce solutions that decay as we move away from the right end of the beam, they must be self-equilibrating, i.e.,

$$\int_{-1}^{1}s(1,\zeta,\epsilon)d\zeta=\int_{-1}^{1}\zeta s_\xi(1,\zeta,\epsilon)d\zeta=0 \text{ for all } \epsilon, \quad (38)$$

the net axial force being identically zero by (18). Thus, $(24)_2$ and (25) imply that

$$\nu_2''(1)=-(2/5)\tilde{E}^{1/2}\omega_0^2\nu_0(1),$$
$$\nu_2'''(1)=-(2/5)\tilde{E}^{1/2}\omega_0^2\nu_0'(1). \quad (39)$$

The First-Order Correction to the Natural Frequencies of Elementary Beam Theory

Let $\lambda_i^2=(\omega_0)_i$, $i = 0, 1, \ldots$ denote the natural frequencies of elementary beam theory and let $\nu_0 = \phi_i$ denote the associated eigenfunctions, normalized so that

$$\int_0^1\phi_i(\xi)\phi_j(\xi)d\xi=\delta_{ij}, \quad (40)$$

where δ_{ij} is the Kronecker delta. To find ω_2, we multiply both sides of (27) by ϕ_i, and integrate from $\xi = 0$ to $\xi = 1$. Noting (21), (22), $(34)_1$, (36), (39), and (40), we find that

$$\omega_2^2=[\nu_2'''(\xi)\phi_i(\xi)-\nu_2''(\xi)\phi_i'(\xi)+\nu_2'(\xi)\phi_i''(\xi)$$
$$-\nu_2(\xi)\phi_i'''(\xi)]_0^1+(2/5)\lambda_i^4\tilde{E}^{1/2}\int_0^1\phi_i''(\xi)\phi_i(\xi)d\xi$$
$$=-(2/5)\tilde{E}^{1/2}\lambda_i^6C_i, \quad (41)$$

where

$$C_i\equiv\lambda_i^{-6}\int_0^1[\phi_i'''(\xi)]^2d\xi$$
$$=\int_0^1[\sinh\lambda_i\xi-\sin\lambda_i\xi-\sigma_i(\cosh\lambda_i\xi+\cos\lambda_i\xi)]d\xi \quad (42)$$

and

$$\sigma_i=\frac{\sinh\lambda_i-\sin\lambda_i}{\cosh\lambda_i+\cos\lambda_i}. \quad (43)$$

With the aid of the numerical tables in Blevins (1979), we find that

$$C_i=\begin{cases}1.321\ \ldots\ ,i=0\\1.471\ \ldots\ ,i=1\\1.252\ \ldots\ ,i=2\\1.181\ \ldots\ ,i=3\end{cases}$$
$$\sim 1 \text{ as } i\to\infty. \quad (44)$$

Thus,

$$(\omega/\omega_0)_i^2=1-(2/5)C_i\tilde{E}^{1/2}\lambda_i^2(H/L)$$
$$+O(H^2/L^2), \quad i=0,1,\ \ldots\ . \quad (45)$$

An analysis of the Timoshenko beam equations, Eqs. (19)–(21) of Duva and Simmonds (1991) showed that if we choose the shear correction factor to be

$$k=(5/3)c, \quad (46)$$

where c is the constant in (8), then Timoshenko theory yields an expression for $(\omega/\omega_0)_i^2$ that is identical to (45) up to the $O(H^2/L^2)$-term. However, as this value of k emerges only *after* an analysis of edge effects, it seems much simpler to abandon Timoshenko theory and instead use the iteration scheme outlined here to improve elementary theory.

Acknowledgments

We thank our colleague, C. O. Horgan, for a careful reading of the manuscript.

References

Blevins, R. D., 1979, *Formulas for Natural Frequency and Mode Shape*, van Nostrand Reinhold, New York.

Duva, J. M., and Simmonds, J. G., 1991, "The Usefulness of Elementary Theory for the Linear Vibrations of Layered, Orthotropic Elastic Beams and Corrections due to Two-Dimensional End Effects," ASME JOURNAL OF APPLIED MECHANICS, Vol. 58, p. 175–180.

Gregory, R.D., and Wan, F. Y. M., 1984, "Decaying States of Plane Strain in a Semi-Infinite Strip and Boundary Conditions for Plate Theory," *J. Elasticity*, Vol. 14, pp. 27–64.

Horgan, C. O., and Simmonds, J. G., 1991, "Asymptotic Analysis of an End-Loaded, Transversely Isotropic, Elastic, Semi-Infinite Strip Weak in Shear," *Int. J. Solids Struct.*, Vol. 27, pp. 1895–1914.

Ladevèze, P., ed., 1985, *Local Effects in the Analysis of Structures*, Elsevier, Amsterdam.

Lin, Y., and Wan, F. Y. M., 1988, "First Integrals and the Residual Solution for Orthotropic Plates in Plane Strain or Axisymmetric Deformation," *Studies in Appl. Math.*, Vol. 79, pp. 93–125.

Simmonds, J. G., 1976, "Recent Advances in Shell Theory," *Advances in Engineering Science* (13th Annual Meeting of the Society of Engineering Science), NASA CP-2001, pp. 617–626.

Downloaded 03 May 2010 to 171.66.16.247. Redistribution subject to ASME license or copyright; see http://www.asme.org/terms/Terms_Use.cfm

Analysis of a Pendulum on a Rotating Arm

Bertram A. Schmidt[1] and David G. McDowell[23]

Introduction

Pendulums with oscillating base motions have been studied by many investigators. Stephenson (1907), Lowenstern (1932), Phelps and Hunter (1965), Ryland and Meirovitch (1977), and Schmidt (1980, 1981, 1983, 1990) present interesting phenomena involving pendulums with imposed oscillations.

In this work, we consider a pendulum suspended on a rotating arm. The system is shown in Fig. 1. The shaft rotates about the y_1-axis with an angular rate ω. The pendulum is pivoted (axis A-A) on an arm rigidly attached to the shaft. This rotation is described by the angle θ. The gravitational vector is in the negative z_1-direction. The length of the arm is R and the length of the pendulum is r. In this investigation r is nearly equal to R, but is smaller than R.

It would appear that there would be one stable equilibrium position: $\theta = 0$. We find that $\theta = \pi$ can also be a stable equilibrium position. This position is made stable by the gravity force which acts with respect to the pendulum as an oscillating force. This causes a small oscillation in θ which, along with gravity, causes an average restoring moment.

The motion is described by one second-order differential equation. We apply a transformation to the linearized version of this and use the method of averaging (see Bogoliuboff and Mitropolskiy (1962)). This shows the extra stable equilibrium position. We also present approximate solutions near this stable equilibrium position. Since we use an approximate differential equation in our analysis, we verify our result with a numerical investigation.

The Analysis

The differential equation which describes the motion is

$$mr^2\frac{d^2\theta}{dt^2}+c\frac{d\theta}{dt}+mRr\omega^2\sin\theta+mr^2\omega^2\sin\theta\cos\theta + mrg\sin\theta\sin\omega t=0,$$

where ω is the angular rate of the shaft, c is the damping coefficient, g is the gravitational constant, m is the mass, t is time, r is the length of the pendulum, and R is the distance from the pivot to the center of the shaft. In this problem we restrict r to be smaller than R and nearly equal to R. To indicate magnitudes of some terms, we introduce a small, positive, dimensionless parameter $\epsilon = ((R-r)/r)^{1/2}$. We establish other dimensionless variables and parameters. Let $\epsilon a = c/mr^2\omega$, $\epsilon\gamma = g/r\omega^2$, and $\tau = \omega t$. The parameters a and γ are positive and independent of ϵ. In terms of these variables and parameters, the equation of motion becomes

$$\frac{d^2\theta}{d\tau^2}+\epsilon a\frac{d\theta}{d\tau}+(1+\epsilon^2)\sin\theta+\sin\theta\cos\theta + \epsilon\gamma\sin\theta\sin\tau=0. \quad (1)$$

In this work, we consider the linear approximation of Eq. (1) near $\theta = \pi$. It is

$$\frac{d^2\phi}{d\tau^2}+\epsilon a\frac{d\phi}{d\tau}-\epsilon^2\phi-\epsilon\gamma\phi\sin\tau=0, \quad (2)$$

where $\phi = \theta - \pi$.

To obtain a system of equations in the standard form for the method of averaging, we apply the transformation $d\phi/d\tau = \epsilon\beta - \epsilon\gamma\phi\cos\tau$, where β is a new variable. This gives a system in the standard form for the method of averaging. It is

$$\frac{d\phi}{d\tau}=\epsilon\beta-\epsilon\gamma\phi\cos\tau$$

$$\frac{d\beta}{d\tau}=\epsilon\gamma(\beta-\gamma\phi\cos\tau)\cos\tau-\epsilon a(\beta-\gamma\phi\cos\tau)+\epsilon\phi. \quad (3)$$

Averaging gives

$$\frac{d\Phi}{d\tau}=\epsilon\mathrm{B}$$

$$\frac{d\mathrm{B}}{d\tau}=-\frac{1}{2}\epsilon\gamma^2\Phi-\epsilon a\mathrm{B}+\epsilon\Phi,$$

or, equivalently,

$$\frac{d^2\Phi}{d\tau^2}+\epsilon a\frac{d\Phi}{d\tau}+\frac{\epsilon^2\gamma^2}{2}\Phi-\epsilon^2\Phi=0, \quad (4)$$

where Φ and B are the averaged variables corresponding to ϕ and β.

If $\gamma^2 > 2$, Eq. (4) yields a damped oscillatory solution or a diminishing exponential solution. This indicates stable equilibrium at $\Phi = 0$. In terms of the original variables and parameters we conclude that $\theta = \pi$ is a stable equilibrium position if $g^2/(\omega^4 r(R-r)) > 2$.

We refer to a theorem of Balachandra and Sethna (1975) to provide validity to our result. This theorem applies to the first approximation of the method of averaging for a more general set of hypotheses than are needed for this problem. By this theorem we can state there is a solution to (2) which approaches the equilibrium solution to (4) as $\epsilon \to 0$ for all τ. This theorem establishes that there is a solution to (2) which approaches zero.

We continue the method of averaging to find more complete approximate solutions near the stable equilibrium solution ϕ

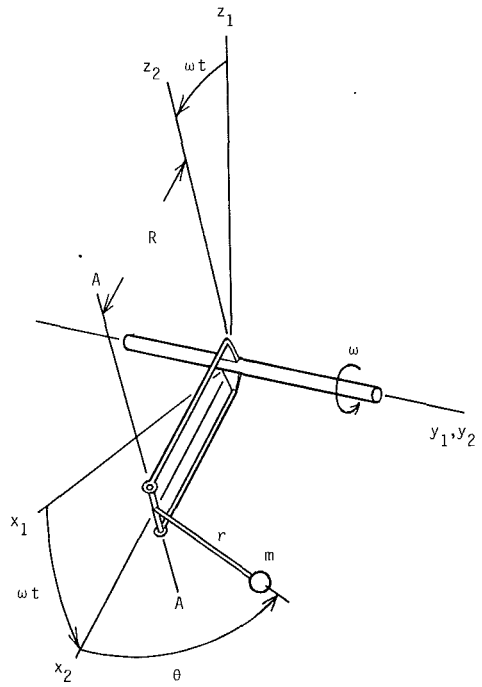

THE PENDULUM

Fig. 1

[23]Department of Mathematics, Central Michigan University, Mount Pleasant, MI 48859.

Manuscript received by the ASME Applied Mechanics Division, Aug. 15, 1990; final revision, Mar. 16, 1991.

Copyright © 1992 by ASME
Downloaded 03 May 2010 to 171.66.16.247. Redistribution subject to ASME license or copyright; see http://www.asme.org/terms/Terms_Use.cfm

Table 1 The method of averaging solution and the numerical solution

τ	Meth. of Av. $\phi \times 10^3$	Num. $\phi \times 10^3$
10	7.625	7.671
20	3.833	3.890
30	1.393	1.459
40	−0.685	−0.643
50	−1.786	−1.760
60	−2.082	−2.072
70	−1.641	−1.638
80	−1.300	−1.302
90	−0.568	−0.568
100	−0.134	−0.135
110	0.205	0.206
120	0.335	0.335
130	0.398	0.398
140	0.277	0.277
150	0.206	0.204

$= 0$. The improved first approximation expresses the slow motion plus the first-order fast part. The improved second approximation gives the slow motion along with the first and second-order fast parts. Following the method of averaging, we find the improved first approximation. It is

$$\phi = \Phi - \epsilon\gamma\Phi \sin \tau, \tag{5}$$

where Φ is a solution to (4). The improved first approximation (5) satisfies (2) through terms of order ϵ, i.e., the error is of order ϵ^2. Continuing the method of averaging, we find the improved second approximation. It is

$$\phi = \Phi - \epsilon\gamma\Phi \sin \tau + \epsilon^2\left[-\frac{\gamma^2}{8}\Phi \cos 2\tau - \epsilon^{-1}2\gamma \frac{d\Phi}{d\tau} \cos \tau - a\gamma\Phi \cos \tau \right], \tag{6}$$

where Φ is a solution to (4). In this problem, the slow Eq. (4) does not change when we consider the second approximation. Equation (6) satisfies (2) through terms of order ϵ^2, i.e., the error is of order ϵ^3.

If interest is restricted to damped oscillatory solutions of (4), $(2\gamma^2 - 4 - a^2 > 0)$, the improved second approximation becomes:

$$\phi = e^{-\frac{1}{2}\epsilon a\tau}\left\{\left[A_1\left(1 - \epsilon\gamma \sin \tau - \frac{\epsilon^2\gamma^2}{8}\cos 2\tau\right) - A_2\epsilon^2\gamma\sqrt{2\gamma^2 - 4 - a^2}\cos \tau\right]\cos \frac{\epsilon}{2}\sqrt{2\gamma^2 - 4 - a^2}\,\tau + \left[A_2\left(1 - \epsilon\gamma \sin \tau - \frac{\epsilon^2\gamma^2}{8}\cos 2t\right) + A_1\epsilon^2\gamma\sqrt{2\gamma^2 - 4 - a^2}\cos \tau\right]\sin \frac{\epsilon}{2}\sqrt{2\gamma^2 - 4 - a^2}\tau\right\}, \tag{7}$$

where A_1 and A_2 are arbitrary constants. This approximate solution satisfies (2) through terms of order ϵ^2. Equation (7) shows ϕ to be made up of fast and slow oscillations with a slowly decaying multiplier.

Since our analysis was applied to a linear approximation of the equation of motion, we made a modest numerical investigation to verify our result. We found a numerical solution to the original differential Eq. (1) using the Runge-Kutta method of order four for this example: $\epsilon = .02$, $a = 2.5$, $\gamma = 4$, $\theta(0) = \pi + .01$, and $\theta'(0) = -.001$. For the step size, we used one tenth. In Table 1 we present some points in the numerical solution and corresponding values given by the second-order method of averaging solution (7). For this example, (7) becomes

$$\phi = .010146e^{-.025\tau}\left\{[.9872(1 - .08 \sin \tau - .0008 \cos 2\tau) - .00075 \cos \tau]\cos \frac{\sqrt{21.75}}{100}\tau + [.10104(1 - .08 \sin \tau - .0008 \cos 2\tau) + .007366 \cos \tau]\sin \frac{\sqrt{21.75}}{100}\tau\right\}. \tag{8}$$

Table 1 shows close agreement between the method of averaging solution, Eq. (8), and the Runge-Kutta solution. The difference between the two solutions appears to be less than 6×10^{-5}.

We conclude $\theta = \pi$ is a stable equilibrium position in the condition $g^2/(\omega^4 r(R - r)) > 2$. It can be noted that stability at the equilibrium position depends on gravity. If g were zero, this equilibrium position would be unstable.

References

Balachandra, M., and Sethna, P. R., 1975, "A Generalization of the Method of Averaging for Systems With Two Time Scales," *Archive for Rational Mechanics and Analysis*, Vol. 58, No. 3, pp. 261–283.

Bogoliuboff, N. M., and Mitropolskiy, Yu, A., 1962, *Asymptotic Methods in the Theory of Nonlinear Oscillations*, Gordon and Breach.

Lowenstern, E. R., 1932, "The Stabilizing Effect of Imposed Oscillations of High Frequency on a Dynamical System," *Philosophical Magazine*, Vol. 13, pp. 458–486.

Phelps, F. M., III, and Hunter, J. H., Jr., 1965, "An Analytical Solution of the Inverted Pendulum," *American Journal of Physics*, Vol. 33, pp. 285–295.

Ryland, G., II, and Meirovitch, L., 1977, "Stability Boundaries of a Swinging Spring With Oscillatory Support," *Journal of Sound and Vibration*, Vol. 51, No. 4, pp. 547–560.

Schmidt, B. A., 1980, "Vibrated Pendulum With a Mass Free to Move Radially," ASME JOURNAL OF APPLIED MECHANICS, Vol. 47, pp. 428–430.

Schmidt, B. A., 1981, "Pendulum With a Rotational Vibration," ASME JOURNAL OF APPLIED MECHANICS, Vol. 48, pp. 200–203.

Schmidt, B. A., 1983, "The Radially Flexible Pendulum Subjected to a High-Frequency Excitation," ASME JOURNAL OF APPLIED MECHANICS, Vol. 50, pp. 443–448.

Schmidt, B. A., 1990, "The Rotationally Flexible Pendulum Subjected to a High-Frequency Excitation," ASME JOURNAL OF APPLIED MECHANICS, Vol. 57, pp. 725–730.

Stephenson, A., 1907, "On a New Type of Dynamical Stability," *Memories and Proceedings of the Manchester Literary and Philosophical Society*, Vol. 52, pp. 1–10.

On Transverse Vibrations of a Rotating Disk of Uniform Strength

Uğur Güven[24]

Transverse, axisymmetric vibrations of a rotating disk of uniform strength is studied. Closed-form solution for the equation of transverse motion is obtained in terms of confluent hypergeometric functions.

1 Introduction

Much work has been done on transverse vibrations of rotating disks, but none of it has considered the effect of the radial displacement on the centrifugal inertia force. In fact, the centrifugal inertia force is a function of radial coordinates and radial displacements. This matter has been first pointed out by E. J. Brunelle and in his work (Brunelle, 1971) the centrifugal inertia force has been taken to be $\rho\Omega^2(r+u)$.

[24]Department of Mechanical Engineering, Yıldız University, Besiktas, Istanbul, Turkey.

Contributed by the Applied Mechanics Division of THE AMERICAN SOCIETY OF MECHANICAL ENGINEERS. Manuscript received by the ASME Applied Mechanics Division, Mar. 31, 1989; final revision, Dec. 20, 1989.

Downloaded 03 May 2010 to 171.66.16.247. Redistribution subject to ASME license or copyright; see http://www.asme.org/terms/Terms_Use.cfm

Table 1 The method of averaging solution and the numerical solution

τ	Meth. of Av. $\phi \times 10^3$	Num. $\phi \times 10^3$
10	7.625	7.671
20	3.833	3.890
30	1.393	1.459
40	−0.685	−0.643
50	−1.786	−1.760
60	−2.082	−2.072
70	−1.641	−1.638
80	−1.300	−1.302
90	−0.568	−0.568
100	−0.134	−0.135
110	0.205	0.206
120	0.335	0.335
130	0.398	0.398
140	0.277	0.277
150	0.206	0.204

$= 0$. The improved first approximation expresses the slow motion plus the first-order fast part. The improved second approximation gives the slow motion along with the first and second-order fast parts. Following the method of averaging, we find the improved first approximation. It is

$$\phi = \Phi - \epsilon\gamma\Phi \sin \tau, \tag{5}$$

where Φ is a solution to (4). The improved first approximation (5) satisfies (2) through terms of order ϵ, i.e., the error is of order ϵ^2. Continuing the method of averaging, we find the improved second approximation. It is

$$\phi = \Phi - \epsilon\gamma\Phi \sin \tau + \epsilon^2\left[-\frac{\gamma^2}{8}\Phi \cos 2\tau - \epsilon^{-1}2\gamma \frac{d\Phi}{d\tau} \cos \tau - a\gamma\Phi \cos \tau \right], \tag{6}$$

where Φ is a solution to (4). In this problem, the slow Eq. (4) does not change when we consider the second approximation. Equation (6) satisfies (2) through terms of order ϵ^2, i.e., the error is of order ϵ^3.

If interest is restricted to damped oscillatory solutions of (4), $(2\gamma^2 - 4 - a^2 > 0)$, the improved second approximation becomes:

$$\phi = e^{-\frac{1}{2}\epsilon a\tau}\left\{\left[A_1\left(1 - \epsilon\gamma \sin \tau - \frac{\epsilon^2\gamma^2}{8}\cos 2\tau\right) - A_2\epsilon^2\gamma\sqrt{2\gamma^2 - 4 - a^2}\cos \tau\right]\cos \frac{\epsilon}{2}\sqrt{2\gamma^2 - 4 - a^2}\,\tau + \left[A_2\left(1 - \epsilon\gamma \sin \tau - \frac{\epsilon^2\gamma^2}{8}\cos 2t\right) + A_1\epsilon^2\gamma\sqrt{2\gamma^2 - 4 - a^2}\cos \tau\right]\sin \frac{\epsilon}{2}\sqrt{2\gamma^2 - 4 - a^2}\tau\right\}, \tag{7}$$

where A_1 and A_2 are arbitrary constants. This approximate solution satisfies (2) through terms of order ϵ^2. Equation (7) shows ϕ to be made up of fast and slow oscillations with a slowly decaying multiplier.

Since our analysis was applied to a linear approximation of the equation of motion, we made a modest numerical investigation to verify our result. We found a numerical solution to the original differential Eq. (1) using the Runge-Kutta method of order four for this example: $\epsilon = .02$, $a = 2.5$, $\gamma = 4$, $\theta(0) = \pi + .01$, and $\theta'(0) = -.001$. For the step size, we used one tenth. In Table 1 we present some points in the numerical solution and corresponding values given by the second-order method of averaging solution (7). For this example, (7) becomes

$$\phi = .010146e^{-.025\tau}\left\{[.9872(1 - .08 \sin \tau - .0008 \cos 2\tau) - .00075 \cos \tau]\cos \frac{\sqrt{21.75}}{100}\tau + [.10104(1 - .08 \sin \tau - .0008 \cos 2\tau) + .007366 \cos \tau]\sin \frac{\sqrt{21.75}}{100}\tau\right\}. \tag{8}$$

Table 1 shows close agreement between the method of averaging solution, Eq. (8), and the Runge-Kutta solution. The difference between the two solutions appears to be less than 6×10^{-5}.

We conclude $\theta = \pi$ is a stable equilibrium position in the condition $g^2/(\omega^4 r(R - r)) > 2$. It can be noted that stability at the equilibrium position depends on gravity. If g were zero, this equilibrium position would be unstable.

References

Balachandra, M., and Sethna, P. R., 1975, "A Generalization of the Method of Averaging for Systems With Two Time Scales," *Archive for Rational Mechanics and Analysis*, Vol. 58, No. 3, pp. 261–283.

Bogoliuboff, N. M., and Mitropolskiy, Yu, A., 1962, *Asymptotic Methods in the Theory of Nonlinear Oscillations*, Gordon and Breach.

Lowenstern, E. R., 1932, "The Stabilizing Effect of Imposed Oscillations of High Frequency on a Dynamical System," *Philosophical Magazine*, Vol. 13, pp. 458–486.

Phelps, F. M., III, and Hunter, J. H., Jr., 1965, "An Analytical Solution of the Inverted Pendulum," *American Journal of Physics*, Vol. 33, pp. 285–295.

Ryland, G., II, and Meirovitch, L., 1977, "Stability Boundaries of a Swinging Spring With Oscillatory Support," *Journal of Sound and Vibration*, Vol. 51, No. 4, pp. 547–560.

Schmidt, B. A., 1980, "Vibrated Pendulum With a Mass Free to Move Radially," ASME JOURNAL OF APPLIED MECHANICS, Vol. 47, pp. 428–430.

Schmidt, B. A., 1981, "Pendulum With a Rotational Vibration," ASME JOURNAL OF APPLIED MECHANICS, Vol. 48, pp. 200–203.

Schmidt, B. A., 1983, "The Radially Flexible Pendulum Subjected to a High-Frequency Excitation," ASME JOURNAL OF APPLIED MECHANICS, Vol. 50, pp. 443–448.

Schmidt, B. A., 1990, "The Rotationally Flexible Pendulum Subjected to a High-Frequency Excitation," ASME JOURNAL OF APPLIED MECHANICS, Vol. 57, pp. 725–730.

Stephenson, A., 1907, "On a New Type of Dynamical Stability," *Memories and Proceedings of the Manchester Literary and Philosophical Society*, Vol. 52, pp. 1–10.

On Transverse Vibrations of a Rotating Disk of Uniform Strength

Uğur Güven[24]

Transverse, axisymmetric vibrations of a rotating disk of uniform strength is studied. Closed-form solution for the equation of transverse motion is obtained in terms of confluent hypergeometric functions.

1 Introduction

Much work has been done on transverse vibrations of rotating disks, but none of it has considered the effect of the radial displacement on the centrifugal inertia force. In fact, the centrifugal inertia force is a function of radial coordinates and radial displacements. This matter has been first pointed out by E. J. Brunelle and in his work (Brunelle, 1971) the centrifugal inertia force has been taken to be $\rho\Omega^2(r+u)$.

[24]Department of Mechanical Engineering, Yıldız University, Besiktas, Istanbul, Turkey.

Contributed by the Applied Mechanics Division of THE AMERICAN SOCIETY OF MECHANICAL ENGINEERS. Manuscript received by the ASME Applied Mechanics Division, Mar. 31, 1989; final revision, Dec. 20, 1989.

Copyright © 1992 by ASME
Downloaded 03 May 2010 to 171.66.16.247. Redistribution subject to ASME license or copyright; see http://www.asme.org/terms/Terms_Use.cfm

In this work, transverse vibrations of a rotating disk of uniform strength is considered. The analysis is based on the plane-stress state assumptions with rotational symmetry of the infinitesimal theory of elasticity. It is assumed that the disk is thin and displacements are small everywhere. Moreover, the actual value of the centrifugal inertia force is taken into account.

2 Variation of Thickness of the Disk of Uniform Strength

The equilibrium equation and tangential strain can be expressed in polar coordinate form as (e.g., Timoshenko and Goodier, 1952)

$$\frac{d}{dr}(hr\sigma_r) - h\sigma_\theta + hr\,F_r = 0 \tag{1}$$

$$\epsilon_\theta = \frac{u}{r} = (\sigma_\theta - \nu\sigma_r)/E \tag{2}$$

where h is the thickness of the disk and F_r is the centrifugal force. The actual value of F_r may be written as follows:

$$F_r = \rho\Omega^2(r+u) \tag{3}$$

where ρ is the mass per unit volume, Ω is the angular velocity, r is the initial undeformed radius, and u is the radial displacement.

If the disk is of uniform strength, the stresses at all cross-sections should be the same (Stodala, 1945; Hartog, 1952), i.e.,

$$\sigma_r = \sigma_\theta = \sigma_o. \tag{4}$$

From (2(1)), (2(2)), (2(3)), and (2(4)), we obtain

$$h = h_o e^{\frac{-\rho\Omega^2}{2}\left[\frac{1}{\sigma_o}+\frac{1-\nu}{E}\right]r^2} \tag{5}$$

where h_o is the thickness of the disk at $r = 0$.

3 Solution of the Equation of Transverse Motion

The equation of the transverse motion of an elementary mass $\rho hr\,\delta_\theta\,\delta_r$ for negligibly small rigidity may be written in the form

$$\rho\frac{\partial^2 w}{\partial r^2} = \frac{1}{hr}\frac{\partial}{\partial r}\left(hr\sigma_r\frac{\partial w}{\partial r}\right) + \frac{\sigma_\theta}{r^2}\frac{\partial^2 w}{\partial\Theta^2} \tag{6}$$

let us take the transverse deflections in the following form

$$w = W(r)\,\cos s\theta\,\cos pt \tag{7}$$

and using relations (2(4)) and (2(5)) in equation (6) we get

$$\frac{d^2W}{dr^2} + \left(\frac{1}{r} - 2kr\right)\frac{dW}{dr} + \left(\frac{\rho p^2}{\sigma_o} - \frac{s^2}{r^2}\right)W = 0 \tag{8}$$

where

$$k = \frac{\rho\Omega^2}{2}\left(\frac{1}{\sigma_o} + \frac{1-\nu}{E}\right)$$

s is an integer, and p is the frequency of vibration.

The general solution of (8) can be written in terms of confluent hypergeometric functions as follows (Slater and Lit, 1960)

$$W = \bar{r}^s e^{kr^2} F\left[1 - \frac{s}{2} + \frac{\rho P^2}{4\sigma_o k};\ 1-s;\ -kr^2\right] \tag{9}$$

and transverse deflections becomes, finally,

$$w = \bar{r}^s e^{kr^2} F\left[1 - \frac{s}{2} + \frac{\rho P^2}{4\sigma_o k};\ 1-s;\ -kr^2\right]\cos s\theta\,\cos pt. \tag{10}$$

References

Brunelle, E. J., 1971, "Stress Redistribution and Instability of Rotating Beams and Disks," *AIAA Journal*, Vol. 9, pp. 758–759.

Hartog, D., 1952, *Advanced Strength of Materials*, McGraw-Hill, New York.

Slater, L. J., and Lit, D., 1960, *Confluent Hypergeometric Functions*, Cambridge University Press, pp. 89–92.

Stodala, A., 1945, *Steam and Gas Turbine*, Peter Smith, New York.

Timoshenko, S., 1964, *Vibration Problems in Engineering*, D. Van Nostrand, New York.

Timoshenko, S., and Goodier, J. N., 1952, *Theory of Elasticity*, McGraw-Hill, New York.

Downloaded 03 May 2010 to 171.66.16.247. Redistribution subject to ASME license or copyright; see http://www.asme.org/terms/Terms_Use.cfm

Journal of Applied Mechanics

Discussion

Stability of Linear Conservative Gyroscopic Systems[1]

B. L. Ly[2]. The author's method yields excellent results, but it requires the determination of some parameters by trial and error. Because zero-parameter criteria are easy to use, the writer feels it is still worthwhile to improve on them. For this reason, the writer has derived a zero-parameter sufficient condition for instability and one for stability of a linear conservative gyroscopic system. He would like to present the findings here as a discussion.

A stable conservative gyroscopic system described by Eq. (2) in the paper admits periodic solutions. Let $x=(u+iv)e^{i\omega t}$, where u and v are real vectors. After the real and the imaginary terms are collected separately, the following equations are obtained:

$$(K-\omega^2 I)u-\omega Cv=0 \tag{5}$$

$$(K-\omega^2 I)v+\omega Cu=0. \tag{6}$$

Eliminate v from (5) and (6) to yield

$$[(K-\omega^2 I)C^{-1}(K-\omega^2 I)+\omega^2 C]u=0. \tag{7}$$

Although (7) is more complicated than (2), it has one major advantage. Namely, an algebraic equation in ω^2 can be obtained by performing an inner product on (7), and it is easier to study the stability of the system from the behavior of ω^2 as revealed by this algebraic equation. It is noted that the inner products $u^T(K-\omega^2 I)C^{-1}(K-\omega^2 I)u$ and u^TCu are equal to zero because C is skew. To obtain a nontrivial algebraic equation, (7) will be premultiplied by u^TC, resulting in

$$(u^Tu)\omega^4-[u^T(CKC^{-1}+K-C^2)u]\omega^2+u^TCKC^{-1}Ku=0, \tag{8}$$

which is the desired algebraic equation.

The system is unstable if ω^2 is negative or complex. On the other hand, the system will be stable (periodic) if ω^2 remains positive. The proposed sufficient condition for instability and that for stability follow from (8) immediately.

A Sufficient Condition For Instability

The system is unstable if any one of the following three conditions is satisfied:

$$u^T(CKC^{-1}+K-C^2)u<0, \tag{9}$$

or

$$u^TCKC^{-1}Ku<0 \tag{10}$$

or

$$\left[\frac{u^T(CKC^{-1}+K-C^2)u}{2u^Tu}\right]^2-\frac{u^TCKC^{-1}Ku}{u^Tu}<0. \tag{11}$$

The Cauchy-Schwartz inequality can be used to show that (11) is implied by

$$u^T(C^{-1}KC+K-C^2)(CKC^{-1}+K-C^2)u-4u^TCKC^{-1}Ku<0. \tag{12}$$

With the identity $u^TAu=u^TA_su$, where $A_s=(A^T+A)/2$, for any real matrix A, $A_s>0$ (or $A_s<0$) is sufficient for $u^TAu>0$ (or $u^TAu<0$). Therefore, a sufficient condition in terms of the operators for the system to be unstable is:

(A.1) $2(K-C^2)+C^{-1}KC+CKC^{-1}<0$, or

(A.2) $CKC^{-1}K+KC^{-1}KC<0$, or

(A.3) $(C^{-1}KC+K-C^2)(CKC^{-1}+K-C^2)-2(CKC^{-1}K+KC^{-1}KC)<0.$

The matrices in the above expressions are symmetric. Their negative-definiteness can be verified by using the Sylvester criteria. The union of the regions defined by (A.1), (A.2), and (A.3) is a domain of instability.

For the two-degree-of-freedom system described by (3) in the paper, the system is unstable if $k_1+k_2+16<0$, or $k_1k_2<0$, or $(k_1+k_2+16)^2-4k_1k_2<0$, according to (A.1), (A.2), and (A.3). The result happens to be the same as the exact solution because all the matrix products are diagonal. For a 2-DOF system, the product of two skew matrices are diagonal.

B Sufficient Condition For Stability

The solution of the gyroscopic system is stable (periodic) if all the following three conditions are satisfied:

$$u^T(CKC^{-1}+K-C^2)u>0, \tag{13}$$

$$u^TCKC^{-1}Ku>0, \tag{14}$$

and

$$\left[\frac{u^T(CKC^{-1}+K-C^2)u}{2u^Tu}\right]^2-\frac{u^TCKC^{-1}Ku}{u^Tu}>0. \tag{15}$$

An approximation will be made to simplify (15). Let us require that (15) be true for all real vectors, including p which is the eigenvector in the eigenvalue problem

$$(CKC^{-1}+K-C^2)p=\lambda p. \tag{16}$$

Then, (15) becomes

$$p^T[(CKC^{-1}+K-C^2)^2-4CKC^{-1}K]p>0. \tag{17}$$

Consequently, a sufficient condition for stability is:

(B.1) $2(K-C^2)+C^{-1}KC+CKC^{-1}>0$, and

(B.2) $CKC^{-1}K+KC^{-1}KC>0$, and

(B.3) $(CKC^{-1}+K-C^2)^2+(C^{-1}KC+K-C^2)^2-4(CKC^{-1}K+KC^{-1}KC)>0.$

The intersection of the regions in (B.1), (B.2), and (B.3) is a domain of stability.

[1] By J. A. Walker and published in the March 1991 issue of the JOURNAL OF APPLIED MECHANICS, Vol. 58, pp. 229–232.

[2] AECL-CANDU Ops., Mississauga, Ontario, L5K 1B2, Canada.

Copyright © 1992 by ASME
Downloaded 03 May 2010 to 171.66.16.247. Redistribution subject to ASME license or copyright; see http://www.asme.org/terms/Terms_Use.cfm

Using the present criterion, the same 2-DOF system in (3) is found to be stable if all the conditions: $k_1k_2+16>0$, $k_1k_2>0$, and $(k_1+k_2+16)^2-4k_1k_2>0$ are satisfied. Again, the result is the same as the exact solution.

The present criteria depend entirely on the characteristics of the system and do not require determination of any parameters. For the simple example, the present criteria give a good result. However, the present method, as any other zero-parameter methods, does not provide a way for improving the results. The author's method, therefore, is superior in this regard and is valuable if a very accurate result is desired.

Mixing in a Closed Room by the Action of Two Fans[3]

F. H. Ling[4]. A mixing problem of practical interest is studied from the viewpoint of chaotic dynamics in this paper. The modeling and the velocity field solution presented in Sections 2–4 are basically correct, but the results in Section 5 are rather misleading.

1 The authors used generalized dimensions to measure how much a trajectory fills the room; this is improper. Since the phase volume of a Hamiltonian system is preserved, its chaotic orbit fills up eventually a finite region in the phase space, and all of the generalized dimensions of the chaotic trajectory should be equal to the embedding dimensions. KAM tori prevent some parts of the phase space from being visited by particle trajectories, but they can not possibly force the chaotic trajectories to occur in a zero volume subspace. Even for a non-Hamiltonian mixing system, it is hard to imagine that the phase volume will shrink to zero.

2 The authors' statement that "the correlation integral method produces a more physical measure than the fractal (Hausdorff) dimension" (Section 5.1) is incorrect. Considering the (fractal) generalized dimensions (Grassberger and Procaccia, 1983),

$$D_q=\frac{1}{1-q}\lim_{\epsilon\to 0}\frac{\ln\sum_{i=1}^{N(\epsilon)}P_i^q(\epsilon)}{\ln(1/\epsilon)},\quad q\geq 0,\ q\neq 1,$$

where $N(\epsilon)$ is the number of nonempty boxes of a partitioning with the length scale ϵ, and $P_i(\epsilon)$ is the probability for a point of a fractal set to fall in box i of the partitioning. It is easy to prove that for a strict self-similar fractal set like the Cantor set, all generalized dimensions are the same. Moreover, if the distribution of the points in a set is uniform, all its generalized dimensions are equal to the embedding dimension. However, this is only an idealized case; almost all numerically generated fractal sets and those existing in nature are not strictly self-similar, and they can often be considered as a combination of several strict self-similar fractal sets. For such a combined set, Ling (1989) proved that the generalized dimensions with $q<1$ such as the capacity ($q=0$) are equal to the maximum of those of the component sets, and the generalized dimensions with $q>1$ such as the correlation dimension ($q=2$) are equal to the minimum of those of the component sets. Therefore, although more details of the fractal set are required for the calculation of the correlation dimension, there is no evidence to indicate that the correlation dimension is physically more meaningful than the capacity. In practical applications, the selection of a certain generalized dimension is guided almost solely by the convenience of computation. No one of the generalized dimensions can be used to measure the uniformity of the mixture.

It is noticed that there are also some new developments in the box-counting algorithm. One may plot the curve of $\ln\sum_{i=1}^{N(\epsilon)}P_i^q(\epsilon)$ versus $\ln(1/\epsilon)$ using box-counting results and measure the slope of its straight portion to determine the generalized dimensions (Ling, 1988; Ling, 1989; Liebovitch and Toth, 1989; Ling and Schmidt, 1991). By using this approach, the correlation dimension can be calculated more efficiently than by using the correlation integral.

3 Unlike the Aref-blinking-vortex system, which is integrable when two vortices act simultaneously, the two fan mixing system discussed in the paper has no apparent integrable limit. The steady case ($T\to\infty$, and the axes of both fans aligned) is very unlikely to be integrable, since the system is spatially three-dimensional, and there is a good chance for chaos to occur even if no time dependence is involved. Therefore, there is no obvious way to relate the dynamics of the present system to that of a near-integrable Hamiltonian system; the arguments in Section 5.2 are rather confusing and misleading.

4 The authors concluded that Lyapunov exponents will give a measure of the mixing rate; this is not true. Although the Lyapunov exponent measures the stretching of a material line in flows, it does not measure the folding of the same line. Both stretching and folding will influence the mixing process, so the Lyapunov exponents may not serve as a measure of the mixing rate. A comparison between the mixing rate evaluated by tracking the deformation of a blob in cavity flows and corresponding Lyapunov exponents confirms this consideration (Ling and Widagdo, 1991). The Lyapunov exponents are useful in the study of mixing mainly because they can be used to identify whether a trajectory is chaotic.

A discussion with G. Schmidt is appreciated.

References

Grassberger, P., and Procaccia, I., 1983, "Measuring the Strangeness of Strange Attractors," *Physica D*, Vol. 9, pp. 189–208.

Liebovitch, L. S., and Toth, T., 1989, "A Fast Algorithm to Determine Fractal Dimensions by Box Counting," *Physics Letters A*, Vol. 141, pp. 386–390.

Ling, F. H., 1989, "On the Fractal Dimensions of a Combined Fractal Set," *Phys. Lett. A*, Vol. 138, pp. 25–28.

Ling, F. H., and Schmidt, G., 1991, "Box-Counting Algorithm and Dimensional Analysis of a Pulsar," *Journal of Computational Physics* to appear.

Ling, F. H., and Widagdo, S., 1991, "Numerical Study of Chaotic Mixing in a Rectangular Cavity," preprint.

Ling, F. H., Xu, N., and Xu, J. H., 1988, "Non-Empty Box-Counting Algorithm for Calculating Fractal Dimensions and Its Applications in EEG Analysis," *Proceedings of The INNS First Annual Meeting*, Boston Sept. 6–10, p. 120.

Author's Closure[5]

The following response uses the same numbering as above.

1 Generalized dimensions were used to characterize "the neighborhood" of mixed particles over *finite* time. In this way, local structure could be discerned.

2 The correlation dimension was chosen (over the Hausdorff dimension) as it is sensitive to inhomogeneity of the distribution of points.

3 Trajectories in the $T=\infty$ limit appeared closed in our numerical simulations suggesting the system is integrable. This was also evidenced by the decrease of dimension and Lyapunov exponent shown in Figs. 2 and 4.

4 Lyapunov exponents may aid in evaluating mixing by measuring the local shear and strain of the flow, as stated in the paper.

[3]By S. Lichter, A. Dagan, W. B. Underhill and H. Ayanle and published in the Sept. 1990 issue of the ASME JOURNAL OF APPLIED MECHANICS, Vol. 57, pp. 762–768.

[4]Department of Chemistry and Chemical Engineering, Stevens Institute of Technology, Hoboken, NJ 07030.

[5]S. Lichter, Department of Mechanical Engineering, Northwestern University, Evanston, IL 60208.

Downloaded 03 May 2010 to 171.66.16.247. Redistribution subject to ASME license or copyright; see http://www.asme.org/terms/Terms_Use.cfm

Using the present criterion, the same 2-DOF system in (3) is found to be stable if all the conditions: $k_1k_2+16>0$, $k_1k_2>0$, and $(k_1+k_2+16)^2-4k_1k_2>0$ are satisfied. Again, the result is the same as the exact solution.

The present criteria depend entirely on the characteristics of the system and do not require determination of any parameters. For the simple example, the present criteria give a good result. However, the present method, as any other zero-parameter methods, does not provide a way for improving the results. The author's method, therefore, is superior in this regard and is valuable if a very accurate result is desired.

Mixing in a Closed Room by the Action of Two Fans[3]

F. H. Ling[4]. A mixing problem of practical interest is studied from the viewpoint of chaotic dynamics in this paper. The modeling and the velocity field solution presented in Sections 2–4 are basically correct, but the results in Section 5 are rather misleading.

1 The authors used generalized dimensions to measure how much a trajectory fills the room; this is improper. Since the phase volume of a Hamiltonian system is preserved, its chaotic orbit fills up eventually a finite region in the phase space, and all of the generalized dimensions of the chaotic trajectory should be equal to the embedding dimensions. KAM tori prevent some parts of the phase space from being visited by particle trajectories, but they can not possibly force the chaotic trajectories to occur in a zero volume subspace. Even for a non-Hamiltonian mixing system, it is hard to imagine that the phase volume will shrink to zero.

2 The authors' statement that "the correlation integral method produces a more physical measure than the fractal (Hausdorff) dimension" (Section 5.1) is incorrect. Considering the (fractal) generalized dimensions (Grassberger and Procaccia, 1983),

$$D_q=\frac{1}{1-q}\lim_{\epsilon\to 0}\frac{\ln\sum_{i=1}^{N(\epsilon)}P_i^q(\epsilon)}{\ln(1/\epsilon)},\quad q\geq 0,\ q\neq 1,$$

where $N(\epsilon)$ is the number of nonempty boxes of a partitioning with the length scale ϵ, and $P_i(\epsilon)$ is the probability for a point of a fractal set to fall in box i of the partitioning. It is easy to prove that for a strict self-similar fractal set like the Cantor set, all generalized dimensions are the same. Moreover, if the distribution of the points in a set is uniform, all its generalized dimensions are equal to the embedding dimension. However, this is only an idealized case; almost all numerically generated fractal sets and those existing in nature are not strictly self-similar, and they can often be considered as a combination of several strict self-similar fractal sets. For such a combined set, Ling (1989) proved that the generalized dimensions with $q<1$ such as the capacity ($q=0$) are equal to the maximum of those of the component sets, and the generalized dimensions with $q>1$ such as the correlation dimension ($q=2$) are equal to the minimum of those of the component sets. Therefore, although more details of the fractal set are required for the calculation of the correlation dimension, there is no evidence to indicate that the correlation dimension is physically more meaningful than the capacity. In practical applications, the selection of a certain generalized dimension is guided almost solely by the convenience of computation. No one of the generalized dimensions can be used to measure the uniformity of the mixture.

It is noticed that there are also some new developments in the box-counting algorithm. One may plot the curve of $\ln\sum_{i=1}^{N(\epsilon)}P_i^q(\epsilon)$ versus $\ln(1/\epsilon)$ using box-counting results and measure the slope of its straight portion to determine the generalized dimensions (Ling, 1988; Ling, 1989; Liebovitch and Toth, 1989; Ling and Schmidt, 1991). By using this approach, the correlation dimension can be calculated more efficiently than by using the correlation integral.

3 Unlike the Aref-blinking-vortex system, which is integrable when two vortices act simultaneously, the two fan mixing system discussed in the paper has no apparent integrable limit. The steady case ($T\to\infty$, and the axes of both fans aligned) is very unlikely to be integrable, since the system is spatially three-dimensional, and there is a good chance for chaos to occur even if no time dependence is involved. Therefore, there is no obvious way to relate the dynamics of the present system to that of a near-integrable Hamiltonian system; the arguments in Section 5.2 are rather confusing and misleading.

4 The authors concluded that Lyapunov exponents will give a measure of the mixing rate; this is not true. Although the Lyapunov exponent measures the stretching of a material line in flows, it does not measure the folding of the same line. Both stretching and folding will influence the mixing process, so the Lyapunov exponents may not serve as a measure of the mixing rate. A comparison between the mixing rate evaluated by tracking the deformation of a blob in cavity flows and corresponding Lyapunov exponents confirms this consideration (Ling and Widagdo, 1991). The Lyapunov exponents are useful in the study of mixing mainly because they can be used to identify whether a trajectory is chaotic.

A discussion with G. Schmidt is appreciated.

References

Grassberger, P., and Procaccia, I., 1983, "Measuring the Strangeness of Strange Attractors," *Physica D*, Vol. 9, pp. 189–208.

Liebovitch, L. S., and Toth, T., 1989, "A Fast Algorithm to Determine Fractal Dimensions by Box Counting," *Physics Letters A*, Vol. 141, pp. 386–390.

Ling, F. H., 1989, "On the Fractal Dimensions of a Combined Fractal Set," *Phys. Lett. A*, Vol. 138, pp. 25–28.

Ling, F. H., and Schmidt, G., 1991, "Box-Counting Algorithm and Dimensional Analysis of a Pulsar," *Journal of Computational Physics* to appear.

Ling, F. H., and Widagdo, S., 1991, "Numerical Study of Chaotic Mixing in a Rectangular Cavity," preprint.

Ling, F. H., Xu, N., and Xu, J. H., 1988, "Non-Empty Box-Counting Algorithm for Calculating Fractal Dimensions and Its Applications in EEG Analysis," *Proceedings of The INNS First Annual Meeting*, Boston Sept. 6–10, p. 120.

Author's Closure[5]

The following response uses the same numbering as above.

1 Generalized dimensions were used to characterize "the neighborhood" of mixed particles over *finite* time. In this way, local structure could be discerned.

2 The correlation dimension was chosen (over the Hausdorff dimension) as it is sensitive to inhomogeneity of the distribution of points.

3 Trajectories in the $T=\infty$ limit appeared closed in our numerical simulations suggesting the system is integrable. This was also evidenced by the decrease of dimension and Lyapunov exponent shown in Figs. 2 and 4.

4 Lyapunov exponents may aid in evaluating mixing by measuring the local shear and strain of the flow, as stated in the paper.

[3]By S. Lichter, A. Dagan, W. B. Underhill and H. Ayanle and published in the Sept. 1990 issue of the ASME JOURNAL OF APPLIED MECHANICS, Vol. 57, pp. 762–768.

[4]Department of Chemistry and Chemical Engineering, Stevens Institute of Technology, Hoboken, NJ 07030.

[5]S. Lichter, Department of Mechanical Engineering, Northwestern University, Evanston, IL 60208.

Copyright © 1992 by ASME
Downloaded 03 May 2010 to 171.66.16.247. Redistribution subject to ASME license or copyright; see http://www.asme.org/terms/Terms_Use.cfm

Stress Analysis of Multilayered Anisotropic Elastic Media[6]

Marek-Jerzy Pindera.[7] The authors should be congratulated for their effort in presenting an efficient algorithm for solving elasticity boundary value problems of the first type (specified surface tractions) in media arbitrarily layered with monoclinic, orthotropic, or transversely isotropic plies (Choi and Thangjitham, 1991). It should be pointed out that the method is also particularly well suited to applications involving mixed boundary conditions. Interfacial crack problems and contact problems belong in this category as the authors themselves state in the closing sentence of the Conclusions section. It is in this class of problems that the power and efficacy of the technique is clearly demonstrated.

The application of the method discussed by the authors to interfacial crack problems in arbitrarily layered media consisting of monoclinic, orthotropic, or transversely isotropic plies has been presented by Chatterjee et al. (1982) and Chatterjee (1987). Derstine et al. (1988, 1989) employed the method to determine the response of arbitrarily laminated graphite/epoxy tubes under external and internal pressure, axial tension and compression, and torsion using a nonlinear constitutive model for the individual plies. Lane (1991) and Pindera and Lane (1991) have recently shown how the method can be employed to solve the frictionless contact problem of an arbitrarily laminated half-plane or a finite thickness laminate of infinite length subjected to a rigid punch of a parabolic profile under the assumption of generalized plane deformation. In both the interfacial crack problem and the contact problem, the asymptotic properties of the local stiffness matrix, together with a well-known relation between Hilbert and Fourier transforms, allow one to reduce the appropriate boundary condition equations to singular Fredholm integral equations of the second kind that can be solved using standard techniques (Erdogan and Gupta, 1972). In the case of the interfacial crack problem, the unknown variables in the integral equations are the crack opening displacement functions whereas in the case of the frictionless contact problem the unknown variable is the contact pressure. The applications of the method to mixed boundary value problems in composites mechanics have recently been summarized by the author (Pindera, 1991a,b).

At this point, it is worthwhile to set the record straight by giving a brief history of the author's involvement with the method discussed by Choi and Thangjitham, which has been referred to as the "local/global stiffness matrix formulation" by the author in the cited references. The author first saw this method while working on the interfacial crack problem in arbitrarily laminated composites with Dr. Chatterjee of the Materials Sciences Corporation during the period 1982–1983. This work is documented in Chatterjee et al. (1982) and Chatterjee (1987). Subsequently, this method was presented in detail by the author in an advanced elasticity course during the spring semesters of 1986 and 1987 while the author was associated with the Engineering Science and Mechanics Department at Virginia Polytechnic Institute and State University. The applications of the method outlined in the course included axisymmetric loading of composite rings or tubes and bending of arbitrarily laminated composite plates with and without interfacial disbonds. A total of 30 M.S. and Ph.D. candidates studied this technique during this period at the above institution. In February of 1987, the author gave a seminar titled "An Efficient Algorithm for Mixed Boundary-Value Problems in Composite Mechanics" to the faculty and graduate students in the ESM Department at Virginia Polytechnic Institute and State University in which this method was outlined and demonstrated with examples. The above is a matter of public record. It is also a matter of public record that Mr. Choi was enrolled in the aforementioned elasticity course in the spring of 1987 and studied this technique along with 14 other students. During the period 1987–1988, Mr. Choi pursued his doctoral studies under the author's guidance, applying the technique to a number of problems in composite mechanics.

With the exception of the information provided above and perhaps one other reference which can be found in Pindera (1991a,b), the authors' outline of the technique's history and development is quite accurate.

References

Chatterjee, S. N., Pindera, M.-J., Pipes, R. B., and Dick, B., 1982, "Composite Defect Significance," Naval Air Development Center Contracts Reports, NADC 81034-60, Warminster, PA, pp. 92–106.

Chatterjee, S. N., 1987, "Three- and Two-Dimensional Stress Fields Near Delaminations in Laminated Composite Plates," *Int. J. Solids Structures*, Vol. 23, No. 11, pp. 1535–1549.

Choi, H. J., and Thangjitham, S., 1991, "Stress Analysis of Multilayered Anisotropic Elastic Media," ASME JOURNAL APPLIED MECHANICS, Vol. 58, pp. 382–387.

Derstine, M. S., Pindera, M.-J., and Bowles, D. E., 1988, "Combined Mechanical Loading of Composite Tubes," CCMS-88-11 Report (VPI-E-88-18), VPI&SU, Blacksburg, Va.

Derstine, M. S., and Pindera, M.-J., 1989, "Nonlinear Response of Composite Tubes Under Combined Thermomechanical Loading," *Composites and Other New Materials for PVP: Design and Analysis Considerations*, D. Hui, T. J. Kozik, G. E. O. Widera, and M. Shiratori, eds., PVP-Vol. 174, ASME, New York, pp. 19–28.

Lane, M. S., 1991, "The Frictionless Contact Problem of Anisotropic Multilayered Media," Ph.D. Dissertation, Civil Engineering Department, University of Virginia.

Erdogan, F., and Gupta, G., 1972, "On the Numerical Solution of Singular Integral Equations," *Quart. J. Applied Mathematics*, pp. 525–534.

Pindera, M.-J., 1991a, "Local/Global Stiffness Matrix Formulation for Anisotropic Multilayered Structures," *Advanced Composites Materials in Civil Engineering Structures*, S. L. Iyer, ed., Proceedings of the ASCE Specialty Conference, Las Vegas, Nev., pp. 313–324.

Pindera, M.-J., 1991b, "Local/Global Stiffness Matrix Formulation for Composite Materials and Structures," *Composites Engineering*, Vol. 1, No. 2, pp. 69–83.

Pindera, M.-J., and Lane, M. S., 1991, "Frictionless Contact of Layered Half Planes," *Proceedings of the Conference on Advances in Elasticity*, ASME Winter Annual Meeting, Atlanta, Ga.

Author's Closure[8]

We appreciate Dr. Pindera's interest in our paper and would like to thank him for providing the additional references. It is very unfortunate, however, that all the mentioned references except Erdogan and Gupta (1972) were not seen by us during our literature search. The main reason for this oversight is that many of the articles were published after or at about the same time we submitted our paper for review (August, 1989). For example, the last reference (Pindera and Lane, 1991) is scheduled to be presented two months after the writing of this closure. Furthermore, many of the aforementioned articles were published in conference proceedings and as internal organization reports which, under many circumstances, are difficult to obtain. We sincerely believe that we have provided a sufficient number of relevant references (16) in our paper. In fact, in order to minimize the length of the paper, we intentionally left out our earlier articles which were not directly related or were published as conference papers and organization reports.

The stiffness matrix method, as used in our paper, was

[6]By H. J. Choi and S. Thangjitham and published in the June 1991 issue of the ASME JOURNAL OF APPLIED MECHANICS, Vol. 58, pp. 382–387.

[7]Associate Professor, Civil Engineering Department, University of Virginia, Charlottesville, VA 22903.

[8]S. Thangjitham, Associate Professor, Department of Engineering Science and Mechanics, Virginia Polytechnic Institute and State University, Blacksburg, VA 24061-0219.

Copyright © 1992 by ASME
Downloaded 03 May 2010 to 171.66.16.247. Redistribution subject to ASME license or copyright; see http://www.asme.org/terms/Terms_Use.cfm

merely a procedure which aided in efficient computation of the results. The method has long been used in the area of structural mechanics. The finite element method as applied to problems in solid mechanics has similar general solution procedure as that of the stiffness method. One obvious difference is that the stiffness matrix method uses the exact solutions for displacements as the interpolation functions.

To comment on any matter unrelated to our paper in this closure is beyond the scope and standards of this journal. However, I would like to point out that it is not uncommon for students to extend basic concepts and techniques obtained from classes to enhance their research work. In fact, graduate courses are purposely designed to help students to develop the neccessary background in their field of research. Nonetheless, the principal author would like to thank Dr. Pindera for introducing some of the basic uses of the stiffness method in his elasticity course.

The Motion of a Sphere on a Rough Horizontal Plane[9]

L. Y. Bahar.[10] This paper suffers from a number of stylistic as well as technical deficiencies, which should have been avoided by the joint effort of the writer and the reviewers. It should therefore be read with caution, in my opinion.

1 Stylistically: Under subheading 2, line 2 should read "... nutates and precesses" instead of "... nutates and proceeds," and the sentence after Eq. (1) should read "... precession, nutation and spin" instead of "... precession, nutation and rotation." In the last paragraph of subheading 3, in line 7, "... rotation" should be replaced by "... spin." and in lines 9 and 12 of the same paragraph, as well as in lines 4 and 6 of the last paragraph of subheading 4, the word "... variance" should be replaced by "... variation." The word variance has a precise meaning in statistics and does not convey the one intended in the paper.

Also, the references are not fully documented. The Journal references of the first two due to Chaplygin are not given, also the date of the first reference should be 1897 and 1987! Interested readers will find the details of both of these references given in Neimark and Fufaev (1972) which is not cited. The references do not contain any information about the languages in which the articles have been written originally, including whether the translations into English are available.

2 Technically: This problem has been completely solved by utilizing Euler's equations of motion with respect to axes of fixed orientation (and not moving axes) which is a reference frame where they assume a particularly simple form, because they become linear in the Cartesian coordinates describing the motion of the center of the sphere. This is because the moments of inertia of a sphere are identical with respect to any orthogonal system of axes passing through its center, which suggests that the simplest choice of a reference frame to use is a space—fixed or inertial frame. It is therefore not surprising that the complete solution to this problem which can be found in recent reprints of such classics as Lamb (1990), Loney (1988), and Routh (1960), as well as more recent texts by Ramsey (1937), Smart (1951), Appell (1953), Atkin (1959), Charlton (1963), Easthope (1964), and Chester (1979) formulate it in rectangular Cartesian coordinates. The same is true of the research literature examplified by Holden and King (1990), in which rolling resistance is added to the usual features.

As seen from all the above references, the choice of an inertial frame in rectangular coordinates uncouples the rotational equations of motion in the angular velocities and reduces the problem to the well-known two-dimensional rotational equations of motion around each of the coordinate axes, on account of spherical symmetry.

A sphere is not a top, and quantities that have particular physical significance for a top such as precession, nutation, and spin have no meaning for a sphere. In addition, they complicate the formulation of the problem by producing nonlinear equations of motion unnecessarily, simply as a result of not taking spherical symmetry into account.

The author's assertion to the effect that "It seems unusual that these solutions are periodic, because under the conditions of friction, it is generally believed that these solutions are decayed" should have indicated that his solution was not physically feasible, despite his experimental observations!

References

Appell, P., 1953, *Traité de Mécanique Rationnelle, Tome II, Dynamique des Systèmes, Mécanique Analytique*, 6th ed., Gauthier-Villars, Paris, pp. 249–253.

Atkin, R. H., 1959, *Classical Dynamics*, John Wiley and Sons, New York, pp. 253–254.

Chester, W., 1979, *Mechanics*, George Allen and Unwin, London, pp. 327–329.

Charlton, F., 1963, *Textbook of Dynamics*, Van Nostrand Co. Ltd., London, pp. 183–186.

Easthope, C. E., 1964, *Three Dimensional Dynamics*, 2nd ed., Butterworths, London, pp. 160–169.

Lamb, H., 1990, *Higher Mechanics*, University Microfilms, Ann Arbor, Mich., (Reprint of the 2nd ed., originally published by Cambridge University Press, 1929), pp. 97–99.

Loney, S. L., 1988, *Dynamics of a Particle and Rigid Bodies*, Surjeet Publications, New Delhi, India (reprint of the 1909 Edition by Cambridge University Press, 1926) pp. 302–304.

Holden, J. T., and King, A. C., 1990, "The Dynamics of a Ball on a Rotating Plane," *Z. angew. Math. Mech.*, Vol. 70, No. 8, pp. 353–355.

Neimark, Ju. I., and Fufaev, N. A., 1972, *The Dynamics of Nonholonomic Systems*, (Translations of Mathematical Monographs), Vol. 33, American Mathematical Society, Providence, R.I., pp. 498–499.

Ramsey, A. S. 1937, *Dynamics*, Part II, Cambridge University Press, London, pp. 155–156.

Routh, E. J., 1960, *The Elementary Part of a Treatise on the Dynamics of a System of Rigid Bodies*, Dover Publications, New York, pp. 220–221.

Smart, E. H., 1951, *Advanced Dynamics, Vol. II, Dynamics of a Solid Body*, MacMillan, London, pp. 222–230.

Author's Closure[11]

First of all, I would like to express my gratitude to Professor Bahar for his comments. I have to say that some of his remarks, particularly on the paper's style and reference documents, are correct.

On the technical side, I would like to provide Professor Bahar with some information: My other paper, "The Motion of a Sphere With Weak Nutation on a Rough Horizontal Plane," which is currently being reviewed by Associate Editor Professor Inman, gives a solution to a sphere with weak nutation. This proves that the solutions presented in my paper are correct.

Professor Bahar quoted many references, and it seems to indicate that the velocity of center and the velocity of contact point has already been solved by others. Even so, the solutions in may paper differ somewhat from the others. By comparison, we can see the differences are striking.

I don't agree with Professor Bahar's comments that precession, nutation, and spin are meaningless for a sphere. Just rotate (or spin) a glass ball (which is often a children's toy)

[9]By J.-Y. Yang, and published in the Mar. 1991 issue of ASME JOURNAL OF APPLIED MECHANICS, Vol. 58, pp. 296–298.

[10]Professor of Applied Mechanics, Department of Mechanical Engineering and Mechanics, Drexel University, Philadelphia, PA 19104.

[11]Professor J.-Y. Yang, Shanghai Teachers' College of Technology, Shanghai, China.

Downloaded 03 May 2010 to 171.66.16.247. Redistribution subject to ASME license or copyright; see http://www.asme.org/terms/Terms_Use.cfm

merely a procedure which aided in efficient computation of the results. The method has long been used in the area of structural mechanics. The finite element method as applied to problems in solid mechanics has similar general solution procedure as that of the stiffness method. One obvious difference is that the stiffness matrix method uses the exact solutions for displacements as the interpolation functions.

To comment on any matter unrelated to our paper in this closure is beyond the scope and standards of this journal. However, I would like to point out that it is not uncommon for students to extend basic concepts and techniques obtained from classes to enhance their research work. In fact, graduate courses are purposely designed to help students to develop the neccessary background in their field of research. Nonetheless, the principal author would like to thank Dr. Pindera for introducing some of the basic uses of the stiffness method in his elasticity course.

The Motion of a Sphere on a Rough Horizontal Plane[9]

L. Y. Bahar.[10] This paper suffers from a number of stylistic as well as technical deficiencies, which should have been avoided by the joint effort of the writer and the reviewers. It should therefore be read with caution, in my opinion.

1 Stylistically: Under subheading 2, line 2 should read "... nutates and precesses" instead of "... nutates and proceeds," and the sentence after Eq. (1) should read "... precession, nutation and spin" instead of "... precession, nutation and rotation." In the last paragraph of subheading 3, in line 7, "... rotation" should be replaced by "... spin." and in lines 9 and 12 of the same paragraph, as well as in lines 4 and 6 of the last paragraph of subheading 4, the word "... variance" should be replaced by "... variation." The word variance has a precise meaning in statistics and does not convey the one intended in the paper.

Also, the references are not fully documented. The Journal references of the first two due to Chaplygin are not given, also the date of the first reference should be 1897 and 1987! Interested readers will find the details of both of these references given in Neimark and Fufaev (1972) which is not cited. The references do not contain any information about the languages in which the articles have been written originally, including whether the translations into English are available.

2 Technically: This problem has been completely solved by utilizing Euler's equations of motion with respect to axes of fixed orientation (and not moving axes) which is a reference frame where they assume a particularly simple form, because they become linear in the Cartesian coordinates describing the motion of the center of the sphere. This is because the moments of inertia of a sphere are identical with respect to any orthogonal system of axes passing through its center, which suggests that the simplest choice of a reference frame to use is a space—fixed or inertial frame. It is therefore not surprising that the complete solution to this problem which can be found in recent reprints of such classics as Lamb (1990), Loney (1988), and Routh (1960), as well as more recent texts by Ramsey (1937), Smart (1951), Appell (1953), Atkin (1959), Charlton (1963), Easthope (1964), and Chester (1979) formulate it in rectangular Cartesian coordinates. The same is true of the research literature examplified by Holden and King (1990), in which rolling resistance is added to the usual features.

As seen from all the above references, the choice of an inertial frame in rectangular coordinates uncouples the rotational equations of motion in the angular velocities and reduces the problem to the well-known two-dimensional rotational equations of motion around each of the coordinate axes, on account of spherical symmetry.

A sphere is not a top, and quantities that have particular physical significance for a top such as precession, nutation, and spin have no meaning for a sphere. In addition, they complicate the formulation of the problem by producing nonlinear equations of motion unnecessarily, simply as a result of not taking spherical symmetry into account.

The author's assertion to the effect that "It seems unusual that these solutions are periodic, because under the conditions of friction, it is generally believed that these solutions are decayed" should have indicated that his solution was not physically feasible, despite his experimental observations!

References

Appell, P., 1953, *Traité de Mécanique Rationnelle, Tome II, Dynamique des Systèmes, Mécanique Analytique*, 6th ed., Gauthier-Villars, Paris, pp. 249–253.

Atkin, R. H., 1959, *Classical Dynamics*, John Wiley and Sons, New York, pp. 253–254.

Chester, W., 1979, *Mechanics*, George Allen and Unwin, London, pp. 327–329.

Charlton, F., 1963, *Textbook of Dynamics*, Van Nostrand Co. Ltd., London, pp. 183–186.

Easthope, C. E., 1964, *Three Dimensional Dynamics*, 2nd ed., Butterworths, London, pp. 160–169.

Lamb, H., 1990, *Higher Mechanics*, University Microfilms, Ann Arbor, Mich., (Reprint of the 2nd ed., originally published by Cambridge University Press, 1929), pp. 97–99.

Loney, S. L., 1988, *Dynamics of a Particle and Rigid Bodies*, Surjeet Publications, New Delhi, India (reprint of the 1909 Edition by Cambridge University Press, 1926) pp. 302–304.

Holden, J. T., and King, A. C., 1990, "The Dynamics of a Ball on a Rotating Plane," *Z. angew. Math. Mech.*, Vol. 70, No. 8, pp. 353–355.

Neimark, Ju. I., and Fufaev, N. A., 1972, *The Dynamics of Nonholonomic Systems*, (Translations of Mathematical Monographs), Vol. 33, American Mathematical Society, Providence, R.I., pp. 498–499.

Ramsey, A. S. 1937, *Dynamics*, Part II, Cambridge University Press, London, pp. 155–156.

Routh, E. J., 1960, *The Elementary Part of a Treatise on the Dynamics of a System of Rigid Bodies*, Dover Publications, New York, pp. 220–221.

Smart, E. H., 1951, *Advanced Dynamics, Vol. II, Dynamics of a Solid Body*, MacMillan, London, pp. 222–230.

Author's Closure[11]

First of all, I would like to express my gratitude to Professor Bahar for his comments. I have to say that some of his remarks, particularly on the paper's style and reference documents, are correct.

On the technical side, I would like to provide Professor Bahar with some information: My other paper, "The Motion of a Sphere With Weak Nutation on a Rough Horizontal Plane," which is currently being reviewed by Associate Editor Professor Inman, gives a solution to a sphere with weak nutation. This proves that the solutions presented in my paper are correct.

Professor Bahar quoted many references, and it seems to indicate that the velocity of center and the velocity of contact point has already been solved by others. Even so, the solutions in may paper differ somewhat from the others. By comparison, we can see the differences are striking.

I don't agree with Professor Bahar's comments that precession, nutation, and spin are meaningless for a sphere. Just rotate (or spin) a glass ball (which is often a children's toy)

[9]By J.-Y. Yang, and published in the Mar. 1991 issue of ASME JOURNAL OF APPLIED MECHANICS, Vol. 58, pp. 296–298.

[10]Professor of Applied Mechanics, Department of Mechanical Engineering and Mechanics, Drexel University, Philadelphia, PA 19104.

[11]Professor J.-Y. Yang, Shanghai Teachers' College of Technology, Shanghai, China.

Copyright © 1992 by ASME
Downloaded 03 May 2010 to 171.66.16.247. Redistribution subject to ASME license or copyright; see http://www.asme.org/terms/Terms_Use.cfm

on a glass table. Actually, through careful observation, we can see what will happen. There is evidence that my experiment and theory prove to be feasible—and my paper was reviewed by many professors before its publication. I believe it was worth publishing.

At the present time, I think that, at least, my way of analysis presented in this paper and the paper "The Motion of a Sphere With Weak Nutation on a Rough Horizontal Plane," can reflect the motion of a sphere comparatively well (in fact, it is not as simple as some people imagine).

I welcome Professor Bahar's further comments and I hope I can contact him directly for such discussion.

The Usefulness of Elementary Theory for the Linear Vibrations of Layered, Orthotropic Elastic Beams and Corrections to Two-Dimensional End Effects[12]

Yi-Yuan Yu.[13] The authors have presented an interesting asymptotic analysis of the end effect on the natural frequencies of linear vibrations of elastic cantilever beams, based on the work of Gregory and Wan (1984). They have also remarked on the works of other authors, including the important contribution of Timoshenko, concerning the effect of transverse shear deformation. Among other things the authors concluded in their abstract and introduction that the Timoshenko beam theory produces an erroneous correction to the frequencies given by the elementary beam theory. This statement is misleading. As the title of the original Timoshenko paper (1921) indicated clearly, his work was "On the Correction for Shear ..." In so far as correction for shear is concerned, the Timoshenko beam theory has *not* produced an erroneous correction to the frequencies of the elementary beam theory, particularly for layered beams, as will be seen presently. The authors further concluded in their abstract and introduction that the correction for end effect is proportional to $\epsilon = H/L$, the correction for shear proportional to ϵ^2, and the most important correction comes from the end effect. However, in their conclusions at the end of the paper, again based on the finding of Gregory and Wan (1984), the authors added the caution that their asymptotic analysis is valid only as $\epsilon \to 0$ and that "For small but finite values of ϵ, it may well be that the coefficients of the ϵ^2-terms are much larger than those of the ϵ-terms." It follows from this statement that, with the influence of such coefficients taken into account, the final total correction for shear may well turn out to be equal to or greater than that for the end effect, thereby reversing the authors' earlier conclusions. In any case, before additional numerical study is carried out on the quantification of the corrections, as contemplated by the authors, they can hardly claim to have reached a definitive conclusion on the relative importance between the correction for shear and correction for end effect, at least from the engineering standpoint, if not from the standpoint of the asymptotic analysis. Based on his experience in vibration analysis of beams, plates, and shells, the writer would like to offer some comments to help clarify the general situation as well as to suggest some special situations for additional numerical work.

The authors also concluded that the elementary beam theory can be applied successfully to layered, orthotropic beams. But the elementary beam theory has always been applied to such beams, as is attested by the various types of analysis of laminated composite beams and plates that are described in many books, such as those by Tsai and Hahn (1980) and Whitney (1987). The success with which the elementary or classical theories can be applied to layered beams and plates, even those weak in shear, depends on a number of factors. As far as vibration analysis is concerned, the most important factors include the geometrical configuration of the beam or plate and the frequency range being considered. For the single-layered and two-layered configurations and low enough frequencies dealt with in this paper, the transverse shear effect is known to be unimportant. For instance, for a single-layered isotropic plate made of steel as ordinarily used in engineering practice, the classical theory can be used to predict accurately natural frequencies as high as, say, 20,000 hertz. Similar conclusions have been reached for two-layered plates by Ren and Yu (1967), who found that the shear effect is small on natural frequencies of predominantly flexural modes.

The transverse shear effect begins to play an important role in a layered beam or plate when the number of layers reaches three, such as in a sandwich beam or plate. As shown by Yu (1959, 1960), when the core of the sandwich is weak in shear, the shear effect in the core can be important even at low frequencies, say, around 100 hertz. The results of his sandwich beam and plate equations that include the shear effect have been confirmed by those given by the exact elasticity theory (Yu, 1960). In addition to infinite sandwich beams and plates and finite ones with simply supported edges, those with clamped edges have further been analyzed by Yu and Lai (1966, 1967). Their results showed that the shear effect is more important in the clamped cases than in the simply supported cases. Later, Dudek (1970) carried out experiments of vibrations of graphite epoxy composite cantilever beams, with natural frequencies as low as around 100 hertz. He found that the frequencies deviated markedly from predictions of the classical beam theory and, for accurate prediction, the Timoshenko beam theory had to be used. It should be noted that the equivalent values of E/G were higher than 4000 for the sandwiches investigated by Yu (1960) and up to 50 for the laminated composites investigated by Dudek (1970). Additional discussions on linear and nonlinear dynamics and vibration of beams, plates, and shells, including sandwiches and laminated composites, may be found in the writer's more recent works (Yu 1989, 1991a–d).

As just mentioned, another primary factor that determines the importance of shear effect is the frequency range under consideration. At high frequencies the shear effect can become important even in single-layered beams and plates. Stimulated by the need to learn about crystal plates used as resonators, R. D. Mindlin made a sustained effort for many years to investigate high-frequency vibrations of both isotropic and anisotropic plates, and his works in this area deserve special attention. He started by developing the equations of an isotropic plate (Mindlin, 1951) that include the transverse shear and rotatory inertia effects and now carry his name (often jointly with the name of E. Reissner, whose important contribution to plate theory was cited and discussed in the aforementioned work by Gregory and Wan). The Mindlin equations are essentially the two-dimensional counterpart of the Timoshenko beam equations. Later, Mindlin (1961) further developed higher-order equations of anisotropic plates. Together with his students, he solved many plate vibration problems on the basis of his equations. For verifying the results of the plate equations, he made use of available experimental results, and he also carried out a most comprehensive analysis of the Rayleigh-Lamb solution for an infinite elastic, isotropic plate, which, as is well known, is based on the exact elasticity theory (Mindlin, 1960).

The last mentioned work of Mindlin (1960) has contributed

[12]By J. M. Duva and J. G. Simmonds and published in the Mar. 1991 issue of the ASME JOURNAL OF APPLIED MECHANICS, Vol. 58, pp. 175–180.

[13]Professor of Mechanical Engineering, Department of Mechanical and Industrial Engineering, New Jersey Institute of Technology, Newark, NJ 07102. Life Fellow ASME.

Copyright © 1992 by ASME
Downloaded 03 May 2010 to 171.66.16.247. Redistribution subject to ASME license or copyright; see http://www.asme.org/terms/Terms_Use.cfm

greatly to the understanding of vibration behaviors of plates. The authors may find the work interesting since, among many other things, it deals with the relations between the frequency spectra of infinite and finite plates, which are applicable to beams as a special case. Thus, he described the process of obtaining the overtones of a finite plate from the frequency spectrum of an infinite plate and went on to point out that the adequacy of plate equations for the prediction of natural frequencies of finite plates depends on the ability of the plate equations to reproduce accurately the frequency spectrum of an infinite plate as compared with the result of the exact elasticity theory. Since the classical beam or plate equations yield only the lowest branch of the frequency spectrum of an infinite beam or plate, the frequency range that can be handled adequately will be limited when the equations are applied to a finite beam or plate. On the other hand, by including the effects of transverse shear and rotatory inertia, a second branch of the frequency spectrum can be generated by the Timoshenko beam theory, and, by further matching the cutoff frequency of this branch with the exact result of elasticity theory in the manner of Mindlin, the frequency range that can be handled adequately is greatly extended. For sandwiches and laminated composites, the transverse shear effect in general can be much more important and often must be considered even for the lowest branch of the frequency spectrum, as has been pointed out earlier. The effect of rotatory inertia plays the same role as in the case of a single-layered beam or plate in making it possible for the beam or plate equations to accommodate a second higher branch of the frequency spectrum. For sandwiches it was further shown by Yu (1960) that the cutoff frequency of this second branch can be much lower than for single-layered beams or plates, which makes the presence of the second branch that much more important for sandwiches. The same is expected to be true for laminated composites.

Finally, it is noted that the value of the shear factor $k = 5/3$ used by the authors below their equations (105) is unusually high.

References

Gregory, R. D., and Wan, F. Y. M., 1984, "Decaying States of Plane Strain in a Semi-infinite Strip and Boundary Conditions for Plate Theory," *Journal of Elasticity*, Vol. 14, pp. 27–64.

Mindlin, R. D., 1951, "Influence of Rotatory Inertia and Shear on Flexural Motions of Isotropic, Elastic Plates," ASME JOURNAL OF APPLIED MECHANICS, Vol. 18, pp. 31–38.

Mindlin, R. D., 1960, "Waves and Vibrations in Isotropic, Elastic Plates," *Proceedings of the First Symposium of Naval Structural Mechanics*, Pergamon Press, pp. 199–232.

Mindlin, R. D., 1961, "High Frequency Vibrations of Crystal Plates," *Quarterly of Applied Mathematics*, Vol. 19, pp. 51–61.

Ren, N., and Yu, Y. Y., 1967, "Flexural and Extensional Vibrations of Two-Layered Plates," *AIAA Journal*, Vol. 5, pp. 797–799.

Timoshenko, S. P., 1921, "On the Correction for Shear of the Differential Equation for Transverse Vibrations of Prismatic Bars," *Philosophical Magazine*, Vol. 41, pp. 744–746.

Tsai, S. W., and Hahn, H. T., 1980, *Introduction to Composite Materials*, Technomic.

Whitney, J. M., 1987, *Structural Analysis of Laminated Anisotropic Plates*, Technomic.

Yu, Y. Y., 1959, "A New Theory of Elastic Sandwich Plates—One-Dimensional Case," ASME JOURNAL OF APPLIED MECHANICS, Vol. 26, pp. 415–421.

Yu, Y. Y., 1960, "Flexural Vibrations of Elastic Sandwich Plates," *Journal of Aero/Space Sciences*, Vol. 27, pp. 272–283.

Yu, Y. Y., and Lai, Jai-Lue, 1966, "Influence of Transverse Shear and Edge Condition on Nonlinear Vibration and Dynamic Buckling of Homogeneous and Sandwich Plates," ASME JOURNAL OF APPLIED MECHANICS, Vol. 33, pp. 934–936.

Yu, Y. Y., and Lai, Jai-Lue, 1967, "Application of Galerkin's Method to the Dynamic Analysis of Structures," *AIAA Journal*, Vol. 5, pp. 793–795.

Yu, Y. Y., 1989, "Dynamics and Vibration of Layered Plates and Shells—A Perspective from Sandwiches to Laminated Composites," *Proceedings of 30th AIAA/ASME/ASCE/AHS/ASC Structures, Structural Dynamics and Materials Conference*, pp. 2236–2245; also to appear in *Proceedings of the First USSR-US Symposium on Mechanics of Composite Materials*, Riga, Latvia, 1989, to be published by ASME.

Yu, Y. Y., 1991a, "Nonlinear Dynamics and Chaos of Buckled Sandwich Beams with Isotropic or Laminated Composite Facings," *Proceedings of the 8th International Conference on Composite Materials*, SAMPE, Covina, Calif., pp. 3-D-1 to 3-D-15.

Yu, Y. Y., 1991b, "Nonlinear Dynamics and Chaos of Buckled Laminated Composite Beams," to appear in *Mechanics of Composite Structures* (to be published in USSR).

Yu, Y. Y., 1991c, "On Equations for Large Deflections of Elastic Plates and Shallow Shells," to be published in *Mechanics Research Communications*, Vol. 18, pp. 373–384.

Yu, Y. Y., 1991d, "Equations for Large Deflections of Homogeneous and Layered Beams with Application to Chaos and Acoustic Radiation," to be published in *Composites Engineering*.

Authors' Closure[14]

We thank Professor Yu for his careful reading of our paper and shall reply to those comments related to its contents; Professor Yu's comments concerning high-frequency vibrations of plates are irrelevant.

First, we acknowledge a semantic problem: we should have written "...Timoshenko beam theory produces an erroneous *asymptotic* correction...". Second, because we take the depth of the beam to be $2H$, our definition of the shear coefficient k in Eq. $(15)_2$ is twice the conventional definition. We apologize for this confusion.

More fundamentally, we believe that Professor Yu's comments are based on a misunderstanding. The theories of Timoshenko and those of Yu for beams and plates are ad hoc—albeit useful—theories, based on *assuming* certain variations of displacements in the thickness direction. In general, these variations are not good point-wise approximations near edges, especially built-in edges, although they often lead to accurate gross quantities such as natural frequencies or buckling loads. In contrast, ours in an *exact* theory, based on a formal asymptotic analysis of the linear equations of elasticity. The limitations of such an analysis are well known: a statement that the remainder in an expansion is $O(\epsilon)$ says nothing about the implied constant that multiplies ϵ; it could be quite large. We acknowledged this limitation in the Conclusions section of our paper, as Professor Yu notes.

The difference between ad hoc and asymptotic theories is also reflected by the role of experiment. In the former, experiments are conducted to verify the soundness of the assumptions; in the latter—barring mathematical errors—the only reason for experiments would be (a) to confirm the underlying assumptions of elasticity theory, (b) to test the validity of idealized boundary conditions, or (c) to empirically estimate the constants associated with certain O-symbols.

On Energy Rate Theorems for Linear First-Order Nonholonomic Systems[15]

T. R. Kane[16] and D. A. Levinson.[17] The author points out a defect in a previously published Note (Kane and Levinson, 1988), but ignores the fact that this defect was remedied in a second Note by the same authors (Kane and Levinson, 1990), a Note whose publication in this journal preceded that of his paper by more than one year.

[14]Submitted by Professors J. Simmonds and M. Duva, Department of Applied Mathematics, University of Virginia, Charlottesville, VA 22903-2422.

[15]By John G. Papastavridis, and published in the June 1991 issue of the ASME JOURNAL OF APPLIED MECHANICS, Vol. 58, pp. 536–544.

[16]Professor of Applied Mechanics, Stanford University, Stanford, CA 94305. Fellow ASME.

[17]Staff Scientist, Lockheed Palo Alto Research Laboratory, Palo Alto, CA 94304. Mem. ASME.

Downloaded 03 May 2010 to 171.66.16.247. Redistribution subject to ASME license or copyright; see http://www.asme.org/terms/Terms_Use.cfm

greatly to the understanding of vibration behaviors of plates. The authors may find the work interesting since, among many other things, it deals with the relations between the frequency spectra of infinite and finite plates, which are applicable to beams as a special case. Thus, he described the process of obtaining the overtones of a finite plate from the frequency spectrum of an infinite plate and went on to point out that the adequacy of plate equations for the prediction of natural frequencies of finite plates depends on the ability of the plate equations to reproduce accurately the frequency spectrum of an infinite plate as compared with the result of the exact elasticity theory. Since the classical beam or plate equations yield only the lowest branch of the frequency spectrum of an infinite beam or plate, the frequency range that can be handled adequately will be limited when the equations are applied to a finite beam or plate. On the other hand, by including the effects of transverse shear and rotatory inertia, a second branch of the frequency spectrum can be generated by the Timoshenko beam theory, and, by further matching the cutoff frequency of this branch with the exact result of elasticity theory in the manner of Mindlin, the frequency range that can be handled adequately is greatly extended. For sandwiches and laminated composites, the transverse shear effect in general can be much more important and often must be considered even for the lowest branch of the frequency spectrum, as has been pointed out earlier. The effect of rotatory inertia plays the same role as in the case of a single-layered beam or plate in making it possible for the beam or plate equations to accommodate a second higher branch of the frequency spectrum. For sandwiches it was further shown by Yu (1960) that the cutoff frequency of this second branch can be much lower than for single-layered beams or plates, which makes the presence of the second branch that much more important for sandwiches. The same is expected to be true for laminated composites.

Finally, it is noted that the value of the shear factor $k = 5/3$ used by the authors below their equations (105) is unusually high.

References

Gregory, R. D., and Wan, F. Y. M., 1984, "Decaying States of Plane Strain in a Semi-infinite Strip and Boundary Conditions for Plate Theory," *Journal of Elasticity*, Vol. 14, pp. 27–64.

Mindlin, R. D., 1951, "Influence of Rotatory Inertia and Shear on Flexural Motions of Isotropic, Elastic Plates," ASME JOURNAL OF APPLIED MECHANICS, Vol. 18, pp. 31–38.

Mindlin, R. D., 1960, "Waves and Vibrations in Isotropic, Elastic Plates," *Proceedings of the First Symposium of Naval Structural Mechanics*, Pergamon Press, pp. 199–232.

Mindlin, R. D., 1961, "High Frequency Vibrations of Crystal Plates," *Quarterly of Applied Mathematics*, Vol. 19, pp. 51–61.

Ren, N., and Yu, Y. Y., 1967, "Flexural and Extensional Vibrations of Two-Layered Plates," *AIAA Journal*, Vol. 5, pp. 797–799.

Timoshenko, S. P., 1921, "On the Correction for Shear of the Differential Equation for Transverse Vibrations of Prismatic Bars," *Philosophical Magazine*, Vol. 41, pp. 744–746.

Tsai, S. W., and Hahn, H. T., 1980, *Introduction to Composite Materials*, Technomic.

Whitney, J. M., 1987, *Structural Analysis of Laminated Anisotropic Plates*, Technomic.

Yu, Y. Y., 1959, "A New Theory of Elastic Sandwich Plates—One-Dimensional Case," ASME JOURNAL OF APPLIED MECHANICS, Vol. 26, pp. 415–421.

Yu, Y. Y., 1960, "Flexural Vibrations of Elastic Sandwich Plates," *Journal of Aero/Space Sciences*, Vol. 27, pp. 272–283.

Yu, Y. Y., and Lai, Jai-Lue, 1966, "Influence of Transverse Shear and Edge Condition on Nonlinear Vibration and Dynamic Buckling of Homogeneous and Sandwich Plates," ASME JOURNAL OF APPLIED MECHANICS, Vol. 33, pp. 934–936.

Yu, Y. Y., and Lai, Jai-Lue, 1967, "Application of Galerkin's Method to the Dynamic Analysis of Structures," *AIAA Journal*, Vol. 5, pp. 793–795.

Yu, Y. Y., 1989, "Dynamics and Vibration of Layered Plates and Shells—A Perspective from Sandwiches to Laminated Composites," *Proceedings of 30th AIAA/ASME/ASCE/AHS/ASC Structures, Structural Dynamics and Materials Conference*, pp. 2236–2245; also to appear in *Proceedings of the First USSR-US Symposium on Mechanics of Composite Materials*, Riga, Latvia, 1989, to be published by ASME.

Yu, Y. Y., 1991a, "Nonlinear Dynamics and Chaos of Buckled Sandwich Beams with Isotropic or Laminated Composite Facings," *Proceedings of the 8th International Conference on Composite Materials*, SAMPE, Covina, Calif., pp. 3-D-1 to 3-D-15.

Yu, Y. Y., 1991b, "Nonlinear Dynamics and Chaos of Buckled Laminated Composite Beams," to appear in *Mechanics of Composite Structures* (to be published in USSR).

Yu, Y. Y., 1991c, "On Equations for Large Deflections of Elastic Plates and Shallow Shells," to be published in *Mechanics Research Communications*, Vol. 18, pp. 373–384.

Yu, Y. Y., 1991d, "Equations for Large Deflections of Homogeneous and Layered Beams with Application to Chaos and Acoustic Radiation," to be published in *Composites Engineering*.

Authors' Closure[14]

We thank Professor Yu for his careful reading of our paper and shall reply to those comments related to its contents; Professor Yu's comments concerning high-frequency vibrations of plates are irrelevant.

First, we acknowledge a semantic problem: we should have written "...Timoshenko beam theory produces an erroneous *asymptotic* correction...". Second, because we take the depth of the beam to be $2H$, our definition of the shear coefficient k in Eq. $(15)_2$ is twice the conventional definition. We apologize for this confusion.

More fundamentally, we believe that Professor Yu's comments are based on a misunderstanding. The theories of Timoshenko and those of Yu for beams and plates are ad hoc—albeit useful—theories, based on *assuming* certain variations of displacements in the thickness direction. In general, these variations are not good point-wise approximations near edges, especially built-in edges, although they often lead to accurate gross quantities such as natural frequencies or buckling loads. In contrast, ours in an *exact* theory, based on a formal asymptotic analysis of the linear equations of elasticity. The limitations of such an analysis are well known: a statement that the remainder in an expansion is $O(\epsilon)$ says nothing about the implied constant that multiplies ϵ; it could be quite large. We acknowledged this limitation in the Conclusions section of our paper, as Professor Yu notes.

The difference between ad hoc and asymptotic theories is also reflected by the role of experiment. In the former, experiments are conducted to verify the soundness of the assumptions; in the latter—barring mathematical errors—the only reason for experiments would be (a) to confirm the underlying assumptions of elasticity theory, (b) to test the validity of idealized boundary conditions, or (c) to empirically estimate the constants associated with certain O-symbols.

On Energy Rate Theorems for Linear First-Order Nonholonomic Systems[15]

T. R. Kane[16] and D. A. Levinson.[17] The author points out a defect in a previously published Note (Kane and Levinson, 1988), but ignores the fact that this defect was remedied in a second Note by the same authors (Kane and Levinson, 1990), a Note whose publication in this journal preceded that of his paper by more than one year.

[14]Submitted by Professors J. Simmonds and M. Duva, Department of Applied Mathematics, University of Virginia, Charlottesville, VA 22903-2422.

[15]By John G. Papastavridis, and published in the June 1991 issue of the ASME JOURNAL OF APPLIED MECHANICS, Vol. 58, pp. 536–544.

[16]Professor of Applied Mechanics, Stanford University, Stanford, CA 94305. Fellow ASME.

[17]Staff Scientist, Lockheed Palo Alto Research Laboratory, Palo Alto, CA 94304. Mem. ASME.

Copyright © 1992 by ASME
Downloaded 03 May 2010 to 171.66.16.247. Redistribution subject to ASME license or copyright; see http://www.asme.org/terms/Terms_Use.cfm

References

Kane, T. R., and Levinson, D. A., 1988, "A Method for Testing Numerical Integrations of Equations of Motion of Mechanical Systems," ASME JOURNAL OF APPLIED MECHANICS, Vol. 55, pp. 711-715.

Kane, T. R., and Levinson, D. A., 1990, "Testing Numerical Integrations of Equations of Motion," ASME JOURNAL OF APPLIED MECHANICS, Vol. 57, pp. 248-249.

Author's Closure[18]

I became aware of Kane and Levinson's (1990) corrective note, to their earlier (1988) paper, late in the spring of 1990; by then I had already completed my paper, sent it, and revised it (Dec. 1989). I believe, however, that Papastavridis (1991) deserved publication anyway for the following prominent reasons:

1 It is formulated in terms of the most general nonholonomic and rheonomic system variables and constraints, and is thus in line with standard advanced dynamics;

2 It makes explicit the energetic effects of nonholonomic (= nonintegrable) rheonomic constraints; and

3 Since it is clearly motivated and fairly self-contained, it can serve as a timely theoretical tutorial for both students and researchers.

All these advantages are absent from Kane and Levinson's "raw" and structureless treatments. In fact, even if Kane and Levinson's (1988) results were correct, it would still take a paper to demonstrate their equivalence with mainstream dynamics.

Dynamics of Nonholonomic Mechanical Systems Using a Natural Orthogonal Complement[19]

John G. Papastavridis[20]. The paper contains a number of theoretical and historical inaccuracies:

1 The opening statement, "The theory of nonholonomic systems arose when the analytical formalism of Euler and Lagrange was found to be inapplicable to the very simple mechanical problems of rigid bodies rolling without slipping on a plane," is eminently false. It is well known that the method of Euler, i.e., the principles of linear and angular momentum, applies to *any* mechanical system, including rolling ones. As for the method of Lagrange, his "Principle of Lagrange" (LP) of 1764 holds for any mechanical system subjected to Pfaffian constraints, holonomic (H) or not. The entire constrained system mechanics rests on LP. Higher-order (or nonlinear) constraints, e.g., control/servo-constraints, require the related higher principles of Gauss/Gibbs, Mangeron/Deleanu, etc.

The original Lagrangean equations of motion of 1780 were indeed restricted to H constraints. However, that limitation of Lagrange's equations, but not of Lagrange's Principle, was easily removed by Routh in 1877: By applying the method of "Euler-Lagrange Multipliers" to LP, he obtained Lagrange-type equations for systems under Pfaffian constraints—H or not. Also, Lagrange himself states in his "Méchanique Analitique" of 1788, p. 46"... in general we shall represent, by $dL=O$, $dM=O$, ..., the equations of condition [i.e., constraints] between these differentials, whether these equations are themselves exact or not, as long as the differentials do not appear except linearly."

2 The fundamental concept of nonholonomicity (NH) was indeed made precise in 1894 by Hertz; although special such problems had been successfully studied by Ostrogradsky in 1858, Minding in 1864, Ferrers in 1873 (see Fig. 1), C. Neumann in 1885, Vierkandt in 1892, et al. But nowhere in their article do the authors supply even a hint as to the precise meaning of NH. Clearly not every rolling constraint is NH; while (outside of control/servo problems) every constraint is or can be brought to Pfaffian form. How does one detect, analytically or otherwise, the NH (≡nonintegrability) or not of a given velocity constraint? Such properties affect critically the equations of motion and their solutions, say, in configuration space; and also their time-integral variational principles. I suspect that the authors (contrary to standard terminology followed by the masters of mechanics for the last hundred years) use the terms kinematic, velocity, and NH synonymously.

3 The relationships among the various equations of motion in NH coordinates and/or NH constraints are not explained. What are their similarities/differences and strengths/weaknesses? And how does one pass from one of them to another?

The complete history of this fascinating topic has never been written. Within the limits of this Discussion I can only say that these equations fall into (i) those based on the kinetic energy T, and (ii) those based on the Gibbs/Appell acceleration energy S. (A third group, initiated by Nielsen in 1935, is based on the gradients of $\dot{T}\equiv dT/dt$. No account of it exists in English.) Both T and S-equations are further subdivided into those in H and NH, or quasi-variables. The most general NH variable T-equations are due to Hamel (1903, 1904), appropriately dubbed by him "The Lagrange-Euler Equations." They uncouple naturally into reaction-free (or kinetic), and reaction containing (or kinetostatic) ones, and, although unmentioned by the authors, constitute the theoretical pinnacle of Lagrangean dynamics. The equations of Ferrers (1872, 1873—what Whittaker (erroneously) calls Ferrers' equations are in reality the Routh equations), C. Neumann (1885), Chaplygin (1895, 1897), Volterra (1898), Appell (1899—not his other famous S-equations), Carvallo (1900, 1901), Voronets (1901), Poincaré (1901), Boltzmann (1902), McMillian (1936) et al., are all special cases of Hamel's; and all result from LP. Figure 1 shows them in increasing order of conceptual power, simplicity, and generality (→). The most general H-variable T-equations are due to Maggi (1896, 1901). A special variable (kinetic) case of them is due to Hadamard (1895, 1899); it was rediscovered, in 1973, by Huston and Passerello. The kinetic and kinetostatic Maggi equations result, respectively, by projection of the Routh equations on the local virtual plane (or null space—the authors' "natural orthogonal complement") and on the normal to it (or range space); Maggi's method also applies to Hamel's equations under additional constraints.

The S-equations, also based on LP (and related to the T-equations by kinematical identities), subdivide into those in H and NH variables. The earliest S-equations in NH variables, but without constraints, are due to Gibbs (1879); and for general Pfaffian constraints and special quasi-variables are due to Appell (1899, and several papers afterwards, until 1925). (The so-called "Kane's equations" of 1961 are theoretically identical to them; and the more general Kane's equations of 1966, are nothing but a special case of the very general nonlinear NH constraint, Schaefer equations of 1951; and all are raw forms of general Hamel results from 1927, 1938, 1949).

4 The statement, "Neimark and Fufaev (1967) gave the first comprehensive and systematic exposition of the mechanics of nonholonomic systems ...," would have been correct had the authors added to its end the words "in English." The earliest systematic reference is due to Heun (1906, in German);

[18]Professor John G. Papastavridis, School of Mechanical Engineering, Georgia Institute of Technology, Atlanta, GA 30332-0405.

[19]By S. K. Saha and J. Angeles and published in the March 1991 issue of the JOURNAL OF APPLIED MECHANICS, Vol. 58, pp. 238-243.

[20]John G. Papastavridis, Associate Professor of Mechanics, School of Mechanical Engineering, Georgia Institute of Technology, Atlanta, GA 30332-0405.

Copyright © 1992 by ASME
Downloaded 03 May 2010 to 171.66.16.247. Redistribution subject to ASME license or copyright; see http://www.asme.org/terms/Terms_Use.cfm

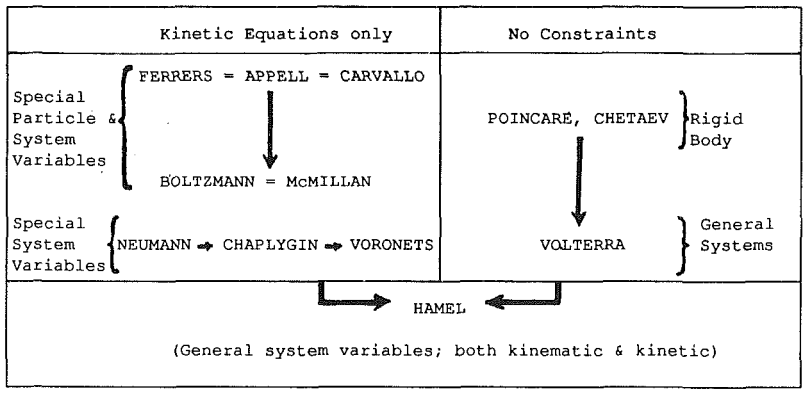

Fig. 1

other classic treatments are due to Prange (1935, in German), Hamel (1949, in German), and Lur'e (1961, in Russian; 1968, in French). (See references of Papastavridis, 1990).

5 The frequent term "nonworking" must be replaced by "virtually nonworking," otherwise, constraint reactions may be working.

6 The term "generalized speed $(-s)$" is incorrect; speed is the (non-negative) magnitude of velocity. The precise term is (contravariant) nonholonomic component $(-s)$ of the velocity vector (or nonholonomic velocity (ies), or quasivelocity (ies)); just as the familiar $\dot{q}_k$ are its holonomic components—see e.g., Schouten (1954).

7 The authors' term "scleronomic" ("rheonomic") must be replaced by the correct one "catastatic" ("acatastatic") (= linear and homogeneous (nonhomogeneous) in the velocity components but with, possibly, time-dependent coefficients); i.e., homogeneous constraints may still be rheonomic. And although Pfaffian constraints can indeed always be brought to castastatic form, it is not explained how this is done and what it means. The authors' rolling constraint (31) is catastatic because their plane (and coordinates used) are inertial. If it had a given motion their constraint could be made catastatic, but it would in general be rheonomic. And how does one handle acatastatic constraints if one must?

8 The authors' Eqs. (17), (35) are very special cases of Hamel's equations; also, in Eq. (35), ω should be $\dot{\omega}$.

9 Finally, below Eq. (18), why not use the standard dynamics term gyroscopic, instead of the (continuum mechanics sounding)" convective inertia terms?"

References

Heun, K., 1906, *Lehrbuch der Mechanik*, I Teil, *Kinematik*, Göschen, Leipzig.

Papastavridis, J. G., 1990, "Maggi's Equations of Motion and the Determination of Constraint Reactions," *J. Guidance, Control and Dynamics*, Vol. 13, No. 2, pp. 213–220.

Schouten, J. A., 1954, *Tensor Analysis for Physicists*, 2nd ed., (corrected printing 1959), Clarendon Press, Oxford, U.K., (Reprinted by Dover, 1989), pp. 194–195.

Author's Closure[21]

We appreciate the special interest with which Professor Papastavridis read the paper under discussion. The discussion of a paper, as we understand it, is intended to set the record straight on confusing or erroneous concepts, leaving aside details like unavoidable misprints and omissions. Professor Papastavridis' discussion helps very little in this regard, as we remark below, taking up his discussion pointwise.

[21]In the absence of the first author, this Closure was written solely by the second author, Professor J. Angeles, Department of Mechanical Engineering, McGill University, Montreal, Quebec H3A 2K6, Canada.

1 We could not agree more with Professor Papastavridis that the principles laid down by J. L. Lagrange in his "Mécanique Analytique," misspelled in the draft of the Discussion that was forwarded to us, hold for any mechanical system, whether holonomic or nonholonomic. We would even go as far as saying that those principles do hold for continuous systems as well. Note that we never said the opposite, either in our opening statement or anywhere else. We did say that Lagrange's formalism, i.e., the procedure whereby a system of governing equations of motion is derived by invoking the independence of the generalized coordinates in use, is not, as such, directly applicable. We believe that this statement is correct. What is not correct, and adds confusion to the discussion, is Professor Papastavridis' allusion to the "method of Euler, i.e., the principles of linear and angular momentum" (sic). We have not found in Euler's works any reference to a method, but are familiar with Euler's *principles* of conservation of momentum and angular momentum (Truesdell and Toupin, 1960), that are applicable to *any* mechanical system. Mixing up methods with principles does not particularly help to set any record straight. We are talking inaccurancies...

2 We did not elaborate on the criteria to identify a set of constraints as nonholonomic because our paper is not of a tutorial nature, but gave some references where the reader can find details. A more modern approach to the characterization of holonomic constraints is given in terms of *involutive distributions* in Isidori (1985). So, where is the inaccuracy here?

3 Again, we could not agree more with Professor Papastavridis in that the history of nonholomic systems has not been written. Neither did we intend to write it in the Introduction of our six-page paper! A more detailed historical account, although by no means a comprehensive one, can be found in Saha (1991). Again, where is the inaccuracy here?

4 We still believe that Neĭmark and Fufaev's is the first *comprehensive and systematic* exposition of the theory of nonholonomic systems, but we are ready to accept that Professor Papastavridis may have a very different concept of what we understand by the above emphasized phrase. Heun (1906) gives a rather short account of nonholonomic systems, but he should not be chastised for that, since his book was meant as an elementary textbook of engineering mechanics at the turn of the century. Even nowadays undergraduate texts of mechanics are not expected to go into much detail when it comes to nonholonomic systems. Unfortunately, Professor Papastavridis does not provide a full reference for Prange's book, as cited in his Discussion. The other books that he cites devote, at most, one chapter to nonholonomic systems. On the contrary, Neĭmark and Fufaev devote their whole book to such systems, including examples with nonmechanical nonholonomic constraints, namely, in the realm of electromachinery. So, again, where is the inaccuracy here?

Copyright © 1992 by ASME
Downloaded 03 May 2010 to 171.66.16.247. Redistribution subject to ASME license or copyright; see http://www.asme.org/terms/Terms_Use.cfm

5 The whole purpose of the natural orthogonal complement is to free the reader from ad hoc concepts such as virtual displacements, quasi-coordinates, and the like, as already expressed in a previous work (Angeles, 1988). What we mean by *nonworking wrench* in the paragraph below Eq. (6) of the paper under discussion is duly explained in that paragraph. We can further say that a nonworking constraint wrench is one developing zero *power* on the mechanical system under study, for any physically possible motion. Note that power is a primitive concept that arises naturally as the inner product of the twist by the wrench, as defined in our paper. Particularly, for conservative systems, a scalar function can be found whose time derivative is the aforementioned power. Such a function, called *work*, does not always exist, but it need not. Once more, where is the inaccuracy here?

6 We accept Professor Papastavridis' definition of *speed*, but follow Kane (1961) in our definition of *generalized speed*. Note that speaking of contravariant components is not within our style, with which we tried to be consistent in this paper, and hence, we avoided dealing with components, whether contravariant or covariant. So, what type of inaccuracy was incurred here? hisotrical? theoretical?

7 Professor Papstavridis has a valid point here. He is right in that we should have meant *catastatic* versus *acatastatic* when we spoke of *scleronomic* versus *rheonomic* constraints, and has set the record straight in this item. As to his question in the same item, we attempt an answer below. In fact, we should have included these facts for the sake of completeness, but lack of space prevented us from expanding on this and other interesting issues. In the case of acatastatic constraints, the counterpart of Eq. (11) of our paper would be

$$\mathbf{At} = \mathbf{b} \qquad (a)$$

where vector $\mathbf{b}$ is independent of the generalized twist $\mathbf{t}$ but is, in general, configuration dependent. This vector can certainly be time dependent as well. Furthermore, it is a rather simple matter to find a vector $\mathbf{t}_0$ such that

$$\mathbf{At}_0 = \mathbf{b} \qquad (b)$$

but due to space limitations, we do not elaborate here on how to find that vector. Moreover, vector $\mathbf{t}$ can now be written as

$$\mathbf{t} = \mathbf{T}\dot{\theta} + \mathbf{t}_0 \qquad (c)$$

where all variables have been explained either in the paper under discussion or above. Upon substitution of $\mathbf{t}$, as given in Eq. (*c*), into Eq. (*a*), we derive

$$\mathbf{AT}\dot{\theta} + \mathbf{At}_0 = \mathbf{b} \qquad (d)$$

but, by virtue of Eq. (*b*), Eq. (*d*) reduces to

$$\mathbf{AT}\dot{\theta} = \mathbf{0}. \qquad (e)$$

And hence, under the assumption that the vector of independent generalized speed $\dot{\theta}$ can be assigned arbitrarily, Eq. (13) of our paper follows, and hence, $\mathbf{T}$ is an orthogonal complement of $\mathbf{A}$. Moreover, upon differentiation of $\mathbf{t}$, as given in Eq. (*c*) above, and substitution of the resulting expression in the uncoupled dynamics equations, Eq. (10), we obtain further

$$\mathbf{MT}\ddot{\theta} = -\mathbf{WMT}\dot{\theta} - \dot{\mathbf{MT}}\dot{\theta} - \mathbf{WMt}_0 - \mathbf{M}\dot{\mathbf{t}}_0 + \mathbf{w}^W + \mathbf{w}^N. \qquad (f)$$

Finally, the coupled dynamics equation are derived upon multiplication of both sides of Eq. (*f*) by $\mathbf{T}^T$, i.e.,

$$\mathbf{T}^T\mathbf{MT}\ddot{\theta} = -\mathbf{T}^T\mathbf{WMT}\dot{\theta} - \mathbf{T}^T\dot{\mathbf{MT}}\dot{\theta} - \mathbf{T}^T\mathbf{WMt}_0 - \mathbf{T}^T\mathbf{M}\dot{\mathbf{t}}_0 + \mathbf{T}^T\mathbf{w}^W \qquad (g)$$

thereby deriving the counterpart of Eq. (14), but applicable to acatastatic systems. If omitting this discussion in our paper produced inaccuracies, we apologize for the omission.

8 We said at the outset in our paper that the natural orthogonal complement is a special type of orthogonal complement; this is why we attach to the foregoing expression the adjective *natural*. Professor Papastavridis is right in pointing out the misprint in Eq. (35): There is a dot missing on top of the ω appearing in the left-hand side. What sort of inaccuracy are we talking about now?

9 We tried to make our paper understandable by a general audience. Note that roboticists would have said "why not use the standard robotics Coriolis and centrifugal forces term?". Again, is this an historical or a theoretical inaccuracy?

In summary, Professor Papastavridis' Discussion and his paper cited therein are paradigms of the confusion that can arise when concepts like virtual quantities and quasi-coordinates are used indiscriminately. As an example, below Eq. (23*b*) of (Papastavridis (1990), the author says: "where $\delta\theta$ = virtual variation or virtual differential of the quasi-coordinate θ and $\omega^k \equiv d\theta^k/dt \equiv \dot{\theta}^k$ (no ordinary derivative, since θ^k does not exist)". So, if the said derivative is no ordinary derivative, what is it? Is it a quasi-derivative? More fundamentally, what do we call derivatives of inexistent quantities? Probably inexistent quasi-derivatives. And, what do we call all that confusion? Is it by any chance an historical inaccuracy? or a theoretical one? Even better, to put our closing remarks in context, should we call Professor Papastavrids' confusion a *quasi-inaccuracy*?

References

References cited in our Closure are to be found in three places, namely, (1) in this Discussion (2) in the paper under discussion, or (3) in the list below

Angeles, J., 1988, *Rational Kinematics*, Springer-Verlag, New York.

Isidori, A., 1985, *Nonlinear Control Systems: An Introduction* (Lecture Notes in Information and Control Sciences), Springer-Verlag, New York.

Saha, S. K., 1991, "Dynamics and Design of Nonholonomic Robotic Mechanical Systems," Ph. D. Thesis, Department of Mechanical Engineering, McGill University, Montreal.

Truesdell, C., and Toupin, R. A., 1960, "The Classical Field Theories," *Encyclopedia of Physiscs*, Vol. III/1, S. Flügge, ed, Springer-Verlag, Berlin-Göttingen-Heidelberg.

Downloaded 03 May 2010 to 171.66.16.247. Redistribution subject to ASME license or copyright; see http://www.asme.org/terms/Terms_Use.cfm

Journal of Applied Mechanics

Book Reviews

Dynamic Fracture Mechanics, L. B. Freund. Cambridge University Press, New York, 1990. 563 pages. Price: $59.50.

REVIEWED BY JOHN W. HUTCHINSON[1]

This monograph covers fundamental aspects of dynamic fracture mechanics which have not previously appeared before in a book format. It is written by one of the foremost contributors to the subject. The monograph pulls together basic mathematical developments which have taken place over the past 20 years or so, and it provides a foundation on which further work can rest. Parts of the subject are far from easy. Unlike the mechanics of quasi-static fracture, there are very few closed-form solutions to problems for dynamically running cracks. This has led to controversy in the interpretation of experiments and in the specification of fracture criteria. In recent years there has been a convergence of opinion among researchers in the field on the underlying concepts and criteria for dynamic fracture. This new state of affairs is reflected in this monograph. Its timing is perfect.

Chapter 1 gives a brief review of the relevant continuum mechanics (linear elasticity for the most part) along with a few pages of some of the mathematical methods employed in later chapters (complex variable theory and Laplace transform methods.) Chapter 1 concludes with a synoptic overview of the central concepts and main theoretical results of dynamic fracture. The next two chapters deal with stationary cracks under dynamic loading, including a discussion of experimental data on the influence of initiation toughness and loading rate. The asymptotic behavior of the stress and strain-rate fields at the crack tip of a running crack is treated in Chapter 4. The effects of inertia, plasticity, and viscosity are all considered and delineated with definitions of the controlling crack-tip intensity measures. The review of the singular crack-tip fields leads naturally to the next chapter on energy concepts which includes the fundamental relation between the dynamic stress intensity factors and the energy release rate, path-independent integrals specialized to various conditions, and weight function methods. Chapters 6 and 7 deal with running cracks in elastic bodies under a variety of conditions including general transient conditions. This is difficult material, but no one is better qualified to write about it than the author. Here is where the mathematical richness of the subject comes out. Equations of motion governing the motion of the crack tip are gone into in detail and a number of examples are discussed. The last chapter focuses on cracks growing in elastic-plastic materials. For the most part, consideration is limited to steady-state growth under conditions of small-scale yielding. Near-tip criteria are invoked to draw conclusions on the role of inertia, plasticity, and strain-rate effects on dynamic toughness.

This is a book that everyone working in fracture or in elasticity with at least an occasional interest in cracks (isn't that everybody?) will want to own. It falls somewhere between a text and a research monograph. It is not likely to stand alone as a text for a graduate course on fracture, but it would serve well for a segment of a course dealing with dynamic fracture.

Plasticity Theory, by J. Lubliner. Macmillan, New York, 1990. 495 pages.

REVIEWED BY B. MORAN[2]

This book is intended as both a textbook for advanced undergraduate and graduate students and a primary reference for researchers in the fields of solid and applied mechanics. Since Hill's *The Mathematical Theory of Plasticity* (Oxford, 1950; 1983 paperback) many important advances in plasticity theory have not been adequately treated in either textbook or monograph. This book addresses many of these developments including modern constitutive theories, continuum thermodynamics, large deformations, and numerical methods. Traditional treatments of elastic-plastic boundary value problems, slip line theory, and limit analysis are also included. The result is a comprehensive account of the field of plasticity as it exists today.

The book contains eight chapters. A generous number of exercise questions are provided in each chapter. Chapter 1: Introduction to Continuum Thermomechanics contains a 68-page introduction to the subject. While many books have been written on this subject, the presentation here is motivated by the desire to make the book self-contained, and it sets the overall tone of the book in terms of both style and pedagogy. The treatment of tensor analysis is in terms of Cartesian components, and large deformation kinematics are deferred to a later chapter. A good deal of emphasis in this chapter and throughout the book is on constitutive theories of inelastic deformation from the viewpoint of internal variables. Chapter 2: The Physics of Plasticity contains an introduction to the

[1]Division of Engineering and Applied Physics, Harvard University, Cambridge, 02138

[2]Department of Civil Engineering, Northwestern University, Evanston, IL 60208. Assoc. Mem. ASME.

Copyright © 1992 by ASME
Downloaded 03 May 2010 to 171.66.16.247. Redistribution subject to ASME license or copyright; see http://www.asme.org/terms/Terms_Use.cfm